NUREG/CP-0142
Vol. 3

Proceedings of the 7th International Meeting on Nuclear Reactor Thermal-Hydraulics NURETH-7

Sessions 12–16

Held at
Sheraton Hotel and Convention Center
Saratoga Springs, New York
September 10–15, 1995

Date Published: September 1995

Compiled by:
R. C. Block, F. Feiner, ANS

Sponsored by
American Nuclear Society
555 N. Kensington Avenue
La Grange Park, IL 60525

American Institute of Chemical Engineers
345 East 47th Street
New York, NY 10017-2392

American Society of Mechanical Engineers
345 East 47th Street
New York, NY 1007-2392

Canadian Nuclear Society
144 Font Street West
Suite 725
Toronto, Ontario, Canada M5J2L7

European Nuclear Society
Secretariat: Monbijoustrasse 5
P.O. Box 5032
CH-3001 Berne, Switzerland

Atomic Energy Society of Japan
No. 1-13, 1-chome
Shimbashi, Minato-ku
Tokyo 105, Japan

Japan Society of Multiphase Flow
Prof. Akimi Serizawa
Department of Nuclear Engineering
Yoshida, Sakyo, Kycto 606-01
Japan

Division of Systems Technology
Office of Nuclear Regulatory Research
U.S. Nuclear Regulatory Commission
Washington, DC 20555-0001

Proceedings prepared by
Northeastern New York Chapter
Amrican Nuclear Society



MASTER

DISTRIBUTION OF THIS DOCUMENT IS UNLIMITED
DT

NUREG/CP–0142, Volume 3, has been reproduced from the best available copy.

DISCLAIMER

This report was prepared as an account of work sponsored by an agency of the United States Government. Neither the United States Government nor any agency thereof, nor any of their employees, make any warranty, express or implied, or assumes any legal liability or responsibility for the accuracy, completeness, or usefulness of any information, apparatus, product, or process disclosed, or represents that its use would not infringe privately owned rights. Reference herein to any specific commercial product, process, or service by trade name, trademark, manufacturer, or otherwise does not necessarily constitute or imply its endorsement, recommendation, or favoring by the United States Government or any agency thereof. The views and opinions of authors expressed herein do not necessarily state or reflect those of the United States Government or any agency thereof.

DISCLAIMER

Portions of this document may be illegible in electronic image products. Images are produced from the best available original document.

ABSTRACT

Technical papers accepted for presentation at the Seventh International Topical Meeting on Nuclear Reactor Thermal-Hydraulics are included in the present Proceedings. Except for the invited papers in the plenary session, all other papers are contributed papers. The topics of the meeting encompass all major areas of nuclear thermal-hydraulics, including analytical and experimental works on the fundamental mechanisms of fluid flow and heat transfer, the development of advanced mathematical and numerical methods, and the application of advancements in the field in the development of novel reactor concepts. Because of the complex nature of nuclear reactors and power plants, several papers deal with the combined issues of thermal-hydraulics and reactor/power-plant safety, core neutronics and/or radiation.

The participation in the conference by the authors from several countries and four continents makes the Proceedings a comprehensive review of the recent progress in the field of nuclear reactor thermal-hydraulics worldwide.

PLANNING COMMITTEE MEMBERS

General Chairman: Richard T. Lahey, Jr.

Vice-Chairman: M. Richard Mendelson

Technical Program Chairman: Michael Z. Podowski

Registration: Thomas M. Sutton

Secretary: Ray G. Gamino

Finance: Hunter B. Currin

Fund Raising: Brian Bielecki and Norman Francis

Publications: Frank Feiner and Robert C. Block

Arrangements: Robert C. Rohr

Publicity: David F. McMullan

Special Events: Jeffrey G. Hoole

Spouse Events: Ann E. Kelly

SCIENTIFIC ADVISORY COMMITTEE

K. Akagawa	Japan
G.F. Hewitt	Great Britian
Y.Y. Hsu	R.C., Taiwan
J. H. Kim	USA
S. Levy	USA
F. Mayinger	Germany
G. Matsui	Japan
U. Mueller	Germany
V. Nakoriakov	Russia
R.I. Nigmatulin	Russia
W. Rohsenow	USA
T. Sakaguchi	Japan
V.E. Schrock	USA
N. Todreas	USA
L.S. Tong	USA

TECHNICAL PROGRAM COMMITTEE

M. Akiyama	Japan	R.E. Henry	USA
K.H. Ardon	Great Britain	G. Hetsroni	Israel
S. Antal	USA	L. Hochreiter	USA
M. Aritomi	Japan	M. Ishii	USA
B. Azzopardi	Great Britain	H. Karwat	Germany
S. Banerjee	USA	G. Kojasoy	USA
F.R. Best	USA	V.S. Krishnan	Canada
B. Boyack	USA	T. K. Larson	USA
N. Brauner	Israel	H. Lemmonier	France
G.P. Celata	Italy	J. March-Leuba	USA
J.H. Cha	South Korea	M. Merilo	USA
A. Clausse	Argentina	F. Moody	USA
M.L. Corradini	USA	H. Nariai	Japan
J.M. Courtaud	France	B. Nigmatulin	Russia
M. Cumo	Italy	H. Ninokata	Japan
V.K. Dhir	USA	O. Nylund	Sweden
G.E. Dix	USA	P.F. Peterson	USA
J.J. Dorning, Jr.	USA	V. Ransom	USA
R.B. Duffey	USA	K. Rehme	Germany
F. Eltawila	USA	D.S. Rowe	USA
M. Epstein	USA	Z. Rouhani	USA
M. Erdman	USA	K. Rust	Germany
S. Ettore	USA	B.R. Sehgal	Sweden
W. Frid	Sweden	A. Serizawa	Japan
M. Golay	USA	B.S. Shiralker	USA
Y.A. Hassan	USA	L. Shotkin	USA
S. Sreepada	USA	J. Weisman	USA
A. Strupczewski	Poland	W. Wulff	USA
L. Szabados	Hungary	G. Yadigaroglu	SWITZERLAND
R. Taleyarkhan	USA	S.T. Yin	CANADA
T.G. Theofanous	USA		

SESSION ORGANIZERS

Almenas, K.
Aritomi, M.
Banerjee, S.
Baratta, A.J.
Best, F.R.
Boyack, B.
Brauner, N.
Catton, I.
Celata, G.P.
Cha, J.H.
Chabard, J.P.
Cheng, L.
Corradini, M.L.
Courtaud, J.M.
Dhir, V.K.
DiMarzo, M.
Dorning, Jr. , J.J.
Eltawila, F.
Frid, W.
Golay, M.W.
Grand, D.
Groeneveld, D.C.
Hassan, Y.A.
Hodge, S.
Hochreiter, L.
Ishii, M.
Karwat, H.
Kojasoy, G.
Krishnan, V.S.
Kurul, N.
Larson, T.K.
Lemmonier, H.
March-Leuba, J.
McMullan, D.
Merilo, M.
Modro, M.
Moody, F.
Nariai, H.
Ninokata, H.
Nylund, O.
Peterson, P.F.
Pilch, M.M.
Ransom, V.H.
Rehme, I.K.
Rouhani, Z.
Rowe, D.S.
Serizawa, A.
Shotkin, L.
Sreepada, S.
Taleyarkhan, R.
Theofanous, T.G.
Todreas, N. E.
Weisman, J.
Wilson, G.
Wright, R.W.
Wulff, W.
Yadigaroglu, G.
Yin, S. T.
Yoder, G. L.

TABLE OF CONTENTS

VOLUME I

Plenary Session - NUCLEAR POWER REACTORS FOR THE 21st CENTURY

"Turning Points in Reactor Design"
E. Beckjord 1

"Resolution of Thermal-Hydraulic Safety and Licensing Issues for the System 80+"
F.L. Carpentino, S.E. Ritterbusch, R.E. Schneider and M.C. Jacob 21

"AP600 Design Certification Thermal Hydraulics Testing and Analysis"
L.E. Hochreiter and E.J. Piplica 43

"Prospects for Bubble Fusion"
R.I. Nigmatulin and R.T. Lahey, Jr. 49

Session 1 - ADVANCES IN TWO-PHASE FLOW MODELING

"A Mechanistic Determination of Horizontal Flow Regime Boundaries Using Void Wave Celerity"
J.-W. Park 76

"A Criterion for the Onset of Slugging in Horizontal Stratified Air-Water Countercurrent Flow"
M.-H. Chun, H.-Y. Nam, B.-R. Lee and Y.-S. Kim 93

"Characterization of Non Equilibrium Effects on High Quality Critical Flows"
E. Camelo, H. Lemonnier, J. Ochterbeck and S. Selmer-Olsen 111

"Local Pressure Gradients Due to Incipience of Boiling in Subcooled Flows"
J. McDuffey and A. Ruggles 131

"Drift Flux Model as Approximation of Two Fluid Model for Two Phase Dispersed and Slug Flow in Tube"
R.I. Nigmatulin 141

"Development, Implementation and Assessment of Specific, Two-Fluid Closure Laws for Inverted-Annular Film-Boiling"
F. de Cachard 166

"Analytical Solution of Laminar-Laminar Stratified Two-Phase Flows with Curved Interfaces"
N. Brauner, Y. Rovinsky and D. Moalem Maron 192

"Velocity of Large Bubble in Liquid-Solid Mixture in a Vertical Tube"
H. Hamaguchi and T. Sakaguchi 212

"About the Statistical Description of Gas-Liquid Flows"
D. Sanz, G. Guido-Lavalle, P. Carrica and A. Clausse 231

"Entropy Analysis on Non-Equilibrium Two-Phase Flow Models"
H. Karwat and Y.Q Ruan 248

"A General Unified Non-Equilibrium Model for Predicting Saturated and Subcooled Critical Two-Phase Flow Rates Through Short and Long Tubes"
D.W.H. Fraser and A.H. Abdelmessih 264

"Predictions of Bubbly Flows in Vertical Pipes Using Two-Fluid Models in CFDS-Flow 3D Code"
A.O. Banas, M.B. Carver and D. Unrau 284

Session 2 - ADVANCES IN BOILING AND CONDENSATION HEAT TRANSFER

"Condensation During Gravity Driven ECC: Experiments with PACTEL"
R. Munther, H. Kalli and J. Kouhia 299

"An Investigation of Condensation From Steam-Gas Mixtures Flowing Downward Inside a Vertical Tube"
S.Z. Kuhn, V.E. Schrock and P.F. Peterson 312

"Study of Condensation Heat Transfer Following a Main Steam Line Break Inside Containment"
J.H. Cho, F.A. Elia, Jr. and D.J. Lischer 336

"Effect of Subcooling and Wall Thickness on Pool Boiling From Downward-Facing Curved Surfaces in Water"
M.S. El-Genk and A.G. Glebov 353

"Numerical Model of Condensation from Vapor-Gas Mixtures for Forced Down Flow Inside a Tube"
R.Y. Yuann, V.E. Schrock and X.M. Chen 377

"A Model for the Performance of a Vertical Tube Condenser in the Presence of Noncondensable Gases"
A. Dehbi and S. Guentay 402

"UPTF-TRAM Experiments for SBLOCA: Evaluation of Condensation Processes in TRAM Tests A6 and A7"
H.G. Sonnenburg, J. Tuunanen and V.V. Palazov 423

"Condensation Heat Transfer Coefficient with Noncondensible Gases for Heat Transfer in Thermal Hydraulic Codes"
S. Banerjee and Y.A. Hassan 434

Session 3 - EXPERIMENTAL METHODS AND INSTRUMENTATION

"Experimental Study of Horizontal Annular Channels Under Non-Developed Conditions"
G. Delgadino, J. Balino and P.M. Carrica 462

"Interfacial Shear Stress in Stratified Flow in a Horizontal Rectangular Duct"
C. Lorencez, M. Kawaji, A. Ousaka and Y. Murao 478

"Quenching Phenomena in Natural Circulation Loop"
H. Umekawa, M. Ozawa and N. Ishida 487

"Measurement of the Interaction Between the Flow and the Free Surface of a Liquid"
K. Okamoto, W.D. Schmidl, O.G. Philip and Y.A. Hassan 497

"The Use of Waveguide Acoustic Probes for Void Fraction Measurement in the Evaporator of BN-350-Type Reactor"
V. Melnikov and B. Nigmatulin 508

"Buoyancy-Driven Flow Excursions in Fuel Assemblies"
J.E. Laurinat, P.K. Paul and J.D. Menna 514

"An Experimental Investigation of the Post CHF Enhancement Factor for a Prototypical ITER Divertor Plate with Water Coolant"
T.D. Marshall, R.D. Watson, J.M. McDonald and D.L. Youchison 532

"Transient Pool Boiling Heat Transfer Due to Increasing Heat Inputs in Subcooled Water at High Pressures"
K. Fukuda, M. Shiotsu and A. Sakurai 554

"Cross-Sectional Void Fraction Distribution Measurements in a Vertical Annulus Two-Phase Flow by High Speed X-Ray Computed Tomography and Real-Time Neutron Radiography Techniques"
G.D. Harvel, K. Hori, K. Kawanishi and J.S. Chang 574

"Two-Phase Velocity Measurements Around Cylinders Using Particle Image Velocimetry"
Y.A. Hassan, O.G. Philip, W.D. Schmidl and K. Okamoto 591

"Characteristics of Turbulent Velocity and Temperature in a Wall Channel of a Heated Rod Bundle"
T. Krauss and L. Meyer 603

"The Coolability Limits of a Reactor Pressure Vessel Lower Head"
T.G. Theofanous and S. Syri 627

Session 4 - MULTIDIMENSIONAL FLOW AND HEAT TRANSFER PHENOMENA

"Numerical Simulation of Multidimensional Two-Phase Flow Based on Flux Vector Splitting"
H. Stadtke, G. Franchello and B. Worth 648

"CFD Simulation of Flow and Phase Distribution in Fuel Assemblies with Spacers"
H. Anglart, O. Nylund, N. Kurul and M.Z. Podowski 673

"Computational Fluid Dynamic Analysis of a Closure Head Penetration in a Pressurized Water Reactor"
D.R. Forsyth and R.E. Schwirian 696

"THEHYCO-3DT: Thermal Hydrodynamic Code for the 3 Dimensional Transient Calculation of Advanced LMFBR Core"
S.G. Vitruk, A.S. Korsun, P.A. Ushakov and B.N. Gabrianovich 711

"Transition to Chaos In a Square Enclosure Containing Internal Heat Sources"
A. Cihat Baytas 720

"ASTRID: a 3D Eulerian Software for Subcooled Boiling Modelling Comparison with Experimental Results in Tubes and Annuli"
E. Briere, D. Larrauri and J. Olive 736

"The Multi-Dimensional Module of CATHARE 2 Description and Applications"
F. Barre, I. Dor and C. Sun 750

Session 5 - CCFL AND FLOODING PHENOMENA

"Reflooding and Boil-Off Experiments in a VVER-440 Like Rod Bundle and Analysis with the Cathare Code"
V. Korteniemi, T. Haapalehto and M. Puustinen 770

"Counter-Current Flow in a Vertical to Horizontal Tube with Obstructions"
P. Tye, A. Matuszkiewicz, A. Teyssedou, A. Tapucu and W. Midvidy 781

"Flooding Characteristics of Gas-Liquid Two-Phase Flow in a Horizontal U Bend Pipe"
T. Sakaguchi, N. Nakamori, T. Ueno, J. Kodama, S. Hosokawa, H. Minagawa and Y. Fujii 804

"CCFL in Hot Legs and Steam Generators and Its Prediction with the Cathare Code"
G. Geffraye, P. Bazin, P. Pichon and A. Bengaouer 815

VOLUME II

Session 6 - NATURAL CIRCULATION AND/OR CONVECTION

"On Heat Transfer Characteristics of Real and Simulant Melt Pool Experiments"
T.N. Dinh, R.R. Nourgaliev and B.R. Sehgal 827

"Passive Decay Heat Removal by Natural Air Convection After Severe Accidents"
F.J. Erbacher, X. Cheng, H.J. Neitzel 846

"Natural Circulation in a VVER Geometry: Experiments with the PACTEL Facility and Cathare Simulation"
P. Raussi S. Kainulainen and J. Kouhia 854

"Parametric Numerical Investigation of Natural Convection in a Heat-Generating Fluid with Phase Transitions"
A.E. Aksenova, V.V. Chudanov, V.F. Strizhov and P.N. Vabishchevich 865

Session 7 - INSTABILITY MECHANISMS, WAVES, AND NONLINEAR DYNAMICS

"Geysering in Boiling Channels"
M. Aritomi, T. Takemoto, J-H Chiang, M. Mori and H. Tabata 875

"Two-Phase Flow Stability Structure in a Natural Circulation System"
Z. Zhou 888

"FIBWR2 Evaluation of Fuel Thermal Limits During Density Wave Oscillations in BWRs"
N. Nik, S.R. Rajan and M. Karasulu 911

"Density Wave Oscillations of a Boiling Natural Circulation Loop Induced by Flashing"
M. Furuya, F. Inada and A. Yasuo 923

"Rayleigh-Taylor Instability of Cylindrical Jets With Radial Motion"
X.M. Chen, V.E. Schrock and P.F. Peterson 933

"Two-Phase Flow Instabilities in Vertical Annular Channel"
I. Babelli, S. Nair and M. Ishii 947

"Problems in Experimental and Mathematical Investigations of the Accidental Thermohydraulic Processes in RBMK Nuclear Reactors"
B.I. Nigmatulin, L.K. Tikhonenko, V.N. Blinkov and A.J. Kramerov 967

"An Investigation of the Stability of a Boiling Water Reactor Under Natural Circulation Conditions Using TRAC-BF-1"
S. Lider, G.E. Robinson, A.J. Baratta and J.G. Refling 978

"Analysis of the Void Wave Propagations: Wave Number Independent Characteristics"
C.H. Song, H.C. No and M.K. Chung 986

"Modeling and Numerical Simulation of Oscillatory Two-Phase Flows with Application to Boiling Water Nuclear Reactors"
M. Rosa and M.Z. Podowski 1003

"Thermal-Hydraulic Instabilities in Pressure Tube Graphite-Moderated Boiling Water Reactors"
G. Tsiklauri and B. Schmitt 1022

"Dynamics of Shock Wave Propagation and Interphase Process in Liquid-Vapour Medium"
B.G. Pokusaev and N.A. Pribaturin 1032

Session 8 - TRANSIENT ANALYSIS AND SIMULATION

"Evaluation of a Main Steam Line Break With Induced, Multiple Tube Ruptures: A Comparison of NUREG 1477 (Draft) and Transient Methodologies - Palo Verde Nuclear Generating Station"
K.R. Parrish 1046

"Application of UPTF Data for Modeling Liquid Draindown in the Downcomer Region of a PWR Using RELAP5/MOD2-B&W"
G. Wissinger and J. Klingenfus 1069

"Plant Data Comparisons for Comanche Peak 1/2 Main Feedwater Pump Trip Transient"
W.J. Boatwright, W.G. Choe, D.W. Hiltbrand, C.V. DeVore and J.F. Harrison 1083

"RBMK-LOCA-Analyses with the ATHLET-Code"
A. Petry, A. Domoradov, A. Finjakin and A. Moskalev 1090

"Small-Break Loss of Coolant Accident in the Updated Pius 600 Advanced Reactor Design"
B. E. Boyack, J.L. Steiner, S.C. Harmony, H.J. Stumpf, and J.F. Lime 1100

"Simulation of a Beyond Design-Basis-Accident With RELAP5/MOD3.1"
J. Banati 1116

"Rapid Depressurization Event Analysis in BWR/6 Using RELAP5 and Contain"
A.K. Muftuoglu and M.A. Feltus 1127

"A Thermal-Hydraulic Code for Transient Analysis in a Channel with a Rod Bundle"
I.D. Khodjaev 1139

Session 9 - ADVANCED WATER REACTOR THERMAL-HYDRAULICS

"Analysis of an AP600 Intermediate Size Loss-Of-Coolant Accident"
B.E. Boyack and J.F. Lime 1153

"A Concept of JAERI Passive Safety Light Water Reactor System (JPSR)"
Y. Murao, F. Araya and T. Iwamura 1169

"Assessment of the Advantages of a Residual Heat Removal System Inside the Reactor Pressure Vessel"
G.M. Gautier 1196

"NRC Review of Passive Reactor Design Certification Testing Programs: Overview, Progress, and Regulatory Perspective"
A.E. Levin 1231

"Flooding of a Large, Passive, Pressure-Tube LWR"
P. Hejzlar, N.E. Todreas and M.J. Driscoll 1224

"SBWR PCCS Vent Phenomena and Suppression Pool Mixing"
P. Coddington and M. Andreani 1249

"Scaling for Integral Simulation of Thermalhydraulic Phenomena in SBWR During LOCA"
M. Ishii, S.T. Revankar, R. Dowlati, I. Babelli, W. Wang, H. Pokharna, M.L. Bertodano, V.H. Ransom, R. Viskanta and J.T. Han 1272

"A Practical View of the Insights from Scaling Thermal-Hydraulic Tests"
A.E. Levin and G.D. McPherson 1291

Session 10 - LIQUID-METAL-COOLED REACTOR THERMAL-HYDRAULICS

"Analysis of Overflow-Induced Sloshing in an Elastic-Wall Vessel Using Physical Component BFC Method"
D. Lu, A. Takizawa and S. Kondo 1302

"Study of Mixed Convective Flow Penetration into Subassembly from Reactor Hot Plenum in FBRs"
J. Kobayashi, H. Ohshima, H. Kamide and Y. Ieda 1313

"Large Eddy Simulation of Mixing Between Hot and Cold Sodium Flows-Comparison with Experiments"
J.P. Simoneau, H. Noe and B. Menant 1324

"Natural Convection Heat Transfer on Two Horizontal Cylinders in Liquid Sodium"
K. Hata, M. Shiotsu, Y. Takeuchi, K. Hama and A. Sakurai 1333

"Evaluation of Wrapper Tube Temperatures of Fast Neutron Reactors Using the Transcoeur-2 Code"
B. Valentin, G. Chaigne and P. Brun 1351

"Simulation of Decay Heat Removal by Natural Convection in a Pool Type Fast Reactor Model - RAMONA with Coupled 1D/2D Thermal Hydraulic Code System"
N. Kasinathan, A. Rajakumar, G. Vaidyanathan and S.C. Chetal 1361

"Conjugate Heat Transfer Analysis of Multiple Enclosures in Prototype Fast Breeder Reactor"
K. Velusamy, V. Balasubramaniam, G. Vaidyanathan and S.C. Chetal 1380

"Computational Modeling for Hexcan Failure Under Core Disruptive Accidental Conditions"
T. Sawada, H. Nimokata and A. Shimizu 1398

Session 11 - CONTAINMENT THERMAL-HYDRAULICS

"Investigations on Sump Cooling After Core Melt Down"
J.U. Knebel 1407

"Containment Atmosphere Response to External Sprays"
J. Green and K. Almenas 1418

"Modelling of Local Steam Condensation on Walls in Presence of Noncondensable Gases. Application to a LOCA Calculation in Reactor Containment Using the Multidimensional GEYSER/ TONUS Code"
L.V. Benet, C. Caroli, P. Cornet, N. Coulon and J.P. Magnaud 1443

"The Modelling of Wall Condensation with Noncondensable Gases for the Containment Codes"
C. Leduc, P. Cost, V. Barthel and H. Deslandes 1456

"An Interpretation of Passive Containment Cooling Phenomena"
B.J. Chung and C.S. Kang 1477

"Detailed Thermal-Hydraulic Computation into a Containment Building"
A. Caruso, I. Flour, O. Simonin and C. Cherbonnel 1489

"Free Convective Condensation in a Vertical Enclosure"
R.J. Fox, P.F. Peterson, M.L. Corradini and A.P. Pernsteiner 1501

"Condensation in the Presence of Noncondensible Gases: AP600 Containment Simulation"
M. Anderson and M.L. Corradini 1519

"Hydrogen Behavior in Ice Condenser Containments"
P. Lundstrom, P. Gango, H. Tuomisto, O. Hongisto and T.G. Theofanous 1535

"Aerodynamics, Heat and Mass Transfer in Steam-Aerosol Turbulent Flows in Containment"
B.I. Nigmatulin, V.A. Pershukov, V.V. Ris, E.M. Smirnov, L.I. Zaichik, A.A. Vinberg, D.V. Sidenkov and V.A. Belov 1555

"GEYSER/TONUS: A Coupled Multi-D Lumped Parameter Code for Reactor Thermal Hydraulics Analysis in Case of Severe Accident"
M. Petit, M. Durin, and J. Gauvain 1574

VOLUME III

Session 12 - FUEL/COOLANT INTERACTION

"On The Constitutive Description of the Microinteractions Concept in Steam Explosions"
X. Chen, W.W. Yuen and T.G. Theofanous 1586

"Correlations Between the Disintegration of Melt and the Measured Impulses in Steam Explosions"
G. Frohlich, A. Linca and M. Schindler 1607

"Analysis of Supercritical Vapor Explosions Using Thermal Detonation Wave Theory"
B.I. Shamoun and M.L. Corradini 1637

"The Numerical Methods for the Development of the Mixture Region in the Vapor Explosion Simulations"
Y.H. Yang, H. Ohashi, M. Akiyama and T. Morii 1653

"Thermal-Hydraulic Behaviors of Vapor-Liquid Interface Due to Arrival of a Pressure Wave"
A. Inoue, Y. Fujii, M. Matsuzaki and M. Takahashi 1663

"Boiling Characteristics of Dilute Polymer Solutions and Implications for the Suppression of Vapor Explosions"
K.H. Bang and M.H. Kim 1677

"Experimental Investigation of 150-KG-Scale Corium Melt Jet Quenching In Water"
D. Magallon and H. Hohmann 1688

"FCI Experiments in the Corium/Water System"
I.K. Huhtiniemi, H. Hohmann and D. Magallon 1712

"Experimental Studies of Thermal and Chemical Interactions Between Oxide and Silicide Nuclear Fuels with Water"
A. Farahani and M.L. Corradini 1728

"The Effect of Constraint on Fuel-Coolant Interactions in a Confined Geometry"
H.S. Park and M.L. Corradini 1743

"The Mixing of Particle Clouds Plunging into Water"
S. Angelini, T.G. Theofanous and W.W. Yuen 1754

"Experimental Studies of Thermal and Chemical Interactions between Molten Aluminum and Water"
A.A. Farahani and M.L. Corradini 1779

Session 13 - THERMAL-HYRAULICS OF SEVERE ACCIDENTS

"Interaction Between the Radiative Flux Emitted by a Corium Melt and Aerosols from Corium/Concrete/Interaction"
M. Zabiego, G. Cognet and P. Henderson 1797

"Modeling of Heat and Mass Transfer Processes During Core Melt Discharge From a Reactor Pressure Vessel"
T.N. Dinh, V.A. Bui, R.R. Nourgaliev, T. Okkonen and B.R. Sehgal 1809

"Results of International Standard Problem No. 36 Severe Fuel Damage Experiment of a VVER Fuel Bundle at the CORA Facility"
M. Firnhaber, L. Yegorova, U. Brockmeir, S. Hagen, P. Hofmann and K. Trambauer 1830

"Oxidation During Reflood of Reactor Core with Melting Cladding"
L.J. Siefken, C.M. Allison, K.L. Davis and J.K. Hohorst.....1851

"Crust Formation and Its Effect on the Molten Pool Coolability"
R.J. Park, S.J. Lee, S.K. Sim and K.J. Yoo.....1863

"Simulation of the Thermalhydraulic Behavior of a Molten Core Within a Structure, with the Three Dimensions Three Components TOLBIAC Code"
B. Spindler, G.-M. Moreau and S. Pigny.....1881

"The Modelling of Core Melting and In-Vessel Corium Relocation in the APRIL Code"
S.W. Kim, M.Z. Podowski, R.T. Lahey, Jr. and N. Kurul.....1889

"CODE PACKAGE "SVECHA: Modeling of Core Degradation Phenomena at Severe Accidents"
M.S. Veshchunov, A.E. Kisselev, A.V. Palagin, A.V. Lemekha, A.M. Volchek, N.V. Yamshchikov, A.V. Boldyrev and A.I. Deryugin.....1914

Session 14 - HEAT TRANSFER WITH PHASE CHANGE; APPLICATIONS TO SEVERE ACCIDENT SITUATIONS

"Experimental Simulation of Water Cooling of Corium Spread Over the Floor of BWR Containment"
F. Moraga, R.T. Lahey, Jr. and M.Z. Podowski.....1930

"SULTAN TEST FACILITY Large Scale Vessel Coolability in Natural Convection at Low Pressure"
S. Rouge.....1949

"An Integral Model for the Calculation of Heat Flux Distribution in a Pool With Internal Heat Generation"
J.M. Bonnet.....1958

Session 15 - COMPUTATIONAL AND MATHEMATICAL MODELING

"Numerical Simulation of Stratified Shear Flow Using a Higher Order Taylor Series Expansion Method"
K. Iwashige and T. Ikeda.....1972

"Application of an Analytical Method for Solution of Thermal Hydraulic Conservation Equations"
M. R. Fakory.....1982

"Numerical Investigation of Heat Transfer in High-Temperature Gas-Cooled Reactors"
G. Chen and S. Anghaie.....1997

"Development of a Graphical User Interface for the TRAC Plant/ Safety Analysis Code"
A.E. Kelly, C.K. Harkins and R.J. Smith.....2003

"A Comparison of the Effect of the First and Second Upwind Schemes on the Predictions of the Modified RELAP5/MOD3"
G. Th. Analytis 2011

"Local Mesh Refinement for Incompressible Fluid Flow With Free Surfaces"
H. Teresaka, H. Kajiwara, K. Ogura, H. Ueda and A. Takizawa 2021

"Level Tracking in Detailed Reactor Simulations"
B. Aktas and J. Mahaffy 2035

"The Sensitivity Analysis by Adjoint Method for the Uncertainty Evaluation of the CATHARE-2 Code"
F. Barre, A. de Crecy and C. Perret 2045

Session 16 - MODEL & COMPUTER CODE VALIDATION & ASSESSMENT

"Development and Assessment of a Modified Version of RELAP5/MOD3"
G. Th. Analytis 2067

"A Study of the Dispersed Flow Interfacial Heat Transfer Model of RELAP5/MOD2.5 and RELAP5/MOD3"
M. Andreani, G.Th. Analytis and S.N. Aksan 2079

"Assessment of Computer Codes for VVER-440/213-Type Nuclear Power Plants"
L. Szabados, Gy. Ezsol and L. Perneczky 2102

"VIPRE Modeling of VVER-1000 Reactor Core for DNB Analyses"
Y. Sung, T.Q. Nguyen and J. Cizek 2112

"CATHARE2 Calculations of SPE4 Test Small Break LOCA on PMK Facility"
E. Laugier and J. Radet 2119

"Quantitative Code Accuracy Evaluation of ISP 33"
H. Kalli, A. Miettinen, H. Purhonen, F. D'Auria, M. Frogheri and M. Leonardi.... 2146

"FARO Base Case Post-Test Analysis by COMETA Code"
A. Annunziato and C. Addabbo 2159

"The Analysis of SCS Return Momentum Effect on the RCS Water Level During the Mid-Loop Operations"
J.K. Seo, J.Y. Yang, S.T. Hwang, and G.C. Park 2169

"An Assessment of RELAP5 MOD3.1.1 Condensation Heat Transfer Modeling with GIRAFFE Heat Transfer Tests"
B.D. Boyer, Y. Parlatan, G.C. Solvik and U.S. Rohatgi 2185

"ATHLET Validation Using Accident Management Experiments"
V. Teschendorff, H. Glaeser and F. Steinhoff 2203

"A Simple Modelling of Mass Diffusion Effects on Condensation with Noncondensable Gases for the Cathare Code"
P. Coste and D. Bestion 2222

"INJECT, and the Modeling of Waste Recycling Processes"
E. Gracyalny and M.L. Corradini 2240

"Some Thermohydraulics of Closure Head Adapters in a 3 Loop PWR"
F. Hofmann, O. Daubert, C. Bertrand, M. Hecker, F. Arnoux-Guisse and O. Bonnin 2250

"Analysis of a Small Break Loss-Of-Coolant Accident of Pressurized Water Reactor by APROS"
S. Al-Falahi, M. Hanninen and K. Porkholm 2263

"Evaluation and Assessment of Reflooding Models in RELAP5/MOD 2.5 and RELAP5/MOD3 Codes Using Lehigh University and PSI-Neptune Bundle Experimental Data"
M. Sencar and N. Aksan 2280

"Overview on CSNI Separate Effects Tests Validation Matrix"
N. Aksan, F. D'Auria, H. Glaeser, R. Pochard, C. Richards and A. Sjoberg 2303

"RELAP5 Analyses of Two Hypothetical Flow Reversal Events for the Advanced Neutron Source Reactor"
N.C.J. Chen, M.W. Wendel and G.L. Yoder 2335

"MELCOR Benchmarking Against Integral Severe Fuel Damage Tests"
I.K. Madni 2349

"Validation of the THIRMAL-1 Melt-Water Interaction Code"
C.C. Chu, J.J. Sienicki and B.W. Spencer 2359

"Experimental Assessment of Computer Codes Used for Safety Analysis of Integral Reactors"
A.A. Falkov, V.S. Kuul, O.B. Samoilov, A.N. Lepekhin and G.N. Polyansky 2384

"Assessment of the SE2-ANL Code Using EBR-II Temperature Measurements"
W.S. Yang and A.M. Yacout 2394

"RELAP5 Model to Simulate the Thermal-Hydraulic Effects of Grid Spacers and Cladding Rupture During Reflood"
C.K. Nithianandan, J.A. Klingenfus and S.S. Reilly 2410

"Validation of Advanced NSSS Simulator Model for Loss-of-Coolant Accidents"
S.P. Kao, S.K. Chang and H.C. Huang 2428

"Severe Accident Simulation at Olkiluoto"
H. Tirkkonen, T. Saarenpaa and L-C Po 2438

VOLUME IV

Session 17 - CHF MODELING AND PREDICTIONS

"The Sudden Coalescence Model of the Boiling Crisis"
P.M. Carrica and A. Clausse 2453

"Role of Heater Thermal Response in Reactor Thermal Limits During Oscillatory Two-Phase Flows"
A.E. Ruggles, A.D. Vasil'ev, N.W. Brown and M.W. Wendel 2470

"Methodology For the Study of the Boiling Crisis in a Nuclear Fuel Bundle"
F. de Crecy and D. Juhel 2480

"An Investigation of Transition Boiling Mechanisms of Subcooled Water Under Forced Convective Conditions"
K-W Lee and S-Y Lee 2489

"A Formal Approach For the Prediction of the Critical Heat Flux in Subcooled Water"
C. Lombardi 2506

"A Comparison of CHF Between Tubes and Annuli Under PWR Thermal Hydraulic Conditions"
C. Herer, A. Souyri and J. Garnier 2519

"New Model for Burnout Prediction in Channels of Various Cross Section"
V.P. Bobkov, N.V. Kozina, V.N. Vinogradov and O.A. Zyatnina 2539

"On the Look-Up Tables For the Critical Heat Flux in Tubes (History and Problems)"
P.L. Kirillov and I.P. Smogalev 2558

"A Comparison of Critical Heat Flux in Tubes and Bilaterally Heated Annuli"
S. Doerffer, D.C. Groeneveld and S.C. Cheng 2583

"Experience Using Individually Supplied Heater Rods in Critical Power Testing of Advanced BWR Fuel"
M. Majed, G. Norback, P. Wiman, G.I. Hadaller, R.C. Hayes and F. Stern 2608

"CHF Considerations for Highly Moderated 100% MOX Fueled PWRs"
D. Saphier and P. Raymond 2621

"General Correlation for Prediction of Critical Heat Flux Ratio in Water Cooled Channels"
R. Pernica and J. Cizek 2636

Session 18 - THERMAL-HYDRAULIC COUPLING IN REACTOR SYSTEMS

"A Study of the Effect of Space-Dependent Neutronics on Stochastically-Induced Bifurcations in BWR Dynamics(*)"
G. Th. Analytis 2654

"Analysis of the Return to Power Scenario Following a LBLOCA in a PWR"
R. Macian T.N. Tyler and J.H. Mahaffy 2669

"Stability Analysis of BWR Nuclear-Coupled Thermal-Hydraulics Using a Simple Model"
A.A. Karve, Rizwan-uddin and J.J. Dorning 2677

"Coupled Calculation of the Radiological Release and the Thermal-Hydraulic Behaviour of a 3-Loop PWR After a SGTR by Means of the Code RELAP5"
W. Van Hove, K. Van Laeken, L. Bartsoen, B. Centner and L. Vanhoenacker 2704

Session 19 - SUBCHANNEL THERMAL-HYDRAULICS

"Analysis of Two-Phase Flow Inter-Subchannel Mass and Momentum Exchanges by the Two-Fluid Model Approach"
H. Ninokata, A. Deguchi and A. Kawahara 2721

"Large Scale Transport Across Narrow Gaps in Rod Bundles"
M.S. Guellouz and S. Tavoularis 2738

"Void Fraction Distribution in a Heated Rod Bundle Under Flow Stagnation Conditions"
V.A. Herrero, G. Guido-Lavalle and A. Clausse 2762

"Numerical Determination of the Lateral Loss Coefficients for Subchannel Analysis in Nuclear Fuel Bundles"
S. Kim and G-C Park 2773

Session 20 - THERMAL-HYDRAULICS OF REACTOR SYSTEMS AND COMPONENTS

"The Low-Power Low-Pressure Flow Resonance in a Natural Circulation Cooled BWR"
T.H.J.J. van der Hagen and A.J.C. Stekelenburg 2785

"Flow Characteristics of Korea Multi-Purpose Research Reactor"
H. Kim, H.T. Chae, B.J. Jun and J.B. Lee 2786

"Analysis of Steam Generator Loss-Of-Feedwater Experiments with APROS and RELAP5/MOD3.1 Computer Codes"
E. Virtanen, T. Haapelehto and J. Kouhia 2806

"Horizontal Steam Generator Thermal-Hydraulics"
O. Ubra and M. Doubek 2815

Session 21 - THERMAL-HYDRAULICS TEST FACILITIES

"ISP33 Standard Problem on the Pactel Facility"
H. Purhonen, J. Kouhia and H. Kalli.....2834

"SPES-2, An Experimental Program to Support the AP600 Development"
M. Tarantini and C. Medich.....2841

"PWR-Related Integral Safety Experiments in the PKL III Test Facility - SBLOCA Under Beyond-Design-Basis Accident Conditions"
P. Weber, K.J. Umminger and B. Schoen.....2856

"SPES-2, AP600 Integral System Test S01007 2" CL to Core Make-Up Tank Pressure Balance Line Break"
M. Bacchiani, C. Medich, M. Rigamonti, O. Vescovi, A. Alemberti and L.E. Conway.....2869

"Investigations on the Thermal-Hydraulics of a Natural Circulation Cooled BWR Fuel Assembly"
H.V. Kok, T.H.J.J. van der Hagen and R.F. Mudde.....2884

"Physical Modelling of a Rapid Boron Dilution Transient"
N.G. Andersson, B. Hemstrom, R. Karlsson and S. Jacobson.....2895

"Further Evaluation of the CSNI Separate Effect Test Activity"
F. D'Auria, S.N. Aksan, H. Glaeser, A. Sjoberg, R. Pochard and J. Lillington.....2904

"Water Hammer Phenomena Occurring in Nuclear Power Installations While Filling Horizontal Pipe Containing Saturated Steam With Liquid"
Y.F. Selivanov, P.L. Kirillov and A.D. Yefanov.....2916

Session 22 - THERMAL-HYDRAULICS AND SAFETY OF NONCOMMERCIAL REACTORS

"Natural Circulation Analysis for the Advanced Neutron Source Reactor Refueling Process II"
R.F. Tucker, S. Dasaradhi, Y. Elkassabgi and G.L. Yoder.....2924

"Cold Source Vessel Development For the Advanced Neutron Source"
P.T. Williams and A.T. Lucas.....2941

"Modeling and Analysis of Thermal-Hydraulic Response of U-Al Reactor Fuel Plates Under Transient Heatup Conditions"
S.N. Valenti, T. Fuketa, S.H. Kim, V. Georgevich, R.P. Taleyarkhan, K. Soyama, K. Ishijima and T. Kodaira.....2957

"Study on Severe Accident Fuel Dispersion Behavior in the ANS Reactor at ORNL"
S.H. Kim, R.P. Taleyarkhan, S.N. Valenti, V. Georgevich and J. Y. Xiang.....2977

"The Phebus FP Thermal-Hydraulic Analysis with MELCOR"
K. Akagane, Y. Kiso T. Fukahori and M. Yoshino 2994

"Flow Excursion Time Scales in the Advanced Neutron Source Reactor"
C.D. Sulfredge 3003

"Thermal-Hydraulics of Wave Propagation and Pressure Distribution Under Hypothetical Fuel-Coolant-Interaction Conditions in the ANS Reactor"
R.P. Taleyarkhan, V. Georgevich, S.N. Valenti and S.H. Kim 3028

"Modeling and Analysis Framework for Core Damage Propagation During Flow-Blockage Initiated Accidents in the ANS Reactor at ORNL"
S.H. Kim, R.P. Taleyarkhan, S.N. Valenti and V. Georgevich 3052

Session 23 - MIXING AND TURBULENCE

"Turbulent Mixed Convection in Vertical and Inclined Flat Channels with the Aiding Flows"
P. Poskas, J. Vilemas, E. Adomaitis, G. Bartkus 3073

"Mixing Phenomena of Interest to Boron Dilution During Small Break LOCAs in PWRs"
H.P. Nourbakhsh and Z. Cheng 3083

"Numerical Boron Mixing Studies for Loviisa Nuclear Power Plant "
P. Gango 3096

"Turbulence Prediction in Two-Dimensional Bundle Flows Using Large Eddy Simulation"
W.A. Ibrahim and Y.A. Hassan 3120

Session 24 - LOCAL FLOW AND HEAT TRANSFER PHENOMENA IN REACTOR CHANNELS

"Statistical Parameter Characteristics of Gas-Phase Fluctuations for Gas-Liquid Intermittent Flow
G. Matsui, H. Monji and M. Takaguchi 3142

"3-D Flow Analyses for Design of Nuclear Fuel Spacer"
Z. Karoutas, C-Y Gu and B. Scholin 3153

"Bubble Behaviour and Mean Diameter in Subcooled Flow Boiling"
O. Zeitoun and M. Shoukri 3175

"Correlation of Critical Heat Flux Data for Uniform Tubes"
T. Jafri, T.J. Dougherty and B.W. Yang 3197

* "A Model of Film Boiling in the Presence of Electric Fields"
P.M. Carrica, V. Masson, A. Clausse, P. DiMarco and W. Grassi 3218

** "A Simple Delay Model for Two-Phase Flow Dynamics"
A. Clausse, D.F. Delmastro and L.E. Juanico 3232

* Paper assigned to Session 14 in the Conference Program
** Paper assigned to Session 11-3 in the Conference Program

PREFACE

Welcome to Saratoga Springs, the place of the first of the NURETH meetings, held in 1980. Since this first meeting, the NURETH series have included: Santa Barbara, California in 1983, Newport, Rhode Island in 1985, Karlsruhe, Germany in 1989, Salt Lake City, Utah in 1992 and Grenoble, France in 1993. Now, after fifteen years, the seventh of the NURETH meetings is being held again in the birth place of the series.

As you probable know, the NURETH meetings have been initiated and sponsored or co-sponsored by the Thermal-Hydraulics Division of the American Nuclear Society. The TH Division has clearly become a leader in establishing and maintaining high technical standards regarding topical meetings in the field of nuclear thermal-hydraulics, paper acceptance criteria for such meetings, and promoting international cooperation and exchange. In particular, the papers accepted for presentation at NURETH-7 and published in these volumes have been thoroughly reviewed by leading experts in their respective fields. Their work, as well as the efforts of the session organizers, are the cornerstones of the high technical quality of this meeting.

The present conference has been organized by the Northeastern New York Section of the American Nuclear Society. In addition, the following organizations have agreed to join the ANS Thermal Hydraulics Division as co-sponsors of NURETH-7: American Institute of Chemical Engineers (AIChE), American Society of Mechanical Engineers (ASME), Canadian Nuclear Society (CNS), European Nuclear Society (ENS), Japanese Nuclear Society (JNS), Japanese Society of Multiphase Flow (JSMF) and the U.S. Nuclear Regulatory Commission.

Except for the invited papers in the plenary session, all the other papers are contributed. They have been divided into twenty-four major topics. These topics cover all major areas of nuclear thermal-hydraulics.

The theme of the NURETH-7 conference is ***Thermal-Hydraulics for the 21st Century***. This theme has been implemented in the program of the meeting through technical papers covering areas such as: progress in analytical and experimental work on the fundamentals of nuclear thermal-hydraulics, the development of advanced mathematical and numerical methods, and the application of advancements in the field in the development of novel reactor concepts. Because of the complex nature of nuclear reactors and power plants, several papers deal with the combined issues of thermal-hydraulics and reactor/power-plant safety, core neutronics and/or radiation.

I hope that both the conference participants and other future readers of this multi-volume edition of NURETH-7 Proceedings will find several new and innovative ideas as the results of the work by the authors representing an outstanding international community of experts from academia and industry.

On behalf of the organizing committee I invite you to actively participate in the conference and wish you a pleasant stay in Saratoga Springs.

Michael Z. Podowski
Technical Program Chairman

ACKNOWLEDGMENTS

The efforts of the authors of both invited and contributed papers included in this volume are gratefully acknowledged. Also acknowledged is the cooperation of the members of the Technical Program Committee and the Scientific Advisory Committee who helped to organize the technical program of the meeting and accomplish its scientific objectives. Special thanks are extended to the session organizers and paper reviewers.

Finally, appreciation is expressed to the U.S. Nuclear Regulatory Commission for their support of the publication of the Proceedings.

ON THE CONSTITUTIVE DESCRIPTION OF THE MICROINTERACTIONS CONCEPT IN STEAM EXPLOSIONS

X. Chen*, W. W. Yuen* and T. G. Theofanous
Center for Risk Studies and Safety,
Department of Chemical and Nuclear Engineering
University of California, Santa Barbara, Santa Barbara, Ca. 93106
Telephone (805) 893-4900 - Fax (805) 893-4927

ABSTRACT

This paper elaborates on the constitutive description of the "microinteraction" model used by the computer code ESPROSE.m to simulate the propagation phase of steam explosions. The approach is based on a series of experiments, in the SIGMA-2000 facility, involving molten drops of tin made to explode under sustained pressure fields; an environment similar to that of a fully-developed large-scale detonation. The experimental ranges cover shock pressures of up to 204 bar, melt temperatures of up to 1800 °C, and a series of isothermal runs, using gallium drops, are also included. The results indicate that, to a first approximation, the basic form of the constitutive laws hypothesized in the original formulation of ESPROSE.m is appropriate. Moreover, through detailed comparison of data with numerical experiments, certain parameters appearing in these laws could be identified quantitatively.

1. INTRODUCTION

The purpose of this paper is to follow up the "microinteractions" idea proposed only recently as the fundamental ingredient of steam explosion physics (Yuen and Theofanous, 1994). The idea owes its origin to the recognition that in fully-developed large-scale detonations, melt fragmentation occurs under a sustained pressure field (as opposed to the sharp-pulse triggers employed in all previous fragmentation studies), and on the observation that under such conditions the debris (fragmented fuel mass) mixes with the coolant found only in the immediate vicinity of the melt-coolant interface (Yuen, et. al. 1992). The rest of the coolant simply does not participate in the ensuing thermal interaction (but it does participate in the wave dynamics process), and the effect on the obtained feedback is enormous – it can produce sustained detonations under much less restrictive conditions on fuel concentration and fragmentation rates.

The first formulation (Yuen and Theofanous, 1994) of the microinteraction model was based on the hypothesized constitutive law that the rate of coolant mixing with the debris is proportional to the melt fragmentation rate. This model produced the first, and still only (see for example, the review by Fletcher and Anderson, 1990, that explains the inconsistencies) consistent comparisons with available experimental results (in the KROTOS facility): from "weak propagations" with tin melt at 1000 °C, to supercritical detonations with aluminum oxide melt at 2300 °C. This model was also utilized to obtain the first results for two-dimensional detonations (open pool geometries), demonstrating thus the important mitigating effect of "venting" due to wave reflections at the free pool surface (Theofanous and Yuen, 1994).

In this paper we examine this constitutive formulation in the light of experiments carried out in the SIGMA-2000 facility especially for this purpose. We use ESPROSE.m to help with

* Also with Mechanical Engineering

the interpretation and in the process we are able to examine the whole microinteraction model of ESPROSE.m in some detail, as well as certain wave dynamics feature of the code.

In this first systematic experimental evaluation of the microinteraction "laws", we concentrate on molten tin drops at temperatures up to 1800 °C, and shock pressures from 68 to 204 bars (1000 to 3000 psi). As a basis of comparison, we carry out also a set of experiments under isothermal conditions with gallium drops (melting point at 30 °C). The results are used to show the existence of a hydrodynamic regime at high pressures, and of a thermally-affected regime at the low end of the pressures considered. Any material dependence is yet to be determined as we undetake experimentation, one-by-one, with each material of interest (namely, Fe and ZrO_2 for reactor applications). However, it is reasonable to expect that, to the extend that the hydrodynamic regime is adequately characterized by the relevant properties (as described below), the behavior at this limit can be adequately predicted. This is **the** important regime from the point of view of assessing the energetics of large-scale detonations. At low pressures thermal effects set in, but this is relevant to the triggering and early escalation stages of an explosion. Preliminary experiments with iron melts at pressure of 68 bar and 1600 °C indicates a thermal effect much stronger than that of tin. This is not surprising considering the heat capacities per unit volume (ρc_p) of iron as compared to that of tin (2 times bigger). The latent heat of iron is also much larger than that of tin (4 times bigger). To fully understand this regime we need extensive experiments with various melts and pressures from essentially ambient up to the range considered here. However, exploring this regime is a lower priority concern, and we are treating it as such.

2. EXPERIMENTAL APPARATUS AND INSTRUMENTATION

The experiments are carried out in the SIGMA facility, employed previously for the study of fragmentation of mercury drops in water (Patel and Theofanous, 1981) under sustained pressure waves and isothermal condition. More recently SIGMA was employed in the study of molten tin drops at temperature up to 1000 °C (Yuen, et. al., 1994). For the present study the facility was upgraded to allow melt drop temperatures up to $\sim$ 2000 °K (hence the SIGMA-2000 name). The whole experimental arrangement is shown in Figure 1, and it can be explained with the help of the schematics in Figures 2 and 3.

The basic component is the shock tube, consisting of an one-meter-long driver section and a two-meter-long expansion section. The design pressure is 1000 bar and with water in the expansion section it allows steady flows/pressures for up to $\sim$ 2.3 ms, before the reflected wave from the bottom end of the tube arrives back to the window area. The window allows an observation area of 2 $\times$ 5 cm, and its midpoint is located 50 cm below the top of the expansion section, which is separated from the driver section with a prescored steel diaphragm. The shock wave is initiated by cracking the diaphragm with the help of a blasting cap which is electrically detonated.

The melt generator, placed typically 5 cm above the window, is illustrated in Figure 3. It is designed to melt and reproducibly release single drops of melt at any desired temperature up to 2073 °K (1800 °C). The test material is placed inside a graphite crucible, surrounded by an induction coil, powered by a 2.5 kW generator. The sample, and to some degree the crucible, can be heated rapidly by the induction currents while the temperature is on-line monitored using K-type thermocouples. When the drop temperature reaches the desired value (typical heating time is about one minute), a mini-plug cylinder (driven by argon gas pressure) is made to snap

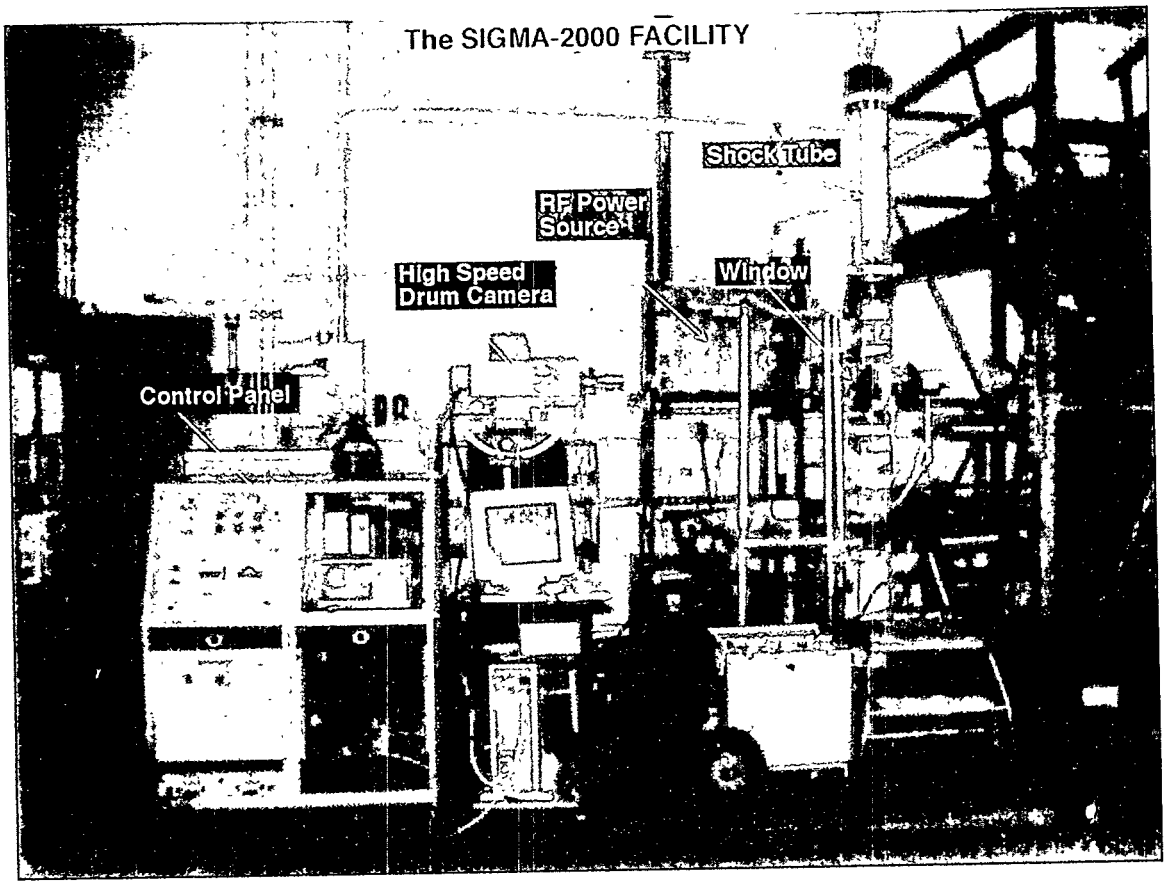


Figure 1: The SIGMA-2000 facility.

open thus releasing a single molten drop. Since at 1300 °C the thermocouple fails, higher temperatures are obtained by an on-line fit and extrapolation of the temperature data (using a PC). The procedure is estimated to have an uncertainty of about ± 30 °C.

The most challenging aspect of the experiment is to obtain the drop-shock interaction near the top of the observation window, so that the event can be observed in its entirety (as the drop translates rapidly and explodes behind the shock). This is achieved by automatically timing the whole experimental sequence, starting with the detection of the molten drop, by means of a laser beam, at the very top end of the window.

The principal experimental data are images of the exploding drops obtained with flash X-ray and high speed movies (so far, these data have been obtained in separate experiments, but under well-reproducible conditions; we have, however, recently developed the capability of simultaneous operation). For the X-ray, we use a Hewitt Packard generator (Model 43734A) capable of a single 25 ns duration flash, that can be timed very precisely on the basis of the shock arrival time at the window. For the movie we use a rotating drum camera run typically at 25,000 frames per second, for a total recording time of 6 ms, under back-lighting conditions.

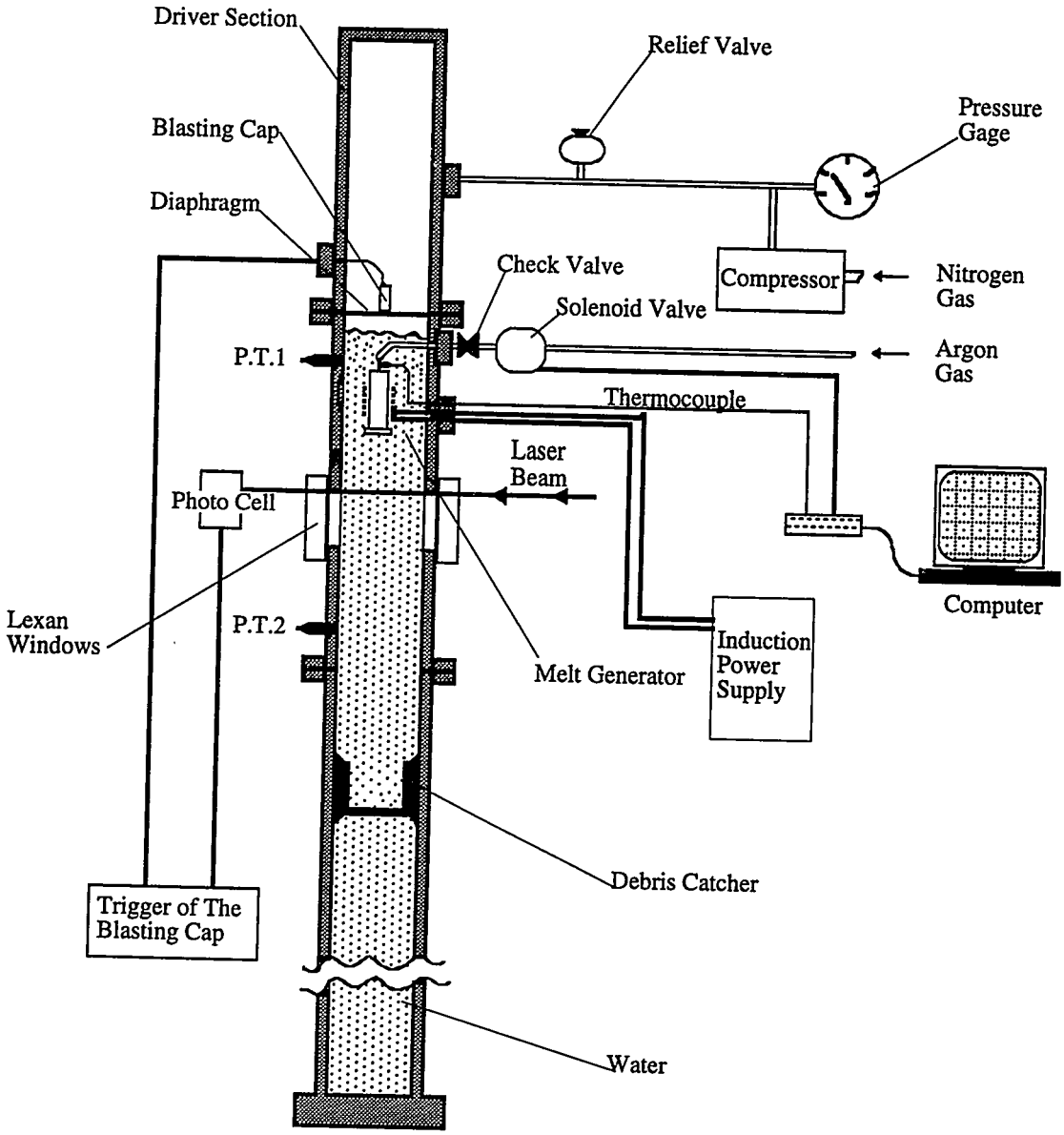


Figure 2: Schematic of the SIGMA-2000 facility (not to scale).

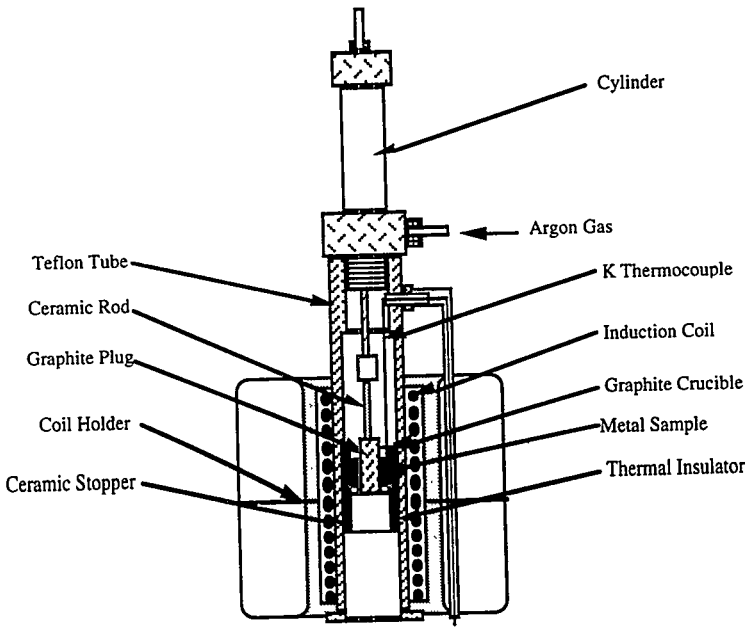


Figure 3: Schematic of the melt drop generator.

Pressures are measured both above and below the window with flush mounted quartz piezo-electric transducers (KISTLER, 607L) having a rise time of 1.5 μs and a 2,000 bar (30,000 psi) maximum range. The signal from the top transducer is used to trigger the X-ray and/or the flash-light for the movie camera. Both transducer signals are recorded in a four-channel digital storage oscilloscope (LeCroy 9304, 175 MHz) and a PC.

Finally, as shown in Figure 2, we employed a debris catcher (which was able to slide up and down the tube following the flow) to collect the debris after each run both for mass and debris size distribution analysis.

3. EXPERIMENTAL PROGRAM AND DATA REDUCTION TECHNIQUES

Critical aspects for the quantitative radiography employed here are the optimization of the X-ray energy level and source position from the object, such as to optimize the film exposure. Moreover, strict quality standards need to be applied in the reproducible development of the exposed film, detailed calibration curves, and witness pieces on every film to allow for the small correction always necessary due to intangible variations in the exposure-development-reading process. With these techniques properly established one can obtain the two-dimensional projection of the fragmenting drop mass distribution at the instant of the X-ray flash. As a means of checking the accuracy of the whole process, the total drop mass was reproducible from the X-ray analysis typically within 10 to 15 %

The high speed movies provide the evolution of images of the ouside envelope of the microinteraction region (consisting of the debris, entrained water, and any steam produced by the interaction), which in turn surrounds any remaining (coherent) drop mass. These data are complementary to those in the X-ray in the following sense. From the X-ray film we can distinguish the fragmented debris mass (as described shortly below), we can thus determine the amount of water mixed with this debris. The movies allow us to expand this information, from the selected time instances of the X-rays, to the complete explosion event.

Analysis of both the movie and X-ray images are done with a digitial scanner (UMAX UC840), and associated software to compute local masses and total volumes. The manner in which the mass corresponding to the debris was identified is described in conjunction with the presentation of data in the next section.

The debris collected from the "catcher" was washed, dried and subjected to sieve analysis. Selected samples were examined and photographed under the electron microscope.

The experimental program involved two materials and runs under seven conditions as summarized in Table 1. The run identifier code includes shock pressure and melt temperature for easy identification in the discussion. Key properties of these melts are given in Table 2. Referring to a remark made in the introduction about iron, the properties of this material are also included. For the tin runs, the water temperature was raised to 90 °C to prevent spontaneous interactions. In addition to one movie run for each entry in Table 1, we have three duplicate runs of T/204/1000 for the X-ray data at three selected instances (0.85, 1.0 and 1.5 ms).

Table 1. Test Conditions for the SIGMA-2000 Experiments

Run ID	Melt	Temperature (°C) (Melt/Water)	Shock Pres. (Bar)	Drop Diameter (cm) (Hor./Ver.)
G/68/45	Galium	45/45	68	0.68/0.46
G/204/45	Galium	45/45	204	0.81/0.39
G/272/45	Galium	45/45	272	0.91/0.56
T/68/1700	Tin	1700/90	68	0.65/0.46
T/204/1800	Tin	1800/90	204	0.63/0.43
T/68/1000	Tin	1000/90	68	0.75/0.41
T/204/1000	Tin	1000/90	204	0.63/0.38

Table 2. Properties of Materials

Material	ρ (gm/cm^3)	σ (dyn/cm)	c_p (J/(g·k)	L (J/g)
Galium	6.07	660	0.371	79.7
Tin	6.10 (T = 1700 °C) 6.47 (T = 1000 °C)	550	0.220	60.7
Iron	7.87	1550	0.449	247

4. EXPERIMENTAL RESULTS

Selected movie image sequences from three representative runs are shown in Figures 4a, 4b and 4c. It is interesting to note that in all cases, the boundary is highly structured, and that

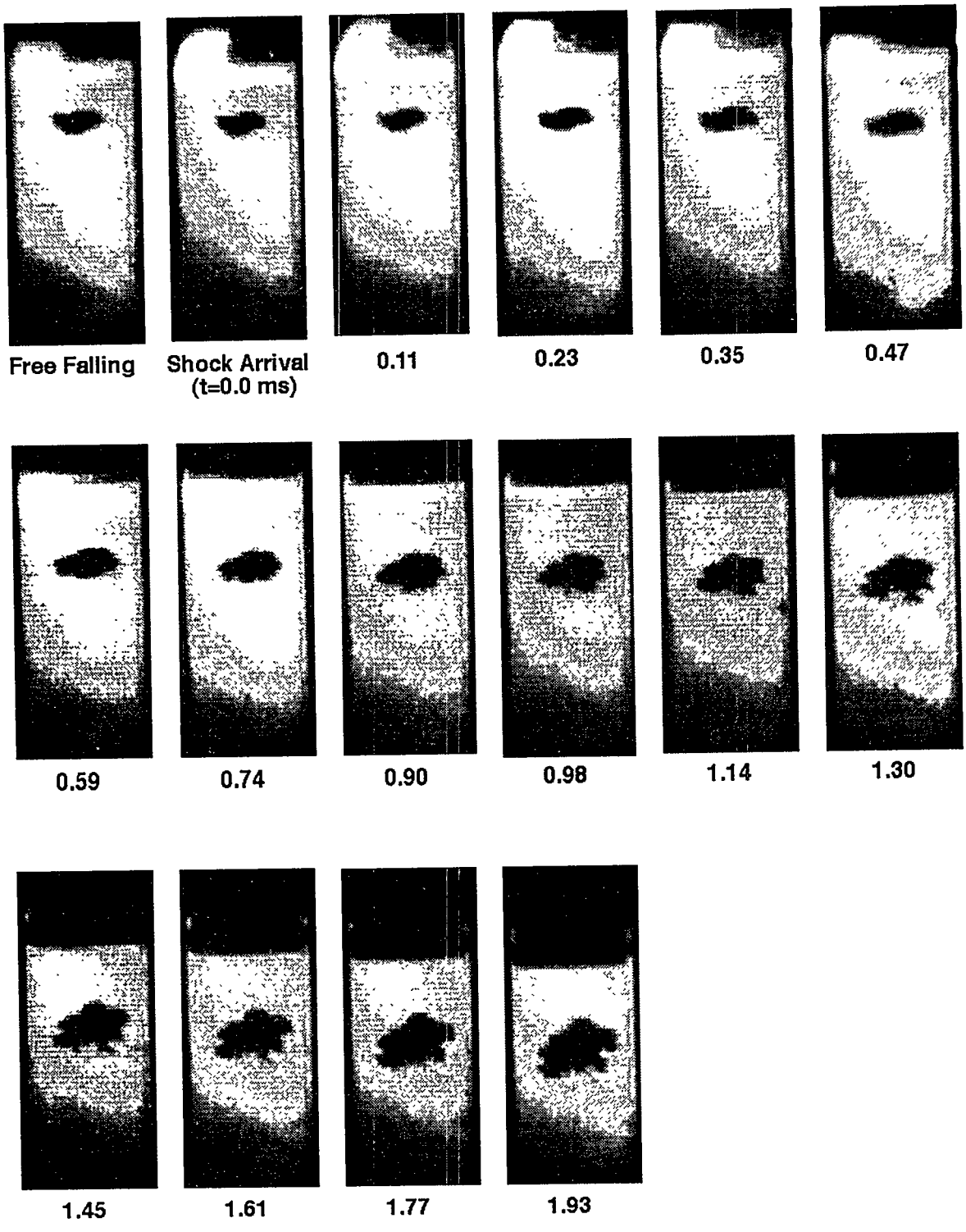


Figure 4a: Movie images of run G/240/45.

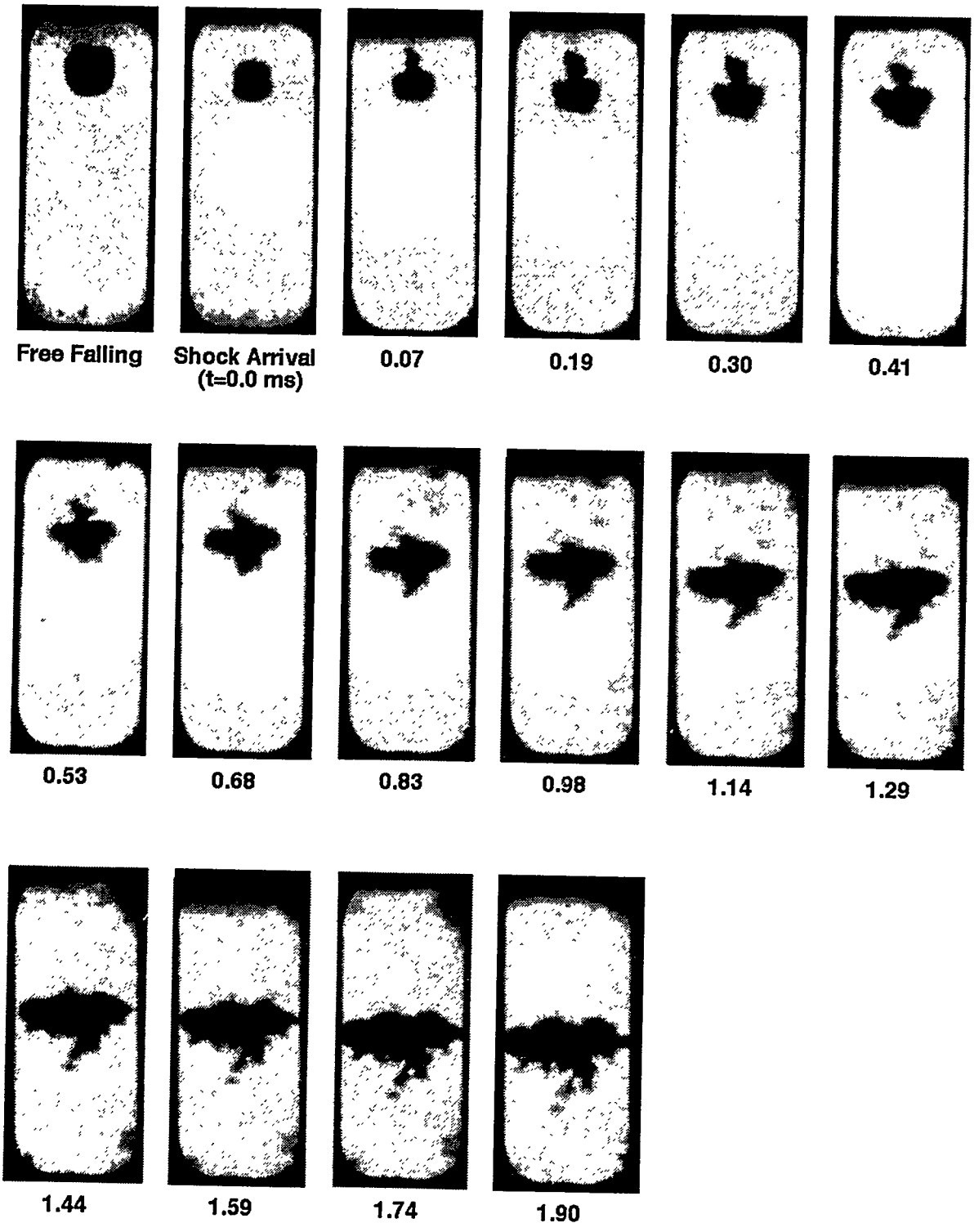


Figure 4b: Movie images of run T/204/1000.

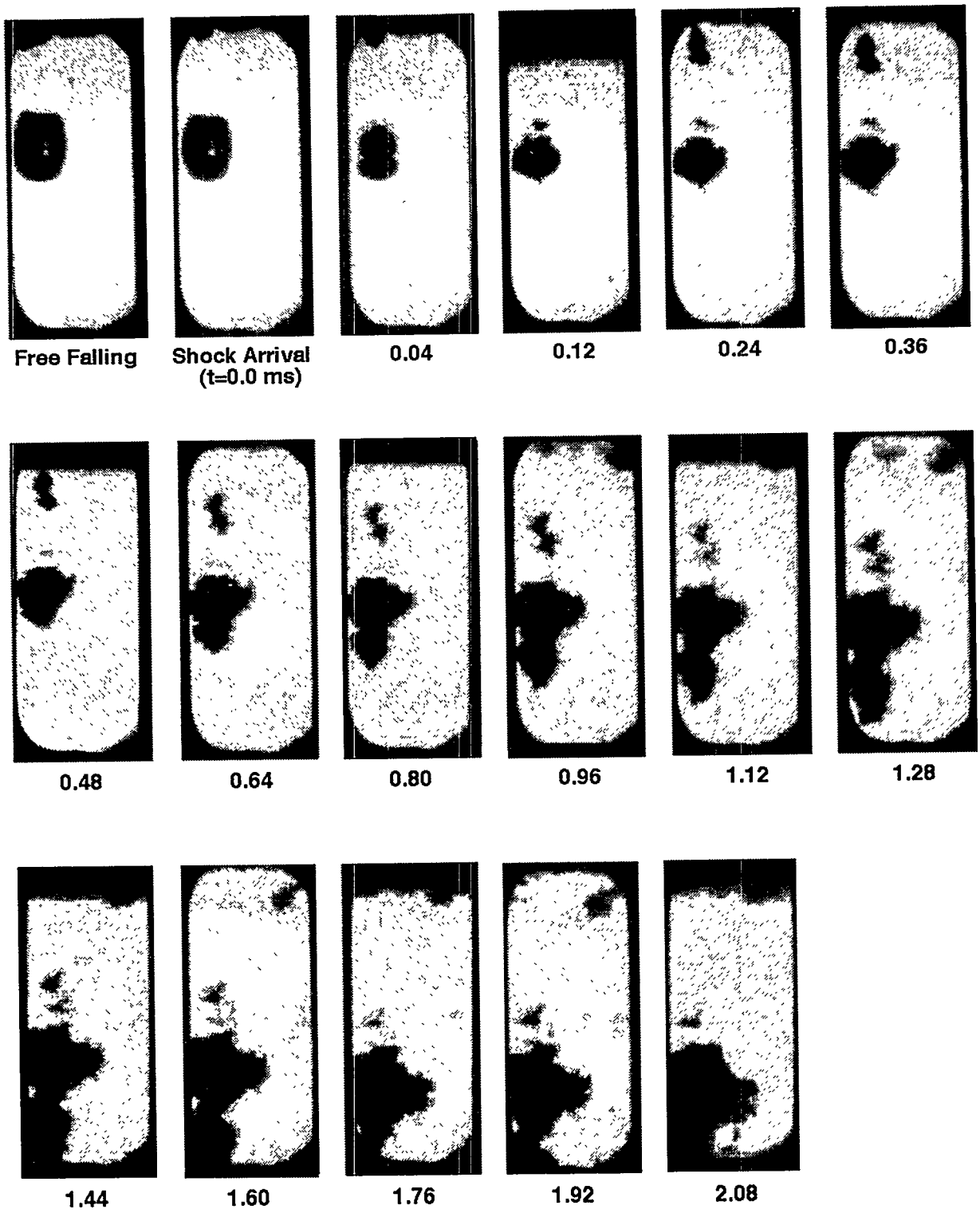


Figure 4c: Movie images of run T/204/1800.

in the non-isothermal runs, the interaction zone develops in a highly irregular fashion. Note however, that even for the high temperature runs the microinteraction zone is quite confined around the drop as found previously (Yuen, et. al. 1994). To obtain an indication of the volume of these zones, these images are integrated (using horizontal slices) assuming axial symmetry (for each slice separately). The uncertainty in carrying out the mechanics of this process is very low, so, the real uncertainty depends on the assumption of axial symmetry, which strictly speaking is not defined at this time. However, an overall perspective can be obtained from the time-wise regularity of the results as well as from the trends between various runs. All the volume results are presented together with analytical interpretations in section 6.

A reconstructed X-ray image is shown in Figure 5, and the mass thickness distribution along a horizontal axis going through the image at an elevation containing the point of maximum mass thickness is given on the top of Figure 6. The sudden drop-off in thickness seen in this figure was used to identify a "boundary" between the still-coherent drop mass and the surrounding debris. This then, in conjunction with the cumulative mass distribution shown in the bottom of Figure 6, was used to determine the fraction of the drop fragmented at the time the shot was taken. For the estimated drop mass, the equivalent diameter is 0.44 cm where the horizonal width of the cutoff thickness region is 0.49 cm and the "average" thickness in this region can be read as $\sim$ 0.4 cm; a consistency which is indicative that the inner region identified as "unfragmented" drop indeed contains no water. The reduced data from all three X-ray runs are presented together with analytical interpretations in section 6.

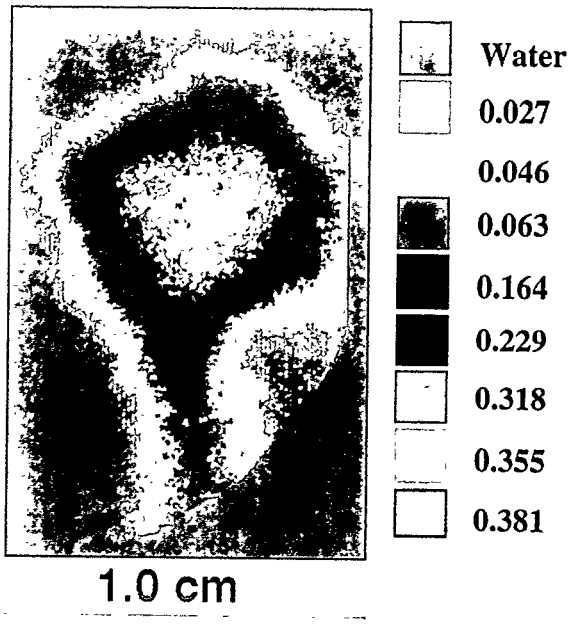


Figure 5: Flash X-ray image of a tin drop (1000 °C) at 0.85 ms after the shock arrival for run T/204/1000.

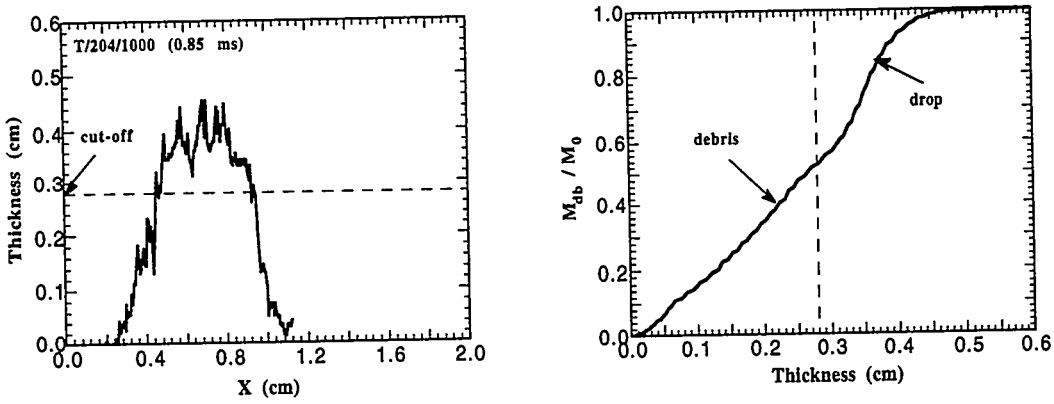


Figure 6: Mass distribution results from the X-ray film shown in Figure 5. The figure on the left represents the mass thickness distribution along horizontal line containing the local area with highest mass concentration. The figure on the right shows the cumulative mass fration distribution.

The debris size distribution from all the tin runs are summarized in Figure 7. We note that the "low pressure", "high temperature" combination gave the maximum fragmentation while the "low pressure", "low temperature" case produced essentailly no fragmentation. The "low" and "high" characterization applied here, are in the perspective of this work. In general, 1,000 °C is not really low since researchers have worked extensively with tin at temperature below 1000 °C, and in the KROTOS experiments, tin melts at 1000 °C were used in attempts to obtain propagating explosions. The present results explain why this was not possible (Yuen, et. al. 1994).

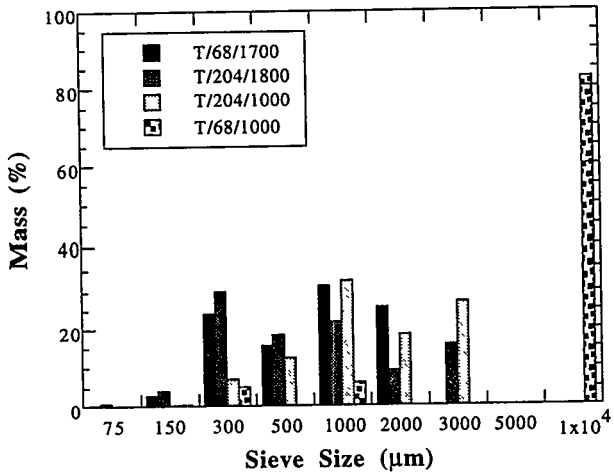


Figure 7: Histogram of fragmented masses from the tin runs. (Data are shown on a pass-basis; that is, the mass fraction shown at each sieve size corresponds to masses caught between it and the next higher size.)

The debris structure can be seen from representative scanning electron micorscope (SEM) photographs collected in Figure 8. The small sample shown for each run was obtained to

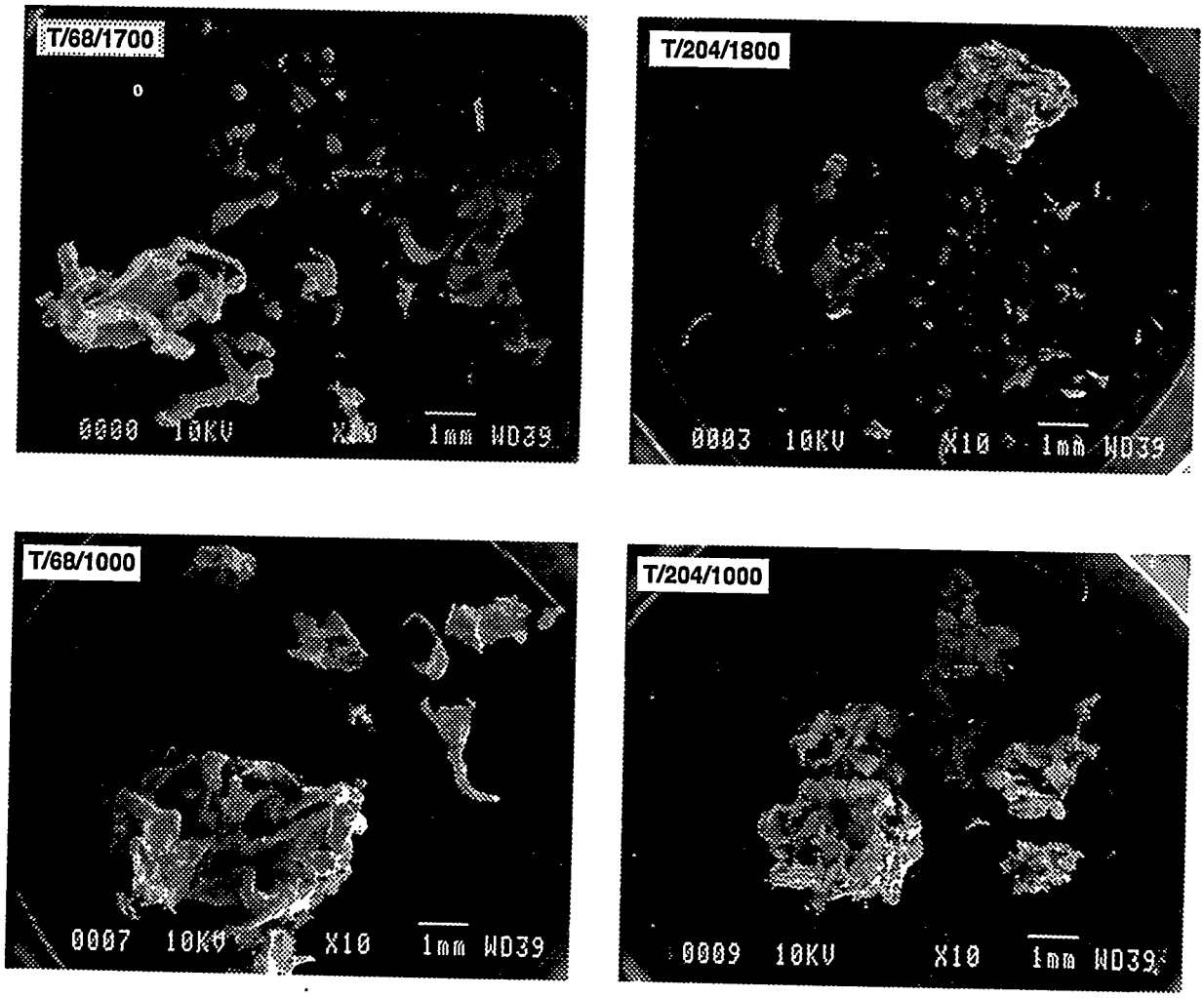


Figure 8: SEM photographs of sample debris collected from four tin experiments (in each photograph, samples of "large", "medium" and "small" debris are presented to illustrate typical characteristic dimensions).

include particles from those in the fine powder range, to intermediate, and large particle sizes. It is interesting to note the highly convoluted morphology of the large particles, even of those at low temperatures, and the smooth shape of the fine particles in the high temperature cases (those are absent in the low temperature runs).

5. THE MICROINTERACTION MODEL IN ESPROSE.m

As noted already we wish to interpret the data presented above in the ESPROSE.m frame. This is done in the next section, by means of ESPROSE.m calculations. In this section, by way of introduction, we provide the key aspects of the model (Yuen and Theofanous, 1995).

In the multifield formulation of ESPROSE.m the materials involved in the microinteraction zone (called the m-fluid) are considered together as a separate field, that is allowed to interact with the other two fields (fuel and liquid coolant) through exchanges of mass, momentum and energy. For our present purposes, we are mainly interested in the continuity equations which are written, for the fuel(f), liquid coolant(ℓ), the microinteraction "field"(m), and the debris(db), as follow:

$$\frac{\partial \rho'_m}{\partial t} + \nabla \cdot (\rho'_m \mathbf{u}_m) = E + J \tag{1}$$

$$\frac{\partial \rho'_\ell}{\partial t} + \nabla \cdot (\rho'_\ell \mathbf{u}_\ell) = -E - J \tag{2}$$

$$\frac{\partial \rho'_f}{\partial t} + \nabla \cdot (\rho'_f \mathbf{u}_f) = -F_r \tag{3}$$

$$\frac{\partial \rho'_{db}}{\partial t} + \nabla \cdot (\rho'_{db} \mathbf{u}_m) = F_r \tag{4}$$

In these equations, the "source terms" F_r and E, represent the rate of fuel fragmentation and the rate of entrainment of liquid coolant into the microinteraction zone respectively. These are the terms that need to be defined before the system of equations (including momentum and energy conservation which are not presented here) can be integrated, and these are the constitutive laws under investigation here. The other source term J represents mass transfer by phase change between liquid coolant and m-fluid. In addition to Eqs. (1) to (4), we have an equation to keep track of the changes in the fuel length scale, written as

$$\frac{\partial}{\partial t}\left(\frac{\theta_f}{D_f}\right) + \nabla \cdot \left(\frac{\theta_f}{D_f}\mathbf{u}_f\right) = \frac{2\theta_f}{D_f^2}\frac{dD_f}{dt} \tag{5}$$

This equation is based on interfacial area transport considerations and includes a "sink" term on the right hand side, representing the length scale changes due to fragmentation (the $\frac{dD_f}{dt}$ term is related to the rate of fragmentation).

The hypothesis made in the original formulation of ESPROSE.m was that the entrainment rate is proportional to the rate of fragmentation (on a volume basis), that is,

$$E = f_e F_r \frac{\rho_\ell}{\rho_f} \tag{6}$$

where f_e is the "entrainment factor". The instantaneous fragmentation rate, F_r, is obtained from a characteristic fragmentation time, t_f, as

$$F_r = \frac{\theta_f \rho_f}{t_f} \tag{7}$$

and the rate of change of the fuel particle diameter is given by

$$\frac{dD_f}{dt} = -\frac{D_f}{3t_f} \tag{8}$$

where the fragmentation time is estimated on the basis of an instantaneous Bond number formulation (i.e. based on the instantaneous differential velocity and drop diameter) obtained by extending an earlier formulation (Patel and Theofanous 1981) to a highly transient regime (Yuen et. al. 1994), that is

$$t_f^* \equiv \frac{|\,\mathbf{u}_f - \mathbf{u}\,|\, t_f}{D_f} \epsilon^{-1/2} = \beta_f \mathrm{Bo}^{-1/4} \tag{9}$$

with

$$\mathrm{Bo} \equiv \frac{3C_d \rho D_f\, |\,\mathbf{u}_f - \mathbf{u}\,|^2}{16\sigma} \qquad \epsilon \equiv \frac{\rho_f}{\rho} \tag{10}$$

This is for the purely hydrodynamic regime, and β_f is evaluated in conjunction with the relevant experiments. For example, based on data available at the time Yuen et. al. (1994) found β_f = 13.7, while Theofanous et. al. (1979) deduced a value of β_f = 10.3. To represent rates of fragmentation higher than this value, due to thermal effect for example, we introduce an augmentation factor, which to a first approximation is treated (here) as a constant. That is, more generally we have

$$t_f' = \frac{t_f}{\gamma_t} \tag{11}$$

and expect that $\gamma_t \rightarrow 1$ at very high pressures, where thermal effect can be expected to be negligible.

To recognize that by the time there is sufficient fragmentation, the turbulence developed and associated mixing effects cannot be expected to subside, even if the fragmentation rate diminishes (because of fuel depletion and/or approaching velocity equilibration), the entrainment rate in ESPROSE.m is kept as a non-decreasing function of time, i.e., it maintains its latest maximum value.

The SIGMA simulations presented in the next section were carried out in 1D with the melt drop at the appropriate location, and with a grid size of 1.25 cm to capture the highly localized

event of interest. A small gas pocket in the melt generator was also simulated. The effect on the wave dynamics is to create an overshoot at the front end of the pressure pulse (this is absent in the absence of this gas pocket), which is both interesting and predictable, as seen in Figure 9.

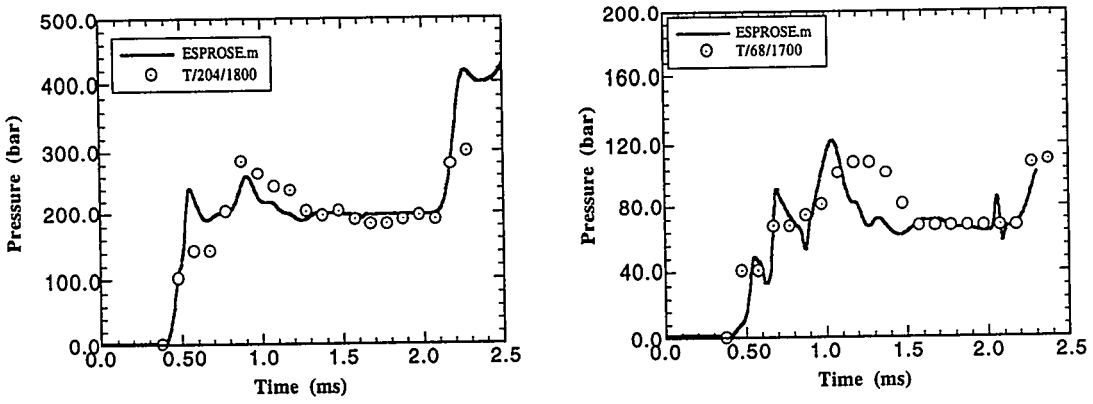


Figure 9: Comparison between ESPROSE.m predictions and measurements of pressure at the transducer below the observation window for runs T/68/1700 and T/204/1800.

6. DATA INTERPRETATIONS AND DISCUSSION

Before the detailed interpretations with ESPROSE.m it is instructive to consider the data in the interpretation of Patel and Theofanous (1981), and Yuen et al. (1994), that suggested a linear relation between the debris mass and dimensionless time, i.e.,

$$\frac{M_{db}}{M_0} = \frac{1}{\beta_{f_0}} t^* Bo_0^{1/4} \tag{12}$$

Now combining this with Eq. (6) we can obtain:

$$\frac{V}{V_0} = 1 + \frac{f_e}{\beta_{f_o}} t^* Bo_0^{1/4} \tag{13}$$

where V includes the unfragmented drop mass and the water entrained into the microinteractions zone. It is important to note that in Eq. (12), β_{f0} represents the total dimensionless fragmentation time based on the "initial" Bond number. It should thus correspond approximately to $\frac{\beta_f}{\gamma_t}$ for the fragmentation model described in the previous section. Eq. (13) is an approximation since it is derived assuming a constant density for the entrained liquid (i.e. isothermal fragmentation).

All the high speed movie data, plotted in the form suggested by Eq. (13), are shown in Figure 10. This figure also contains lines of Eq. (13) with the values $f_e = 7$, $\beta_f = 9$ and $\gamma = 1, 2, 4.2$. The specific values of these parameters are determined from interpretation of the fragmentation data with ESPROSE.m which is described below. A distinctive trend of the

data can clearly be identifed. As pressure increases, the fragmentation behavior approaches the "hydrodynamic regime" as represented by the isothermal gallium runs. The effect of temperature appears to be rather secondary.

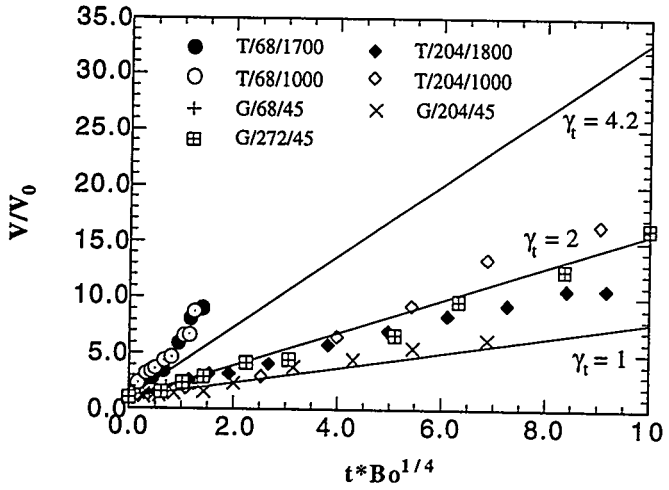


Figure 10: Transient behavior of the mixing volume for the seven tests.

A representative set of pressure transients, and volume fraction distributions of fuel, debris, and m-fluid obtained from ESPROSE.m with given values of the three constants (β_f, f_e, and γ_t) is shown in Figure 11. The following approach was followed in the parameter identification exercise, using such numerical experiments.

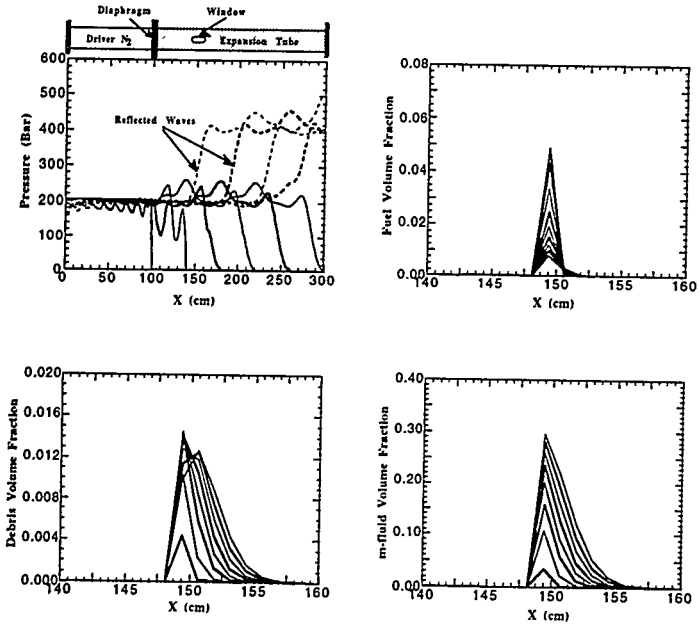


Figure 11: A typical set of pressures, volume fraction distributions for fuel, debris and m-fluid predicted by ESPROSE.m (Run T/204/1000) at 0.25 ms intervals. (The debris and m-fluid volume fraction distribution begin at 0.5 ms.)

First, we re-examine the old X-ray mercury fragmentation data (Yuen et al., 1994) to determine the value of β_f in the ESPROSE.m formulation that produces the same rates of fragmentation. The results are shown in Figure 12. As expected, the entrainment f_e has essentially no effect on the predicted fragmentation. Based on this comparison, the value of β_f is determined to be 9. The value of 13.7 quoted by Yuen et al. (1994) was based in a very early version of the ESPROSE code and an approximate treatment of the instantaneous Bond number formulation. On the other hand, the value of β_f is actually quite close to the 10.3 value of Theofanous et. al. (1979) noted above.

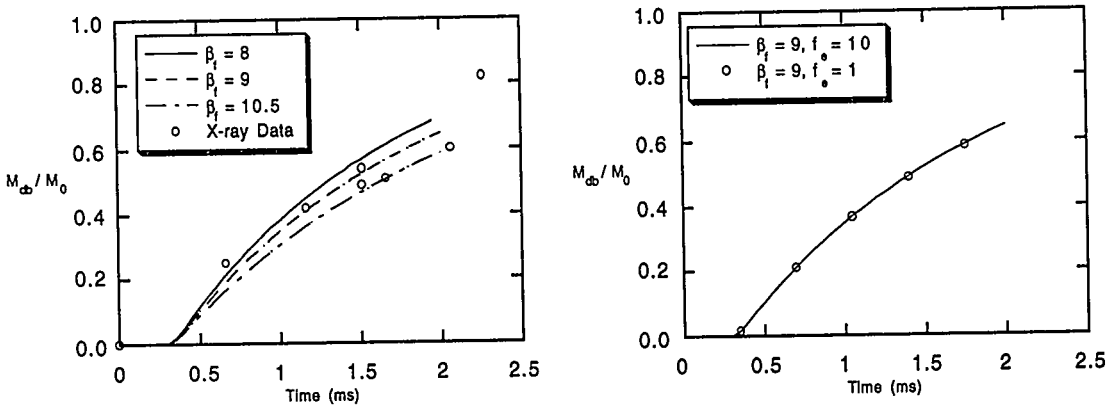


Figure 12: Comparison between ESPROSE.m predictions and the old fragmentation data for mercury at 340 bar. The left figure shows the effect of β_f with $f_e = 10$. The right figure shows the effect of f_e with $\beta_f = 9$.

With the β_f fixed, numerical experiments are next ran to determine an appropriate value of f_e using comparisons of predicted and measured total mixing volume (volume of the drop, debris and entrained coolant) of the three gallium runs. As shown in Figure 13, there is some explicit dependence on pressure. However the general trends are reasonable, in the perspective of the highly coupled nature of the phenomenon, and of the data being analyzed here, and allow us to make a first order choice of this parameter, f_e, in the range of 7 to 10. From the model described in section 5, one can recognize that higher values lead to lower peak explosion pressure, so a value of 7 can be considered as reasonably conservative for highly developed detonations. This is the value used in sample calculations with ESPROSE.m so far (Yuen and Theofanous 1994 and Theofanous and Yuen 1995).

Next the X-ray tin data are examined with the values of β_f and f_e fixed at 9 and 7 respectively. We find that some augmentation of the fragmentation rate is required. With a value of γ_t = 2, the comparison of the data is reasonable, as shown in Figure 14. Also on Figure 14, we can see that the sensitivity to γ_t is not great. The value of γ_t is in fact consistent with the movie data, and the other high pressure run (T/204/1800) as shown in Figure 15. For the low pressure runs, a much higher enhancement factor is necessary (γ_t = 4.2) to produce the agreement seen in Figure 15. A summary of the microinteraction parameters determined from the tin data is shown in Table 3.

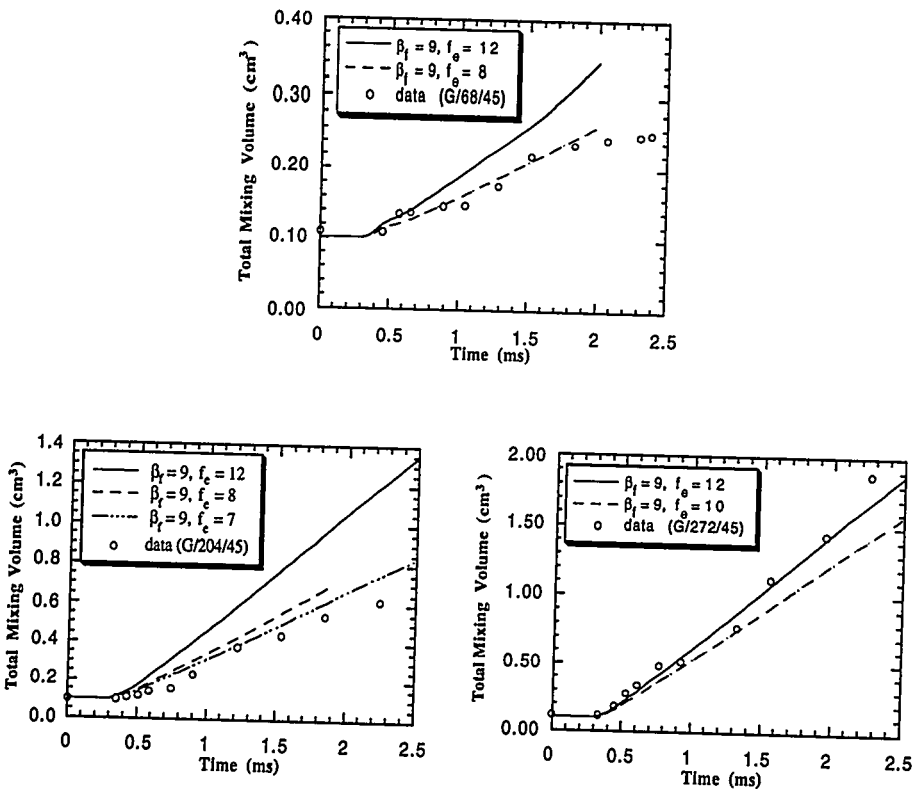


Figure 13: Comparison between the predicted and measured mixing volumes for the isothermal gallium/water runs. Time zero corresponds to the moment of diaphragm rupture.

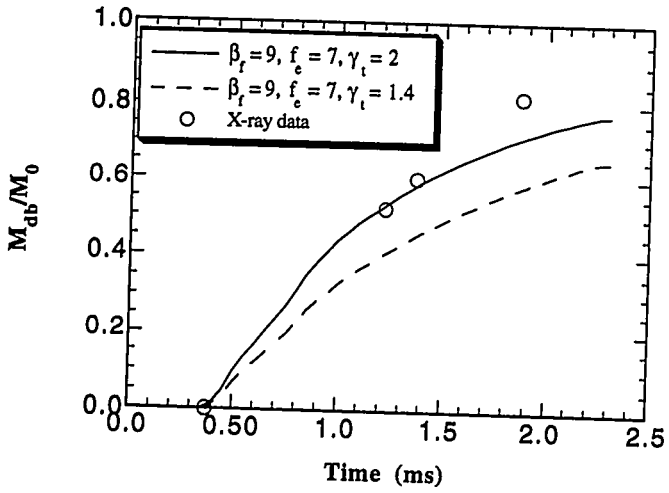


Figure 14: Comparison between the ESPROSE.m prediction ($\beta_f = 9$, $\gamma_t = 2$) with the fragmentation data for the present X-ray tin runs (T/204/1000). Time zero corresponds to the time of the diaphragm rupture.

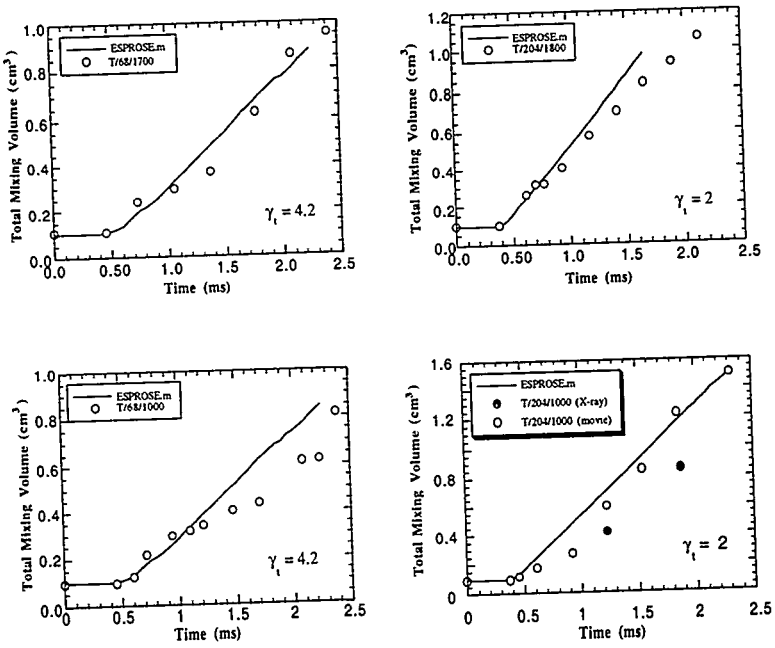


Figure 15: Comparison between the predicted (with $\beta_f = 9$, $f_e = 7$) and measured mixing volumes for all present tin movie runs. Time zero corresponds to the moment of diaphragm rupture. For run T/204/1000, the data points from the X-ray runs are also presented.

Table 3. Microinteraction Model Parameters

Run ID	Temperature Melt/Water °C	Pressure (bar)	β_f	f_e	γ_t
T/68/1700	90/1700	68	9	7	4.2
T/204/1800	90/1800	204	9	7	2
T/68/1000	90/1000	68	9	7	4.2
T/204/1000	90/1000	204	9	7	2

7. CONCLUSIONS

The purpose of this paper is to present the first systematic evaluation of the microinteractions model used in the ESPROSE.m code to compute the propagation phase of steam explosions. The approach is basically experimental, using the SIGMA-2000 facility to observe exploding tin drops under conditions that simulate those found in large scale, fully developed detonations. The results indicate that to a first approximation, the basic form of the constitutive laws hypothesized in the original formulation of ESPROSE.m is appropriate. Moreover, the results clearly show that under high pressure conditions a hydrodynamic regime dominates the behavior. The data in conjunction with numerical experiments have allowed to determine the numerical constants in

the formulation of the hydrodynamic regime, and to attempt a first quantification of the thermal regime.

ACKNOWLEDGEMENTS

This work was funded by the U.S. Department of Energy's Advanced Reactor Severe Accident Program (ARSAP) through ANL subcontract No. 23572401. We are grateful to Mr. Steven Sorrell (DOE) and Mr. Stephen Addition (TENERA) for their key roles in programmatically supporting this program.

NOMENCLATURE

Bo	Bond number, Eq. (10)
C_d	drag coefficient
c_p	specific heat
D	drop diameter
E	mass entrainment rate
f_e	entrainment factor, Eq. (6)
F_r	fragmentation rate
L	latent heat
M	mass
t	time
t_f^*	dimensionless complete fragmentation time of one fuel particle, Eq. (9)
$\mathbf{u}$	velocity vector
V	mixture volume (including melt drop and microinteraction zone)

Greek

β_f	fragmenation coefficient,, Eq. (9)
γ_t	thermal enhancement factor
ϵ	density ratio, Eq. (10)
θ	volume fraction
ρ	microscopic density
ρ'	macroscopic density, Eqs. (1) to (4)
σ	surface tension

Subscript

db	debris
f	fuel (also, fragmentation)
ℓ	liquid
m	m-fluid (m-field)
0	initial value

REFERENCES

1. Fletcher D. F. and R. P. Anderson (1990), "A Review of Pressure Induced Propagation Models of the Vapor Explosion Process," Progress in Nuclear Energy, Vol 23, pp. 137-179.

2. Patel, P. D. and Theofanous, T. G. (1981), "Hydrodynamic Fragmentation of Drops," Journal of Fluid Mechanics, Vol. 103, 1981, pp. 207-223.

3. Theofanous, T. G., M. Saito and T. Ethimiadis (1979) "The Role of Hydrodynamic Fragmentation in Fuel-Coolant Interactions," Fourth CSNI Specialist Meeting on Fuel-Coolant Interactions in Nuclear Reactor Safety, Bournemouth, England, April 2–5, 1979, CSNI Report No. 37, Vol. 1, 112, Paper FC14/P5.

4. Theofanous, T. G. and W. W. Yuen (1994), "The Prediction of Dynamic Loads from Ex-Vessel Steam Explosion," Proceeding of the International Conference on New Trends in Nuclear System Thermohydraulics, Pisa, Italy, 1994, Vol. 2, pp. 257-270.

5. Yuen, W. W., X. Chen and T. G. Theofanous (1994), "On the Fundamental Microinteractions that Support the Propagation of Steam Explosion," Nuclear Engineering and Design, 146 (1994), pp. 133-146.

6. Yuen, W. W. and T. G. Theofanous (1994), "The Prediction of 2d Thermal Detonations and Resulting Damage Potential," Proceeding of the CSNI Specialists Meeting on Fuel-Coolant Interaction, NUREG/CP 0127, March 1994, pp. 233-250.

7. Yuen, W. W. and T. G. Theofanous (1995) "ESPROSE.m: A Computer Code for Addressing the Escalation/Propagation of Steam Explosions," DOE/ID-10501, April 1995.

Submitted to the 7th International Meeting on Nuclear Reactor Thermal-Hydraulics (NURETH-7) in Saratoga Springs (USA), Sept. 10-15, 1995

Correlations between the Disintegration of Melt and the Measured Impulses in Steam Explosions

G. Fröhlich, A. Linca and M. Schindler

Institut für Kernenergetik und Energiesysteme, University of Stuttgart (Germany)

Abstract

To find out correlations in steam explosions (melt water interactions) between the measured impulses and the disintegration of the melt, experiments were performed in three configurations i.e. stratified, entrapment and jet experiments. Linear correlations were detected between the impulse and the total surface of the fragments. Theoretical considerations point out that a linear correlation assumes superheating of a water layer around the fragments of a constant thickness during the fragmentation process to a constant temperature (here the homogeneous nucleation temperature of water was assumed) and a constant expansion velocity of the steam in the main expansion time. The correlation constant does not depend on melt temperature and trigger pressure, but it depends on the configuration of the experiment or of a scenario of an accident. Further research is required concerning the correlation constant. For analysing steam explosion accidents the explosivity is introduced. The explosivity is a mass specific impulse. The explosivity is linear correlated with the degree of fragmentation. Knowing the degree of fragmentation with a proper correlation constant the explosivity can be calculated and from the explosivity combined with the total mass of fragments the impulse is obtained which can be used to an estimation of the maximum force.

1. Introduction

Steam explosions are caused by a rapid heat transfer from the hot melt (fuel) to the water (coolant). For this procedure a fragmentation process is necessary in which the melt is disintegrated. This disintegration of the melt leads to an enhancement of the heat transfer area between melt and water. Hereby the water is superheated combined by a pressure increase and an explosive vaporization of the water. The impulses which were generated during steam explosions must be correlated with the degree of disintegration of the melt.

In literature the violence of a steam explosion is either characterized by the degree of disintegration of the melt analysed after steam explosion or by the pressure and force respectively generated during steam explosion. Up to now nobody has published a correlation between the disintegration of the melt and the generated pressures or forces. The option of this paper is to investigate the kind of correlation between both conceptions of violence. For these investigations firstly, experiments in stratified configuration were chosen, i.e. a water layer is overlying a melt layer. In comparison to entrapment and jet experiments in stratified experiments larger masses of melt and water can interact if an effective trigger is used. The degree of melt disintegration was determined by a fragment analysis of the solidified melt fragments in a steam explosion. The forces generated during steam explosions in the so-called layer experiments were measured by force transducers.
The experimentally obtained correlation of layer experiments is backed up by theoretical consideration and by experiments in other configurations.

2. Stratified Experiments

The stratified experiments were carried out in a set-up that was already used for studying interactions between molten lava and water (s. p. 7 to 20 of /1/ or p. 342 to 344 of /2/). This set-up was called TEE-Haus which is an abbreviation of thermal explosion experiments and the German word "Haus" that is the English word "house", which should suggest the shape and dimension of the set-up (s. Fig. 1). The central element of the TEE-Haus is a steel crucible containing melt and water which is positioned on a substructure recording device that is marked with (1) in Fig. 1 (magnified in Fig. 2). The

crucible is opened to the room inside of the TEE-Haus, i.e. the rim of the crucible is on the same level as the bottom of the TEE-Haus. The crucible is placed inside a coil. The coil is contacted with a 30 kW middle frequency generator by the railing (2). Sliding doors (3) are installed in the four sides of the TEE-Haus. For the observation of the explosions, in the center of each sliding door a acrylic glass window is inserted. Smaller acrylic glass windows are installed in the four sides of the roof. Through one of them a video camera (4) was monitoring the course of events. The steam explosion was triggered by an air gun pellet (5).

Fig. 2 shows the steel crucible (6) which is surrounded by an electric coil (7) for heating up the melt (8). After heating up water flooded into the crucible through a pipe (9) and formed a water layer which was separated by a vapor film from the melt layer. A heat screen plate (10) and a metall cylinder (11) cooled by water protect both force transducers (12) from heating up. Below the metall plate (13) a crank wheel (14) allows to adjust the position of the crucible rim to the level of the bottom of the TEE-Haus.

The stratified experiments were performed with melt of an alloy of copper and 20 weight percentage of tin (CuSu20). After having flooded water into the crucible, a vapor film is built up and separates the water from the melt (s. Fig. 2). For the ignition of a steam explosion the vapor film must collapse. To achieve the collapse of the vapor film in the stratified experiments a shock wave was produced in the melt water system by firing an air gun pellet into the crucible. The shock wave triggers the vapor film collapse. After vapor film collapse a fragmentation process starts. The fragmentation process takes place in a fragmentation zone (s. Fig. 3) which starts from the interface of water and melt and grows to a maximum thicknes z_o. The fragmentation process enhances the contact area between water and melt causing a rapid heat transfer from the melt to the water which leads to an explosive vaporization of water accompagnied by an eruption of a mixture of melt fragments, water and steam out of the crucible into the TEE-Haus. During explosion the both force transducers (s. Fig. 2) record the vertical force component as a function of time $F_z(t)$. Two force transducers were used in order to get two measuring ranges, because the maximum force may vary in a wide range. The curve with the best resolution was used for integration with respect to time to get the impulse. An example for a force time curve of a stratified experiment is to be seen in Fig. 4.

After the end of the explosion the erupted melt fragments were caught in the TEE-Haus collected and analysed with respect to their size distribution. For that a sieve analysis was used. Standardized sieves were taken with 15 mesh sizes (s. Tab. 1). The fragment masses remaining on each sieve after the sieving procedure were weighted.

Since heat transfer depends on the surface of the fragments, this surface was estimated which was done by supposing that all fragments may be spheres and have average diameters corresponding to the special mesh sizes of the sieves. Thus on the sieve i were lying spheres of the average diameter d_i

$$d_i = \frac{a_i + a_{i+1}}{2} \qquad (1)$$

Here a_i and a_{i+1} are the width of the meshes of the sieves i and i+1 respectively where the sieve i+1 has the next larger mesh width to the sieve i, so that the fragments smaller than a_{i+1} fall on the sieve i and from these fragments all which are smaller than a_i do not stay on this sieve i.
Knowing the measured mass m_i of the fragments of all k(=15) sieves the total surface A_f of all melt fragments of a stratified experiment is on these assumptions:

$$A_f = \frac{6}{\rho} \sum_{i=1}^{k} \frac{m_i}{d_i} \qquad (2)$$

where ρ is the density of the solidified melt.

Nine experiments were carried out in stratified configuration actually with CuSn20 melt at three melt temperatures of 1150, 1250 and 1350°C and water of 20 °C. The crucible of an inner diamter of 50 mm was filled to a hight of about 40 mm with melt and of about 25 mm with water. For triggering an air gun pellet of a caliber of 4,5 mm with an impact velocity of about 175 m/s was used. The results are listed in Tab. 2 and plotted in the diagram of Fig. 5 (for more experimental details s. /3/). The diagram shows that the results can be approximated by a straight line. Thus a linear correlation is detected between the impulse in form of the time integral of the force acting on the bottom of the crucible and the total surface area of the fragments:

$$\int_{t=0}^{\infty} F_z(t)\ dt = C_L A_f \quad . \qquad (3)$$

C_L is a constant which is equal to the slope of the straight line in the diagram of Fig. 5 $C_L \approx 17.4$ Ns/m² (inaccuracy: ± 0.2 Ns/m²).

3. Theoretical Considerations

With equation (3) a correlation between two characteristic values of steam explosions (impulse and area of fragments) is to be detected. To find out the assumptions that lead to such a correlation, theoretical considerations were used.

In the fragmentation zone (s. Fig. 3) all fragments are supposed to be spherical and surrounded by water which is only heated up in a small layer s to the homogeneous nucleation temperature T_{hom}. All fragments are supposed to have the same course of surface temperature because they come from a melt of uniform temperature. Therefore the layer s is considered to be equal around all fragments. Thus the water mass surrounding the fragments by a layer of the thickness s is:

$$m_w = s \cdot \rho_{wa} \cdot A_f \qquad (4)$$

ρ_{wa} is the density of water and A_f is the surface of all fragments of an experiment.

It is assumed that only this water mass is vaporized which is superheated to the homogeneous nucleation temperature T_{hom}. Supposing that the transformation from water mass m_w to steam and the expansion of the steam occurring so rapidly that heat transmission to the environment is negligable, the energy balance for this transformed water mass is:

$$c_w (T_{hom} - T_0)\, dm_w - h dm_w + p_D dV_D = 0 \qquad (5)$$

c_w, h and T_0 are the specific heat, varporization heat and initial temperature of the water respectively. V_D and p_D are the volume and pressure of the generated steam respectively.

Differentiation of equation (5) in respect to time leads to

$$[c_w (T_{hom} - T_0) - h] \frac{dm_w}{dt} + p_D \frac{dV_D}{dt} = 0 \qquad (6)$$

where

$$\frac{dV_D}{dt} = A_c \frac{dz}{dt} = A_c v_z \quad . \qquad (7)$$

In equation (7) it is assumed that in stratified experiments the fragmentation zone extends along the cross-section A_c of the crucible with a thickness z_0 (s. Fig. 3). Thus vaporization extends along this diameter and changes its volume only in vertical direction which implies that the steam expansion is only governed by the velocity component v_z.

If equation (7) is introduced into equation (6) and due to an integration with respect to time t it is

$$[c_{wa} (T_{hom} - T_0) - h] m_w = \int_{t=0}^{\infty} p_D (t) A_c v_z dt \qquad (8)$$

The pressure p_D of the steam is transient. The direction of p_D is perpendicular to the surface of the steam volume, corresponding to the geometrical situation of Fig. 3:

$$p_D (t) A_c = F_z (t) \qquad (9)$$

Here, F_z is the force acting upward. The force acting downward has the same amount but acts in the reverse direction. This force acts through the underlying melt on the bottom of the crucible and from here through the screen plate (s. Fig. 2) and metal cylinder on the calibrated force transducers because of the mechanical principle "actio

equal reactio". Tus the amount of F_z in equation (9), (10) and (11) is the same as in equation (3).

Substitution of (4) and (9) in (8) leads to

$$\int_{t=0}^{\infty} F_z(t)\, v_z dt = s\rho_{wa}\,[\,c_{wa}\,(T_{hom}-T_0)\; -\; h\,]\,A_f \quad . \qquad (10)$$

Equation (10) differs from (3) only by the velocity v_z which is within the integral of the left side of (10).

v_z is a function of time which does not change as quicly as F_z. Due to the generalised sentence of the mean value of the integral calculus, the left side of equation (10) can be transformed:

$$\int_{t=0}^{\infty} F_z(t)\, v_z(t)\, dt = \overline{v_z} \int_{t=0}^{\infty} F_z(t)\, dt \qquad (11)$$

Thus a comparison of (3), (10) and (11) leads to

$$C_L = \frac{s\rho_{wa}[\,C_{wa}(T_{hom}\; -\; T_o)\; -h\,]}{\overline{v_z}} \quad . \qquad (12)$$

Although v_z begins at zero it may increase very fast to a constant value because of friction effects. The melt temperature is not involved in equation (11) which agrees with experimental results. Therefore the assumption of heating up the water before its vaporization to a constant temperature as the homogeneous temperature is justified.

4. Experiments in other configurations

The correlation between the impulse and the surface of the fragments was also examined by experiments in entrapment and jet configuration which were called in the following entrapment experiments or jet experiments. The entrapment experiments were carried out in the same set-up (the TEE-Haus) as the stratified experiments. Only the water

insertion into the crucible was different i.e. water was injected by a tube into the melt near the bottom of the crucible (s. Fig. 6). Furthermore the entrapment experiments were carried out with tin melt instead of CuSn20. The temperature of the tin melt was 650°C in six experiments and in one experiment 1000°C. The crucible had an inner diameter of 50 mm and was filled to a hight of 60 mm with melt. 10,9 g water were injected with a velocity of 2 m/s by a tube of 3,5 mm in diameter. Again an air gun pellet of a caliber of 4,5 mm was used for triggering. Tab. 3 contains the results of the entrapment experiments which are plotted in Fig. 7 (for more experimental details s. /3/). Since all points are near a regression line there can also be detected a linear correlation between the impulse and the surface of the fragments:

$$\int_{t=0}^{\infty} F_z(t)\,dt = C_E A_f \qquad (13)$$

The constant C_E of entrapment experiments is $C_E \approx 5.4$ Ns/m^2 (inaccuracy: ± 0.9 Ns/m^2).

The set-up used for the jet experiments was designed for multi jet experiments (s. Fig. 1 of /4/ or p. 210 of /5/). But here only one tin jet was chosen. Fig. 8 shows a sketch of this set-up. The container (1) filled with 80 l water is installed on a plate (2). The melt container (3) is pivoted in a box (8) which is hanging on a rail (4) and fixed with two screws (5a/5b). A melt jet can leave the melt container through an open hole (10) if a pull on the wire (9) turns the melt container by an angle of 90°C. Hereby a light barrier (12) is interrupted which led after a dwell time to an underwater bridge wire explosion at the wire fixing device (13). Then the wire explosion produces a shock wave and a water flow. The water flow is screened by the plate (14) while the shock wave passes the plate and reaches the melt jet in the water. If the shock wave is large enough steam explosions are triggered. The pressure peaks of the wire explosion as well as that of the steam explosion is measured by the pressure transducer (15). It is possible to cool the water of the container (1) by the thermostat (7) and to heat it up by two immersion heaters (6a/6b).

The jet experiments were carried out with molten tin of 650°C. The water temperature was 70°C. The trigger pressure p_{Tr} was varied stepwise from 0.95 to 6 MPa in the 20 jet experiments (s. the third column of Tab. 4). An example of the measured pressure

record is given in Fig. 9. The pressure peaks of the tin water interactions are indicated by numerals and the peaks of the trigger (from wire explosion) are indicated by small letters. The main peak of the trigger (indicated with letter "a") was larger than the upper limit of the chosen measuring range. Thus this pressure peak of trigger was cut (for more experimental details s. /3/). But therefore the maxima of the pressure peaks of the the interactions could be measured more exactly.

In jet experiments pressure was measured instead of force (s. number 15 of Fig. 8). Furthermore in jet experiments a time resolution of the pressure could not be recorded (s. Fig. 9). Thus, the sum of the measured pressure peaks $\sum_{i=1}^{n} p_i$ of an experiment were used instead of the impulse to characterize the violence of the steam explosion in jet experiments. The sum of the pressure peaks can be regarded as a reduction of the impulse with respect to area and time.

Tab. 4 contains the results and in Fig. 10 the sum of the pressure peaks is plotted versus surface area A_f of the fragments which were determined by sieve analysis as in stratified and entrapment experiments and calculated by equation (1) and (2).

In Fig. 10 the points can be approximated by straight line or by the correlation:

$$\sum_{i=1}^{n} p_i = C_J A_f \qquad (14)$$

The value of the constant C_J is: $C_J \approx 25{,}5$ MPa/m², (inaccuracy: ± 0,6 MPa/m²).

5. Conclusions

Here with equation (3) and (12) for the first time correlations are given between the violence determined on the surface of the fragments and the violence determined on the impulse which is obtained by measurements of the force and an integration with respect to time. Thus also the latter quantity becomes independent of time and can be compared

with the first one. In the latter case however more information is contained than in the first one because of the additional knowledge of the transient force.

It was found that in all three configurations (stratified, entrapment and jet) the impulse or the reduced impulse is linear proportional to the surface of the fragments. The correlation constant however depends on the kind of configuration.

The correlation constant of the stratified experiments C_L is much larger than the one of the entrapment experiments C_E. Obviously in stratified experiments a larger percentage of fragments is directly fragmented by water melt contact (thermal fragmentation) than in entrapment experiments. In the latter case the melt water interaction occurred near the bottom of the crucible. Thus the melt in the upper part of the crucible was accelerated like a plug by the high pressure of the steam explosion and in consequence this melt plug fragmented by hydrodynamical effects. But only these fragments which are generated by water and melt contact are involved in producing steam. As a consequence the impulses in entrapment experiments are smaller than those in stratified experiments for the same surface of fragments.

Since the correlation constant of jet experiments C_J (due to the reduction of measurements) has not the same dimension as the other correlation constants, a comparison is not adequate. The linear correlation between the sum of the pressure peaks and the surface of the fragments indicates that all pressure peaks had the same time base approximately and the pressure transducer was positioned at a representative point. To get an appropriate constant C_J for comparisons jet experiments should be performed with better time resolution and with three force transducers (one in each space coordinate) or many pressure transducers alternatively.

Thus the experimentally detected linear correlation can be formulated

$$\int_{t=0}^{\infty} F(t)\, dt = C \cdot A_f \qquad (15)$$

where C is a constant which depends on the configuration of the experiment or the given scenario of an accident.

Since in equation (15) total quantities (total fragment area and impulse) are correlated, also specific quantities must be correlated. Deviding equation (15) by the total mass of fragments m_f leads to

$$E_x = C \cdot S_f \qquad (16)$$

Here E_x is the explosivity which is defined by

$$E_x = \frac{1}{m_f} \int_{t=0}^{\infty} F(t)\, dt \qquad (17)$$

The explosivity is the mass specific impulse which is a proper quantity to classify the violence of melt water interactions. The TEE-Haus would be a good facility for measuring the explosivity of melts at defined initial conditions.

S_f is the fragmentation degree or a specific fragment area i.e. fragment area per mass unit (for instance cm^2/g, s. Fig. 11 of /6/):

$$S_f = \frac{A_f}{m_f} \qquad (18)$$

Relation (16) can be important in accident analyses. It is evident that after an accident where destructions caused by steam explosions have taken place fragments of the solidified melt have to be produced. Thus after the accident of the coal power plant of the IAW in Zolling (Bavaria in Germany) on March 23rd 1987 representative masses of solidified slag fragments could be found at pillars and walls of the plant (for more details s. p. 4-5 to 4-42 of /7/).

With this representative masses of slag fragments the fragmentation degree S_f with (18) could be determined whereas only a small part of the total fragments were analysed. By knowing an appropriate correlation constant C for the accident szenario the explosivity E_x could have been calculated with equation (16). The total fragment mass involved in the steam explosion at the analysed accident could be estimated from the difference between the melt mass of normal operation of the coal power plant and the solidified melt mass of large slag lumps which were found after the accident. Using the explosivity and the total mass of the fragments m_f the impulse can be calculated with equation (17). From the impulse and informations about the duration of the explosion (e.g. recorded by a microphone) the maximum forces which occured in the accident can be estimated.

6. Summary

Till now the violence of a steam explosion was determined either by analysing the degree of fragmentation or by measuring the transient forces or pressures during steam explosions. Here investigations were performed to find out correlations between both conceptions of violence. Therefore experiments were carried out in three configurations i.e. stratified, entrapment and jet experiments. In stratified and entrapment experiments during explosions force transducers were used to measure the transient force and in jet experiments a pressure transducer measured the transient pressure. In all three cases the mass distribution of the fragments was determined by sieve analysis and the total area of fragments was estimated by assuming spherical shapes for all fragments. Linear correlations were detected either between the impulse or the sum of pressure peaks and the total area of fragments. Using the sum of the pressure peaks instead of the impulse means a reduction of resolution of measurements; but in jet experiments installation of pressure transducers is usual.

Theoretical considerations point out that a linear correlation between impulse and total area of fragments assumes superheating of a water layer around the spherical fragments of a constant thickness during the fragmentation process to a constant temperature as the homogeneous nucleation temperature of water and a constant expansion velocity of steam in the main expansion time.

The correlation depends on the configuration of the experiment because of the different percentage of thermal and hydrodynamical fragmentation. The correlation constant does not depend on the melt temperature and different trigger pressures. Further research is required concerning the correlation constant especially its range has to be studied.

Dividing the experimentally detected correlation between the impulse and the total area of fragments by the total mass of fragments leads to a linear correlation of specific quantities as the explosity and the degree of fragmentation. The explosity is the mass specific impulse and the degree of fragmentation is the mass specific surface of fragments. In analyses after an accident the correlation of the explosity and the degree of

fragmentation can be used to estimate the maximum pressure or force occurred during explosion.

References

/1/ G. Fröhlich, B. Zimanowski, V. Lorenz, V. Bayer, E. v. Berg, M. Khan and M. Schindler, "Experiments on simulating of phreatomagmatic explosions and comparing investigations" (in German), IKE Report, IKE Nr. 2-97 (1992).

/2/ B. Zimanowski, G. Fröhlich and V. Lorenz, "Quantitative experiments on phreatomagmatic explosions", Journal of Volcanology and Geothermal Research 48, 341-358 (1991).

/3/ A. Linca, "Experimental investigations on the relationship between fragmentation degree and violence of steam explosions", (in German), Dissertation, University of Stuttgart (in preparation).

/4/ G. Fröhlich, "Propagation of fuel-coolant interactions in multi-jet experiments", NURETH-4 Proc. 4th Intern. Topical Meeting in Nuclear Reactor Thermal-Hydraulics, 1, 282-289 (1989).

/5/ G. Fröhlich, "Propagation of fuel-coolant interactions in multi-jet experiments with molten tin, Nucl. Engrg. Des. 131, 209-221 (1991).

/6/ G. Fröhlich, G. Müller and H. Unger, "Experiments with water and hot melts of lead", J. Non-Equil. Thermodyn. 1, 91-103 (1976).

/7/ G. Fröhlich, H. Unger, A. Linca and A. Schatz, "Possible contribution of violent steam explosions in the accident of the melt furnace coal power plant Zolling block 3 of the IAW", (in German), IKE Report, IKE Nr. 2-84, ages (1988).

Nomenclature

Symbol	Dimension	Meaning
A_c	m^2	cross section of the crucible
A_f	cm^2	total surface of the melt fragments
a_i	µm	mesh width of sieve i
C	Ns/m^2	correlation constant
C_E	Ns/m^2	correlation constant of entrapment experiments
C_J	MPa/m^2	correlation constant of jet experiments
C_L	Ns/m^2	correlation constant of stratified experiments
c_w	J/kg	specific heat capacity
d_i	µm	average diameter of fragments on sieve i
E_x	Ns/kg	explosivity
$F_z(t)$	N	transient force in vertical direction
h	J/kg	vaporization heat of water
i	-	number
k	-	number
m_f	g	total fragment mass
m_i	g	fragment mass on sieve i
m_w	g	mass of superheated water
n	-	number
p_D	MPa	pressure of steam
p_i	MPa	pressure of peak i
S_f	m^2/kg	fragmentation degree
s	µm	thickness of superheated water
T_{hom}	°C	homogeneous nucleation temperature of water
T_{sm}	°C	melt temperature
T_o	°C	initial temperature of water
t	s	time
V_D	m^3	volume of steam
v_z	m/s	velocity component in vertical direction
$\overline{v}_z$	m/s	mean value of v_z with respect to time
z_o	cm	maximum thickness of the fragmentation zone in layer experiments
ρ	m^3/kg	density of melt

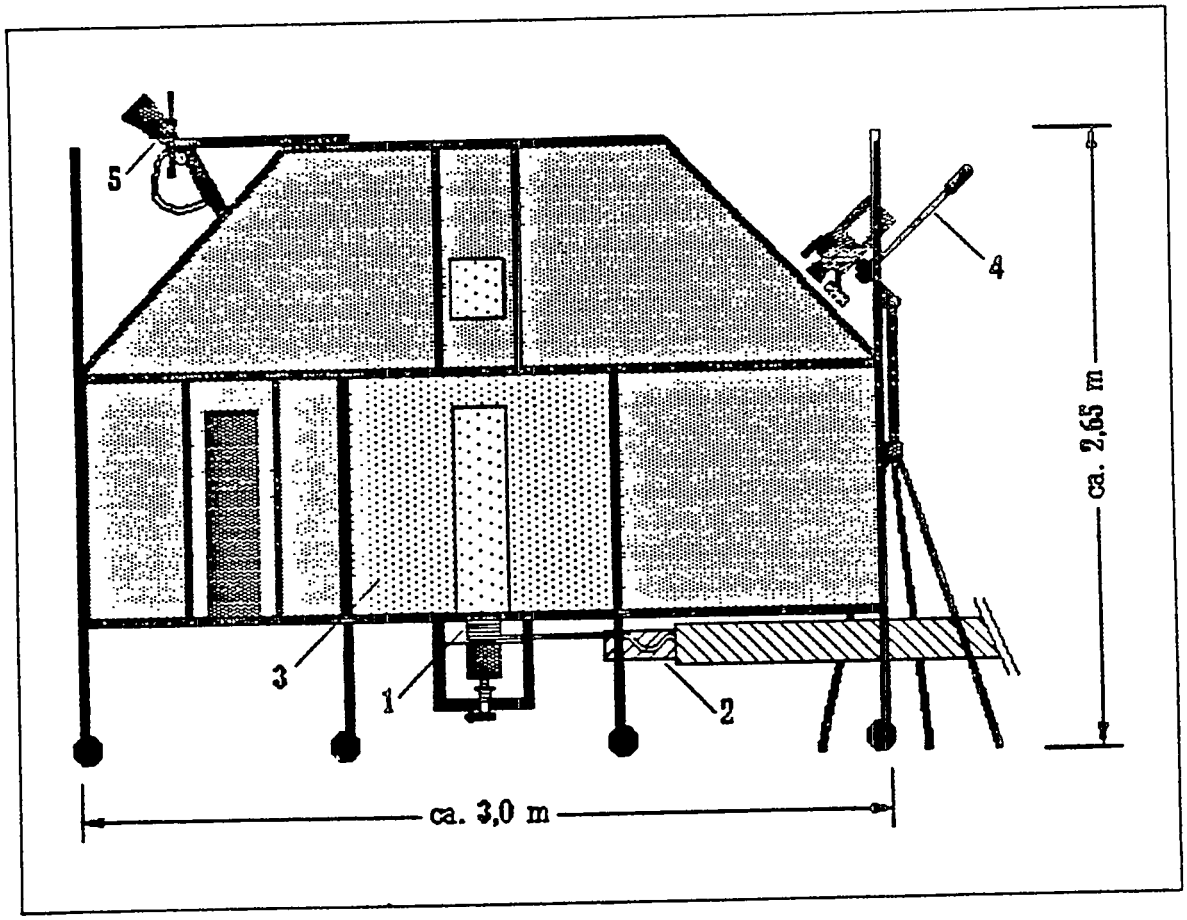


Fig. 1: View of the outside of the TEE-Haus, the set-up of layer and entrapment experiments

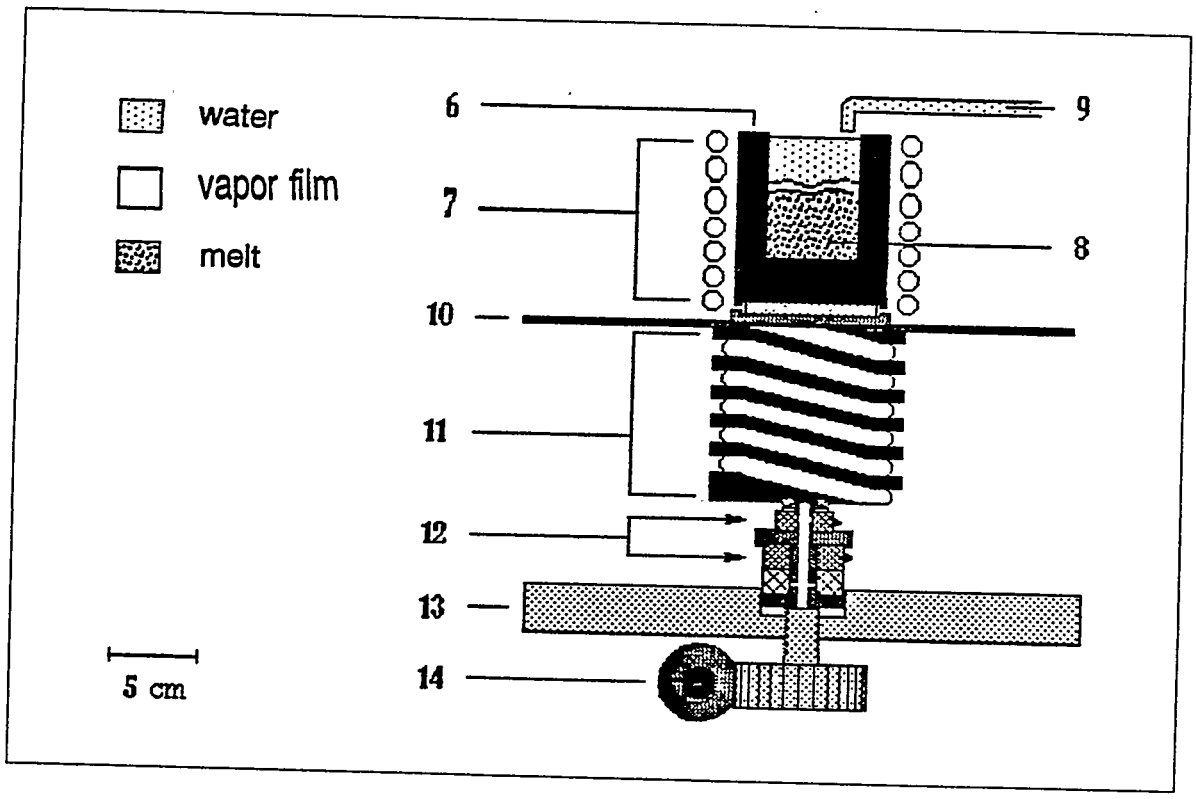


Fig. 2: Crucible with substructure

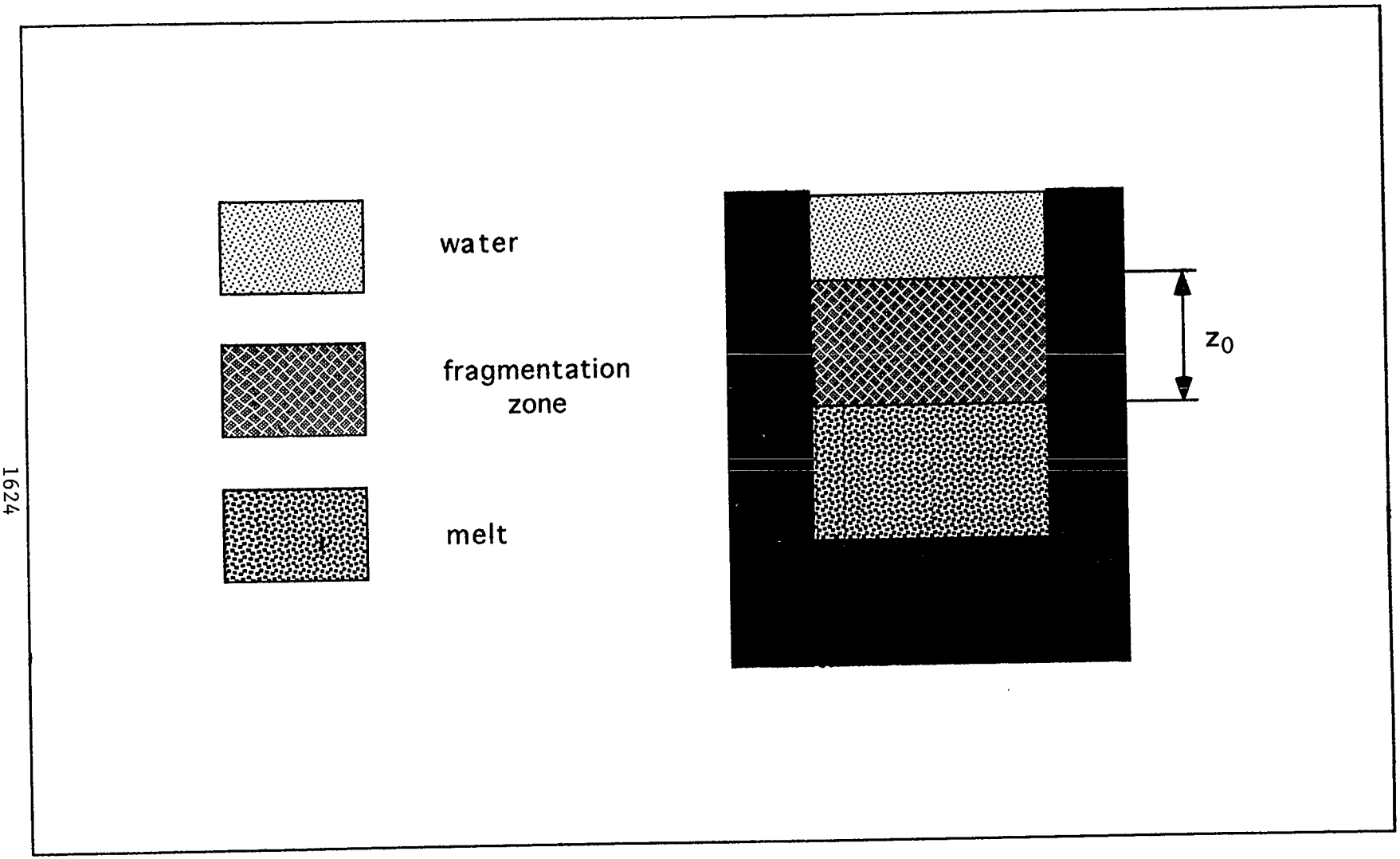


Fig. 3: Maximum extension of the fragmentation zone

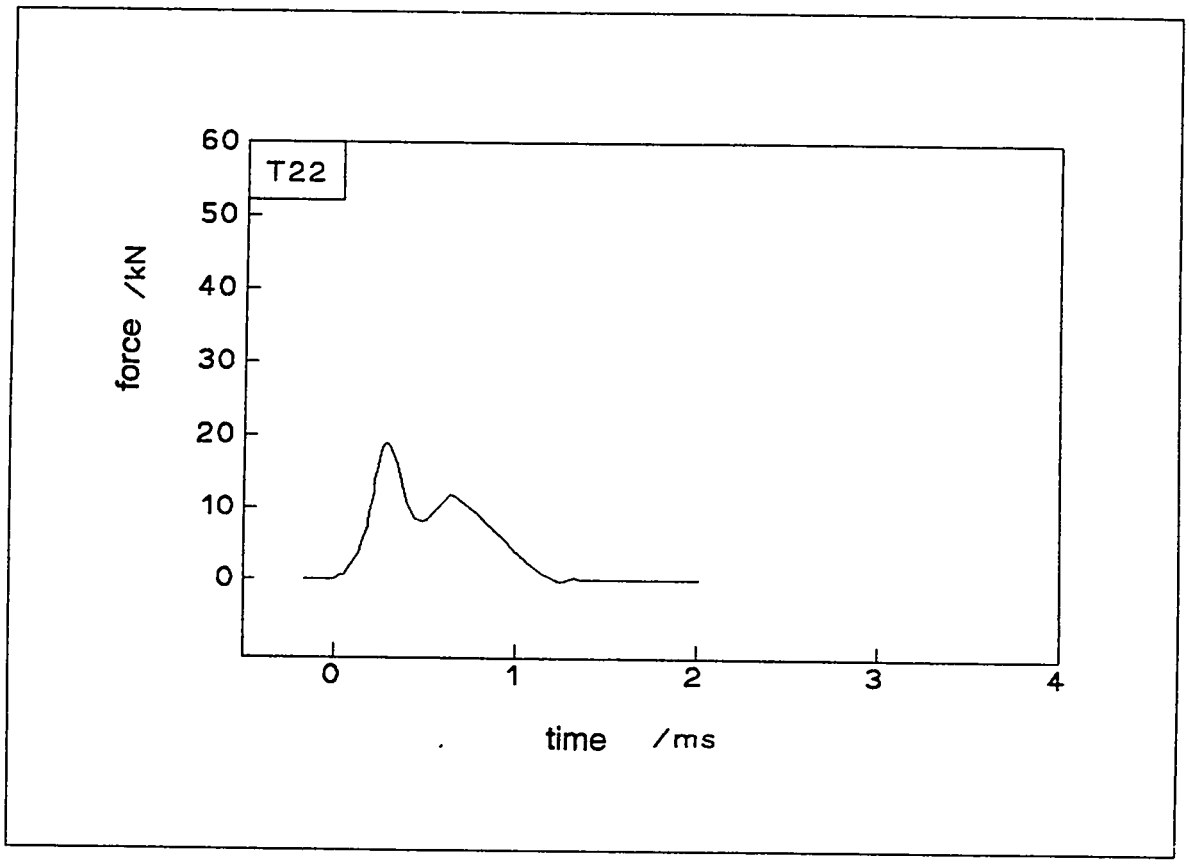


Fig. 4: Measured force of the layer experiment T 22

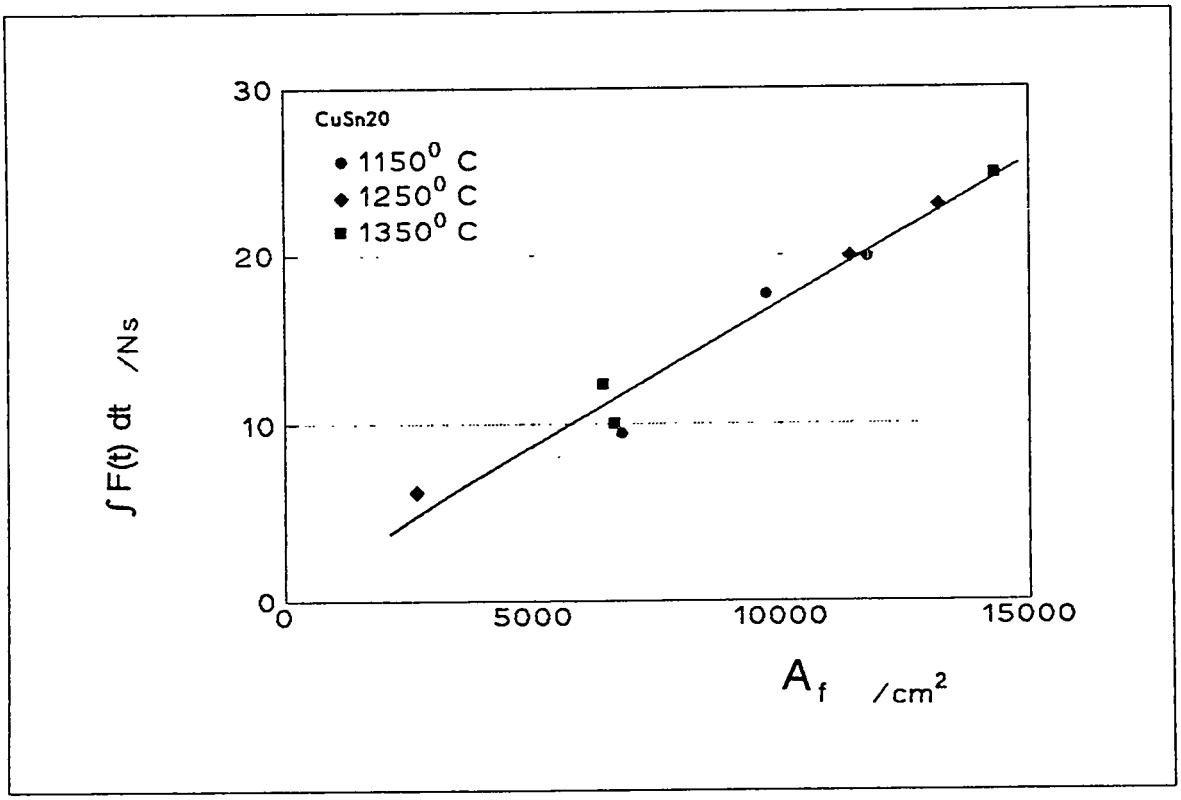


Fig. 5: Plot of impulse versus total surface of fragments of layer experiments

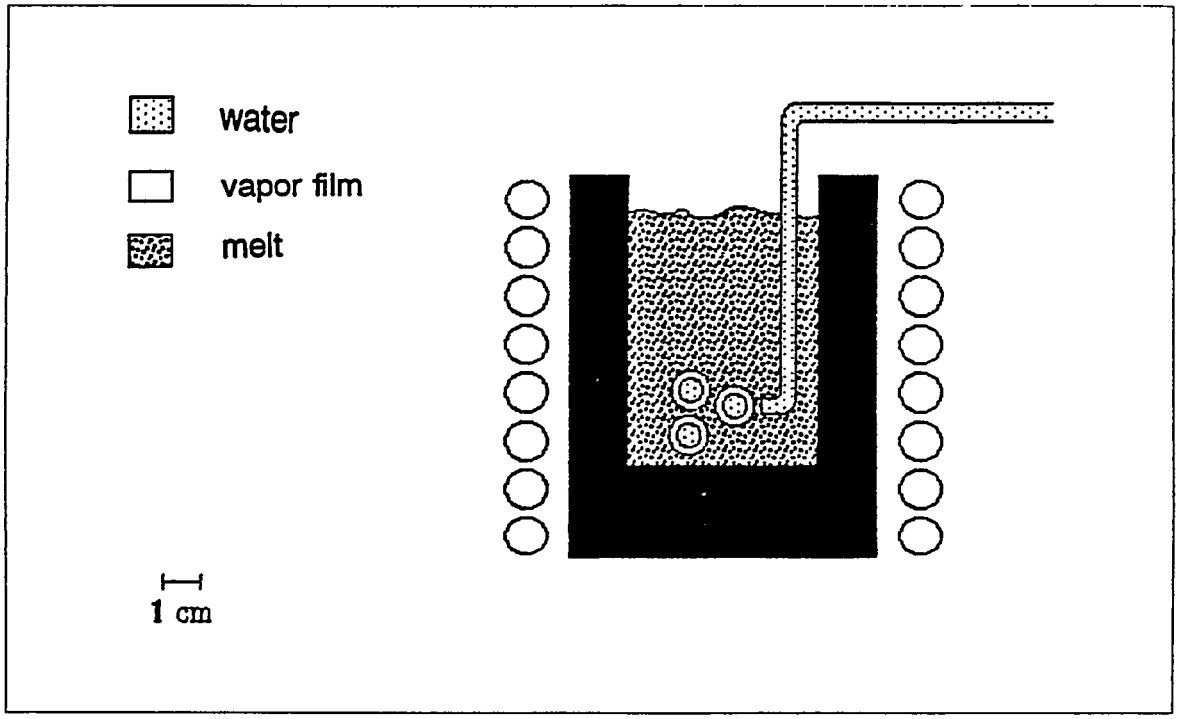


Fig. 6: Water injection in the crucible of the entrapment experiments

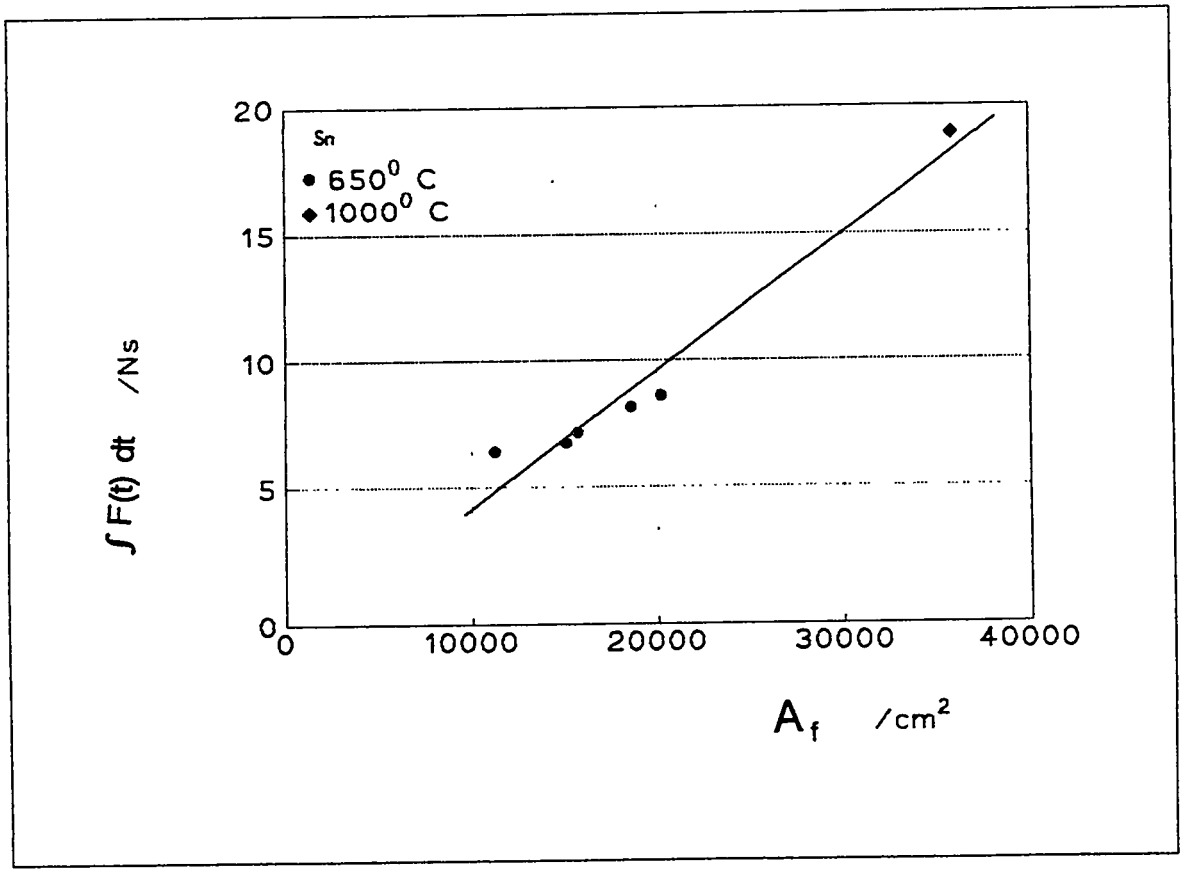


Fig. 7: Plot of impulse versus total surface of fragments of entrapment experiments

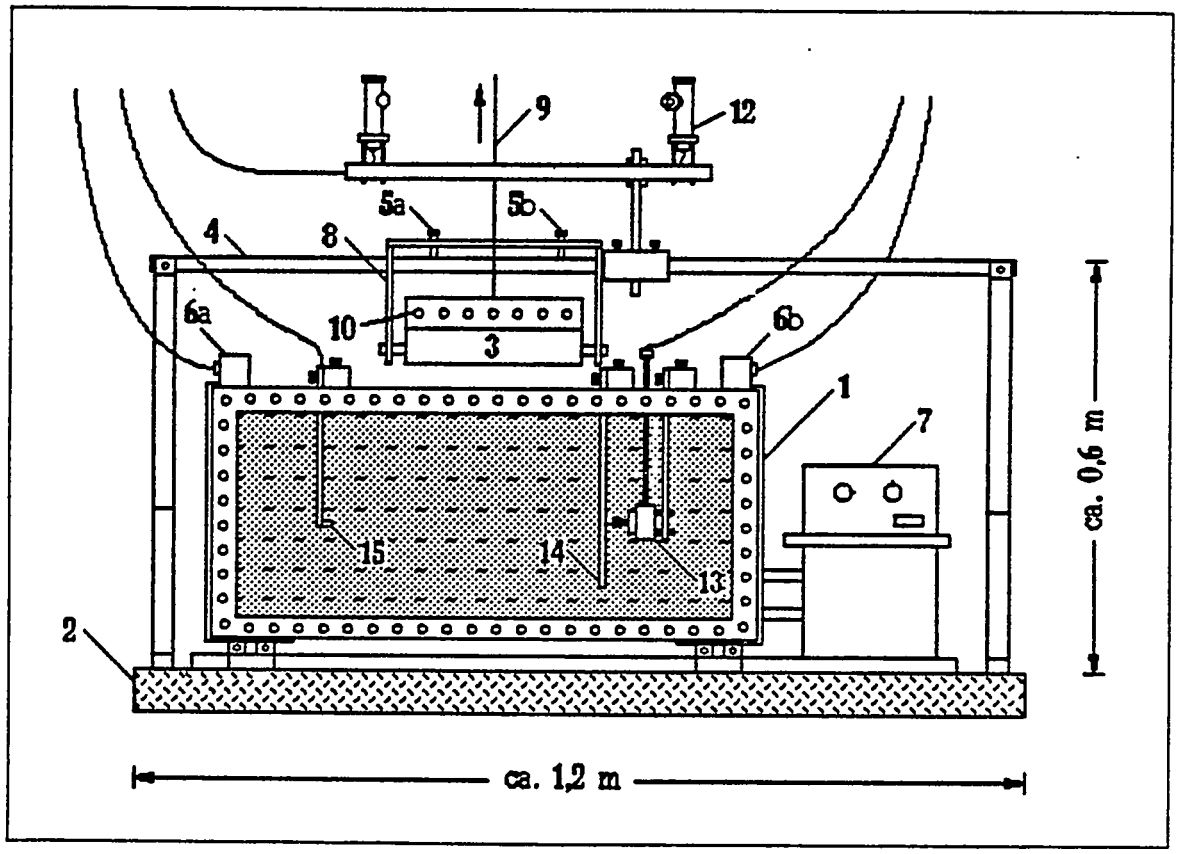


Fig. 8: View of the outside of the set-up of the jet experiments

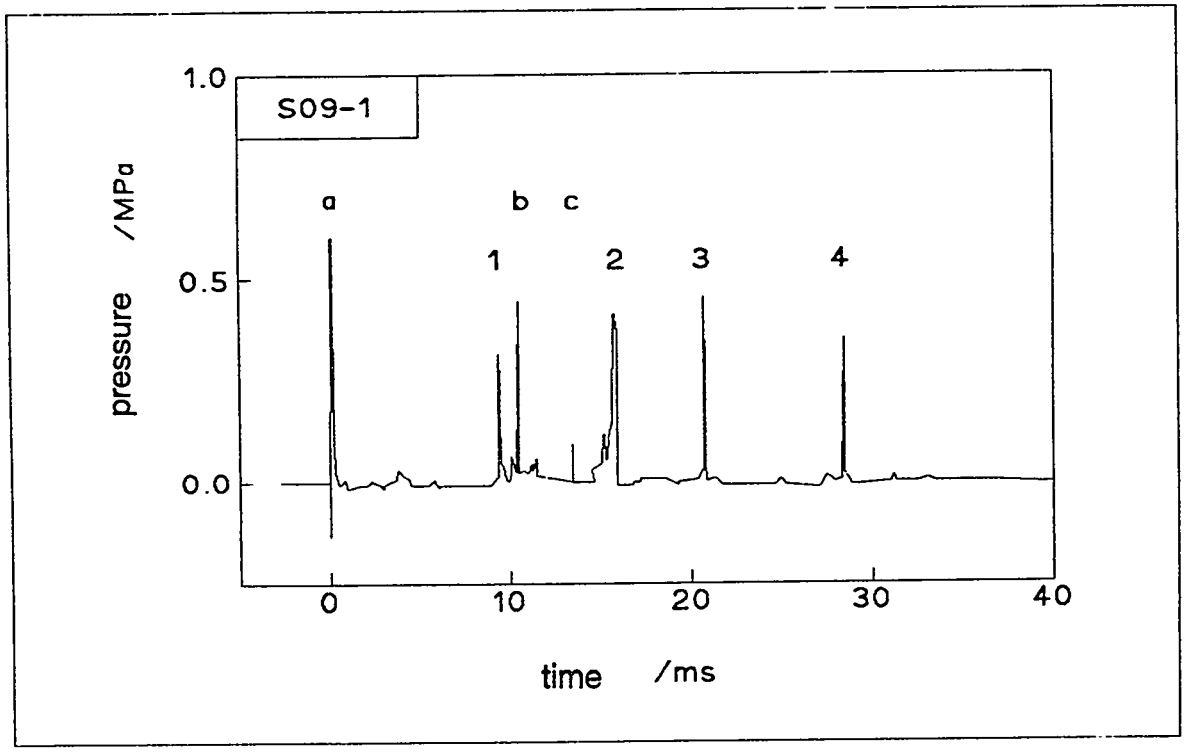


Fig. 9: Pressure peaks of the jet experiment S 09-1

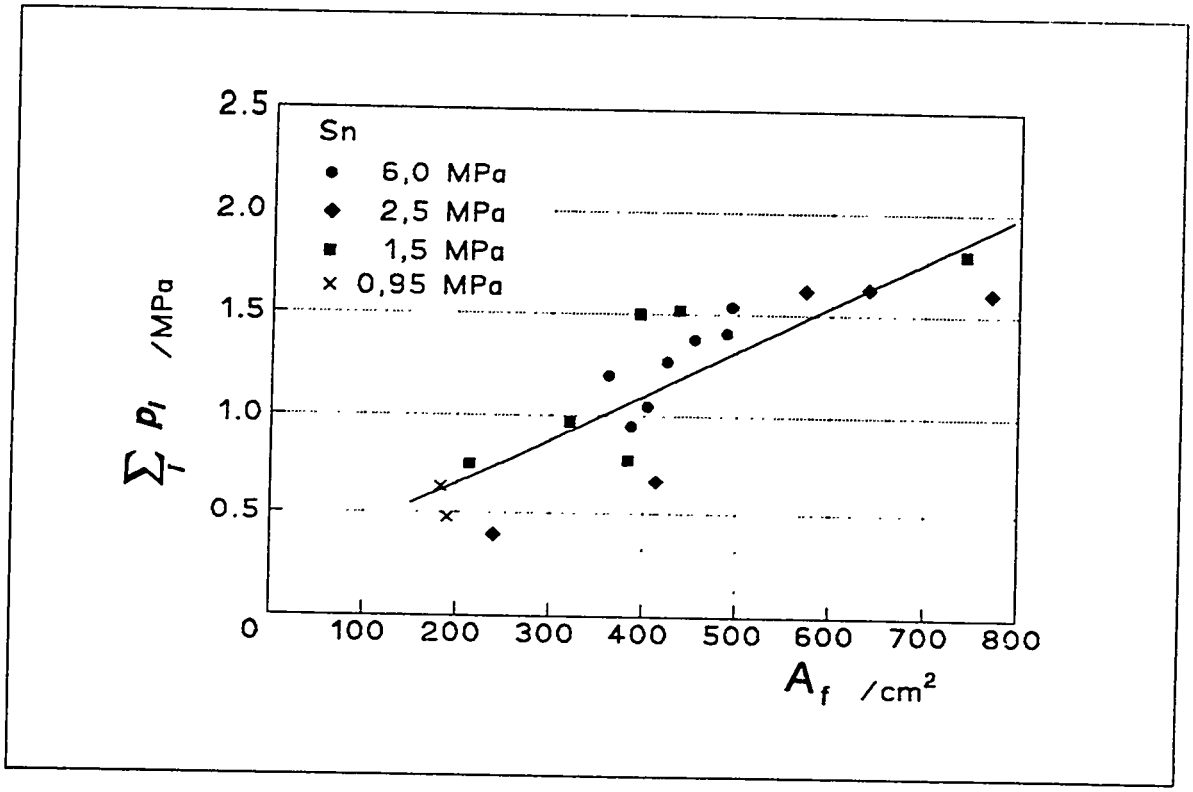


Fig. 10: Plot of the sum of the peaks versus total surface of fragments of jet experiments

a_i
20 µm
32 µm
45 µm
63 µm
90 µm
125 µm
180 µm
250 µm
355 µm
500 µm
710 µm
1000 µm
1400 µm
2000 µm
2800 µm

Table 1: Width of the meshes of the used sieves

	Exp. Nr.	T_{Sm} ° C	m_f g	A_f cm^2	$\int F(t)\,dt$ Ns
1	T21	1350	159	6417	12,4
2	T22	1350	196	6656	10,0
3	T23	1250	218	13197	22,9
4	T24	1250	260	11416	19,9
5	T25	1150	262	9716	17,7
6	T26	1250	89	2648	5,9
7	T28	1150	218	6794	9,4
8	T29	1150	195	11759	19,8
9	T30	1350	227	14304	24,8

Table 2: Results of the layer experiments (measuring errors: $\Delta T = \pm 1$ °C, $\Delta m_f = \pm 1$ g; $\Delta A_f = \pm 4$ cm², $\Delta \int F(t)dt = \pm 0{,}2$ Ns)

	Exp. Nr.	T_{Sm} °C	m_f g	A_f cm^2	$\int F(t)\,dt$ Ns
1	Z02	650	335	15078	6,7
2	Z04	650	380	15677	7,1
3	Z05	650	480	11244	6,4
4	Z06	650	413	18555	8,1
5	Z09	650	401	20221	8,5
6	Z10	1000	470	35860	18,9

Table 3: Results of the entrapment experiments (measuring errors: $\Delta T = \pm 1$ °C, $\Delta m_f = \pm 1$ g, $\Delta A_f = \pm 4$ cm^2, $\Delta \int F(t)dt = \pm 0{,}2$ Ns)

	Exp.-Nr.	p_{Tr} MPa	$\sum_i p_i$ MPa	A_f cm^2	m_f g
1	S09-1	6,0	1,55	492	21,6
2	S09-2	6,0	1,41	487	19,4
3	S09-3	6,0	0,95	386	16,5
4	S09-4	6,0	1,38	453	19,8
5	S09-5	6,0	1,27	424	18,2
6	S09-6	6,0	1,20	361	16,5
7	S09-7	6,0	1,05	403	14,2
8	S10-2	2,5	0,67	413	21,2
9	S10-6	2,5	1,63	639	32,3
10	S10-7	2,5	1,61	770	37,4
11	S10-8	2,5	0,39	239	12,3
12	S10-9	2,5	1,62	571	30,4
13	S11-2	1,5	1,52	435	20,9
14	S11-5	1,5	0,78	383	20,8
15	S11-6	1,5	1,80	743	37,8
16	S11-7	1,5	0,97	320	13,9
17	S11-8	1,5	1,50	394	20,2
18	S11-9	1,5	0,76	213	11,1
19	S12-2	0,95	0,64	183	8,5
20	S12-3	0,95	0,48	190	8,1

Table 4: Results of the jet experiments (measuring errors: $\Delta p_{Tr} = \pm 0{,}03$ MPa, $\Delta \Sigma$ pi = $\pm 0{,}03$ MPa, $\Delta A_f = \pm 2$ cm^2, $\Delta m_f = \pm 0{,}5$ g)

Analysis Of Supercritical Vapor Explosions Using Thermal Detonation Wave Theory

B.I. Shamoun, M.L. Corradini

Department of Nuclear Engineering and Engineering Physics
University of Wisconsin-Madison, WI 53706. U.S.A
(608) 263-4447, (608) 263-2196

Abstract

The interaction of certain materials such as Al_2O_3 with water results in vapor explosions with very high (supercritical) pressures and propagation velocities. A quasi-steady state analysis of supercritical detonation in one-dimensional multiphase flow was applied to analyze experimental data of the KROTOS (26-30) set of experiments conducted at the Joint Research Center at Ispra, Italy. In this work we have applied a new method of solution which allows for partial fragmentation of the fuel in the shock adiabatic thermodynamic model. This method uses known experiment values of the shock pressure and propagation velocity to estimate the initial mixing conditions of the experiment. The fuel and coolant were both considered compressible in this analysis. In KROTOS 26, 28. 29. and 30 the measured values of the shock pressure by the experiment were found to be higher than 25, 50, 100, and 100 Mpa respectively. Using the above data for the wave velocity and our best estimate for the values of the pressure, the predicted minimum values of the fragmented mass of the fuel were found to be 0.026. 0.04, 0.057, and 0.068 kg respectively. The predicted values of the work output corresponding to the above fragmented masses of the fuel were found to be 40, 84, 126. and 150 kJ respectively, with predicted initial void fractions of 11%, 12.5%, 8%, and 6% respectively.

1 Introduction

Over the last few decades the vapor explosion phenomenon has been of concern to safety analysts due to its implications for many industrial applications. In a nuclear reactor, for example, the Loss Of Coolant Accident (LOCA) and the malfunctioning of the emergency cooling system results in a dramatic increase in the temperature of the fuel materials due to the decay heat produced by fission products. Given a prolonged absence of cooling, the temperature reaches the melting point of the fuel. the melt falls down to the bottom of the reactor vessel and mixes with residual water where the vapor explosion process could occur and may threaten the integrity of the

pressure vessel and containment; due to its expansion work or dynamic pressures [1]. Vapor explosions have also been observed in some other fields of applications such as in the metal casting industries [2]. the paper industries [3], the transportation of natural gas [4] and others.

Since the vapor explosion is considered to be a rather complicated multiphase phenomenon, we have not seen a complete theoretical model that can simulate the whole process in which the predicted results match those obtained from the experiments. In the previous study of subcritical vapor explosions [5] we discussed the shock adiabatic thermodynamic model which was originally proposed by Board and Hall in 1974 [6]. It was shown that the assumption of total thermal energy transfer from the fuel to the coolant in this model leads to the prediction of upper bound for the shock pressure and work output. A modified model was, therefore. suggested such that a partial fragmentation of the fuel is allowed in the explosion using a new method of solution. The modified model uses known experiment values of the shock pressure and propagation velocity to predict the initial conditions and work output of the experiment. The model formulation and assumptions are shown in Appendix A. In the present work we have tried to apply this model in the analysis of supercritical vapor explosions. To avoid any errors that might be generated as a result of using constant fuel thermodynamic properties at very high temperature and pressure, a complete set of fuel equations of state were derived and shown in Appendix B.

The Hugoniot theory employed in the shock adiabatic model to simulate the vapor explosion phenomenon is based on the suggested analogy between chemical detonation and thermal detonation by Board et al. If the analogy exists. there is only one state on the Hugoniot where the explosion is steady state and self-sustained. This state corresponds by analogy to the Chapman-Jouguet detonation state (CJ state).At the CJ state. the velocity of the materials is the sonic velocity, the entropy is minimum. and the Rayleigh line which connects the initial state of the mixture to any other state is tangent to the Hugoniot. The CJ state is determined by solving the Hugoniot equation given the initial mixture conditions. The general form of this equation is given by,

$$(h_1 - h_2) + (p_1 - p_2)(v_2 + v_1) = 0 \qquad (1)$$

Our method of solution suggests that if the shock pressure and the propagation wave velocity of the mixture are given by the experiment, it is possible to solve the Hugoniot equation for the initial conditions using an iterative method. Thus, one is able to determine the mass fraction of the fragmented fuel and estimate the work output given closure relation.

According to the detonation theory, the CJ solution to the Hugoniot equation is determined if the predicted velocity equals the measured prop-

agation velocity from the experiment. The homogeneous sound speed of multicomponent mixture was used to calculate the propagation velocity in this analysis. The general expression of the sound speed of two components mixture is given by the following equation.

$$u_{sound} = \frac{1}{\{\frac{1}{v_{mix}}[\frac{x_1 v_1^2}{c_1^2} + \frac{x2v_2^2}{c_2^2}]\}^2} \tag{2}$$

Using the velocity criterion to determine the solution to the Hugoniot equation, however, showed that a family of Hugoniot solutions can be generated such that each solution corresponds to a certain fractional value of the fragmented fuel in the explosion. To determine which one of these solutions represents the actual CJ solution another piece of information is required.

D.L. Frost, J.H.S Lee and G. Ciccarelli [11] discussed the sonic velocity criterion in selecting the solution to the Hugoniot equation at the CJ point and found that this criterion is not equivalent to drawing a tangent to the Hugoniot curve. Thus in order to determine a single solution to the Hugoniot equation at the CJ state, the tangency condition of the Rayleigh line must be satisfied. The solution obtained by satisfying this condition is also found to be self-consistent thermodynamically and corresponds to the minimum entropy change.

In the present work, the Hugoniot analysis has been carried out by applying the conservation laws of mass, momentum and energy to a one-dimensional homogeneous mixture of Al_2O_3 and water to analyze the experimental data of supercritical vapor explosions. This creates a special challenge to such analysis since no vapor exists in the explosion zone after the explosion propagates. The general model used in this investigation is based on that used in the previous work [5] to analyze the subcritical vapor explosion of tin and water FCI.

2 Results and Discussion

The KROTOS set of experiments (26-30), conducted at the Joint Research Center at Ispra, Italy to study the melt-coolant premixing and vapor explosion in 1-D geometry, was chosen as our benchmark experiments in this analysis [7]. In this set of experiments ceramic fuel Al_2O_3 at 2573-2673 K and water at different subcooling temperatures were used to simulate typical nuclear reactor materials during an FCI. The shock pressure measured as a result of the explosion in this set of experiments is supercritical. The uncertainty in the measured values of the pressure, however, is relatively high since most of the pressure gages were maxed out. Nevertheless, our objective in choosing KROTOS 26-30 tests is to perform the Hugoniot calculations in

the supercritical region of the p-v diagram where the vapor does not exist in the explosion zone.

The data obtained from the experiments are the shock pressure and propagation velocity. The work output was not measured during these experiments. Therefore, we tried to estimate the experimental work output using the data measurement of the pressure entering and exiting the test tube with two different methods.

Method 1

The experimental work output (i.e., kinetic energy) is approximated by the mechanical impulse delivered to the slug of the mixture in the test tube, where the explosion takes place. Assuming a 1-D flow and applying Newtons first law, the velocity can be related to the impulse as follows

$$u = \frac{A \int_{t_1}^{t_2} p dt}{m_{mix}} = \frac{AI}{m_{mix}} \tag{3}$$

where A is the cross section area of the test tube ($78.5cm^2$). The work output can then be obtained from the following equation.

$$work = \frac{m.u^2}{2} = \frac{(IA)^2}{2m_{mix}} \tag{4}$$

It should be noted that the value of the impulse depends on the duration of the pulse $(t_2 - t_1)$. The results of the work output obtained using this method for KROTOS 26-30 are shown in table 1.

Method 2

In this method the experimental work output is approximated to the compression work done to the air in the vessel as a result of the explosion. The air was considered as an ideal gas and the work was found using the following equation.

$$work = \frac{[p_2 v_2 - p_1 v_1]}{\gamma_{air} - 1} m_{air} \tag{5}$$

where γ_{air} is the specific heat ratio for air taken to be 1.4, and m_{air} is the mass of the air in the vessel, 0.35 kg. The results of the work output obtained using this method are shown in table 2.

It is clear from tables 1 and 2 that the work output is not the same for any given experiment. The main reason of this disrepancy is the uncertainty in the measurement of the pressure as it was mentioned earlier. In general, these two methods underestimate the actual work output since the losses were not considered during these calculations.

experiment no.	pressure transducer	total mass of mixture [Kg]	pressure pulse [bar]	time [ms]	Impulse [KPa.m^2.sec]	kinetic energy [KJ]
KROTOS-26	K2	8.63	260.0	1.8	367.5	8.0
KROTOS-28	K3	8.643	502.0	1.0	395.0	9.0
KROTOS-29	K3	9.18	1040.0	1.2	980.0	52.0
KROTOS-30	K3	8.95	1060.0	1.5	1248.3	87.0

Table 1: Summary of estimated experimental work output of method 1.

experiment no.	pressure transducer	air pressure at state 2 [bar]	air spec. vol. at state 2 [m^3/Kg]	work per unit mass of air [KJ/Kg air]	work [KJ]
KROTOS-26	C2	1.5	0.644	27.0	9.5
KROTOS-28	C2	4.0	0.320	104.6	36.0
KROTOS-29	C3	4.5	0.294	115.5	40.0
KROTOS-30	C2	8.0	0.195	175.0	70.0

Table 2: Summary of estimated experimental work output of method 2.

The predicted work output by the model due to the mixture expansion behind the shock from the high pressure state to the end of state pressure was calculated using the following equation.

$$W_{23} = \Delta e_{23} - K.E - W_{comp} \tag{6}$$

$$\Delta e_{23} = (m_f e_{f2} + m_{c2} e_{c2}) \tag{7}$$

$$K.E. = (m_f + m_c)\frac{(u_1 - u_2)^2}{2} \tag{8}$$

where:

W_{23} : work output due to the expantion process.
m : mass,
e : internal energy,
$K.E.$: kinetic energy of the materials behind the shock,
$(u_1 - u_2)$: velocity of the materials behind the shock front in the lab frame,
subscripts f and c refer to the fuel and coolant respectively,
subscripts 1,2,3 refer to states 1,2,3 respectively.

Analysis of KROTOS 26

In this test, 1.0 kg of molten Al_2O_3 at 2573 K was mixed with 7.2 kg of water at 40 K subcooled. A steam explosion occurred in this test resulted in an explosion pressure greater than 25 MPa and a propagation wave velocity of 650 m/sec. The estimated value of the experimental work output was found to be $\sim$ 10 kJ.

The Hugoniot calculations were performed using the above experimental data output. The average value of the shock pressure was estimated by the authors to be 26 MPa during these calculations. The results obtained are as follows. The predicted minimum mass of the fragmented fuel in the explosion was found to be 0.026 kg, which represents 2.6% of the total mass of the fuel originally mixed with water. The predicted work output by the model corresponding to the above fragmented mass of the fuel was found to be 40 kJ. The initial void fraction of vapor in the mixing phase was found to be 11%.

It should be noted that the solution to the Hugoniot equation which produced the above results was determined by satisfying the conditions applied by detonation theory to the thermal detonation. That means for the given experimental shock pressure the predicted homogeneous sound speed of the mixture behind the shock equals to the measured speed from the experiment, the Rayleigh line is tangent to the Hugoniot curve at the CJ-point.

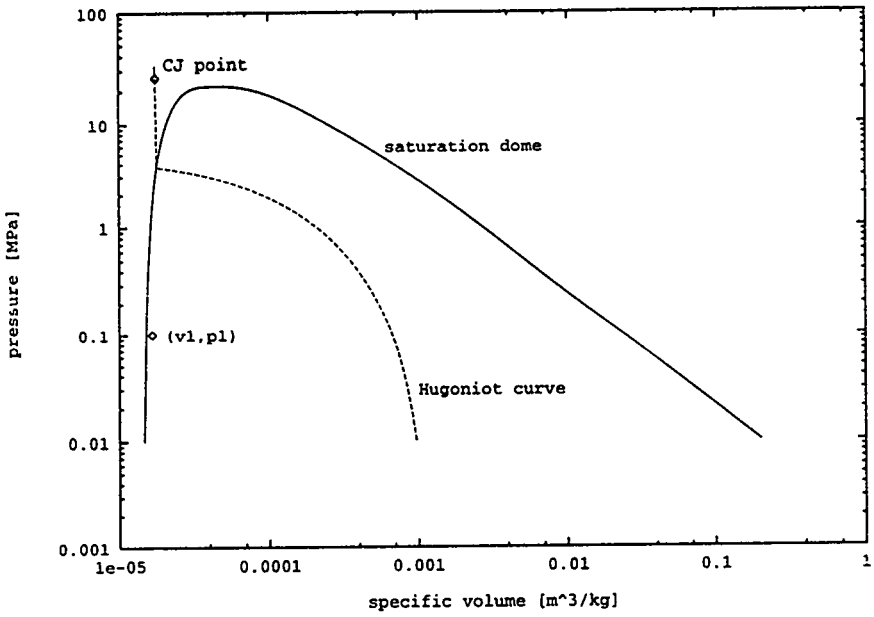


Figure 1: Hugoniot curve for Al2O3-water. KROTOS-26.

and the change in the entropy along the Hugoniot curve is a minimum at the CJ-point. The Hugoniot curve was plotted on the p-v diagram and shown in figure 1. Figure 2 shows the tangency of the Rayleigh line to the Hugoniot curve at the CJ point.

The higher value of the predicted work output compared to the estimated experimental work output is not surprising, however, since there are many factors that could cause this discrepancy. First, the isentropic expansion of the mixture behind the shock suggested by the shock adiabatic thermodynamic model overestimates the work output. Second, the inaccurate methods used to estimate the experimental work also contributes to this difference. Third, the uncertainty in the pressure measurements has a major influence on the stability of the Hugoniot calculations in general. We should also mention that our assumption of the initial and final temperatures of the vapor T_{v1} and T_{v2} could also have its effect on the results (see Appendix A). Nevertheless, the new model shows a great improvement in the predicted results obtained compared with the original model or any other models.

Analysis of KROTOS 28

In this test, 1.443 kg of molten Al_2O_3 at 2673 K was mixed with 7.2 kg of water at 13 K subcooled. The explosion pressure measured during the experiment was found to be greater than 50 MPa. The corresponding prop-

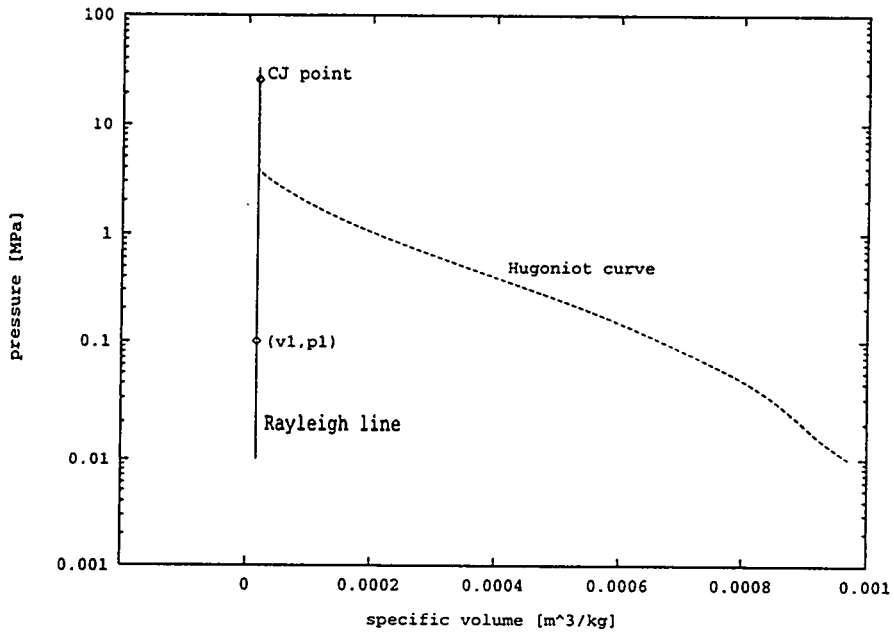


Figure 2: Rayleigh line and Hugoniot curve for Al2O3-water, KROTOS-26.

agation wave velocity was found to be 830 m/sec. The estimated value of the experimental work output was found to be $\sim$ 25 kJ.

The results predicted by the model using the above experimental data are the following. The minimum mass of the fragmented fuel was found to be 0.04 kg (2.8% of the total mass of the fuel). The predicted work output corresponding to the above value of the fragmented mass of fuel was found to be 84 kJ. The initial void fraction of vapor was found to be 12.5%. The explosion pressure in this analysis was estimated to be 55 MPa.

The effect of decreasing the subcooling temperature on the value of the work output did not show up in this test clearly, although the void has increased somewhat. The predicted work output, however, in this test was higher than that in KROTOS 26, since the difference in the fuel mass in these two tests dominates the explosion calculational results. The Hugoniot curve and the tangency of the Rayleigh line to the Hugoniot curve on the p-v diagram are shown in figures 3 and 4 respectively.

Analysis of KROTOS 29

In this test, 1.53 kg of Al_2O_3 at 2573 K was mixed with 7.65 kg of water at 80 K subcooled. The explosion in this test was self-triggered. It was reported that all the pressure transducers attached to the test tube were broken. An explosion pressure greater than 100 MPa, however, was recorded by the K3

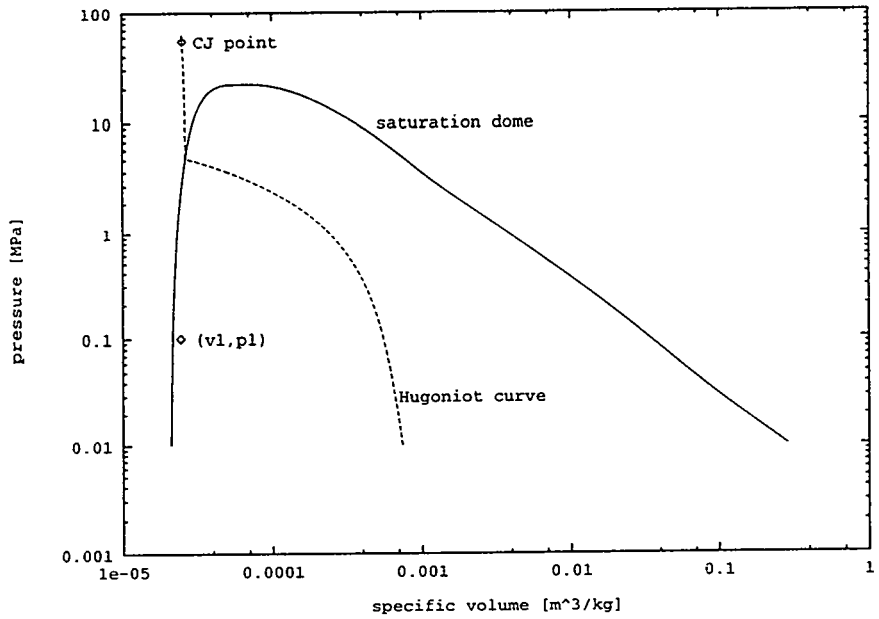


Figure 3: Hugoniot curve for Al2O3-water. KROTOS-28.

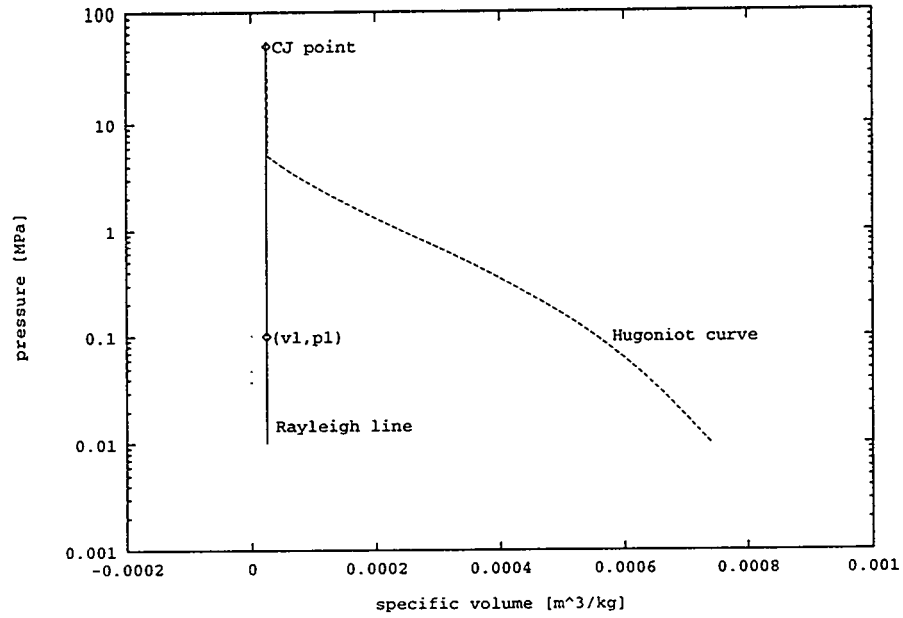


Figure 4: Rayleigh line and Hugoniot curve for Al2O3-water. KROTOS-28.

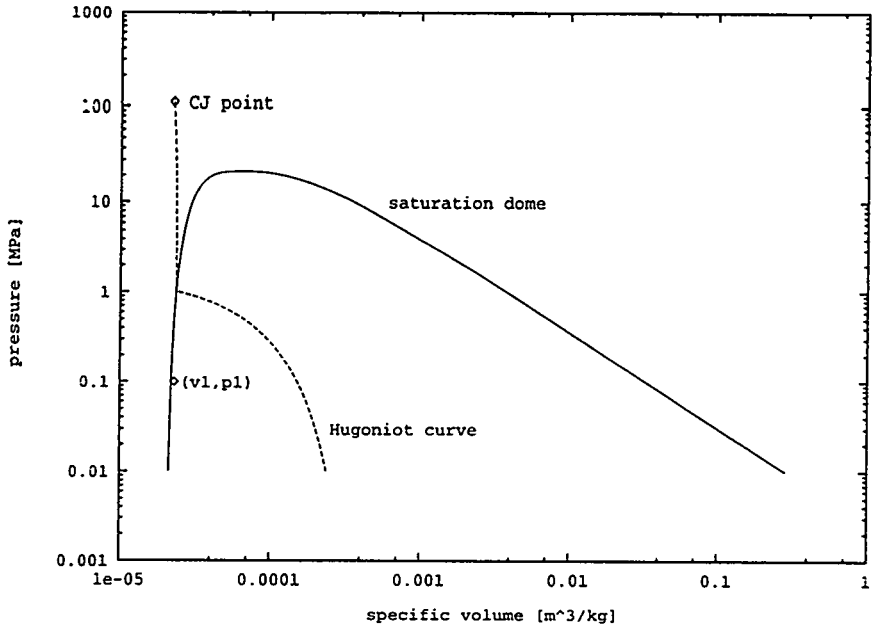


Figure 5: Hugoniot curve for Al2O3-water, KROTOS-29.

pressure transducer. The propagation wave velocity was found to be 1145 m/sec. The estimated value of the experimental work output was found to be $\sim$ 50 kJ.

Using the above experimental data with an estimated value of 110 MPa for the shock pressure, the Hugoniot calculations showed that the minimum mass of the fragmented fuel is 0.057kg (3.7% of the total mass of the fuel). The predicted work output was found to be 126 kJ. The initial void fraction of the vapor was 8%. The predicted work output in this experiment appeared to be greater than that obtained in the KROTOS 26 and KROTOS 28 tests. This is not surprising since the decrease in the subcooling temperature of the water is expected to increase the explosion pressure and the propagation velocity and make the explosion more violent. The Hugoniot curve and the Rayleigh line with the Hugoniot curve for this test were plotted and shown in figures 5 and 6 respectively.

Analysis of KROTOS 30

A mass of 1.516 kg of Al_2O_3 at 2573 K was mixed with 7.45 kg of water at 80 K subcooled. This test was a repetition of KROTOS 29 to avoid self-triggering of a vapor explosion by introducing some modification to the test tube. However, these modifications did not inhibit the spontaneous triggering and another spontaneous explosion resulted.

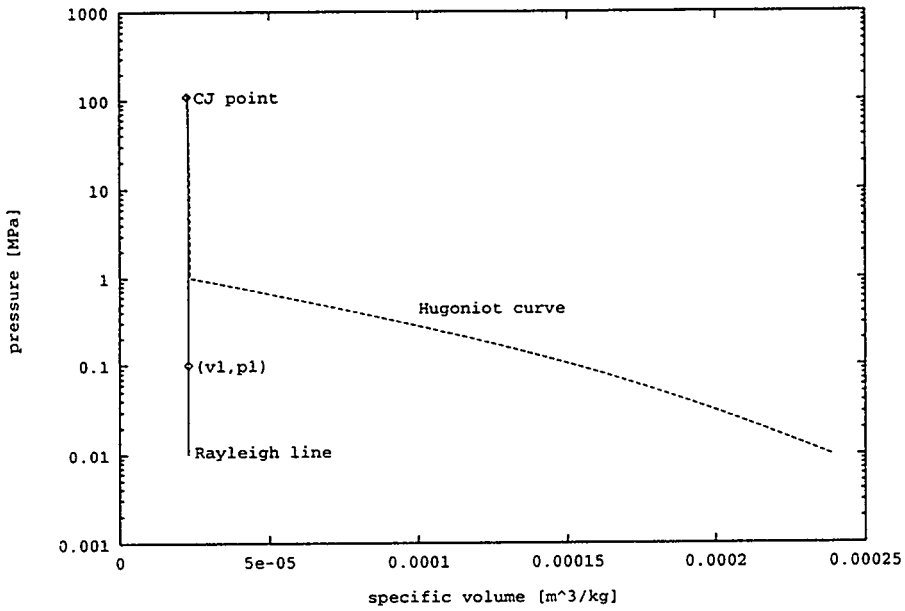


Figure 6: Rayleigh line and Hugoniot curve for Al2O3-water, KROTOS-29.

An explosion pressure greater than 100 MPa and a propagation wave velocity of 1300 m/sec were obtained in this experiment. It was reported. however, that four out of seven pressure transducers were blown out of the test tube and destroyed. Also, due to the strong water hammer, the twelve bottom plate bolts were plastically elongated up to 6 mm and the test tube diameter was distended by 1%. It was assumed that the impact pressure must have been at least 150 MPa, [12]. Based on this experimental data. one can conclude that the explosion was more energetic in KROTOS 30 than KROTOS 29, although almost same conditions were employed in running both experiments. The estimated value of the work output in this experiment was found to be $\sim$ 80 kJ.

In the calculations, the shock pressure was taken to be 150 MPa. The results obtained from this analysis are as follows. The minimum mass of the fragmented fuel was found to be 0.068 kg, (4.5% of the total mass of the fuel). The predicted work output was found to be 150 kJ. The initial void fraction of the vapor was found to be 6%. The plots of the Hugoniot curve and the Rayleigh line with the Hugoniot curve on the p-v diagram for this test are shown in figures 7 and 8 respectively.

The computational method used to analyze the KROTOS (26-30) set of

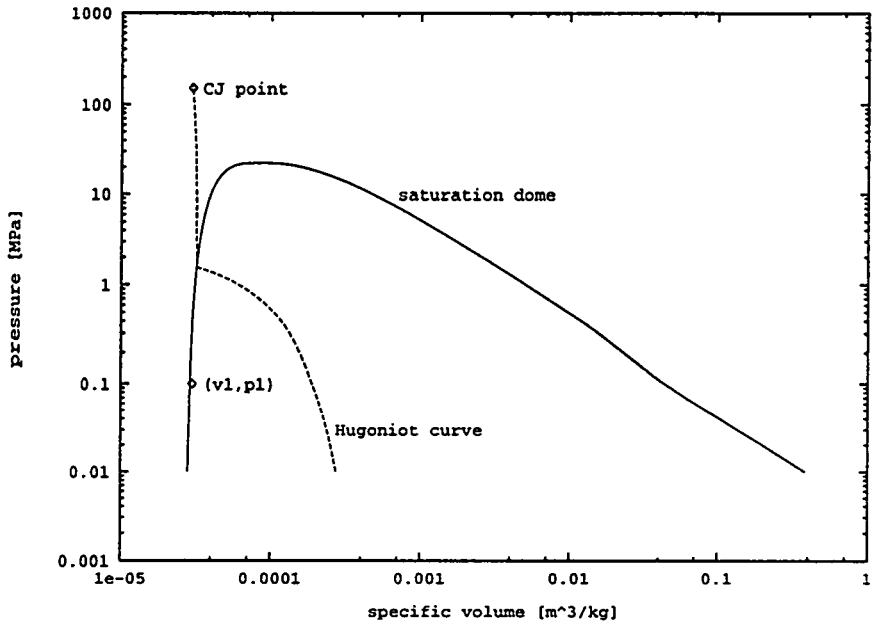


Figure 7: Hugoniot curve for Al2O3-water. KROTOS-30.

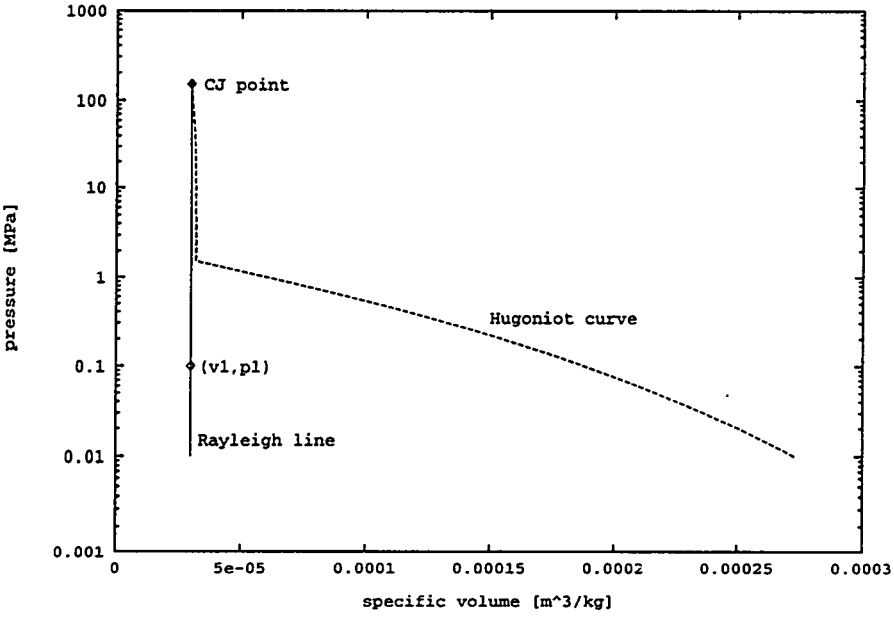


Figure 8: Rayleigh line and Hugoniot curve for Al2O3-water, KROTOS-30.

experiments using Al_2O_3-water mixture shows that the predicted value of the work output varies with the mass fraction of the fragmented fuel. The predicted work by the model, however, was always higher than the estimated experimental work output. There are two main reasons for this discrepancy: the uncertainty in the pressure measurements during the these experiments could have underestimated the actual pressure and. therefore, the work output. second, it is well known that the predicted work by the thermodynamic model is always higher than the measured work from the experiment because of the assumption that various processes occur adiabatically with no irreversibilities.

3 Conclusion

In this paper we have examined the supercritical explosions of Al_2O_3 with water using a modified thermodynamic model for the explosion detonation. The proposed model has been successfully applied to analyze the supercritical vapor explosion such that the condition of complete fragmentation of the fuel in an energetic FCI is relaxed. The new model can be used to predict the mass fraction of the participating materials in the vapor explosion process. The main features of this work are as follows.

1. A new method of solution has been developed using known experimental values of the shock pressure and propagation velocity to estimate the initial conditions of the experiment and the work output.

2. Use of the proposed model for the analysis of thermal detonation suggests that the tangency condition is the most reliable condition to determine the unique solution in the Hugoniot calculations.

3. Uncertainty analysis of the pressure on the predicted results is required in order to check the validity of the new modified model.

4. We suggest that a comparison be made between our thermodynamic model and a mechanistic model to observe the differences in the predicted results.

Nomenclature

A	cross section area of the test tube
c_1. c_2	sound speed of components 1, and 2 in the mixture
c_p	specific heat
h_1. h_2	specific enthalpy at states 1 and 2
h_c	specific enthalpy of the coolant

h_f	specific enthalpy of the fuel
h_{ref}	reference specific enthalpy
I	mechanical impulse
m_{air}	mass of air
m_{mix}	mass of the mixture
p_1, p_2	system pressure at states 1 and 2
s_1, s_2	specific entropy at states 1 and 2
s_c	specific entropy of the coolant
s_f	specific entropy of the fuel
s_{ref}	reference specific entropy
t	time
T_2	equilibrium mixture temperature at states 2
T_{f1}	fuel temperature at states 1
T_{L1}	liquid coolant temperature at states 1
T_{ref}	reference temperature
T_{v1}, T_{v2}	vapor temperatures at states 1 and 2
u_1, u_2	velocity of the mixture in front and behind the shock
v_1, v_2	specific volume of the mixture at states 1 and 2
v_f	specific volume of the fuel
v_c	specific volume of the coolant
x_1, x_2	mass fraction of components 1 and 2 in the mixture
x_f	total mass fraction of the fuel in the mixture
x_i	mass fractions of the ith component in the mixture
x_{L1}, x_{L2}	mass fraction of the liquid coolant at states 1 and 2
x_{v1}, x_{v2}	mass fraction of vapor at states 1 and 2
y_c	mass fraction of coolant participating in the explosion
y_f	mass fraction of fuel participating in the explosion

Greek Symbols

β	volumetric thermal expansion coefficient
γ	specific heat ratio of steam
γ_{air}	specific heat ratio of air
κ	isothermal coefficient of compressibility

Subscripts

1	state 1 conditions
2	state 2 conditions
c	coolant
f	fuel
i	ith component

L	liquid
ref	reference state
v	vapor

References

[1] Corradini, M. L., Kim, B. J. and Oh, M. D. "Vapor Explosion in Light Water Reactors: A Review of Theory and Modeling," *Progress in Nuclear Energy*, Vol. 22, No. 1, pp. 1-117, 1988.

[2] G. Long, "Explosion of Molten Metals in Water: Causes and Preventation," Metals Progress, vol. 71, 107-112, 1957.

[3] Grace, T.M. (1985) "Energetics of Smelt/Water Explosion," Project 3575, The Institute of Paper Chemistry, Appleton, Wisconsin.

[4] D.L. Katz and C.M. Sliepcevich "Liquefied Natural gas/water Explosion: cause and effect," Hydrocarbon Process. Vol. 50, 240-244. 1971.

[5] B.I. Shamoun, M.L. Corradini "Analytical Study Of Subcritical Vapor Explosion Using Shock Wave Theory," submited for publication to Nuclear Technology.

[6] S.J. Board and R.W. Hall, "Propagation of Thermal Explosions Part2: A Theoretical Model," Central Electricity Generating Board Report RD/B/N3249, 1974.

[7] H. Hohmann, M. Field, K. Klein, H. Schins, "Experimental Data Collection." Joint Research Center, Safety Technology Institute, Ispra. Italy Technical Note No. 1.92.115, November 1992.

[8] L. Haar, J.S. Gallagher, and G.S. Kell, "NBS/NRC Steam Tables: Thermodynamic and Transport Properties and Computer Program for Vapor and Liquid States of Water in SI Units," Hemisphere Pub., 1984.

[9] McCahan S. and Shepherd J.E., "A Thermodynamic Model For Aluminum-Water Interaction," Proceeding of the CSNI Specialists Meeting on Fuel-Coolant Interaction, Santa Barbara, California, NUREG/CP-0127, January 1993.

[10] National Bureau of standards, "JANAF Thermochemical Tables." National Standard Reference Data Series, 3rd Edition. 1985.

[11] D.L. Frost, J.H.S. Lee and G. Ciccarelli, "The use of Hugoniot analysis for the propagation of vapor explosion waves." Shock Waves, Vol. 1. pp. 99-110, March 1991.

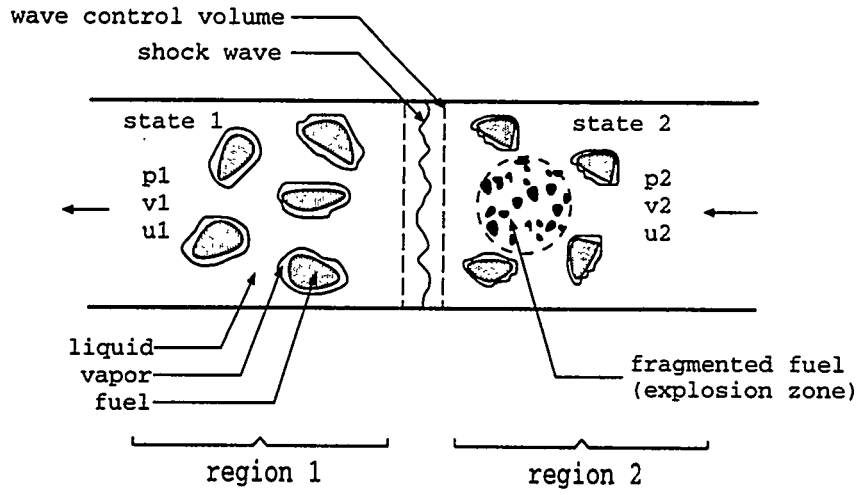


Figure 9: Schematic diagram of the reaction regions 1 and 2 separated by a shock wave.

[12] H. Hohmann, D. Magallon, H. Schins, A. Yerkess, "FCI Experiments In The Aluminum Oxide/Water System," Proceeding of the CSNI Specialists Meeting on Fuel-Coolant Interaction, Santa Barbara, California. NUREG/CP-0127, January 1993.

A Model Formulation

The proposed model considers that the control volume behind the shock consists of two zones; the explosion zone and the nonexplosion zone. The conceptual picture of the FCI system before and after the explosion is shown in figure 9. In the explosion zone we consider that there is a specific mass fraction of the fuel which is fragmented and transfers its thermal energy to the coolant. The fuel-coolant mixture in this zone attains thermal and mechanical equilibrium at a high pressure. In the nonexplosion zone, however, we assume that the remaining fuel that is not fragmented maintains mechanical equilibrium but is thermally isolated from the coolant. The fuel and liquid coolant temperatures in the nonexplosion zone are taken to be the initial temperatures of the fuel and coolant just before the explosion. Whereas the vapor temperature in the interfacial region between the fuel and coolant is treated explicitly. It is assumed that the remaining vapor undergoes an adiabatic compression from state 1 to state 2, therefore, its temperature is given by the following equation.

$$T_{v2} = T_{v1}(\frac{p_2}{p_1})^{\frac{\gamma-1}{\gamma}} \tag{9}$$

It should be mentioned that the initial vapor temperature T_{v1} was taken to be 400 K in the analysis. In front of the shock, the undisturbed region of the fuel-coolant mixture is initially assumed in mechanical equilibrium and thermal disequilibrium. The upstream and downstream mixtures which are separated by the shock are both assumed homogeneous in the analysis. The conservation equations of mass, momentum and energy together with the second law of thermodynamics can, therefore, be applied to two regions across the shock as follows,

$$\frac{u_1}{v_1} = \frac{u_2}{v_2} \tag{10}$$

$$p_1 + \frac{u_1^2}{v_1} = p_2 + \frac{u_2^2}{v_2} \tag{11}$$

$$h_1 + \frac{u_1^2}{2} = h_2 + \frac{u_2^2}{2} \tag{12}$$

$$s_2 \geq s_1 \tag{13}$$

The specific quantities in the above equations are obtained in terms of the mass fractions of a homogeneous mixture components as follows.

$$v = \sum_{i=1}^{n} x_i v_i \tag{14}$$

$$h = \sum_{i=1}^{n} x_i h_i \tag{15}$$

$$s = \sum_{i=1}^{n} x_i s_i \tag{16}$$

Therefore, the specific quantities of the mixture at region 1 and region 2 of the FCI system can be written as the following.

Region 1 :

$$v_1 = x_f\ v_f(p_1, T_{f1}) + x_{L1}\ v_c(p_1, T_{L1}) + x_{v1}\ v_c(p_1, T_{v1}) \tag{17}$$

$$h_1 = x_f\ h_f(p_1, T_{f1}) + x_{L1}\ h_c(p_1, T_{L1}) + x_{v1}\ h_c(p_1, T_{v1}) \tag{18}$$

$$s_1 = x_f\ s_f(p_1, T_{f1}) + x_{L1}\ s_c(p_1, T_{L1}) + x_{v1}\ s_c(p_1, T_{v1}) \tag{19}$$

Region 2 :

$$v_2 = y_f\ x_f\ v_f(p_2,T_2)\ +\ (1-y_f)\ x_f\ v_f(p_2,T_{f1})\ +\ y_c\ (1-x_f)\ v_c(p_2,T_2) + (1-y_c)\ (1-x_f)\ [x_{v2}\ v_c(p_2,T_{L1})\ +\ x_{L2}\ v_c(p_2,T_{v2})] \quad (20)$$

$$h_2 = y_f\ x_f\ h_f(p_2,T_2)\ +\ (1-y_f)\ x_f\ h_f(p_2,T_{f1})\ +\ y_c\ (1-x_f)\ h_c(p_2,T_2) + (1-y_c)\ (1-x_f)\ [x_{v2}\ h_c(p_2,T_{L1})\ +\ x_{L2}\ h_c(p_2,T_{v2})] \quad (21)$$

$$s_2 = y_f\ x_f\ s_f(p_2,T_2)\ +\ (1-y_f)\ x_f\ s_f(p_2,T_{f1})\ +\ y_c\ (1-x_f)\ s_c(p_2,T_2) + (1-y_c)\ (1-x_f)\ [x_{v2}\ s_c(p_2,T_{L1})\ +\ x_{L2}\ s_c(p_2,T_{v2})] \quad (22)$$

B Thermodynamic States

The thermodynamic properties of the coolant (water in our case) are provided by the program package of the NBS/NRC steam tables [8]. Such tables are not available for the fuel. Therefore, the caloric equation of state and the Maxwell relations were used to derive the necessary equations to calculate the specific properties of the fuel. The specific volume of the fuel as a function of the pressure and temperature can be written as

$$v = v(p,T) \quad (23)$$

$$dv = (\frac{\partial v}{\partial T})_p\ dT + (\frac{\partial v}{\partial p})_T\ dp \quad (24)$$

The above equation can be written in terms of the volumetric thermal expansion coefficient β and the isothermal coefficient of compressibility κ as follows

$$\frac{dv}{v} = \beta dT + \kappa dp \quad (25)$$

where:

$\beta = \frac{1}{v}(\frac{\partial v}{\partial T})_p$

$\kappa = \frac{1}{v}(\frac{\partial v}{\partial p})_T$

The specific enthalpy and entropy can be regarded as a function of pressure and temperature: h = h(p,T) and s = s(p,T) respectively. The differentials of these functions are

$$dh = c_p\, dT + [v - T(\frac{\partial v}{\partial T})_p]\, dp \tag{26}$$

$$ds = \frac{c_p}{T}\, dT - (\frac{\partial v}{\partial T})_p\, dp \tag{27}$$

Equations (17-19) can be integrated from any reference state to any final state in which the final forms of v, h, and s quantities as a function of the pressure and temperature are given by the following equations.

$$v(p,T) = v_{ref}\ exp[\beta(T - T_{ref}) - \kappa(p - p_{ref})] \tag{28}$$

$$h(p,T) = h_{ref} + \int_{T_{ref}}^{T'} c_p\, dT - \frac{v_{ref}(1 - \beta T)}{\kappa}\, exp[\beta(T - T_{ref})] \{exp[-\kappa(p - p_{ref}) - 1]\} \tag{29}$$

$$s(p,T) = s_{ref} + \int_{T_{ref}}^{T'} \frac{c_p}{T}\, dT + \frac{v_{ref}\beta}{\kappa}\, exp[\beta(T - T_{ref})] \{exp[-\kappa(p - p_{ref}) - 1]\} \tag{30}$$

It should be noted that the latent heat of melting and the entropy of melting should be included in equations (21) and (22) if the fuel temperature is above melting point.

The values of the volumetric thermal expansion coefficient β and the isothermal coefficient of compressibility κ for solid Al_2O_3 were taken to be $5.0 \times 10^{-5}\ K^{-1}$ and $2.8 \times 10^{-12}\ Pa^{-1}$ respectively. [9]. However, these parameters are not available for liquid Al_2O_3. Therefore, the same values were used for solid and liquid Al_2O_3. The form of the specific heat equation for solid and liquid Al_2O_3 as a function of temperature [10] was taken to be

$$c_p(T) = a + b.10^{-3}T + c.10^{-6}T^2 + d.10^5T^{-2} \tag{31}$$

For solid Al_2O_3, $a = 1212.1$, $b = 68.98 \times 10^{-3}$, $c = 0$, *and* $d = -5.31 \times 10^7$. For liquid Al_2O_3, $a = 1887.64$, $b = 0$, $c = 0$, $d = 0$.

The Numerical Methods for the Development of the Mixture Region in the Vapor Explosion Simulations

Y.Yang . H.Ohashi and M.Akiyama
Department of Quantum Engineering and Systems Science
University of Tokyo
7-3-1 Hongo. Bunkyo-ku. Tokyo, 113. Japan
T.Morii
Mitsubishi Heavy Industries. Ltd.
3-3-1 Minatomirai. Nishi-ku. Yokohama, 220 Japan

Abstract

An attempt to numerically simulate the process of the vapor explosion with a general multi-component and multi-dimension code is being challenged. Because of the rapid change of the flow field and extremely nonuniform distribution of the components in the system of the vapor explosion, the numerical divergence and diffusion are subject to occur easily. A dispersed component model and a multi-region scheme, by which these difficulties can be effectively overcome, were proposed. The simulations have been performed for the processes of the premixing and the fragmentation propagation in the vapor explosion.

1 Introduction

The vapor explosion caused by the contact of hot molten metal liquid with low boiling temperature cold liquid is important for safety problems in the nuclear industries. The phenomenon of the vapor explosion is an acutely changing process with very high speed heat and mass transfer. There are serious nonuniformity and changeability for the physical variables both in space and time. The divergence and numerical diffusion are the biggest difficulties in the simulations of such a kind of problems, especially in those multi-dimensional simulations. By now, only limited number of successful simulations for the phenomenon, especially after the stage of the premixing, with multi-dimensional codes were published [1]. However, the system of a vapor explosion is a multi-component system. Besides the continuous phase of coolant and the input component of high temperature melt drop, some news components, such as vapor and fine melt fragments, will be produced in the process, whose distributions are strongly dependent on the distribution of the melt drops. Moreover, the coherent fragmentation is also dependent on the sites of melt drops. Therefore, for the system with non-uniformly sparsely dispersed melt drops, the high-dimensional simulations are highly desired.

The authors are making an effort to simulate the whole process of a small scale vapor explosion with a multi-dimensional , multi-component and multi-field thermalhydaulic code . A general purpose code named CHAMPAGNE which was developed by Morii,T [2] was employed in the simulation. To avoid the divergence and numerical diffusion, some models and computing schemes used in the code were modified, hence the code is renamed as CHAMP/VE. Combining with the constitutive relationships associated with the physical processes in the vapor explosion, up to now, we have successfully simulated the premixing and fragmentation stages in the simple vapor explosion problems. The detailed modeling and some results can be found in another paper [5]. In this paper,

only the numerical treatments for this special problem will be discussed. One of the main improvement is the use of dispersed component model and the multi-region scheme.

Some simple metal drop pouring processes were taken as the sampling simulation cases. In these cases, the metal drops are poured continuously or discontinuously into a container full of quiet coolant. With the penetration of the hot metal drops, the coolant nearby the drops evaporizes and forms a vapor film covering the drops. Under certain triggering conditions, the metal drops break into fragments and the film changes into vapor bubbles. In this ideal system, metal drops and the products, such as vapor film, bubbles and fragments, are considered as the dispersed components, which justifies the adoption of a dispersed component model in the calculation.

Usually, in Eulerian multi-component codes, it is assumed that each component continuously distributed throughout the calculation zone. Therefore, at least, a infinitesimal fraction of components have to be assumed even in place where it does not actually exist. This assumption will bring out the numerical diffusion, especially for the components with lower volume fraction. In the small scale vapor explosion system, the volume fraction of the hot metal drops is very small and cannot spread over the whole system even by the end time of the calculation. But, due to the extremely large temperature difference with the coolant, this small fraction of metal does lead to strong transfers in components and changes in various physical parameters. Therefore, it is very important to correctly determine the distribution of this component. The numerical diffusion leads to the additional interactions where the metal drops do not exist, and on the contrary, reduces interactions where they really exist. In order to get rid of the effect of numerical diffusion, a multi-region scheme was developed in this paper.

The above two numerical methods used in the calculation will be discussed below.

2 The Numerical Treatments

2.1 Dispersed Component Model

- The flow Pattern

In the multi-component CHAMPAGNE code, each component is considered as a continuously distributed fluid. Under this assumption, the fundamental conservation equations of mass, momentum and energy for continuous fluid are solved for each component individually. The interactions between components are treated as the source terms in each equation. Thus, these equations can be written in a general form as below:

$$\frac{\partial}{\partial t}(\alpha_k \rho_k \Phi_k) + \frac{\partial}{\partial x_j}(\alpha_k \rho_k u_{kj} \Phi_k) = \frac{\partial}{\partial x_j}(\lambda_k \alpha_k \frac{\partial \Phi_k}{\partial x_j}) + S_k, \tag{1}$$

where k is the index for the components, α is the volume fraction, Φ represents the main physical quantities, i.e. 1 for mass , velocity u_i for momentum and energy e for energy conservation equations. λ is the diffusion efficient, i.e. 0 for mass, μ for momentum and k/C_p for energy equations. S is the source term, referring to mass generation in mass equation, pressure gradient, gravitation and interfacial forces between components in momentum equation, energy exchange between components in energy equations.

By applying these equations on the fluid components, each component is continuously distributed without any separation by other components. The existence of other components only take effects on sources and flow areas. The convection and diffusion are transformed inside each component itself.

Physically, this assumption for continuously distributed fluid is not reasonable for the discontinuity among components, especially for those existing in forms of particles, such as drops, bubbles or solid spheres. Because there are no exchanges (such as mass transfer, momentum or energy diffusion) between the separate particles, if the volume scale of each particle is smaller than that of a computational grid, there is also no diffusion between grid and grid. For example, because the conductivity of the melt is very large, if the continuously distributed fluid assumption is used, the conduction inside the melt will lead the temperature to become uniform in a very short time period, which will make some unexpected results such as the additional evaporization near the melt with lower temperature or the lack of the vapor near the melts with high temperature.

To cut the direct relationship between the particles of the same component, it is best to use the discontinuous models. Although all the discontinuous components in this discussing system are liquids, we take these components as solid particles except that the volume changes with the time. Therefore, the fundamental equations for the discontinuous components take the particle forms :

Mass Equations

$$\frac{\partial \rho_k V_k}{\partial t} + \frac{\partial}{\partial x_j}(\rho_k V_k u_{kj}) = \sum_q \Gamma_{qk}. \tag{2}$$

Momentum Equations

$$\frac{\partial}{\partial t}(V_k \rho_k u_{ki}) + \frac{\partial}{\partial x_j}(V_k \rho_k u_{kj} u_{ki}) = -\frac{\partial V_k p}{\partial x_i} - V_k \rho_k g_i + \sum_q F_{qk} + S_f, \tag{3}$$

Energy Equations

$$\frac{\partial}{\partial t}(V_k \rho_k e_{ki}) + \frac{\partial}{\partial x_j}(V_k \rho_k u_{kj} e_{ki}) = \sum_q Q_{qk} + \Phi_f, \tag{4}$$

$$k, q = v, d, f, b,$$

where, V_k is the particle volume of component k. Here, the diffusion terms are not included in the equations for the particles which are smaller than the grids, i.e, the temperature and velocity are unity inside a particle.

- Iteration Algorithm

In the CHAMPAGNE code, the iteration scheme so-called IPSA algorithm is employed, which is developed from the single phase iteration scheme of SIMPLE, to solve the fundamental equations. One of the emphasis of the scheme is that the pressure is computed from a so-called pressure modification equation which comes from substituting the momentum equation into the mass equation. In the multi-componental system, the total mass is the sum of each component and the local pressure is same for each component. Therefore, in the IPSA method, the pressure modification equation is derived by substituting the momentum equation of each component into the total mass equation. In

the concept of continuously distributed fluid, this treatment has no problem. But for the dispersed components, if the size of each particle is small enough, the direct contribution to the pressure field is small. The use of the total mass equation for the pressure modification equation will cause numerical divergence easily. For this sake, only the mass equation of continuously distributed components is used for the pressure modification equation in the newly developed CHAMP/VE code.

By using equations (2) - (4) for the dispersed components and equation (1) for the continuous component as well as the above pressure iteration algorithm, numerical divergence can be effectively avoided. This treatment is called the dispersed component model.

2.2 Multi-region Scheme

- The Distribution of Components

Let's consider the distribution of components in a system of the vapor explosion. According to distribution of each component in the system, we can divide the system into several regions. In the system of pouring case of a vapor explosion, the regions can be: (1) single component region (only the single coolant exists), (2) four components mixture region (with melt drops, vapor films, bubbles and coolant) and (3) five components mixture region (includes additional fragments). At least, a single component region and a mixture region can be roughly classified. Figure 1 shows the conceptual map of the regions in a pouring vapor explosion system.

As had been mentioned before, in many multi-components code, it is assumed that each component is distributed over all the computed regime, so that some unnecessary calculations on regions without the distribution of components have to be performed . This kind of treatment is apt to induce numerical diffusion.

In face, it is not necessary to do the calculation for the components on the non-existing region. Following this point of view, we use a multi-region method in our simulation. The calculation regime consists of two regions: a single component region and a mixture region. Thus, each component is computed only in the region where it does exactly exist.

- The Boundary Tracking Technique

Since the dispersed components are particles with certain diameters, it is not a diffusion problem for concentration . The mixture region can be identified by the appearance of the dispersed components. Therefore, the location of the mixture region boundary (or called region surface) is decided by the motion of the particle on the front of the mixture region. The motion equation of a particles with the Lagrange method can be expressed as:

$$\frac{d}{dt}(V_k \rho_k u_{ki}) = -\frac{\partial V_k p}{\partial x_i} - V_k \rho_k g_i + \sum_q F_{qk} + S_f. \tag{5}$$

Then, the location of the particles is decided by both the magnitude and direction of the velocity,

$$\frac{dl}{dt} = V_k. \tag{6}$$

The surface location is determined by the farthest location of the particle away from the mixture region. The explicit differential form of the above equation is used.

The principle of the idea is simple, but the difficulty is the determination of the region surface cells which is needed in the numerical differential equations. In our model, we define two kinds of cells: the original fixed cells which are the same as the usual cells as if there is only one region and the surface moving cells which appear only on the boundary of the mixture region. The continuous component is computed on the fixed cells while the dispersed components on a hybrid of the two kinds of cells. Figure 2 shows numerical treatment for the development of the mixture region boundary. The size on the boundary side of a surface cell is the length of the straight line of the boundary through the fixed cell, as shown in the figure. The solid dots represent the side points of the surface cells at some time instant. After a time step, the particles on these points reach to new sites which are expressed as the empty dots in the figure. Connecting the two new sites reached by the particles on the both side of the old surface cell with straight line, the points of intersection with the original fixed cell are selected as the candidate locations of the new surface cell points. Comparing all the new candidate locations of each dispersed component, the farthest location from the mixture region is selected as the new boundary of the mixture region. A modifying of this new boundary then must be made after checking if there is any particles inside the region going out of the new determined region. The parameters in those new surface cell points have the values of linear interpolation of the values on the old surface cell points.

3 Calculations and Results

3.1 Cases for Validation

Some simple cases were used to verify the usefulness of the multi-region treatment. The calculations were performed by assuming that some melt at a given inlet velocity and a volume fraction were pouring into a pool full of coolant. Figure 3 to 5 show the results of comparison between the uniform region scheme and the multi-region scheme both of one dimensional and two dimensional cases. The calculation region was divided into 20 cells for one dimension and 5 cells in the radial direction and 17 cells in the vertical direction for two dimension. In two dimension cases, the pouring area is within 2 cells near the center line of the pool and the results shown were obtained at the center line.

Figure 3 and 4 were obtained by ignoring heat transfer and all forces, such as drag, gravitation and the pressure gradient. In theory, the velocity and the void fraction should keep constants inside the mixture region, but the uniform region scheme induces the numerical diffusion significantly on the cells near the boundary of the mixture region . All the parameters calculated will be diffused, which make the value become lower than the real value as shown in the figure at the boundary of the mixture region. But the decrease of the velocity will induce mass accumulation, which can compensate for deficit caused by the numerical diffusion. As a result, the obtained value of volume faction is dependent on the overall effects both of the numerical diffusion and of the mass accumulation. If the effect of the former is larger than the latter, the volume faction will be less than the real value, as shown in figure 3a. Otherwise, it will be larger than the real value, which is quite evident at the cells near of the boundary as shown in figure 4a. The results in

figure 3b and 4d show that the multi-region scheme can avoid the numerical diffusion on the boundary of the mixture region and therefore the mass accumulation can also be reasonably avoided.

The numerical diffusion is more significant on the conditions of lower inlet velocities. Fig. 5 and 6 show the results for melt falling only under the gravity with the inlet velocities of 3.0 ms^{-1} and 0.3 ms^{-1}. In higher inlet velocity cases, the numerical diffusion can be effectively compensated by the mass accumulation, so that the results obtained from the uniform region scheme is close to the results from the multi-region scheme. But at lower inlet velocity, the reduction of the volume fraction is evident. However, we can not judge that the larger the inlet velocity is, the more effective the compensation is, because at much higher velocity, the accumulation will become dominating.

From these simple examples, we have seen that the use of the uniform region treatment will make the results far from the real value sometimes and it is not easy to estimate the error caused by the numerical diffusion. The error will bring large indeterminateness to distribution of variables because of the large transfers between components. We can then say that the treatment of the multi-region is necessary.

3.2 Cases of the Vapor Explosions

Two kinds of melt drop inlet conditions were considered for the calculations of the vapor explosions. One is the continuous melt drop pouring case and the other is the two or more group drop falling down at different instants. The components in the system include four dispersed components (melt drops, fragments, vapor films and bubbles) and one continuous component (coolant). The fragments are produced from the fragmentation of the melt drops and the vapor bubbles were assumed to be transformed from the vapor films collapsing when the fragmentation takes place. Each of the dispersed components has an estimated initial diameter and could be changed with the mass transfer but keep the total number unchanged once they are produced.

For the vapor film was supposed to be around the melt drop before the drop fragments, the velocity of the vapor film was taken to have the value of the melt drop. The heat transfer between melt, vapor film and coolant was assumed to be by a combination of stable film boiling and radiation before the fragmentation.

The fragmentation theories both based on the hydrodynamic and thermal fragmentation were taken into account. The first model was used in the case of continuous pouring inlet condition, and the second model was used in the two or more groups of melt drops falling cases to investigate the behavior of the spontaneous fragmentation propagation.

The inlet of the pool was treated as a free surface, which could rise with the increasing of the whole volume as the melt progressed and the vapor generated.

The dispersed model was employed in both of the inlet conditions while the multi-region scheme was used only on the continuous pouring case.

The calculated two-dimensional zone has a width of 370 mm and a height of 600 mm. The melt inlet region has a width of 150 mm. The inlet volume fraction and diameter of melt were taken as 0.002 and 6mm, together with the inlet velocity of 5.0 ms^{-1}. The mesh is taken as 10×20.

The calculations was performed using a finite difference grid with 10 cells in radial direction and 20 cells in the vertical direction. The time step was adjustable and the

maximum was 1×10^{-5}s.

Because this paper is focus on the discussion of the numerical treatments used in the calculations of a vapor explosion, only the results of a test calculation for a continuous pouring case in the stage of fragmentation is shown here. The fragmentation is assumed to take place from the beginning of pouring. The fragmentation was based on the difference of the velocities [3][4]. Figure 7 to 9 show the contours of volume fraction of melt, vapor and fragmentation in a case of a vapor explosion. The development of the mixture region boundary can also be clearly shown in the figures.

4 Conclusion

The authors are trying to simulate the process of a vapor explosion by using a general multi-dimensional, multi-component and multi-field thermal-hydraulic code. To avoid or control the numerical divergence and diffusion, some numerical treatments have been developed. Up to now, two stages of premixing and fragmentation propagation have been calculated [5]. Because there is still some unsolved problems left on the applications for the simulation of the process of a vapor explosion, such as the triggering model does still not included into the code to date, the comparison with the experimental data has not been done. It is the next arm for the authors.

Nomenclature

English Symbols

e	energy
F	force per unit volume
g	gravitation
p	pressure
Q	heat source
u	velocity
V	Volume of a particle
S	source
t	time

Greek Symbols

α, f	volume fraction
Γ	mass generation
Φ	Physcal variables

Subscript

b, c, d	bubble, coolant. drop
f, v	fragment, vapor

References

[1] T.G.Theofanous. "The Study of Steam Explosions in Nuclear Systems" *Proc. Int. Semi. on the Phy. of Vapor Explosion*. Tomakomai,1993

[2] T.Morri et al. "Development of the Multi-Phase Flow Simulation Code" *Proc.Multi-Phase Flow Symposium* (1993), B17

[3] C.B.Carachalios, et al "A Transient Two-phase Model to Describe Thermal Detonations based on Hydrodynamic Fragmentation " *Proc, Int. Meeting on LWR Severe Accident Evaluation*, Cambridge, Massachusetts, 1983

[4] D.F.Fletcher et al "A Mathematical Model of Melt/Water Detonations" *Appl. Math. Modelling*, 13, p339-347 (1989)

[5] Y.Yang et al. "A Two-Dimensional Numerical Simulation of the Fragmentation Propagation in the Vapor Explosion" *Paper in the 3th Int. Conf. on Nucl.Eng.*. Kyoto, Japan. April, 1995

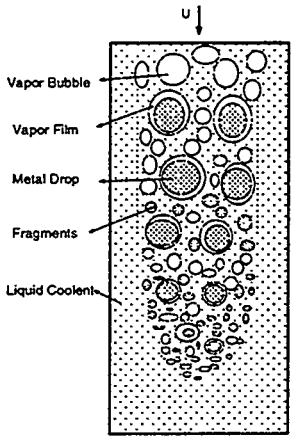


Figure 1: Components and regions in pouring case of a vapor explosion

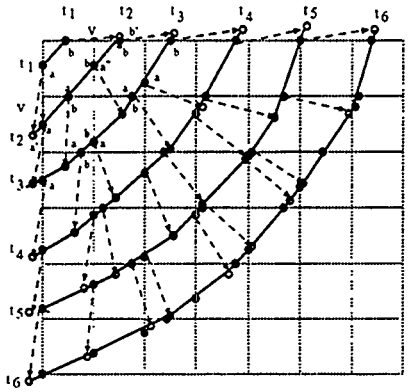


Figure 2: Arrangement and development of the surface cells of mixture region

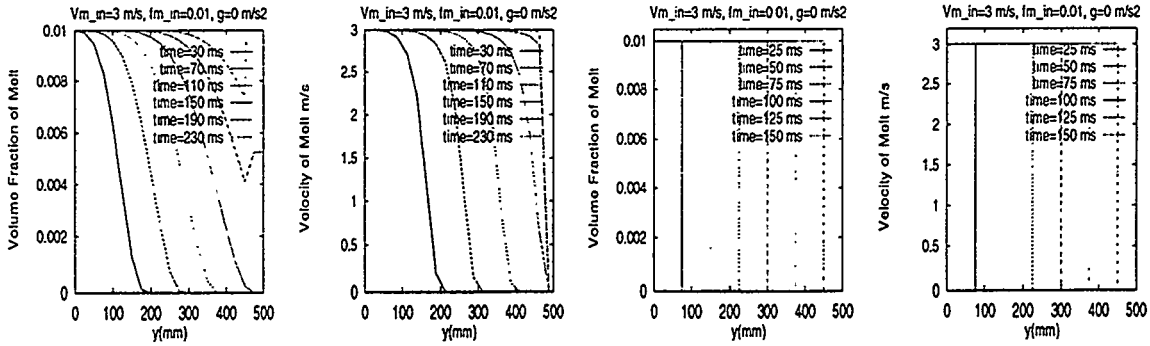


Figure 3: The 1D results of validation cases without any forces
(The data is got form the center line in vertical diraction)

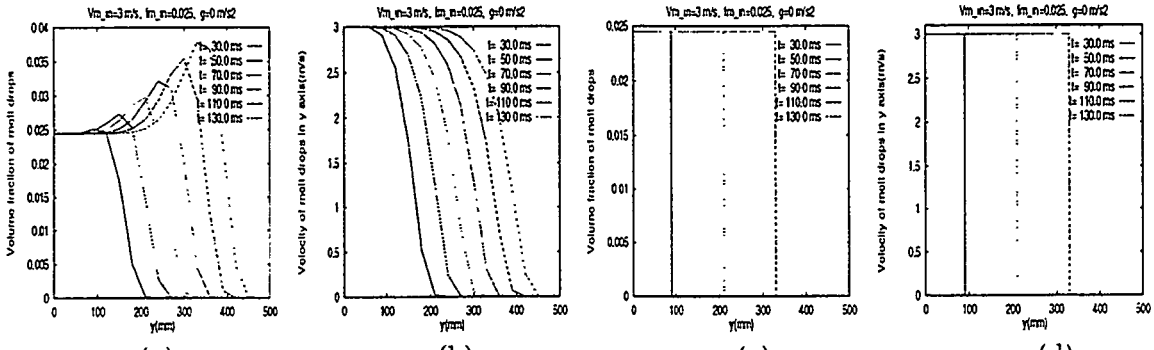


Figure 4: The 2D results of validation cases without any forces

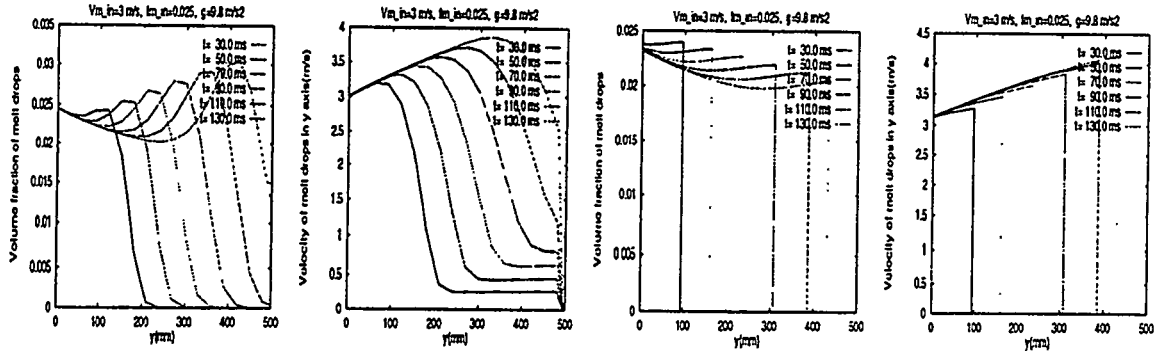


Figure 5: The 2D results of validation cases under the gravity
(Inlet velocity is 3.0 m.s)

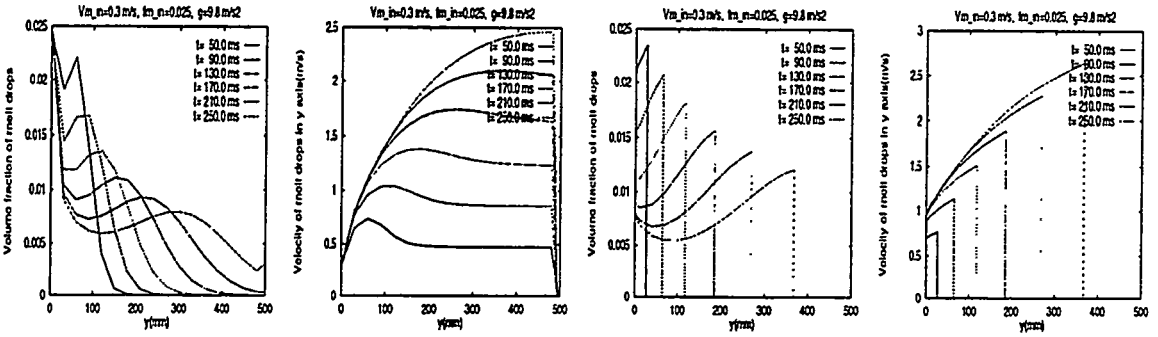


Figure 6: The 2D results of validation cases under the gravity
(Inlet velocity is 0.3 m.s)

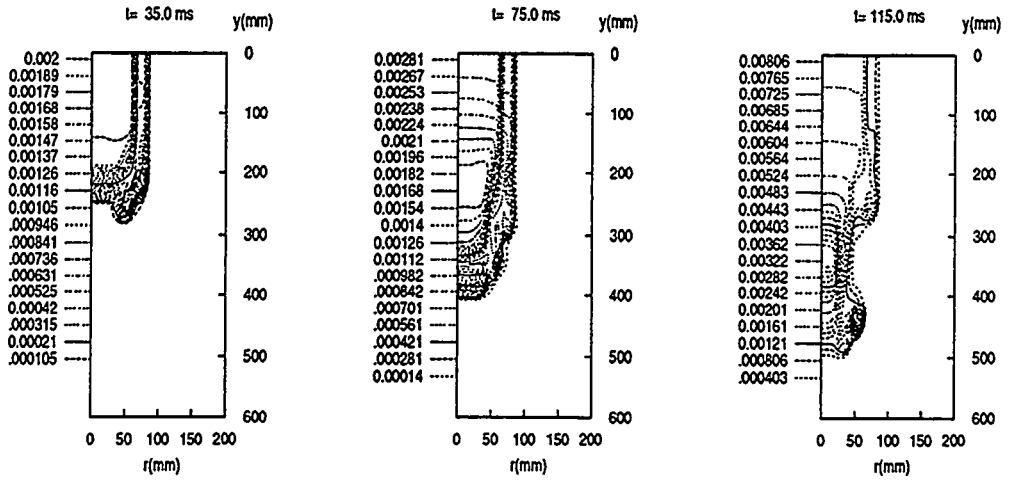


Figure 7: The volume fraction of melt Drops in the case of vapor explosion

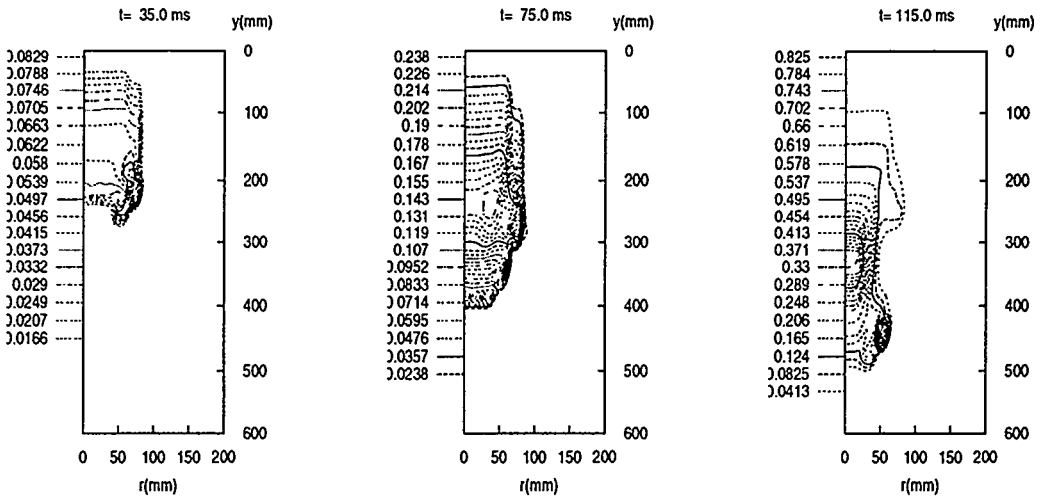


Figure 8: The volume fraction of vapor in the case of vapor explosion

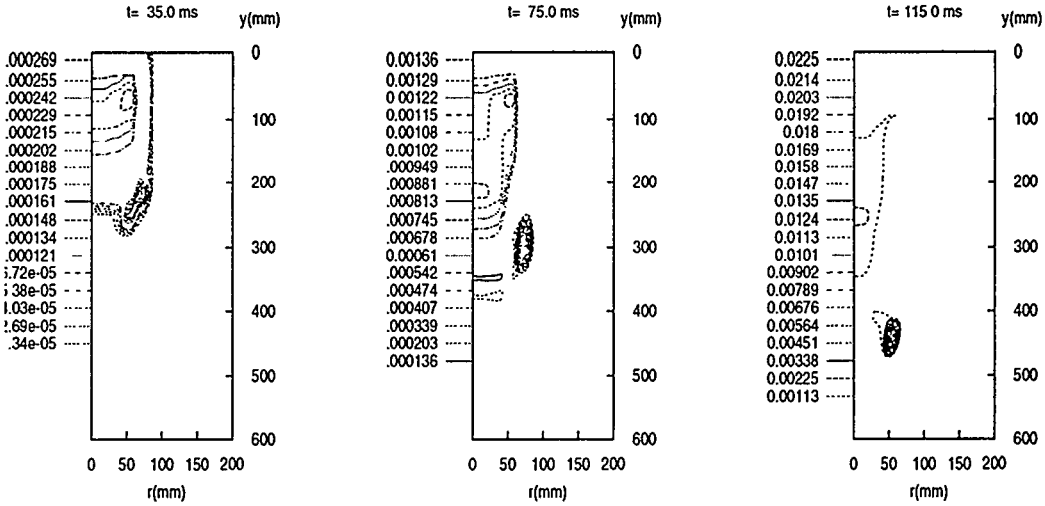


Figure 9: The volume fraction of fragments in the case of vapor explosion

Thermal-Hydraulic Behaviors of Vapor-Liquid Interface due to Arrival of a Pressure Wave

Akira Inoue , Yoshifumi Fujii , Mitsuo Matsuzaki , Minoru Takahashi
Research Laboratory for Nuclear Reactors, Tokyo Institute of Technology,
2-12-1 Ookayama, Meguro-ku, Tokyo 152,Japan
TEL:81-03-5734-3059, FAX:81-03-5734-2959

Abstract

In the vapor explosion, a pressure wave (shock wave) plays a fundamental role for triggering, propagation and enhancement of the explosion. Energy of the explosion is related to the magnitude of heat transfer rate from hot liquid to cold volatile one. This is related to an increasing rate of interface area and to an amount of transient heat flux between the liquids. In this study, the characteristics of transient heat transfer and behaviors of vapor film both on the platinum tube and on the hot melt tin drop, under same boundary conditions have been investigated. It is considered that there exists a fundamental mechanism of the explosion in the initial expansion process of the hot liquid drop immediately after arrival of pressure wave. The growth rate of the vapor film is much faster on the hot liquid than that on the solid surface. Two kinds of roughness were observed , one due to the Taylor instability, by rapid growth of the explosion bubble, and another, nucleation sites were observed at the vapor-liquid interface. Based on detailed observation of early stage interface behaviors after arrival of a pressure wave, the thermal fragmentation mechanism is proposed.

I. Introduction

In the vapor explosion which is occasionally caused in liquid-liquid system with a big temperature difference, a pressure wave (shock wave) plays a fundamental roles for the triggering, propagation and enhancement of the vapor explosion. Energy of explosion depends upon the high heat flow from hot liquid to cold volatile liquid, which is related to an increasing rate of the interface area and to an amount of transient heat flux between the liquids . As a result of sudden transient heat flux between liquids and the phase change, intensive flow is induced with a pressure wave. The vapor explosion region is expanded as the pressure wave is propagated.

Many studies for the vapor explosion of single drop have been done to date. The roles of the single drop test were to simplify complex phenomena of vapor explosion and to investigate their mechanisms and the fundamental criteria which caused explosions. Especially, single drop test triggered by a pressure pulse was important as a local simulation of large scale explosion in the coarse mixture.

Observation of single drop vapor explosion under a pressure pulse is represented by Nelson's experiment [1]. He observed the pressure triggered explosion of an iron oxide drop ,which is melted by a laser in the air and dropped in the pool water by a high speed movie.

Fundamental aspects of vapor explosion are the mechanisms to produce big and highly transient heat flow which is enough to support energy of explosion. Fragmentation and mixing of both liquids at an arrival of a pressure wave have been believed to be the main mechanisms to

produce such transient heat flow between liquids. As for single drop explosion triggered by a pressure pulse, the thermal induced fragmentation becomes more important than the hydrodynamic one, because transient high flow can not be expected there.

It is well known by theoretical analysis of Plesset & Chapman [2], and the experimental verification [3], that when a cavitation bubble is collapsed near wall region, a liquid microjet is formed at the interface.

Buchanan[4] proposed the microjet penetration model followed to the cavitation theory. He thought that when a bubble shaped vapor film formed around a hot drop is collapsed, similar micro-jets are generated around the drop. When the liquid microjet penetrates into the hot metal, the top is reformed like top of mushroom and disintegrated into fine particles by the shear between fluids. He thought two kinds of vapor generation processes from the trapped fine particles, one is normal heat transfer and the other, the homogeneous nucleation. However, it is pointed out for this model whether bubbly configuration can be formed in the vapor film around the drop or not [5].

Kim & Corradini[6] proposed that the interface waves which are occurred by the Taylor instability during collapse and re-growth of vapor film forms an array of microjets around the hot drop ,when the vapor film is collapsed by arrival of a pressure wave. The micro jets are penetrated into hot melt drop, when the inertia forces exceed the stress of the surface tension. The penetrated liquid jet is disintegrated into fine fragments by shear force and then remains in some depth. When the fine particles are heated and evaporated in the hot metal, a part of hot metal covering the fine particles are blown off. One good points of the model is that the fragmentation mass rate can be derived from the model. For this model , there are some doubts that whether the micro jet can be formed or not, when the wavy interface is collapsed and whether the micro jet (when it can be formed) can be penetrated into the hot drop.

One of authors previously analyzed the dynamics of vapor film under a pressure wave[7] and found that the high pressure was generated when thickness of the vapor film became less than 50 μ m. Authors verified analytically in the previous report[8] that there were enough time to develop the Taylor instability at the both interfaces of liquid and melt drop before the vapor film collapses and proposed the single drop explosion model. Diameter of fragmented droplet was derived from the wave length of the maximum growth rate of the instability.

Ochiai & Bankoff [9] proposed "the splash theory". Because initial vapor film is wavy, collapse of vapor film does not occur coherently but limited in the local area on the drop. When vapor film collapses locally and liquid-liquid direct contact is realized, the liquid interface is pushed away by high vapor pressure explosively generated by the spontaneous nucleation and then on the contrary, a part of the perimeter falls back to the interface and liquid-liquid direct contact occurs there. In this way, the interaction region propagates over peripherally around the drop.

Ciccarelli [10] tried to observe single drop explosion process by using X-ray spot camera matching with a high speed movie camera and found that when a large bubble including the hot drop was growing ,surface of the hot drop became unstable and formed several spikes. From the top of the spikes, fine particles dispersed. They thought that the local high impact pressures around the hot drop squeezed the melt metal at low pressure locations and formed the interface unstable like a spike. They verified that a pair of pressure pulses generated by two exploding wires which are attached near water-melt metal interface, caused the similar type interface instability.

Nelson et.al.[11] investigated photographical-ly mechanism of the fragmentation process for the pressure triggered single drop explosion. They found that a melt drop expand rapidly after the collapse of vapor film (Stage 4 in the paper) and thought that this expansion was caused by the entrapped water. They supposed that the en-trapping had occurred by micro-jets penetration, when the cavitation bubbles generated around the hot drop or the interface waves which are generated by the Taylor instability, were collapsed. Though this was a very important evidence for the explosion, they did not continue further investigation. For the vapor explosion it

is considered that the initial growth process of vapor film around a hot metal plays a fundamental mechanism for the single drop explosion.

In this study,

1) Relation between the transient heat transfer rate and the behavior of vapor film around the Joule heated platinum tube is investigated as a typical example for behaviors of vapor film under a pressure pulse.

2) Transient behaviors of vapor-liquid surface both on melt tin drop and on platinum tube are observed in the same coolant condition especially to investigate initial stage of fragmentation and explosion.. A high speed image converter camera was used to observe such high transient behaviors.

3) The thermal induced fragmentation mechanism is discussed following to the transient behaviors of the vapor film around the hot metal drop.

II. Experimental device

An experimental device for measurement of the transient heat transfer and for observation of the single drop explosion is shown in Fig.1. Liquid heated up in a storage tank enters and rises up through the test section for two−dimensions observation and flows back again into the storage tank. Flow speed of circulated water was kept less than 5cm/s in the test section. Pressure pulse is generated by hitting of a metal plate which is installed at the bottom end of the test section. A piston derived by gas pressure is used to hit the plate. The pressure pulse is controlled by adjusting the impact velocity of the piston driven by the gas pressure.

As described Fig.2 , the test section has a pair of windows at 30mm wide and 130mm long ,which are made of quartz or resin plates of approximately 20mm in thickness. The cross section of the test channel is rectangular of 50mmx4mm. A pair of piezo type pressure transducers are installed at the side wall of 30mm upper and bottom from the center.

In the case of transient film boiling on the solid surface , a platinum tube of 2.3mm outer diameter and 15mm long is installed horizontally at the center of the test section and is heated by
controlled DC power source. Two platinum wires of 0.1mm dia. are welded at the distance of 4mm in the center region of the tube to measure wall temperature to detect the resistance change by the Kervin Bridge method. And transient heat flux $q_w(t)$, is obtained by the Joule heating and the wall temperature change as follows.

$$q_w(t) = I(t)V(t)/(\pi\, d_m l_m) + \rho_m C_{pm} \delta_m dT_m(t)/dt \qquad (1)$$

where, I and V are current and voltage drop in the measured part of the Pt tube which has diameter d_m, and length l_m ,between measurement taps respectively. ρ_m, C_{pm}, δ_m and T_m denote density, specific heat, thickness and temperature of the Pt tube.

On the other hand, for the injection test of single metal drop, a drop machine which is composed of a piston with drive controller is attached on the top part of the test section. The machine is designed so as to heat 1−2cc of metal lump up to 700℃ and to drop automatically into liquid of the test section. Through upper part of the observation window, a laser beam is projected and when the signal liquid drop crosses the beams, the driving piston for pressure pulse is actuated. High speed photographs were taken by a image converter camera of NAK Corporation, which is able to take max. 20 million frame per second. To get good timing of the drop test, the camera is started by the triggering signal from P1 pressure transducer which is attached at the side wall of 30mm upstream region. The traveling time of a pressure wave is 20−30 μ s over the distance from location of a piezo pressure transducer (P1) to the test drop position which is approximately 30mm. Then the first photograph starts 20−30 μ s in advance of pressure wave arriving.

Ⅲ. Experiment results

1. Transient behaviors of vapor film and heat transfer on platinum tube

Behaviors of the vapor film, the temperature and the heat flux on the Pt tube wall at arrival of a pressure wave are shown in Fig.3. It was observed that the wall temperature rises at first at the arrival of pressure wave and then drops sharply. This temperature rise is considered to be a result of transient compression of vapor near the wall. For the successive photographs, existence and behaviors of the vapor film on the Pt tube can be discriminated by the reflection of light from interface of vapor-liquid or solid wall. The vapor film looks collapse at about 120 μ s after arrival of pressure wave. During this period, transient heat flux keeps higher value. Then, the ring shape winkles of the vapor film are formed around the tube. In the experimental condition, the peak of heat flux occurs at about 120 μ s which corresponds to minimum thickness of the vapor film. In a photograph, the growth rate of the vapor film on the platinum is slow. The thickness of the film is kept thin until around 1ms.

Time histories of wall temperature and heat flux in the various initial wall temperature are shown in Fig. 4. When the initial wall tempera-ture increases higher than 300 ℃, the peak heat flux becomes smaller. This means the vapor film becomes thicker and harder to collapse when the wall temperature increased. The bold line in the Fig.4−(b) indicates the corresponding numeri-cal results using the analysis which was developed in the previous report[7].

The analytical results for the transient temperature behaviors almost coincide with the experimental ones. The behaviors of other parameters, heat flux at vapor-metal interface: qw, heat flux at vapor-liquid interface: ql, pressure in the vapor film: Pg and thickness of the film: χ are indicated in the Fig.5 respectively. Then, in the following investigations, the findings from the analytical results were considered.

2. Vapor film behaviors around the hot tin drop and its fragmentation

Figure 6 shows the successive photographs around the hot tin drop when 2 gr of tin at 500℃ is dropped into subcooled water of 20K. Photographs (a) to (c) are observed at high speeds corresponding to 20,000 f/s 50,000 f/s and 10,000 f/s respectively. Because of a distance of 30mm from the drop to side wall, significant pressure pulse by the explosion was not measured clearly. However, the explosion had taken place.

Behaviors of vapor-liquid interface around melt drop after arrival of a pressure wave are summarized in Fig. 7 , that is,

① When vapor film around melt drop collapses, reflection of light from vapor-water interface is extinct and changes dark. :120−140 μ s

② Many white speckles which are considered vapor sites dimly appear in the next photograph of 20 μ s later. :140−160 μ s

③ Vapor-liquid interface around the melt drop begins to grow. :180−200 μ s

④ Three dimensional wave with the length less than 1 mm is observed in the vapor-liquid interface. :500−900 μ s

⑤ The bumpy interface with bubbly like spots appears at the interface and grow with time. :700 μ s−3 ms

⑥ Surface of metal drop is disturbed like hempyarn and fragmentation is promoted. :700 μ s−3 ms

The initial growth rate in ③ looks uniform around the drop and is not affected by the

directions of pressure wave propagation and gravity force. Interfacial wave observed in ④ is thought to be the Taylor instability developed by rapid increase of the pressure in the vapor layer. A bumpy interface observed at ⑤ is formed by evaporation sites including fragmented particles which are dispersed but remained near the interface.

Radial changes of the vapor-liquid interfaces in the vertical direction both on Pt tube and on melt tin drop are examined in the Fig. 8. In the case of the melt tin drop, sudden growth is started at around 200 μ s. The radial growth rate is about 20m/s, that is dR/dt=20m/s. On the other hand, the growth rate on the Pt surface remains at small value over the same period.

IV. Thermal fragmentation mechanism and discussions.

Related to above observations of the transient vapor film , two fundamental aspects related to the vapor explosion would be pointed out.

a) Many white speckles which means the spontaneous nucleation sites are observed in the short time less than 20 μ s right after collapse of vapor film.

b) The growth of the melt tin drop starts in the early stage of 60−80 μ s after the collapse of vapor film. The growth rate is extremely fast compared to growth rate of vapor film on the platinum tube.

These behaviors in the starting period of vapor explosion include some of fundamental mecha-nism of the explosion. The distance from the tin drop to upper free surface is approximately 7.5 cm and then round traveling time of a shock wave in the liquid is estimated about 110 μ s. This value corresponds to the acoustic constrain time in this test section. However, it is too long compared with the nucleation time of 20 μ s observed in this experiment. Accordingly, it is thought that the acoustic constraint for start of vapor generation is not workable.

As for b), two cases are considered, one is the melt tin drop itself expands and the other is the vapor film around the drop grows very fast, because high speed photograph can only get the behaviors of the vapor-liquid interface. The vapor film can save superheat energy both in the vapor layer and in the thermal boundary layer of the liquid during its collapsing phase by the elevated pressure and can release them to the vapor film in the growth phase. However, these situations are the same as those of the vapor film on the Pt tube. Then, other mechanism to promote rapid vapor generation must be sought.

As one of the mechanism where the expansion occurs inside the melt tin, it is considered that when vapor film around a drop collapses by pressure wave, impact shocks locally generated on the interface attack into inside of the drop and reflect one another there, minus pressure is caused there. Then the drop disintegrates itself internally by cavitation. However, it is not realistic because a large negative pressure is needed to promote cavitation inside the metal.[5] Further, if we see the fact that the second explosion is generally more violent than the first one [1], this must be the fragmentation mechanism where an UN-interacted mass of the drop is remaining therein. Then the cavitation induced fragmen-tation is not suitable.

There are several plausible fragmentation mechanisms as described in the introduction. When mechanisms of fragmentation at arrival of the pressure wave are discussed, it is important to give considerations for the propriety on scales of space and time. About micro-jets which is generated at collapsing of initial wavy interface, the formation of bumpy holes of mm order size was not observed by high speed photographs on the surface of metal at the time of collapsing, but the surface was found rather smooth. Further, the significant wave motion of vapor film is observed on upper part of melt drop but the interface on bottom side part is found to be flat and smooth. The growth rate of the melt drop in the initial period is observed to be uniform in all directions. Initial wave motion of several mm order around the drop is too coarse to explain the uniform growth. More fine mechanism is needed to explain initial phase of the explosion.

It was found experimentally by Ciccarelli[10] that the instability wave on the hot drop

observed by the X-ray photograph is quite similar to that observed at the water-liquid metal interface with two artificial pressure spots. However, as the growth time of the instability is of order of ms, this looks too long to explain the initial growth of the drop surface which is of 100 μ s order. Therefore, it is needed to find more fine structure interface instability.

According to the previous analysis [8] of transient vapor film at arrival of a pressure wave, the relations between the minimum vapor film thickness and the vapor pressure on the platinum tube are indicated in Fig. 9 in the various conditions. These relations are not changed for the vapor film on the melt tin drop. When vapor film thickness become less than 10 μ m, pressure in the film reaches more than 10MPa. The generated pressure creates large acceleration from vapor toward the liquid. Then the Taylor instability takes place at the vapor-liquid interface .

The acceleration α, at the vapor-liquid inter-face around the drop of which radius is R_m and the most unstable wave length λ^*, are described as,

$$\alpha=(P_v-P_\infty) / (\rho_l R_m) \tag{2}$$

and

$$\lambda^*=(2/3)^{3/2}\pi\{\alpha(\rho_l-\rho_v)/\sigma\}^{-1/2} \tag{3}$$

where R_m, P_v, P_∞ and σ are the radius of the drop, the vapor pressure , pressure where is enough apart from the drop and surface tension respectively.

The growth rate of the Taylor instability is proportional to $e^{n^*t^*}$, where n^* is described as,

$$n^*=[(2/3)^{3/2}\{(\rho_l-\rho_v)\alpha\}^{3/2}\{(\rho_l+\rho_v)*\sigma\}^{1/2}]^{1/2} \tag{4}$$

From Eq.(3), when Rm is equal to 1.5mm, relations among λ^*, $(P_{vp}-P_\infty)$ and growth time t^*, which is the time that instability grows to $e^{n^*t^*}$ times larger than the initial value, are indicated in the Fig. 10.

From Fig. 10, λ^* and t^* are estimated at $e^{n^*t^*}=100$ respectively,

$\lambda^*=$ 100 μ m, $t^*=$ 20 μ s at P_v = 1MPa

and

$\lambda^*=$ 40 μ m, $t^*=$ 5 μ s at P_v = 10MPa

and it can be considered that size of fragmented particle is of the order of λ^*. In this conditions ,time to grow up to 100 times of initial disturbance is about 5 μ s . It is verified that the growth time of the Taylor instability is less than the collapse time [8]. Based on above considerations, the mecha-nism of vapor-fluid interface described in the Fig. 11 is proposed.

Stage 1: (①–④ in Fig.11)

When the vapor film begins to collapse under the pressure wave of several atmosphere and as the thickness decreases to around 50 μ m, the vapor pressure exceeds the pressure wave. In this period, the wave motion at the vapor - liquid interface is kept at the same configuration as the initial one which wave length is several mm. However, when the vapor film decreases to less than 10 μ m, the vapor film pressure goes up to more than 10MPa and the Taylor instability grows up rapidly at the vapor-liquid interface. The wave developed by the Taylor instability would be fine. The wave length is estimated about 10 to 50 μ m which is less than 1 order smaller than

initial wave length.

The interfacial waves around the drop might be developed to the non-linear ones with the sharp crests. The vapor film locally collapses keeping the same configuration. Then, the sharp crests thrust or penetrate into the hot melt drop. Impact velocity of the interface becomes around 10m/s when the drop radius is 2mm and the vapor layer thickness is 0.3mm under pressure wave of 1MPa.

The initial liquid-liquid contacts take place in supercritical state, when the interface temper-ature is higher than the critical temperature of the liquid. When the impact pressure leaves from interface, vapor is generated by the homogeneous nucleation. Or it is generated by the sponta-neous nucleation when the interface temperature is between the critical temperature and the spontaneous one respectively. That is, vapor is generated immediately after collapse in both cases and liquid-liquid contact be realized from the wave crests by the homogeneous or the spontaneous nucleation. Increase of heating surface area with fine wave structure conducts to rapid evaporation to support the growth of the initial period around the drop. The white many speckles observed at ② in the Fig.7 are the vaporization sites of the fine microjet spots.

Stage 2: (④–⑥ in Fig.11)

The impact of vapor film occurs locally, because the initial vapor film thickness before the collapse are locally difference. When the initial collapses of vapor film occurred at several locations around the drop, the pressure spots are transiently generated there. As pointed out by Ciccarelli, these pressure spots work to squeeze the melt drop and to bring up interfaces staying under lower pressures around them. However, the pressures around the high pressure spots gradually start to increase in this period and liquid inertia force increase toward the melt drop simultaneously. Then, even if local large peak pressures would be generated, the instability of drop surface would be suppressed in this period. We can see these situations from high speed photographs in Fig.6–(a) where the coarse surface roughness are not observed during a hundred microsecond ,until almost all surface around the melt drop is collapsed.

On the other hand , in the later period of the local impacts which correspond to impacts at initial thicker film positions, local pressures of earlier period impact place are rapidly decreased by the reflection and expansion of vapor film there and the local inertia forces are directed toward liquid from vapor. In this period (several hundred micro second after the collapse), local peak pressures would be able to squeeze the low pressure interfaces, and further cause the local swell surface there. From crests of the "squeezed waves" of melt drop, fine particles with high temperature break spray and fly through the vapor layer.

Stage 3: (⑥–⑦ in Fig.11)

As described in the previous report[8], the fine particles fly and disperse through the vapor layer which has already grown around the hot melt drop. They attack and penetrate the vapor-liquid interface of the large explosion bubble. However, the stopping distance of these fine particles with vapor film would be small. Then they stay near the interface region and keep to supply the vapor to the large bubble. The bubbly like spots at the interface which were described at ⑤ of previous section is occurred by these particles near interface.

Recently, transient two-dimensional analysis for behaviors of the interfacial region between water and tin drip was done by the CIP numerical scheme . In the numerical results , water micro jet could not penetrated into the tin surface . When the micro jet attacked on the tin surface , the top of the micro jet was spread out like a cap of mushroom. Instead, the small perturbation waves were observed on the contact interface region of the top.

V. Conclusions

Transient behaviors of vapor films both on the platinum tube and on the melted tin drop at arrival of a pressure wave were observed by the high speed image converter camera. From the detailed investigations of the observation results and the previous analysis, the following con-conclusions are deduced.

1.The peak transient heat flux on the platinum tube under pressure pulse decreases when wall temperature becomes higher than 300℃.

2.Behaviors of vapor film in collapsing period on the tin drop under a pressure pulse looks the same as one on the platinum tube. However, the growth rate of the vapor liquid interface on the tin drop is much higher than that on the platinum(solid surface).

3.For the nucleation after collapse of vapor film, the acoustic constraint period is not plausible and a cloud of white spot which is considered a cloud of nucleation sites are observed in less than 20 μ s after collapse.

4.In the rapid growth period of explosion bubble, two kind of irregularities were observed on the vapor liquid interface. One is occurred by the Taylor instability due to rapid growth of explosion bubble and another comes from hot fine particles which stays near the interface .

5.Behaviors and mechanism of thermal fragmentation of single hot drop at the arrival of a pressure wave is proposed.

References:

[1] Nelson L.S. & Duda P.M. 'Steam Explosion Experiments with Single Drops of Iron Oxide Melted with CO2 Laser', Part 1,NUREG/CR-2295(1981) and Part 2, NUREG/ CR-2718(1984).

[2] Plesset M. S. & Chapman,R.B. ' Collapse of an Initially Spherical Vapor Cavity in the Neighborhood of a Solid Boundary',J. Fluid Mech., Vol. 47,(1971)283-290.

[3] Lauterborn, W. & Bolle H.,'Experimental Investigations of Cavitation-Bubble Collapse in the Neighbourhood of a Solid Boundry', J. Fluid Mech. Vol.72, Part2 (1975)391-399.

[4]Buchanan D. J.,' A Model for Fuel-Coolant Interactions,J. Phys. D:Appl. Phys., Vol.7 (1974)1441-1457.

[5] Corradini et. al.,'Vapor Explosions in Light Water Reactors: A Review of Theory and Modeling', Progress in Nuclear Energy, Vol.22, N0.1, (1988)1-117.

[6] Kim. B and Corradini M. L.,'Modeling of Small Scale Droplet Fuel/Coolant Interactions', Nucl. Sci. Enging, Vol.98 (1988) 16-28.

[7] Inoue A.et. al.," Study on Transienteat Transfer of Film Boiling due to Arrival of Pressure Shock", Proc. 7th Int. Heat Trans. Conf. Vol.5 (1982)403-408.

[8] Inoue, A.et.al.,"An Analytical Model on Vapor Explosion of a High Temperature Molten metal Drop in Water Induced by a Pressure Pulse",
Proc. NURETH-4 and Chem. Eng. Comm. Vol.118, (1992)189-206.

[9] Ochiai,M. & Bankoff,S.G.," Liquid-Liquid Contact in Vapor Explosion", Proc.Int. Conf. Fast Reactor Safety, Am. Nucl. Soc. (1976).

[10] Ciccarelli,G.,"Investigation of Vapor Explo-sions with Single Molten Metal Drops in Water Using Flash X-Ray",PhD Thesis, Dept. Mech. Enging, McGill Univ. Canada (1991)

[11] Nelson, S. L. et.al. "Phtotographic Evidence for the Mechanism of Fragmenta- tion of a Single Drop of melt in Triggered Steam Explosion Experiments", J. Non- Equilib. Thermodyn. Vol.13(1988)27-55.

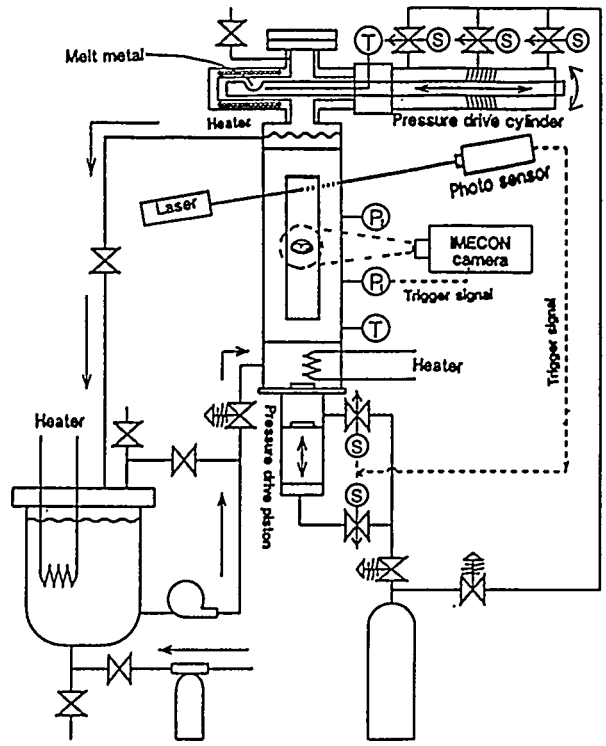


Fig. 1 Experimental system

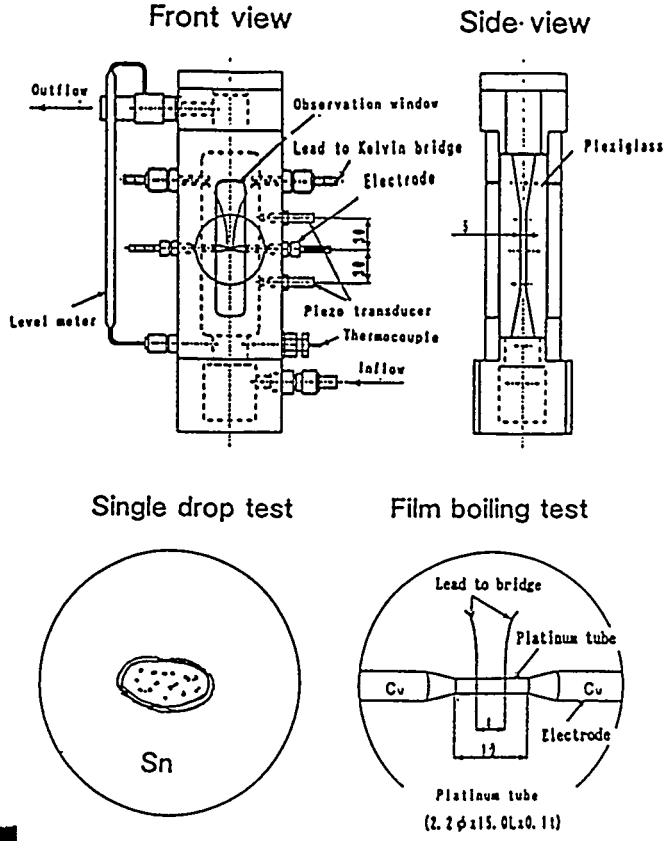


Fig. 2 Test section

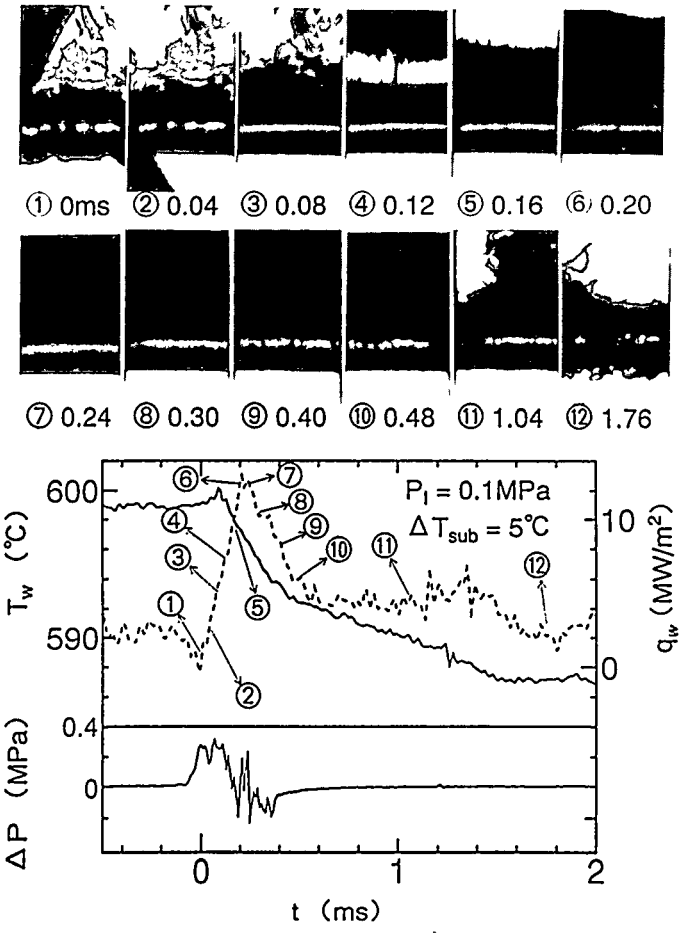


Fig. 3 Behaviors of vapor film around Pt tube, wall temperature, T_w and heat flux, q_w at arrival of a pressure wave, ΔP

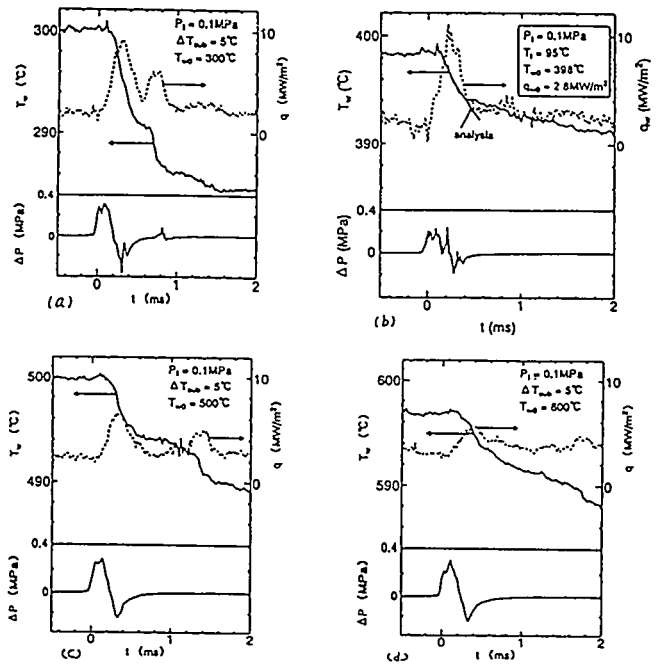
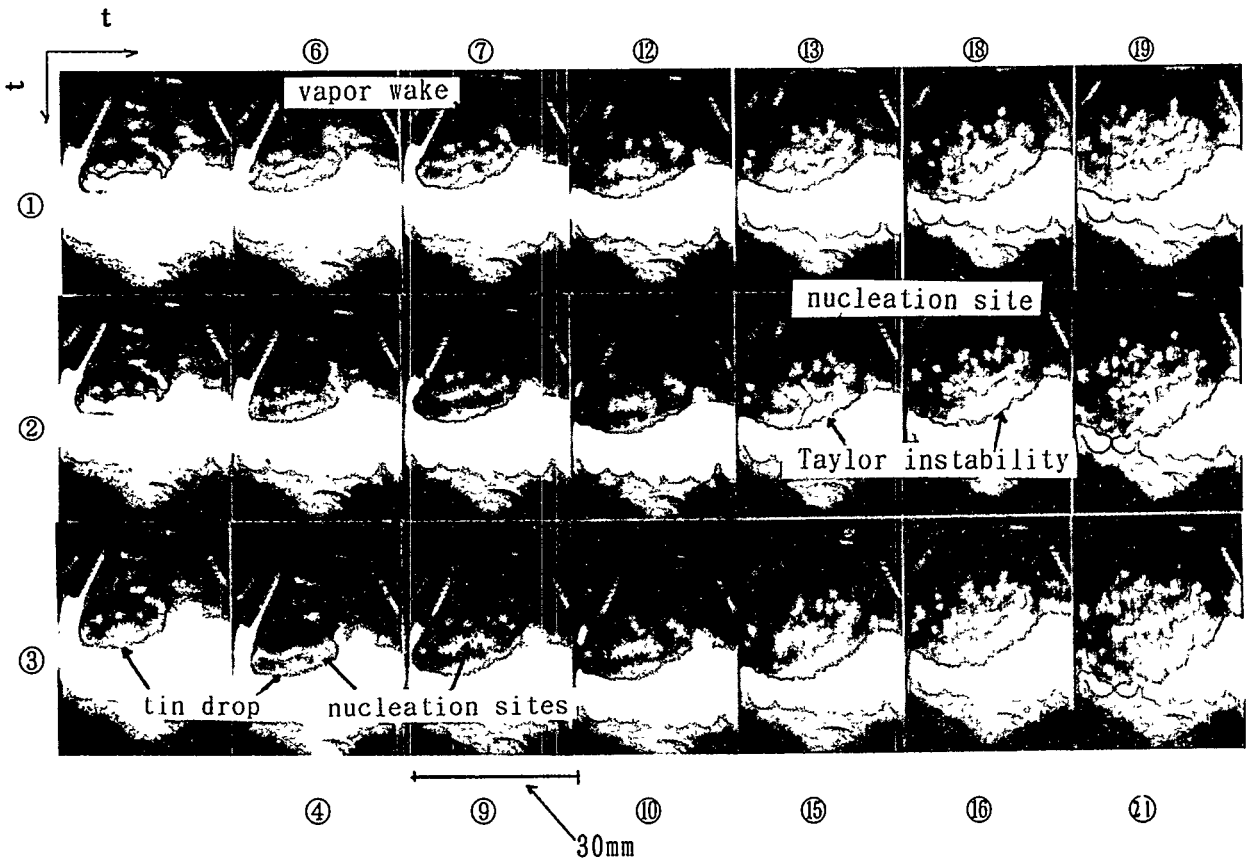


Fig. 4 Time histories of T_w and q_w under pressure wave, ΔP at various initial wall temperature



(a) 20, 000 frames/sec

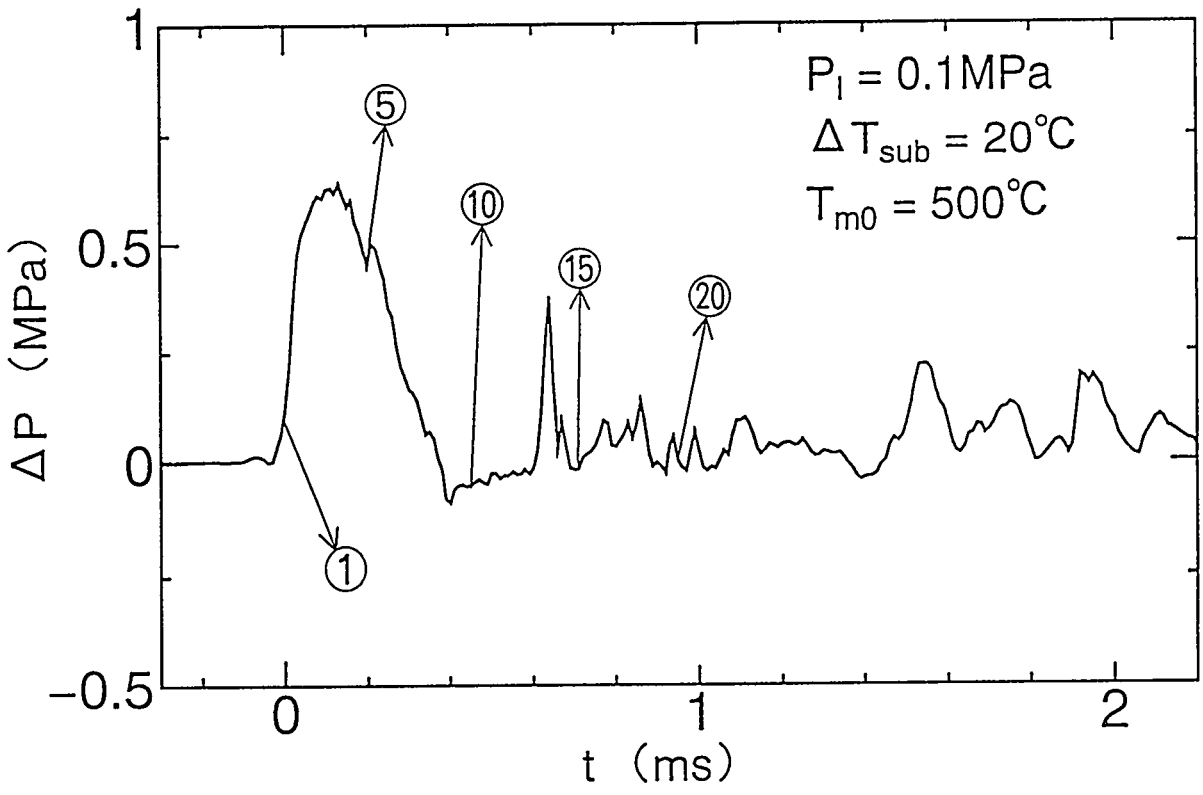
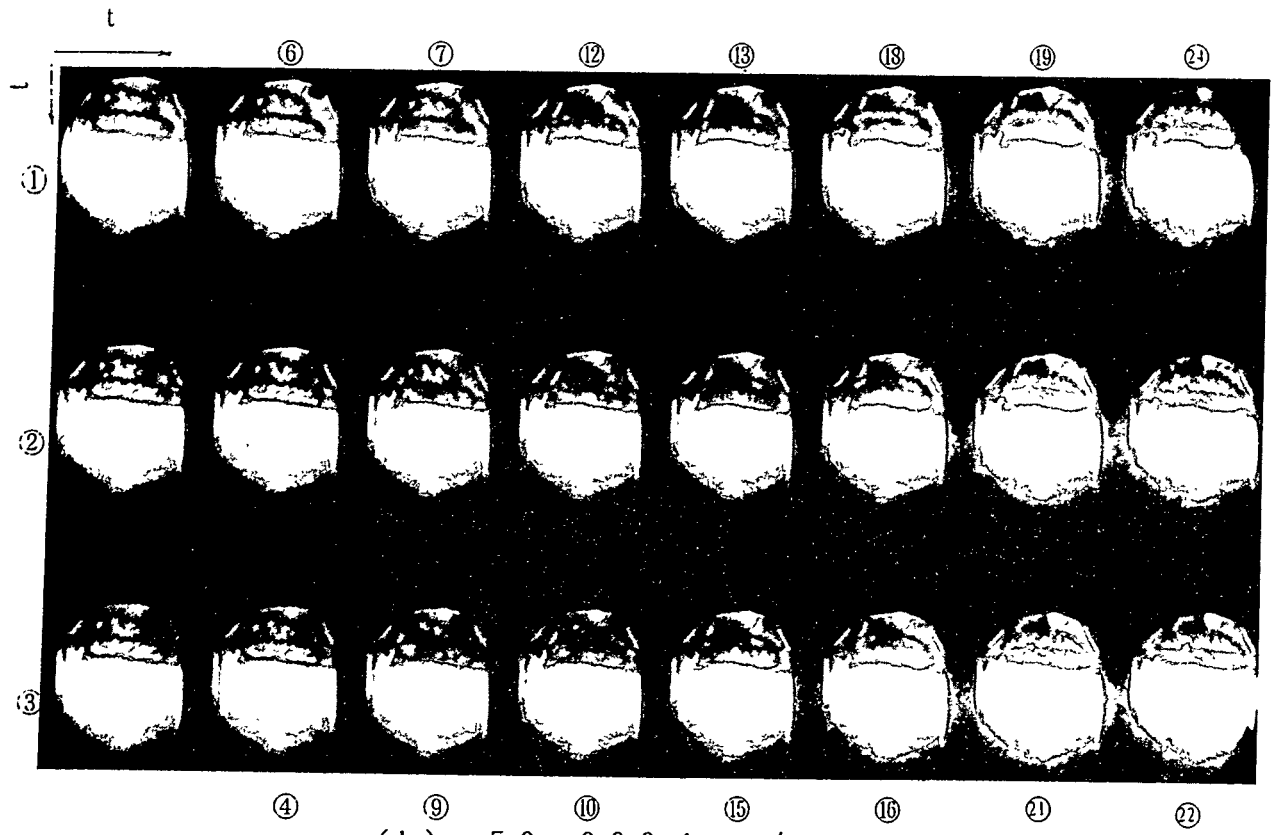
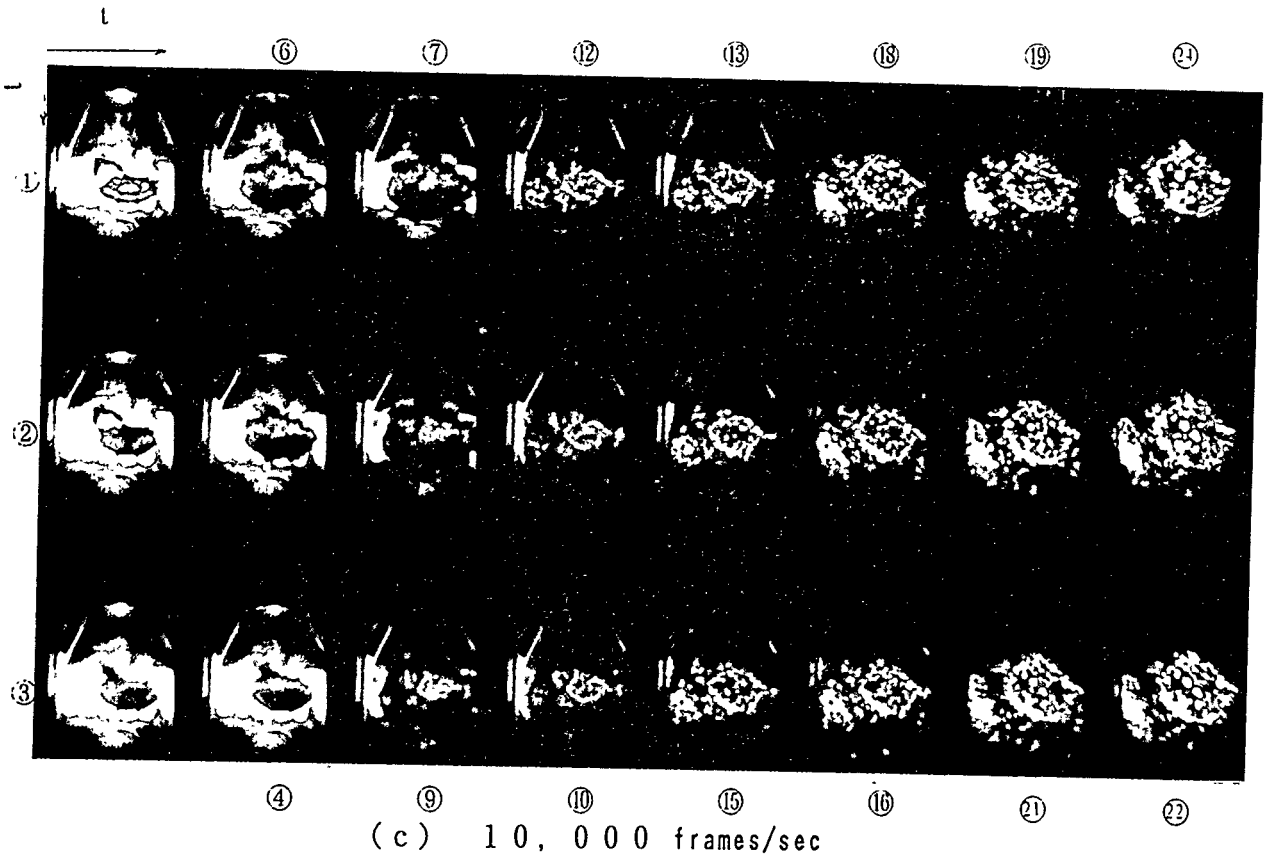


Fig.6 (a) Continuous photographs of a tin drop at arrival of a pressure pulse. Initial tin temp, Tmo=500 ℃ Water subcooling, △ Tsub=20 K.



(b) 50,000 frames/sec



(c) 10,000 frames/sec

Fig.6 **(b) and (c)**, Continuous photographs at faster and slower speeds than (a) when a pressure pulse arrives at a tin drop. All experimental conditions are the same with those in Fig. 6 (a).

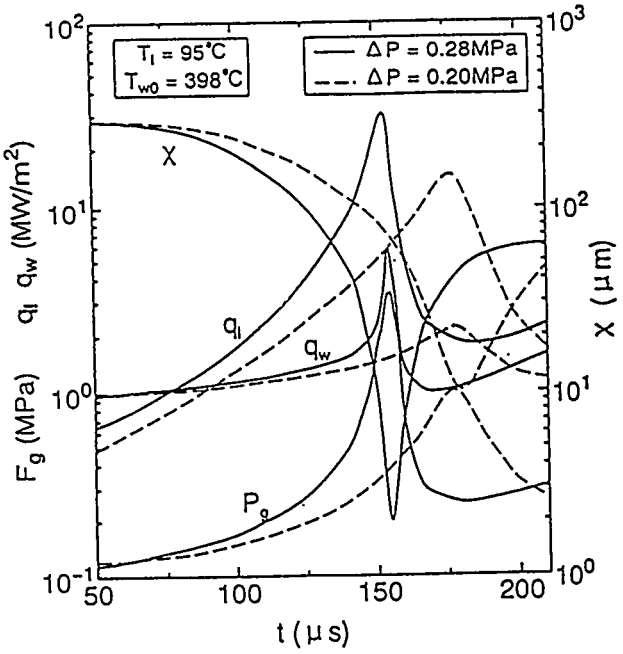


Fig. 5 Analytical results of time histries for heat fluxes at wall, q_w, and vapor-liquid interface, q_l, thickness, χ, and pressure, P_g, of vapor film.

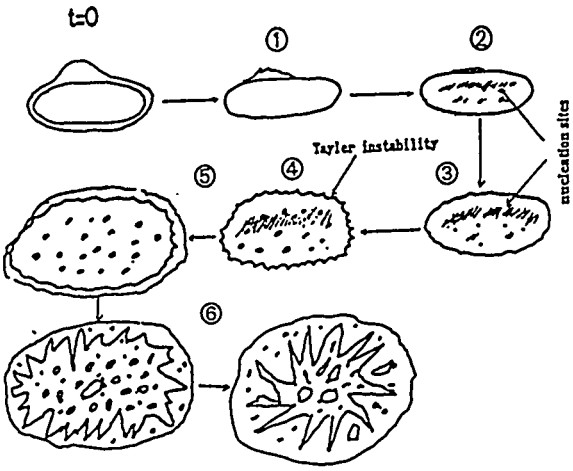


Fig. 7 Behaviors of vapor-liquid interface around a melt tin drop after arrival of pressure wave

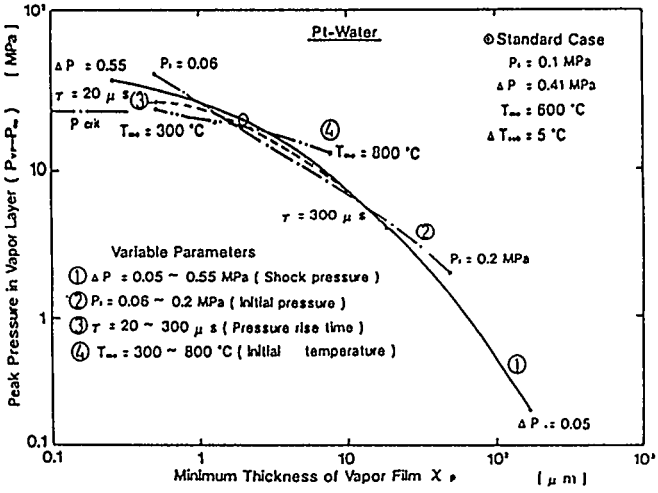


Fig. 9 Relation between peak pressure, $(P_{vp}-P_\infty)$ and minimum thickness of vapor film, χ_p

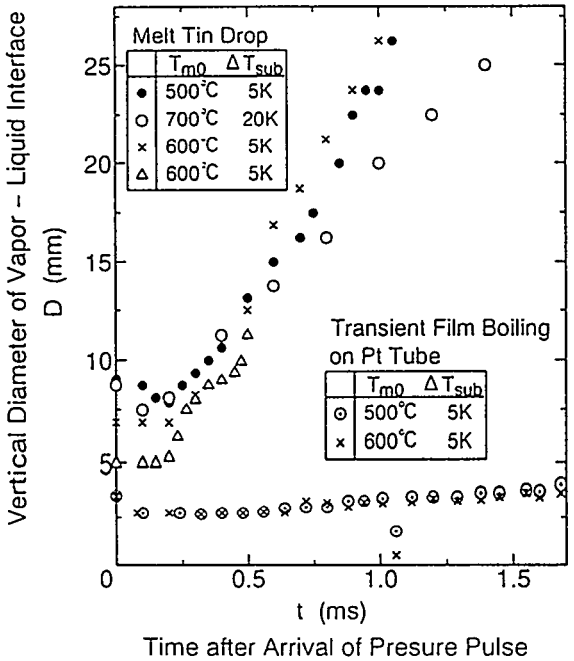


Fig. 8 Growth rates of vapor-liquid interface in vertical direction around melt tin drop and platinum tube

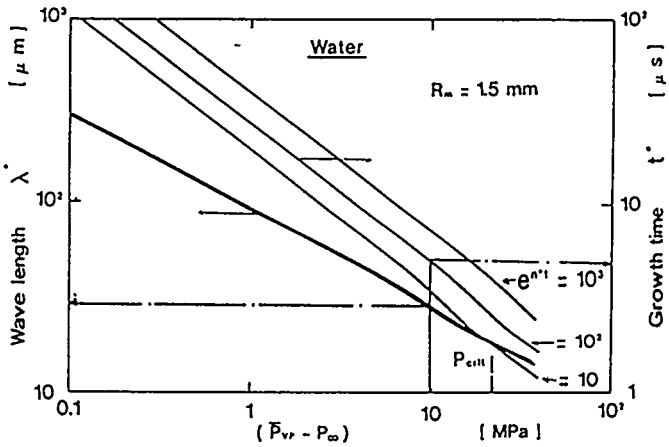


Fig. 10 Relations among averaged peak pressure, $(P_{vp}-P_\infty)$, wave length, λ^*, and growth time, t^* of the most instable wave of Tayler instability

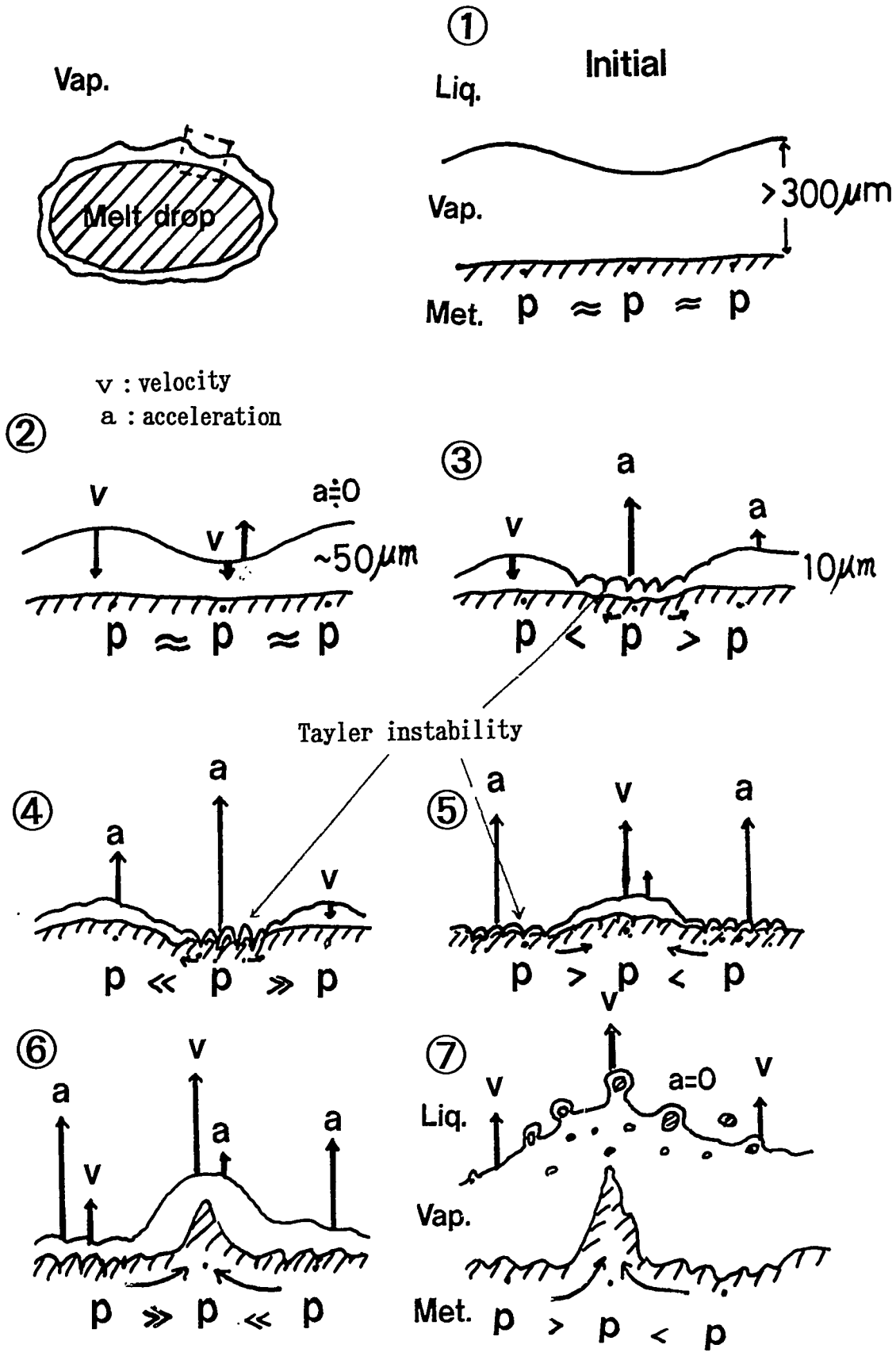


Fig. 11 Proposed mechanism of vapor-fluid interfaces at arrival of pressure wave

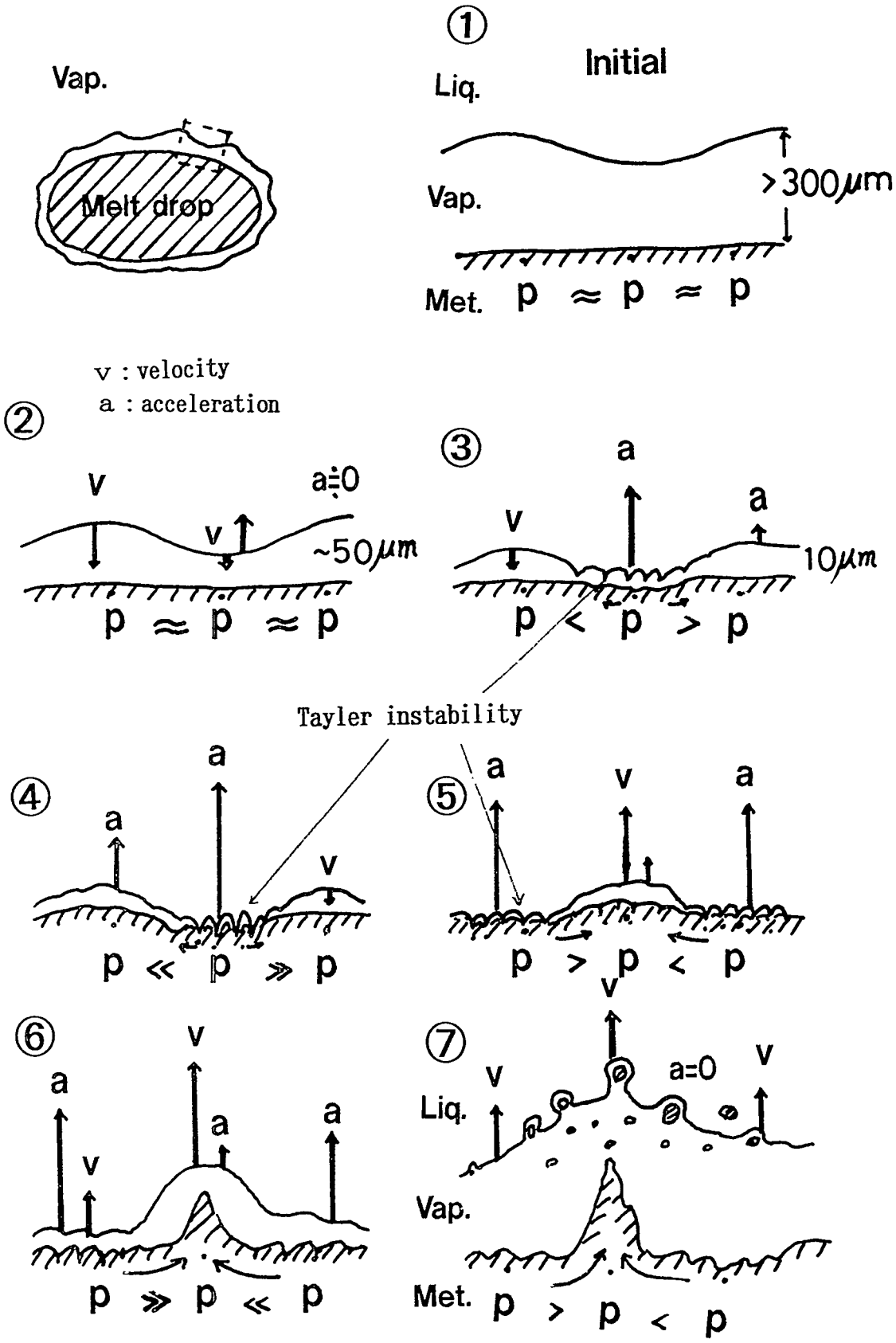


Fig. 11 Proposed mechanism of vapor-fluid interfaces at arrival of pressure wave

BOILING CHARACTERISTICS OF DILUTE POLYMER SOLUTIONS AND IMPLICATIONS FOR THE SUPPRESSION OF VAPOR EXPLOSIONS

K.H. Bang and M.H. Kim
Dept. of Mechanical Engineering, Pohang University of Science and Technology
San 31 Hyoja Dong, Pohang, S. Korea

Abstract

Quenching experiments of hot solid spheres in dilute aqueous solutions of polyethylene oxide polymer have been conducted for the purpose of investigating the physical mechanisms of the suppression of vapor explosions in this polymer solutions. Two spheres of 22.2mm and 9.5mm-diameter were tested in the polymer solutions of various concentrations at 30℃. Minimum film boiling temperature(ΔT_{MFB}) in this highly-subcooled liquid rapidly decreased from over 700℃ for pure water to about 150°C as the polymer concentration was increased up to 300ppm for 22.2mm sphere, and it decreased to 350℃ for 9.5mm sphere. This rapid reduction of minimum film boiling temperature in the PEO aqueous solutions can explain its ability of the suppression of spontaneous vapor explosions. The ability of suppression of vapor explosions by dilute polyethylene oxide solutions against an external trigger pressure was tested by dropping molten tin into the polymer solutions at 25°C. It was observed that in 50ppm solutions more mass fragmented than in pure water, but produced weaker explosion pressures. The explosion was completely suppressed in 300ppm solutions with the external trigger. The debris size distributions of fine fragments smaller than 0.7mm were shown almost identical regardless of the polymer concentrations.

I. INTRODUCTION

Vapor explosions, or so-called Fuel-Coolant Interactions(FCIs), are physical processes in which very rapid energy transfer occurs between a hot liquid and a volatile, colder liquid when the two liquids come into a sudden contact. The high heat transfer rate associated with fine fragmentation of the liquids causes rapid vaporization of the cold liquid and the resulting high pressure mixture expands against the low-pressure surroundings. Since this process has the potential of destructive mechanical energy release and high pressure load to the system, it has been a safety concern in severe nuclear reactor accidents as well as many industrial accidents in metal foundries and paper mills.

While many investigators have conducted experiments and developed physical models of vapor explosions in order to understand the physical mechanisms and to quantify the potential hazard, a way of preventing or mitigating vapor explosions has been also sought. Long[1], for example, reported that the explosive interactions of molten aluminum and water in aluminum industry were caused by the rapid vaporization of water entrapped between the melt and container bottom surface and suggested that a coated container surface prevent the explosive interactions. Another way of studying the suppression of steam explosions has been the change of the physical properties of water, in particular, viscosity and surface tension. These properties were altered by dissolving small amount of additives such as polymers and surfactants. A numerous studies have been reported on the effects of such additives on the suppression of vapor explosions. The studies of surface tension effects[2-4] indicates that

dilute solutions of surfactants have a mitigating effect on both spontaneous and triggered vapor explosions, but there has been no observation of complete suppression of the explosion. Also it was reported that the surfactants increased the efficiency of explosions at certain range of coolant temperature (~20°C)[3].

One of the most useful features of polymers is their ability to increase the viscosity of a liquid in which they are dissolved, even at low concentrations. Also, dilute aqueous polymer solutions have been studied for many years in the area of drag reduction in turbulent flows and thermal systems. For this reason, many kinds of polymers have been studied for the effects of coolant viscosity on the suppression of vapor explosions and some polymers were reported to show the ability of suppression[5,6]. The cut-off concentration depended on the type of polymers, as high as 240 times higher viscosity than pure water for triggered explosions of iron oxide and water[6]. Such high viscosity seems to discourage a practical application of the results.

Recently, Ip et al.[7] reported that the dilute aqueous solution of polyethylene oxide(PEO) showed the ability to suppress spontaneous vapor explosions at low viscosity increase. They conducted small-scale experiments of dropping 12g of molten tin into dilute PEO solutions and observed that spontaneous explosions were markedly suppressed when the polymer solution was twice viscous as pure water. This result of PEO solutions was tested again in the large-scale experiments by Park et al.[8]. In these experiments, molten tin up to 5kg was dropped into the polymer solutions at room temperature and no explosive event was observed even at low viscosity increase (about two fold) and external triggering. The ability of suppression of vapor explosions by the dilute PEO solutions seems to be a promising result for preventing violent vapor explosions, however, the physical mechanism of the suppression effects and the effect of external trigger on the cut-off viscosity has not been clearly identified.

In the present study, quenching experiments of hot solid spheres in dilute water solutions of polyethylene oxide have been conducted for the purpose of investigating the physical mechanisms of the suppression effects, and also the effect of external trigger has been tested in small-scale experiments of dropping molten tin into the PEO aqueous solutions. This paper reports the observations of pool boiling characteristics of the polymer solutions and the effect of external triggering.

II. POOL BOILING EXPERIMENTS

II.A. Experimental Apparatus

The apparatus was designed for both boiling experiments of solid spheres and small-scale vapor explosion experiments. For pool boiling experiments, the apparatus consisted mainly of test chamber, furnace, trigger device, and the test sphere assembly. Figure 1 shows a schematic of the experimental apparatus. The test chamber was an open-topped rectangular construction using clear polycarbonate plates for the purpose of visual observation. The inner dimensions of the chamber were 150mm in height and 90mm each side. The base of the chamber was a movable circular disk sealed with an o-ring. A pressure wave was produced by tapping this plate using a pneumatic cylinder when the effect of an external disturbance was investigated. On a side wall of the chamber a T-type thermocouple was inserted to monitor pool temperature and a piezoelectric pressure transducer(PCB Model 112) was flush-mounted to measure dynamic pressure produced in transient boiling. A charge amplifier was used to amplify the signals from the pressure transducer. The pool temperature was controlled by circulating water through a copper coil immersed into the pool and a constant-temperature bath.

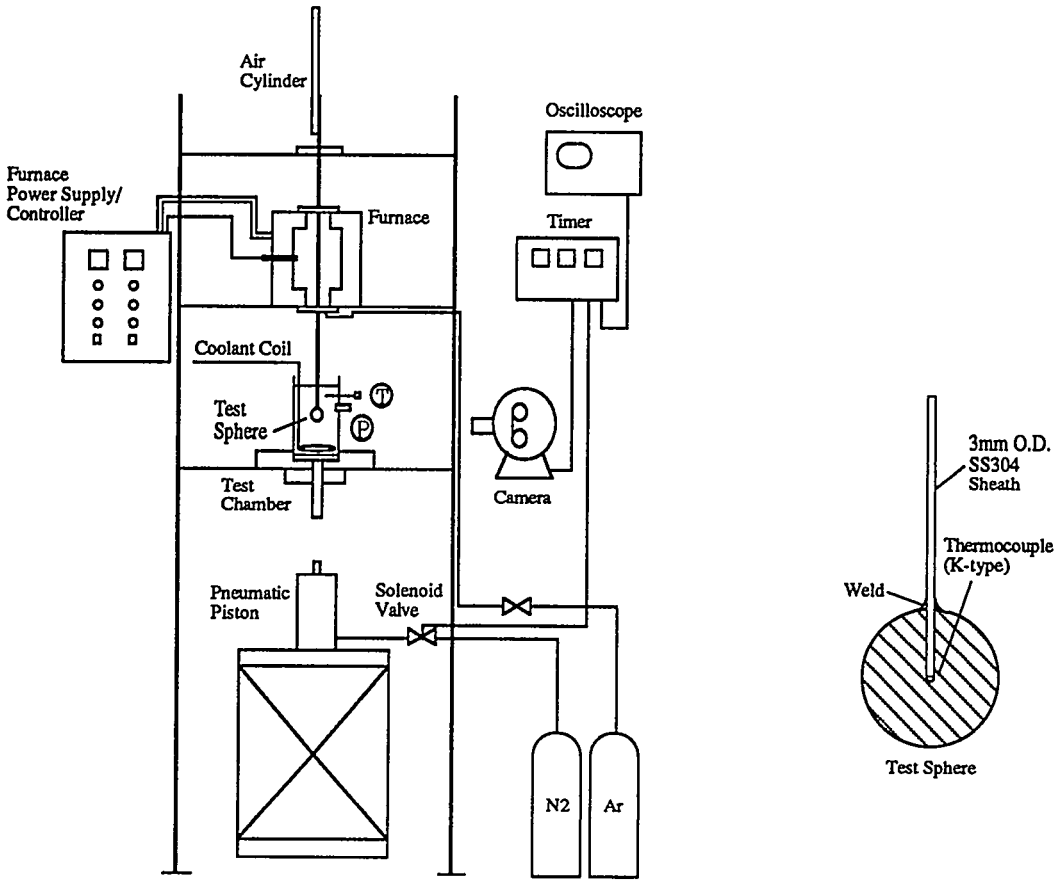


Fig.1. Experimental Apparatus

An electric furnace was used for heating the test sphere. It was fabricated using two half-cylinder heaters of 1.3kW capacity in total. A K-type thermocouple was inserted into the inner space of the furnace and connected to a temperature controller to regulate the furnace temperature at a desired temperature. The furnace was continuously purged with argon gas to minimize the surface oxidation of the test sphere.

The test spheres were stainless steel 304 balls and two sizes were used; 22.2mm and 9.5mm in diameter. To measure the transient temperature of the sphere, the sphere was drilled to the center and a K-type thermocouple, sheathed with 3mm outer-diameter stainless steel tube, was inserted to the center position and the sheath was welded at the sphere surface. To obtain fast sampling of the thermocouple signal, an electronic ice-point compensator and a millivolt amplifier were placed between the thermocouple and the digital oscilloscope. The sphere was mounted by an air cylinder for easy and fast release from the furnace to the test chamber. The release of the sphere, data acquisition trigger, and all other motions in the apparatus were controlled using a set of electronic timers.

The polymer solutions were prepared by adding slowly the dry PEO polymer of average molecular weight of 4×10^6 in powder form into distilled water in a large beaker while the water

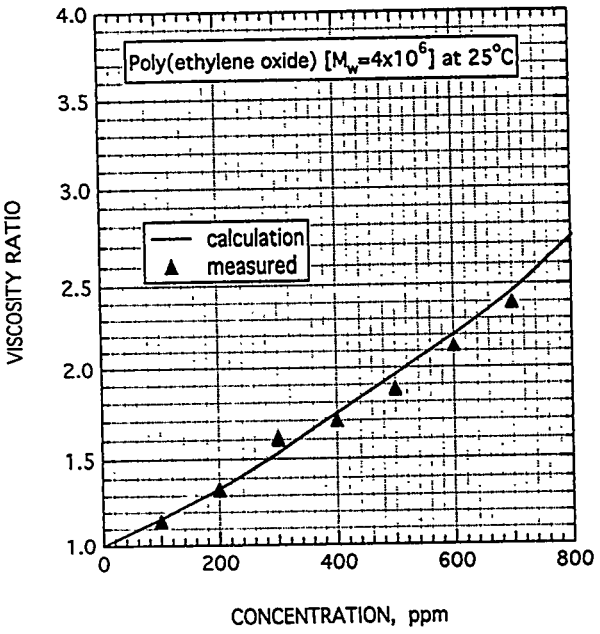


Fig.2. Viscosity Increase of Aqueous Solutions of Polyethylene Oxide

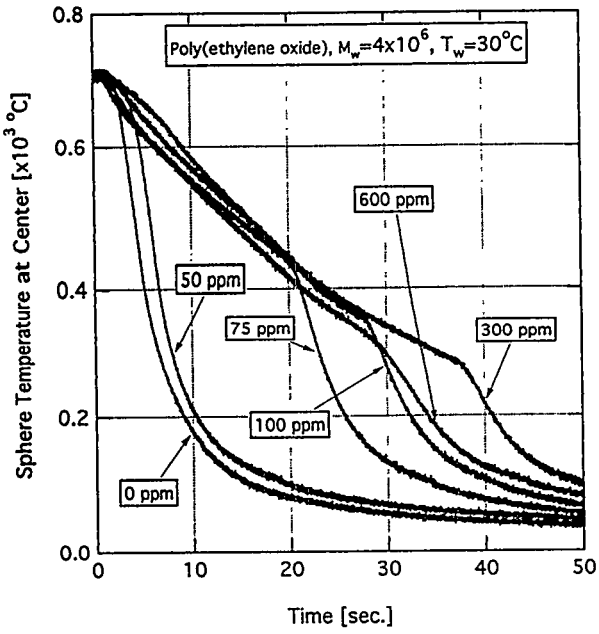


Fig.3. Temperature-Time Traces of 22.2mm Sphere in Various Polymer Concentrations

was stirred using a motor-driven stirrer at about 300rpm. Then, the stirring was continued for another 4 to 8 hours depending on the concentration until the polymer dissolved completely. The viscosity of the solution was measured with a size 50 Cannon-Fenske type capillary viscometer. Figure 2 shows the viscosity increases of the polyethylene oxide solutions at various concentrations. In this figure, calculations of solution viscosity using the MHS equation[10] are compared with the measured viscosity and a good agreement is observed.

II.B. Data Reduction

To obtain the sphere surface temperature from the measured temperature-time trace at the center of the sphere, the inverse conduction problem was solved. Since for the stainless steel sphere, the Biot number is greater(>0.1), the lumped capacity model may not be accurate enough for the present cases. Knowing the temperature of the center of the sphere as a function of time and the time of minimum film boiling point from the pressure signal, the surface temperature and heat transfer coefficient were calculated by solving 1-D transient conduction equation for the sphere with convective boundary condition[9]. The solution was obtained by assuming constant thermophysical properties and uniform and constant heat transfer coefficient.

II.C. Results and Discussions

Pool boiling of hot solid spheres in dilute polyethylene oxide solutions at primarily room temperature (30°C) was investigated. In pure water at 30°C, the sphere at initially 700°C quenched rapidly and it was obviously in nucleate boiling regime from the beginning as confirmed also from the visual observation. Such difficulty of sustaining stable film boiling in

such highly subcooled water was also observed in the past work[11].

However, in the polymer solutions, the boiling behavior markedly changed. Figure 3 and Figure 4 show the temperature-time traces of the two spheres quenched from the same initial temperature of 700°C, but in the polymer solutions of various concentrations. The sphere quenched slowly in film boiling regime and, for instance, this boiling mode lasted for 35 seconds in 300ppm solution for 22.2mm diameter sphere. The visual observation showed clearly the three modes of boiling; (a) stable film boiling, (b) film collapse, and (c) nucleate boiling. Also in the polymer solutions, the collapse of vapor film around the sphere was clearly identified such that a big sound was heard and, at this point, a pressure peak was recorded in the pressure transducer signal as shown in Fig.5. This pressure peak is a more accurate indication of the minimum film boiling point than the point of the beginning of rapid temperature decrease, which past investigators often assumed for the transition point.

In Fig.5, the calculated temperatures at the surface and the center of the sphere are plotted together with the measured center temperature. It shows a good agreement between the measurement and calculation of the center temperature except the early time. This is because the heat transfer rate was relatively higher in this early period of initial contact between the sphere and the liquid.

From the calculated surface temperatures of the spheres, the minimum film boiling temperature differences ($\Delta T_{MFB}=T_W-T_{SAT}$) were obtained and shown in Fig.6 as a function of polymer concentration. In this figure, the value for the pure water is shown together for comparison, which was obtained from the extrapolation of the data up to 50°C of subcooling obtained by Dhir and Purohit[11]. For 22.2mm diameter sphere, the minimum film boiling temperature decreased rapidly from over 700°C for pure water to about 150°C as the

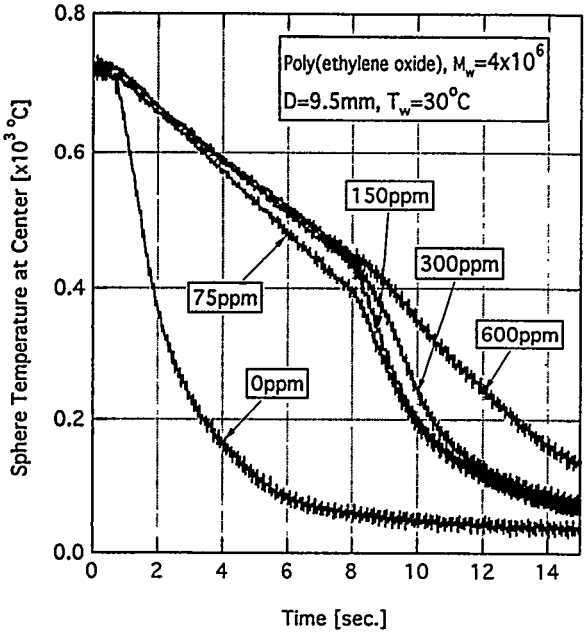


Fig.4. Temperature-Time Traces of 9.5mm Sphere in Various Polymer Concentrations

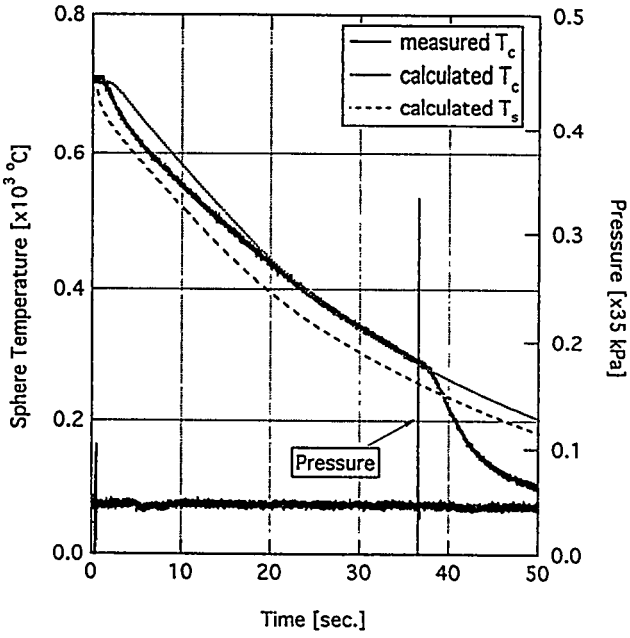


Fig.5. Comparison of Measured and Calculated Temperature Traces

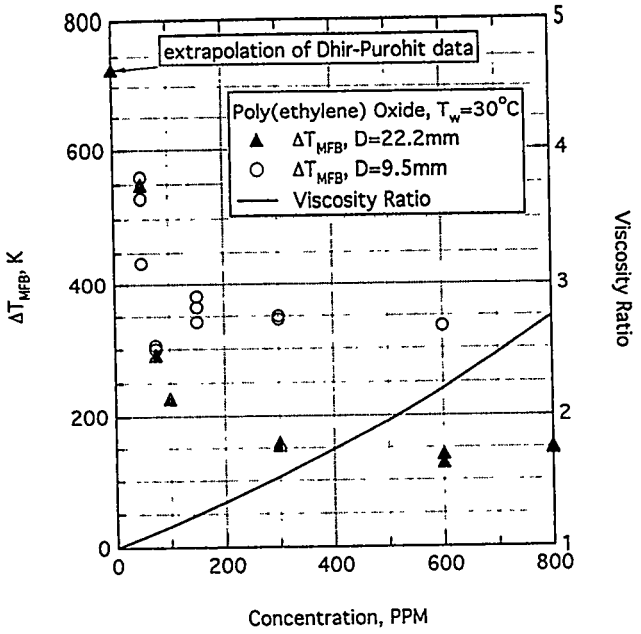


Fig.6. Minimum Film Boiling Temperatures vs. Polymer Concentration

concentration was increased up to 300ppm, and it did not decreased further from this level when the concentration was further increased. Such trend persisted also for 9.5mm diameter sphere except that the reduction is smaller, down to about 350°C. This is the major unique observation in the present study for the effect of dilute aqueous solution of polyethylene oxide on pool boiling, and this seems to be the key mechanism in explaining the ability of vapor explosion suppression by these polymer solutions.

The present results are, however, contrast to the results obtained by Rouai and Abdel-Khalik[12] in the past. They conducted similar experiments using 4.76mm and 6.38mm-diameter brass spheres at 90°C pool temperature. Their results showed that the PEO solutions increased minimum film boiling temperature. It is, however, noted that in these two experiments the pool temperatures are severely different. Therefore, in order to identify the cause of the disagreement, a series of tests using 9.5mm-diameter sphere were conducted in heated pool to 80°C and the temperature-time traces are shown in Fig.7. Again in these heated pool tests, the sphere quenched in film boiling in the polymer solutions much longer than in pure water. Also, the heat transfer rates seemed to be almost same regardless of the polymer concentration by noting the same slopes of temperature in film boiling regime. In pure water at 80°C, the minimum film boiling temperature difference was 440°C and it was 350°C in 300ppm PEO solution. For pure water, the present result is higher than the Dhir and Purohit's data of 260°C for 19mm and 25.4mm-diameter spheres and 20°C water subcooling. For 10°C water subcooling, Rouai and Abdel-Khalik reported 80°C of minimum film boiling temperature difference and it is 180°C from the Dhir and Purohit's data. In these comparison, one of the major differences in the experimental conditions is the sphere diameter whose effects on the minimum film boiling seems to need further investigation. For PEO solutions, one notes that the PEO polymer chains in aqueous solutions retain to a greater or lesser extent the helical conformation and the melting point of these helical sections is around 40°C[10]. This may cause an instability of the properties of PEO aqueous solutions kept at high temperature for a

long period of time.

It is noted that the solution viscosity increases nearly linearly with the concentration, while the minimum film boiling temperature in the solutions drops rapidly within the range of 100ppm and stays unchanged in higher concentrations. This indicates that the viscosity may not be the only contributing parameter for this change of minimum film boiling temperature in polymer solutions. One may also note that currently existing models of minimum film boiling temperature[13] do not contain liquid viscosity in the equations. The change of surface tension of PEO aqueous solutions is reported to be negligible[7]. Therefore, it is suggested that the interfacial phenomena at the vapor-liquid interface in which polymer is dissolved may play a greater role in such change of minimum film boiling temperature, particularly with a linear-chain polymer like PEO.

The rapid reduction of minimum film boiling temperature in the PEO aqueous solutions may explain its ability of the suppression of spontaneous vapor explosions. That is, in the polymer solutions, a drop of molten metal undergoes more stable film boiling at even low temperature. Thus at the time that the vapor film becomes unstable, which is often considered as one of the plausible triggering mechanisms of spontaneous vapor explosions, the drop surface is already frozen, preventing disintegration of the drop. This is why a spontaneous explosion is less likely in the polymer solutions.

In the case when an external disturbance like a pressure wave exists, the vapor film can be destabilized before the surface cools down to minimum film boiling condition. In order to investigate the effect of an external disturbance, a series of tests were conducted in which the base of the test chamber was tapped to produce pressure waves. Figure 8 shows the temperature traces of the sphere when the pressure wave was applied five seconds after the sphere was dropped into water. In 300ppm solutions, the vapor film collapsed by the disturbance. In 600ppm solutions, however, stable film boiling was recovered after a short period of vapor film disturbance. Therefore, it is likely that the polymeric additive makes the vapor film more stable against an external disturbance.

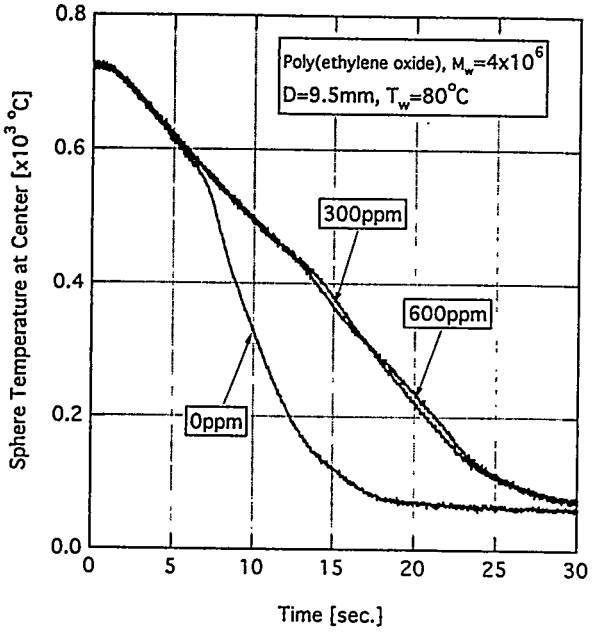


Fig.7. Temperature-Time Traces of 9.5mm Sphere at 80°C

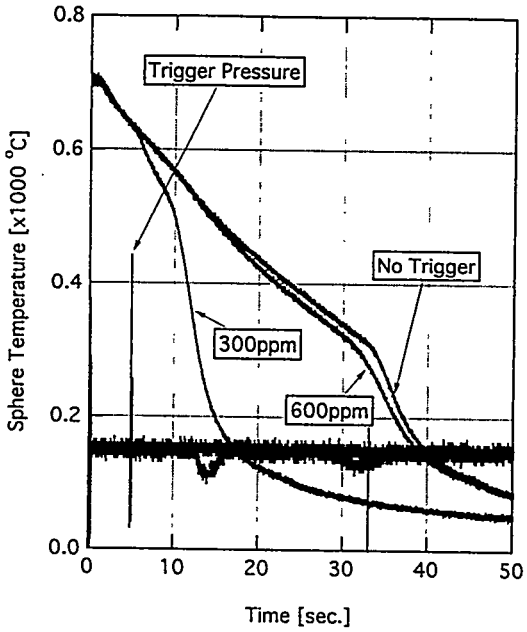


Fig.8. Effect of External Disturbance on Film Boiling

III. TIN/WATER INTERACTIONS

III.A. Experimental Apparatus and Procedure

The apparatus used in the boiling experiments was used again for tin/water triggered vapor explosion experiments by replacing the test sphere assembly with a pipet-type quartz tube for melting the tin. A smaller quartz rod was inserted inside the tube to close the bottom hole until molten tin drop was released and the tube was filled with argon gas before loading into the furnace. A paper filter was placed on the bottom disk of the test chamber to collect the posttest debris after the water was drained.

When the melt temperature reached the desired value, the tube was lowered further down to the inner bottom of the furnace to reduce the drop height to 10cm for minimizing air entrainment by the falling melt drop. The melt was released from the tube by raising the plug rod using a small pneumatic cylinder. The mechanical trigger by hitting the bottom disk of the test chamber was applied when the drop was falling by the middle of the pool. The pressure was recorded at 100kHz rate.

III.B. Results and Discussions

The ability of the suppression of vapor explosions by dilute polyethylene oxide solutions against a weak external trigger pressure was tested by dropping 3.8g of molten tin into the solutions. This amount of tin mass produced two or three drops of molten tin when released from the quartz tube. In most tests, tin temperature was 900°C and the pool temperature was 25°C. The external pressure peak was about 50kPa and this value may represent the pressure of vapor film collapse or local pressure spikes which can be produced when larger mass is dropped.

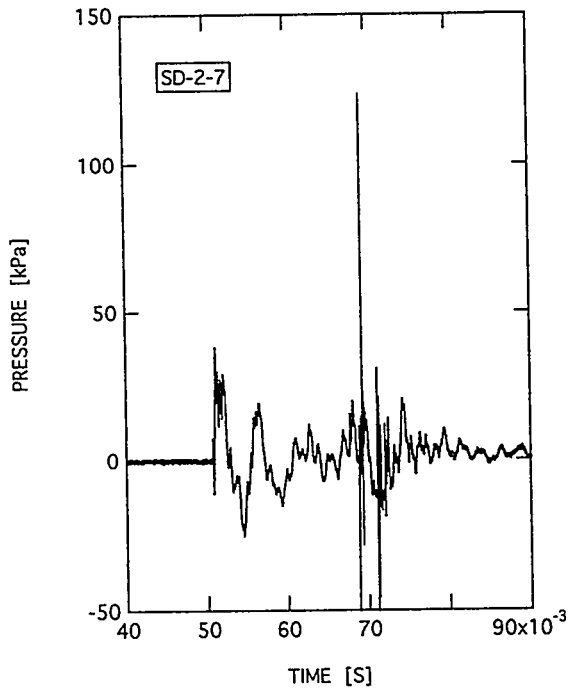


Fig.9.Typical Pressure Trace in Triggered Interaction of Tin in Pure Water

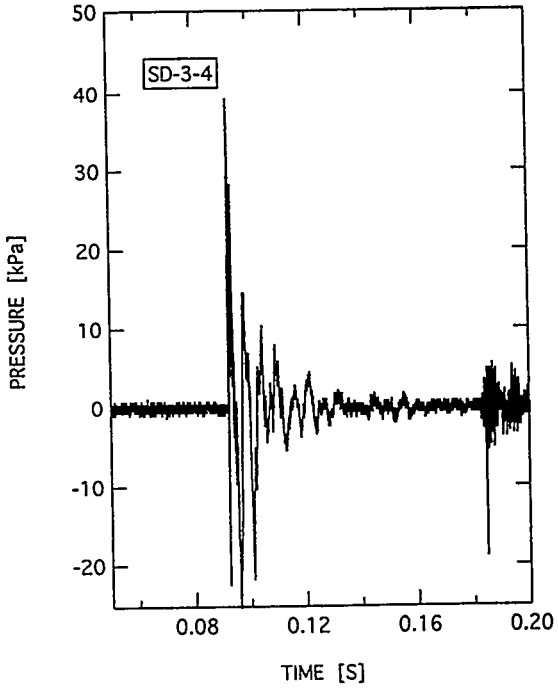


Fig.10.Typical Pressure Trace in Triggered Interaction of Tin in 50ppm PEO Solution

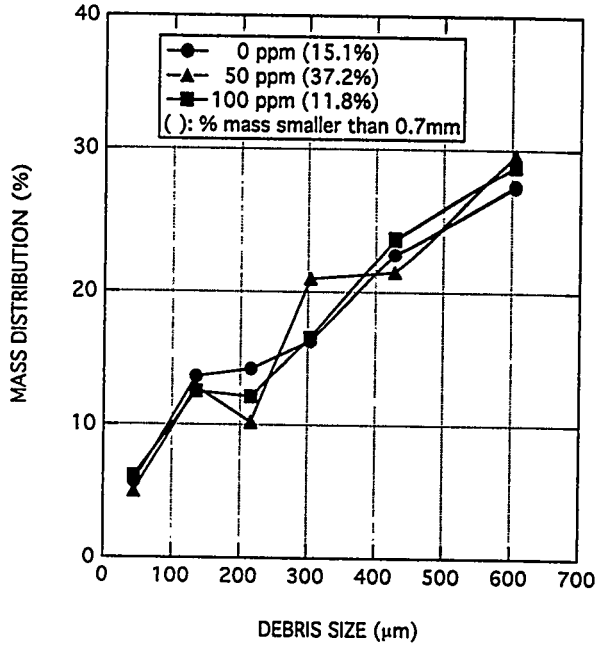


Fig.11. Debris Size Distributions of Particles Smaller than 0.7mm

In pure water, most tests showed a partial or complete fragmentation of the drop and the explosion pressure peaks were relatively low, ranging from 50 to 150kPa. Figure 9 shows a typical pressure trace in pure water tests. The delay time of explosion peak pressure from the trigger widely ranged up to 20 milliseconds. In 50ppm solutions of PEO, more fraction of the melt fragmented than in pure water. However, the pressure traces showed many peaks of much



Fig.12. Electron Microscope Photographs of the Debris from Pure Water (left) and 100ppm PEO Solution (right)

smaller value of under 10kPa as shown in Fig.10 for a typical pressure trace and the delay time of these peaks were longer up to 100 milliseconds. In 100ppm solutions, the peak pressures were at the negligible level, but the melt was still partially fragmented at the level of pure water cases. When 300ppm solutions were tested, no fragmentation was observed in all 5 tests.

In all tests, the collected debris were dried and sieved. As observed in most other experiments using tin, a large fraction of the debris appeared as a single porous piece with rough and stretched surfaces rather than separate particles. When the particles smaller than 0.7mm were sieved, the mass distributions of these fine particles are as shown in Fig.11. As seen in this figure, an almost identical distribution of these fine fragments was observed regardless of the polymer concentrations. The fraction of these smaller fragments to the total mass was 37% in 50ppm solutions, which was higher than for pure water and 100ppm cases. The pictures of the debris between 90μm and 180μm taken by a scanning electron microscope are shown in Fig.12. Many of these particles look strecthed, much different from the spherical shape.

IV. CONCLUSION

Quenching experiments of hot solid spheres in dilute aqueous solutions of polyethylene oxide polymer have been conducted for the purpose of investigating the physical mechanisms of the suppression of vapor explosions in this polymer solutions. Two spheres of 22.2mm and 9.5mm-diameter were tested. It was heated to 700°C in a furnace and immersed into polymer solutions of various concentrations at 30°C. The key observation in this study was that minimum film boiling temperature(ΔT_{MFB}) in this highly-subcooled liquid rapidly decreased from over 700°C for pure water to about 150°C as the polymer concentration was increased up to 300ppm for 22.2mm sphere, and it decreased to 350°C for 9.5mm sphere. This rapid reduction of minimum film boiling temperature in the PEO aqueous solutions may explain its ability of the suppression of spontaneous vapor explosions. It was also observed that the vapor film behaved more stable against an external disturbance at higher polymer concentrations.

The ability of suppression of vapor explosions by dilute polyethylene oxide solutions against an external trigger pressure(50kPa peak) was tested by dropping 3.8g of molten tin heated to 900°C into the solutions at 25°C. It was observed that in 50ppm solutions more mass fragmented than in pure water, but produced weaker explosion pressures. The explosion was completely suppressed in 300ppm solutions with the external trigger. The debris size distributions of fine fragments smaller than 0.7mm were shown almost identical regardless of the polymer concentrations.

In order to apply such dilute polymer solution technique to the prevention and mitigation of energetic fuel-coolant interactions in severe nuclear accidents, such suppression ability must be tested over wider ranges of conditions such as melt material and coolant temperature, and the aging effect of polymer solutions must be taken into consideration.

ACKNOWLEDGMENT

This work has been supported by the Korea Science and Engineering Foundation through the Advanced Fluids Engineering Research Center at Pohang University of Science and Technology. The authors wish to thank the Institutions for the financial support.

REFERENCES

[1] G. Long, "Explosion of Molten Aluminum in Water - Cause and Prevention," Metal Progress, 71, 107-112 (1957).

[2] K.M. Becker and K.P. Lindland, "The Effects of Surfactants on Hydrodynamic Fragmentation and Steam Explosions," KTH-NEL-50, Royal Inst. of Tech. Stockholm, Sweden (1990).

[3] M. Baker, "Single Droplet Studies with the Addition of a Surfactant," M.S. Thesis, Univ. of Wisconsin-Madison (1990).

[4] M.G. Kowal, M.F. Dowling and S.I. Abdel-Khalik, "Effects of Surfactants on the Likelihood and Severity of Steam Explosions," CSNI-FCI Specialists Mtg., Santa Barbara, CA (1993).

[5] L.S. Nelson and K.P. Guay, "Suppression of Steam Explosions in Tin and Fe-Al_2O_3 Melts by Increasing the Viscosity of the Coolant," High Temp.- High Pressure, 18, 107 (1986).

[6] H. Kim, "Single Droplet Vapor Explosion Experiments," Ph.D Thesis, Univ. of Wisconsin-Madison (1987).

[7] B.M. Ip, M.F. Dowling and S.I. Abdel-Khalik, "Suppression of Vapor Explosions by Dilute Aqueous Polymer Solutions," Nucl. Sci. Eng., 113, 300-313 (1992).

[8] H.S. Park, M.L. Corradini, and K.H. Bang "The Effect of Coolant Additives on Fuel-Coolant Interactions," Proc. of 2nd Int. Conf. on Multiphase Flow, 3, VE33-40, Kyoto, Japan (1994).

[9] A.F. Mills, Heat Transfer, Irwin (1992).

[10] P. Molyneux, Water-Soluble Synthetic Polymers: Properties and Behavior, Vol. I, CRC Press (1982).

[11] V.K. Dhir and G.P. Purohit, "Subcooled Film-Boiling Heat Transfer from Spheres," Nucl. Eng. Des., 47, 49-66 (1978).

[12] N.M. Rouai and S.I. Abdel-Khalik, "Pool Boiling of Drag-Reducing Polymer Solutions," Appl. Sci. Res., 40, 209-222 (1983).

[13] V.P. Carey, Liquid-Vapor Phase Change Phenomena, Hemisphere (1992).

EXPERIMENTAL INVESTIGATION OF 150-KG-SCALE CORIUM MELT JET QUENCHING IN WATER[a]

D. Magallon and H. Hohmann

European Commission
Joint Research Centre
Safety Technology Institute
I - 21020 Ispra (Va)

ABSTRACT

The paper compares and discusses the results of two large scale FARO quenching tests known as L-11 and L-14, which involved, respectively, 151 kg of w% 76.7 UO_2 + 19.2 ZrO_2 + 4.1 Zr and 125 kg of w% 80 UO_2 + 20 ZrO_2 melts poured into 600-kg, 2-m-depth water at saturation at 5.0 MPa. The results are further compared with those of two previous tests performed using a pure oxidic melt, respectively 18 and 44 kg of w% 80 UO_2 + 20 ZrO_2 melt quenched in 1-m-depth water at saturation at 5.0 MPa. In all the tests, significant breakup and quenching took place during the melt fall through the water. No steam explosion occurred. In the tests performed with a pure oxide UO_2-ZrO_2 melt, part of the corium (from 1/6 to 1/3) did not breakup and reached the bottom plate still molten whatever the water depth was. Test L-11 data suggest that full oxidation and complete breakup of the melt occurred during the melt fall through the water. A proportion of 64% of the total energy content of the melt was released to the water during this phase (~1.5 s), against 44% for L-14. The maximum temperature increase of the bottom plate was 330 K (L-14). The mean particle size of the debris ranged between 3.5 and 4.8 mm.

1. INTRODUCTION

The FARO tests have been designed to provide data on mixing and quenching of large masses of real corium melt in water under severe accident prototypical conditions [1, 2]. Quantities of the order of 150 kg of UO_2-ZrO_2 and UO_2-ZrO_2-Zr mixtures are used. Basically, the penetration of the molten corium into the water of the lower plenum and its subsequent settling on the bottom head of the RPV are simulated. So far, the knowledge in this area was based essentially on small scale, simulant and separate effect experiments. The computer models for describing mixing and quenching phenomena were validated against this data base. It revealed to be insufficient to explain the facts

[a]The present FARO-LWR Test Programme is performed in collaboration with USNRC in the frame of Technical Exchange Agreement n° 4086-90-09 TG ISP USA.

that occurred in the TMI-2 accident and, particularly, why the reactor pressure vessel did not fail under the accident conditions [3, 4].

In FARO, the melt quantity is still of two orders of magnitude lower than expected in a real accident (e.g., TMI-2 accident), but it is one order of magnitude higher than what has been experimentally performed so far in the field using real material [5]. Furthermore, the depth of water (up to 2 m), the system pressure and temperature (up to 10 MPa and 573 K), the melt delivery conditions (flow rate, release by gravity) are realistic and the volumes involved scale the reactor case. Thus, the data represent a major contribution in evaluating the potential of water to quench the core material before it reaches the bottom of the reactor pressure vessel, the subsequent early thermal load on the bottom structure and to characterise the debris structure. They complement the data from simulant and small scale experiments in validating the computer models for melt/water mixing and quenching.

So far, high pressure core melt down scenarios have been simulated. Two preliminary tests known as L-06 and L-08 were performed with 18 and 44 kg of pure oxide w% 80 UO_2 + 20 ZrO_2 melts poured into 1-m-depth water at saturation at 5.0 MPa (537 K) from a nozzle of diameter 100 mm [2]. They have shown that, although significant breakup and thus quenching of the melt occurred, part of the corium (~1/3) reached the bottom plate still molten. Nevertheless, the thermal load on the bottom plate remained rather mild with a temperature increase of the plate contact face around 275 K.

Two larger size tests known as L-11 and L-14 have been performed. They involved, respectively, 151 kg of w% 76.7 UO_2 + 19.2 ZrO_2 + 4.1 Zr and 125 kg of w% 80 UO_2 + 20 ZrO_2 melts quenched in 600-kg, 2-m-depth water at saturation at 5.0 MPa. These tests, together with the two preliminary tests, allow quantifying the effect of melt mass, H_2 generation and water depth on the quenching process.

In the paper the results of the large melt mass tests are reported and compared with those of the two lower size tests. Particular attention is paid to the evaluation of the influence of the melt oxidation on the quenching process.

2. DESCRIPTION OF THE EXPERIMENTS

2.1. Test Apparatus

The experimental arrangement for performing the FARO large size tests is shown in Figure 1. The interaction vessel TERMOS (designed for 10 MPa, 573K) is connected to the UO_2-ZrO_2 melting furnace via the release channel and isolated from it during interaction by the valve SO2. After melting in the FARO furnace, the melt is first delivered to the release vessel, and then released into the water. The release vessel, located in the upper head (so-called dome)

of the test vessel, can contain Zr wire distributed in the volume. In that case (L-11 test) the superheated oxide melt coming from the furnace induced the melting of the zirconium and the formation of a UO_2-ZrO_2-Zr mixture.

The test vessel TERMOS is connected downstream to a condenser via a steam/water separator and exhaust valves (Figure 2). The purpose of this unit is to vent and condense part of the steam produced during the melt quenching should the pressure in the interaction vessel TERMOS exceed a pre-established value (9.3 MPa for the tests reported here). The high pressure steam/water separator is connected to TERMOS by a pipe with an internal diameter of 146 mm. From the separator the steam is distributed to four circuits, each including an exhaust valve (actually full lift safety valve) with a discharge diameter of 32 mm. Downstream to the valves the steam is vented to a low pressure condenser (design pressure 0.8 MPa). The unit was conservatively designed on the basis of predictions from several computer models. Non-condensable gases (such as the hydrogen produced by oxidation of the melt or the argon possibly initially present in TERMOS) can be stored in the 2.5 m^3 free-board volume of the condenser.

2.2. Test Procedure

Initially, the release vessel is at the same low pressure as the furnace (0.2 MPa). After transfer of the UO_2-ZrO_2 mixture to the release vessel, the intersection valve SO1 and the isolation valve SO2 are closed, and the release vessel is pressurised to the TERMOS pressure (i.e., 5.0 MPa) by using an argon supply. Upon pressure equalisation, the two melt catcher flaps automatically open. The lower flap allows the melt to be released to the water by gravity. The side flap, of the same diameter as the melt release flap, prevents against pressure differences between the release vessel and TERMOS during the melt release. After mixing with the water, the corium is collected in the debris catcher. If the pressure in the TERMOS vessel reaches the threshold pressure of the exhaust valves, steam/gas venting to the condenser occurs.

2.3. Instrumentation

The principal quantities measured in the test vessel during the corium quenching are pressures and temperatures both in the freeboard volume and in the water, and temperatures in the debris catcher bottom plate. Tungsten ultrasonic temperature sensors are mounted in the release vessel for measuring the temperature of the melt. A total of about 250 signals are loaded to 6 different recorders of the data acquisition system.

Five KELLER® pressure transducers (piezoresistive, 5-kHz frequency response) measure the vessel pressurisation. Four VIBRO-METER® pressure transducers (piezoelectric, 15-kHz frequency response) are located at four dif-

ferent elevations in the water for rapid transient records in case of an energetic FCI.

Fifteen K-thermocouples are placed off-centre (at radius between 190 and 300 mm) at different elevations above elevation 2000 mm (initial level of the water). Initially, all these thermocouples are therefore in the gas-phase region but actually, because of the level swell, only some of them will measure the temperature of the gas-phase during the interaction (see section 4). Ten of these fifteen thermocouples, placed between the exit of the release vessel and the initial level of the water, are protected from radiation of the melt jet by large shells. One thermocouple on the centreline of the vessel, 250 mm below the lower face of the release flap, detects the passage of the melt. The opening of the melt catcher flaps is indicated by the rupture of two 0.5 mm K-thermocouples. Forty-three water K-thermocouples are distributed at different axial and radial locations in the water. They are used to determine the downward progression and radial expansion of the melt jet. Those not destroyed during melt penetration record the long time water temperature histories. In particular, eleven are placed on the centreline every 0.20 m and are sustained by thin (0.2 mm) stainless steel wires crossing the test section, and fourteen are located in the debris catcher region. Gas-phase and water thermocouples are 0.5 mm in diameter. Sixteen thermocouples of 1.6 mm in diameter are imbedded into the bottom plate of the debris catcher for measuring the thermal load on the plate.

The level swell is measured by means two continuous level-meters based on the time domain reflectrometry method. In tests L-11 and L-14, the level-meters were placed at radius 280 mm, 180° apart from each other. Experimental probes based on the absorption of hydrogen by palladium are used as an attempt to quantify the hydrogen produced by oxidation of the zirconium.

The instrumentation includes also absolute pressure transducers and thermocouples in the separator, on the downstream side of each valve and in the condenser. A mass spectrometer is connected to the condenser for a qualitative indication of the gas composition. Water level measurements are made by differential pressure probes mounted both in the separator and in the condenser. Magnetic indicators show the ON/OFF positions of the exhaust valves.

3. EXPERIMENTAL CONDITIONS

Table 1 summarises the experimental conditions of large size tests L-11 and L-14, together with those of tests L-06 and L-08 made with reduced quantities of melt and water. For test L-11, the discharged mass indicated in Table 3 takes into account five kilograms of debris which deposited in the separator. The main difference between L-11 and L-14 is the quality of the melt. The measured melt temperature in L-14 is 250 K higher than the estimated value for L-11. However, due to the difference of the melting point of the two mixture

(2860 K for L-14 mixture and 2723 K for L-11 mixture), the difference in superheating is only around 100 K.

Table 1. Summary of experimental conditions

Test n°				L-06	L-08	L-14	L-11
Melt	composition	UO_2	w%	80	80	80	76.7
		ZrO_2	w%	20	20	20	19.2
		Zr	w%	0	0	0	4.1
	temperature		K	2923[a]	3023[a]	3073±50[b]	2823[a]
	discharged mass		kg	18	44	125	151
	hydrostatic head in release vessel		m	0.34	0.47	0.57	0.59
	Δp delivery			~gravity[c]	~gravity[c]	gravity	gravity
	initial discharge diameter		m	0.1	0.1	0.1	0.1
	free fall in gas		m	1.66	1.53	1.04	1.09
Water	mass		kg	120	255	623	608
	height		m	0.87	1.00	2.05	2.00
	diameter of water container		m	0.470	0.710	0.710	0.710
	initial mean temperature		K	539	536	537	535
	fuel/coolant mass ratio			0.15	0.17	0.21	0.25
Free-board	gas composition	steam	w%	83	70	77	77
		argon	w%	17	30	23	23
	volume		m^3	0.464	0.875	1.260[d]	1.280[d]
	initial pressure		MPa	5.0	5.8	5.0[d]	4.9[d]
	initial mean temperature		K	543	536	536	536
Exhaust valves	start opening pressure P_s		MPa	-	-	9.3 ± 0.15	
	full opening pressure[e]			-	-	1.05 P_s	
	full opening time[e]		s	-	-	< 0.1 from 1.05 P_s	
	flow area at full opening[e]		m^2	-	-	8.04×10^{-4}	
	sensitivity to back pressure[e]			-	-	no if < 0.5 P_s	
Condenser	overall volume		m^3	-	-	4.0	
	water mass		kg	-	-	1440	
	initial water temp.		K	-	-	290	

[a]Inferred from measurements in previous test; [b]Measured in the test; [c]Damped oscillatory behaviour of the pressure observed in the release vessel during melt delivery (+0.26/-0.15 MPa maximum amplitudes around the system pressure for L-08 at the beginning of melt delivery); [d]Includes separator and piping up to exhaust valves; [e]Valve manufacturer data: proportional opening up to 1.05 P_s corresponding to 20% of full discharge capacity, then full opening.

In test L-11, about 1000 twisted pieces of Zr wire of 1.2 mm in diameter (7 kg) were uniformly distributed in a volume of the release vessel which corresponded to the volume to be occupied by the melt after mixing. We have verified that in case of a reduced quantity of oxide melt with respect to that foreseen, that part of Zr which remained above the mixture did not melt. This indicates that the melting process of the Zr by the oxide melt is rather continuous and soft as the oxide melt penetrates into the Zr bed.

In test L-11, the time period from the start of release of the oxide melt from the furnace to the start of the full mixture delivery to the water was 8.7 s. The leading front of the oxide melt reached the Zr about 1 s after start of release from the furnace, and the release time of the oxide melt from the furnace was about 2 s. This means that all the melt was hold for 5.7 s in the release vessel before delivery to the water. In these conditions, it is very likely that the phases had not sufficient time to segregate and, therefore, that a uniform mixture which was delivered to the water.

4. EXPERIMENTAL RESULTS

Table 2 summarises the main experimental results of the four tests. For all the tests, time zero in the figures corresponds to the start of melt delivery from the release vessel to the water, at the end of the pressure equilibration phase. Essentially the measured quantities and some timing data deduced from the thermocouple signals are reported here. All other data deduced from the measured quantities are presented and discussed in Section 5.

4.1. Pressure

Pressure histories in TERMOS are reported in Figure 3 (-1s<time<40s or end of data acquisition) and Figure 4 (-1s<time<6s). The curves present two main maxima. The first maximum should roughly correspond to the end of the melt fall (approximately end of melt jet breakup). A maximum pressure of 10 MPa was reached at time 2.15 s for L-11 despite 48 kg of steam were discharged to the condenser starting at time 1.50 s (9.3 MPa, see section 4.2). In test L-14, the maximum pressure was only 7.8 MPa reached at time 2.45 s. The rate of pressure increase in L-11 was twice as high as in L-14. The second maximum occurred during the debris cooling phase at time 22 s for L-11 (7.7 MPa) and at time 30 s for L-14 (8.3 MPa).

In tests L-06 and L-08, the pressure increases before melt/water contact were 0.4 MPa and 0.3 MPa, respectively. This corresponds to 36% and 18% of the maximum pressure increases measured in these tests during the melt fall stage [2]. The pressure increases before melt/water contact were 0.3 MPa for L-11 and 0.1 MPa for L-14, i.e., 6% and 4% respectively of the maximum pressure increases observed during the melt fall stage. When comparing these numbers,

it should be kept in mind that in tests L-11 and L-14 the volume and surface exposed to the jet in the gas-space were 40% smaller than in L-08 (mainly due to the shorter distance between the release nozzle and the water surface), and the total free-board volume was 33% higher (due to the presence of the separator and piping directly connected to TERMOS).

Table 2. Summary of experimental data

Test n°			L-06	L-08	L- 14	L-11
Melt	delivery time	s	0.28	0.37	~ 1	~ 1
	mean mass flow rate	kg/s	64	119	125	151
	final discharge diameter	m	0.084	0.095	0.092	0.095
	broken up	kg	12	30	105	151
	conglomerated on bottom plate	kg	6	14	20	0
	mean size of fragments	mm	4.5	3.8	4.8	3.5
	melt/debris rejection		no	no	no	no[a]
Bottom Plate	maximum temperature increase[b]	K	n.a.	275	330	20
	state		intact	intact	intact	intact
Pressure Increase	before melt/water contact	MPa	0.4	0.3	0.1	0.3
	melt fall stage maximum	MPa	1.1 (t=1.2s)	1.8 (t=1.2s)	2.8 (t=2.4s)	5.1 (t=2.15s)
	long term maximum	MPa	1.6 (t=12s)	1.8 (t=20s)	3.4 (t=30s)	2.8 (t=22s)
	maximum rate	MPa/s	1.6	3.3	2.4	4.8
	steam explosion		no	no	no	no
Temp. Increase	gas phase (uppermost region of test vessel)	K	40	43	77	67[d]
	water	K	15	23	28	27
Level swell	maximum indicated by level-meters	m	0.130[c] (t=0.8s)	0.410 (t=1.15s)	1.100 (t=2.1s)	1.00[d] (t=1.1s)
Venting Phase	start time	s				1.5
	duration	s	-	-	-	3.8
	debris in separator	kg	-	-	no	5(< 1mm)
	water added to separator	kg	-	-	venting	11
	water added to condenser	kg	-	-	venting	48
	pressure increase in condenser	MPa	-	-	in this	0.17
	mean water temperature increase in condenser	K	-	-	test	20

[a]About 5 kg of debris <1 mm found in the separator; [b]Contact face; [c]Inferred from thermocouples; [d]Probably not the absolute maximum.

4.2. Venting in Test L-11

Gas-steam venting occurred only in test L-11. In Figure 5 are compared the pressure histories in TERMOS and at the outlet of the separator during the venting phase. As expected, the TERMOS and separator traces are identical up to the time at which the gas started discharging to the condenser (time 1.50 s). Then, the pressure difference between TERMOS and separator indicates the fluid flow through the connecting pipe. Venting started at 9.3 MPa (pressure threshold of the exhaust valves), but the pressure continued to increase up to reaching about 10.0 MPa in the TERMOS vessel.

This pressure-overshoot was due to the fact that the venting system never reached its full discharging capabilities. The exhaust valves are sensitive to the pressure at the outlet of the separator. This pressure never increased beyond 9.7 MPa which was the lower limit for a full opening of the valves. Because of the ±0.15 MPa uncertainty on the set pressure, some valves opened completely, but some only partially. Although a pressure difference between TERMOS and the separator is perceptible only up to time 3.15 s in Figure 5, a residual gas discharge through the valves continued up to time 5.0 s, i.e. when the pressure reached 7.3 MPa (clearly evidenced in Figures 3 and 5 by the start of vessel pressure recovery at that time). A detailed analysis of the venting scenario is found in [6].

4.3. Hydrogen Production in Test L-11

The experimental probes for measuring the hydrogen did not give any usable data for determining neither the quantity of hydrogen produced nor the production rate. Analyses to try to provide data on hydrogen production from the pressure and temperature measurements both in the test vessel and in the condenser are in progress. Qualitatively, the presence of a significant amount of hydrogen was ascertained in the condenser by the mass spectrometer just after the venting phase. X-ray diffraction analysis of the debris indicated that Zr was no longer present as a metallic phase in the debris. This, however, is not sufficient to definitely conclude that all the Zr present in the mixture was oxidised during the interaction. On the other hand, by comparing the L-11 and L-14 results (see section 5.2) it may be deduced that the presence of Zr in the mixture had a strong influence on the quenching process and that the Zr was probably fully oxidised at the end of fall stage of the melt.

4.4. Level Swell

The level swell values reported in Table 2 correspond to the maximum value indicated by the level-meters. Figure 6 shows the level-meter indications for tests L-11 and L-14. In test L-11, the level-meter data was only recorded within the calibration range, i.e., 2300 mm and 3000 mm for LTC 1 and LTC 2, respectively. However, it is clear from Figure 6 that this level was not the

absolute maximum for L-11. The mean rate of increase of the level is calculated to be approximately 1.4 m/s for L-11 and 0.6 m/s for L-14, respectively. Linear extrapolation of the signal of LTC 2 in test L-11 gives a level swell value of 2.1 m at the time of the valves opening (1.5 s), i.e., that the two-phase water would have occupied all the free-board volume. Thus, it is likely that a two-phase flow occurred in the communication pipe between TERMOS and the separator during the venting phase, and that most of the water added to the separator during that phase (about 11 kg) resulted from this two-phase flow.

Assuming that all the water participated homogeneously for quenching the melt, one finds values of the integral void fraction corresponding to the maximum level swell equal to 0.5 and 0.35 for L-11 and L-14, respectively. These values have to be considered as minimum values, because probably not all the water had participated in the mixing.

4.5. Temperatures

As already noticed in [2] for FARO tests L-06 and L-08, it is very difficult to establish the temperature of the steam produced during the first seconds of the interaction. This is due to the large disturbances created by the steam generation itself on the gas-phase temperature field, and also to the difficulty for thermocouples in measuring transient steam superheating. Locally, temperatures up to 86 K above initial ones were measured in test L-06 near the surface of the water. This value tended to decrease at higher elevations in the test vessel. In the uppermost regions of the test-vessel, the temperature increase was about 40 K maximum.

In tests L-11 and L-14, most of the thermocouples which were initially in the gas space were reached by the two-phase water because of the important level swell noticed in these tests. Thus, an evaluation of the steam temperature is even more difficult than in tests L-06 and L-08, where a limited level swell was observed. Temperature traces at different elevations above level 2000 are reported in Figures 7 and 8a for L-11 and L-14, respectively. At the very beginning of the melt penetration into the water, all the thermocouples measured the temperature of the steam and the traces are similar. As the thermocouples are reached by the two-phase water, the temperature drops towards values similar to that measured below level 2000. This behaviour is particularly well evidenced for L-14 (Figure 8a and 8b). Only the uppermost thermocouples (levels 3650 and 4115), were not reached by the two-phase mixture and actually indicate temperatures of the steam at these locations (maximum 613 K at time 2.0 s, i.e., 77 K increase). This value is about 30 K higher than the values at similar elevations for tests L-06 and L-08 (see Table 2). After a few seconds, when the initial strong disturbances generated by the falling jet have damped, all the other thermocouples, including those below level 2000, indicate temperature homogenisation with values close to saturation.

For L-11 (Figure 7), it was not possible to determine unambiguously a temperature of the steam produced because a two-phase steam-water mixture probably occupied the whole free-board volume. The value of the increase indicated in Table 2 (67 K) corresponds to the maximum measured by thermocouples at level 4115, just before venting.

4.6. Debris

Figure 9 shows a photograph of the debris of test L-11 (UO_2-ZrO_2-Zr melt) as found in the debris catcher. All the debris on the bottom plate (146 kg) was a fragmented debris. In addition, 5 kg of particles (size of the order of 1 mm) were found in the separator, probably drained out of the TERMOS vessel during the gas discharge.

This contrasts with the pure oxide melt tests (L-06, L-08, L-14), in which only partial breakup was observed. The debris resulting from those tests consists of a conglomerate ("cake") in contact with the bottom plate and overlaying fragments (loose debris similar to that of test L-11). In tests L-06 and L-08 performed with 1 m of water, the proportion of melt which formed the cake was 1/3 of the total, i.e., 6 kg and 12 kg, respectively. This proportion was 1/6 (i.e., 20 kg) in test L-14 performed with 2.05 m of water. Figure 10 shows a photograph of the cake found in test L-14. It corresponds to a part of the corium which reached, still in a molten state, the bottom plate and did not further fragment. The surface of the cake was bright smooth, without any evidence of cracks on it. However, it was very brittle and broke easily into pieces during removal.

Particles which formed the loose debris were completely separated from each other in all the tests. Only this loose debris (e.g., 105 kg for test L-14, see Table 2) was sieved for determining the particle size distribution. Although the debris resulting from UO_2-ZrO_2 melt quenching is generally brittle [2], visual observations of debris samples pre- and post- sieving did not indicate any further break of the particles due to the sieving process. The particle size distributions are reported in Figure 11. The mean particle sizes range between 3.5 (L-11) and 4.8 mm (L-14). The proportion of fragments larger than 6 mm in L-14 is significantly higher than in all the other tests (40% against 20%-26%).

4.7. Bottom Plate

The thermal load resulting from test L-11 (complete breakup of the melt) was negligible, with a maximum temperature increase of the plate equal to 20 K. Also in the other tests the temperature increase remained mild, with a maximum increase of the contact face of 330 K measured in test L-14 (Figure 12) in the region where the cake formed. Neither adherence to nor pitting of

the plate was noticed. Only a brown coloured spot evidenced the position of the conglomerate melt on the plate in test L-14.

5. ANALYSIS AND DISCUSSION OF MEASUREMENTS

5.1. Jet Breakup

The melt downward progression data are summarised in Table 3. The melt leading edge position as a function of time was detected from the centre-line water thermocouple signals. As indicated in footnote *c* of Table 1, the over-pressurisation of 0.26 MPa observed in the release vessel at the start of melt delivery in test L-08 was responsible for the elevated melt velocity at water contact. For the pure oxide melt tests, it may be concluded that the melt jet breakup length was larger than the water depth because molten material reached the bottom plate. Only a mean melt descent velocity was calculated for these tests as reported in Table 3.

For test L-11, the centre-line water thermocouple responses are reported in Figure 13a. The interspacing of the thermocouples was 200 mm, except very near to the bottom plate where thermocouples were placed at 10 and 5 mm from the plate. It is seen that down to elevation 600, the progression of the melt is difficult to establish from the thermocouple signals. On the contrary, from elevation 600 down to the plate, the departure of the temperatures from their initial values can be easily tracked. A melt front progression history is reported in Figure 13b. Figures 13a and 13b suggest that the melt downward progression occurred in two main regimes: one, where the melt progressed at a mean velocity of 2.5 m/s; another, where the melt progressed at a constant velocity of 1.2 m/s. As was made in the analysis of the CCM test series of Argonne [5], the breakup length was determined as the depth where the slope changes in Figure 13b. A value in the range of 1.2-1.4 m is found. One has to note that this value is referred to the original free surface of the water (i.e., 2 m above the bottom plate). Actually, at the time the melt reached the depth of 1.4 m (time 1.1 s), the level swell was around 1 m (i.e., the water-steam two-phase free surface was 3 m above the bottom plate and very near - 85 mm - to the melt release nozzle).

The fact that in test L-11 there is a breakup length shorter than the water depth suggests that all the melt experienced breakup before settling on the bottom plate. It is noted that the melt velocity before complete breakup in L-11 was twice as small as in L-14. The water-steam two-phase free surface was 2.3 m above the bottom plate when the melt front contacted the bottom plate in test L-14 (at time 0.9s).

Table 3. Melt downward progression data

Test n°		L-06	L-08	L-14	L-11
mean velocity in gas phase	m/s	4	5	2.9	2.9
velocity at melt/water contact (estimated)	m/s	6.0	10.0	5.6	5.7
mean velocity in water	m/s	2.3	3.7	4.8	2.5 /1.2[a]
dimensionless breakup length L/D[b]		>8.7	>10.0	>20.5	14

[a]2.5 m/s: mean value from level 2.00 m down to ~0.6 m; 1.2 m/s=constant: from ~0.6 m down to bottom plate; [b]L: breakup length; D: initial discharge nozzle diameter.

5.2. Role of the Presence of Zr Metal in Test L-11

From the results of the X-ray analysis of the debris it can be concluded that Zr was not any more present as a metal. This suggests that all the 6.2 kg of metallic zirconium present in the mixture completely oxidised during the test. A number of observations further suggests that the melt oxidation was completed at the end of the melt fall stage and that this was the reason for the intensive breakup observed.

First, the rate of pressure increase (Figure 14) is dramatically higher for L-11 than for L-14 for all the melt fall phase. The maximum pressure increase at the end of the melt fall stage can be estimated to 8.0 MPa for test L-11 (in case of no steam venting) against 2.8 MPa for test L-14. The differences in mass and flow rates cannot account for this large differences in pressurisation. For the longer term, no difference of the pressure behaviour is noticed between the tests.

Second, it has been established that probably the melt experienced complete breakup between 0.8 m and 0.6 m before reaching the bottom plate in L-11. This contrasts with all the tests performed with pure oxide melts and, particularly, with L-14 where 20 kg of molten corium settled on the plate.

Third, from the analysis of the water thermocouple responses, it results that the depth of 1.4 m, where the melt was completely broken up, was reached by the melt before the opening of the venting valves (1.1 s against 1.5 s). On the contrary, the bottom plate was reached by the corium a little later (1.6 s) without inducing any change in the settling velocity. The melt trailing edge is estimated [7] to have penetrated into the water at time ~1.2 s (taking into account the level swell), i.e., also before the venting valves opened. It can be concluded that the venting phase did not influence the quenching process.

Thus, the contribution of the melt oxidation to the enhanced pressurisation and melt quenching noticed in test L-11 with respect to L-14 can be attributed to three separate factors. First, the partial pressure of the hydrogen pro-

duced contributed for approximately 0.50 MPa (0.272 kg at 573 K) to the total pressure of the system. Second, assuming that the oxidation was due to the Zr/H_2O reaction only, the heat of reaction added 20 % more energy to the system. Third, the melt oxidation increased breakup during the fall stage, which further enhanced the production of steam.

A question remains on whether the Zr was fully oxidised during the melt fall by the Zr/H_2O chemical reaction, or had been already partially or totally oxidised by the $(U,Zr)O_2$ melt in the release vessel where the melt rested for 5.7 s before being discharged to the water. In this case, the effects described above would have been the consequences of a combination of both Zr/H_2O and $(U,Zr)O_{2-x}/H_2O$ chemical reactions.

5.3. Calculation of the Quenching Rate

From the pressure and temperature data it is possible to calculate the quenching rate and the energy released to the steam-water system as a function of time. The following formula are used for constant volume:

$$E = m_{liq}h_{liq} + m_{vap}h_{vap} = m_{tot}h_{liq} + \frac{V}{\nu_{vap}}\left(h_{vap} - h_{liq}\right)$$

$$P = \frac{dE}{dt} = m_{tot}\frac{dh_{liq}}{dt} + V\frac{d}{dt}\left[\frac{h_{vap} - h_{liq}}{\nu_{vap}}\right]$$

where:

E	energy of the system;
P	quenching rate;
m_{liq}	mass of liquid water;
m_{vap}	mass of steam;
m_{tot}	$= m_{liq} + m_{vap}$ = constant;
h_{liq}	enthalpy of liquid;
h_{vap}	enthalpy of steam;
ν_{vap}	specific volume of steam;
V	freeboard volume.

Calculations have been performed by using for h_{liq} the values corresponding to the time dependent space average temperature of the water, and for h_{vap} and ν_{vap}, the values corresponding to saturation conditions at the total pressure of the system. The results are presented in Figures 15a (energy release) and 15b (quenching rate) and are summarised in Table 4. However, for test L-11 the above formula cannot be applied beyond time 1.5 s because of the steam discharge to the condenser. For this phase (dotted curves in the figures) an approximation was made taking into account the valves opening following a se-

quence described in [6]. It is noted in Figure 15b that the maximum quenching rate for test L-11 was reached before the steam venting started.

Table 4. Energy release and quenching rate

Test n°		L-06	L-08	L- 14	L-11
energy of the melt: E_{melt}	MJ	27	66	188	225 (265[a])
energy released at first pressure maximum (~ melt fall): E_{fall}	MJ	6	24	83	170
ratio E_{fall} / E_{melt}		0.22	0.36	0.44	0.76 (0.64[a])
E_{fall} per kg of broken up melt	MJ/kg	0.50	0.80	0.79	1.13
E_{fall} per kg of melt	MJ/kg	0.33	0.55	0.66	1.13
maximum quenching rate: P_{max}	MW	7	22	57	157
P_{max} per kg of broken up melt	MW/kg	0.58	0.73	0.54	1.04
P_{max} per kg of melt	MW/kg	0.39	0.50	0.46	1.04

[a]Including the energy of the Zr/H_2O chemical reaction, i.e.~40 MJ.

It is seen from Table 4 that the fraction of energy released during the melt fall phase with respect to the energy content of the melt increases with increasing melt and water masses (or water depth) from 0.22 for L-06 to 0.64 for L-11. However, related to the mass of broken up debris, the values are almost the same for L-08 and L-14 (0.80 and 0.79, respectively). It can be deduced that, in the test conditions, the quenching process during the melt fall phase was essentially the same whatever the melt mass and the water depth, and that the dimensions of the debris (in the range 3.8 - 4.8 mm) had little influence on the global heat exchange. In this case, the difference between L-11 and L-14 (1.13-0.79 = 0.34 MJ/kg) could be attributed to the heat of the chemical Zr/H_2O reaction only. This corresponds to 51 MJ for 151 kg of melt. Taking into account the uncertainties of these global estimates, the value compares remarkably well with the theoretical value of 40 MJ, and seems to indicate that all the Zr was oxidised during the melt fall stage.

The maximum quenching rate increases from 7 MW for L-06 to 157 MW for L-11 (Table 4). Related to the melt mass, the differences are in the range 0.39 - 1.04 MW per kilogram of available melt and in the range 0.58 - 1.04 MW per kilogram of broken up melt. In contrast with the energy values per kilogram of broken up melt, the difference in quenching rates is noticeable between L-08 and L-14 (0.73 MW/kg against 0.54 MW/kg), which may be due to the difference between the melt entry velocities (10 m/s for L-08 - mainly because of the oscillatory behaviour of the injection pressure, see Tables 1 and 3 - against 5.6 m/s for L-14).

5. CONCLUDING REMARKS

The main objectives of the two large melt mass tests in FARO have been achieved. The data related to melt jet breakup, energy release, the debris structure, bottom plate thermal load and the importance of the zirconium oxidation have been determined. Although the number of tests performed so far is limited, some aspects of corium mixing and quenching in water which could not be available from simulant and small scale experiments have been evidenced. In particular, it has been found that, in the test conditions:

- The energy released to the water during the corium fall by the part of the melt which experienced breakup amounted to 0.80 MJ/kg for a pure oxide w% 80 UO_2 + 20 ZrO_2 melt. This data did not depend on the melt mass (44 to 151 kg) and the water depth (1 to 2 m);
- In test L-11, the 151 kg of w% 76.7 UO_2 + 19.2 ZrO_2 + 4.1 Zr melt was probably completely oxidised at the end of the melt fall phase, which increased the energy released during that phase to 1.13 MJ/kg;
- The addition of metallic zirconium to a UO_2-ZrO_2 melt enhanced the early quenching of the melt with respect to the pure oxide melt, and, consequently, led to a significant increase of the steam production and vessel pressurisation, and to a decrease of the thermal load on the bottom plate;
- Part of the melt reached the bottom plate still molten in all tests with pure oxide melts (1/6 to 1/3). A complete breakup of the melt occurred within a depth of 1.2-1.4 m in the case with metallic zirconium in the corium mixture;
- In all cases, the mean particle size of the broken up debris ranged between 3.5 to 4.8 mm;
- The maximum measured temperature increase of the bottom plate was 330 K in the case molten material deposited on it.

Obviously, to draw more definite conclusions on the quenching of large masses of corium requires to perform further tests in similar conditions with improved instrumentation in order to confirm these data and interpretations.

ACKNOWLEDGEMENTS

The authors greatly acknowledge the work and efforts of the whole FARO experimental team. Extensive discussions with A. Annunziato and A. Benuzzi greatly helped in analysing the experimental results.

REFERENCES

[1] CORRADINI M.L. and H. HOHMANN, Multi-Phase Flow Aspects of Fuel-Coolant Interactions in Reactor Safety Research, Nucl. Engrg. Des. 145 (1993) 207-215.

[2] MAGALLON D. and H. HOHMANN, High Pressure Corium Melt Quenching Tests in FARO, CSNI Specialist Meeting on Fuel Coolant Interaction, Santa Barbara (CA), 5-8 Jan. 1993, NUREG/CP-0127 (March 1994).

[3] STICKLER L. A., J.L. REMPE, S.A. CHAVEZ, G.L. THINNES, S.D. SNOW, R.J. WITT, M.L. CORRADINI and J.A. KOS, Calculations to Estimate the Margin to Failure in the TMI-2 Vessel, NUREG/CR-6196 (February 1994).

[4] WOLF J.R. et al. (13 co-authors), TMI-2 Vessel Investigation Project Integration Report, NUREG/CR-6197 (March 1994).

[5] WANG S.K., C.A. BLOMQUIST, B.W. SPENCER, L.M. MAC UMBER and J.P. SCHNEIDER, Experimental Study of the Fragmentation and Quench Behavior of Corium Melts in Water, Nat. Heat Transfer Conf., ANS, 1989.

[6] ANNUNZIATO A., C. ADDABBO, FARO Base Case Post-Test Analysis by COMETA code, NURETH 7, Saratoga Springs , NY, 10-15 September 1995.

[7] BENUZZI A. and D. MAGALLON, FARO-LWR Programme: Base Case Test (L-11) Quick-Look Report, Technical Note I.94.55, JRC-Ispra (April 1994).

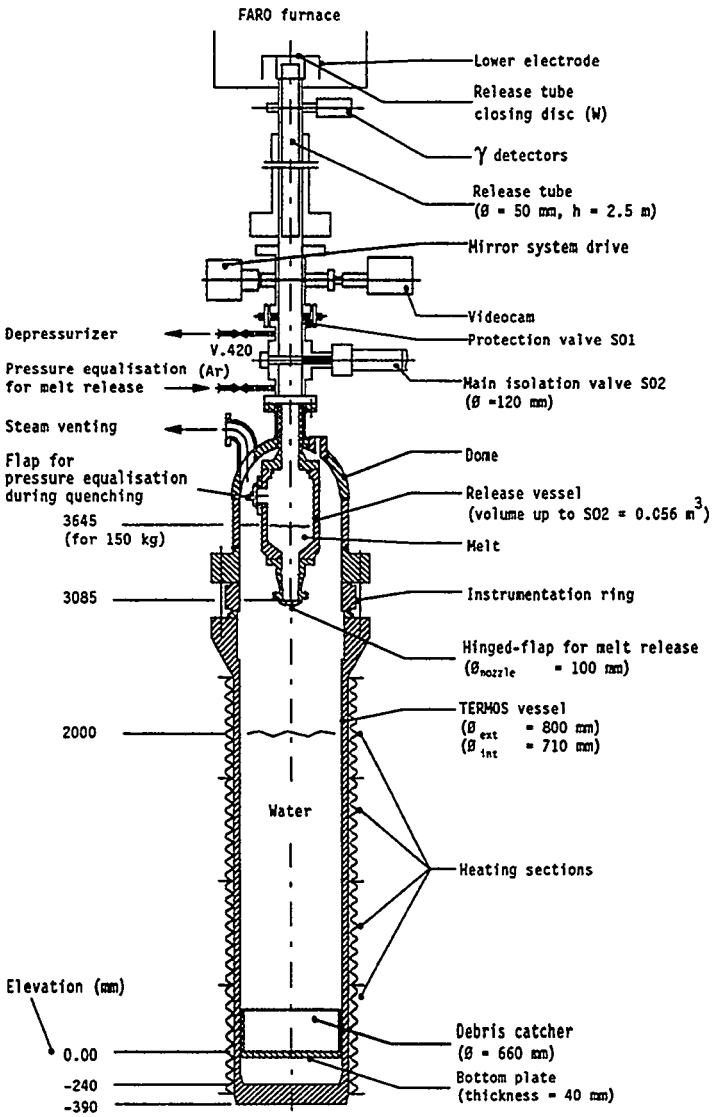


Figure 1. FARO Test Arrangement.

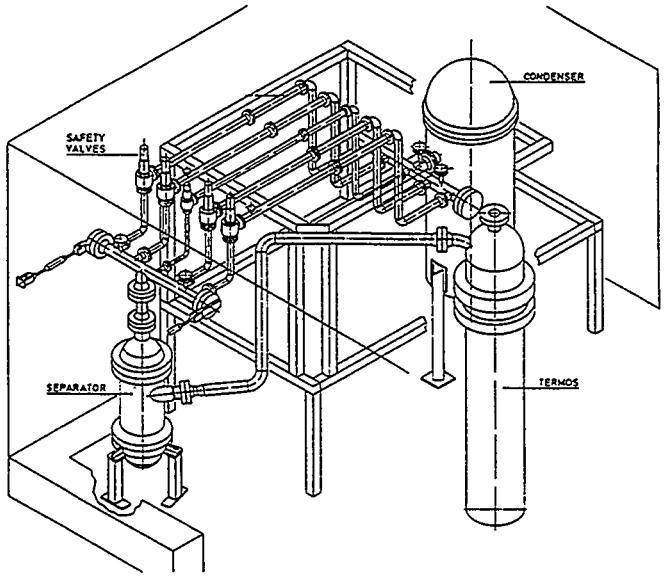


Figure 2. FARO Venting System.

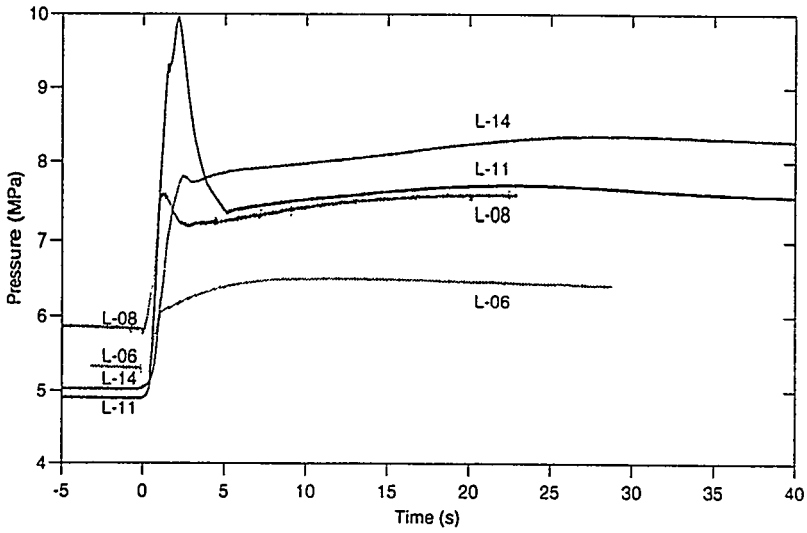


Figure 3. Test Vessel Pressure (-5 s < time < 40 s).

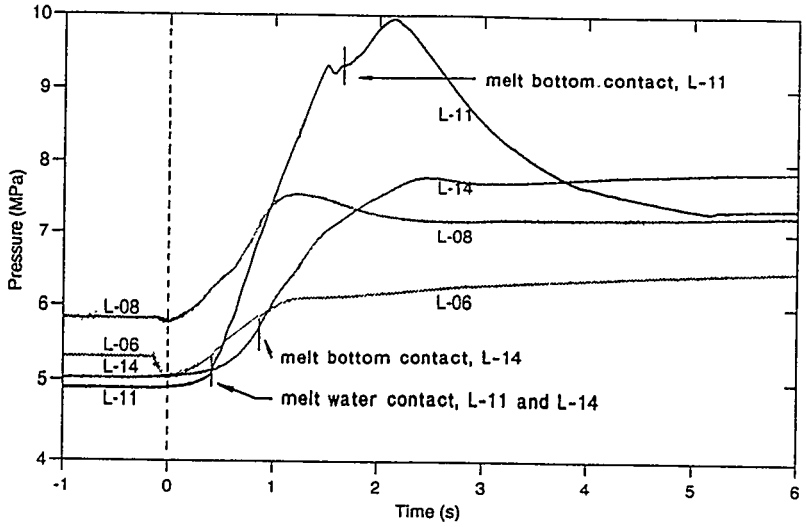


Figure 4. Test Vessel Pressure (-1 s < time < 6 s).

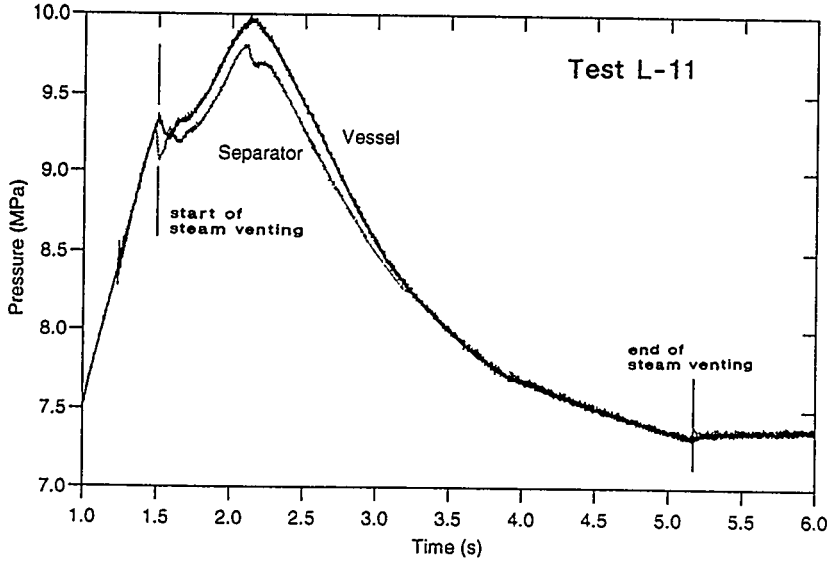


Figure 5. Test Vessel and Separator Pressures (1 s < time < 6 s).

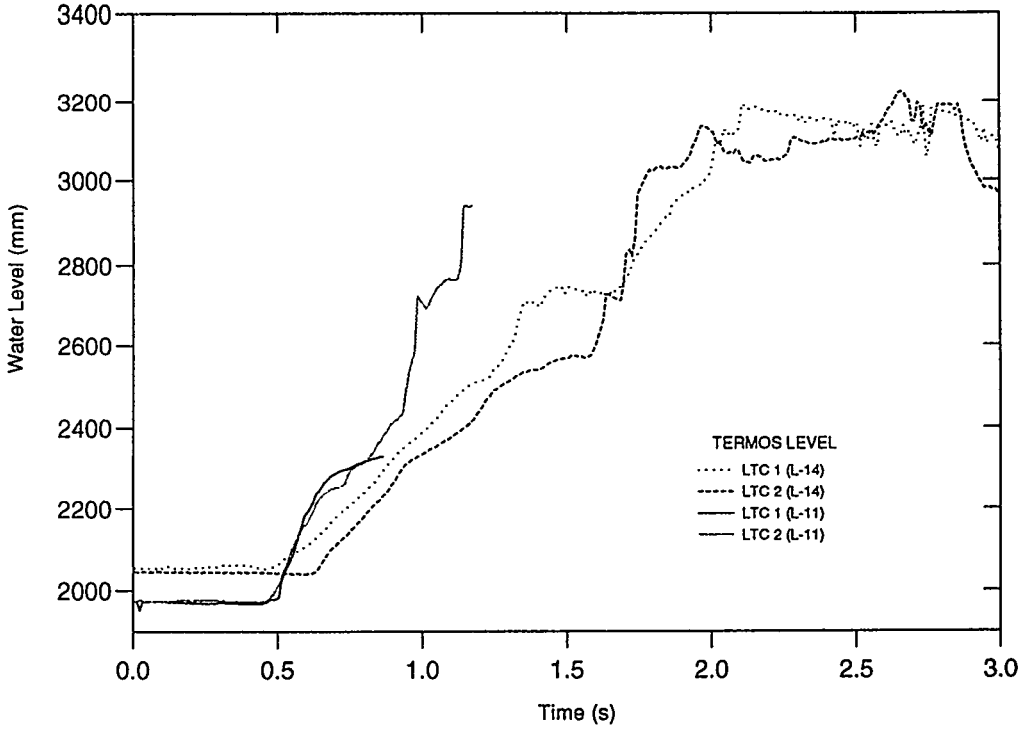


Figure 6. Water Level in Tests L-11 and L-14.

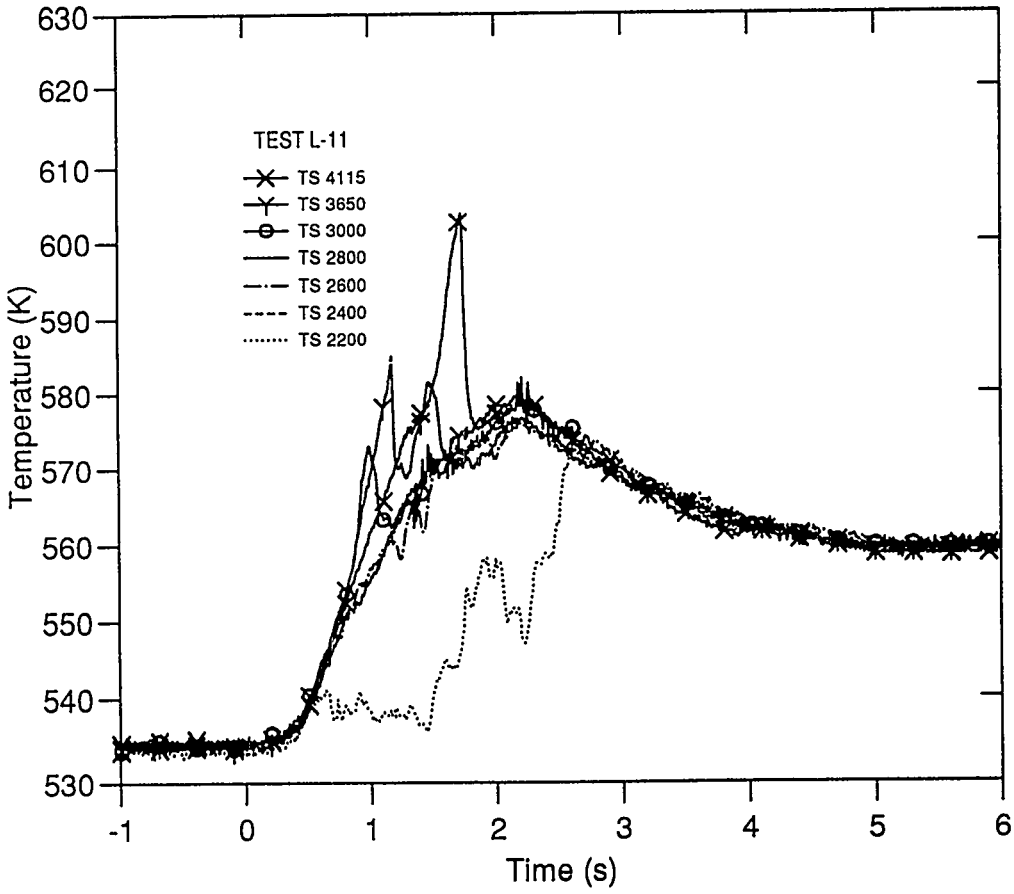


Figure 7. Temperatures in TERMOS Free-board Volume at Different Elevations in Test L-11.

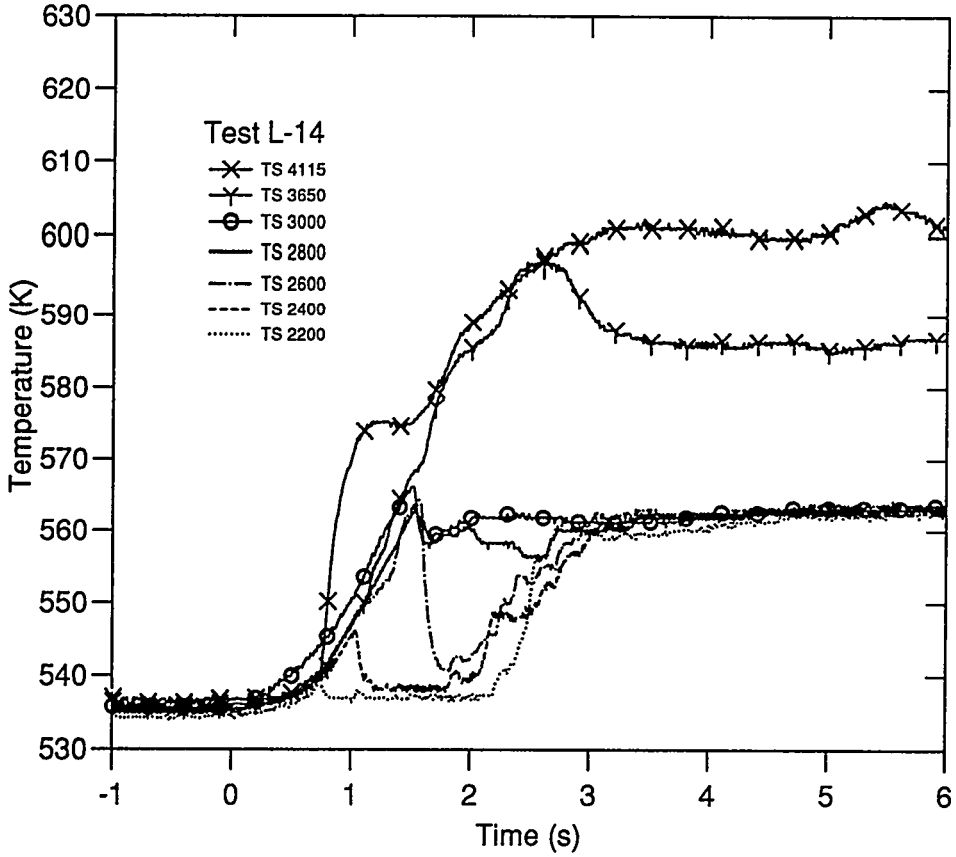


Figure 8a. Temperatures in TERMOS Free-Board Volume at Different Elevations in Test L-14.

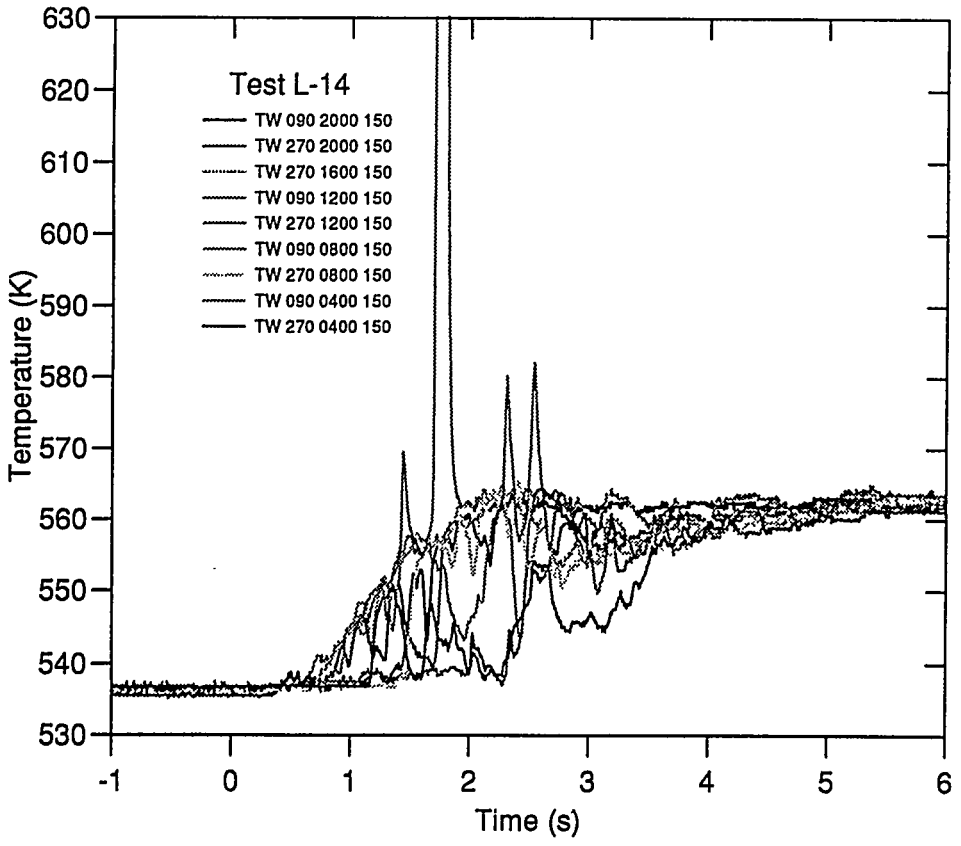


Figure 8b. Temperatures in Water (below level 2000) at Different Elevations in Test L-14 (radius 150 mm, azimuth 90° and 270°).

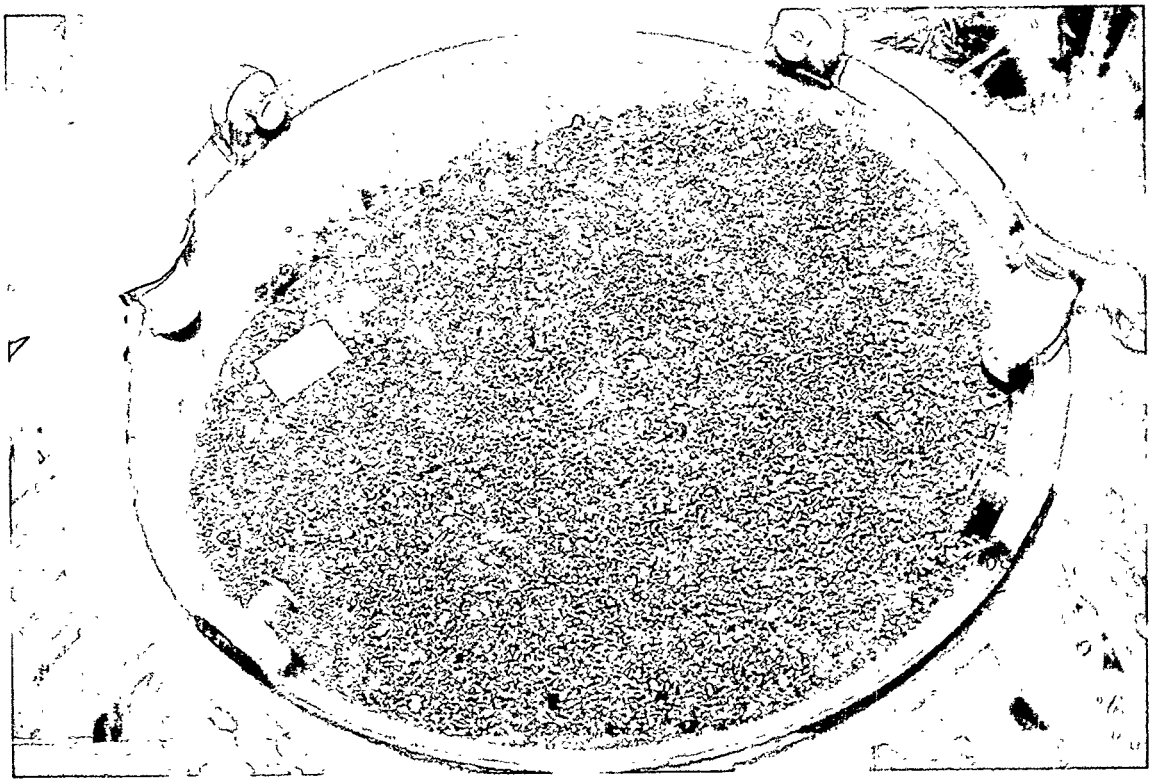


Figure 9. Photograph of the Debris of Test L-11.

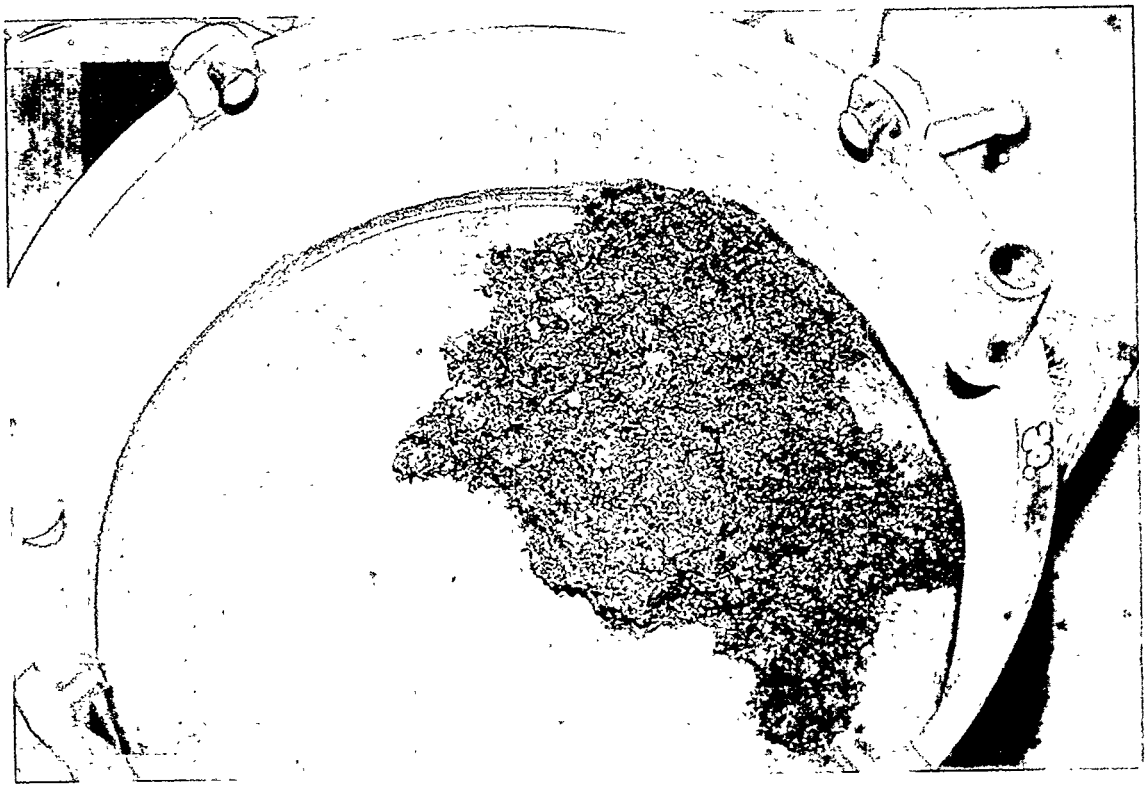


Figure 10. Photograph of the "Cake" of Test L-14.

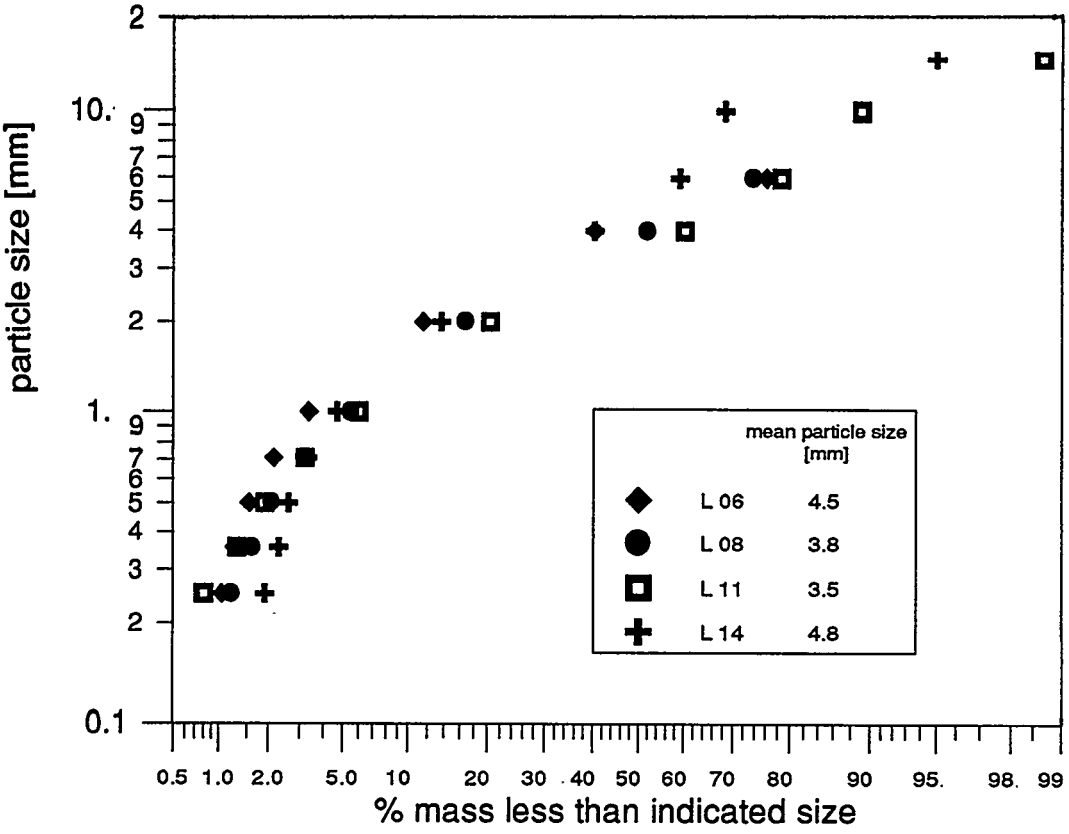


Figure 11. Particle Size Distribution.

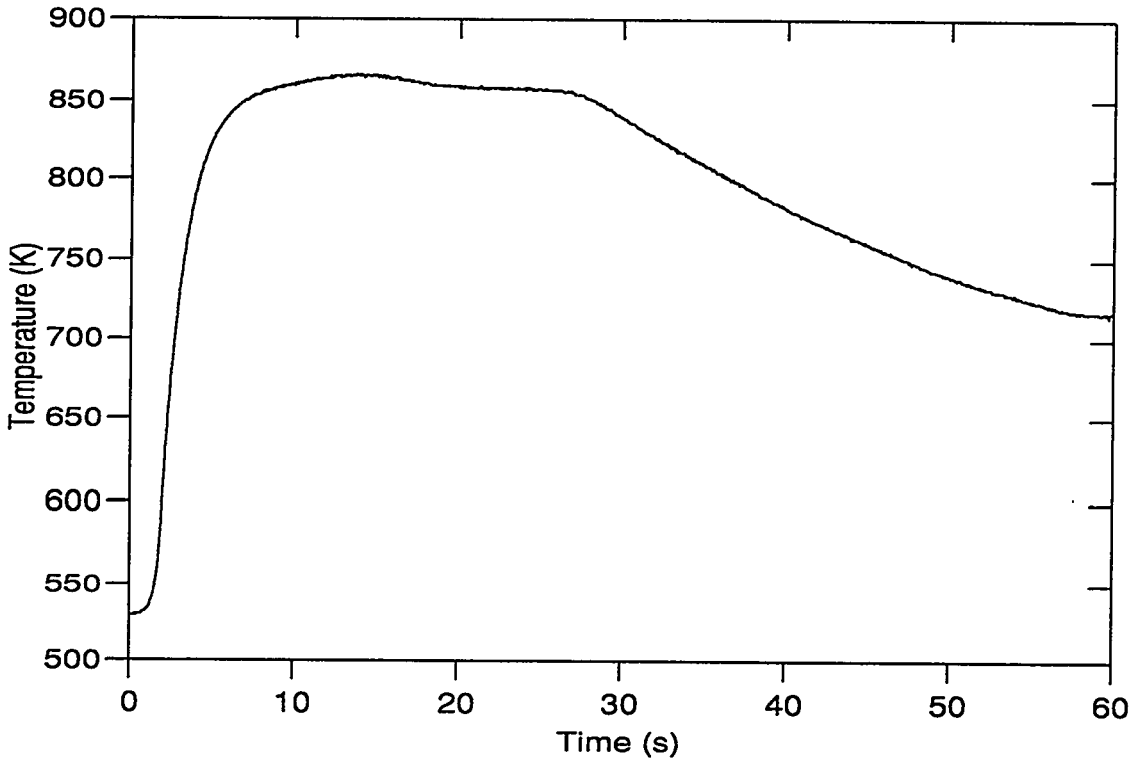


Figure 12. Temperature of the Contact Face of the Bottom Plate in Test L-14.

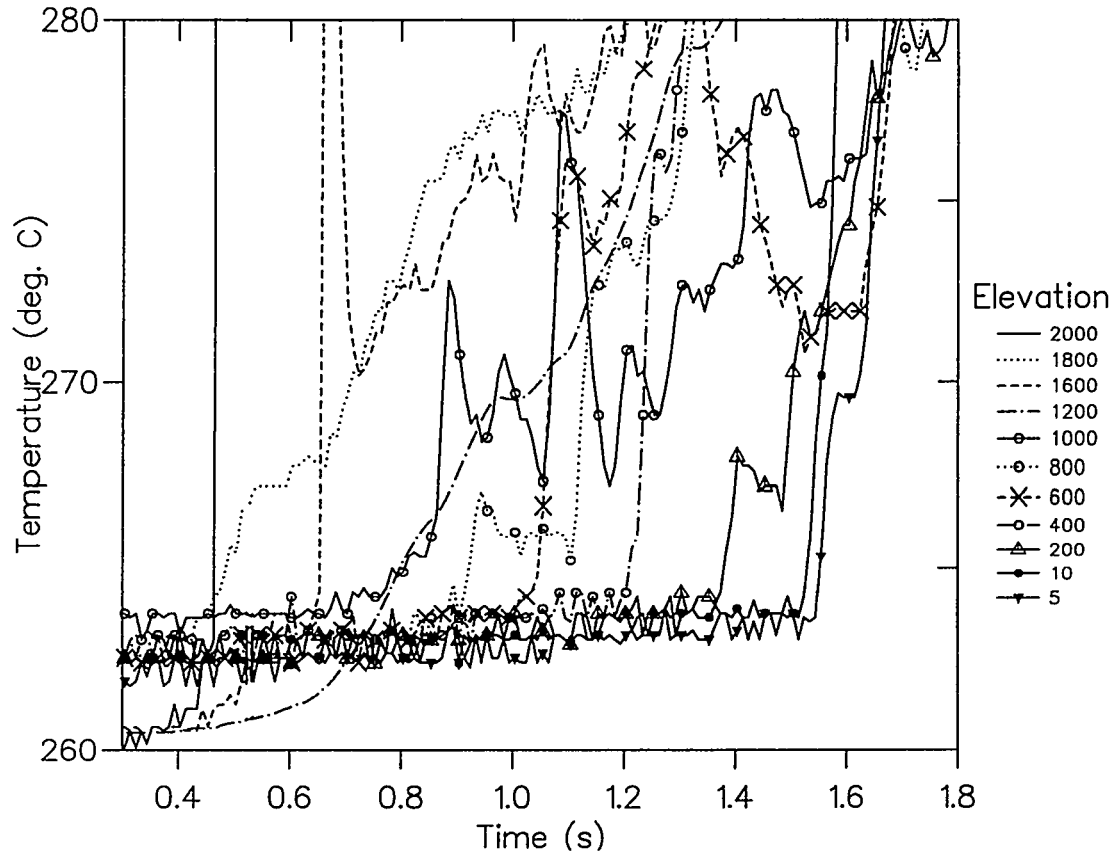


Figure 13a. Response of the Centre-Line Water Thermocouples in Test L-11.

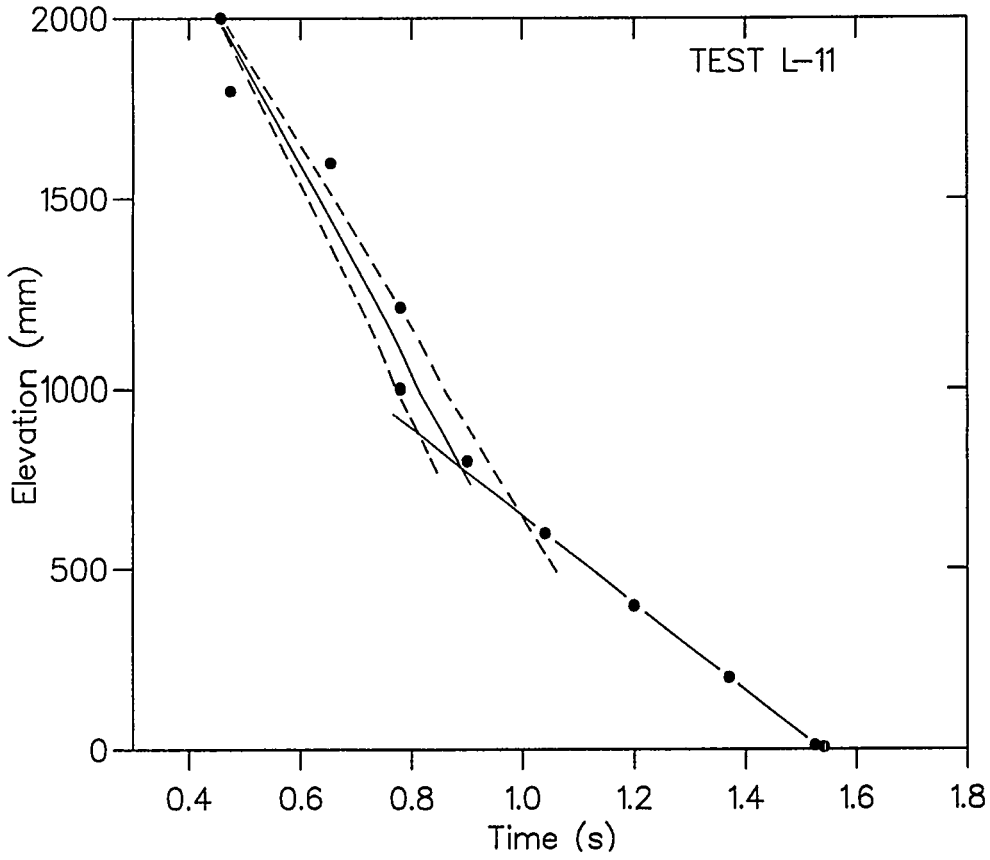


Figure 13b. Melt Down Progression in Test L-11.

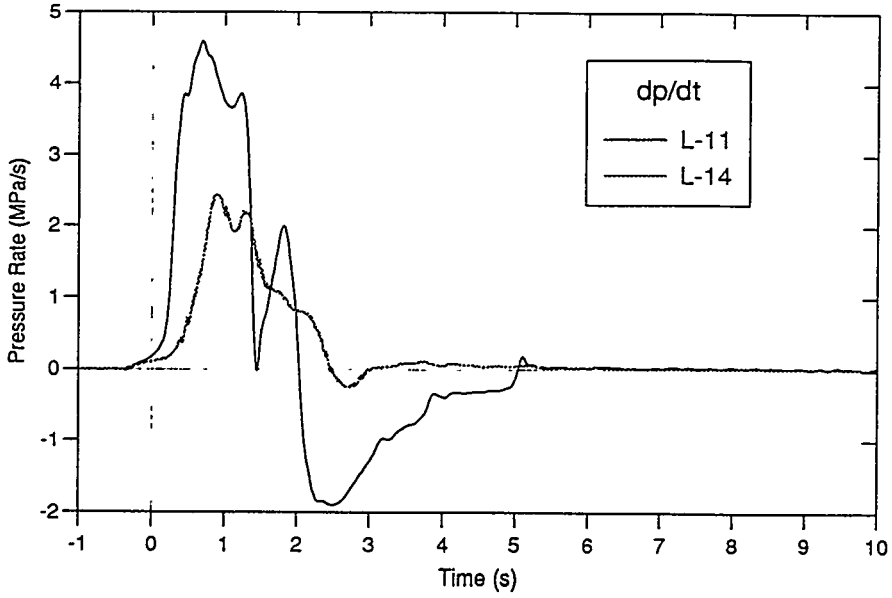


Figure 14. Pressure Increase Rate.

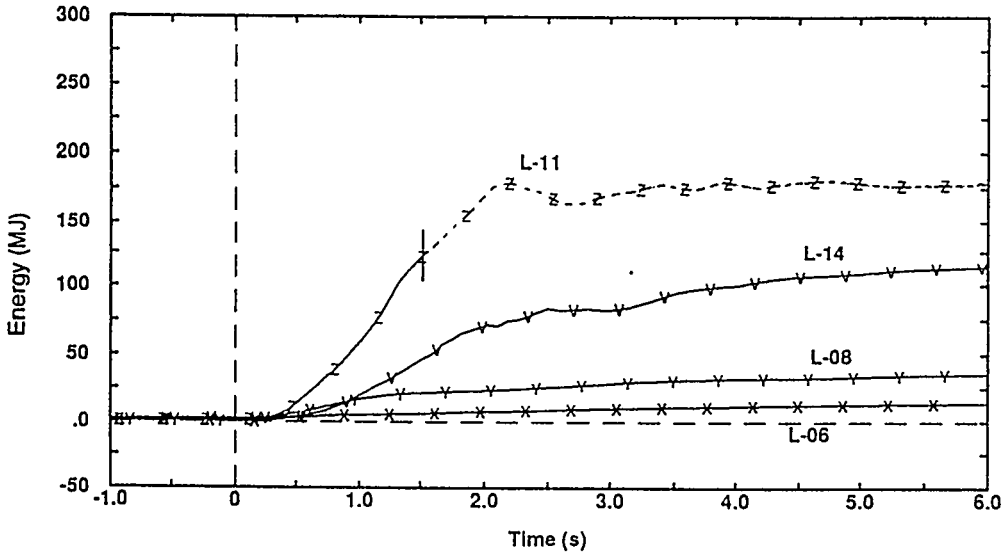


Figure 15a. Energy Released to the Water.

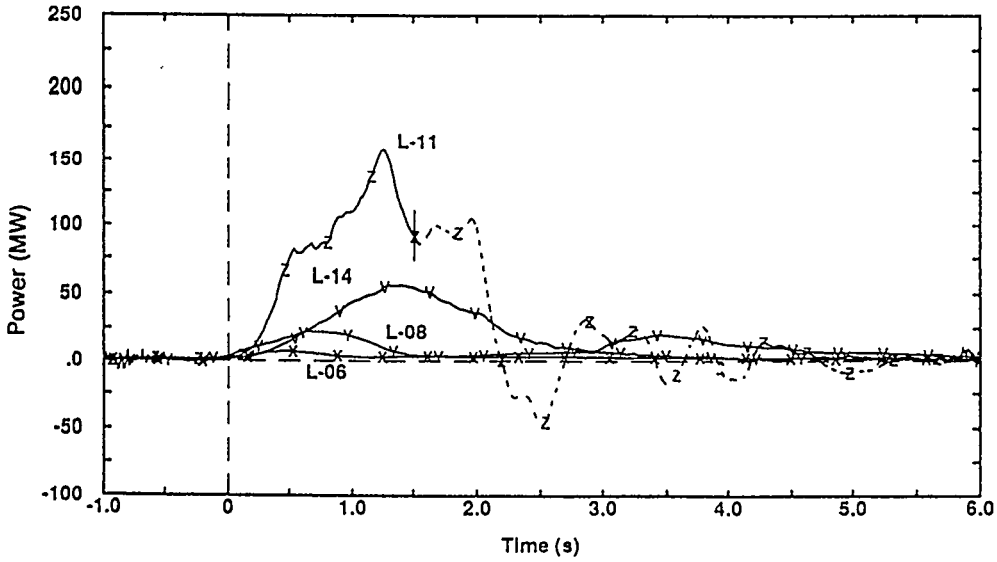


Figure 15b. Quenching Rate.

FCI EXPERIMENTS IN THE CORIUM/WATER SYSTEM

I. Huhtiniemi, H. Hohmann, D. Magallon
European Commission[1]
Joint Research Centre
Safety Technology Institute
I - 21020 Ispra (Va)

Abstract

The KROTOS fuel coolant interaction (FCI) tests aim at providing benchmark data to examine the effect of fuel/coolant initial conditions and mixing on explosion energetics. Experiments, fundamental in nature, are performed in well-controlled geometries and are complementary to the FARO large scale tests. Recently, a new test series was started using 3 kg of prototypical core material (80 w/o UO_2, 20 w/o ZrO_2) which was poured into a water column of $\leq$ 1.25 m in height (95 mm and 200 mm in diameter) under 0.1 MPa ambient pressure. Four tests have been performed in the test section of 95 mm in diameter (ID) with different subcooling levels (10–80K) and with and without an external trigger. Additionally, one test has been performed with a test section of 200 mm in diameter (ID) and with an external trigger.

No spontaneous or triggered energetic FCIs (steam explosions) have been observed in these corium tests. This is in sharp contrast with the steam explosions observed in the previously reported Al_2O_3 test series which had the same initial conditions of ambient pressure and subcooling. The post-test analysis of the corium experiments indicated that strong vaporisation at the melt/water contact led to a partial expulsion of the melt from the test section into the pressure vessel. In order to avoid this and to obtain a good penetration and premixing of the corium melt, an additional test has been performed with a larger diameter test section. In all the UO_2–ZrO_2 tests an efficient quenching process (0.7–1.2 MW/kg-melt) with total fuel fragmentation (mass mean diameter 1.4–2.5 mm) was observed. Results from Al_2O_3 tests under the same initial conditions are also presented for further confirmation of the observed differences in behaviour between Al_2O_3 and UO_2–ZrO_2 melts.

[1] Performed in collaboration with the USNRC in the frame of Technical Exchange Agreement N° 4086-90-09 TG ISP USA

1 Introduction

In the event of a severe reactor accident a significant fraction of the core may melt and pour down into the lower plenum of the reactor pressure vessel. Unless outside cooling of the vessel wall is provided, the vessel integrity might be threatened and eventually core material could enter into the reactor cavity. In many countries the accident management strategies for such situations are based on having water in the cavity to quench the melt and ultimately to obtain a coolable configuration of debris on the basemat. However, such a strategy relies on the fact that no highly energetic fuel coolant interactions (FCI) will take place or that the cavity structures are sufficiently strong to cope with loads due to such an explosion.

Active modelling work is currently underway in several research centres to investigate FCIs and, in particular, different stages of it, pre-mixing, triggering, propagation and expansion (in the case of an explosion), which determines the energetics and structural loading [7, 10]. To support these modelling efforts, fundamental experimental investigations are being performed in the KROTOS facility at JRC-Ispra. These experiments are aimed at providing benchmark data to examine the effect of fuel-coolant initial conditions and mixing on explosion energetics. Detailed data is needed where mixing and explosion processes occur under controlled conditions. With such data one can also validate in small scale the fuel coolant mixing models such as IFCI (Sandia Nat. Lab., [4]), TEXAS-III (Univ. of Wisconsin, [9]), PM-ALPHA (Univ. of California [1]) and COMETA (JRC, [2]) and explosion models such as ESPROSE.m (Univ. of California, [10]), IDEMO (IKE, [3]) and TEXAS-III. These models are currently actively in use to analyse KROTOS test results with an aim to improve their predictive capabilities so that reliable extrapolation of results to the reactor scale could be achieved.

The KROTOS facility is used for FCI studies in the molten $UO_2 - ZrO_2$/water system in conjunction with the large-scale FARO facility [6]. The objectives of the current tests are to investigate in 1-D and 2-D geometries the premixing of molten fuel jets with nearly saturated and subcooled water and subsequently, the potential for an energetic interaction. During every experiment the dynamic pressurisation of the test section and pressure vessel, as well as the water and cover gas temperatures, and water level swell are measured. Post-test debris analyses provide additional qualitative information about explosion efficiency.

2 KROTOS Facility

Fig. 1a illustrates the main components of the facility: the radiation furnace, release tube, pressure vessel and test section. A pre-test series with $UO_2 - ZrO_2$ melts showed that some modifications of the facility were required with respect to the previous test series with molten Al_2O_3. At high temperatures (up to 3273 K), involved in the UO_2 melting, the use of graphite heaters caused material problems due to unexpected chemical reactions. Therefore,

the graphite heater elements had to be replaced by tungsten heaters. The pre-tests also demonstrated that helium was better suited as furnace cover gas than argon. Furthermore, due to the high temperatures in these tests only tungsten could be used as the material for the melt crucible and the puncher (the device for perforating the crucible bottom), see Fig. 1b. Extensive work had to be done to refine the sophisticated fabrication techniques to machine the bottom membrane of the tungsten crucibles according to the required dimensions (0.2-0.3 mm thickness).

2.1 Furnace

The furnace consists of a cylindrical tungsten heater element which enclose the crucible containing the melt material. The crucible is held in place by means of a pneumatically operated release hook. Eight concentric tungsten, molybdenum and steel radiation shields are radially placed around the heater element. The top and bottom parts of the heated zone are insulated with thermal screens to reduce heat losses to the surroundings. The furnace is covered with a bell-shaped, water-cooled lid designed to withstand 0.25 MPa over-pressure (Ar, He) or vacuum. The 3-phase electric power supply has a maximum voltage of 30 V and a maximum power of 130 kW.

Depending on the crucible design, melt masses in the range of about 1 to 10 kg can be used. Maximum achievable temperatures in the furnace are of the order of 3273 K. The melt temperature is controlled by an optical pyrometer measuring the wall temperature of the crucible.

2.2 Pressure Vessel and Test Section

The lower part of the KROTOS facility consists of a pressure vessel and test section, both made of stainless steel. The pressure vessel is designed for 2.5 MPa at 493 K. It is a cylindrical vessel of 0.4 m inner diameter and 2.21 m in height (volume: 0.290 m^3) with a flat bottom plate and flanged flat upper head plate. A number of feed-throughs exist in this vessel for auxiliary gas and water connections and mounting of instrumentation.

Two test sections of different diameter, one of which is illustrated in Fig. 1a, are utilised in this test series. The test sections consist of strong stainless steel tube either of inner diameter 95 mm and outer diameter 135 mm (designated as the narrow test section) or 200 mm and 240 mm (designated as the wide test section), respectively. Both of them can contain water at variable heights up to about 1.25 m. The bottom of both the test sections can be closed by either a flat plate or with a gas trigger device.

In some of the first experiments with Sn and Al_2O_3, spontaneous interactions occurred near the water surface [5], therefore additional means had to be introduced to improve the penetration of melt into the water and to minimise the risk of an early steam explosion. One of these measures consisted in providing the experimental tube with a 2 mm thick Plexiglas liner, thus avoiding direct contact between the melt and the wall of the test section.

At the upper part of the narrow test section, 20 holes (diameter 50 mm) allow the vapour venting into the pressure vessel volume. A steel vessel of 205 mm inner diameter is mounted around the part of the test section with the holes. This vessel fills up with water to the test section water level and level meters are placed there to measure the water level swell during melt-coolant premixing, see Fig. 1c. The level meter vessel is not used with the wide test section. Instead, two level meters are mounted along the inside wall of this test section.

In some tests a trigger device is attached at the bottom of the test section. The gas trigger device used in this test series is shown in Fig. 1d. The gas chamber volume of 15 cm^3 can be charged to a pressure of up to 20 MPa (argon) and is closed by a 0.1–0.2 mm thick steel membrane. After melt penetration down into the lower region of the test section, the mechanic destruction of the membrane delivers a pressure pulse propagating vertically upwards through the mixture of melt, water and steam. The gas trigger device is activated either by a thermocouple signal (normally TC 2 or 3) or by a backup time delay circuit.

2.3 Instrumentation and Data Acquisition

Pressures, temperatures and water level swell are the main experimental parameters measured in the KROTOS test section during melt-coolant interactions.

Up to fourteen piezo-electric pressure transducers of different types (e.g. KISTLER, designated as K0, etc.) and pressure ranges (up to 100 MPa) are used in the test tube to monitor the pressure in the interaction zone and in the gas trigger device. The pressure increase in the cover gas atmosphere can be detected at six positions in the pressure vessel by means of piezo-resistive pressure transducers (type KELLER, designated as C1, etc.). All pressure transducers have response frequencies of >10 kHz and the signals are normally recorded on transient recorders with a sampling time of 20 μs. The positions of the pressure transducers with respect to the bottom plate upper surface of the test section are given in Table 1.

Several thermocouples (K-type) are used to measure the temperatures of the gas atmosphere and the water in the test section, and to detect the position of the melt jet leading edge during its penetration into the water. In order to improve the response times, thermocouples of 0.5 mm diameter are used. The thermocouples installed at the test section axis are positioned at the same elevations as the K-transducers and designated as TC 1, etc.

Table 1: Pressure Transducer Locations

KISTLER	Pos.* [mm]	KELLER	Pos.* [mm]
K0	0	C1/C11	140
K1	150	C2/C12	1450
K2	350	C3/C13	1780
K3	550		
K13	550		
K4	750		
K5	950		

* Measured from the bottom plate of the test section

The contact with melt leads to immediate destruction of the thermocouples therefore no information of the trailing edge of the melt can be obtained with them. In general, extra sensors such as photocells, photoresistors and magnetic field detectors were introduced in the upper part of the test section above the water level in order to detect both the beginning and the duration of the melt release from the crucible without contacting the melt jet. However, these techniques were still at development stage during this test series and they have failed to provide reliable data so far.

Water level measurement is required for the estimation of the integral vapour fraction in the mixing zone. Two different kinds of level meters, an inductive (with a moving float) and TDR-type (Time Domain Reflectometry), are used to measure the level swell during the premixing phase. The tests with the narrow test section utilise one of each of these types in a separate level meter vessel (placement illustrated in Fig. 1c). In the tests with the wide test section, only TDR-type of level meters are used, because they are more robust and insensitive to thermo-mechanical loads that might be imposed during a test.

It is important to note that the level meters in general do not function well in highly voided regions. However, the fast response time ($\geq$ 1 kHz) of the TDR sensor and its ability to detect gas/water surface intersecting it give confidence in the measurements of the level swell even in the initial phase of mixing where high void fractions are expected. Qualitative check by visual observation of both types of level meters has been made in a transparent test section mock-up. Furthermore, a calibration of the level meters was done prior to each test with water (no void).

The KROTOS data acquisition system consists of several transient data recorders. Pressure transducer and level swell probe signals are recorded using a transient recorder (Yokogawa 1600) with high data sampling rates of 50 kHz over a time period of about 5 seconds. Ther-

mocouple data (8–12 channels) were also recorded at quite high sampling rate of 1 kHz (Yokogawa 1100) in most tests to capture the timing of the melt front progression accurately. A RACAL analog tape recorder and an HP 75000 data acquisition system are used to record the long term behaviour of the system as well as provide a data backup system. Data reduction and processing is done remotely using a PV-WAVE data analysis package in an HP 712 workstation which is connected to the KROTOS site via a TCP/IP network link.

3 KROTOS Test Procedure

After having reached the desired melt temperature (3018–3063 K), the crucible containing the UO_2–ZrO_2 melt (about 3 kg, density 7960 kg/m^3) is released from the furnace and falls by gravity through a 4 m long release tube of 95 mm inner diameter. Half-way down the tube, a rapid-acting slide valve separates the furnace from the test section below. This valve closes immediately after the crucible has passed. During its fall, the crucible cuts a copper wire generating the zero time signal for the data acquisition. Finally the crucible impacts onto a retainer ring at the end of the tube where a conical shaped metallic puncher breaks the bottom of the crucible thus allowing the melt to pour out (Fig. 1b). The exit of the melt can be blocked by some hundreds of milliseconds by a sacrificial disk of low melting point metal placed beneath the puncher (used only in KROTOS 35). In this way the melt is slowed down to gravity release conditions. The melt jet diameter is defined by guiding the melt through a funnel of high temperature refractory material with an exit diameter of 30 mm. The melt arrival is detected with a thermocouple (TC 7) just at the exit of the funnel which, in turn, is located about 0.46 m above the water free surface. Another thermocouple (TC 6) is located about 10 mm above the water surface to allow for estimation of the velocity of the jet at the melt-water contact. The melt injection phase has been observed visually in numerous tin and Wood's metal simulant tests which were performed in a transparent test section mock-up. These tests demonstrated a coherent jet injection and verified the operation of the level meters. After the jet has penetrated sufficiently deep into the water column, either a thermocouple signal or a predetermined time delay can be used to activate the destruction of the membrane of the gas trigger device to generate a pressure pulse that propagates vertically upwards through the melt/water mixture in order to trigger a steam explosion. After the test, all the debris is collected, photographed and sieved. The debris is inspected before and after the sieving in order to detect any changes in debris form caused by sieving process. Finally the internal parts of the test facility are decontaminated before the preparations for the next test can be started.

4 KROTOS Experimental Results

Five experiments with $UO_2 - ZrO_2$ have been performed. The objective of this test series was to study premixing of $UO_2 - ZrO_2$ melts with water at both low and high subcoolings and to determine if an energetic FCI could take place under such conditions. The main test parameters and results are summarised in Table 2. The KROTOS test programme has been evolutionary in nature, the outcome of previous results contributing significantly to the planning of the future experiments. To reduce the number of test variables, the following parameters have been fixed in these tests: the initial system pressure (0.1 MPa), release nozzle diameter (30 mm), fall height ($\sim$ 0.46 m) and the water depth ($\sim$ 1.1 m).

In the next sections a brief description of the tests and results is given. The discussion is subdivided into two classes as "saturated water conditions" and "subcooled water conditions" following the same convention as before when the results of the Al_2O_3/water system were reported in [5].

4.1 KROTOS Experiments in "Saturated Water Conditions"

In the KROTOS 32 test, approximately 3 kg of $UO_2 - ZrO_2$ was heated up to 3063 K in a tungsten crucible. After the test sequence initiation, the crucible was released and fell down onto the puncher. Since the test was performed without a brake disk, the melt was free to stream out through the punctured crucible bottom and funnel into the water without any time delay. A Plexiglas liner (2 mm thick) was used in the test section to reduce the risk of a spontaneous steam explosion upon the melt contacting the walls of the test section.

The thermocouple data gives an estimate of 4.2 m/s for the leading edge velocity using the thermocouples TC 6 and TC 7 as melt arrival indicators. This value is significantly lower than the theoretical value considering a gravity release of the melt from the furnace. Evidently, the puncher and funnel assembly slowed down the release rate. Thermocouples in the water allowed for the estimation of the melt velocity after penetration into the water. The estimated velocity of the melt jet between TC 5 and TC 6 was approximately 1.5 m/s. The thermocouple data demonstrates that the coherent jet penetrated at least down to TC 5.

No energetic interactions occurred, and the pressurisation of the freeboard volume was mainly due to the steam generation of the melt (see Fig. 2). The different phases of the melt injection can be distinguished in the pressure history. At about 200 ms after cutting the trigger wire, the crucible impacts the puncher creating a small spike which can be seen in Fig. 2. Immediately afterwards, the start of the melt pour increases the pressure rapidly due to the heating of the cover gas up to 0.06 MPa (220–300 ms). The pressurisation rate changes when the melt jet penetrates the water column due to energy transfer to the water. Once the melt

Table 2: KROTOS $UO_2 - ZrO_2$ Test Conditions and Results

KROTOS Test N°				32	33	35	36	37
Melt	composition	UO_2	[w/o]	80.8	81.2	79	79	79
		ZrO_2	[w/o]	19.2	18.8	21	21	21
	charged mass		[g]	3030	3170	3102	3027	3222
	temperature		[K]	3063	3063	3023	3025	3018
	brake disk			no	no	yes[a]	no	no
	initial jet diameter		[mm]	30	30	30	30	30
	free fall in gas		[m]	0.46	0.46	0.46	0.46	0.44
Coolant	Water mass		[kg]	7.1	7.7	7.7	7.7	34.5
	height		[m]	1.08	1.08	1.08	1.08	1.105
	inital temperature		[K]	351	298	363	294	294
	subcooling		[K]	22	75	10	79	79
Test Section	initial pressure (He)		[MPa]	0.1	0.1	0.1	0.1	0.1
	internal diameter		[mm]	95	95	95	95	200
	Plexiglas liner			yes	no	no	no	no
	gas trigger			no	no	yes	yes	yes
Results	confirmed penetration			TC 5	TC 4	n.a.[b]	TC 5	TC 4
	depth of the melt jet							
	maximum pressurisation		[MPa]	0.23	0.14	0.17	0.13	0.07
	steam explosion			no	no	no	no	no
	total debris[c]		[g]	2608	2802	1424	2801	2925
	debris in test section		[g]	1402	1705	331	1142	2925

[a]Tin/Woods metal alloy (T_m ~413 K).
[b]Thermocouple wires destroyed by melt ejection from the test section.
[c]Found in test section, level-meter vessel and pressure vessel.

has penetrated and mixed with the water, the pressurisation rate increases again because of the enhanced heat transfer due to melt breakup. The pressure increase reached approximately 0.23 MPa and then the pressurisation fell quickly to the quasi steady-state value of about 0.05 MPa due to condensation onto cool walls.

The debris size distribution for KROTOS 32 is plotted in Fig. 5. The mass mean size of the debris is about 2.5 mm. The large particles of the debris consisted mainly of irregular shaped particles with some agglomerates. The smaller particles were more spherical in shape. An estimate of debris quenching rate can be obtained by assuming that the pressurisation of the freeboard volume was caused solely by saturated steam with negligible bulk water heating and that all the melt participated (i.e. entered into the water). This simple analysis gives an estimate of 0.7 MW/kg-melt for the maximum melt quenching rate during the mixing phase.

The KROTOS 35 test was essentially a repeat of the KROTOS 32 experiment except that the test section did not have a Plexiglas liner and a Woods metal-tin brake disk was installed to reduce the melt release rate. Additionally, a gas trigger device was mounted. The gas trigger was configured to trigger when TC 3 sensed the melt arrival.

After the initial melt injection, a rapid pressurisation was observed. This initial rapid pressurisation of the cover gas lasted longer than in KROTOS 32 because of the longer duration of the melt release. The observed peak pressurisation of 0.17 MPa is lower than in KROTOS 32, because a significant amount of melt (about 1.1 kg) was blocked in the release funnel and, furthermore, vigorous steaming lead to expulsion of significant fraction of unquenched melt (77 % of the injected melt mass). Some of melt swept out from the test section damaged the thermocouple and level-meter cables on the outside of the test section. Thus the trigger device activated only after the set time delay (2.6 s) rather than with the TC 3 signal. No steam explosion took place. However, the time delay might have been too long for an appropriate triggering, i.e. it is believed that significant fraction of the melt was already quenched.

4.2 Experiments in "Subcooled Water Conditions"

The KROTOS 33 test was essentially a repeat of the KROTOS 32 test except that the water subcooling was higher (75 K) and that the Plexiglas liner was removed from the test section. The same method as in KROTOS 32 was used to estimate the leading edge velocity. The TC 6 and TC 7 data indicated a somewhat higher velocity of 8 m/s prior to melt penetration into the water. This is also confirmed by the shorter duration (220–270 ms) of the cover gas pressurisation (up to $\sim$ 0.02 MPa) shown in Fig. 2. Once in the water, the jet decelerated rapidly from the average velocity of 4.4 m/s between TC 6 and TC 5 to 0.9 m/s between TC 5 and TC 4. Due to the higher subcooling, the pressurisation of the expansion volume is less than in KROTOS 32 with a maximum of about 0.14 MPa and a quasisteady-state level of about 0.025 MPa, see Fig. 2.

The debris size distribution for KROTOS 33 is plotted in Fig. 5. The morphology of the debris was the same as in KROTOS 32. One larger piece of material weighing 88.8 g was recovered from the level meter vessel. The particle sizes are somewhat smaller than in the near saturation conditions (KROTOS 32) with the mass mean size of about 2 mm (excluding the piece mentioned above). Accordingly, the estimate of the melt quenching rate (1.2 MW/kg-melt) is higher than in KROTOS 32.

The KROTOS 36 test was performed with the same conditions as KROTOS 33 except that a trigger device was mounted. The trigger device was set to activate with the TC 3 signal as in the KROTOS 35 test. Moreover, the results from the KROTOS 35 test allowed for a better estimate of the appropriate backup time delay for triggering. Melt injection was

successful but again vigorous steaming at the melt-water contact lead to a partial expulsion of the melt from the test section. The gas trigger device was activated by the TC 3 signal at 1.6 s. However, no energetic propagating explosion was observed. Immediate rapid pressurisation and melt sweep-out lead to the conclusion that the melt mass participating in the premixing process was limited due to the flow constraint imposed by the narrow test tube.

The KROTOS 37 test was a repeat of the KROTOS 36 test with a new, larger diameter test section (200 mm vs. 95 mm). The larger test section was utilised to reduce the superficial steam velocity above the water thus reducing early (fall stage) jet breakup, levitation and sweep-out of the melt as observed in previous tests. In KROTOS 37, the melt jet was successfully injected into the test section with an insignificant amount of sweep-out. The coherent melt jet penetrated at least down to the TC 4 level. The trigger activated with the TC 3 signal at 1.0 s, but no interaction was observed. However, due to the larger test section, the amplitude of the propagating trigger pulse was reduced from the previous tests because the trigger energy (200 J) was kept constant. The maximum pressurisation, shown in Fig. 3, was lower than the previous one (KROTOS 33) because of the greater mass of subcooled water (34.5 kg).

A total fragmentation of the injected melt mass was observed. The resulting debris size distribution for KROTOS 37 is plotted in Fig. 5. The particle sizes are somewhat smaller (1.4 mm) than observed under the same initial conditions but with the narrow test section (KROTOS 33). In the CCM-1 test, which was performed at Argonne National Laboratory [8] with similar initial conditions (P$\sim$ 0.1 MPa, $\Delta T_{sub} \sim$ 43 K), but with corium thermite melt, the mass mean particle size was 2.3 mm.

The estimate of the melt quenching rate (0.13±15% MW/kg-melt, uncertainty due to non-linearity of the slope of the pressure increase) is significantly lower than in the tests with the narrow test section indicating more efficient bulk heating of the water which was not considered in the simple analysis and was not measured in the KROTOS 37 test during the mixing phase. By considering only the steam generation in the CCM-1 test, a melt quenching rate of about 0.09 MW/kg-melt is obtained which compares well with the KROTOS 37 data. However, in the CCM-1 test a significant fraction of energy was deposited into the water, so that the total melt quenching rate was about 0.8 MW/kg-melt which is comparable to the estimates in the KROTOS tests with the narrow test section (with less water) and to the results from FARO test analysis (including the bulk water heating). Therefore, it is likely that the bulk water heating in KROTOS 37 was at least as effective as in the CCM-1 test because of the higher initial subcooling and the smaller average particle mass mean diameter.

It is interesting to contrast the $UO_2 - ZrO_2$ results with the previous ones from the Al_2O_3 test series where supercritical explosions were observed [5]. Such a comparison is shown in Table 3 where the initial conditions and some results of the the Al_2O_3 and $UO_2 - ZrO_2$ are tabulated. In order to make consistent comparisons, it was imperative to repeat an Al_2O_3 test with the larger diameter test section to see if lessening the constraint of the narrow test tube

would indeed affect the outcome (normally an energetic interaction). Such a test (KROTOS 38) was performed with 1.5 kg of Al_2O_3 (at 2665 K), see Table 3. A spontaneous energetic explosion took place before the trigger system was activated. Peak dynamic pressures up to 67 MPa were observed in the test section. The pressurisation of the freeboard volume for this test is shown together with the KROTOS 37 result in Fig. 3. A different type of premixing behaviour with $UO_2 - ZrO_2$ and Al_2O_3 is evident by comparing the initial steaming rates. Significantly greater steam generation with the $UO_2 - ZrO_2$ melt is further illustrated by the level swell data, shown in Fig. 4. This preliminary data would therefore suggest that less breakup of the melt occurred and that the void fraction in the mixing region was smaller prior to triggering in the case of Al_2O_3. However, due to the steam explosion the debris is significantly finer than in the $UO_2 - ZrO_2$ tests, see Fig. 5. Fig. 5 also indicates that about 65 % of the interacting Al_2O_3 melt mass fragmented in particles of less than 250 μm in diameter. In this investigation it was assumed that these particles participated in the explosion process. The efficiency of this explosion process is then the ratio of the kinetic energy to the thermal energy content of the melt which participated in the process. The kinetic energy of the mixture mass was determined from the dynamic pressurisation of the test section which allowed to estimate the impulse ($\int p\ dt$) deposited into the water column. Using this approach and the experimental data from KROTOS 38, an explosion efficiency of 1.8 % was calculated.

These observations have important implications concerning tests with Al_2O_3 simulants performed at various research centers. The differences between $UO_2 - ZrO_2$ and Al_2O_3 melts, in this respect, should be well understood. Currently, experimental investigations are pursued to study the differences between the prototypic $UO_2 - ZrO_2$ melts and Al_2O_3 simulant melts in parallel with general objectives of the KROTOS programme.

5 Conclusions

Concerning KROTOS tests, it is important to note that the following conclusions are based on preliminary trends observed with only a few tests and need to be confirmed with further tests. The experimental results from the KROTOS $UO_2 - ZrO_2$ programme so far indicate:

- Significant breakup of the melt into relatively fine debris (~1–3mm),
- No energetic interactions within the range of the following investigated parameters: low subcooling (10–20 K), high subcooling (~80 K) and external trigger (energy of 200 J),
- Due to lack of energetic interactions so far with $UO_2 - ZrO_2$ melts, the data on effects of geometric constraints on explosions and the far field effects are limited to results from Al_2O_3 tests,

Table 3: Al_2O_3 Tests with Similar Initial Conditions as KROTOS 33 and 37

KROTOS Test N°			30	33	37	38
Melt	composition		Al_2O_3	UO_2–ZrO_2	UO_2–ZrO_2	Al_2O_3
	charged mass	[g]	1516	3170	3222	1533
	temperature	[K]	2573	3063	3018	2665
	brake disk		no	no	no	no
	initial jet diameter	[mm]	30	30	30	30
	free fall in gas	[m]	0.46	0.46	0.44	0.44
Coolant	Water mass	[kg]	7.7	7.7	34.5	34.5
	height	[m]	1.08	1.08	1.105	1.105
	initial temperature	[K]	294	298	294	294
	subcooling	[K]	79	75	79	79
Test	initial pressure	[MPa]	0.1	0.1	0.1	0.1
Section	internal diameter	[mm]	95	95	200	200
	Plexiglas liner		yes	no	no	no
	gas trigger		no	no	yes	yes[a]
Results	confirmed penetration depth of the melt jet		TC 3	TC 4	TC 4	TC 3
	max. dynamic pressure[b]	[MPa]	> 100	–	–	67
	steam explosion		yes	no	no	yes
	total debris	[g]	1400	2802	2925	1523
	debris <250 μm	[g]	1210	136	116	934
	debris <100 μm	[g]	1000	37.4	41.2	545
	explosion efficiency	[%]	1.6	–	–	1.8

[a]Spontaneous explosion took place before triggering.
[b]In the test section.

- Simple analysis using steaming rates indicate melt quenching rates of 0.7–1.2 MW/kg-melt in the narrow test section. The observed melt quenching rates in larger scale FARO facility are comparable to the rates observed in the KROTOS tests.
- Significant differences between the behaviour of prototypic $UO_2 - ZrO_2$ and simulant Al_2O_3 melts have been observed and more data is needed to understand them.

ACKNOWLEDGEMENTS

The authors greatly acknowledge the work and efforts of the whole KROTOS team.

References

[1] S. Angelini, W. W. Yuen, and T. G. Theofanous. Premixing-related behaviour of steam explosions. In CSNI Specialist Meeting on Fuel Coolant Interactions, NUREG/CP-0127, 1994.

[2] A. Annunziato and C. Addabbo. COMETA (COre MElt Thermalhydraulic Analysis): a computer code for melt quenching analysis. In Int. Conf. on New Trends in Nuclear System Thermohydraulics, Pisa 1994.

[3] M. Bürger, M. Buck, K. Müller, and A. Schatz. Stepwise verification of thermal detonation models: Examination by means of the KROTOS experiments. In CSNI Specialist Meeting on Fuel Coolant Interactions, NUREG/CP-0127, 1994.

[4] F. J. Davis and Young M. F. Integrated fuel-coolant interaction (IFCI) code. NUREG/CR-6211 , Sandia Nat. Laboratory, 1994.

[5] H. Hohmann, D. Magallon, H. Schins, and A. Yerkess. FCI experiments in the aluminumoxide/water system. In CSNI Specialist Meeting on Fuel Coolant Interactions, NUREG/CP-0127, 1994.

[6] D. Magallon and H. Hohmann. Experimental investigation of 150-kg-scale corium melt jet quenching in water. To be published, in NURETH-7, 1995.

[7] J. Murphy and M. Corradini. An assessment of ex-vessel FCI energetics for ALWRs. In Int. Conf. on New Trends in Nuclear System Thermohydraulics, Pisa 1994.

[8] B. W. Spencer, K. Wang, C. A. Blomquist, L. M. McUmber, and J. P. Schneider. NUREG/CR-6133, Argonne Nat. Laboratory, 1994.

[9] J. Tang. Modeling of the Complete Process of One-dimensional Vapor Explosions. PhD thesis, Univ. of Wisconsin, Madison, 1993.

[10] T. G. Theofanous and W. W. Yuen. The prediction of dynamic loads from ex-vessel steam explosions. In Int. Conf. on New Trends in Nuclear System Thermohydraulics, Pisa 1994.

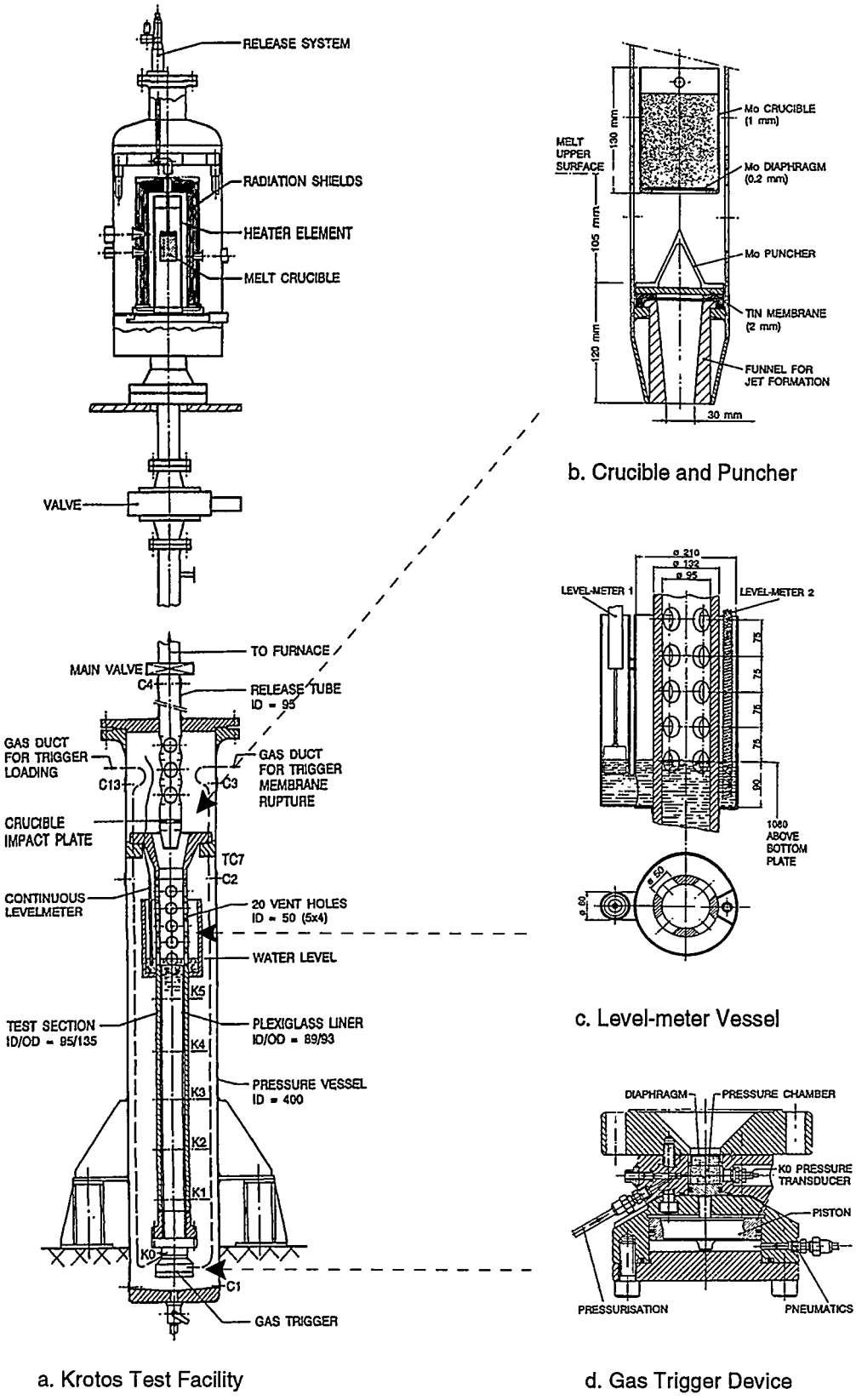


Figure 1: Krotos Test Facility

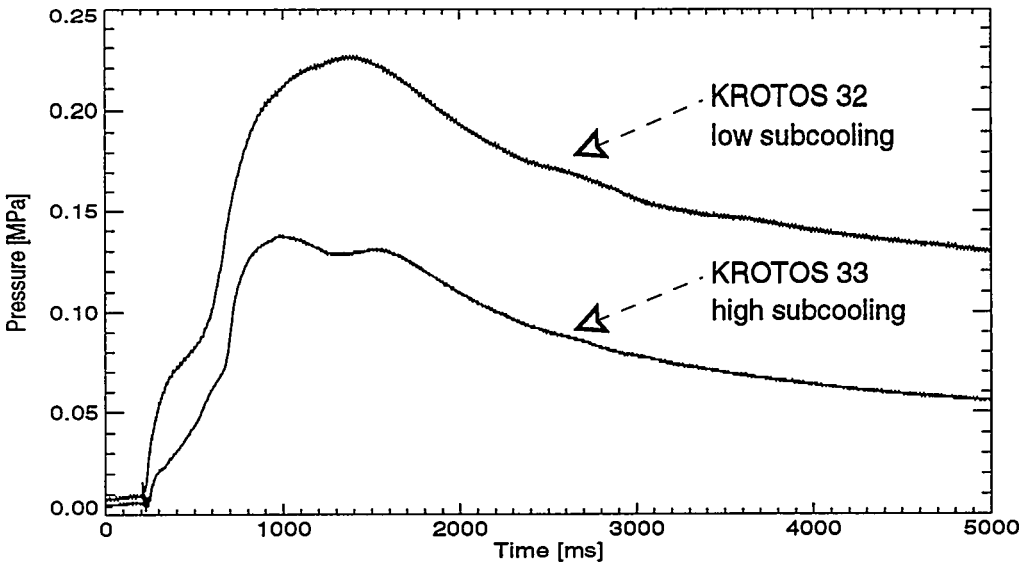


Figure 2: Pressurisation: Subcooled vs. Near Saturated

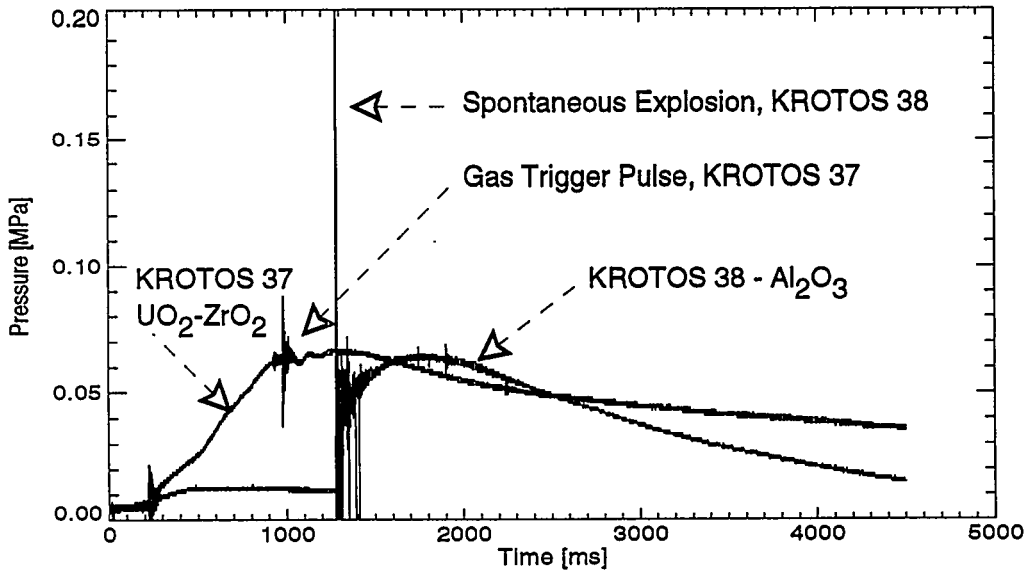


Figure 3: Pressurisation: UO_2-ZrO_2 vs. Al_2O_3

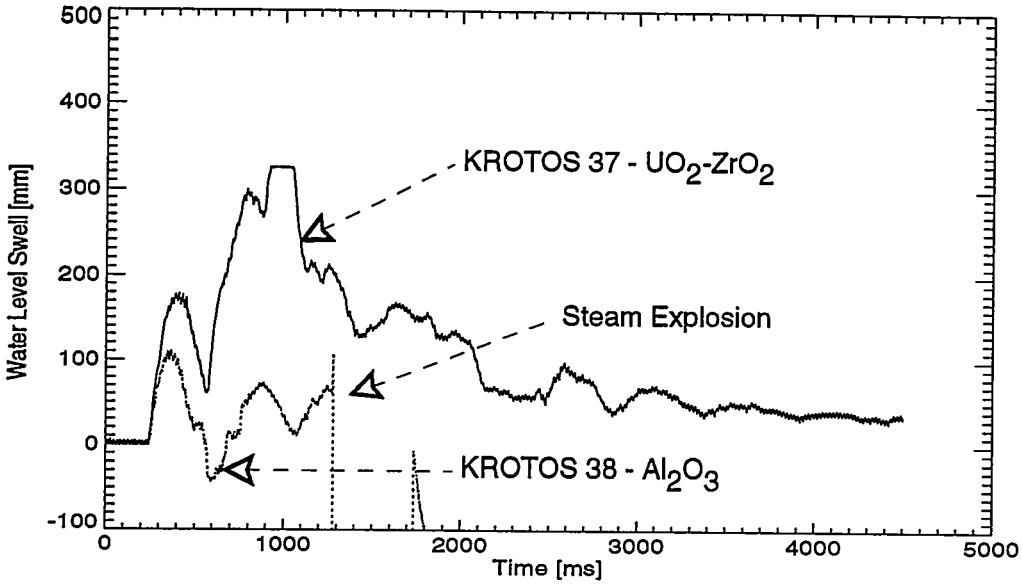


Figure 4: Level Swell: UO_2-ZrO_2 vs. Al_2O_3

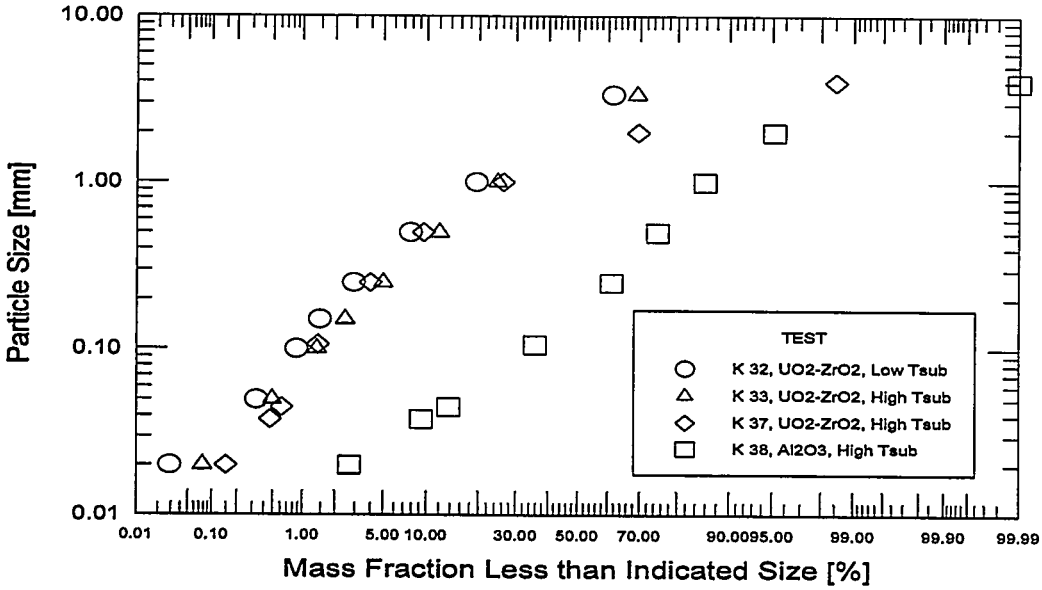


Figure 5: Particle Size Distribution in Selected Tests

Experimental Studies of Thermal and Chemical Interactions Between Oxide and Silicide Nuclear Fuels with Water

Ali A. Farahani and M. L. Corradini
Mechanical Engineering Department
University of Wisconsin - Madison, 53706

Abstract

Given some transient power/cooling mismatch in a nuclear reactor and its inability to establish the necessary core cooling, energetic fuel-coolant interactions (FCI's, commonly called 'vapor explosions') could occur as a result of the core melting and coolant contact. Although a large number of studies have been done on energetic FCI's, very few experiments have been performed with the actual fuel materials postulated to be produced in severe accidents. Because of the scarcity of well-characterized FCI data for uranium alloys in noncommercial reactors (cermet and silicide fuels), we have conducted a series of experiments to provide a data base for the foregoing materials. An existing 1-D shock-tube facility was modified to handle depleted radioactive materials ($U_3O_8 - Al$, and $U_3Si_2 - Al$). Our objectives have been to determine the effects of the initial fuel composition and temperature and the driving pressure (triggering) on the explosion work output, dynamic pressures, transient temperatures, and the hydrogen production. Experimental results indicate limited energetics, mainly thermal interactions, for these fuel materials as compared to aluminum where relatively more chemical reactions occur between the molten aluminum and water.

Introduction

An energetic FCI is a process in which a hot liquid, 'fuel', transfers its internal energy to a colder and more volatile liquid, 'coolant', hence, generating high pressure vapor. Potential damage from the explosive expansion of this high pressure vapor include, but are not limited to, shock wave dynamic loading, kinetic energy of the accelerated mixture caused by the expansion of coolant vapor, and possible combustion of the generated hydrogen, if the fuel is oxidized by the coolant.

Vapor explosions have been an important topic in the safety analysis of nuclear reactors. Energetic FCI's could occur as a result of the core melt in case of a severe accident in a nuclear reactor. These explosions threaten the integrity of the reactor vessel [1] and possibly the containment building should they occur outside the reactor vessel.

Data concerning pressure generation, explosion work, and the extent of oxidation for the interaction between aluminum-uranium fuels with water are very limited. Actually no data could be found on the vapor explosion of the above materials and liquid water except for the Borax I accidental explosion and the Spert ID test, in both of which molten uranium-aluminum alloys/water interactions caused the destruction of the reactors. A survey of literature on FCI after uranium-aluminum

core melt by Martinson [2] reports of only few laboratory experiments [3] and [4] where the chemical reaction between molten aluminum-20 wt.% U with water vapor has been studied. All of this data has been from transient experiments where steam is passed over a liquid metal sample of known initial temperature.

To understand the fundamentals of FCI behavior better, simple experimental geometries must be designed to provide unambiguous data for analysis. Although a large amount of work has been done on energetic FCI's, very few experiments have been performed with aluminum fuel alloys used in noncommercial nuclear reactors (e.g., cermet and silicide fuels) in simple geometries where relatively precise measurements of work, impulse, and hydrogen generation were made.

This paper presents the results of the first series of the FCI experiments we have conducted to provide a data base for the cermet and silicide fuels. Our objectives have been to study the triggering, transient pressures, work potential, and hydrogen generation phenomena of energetic FCI using aluminum fuel alloys (U_3O_8-Al and U_3Si_2-Al) and water in the simple geometry of a 1-D shock tube apparatus. The shock tube provides a straight forward method for controlling fuel-coolant contact, with the independent variables being the fuel and coolant composition, initial masses and temperatures as well as the driving pressure that forces fuel-coolant contact. In a shock tube geometry, stratified layers in our experiments, with control over the contact surface and the impact strength, a vapor explosion can be forced to occur. The dynamic pressures resulting from this vapor explosion inside the constrained geometry of a shock tube are greater than those resulting from a vapor explosion in the less constrained geometry of an open tank in a dropping experiment.

Experimental Setup

The experimental setup consists of two separate apparatus:

- shock tube
- partial pressure analyzer

The shock tube, a long vertical tube, is the environment in which the actual fuel coolant interactions occur. A partial pressure analyzer apparatus is used as a tool to determine the extent of the FCI by measuring the amount of the hydrogen produced from the exothermic chemical reaction between the aluminum content of the fuel and water.

The major components of the shock tube facility are shown in figure 1. The vertical tube consists of two stainless steel tubes and one inconel 600 holder. The middle section (compression tube), 1-in I.D., 1.5-in O.D., 6.6 ft long 304 stainless steel tube, holds the coolant (water, in our case). The lower section, reaction tube or holder (both names are used interchangeably in this report), .984-in I.D., 1.5-in O.D., 5.6-in long inconel 600, holds the melt. The melt itself is contained in a 321 stainless steel crucible which is placed inside the reaction tube. The upper section (expansion vessel), 3-in I.D., 3.5-in O.D., 20-in long 304 stainless steel tube, serves as a gas volume in which argon is introduced to pressurize the coolant. A kapton foil, which separates the compression and the reaction tubes, will burst at a specific pressure depending on its thickness and the coolant will impact the fuel as a result.

Figure 2 shows the components of the partial pressure analyzer device. This device is designed to measure the hydrogen concentration in the gas volume above

the coolant column in the shock tube. A high vacuum is achieved using a turbo-molecular pump while the partial pressures are measured by a quadrupole mass spectrometer with the mass range from 0 to 64 amu.

Measurement and Data Acquisition Devices

Four E type thermocouples (TC0-TC3), which measure coolant temperatures along the shock-tube, have their tips inserted into the tube wall up to 0.35 in. TC4, an E type thermocouple located at the top of the shock-tube, measures the gas temperature in the expansion vessel. Fuel temperature is measured by a K type thermocouple with its tip inserted 0.1 inch in a gap provided at the bottom of the crucible. All of the thermocouples are ungrounded, sheathed, and have a $\sim \frac{1}{16}$ inch O.D. Thermocouples' signals are processed by the Keithley Data Acquisition System 500 (DAS 500) and stored in a PC. Temperature measurements are taken every 30 msec.

Dynamic pressures are measured by five miniature, quartz, charge mode (PCB Piezoelectronics series 112A03) pressure transducers, which are chosen because of their short rise time (2μsec), good sensitivity (1pC/psi), and range (up to 15,000 psi). These transducers are located at the same level along the shock-tube as their corresponding thermocouples. Each transducer is connected to a charge amplifier (PCB Piezoelectronics model 462A) for amplifiying and converting the charge ouput of the transducer into a voltage signal. The charge amplifiers have a range selection capability which determines the maximum pressure that will be measured, hence, increasing the digitalization resolution.

Analog transient pressure signals out of the charge amplifiers are digitized and stored temporarily by a LeCroy data acquisition system comprising a Camac frame, two 12-bit digitizers (LeCroy 8200), two memory modules (LeCroy 8800A), and a Camac to GPIB interface. Each digitizer has four input channels with a maximum of 1 MHz sampling rate per channel. The storing period is determined by the sampling frequency. For example, at 125 μsec sampling period only 1 second of the transient event can be stored. This limits our ability to capture transient pressure frequencies that are much larger than the sampling period which is set by an external clock. The transient pressure digitalization and storage are controlled by Waveform Catalyst, an instrumentation control software from LeCroy, which is run on a personal computer.

A strain-gauge pressure transducer, with 0-500 psig pressure range model 175A purchased from Robinson-Halpern Co., is used to measure and monitor the pressure in the expansion vessel before, during, and after each experiment. The output of this gauge is processed the same way as the thermocouples.

A review of the available literature [5, 6] provided us with very limited information about the thermodynamic properties of U_3O_8-Al. The thermodynamic properties of U_3O_8-Al and U_3Si_2-Al are not completely known to us at the moment. Wherever needed, the unknown properties are found using the ideal gas mixture techniques. The review by Peacock [6] on the available information on thermodynamic properties of U_3O_8 and U_3O_8-aluminum are used where available.

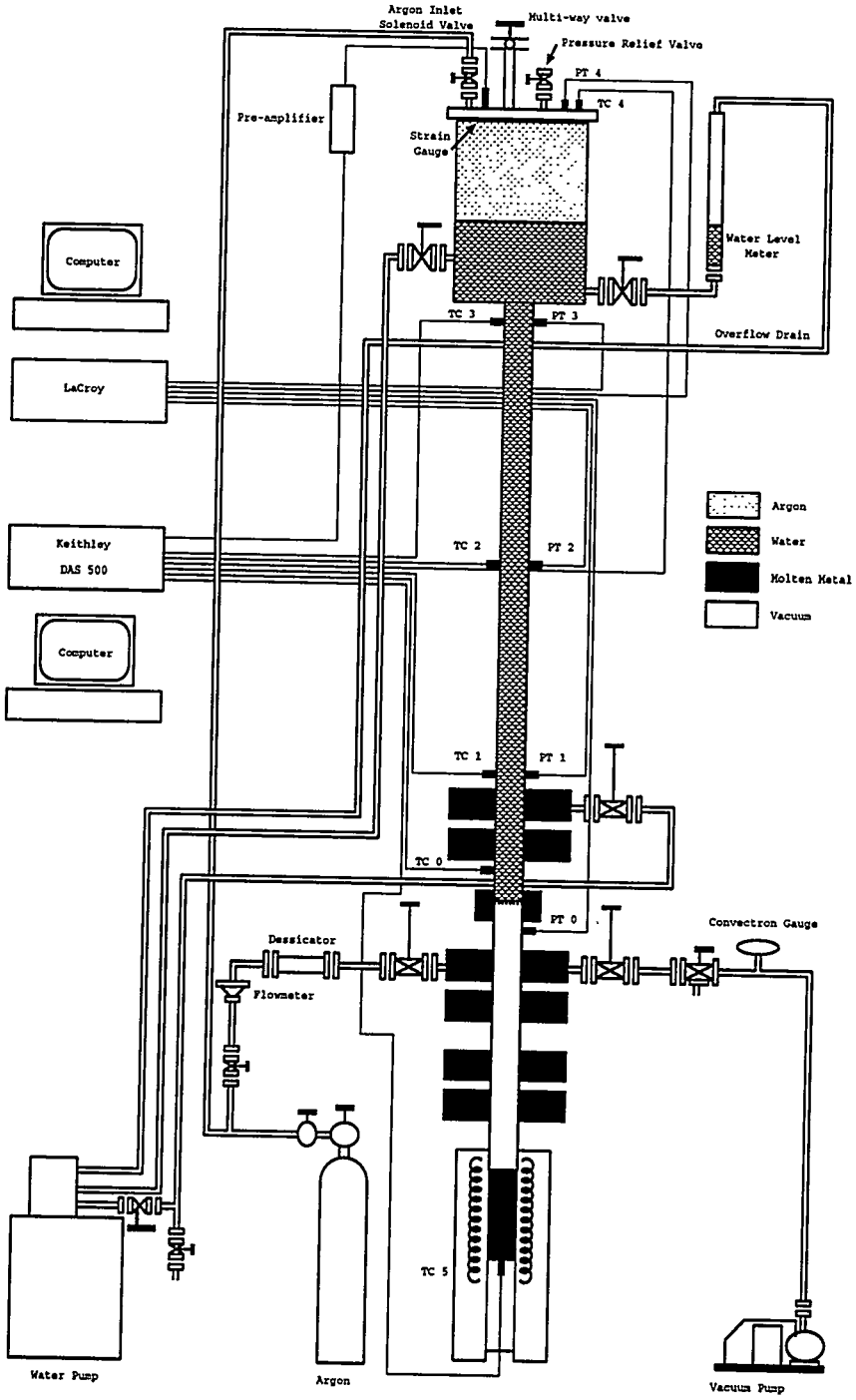


Figure 1: The shock-tube with measurement and data acquisition devices.

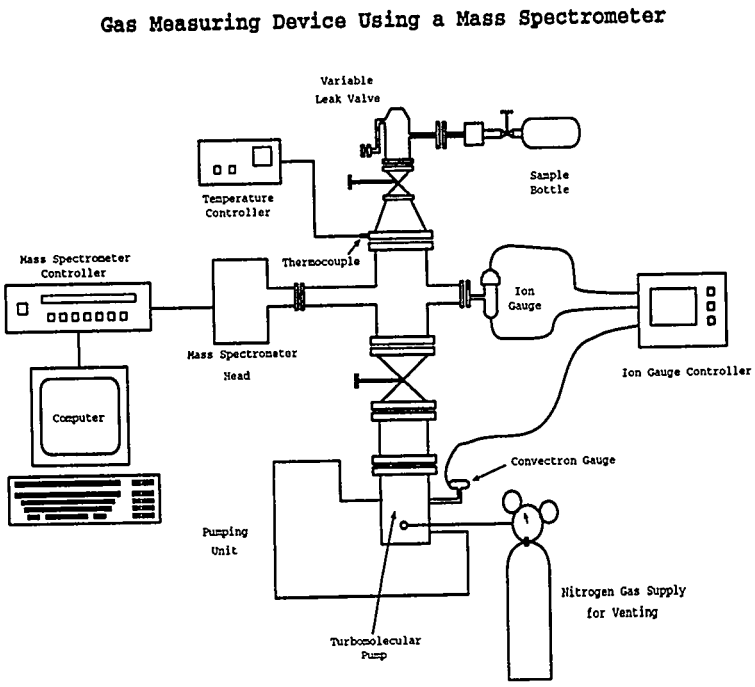


Figure 2: The partial pressure analyzer device.

Experimental Procedure

Depleted radioactive fuels are obtained from our stock, sent to us from Westinghouse Savannah River Company. The fuel pellets are crushed using a hydraulic crusher and then ~12 cc of it is weighed and poured into a crucible. The rupture disk is prepared by cutting a circle, the size of its housing, from a kapton sheet.

After installation of the rupture disk assembly, reactor quality water is pumped by a Haake constant temperature circulator, which is used to control the water temperature, into the shock tube to a pre-detetermined level. The crucible is then loaded into the reaction tube (inconel 600) and attached to the shock tube using stainless steel gaskets. Following this, the volume between the fuel and the rupture disk is vacuumed and checked for any leaks. A Pirani type vacuum gauge supplied by Granville-Phillips monitors the pressure inside this volume. After this, the ceramic fiber radiant heater is attached to the reaction tube. A 700 W heater with a maximum operating temperature of 1200 °C was used in low temperature experiments. However, because of the problems with the aluminum reacting with the stainless steel crucible at high temperatures, a 2600 W heater with a maximum operating temperature of 1300 °C was used in the high temperature experiments (900 °C and up).

The fuel inside the crucible is heated while the volume above the fuel is continuously purged with argon and kept at 5 Torr. This purging of argon is done to prevent the molten fuel from forming any oxide layer prior to its contact with water. When the fuel reaches the desired temperature, argon gas will be diverted

to a solenoid valve that opens up into the expansion vessel. The heater and the vacuum pump are turned off and the three-second countdown starts. After the countdown, the solenoid valve opens up and allows the argon gas to pressurize the water column, which will eventually rupture the diaphragm.

Sample gases are collected inside 50 cc bottles one and five minutes after the completion of each test. The partial pressure of specific gas components making up the total pressure of the sample bottle will then be measured using a mass spectrometer. Partial pressure measurements are usually made at total pressures less than 5×10^{-6} Torr in order to remain below the region of non-linear effects of our mass spectrometer.

Experimental Results

FUEL	Expt. No.	m_f gram	T_f °C	P_{dr} MPa	H_{fuel} m	H_{fall} m
EMPTY CRUCIBLE	7R	0.0	25	.566	0.0	0.435
	8R	0.0	21.9	.555	0.0	0.435
	9R	0.0	22.1	1.177	0.0	0.435
	53	0.0	723.5	.523	0.0	0.435
	55	0.0	710.3	.555	0.0	0.435
	57	0.0	893.2	.584	0.0	0.435
	61	0.0	901	1.159	0.0	0.435
	62	0.0	902	1.187	0.0	0.435
	66	0.0	993.4	.570	0.0	0.435
U_3O_8-Al	71	32.90	723.4	.563	0.031	0.404
	74	29.66	903.5	.580	0.031	0.404
	75	28.58	902.9	.553	0.031	0.404
	76	28.68	901.6	1.127	0.031	0.404
	77	26.75	903	1.044	0.031	0.404
	78	28.13	767.8	.537	0.031	0.404
	79	28.62	1004.8	.593	0.031	0.404
U_3Si_2-Al	59	33.46	908.6	.552	0.031	0.404
	60	30.29	895.6	.560	0.031	0.404
	63	32.46	902.3	1.155	0.031	0.404
	64	33.61	895.1	1.155	0.031	0.404
	65	31.74	768	.532	0.031	0.404
	67	32.97	1032.1	.600	0.031	0.404

Table 1: A list of the preliminary experiments

Table 1 shows the list of the 22 successful experiments performed in our initial series investigating the effects of fuel composition, initial fuel temperature, and driving pressure on the energetics of vapor explosions. The height of the fuel inside the crucible, H_{fuel}, and the vertical distance between the rupture disk and the top of the fuel surface, H_{fall} are also shown in table 1. The experimental matrix

includes three different fuel compositions; the empty crucible, U_3O_8-Al, and U_3Si_2-Al having aluminum weight concentrations of 0%, 40%, and 43.5%, respectively. To check the performance of the experimental design, we performed the scoping experiments with the crucible and the water at room temperature. The empty crucible and the other fuel composition experiments have been carried out at three other initial temperatures of ~750 °C , ~900 °C, and ~1000 °C. The lower end of the initial temperature region, 750 °C, was chosen so that the existence of a homogeneous aluminum melt inside the crucible is guaranteed.

The aluminum based fuels, used here, do not melt completely in the temperature range of 750 to 1000 °C rather they form a mixture of solid and partially melted aluminum. This temperature range was chosen since it represented the predicted range of initial temperatures for particular severe accident scenarios in noncommercial reactors.

The second independent variable of interest is the driving pressure which accelerates the liquid column downward. The effects of driving pressure on the energetics of the interaction have been investigated using diaphragm of 1 and 2 mils in thicknesses that rupture at 5 and 10 bar, respectively.

Table 2 lists the important initial and boundary conditions for the 1st series of the experiments. The experiments were carried out in a random order to insure that the results were not affected significantly by the changes in the characteristics of the experimental design. To investigate the reproducibility of the experimental results, we performed a minimum of two experiments for any given initial conditions. The reproducibility of the experimental results can be seen by comparing the results as listed in table 3 and Farahani [7].

Coolant Temperature (°C)	23 ~ 27
Mass Fraction of Al	.40 ~.435
Water Column ID (cm)	2.54
Crucible ID (cm)	2.22
Coolant Height (m)	2.60
Vacuum Height (m)	.40
Coolant Mass (Kg)	1.95
Total Fuel Mass (gram)	28 ~ 35
Fuel Volume (cc)	11.5 ~ 12.5
Coolant Volume (cc)	1950
Mass Ratio (M_c/M_f)	55.7 ~ 69.6
Volume Ratio (V_c/V_f)	156 ~ 170

Table 2: The initial and the boundary conditions for the 1st series of the experiments.

Dynamic pressure traces, fuel and water temperatures, and gas concentrations were the measured quantities in each experiment. The pressure and the temperature

profiles along the shock tube for all the experiments listed in table 1 are included in a detailed report by Farahani [7].

Pressure Profiles

Dynamic pressure measurements were made at 5 different locations along the shock tube (see figure 1 for the locations of the pressure transducers). The PT0 transducer measures the pressure in the region below the rupture disk. The measured pressure by PT0 is positive as long as the pressure at the location of the transducer during the experiment does not fall below the initial vacuum pressure. The gas pressure in the expansion vessel is measured by PT4. Figures 3 through 5 show the pressure traces for typical experiments conducted for this initial test series.

A typical pressure trace for the impact of a pressurized water column upon the surface of an empty crucible is shown in figure 3. The value of the pressure at the peak of the first rise in the PT4 trace corresponds to the injection pressure as measured by the strain gauge transducer and is noted on the plot. The traces in the figure 3 and others are shown between 0 to 1000 msec. The zero msec does not correspond to the beginning of the experiment; but, it is recalibrated here in order to eliminate the unnecessary data from the opening of the solenoid valve until some time before the diaphragm ruptures.

The generation of water vapor and hydrogen gas can contribute significantly to the pressurization of the argon gas during the experiment. The increase of the pressure inside the expansion vessel beyond the initial driving pressure is part of the work done by the FCI, see figures 4 and 5.

Gas Measurements

Two gas samples, taken at one and five minutes after the experiment from the expansion vessel, were collected to measure their constituent concentrations to determine the extent of the chemical reaction between the aluminum part of the fuel and water. Table 3 gives values for the measured hydrogen mass and the wt% of the aluminum content of the fuel that was oxidized in the initial experiments. The wt% of the aluminum content of the fuel oxidized is based on the assumed stoichiometric reaction between the measured hydrogen mass with aluminum.

Data Analysis

The pressurized gas in the expansion vessel in our shock tube apparatus is a triggering device that can force the collapse of the vapor film, force liquid-liquid contact, and trigger an explosive interaction. The pressure difference across the water column along with the weight of the water are the contributing forces that accelerate the coolant toward the fuel surface. The higher the driving pressure, the greater will be the coolant impact velocity for a given fall distance. Driving pressures of ~5 and ~10 bars have been thus far used. A comparison of the results of expts 76 and 77 with those of expt 75 show that the amount of the chemical reaction between the aluminum content of U_3O_8-Al and water decreased when the driving pressure was increased from ~5 bar to ~10 bar. This conclusion was based on the results of not only expt75 but also expts 72 and 73, not detailed here, where approximately

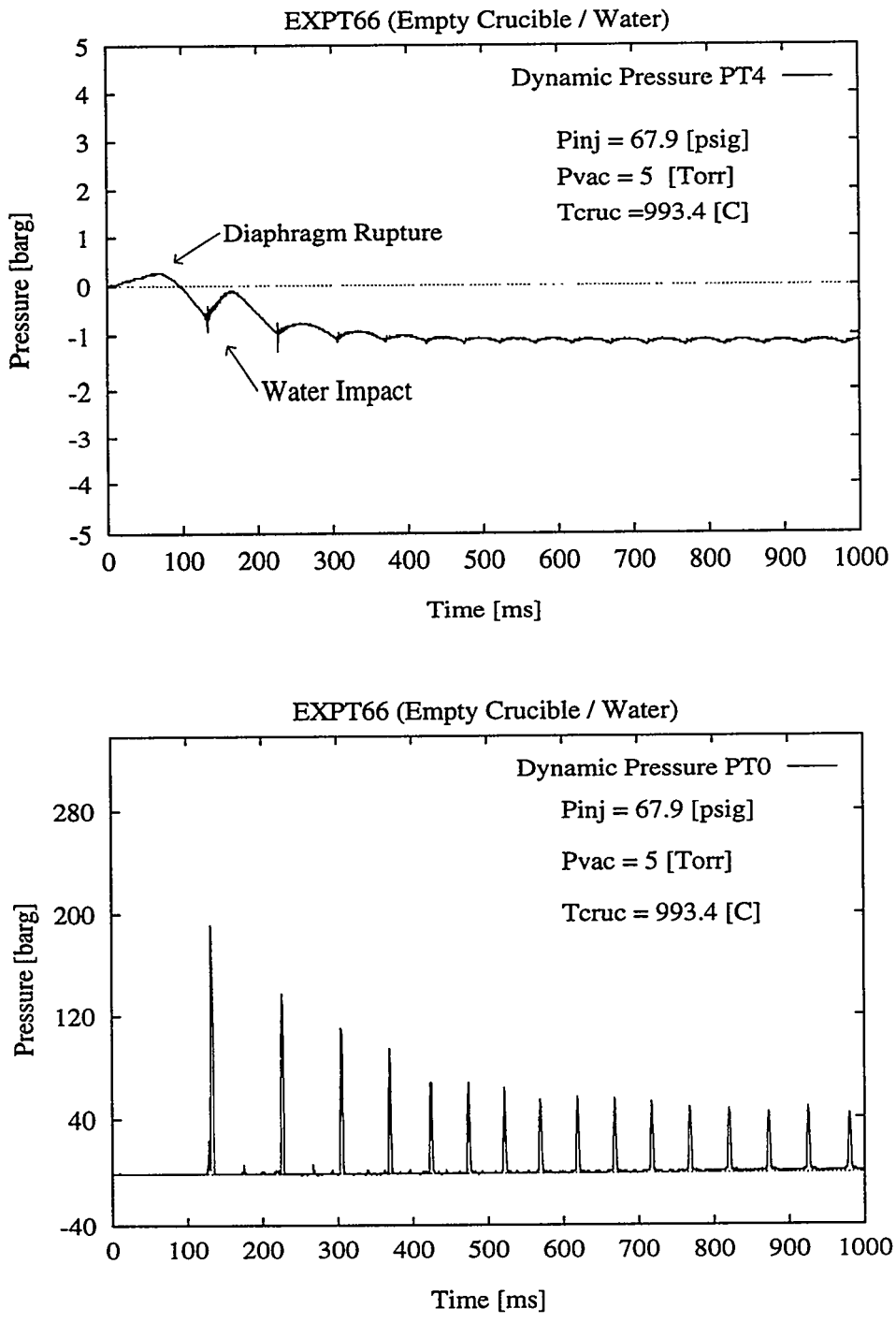


Figure 3: Gas vessel and reaction vessel pressure traces for experiment 66.

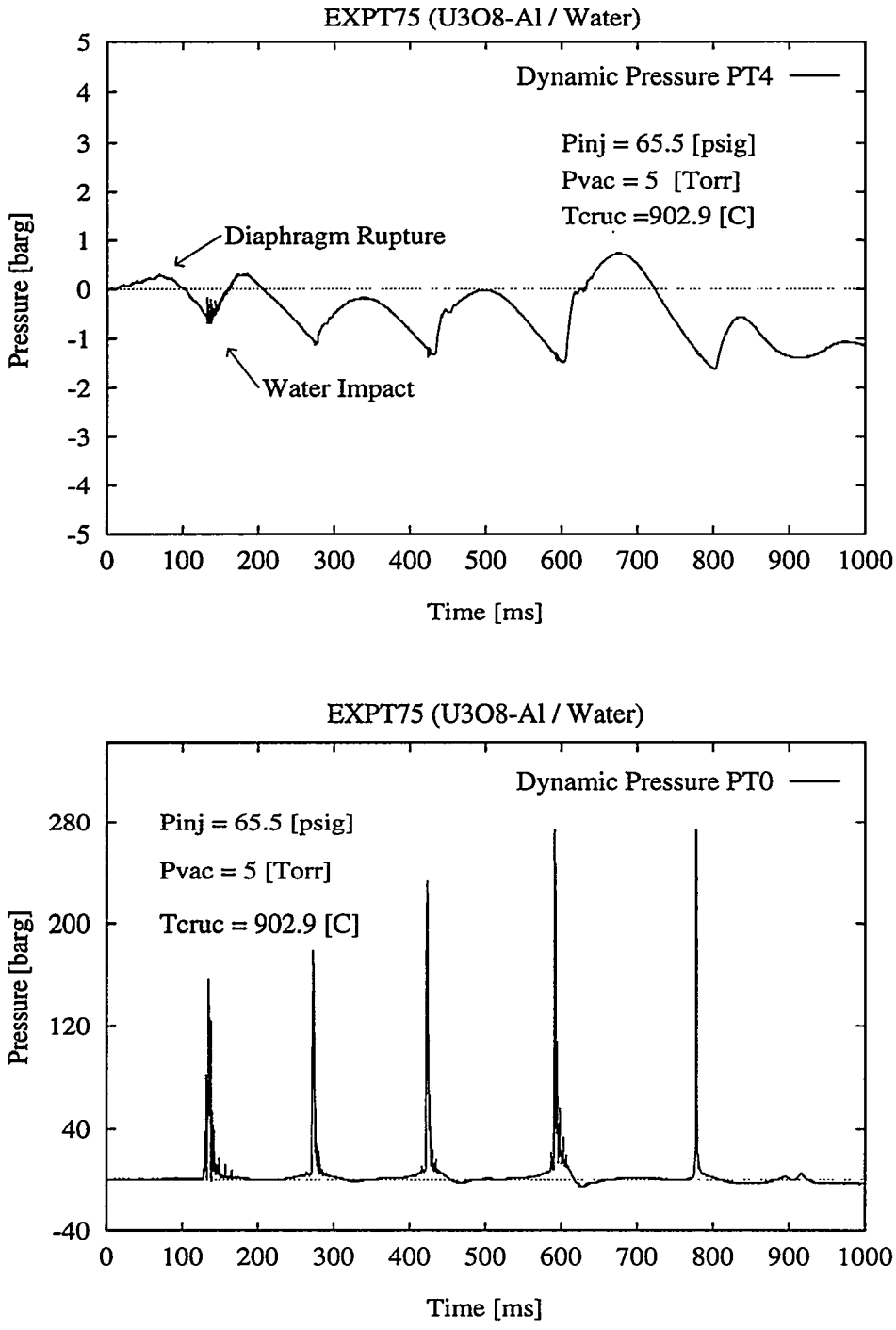


Figure 4: Gas vessel and reaction vessel pressure traces for experiment 75.

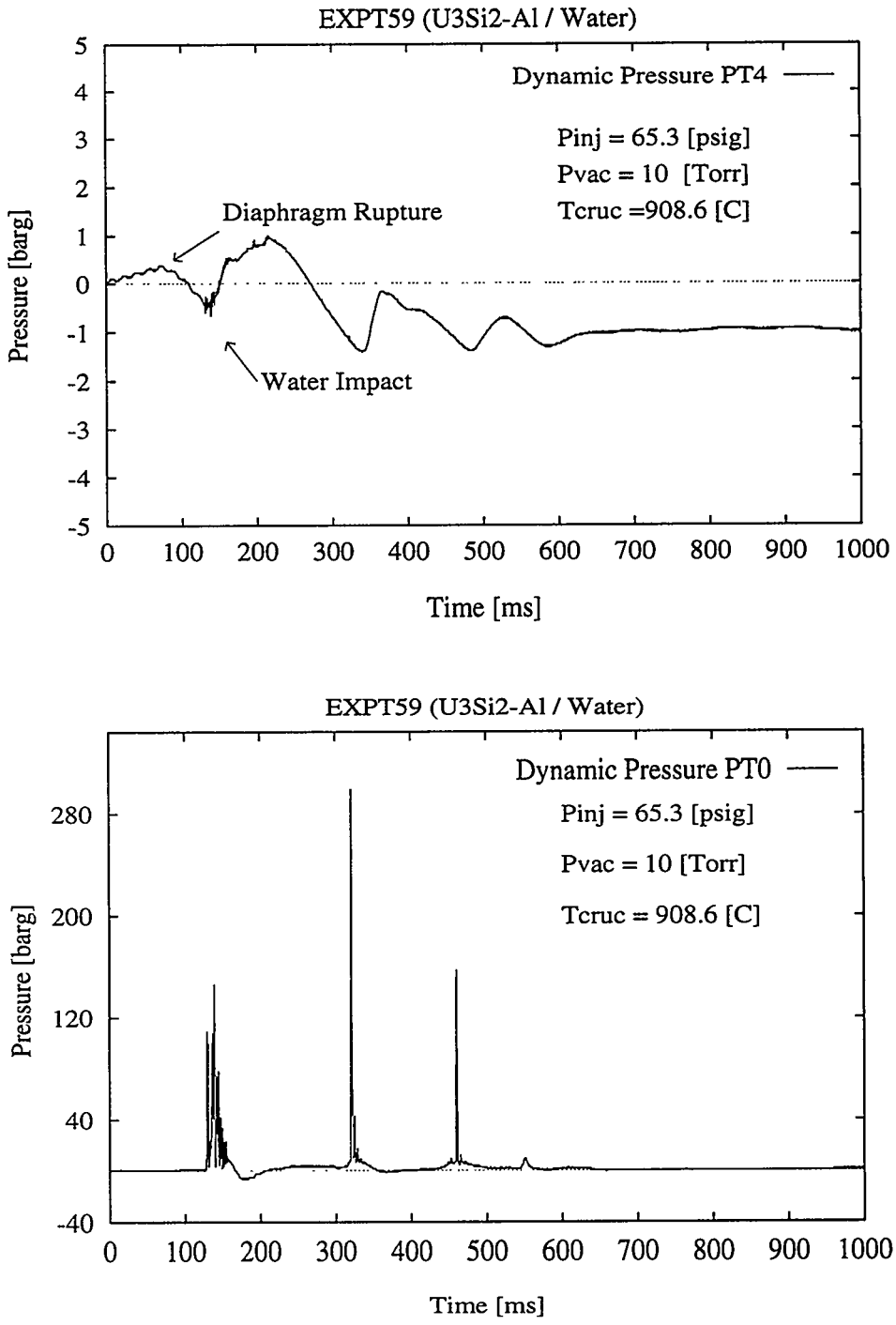


Figure 5: Gas vessel and reaction vessel pressure traces for experiment 59.

FUEL	Expt. No.	m_f gram	T_f °C	m_{Al} gram	m_{H_2} mgram	wt% Al reacted
EMPTY CRUCIBLE	7R	0.0	25	0.0	0.0	0.0
	8R	0.0	21.9	0.0	0.0	0.0
	9R	0.0	22.1	0.0	0.0	0.0
	53	0.0	723.5	0.0	0.0	0.0
	55	0.0	710.3	0.0	0.0	0.0
	57	0.0	893.2	0.0	0.0	0.0
	61	0.0	901	0.0	0.0	0.0
	62	0.0	902	0.0	0.0	0.0
	66	0.0	993.4	0.0	0.0	0.0
U_3O_8-Al	71	32.90	723.4	13.07	10.97	0.7
	74	29.66	903.5	11.86	0.0	0.0
	75	28.58	902.9	11.43	26.2	2.0
	76	28.68	901.6	11.47	0.0	0.0
	77	26.75	903	10.70	2.1	0.2
	78	28.13	767.8	11.25	21.2	1.7
	79	28.62	1004.8	11.45	6.0	0.5
U_3Si_2-Al	59	33.46	908.6	14.56	1.2	0.1
	60	30.29	895.6	13.18	13.4	0.9
	63	32.46	902.3	14.12	0.0	0.0
	64	33.61	895.1	14.62	1.3	0.1
	65	31.74	768	13.81	0.0	0.0
	67	32.97	1032.1	14.34	8.0	0.5

Table 3: A list of the hydrogen mass as measured and the wt% of aluminum oxidized for the preliminary experiments.

2% of the aluminum mass had reacted with water. The results from expt 74 are different than those of expts 75 because the fuel did not disperse into the water column upon the contact rather it formed a solid cylindrical block (see [7]); hence, the interaction looked like that of an empty crucible experiment.

In all of the experiments conducted thus far, the water impacted the fuel several times, see figures 3 to 5. The maximum pressure was observed on the first impact in the experiments performed with empty crucibles (figure 3) as expected due to the lack of any molten fuel fragmentation. The maximum pressure occurred on the second peak in silicide fuel experiments (figure 5). Although the maximum pressures obtained by PT0 in experiments with different fuel compositions did not reveal any major differences among them, the differences in the effects of thermal interactions were more evident in the PT4 traces, the plots on the top of the figures 3 to 5. A larger pressure value on any peak larger than the maximum pressure on the first peak, as measured by PT4, is suggestive of the work done by the FCI for this geometry.

The amount of the hydrogen generated during the FCI is measured and used to

calculate the extent of the chemical reaction between the aluminum content of the fuel with water. Some of the results of hydrogen measurements based on the values given in table 3 are as follows:

- In experiments with empty crucibles no hydrogen gas was found as expected.
- The percentage of the aluminum content of the oxide and silicide fuel that reacted with water remained the same at $\leq$2% in all experiments.

	Fuel	Temp (^oC)	P_{dr} (psig)	Work (J)	Pk P (MPa)	Oxide (%)
ex55	Empty	710	66	48	18	0.
ex65	Silicide	768	62	80	15	0.
ex78	Oxide	768	63	114	13	1.7
ex57	Empty	893	70	103	18	0.
ex59	Silicide	909	65	138	15	0.
es75	Oxide	903	66	>136	16	2.0
ex61	Empty	901	153	106	27	0.
ex63	Silicide	902	153	192	20	0.
ex76	Oxide	902	149	151	22	0.

Table 4: The Summary of the Results; W = Work Output, Oxide = %of the Fuel Oxidized, Pk P = Peak Pressure

The work done on the expansion gas by the thermal- and/or chemical-type vapor explosion between the hot metal and water is a small part of the total energy transfer from the FCI to the mixture. Significant portions of the thermal and chemical energy of the fuel are used to heat the coolant and generate water vapor. The ideal way to calculate the work from the explosion requires the knowledge of the pressure and the volume of the generated vapor at any instant. However, the work from the vapor explosion can be determined indirectly, by calculating the coolant acceleration due to the expanding vapor. A third method, which estimates the work from the explosion by calculating the work required to compress the expansion gas from state one (the end of the gas expansion process) to state two (the end of the expansion gas compression by the upward motion of the coolant), is employed here to compare the amount of the work from the explosion for each fuel type.

$$du_g = dw_{c-g} + dq_{c-g} \tag{1}$$

where du_g, dw_{c-g}, and dq_{c-g} are the change in the internal energy of the gas, the work done by the coolant on the gas, and the heat transferred from the coolant to the gas, respectively. The compression process is assumed to be isentropic ($dq_{c-g} = 0.$ and $PV^\gamma = constant$), so that the gas volume at the end of the compression process can be approximated.

$$du_g = dw_{c-g} \tag{2}$$

$$\Delta u_g = \Delta w_{c-g} \tag{3}$$

For an ideal gas with constant properties

$$\Delta w_{c-g} = c_v(T_2 - T_1) \tag{4}$$

$$\Delta w_{c-g} = \frac{P_2 v_2 - P_1 v_1}{1 - \gamma} \tag{5}$$

The isentropic assumption underestimates the work output from the explosion.

The maximum dynamic pressures on the first impact of the coolant with the fuel and the estimated work output during any impact are tabulated in table 4. Figure 6 shows the ratio of the gas compression work (influenced by FCI) to the gas expansion work (affected by water impact) for all the hot experiments (where the crucible temperature is above 700 °C). Because the expansion work is not the same for all the experiments, then he ratio of the compression work to the expansion work is a better way of comparing the energetics of the interactions.

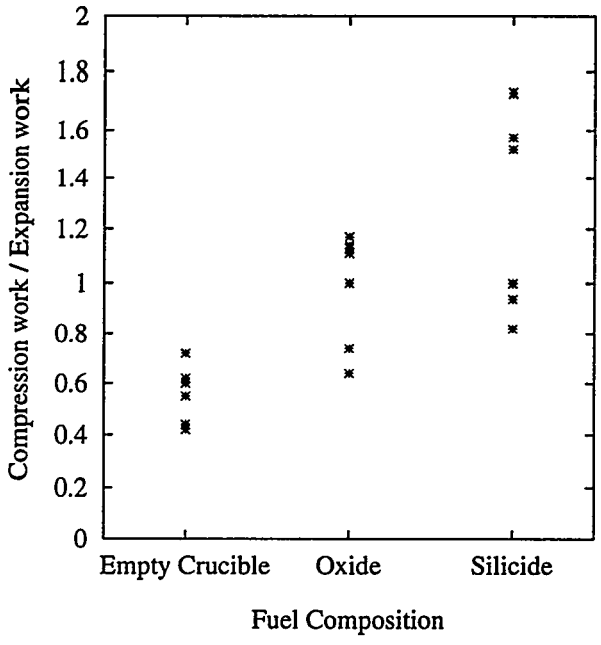


Figure 6: The relative FCI energetics for all the hot experiments.

Conclusions

The amount of the work output and the peak pressures are not significantly different for all the experiments reported in table 3. Previously, it had been assumed that no chemical reaction occurred between these fuels and water as long as the fuel temperature remained below 1500 °C. The idea was that the chemical reaction occurred when the fuel (alloyed with aluminum) was in the liquid phase and the fuel would not be in the liquid phase for the fuel temperatures below 1500 °C. The results of our small scale experiments (~30 gram shots of the fuel) show that the nuclear fuels, both silicide and oxide, did chemically react with water (see table 3), based on the mass of the evolved hydrogen. However, all the fuel and coolant interactions for this first series of the experiments have been thermally dominated interactions. This is in difference to experiments with aluminum, without any nuclear fuels, where energetic FCI's with significant chemical reaction resulted in one order of magnitude larger dynamic pressures and explosion work in our test apparatus [8] and in past experiments.

Acknowledgement

We would like to thank J. Krueger for his help in the laboratory and the DOE and the Savannah River Site for their partial support of this work.

References

[1] R. W. Miller, A. Sola, and R. K. McCardell, **Report of the Spert I Destructive Test Program on an Aluminum, Plate-Type, Water-Moderated Reactor**, IDO-16883, June 1964

[2] Z. R. Martinson, **Survey of Literature on Particle Size, Surface Areas, Oxidation and Pressure Generation After Uranium-Aluminum Core Melt**, EG&G Report PG-T-89-003, Feburary 1989

[3] W. F. Zelezny, **Metal - Water Reactions: Rates of Reaction of Aluminum and Aluminum - Uranium Alloys with Water Vapor at Elevated Tempeatures**, IDO-16629, Nov. 1960

[4] A. Robertson and A. J. Rostron, **Reaction of Molten Al and of Al-20 wt. % U with Water Vapor**, Corrosion Science, 1965, Vol. 5, pp. 425-447

[5] R. W. Knight, **Observation in the Manufacture of Aluminum-Based Research Reactor Fuel Elements**, ORNL/TM-11809, July 1993

[6] H. B. Peacock, **Properties of U_3O_8-Aluminum Cermet Fuel (U)**, WSRC-RP-89-981, Rev. 1, March 1990

[7] Ali Farahani, **Experimental Studies of Thermal and Chemical Interactions Between Molten Aluminum and Aluminum Fuel Alloys with Water**, Preliminary Report, University of Wisconsin-Madison, August 1994

[8] Ali Farahani and M. L. Corradini, **Experimental Studies of Thermal and Chemical Interactions Between Molten Aluminum and Water**, Submitted for Presentation and Publication in NURETH-7 Proceedings

The Effect of Constraint on Fuel-Coolant Interactions in a Confined Geometry

Hyun-sun Park and Michael L. Corradini

Dept. of Nuclear Engineering and Engineering Physics,
University of Wisconsin - Madison, U.S.A
(Phone) (608) 263-4447, (Fax)(608) 262-6707

Abstract

A Fuel-Coolant Interaction (FCI or vapor explosion) is the phenomena in which a hot liquid rapidly transfers its internal energy into a surrounding colder and more volatile liquid. The energetics of such a complex multi-phase and muti-component phenomenon is partially determined by the surrounding boundary conditions. As one of the boundary conditions, we studied the effect of constraint on FCIs. The WFCI-D series of experiments were performed specifically to observe this effect. The results from these and our previous WFCI tests as well as those of other investigators are compared.

1 Introduction

An energetic Fuel-Coolant Interaction(FCI or vapor explosion) is the phenomenon in which a hot liquid releases its energy explosively into a surrounding volatile and cold liquid when these fluids come into contact with each other. This phenomenon has been a concern in several industries including the nuclear industry [1] [2]. In particular, molten fuel generated due to a severe accident in a nuclear reactor may contact residual water either inside or outside of the reactor vessel. Such a contact could result in an FCI.

The FCI has been identified by four unique phases: mixing, triggering, propagation and expansion phases [3]. In the mixing phase, if hot liquid pours into cold liquid, the hot liquid will be slowly fragmented to smaller sizes and mixed with the cold liquid. Both hot and cold liquids will be separated by a vapor film if the surface temperature of the hot liquid is sufficient to maintain this film. In the triggering phase, such a metastable vapor film collapses locally due to a disturbance, and therefore very rapid heat transfer and local high pressures are generated. This local explosion provides a trigger source to generate explosions in the adjacent mixture. These reactions produce a spatial propagation of the explosion. High heat transfer rates from hot to cold liquids produce rapid vapor volume increases which may cause mechanical damage to the surrounding system constraint.

To determine thresholds and quantify such destructive energy which results from FCIs, numerous investigations have been conducted experimentally and theoretically over the last several decades. Because of the complexity of the multiphase phenomena, there are limited quantitative data available to help understand the phenomena. Early research on this phenomena has focused more on the FCI prevention than on the basic mechanisms of FCIs [4]; e.g., properties, initial conditions and thresholds at which the explosion occurs or is suppressed. More systematic research, following the above work, has been performed to investigate the cause of the phenomenon experimentally and theoretically using small scale single drop analysis [2]. Following the Reactor Safety Study(WASH-1400) [5] and then the TMI accident, phenomena related to severe accidents in nuclear power plant has been studied. Most recently FCI research on mixing and energetics has become much more quantitative in its measurements for each of the FCI stages and associated hazards. The WFCI facility [6] has recently been designed and constructed to produce data for understanding the phenomenon under larger scale conditions and benchmarking numerous theoretical investigations and models. The facility was specifically designed as a controlled one-dimensional geometry ($\frac{L}{D}$>10) to reduce complexity and geometric dependency.

In this study, we endeavored to observe experimentally the effect of axial constraint and compared these results to our previous tests and to those of others. Specific comparison data [7, 8, 9] were chosen because of their similarity in geometry, materials, and experimental conditions as well as their completeness in data measurement.

2 Past Experiments

Hall *et al.* [7] investigated tin/water vapor explosions in a long tube geometry. The main test tube was of 0.85-1.0 m in length, 25 mm inner diameter with an outer tube diameter of 50 mm. The test vessel was filled with water at 85-95 °C. The Molten tin as fuel at 600-750 °C is poured into the top of the inner tube. They observed self-sustaining shock propagations and shock escalation.

Baines' facility [7] is a predecessor to our current design of the WFCI facility. The test section is about 1 m long and the horizontal cylinder is about 3 m long with the same inner diameter of 29.5 mm. The test section, made of stainless steel, was initially filled with cold water and electrically heated up to about 90 °C, but the water at the bottom remained cold, typically about 20 °C to induce self-triggering when the melt reached this section. The temperature of the tin as a fuel is at about 800 °C with a mass of approximately 0.5 to 0.8 kg. The expansion velocity was measured by a signal from the magnetic piston in the horizontal tube. He observed that the explosion efficiencies were low with measured kinetic energy yields less than 0.4 % of the thermal energy in the fuel, and propagation velocities were about 100 m/s. The explosion mixtures produced were relatively 'weak' with the tin volume fraction in the range of 0.08 to 0.14.

The KROTOS facility is equipped with an inner test chamber and outer containment vessel to confine the interaction against the surrounding environment. The facility is not equipped with a system for direct measurement of work output, but it can be roughly estimated using the transient pressure of the pressure vessel and dynamic pressures of the explosion event. Several tests with different fuel materials (formerly tin/water, and currently Al_2O_3/water, and UO_2+ZrO_2/water) are being conducted. In the KROTOS-21 test [9], for example, molten tin was used as a fuel with a mass of 7.5 kg and temperature of 1150 °C and water was used as a coolant with a temperature of about 85 °C. A highly pressurized gas chamber with a volume of 12 ml and pressure of less than 15 MPa was mounted at the bottom of the test section as an external triggering device. They measured explosion pressure pulses of about 5 MPa and explosion velocities in the range of 200 to 250 m/s using five pressure transducers located vertically on the test tube.

The WFCI facility is equipped with a direct method of work output measurement. Since the interaction zone is allowed to expand in only one direction, the measured speed of the expansion in the direction directly corresponds to the expansion of the interaction zone. The WFCI experimental series for testing the effect of system constraint on the FCIs is named WFCI-D. All details are discussed in the following section.

3 Effect of Boundary Condition

The energetics of the FCI could be affected by several initial and boundary conditions. Results obtained from large scale experiments currently being conducted in WFCI and KROTOS facilities have produced FCI energetic yields with less than a few percent conversion ratio, which is defined as the ratio of the explosion work to the initial fuel thermal energy. These ratios are an order of magnitude lower than the maximums obtained by a thermodynamic analysis [3]. These large differences between the ideal and real cases result from several factors in the initial and boundary conditions of the FCIs.

3.1 Radial Constraint

The geometrical effect could play an important role in the FCI energetics. Frost *et al.*[10] investigated the degree of geometrical constraint required to sustain propagation of vapor explosions. In their

experiments an array of melt droplets were injected into a narrow channel as a radial constraint (or confinement). The explosive interaction produced a shock propagation with a speed of about 50 m/s. Without the radial constraint, incoherent sequential explosions of the drops still occurred. If there was no confinement, the propagation velocity was decreased by an order of magnitude to 5-10 m/s. They found a high degree of radial constraint was required to sustain a propagating explosive interaction. Also they observed interactions initiated in a radially unconstrained cylindrical geometry always failed to propagate after a short distance. In the recent KROTOS and WFCI tests, this high degree of radial constraint has been maintained and vapor explosion propagations commonly result. The presence of a strong radial wall constraint in these one-dimensional experiments is necessary to simulate a 'slice' of a larger scale fuel-coolant mixture which would provide the radial confinement in larger scale explosions. The relationship between the scale of experimental geometries and fuel-coolant mixtures is a crucial factor in deciding the degree of geometrical constraint needed to bound the effect of larger scales and sustain propagations. It is our belief that a strong radial constraint maximizes energetics for a particular fuel-coolant mixture.

3.2 Presence of Porous Fuel Plugs

For tests with a high degree of radial constraint and a one-dimensional interaction zone in the axial direction, such as the KROTOS and WFCI tests, highly irreversible processes can be observed, when the shock pressure waves produced by an explosive interaction pass through highly multiphase-multicomponent mixtures. Some portion of their energy will be dissipated during the interaction and then the shock pressures decrease and pulse widths broaden. Eventually, these effects may reduce the shock impulse and the expansion work on the surrounding system.

In the WFCI tests, Park *et al.*[11] demonstrated the presence of multiple shock wave propagations through an axial interaction zone with the presence of a rigid boundary at the top of the test section (i.e., slide gate). In particular with the KROTOS tests, similar multiple wave propagations even without a solid boundary at the top of the test section have been observed. Post-test analysis shows that about fifteen percent of the total debris was packed in a region near the top of the fuel-coolant mixture, presumably caused by the mixing during the fuel pouring time and subsequent freezing during the FCI. The hypothesis is that this 'porous plug' of melt provided a 'semi-rigid' boundary at the top of the mixture. This boundary not only can dissipate the explosion impulse and expansion, but also aids as a point of shock reflection for downward FCI propagation.

3.3 Fuel Participation in Fuel-Coolant Interactions

In the thermodynamic analysis, it has been historically assumed that the total amount of fuel and coolant are completely mixed together and participate in the FCI. It is one of the key reasons for the large pressure and work output estimated by such models. This assumption is unrealistic and partial participation of the fuel and coolant during the explosion has been recognized in recent analyses of tests. Park *et al.*[11] analyzed experimental results using a thermal detonation model to match the explosion pressures and propagation velocities obtained from their experiments and thus estimated the initial mixing conditions. They found only a few percent of the fuel mass need to be involved in the explosive interaction to produce the shock pressures, propagation speeds and estimated work outputs. Such analyses have been also applied to recent KROTOS tests [12] for high temperature oxides and similar conclusions were reached.

3.4 System or Axial Constraint

In general, during an energetic FCI the peak pressurization and the mechanical work potential depend on the system constraint. From a hydrodynamic or mechanical point of view, the system constraint was originally categorized by Cho *et al.*[13] as acoustic and inertial. They considered the system constraint in developing their parametric models as the acoustic and inertial system, based on two different timescales

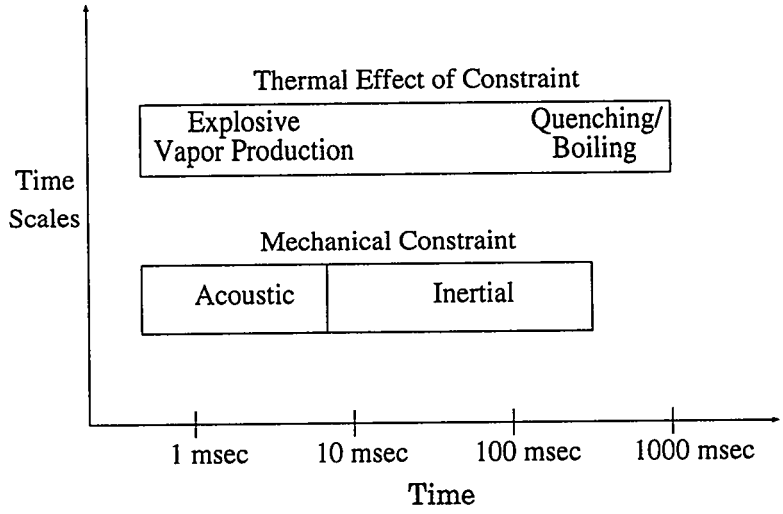


Figure 1: Time Scales with respect to the System Constraint

for potential mechanical damage as shown in Figure 1. The first is the time for acoustic relief. During this timescale (so called acoustic unloading time) the pressure shock wave builds within the fuel-coolant mixture in the explosion chamber. It is determined by the time for a shock pressure front to travel through the mixture and system constraint above it to the nearest free reflecting surface and with a rarefaction wave back to the interaction zone. It is approximately equal to 2L/c, where L is the distance from the interaction zone to the nearest free reflecting surface and c is the velocity of sound in the media. The second is the time for the inertial expansion of the fuel-coolant mixture. In this time period, the mass of the liquid column and fuel-coolant mixture itself can be accelerated upwards by the expanding mixture pressure.

From a thermal point of view, however, the timescale for explosion expansion, related to the system constraint may be divided into two time periods: one is a time period for heat transfer between the rapidly fragmented fuel and the adjacent coolant causing vapor production and another is the time period for fuel quenching by heating the surrounding coolant without significant vapor production. Those two time periods are plotted for comparison with the mechanical timescales in Figure 1. During the first time period, since the vapor production rate is directly proportional to the fuel quenching rate, more energetic FCIs may be expected as the time increases. This is because as more time is made available, larger vapor pressures driving the explosion can result, with minimal slug expansion. If the time continues to increase into the second period, however, less energetic interactions are anticipated. Under these circumstances the vapor production rate becomes smaller than the fuel quenching rate as the slug expansion becomes appreciable and coolant bulk heating begins to dominate. The system constraint directly affects these timescales since it controls both the acoustic and inertial timescales through its variation and its effect on fuel-coolant energy exchange.

In our WFCI facility, we can directly test the system (axial) constraint effect of an FCI by varying the total slug mass within the expansion tube.

4 Experiments

4.1 Experimental Facility and Procedures

The WFCI facility has been designed to perform fundamental experiments in energetic fuel-coolant interactions. It allows for controlled initial and boundary conditions and is able to more precisely

measure the fuel-coolant mixing process and the energetics from the explosion. It specifically allows measurement of spatial and temporal shock pressure histories, explosion propagation velocities, work outputs and fragmented fuel debris.

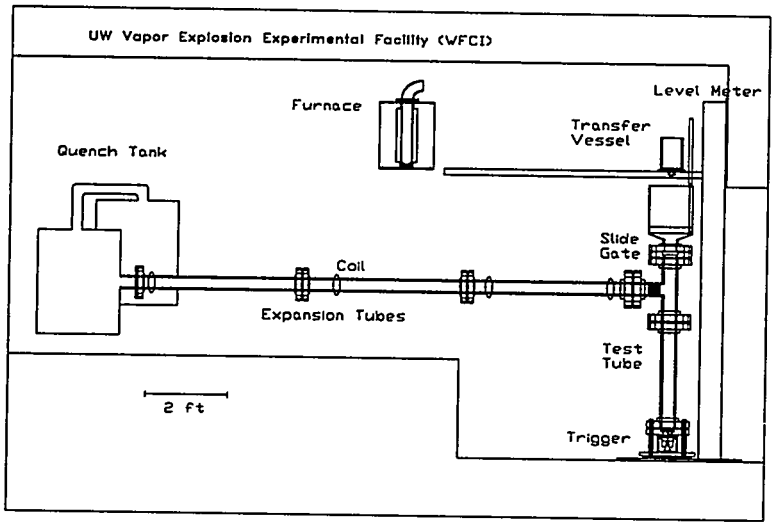


Figure 2: Schematic of the Wisconsin Fuel-Coolant Interaction (WFCI) Facility

The WFCI facility consists mainly of vertical test tubes, expansion tubes, an external triggering device, and furnace as shown in Figure 2. The vertical test section (1.5 m) and the horizontal expansion tubes (3.6 m) are constructed from thick walled stainless steel pipe with an internal diameter of 87.3 mm. At the top of the test section a fast acting slide gate is located and closed after the melt is poured but prior to explosion triggering. The bottom end of the test section is a piston (trigger) which produces a shock wave via impact by a magnetic hammer mounted underneath. The melt is generated in an electric furnace, delivered by a ceramic transport vessel to the top of the vertical test tube. The melt is poured into the vertical test tube by opening the plug at the bottom of the transfer vessel. A few seconds later the slide gate and bypass valve are closed and the external triggering device and data acquisition system are simultaneously actuated. The automatic sequences are shown in Figure 3. The explosion pressures are measured by a set of eight dynamic pressure transducers and the explosion propagation speed is obtained from these pressure traces. The explosion work yield is measured by knowing the system mass with the velocity determined by a set of coils wound on the expansion tubes which detect the passage of a magnet within the piston inside the expansion tubes.

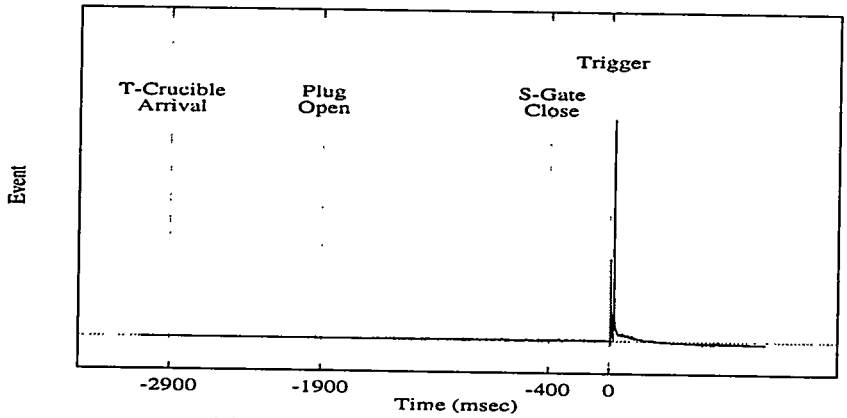


Figure 3: Typical Experimental Sequence

In this series of experiments, the degree of constraint for fuel-coolant interactions is determined by the total mass of coolant in the expansion tube and additional high density lead slugs (73 mm diameter and 100 mm long each) in the expansion tube. The experimental conditions of the WFCI-D series and other series are shown in Table 1.

4.2 Data Acquisition

The main physical parameters measured in the WFCI experiments are transient pressures, temperature, and level swell histories as well as piston-slug displacement during the fuel-coolant interactions. Temperatures of the furnace, fuel, and water are monitored by K-type thermocouples located at the furnace, water-loop, magnet trigger piston and test tubes. A video camera records the whole sequence of the experiment.

The test section was designed to accommodate up to eight high sensitivity piezo-electric pressure transducers (PCB series 112A) for pressure signals during the explosion and the mixing phase. These are flush-mounted on the test tube. Each transducer is connected to a charge amplifier (PCB Model 462A) for converting electrostatic charge (1.0 pC/psi nominally) into a voltage output. The charge amplifier has multi-range (unit/volt) capability, thus a higher resolution can be obtained in the digitization at fixed fits by adjusting the full voltage scale. All pressure transducers have response frequencies greater than 10 kHz and the signals are recorded via a high speed analog/digital buffer interface (up to 1 MHz).

Table 1: Experimental conditions and brief results of the WFCI-D series

WFCI Series	M_{slug}[1] (kg)	T_m[2] (°C)	T_w[3] (°C)	P_{trig}[4] (MPa)	M_{melt}[5] (kg)	Results
D-01	0.53	901	84.3	3.0	3.19	TE[6]
D-02	42.2	911	84.6	3.0	3.31	TE
D-03	42.2	877	84.1	3.0	3.51	TE
D-04	56.8	901	86.6	3.0	3.19	TE
D-05	71.2	819	82.9	3.0	2.91	SE[7]
D-06	71.2	889	83.6	3.0	3.01	TE
A-02	23.4	980	85.0	3.0	3.73	TE
A-05	23.4	940	85.0	3.0	3.58	TE
C-01	23.4	978	85.0	3.0	3.31	TE
C-05	23.4	881	85.0	3.0	3.09	TE

The location of the magnet embedded piston in the expansion tube as a function of time is measured by installing electrical coils along the expansion tube that sense the piston passing each coil location at a particular time. Since all the explosion expansion products are directed through this tube, the explosion expansion work can be calculated from these data.

A PC based CAMAC system (LeCroy) is used for digitizing and storing the fast transient signals from the instruments. It has four 12-bit digitizers (LeCroy 8200) with a 32 K memory module (LeCroy 8800A). Each digitizer has four input channels with 1 MHz maximum sampling rate per channel.

[1] Slug mass in the expansion tube
[2] The initial molten fuel temperature
[3] The initial coolant temperature
[4] The external trigger peak pressure
[5] The molten fuel mass collected inside
[6] Triggered Explosion
[7] Spontaneous Explosion

5 Results and Discussion

A total of six experiments of the WFCI-D series were conducted to investigate the axial constraint effect on fuel-coolant interactions. The axial constraint on the system was provided by the additional mass in the expansion tube. The total slug mass used in each test is shown in Table 1. The conversion ratio of this series of experiments was plotted in Figure 4 with respect to the total slug mass. In this figure, other test [7, 8] results are also plotted for comparison.

For the KROTOS-21 test, the system (axial) constraint is assumed to be zero to be consistent with the method applied in the WFCI test; i.e., the slug mass is defined as the fluid above the actual fuel-coolant mixture. The conversion ratio for KROTOS-21 was not directly measured but estimated from the TEXAS simulation [14], which produced the maximum work output of 1100 J. Also, the total mass of the fuel for the total thermal energy used in the calculation was 5.4 kg, which was measured after the experiment and called "the probable-mixed mass". For Hall's experiment, the constraint was also assumed to be the same as the KROTOS-21 test since it has the same geometrical configuration as the KROTOS facility. The conversion ratio for their tests was determined from the impulse of the explosion pressures they measured in a range from 150 J to 250 J. The conversion ratio corresponding to those impulses is in a range from 0.06 to 0.25%.

For Baines' experiment, he determined the conversion ratios to be 0.18 to 0.38% using a similar measurement method to our apparatus. The WFCI-D-01 test was conducted without water in the expansion tube but still the piston with mass of 0.53 kg was considered as the axial system constraint. This experiment provided the lowest bound of the system constraint in this system.

To illustrate the effect of the fuel quenching time on the FCI energetics, the WFCI-B series of tests are considered. In these tests shown in Table 2, explosions occurred in a random fashion, since an external trigger was not used. These tests show that the conversion ratio tends to decrease as the dwell time to the explosion, t_{exp}, increases. This suggests that the effect of the fuel quenching is effective in reducing the FCI energetics during this mixing time period.

Table 2: Summary of Timing in some of WFCI Experiments

Test Series	M_{slug} kg	CR[8] %	t_{exp}[9] msec[11]	Δt_{slug}[10] msec
D-01	0.53	0.096	9.66	107.1
D-02	42.2	0.420	9.01	416.1
D-03	42.2	0.530	8.21	376.1
D-04	56.8	-	8.58	-
D-05	71.2	0.348	-307.7	622.2
D-06	71.2	0.301	8.58	636.1
A-02	23.4	0.190	8.21	358.0
A-05	23.4	0.325	12.04	283.6
B-01	23.4	0.155	1189.2	392.4
B-02	23.4	0.302	663.4	332.0
B-03	23.4	0.456	-67.8	228.8
C-01	23.4	0.383	9.31	260.0
C-05	23.4	0.317	13.97	319.5

In Figure 4, the conversion ratio and the duration time of the piston movement in the expansion tube were plotted with respect to the axial constraint. The linearly fitted line for Δt_{slug} was obtained from

[8] Conversion ratio which are re-evaluated [6],[11]

[9] Time of the explosion occurred

[10] Time between the slug begins to move and arrives at the tube exit

[11] Time zero is set by the time of the external trigger activated

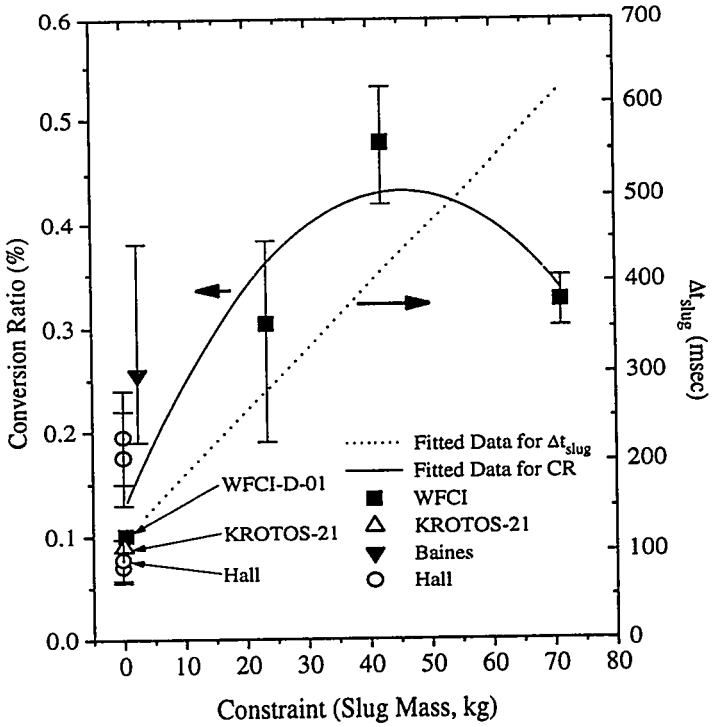


Figure 4: Conversion Ratio and Δt_{slug} with respect to various slug masses

the data in Table 2 with a standard deviation of about 50 ms. This figure shows that the conversion ratio increases with an increase in the axial constraint up to about 50 kg, then slowly decreases. However, Δt_{slug} keeps increasing with the axial constraint. As noted in the previous discussion for the system constraint a possible reason can be linked to the two different time periods associated with fuel fragmentation. If the axial constraint increases, the duration time of the piston movement will increase and eventually it provides more time for mixture energy exchange. It initially increases the FCI energetics since the fuel quenching is not significant during this time period. However, if Δt_{slug} increases with the increase of the system constraint, the conversion ratio decreases since the fuel quenching becomes dominant during that time period. In this experiment, the turning point occurs within a range of 450 to 550 ms for the Δt_{slug}.

Another way to explain the observed results may be helpful. Above a certain degree of system constraint, if the system is not allowed to expand, additional vapor generation causes a system pressure increase. Such a pressure build-up eventually changes the heat transfer characteristics of the fuel-coolant-vapor system. If the system pressure increases, the vapor generation rate tends to decrease and heat transfer among those phases is enhanced. Those two effects eventually suppress the FCI energetics. As an extreme case, if the system is bounded by a nearly infinite constraint within a time scale in which vapor generation is dominant, suppression of the explosive interaction is most likely, as shown in the case of the deep undersea volcanic explosion.

Figure 5 shows the pressure history of the WFCI-D-04 test. This data illustrates the typical pressure history of the WFCI experiments. The plot presents the pressure histories measured with eight pressure transducers from bottom to top of the test section. It clearly shows pressure propagation and escalation from the bottom of the test section. The bottom two plots show the typical pressure trace of the external trigger. The external trigger was provided at about 3 MPa with a pulse width of about 0.1 to 0.2 ms at its half height to all D series experiments. The trigger shock traveled with a speed of 1530 m/s from the first transducer to the second one. However, the speed of the shock dropped to about 290 m/s and the shape of the shock was changed at the third transducer location. This indicates no melt had

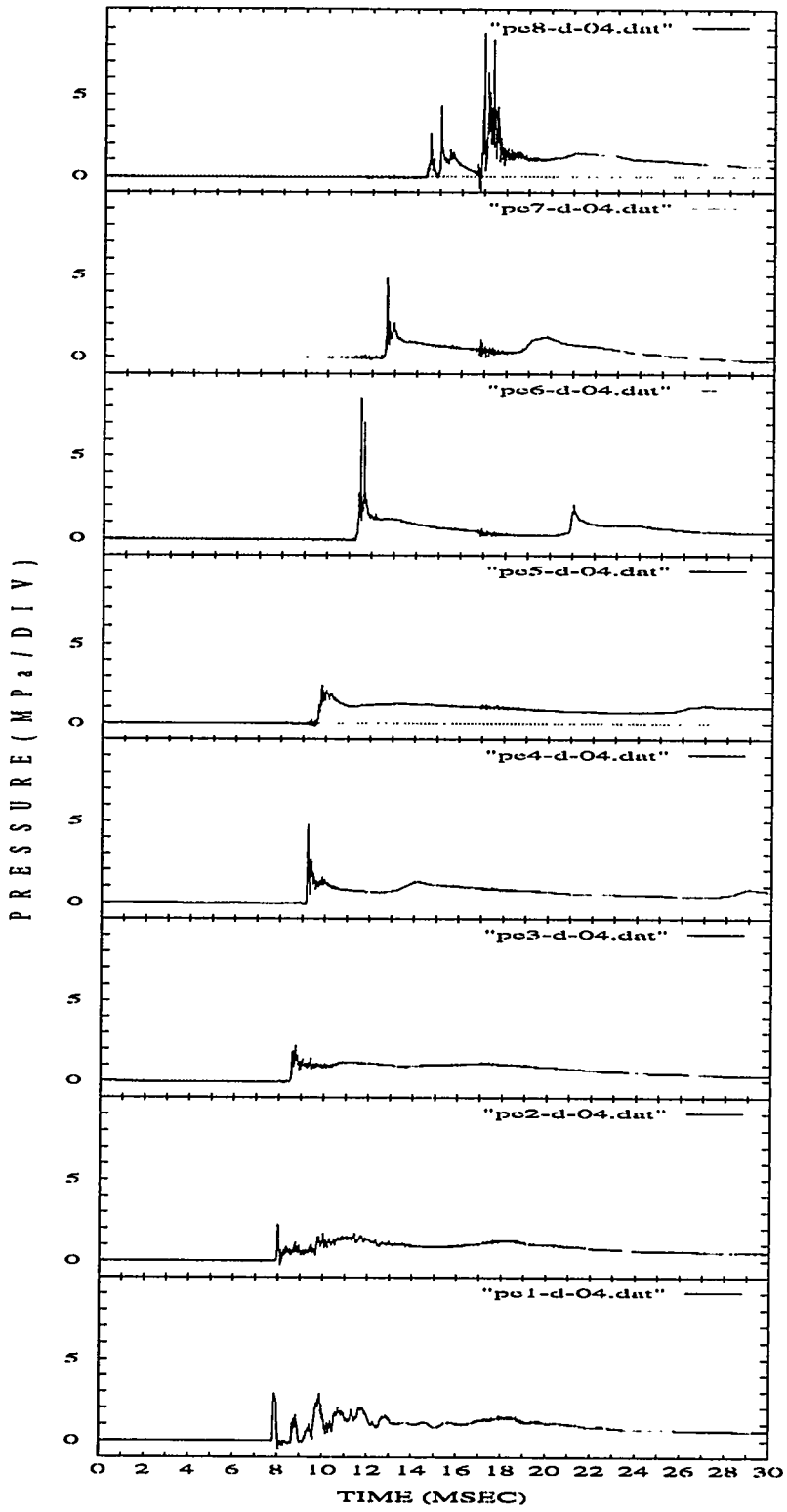


Figure 5: Pressure Traces of WFCI-D-04 Test with a total constraint mass of 56.8 kg

reached the location of the second transducer and the leading edge of the fuel melt is located in between the second and the third pressure transducers which is about 1.1 m below the slide gate. After that point, the shock generated by the explosive interaction, with less than 0.1 ms peak rising time, travelled with different speeds from 290 down to 80 m/s. These speeds can be explained by the condition of the mixture; i.e., high vapor void fractions from the bottom to the top of the explosion tube.

6 Conclusions

The effects of the system constraint on energetic fuel-coolant interactions were investigated. From the experimental results of the WFCI-D series, the conversion ratio increased up to a certain degree of constraint and then decreased with increasing an system constraint. It may suggest that there is a maximum threshold of the explosion energy conversion with respect to the system constraint. This maximum point will be determined by the two time periods as discussed before. Up to this point, the FCI energetics increases since the time of the energy exchange between the fuel and coolant increases with an increase in the system constraint without significant fuel quenching. With regard to the FCI expansion time increase, with more system constraint provided, the fuel quenching time plays a more dominant role in the FCI energetics. The effect of the fuel quenching time was demonstrated in the WFCI-B series of tests with a fixed degree of system constraint. Above that limit, however, the FCI energetics may be reduced since the fuel quenching effect is more significant.

Work is continuing to observe the effects of fuel and coolant masses as the key initial conditions which interact with the system constraint.

ACKNOWLEDGEMENT

This work was supported by the US Nuclear Regulatory Commission (NRC) and was performed at University of Wisconsin-Madison. The authors thank Dr. I. S. Kim from Korea Atomic Energy Institude in Korea for his help and valuable discussions.

References

[1] Reid, R. C., "Rapid Phase Transitions From Liquid to Vapor," *Adv. Chem. Eng.*, **12**, pp 105~208, (1983).

[2] Corradini, M. L., Kim, B. J., and Oh, M. D., "Vapor Explosions in Light Water Reactors; A Review of Theory and Modeling," *Progress in Nuclear Energy*, Vol. **22**, No. 1, pp 1~117, (1988).

[3] Board, S. J., and Hall, R. W., "Recent Advances in Understanding Large-Scale Vapor Explosion," *The 3rd Specialist Meeting on Sodium Fuel Interactions*, Tokyo, PNC N251, 76-12, pp 249~283, (1976).

[4] Long, G., "Explosion of Molten Aluminum in Water - Cause and Prevention," *Metals Progress*, **71**, pp 107~112, (1957).

[5] Nuclear Regulatory Commision, "Reactor Safety Study; An Assessment of Accident Risks in U.S. Commercial Nuclear Power Plants," *Report NUREG-75/0114 (WASH-1400)*, October (1975).

[6] Park, H. S., Yoon, C., Bang, K. H. and Corradini, M. L., "Vapor Explosion Escalation/Propagation Experiments and Possible Fragmentation Mechanisms," *International Seminar on Physics of Vapor Explosion; Oji Seminar*, Tomakomai, Hokkaido, Japan, Oct 25~29, (1993).

[7] Hall, R. W., Board, S. J., and Baines, M., "Observations of Tin/Water Thermal Explosions ina Long-tube Geometry; Their Interpretation and Concequences for the Detonation Model," *Proc. 4th CSNI Specialists Meeting on Fuel-Coolant Interactions in Nuclear Reactor Safety*, 2, 450~476, Bournemouth, England, 2~5 April, (1979).

[8] Baines, M., "Preliminary Measurements of Steam Explosion Work Yeilds in a Constraint System," *1st U.K National Heat Transfer Conference on Heat Transfer, Inst. Chem. Eng. Symp.*, No. 86, pp 97~108, Leeds (1984).

[9] Shins, H., Zeyen, R., Hohmann, H., Bürger, M., Müller, K., Buck, M., Cho, S. H., Schatz, A., "Analysis of Thermal Detonation Experiments by means of a Transient Multiphase Detonation Code," *Proc. 4th Int. Topical Meeting on Nuclear Reactor Thermal Hydraulics ; NURETH-4*, Karlsruhe, K. F. G., (1989).

[10] Frost, D. L., Bruckert, B., and Ciccarelli, G., "The Role of Confinement in the Propagation of Vapor explosions," *International Seminar on Physics of Vapor Explosion; Oji Seminar*, Tomakomai, Hokkaido, Japan, Oct 25~29, (1993).

[11] Park, H. S., Yoon, C., Bang, K. H., and Corradini, M. L., "Experiments on the Trigger Effect for 1-D Large Scale Vapor Explosion" *Proc. New Trends in Nuclear System Thermodynamics*, Pisa, Italy, May 30~June 2, 271~280, (1994).

[12] Shamoun, B. I., and Corradini, M. L., "Analysis of Supercritical Vapor Explosion Using Thermal Detonation Wave Theory," *7th International Meeting on Nuclear Reactor Thermal-Hydraulics*, Saratoga, Spring, NY, USA, September 10~15, (1995).

[13] Cho, D. H., Ivins, R. O., and Wright, R. W., "Pressure Generation by Molten Fuel-Coolant Interaction under LMFBR Accident Conditions," *Proc. of Conf. on New Develpments in Reactor Mathematics and Applications*, Idaho Falls, CONF-71032 (Vol.1), pp 25~49, March (1971).

[14] Tang, J., and Corradini, M. L., "Modeling of the complete Process of one-dimensional Vapor Explosions," *OECD-CSNI Specialist Meeting*, Santa Barbara, CA, January 5~8 (1993).

THE MIXING OF PARTICLE CLOUDS PLUNGING INTO WATER

S. Angelini, T.G. Theofanous and W.W. Yuen

Center for Risk Studies and Safety
Departments of Chemical & Nuclear and
Mechanical & Environmental Engineering
University of California, Santa Barbara, CA 93106

ABSTRACT

This work addresses certain fundamental aspects of the premixing phase of steam explosions. At issue are the multifield interaction aspects under highly transient, multidimensional conditions, and in presence of strong phase changes. They are addressed in an experiment (the MAGICO-2000) involving well-characterized particle clouds mixing with water, and detailed measurements on both external and internal characteristics of the mixing zone. Both cold and hot (up to 1500^oC) particle clouds are considered in conjunction with saturated and subcooled water pools. The PM-ALPHA code is used as an aid in interpreting the experimental results, and the exercise reveals good predictive capabilities for it.

1. INTRODUCTION

This paper describes certain fundamentally-oriented experiments with particle clouds plunging into water. Of special interest are the dynamics of the (transient) interaction, the multidimensional behavior, and, in the case of hot particles, phase-change phenomena and the resulting void fractions in the mixing region. While in a broad sense the subject could be classified under the well-established field of "fluidization," it is, for the most part, outside the main realms investigated previously. That this is so is not immediately obvious, but it will be demonstrated by the results of the present work.

Our present interest derives from the study of steam explosions. It is known that such explosions propagate through coarse-scale mixtures (the "premixtures") of a "hot" liquid (usually a melt) into a coolant (typically water). In the metastable state of a premixture the hot liquid is surrounded by vapor blankets (film boiling), and depending on the particulars of the interaction (size of mixing zone, temperature of melt, coolant subcooling, etc.) it may contain more or less voids (that is, vapor as the third component). It is now possible to compute this propagation, and the resulting shock pressures to the surrounding structures (Theofanous and Yuen, 1994) provided the spatial distributions of the premixture constitutents are known at the instant that an explosion is triggered. Thus, the study of "premixing" as a phenomenon provides the key link between the independent variables that characterize a melt-pour scenario (i.e., pour geometry, quantities, water pool geometry and subcooling), and the resulting explosion itself.

Clearly, the use of particle clouds limits the context, for even if a melt was to enter the water not as a coherent mass, but in a more-or-less broken-up state, under most conditions, additional break-up would be expected during premixing. Still, this limited context (one that may be called "idealized premixing") is extremely attractive. The reasoning can be summarized as follows:

(1) Absence of break-up allows complete characterization—a "must" for deep understanding of the phenomena, and unambiguous testing of analytical/predictive capabilities.

(2) Collective-particle (cloud) behavior is of central significance, even in the presence of break-up—deep understanding of such behavior is an essential prerequisite to understanding the whole process (including break-up).

(3) Deep understanding of idealized premixing can provide important insights, if not quantitative bounds (such as on the degree of voiding) on the behavior of real premixtures.

(4) Finally, the approach can lead to the creation and study of liquid-particle clouds, as a means of getting to the fundamentals of propagation—i.e., the study of propagation under well-defined premixture conditions and triggers.

This line of inquiry has begun already with the MAGICO experiments (Angelini et al., 1994a), involving mostly hot particle clouds, and the Berkeley Nuclear Laboratory (BNL) program (a portion actually carried out at Oxford University), involving mostly isothermal, two-dimensional clouds (a flow field as slice with thickness slightly larger than the particle diameter) (Hall and Fletcher, 1994), while related efforts have been announced (and are probably underway) also in France (Berthoud and Valette, 1994) and in Germany (Jacobs, 1994). In the same context, the MIXA experiments (Denham et al., 1992; Fletcher and Denham, 1994) in Winfrith, UK, and the ALPHA experiments (Yamano et al., 1994) in JAERI, Japan, should probably also be mentioned. They both involve melts broken up into particle clouds prior to entering the water, although complete characterization of the melt particle sizes has not been made available. At the other extreme we have the more "integral" type experiments, FARO (Magallon et al., 1994) and ALPHA being currently the more prominent, in which more-or-less coherent melt masses are let to fall into water. The present work is an outgrowth and continuation of the MAGICO experiment just mentioned. In a related effort, the PM-ALPHA code is being developed (Amarasooriya and Theofanous, 1991; Yuen and Theofanous, 1995), and we make use of it here to aid in the interpretations.

The MAGICO experiment involved liter quantities of steel particles at temperatures up to 900^oC, plunging with velocities of $\sim 2m/s$ into saturated water pools of 0.25 and $0.5m$ in depth. The major thrust in the new experiment is to achieve particle temperatures of up to 2000^oC, hence the name, MAGICO-2000. At this temperature level radiation heat transfer becomes rather significant and leads (according to the PM-ALPHA calculations carried out in the design phase) to extensive voiding of the premixture—well above the $\sim$60% value reached in the original MAGICO tests. Another key objective in the design was to increase the duration of the interaction (i.e., advance from small scale to intermediate scale behavior). This was achieved by increasing the total volume of the particulate and the pool depth, which also allows much higher inlet velocities. Finally, around these two main anchors, we built an experimental program covering wide ranges of particle density, particle sizes, and water subcooling. Experiments were carried out in both axisymmetric and Cartesian (2D) geometries.

Following the description of the experimental apparatus, procedures and measurement techniques (Section 2), the test program and results are given in two main parts, covering the isothermal and high temperature runs, in Sections 3 and 4 respectively. A summary of key findings is given under concluding remarks in the last section.

2. EXPERIMENTAL APPARATUS, PROCEDURES, AND MEASUREMENT TECHNIQUES

The principal experimental objective was to generate uniform particle clouds at temperatures approaching $2000^{o}C$, and it was met by a special purpose "furnace" designed and built in our laboratory. The central element of it is a graphite block, machined into a matrix of parallel holes and slots, as illustrated in Figure 1. The holes are to contain the particles during heating—an arrangement of miniature doors (a total of 5 doors, one door per row of particles) are used for this –and the particles are released on command by simultaneously opening all the doors. Heating is accomplished by passing a high electrical current through the graphite "resistor," formed by the combination of holes and slots, from one end of the block to the other. The total power available by the transformer is $12.5kW$, and it is sufficient to reach the 1500 to $2000^{o}C$ range in 7 to 10 hours. The heating is gradual, to minimize thermal gradients/stresses and allow time for thermal equilibration between the graphite and the particulate load.

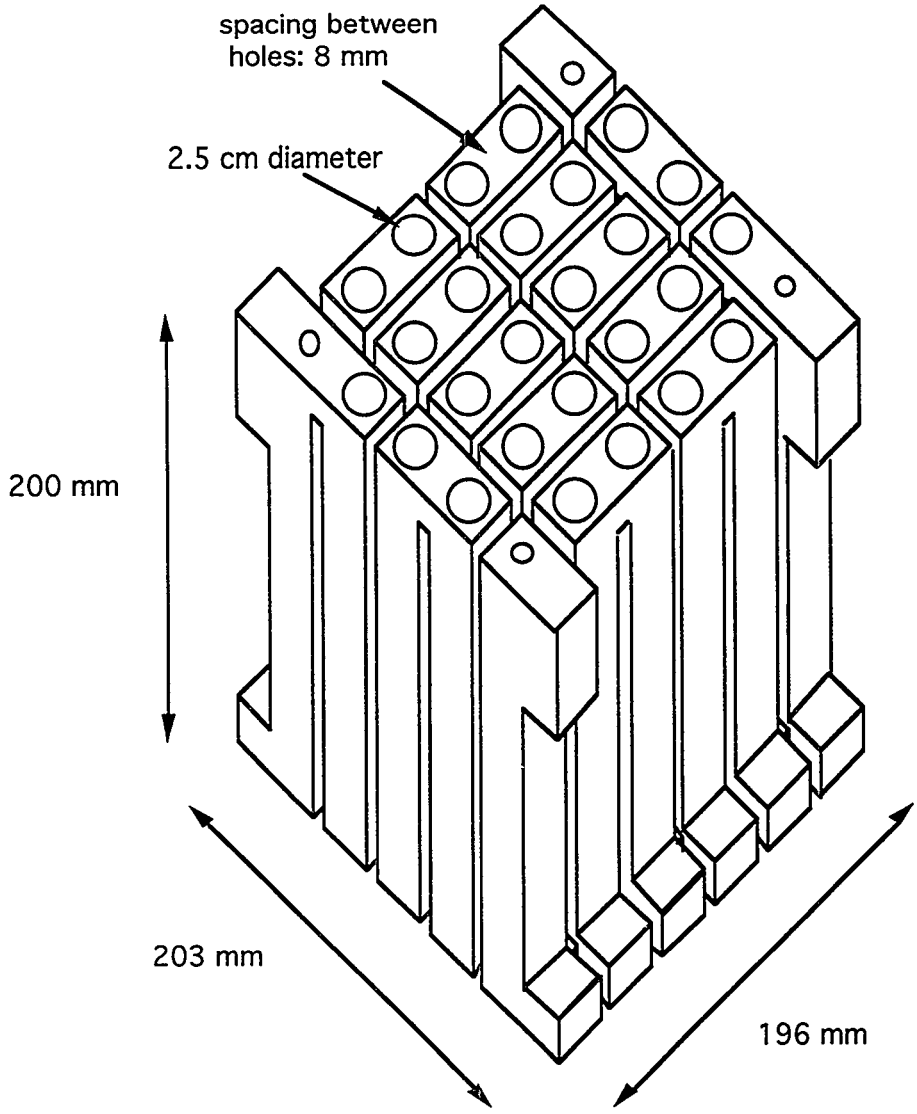


Fig. 1: Heating element in MAGICO-2000.

Major development work was required (for details see Angelini, 1995) to support such a "hot" block, to build and properly operate the miniature doors, to thermally insulate the whole structure, and to create the necessary inert containment for it. Both the thermal insulation barrier and the outer inert containment are provided with mechanisms to allow the particle cloud through, while still protecting the hot graphite block from atmospheric air, and from the steam generated when the particles plunge into the water pool beneath. The overall arrangement is illustrated schematically in Figure 2.

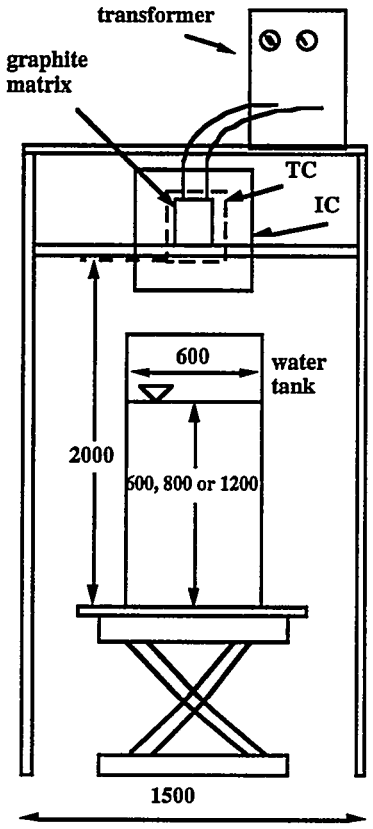


Fig. 2: Schematic of MAGICO-2000. All dimensions are in mm.
TC indicates the thermal containment, IC indicates the inert containment.

The various particulate materials utilized in the experiments, and respective densities, sizes, and shapes are listed in Table 1. This table also shows the melting points and maximum temperatures attained so far with each one of them. At still higher temperatures the particles tend to "stick" to each other in such a manner as to prevent the full and reproducible release needed to form a uniform cloud. Recently, we have developped techniques that inhibit these surface interactions and thus allow us to achieve temperatures of $\sim 2000^{o}C$.

Experiments were conducted in two series. One, addressing momentum interactions, involved isothermal (room temperature) pours—the "cold" runs. The other included phase change effects and was carried out with high temperature pours—the "hot" runs. Experimental conditions are summarized in Tables 2 and 3 for the "cold" and "hot" runs respectively. In addition, we have carried out cold single-particle runs (they are not included in this table) for the purpose of testing experimental techniques and PM-ALPHA in the "dilute" particle limit, under conditions for which an analytical comparison is possible. These runs will be referred to by the particle size and the material used.

Table 1. Materials Utilized in this Study and Their Key Characteristics

Material	Shape	Dimensions (mm)	Density (g/cm^3)	Melting Point (°C)	Max. Temp. (°C)
ZrO_2	Spherical*	2.4–3.4	5.5	2600	1500
ZrO_2	Spherical	6.3	5.5	2600	1500
Al_2O_3	Spherical	1.5–2.5	3.5	1950	900
SiC	Rough Chips**	1.0–4.0	3.1	2200***	1200
Steel	Spherical	2.4	7.9	1400	1000

*Slightly off-spherical
**Typical chip has dimensions 1.5×2×3 mm
***Dissociation point for SiC

Table 2. Specification of the Cold Runs

Run	Particulate	Size Range [mm]	Total Mass [kg]	Plunging Velocity [m/s]	Inlet Volume Fraction [%]	Cloud Length/ Diameter* [cm]	Pool Geometry/ Depth [cm]
MA.AX	Al_2O_3	1.5-2.5	5.4	5.0	9.4	43/22.0	60×60/60
MA.CR	Al_2O_3	1.5-2.5	5.4	5.0	9.4	43/22.0	60×30/60
MZ.AX	ZrO_2	2.4-3.4	8.6	5.0	10.9	37/22.0	60×60/60
MZ.CR	ZrO_2	2.4-3.4	8.6	5.0	10.9	37/22.0	60×30/60
MZD.AX	ZrO_2	2.4-3.4	8.6	4.0	10.9	37/22.0	60×60/120
MF.AX	Steel	2.4	12.2	5.0	13.3	37/20.0	60×60/60
MF.CR	Steel	2.4	12.2	5.0	13.3	37/20.0	60×30/60

*Equivalent diameter

Table 3. Specification of the Hot Runs

Run	Particulate/ Size Range [mm]	Total Mass [kg]	Pour Equivalent Diameter [cm]	Pour Duration [s]	Plunging Velocity [m/s]	Inlet Volume Fraction [%]	Particle Temp. Range [°C]	Water Subcooling/ Depth [°C/cm]
Z1500/0-1	ZrO_2/2.4-3.4	6.2	22.5	0.33	5.0	1.71	1300-1450	0/60
Z1500/0-2	ZrO_2/2.4-3.4	6.2	22.5	0.33	4.8	1.71	1300-1450	0/80
Z1500/3-4	ZrO_2/2.4-3.4	8.0	22.5	0.33	4.8	2.21	1300-1450	3/80
Z1500/18-5	ZrO_2/2.4-3.4	8.6	22.5	0.33	4.8	2.38	1300-1450	18/80
S1200/0-6	SiC/1.0-4.0	2.85	22.0	0.33	4.8	1.46	1150-1200	0/80

In loading the particles into the graphite block we found a packing fraction of $\sim 60\%$. From the overall geometry (fraction of hole area to the total), we can compute that an ideal, frictionless, pour should produce a cloud of dimension similar to the graphite block with a particle volume fraction of $\sim 26\%$. Accelerating under freefall this cloud would arrive at the pool surface (normally $\sim 1.4m$ below) with a velocity of $5m/s$. The freefall was confirmed from the experiments; the cloud, however, was found to be considerably elongated (see Tables 2 and 3) as compared to the ideal height of $20cm$ (the height of the holes). Moreover, the elongation was significantly greater in the hot runs as compared to that in the cold runs. Since frictional resistances, between the particles and graphite wall, are responsible for this elongation, the above trends indicate that the high temperatures aggravate this friction. Alternatively, it may be that this frictional limitation is aggravated by the same surface interactions that yield at higher temperatures the particle "sticking" mentioned above and is responsible for introducing a "delay" in the flow of each particle once the support has been removed. More work is being done to better map the particle volume fraction within the cloud, but for the time being from the dimensions of the cloud prior to impact we can find a value of average particle volume fraction, and this is given for each run in Tables 2 and 3. A ZrO_2 particle cloud pouring at $1500°C$ is shown in Figure 3.

Even though both the graphite matrix and the water tank have a square cross-section this geometry is referred to as "axisymmetric." This is to indicate our view of it as approximately axisymmetric, since via slight redistribution during the freefall the cloud cannot really be distinguished from a cylindrically shaped one (also note in Figure 1 that with the 4 corner holes missing, the equivalent cross section is already quite round), and more importantly, its interaction with the water is "all around" (largely axisymmetric). This is to be distinguished from the "Cartesian" geometry tank in which the width in one direction is reduced to be approximately equal to that of the pour, forcing the interaction with water to be two-dimensional on a "plane." The main reason for this second geometry, which was employed only for some of the cold runs, was to be able to see clearly "behind" the mixing region—after the tail end of the cloud had entered the water. In addition, it was interesting to distinguish experimentally this effect of geometry—we would expect the 2D cloud to penetrate more slowly than the axisymmetric one—and provide another test point for computer codes. The designations "AX" and "CR" are used in the name of the cold runs for the axisymmetric and Cartesian geometries respectively.

The interactions were recorded on video at the rate of 30 frames per second, and at selected instances by X-ray radiographs. The video records were scanned and made available as electronic files into the computer for further processing. From these we could easily extract histories of the interaction penetration front, evolution of the interaction zone shape, rise of water (surrounding the interaction zone) level, and heights of the two-phase spray ("dome") forming above the interaction in the hot runs. Both local (covering the water tank) and global (including the elevation of cloud formation immediately below the furnace) videos using Sony Hi8 camcorders were obtained. The flash X-rays were generated by a Hewlett Packard model 43734 generator equipped with a soft X-ray tube with variable energy capability of up to $360kV$. We optimized the energy level and position of the tube relative to the film (see Figure 4) for the purposes of each type of run. For the cold runs our interest was to be able to delineate any regions of high particle concentration, created through the interaction of the high-velocity cloud with the water. Such regions were predicted by the numerical simulations (PM-ALPHA), but certainly they could not be detected in the video records. The other interest in this part of the investigation was in exploring the possible existence of a "hole" predicted to form immediately behind the submerged particle cloud, and an interesting dynamic of "closing in" a short time later. To maximize clarity, these runs were conducted in what we referred to as the Cartesian geometry.

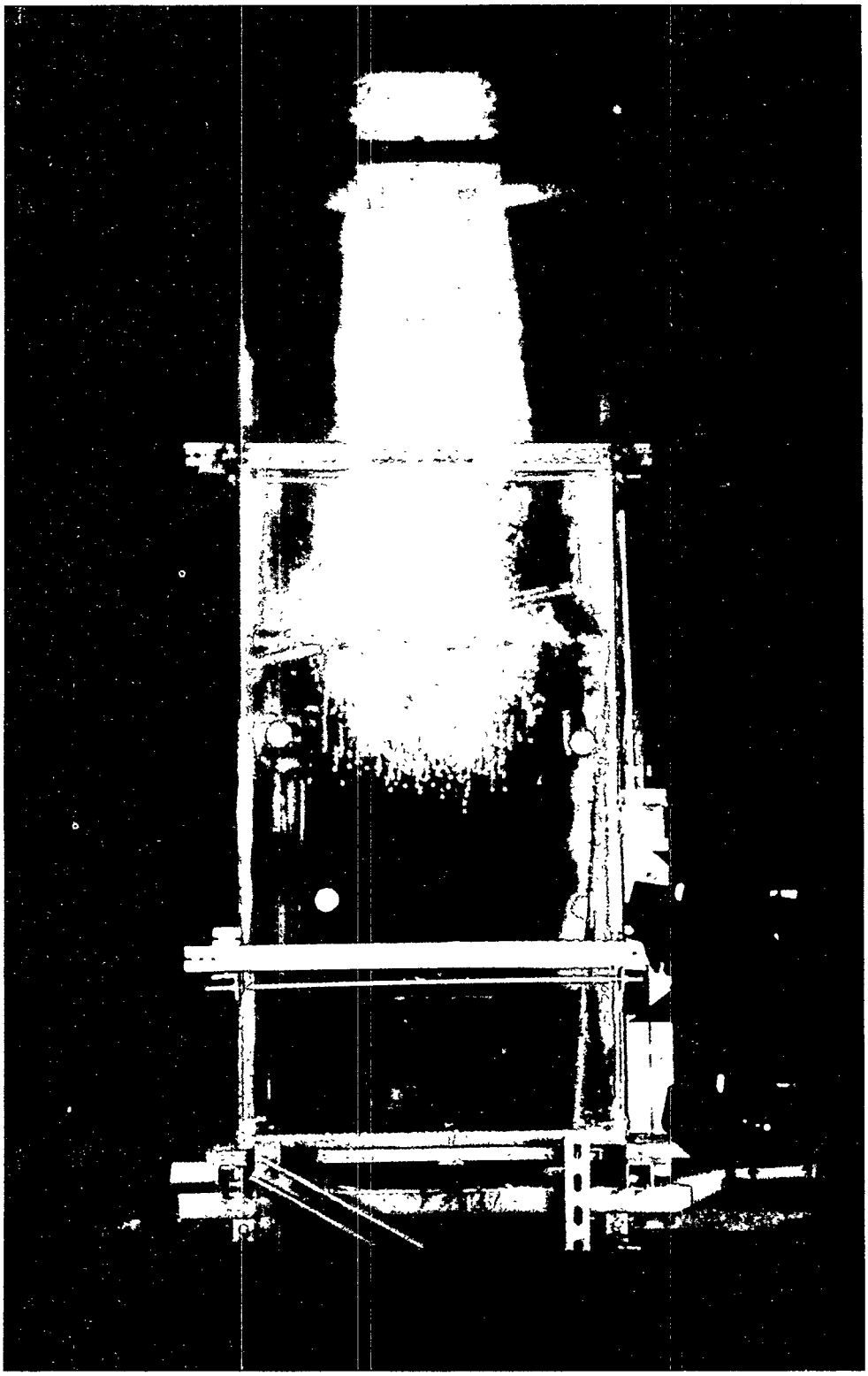


Fig. 3: Zirconium Oxide pour at $1500°C$.

For the hot runs, our major interest was to measure the void fractions within the interaction zone. Fortunately this became possible because, as discussed above, the particle volume fractions obtained in the hot runs were sufficiently low to allow, in between the particles, regions providing sight lines from the X-ray source to the film, involving only steam or water. The average void fraction along such lines (regions) could be measured using calibrations, obtained *in situ*, with known quantities of void. The approach is similar to that developed in the original MAGICO experiment (Theofanous, 1993). To further optimize discrimination here, without significantly affecting the geometry, we make use of the two "windows" shown in Figure 4. They are simply empty beakers, $7.5cm$ in diameter and $7.5cm$ long, used to remove a total of $15cm$ of water from the X-ray path, thus enhancing the sensitivity of the measurement. The uncertainties in this measurement will be discussed together with the presentation of results. The same applies for the uncertainties in the measurement of the rise of the water level and of the heights of the two-phase spray. The advancements of the fronts in the pool involve determination of position and time, and they are made with an accuracy of $\pm 3cm$ and $\pm 0.015s$ respectively. These are small, for our purposes, and they are reflected in the size of the symbols used in the figures.

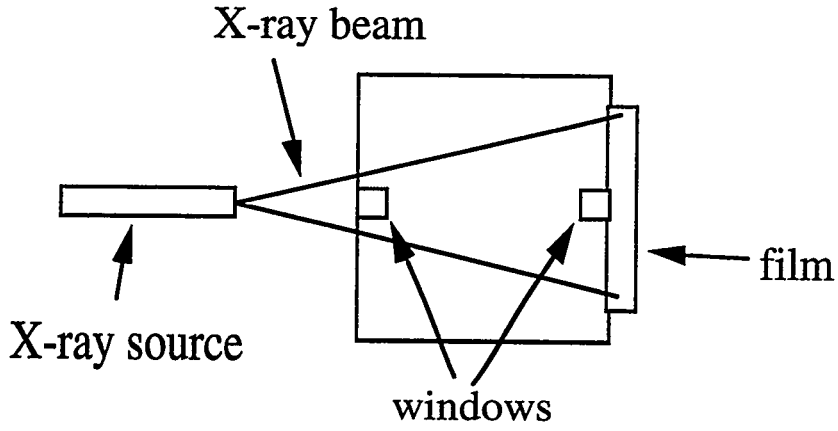


Fig. 4: Top view of X-ray arrangement in hot runs.

Temperatures were measured continuously during heatup, using both K- and C-type thermocouples, positioned at various locations within the particulate and the graphite matrix. The maximum temperature difference is shown in Table 3, and it is indicative of the uncertainty in initial cloud temperature.

Code predictions will be shown alongside the presentation of the experimental results. The code is the version documented by Angelini et al., 1994b, and the inputs for each run are according to the specifications given in Tables 1 through 3. Only the following additional clarifications are necessary:

1. The axisymmetric geometry was modeled by matching the cross-sectional area of the tank. The pour area was modeled by matching, to the closest integer number of computational cells (of size $3 \times 3cm$), the cross-sectional area of the experimental pour as obtained from the videos prior to impact on the water (the cloud appeared to expand slightly during the freefall); this involved a difference between actual pour and simulated pour of about 16% for the cold runs and 12% for the hot runs. Accordingly, the particle volume fraction has been adjusted from the average value listed in Tables 2 and 3 in order to conserve the

total particle mass; sensitivity studies showed little or no effect due to this small change in particle volume fraction.

2. Calculations in the dilute limit, for comparison with the single-particle runs, were carried out by releasing a "mini-cloud" (a packet of particles covering just one computational cell) with a particle volume fraction of 1%. That the single-particle behavior was approached was confirmed with calculations using 0.5 and 0.1% particle volume fractions that yielded the same results.
3. To determine more precisely the position of the fronts in the Eulerian calculation, we superposed Lagrangian tracer particles, made to move with the local (cell) velocity of the particulate field.
4. For the hot runs, the code calculations were carried out with a particle temperature at the middle of the range shown in Table 3. The results were not sensitive to any specification within the respective ranges.

3. RESULTS FROM THE COLD RUNS

All the front-propagation results from the axisymmetric cold runs are summarized in Figures 5 through 10. Figures 5 and 6 refer to single-particle runs and calculations, and they include the analytically determined terminal velocities (sphere in Newton regime, constant drag coefficient $C_D = 0.44$). These comparisons are indicative of the accuracy of the experimental and data reduction procedures and the appropriateness of the analytical approach. The small deviation in terminal velocities seen for Al_2O_3 may be due to micro-bubbles trapped on the surface of the highly porous particle—such an effect appearing more pronounced given the low density of Al_2O_3. The next three figures (7 through 9) show the collective particle effect in producing a faster-penetrating front and the influence of the particle density on this phenomenon. The faster-penetrating front is the result of the prolonged inflow of particles into the mixing region which causes an overall alteration of the velocity fields. This will be discussed more in detail later. There is some discrepancy between experiment and calculation, and this appears to increase as the particulate density decreases, and from the visual records it also appears to be associated with instabilities on the cloud front. These results are highly reproducible. Remarkably, a relatively small reduction in inlet velocity (from 5 to $4m/s$) is sufficient to suppress these instabilities, as shown in Figure 10.

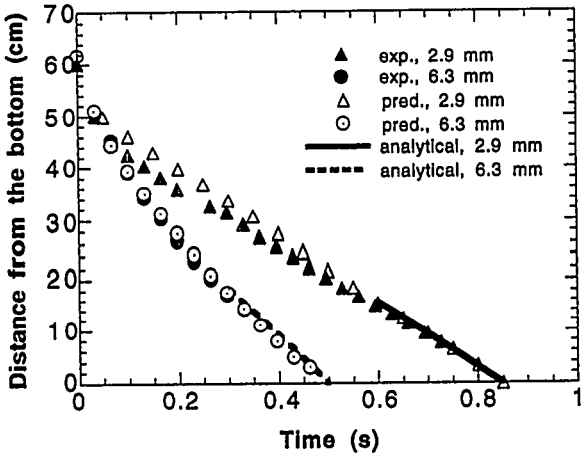


Fig. 5: Advancement of single particles, ZrO_2.

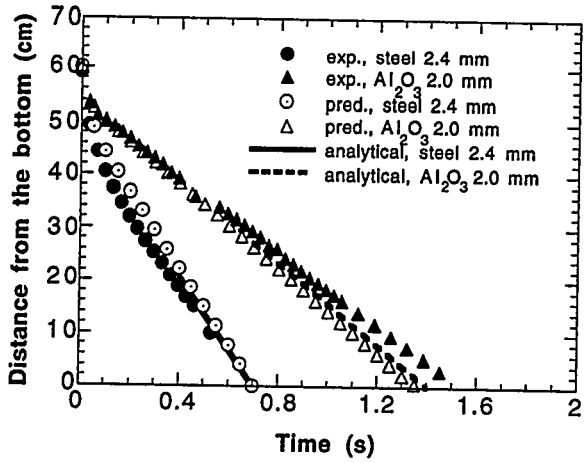


Fig. 6: Advancement of single particles, steel and Al_2O_3.

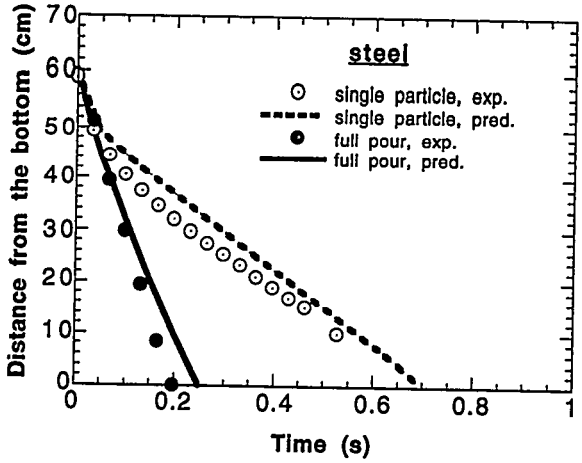


Fig. 7: Comparison between full pour (MF.AX) and single particle, steel.

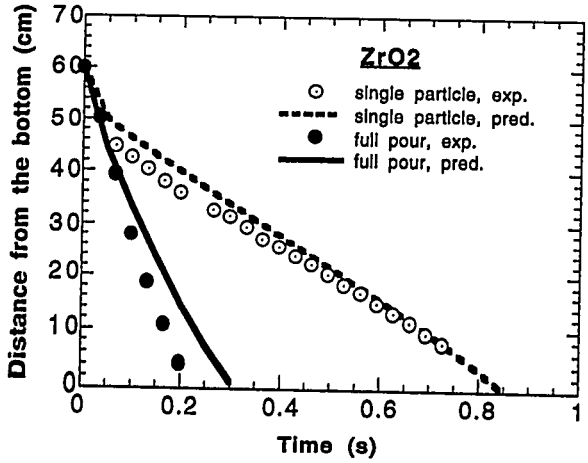


Fig. 8: Comparison between full pour (MZ.AX) and single particle, ZrO_2.

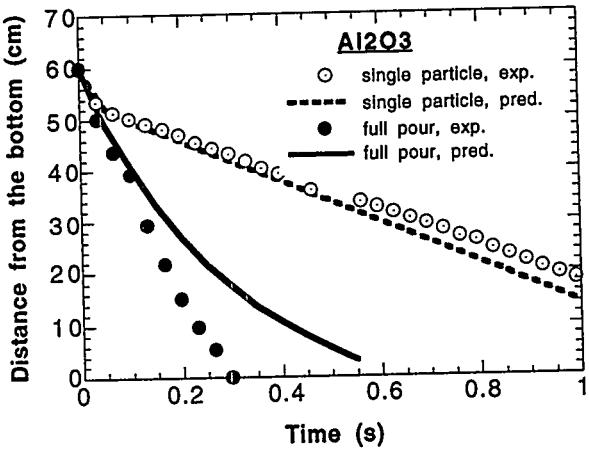


Fig. 9: Comparison between full pour (MA.AX) and single particle, Al_2O_3.

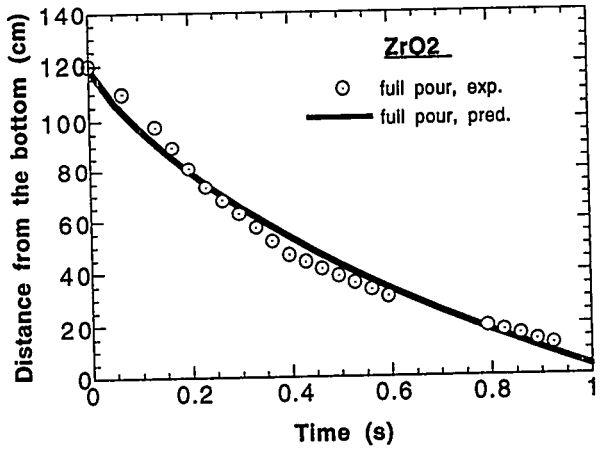


Fig. 10: Advancement of full pour of ZrO_2 particles in $1.2m$ pool (MZD.AX).

The morphology of the front in all four cases discussed here is shown in Figure 11. This figure, representing a two-dimensional projection of the three-dimensional fronts, is not very powerful in depicting the extent of the instabilities, although it allows to discern the difference in behavior between the "stable" steel and the "unstable" lighter materials.

The radiographs from two Cartesian geometry runs employing a full pour of ZrO_2 particles (MZ.CR), taken at 0.15 and 0.25 seconds after the first contact with water, are shown in Figures 12 and 13 respectively. These figures show the formation of a "hole-in-the-water" behind the cloud and the dense packing produced at the front. Both of these phenomena were predicted by PM-ALPHA during our work with the axisymmetric runs and motivated our investigations in the Cartesian geometry. According to our calibration, the quantity of water present in the hole region is negligible, but a few particles can be identified in it. The various regions are much more clearly identifiable in the original X-ray (than in the reproduction given here), and outlines of them are shown superposed with the PM-ALPHA results in Figures 14 and 15. Note that the essential features, such as hole shape, including the necking-in phenomenon shown in Figure 15,

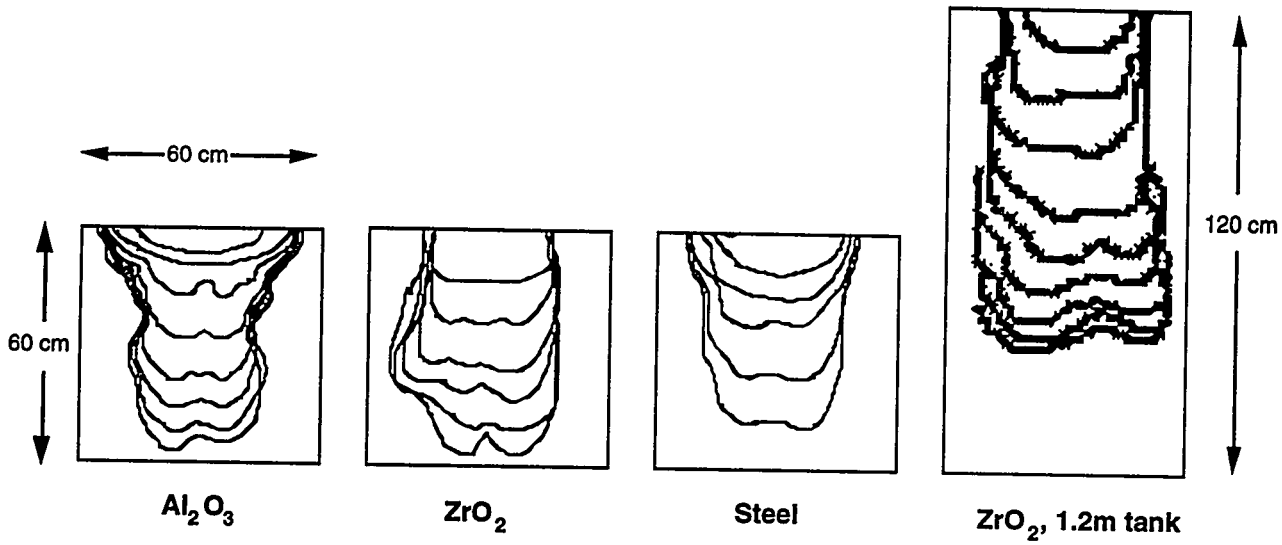


Fig. 11: Front morphologies in the cold runs in axisymmetric geometry. Contour lines are $0.033s$ apart in the $60cm$ runs and $0.066s$ apart in the $1.2m$ run.

and the position of the densely-packed region of particles are well-captured in the computation. Also in Figure 15, we can see the presence of the instability that is responsible for the experimental front overtaking the calculation, as discussed already for the axisymmetric runs.

These instabilities are indeed present also in the Cartesian geometry. That the behavior in this geometry is closely related to that in the axisymmetric one is demonstrated in Figures 16 through 18, which compare directly the two behaviors. In Figures 16 and 17 (steel and ZrO_2, respectively) the basic behavior that the planar geometry slows down the penetration is quite evident in both experiments and the computations—indeed, the agreement with the degree of reduction is quantitative. These figures also show that the degree of discrepancy between experiments and computations due to the instabilities is quantitatively similar in the two geometries. However, in the Al_2O_3 case, Figure 18, the instabilities overwhelm the whole behavior to such an extent that the "constraint" of the planar two-dimensionality cannot be felt. This relates to the smaller wave length (found in this case) as compared to the depth of the flow field. The front morphologies (again projections) in the Cartesian runs are reproduced in Figure 19.

The X-ray images are useful in explaining the above-mentioned alteration of velocity fields. The continuous transfer of momentum from the particle cloud to the water results in large displacements of the water itself and the generation of a hole in the region behind the front. The presence of this hole implies that, aside from the first ones, the particles are falling through a gap, therefore not decelerating until they reach the front. Here their momentum is dissipated in further displacing the water ("pushing" it away) and aiding the front in its advancement, which thus results to be faster than that of a single particle. This behavior is quite different from that observable in a sedimenting bed: in this case, from an initial uniform suspension of particles in a liquid, gravity starts a downward motion of the particles, but the achieved terminal velocity is

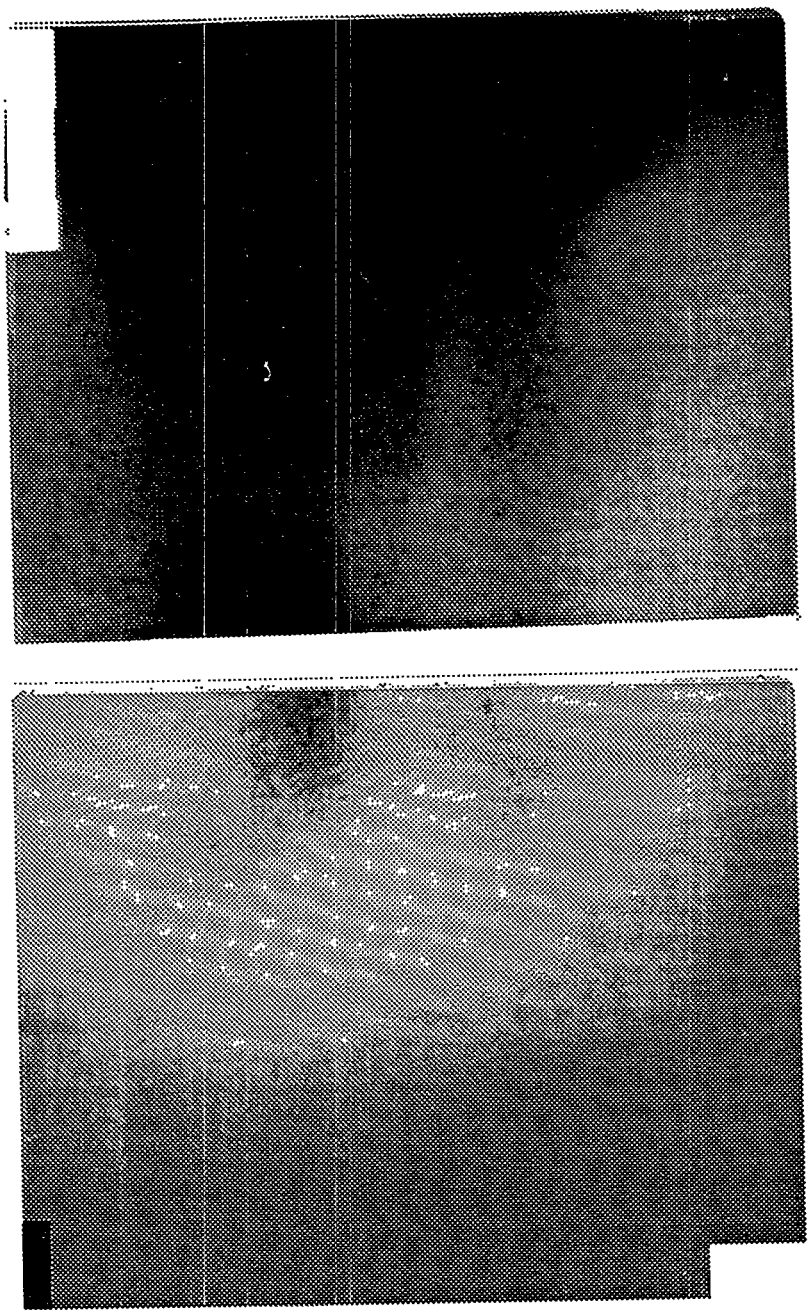


Fig. 12: Reproduction of X-ray images taken $0.15s$ after impact of a pour of ZrO_2 particles on water (MZ.CR). The white area is given by the boundaries of the cassettes containing the X-ray films.

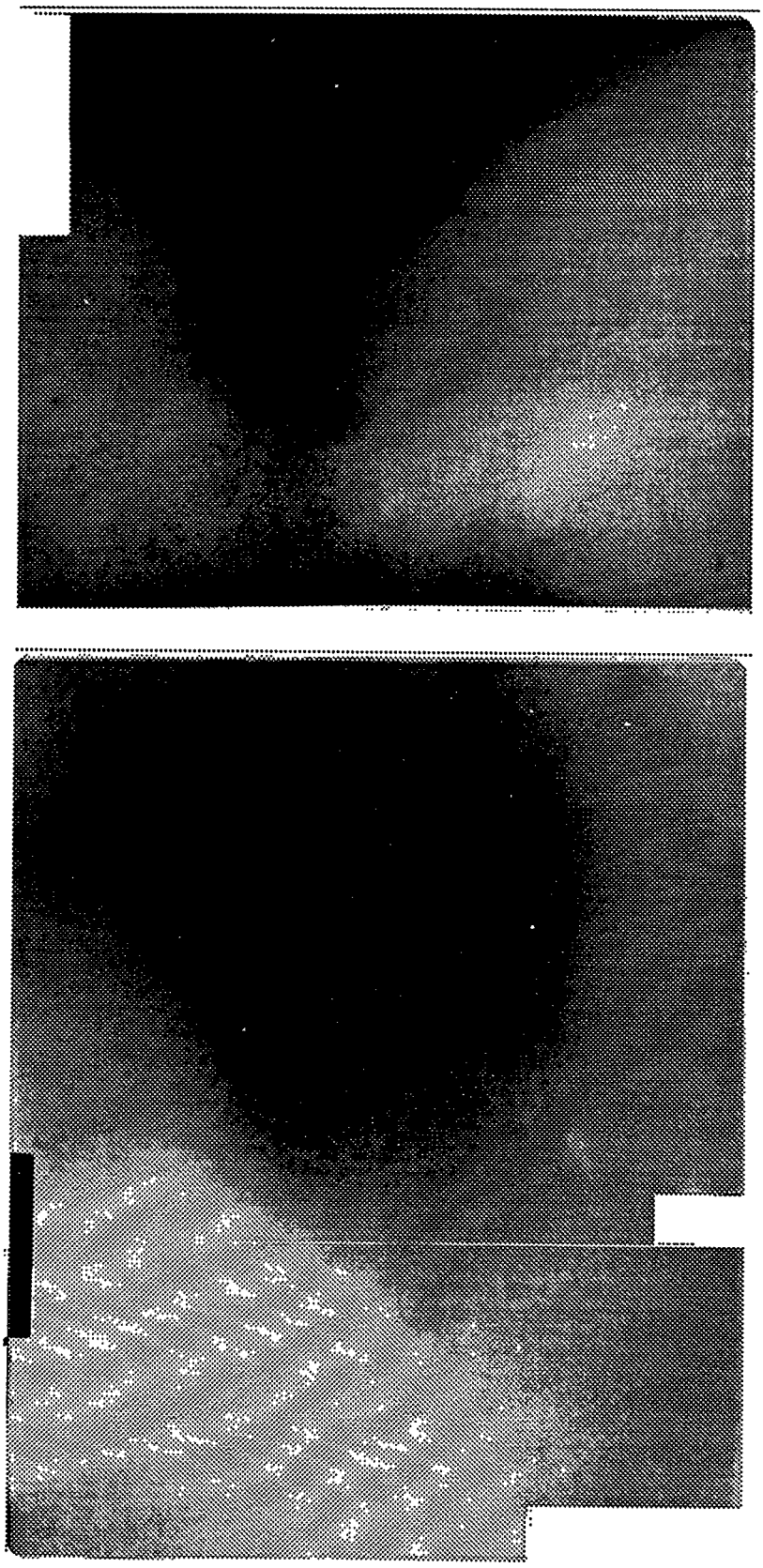


Fig. 13: Reproduction of X-ray images taken $0.25s$ after impact of a pour of ZrO_2 particles on water (MZ.CR). The white area is given by the boundaries of the cassettes containing the X-ray films.

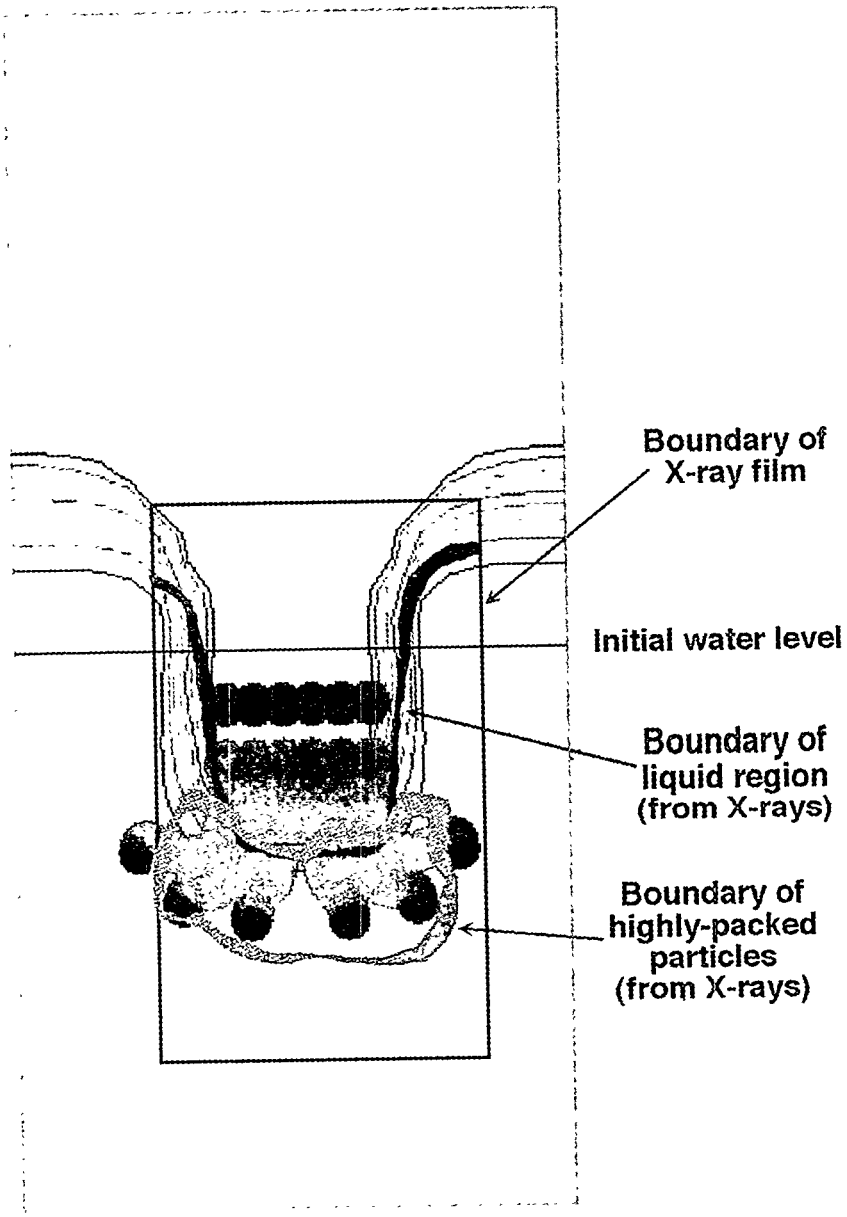


Fig. 14: Superposition of contour lines from X-ray films onto predictions from PM-ALPHA. ZrO_2 cold run (MZ.CR), $0.15s$ after impact of particles on water. The prediction shows the void fraction contour lines at intervals of 10%, starting at 10%. The dots are representative of particle location (Lagrangian tracer particles). Particle volume fraction is about 18% in the zone of the red dots and about 2% in the zone of the dark blue dots.

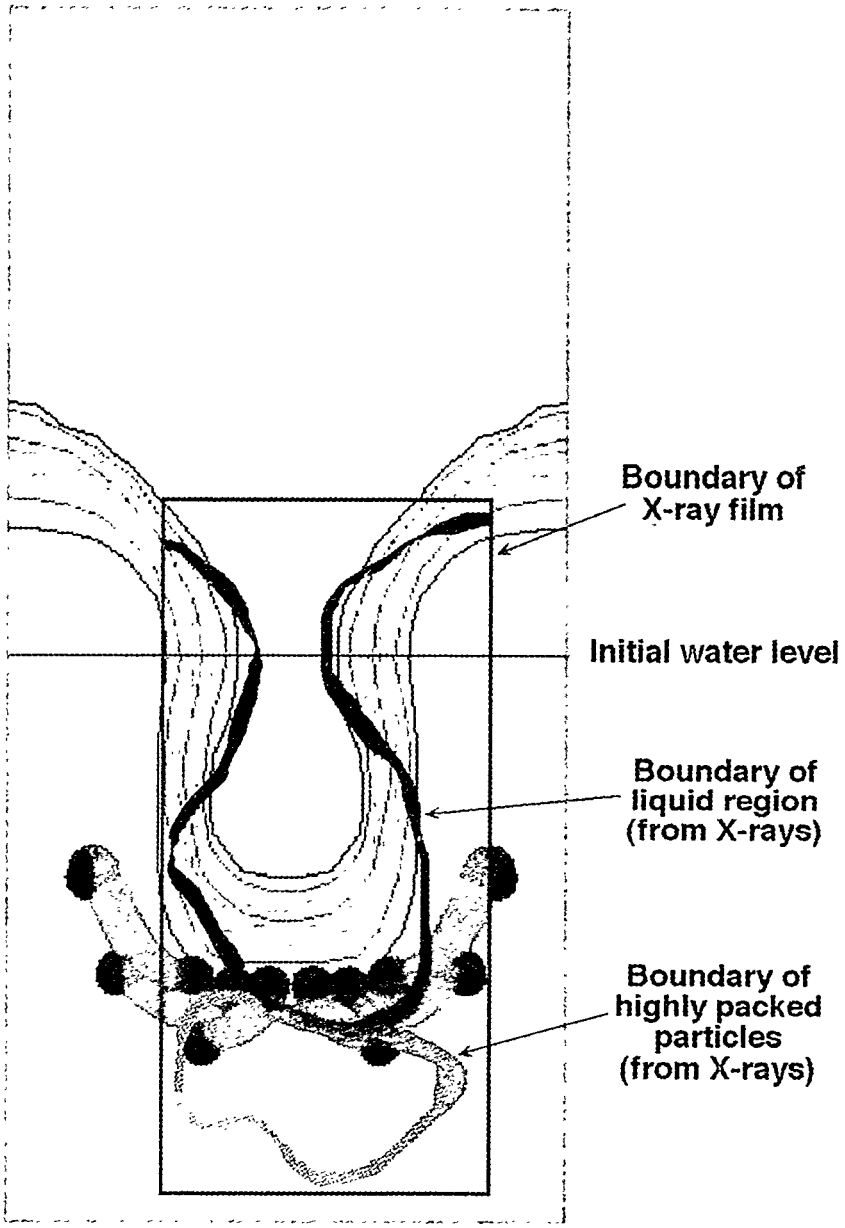


Fig. 15: Superposition of contour lines from X-ray films onto predictions from PM-ALPHA. ZrO_2 cold run (MZ.CR), $0.25s$ after impact of particles on water. The prediction shows the void fraction contour lines at intervals of 10%, starting at 10%. The dots are representative of particle location (Lagrangian tracer particles).

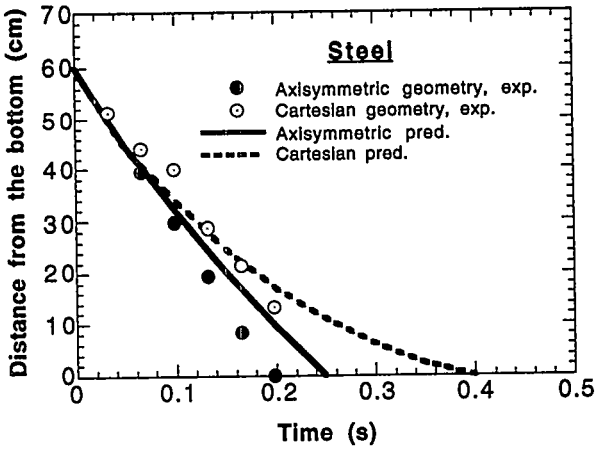


Fig. 16: Comparison between front advancements in MF.AX and MF.CR.

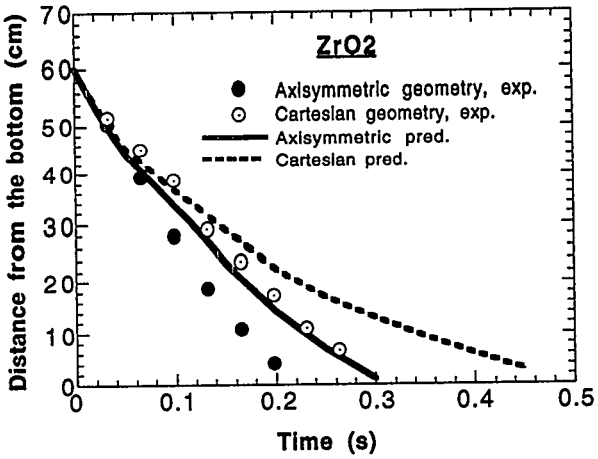


Fig. 17: Comparison between front advancements in MZ.AX and MZ.CR.

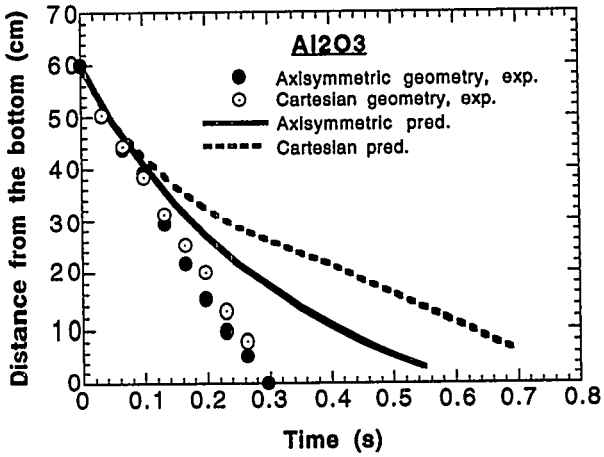


Fig. 18: Comparison between front advancements in MA.AX and MA.CR.

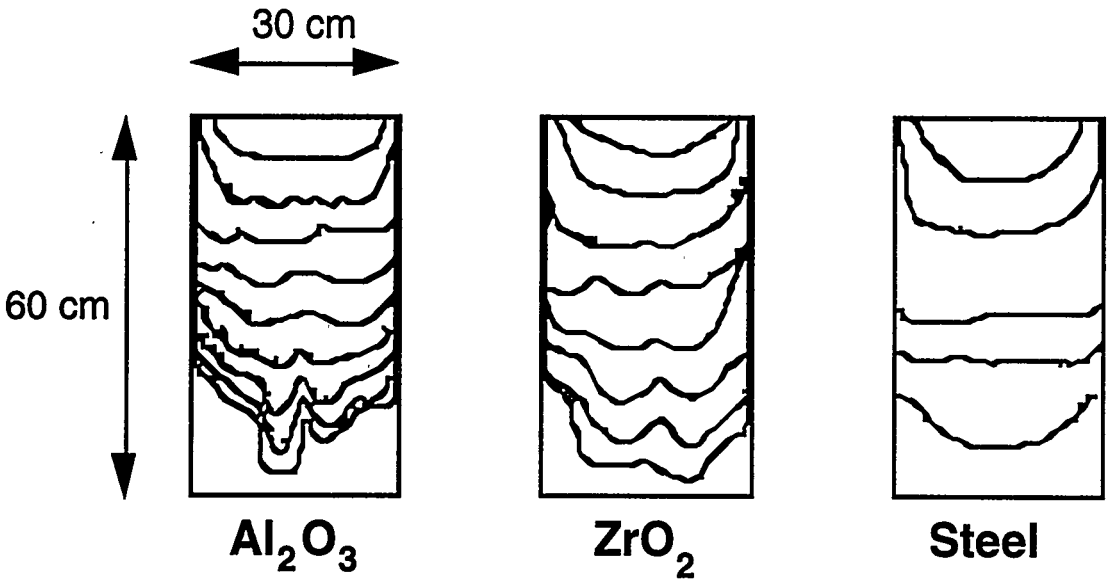


Fig. 19: Front morphologies in the cold runs in Cartesian geometry. Contour lines are $0.033s$ apart.

always *lower* than that for a corresponding single particle (Mirza and Richardson, 1979). This is due to the increased resistance that the liquid finds in moving upwards through the sedimenting particles in the one-dimensional geometry. It is interesting to note, however, that even in our experiments, once the inflow of particles ends, such a sedimenting behavior is asymptotically reached, as Figure 20 clearly shows: here we compare the advancement of the particle front for runs MZ.AX (already in Figure 8) and MZD.AX (already in Figure 10). Initially the two cases behave very similarly, the difference in slope being due to the lower impact velocity in the $1.2m$ run; however, shortly after the inflow of particle ends, the front in run MZD.AX undergoes a deceleration, with a velocity quickly approaching the terminal velocity of a corresponding single particle, represented by the continuous line (the front in run MZ.AX reaches the bottom before any deceleration can be detected). PM-ALPHA very effectively captures this aspect of the flow.

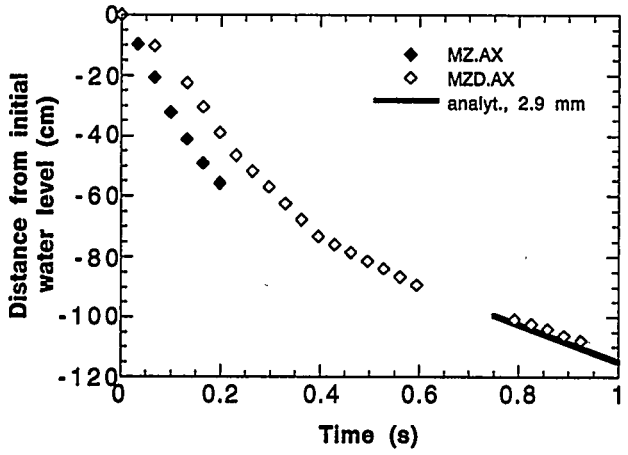


Fig. 20: Sedimenting behavior in deep pools.

4. RESULTS FROM THE HOT RUNS

The penetration behavior and instabilities in these runs were found to be quite similar to those observed in the cold runs. The results are summarized in Figure 21. The behavior for run Z1500/0-2 is very similar to Z1500/0-1, which is not included in Figure 21. We note that subcooling appears to aggravate, somewhat, the instabilities. These are responsible for the apparent disagreement in the figure: "waves" of particles stretching past the bulk of the cloud, the latter being closer to the prediction. We also note an indication of reversal in trend, compared to the cold runs: here the light cloud (SiC) is not nearly as unstable! Under strong vapor flux due to intensive boiling the light cloud decelerates rather quickly and comes almost to a halt (both in the experiment and in the calculation). The front morphologies for runs Z1500/0-2, Z1500/3-4 and Z1500/18-5 are illustrated in Figure 22, from which one can see the different behavior of the instabilities due to subcooling.

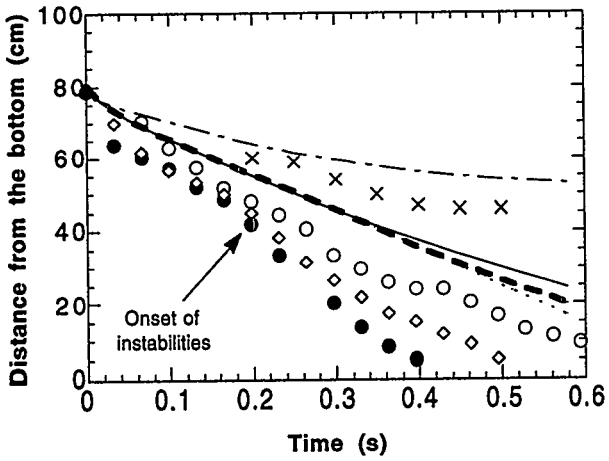


Fig. 21: Advancement of the front in hot runs. Experimental data (predictions): o (continuous line) is Z1500/0-2, • (dashed line) is Z1500/3-4, ◇ (dotted line) is Z1500/18-5, × (dash-dot line) is S1200/0-6.

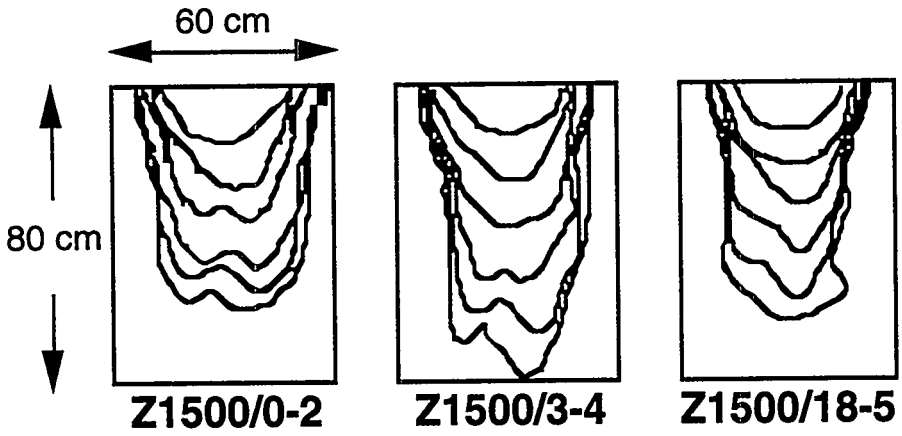


Fig. 22: Front morphologies in the hot runs. Contour lines are 0.066s apart.

While the instabilities express a local behavior, albeit an interesting one, of much greater significance for our purposes are the overall mixing zone development, the void fraction in it, and the related flow behavior around it. In particular, the water level around it provides a measure of the overall void history as a result of phase change phenomena, while the spray dome above it provides an indication of the steaming rate resulting from the interaction. These key behaviors are presented below. Only a small sample of the results is possible within the space available; complete details have been documented and discussed by Angelini (1995).

Void fraction measurements

The measurement of void fraction is limited to the chordal average through a small region $15cm$ below the initial water level. It is the only "local" measurement among those presented here and thus strongly depends on the characteristics of the evolution of the interaction in its detail, rather than on a global behavior. As such, the measurement not only provides insight into premixing, but represents probably the most important test for computer codes.

The local void fractions found experimentally in runs Z1500/0-2 and Z1500/3-4 are compared to the predictions in Figure 23; the experimental value has been taken $0.35s$ ($+0.05s$ uncertainty) after first impact of particles on the water. The analysis of the X-ray film is based on 8 calibration films in which steps of void of known length were placed in the tank. Comparison between these films and those taken during the hot runs is facilitated by the presence of witness marks and allows us to place the uncertainty within the range shown.

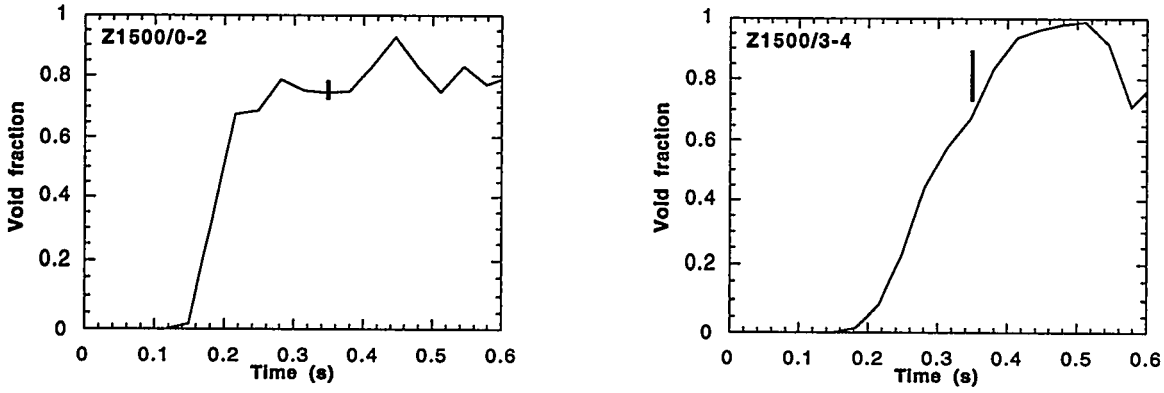


Fig. 23: Comparison between void fraction measured in runs Z1500/0-2 and Z1500/3-4 and corresponding PM-ALPHA predictions.

As expected, the prediction suggests that the effect of $3°C$ subcooling is to introduce a delay time in the onset of voiding. After this delay extensive voiding of the mixing region is reached, somewhat more gradually, but at even higher levels (up to 100%) than the saturated case, temporarily. This is confirmed by the experimental measurements. The highly subcooled run, Z1500/18-5, produced, in agreement with the calculation, an insignificant void (as judged by the level swell to be discussed shortly below). It was below the detection limit of the X-rays ($\sim$ 25%). In run Z1500/0-1 void fractions by X-rays were not measured.

In run S1200/0-6 the combination of low particle density and intensive vapor generation causes the particles to undergo a strong deceleration, as already seen in Figure 21. The ensuing particle accumulation, below and around the detection region, is responsible for essentially complete voiding of that region, and a measurement of 100% void fraction is obtained. The low

particle density in this case, synergistically with the vapor production and associated momentum interaction produces quite different axial particle distributions than in the ZrO_2 runs. This is illustrated in Figure 24. Note in particular that in the ZrO_2 runs the X-ray is taken well behind the front, and in the trailing side of the descending particle cloud (behind the concentration peak) while in the SiC run the front has just passed through this location, the particle concentration is low, and on the rise as the main portion of the descending cloud is approaching. The peak in this cloud is narrower and quite high. Due to this singular behavior the comparison with the prediction is rendered in the form of Figure 25. Note that within a few centimeters away the prediction gives a rather broad voided zone with a void fraction of $\sim 90\%$ as compared to the measured $\sim 100\%$.

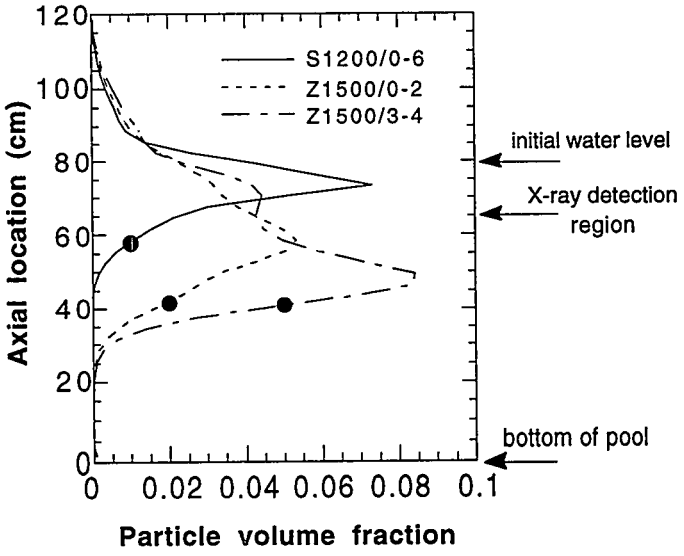


Fig 24: Predicted particle volume fractions in hot runs at time of X-ray trigger. The black dot identifies the location of the front according to the prediction.

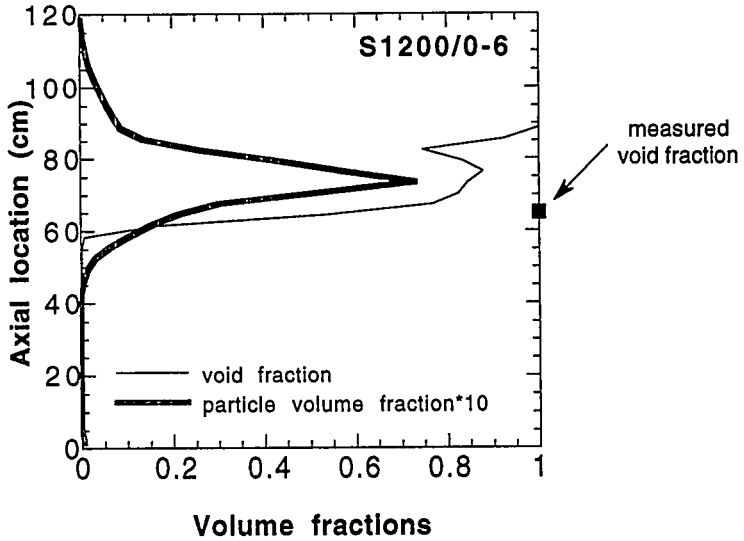


Fig 25: Volume fraction distributions in run S1200/0-6.

By contrast, as can be seen in Figure 26, the X-ray in run Z1500/0-2 was obtained away from the front and the associated (singular) high-sensitivity region. In run Z1500/3-4 the presence of subcooling is responsible for three distinct singular regions: the void distribution presents a maximum which is lagging the peak in the particle cloud because of the time required for the water to reach saturation first. At an even higher location, the void fraction collapses temporarily because of recirculation of subcooled water that is being displaced by the front. Incidentally, the X-ray happens to have caught the region of high void fraction.

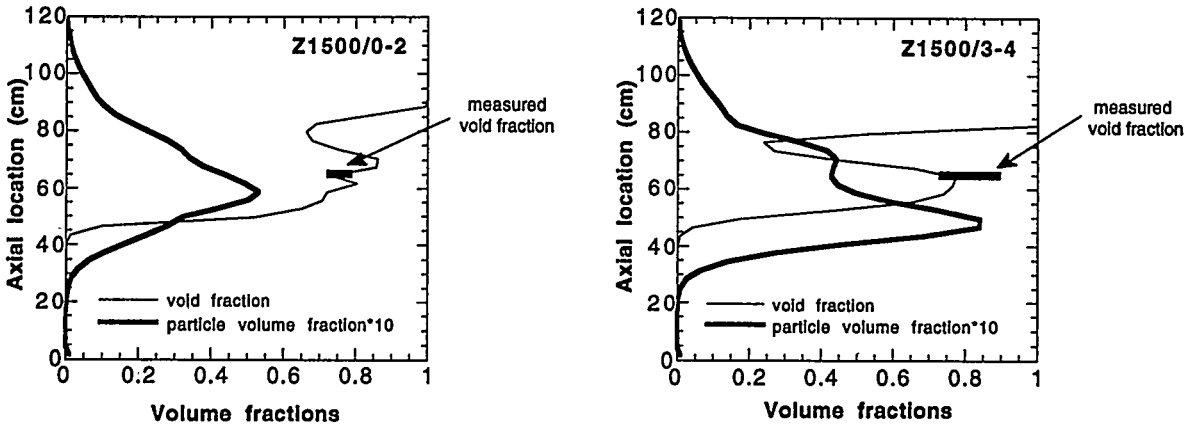


Fig. 26: Volume fraction distributions in ZrO_2 runs.

Water level swells

The level swells for runs Z1500/0-2 and Z1500/18-5 are shown in Figure 27. The uncertainty in measurement is in locating the somewhat disturbed (and disrupted) interface. For the calculation the upper and lower limits shown correspond to the 50% and 90% liquid fraction contours at the interfacial region—they are indicative of the water level. The important trends in this figure are that $18°C$ subcooling suppresses voiding almost completely, and that the void in the mixing zone for the saturated run peaks out and contracts. This latter effect is indicative of the flow reversal phenomenon (in the water surrounding the mixing zone) and the ETHICCA phenomenon described previously (Angelini et al., 1994b).

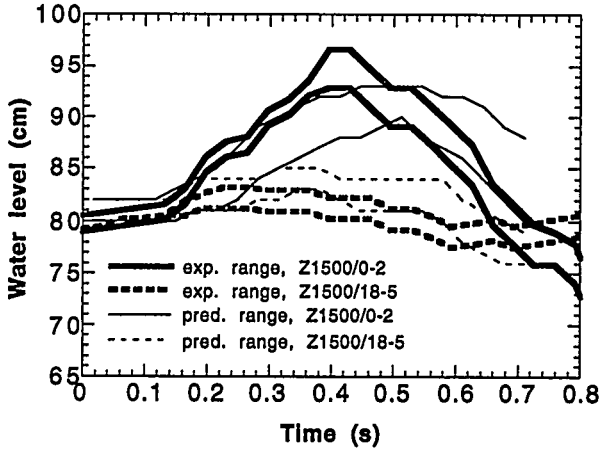


Fig. 27: Water level swells for runs Z1500/0-2 and Z1500/18-5. Predictions refer to 50% and 90% liquid contour lines.

In run S1200/0-6 because of the shallow penetration these phenomena are less discernible, especially since the interface broke sufficiently to make measurements impossible beyond $0.3s$ (the comparison up to this time with the calculation is similar to that in Figure 27). For runs Z1500/0-1 and Z1500/3-4 the behavior is very similar to that of Z1500/0-2.

Height of spray dome

The heights of the spray dome above the initial water level for runs Z1500/0-1 and Z1500/18-5 are shown in Figure 28. The experimental data are represented by bars which incorporate the uncertainty in their measurement, and the prediction corresponds to the position of the 2% liquid volume fraction contour line (contour lines between 1 and 5% form a rather narrow band). Results similar to those of Z1500/0-1 are obtained in runs Z1500/0-2 and S1200/0-6, while for run Z1500/3-4 these data were not available. From this figure we see that in the presence of $18°C$ subcooling the spray dome is almost nonexistent and forms only after all the particles have entered the tank ($\sim 0.4s$), again suggesting that for this run evaporation is almost completely suppressed. The calculation predicts the same behavior. On the contrary, in saturated water large amounts of vapor are produced that escape the tank dragging liquid along with them from early in the mixing (note that the computational grid in the simulation of Z1500/0-1 is limited to $60cm$ above the initial water level). It is worth pointing out the difference in scales between Figures 27 and 28: the water level grows by a maximum of $15cm$, as opposed to $70cm$ and more for the spray dome. Although both behaviors are linked to the vapor generation in the mixing region, they are completely distinguishable.

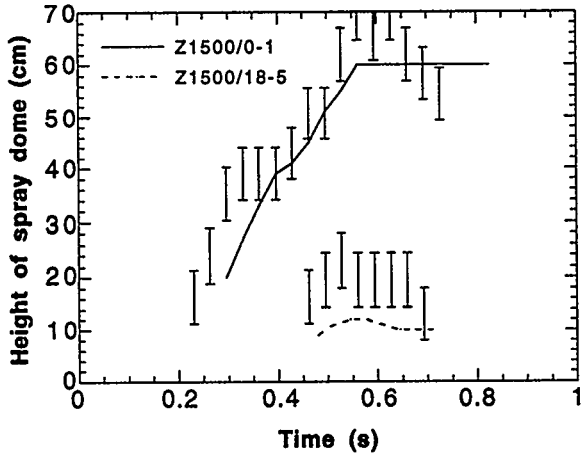


Fig. 28: Height of spray dome above initial water level for runs Z1500/0-1 and Z1500/18-5.

5. CONCLUDING REMARKS

The MAGICO-2000 facility and the associated measurement techniques provide a unique capability to produce uniform particle clouds of temperatures up to $1500°C$, currently, for the study of detailed interaction with water pools. Interesting phenomena identified under isothermal conditions are the formation of densely packed regions at the penetrating front, the formation of a "cavity" behind relatively dense clouds ($10 \div 14\%$ volume fraction), the development of instabilities (finger-like) at the penetrating front, and the slowing-down effect of a motion restricted to planar symmetry. Interesting phenomena quantified in hot pours include local voiding in the

mixing zone, global voiding through the level swell, the formation of a two-phase spray dome about the mixing zone, and the effects of slight (3^oC) and moderate (18^oC) subcooling on the above. Calculations with the PM-ALPHA code helped to interpret and probe in much greater detail than is feasible experimentally into these phenomena, and showed the importance of the details for the correct simulation of the process. Only the front instability was not captured by the numerical model. All these comparisons are expected to contribute significantly to an overall scheme of code verification appropriate for the intended applications.

6. ACKNOWLEDGEMENTS

This work was funded by the U.S. Department of Energy's Advanced Reactor Severe Accident Program (ARSAP) through ANL subcontract No. 23572401. We are very grateful to Mr. Tony Salmassi, who was instrumental in the design and the construction phases of the MAGICO-2000 facility. We would also like to acknowledge the contribution of Mr. Sam Ameen (Aweto Custom Printing) in the development of X-ray radiography for void fraction measurements. Messrs. Steven Sorrell (DOE) and Stephen Additon (TENERA) played a key role in programmatically supporting this project.

7. REFERENCES

1. Amarasooriya, W.H. and T.G. Theofanous (1991) "Premixing of Steam Explosions: A Three-Fluid Model," *Nuclear Engineering & Design* **126**, 23-39.

2. Angelini, S. (1995), "The dynamics of hot particle clouds plunging into water," PhD thesis, University of California at Santa Barbara.

3. Angelini, S., E. Takara, W.W. Yuen and T.G. Theofanous (1994a) "Multiphase Transients in the Premixing of Steam Explosions," *Nuclear Engineering & Design*, **146**, 83-95.

4. Angelini, S., W.W. Yuen and T.G. Theofanous (1994b) "Premixing-Related Behavior of Steam Explosions," Proceedings CSNI Specialists Meeting on Fuel-Coolant Interactions, Santa Barbara, CA, January 5-8, 1993, NUREG/CP-0127, March 1994, 99-133.

5. Berthoud, G. and M. Valette (1994) "Calculations of the Premixing Phase of an FCI with the TRIO MC Code, Proceedings CSNI Specialists Meeting on Fuel-Coolant Interactions, Santa Barbara, CA, January 5-8, 1993, NUREG/CP-0127, March 1994, 27.

6. Denham, M.K., A.P. Tyler and D.F. Fletcher (1992) "Experiments on the Mixing of Molten Uranium Dioxide with Water and Initial Comparisons with CHYMES Code Calculations," Proceedings of the Fifth International Topical Meeting on Reactor Thermal Hydraulics (NURETH-5), Salt Lake City, UT, September 21-24, Vol VI, 1667.

7. Fletcher, D.F. and M.K. Denham (1994) "Validation of the CHYMES Mixing Model," Proceedings CSNI Specialists Meeting on Fuel-Coolant Interactions, Santa Barbara, CA, January 5-8, 1993, NUREG/CP-0127, March 1994, 89.

8. Hall, R.W. and D.F. Fletcher (1994) "Validation of CHYMES: Simulant Studies,"Proceedings CSNI Specialists Meeting on Fuel-Coolant Interactions, Santa Barbara, CA, January 5-8, 1993, NUREG/CP-0127, March 1994, 70.

9. Jacobs, H. (1994) "Analysis of Large-Scale Melt-Water Mixing Events," Proceedings CSNI Specialists Meeting on Fuel-Coolant Interactions, Santa Barbara, CA, January 5-8, 1993, NUREG/CP-0127, March 1994, 14.

10. Magallon, D. and H. Hohmann (1994) "High Pressure Corium Melt Quenching Tests in Faro," Proceedings CSNI Specialists Meeting on Fuel-Coolant Interactions, Santa Barbara, CA, January 5-8, 1993, NUREG/CP-0127, March 1994, 1.

11. Mirza, S. and J.F. Richardson (1979) "Sedimentation of Suspensions of Particles of Two or More Sizes," *Chemical Engineering Science*, **34**, 447-454

12. Theofanous, T.G. (1993) "The Study of Steam Explosions in Nuclear Systems," International Seminar on Physics of Vapor Explosion, Tomakomai, Hokkaido, Japan, October 25-28, pp.5-26.

13. Theofanous, T.G. and W.W. Yuen (1994) "The Prediction of Dynamic Loads from Ex-Vessel Steam Explosions," Proceedings, International Conference "New Trends in Nuclear System Thermohydraulics," Pisa, May 30–June 2, 1994, 257-270.

14. Yamano, N., J. Sugimoto, Y. Maruyama and K. Soda (1994) "Studies on Fuel Coolant Interactions during Core Melt Accident of Nuclear Power Plant," Proceedings CSNI Specialists Meeting on Fuel-Coolant Interactions, Santa Barbara, CA, January 5-8, 1993, NUREG/CP-0127, March 1994, 271.

15. Yuen, W.W. and T.G. Theofanous (1995) "PM-ALPHA: a Computer Code for Addressing the Premixing of Steam Explosions," DOE/ID-10502, May 1995

Experimental Studies of Thermal and Chemical Interactions Between Molten Aluminum and Water

Ali A. Farahani and M. L. Corradini
Mechanical Engineering Department
University of Wisconsin - Madison, 53706

Abstract

The possibility of rapid physical and chemical aluminum/water interactions during a core melt accident in a noncommercial or experimental reactor (e.g., HFIR, ATR), has resulted in extensive research to determine the mechanism by which these interactions occur and propagate on an explosive time scale. These events have been reported in nuclear testing facilities, i.e., during SPERT 1D experiment, and also in aluminum casting industries. Although rapid chemical reactions between molten aluminum and water have been the subject of many studies, very few reliable measurements of the extent of the chemical reactions have thus far been made. We have modified an existing 1-D shock tube facility to perform experiments in order to determine the extent of the explosive thermal/chemical interactions between molten aluminum and water by measuring important physical quantities such as the maximum dynamic pressure and the amount of the generated hydrogen. Experimental results show that transient pressures greater than 69 MPa with a rise time of less than 125 μsec can occur as the result of the chemical reaction of 4.2 grams of molten aluminum (~15% of the total mass of the fuel of 28 grams) at 980 °C with room temperature water.

Introduction

An explosion involves the rapid conversion of energy from one form (i.e., metastable state) to another (e.g., kinetic energy). An energetic fuel-coolant interaction (FCI, commonly called a 'vapor explosion') is such a process in which a hot liquid, 'fuel', transfers its internal energy to a colder and more volatile liquid, 'coolant', in a very short time. A vapor explosion is triggered when the pre-existing vapor film around the fuel is either deformed or collapsed. Potential damage from vapor explosions include, but are not limited to, shock wave dynamic loading, kinetic energy of the accelerated mixture caused by the expansion of coolant vapor, and possible combustion of the generated hydrogen, if the fuel is oxidized by the coolant.

Vapor explosions occur in industry and nature where cold and hot liquid can come into contact with each other. Aluminum casting industries have long been plagued with explosions caused by accidental contact of molten aluminum with cooling water [1]. Vapor explosions have been an important topic in the safety analysis of nuclear reactors. Given a transient power/cooling mismatch in a nuclear reactor and the plant inability to establish the necessary prolonged core cooling, energetic FCI's could occur as a result of the core melt.

This paper presents the results of the first series of the FCI experiments we have conducted to study the triggering and fragmentation, transient pressures, and

hydrogen generation phenomena of energetic FCI's between molten aluminum and water in the simple geometry of a 1-D shock tube apparatus. Molten metal/water FCI tests have been performed in three different geometries: stratified layers, fuel liquid dispersed in a continuum of coolant liquid, and coolant liquid dispersed in a continuum of fuel liquid. In a shock tube geometry, a vapor explosion can be forced to occur with stratified layers and with control over the contact surface and the impact strength. This is in difference to dropping experiments where external triggers are often used to initiate the explosions. The dynamic pressures resulting from the vapor explosion inside the constrained geometry of a shock tube are greater than those resulting from a vapor explosion in the less constrained geometry of an open tank in a dropping experiment. In addition, the ability of a shock tube in containing the explosion makes it more attractive than the open geometry experiments where the experimental apparatus is substantially damaged after each energetic explosion (see [2] and [3]). Nelson et al. [4] permanently damaged their apparatus in the only experiment where they observed significant chemical reactions of ~10 grams of aluminum at 1773 K with water. Based on these events, and the works of Wright et al.[5] and Darby et al. [6] all of whom used a strong tube (stratified layer) geometry, it appeared to us that a shock tube may be a simple one-dimensional geometry from which reliable data could be gathered.

Experimental Setup

The experimental setup consists of two separate apparatus:

- shock tube
- partial pressure analyzer

The shock tube, a long vertical tube, is the environment in which the actual fuel coolant interactions occur. A partial pressure analyzer apparatus is used as a tool to determine the extent of the FCI by measuring the amount of the hydrogen produced from the exothermic chemical reaction between the aluminum content of the fuel and water.

The major components of the shock tube facility are shown in figure 1. The vertical tube consists of two stainless steel tubes and one inconel 600 holder. The middle section (compression tube), 1-in I.D., 1.5-in O.D., 6.6 ft long 304 stainless steel tube, holds the coolant (water, in our case). The lower section, reaction tube or holder (both names are used interchangeably in this report), .984-in I.D., 1.5-in O.D., 5.6-in long inconel 600, holds the melt. The melt itself is contained in a 321 stainless steel crucible which is placed inside the reaction tube. The upper section (expansion vessel), 3-in I.D., 3.5-in O.D., 20-in long 304 stainless steel tube, serves as a gas volume in which argon is introduced to pressurize the coolant. A kapton foil, which separates the compression and the reaction tubes, will burst at a specific pressure depending on its thickness and the coolant will impact the fuel as a result.

Figure 2 shows the components of the partial pressure analyzer device. This device is designed to measure the hydrogen concentration in the gas volume above the coolant column in the shock tube. A high vacuum is achieved using a turbo-molecular pump while the partial pressures are measured by a quadrupole mass spectrometer with the mass range from 0 to 64 amu.

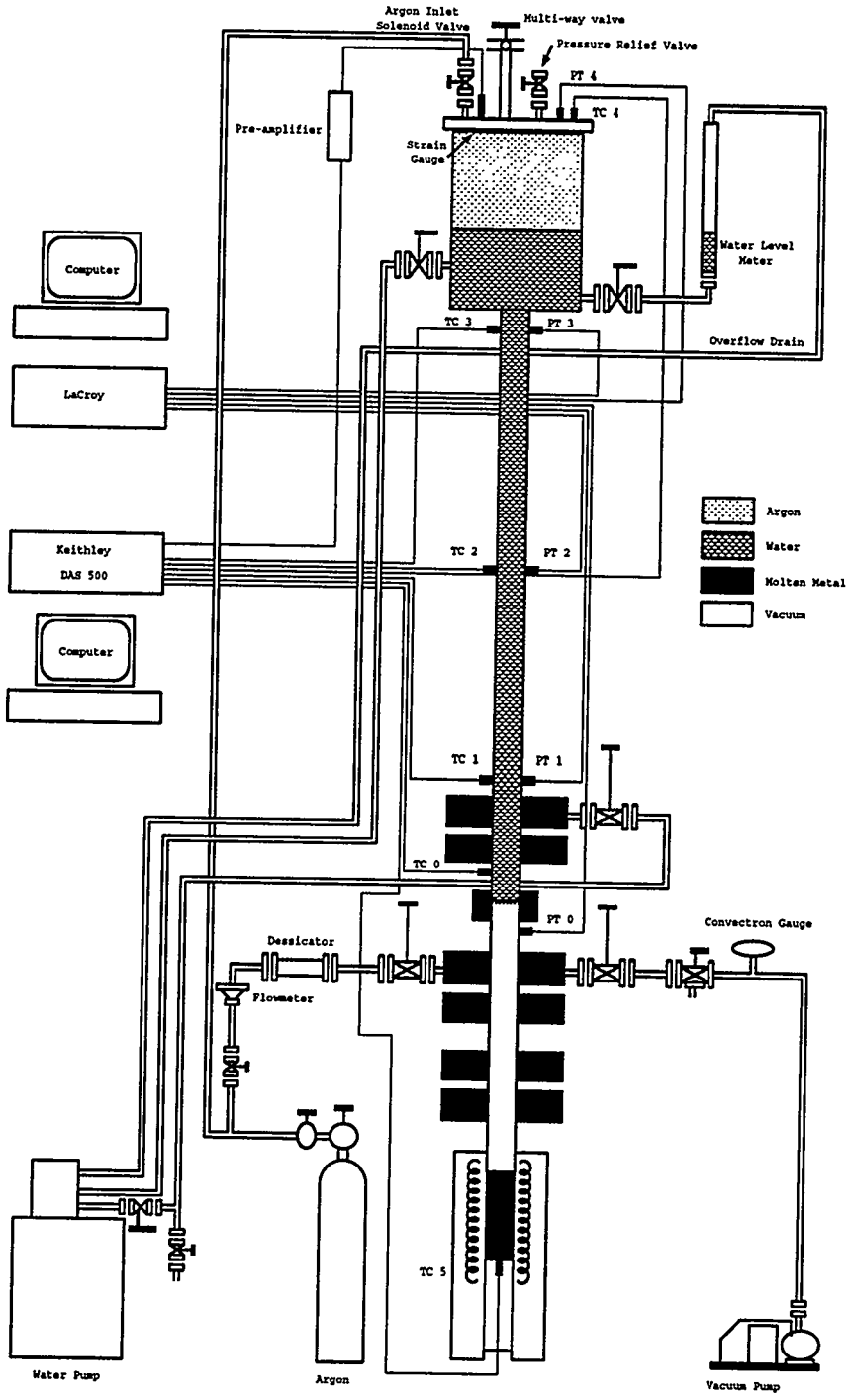


Figure 1: The shock-tube with measurement and data acquisition devices.

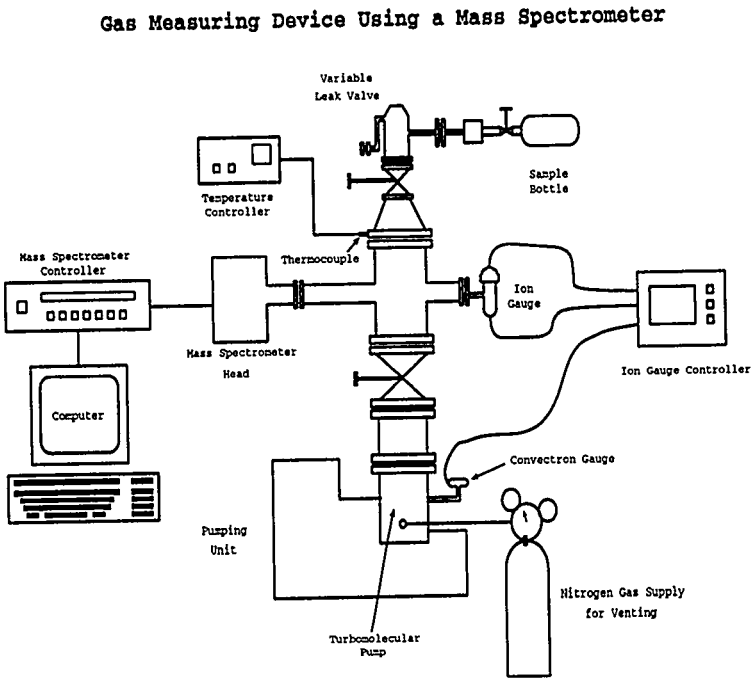


Figure 2: The partial pressure analyzer device.

Measurement and Data Acquisition Devices

Four E type thermocouples (TC0-TC3), which measure coolant temperatures along the shock-tube, have their tips inserted into the tube wall up to 0.35 in. TC4, an E type thermocouple located at the top of the shock-tube, measures the gas temperature in the expansion vessel. Fuel temperature is measured by a K type thermocouple with its tip inserted 0.1 inch in a gap provided at the bottom of the crucible. All of the thermocouples are ungrounded, sheathed, and have a $\sim \frac{1}{16}$ inch O.D. Thermocouples' signals are processed by the Keithley Data Acquisition System 500 (DAS 500) and stored in a PC. Temperature measurements are taken every 30 msec.

Dynamic pressures are measured by five miniature, quartz, charge mode (PCB Piezoelectronics series 112A03) pressure transducers, which are chosen because of their short rise time (2μsec), good sensitivity (1pC/psi), and range (up to 15,000 psi). These transducers are located at the same level along the shock-tube as their corresponding thermocouples. Each transducer is connected to a charge amplifier (PCB Piezoelectronics model 462A) for amplifiying and converting the charge ouput of the transducer into a voltage signal. The charge amplifiers have a range selection capability which determines the maximum pressure that will be measured, hence, increasing the digitalization resolution.

Analog transient pressure signals out of the charge amplifiers are digitized and stored temporarily by a LeCroy data acquisition system comprising a Camac frame, two 12-bit digitizers (LeCroy 8200), two memory modules (LeCroy 8800A), and a

Camac to GPIB interface. Each digitizer has four input channels with a maximum of 1 MHz sampling rate per channel. The storing period is determined by the sampling frequency. For example, at 125 μsec sampling period only 1 second of the transient event can be stored. This limits our ability to capture transient pressure frequencies that are much larger than the sampling period which is set by an external clock. The transient pressure digitalization and storage are controlled by Waveform Catalyst, an instrumentation control software from LeCroy, which is run on a personal computer.

A strain-gauge pressure transducer, with 0-500 psig pressure range model 175A purchased from Robinson-Halpern Co., is used to measure and monitor the pressure in the expansion vessel before, during, and after each experiment. The output of this gauge is processed the same way as the thermocouples.

In our early experiments with molten aluminum in the stainless steel crucibles, we encountered undesirable chemical reactions between the two metals at temperatures above 750 °C. Some of our crucibles were permanently damaged beyond any further use due to aluminum corrosion. To prevent the aluminum from contacting the naked crucible's wall, we applied a thin layer of boron-nitrate coating to the inner wall of the crucible. The boron-nitrate coating did not stop the aluminum from corroding the crucible's wall. After reviewing a report by Tutu et al. [7], a more powerful heater was used to heat up the fuel at a faster rate, thus minimizing the available time for aluminum-steel chemical reaction at high temperatures.

Experimental Procedure

Approximately 30 grams ($\sim$ 12 cc) of rectangular pieces of aluminum 6061-T6, that are sawed off from the plates sent to us from Savannah River Site heavy water reactor, is loaded into a crucible. The rupture disk is prepared by cutting a circle, the size of its housing, from a kapton sheet.

After installation of the rupture disk assembly, reactor quality water is pumped by a Haake constant temperature circulator, which is used to control the water temperature, into the shock tube to a pre-detetermined level. The crucible is then loaded into the reaction tube (inconel 600) and attached to the shock tube using stainless steel gaskets. Following this, the volume between the fuel and the rupture disk is vacuumed and checked for any leaks. A Pirani type vacuum gauge supplied by Granville-Phillips monitors the pressure inside this volume. After this, the ceramic fiber radiant heater is attached to the reaction tube.

The fuel inside the crucible is heated while the volume above the fuel is continuously purged with argon and kept at 5 Torr. This purging of argon is done to prevent the molten fuel from forming any oxide layer prior to its contact with water. When the fuel reaches the desired temperature, argon gas will be diverted to a solenoid valve that opens up into the expansion vessel. The heater and the vacuum pump are turned off and the three-second countdown starts. After the countdown, the solenoid valve opens up and allows the argon gas to pressurize the water column, which will eventually rupture the diaphragm.

Sample gases are collected inside 50 cc bottles one and five minutes after the completion of each test. The partial pressure of specific gas components making up the total pressure of the sample bottle will then be measured using a mass spectrometer. Partial pressure measurements are usually made at total pressures

less than 5×10^{-6} Torr in order to remain below the region of non-linear effects of our mass spectrometer.

FUEL	Expt. No.	m_f gram	T_f °C	P_{dr} MPa	H_{fuel} m	H_{fall} m
EMPTY CRUCIBLE	7R	0.0	25	.566	0.0	0.435
	8R	0.0	21.9	.555	0.0	0.435
	9R	0.0	22.1	1.177	0.0	0.435
	53	0.0	723.5	.523	0.0	0.435
	55	0.0	710.3	.555	0.0	0.435
	57	0.0	893.2	.584	0.0	0.435
	61	0.0	901	1.159	0.0	0.435
	62	0.0	902	1.187	0.0	0.435
	66	0.0	993.4	.570	0.0	0.435
Al 6061-T6	31	31.80	889.1	.562	0.034	0.401
	32	25.72	773.6	.552	0.028	0.407
	33	25.72	766.5	.516	0.028	0.407
	34	28.48	980.3	.578	0.031	0.404
	35	28.18	967.9	.537	0.031	0.404
	36	29.45	1022.9	.494	0.032	0.403
	37	29.41	1010.8	.485	0.032	0.403

Table 1: list of the preliminary experiments

Experimental Results

Table 1 shows the list of the 16 successful experiments performed investigating the effects of the initial fuel temperature and driving pressure on the energetics of vapor explosions between molten aluminum and water. To check the performance of the experimental design, we performed the scoping experiments with the crucible and the water at room temperature and the experimental peak pressures and the acoustic relief time were in good agreement with the theoretical results. The experiments have been carried out at four other initial temperatures of ~750 °C , ~900 °C, and ~1000 °C. The lower end of the initial temperature region, 750 °C, was chosen so that the existence of a homogeneous aluminum melt inside the crucible is guaranteed. The maximum temperature for safe operation of our apparatus is ~1100 °C at which point the crucible can be easily ruptured due to the combined effects of aluminum corrosion and water hammer pressure. The crucible used in Expt. 39 (not reported here) failed when water column with a driving pressure of 0.399 MPa impacted upon molten aluminum at 1107.3 °C.

The second independent variable of interest is the driving pressure which accelerates the liquid column downward. The effects of driving pressure on the energetics of the interaction have been investigated using diaphragm of 1 and 2 mils in thick-

nesses that rupture at ~5 and ~10 bar, respectively. The one mil rupture disk, however, failed unexpectedly at pressures below 5 bar in some of the higher temperature experiments, i.e., Expts. 36 and 37.

The experiments were carried out in a random order to insure that the results were not affected significantly by the changes in the characteristics of the experimental design. To investigate the reproducibility of the experimental results, we have tried to perform a minimum of two experiments for any given initial conditions. The reproducibility of the experimental results can be seen by comparing the results as listed in table 3 and Farahani [8].

Dynamic pressure traces, fuel and water temperatures, and gas concentrations were the measured quantities in each experiment. The pressure and the temperature profiles along the shock tube for all the experiments listed in table 1 are included in a detailed report by Farahani [8]. Table 2 lists the important initial and boundary conditions for the 1st series of the experiments.

Coolant Temperature (°C)	**23 ~ 27**
Driving Pressure (MPa)	**.343 ~1.187**
Water Column ID (cm)	**2.54**
Crucible ID (cm)	**2.22**
Coolant Height (m)	**2.60**
Vacuum Height (m)	**.40**
Coolant Mass (Kg)	**1.95**
Total Fuel Mass (gram)	**25 ~ 32**
Fuel Volume (cc)	**11.67 ~ 12.92**
Coolant Volume (cc)	**1950**
Mass Ratio (M_c/M_f)	**61 ~ 78**
Volume Ratio (V_c/V_f)	**151 ~ 167**

Table 2: The initial and boundary conditions in the 1st series of the experiments.

Pressure Profiles

Dynamic pressure measurements were made at 5 different locations along the shock tube (see figure 1 for the locations of the pressure transducers). The PT0 transducer measures the pressure in the region below the rupture disk. The measured pressure by PT0 is positive as long as the pressure at the location of the transducer during the experiment does not fall below the initial vacuum pressure. The gas pressure in the expansion vessel is measured by PT4. Figures 3 through 5 show the pressure traces for typical experiments conducted for this initial test series.

A typical pressure trace for the impact of a pressurized water column upon the surface of an empty crucible is shown in figure 3. The value of the pressure at the

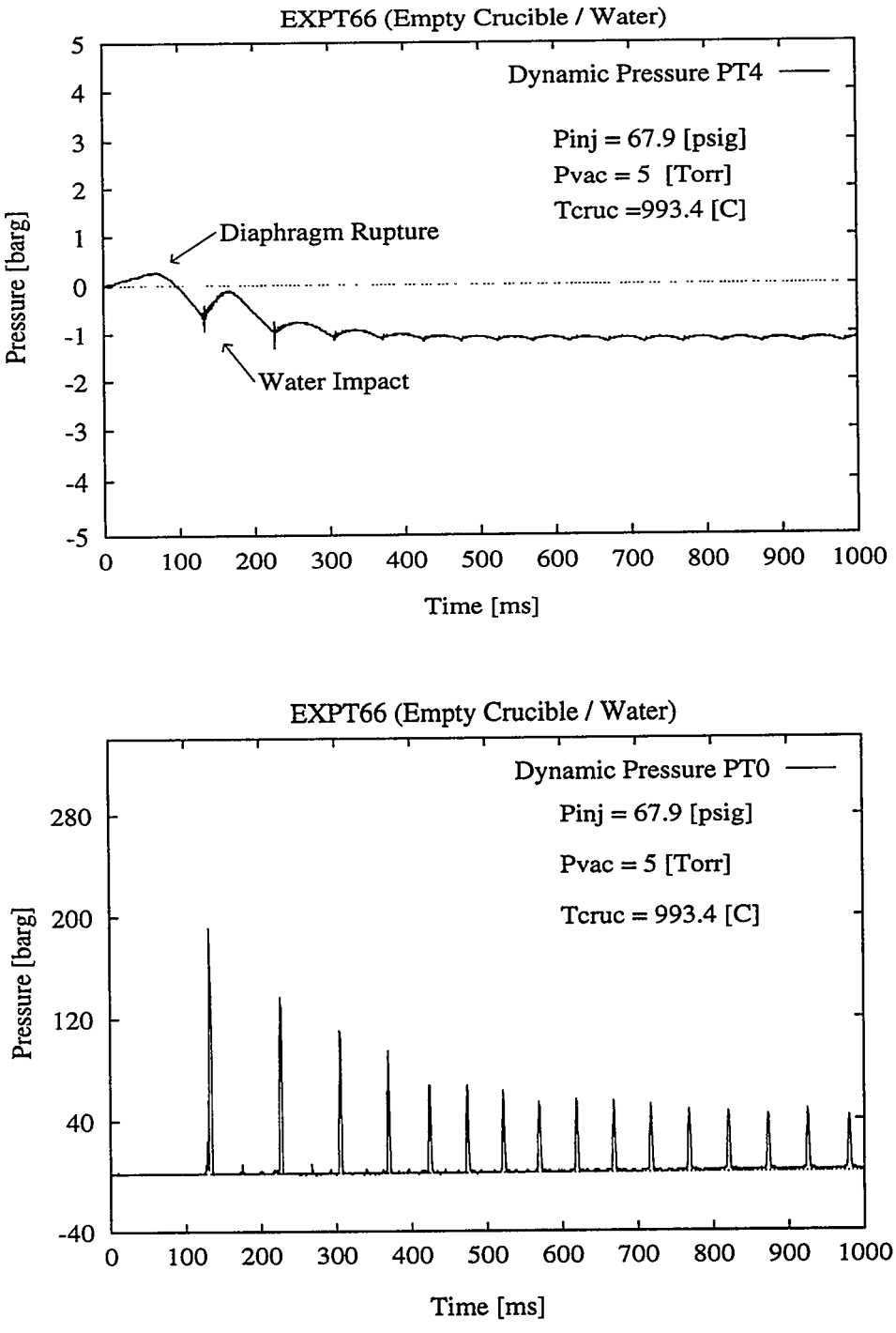


Figure 3: Gas vessel and reaction vessel pressure traces for experiment 66.

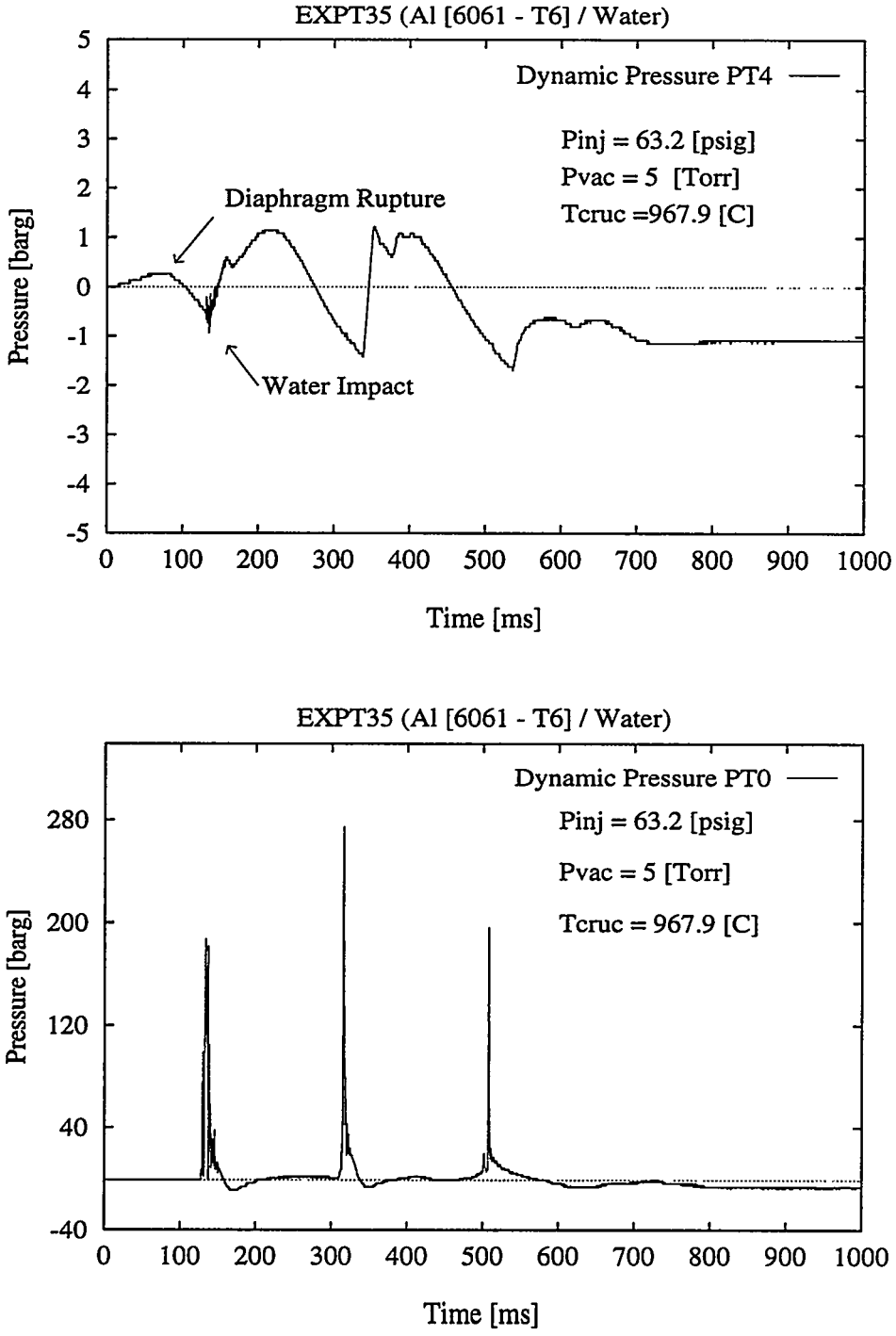


Figure 4: Gas vessel and reaction vessel pressure traces for experiment 35.

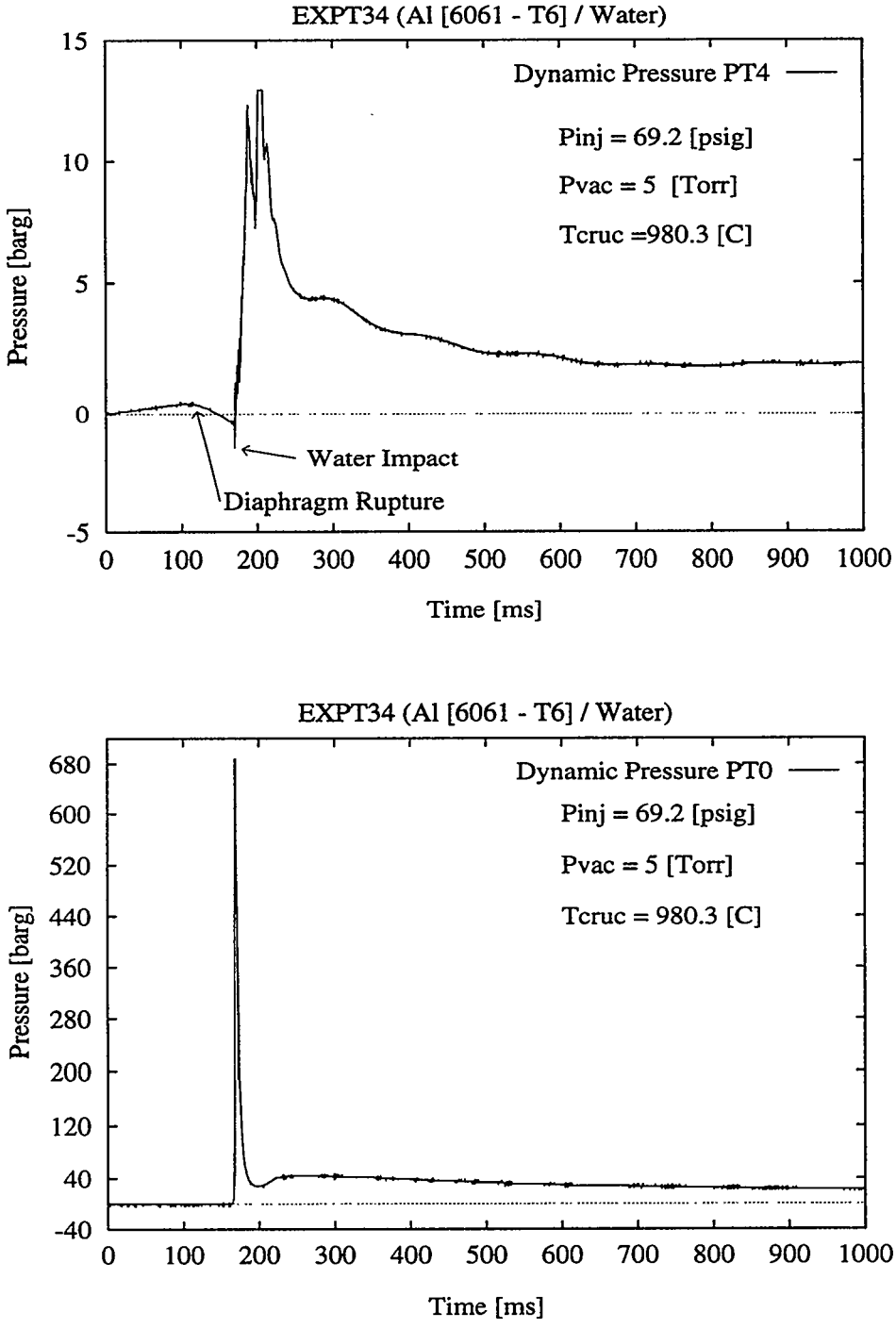


Figure 5: Gas vessel and reaction vessel pressure traces for experiment 34.

peak of the first rise in the PT4 trace corresponds to the injection pressure as measured by the strain gauge transducer and is noted on the plot. The traces in the figure 3 and others are shown between 0 to 1000 msec. The zero msec does not correspond to the beginning of the experiment; but, it is recalibrated here in order to eliminate the unnecessary data from the opening of the solenoid valve until some time before the diaphragm ruptures.

The generation of water vapor and hydrogen gas can contribute significantly to the pressurization of the argon gas during the experiment. The increase of the pressure inside the expansion vessel beyond the initial driving pressure is part of the work done by the FCI.

Temperature Profiles

Figures 6 and 7 show the water and fuel temperature traces for the above experiments. The T1 thermocouple is located at the same axial location as PT1. The temperature traces are plotted for an approximate time interval of 4 or 5 seconds. The initial time in the plots, 3 sec, corresponds to the end of the three second countdown and the opening of the solenoid valve. The Keithley data acquisition system continues to record data for a period of three seconds after a signal from PT0. The signal from PT0 corresponds approximately to the time of the rupture disk failure. The rupture disk failure time is noted in all of the temperature plots.

Gas Measurements

Two gas samples, taken at one and five minutes after the experiment from the expansion vessel, were collected to measure their constituent concentrations to determine the extent of the chemical reaction between the aluminum part of the fuel and water. Table 3 gives values for the measured hydrogen mass and the wt% of the aluminum content of the fuel that was oxidized in the initial experiments. The wt% of the aluminum content of the fuel oxidized is based on the assumed stoichiometric reaction between the measured hydrogen mass with aluminum.

Data Analysis

The pressurized gas in the expansion vessel in our shock tube apparatus is a part of the triggering device that forces the collapse of the vapor film, forces liquid-liquid contact, and triggers a vapor explosion. The pressure difference across the water column along with the weight of the water are the contributing forces that accelerate the coolant toward the fuel surface. The higher the driving pressure, the greater will be the coolant impact velocity for a given fall distance. Driving pressures of $\sim$5 and $\sim$10 bars have been thus far used. A comparison of the results of expts 35, 36, and 37 with those of expt 34 show that the amount of the chemical reaction between molten aluminum and water increased when the driving pressure was increased from .485 MPa to .578 MPa. The rupture disks in experiments 35 to 37 were ruptured unexpectedly at pressures lower than .560 MPa. The sifting of the aluminum residue collected from Expts. 31 to 34

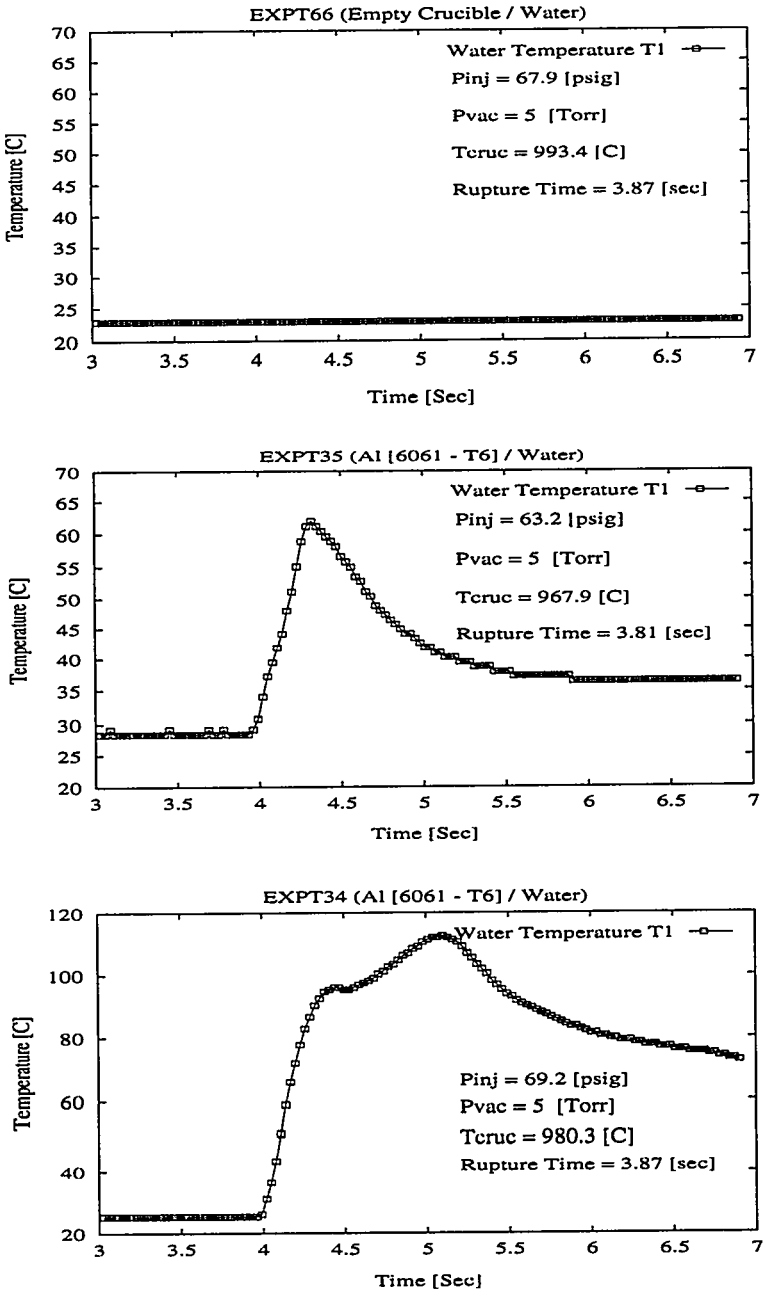


Figure 6: Water temperature traces for Expts. 66, 35, and 34.

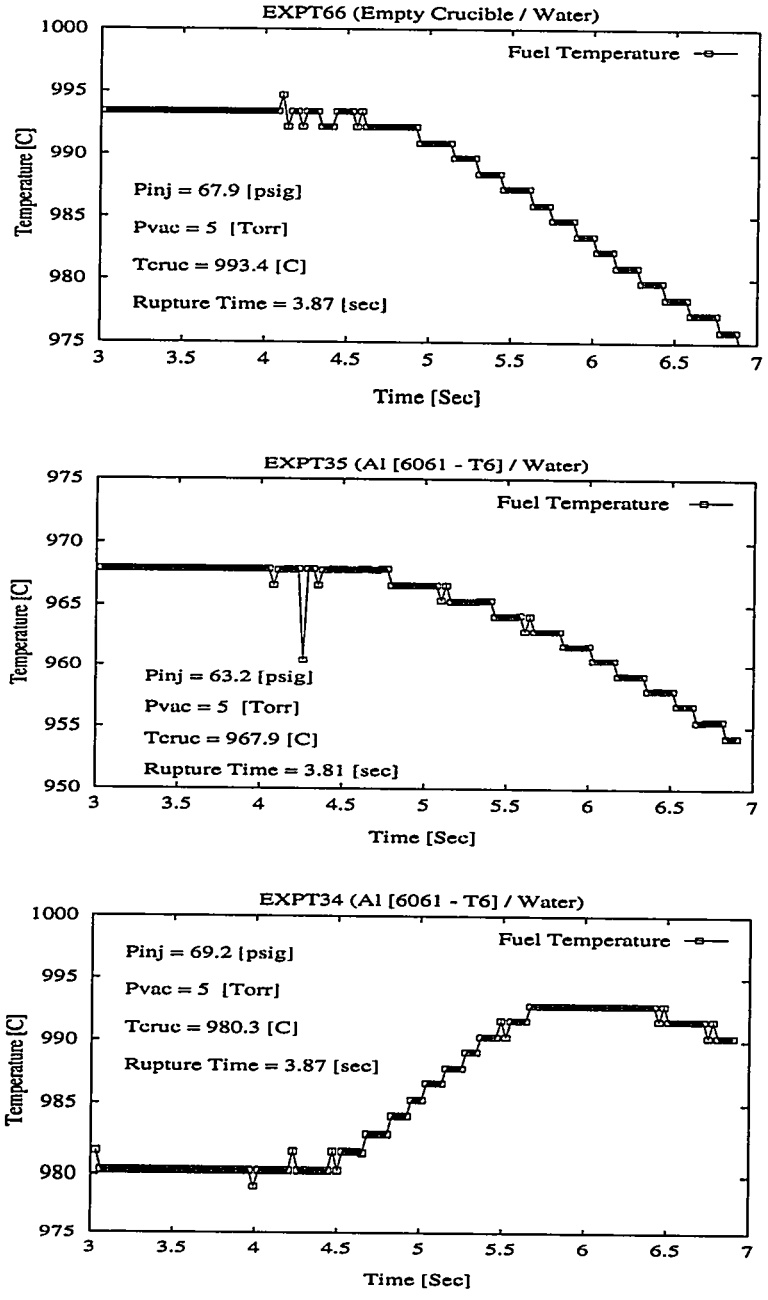


Figure 7: Fuel temperature traces for Expts. 66, 35, and 34.

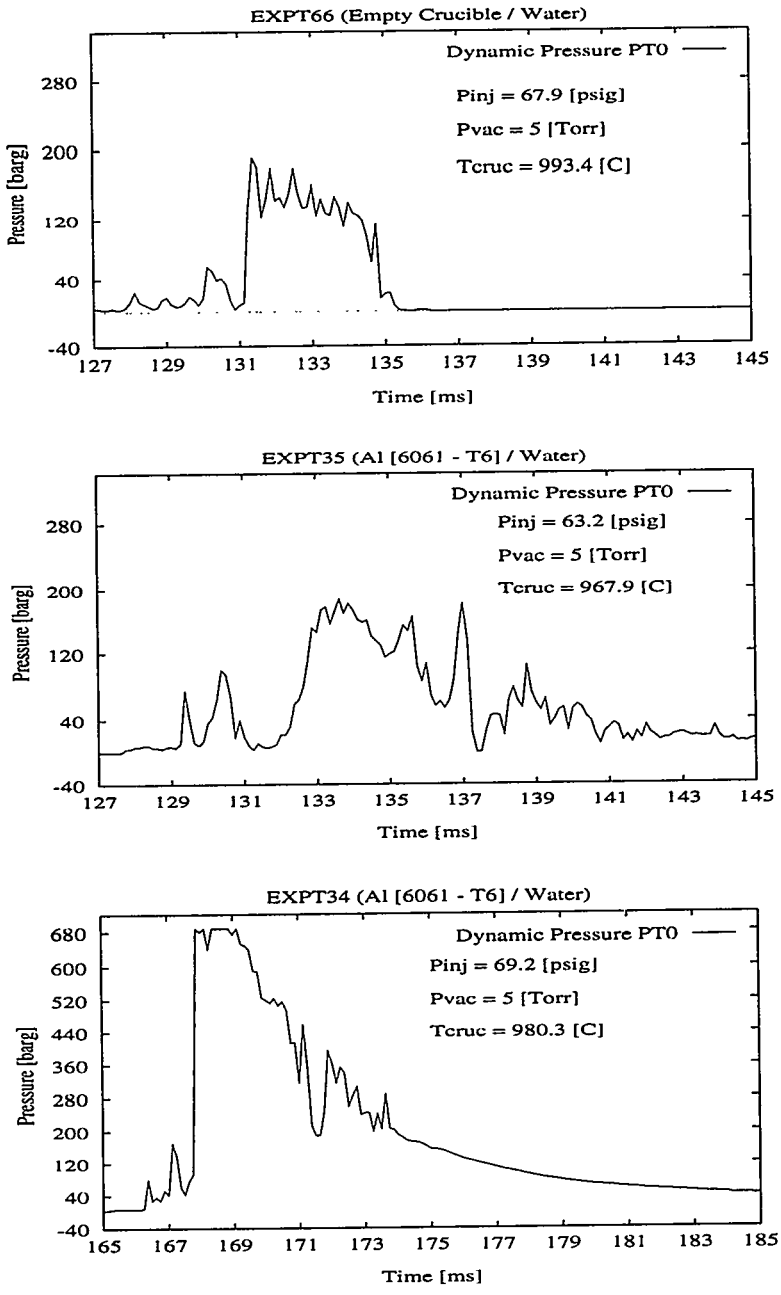


Figure 8: Rescaled pressure traces of the initial water impact upon the fuel for Expts. 66, 35, and 34.

revealed notable differences between the debris size distribution for the experiment with aluminum ignition in it (Expt. 34) and that of the other experiments (see Fig. 5.1 in [8]). Much of the debris were core-like in shape and were made of agglomerates of smaller particles.

Dynamic pressures much larger than those due to only hydrodynamic effects (~20 MPa) were observed in Expt. 34 when water at room temperature impacted upon aluminum at 980 °C. The actual transient pressure was greater than 69 MPa, which was the maximum pressure that could be measured by PT0 transducer due to charge amplifier settings, with a rise time of less than 125 μsec. The water column impacted the aluminum only once in Expt. 34 compared to several impacts of water upon the fuel surface in all other experiments (see figures 3 to 5). The absence of additional water impacts suggests the presence of large amounts of water vapor and hydrogen at sufficiently high pressures. The scaled PT0 trace for Expt. 34 in figure 8 shows the condensation of the existing steam in the form of a tail in the pressure trace which is absent from plots for Expts. 66 and 35 in figure 8. The impact of water upon liquid surfaces of molten aluminum generates a series of pressure oscillations suggestive of coarse fuel and coolant mixing unlike the pressure plateau seen in the hot solid impact, like in empty crucible experiments where no mixing or fragmentation occurs (see Fig. 8 for the scaled plots for the initial impact of the Expts. 66 and 35).

FUEL	Expt. No.	P_{dr} (MPa)	T_f °C	Work (J)	m_{H_2} mgram	wt% Al reacted
EMPTY CRUCIBLE	7R	.566	25	(–)	0.0	0.0
	8R	.555	21.9	(–)	0.0	0.0
	9R	1.177	22.1	(–)	0.0	0.0
	53	.523	723.5	71.6	0.0	0.0
	55	.555	710.3	47.9	0.0	0.0
	57	.584	893.2	86.4	0.0	0.0
	61	1.159	901	105.8	0.0	0.0
	62	1.187	902	158.2	0.0	0.0
	66	.570	993.4	58.1	0.0	0.0
Al 6061-T6	31	.562	889.1	114.9	67.9	1.9
	32	.552	773.6	111.0	2.4	0.1
	33	.516	766.5	141.4	25.3	0.8
	34	.578	980.3	> 892	476.4	14.9
	35	.537	967.9	202.0	20.3	0.6
	36	.494	1022.9	219.9	24.7	0.7
	37	.485	1010.8	153.9	48.9	1.5

Table 3: The list of the measured hydrogen mass and calculated compression work for the initial experiments.

The increase in the fuel temperature of the aluminum in Expt. 34 due to relatively significant chemical reaction can be easily seen in Fig. 7. This is in

contrast to other experiments where the fuel temperature decreases upon the water impact. Finer debris and larger amount of the chemical reactions caused a larger increase in water temperature, as measured by T1 thermocouple, in Expt. 34 (~90 °C) compared to ~35 °C in Expt. 35.

Table 3 shows that, except for Expt. 34, only less than 2% of the total mass of the fuel in each experiment has reacted with water. As explained previously, we conducted a few unsuccessful experiments to reproduce the initial conditions like those of Expt. 34. It is our belief that future experiments should further investigate the effect of the driving pressure (using 2 mil rupture disks) at 1000 °C fuel temperature.

The ideal way to calculate the work from the explosion requires the knowledge of the pressure and the volume of the generated vapor at any instant. However, the work from the vapor explosion can be determined indirectly, by calculating the coolant acceleration due to the expanding vapor. A third method, which estimates the work from the explosion by calculating the work required to compress the expansion gas from state one (the end of the gas expansion process) to state two (the end of the expansion gas compression by the upward motion of the coolant), is employed here to compare the amount of the work from the explosion for each fuel type.

$$du_g = dw_{c-g} + dq_{c-g} \tag{1}$$

where du_g, dw_{c-g}, and dq_{c-g} are the change in the internal energy of the gas, the work done by the coolant on the gas, and the heat transferred from the coolant to the gas during the compression process, respectively. The compression process is assumed to be isentropic, so that the work required to compress the gas is minimum ($dq_{c-g} = 0.$ and $PV^{\gamma} = constant$). The isentropic assumption enables us to approximate the gas volume at the end of the compression process.

$$du_g = dw_{c-g} \tag{2}$$

$$\Delta u_g = \Delta w_{c-g} \tag{3}$$

For an ideal gas with constant properties

$$\Delta w_{c-g} = c_v(T_2 - T_1) \tag{4}$$

$$\Delta w_{c-g} = \frac{P_2 v_2 - P_1 v_1}{1 - \gamma} \tag{5}$$

The isentropic assumption underestimates the work output from the explosion.

The amount of the work for compressing the gas inside the expansion vessel for all the hot experiments (where the crucible temperature is above 700 °C) is reported in table 3. The reported work values although different, don't show a significant difference between empty crucible experiments and aluminum experiments. Because the compression work is affected by the impact of the coolant column upon the molten fuel (expansion process), the ratio of these two values is a better indicator for the energetics of FCI. Figure 9 shows that the work ratio is always below unity for empty crucible experiments and larger than one for aluminum experiments. It is worth mentioning that the same work ratio is below two for cermet and silicide fuels (see [9]) and galium, tin, and lead (see [10]).

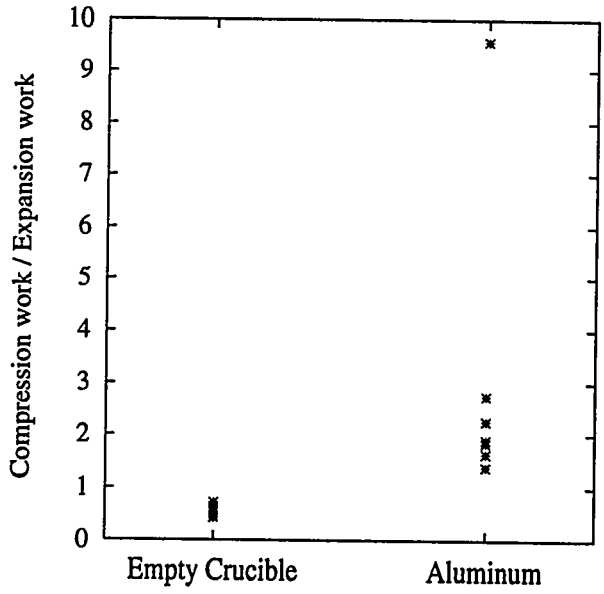


Figure 9: The relative FCI energetics for all the hot experiments.

Conclusions

Energetic FCI's with significant chemical reaction in experiment 34 resulted in one order of magnitude larger dynamic pressures and explosion work. The results of the experiment 34 show that aluminum ignition can occur in small scale experiments at a temperature which lies between those reported in large scale experiments (see [3]) and drop size experiments (see [4]). Although similar experiments to experiment 34 (experiments 35, 36, and 37) were conducted, the results were different (see table 3). One could speculate, based on the results of the experiments conducted thus far, that alumiunm ignition at about 980 °C although possible, is not assured. Our speculation is similar to that from Alexis W. Lemmon [11] who observed that very violent explosions did not occur in all experiments where tap and distilled water interacted with molten aluminum at about 1000 °C under similar initial conditions.

Acknowledgement

We would like to thank J. Krueger for his help in the laboratory and the DOE and the Savannah River Site for their partial financial support of this work.

References

[1] G. W. P. Rengstroff, A. W. Lemmon Jr., and A. O. Hoffman, **Review of Knowledge on Explosions Between Molten Aluminum and Water to the Aluminum Association**, April 11, 1969, Battelle Memorial Institute

[2] G. Long, **Explosions of Molten Aluminum in Water - Causes and Prevention**, Metal Progress, Vol. 71, May 1957, pp 107-112

[3] M. J. Rightly and D. B. Beck, **NPR/FCI EXO-FITS Experiment Series Report**, SAND91-1544, 1993, Sandia National Laboratories

[4] L. S. Nelson, P. M. Duda, and D. A. Hyndman, **Thermal- and Ignition-Type Steam Explosions of Single Drops of Molten Aluminum**, Trans. American Nuclear Society 1991, 64

[5] R. W. Wright and G. H. Humberstone, **Dispersal and Pressure Generation by Water Impact upon Molten Aluminum**, Transactions, American Nuclear Society, Vol. 9, 1966, pp 305-306

[6] K. Darby, R. C. Pottinger, N. J. M. Rees, and R. G. Turner, **The Thermal Interaction Between Water and Molten Aluminum Under Impact Conditions in a Strong Tube**, In Engineering of Fast Reactors for safe and reliable operation, Vol. II., Karlsruhe, Oct. 192,1973

[7] N. K. Tutu, C. C. Finfrock, J. D. Lara, C. E. Schwarz, and G. A. Greene, **Dissolution of a 316L Stainless Steel Vessel by a Pool of Molten Aluminum**, BNL 52366, January 1993

[8] Ali Farahani, **Experimental Studies of Thermal and Chemical Interactions Between Molten Aluminum and Aluminum Fuel Alloys with Water**, Preliminary Report, University of Wisconsin-Madison, August 1994

[9] Ali Farahani and M. L. Corradini, **Experimental Studies of Thermal and Chemical Interactions Between Cermet and Silicide Nuclear Fuels with Water**, Submitted for Presentation and Publication in NURETH-7 Proceedings

[10] G. Vokovic, **Liquid-Metal/Water Interactions in a Shock-Tube Geometry**, PhD Thesis, Department of Nuclear Engineering and Engineering Physics, University of Wisconsin-Madison, 1994

[11] Alexis W. Lemmon, **Explosions of Molten Aluminum and Water**, Conference Proccedings of The Metallurgical Society of AIME, Light Metals 1980, pp 817-836

INTERACTION BETWEEN THE RADIATIVE FLUX EMITTED BY A CORIUM MELT AND AEROSOLS FROM CORIUM/CONCRETE INTERACTION

M. Zabiégo*, **G. Cognet**
CEA - DRN/DER/SERA - CE Cadarache - 13108 Saint-Paul-Lez-Durance - France.

D. Henderson
NEEP Dept. - University of Wisconsin - 1500 Johnson Drive - Madison - WI 53706 - USA.

ABSTRACT

In this paper we present a one-dimensional numerical model that deals with radiative transfer in a medium where aerosols are present. This model is written with the aim of performing radiative transfer calculations in the framework of severe Pressurized Water Reactor accidents, especially during the last stage of such an accident (Molten Core Concrete Interaction (MCCI)) when aerosols are very numerous .
We explain the theoretical basis of our model, writing the general radiative transfer equation, knowing that aerosol droplets participate in radiation transport. We then simplify this equation for a one-dimensional medium and we propose to solve it using the spherical harmonics approximation. This gives us the radiative intensity and we can then deduce the radiative flux.
Aerosol optical properties (extinction and scattering coefficients) are also required in such a calculation. They are determined using Rayleigh or Mie theory, depending on the aerosol size.
In order to provide an example of results one can expect from such a calculation, we applied our model to a test problem with given aerosol size and concentration distributions. Our example does not model any experiment explicitly but the physical conditions used are very close to the L4 test from the Advanced Containment Experiment (ACE) program (Argonne National Laboratory, 1988-1990).

INTRODUCTION

In the later phase of a severe PWR accident, the corium could reach very high temperatures, becoming a strong thermal radiation emitter and damage the containment. Therefore, to better assess the downward and upward heat fluxes, it is of a great interest to determine the amount of energy emitted by the corium pool and received by the containment.

The main difficulty in estimating the upward fluxes is due to the presence of aerosols which participate in the energy transfer between the melt surface and the walls. Depending on the composition of the concrete and the melt and gas temperature, the concentration of suspended particles could reach high values and consequently the thermal radiation from the melt could be strongly reduced [1].
Most computer codes (CONTAIN [2] and WESCHL [3] for example) do not calculate precisely the aerosol effect on the radiation emitted by the corium pool. They usually determine an average opacity above the corium pool. The theoretical work that we present here is certainly too fundamental to be included in a severe accident computer code; however we intend to deduce from this work a simplified model which could better take into account the role played by the aerosols.

The aim of this paper is to present a radiative transfer study in a medium where aerosols are numerous and play a significant role in heat exchanges. We first write the radiative transfer equation in a medium that can scatter, absorb and emit radiation [4, 5]. This gives us an integro-differential equation for the intensity; we propose to solve it using the spherical harmonics approximation [4] and to deduce the radiative flux.

---

* Present address: NEEP Dept.- University of Wisconsin - Madison - WI 53706 - USA

Coefficients of the this equation are functions of aerosol optical properties. Depending on the value of the ratio between the droplet size and the wavelength, we use Rayleigh (for small droplets) or Mie (for large droplets) theory to calculate scattering and extinction coefficients [6]. For that step in the calculation, it is necessary to know the aerosol size distribution as well as their concentration in the studied volume.

We describe the numerical scheme of the calculation and provide results for the radiative flux and optical coefficients in the studied volume with given aerosol features and temperature profile. We can not precisely compare our results to experimental ones but, nevertheless, we obtain the flux within an order of magnitude of the value measured from ACE-test L4.

I RADIATIVE TRANSFER

We propose here a numerical model that deals with radiative transfer in a participating medium. We suppose that vapor and aerosols are present in the medium and that those aerosols can scatter, absorb and emit radiation. Aerosol size distribution and concentration are known, estimated from experimental results or from a special modeling. We now present the theoretical basis of our study.

I.1. Radiative Transfer Equation [4, 5].

The first step of a radiative transfer calculation is to write the radiative transfer equation (RTE) (which is the energy balance) in the studied medium. Let us describe the RTE with the following notations:
In general, the optical properties of the medium are functions of the wavelength of the radiation. However, by making the assumption of a gray medium, we use the average properties of the medium (which is discussed in section II)

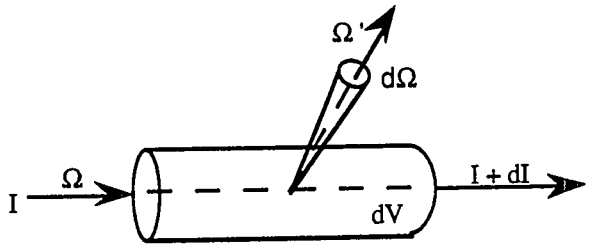


Figure 1: Geometry used to write the RTE

I is the incident radiation in the direction Ω and dI is the variation of I due to the medium.
In this geometry, the steady state RTE is written:

$$\frac{\partial I}{\partial l}(l,\Omega) = -(K_a(l)+K_s(l))\, I(l,\Omega) + K_a(l)\, I_B(T(l)) + \frac{K_s(l)}{4\pi} \int_{4\pi} I(l,\Omega)\, p(\Omega',\Omega)\, d\Omega \ . \qquad (1)$$

This equation represents the evolution of the radiative intensity (I) while it passes through the studied volume. The right side of this equation is composed by three different terms that will cause the intensity I to change. These terms are:

1. extinction by absorption (K_a is the absorption coefficient) and out-scattering (K_S is the scattering coefficient). This first part represents the energy removed from the initial beam.

2. emission: this second term represents the energy added to the beam, due to the aerosol emission at their temperature. Aerosols are considered to be black bodies.

3. in-scattering: this is the energy added to the beam due to scattering inside the studied volume. This term depends on the phase function (p). p gives the probability for the incident wave traveling in the direction Ω to be scattered along the direction Ω' about dΩ.
Notice that p=1 for isotropic scattering.

Solving (1) will allow us to calculate the radiative flux defined by:

$$q_R = \int_{4\pi} \Omega I(l,\Omega) d\Omega \ . \tag{2}$$

From now on, we will consider a one-dimensional model depicted as follows:

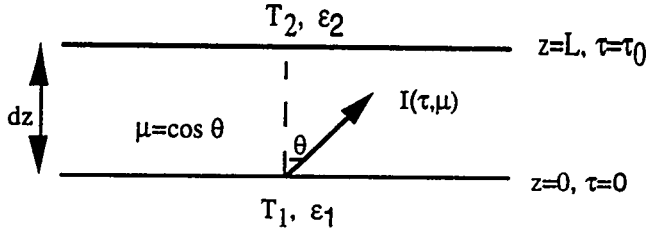


Figure 2: one-dimensional medium

where dz is the thickness of the slab, T_i are the boundary temperatures, ε_i are the boundary emissivities, τ is the optical thickness and I is the radiative intensity.

The steady state RTE at the given position (z, μ) is:

$$\mu \frac{\partial I}{\partial z}(z,\mu) + K_e(z)\, I(z,\mu) = K_a(z)\, I_B(T) + \frac{1}{2} K_s(z) \int_{-1}^{1} p(\mu,\mu')\, I(z,\mu')\, d\mu' \tag{3}$$

where $I_B(T)$ is the Planck function for a black body and $K_e(z)$ is the extinction coefficient defined by:

$$K_e(z) = K_a(z) + K_s(z) \ . \tag{4}$$

It is generally more convenient to rewrite the RTE with respect to the optical variables, namely the scattering albedo:

$$\omega(z) = \frac{K_s(z)}{K_e(z)} \tag{5}$$

and the optical thickness τ, such that $d\tau = K_e(z)\, dz$.

Then, the RTE becomes:

$$\mu \frac{\partial I}{\partial \tau}(\tau,\mu) + I(\tau,\mu) = (1-\omega(\tau))\, I_B(T) + \frac{\omega(\tau)}{2} \int_{-1}^{1} p(\mu,\mu')\, I(z,\mu')\, d\mu' \ . \tag{6}$$

This last equation represents the integro-differential equation that we solve to perform our radiative transfer study and determine the upward radiative flux:

$$q(\tau) = \int_{0}^{1} \mu I(\tau,\mu) d\mu \ . \tag{7}$$

To do so, we chose to use the spherical harmonics approximation, from among the different methods proposed in literature.

I.2. Spherical harmonics approximation (or P-N method) [4]

The idea of this method is to expand the radiative intensity and the scattering phase function in series of Legendre Polynomials:

$$I(\tau,\mu)=\sum_{m=0}^{N=\infty}\frac{2m+1}{4\pi}P_m(\mu)\,\Psi_m(\tau)$$

$$p(\mu,\mu')=\sum_{n=0}^{N=\infty}(2n+1)\,f_n\,P_n(\mu)\,P_n(\mu') \qquad (8)$$

where P_n are the Legendre Polynomials, Ψ_m are functions to be determined and f_n are coefficients such that, for isotropic scattering, $f_0=1$ and $f_{n\neq 0}=0$. With the P-N method, direction and position variables are separated.

Replacing this development into the RTE and using the orthogonality and recurrence relationships of the Legendre polynomials leads to:

$$(m+1)\Psi'_{m+1}(\tau)+m\Psi'_{m-1}(\tau)+(2m+1)(1-\omega f_m)\Psi_m(\tau)=4\pi\,(1-\omega)\,I_B(T)\,\delta_{0m} \qquad (9)$$

where δ_{0m} is the Kronecker symbol, (') corresponds to the first derivative and m is an integer positive or equal to zero.
This is a system of (m+1) coupled differential equations. We are going to simplify the resolution of this system by using the P1 approximation.

I.2.1. P1 approximation [4]

The order of the approximation corresponds to the number of terms in the series, namely N. (P1 approximation means N=1). We will now consider isotropic scattering and the system of equations. reduces to:

$$\Psi'_1(\tau)+(1-\omega)\Psi_0(\tau)=4\pi(1-\omega)I_B(T)$$
$$\Psi_0(\tau)+3\Psi_1(\tau)=0\ . \qquad (10)$$

Using the orthogonality relation of the Legendre polynomials, Ψ_0 and Ψ_1 can be related to I by:

$$\Psi_0(\tau)=2\pi\int_{-1}^{1}I(\tau,\mu)\,d\mu$$
$$\Psi_1(\tau)=2\pi\int_{-1}^{1}\mu\,I(\tau,\mu)\,d\mu\ . \qquad (11)$$

These expressions help to give a physical meaning to Ψ_0 and Ψ_1: they are the first two moments of the intensity and can be identified as the incident radiation (Ψ_0) and the net radiative flux (Ψ_1). From now on, we will write I_0 and I_1 instead of Ψ_0 and Ψ_1 in all our expressions.

Using these notations, I is expressed (from Equ.8) with respect to its first moments by:

$$I(\tau,\mu)=\frac{1}{4\pi}\left[I_0(\tau)+3\mu\,I_1(\tau)\right] \qquad (12)$$

with the closing relation:

$$I_1(\tau)=-\frac{1}{3}I'_0(\tau) \qquad (13)$$

and the RTE becomes finally:

$$\frac{\partial^2 I_0}{\partial \tau^2}(\tau)=3(1-\omega)\left[I_0(\tau)-4\pi I_B(T)\right] . \tag{14}$$

I.2.2 Boundary conditions

We employ the Marshak boundary conditions. To calculate them, we first have to write an energy balance on each boundary:

$$\begin{aligned} I(0,\mu) &= \varepsilon_1 I_B(T_1)+(1-\varepsilon_1)I(0,-\mu) \qquad \mu>0 \\ I(\tau_0,-\mu) &= \varepsilon_2 I_B(T_2)+(1-\varepsilon_2)I(\tau_0,\mu) \qquad \mu<0 \end{aligned} \tag{15}$$

Then, following the spherical harmonics method, we multiply both sides of these equations by $Y_n(\mu)$ and integrate over μ [4].

This way, the boundary conditions are suitable to the P-N approximation (P1 here) and there is no more angular dependency. The results for Marshak boundary conditions (for the geometry shown on Fig.2) are:

$$\begin{aligned} I_0(0) + \frac{2(2-\varepsilon_1)}{\varepsilon_1} I_1(0) &= 4\pi I_B(T_1) \qquad \text{for } z=0,\ T=T_1,\ \varepsilon=\varepsilon_1 \\ I_0(\tau_0) - \frac{2(2-\varepsilon_2)}{\varepsilon_2} I_1(\tau_0) &= 4\pi I_B(T_2) \qquad \text{for } z=L,\ T=T_2,\ \varepsilon=\varepsilon_2 \end{aligned} \tag{16}$$

I.3. Aerosol optical properties [6]

To compute the radiative transfer equation, it is necessary to determine the aerosol optical properties: the scattering and extinction coefficients used to calculate ω and τ. Depending on the relative value of the particle size (radius r) to the wavelength (λ) of the incident radiation, one can use three different theories. Let us define the Mie parameter α by:

$$\alpha=\frac{2\pi r}{\lambda} . \tag{17}$$

If r is much smaller than λ ($\alpha < 0.2$) then, the Rayleigh theory applies.
If r is of the order of magnitude of λ ($\alpha \approx 1$) then the Mie theory applies.
If r is greater than λ ($\alpha > 300$) we are in the optical geometry domain.

In our case, we can either be in the Mie theory domain (for large aerosols) or in the Rayleigh theory domain (for small aerosols). Those two theories allow us to calculate the extinction and scattering efficiencies (Q_e and Q_S), which are directly related to the extinction and scattering coefficients by:

$$\begin{aligned} K_a &= \int_{\text{over all r}} \pi r^2 Q_a(r) N(r)\, dr \\ K_s &= \int_{\text{over all r}} \pi r^2 Q_s(r) N(r)\, dr . \end{aligned} \tag{18}$$

The result using the Mie theory is:

$$Q_s = \frac{2}{\alpha^2} \sum_{n=1}^{\infty} (2n+1)\,(|a_n|^2 + |b_n|^2)$$

$$Q_e = \frac{2}{\alpha^2} \sum_{n=1}^{\infty} (2n+1)\,\mathrm{Re}(a_n + b_n) \qquad (19)$$

where a_n and b_n are the Mie coefficients; and the result using the Rayleigh theory is:

$$Q_s = -\,4\alpha\,\mathrm{Im}\left(\frac{m_c^2 - 1}{m_c^2 + 2}\right)$$

$$Q_e = -\,4\alpha\,\mathrm{Im}\left(\frac{m_c^2 - 1}{m_c^2 + 2}\right) + \frac{8}{3}\alpha^4 \left|\frac{m_c^2 - 1}{m_c^2 + 2}\right|^2 . \qquad (20)$$

Those efficiencies (both from Mie and Rayleigh theory) depend on:
- the Mie parameter (therefore the aerosol radius),
- the real and imaginary parts of the complex index of refraction $m_c = n_r - ik_i$.

II. MODELING

We describe here the main features of the one-dimensional numerical model.
Consider a slab (as the one defined by Fig. 2) with two boundaries such that T_2 is lower than T_1.
The model takes into account the radiative transfer through a given aerosol cloud (the size and concentration distribution with respect to the elevation in the medium are known).

Description:

Given aerosol data as function of the position, we calculate the extinction and scattering coefficient profiles into the volume.
Then, to determine the intensity distribution, we solve the radiative transfer equation (given in the P1 approximation by Eq. 14). To match the aerosol distribution we write this equation in the z-coordinate. It is important to remember here that, from the structure of the aerosol cloud (different sizes and concentrations at each elevation), the extinction coefficient depends on the position. Then, the RTE becomes:

$$\frac{d^2 I_0}{dz^2}(z) = 3K_e^2(z)(1-\omega(z))\left[I_0(z) - 4\pi I_B(T(z))\right] + \frac{1}{K_e(z)}\frac{dK_e(z)}{dz}\frac{dI_0(z)}{dz} \qquad (21)$$

where $I_B(T)$ is the Planck black body function at a given temperature.
The above equation is solved by using a central finite difference scheme for the second derivative of I_0 and a forward scheme for the first derivative of I_0 and K_e. Equations (7), (10) and (12) are then used to calculate the radiative flux:

$$q_R(z) = \frac{1}{4} I_0(z) - \frac{1}{6}\frac{1}{K_e(z)}\frac{dI_0(z)}{dz} \qquad (22)$$

The boundary conditions are those given by expression (16) except that we suppose that the upper boundary does not send any energy (no emission and no reflection) into the medium. Therefore, in the z-system, Eq. (16) becomes:

$$I_0(0) - \frac{1}{3K_e(0)} \frac{2(2-\varepsilon_1)}{\varepsilon_1} \frac{dI_0(z)}{dz}\Big)_{z=0} = 4\pi I_B(T_1)$$

$$I_0(L) + \frac{2}{3K_e(L)} \frac{dI_0(z)}{dz}\Big)_{z=L} = 0 \qquad (23)$$

We also use a finite difference scheme to include these equations in our system.

Remark:
We investigated the behavior of the extinction coefficient with respect to the wavelength (λ) for two given values of the aerosol radius (r_1 and r_2) ; those values were chosen so that α (the Mie parameter given by (17)) was in the Mie domain for r_1 and in the Rayleigh domain for r_2. For each calculation r was fixed but λ (and then α) followed the temperature profile (see Fig. 3). The results showed little variations of the extinction coefficient with λ. Therefore, we decided to assume a gray medium.

III. RESULTS AND DISCUSSION

To give an example of the kind of result we could expect, we place our study into the framework of severe water reactor accident analysis. We are especially interested in the last stage of such an accident, when the corium interacts with the concrete basemate (MCCI). This phenomena generates a large amount of aerosols mainly composed of numerous products issuing from concrete decomposition.
Experimental programs have been performed to study the aerosol behavior. For this work we chose the example of the Advanced Containment Experiment program that took place in Argonne National Laboratory (1988-1990). Results, for example, from test L4 showed that the aerosol cloud is essentially composed of Silicium products and that the dominating species was SiO_2 [13].

Hypothesis:
Following [8] we chose to consider a cubic temperature profile in the gas layer above the corium melt (Fig. 3).

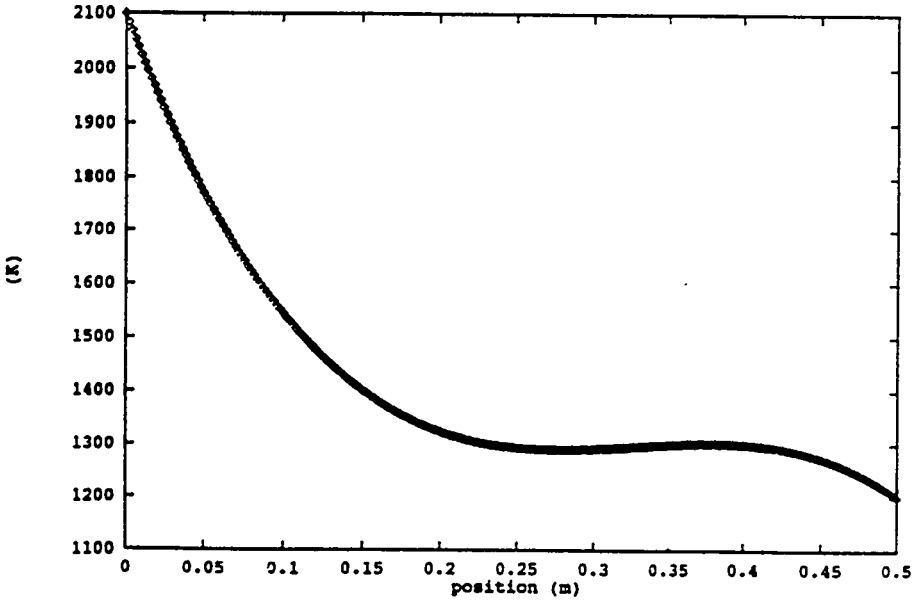


Figure 3: Temperature profile.

Figures 4 and 5 give the aerosol concentration and size distribution with respect to the position into the studied volume. These curves are idealized: their shapes are estimated from a one-dimensional

monocomponent aerosol generator described in [9]. In this generator, the medium (an Argon flow with a constant upward velocity equals to 3.2 cm/s) is over-saturated with SiO_2 vapor and aerosols are produced by homogeneous nucleation [10]. Aerosols grow by condensation/evaporation of vapor molecules and by aerosol droplet thermal coagulation [11]. This model takes into account aerosol settling, depending on the droplet size and the gas velocity [12].

In our example, the aerosol size distribution is a gaussian curve centered 3 cm above the pool with a most probable value of 2.4 micrometers (see Fig. 5). It has to be pointed out that above 4 cm the aerosol radii are quite small (10^{-10} to 10^{-9} m). Although very small, these aerosols are very numerous and the aerosol concentration remains around 0.4 kg/m^3 (see Fig. 4) for the next 45 cm.

Below 2 cm in the domain that we consider, the medium is not enough over-saturated, aerosol nucleation can not occur and radii and concentrations are equal to zero.

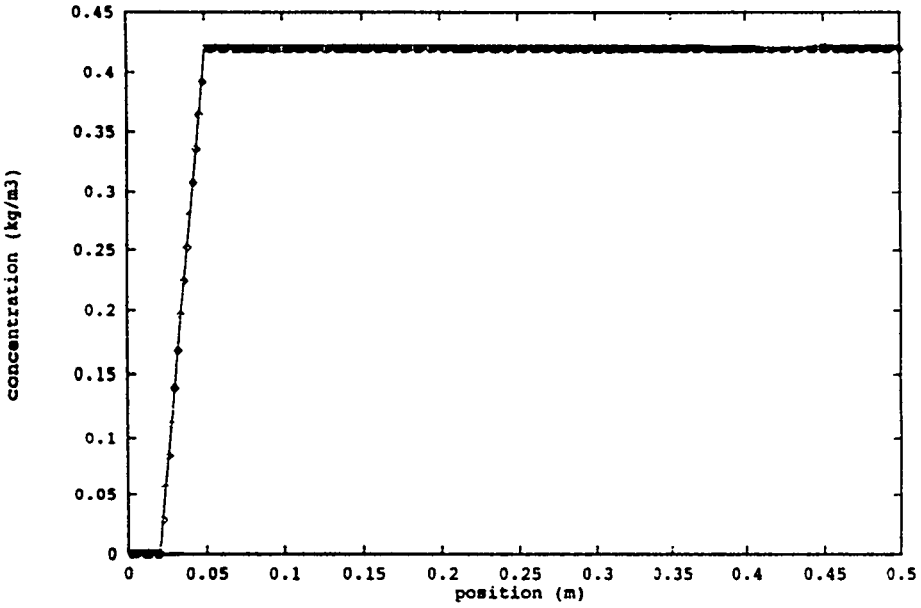


Figure 4: Aerosol concentration profile.

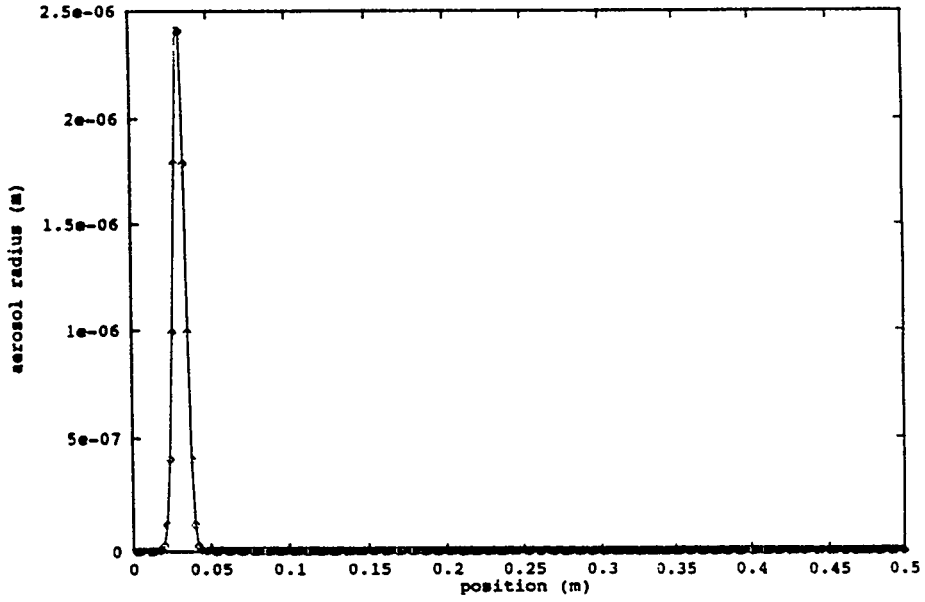


Figure 5: Aerosol size distribution.

Figures 6, 7 and 8 show the aerosol optical properties: absorption coefficient, scattering coefficient and extinction coefficient with respect to the position. We notice that scattering only dominates for big aerosols which are present only on a very small part of the domain. Elsewhere, the absorption coefficient is the most important. The resulting extinction coefficient (Fig. 8) is very peaked around 3 cm.

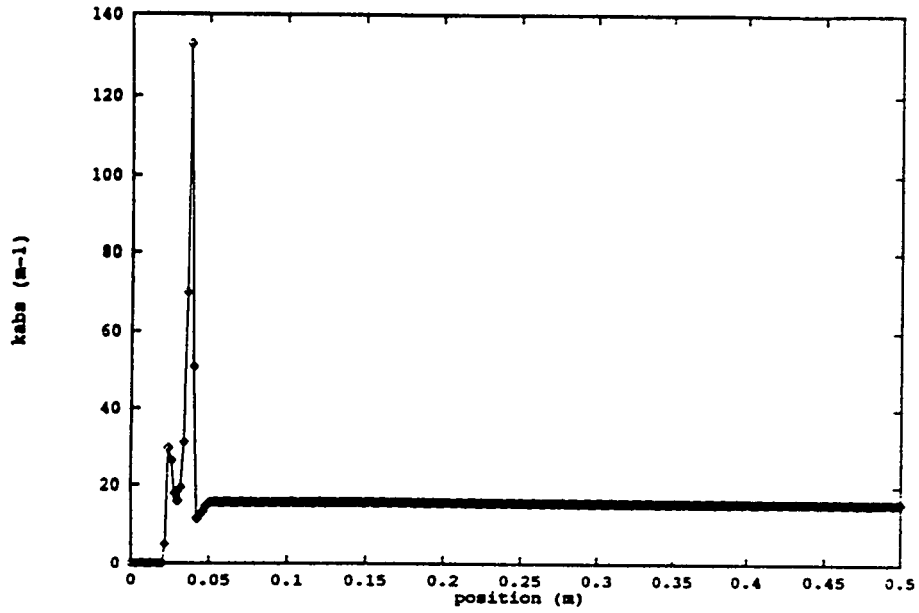


Figure 6: Absorption coefficient with respect to the position.

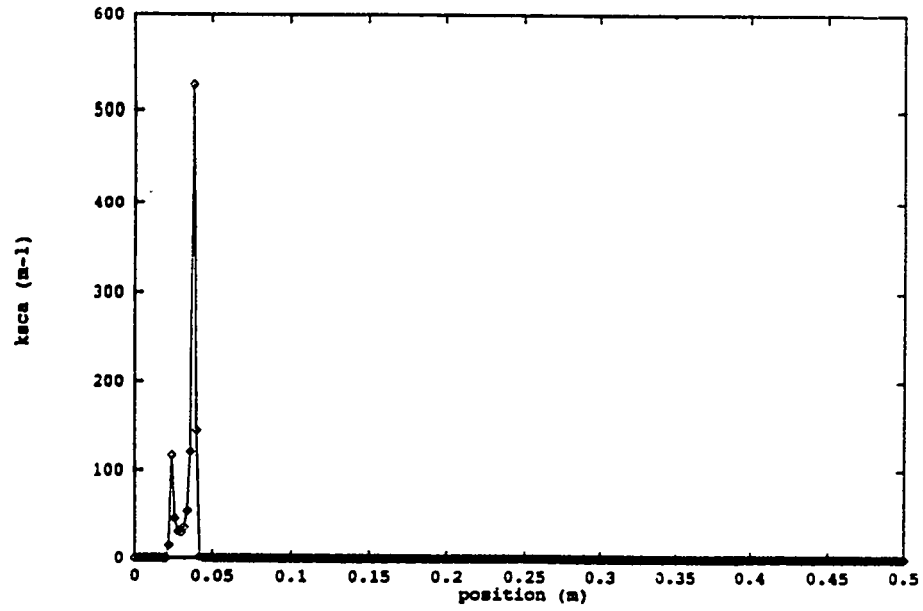


Figure 7: Scattering coefficient with respect to the position.

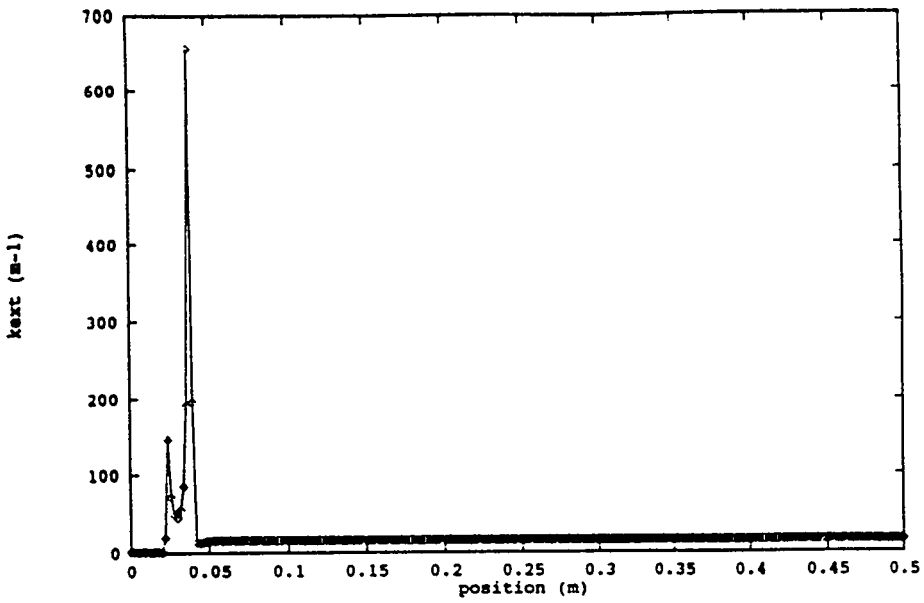


Figure 8: Extinction coefficient with respect to the position.

We previously explained that there are no aerosols below a certain position (2 cm). However, as vapor is certainly present in this area, we chose to set the extinction coefficient to 1.0 m^{-1}, to represent the small absorption due to the vapor molecules.
Figures 4 to 8 are then consistent and define the properties of the medium in which the thermal radiation from the corium pool propagates.

Here are the numerical data we use to perform our calculation:

Temperature of the corium pool:	2100 K (see Fig. 3)
Emissivity of the corium pool:	0.9
Temperature of the upper boundary:	1200 K (see Fig. 3)
Thickness of the layer:	0.5 m
Spatial step:	2.10^{-3} m
Aerosol size distribution:	Gaussian curve (see Fig. 5)
Aerosol concentration distribution:	See Fig. 4
Aerosol complex index of refraction:	$m_c = 4.07 - 0.095i$ [13]
Radiation wavelength:	$\lambda = 1.5.10^{-6}$ m

Results:
Figure 9 shows the radiative flux distribution in the domain of interest. The calculated flux at the top of the enclosure (z=0.5 m) is about 0.15 MW/m^2. A precise comparison between our calculations and the experimental results is not possible. However, from experimental curves for the sidewall power loss and the lid power loss, one can estimate the "true upward heat loss" from a correction to radiative losses to the sidewall. If ACE was a one-dimensional experiment, the out-going flux is calculated to be around 0.11 MW/m^2 for test L4. One notes that our one-dimensional analysis results are in good agreement.

This example shows how the radiative flux can be strongly reduced, due to the presence of aerosol droplets at high concentration:

z = 0 m -> $q_R = 1.0$ MW/m^2
z = 0.5 m -> $q_R = 0.15$ MW/m^2.

It has been reduced by a factor 6 to 7 between the corium pool and the upper boundary.

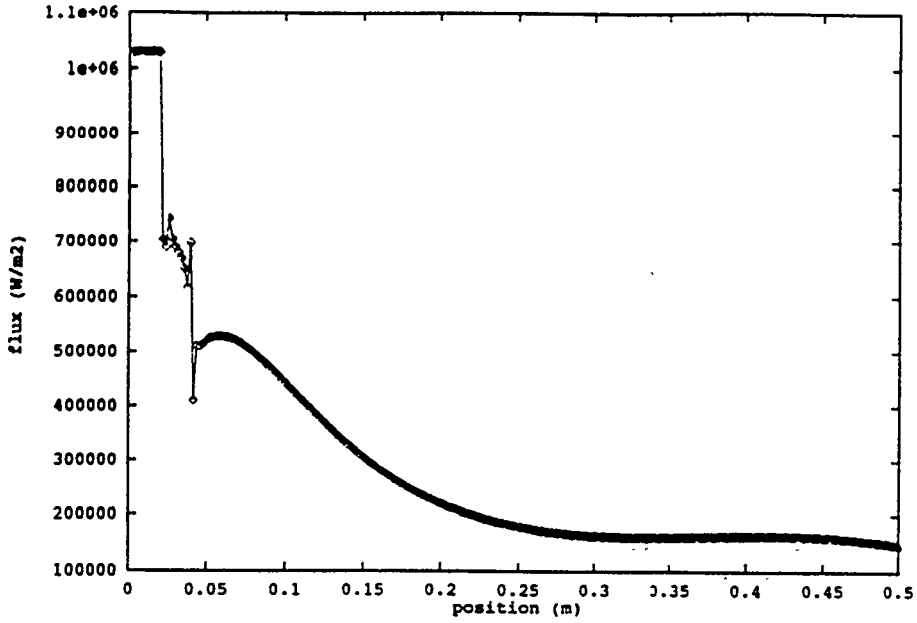


Figure 9: Radiative flux with respect to the position.

CONCLUSION

We presented here a one-dimensional model to perform a radiative transfer calculation in a dense aerosol cloud. Aerosol optical properties were determined by the Rayleigh or Mie theory, depending on their size. The radiative transfer equation was then solved, using the first order spherical harmonics approximation (P1) and the radiative flux was calculated. An example of the radiative flux distribution for given aerosol size and concentration distributions in the medium was presented. We could not perform any precise comparison with experimental data. However, from experimental curves, we could estimate the "true upward heat loss" from a correction to radiative losses to the sidewall. Our results were in good agreement with an one-dimensional estimate of the experimental results.

One can note that the aerosol cloud strongly reduced the upward heat losses by participating in the heat exchange.

ACKNOWLEDGMENTS

The authors would like to acknowledge Drs. Claire De Pascale (CEA. France), Nadia Coulon (CEA. France) and Patrick Vigliano (Université Aix-Marseille I, France) for helpful comments and ideas.

We are also very grateful to Prof. Michael Corradini (University of Wisconsin, Madison. USA) for fruitful discussions and advice.

NOMENCLATURE

I	= radiative intensity, W/m^2
I_B	= black body intensity (Stefan law), W/m^2
I_i	= moments of the radiative intensity, W/m^2
k_i	= imaginary part of the complex index of refraction
K_a	= absorption coefficient, m^{-1}
K_e	= extinction coefficient, m^{-1}

K_s = scattering coefficient, m^{-1}
l = given distance, m
m_c = complex index of refraction
n_r = real part of the complex index of refraction
$p(\Omega,\Omega')$ = phase function
P_n = Legendre polynomials
q_R = radiative flux , W/m^2
Q_e = extinction efficiency
Q_s = scattering efficiency
r = aerosol radius, m
T = temperature, K
Y_n = spherical harmonics

Greek letters:

α = Mie parameter
ε_i = boundary (i=1 or 2)
λ = radiation wavelength, m
μ = cos θ (see figure 2)
τ = optical thickness
σ = Stefan constant
ω = scattering albedo

REFERENCES

[1] Fink J.K., Thompson D.H., Spencer B.W., Sehgal B.R. - Aerosol release during large scale integral MCCI test in ACE program - presented at the OECD CSNI Specialist Meeting on Core Debris Concrete Interaction - Karlsruhe, Germany, April 1-3, 1992.

[2] Murata K.k. *et al.* - User's manual for CONTAIN 1.1: a computer code for severe nuclear reactor accident containment analysis - NUREG/CR-5026 - 1989.

[3] Reinman M., Murfin W.B. - The WECHSL code: a computer program for the interaction of a core melt with concrete - KfK 2890 - 1981.

[4] Ozisik N. - Radiative transfer and interaction with conduction and convection - Wiley & Sons - 1973

[5] Hottel H.C. Sarofim A.F. - Radiative transfer - McGraw Hill book compagny - 1967

[6] Van de Hulst H.C. - Light scattering by small particles - Dover Publication, New York - 1981

[7] Fink J.K. - ACE MCCI test L4: test data report, aerosol analysis - ACE-TR-C10 vol2. 1990

[8] Furukawa O., Furutani A., Hattori N., Iguchi T. - Experimental study of heat transfer through cover gas in the LMFBR - Liquid metal engineering and technology, BNES London - 1984.

[9] Zabiégo M., Lambert E., Cognet G. - Aerosol generation and growth in the later phase of a severe reactor accident- Proceedings of the International Conference on "New Trends in Nuclear System Thermohydraulics" Pisa, Italy, May 30th to June 2nd 1994.

[10] Dunning W.J. - General and theoretical introduction to nucleation - in Nucleation edited by Zettlemoyer A.C., Dekker, New York - 1969.

[11] Hinds W.C. - Aerosol technology: properties, behavior and measurement of airbone particles - J. Wiley & Son - 1982.

[12] Fuchs N.A. - The mecahnics of aerosols - Pergamon Press - 1964.

[13] Lide D.R. - Handbook of chemistry and physics - 72nd edition - 1991-1992.

MODELING OF HEAT AND MASS TRANSFER PROCESSES DURING CORE MELT DISCHARGE FROM A REACTOR PRESSURE VESSEL

T.N. Dinh, V.A. Bui, R.R. Nourgaliev, T. Okkonen and B.R. Sehgal

Royal Institute of Technology, Division of Nuclear Power Safety
Brinellvägen 60, 10044 STOCKHOLM, SWEDEN
Fax:(46) (8) 790-76-78, e-mail: nam@ne.kth.se

Abstract

The objective of the paper is to study heat and mass transfer processes related to core melt discharge from a reactor vessel in a severe light water reactor accident. The phenomenology of the issue includes (1) melt convection in and heat transfer from the melt pool in contact with the vessel lower head wall; (2) fluid dynamics and heat transfer of the melt flow in the growing discharge hole; and (3) multi-dimensional heat conduction in the ablating lower head wall. A program of model development, validation and application is underway (i) to analyse the dominant physical mechanisms determining characteristics of the lower head ablation process; (ii) to develop and validate efficient analytical/computational methods for estimating heat and mass transfer under phase-change conditions in irregular moving-boundary domains; and (iii) to investigate numerically the melt discharge phenomena in a reactor-scale situation, and, in particular, the sensitivity of the melt discharge transient to structural differences and various in-vessel melt progression scenarios. The paper presents recent results of the analysis and model development work supporting the simulant melt-structure interaction experiments.

1 INTRODUCTION: PHENOMENOLOGY AND PROBLEMS

In a light water reactor core meltdown accident (severe accident), the molten core material could cause a failure of the lower head of the reactor pressure vessel (RPV), if sufficient internal or external cooling of the vessel could not be provided. Depending on the vessel design and accident sequence in question, the lower head integrity could be lost due to a global or local creep rupture of the lower head wall or - if the lower head had penetrations - a local penetration failure [1]. With a local creep or penetration failure the growth of the initial lower head failure site, due to heat transfer from the ejected melt (corium) at a higher temperature ($T_f \sim 2000 - 3000K$) than the vessel melting point ($T_{w,mp} \sim 1790K$), could enhance the melt ejection rates. Melt-induced loads on the containment and any further accident progression - involving interactions between core melt and the coolant, structures and atmosphere in the reactor cavity of a pressurized water reactor (PWR) or in the pedestal (lower drywell) or suppression pool of a boiling water reactor (BWR) - would largely depend on the melt ejection characteristics.

Previous work on melt interactions with the vessel wall has been largely analytical [1], except for the experiments conducted at SNL; for a relevant review, see [2]. These experiments, on hole ablation, were performed with iron-alumina thermite and covered a limited range of

the hole ablation problematics. The experimental data received from these experimental studies have been used to evaluate the ablation rate formula implemented in the integrated severe accident computer codes like MELPROG and MELCOR. For the hole ablation issue, phenomenological models have recently been developed by Pilch [2]. Most recent studies employed a one-dimensional formulation which equates the energy required to melt the wall material (steel, crust, etc.) to the energy transferred from the molten fuel passing through the orifice. Comparing to former studies [3],[4], these methods employed the difference between the temperature of the molten fuel (T_f) and the melting temperature of the wall ($T_{w,mp}$), instead of the difference between the temperature of the molten fuel (T_f) and its melting point ($T_{f,mp}$). The analytical relationships have shown that the past experiments did not cover the range of characteristic numbers typical for either local penetration failures or a circumferential vessel creep rupture [5]. Because the models have been based on experimental observations and data obtained in a relatively narrow range, it is not clear that the assumptions on physical mechanisms and correlations made in the above-mentioned models of the hole ablation process will hold for reactor-scale situations. The lack of experimental evidence supporting or contradicting the applied melt ejection and hole growth models was emphasized also in the recent DCH study for the Zion PWR [5].

Melt ejection and lower head ablation experiments, using an oxidic melt material ($T_f \sim 1000 - 1500K$) discharged from a vessel with a low-melting-point, metallic lower head ($T_{w,mp} \sim 600 - 900K$), are underway at the Royal Institute of Technology (KTH), Stockholm. Up till now we have been working with the oxidic, glass-type melt mixture $PbO - B_2O_3$ (80-20 wt%). It has a melting point of about 900K and its melt-phase viscosity of about 0.1 Pa.s increases under freezing, a characteristic of the core melt as well. In the scoping tests on vessel ablation, pure lead with a melting point of 600K has been used as the lower head material. The integral scaling is based on the method introduced by Pilch in [2]. It has been shown that we need melt volumes of the order 10-100 liters to reach integral process characteristics relevant for such reactor cases, where the initial lower head failure site is small compared to the vessel melt contents. In the scoping experiments that we have performed so far with melt volumes of about 3-7 liters, the melt has been quite much superheated; the lead plate thickness has been varied in the range of 2-4 cm [6]. To support the design and the analysis of the experimental results, as well as their use for reactor cases, a detailed analytical model is being developed. In the present paper, we will focus on physical modeling.

For reactor safety analyses and accident management considerations, the primary interests are the *hole growth dynamics* [$D_{hole}(t)$] and *melt discharge flow parameters* (melt flow rate, superheat, composition). In this sense, all potentially significant aspects have to be identified and evaluated for reactor-specific scales and conditions. The considerations of phenomenology are built around three key elements: the thermal-hydraulic behavior of core melt in the vessel lower head, the fluid dynamics and heat transfer in the melt ejection hole, and the thermal and physical (phase-change, mass-transfer) response and feedback of the lower head wall, during core melt discharge from the RPV; see Fig.1.

For melt pool thermohydraulics, the flow fields in the pool during the discharge process are related to phenomena of large uncertainties. Because the convective heat fluxes (from melt flow to discharge hole boundaries) form the driving mechanism of vessel ablation, the heat transfer characteristics of a laminar entry region in experiments and those of a turbulent entry region in prototypic situations have to be analysed in an accurate manner. Based on tentative identification, ranking and evaluation of related physical mechanisms, the most critical phenomena are considered to be crust formation and relocation dynamics, temperature dependence of melt properties, and multi-dimensional heat conduction and ablation front propagation in the vessel

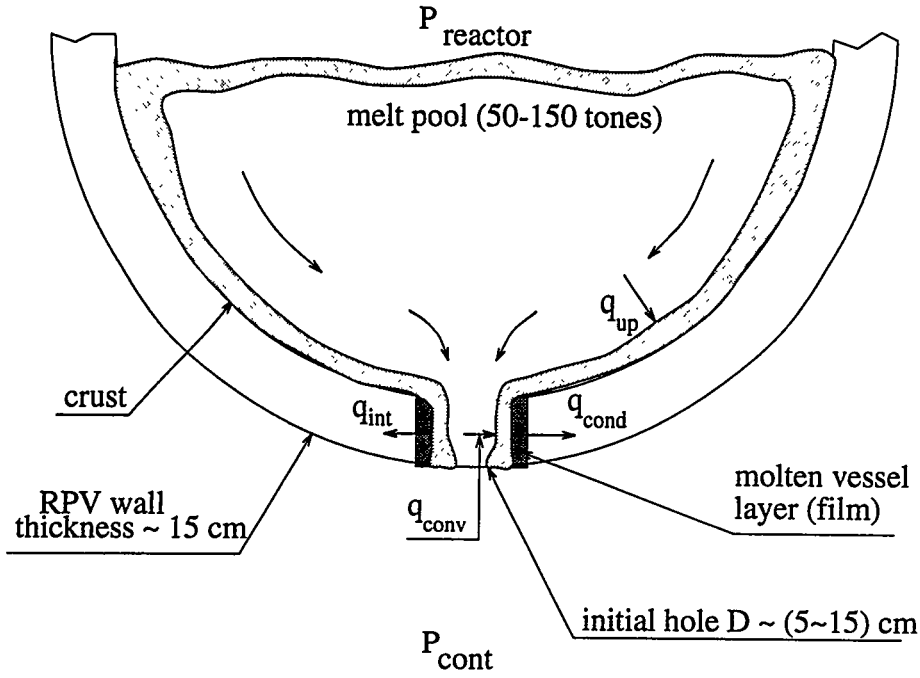


Figure 1: Overall scheme of the hole ablation phenomenology.

wall beneath the crust.

The basic objective of model development is to study the phenomenological scalability of experiments, the quality of correlative models, and the physics of limiting mechanisms. In order to ensure direct applicability of the data base, all effects should be confirmed to be prototypical from the melt flow, heat transfer, wall behavior and crust integrity point of view. Because this is hard to achieve, we must be able to differentiate between various effects dominating in our tests and to address their relevance to the reactor case. Analytical modeling helps considerably in this task. The limiting mechanisms are attacked (first) separately, and separate effects data are used to validate analytical modeling. The major advantage of the models described in this work is that we have intended to employ - whenever reasonable - only first-principle formulations or well-supported assumptions on physical mechanisms. Such an approach avoids direct applications of empirical correlations in studying *separate effects*. Calculational data obtained are used to assess the applicability of available correlations for heat transfer and then friction under prototypical and experimental conditions of interest. Furthermore, new or modified correlations can be employed in the integrated code HAMISA to describe multi-dimensional effects of the ablation processes.

2 MODELING OF MELT DISCHARGE AND VESSEL WALL ABLATION

In order to approach the subject, we employ a stepwise research scheme. In the first stage, the modeling efforts emphasize *integrated thermal hydraulics* of the melt ejection and lower head ablation processes. The code named HAMISA.1D [1] has been developed to perform sensitivity estimates of a set of phenomena involved in the melt ejection process and to do scaling calculations for the experimental facility design. The code considers two basic cases: (1) lower head failure and core melt discharge in the RPV configuration; and (2) experimental cases with some

[1]The HAMISA stands for Hole Ablation Modeling In Severe Accidents.

metallic material as the lower head and oxidic material as the corium simulant. The mathematical models of the HAMISA.1D include point kinetics of mass and energy conservation in the melt pools, a set of transient, one-dimensional equations of mass, momentum and energy conservation of melt flow in the growing discharge hole, as well as the closure correlations required. These equations form a set of non-linear differential equations integrated within a time loop and along the hole. The fourth-order Runge-Kutta method is applied for numerical treatment. The code determines discharge flow rate from the so-called P-SOLUTION algorithm, and performs the melting calculations in an axisymmetric geometry for melt-plate heat transfer and tracking of the ablation front. Thus, the code can provide the hole ablation rate, $\dot{D}_{hole}(t,z)$, and the melt mass discharge rate, $U_{ejection}(t)$, as function of time, and the results can then be compared to the data obtained in the experiments. The code varies the melt properties, e.g., viscosity and thermal conductivity, as function of temperature. The accuracy of the numerical methods employed has been tested against analytical solutions available for limiting cases. Furthermore, the HAMISA.1D code has been used to describe the SNL tests, with reasonable agreement between calculational results and data. Results of the HAMISA.1D calculations have been presented elsewhere [6].

In general, the *dynamic analysis* has shown that the calculational results of the 1-D and transient models are similar to the results obtained with simplified models [2]. This fact can be explained by the short time period of the discharge process analysed and the similar approach applied to define the ablation rate. One should also note that large melt superheats and small temperature differences between melting points of simulant (thermite melt) and vessel wall metal in the previous experiments could have dampened thermal effects of crust formation (if any). Furthermore, calculations performed for reactor-specific situations demonstrate significant bifurcations of ablation dynamics depending on whether a stable crust layer exists or not. The presence of the crust involves lower rates of vessel wall ablation in the initial phase, amplifying thereby the effects of pre-heating and heat conduction in vessel wall and test plates. Due to such spatial and temporal complications, detailed multidimensional and dynamical analyses were considered to be necessary in order to support experimental design and interpretation, as well as extrapolation of the experimental results to reactor conditions.

2.1 Melt pool thermal hydraulics

The thermal hydraulics of the melt pool in the hole ablation problematics has specific goals that are (i) to evaluate the thermal state of the RPV wall and the thickness/composition of the crust lying on the lower head prior to the discharge process, and (ii) to model the forced convection and heat transfer phenomena during melt discharge from the RPV. For the purpose of this study, a model has been developed and employed to describe two-dimensional fluid flow and heat transfer in a complex geometry [7]. The modified low-Reynolds-number turbulence model is applied to predict heat transfer characteristics from the melt pool to its frozen boundaries [8]. The heat fluxes obtained are then employed to calculate quasi-static thickness of the crust between the melt pool and the vessel wall [2]. During the melt discharge process, heat fluxes from melt flow to the crust-vessel wall structure can remelt such crust (solidified fuel) layers. Calculations performed show that under both experimental and prototypical conditions, the pool flow during the discharge processes is mostly laminar. This is due to the low vessel overpressurization in our experiments, and the large ratio between the melt pool radius and the discharge hole radius in reactor cases.

[2] In this section, the crust refers to solidified fuel on the inside of the RPV lower head.

2.1.1 Heat transfer results

The laminar model was used to analyse geometrical and regime effects on heat transfer to the top surface of the vessel wall during the melt discharge process in small-scale experiments and in prototypical situations. Both the oxidic melt simulant and core melt were employed as the respective working fluids, with temperature dependent viscosity. For experimental conditions the Nusselt number, Nu_{up}, is shown to depend on the Reynolds number, Re_{hole}, the ratio between the pool radius and the discharge hole radius ($\frac{r_{pool}}{r_{hole}}$), and the dimensionless distance from the hole inlet, r^*, as follows:

$$Nu_{up} \simeq 1.2 \cdot Re_{hole}^{1/2} \left(\frac{r_{pool}}{r_{hole}}\right) \cdot (r^*)^{-2/3} \tag{1}$$

A limited number of calculations also have been performed for reactor-specific conditions. In general, the Nusselt number, Nu_{up}, obeys eq.(1). The correlation developed ($\pm 20\%$ for near-hole regions) can be applied to assess the remelting process of crust overlying the top surface of the vessel wall and test plate.

2.1.2 Flow fields results

In analyses of the melt pool flow fields during discharge one needs to know the conditions (overpressure, geometry of pool and hole, viscosity, melt volume) under which significant non-uniformities (central suppression) of the melt surface could occur. This process is ofren referred to as blowthrough phenomena, which have been studied extensively. Prototypical (reactor) situations under consideration might involve several complications. For instance, an overlying crust in the molten pool in the reactor vessel lower plenum may influence the free surface flows associated with gas blowthrough. However, such detailed effects are yet to be addressed in further experiments and analyses and are out of the scope of the present study.

In general, first-principle modeling of the gas blowthrough processes would eventually include the task of determining the interfacial geometry. This would be a very laborious computational exercise, and a reliable numerical scheme would have to be developed for dynamic free surface tracking with 3D vortex flows in complex geometry domains. In addition, this problem might have a continuum of solutions corresponding to arbitrarily prescribed interface shapes. Furthermore, physical situations in question might be highly unstable, necessitating thus flow instability analysis [10]. We are not aware of extensive computational efforts in predicting gas blowthrough dynamics. In contrast, several correlations have been obtained through the past studies, which have been derived mainly from dimensional analysis and empirical fitting with the experimental data; see e.g. [9]. Gluck et al. proposed a correlation for gas blowthrough onset in flat and hemispherical bottomed cylinders [12],[13],

$$\frac{H_{pool,gb}}{D_{hole}} = 0.43 \frac{D_{pool}}{D_{hole}} tanh\left(Fr^{1/2} \frac{D_{hole}}{D_{pool}}\right) \tag{2}$$

Recently, Pilch and Griffith have collected and examined a number of correlations describing gas blowthrough in regard to their applicability to accident situations with core melt discharge from RPV [11]. It was also noted in ref.[11] that only the Gluck correlation embodies the effects

of tank diameter and the data base of this correlation spans the range of the Froude number $Fr = \frac{U_{ejection}}{\sqrt{g \cdot D_{hole}}}$ and D_{pool}/D_{hole} values of reactor applications. Therefore, the Gluck correlation was recommended for use in DCH analyses. However, it could be shown that there are no significant effects of the ratio $\frac{D_{pool}}{D_{hole}}$ under the RPV hole ablation and melt discharge conditions (i.e. D_{pool} ~3.6m and D_{hole} in the range 0.05-0.5m).

In the present work, we are interested in the onset of gas blowthrough, rather than the annular gas-liquid discharge flow dynamics. For this purpose, a quasi-steady 2-D formulation is used to calculate flow and pressure fields in a test crucible and RPV lower plenum with melt discharge through holes of different sizes. It can be shown that the boundary layer thickness in the hemispherical pool is so small that the whole flow field could be treated as potential flow. Nevertheless, the grid independence of numerical solutions has been examined, based on results of comparative calculations with computational meshes of different refinements. Calculations employing a low-Reynolds-number turbulence model indicates that shear-induced turbulence generation takes place only nearby the hole inlet and does not affect the pressure field results of interest. The laminar model is then applied to calculate flow and pressure fields.

Fig.2 describes the calculated velocity field in a hemispherical lower head during the core melt discharge process. Calculational data of dynamic pressure field were analysed to evaluate potential "crater formation" in the melt pool. First, dynamic pressure distributions on various elevations from the lower plenum bottom are compared to hydraulical heads of the respective melt column; see Fig.3. It is hypothesized in the present work that at the critical pool depth the maximum variation of the dynamic pressure (i.e. above the discharge hole) is equal to the corresponding hydraulical head, inducing such deformation of the free surface that enables gas entrainment into the discharge flow. Fig.4 depicts the technique used to determine the blowthrough onset. Comparison of numerically determined critical pool depth with the experimental correlation of Gluck et al. for the hemispherically bottomed cylinders is given in Fig.5. One can see that a good agreement is achieved for the parameter ranges of interest.

It is worth noting here that the present work assumes (at least partial) depressurization of the reactor coolant system prior to the melt discharge, i.e. the discharge flow rates are in the intermediate range of 3-10m/s. The moment when a melt pool crater starts to dominate the flow patterns in reactor cases can be evaluated in the integrated HAMISA modeling using the Gluck correlation. In addition, the relative critical pool depth ($k_{crater} = \frac{H_{pool,gb}}{D_{hole}}$) is decreased with increasing discharge hole diameter. It is shown that annular-type discharge regimes can occur only at the very end of the ablation and discharge process. For an initial melt mass of 100 tonnes, fractions of melt mass discharged in annular-type regime have been evaluated to be in the ranges 2-5% and 4-10% for cases with and without crust, respectively [3].

2.2 Discharge hole thermal hydraulics

In this section, we present some results of studies of heat, mass and momentum transfer related to core melt ejection through a circular hole in the RPV lower head. The control-volume based model has been developed to solve Navier-Stokes and energy equations in 2-D axisymmetric, narrowing channels with a constant wall-temperature boundary condition [7]. Axial diffusion of both momentum and heat as well as viscous dissipation are taken into account in the numerical simulation. Additionally, a low-Reynolds-number model of turbulence is applied due to the presence of laminar, transition-to-turbulence and turbulent regimes in reactor-scale processes.

[3] Note that crust affects the hole growth and the hole size.

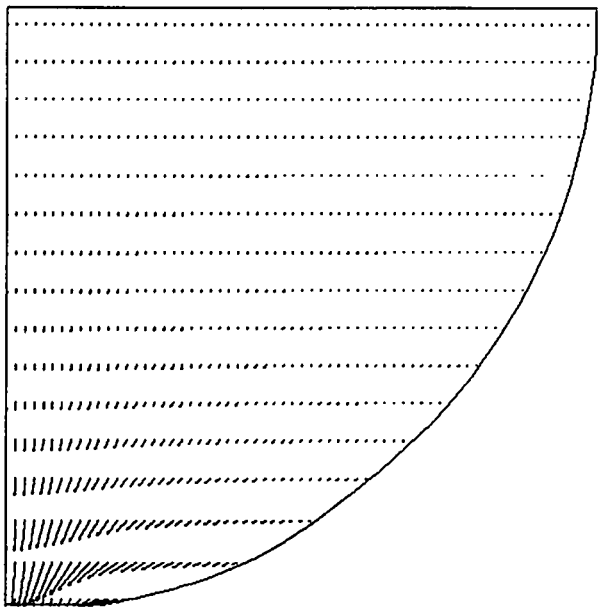


Figure 2: The velocity field during the core melt discharge process: $U_{ejection}$ = 10m/s, D_{hole} = 0.5m, D_{RPV} = 3.6m. The computational mesh for the lower plenum section 50x50.

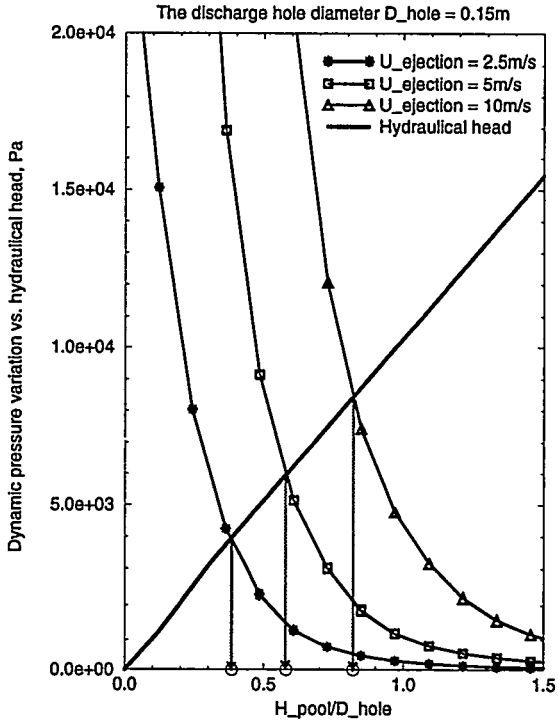


Figure 4: Determination of gas blowthrough onset from the dynamic pressure and hydraulical head of the liquid column above the hole (○ corresponds the critical pool depths).

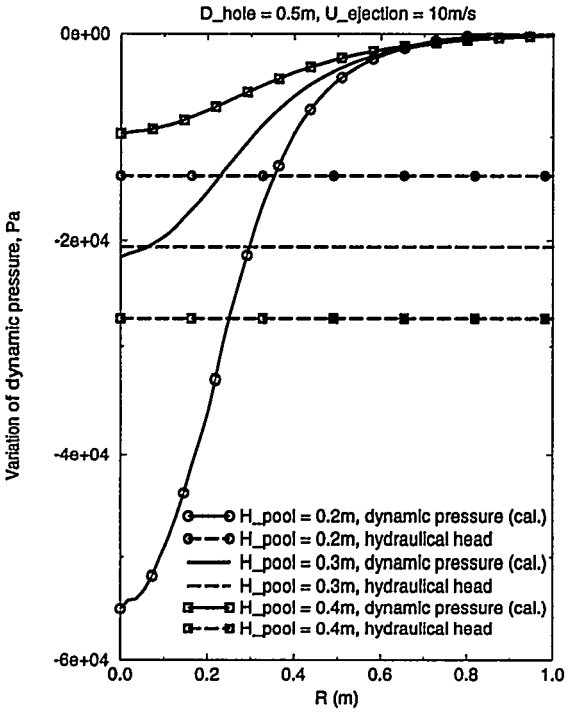


Figure 3: Calculated radial distributions of the dynamic pressure in core melt pool.

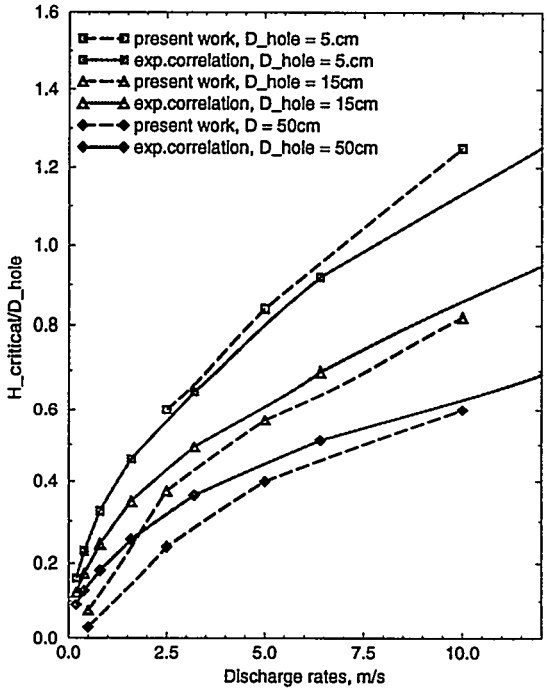


Figure 5: Comparison with the experimental correlation of Gluck et al.

By employing the first-principle-modeling approach, it is possible to examine the following set of specific effects: variation of viscosity and conductivity across the boundary layer due to freezing of the core melt near the wall, variation of velocity/temperature profiles at the hole inlet, variation of (narrowing) channel geometry, and variation of fluid Prandtl number. For limiting cases of interest, the calculational results obtained compare satisfactorily with previous boundary layer solutions, calculational results and experimental data found in the literature.

2.2.1 Experimental conditions

Since Reynolds numbers in experiments are sufficiently low, laminar flow is the most probable experimental regime. That is why detailed analysis of thermal hydraulics within the discharge hole under experimental conditions must be carried out in order to address the relevance of experiments to prototypical reactor conditions.

Pressure drop.

The apparent Fanning friction factor corresponds to pressure drop in a certain flow length through the duct. In a tube with its frictionless infinite upstream extent ($-\infty < z < 0$), the apparent Fanning friction factor is defined as follows:

$$f_{app}(z_*) = \frac{P(-\infty) - P(z_*)}{2Re_{hole}z_*} \tag{3}$$

In calculations presented in Table 1, it is assumed that the viscosity varies strongly in the sublayer ($0.95 < \frac{r}{r_{hole}} < 1$). The maximum value of the viscosity at the wall is as much as 25 times greater than the bulk viscosity. It can be seen that in the vicinity to the entrance, the property variation leads to more than two times higher values of the apparent Fanning friction factor. Note that z_* in the range of $10^{-4} - 10^{-3}$ characterizes parameters of experiments under consideration.

Table 1: The apparent Fanning friction factor.

$z_* = \Delta z/(D_{hole} \cdot Re_{hole})$	Apparent friction factor	
	μ_{fs} = var	μ_{fs} = const
$3.138 \cdot 10^{-4}$	464.3	222.8
$1.256 \cdot 10^{-3}$	170.9	102.9
$7.034 \cdot 10^{-3}$	60.9	44.7
$9.166 \cdot 10^{-1}$	19.4	16.3

The Nusselt number.

Table 2 presents results of heat transfer calculations for four cases. The first case is the standard case without property variation. The second case shows effects of the above-described variation of viscosity across the sublayer on heat transfer. The third and fourth cases include variations of both viscosity and conductivity across the sublayer. The conductivity is decreased near the wall parabolically. Values of the fluid conductivity in the wall-fluid interface are

two and ten times smaller than that of the bulk conductivity, for the third and fourth cases, respectively. Values of the Reynolds number are constant for four cases, and equal to 500. In fact, the effects of property variations on heat transfer are even greater than those shown in Table 2, due to the fact that the discharge mass flow rates are also reduced (see Table 1 for the apparent Fanning friction factor). Similar calculations have also been performed for reactor processes by means of the low-Reynolds-number turbulence model. Most notably, there is also a laminar boundary-layer flow development in the very short section of the discharge hole ($z_+ \sim 10^{-6}$). However, there are two different factors affecting effects of temperature dependence of fluid properties on heat transfer rates. First, the lower are the values of z_+, the more significant are the effects of fluid properties, due to the smaller thickness of the boundary layer with property variation. Second, the Reynolds numbers are higher under prototypical conditions, which decreases temperature variations along and across the flow sections.

At the present range of applications, one can conclude that temperature dependence of transport properties needs to be accounted for in evaluation of pressure drop and heat transfer coefficients inside the discharge hole. However, there remains the principal question about *real* variations of melt properties in temperature range near the melt solidus point. Due to large uncertainties of heat transfer rates in (short) discharge holes under prototypical situations, experimental data with higher Reynolds numbers employing melt simulants with temperature-dependent viscosity are required to confirm order-of-magnitude assessments of convective heat fluxes and formulation of boundary conditions for a freezing melt flow with a wide mushy region [$\Delta T_{mushy} = (T_{liquidus} - T_{solidus}) \sim$ (150-200)K].

Analyses performed for converging ducts show dual effects of such geometry: narrowing channels cause a flow laminarization but can also expose channel walls to direct hotter melt entering from the pool into the hole-wall boundary layer. Such aspects require further modeling work coupling melt thermal hydraulics in the hole and the pool. Thermal convection for non-Newtonian fluid in the (laminar/turbulent) entry region of a duct is another fundamental aspect that could change heat transfer rates as much as two times. It is not certain whether the core melt and its oxidic simulant act in accordance with Newtonian formulation, especially for cases with small melt superheats above the melt solidus point.

Table 2: The Nusselt number in laminar flows.

$z_+ = \Delta z/(D_{hole} \cdot Pe_{hole})$	Nusselt numbers			
	μ, k = const	μ = var	μ, k = var; $\frac{k_w}{k_b}$=0.5	μ, k = var; $\frac{k_w}{k_b}$=0.1
$3.138 \cdot 10^{-4}$	22.21	15.81	14.47	11.70
$1.256 \cdot 10^{-3}$	11.56	9.82	9.34	8.19
$7.034 \cdot 10^{-3}$	5.82	5.39	5.26	4.92
$9.166 \cdot 10^{-1}$	3.65	3.44	3.37	3.21

Discharge coefficient.

In most scaling studies and previous models, velocities of melt ejected from the vessel are calculated by means of Bernoulli's equation [eq.(4)] with discharge coefficient C_D, in the range of (0.6-1).

$$U_{ejection} = C_D\sqrt{\frac{2\Delta P_{hole}}{\rho_f}} \tag{4}$$

where $\Delta P_{hole} = \rho_f g H_{pool} + P_{reactor} - P_{containment}$. The calculational results for melt ejected through holes (in a 2-D axisymmetric steady-state formulation) show the general applicability of eq.(4) for conditions of interest. Specifically, it is true for prototypical situations, due to the low viscosity of core melt, $\mu_f \sim 0.005$ Pa.s, and the relatively small thickness of the vessel wall, L_{wall}, compared to discharge hole diameters, D_{hole} (L_{wall}/D_{hole} <1 in the most vessel ablation phase). However, in our experiments oxidic melt simulant has a higher viscosity ($\mu_{fs} \sim 0.1$ Pa.s), the test plate is relatively thicker and vessel overpressure is smaller. In such a case, the fluid-wall friction along the hole, ξ_{f-w}, should be taken into account. In order to facilitate developments of the fast-running HAMISA code, it is proposed to calculate the pressure drops due to flow resistances in an orifice [eq.(5)] by means of a loss coefficient ($K_{loss} = 1/\sqrt{C_D}$), whereas the discharge flow velocity is determined from solution of momentum equations along the hole [eq.(6)].

$$\Delta P_{orifice} = \frac{K_{loss}\rho_f U_{f,ave}^2}{2} \tag{5}$$

$$\frac{dP_f}{dz} = -\rho_f U_f \frac{dU_f}{dz} - \rho_f \frac{dU_f}{dt} - \rho_f g - \frac{\xi_{f-w}(z)\rho_f U_f(z) \mid U_f \mid}{2D_{hole}} - \frac{2 \cdot P_f}{D_{hole}} \frac{dD_{hole}}{dz}$$
$$-U_f \rho_f \left[\frac{dU_f}{dz} + \frac{2U_f}{D_{hole}} \frac{dD_{hole}}{dz}\right] - \frac{2\rho_f U_f}{D_{hole}} \frac{dD_{hole}}{dt} \tag{6}$$

with $\Delta P_{f-w,hole} = \Delta P_{hole} - \Delta P_{orifice}$ as the given pressure drop in the hole. These equations together with mass conservation equation form a method (to calculate melt ejection rates from a vessel) that is more general than the conventional Bernoulli's equation. As already mentioned, the method is crucial when analysing experimental processes.

Calculations performed for reactor-scale melt discharge processes also show an increase in hole pressure drop due to temperature dependence of melt viscosity. However, as shown above (see section 2.2.1) when discussing the discharge coefficient, C_D, the fluid-wall friction inside the hole has a minor effect for ejection rates. A more detailed discussion is therefore not necessary.

2.2.2 Prototypical conditions

Typically core melt flows in the discharge hole under prototypical conditions have very high Reynolds numbers (Re in the range 10^5 - $5{\cdot}10^6$), depending, mainly, on the reactor system overpressurization and the size of local failure site (hole diameter). The forced convection heat transfer within the discharge hole may be characterized by development of laminar boundary layer at the very entry region and its transition to turbulent. Nusselt numbers in the laminar flow region and turbulent region can be determined by Schlichting's correlation [eq.(7)] and von Kárman's correlation [eq.(8)], respectively [15].

$$Nu = 0.332 \cdot z_+^{-1/2} \cdot Pr^{-1/6} \tag{7}$$

$$Nu = \frac{0.0288 \cdot Re^{3/5} \cdot z_+^{-1/5} \cdot Pr^{4/5}}{1 + 0.85 \cdot Re^{-1/5} \cdot z_+^{-1/10} \cdot Pr^{-1/10} \left\{ Pr - 1 + ln[1 + \frac{5}{6}(Pr - 1)] \right\}} \quad (8)$$

In contrast to the fact that Eqs.(7-8) were obtained, originally, for boundary layers over the flat plate, they are given here in the form of Nu numbers based on the channel diameter. These correlations along with current results of solving the fluid flow and heat transfer problem within the hole are presented in Figs.6-8. One can see that the method of two-dimensional turbulent flow modeling employed in the present work is able to reproduce heat transfer laws related to boundary-layer development. Correlations of Dittus-Boelter and Petukhov et al. [16] for heat transfer in developed flows are also given for comparison.

Despite of the quantitative agreement achieved between computational results and experimental correlations, it is worth noting that there exist significant difficulties in turbulence modeling of the thermally and hydrodynamically developing flows. An attempt has been made towards accounting for anisotropic effects in the thermally developing and developed flows [14]. However, the absence of experimental data for $z_+ < 10^{-5}$ still renders uncertainties of predicting heat transfer in the very entry region of high-Reynolds-number flows (Re numbers up to 10^7 and z_+ in the range $10^{-7} - 10^{-5}$). Thus, further work on validation and application of the model developed must focus on effects of Re and fluid Pr numbers, as well as possible effects of temperature dependence of physical properties in the thermal boundary layer.

Eqs.(7-8) have also been used in the THIRMAL analysis [17]. However, the criterion of laminar-to-turbulence transition was taken as $Re_{z,trans} = \rho_f U_{ejection} Z_{trans}/\mu_f = 5 \cdot 10^5$. Such a selection of $Re_{z,trans}$ is perhaps based on data of some measurements in the past. Most of such data are related to small diameter channels or flat plates. As a result, the authors of the work [17] showed that the minimum heat transfer coefficient will be either at the channel exit or at the location where the laminar-to-turbulent transition occurs. It can be seen also in Figs.7-8, which indicate very sharp changes of Nusselt numbers by the THIRMAL model. Such a selection of $Re_{z,trans}$ provides relatively small final hole sizes determined by the local erosion rate.

The present two-dimensional modeling of heat transfer in simultaneously developing turbulent flows, however, indicates that the transition might occur at much smaller $Re_{z,trans}$. Results of computations performed for the range of Reynolds number from 10^4 up to $7.5 \cdot 10^6$ indicates $Re_z = 10^5$ as the most probable value of $Re_{z,trans}$ for the large-diameter (more than 5cm ID) circular channels. In the prototypical range of Re numbers ($Re \sim 10^6$), the laminar-to-turbulent transition would take place near the hole entry. Furthermore, one has to account for turbulence in melt flow coming to the hole inlet. In such a case, the boundary layer might become turbulent from the inlet leading edge of the discharge hole. This might also be seen from Fig.9, which depicts a monotonic decrease of Nusselt numbers for hydrodynamically developed flow (in the thermal entrance region) already at low Re numbers ($Re = 4 \cdot 10^4$). Two other calculated lines of the local Nusselt number along the channels are also presented in the figure for simultaneously developing flows with $Re_{hole} = 10^4$ and $5 \cdot 10^4$.

In addition, the physical picture involves several complications due to geometry of the hole (variation of flow cross-section) and convection with freezing/melting processes. Nevertheless, presuming forced convection heat transfer as the governing mechanism, the present analysis indicates that the axial profile of heat transfer coefficient, and, therefore, also the wall ablation rate, are decreasing monotonically towards the hole exit.

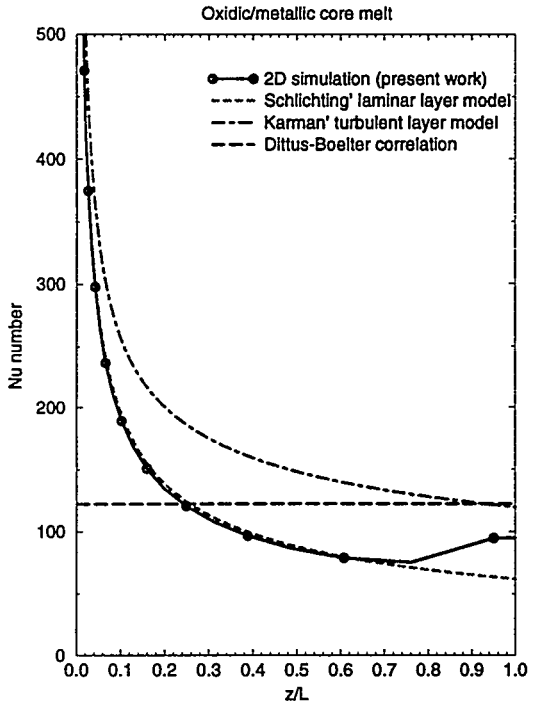


Figure 6: Forced convection heat transfer within the discharge hole: $Re_{hole} = 10^5$, $Pr = 0.2$, L is the hole length.

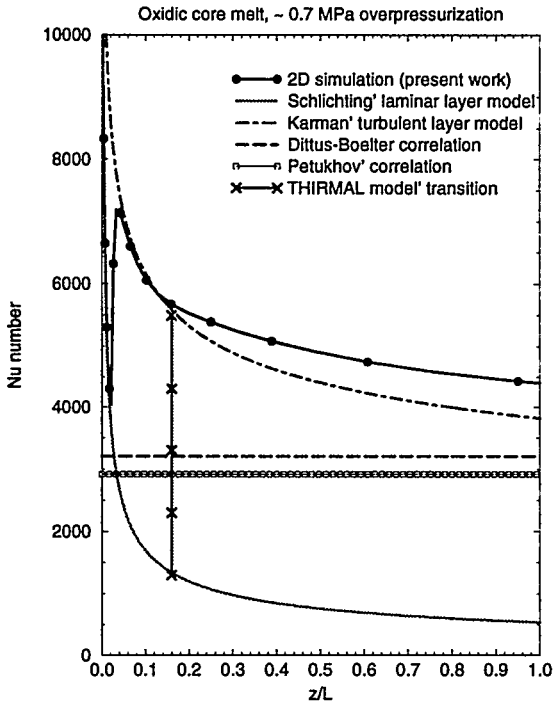


Figure 8: Forced convection heat transfer within the discharge hole: $Re_{hole} = 3 \cdot 10^6$, $Pr = 0.82$, L is the hole length.

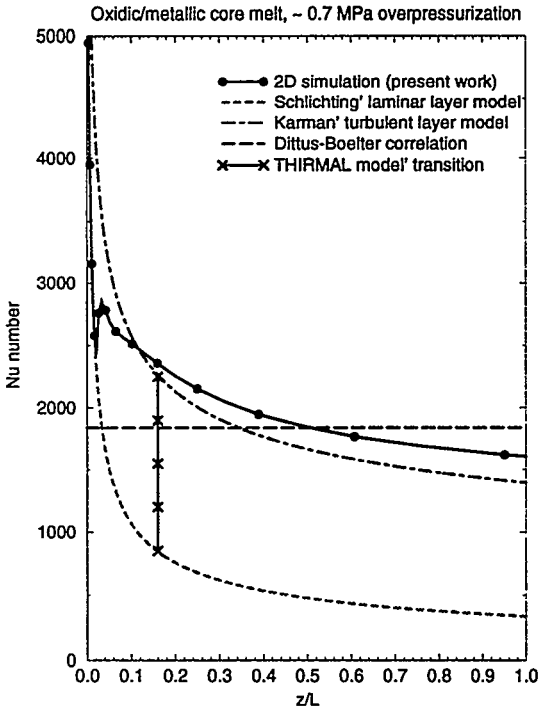


Figure 7: Forced convection heat transfer within the discharge hole: $Re_{hole} = 3 \cdot 10^6$, $Pr = 0.2$, L is the hole length.

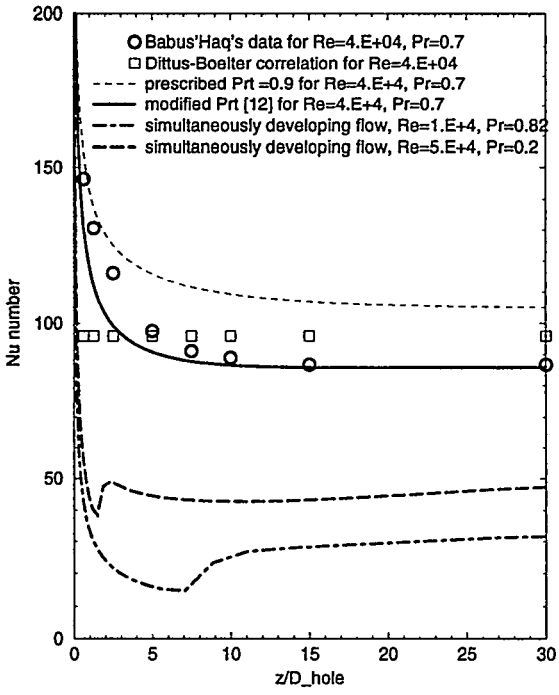


Figure 9: Local Nusselt number in the thermal entrance region: $Re_{hole} = 4 \cdot 10^4$, $Pr = 0.7$.

2.3 Crust behavior within the discharge hole

In the hole ablation problematics, the crust behavior plays the most important role. The physics of (thermal and mechanical) crust behavior during the *melt discharge* process has attracted a very limited number of experiments and analyses so far. The phenomena of crust formation, growth, remelting and mechanical instability have been considered mainly for the LMFBR program and in lower head failure analyses, when predicting core melt penetration distance (transient freezing) in steel tubes and potential localized failure caused by core melt jet impingement against the vessel lower head; a relevant review can be found in [1]. Most notably for the purpose of the present work, the unsteady growth and decay of a frozen layer (crust) in a liquid flowing past a non-melting wall was studied by Epstein in ref.[18], in which an integral method (employing second-order polynomials for temperature profile) was developed. The method was then applied to calculate time characteristics in a tube flow with solidification in the liquid flow and melting in the initially solid wall [19]. However, no direct observations nor measured data on the dynamic behavior of the crust and molten wall layer have been reported from low-temperature simulant (say, Freon-ice wall system) or higher-temperature melt experiments.

The crust formation and existence determine the vessel wall ablation regime. On the other hand, the crust characteristics depend on thermal-hydraulic processes in the melt flow and in the lower head wall. The approaches of some recent studies [2],[3] have been partially contradictory. If there is a stable crust, the melt superheat (say, 10-200K in reactor cases) forms the heat-driving temperature difference ($\Delta T_{ref} = T_f - T_{f,mp}$), while without crust the ablation could be much more rapid, as controlled by the difference between the melt temperature and the wall melting point (say, $\Delta T_{ref} = T_f - T_{w,mp}$ = 2700-1700 $\sim$ 1000K). If the difference in melt-wall heat transfer were about ten, as it could be between the limiting cases, the relative growth of initially small hole ($\propto \Delta T_{ref}^{1/3}$ [2]) could differ by a factor of two or more.

In order to assess possibilities of crust formation, growth and existence during the melt discharge processes in both prototypical and experimental conditions, we have considered a set of physical mechanisms, including conduction-controlled crust growth, crust remelting process due to convective heat fluxes from melt flow, q_{conv}, convection-induced crust sweep-out by melt flow and falling film of molten vessel wall beneath the crust. It was shown that although the remelting time periods, $\tau_{cr,remelt}$, are rather short for characteristic values of crust thickness, the remelting times are as much as 3-5 times larger than the characteristic times of the conduction-controlled crust growth, $\tau_{cr,growth}$, for the given values of crust thickness, $\delta_{f,crust}$; see Table 3. The most important parameter (for ex-vessel melt progression) is the diameter of the melt jet ejected out of the vessel. At the hole leading edge, the heat transfer rates are relatively small, especially in the initial phase of the discharge process. Hence, the crust growth and existence are promoted. Further, limiting mechanisms of convection-induced crust dynamics are considered to evaluate typical values of the crust thickness. Order-of-magnitude assessments for crust-related parameters in reactor situations and KTH experiments are given in Table 4. It can be seen that values of the crust thickness are about 0.5 mm under both prototypical and experimental conditions. Such crust thicknesses are applied to the outlet leading edge of the discharge hole, since the crust life times are calculated by using the total length of the hole. The time characteristics related to the hole ablation process (ablation time, convection-controlled crust life time) are similar in both cases of interest.

Under the HAMISA code development, a number of models have been selected and developed to describe the crust formation and wall melting processes. Originally, a separate-layer model was proposed to model the thicknesses of the crust, $\delta_{f,crust}$, and of the molten wall layer, $\delta_{w,ml}$.

Table 3: Crust formation and remelting.

PARAMETERS	REACTOR				EXPERIMENTS (KTH)		
$\rho_{f,crust}$, kg/m^3 H_{fusion}, J/kg	8000 $3{\cdot}10^5$				6000 $2.5{\cdot}10^5$		
q_{conv}, MW/m^2	1	5	10	20	3	6	9
$\frac{\partial \delta_{f,crust}}{\partial t}$, mm/s	0.4	2	4	8	2.4	4.8	7.2
$\delta_{f,crust}$, mm	1	0.2	0.1	0.05	0.5	0.25	0.1
$\tau_{cr,remelt}$, s	2.5	0.1	0.025	0.006	0.2	0.06	0.015
$\tau_{cr,growth}$, s	0.5	0.04	0.01	0.0025	0.06	0.015	0.005

Table 4: Dynamics of the crust within the discharge hole.

PARAMETERS	REACTOR		EXPERIMENTS (KTH)	
Film-driven crust dynamics				
Typical ablation rate, V_{ab}, mm/s	3-10 (ave: 6)		1-6 (ave: 3)	
Vessel/plate thickness, L_{wall}, m	0.15		0.02-0.05	
$\delta_{w,ml}$, mm	1	0.5	1	0.5
$U_{film} = V_{ab}L_{wall}/\delta_{w,ml}$, m/s	0.9	1.8	0.06 - 0.15	0.12 - 0.3
$\tau_{film,conv} = L_{wall}/U_{film}$, s	0.16	0.08	0.25	0.10
Melt flow-driven crust dynamics				
$U_{ejection}$, m/s	3 - 10		0.3 - 1	
Re_{hole}	$(0.7\text{-}2.3){\cdot}10^6$		900-3000	
ξ_{f-cr}	$0.3164{\cdot}Re_{hole}^{-1/4}$		$16/Re_{hole}$	
$U_{fbl} = U_{ejection}\sqrt{\frac{\xi}{8}}$, m/s	0.1 - 0.3		0.02 - 0.1	
$\tau_{fbl,conv} = L_{wall}/U_{fbl}$, s	1.5 - 0.5		1.5 - 0.2	
$\tau_{cr,res} = min(\tau_{film,conv}, \tau_{fbl,conv})$, s	0.1		0.15	
$\delta_{f,crust}$, mm (for $\tau_{cr,growth} = \tau_{cr,res}$)	0.5		0.6	

The formulation of the three-layer model is general (see, e.g. ref.[19]), using heat conduction and heat balance across the layers (of crust, molten wall and solid wall) to simulate their transient behavior. Finite-difference method is used to solve heat transfer problems in conjugated domains with phase-change boundary mobilization. However, the heat conduction is not the only heat transfer regime in the layer of molten wall as it has been assumed in most previous works, including the above-referred one [19]. There are large uncertainties in describing the behavior of molten wall layer (beneath the crust) due to shear stress from melt flow through crust layer and flow dynamics of a falling film. Therefore, a simplified approach to the treatment of the crust within the discharge hole has been taken in the first-order integrated analysis, by assuming that heat conduction is the dominant process in the initial ablation phase when the thickness of the molten wall layer is less than a critical value ($\delta_{w,ml} < \delta^*_{w,ml}$), say $\delta^*_{w,ml}$ = 1mm for experimental conditions. Then, two equations of heat conduction and phase change in crust and molten wall layers are applied

$$\rho_{f,crust} H_{fusion,crust} \frac{d\delta_{f,crust}}{dt} = -\kappa_{f,crust} \frac{T_i - T_{f,mp}}{\delta_{f,crust}} - q_{conv} \tag{9}$$

$$\rho_w H_{fusion,w} \frac{d\delta_{w,ml}}{dt} = -\kappa_w \frac{T_i - T_{w,mp}}{\delta_{w,ml}} - q_{cond} \tag{10}$$

where

$$T_i = \frac{\frac{\kappa_{f,crust} T_{f,mp}}{\delta_{f,crust}} + \frac{\kappa_w T_{w,mp}}{\delta_{w,ml}}}{\frac{\kappa_{f,crust}}{\delta_{f,crust}} + \frac{\kappa_w}{\delta_{w,ml}}}$$

Should the thickness of molten wall layer reach its critical value, the equation $\delta_{w,ml} = \delta^*_{w,ml}$ is assumed for the following ablation phase. In such a case, the thickness of the crust layer is calculated from eq.(11), and the heat flux imposed on the phase-change interface, q_{int}, is defined from eq.(12).

$$\rho_{f,crust} H_{fusion,crust} \frac{d\delta_{f,crust}}{dt} = -q_{conv} + \frac{T_{f,mp} - T_{w,mp}}{\frac{\kappa_{f,crust}}{\delta_{f,crust}} + \frac{\kappa_w}{\delta^*_{w,ml}}} \tag{11}$$

$$q_{int} = -\kappa_w \frac{T_{w,mp} - T_i}{\delta^*_{w,ml}} \tag{12}$$

In the present work, the calculated values of q_{int} are used as the boundary condition to the problem of vessel wall heat conduction and ablation analysed below; see, e.g., eq.(13). The crust-related assumptions need to be verified, when more experimental observations and data become available. If so, the dynamics of the crust within the discharge hole and the role of the crust in heat transfer-controlled ablation process can be shown more explicitly for prototypical situations. Most notably at the moment, the dynamics of the molten wall layer requires substantial modeling and experimental efforts to clarify its phenomenology. After that, a general treatment of the crust within the discharge hole could be developed as the uncertainties in describing the flow of the molten wall layer would not be overriding details of heat transfer in the crust.

2.4 Vessel wall heat conduction and ablation

In this section we will examine effects of preheating and multi-dimensional heat conduction in the vessel wall and test plate. Preliminary assessments for experiments employing lead (as well as aluminum and tin) as metallic lower head models show significant transients in the test plate's temperature field prior and during melt discharge. As it takes time (15-30s) for melt discharge process to start after the first melt-wall contact, the thermal front could already penetrate through the relatively thin metallic layers (2-4cm) of the test plate due to large values of thermal diffusivity ($\alpha = 20 - 40 \cdot 10^{-6} \mathrm{m}^2/\mathrm{s}$) of vessel materials (metals) used. The HAMISA.2D/WALL model has been developed to describe *two-dimensional heat conduction with phase change.* An efficient numerical technique has been developed to solve two-dimensional heat conduction equation in complex geometry domains with moving phase-change boundary. The idea of the method developed is to have a dominant direction of boundary mobilization, that is the ablation front along the hole. The heat conduction in the remaining direction is taken into account in a semi-implicit manner. The moving rate of phase-change boundary of a given strip (horizontal layer) in cylindrical coordinate system (r, z) is defined through the difference between the heat

flux imposed on the interface, q_{int}, and that taken away by heat conduction, q_{cond}, as follows (see also Fig.1)

$$V_{ab}(z,t) = \frac{\sqrt{r_o^2 + \frac{2(q_{int}-q_{cond})r_o\Delta t}{\rho_w H_{fusion,w}}} - r_o}{\Delta t} \tag{13}$$

where r_o is the position of the melting front at time t_o, and Δt is time step, $\Delta t = t - t_o$. Calculated values of V_{ab} are then used to track the phase-change interface. Calculations by means of the HAMISA.2D/WALL model were performed for conditions of hole ablation experiments. Results of calculations for cases with and without crust are presented in Figs.10-13.

It can be seen from Figs.11,13 that roughly similar diameters for the final hole were predicted for two cases. Nevertheless, transient temperature fields in the test plate during melt discharge process are *sensitive* to the given boundary conditions, i.e. crust presence (18s process; see Fig.10) or absence (7s process; see Fig.12). Therefore, data of thermocouples installed inside the test plate and reduced data on ablation dynamics could be used to assess heat fluxes from melt flow to the test plate. Consequently, existence of the crust can be evaluated. Large openings of the hole at its inlet are due to entrance effects on heat transfer and additional pre-heating of the test plate (from molten pool's flow above) prior to melt front propagation. Qualitatively, calculational results of final hole formation (see Fig.14) and ablation dynamics agree with observations from the KTH scoping experiments on vessel hole ablation. Firstly, the geometry of the final hole indicates effects of the hole entry region on heat transfer and of the two-dimensionality of heat conduction in the test plate. Future experiments are required to quantify heat transfer coefficient within the hole. Influence of pool geometry (ratio of pool and hole diameters) on flow turbulence, velocity and temperature profiles at the hole inlet must be taken into consideration in experimental data analysis. Secondly, it has been observed for the discharge hole exit that the hole growth rate has been accelerated towards the end of the process, rendering thus a basis for assuming crust existence, at least, at the hole exit (compare cases 1 and 2 in Figs.11,13. However, in order to observe, more decisively, crust existence from measurement data in future experiments, one has to provide small ratios $\frac{T_{fs}-T_{fs,mp}}{T_{fs}-T_{w,mp}}$, i.e. the melt temperature has to be much less above the melt liquidus than above the wall melting point. Under such conditions, the effect of the crust could lead to distinctive bifurcation of the final hole geometry.

Depicting a regime pattern of hole ablation phenomenology, one could imagine three extreme regions: (a) no melting of the wall; (b) rapid ablation of the wall; and (c) simultaneous existence of the crust layer and propagation of the melting front in the wall. Actually, the experimental and analytical simulations have to be able to describe such *regime transitions*. Also, simulant, low-temperature separate effects tests are envisioned to study the crust formation without melting of the wall, and with melting of the wall including rapid ablation without crust formation. Apparently, during a (reactor/experiment) process, the transient can lead to dynamical change of the state, from the (a)-region to the (c)-region, and perhaps further to the (b)-region. Such considerations are important to confirm the reproducibility and correct interpretation of our experiments. Analyses performed with the help of the HAMISA.2D/WALL model allow us to define the thermal state of the test plate (the initial and boundary conditions of hole ablation problem), to set requirements for melt pouring (from melt generation vessel into test crucible) times, and to design the test plates. In addition to the above-mentioned scaling aspects, analytical predictions of the thermal behavior of test plates are necessary to avoid the possibility of processes other than ablation, such as creep rupture.

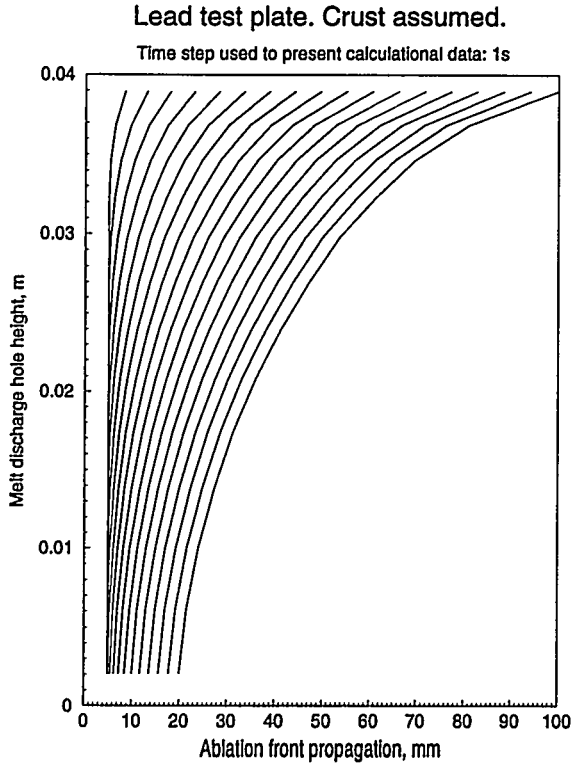


Figure 10: Case 1: $T_f - T_{f,mp} = 200\text{K}$.

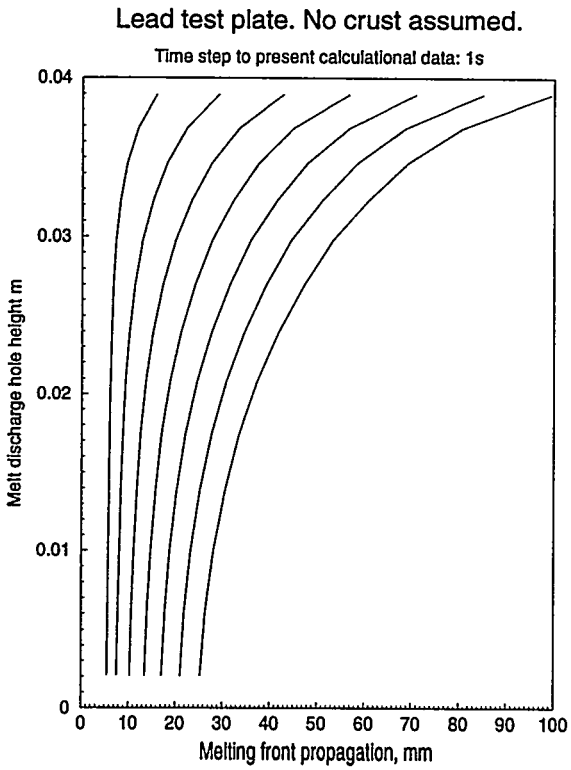


Figure 12: Case 2: $T_f - T_{w,mp} = 500\text{K}$.

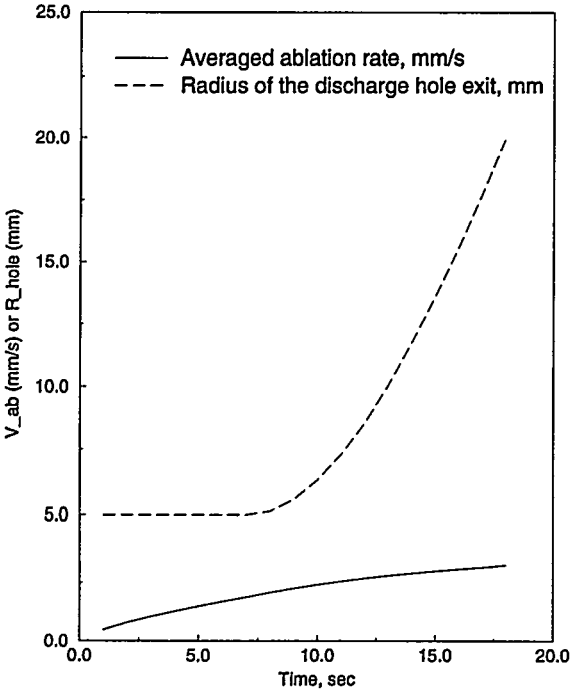


Figure 11: HAMISA simulation of KTH hole ablation experiment: case 1.

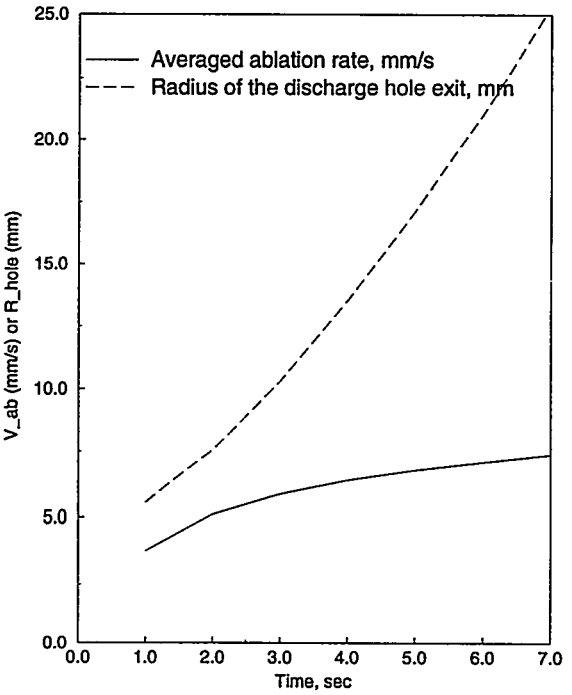


Figure 13: HAMISA simulation of KTH hole ablation experiment: case 2.

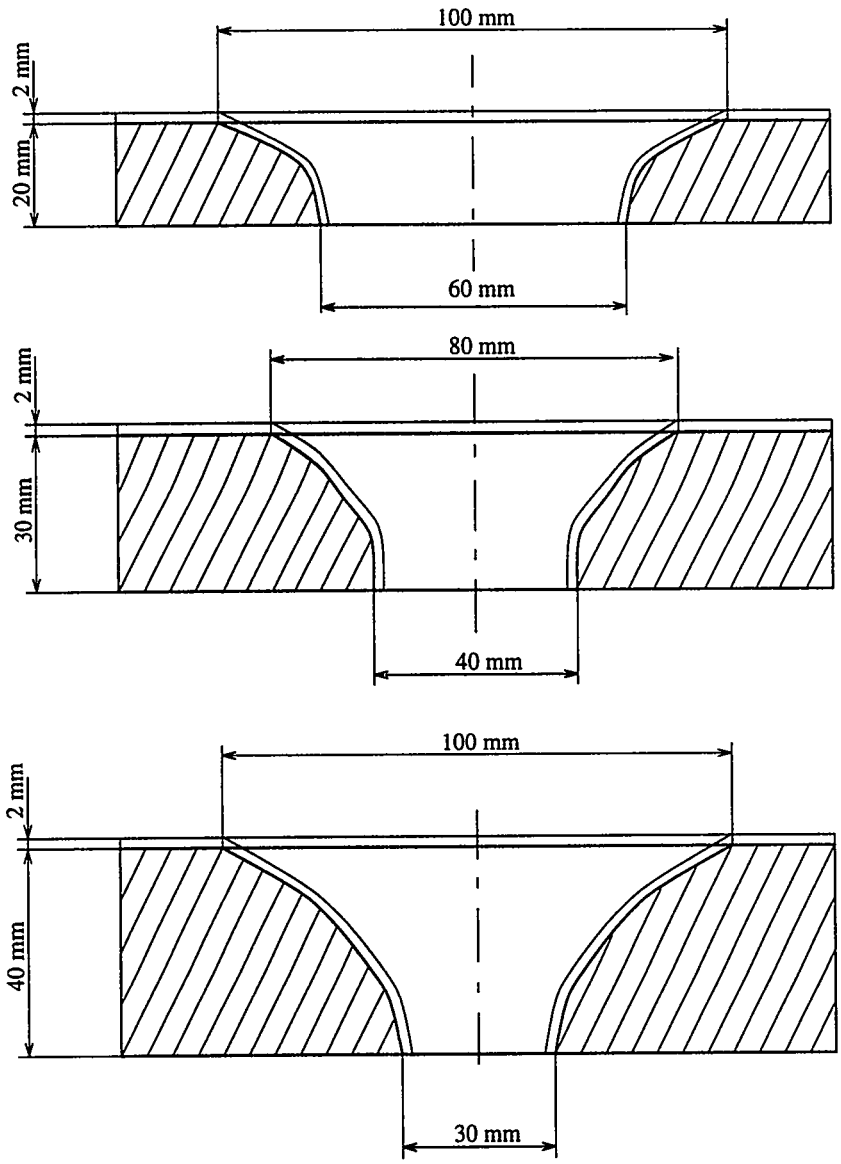


Figure 14: Final hole geometry in the KTH scoping hole ablation experiments: observations on 3 plates.

3 SUMMARY

The paper describes the model development work at the Royal Institute of Technology, Stockholm, to study the core melt discharge and reactor pressure vessel (RPV) lower head ablation. The objective of the study is to provide understanding of the physics of these complicated melt-structure interaction processes. Both phenomenological and computational models are under development to treat together the dynamically coupled processes of melt flow, heat transfer to vessel wall, and the hole ablation. The most difficult, and the most uncertain, part of the modeling is the thermal and mechanical behavior of the crust, which can form a limiting mechanism for lower head ablation in severe light water reactor accidents. Other significant phenomena (such as penetration hole entrance effects, multi-dimensional heat conduction and phase change in lower head wall, melt pool thermal hydraulics) also have been discussed in detail. By taking advantage of these developments, we believe, it is possible to reduce the uncertainties in the quantification of the continued enlargement of the initial failure site in the RPV lower head.

As a link between reactor processes and experiments, the model development work has been oriented to confirm relevance and completeness of the research efforts on hole ablation.

Calculations using the mechanistic models developed have confirmed the effects of core melt (momentum and heat) transport properties and their temperature dependence. The current modeling has also highlighted the importance of the wall thickness and thermal properties in scaling considerations of the hole ablation experiments. Further progress in model development and validation relies on applications to various aspects of hole ablation experiments and separate effects tests. The HAMISA code, when validated against related experiments, will form the basis to analyse hole ablation dynamics for reactor situations of interest.

ACKNOWLEDGEMENT

The authors would like to thank Dr. M.M. Pilch of Sandia National Laboratories for all the information he has provided us on the melt discharge subject. Special thanks are due to Mr. J. Anderson , who has been performing the hole ablation scoping experiments at KTH.

NOMENCLATURE

Arabic letters

C_D	Discharge coefficient (-), see eq.(4)
D	Diameter (m)
f_{app}	Apparent friction factor (-), see eq.(3)
Fr	Froude number, $Fr = \frac{U_{ejection}}{\sqrt{g \cdot D_{hole}}}$ (-)
g	Gravitational acceleration (9.81 m/s^2)
h	Heat transfer coefficient (W/m^2·K)
H	Melt pool level (m)
H_{fusion}	Heat of fusion (J/kg)
L, L_{wall}	Given thickness of the RPV wall (m)
Nu	Nusselt number, $Nu = \frac{hD_{hole}}{\kappa_f}$
Nu_{up}	Nusselt number, $Nu_{up} = \frac{q_{up}(r^*)D_{hole}}{\kappa_f(T_f - T_{f,mp})}$ (-)
P	Pressure (Pa)
Pe_{hole}	Peclet number, $Pe_{hole} = Re_{hole} \cdot Pr_f$ (-)
Pr	Prandtl number, $Pr = \mu C_p/\kappa$ (-)
r	Radius or distance from the hole symmetry line (m)
r^*	Dimensionless radius, $r^* = \frac{r - r_{hole}}{r_{pool} - r_{hole}}$ (-)
Re_{hole}	Reynolds number based on D_{hole}, $Re_{hole} = \rho_f U_{ejection} D_{hole}/\mu_f$ (-)
Re_z	Reynolds number based on Z, $Re_z = \rho_f U_{ejection} Z/\mu_f$ (-)
q	Heat flux (W/m^2)
t	Time (s)
U	Velocity in z-direction (m/s)
V	Velocity in r-direction (m/s)
z, Z	z-coordinate (m)
z_+	Dimensionless z for heat transfer data, $z_+ = \Delta z/(D_{hole} \cdot Pe_{hole})$ (-)
z_*	Dimensionless z for friction data, $z_* = \Delta z/(D_{hole} \cdot Re_{hole})$ (-)

Greek letters

δ	Thickness of layers (m)
κ	Heat conductivity (W/m·K)
μ	Dynamic viscosity (Pa·s)

ρ	Density (kg/m^3)
τ_{growth}	Solidification time scale (s)
τ_{remelt}	Remelting time scale (s)
τ_{conv}	Convection time scale (s)
τ_{res}	Residence time scale (s)
ξ	Friction coefficient
ΔP	Pressure difference (Pa)
Δt	Time step (s), see eq.(13)
Δz	Distance from the discharge hole inlet (m)

Subscripts

ab	Vessel wall ablation
cond	Conduction
conv	Convection
cr,crust	Crust of core melt or simulant material
f	Core melt flow
fbl	Boundary layer of discharge flow
film	Falling film characteristics of the molten wall layer
fs	Simulant material of core melts
gb	Gas blowthrough
hole	Discharge hole
int	Interface
ml	Molten layer
o	Reference value
pool	In-vessel melt pool
t	Turbulent
transition	Laminar-to-turbulent transition
up	Upper surface of the crust overlying the vessel wall
w	Vessel lower head wall or its model

References

[1] J.L.Rempe et al., *"Light Water Reactor Lower Head Failure Analysis"*. NUREG/CR-5642. USNRC. 1992.

[2] M.M. Pilch, *"Continued Enlargement of the Initial Failure Site in the Reactor Pressure Vessel"*. Appendix J of [5].

[3] *"Zion Probabilistic Safety Study"*. Commonwealth Edison Co., Chicago, IL. 1981.

[4] J.J. Sienicki and B.W Spencer, Superheat Effects on Localized Vessel Breach Enlargement During Corium Ejection, *Trans. ANS*, Vol. 52, 1986, pp.522-524.

[5] M.M. Pilch, H. Yan and T.G. Theofanous, *"The Probability of Containment Failure by Direct Containment Heating in Zion"*. NUREG/CR-6075. SAND93-1535. June 1993.

[6] B.R. Sehgal, J. Andersson, T.N. Dinh and T. Okkonen, "Scoping Experiments on Vessel Hole Ablation During Severe Accidents", *Proceedings of the Workshop on Severe Accident Research in Japan, SARJ-4*, Japan, Oct.-Nov., 1994

[7] T.N. Dinh and A.A. Popov, "Molten Corium - Reactor Vessel Interaction: Scaling and Other Aspects", *ASME 1993 Winter Annual Meeting.* New Orleans, Louisiana, USA. December 1993. Section 14C: Advanced Nuclear Power Plants. ASME paper 93-WA/HT-81, 1993.

[8] T.N. Dinh and R.R. Nourgaliev, "On Turbulence Modeling of Large Volumetrically Heated Liquid Pools", *Nuclear Engineering and Design*, 1995 (in press).

[9] C. Smoglie and J. Reimann, "Two-Phase Flow Through Small Branches in a Horizontal Pipe with Stratified Flow", *Intern.J. of Multiphase Flow*, Vol.12, N.4, pp.609-625 (1986)

[10] T. Yonomoto and K. Tasaka, "Liquid and Gas Entrainment to a Small Break Hole from a Stratified Two-Phase Region", *Intern.J. of Multiphase Flow*, Vol.17, N.6, pp.745-765 (1991)

[11] M.M. Pilch and R.O. Griffith, *"Gas Blowthrough and Flow Quality Correlations for use in the Analyses of High Pressure Melt Ejection (HPME) Events"*, SAND91-2322, Sandia National Laboratories, Albuquerque, NM, 1992.

[12] D.F. Gluck, J.P. Gille, D.J.Simkin and E.E. Zukowski, "Distortion of the Liquid Surface under Low g Conditions", *Aerospace Chemical Engineering*, ed. D.J. Simkin, Vol.62, No.61, p.150, AIChE, NY (1966)

[13] D.F. Gluck, J.P. Gille, E.E. Zukowski, and D.J.Simkin, "Distortion of a Free Surface during Tank Discharge", *J. Spacecraft*, 3., p.1691 (1966)

[14] V.A. Bui and T.N. Dinh, "An Approximation of Turbulent Prandtl Number in Thermally Developing Flows", *Proceedings of the Second CFD Colloquium on Process Simulation*, Helsinki University of Technology, Espoo, Finland, June 1995

[15] H. Schlichting, *"Boundary Layer Theory"*, Sixth Edition, McGraw-Hill Book Company, 1968

[16] F.P. Incropera and D.P. de Witt, *"Fundamentals of Heat and Mass Transfer"*, Third Edition, John Willey & Sons, 1990

[17] J.J. Sienicki, C.C. Chu, B.W. Spencer, W. Frid, and G. Löwenhielm, "Ex-Vessel Melt-Coolant Interactions in Deep Water Pool: Studies and Accident Management for Swedish BWRs", *Proceedings of the CSNI Specialist Meeting on Fuel-Coolant Interactions*, Santa Barbara, January 5-8, 1993, NUREG/CP-0127, NEA/CSNI/R(93)8

[18] M. Epstein, "The Growth and Decay of a Frozen Layer in Forced Flow", *Intern.J. Heat Mass Transfer*, Vol.19, pp.1281-1288 (1976)

[19] A. Yim, M. Epstein, S.G. Bankoff, G.A. Lambert, and G.M. Hauser, "Freezing-Melting Heat Transfer in a Tube Flow", *Intern.J. Heat Mass Transfer*, Vol.21, pp.1185-1196 (1978)

Results of International Standard Problem No. 36 Severe Fuel Damage Experiment of a VVER Fuel Bundle at the CORA Facility

M. Firnhaber[1)], L. Yegorova[2)], U. Brockmeier[3)],
S. Hagen[4)], P. Hofmann[4)], K. Trambauer[1)]

[1)] Gesellschaft für Anlagen- und Reaktorsicherheit, 50667 Köln, Germany

[2)] Nuclear Safety Institute of Russian Research Center, 123182 Moscow, Russia

[3)] Ruhr-University of Bochum, 44780 Bochum, Germany

[4)] Kernforschungszentrum Karlsruhe, 76133 Karlsruhe, Germany

ABSTRACT[1]

International Standard Problems (ISP) organized by the OECD are defined as comparative exercises in which predictions with different computer codes for a given physical problem are compared with each other and with a carefully controlled experimental study. The main goal of ISP is to increase confidence in the validity and accuracy of analytical tools used in assessing the safety of nuclear installations. In addition, it enables the code user to gain experience and to improve his competence.

This paper presents the results and assessment at the blind ISP No. 36, which deals with the early core degradation phase during an unmitigated severe LWR accident in a Russian type VVER. Representatives of 17 organizations participated in the ISP using the codes ATHLET-CD, ICARE2, KESS-III, MELCOR, SCDAP/RELAP5 and RAPTA. Some participants performed several calculations with different codes. As experimental basis the severe fuel damage experiment CORA-W2 was selected. The main phenomena investigated are thermal behavior of fuel rods, onset of temperature escalation, material behavior and hydrogen generation.

In general, the calculations give the right tendency of the experimental results for the thermal behavior, the hydrogen generation and, partly, for the material behavior.

[1] This work was sponsored by the German Ministry for Education, Science, Research and Technology under the contract No. RS 871 A.

However, some calculations deviate in important quantities - e.g. some material behavior data - showing remarkable discrepancies between each other and from the experiments.

The temperature history of the bundle up to the beginning of significant oxidation was calculated quite well. Deviations seem to be related to the overall heat balance. Since the material behavior of the bundle is to a great extent influenced by the cladding failure criteria a more realistic cladding failure model should be developed at least for the detailed, mechanistic codes. Regarding the material behavior and flow blockage some models for the material interaction as well as for relocation and refreezing requires further improvement.

INTRODUCTION

An International Standard Problem (ISP) Exercise is defined as a comparative exercise in which predictions with different computer codes for a given physical problem are compared with each other and a carefully controlled experimental study. The main goal of ISP is to increase confidence in the validity and accuracy of analytical tools which are used in assessing the safety of nuclear installations /1/. Moreover, it enables the code user to gain experience and to improve his competence. The related calculation can be performed with or without previous knowledge of the experimental results. Therefore two approaches of performing a standard problem exercise can be defined, "open" or "blind".

Accepting a proposal of the Federal Republic of Germany the Principal Working Group (PWG) No. 2 of CSNI offered the experiment CORA-W2 /2/ on severe core damage as International Standard Problem No. 36 (ISP36) to its member countries. It was conducted as a blind standard problem, i.e. only the experimental boundary conditions were given to the participants prior to performing the calculation. ISP36 was initiated in December 1993, the first workshop took place in February 1994 and the second in February 1995.

17 organizations from 9 Eastern and Western countries participated in the ISP submitting 22 calculations (s. Table 1 and 2). They employed the severe accident codes

ATHLET-CD /3/, ICARE2 /4/, KESS III /5/ MELCOR /6/, RAPTA /7/ and SCDAP/RELAP5 /8/.

ISP36 is the third ISP on severe fuel damage aspects. The first one (ISP28) was performed in 1990/1991 using PHEBUS-SFD B9+ experiment as basis for the data comparison /9/ and the second one (ISP31) /10/ is based on the experiment CORA-13.

OBJECTIVES OF INTERNATIONAL STANDARD PROBLEM NO. 36

During an unmitigated severe LWR accident the core material reaches temperatures significantly higher than 1200° C. This causes core damages in a large variety of forms, i.e. chemical interactions of the different materials, melting, relocation, blockage formation, hydrogen generation and further more embrittlement and fragmentation of the cladding on cooldown and quenching. To predict the course of the accident and to mitigate the accident a detailed knowledge of the core meltdown behavior is necessary. Experimental results and code predictions can be used to quantify the safety margins presently existing in the safety systems of operating reactors, and to explore possibilities of ending a high temperature transient before it can lead to the formation of a ceramic melt pool in the core or even more an uncontrolled core meltdown. For demonstrating the capability of current computer codes to model and to calculate the initial phase of core meltdown of a severe accident with sufficient accuracy, the OECD-CSNI decided to propose a further fuel degradation standard problem.

The general objectives of the International Standard Problem No. 36 (ISP36) are to analyze the heatup and early degradation of a Russian type VVER fuel element with B_4C- absorber rods at the CORA facility and to examine the reliability and precision of the severe accident computer codes used.

In more detail the objectives are the comparison and investigation of the following physical variables and phenomena:

- Temperature behavior of selected fuel and absorber rods,

- Onset of temperature escalation as a result of the exothermal zirconium/ steam interaction,
- Extent of zirconium cladding oxidation,
- Liquefaction process of stainless steel spacers and B_4C-absorber rods,
- Extent of UO_2 and ZrO_2 dissolution by molten zirconium,
- Oxidation of metallic melt containing zirconium,
- Formation of blockages, its extent and location,
- Timing and magnitude of hydrogen generation.

EXPERIMENT CORA-W2

The experiment CORA-W2 was performed in the CORA out-of-pile facility /2/, which is designed to investigate the behavior of LWR fuel elements under severe fuel damage accident conditions. In the experiment the decay heat is simulated by electrical heating. Great emphasis is given to the fact that the test bundle contains all materials used in light-water reactor fuel elements, to investigate the different material interactions. Pellets, claddings, grid spacers, absorber rods and the pertinent guide tubes are typical of those of commercial LWR with respect to their compositions and radial dimensions (s. Fig. 1).

Test CORA-W2 was performed with a fuel bundle simulator which was assembled from original VVER bundle material. The major differences are the hexagonal rod array, Zr1%Nb as cladding material instead of Zry-4 as well as B_4C absorber rod with stainless steel guide tube and stainless steel grid spacers.

The central part of the facility is the fuel rod bundle, which contains 19 rods in a hexagonal array: 13 heated rods, 5 unheated rods and 1 B_4C absorber rod. The tungsten heaters have an effective length of 1024 mm and three spacer grids are used to maintain the positions of the rods. To conduct the steam through bundle, it is surrounded by a Zr1%Nb shroud with Zirconia insulation and a high-temperature shield to minimize the heat losses.

The test sequence can be divided into the gas preheat phase, the transient phase with a duration of 1 500 s and the cooling phase. During the gas pre-heat phase the bundle is heated by an argon flow of 793 K. The transient phase is performed by raising the electric power input from 2 to 14 kW at a constant rate and by introducing a steam flow of approximately 4 g/s into the system. The cooling phase starts after the transient phase by switching off the electrical power.

COMPUTATIONAL MODELS USED

The computational models used for the ISP36 calculations are defined by both the models provided by the codes and the specific input decks defined by the participants. The basic modeling aspects particularly as regards the ISP36 calculations are summarized below in terms of nodalization scheme, thermal hydraulics, structure heat-up, material oxidation and hydrogen generation, mechanical rod behavior and cladding failure, chemical interactions, and material relocation.

The basic constructional elements to be nodalized in the CORA bundle are the three types of rods (heated, unheated, and absorber rods), the shroud, the HTS, the flow sub channels in the bundle, the bypass flow channel and the spacer grids. A further governing nodalization characteristic is the treatment of the flow channels. For most ISP36 calculations, two flow channels have been defined, one representative channel for the bundle flow (inside the shroud) and the other for the bypass flow. The codes uniformly apply quasi one dimensional formulations of the conservation equations coupled to constitutive equations for the modeling of heat and mass transfer between the fluid phases and between fluid and structures. True cross flow modeling is not possible in terms of momentum mixture.

Generally, the codes provide two types of models for structure heat-up, so called heat structures for energy balances in structures maintaining their integrity during core degradation and core structure for energy balances of degrading geometries. Core structures apply two dimensional thermal energy equations including sources due to oxidation, fission product decay and relocating material.

Regarding material oxidation and hydrogen generation, most of the calculations performed for ISP36 are based on rate equations for oxidation (some used a diffusion

model). Only partially the rate coefficients have been adapted to treat the Zr1%Nb material of the VVER-type of cladding. Most of the codes treat inside oxidation after the burst of the cladding. Melt oxidation models - so far available - are thoroughly based on rate equations for intact rods. For the rate calculation of melt mixtures consisting of U-Zr-O, UO_2 and ZrO_2, the mixture layers in the respective axial zones are rearranged to show a vertically stratified structure with the Zr component forming one layer in this structure. Besides Zr, most of the codes provide oxidation models for stainless steel and some (e.g. MELCOR) for B_4C too.

The most important models for early phase structure mechanics are those for ballooning with subsequent cladding rupture and for the breach of oxide shells containing molten U-Zr-O mixtures and absorber materials. Except MELCOR, all codes used for ISP36 provide ballooning models, varying from highly mechanistic codes accounting for material anisotropics and circumferential temperature gradients (SCDAP/RELAP5) to more empirical (ICARE) based on specific experiments. The models for oxide shell breach have significant impact on the amount of liquid U-Zr-O mixtures and the onset of relocation of liquid materials including U-Zr-O and absorber material eutectic mixtures. The impact on the amount of U-Zr-O mixtures is due to the fact that the oxide shell keeps the mixture within the reaction zone, i.e. the chemical dissolution process lasts until the shell breaches and the mixture is released to outside of the fuel rod.

Chemical interactions important for CORA-W2 are the fuel rod UO_2-Zr-ZrO_2 and the absorber rod B_4C-Stainless Steel (SS) eutectic interactions. The B_4C absorber rods are a specific feature of VVER type bundles. The B_4C absorber material is surrounded by a SS cladding and a SS guide tube. Consequently, as far as the outer oxidized steel shell is intact, the chemical interactions of interest are those between B_4C and SS. Some of the codes in principle provide models for the dissolution of SS by B_4C. However they are either coupled to certain geometric situations (SCDAP/ RELAP5 model for BWR absorbers) or they are rather simple by just providing an eutectic temperature leading to an instantaneous liquefaction (ATHLET-CD). Both, mechanistic models for radial spreading of absorber material and for chemical interactions of B_4C-SS-ZrO_2 are presently not available in the codes.

All the codes used for ISP36 provide models for axial relocation (candling), only some (e.g. MELCOR) have simple models for radial relocation. The approaches underlying the candling models differ widely from highly mechanistic (ATHLET-CD, KESS) to

basically parametric (MELCOR). Generally, the models are based on the assumption of a given relocation velocity (in MELCOR essentially infinitively high) and of a given arrangement of the melt leaving the rod on its outer side (film or certain number of rivulets or droplets).

COMPARISON OF ANALYTICAL AND EXPERIMENTAL RESULTS

For comparison purpose the experimental and analytical results are grouped in overlay plots according to the codes used. The most important results are discussed here (only the results of one code group are shown here in the figures as an example). The different curves are labeled according Table 1 and 2, which gives the name of the organization and the code version used. In more detail the results are given in /11/.

Fuel and Cladding Temperature

During the heatup phase the temperature behavior is quite well calculated between 3000 and 4000 s by most of the participants with a spread of about 150 K (Fig. 2). But this temperature spread results in a large spread in time of onset of temperature escalation which spans more than 300 s. Most of the calculations show an onset which is to late compared to the experiment. Since no thermocouple survived the high temperature after the temperature escalation only an estimate from material investigations of the maximum temperature can be given, which ranges from 2250 K to 2500 K. The comparison shows that most of the calculations lie within this temperature band or underestimate it, except SCDAP/ RELAP5 which deviates is to higher temperatures.

Zirconium Oxidation

The distribution of oxidized Zr is given in Fig. 3. The post test examination shows that above elevation 250 mm approximately 20 to 30 % of solid, unmolten Zr is oxidized with a maximum of 55 % at elevation 300. The oxidation of the molten Zr is not included in the experimental values, but in the calculational results. With some exception the ATHLET-CD and MELCOR calculations meet this oxidation level, the SCDAP/RELAP5 calculation overestimate and the ICARE calculation underestimate

the oxidation. Nearly all calculations determined the maximum of the oxidation at a much higher level (450 mm to 650 mm).

Absorber Material (B_4C) Total Mass

In Fig. 4 the B_4C total mass distribution is plotted compared to the mass per length of 0.64 kg/m of the intact bundle and to the calculated data. Above elevation 500 mm all of the B_4C was dissolved by SS and relocated to lower positions. At the lower end of the bundle the B_4C mass per length increased to nearly 1 kg/m. All but one ATHLET-CD calculation (GRSA) underestimated the B_4C relocation considerably due to an underestimate of the temperature in the lower bundle half.

UO_2 Total Mass

The initial value of the UO_2 total mass per rod is 0.65 kg/m. During the test a small amount, mainly in the upper part of the bundle was dissolved or relocated. Only some calculations (1 MELCOR, 2 SCDAP/RELAP5, 1 ATHLET- CD) got the right tendency of the UO_2 distribution (s. Fig. 5).

Core Blockage

The core blockage is given in Fig. 6. Due to the material relocation a core blockage of 25 % relative to the originally free flow area, was measured at elevation 200 mm. In the upper part of the bundle, the flow area is slightly increased (about 10 %). The ICARE and some MELCOR calculations show the tendency of core blockage adequately, despite the lack of suitable models, but not all calculate the correct maximum. ATHLET-CD and SCDAP/RELAP5 calculated only positive flow blockages due to the fact that the cladding and pellet stack in the upper part of the bundle stayed in place.

H_2 Generation

The measured H_2-generation rate between 4100 s and 4600 s is approximately 0.13 g/s. As can be seen in Fig. 7 most of the calculations under- or overestimated the rate considerably. The same tendency is shown by the accumulated hydrogen generation, which was measured with a total of 68 g (s. Fig. 8).

ASSESSMENT OF ISP36 AND CONCLUSIONS[2]

In general, the calculations give the correct tendency of the experimental results. However, some calculation show major differences from the experimental results, mainly in the area of material behavior.

The temperature history of the bundle up to the point of the beginning of significant oxidation was calculated quite well. Deviations seem to be related to the overall heat balance. The material behavior of the bundle is to a great extent influenced by the absorber rod material, the cladding failure criteria and by the interaction between the stainless steel grid spacer and the cladding, as could be demonstrated by the SCDAP/RELAP5 grid spacer model. A more realistic cladding failure model should be developed at least for the detailed, mechanistic codes. For the integral codes, like MELCOR improved cladding failure criteria might be sufficient.

The time history of the hydrogen generation is strongly influenced by local effects like bypass flow, steam starvation and relocated metallic melt. Due to the large deviations between measurements and calculations it can be concluded that either the existing models were not applied properly or the measurements might have a too large error band. For the total amount acceptable agreement could be achieved, if the code calculated the total amount of oxidized Zr correctly.

The B_4C absorber rod failed relatively early due to interaction of B_4C and SS-cladding as well as SS-guide tube. Subsequently the melt of absorber rod material attacks the fuel rod claddings. Regarding the material interactions and flow blockage larger differences occur between calculated and measured data because of inappropriate models for the material relocation and refreezing, and the lack of models for interaction of absorber rod material and the fuel rods.

In general the ISP showed that basically the code calculated the overall thermal bundle behavior sufficiently correct. Some material interactions and relocations have been fairly well simulated. But especially for detailed mechanistic codes the modeling of material interactions and failure criteria (fuel rod cladding and absorber rod) should be further developed. This assessment reflects the early core degradation processes only. It is obvious, that further modeling effort and international exercises should be

[2] The results are still in the process of being reviewed inside OECD

directed to the late phase core degradation.ISP36 documented the importance of actions of this kind. It provided a forum for the international community enhancing the experience in performing SFD-computations, it serves as an excellent basis for comparative assessment of the codes, and it thus may have a great impact on further code development acting into the same direction as independent peer reviews.

Literature

/1/ CSNI; Standard Problem Procedure; CSNI Report No. 17, January 1984

/2/ S. Hagen et al.
Results of Severe Fuel Damage Experiment CORA-13
KfK 5363, October 1994

/3/ K. Trambauer, H. Ball,
J. D. Schubert
Entwicklung des Rechenprogramms ATHLET-SA zur Analyse schwerer Störfälle
GRS-A-1937
Gesellschaft für Anlagen- und Reaktorsicherheit mbH, 1992

/4/ R. Gonzalez, P. Chatelard, F. Jacq
ICARE2 Version 2 MOD0 and MOD0.1
Description of Physical Models, Institut de Protection et de Suréte Nucléaire, Note Technique DRS/ SEMAR 92/94, CEA, France, 1992

/5/ K.-D. Hocke et al.
KESS-III, Ein Programmsystem zur Simulation auslegungsüberschreitender Störfälle in Leichtwasserreaktoren
IKE 2-93, Stuttgart, January 1991

/6/ R.M. Summers et al
MELCOR 1.8.2 Computer Code Manual;
Volume 1: Primer and User's Guides;
Volume 2: Reference Manuals and Programmers Guides,
Sandia National Laboratories, USA, 1993

/7/ RAPTA
(to be published)

/8/ C. M. Allison, et al
SCDAP/RELAP5/MOD3.1
Code Manual; Volumes 1-5
NUREG/CR-6150, EGG-2720, 1994

/9/ B. Adroguer et al
OECD/NEA/CSNI International Standard Problem ISP 28
PHEBUS-SFD B9+ Experiment on the Degradation of a PWR Core Type
Comparison Report, NEA/CSNI/ R(92)17, December 1992

/10/ M. Firnhaber et al.
OECD/NEA/CSNI International Standard Problem No. 31
CORA-13 Experiment on Severe Fuel Damage
CSNI Report NRA/CSNI/R(93)17, July 1993
GRS 106, KFK 5287

/11/ M. Firnhaber et al.
OECD/NEA/CSNI International Standard Problem No. 36
CORA-W2 Experiment on Severe Fuel Damage
CSNI/GRS/KfK-Report

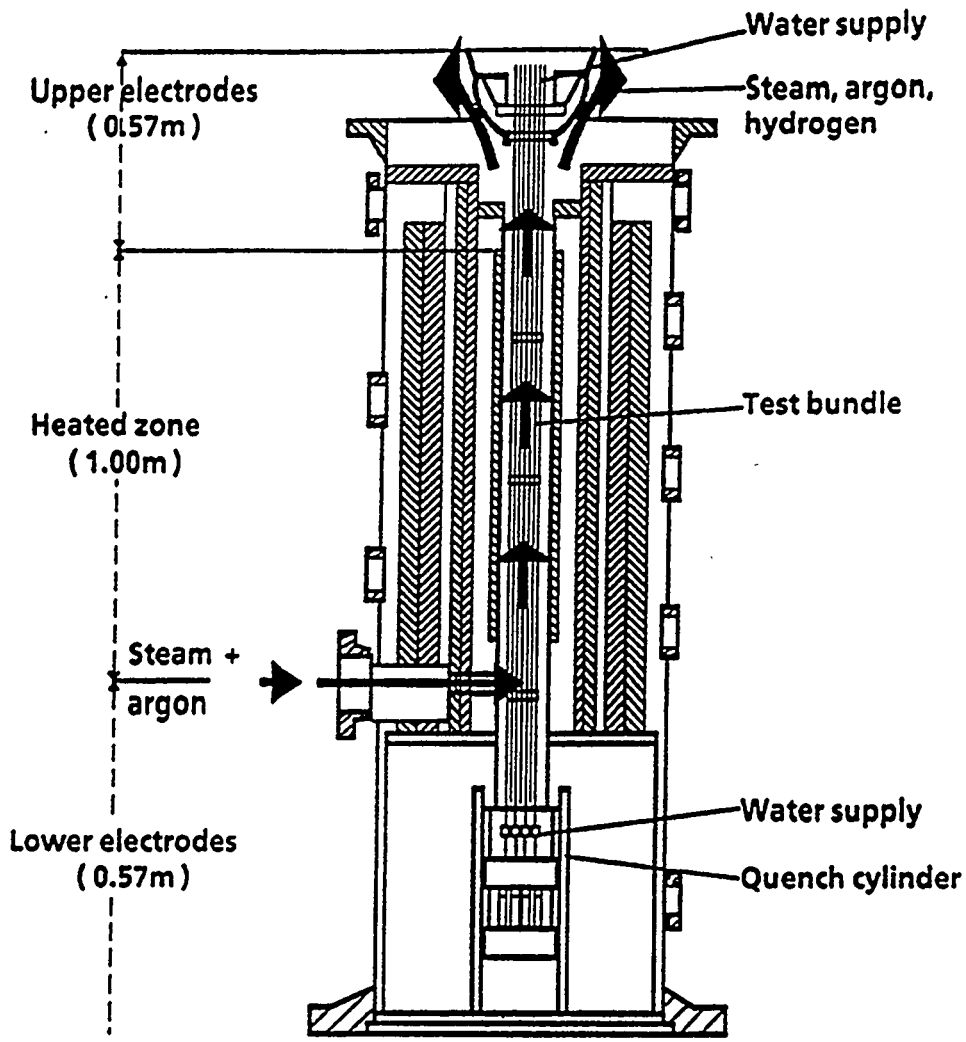
Tab. 1: Participants

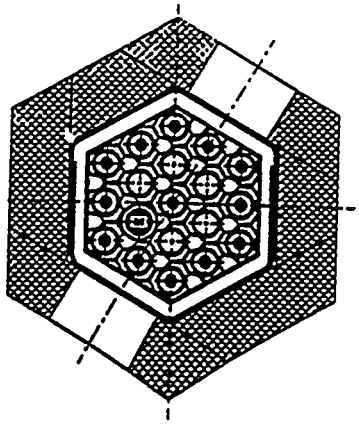
Legend	Participant
AEA	Atomic Energy Authority, Dorchester, UK
ARS	All - Russian Scientific and Research Institute of Inorganic Materials, Moscow, Russia
GID	EDO Gidropress, Podolsk, Russia
ENE	Ente per le Nuove Tecnologie, L'Energia e L'Ambiente, Bologna, Italy
GRS	Gesellschaft für Anlagen- und Reaktorsicherheit (GRS) mbH, Cologne, Germany
IKE	Institut für Kernenergietechnik, Stuttgart, Germany
KFI	Atomic Energy Institute, Budapest, Hungary
NRI	Nuclear Research Center Rez, Rez, Czech Republic
NUP	Nuclear Power Engineering Corporation, Tokyo, Japan
OKB	OKB Mechanical Engineering, Nizhny Novgorod, Russia
RAS	Russian Academy of Science Nuclear Safety Institute, Russia, Moscow
RDI	Research and Development Institute of Power Engineering, Moscow, Russia
RRC	Nuclear Safety Institute RRC "Kurchatov Institute", Moscow, Russia
TUD	Technical University of Dresden, Dresden, Germany
UBO	Ruhr-University of Bochum, Bochum, Germany
VTT	Technical Research Center of Finland, Espo, Finland

Tab. 2: Codes Used by Participants

Legend[1]	Code Used	Legend	Code Used
AEAM	MELCOR 1.8.2	TUDK	KESS III 1.0 WWER
GIDM	MELCOR 1.8.2	NRII	ICARE2 MOD 1 Release Dec. 1993
KFIM	MELCOR 1.8.2	RASI	ICARE2 MOD 1.0
NUPM	MELCOR 1.8.2, COR modified	RRCI	ICARE2 V2 MOD 1.0
OKBM	MELCOR 1.8.2	UBOI	ICARE2 V2 MOD 0
UBOM	MELCOR 1.8.2	ARSR	RAPTA-SFD
GRSA	ATHLET-CD MOD 1.1B 0.1V	ENES	SCDAP/RELAP5/MOD 2
RASA	ATHLET-CD MOD 1.1B 0.1V	RDIS	SCDAP/RELAP5/MOD 2.5
RRCA	ATHLET-CD MOD 1.1B 0.1V	RRCS	SCDAP/RELAP5/MOD 3.1
UBOA	ATHLET-CD MOD 1.1B 0.1V	UBOS	SCDAP/RELAP5/MOD 3.0 7o
IKEK	KESS III 1.3	VTTS	SCDAP/RELAP5/MOD 3 V7af

1 The first 3 letters stand for the institution (see Tab. 1) and the 4th for the code used (A = ATHLET-CD, I = ICARE2, K = KESS III, M = MELCOR, R = RAPTA-SFD, S = SCDAP/RELAP5).





CORA - W2

Fig. 1: CORA Test Facility and fuel rod arrangement

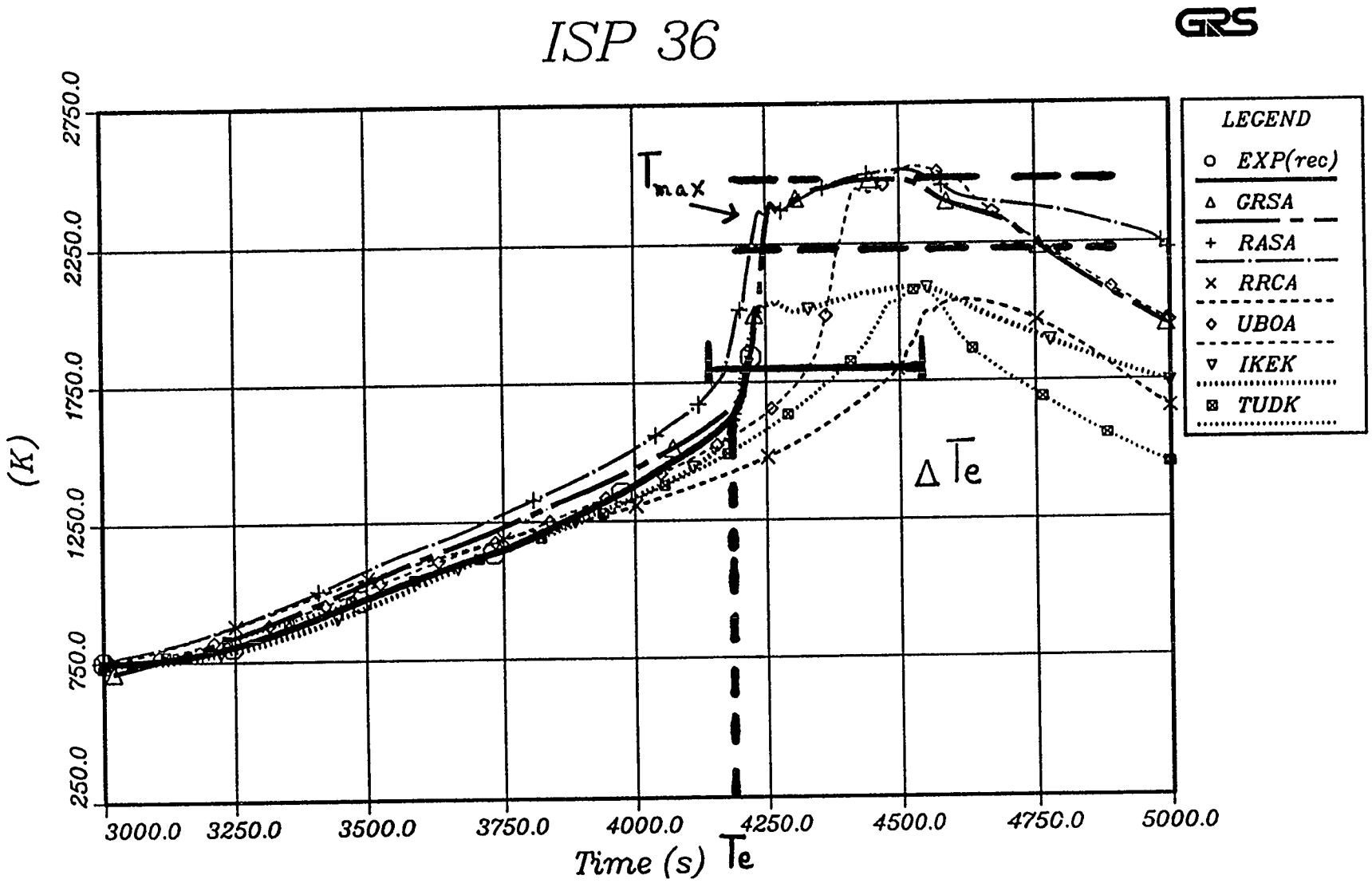


Figure 2: Fuel Temperature (TU02 0750); Codes: ATHLET-CD, KESS III

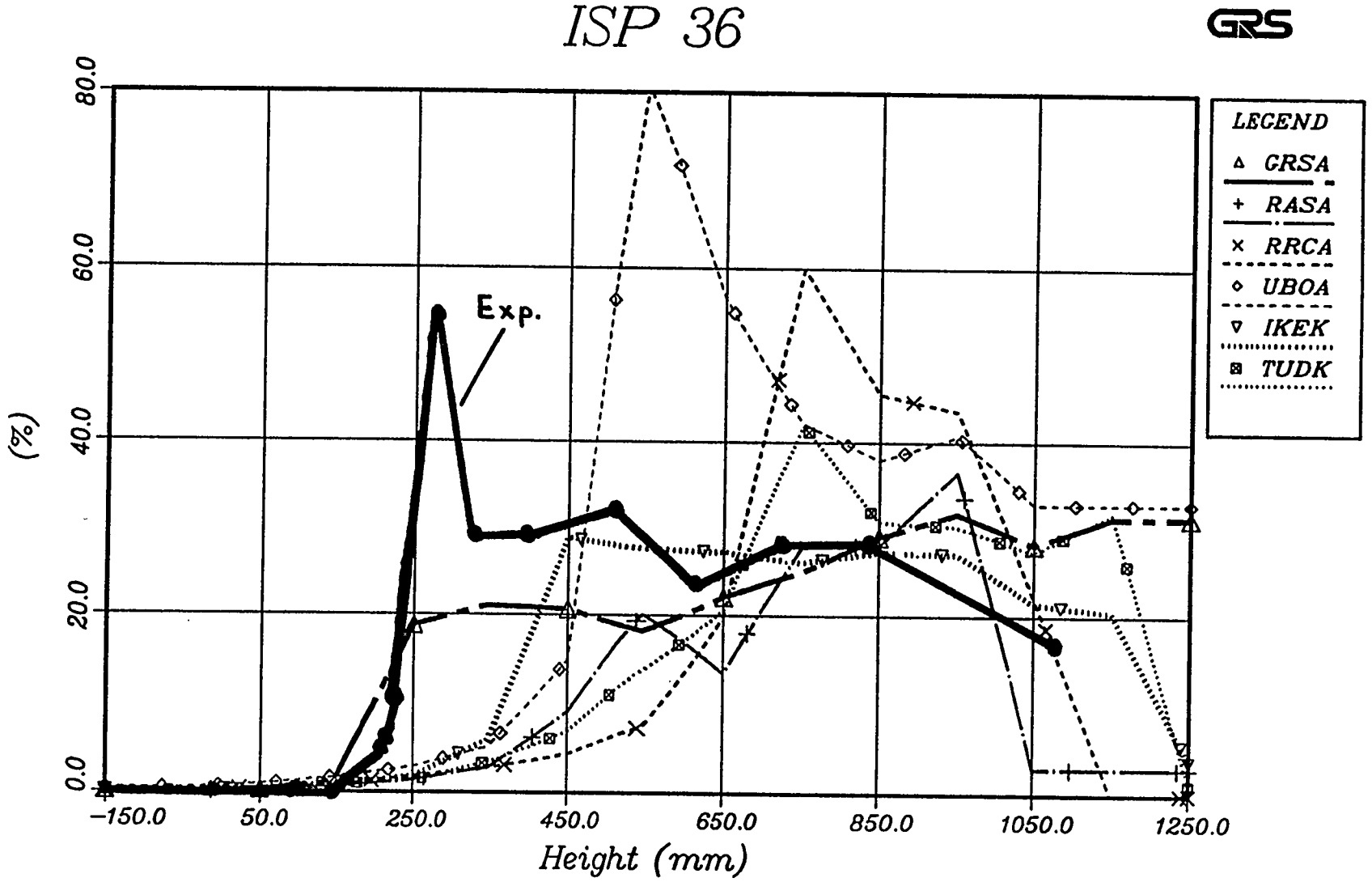


Figure 3: Zr Oxidized, Bundle, Orig. Pos. (Z0B0 4900); Codes: ATHLET-CD, KESS III

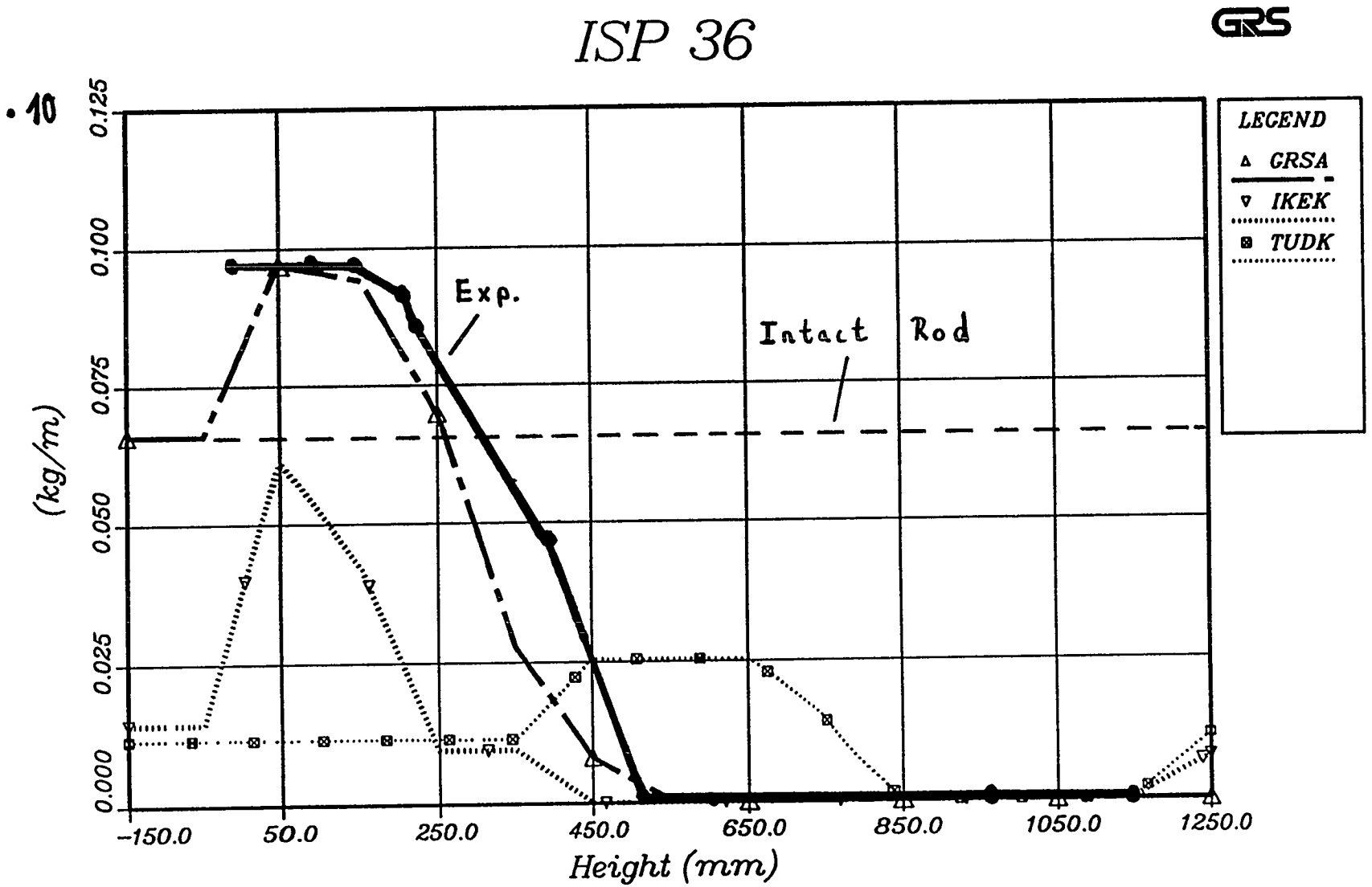


Figure 4: B_4C Total Mass (B_4CT 4900); Codes: ATHLET-CD, KESS III

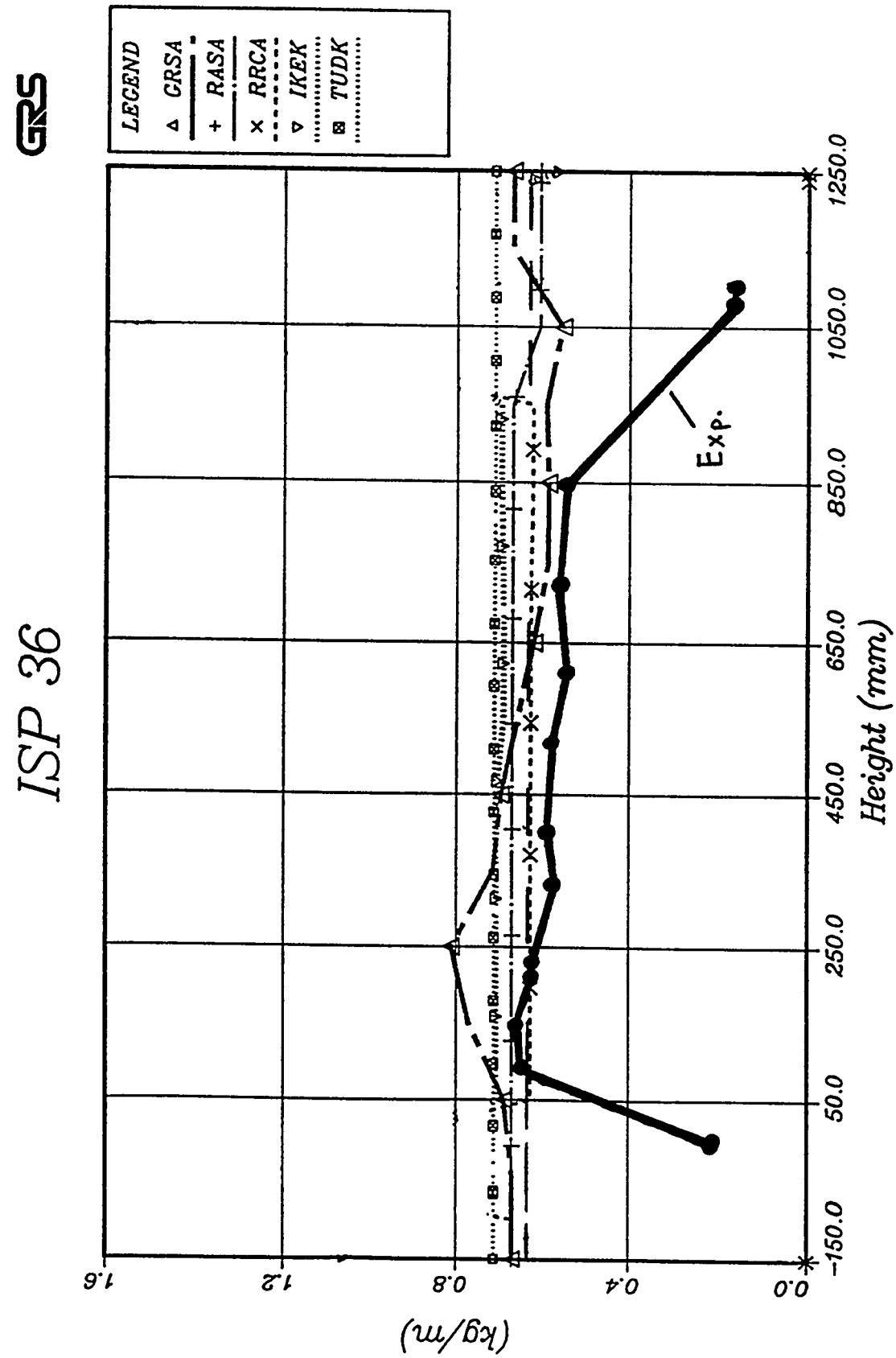


Figure 5: UO_2 Total Mass (UO_2T 4900); Codes: ATHLET-CD, KESS III

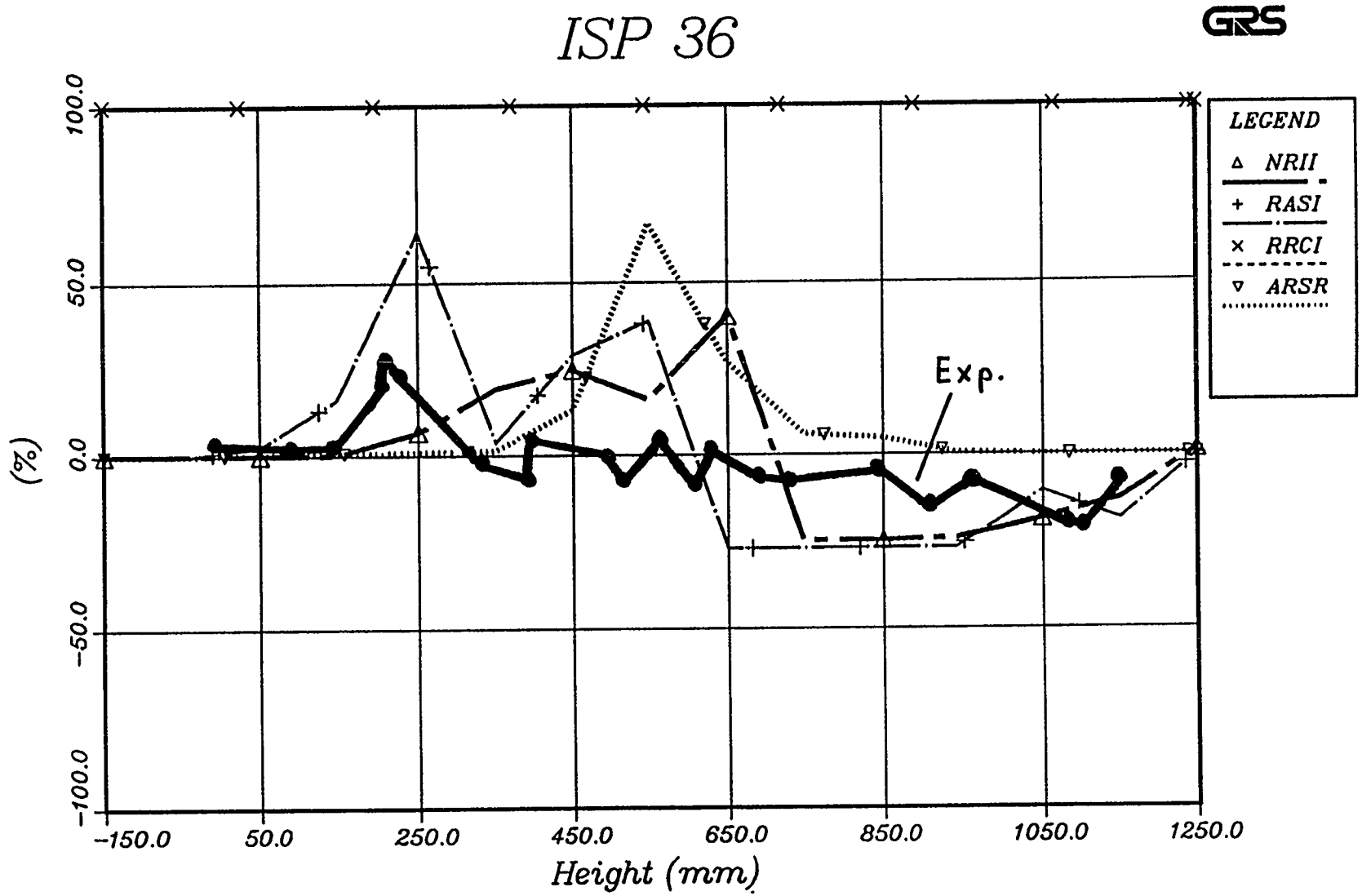


Figure 6: Core Blockage (COBL 4900); Codes: ICARE2, RAPTA-SFD

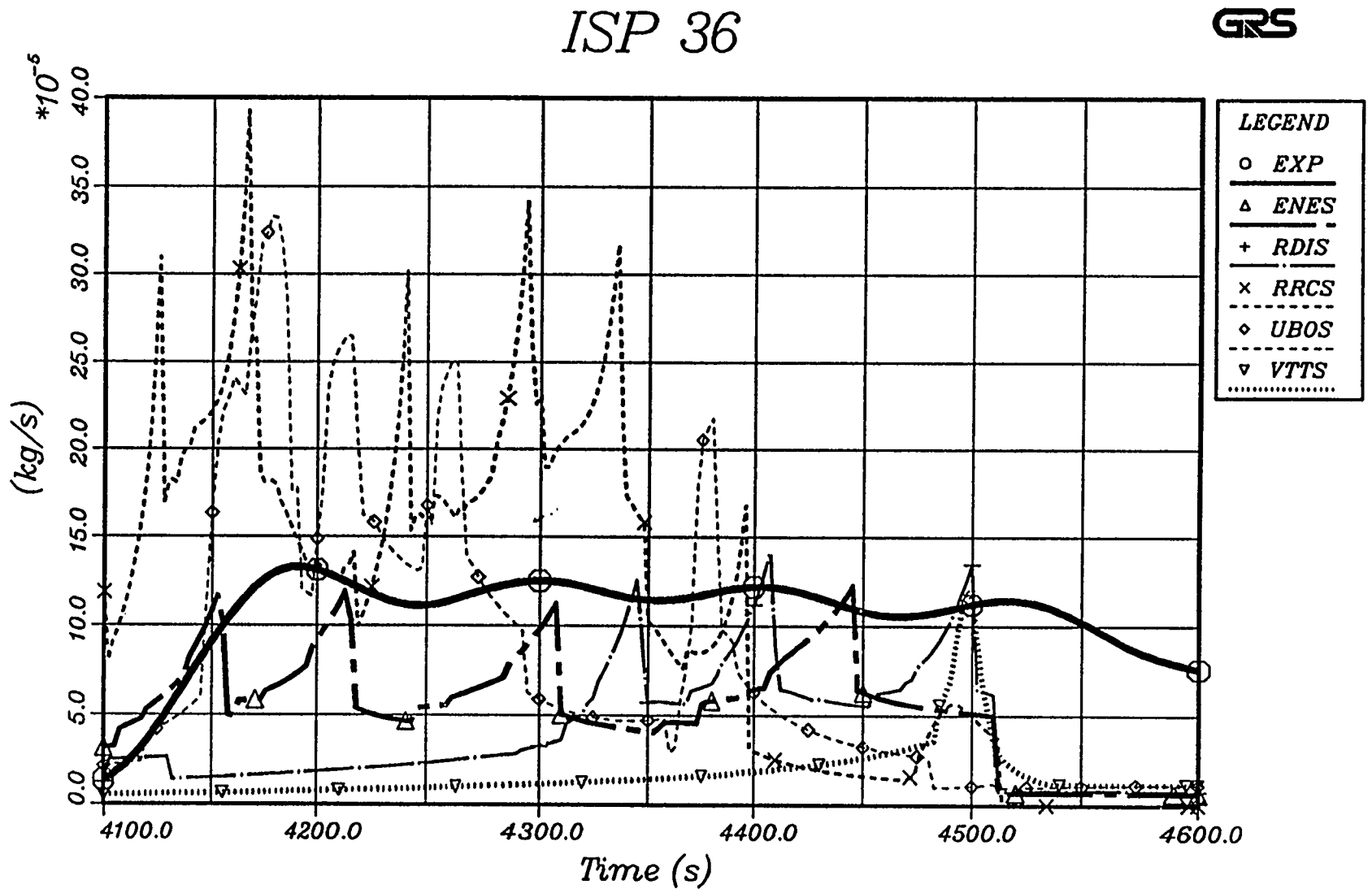


Figure 7: Hydrogen Generation Rate, Bundle + Shroud (HRBS); Code: SCDAP/RELAP5

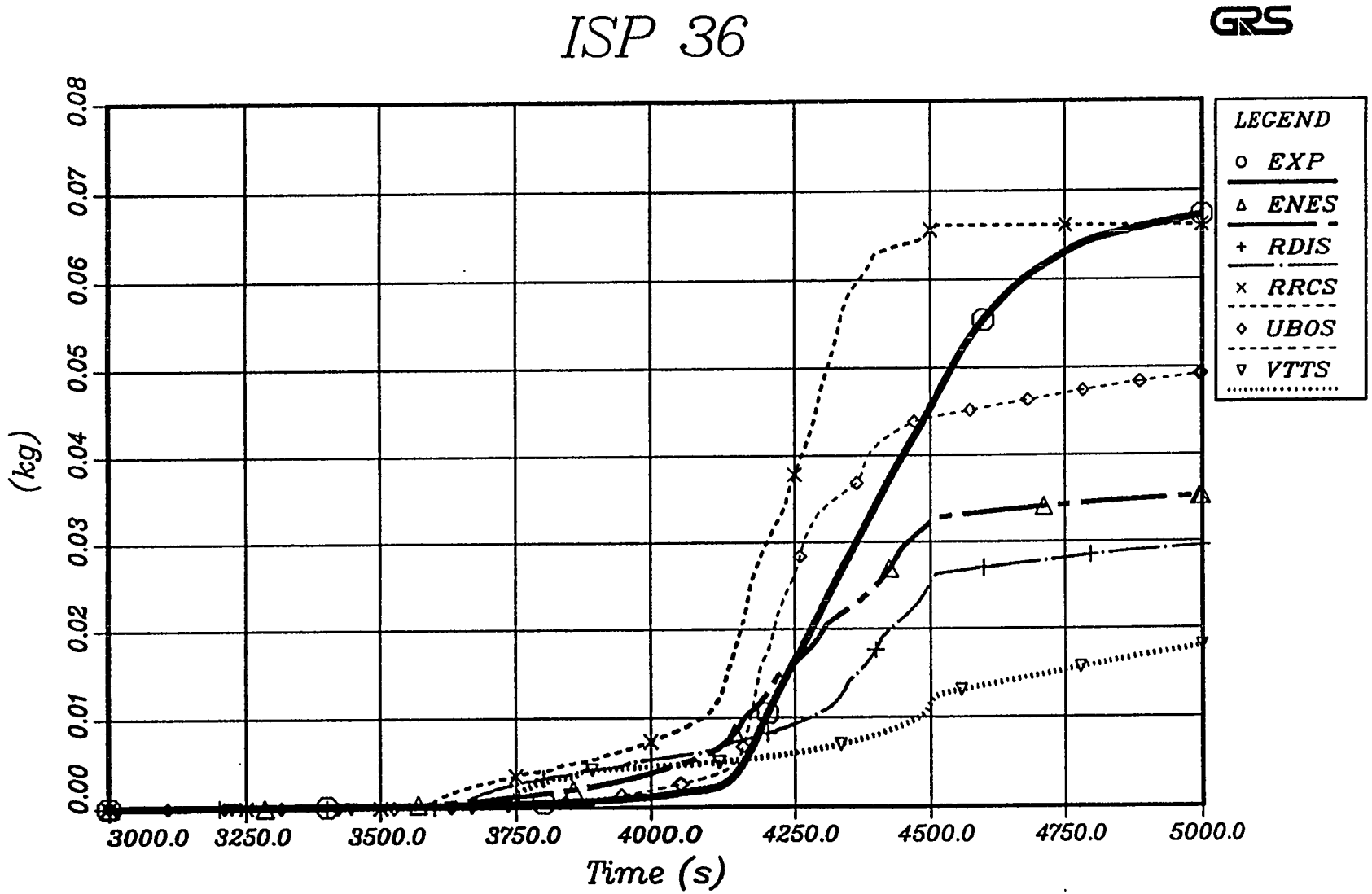


Figure 8: Acc. Hydrogen Generation, Bundle + Shroud (HABS); Code: SCDAP/RELAP5

Oxidation During Reflood of Reactor Core With Melting Cladding

L. J. Siefken

C. M. Allison

K. L. Davis

J. K. Hohorst

Abstract

Models were recently developed and incorporated into the SCDAP/RELAP5 code for calculating the oxidation of fuel rods during cladding meltdown and reflood. Experiments have shown that a period of intense oxidation may occur when a hot partially oxidized reactor core is reflooded. This paper offers an explanation of the cladding meltdown and oxidation processes that cause this intense period of oxidation.

Models for the cladding meltdown and oxidation processes are developed. The models are assessed by simulating a severe fuel damage experiment that involved reflood. The models for cladding meltdown and oxidation were found to improve the calculation of the temperature and oxidation of fuel rods during the period in which hot fuel rods are reflooded.

1. Introduction

This paper describes models for the oxidation of light water reactor fuel rods with cladding that melts and slumps during a severe accident. Oxidation of slumped material may result in a significant increase in the oxidation that began when the material being oxidized was configured as part of intact fuel rods. The oxidation of the slumped material thus has the potential of significantly influencing the damage progression and the hydrogen production occurring during a severe accident.

2. Kinetics Equation for Oxidation of Liquefied Material

The oxidation of liquefied Zircaloy and UO_2 is represented as a diffusion controlled process using an approximate parabolic rate law.[1] The parabolic rate law constants for 100% Zircaloy and 100% UO_2 have been well defined through experiments.[2] For mixtures of Zircaloy and UO_2, U-Zr-0, the experimentally determined constants are extremely limited. Therefore, the calculation of rate constants for U-Zr-O is based upon the assumption that the rate constant changes linearly with the mass fraction of UO_2 in the mixture. As shown on Figure 1, the comparison of a calculated rate constant with a correlation developed from data for a mixture of 85 mol% Zr and 15 mol% UO_2 by Prater and Courtright[3] shows good agreement at temperatures below 2000 K. The variation at higher temperatures is due to the differences in the rate constant for Zircaloy used in SCDAP/RELAP5, based upon a correlation developed by Urbanic and Heidrick[4] for temperatures above 1850 K, and a similar correlation developed by Prater and Courtright.[3]

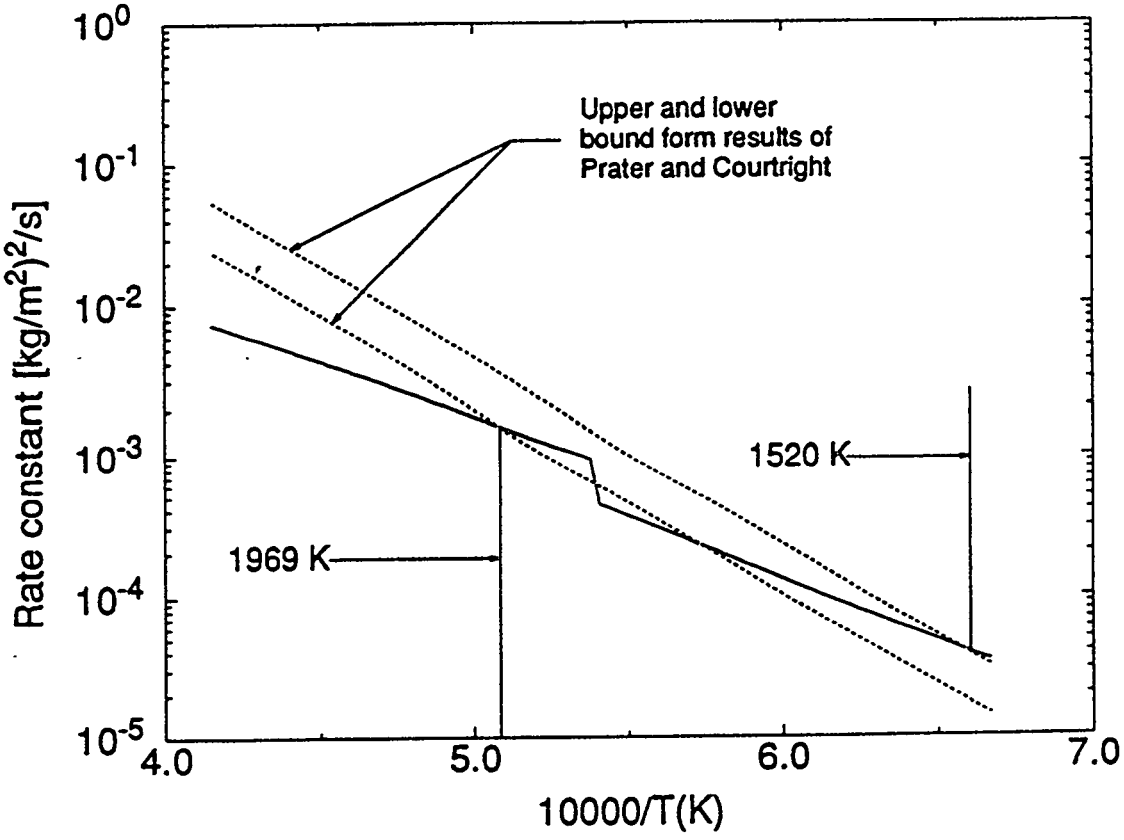


Figure 1. Parabolic rate constant for mixture of 85 mol% Zr and 15 mol% UO_2.

Although there is significant difference in the rate constant data for these high temperatures, assessment of the code for Zircaloy oxidation using a wide variety of bundle heating and melting experiments indicates that the Urbanic and Heidrick[4] correlation provides better overall agreement with the data than the Prater and Courtright correlation.[5]

The large variation in rate constants at high temperatures is normally not important in bundle heating and melting experiments because the maximum oxidation rates are limited by the availability of steam at the surface of the material. In the SCDAP/RELAP5 models, the limits on oxidation due to steam availability are represented using two related models. First, the diffusion of steam to the surface of liquefied material is limited using a mass/heat transfer analogy to determine a mass diffusion rate constant. Second, the driving potential for the diffusion process is determined by the local steam bulk mass flow. That is, as the steam is replaced by hydrogen during the oxidation process, the bulk concentration of steam in the flow channel is reduced correspondingly. The oxidation rate is also limited at high temperatures by the availability of unoxidized material. The oxidation process is normally terminated because the material either becomes completely oxidized or relocates to a colder region where the oxidation rate is effectively zero.

3. Oxidation of droplets of liquefied fuel rod material

Meltdown of the cladding of fuel rods may have a significant impact on the subsequent damage progression that occurs in a reactor core. In some cases, meltdown may result in a rapid increase in the oxidation rate of the reactor core. In other cases, meltdown may result in the blockage of coolant flow. The modeling of cladding meltdown is empirical in nature and is based on the observed behavior of melting and relocating cladding of fuel rods. A theoretical analysis performed by Dussan and Chow[6] showed that a mechanistic model depicting the motion of a drop flowing down a surface in response to gravity requires correlations that define the contact angles as a function of the velocity of the moving drop. These correlations for advancing and receding contact angles as a function of velocity are not available for a mixture of Zr-U-O flowing down the surface of a fuel rod. Thus an empirical model for the configuration and motion of drops of Zr-U-O has been developed that is based on observations of cladding meltdown during experiments that subjected fuel rods to severe damage. The observations used to develop these models are primarily obtained from the CORA experiments[7,8] and supplemented by results from post irradiation examinations (PIE) of several other severe fuel damage experiments.[9,10] The development of the new oxidation model used during reflood and clad relocation is described in the following section.

3.1 Experimental observations of fuel rod meltdown

An example of the configuration of a fuel rod with cladding meltdown is shown in Figure 2. This figure was taken during the post test examination of the damaged CORA-13 fuel bundle.[8] A significant result that is shown in Figure 2 is that the slumped material is in the configuration of drops. Other severe fuel damage experiments such as CORA-7 have shown a similar behavior for liquefied fuel rod material that has slumped.[11] The characteristics of slumping material considered to be the most important are summarized in Table 1. The average velocity of slumping drops is estimated to be 0.05 m/s. The drops are observed to have a wide range of velocities, with some drops slumping as slowly as 0.01 m/s and some as rapidly as 1.0 m/s. The definition of the contact angles used to characterize the configuration of the drops is shown in Figure 3.



Figure 2. Posttest view of bundle CORA-13.

Table 1. Characteristics of meltdown of fuel rod cladding.

Characteristic Number	Description of Characteristic
1	*Relocated material is in the configuration of drops*
2	*Drops slump at velocity of about 0.05 m/s.*
3	*Advancing contact angle is about 100 degrees.*
4	*Receding contact angle is about 80 degrees.*

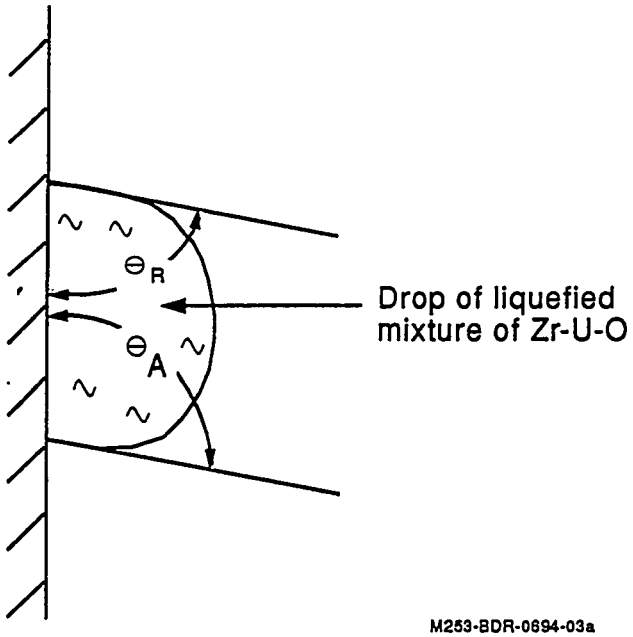


Figure 3. Configuration of drop of liquefied material suspended on surface of fuel rod.

3.2 Breach of Cladding Oxide Layer

The release of droplets of a liquefied mixture of cladding and dissolved fuel is caused by a breach of the cladding surface ZrO_2 layer. To determine if a breach in a shell of cladding oxide occurs, criteria based on well defined parameters are used. Variables defining the criteria are temperature, extent of oxidation of the cladding, and the fraction of liquid in the fluid at the surface of the fuel rods. Liquid droplets of water in contact with an oxide shell that contains a mixture of liquid cladding and dissolved fuel are assumed to disrupt the shell.

3.3 Configuration and Relocation of Liquefied Zr-U-O

This step of the modeling calculates the configuration and relocation of liquefied Zr-U-O that pours through a breach in the ZrO_2 layer and slumps downward until solidifying. The configuration of the slumping material is taken into account in calculating the oxidation of the slumping material. The relocated material that is released by a breach is assumed to be configured as an array of drops as shown in Figure 4.

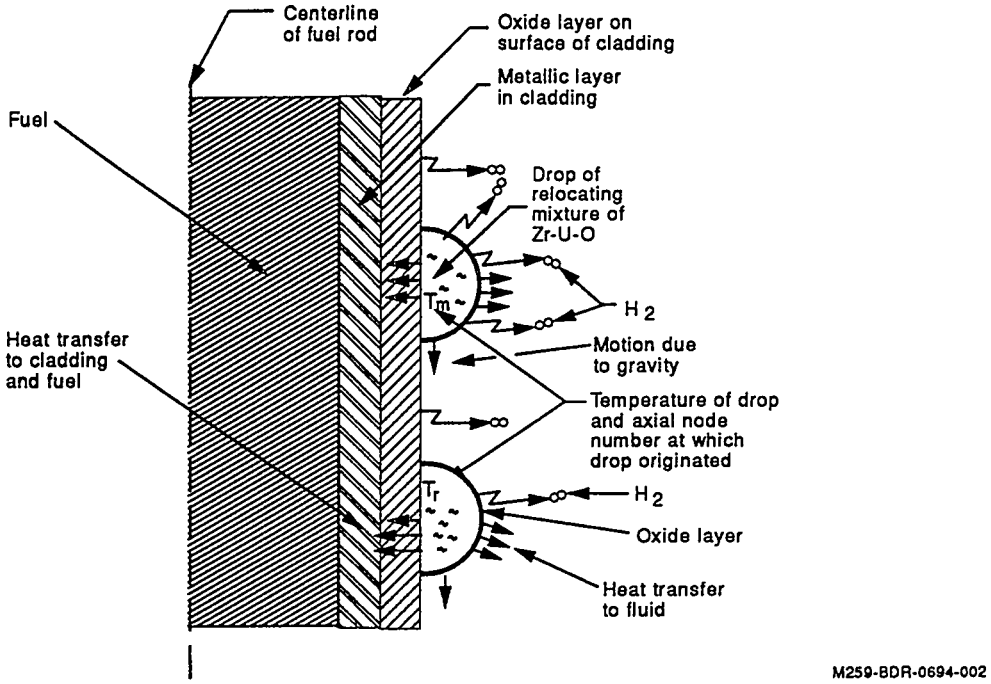


Figure 4. Cross section of fuel rod with oxidation of relocating material and intact section of fuel rod.

The size and surface area wetted by each drop of slumping material is calculated based on the application of the Dussan and Chow[6] lubrication theory. In order to calculate the radius of the drops of slumping material, two simplifying assumptions are required. The first assumption is that the drops are in the shape of a hemisphere and the second is that the area wetted by moving drops is 10% larger than the area wetted by static drops. For values of wetting angles shown in Table 1, and using value of 0.45 N/m for surface tension and 7000 kg/m^3 for a drop density, a drop radius of 2.5 mm is calculated. This value is in agreement with the size of the drops observed in the cladding meltdown experiments, shown in Figure 2.

The oxidation of the drops of Zr-U-O on the outside surface of the fuel rod may result in a significant amount of heat generation. Oxidation of these drops occurs very rapidly because the hot metallic material released from the protective oxide shell on the cladding surface is exposed directly to steam. The rate of oxidation is limited, in most cases, by the availability of steam in the vicinity of the drops and by the rate of mass transfer between the steam and hydrogen at the surface of the drops. Heat generation in the fuel rod due to oxidation is calculated based on the configuration shown in Figure 4. The oxidation of the portion of the fuel rod surface covered with drops is represented by the drop oxidation model and the oxidation of the uncovered portion of the fuel rod is represented by the oxidation model for intact fuel rods. Drops are identified according to the axial node at which they originated. This distinction takes into account the different extents of oxidation of drops that have different times of origin. When a breach occurs at an axial node, all the liquefied material inside the fuel rod is assumed to be simultaneously released to the surface of the fuel rods and to form drops.

Oxidation at an axial node with drops of relocated material is calculated in three steps. First, the change in weight gain per unit surface area is calculated. This calculation takes into account the temperature of the drop, the composition of the mixture of Zr-U-O in the drop, the spalling of the oxide layer due to contact with water which exposes the metallic part of the drop to steam, and the limitation on

the rate of mass transfer. Second, the rate of heat generation for each drop is calculated taking into account the surface area and composition of the drop. Third, the surface area of the axial node not covered with drops is calculated and used to calculate the heat generation due to oxidation of the uncovered portion of the cladding.

Drops released from a breach in the cladding surface flow downward. Dussan and Chow[6] determined that the downward velocity of a falling drop can be mathematically approximated, although the exact velocity due to gravity of a falling drop must be determined from experimental results. A limited survey of experimental results showed that the average velocity of a moving drop is about 0.05 m/s. Experimental data is currently too limited to develop a correlation relating the downward velocity of falling drops to parameters such as the temperature and composition of the drop. Thus the downward velocity of the drop is assumed to be 0.05 m/s if the drop temperature is greater than the solidus temperature of material in the drop and 0.0 m/s if the drop temperature is less than the solidus temperature.

The experimentally determined value for drop velocity can be compared to the theoretical value calculated on the basis of assumed values for the rate of change in velocity with respect to the change in the advancing and receding contact angles. Since the change in contact angles with respect to velocity has not been measured, the contact angles are conjectured to linearly increase by a value of $\pi/36$ as the velocity of the drop changes from 0 to 0.05 m/s. If these assumptions are applied, the theoretical value for downward velocity is calculated to be 0.02 m/s. The estimated value from experimental data of 0.05 m/s. In view of the large uncertainties in material properties, the theoretical and experimentally based values are considered to be in fair agreement and the assumption made to calculate drop size was not unreasonable.

The temperature of the drops is calculated taking into account the heatup of the drop due to oxidation and the transfer of heat from the drop to the substrate on one side of it and to the fluid on the other side. The heat transfer process modeled is shown in Figure 5. A temperature wave propagates into an axial slice of the fuel rod beginning the instant the drop of relocating material comes in contact with the surface of the axial slice. The amount of heat transferred into the axial slice is calculated using the integral method.[12] Transient heat flux at the surface of each axial slice is calculated assuming that the temperature of the surface changes from the cladding temperature to the drop temperature the instant that the drop comes in contact with the surface. The distance propagated by the temperature wave is proportional to the square root of time. The temperature change of falling drops is calculated in five steps; (1) calculate the length of time the axial slice is covered by the flowing mixture; (2) calculate the amount of heat conducted into the axial slice from the time the leading edge on the drop contacted the surface of the slice to the time that the receding edge covered the surface of the slice, (3) calculate the amount of heat transferred from the drop to the surrounding fluid during the time the drop covered the axial slice, (4) calculate the heat generation in the drop, and (5) calculate the temperature change of the drop during the time step. The heat transfer from the drop to its cladding substrate is accounted for by the heat conduction model of the intact fuel rod. The heat generation term for the cladding includes the heat transfer from the drop to the cladding. The term that accounts for the transfer of heat from the fuel rod to the fluid is incremented to also account for the heat transfer from the drop to the fluid.

After drops have frozen and become static, the drops are represented as being part of the cladding. First, the equilibrium temperature is calculated for the drops and the fuel rod at the axial node at which the drops solidified. This calculation of equilibrium temperature adds the internal energy of the drops to the fuel rod internal energy term. The subsequent representation of the drops is performed using the heat

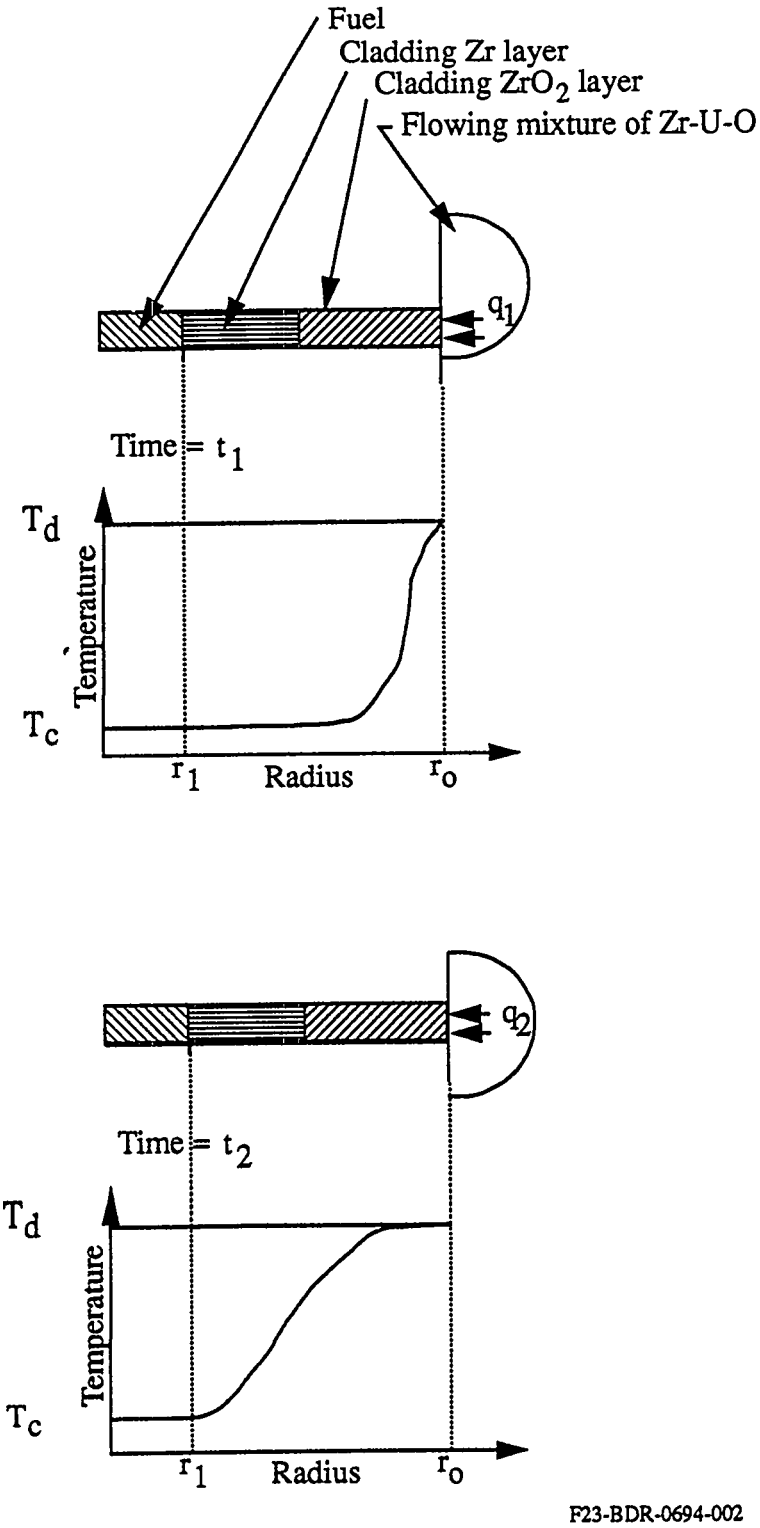


Figure 5. Heat transfer from flowing mixture into axial slice of fuel rod.

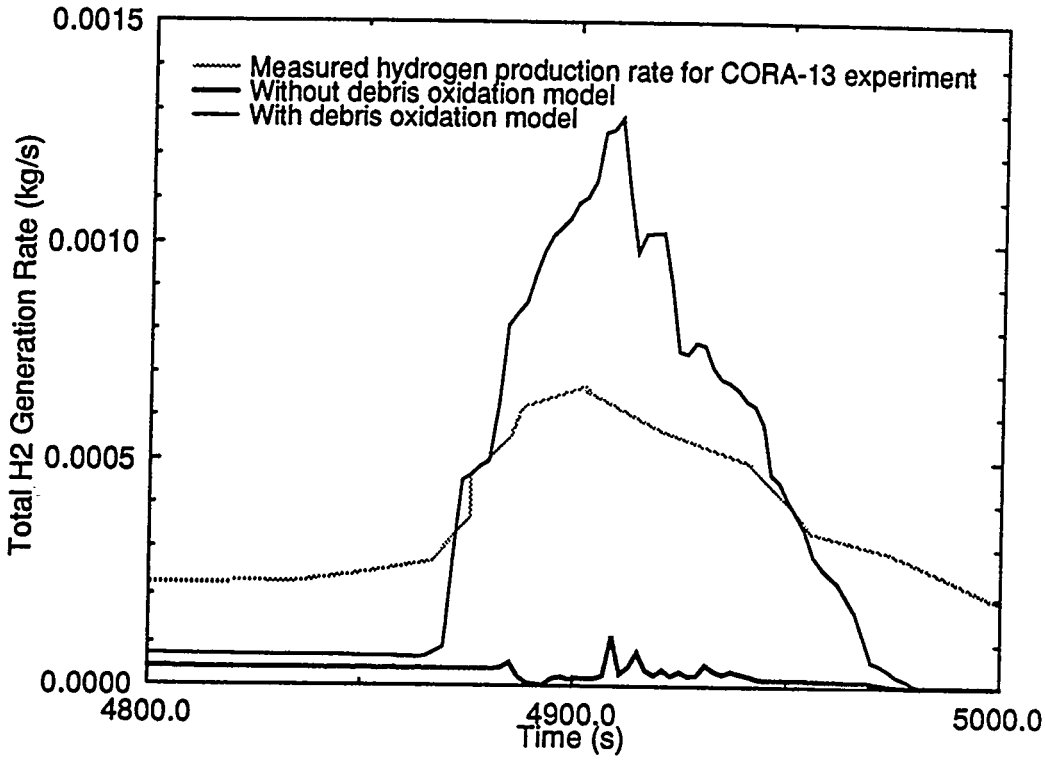


Figure 6. Calculated hydrogen production rate during reflood period.

conduction model for intact fuel rods. The heat capacity of the drops is taken into account in calculating the effective heat capacity of the cladding and the oxidation of the drops is taken into account in calculating the oxidation of the cladding. If the drops heat up to the point of liquefaction, then the drops are calculated to move in response to gravity and the temperature of the drops is again calculated.

Shattering of the oxide layer on frozen drops is assumed to occur as for the oxide layer on intact cladding.[1] If the drops of relocated cladding are above a temperature of 1150 K and are contacted by drops of water, then the oxide layer is considered to shatter and expose the metallic part of the drop directly to steam. The shattering is assumed to occur over the entire interface area between the oxide layer and its metallic substrate. The oxide layer is not modeled as continuously shattering but is considered to shatter after the layer has attained a threshold value for the weight gained since the last shattering. An exact threshold value needs to be determined experimentally.

4. Results

The new oxidation models had a significant impact on the predicted response of the CORA-13 bundle during reflood. Even though the code was previously able to predict the sharp burst of hydrogen observed during the reflooding of the experimental bundle, the cumulative hydrogen generation, peak oxidation rate, and the associated bundle temperature excursion during reflood was underpredicted. With the new model these discrepancies were either significantly reduced or eliminated. For example, the cumulative hydrogen generation predicted without the new models was 70 g, and with the models is 144 g. The measured value was 210 g. The calculated value is less than the measured value in part because the calculations did not represent structures above the test bundle that oxidized. Figure 6 shows the predicted

hydrogen production rate during the reflood phase of the experiment. The peak oxidation rate occurring during reflood was increased by a factor of ten by the addition of the new models. The new rate is in much better agreement with the experiment as well. The sharp rises in hydrogen production are due to the shattering of the oxide layer as reflood water comes in contact with the hot fuel rod and the oxidation of the newly exposed Zircaloy. The percentage of the total hydrogen production that occurred during the reflood period of the experiment was calculated to be 48%, which is the same as the measured value.

The temperature response during reflood was also much improved as indicated in Figure 7. This figure shows the calculated fuel rod temperatures at the 750 mm elevation for both cases along with the measured temperature at the 1150 mm elevation. The 1150 mm elevation is above the directly heated region of the bundle and is the closest location to the 750 mm elevation for which measurements are available. Thermocouples at the 750 mm for the fuel rods had failed during the experiment prior to reflood although the estimated peak temperatures at this location were compable to those at 1150 mm elevation. Calculated temperatures at the 1150 mm elevation were not available because the region above the heated partion of the test bundle was not represented in the calculations.

The uncertainty in the measured temperatures is estimated to be ± 20%. The calculated temperatures fall within the range of uncertainty of the measure temperatures.

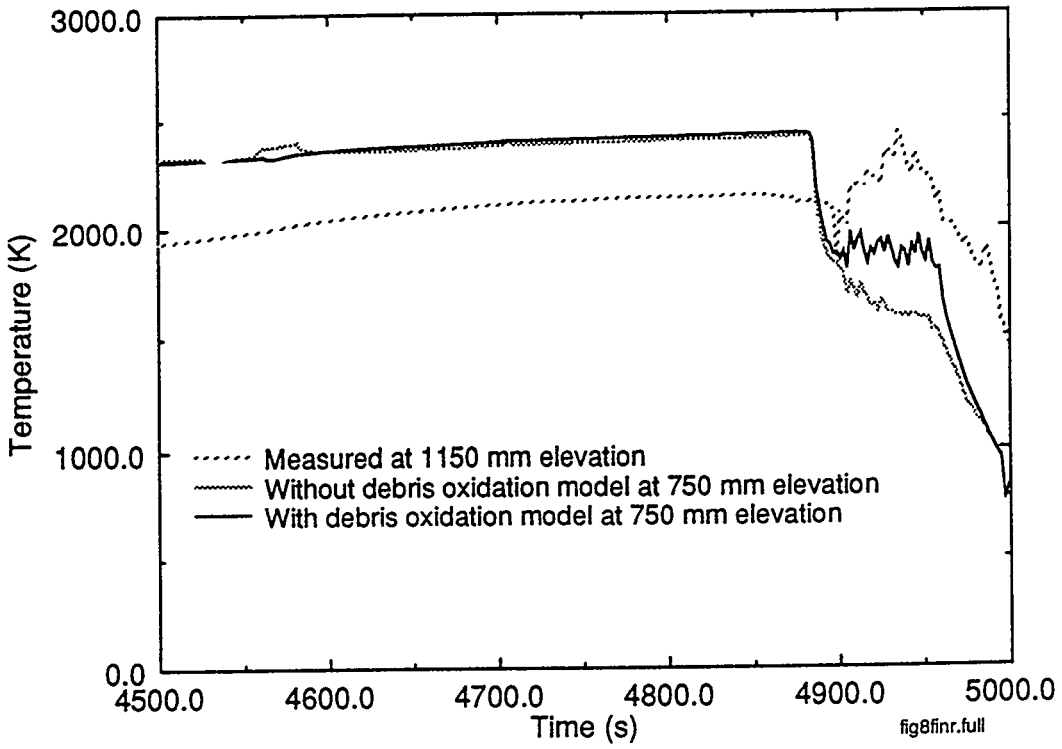


Figure 7. Calculated fuel rod temperatures at the 550 mm elevation compared to measured upper bundle temperatures for the CORA-13 experiment.

5. Conclusions

Models have been developed to calculate the oxidation of a reactor core as it degenerates during a severe accident. The models indicate that the quenching of a hot and partially oxidized reactor core may result in an oxidation excursion and the production of a large amount of hydrogen. The oxidation excursion is triggered by the release of liquefied metallic material at the same time that a large amount of steam is available to fuel the oxidation excursion. A limited amount of assessment of these models has been completed. The assessment to date indicates that the models are in good agreement with CORA-13 experimental result. Further assessment of the models and further evaluation of the experimentally determined parameters which the model uses are planned for the future. The experimentally determined parameters to be further evaluated include: (1) velocity of drops of slumping material, and (2) temperature range for which an oxide layer shatters during reflood.

6. References

1. C. M. Allison et al., *SCDAP/RELAP5/MOD3.1 Code Manual, Volume II; Damage Progression Model Theory*, NUREG/CR-6150, EGG-2720 Volume 2, October 1993.
2. J. K. Hohorst et al., *SCDAP/RELAP5/MOD2 Code Manual, Volume 4: MATPRO--A Library of Materials Properties for Light-Water-Reactor Accident Analysis*, NUREG/CR-5273, EGG-2555, February 1990.
3. J. T. Prater and E. L. Courtright, *Properties of Reactor Fuel Materials at High Temperature*, NUREG/CR-4891, July 1987.
4. Urbanic and Heidrick, V. F. Urbanic and T. R. Heidrick, *"High Temperature Oxidation of Zircaloy-2 and Zircaloy-4 in Steam," Journal of Nuclear Materials*, 75, 1978, pp 251-261.
5. C. M. Allison et al., *SCDAP/RELAP5/MOD3.2 Code Manusl, Volume V, Development Assessment*, NUREG/CR-6150, EGG-2720 Volume 5, October 1993.
6. E. B. Dussan V and Robert Tas-ping Chow, "On the Ability of Drops or Bubbles to Stick to Non-Horizontal Surfaces of Solids," *Journal of Fluid Mechanics*, Vol. 137, pp 1-29, 1983.
7. S. Hagen, L. Sepold, P . Hofmann and G. Schanz, *Out of Pile Experiments of LWR Severe Fuel Damage Behavior, Tests CORA-C and CORA-2*, KfK 4404, September 1988.
8. S. Hagen et al., *Results of SFD Experiment CORA-13 (OECD International Standard Problem 31)*, KfK 5054, February 1993.
9. S. M. Jensen, D. W. Åkers and B. A. Pregger, *Postirradiation Examination Data and Analysis for OECD LOFT Fission Product Experiment LP-FP-2, Volumes 1 and 2*, OECD LOFT-T-3810, December 1989.
10. D. A. Petti et al, *PBF Severe Fuel Damage Test 1-4 Test Results Report*, NUREG/CR-5163, EGG-2542, EG&G Idaho, Inc., December 1986.
11. P. Hofmann, S. Hagen, G. Schranz and L. Sepold, Material Behavior in the Large PWR Bundle Experiment CORA-7, International CORA Workshop, September 23 - 26, 1991, Karlsruhe, Germany.
12. T. R. Goodman, *"Application of Integral Methods to Transient Nonlinear Heat Transfer,"* Advances in Heat Transfer, 1 (1964), pp 51-120.

Crust Formation and Its Effect on the Molten Pool Coolability

R. J. Park, S. J. Lee, S. K. Sim, and K. J. Yoo

Severe Accident Research Group
Korea Atomic Energy Research Institute
P.O. Box 105, Daeduk-Danji, Taejon,
KOREA, 305-600
Tel) 82-42-868-2691
Fax) 82-42-861-2574
E-mail) r270prj@crayc90.seri.re.kr

Abstract

Experimental and analytical studies of the crust formation and its effect on the molten pool coolability have been performed to examine the crust formation process as a function of boundary temperatures as well as to investigate heat transfer characteristics between molten pool and overlying water in order to evaluate coolability of the molten pool. The experimental test results have shown that the surface temperature of the bottom plate is a dominant parameter in the crust formation process of the molten pool. It is also found that the crust thickness of the case with direct coolant injection into the molten pool is greater than that of the case with a heat exchanger. Increasing mass flow rate of direct coolant injection to the molten pool does not affect the temperature of molten pool after the crust has been formed in the molten pool because the crust behaves as a thermal barrier. The Nusselt number between the molten pool and the coolant of the case with no crust formation is greater than that of the case with crust formation. The results of FLOW-3D analyses have shown that the temperature distribution contributes to the crust formation process due to Rayleigh-Benard natural convection flow.

1. INTRODUCTION

From a nuclear reactor safety point of view, much attention has been given to the corium pool coolability[1, 2, 3]. If energetic FCI(Fuel Coolant Interaction) is not occurring when the water is injected into the corium pool during a hypothetical severe accident, the crust can be formed over the corium pool. Due to the complexity of the corium pool coolability phenomena, crust formation process of the corium pool and its effect on the corium pool coolability have not been clearly understood.

If the crust is formed around the deep corium pool, corium coolability is degraded because the crust behaves as a thermal barrier[4] between the coolant and corium pool. The crust formation of the corium pool is a very important phenomenon to understand the range of corium pool coolability configuration in the core, in the lower plenum, and in the reactor cavity. For

this reason, the crust formation process of the corium pool should be understood more precisely. Many macroscopic studies have been performed in the field of corium pool coolability[5, 6, 7], but few microscopic studies on the crust formation phenomena and heat transfer mechanisms around the crust have been performed. Therefore, it is necessary to estimate the crust formation characteristics and its effect on the corium pool coolability.

Experimental and analytical studies on the crust formation of the corium pool in a hypothetical severe accident of nuclear power plant have been performed. The objectives of this study are to investigate the crust formation processes by changing the boundary temperatures and the coolant injection methods for understanding the thermal barrier behavior of the crust as well as the heat transfer characteristics between the corium pool and the overlying water.

Steady state tests on the crust formation in the molten pool have been performed for the case with non boiling situations. Experiments for a case of direct coolant injection into the test section and a case of using heat exchanger have been performed to investigate the crust formation characteristics as a function of corium pool temperature and the coolant conditions contacting with the corium pool. Analytical studies have been performed to validate and to evaluate the test results using FLOW-3D computer code[8]. The results can be used to validate the crust formation process models of the molten pool presently used in the severe accident computer codes and to understand the insight of the crust formation phenomena of the molten core material pool.

2. EXPERIMENTAL APPARATUS AND PROCEDURES

Steady state tests of the crust formation on the molten pool have been performed to investigate the crust thickness and heat transfer characteristics around the crust as a function of the coolant injection conditions and setting temperatures of the top of the coolant and the bottom surfaces of the molten pool. As shown in Figure 1, test facility is consisted of four parts, namely, test section, coolant injection system, data measuring system, and data acquisition system. The size of rectangular test section was 15 cm in height, 15 cm in depth, and 45 cm in width. A 2 kW heater was installed to maintain the uniform temperature of lower plate at the horizontal bottom surface of the test section. A 5 mm thick STS304 stainless steel plate was installed between the heater and the inner side of test section. And a 3 mm thick copper plate was installed to maintain the uniform temperature of the bottom plate of the heat exchanger at the horizontal top surface of the test section for the case of using heat exchanger.

The pyrexglass was used for the visual inspection of the inside of the test section at the vertical front and back surfaces. Three pipe lines of coolant inlet/outlet and low melting alloy drain, and two thermocouple outlet lines were installed at the two vertical sides made of 5 mm thick STS304 stainless steel.

The sides of the test section were well insulated with a 3 cm thick Fiberfrax insulation material to reduce heat loss to the environment.

Two coolant pipe lines of heat exchanger and direct injection into the test section were installed to provide the coolant. The coolant region inside of test section has a closed system for the case with heat exchanger, but it has a part of open loop for the case with direct coolant injection into the test section. A 605 Di/R digital pump was installed to provide uniform mass flow rate of coolant at the coolant injection pipe line. A heater and a thermocouple were installed in a water storage tank to maintain the injection temperature of coolant for the case with direct coolant injection into the test section.

The measuring system included 39 copper constant thermocouples(type T) and the digital pump speed. Measurements of the temperature distribution of the inside of test section were made with 30 thermocouples. They were placed in two Teflon bars located at one-half and three-fourths of the width of test section. The crust thickness was calculated by interpolation of the measured low melting alloy temperature applying Stefan condition, which phase change occurred at melting temperature. The mass flow rate of direct coolant injection into the test section was calculated by conversion of the measured digital pump speed.

A data acquisition system based on IBM 486 personal computer was used in this test. Heater power and coolant mass flow rate were controlled to maintain uniform temperature of the bottom of the molten pool and the top plate of the test section for the case with heat exchanger. Heater power and coolant injection tank power were controlled to maintain uniform temperature of the bottom plate of the test section and the coolant for the case with direct coolant into the test section. The heat transfer coefficients between the corium pool and the crust have been estimated by performing a total energy balance, integrated bottom heat flux, latent energy of the corium mass frozen, integrated top heat flux, and energy loss to the environment.

The test parameters were coolant injection condition, which is a direct coolant injection into the test section and a heat exchanger, setting temperature of the heat exchanger from 30 °C to 60 °C, bottom plate setting temperature of the molten pool from 80 °C to 100 °C, setting temperature of direct coolant injection into the test section from 40 °C to 60 °C, and the mass flow rate of direct coolant injection into the test section from 2.48 kg/min to 6.50 kg/min. The simulant material for the corium melt was low melting alloy(wood metal's with composition in weight percent: Bi=49.92, Pb=13.28, Sn=13.28, Cd=9.85) of which melting temperature was 70 °C as a corium. The low melting alloy had a density of 9383.2 kg/m^3, a specific heat 167.5 J/kgK, a coefficient of volumetric expansion 0.00022 1/K, a thermal conductivity 18.8 W/m.K and a kinematic viscosity 2×10^{-7} m^2/s. The distilled water was used as a coolant. The depth of low melting alloy was 7.5 cm.

If a temperature distribution of the low melting alloy and the water region does not change as time increases, it is assumed to be reached a steady state condition for one test in the given test parameters such as coolant injection condition, bottom plate setting temperature of the molten pool, setting temperature of the heat exchanger, setting coolant temperature of direct injection, and the mass flow rate of direct coolant injection. Twenty five steady state tests have been performed in the present study.

3. EXPERIMENTAL RESULTS AND DISCUSSION

Figure 2 shows temperature distribution at the central part of the test section as a function of the coolant injection mass flow rate from 2.48 kg/min to 6.50 kg/min for the case with direct coolant injection into the test section. The lower part of the dotted line is a low melting alloy region and the upper part of the dotted line is a water region. In the low melting alloy region, the part of which temperature is higher than 70 °C is in liquid state and the other part is in solid state.

As shown in the Figure 2, natural convection heat transfer contributes to the temperature distribution in the molten pool. Although the crust was not formed as the direct coolant injection mass flow increased from 2.48 kg/min to 3.93 kg/min, the temperature of molten pool has changed. Since the top surface temperature of molten pool is lower than 70 °C, the thin crust is formed at the case of 5.41 kg/min of direct coolant injection mass flow rate into the test section. As the crust behaves a thermal barrier, the temperature of the molten pool is not increased as mass flow rate of direct coolant injection increases. From this result, it is concluded that increasing mass flow rate of direct coolant injection into the corium pool does not affect the temperature increase after the crust has been formed in the molten pool, because the crust behaves as a thermal barrier.

Figure 3 shows temperature distribution at the central part of the test section as a function of the bottom plate setting temperature of the molten pool for the case with direct coolant injection into the molten pool. Natural convection heat transfer in the molten pool contributes to the temperature distribution in the cases of 90 °C and 100 °C of the bottom plate setting temperature of molten pool. But the natural convection heat transfer is not fully developed in the case of 80 °C of the bottom plate setting temperature of the molten pool, because the buoyancy force decreases. The crust is not formed in the case of 100 °C of the bottom plate setting temperature of the molten pool. But more than 50 % of the overall molten pool has been solidified in the case of 80 °C of the bottom plate setting temperature of the molten pool. From this result, it is concluded that the bottom plate setting temperature is very important for the crust formation process of the molten pool for the direct coolant injection case.

Table 1 shows the heat transfer rate for the case with direct coolant injection into the test section in the molten pool. The range of the Rayleigh Number in the

tests is from 10^4 to 10^6. The Rayleigh number can be determined by setting temperature difference between the top and the bottom plates. The Nusselt number is defined by the ratio between convective heat transfer rate and conductive heat transfer rate. As shown in the Table 1, the upper part Nusselt number of the molten pool of the case with no crust formation is greater than that of the case with crust formation, because the crust behaves as a thermal barrier.

Figure 4 shows temperature distribution at the central part of the test section as a function of the bottom plate setting temperature for the case of using heat exchanger. As shown in Figures 4.1 and 4.2, temperature of the molten pool is almost uniform because of natural convection flow by buoyancy force for the cases with bottom plate setting temperatures of 90 °C and 100 °C. But the natural convection flow is not effective for the case with bottom plate setting temperature of 80 °C because the buoyancy force decreases as shown in Figure 4.3. The setting temperature change of heat exchanger is not effective to the crust formation of molten pool because of natural convection flow for the case with bottom plate setting temperatures of 90 °C and 100 °C. But the setting temperature of the heat exchanger is important for the crust formation of molten low melting alloy for the case with bottom plate setting temperature of 80 °C, because intensity of natural convection flow decreases. From this result, it is concluded that the bottom plate setting temperature is very important for the crust formation process of the molten pool for the heat exchanger case.

Table 2 shows the heat transfer rate for the case of using heat exchanger. The range of the Rayleigh Number in the tests is from 10^4 to 10^6 similar to the direct coolant injection case. Since the crust behaves as a thermal barrier, the upper part Nusselt number of molten pool of the case with no crust formation is greater than that of the case with crust formation similar to the case of the direct coolant injection. The crust starts to form initially for the cases of the top plate heat exchanger setting temperature of 32.0 °C and the bottom plate molten pool setting temperature of 100 °C, the top plate heat exchanger setting temperature of 42.5 °C and the bottom plate molten pool setting temperature of 90 °C, the top plate heat exchanger setting temperature of 57.5 °C and the bottom plate molten pool setting temperature of 80 °C. More than 50 % of the overall molten pool has been solidified in the case of the bottom plate molten pool setting temperature of 80 °C and the top plate heat exchanger setting temperature of 40 °C.

Comparing the results of Table 1 with Table 2, it is concluded that the crust thickness of the case with direct coolant injection into the test section is greater than that of the case of using heat exchanger. The test results show that the bottom plate molten pool and the top plate heat exchanger setting temperatures are dominant parameters in the crust formation process of the molten pool. Especially, the bottom plate molten pool setting temperature is the key factor of the crust formation process because it is very effective to the natural convection heat transfer.

4. ANALYTICAL RESULTS AND DISCUSSION

Analytical study has been performed to validate and evaluate the test results for the case of using heat exchanger. Many studies have been performed on natural convection heat transfer to develop the heat transfer correlation for the case with no crust formation and high Prandtl number[9, 10, 11]. The natural convection of molten pool during a hypothetical severe accident can be defined by low Prandtl number and crust formation. Natural convection heat transfer of the molten pool have been calculated using FLOW-3D version 3.3 computer code in the present study. But natural convection with crust formation can not be calculated because the code is not capable of crust formation modeling.

The FLOW-3D input model has been developed for two dimensional, steady state, buoyancy, laminar flow, and heat transfer. Two vertical sides were assumed to be adiabatic. And two horizontal sides were maintained at the setting temperatures. Figures 5 and 6 show velocity field and temperature contour of the molten pool in the cases of the bottom plate molten pool setting temperature of 100 °C, 90 °C, and 80 °C. The top surface temperature is 70 °C in three cases. The height of molten pool is 7.5 cm in the cases of the bottom plate molten pool setting temperatures of 100 °C and 90 °C. The height of molten pool is 3.2 cm in cases of bottom plate molten pool setting temperature of 80 °C because the crust thickness was 4.3 cm in the experiment. As shown in the Figure 5, three Rayleigh-Benard natural convection cells are developed in the case of bottom plate molten pool setting temperature of 100 °C, four cells are developed in the case of bottom plate molten pool setting temperature of 90 °C, and six cells are developed in the case of bottom plate molten pool setting temperature of 80 °C. The Rayleigh-Benard natural convection cells are depended on the temperature difference between the top and bottom, and the height(aspect ratio) of molten pool.

The natural convection flow pattern by the buoyancy force contributes to the temperature distribution of the test section, as shown in Figure 6. Temperature of the molten pool which upper flow pattern occurred is higher than that of the molten pool which lower flow pattern occurred. From the calculation results using the FLOW-3D computer code on the crust formation test, the Rayleigh-Benard natural convection flows of the molten low melting alloy pool and the water by the buoyancy force contribute to the crust formation of molten pool. As shown in the Figure 3.2, the average temperature of molten pool is about 80 °C in the case of bottom plate molten pool setting temperature of 90 °C, but the average temperature of molten pool were about 84 °C in the FLOW-3D calculation. Since heat losses to the environment was not considered in the FLOW-3D analysis, the average temperature of molten pool in the FLOW-3D calculation is higher than that of molten pool in the experiment.

5. CONCLUSIONS

Experimental and analytical studies on the crust formation and associated heat transfer mechanisms of the molten pool during a hypothetical severe accident of nuclear power plant have been performed to investigate the crust formation process as a function of boundary temperature and the coolant injection conditions as well as the heat transfer characteristics between the molten pool and the overlying water in order to understand the moltel pool coolability phenomena. The experimental test results have shown that the bottom plate setting temperature is the influential parameter in the crust formation process of the molten pool. It is also found that the crust thickness of the case with direct coolant injection into the molten pool is greater than that of the case with heat exchanger. Increasing mass flow rate of direct coolant injection into the molten pool does not affect the molten pool temperature after the crust has been formed in the molten pool because the crust behaves as a thermal barrier. The heat transfer rate between the molten pool and the coolant of the case with no crust formation is greater than that of the case with crust formation due to the fact that the crust behaves as a thermal barrier. The results of the FLOW-3D computer code analyses have shown that the temperature distribution contributes to the crust formation process due to Rayleigh-Benard natural convection flow. Since heat losses to the environment were not considered in the FLOW-3D analysis, the average temperature of molten pool in the FLOW-3D calculation is higher than that of molten pool in the experiment. To apply the results of this study for the actual reactor situations, further studies are needed for the case of high Rayleigh Number, the cases with coolant boiling, and to analyze difference between internal heating and bottom heating. The results of these studies will be used to develop the crust formation models of molten core material pool in the core and in the lower plenum.

REFERENCES

[1] M. Epstein, "The MACE Internally-Heated Corium Pool: Was It a Thermal Oscillator ?," ANS Proceedings : '92 National Heat Transfer Conference (1992)

[2] J. M. Bonnet and J. M. Seiler, "Coolability of Corium Spread on to Concrete Under Water, the PERCOLA Model," ANS Proceedings : '92 National Heat Transfer Conference (1992)

[3] T. Ginsberg, J. Klein, J. Klages, Y. Sanborn, C. E. Schwarz, J. C. Chen, and L. Wei, "An Experimental and Analytical Investigation of Quenching of Superheated Debris Beds Under Top-Reflood Conditions," NUREG/CR-4493(1986)

[4] F B. Cheung, "Periodic Growth and Decay of a Frozen Crust over a Heat Generating Liquid Layer," J. of Heat Transfer Vol. 103, 369-375 (1981)

[5] W. W. Tarbell, D. R. Bradley, R. E. Blose, J. R. Ross, and D. W. Gilbert, "Sustained Concrete Attack by Low-Temperature Fragmented Core Debris," NUREG/CR-3042 (1987)

[6] R. E. Blose, J. E. Gronager, A. J. Suo-Anttila, J. E. Brockmann, "SWISS : Sustained Heated Metallic Melt/Concrete Interactions with Overlying Water Pool," NUREG/CR-4727 (1987)

[7] B. W. Spencer, M. T. Farmer, M. Merilo, "Status of Melt Attack and Coolability Experiment(MACE)," CSARP Review Meeting, Bethesda, Maryland (1993)

[8] CFDS-FLOW3D Release 3.3: Users Manual, CFD Services, Harwell Laboratory, Oxfordshire, United Kingdom, June 1994

[9] F. Mayinger, P. Fritz, H. H. Reineke, L. Rinkleff, R. Schramm, and U. Steinerenner, "Theoreical and Experimental Research on the Behaviour of Core Melt in a Reactor Containment and on the Basemat Concrete, BMFT RS 166- 79-05 (1980)

[10] M. Keyhani, L. Chen, and D. R. Pitts, "The Aspect Ratio Effect on Natural Convection in an Enclosure with Protruding Heat Sources," J. of Heat Transfer Vol. 113, 883 - 891 (1991)

[11] J. D. Gabor, L. Baker, J. C. Cassulo, J. D. Erskine, and J. G. Warner, "Heat Transfer to Curved Surfaces From Heat Generating Pools," Journal of Heat Transfer Vol. 102, 519-524 (1980)

Table 1. Heat transfer rate for the case with direct coolant injection into the test section in the molten pool region.

Set Temp. of Bottom (℃)	Coolant Inj. Temp. (℃)	Coolant Inj. Mass Flow Rate(kg/min)	Heat Flux (W/m^2)	Rayleigh Number	Lower Part		Upper Part		Crust Thickness (cm)
					h(W/m^2K)	Nusselt N.	h(W/m^2K)	Nusselt N.	
100.0	60.0	2.48	1.49E5	7.00E5	1.24E4	296.7	2.25E4	537.8	0.0
100.0	50.0	2.48	1.70E5	7.84E5	1.42E4	338.1	1.96E4	468.4	0.0
100.0	50.0	3.93	1.74E5	8.31E5	1.20E4	287.2	1.60E4	383.1	0.0
100.0	50.0	5.41	1.76E5	9.70E5	1.41E4	337.1	1.30E4	312.1	0.12
100.0	50.0	6.50	1.82E5	9.39E5	1.46E4	348.5	1.36E4	322.7	0.20
90.0	60.0	2.48	4.02E4	5.57E5	3.02E3	72.2	4.02E3	95.9	0.73
90.0	50.0	2.48	9.29E4	4.92E5	1.24E4	295.9	7.43E3	177.5	1.01
90.0	40.0	2.48	1.20E5	3.69E5	8.91E3	212.9	1.85E4	147.3	1.60
80.0	60.0	2.48	1.74E4	1.30E5	2.17E3	51.8	5.79E3	66.1	2.25
80.0	50.0	2.48	3.29E4	2.14E4	3.65E3	87.2	1.09E4	67.0	4.62

Table 2. Heat transfer rate for the case of using heat exchanger in the molten pool region.

Set Temp. of Bottom (℃)	Set Temp. of Top (℃)	Heat Flux (W/m^2)	Rayleigh Number	Lower Part		Upper Part		Crust Thickness (cm)
				h(W/m^2K)	Nusselt N.	h(W/mK)	Nusselt N.	
100.0	50.0	1.71E5	7.38E5	1.57E4	375.8	2.05E4	489.9	0.0
100.0	40.0	1.73E5	8.54E5	1.24E4	295.9	2.03E4	485.1	0.0
100.0	32.0	1.82E5	1.16E6	1.17E4	280.5	1.26E4	299.8	0.02
100.0	30.0	1.82E5	1.09E6	1.17E4	279.9	1.25E4	299.2	0.11
90.0	50.0	1.16E5	7.13E5	1.16E4	277.9	1.32E4	316.2	0.0
90.0	42.5	1.18E5	7.58E5	1.32E4	281.0	1.32E4	281.0	0.01
90.0	40.0	1.39E5	7.31E5	1.39E4	331.0	1.39E4	331.0	0.09
90.0	30.0	1.46E5	6.11E5	1.46E4	348.1	1.46E4	348.1	0.52
90.0	25.0	1.46E5	5.27E5	1.42E4	338.1	1.50E4	359.0	0.86
80.0	60.0	4.75E4	2.38E5	1.06E4	248.9	2.99E4	714.4	0.0
80.0	57.5	4.23E4	3.42E5	6.50E3	155.4	1.21E4	288.4	0.25
80.0	50.0	4.23E4	1.20E5	6.04E3	144.2	1.41E4	336.5	2.38
80.0	40.0	5.45E4	5.29E4	7.79E3	186.0	1.82E4	433.9	3.61
80.0	30.0	6.62E4	2.95E4	9.45E3	219.0	2.21E4	526.8	4.30
80.0	25.0	7.65E4	2.01E4	1.09E4	260.9	2.55E4	608.7	4.68

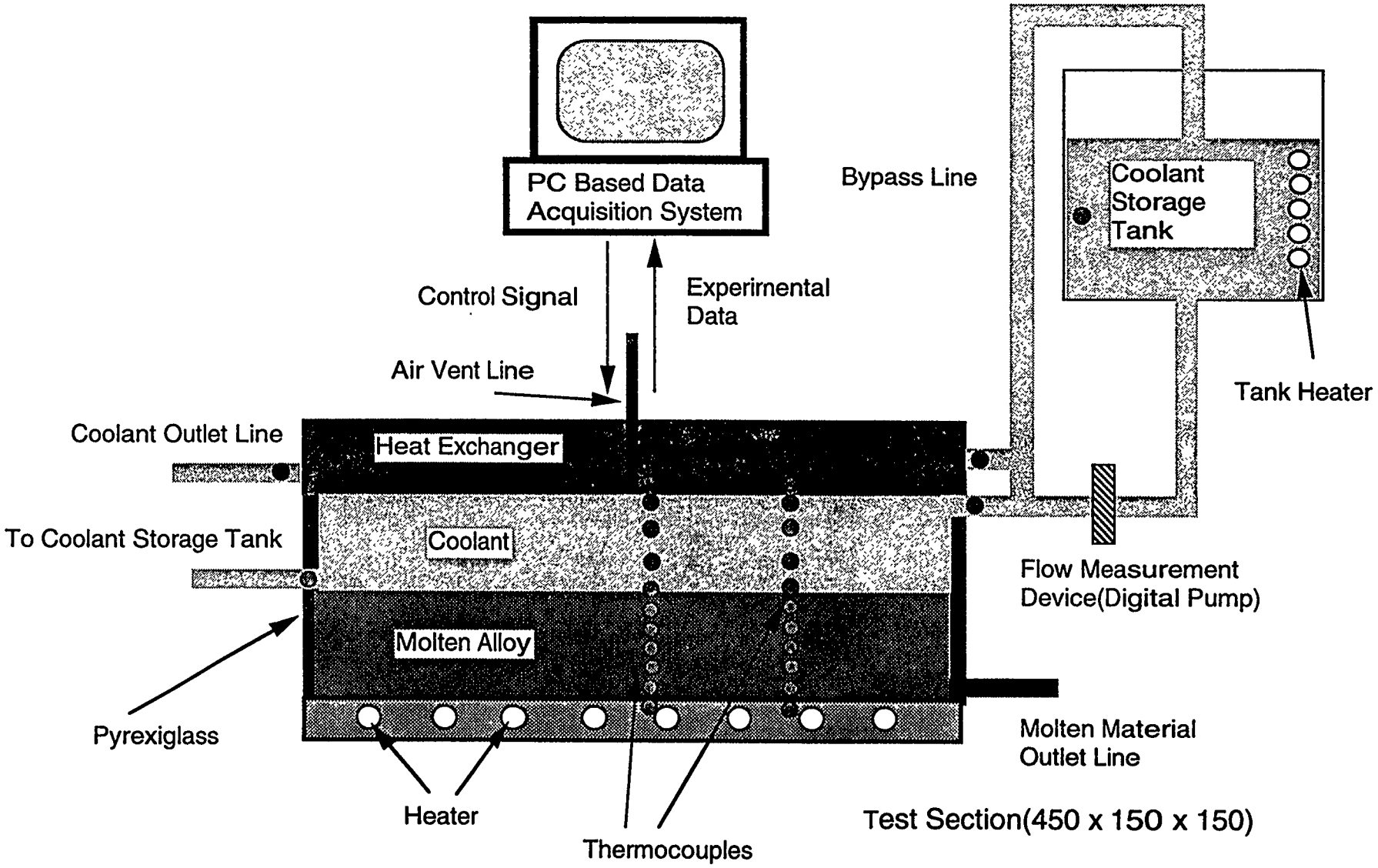


Figure 1. Schematic diagram of crust formation experimental apparatus.

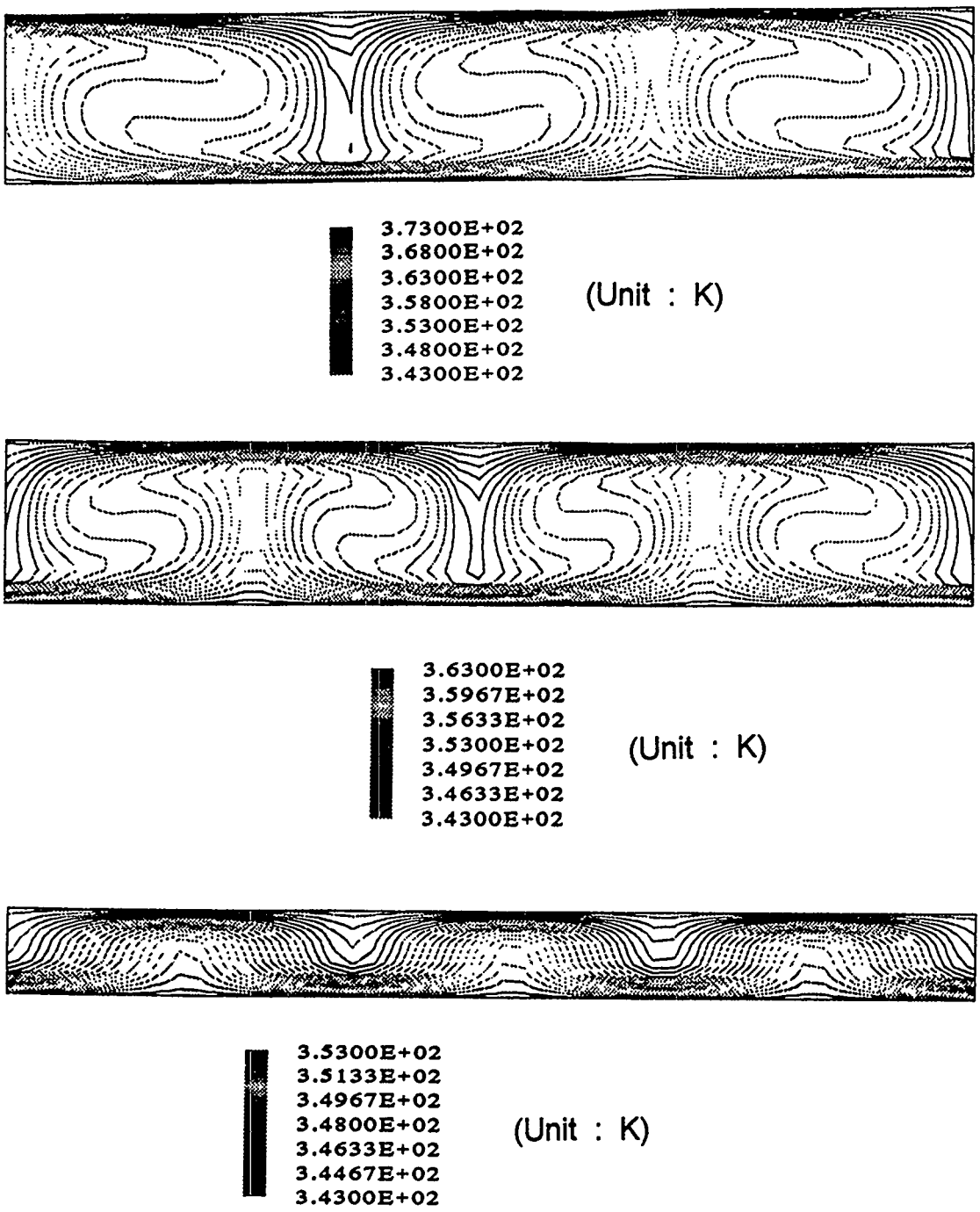


Figure 6. Calculated temperature profiles of the molten pool.

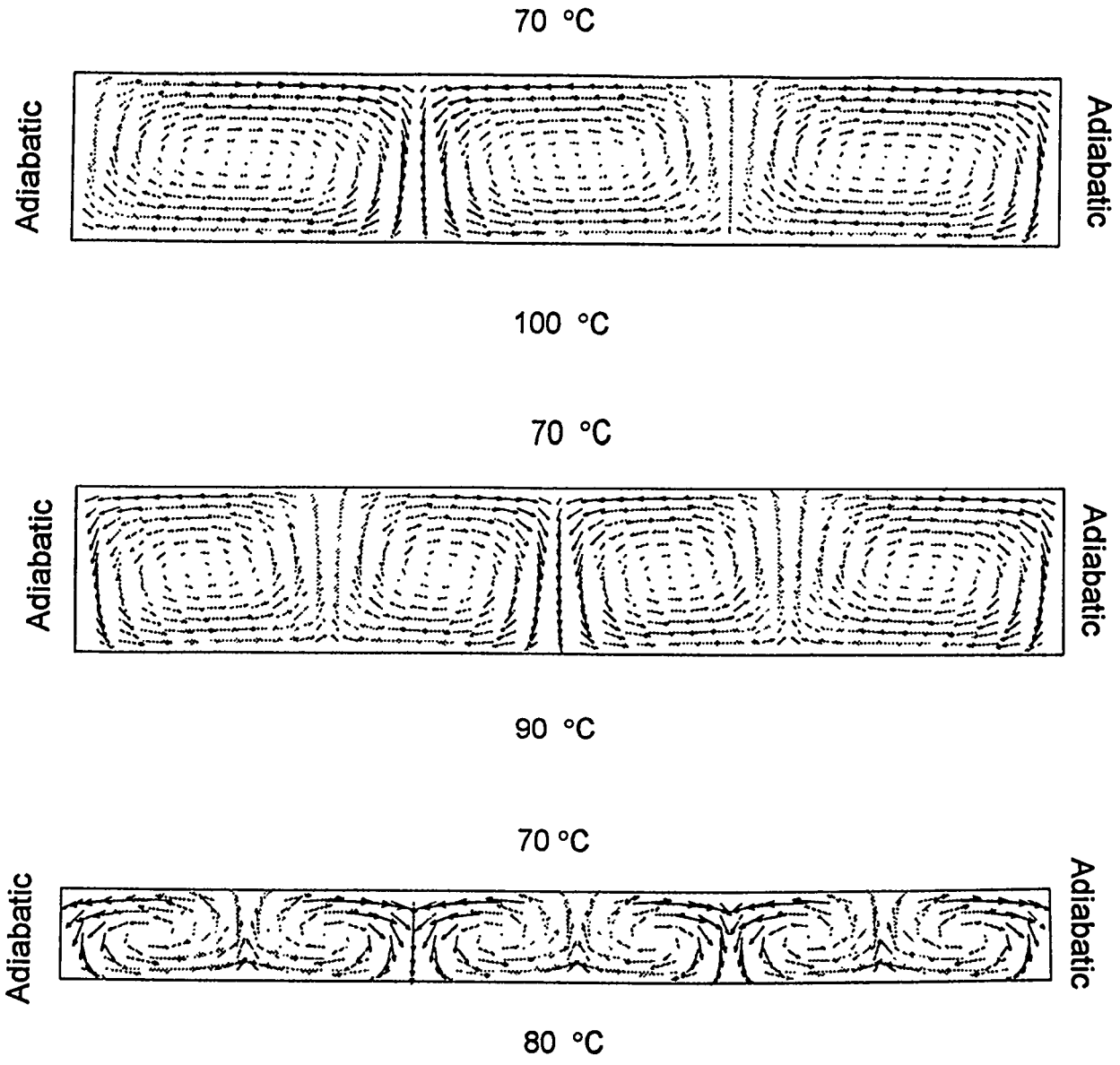


Figure 5. Calculated velocity vectors of the molten pool.

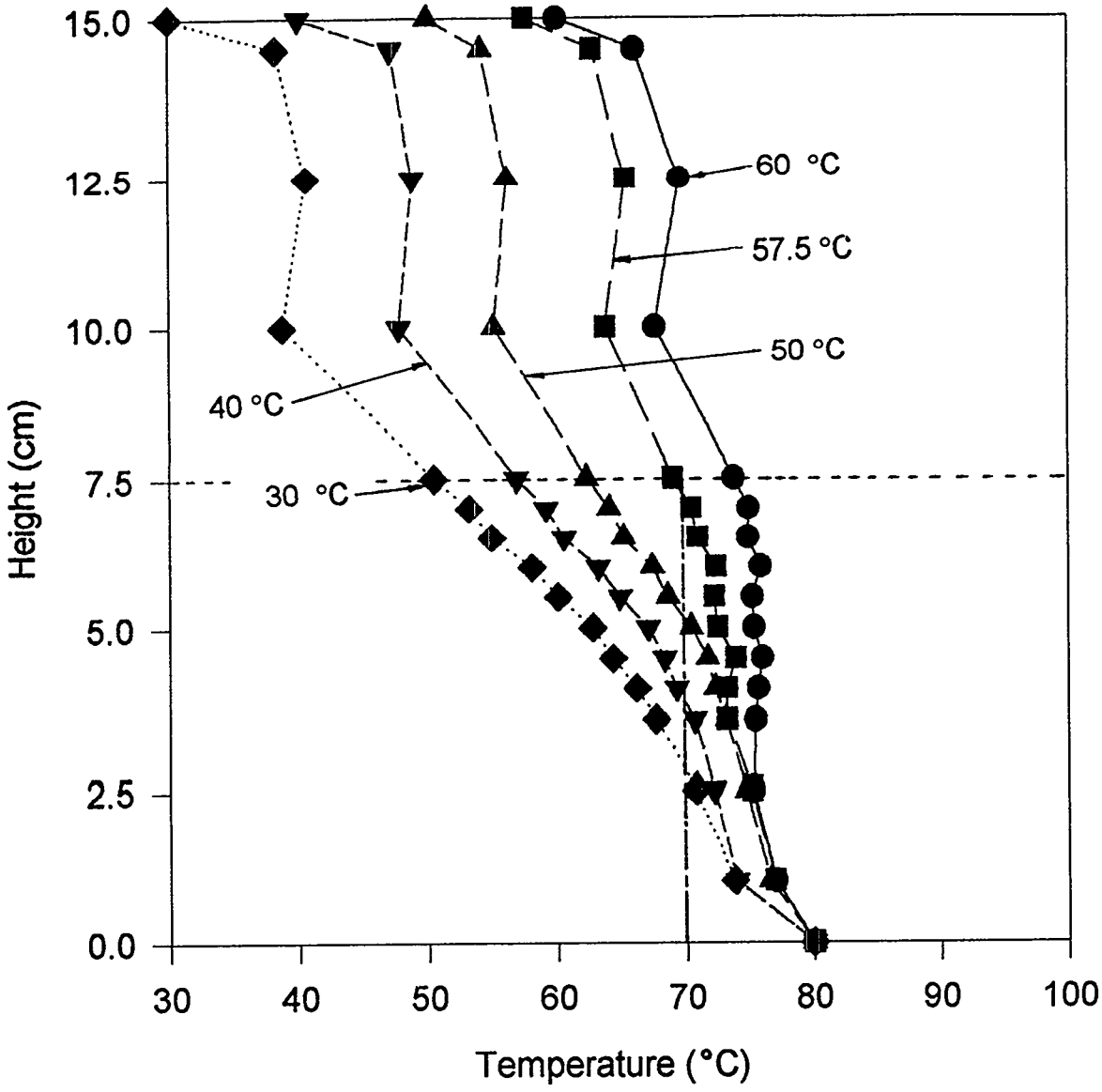


Figure 4.3 Measured temperature profiles of the inside of test section as a function of the setting temperature of heat exchanger (setting temperature of the bottom plate = 80 °C).

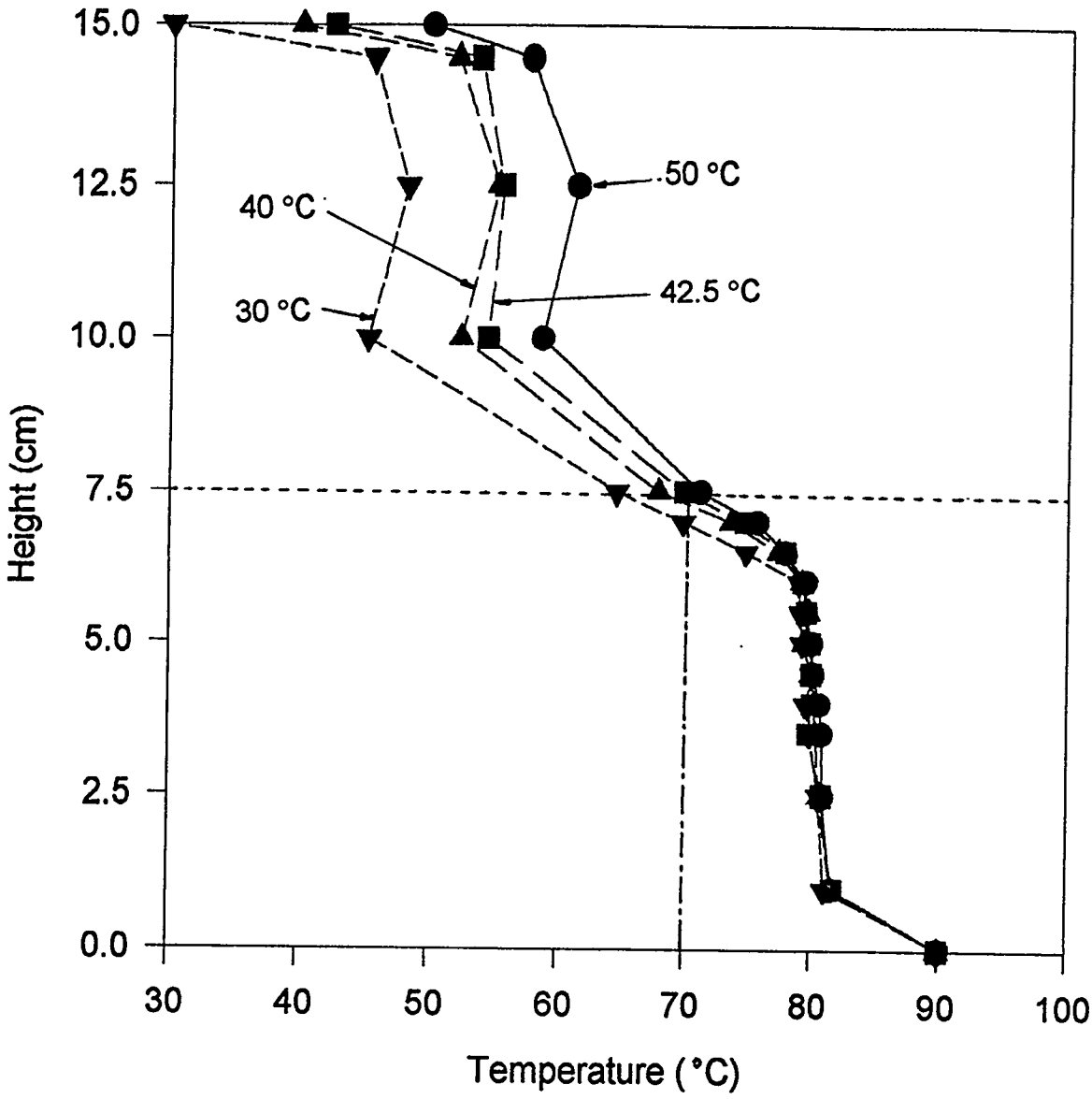


Figure 4.2 Measured temperature profiles of the inside of test section as a function of the setting temperature of heat exchanger (setting temperature of the bottom plate = 90 °C).

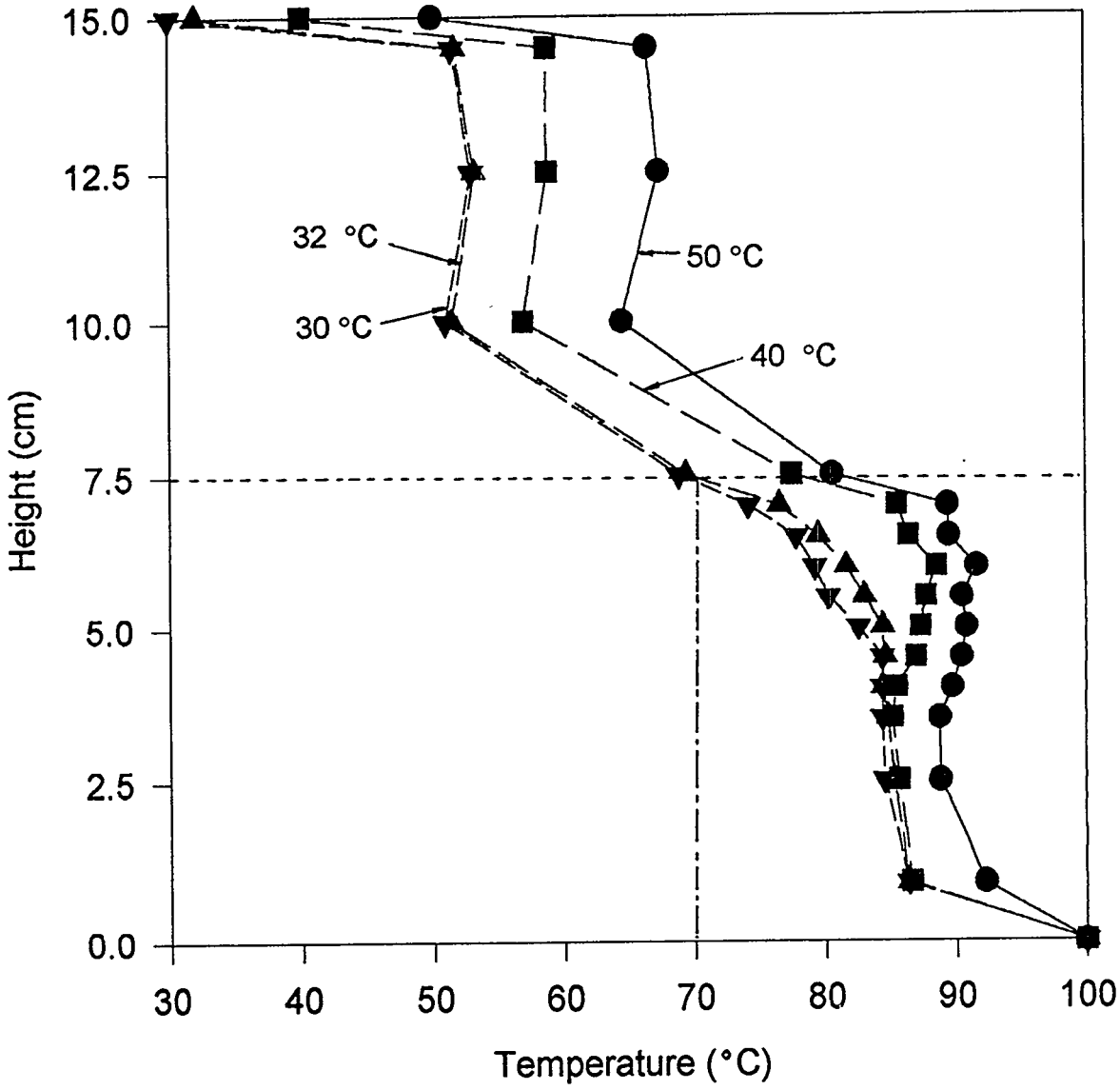


Figure 4.1 Measured temperature profiles of the inside of test section as a function of the setting temperature of heat exchanger (setting temperature of the bottom plate = 100 °C).

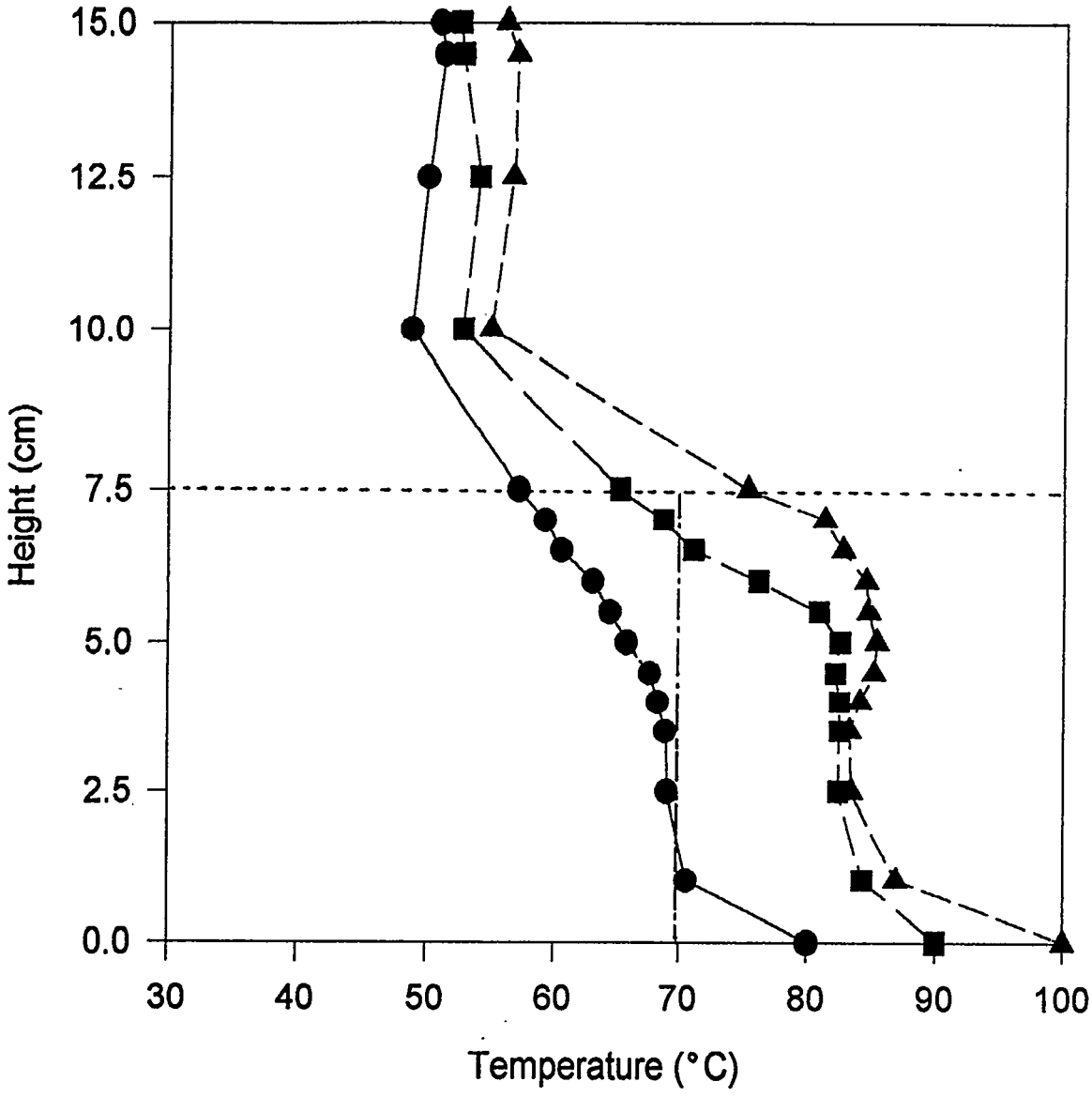


Figure 3. Measured temperature profiles of the inside of test section as a function of setting temperature of the bottom plate (setting temperature of direct coolant injection = 50 °C, coolant injection mass flow rate = 2.48 kg/min).

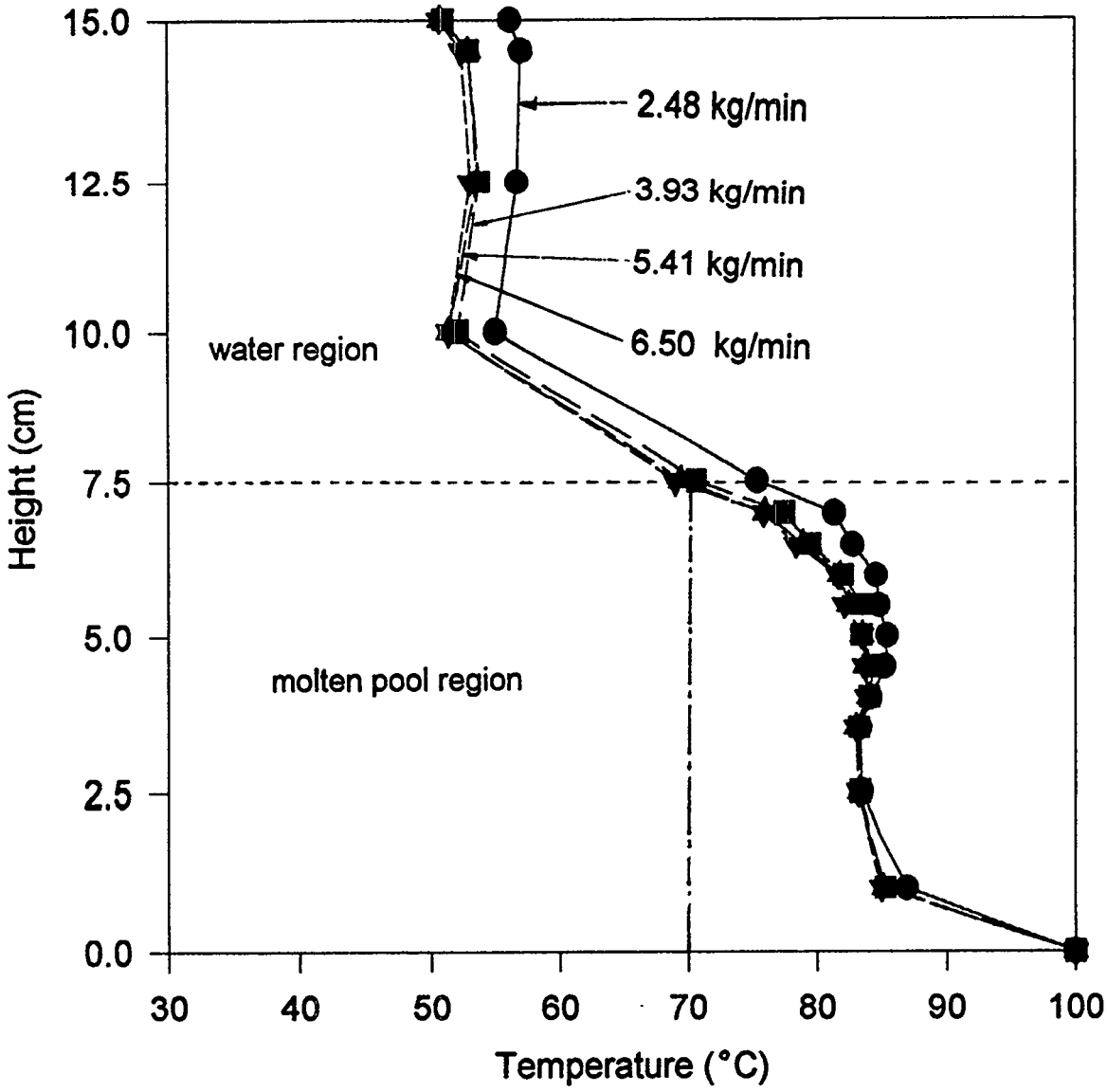


Figure 2. Measured temperature profiles of the inside of test section as a function of the coolant injection mass flow rate (setting temperature of direct coolant injection = 50 °C).

SIMULATION OF THE THERMALHYDRAULIC BEHAVIOR OF A MOLTEN CORE WITHIN A STRUCTURE, WITH THE THREE DIMENSIONS THREE COMPONENTS TOLBIAC CODE

B. SPINDLER, G.-M. MOREAU, S. PIGNY

Commissariat à l'Energie Atomique, FRANCE, Direction des Réacteurs Nucléaires
Département de Thermohydraulique et de Physique, Service de Thermohydraulique des Réacteurs
Centre d'Etudes Nucléaires de Grenoble, 17 rue des Martyrs, F38054 GRENOBLE CEDEX 9

ABSTRACT

The TOLBIAC code is devoted to the simulation of the behavior of a molten core within a structure (pressure vessel or core catcher), taking into account the relative position of the core components, the wall ablation and the crust formation. The code is briefly described: 3D model, physical properties and constitutive laws, wall ablation and crust model. Two results are presented: the simulation of the COPO experiment (natural convection with water in a 1/2 scale elliptic pressure vessel), and the simulation of the behavior of a corium in a PWR pressure vessel, with ablation and crust formation.

1. INTRODUCTION

Frame

In the frame of severe accident studies, the behavior of a molten core has to be predicted. Numerous physical processes are involved in these studies and a predictive tool is of great interest in order to investigate several situations, geometries, or events. The purpose of the TOLBIAC code is the simulation of the behavior of a molten core within a structure (pressure vessel or external core catcher). The ame of the code is not to describe the successive phases of the degradation of a reactor core, in a situation of severe accident. In a pressure vessel or in a core catcher, the simulation with TOLBIAC takes place after the evaporation of the existing water, if any, and also after melting of the corium debris, depending of their volume, their heat exchange surface and the residual power.

The TOLBIAC code user has to define the initial composition and temperature of the molten core, according to what he can imagine or calculate if possible. The TOLBIAC code mainly gives, during the time of the simulation, the pool temperature field (in a 3D meshing), and the wall temperatures and thicknesses.

The three dimensions three phases model is what distinguishes the TOLBIAC code from other codes describing the behavior of a molten pool. However the closure of such a model needs some constitutive laws. Their assessment is not easy, because experiments with true materials or full scale are scarce and poorly instrumented.

TOLBIAC specifications

The thermal conductivity is about ten times higher for the metals than for the oxides, and consequently the heat transfer coefficients are in the same ratio. The other physical properties also depend on the component, and mainly the density. The major part of the residual power is generated in the heavy oxides and not in the whole volume. The zirconium may be oxidized by the gases in an exothermal reaction.

The relative position of the components has consequently to be known. A 3D discretization was then chosen, with three components: a liquid metal phase, a liquid oxide phase and a gas phase. The following main phenomena can be simulated: metal-oxide stratification, residual power, wall heat transfer, free surface heat transfer (radiation, or heat transfer with a water pool), wall ablation, crust formation.

2. The 3D model

The three phases

The model describes the different phases as a mixture of several materials, with a single velocity field, and a single temperature field for each phase. Only the most present in terms of mass are taken into account, because materials in low quantities are of no influence on the physical properties. The residual

power is defined by the code user with several parameters: the initial power at the time the simulation begins, the coefficient controlling the decay of the residual power, and the proportion of residual power generated respectively in the oxide and in the metal phases. The residual power is not calculated with a peculiar model describing the behavior of the fission products.
The metal liquid phase is a mixture of iron, zirconium, nickel and chromium, defined by the code user. It is characterized by its own volumetric fraction, temperature and velocity fields.
The oxide liquid phase is characterized by its own temperature and velocity fields. It is divided into light and heavy oxides, each with its own volumetric fraction. The heavy oxides are a mixture of uranium dioxide and zirconia. The light oxides, issued from the concrete ablation, are a mixture of alumina, silica and lime, or zirconia, depending on the nature of the concrete. Finally the gas phase, characterized by its volumetric fraction and velocity fields, is a mixture of carbone dioxide and water vapor, issued from the concrete ablation.

System of equations

Four mass balance equations are used (metals, oxides, light oxides and gases). The source and sink terms of these equations are the following:

component	**source or sink terms for the mass balance equations**		
	ablation	oxidization	crust formation
metals	Γ_A	$-\Gamma_{AD}$	$-\Gamma_{Ac}$
oxides	Γ_D	$+\Gamma_{AD}+\Gamma_{gD}$	$-\Gamma_{Dc}$
light oxides	Γ_x		$-\Gamma_{Xc}$
gases	Γ_g	$-\Gamma_{gD}$	

The nature of the ablation source terms depends on the wall material: metal (for instance the pressure vessel), heavy oxide (for instance zirconia), or light oxides and gases (for instance concrete). The oxidization terms appear in the case of a concrete wall ablation with a source of gases. The exothermic reaction between the gases (water and carbone dioxide) and the zirconium is taken into account.
Two energy balance equations are used (metals and oxides). The energy of the gas phase is not taken into account, due to its negligible value compared to the energy of the metal and oxide phases. The temperature of the gas phase is taken as the temperature of the liquid phase around. The source and sink terms of the energy balance equations are the following:

component	**source or sink terms for the energy balance equations**					
	ablation	oxidization	interface	power	wall	crust formation
metals	$\Gamma_A.H_{Ao}$	$-\Gamma_{AD}.H_A$	$-Q_{AD}$	Q_{Aq}	Q_{Aw}	$-\Gamma_{Ac}.H_{Ac}$
oxides	$\Gamma_D.H_{Do}$	$(\Gamma_{AD}+\Gamma_{gD}).H_D$	$+Q_{AD}$	Q_{Dq}	Q_{Dw}	$-\Gamma_{Dc}.H_{Dc}$

The mass issued from the wall ablation is supposed to be at the fusion temperature of the wall material. The interface term corresponds to the heat exchange between the two liquid phases, and depends on the interfacial area. Part of the residual energy may be generated in the metal phase, according to the user's choice. The wall heat transfer is controlled by heat transfer coefficients. The enthalpy corresponding to the crust formation is calculated at the solidus temperature of the considered liquid phase.
Finally, three momentum balance equations are written (metals, oxides and gases), projected in each direction. The interfacial shear stress between the phases is taken into account, as well as the wall shear stress.
In addition, a diffusion term is included in the energy and momentum equations, in order to take account of the effect of the viscosity and conductivity. Up to now only the molecular viscosity and conductivity are considered. The assessment of the code will show if aturbulence model is needed.
Apart from the hydraulic equations, the temperatures in the walls are calculated by solving a 1D conduction equation, one for each part of the wall facing a cell of the hydraulic meshing.

Geometry

The variation of the volume, the flow areas, the exchange surface and the wall thickness of the cells, due to the wall ablation or crust formation, are taken into account. The cells geometry is calculated explicitly at each time step, and depends on the ablation velocity and crust thickness.

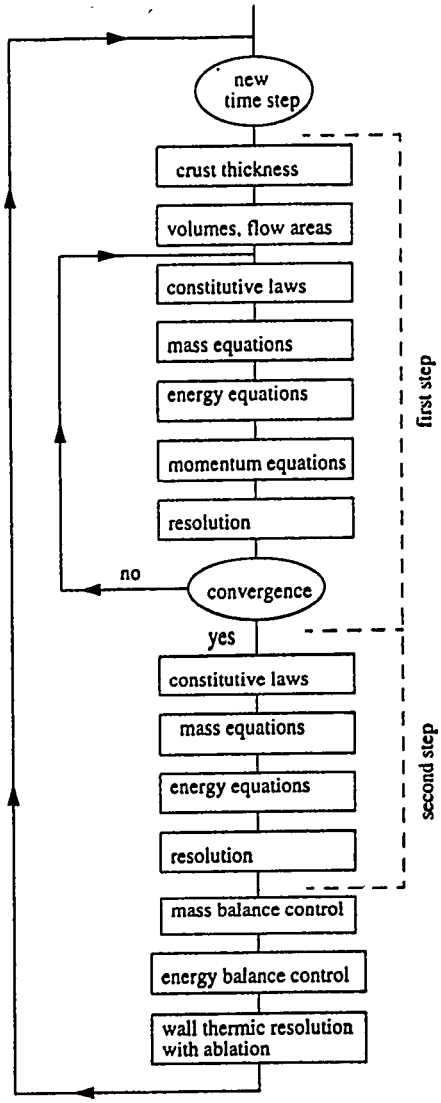


Fig. 1 Main steps of the calculation scheme

Numerical features

In figure 1 is presented a diagram of the main steps of the calculation scheme.

The equations are discretized with a finite difference scheme on a staggered spatial meshing, and with the donor-cell method.

The numerical integration uses a two-step numerical method, in order to avoid the time step Courant limitation. This method is issued from the 3D module of the CATHARE code [1]. The first step (predictor) is written with a quasi-implicit scheme. The equations are written in a non-conserving form. The non-linear system of equations is solved through a Newton-Raphson iteration procedure. Simple arithmetic manipulations reduce the linear system by considering only the pressure as unknown. This reduction leads to a Jacobian linear system with a highly sparse matrix. A second step (corrector) is used to restore the conservation. It involves a fully implicit set of equations for the scalar quantities. The mass and energy balance equations generate one linear system for each phase. Since these systems have the same sparse structure as the predictor Jacobian matrix, they can be solved using the same method.

The resolution of the wall thermal equations uses a fully implicit difference scheme.

3. Physical properties

The physical properties of the components are not well known, particularly in the case of mixing of several materials. Two of them are of great importance: the solidus temperature and the viscosity of the oxides.

The solidus temperature is a key parameter for the crusts formation and hence the wall heat transfer coefficient. The values used in TOLBIAC are deduced from curves calculated with the code GEMINI2 of THERMODATA [2].

The oxides viscosity highly depends on the light oxides concentration, and controls the diffusion effects. Its values in TOLBIAC are adapted from the curves of Gonzales [3], who pointed out some inconsistencies in the values of the literature. The other properties of the components are classically deduced from the values of each material with a mass or a volume balance.

4. Constitutive laws

Presentation

The constitutive laws are correlations from the literature, or simple models which lead to consistent trends. Further works concerning the code assessment will provide new or improved correlations. However the uncertainties concerning the physical properties, the initial conditions and the crusts behavior for instance, are large enough so that a good precision of the constitutive laws is probably not necessary, and not reachable.

Flow configurations

The peculiarity of a three dimensions three phases model is to calculate the relative position of the three phases (oxide, metal and gas). The result depends on the densities and the constitutive laws. Among the constitutive laws, the three interfacial shear stresses (metal-oxide, metal-gas and oxide-gas) are the key parameters which control the phase mixing or stratification.

In a molten corium pool with no gas generation at the wall, the sedimentation of the oxide and metal phases rapidly occurs. In the bottom of the structure, the oxides generated by the wall ablation mix with the oxides. The oxides generated in the metal layer either flow up or down, depending on their density.

The sedimentation remains, except along the wall. Reciprocally the metals generated by the wall ablation either mix with the metal phase or flow up in the oxide layer. When no gas is generated at the wall, the stratified configuration concerns then the main part of the structure, during a long time, until a sufficiently large amount of light oxides are generated, so that the oxide phase becomes lighter than the metal phase. An inversion of the stratified layers then occurs: metals at the bottom and lightened oxides at the top.
On the other hand, when the walls are made of concrete, their ablation generates a gas flow through the corium pool. If this gas flow is sufficiently high, its influence prevails with respect to the natural convection. Hence the three phases in the pool mix.
In each case (gas generation or not) the flow configuration is the result of a calculation (momentum equation, in which the key parameters are the gravity and interfacial shear stresses terms). During a simulation, the flow configuration may vary, depending on the relative densities of the phases, or the beginning or termination of ablation.
These two types of flow configuration (stratification or mixing) correspond to different sets of constitutive laws. Taken into account the first needs of the code users, the first constitutive laws developed correspond to stratification. They are briefly presented here.

Energy balances

For the interfacial energy transfer coefficient in a stratified configuration, the natural convection correlation of Haberstroh and Reinders [4] is used. For the wall heat transfer, natural convection correlations are used (Haberstroh and Reinders [4] for an horizontal wall and Chawla and Chan [5] for a vertical wall). These correlations are written with a Rayleigh number ($Ra=g.\Delta T.\beta.L^3.\rho^2.Cp.\lambda^{-1}.\mu^{-1}$) based on a temperature difference. The correlations of Steinberner and Reineke [6] written with a Rayleigh number based on a volumetric heat power ($Ra=g.Q.\beta.L^5.\rho^2.Cp.\lambda^{-2}.\mu^{-1}$) can also be chosen. However these last correlations can only be chosen if a volumetric power is present.
If a crust exists between the wall and the molten corium, the exchange temperature used in order to evaluate the wall heat flux is not the wall temperature, but the solidus temperature, supposed to be the crust temperature at the pool side. The crust model is described hereafter.
Besides, for the upper surface of the molten pool, either a radiative heat transfer or an exchange with a water pool is taken into account. The crust formation at the upper surface is also considered.

Momentum balances

For the interfacial momentum transfer, simple models are used, depending on the density and volumetric fraction, with two different constants, one for a stratified configuration, the other for a mixed flow configuration. A wall momentum transfer is considered, depending on the flow configuration. If there is no gas generation at the wall, a classical friction factor model is used, with the whole structure diameter or height used as hydraulic diameter. If gases are generated at the wall, no shear stress is taken into account for the liquids.

5. Crust formation

Wall crust

A crust appears along the wall if the solidification temperature of the liquid component is between the liquid pool temperature and the wall temperature. Typically, at the beginning of a transient, the wall is at the ambient temperature, whereas the corium is hot. Hence a crust appears and grows. When the wall temperature increases, the crust thickness progressively decreases and the crust disappears if the wall temperature becomes larger than the solidification temperature.
The crust thickness is calculated using a heat balance in the crust, where the following terms are taken into account: the pool to crust heat flux, the residual power in the crust, the crust to wall heat flux, the heat stored in the crust and the solidification heat. In order to simplify the model, it is supposed that the temperature profile in the crust is stationary, and the crust physical properties are constant, which yields a parabolic temperature profile in the crust. After rearrangement, the following equation is obtained:

$$-\frac{de}{dt}\cdot\left[\rho\cdot H_{LS}+\rho\cdot Cp.\frac{T_{sol}-T_w}{2}-\rho\cdot Cp.\frac{Q.e^2}{4.\lambda}\right]$$

$$=h_b.(T_b-T_{sol})+\frac{\rho\cdot Cp.e}{2}.\frac{d(T_{sol}-T_w)}{dt}-\frac{\lambda\cdot(T_{sol}-T_w)}{e}+\frac{Q.e}{2}$$

This equation, giving the crust thickness variation, is solved by mean of a Newton iterative method.

Crust at the surface of the pool

The principle of the crust formation at the surface of the pool is the same as the wall crust, except that the wall temperature is replaced by the crust external surface temperature. This surface temperature is not known and depends on what exists above the pool (water or not). Hence the model giving the crust thickness is more complicated, because the crust thickness and the surface temperature are both to be determined. The energy balance of the crust is written with the same principles as for the wall crust. A second equation is written for the heat transfer at the surface: radiative heat transfer, or heat transfer with water, with the boiling curve giving the heat transfer coefficient h_{ext}. After rearrangement, the two equations obtained are the following:

$$-\frac{de}{dt} \cdot \left[\rho \cdot H_{LS} + \rho \cdot Cp \cdot \left(\frac{2+A}{1+A}\right)^2 \cdot \left(\frac{T_{sol}-T_{ext}}{2\cdot(2+A)} - \frac{Q\cdot e^2}{4\cdot\lambda}\right)\right]$$

$$-\frac{\rho \cdot Cp \cdot e}{2\cdot(1+A)} \cdot \frac{dT_{sol}}{dt} - \frac{\rho \cdot Cp \cdot e^2}{2\cdot\lambda \cdot (1+A)^2} \cdot \left(T_{sol}-T_{ext}+\frac{Q\cdot e^2}{2\cdot\lambda}\right) \cdot \frac{dh_{ext}}{dT_{sur}} \cdot \frac{dT_{sur}}{dt}$$

$$= h_b \cdot (T_b - T_{sol}) - \frac{h_{ext}\cdot(T_{sol}-T_{ext})}{1+A} + Q\cdot e \cdot \frac{2+A}{2\cdot(1+A)}$$

$$\left[T_{sur}-T_{ext}-\frac{1}{(1+A)^2}\cdot\left(T_{sol}-T_{ext}+\frac{Q\cdot e^2}{2\cdot\lambda}\right)\right] \cdot \frac{dh_{ext}}{dT_{sur}} \cdot \frac{dT_{sur}}{dt} + h_{ext} \cdot \frac{dT_{sur}}{dt}$$

$$= \frac{h_{ext}}{1+A} \cdot \frac{dT_{sol}}{dt} - \frac{h_{ext}}{(1+A)^2} \cdot \left[(T_{sol}-T_{ext}) \cdot \frac{h_{ext}}{\lambda} - \frac{Q\cdot e\cdot(2+A)}{2\cdot\lambda}\right] \cdot \frac{de}{dt}$$

$$with\ A = \frac{h_{ext}\cdot e}{\lambda}$$

These equations are solved with a Runge-Kutta method.

6. Ablation

The ablation velocity is obtained by the wall thermic model resolution. The energy balance takes into account the melting heat. A fine meshing is defined near the melting front. When a cell is entirely molten, it is withdrawn from the energy balance, by setting its heat capacity to a negligible value.

7. Natural convection in a volume

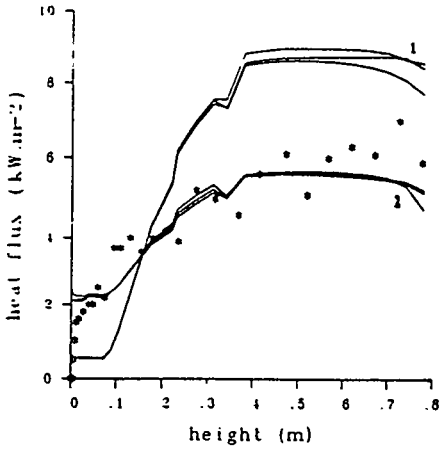
Presentation

The COPO experiment [7] simulates with water the behavior of molten core in the elliptic pressure vessel of a VVER reactor, with a two-dimensional slice in a linear scale 1/2. The height of the pool is 0.80 m. The simulant fluid is water, with some zinc sulfate added in order to adjust the electric conductivity for Joule heating. The side, bottom and top walls are cooled, and the measurements give the wall temperature and the power dissipated in the water. However, some thermal losses are to be noticed in the COPO facility, since the wall heat exchanges balance only 83 % of the total Joule heating. The effective heat power used in the simulation is then reduced compared to the annonced value.

Results

Test fh2 is simulated with TOLBIAC, in a 20x20 meshing. The initial pool temperature is 349 K, the effective heat power is 34.25 $kW.m^{-3}$, and the wall temperature is 336.8 K. The Rayleigh number based on the heat power, corresponding to this test is $Ra = 1.6.10^{15}$. The calculation time is sufficiently long so that a steady state is reached. Actually no steady state is reached because eddies develop under the top wall, which are continually changing. This phenomenon correspond to what is observed in the experiment. However, the heat flux at the side and bottom walls become stable (fig. 1).

Two simulations were performed. The first one with the correlations of Steinberner and Reineke and the second one with Nusselt numbers derived from the Copo measurements.



Simulation 1
Top: $Nu = 0.345.Ra^{0.3233} = 1200$
Side: $Nu = 0.85.\ Ra^{0.190} = 660$
Bottom: $Nu = 1.389.\ Ra^{0.095} = 39$

Simulation 2
Top: Nu = 1800
Side: Nu = 560
Bottom: Nu = 220

Fig. 1: COPO, bottom and side wall heat flux ($kW.m^{-2}$) versus height (m).
1: TOLBIAC with Steinberner and Reineke correlations (curves at different times).
2: TOLBIAC with Nusselt numbers derived from the experiment (curves at different times).
*: COPO measurements.

The side and bottom wall heat flux are presented on figure 1, in comparison with the measured ones. For each calculation, several curves are plotted, corresponding to different times, and showing the non stationary behavior of the upper part of the pool. The correlations of Steinberner and Reineke give results far from the experiment, because the top heat exchange is largely underestimated by these correlations, which are derived from measurements in square cavities.

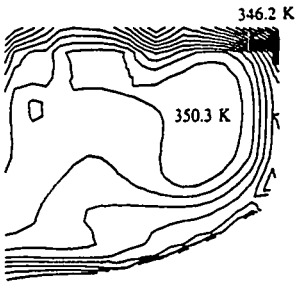


Fig. 2: COPO, temperature field calculated with Nusselt numbers derived from the experiment. Temperature difference between two curves: 0.25 K.

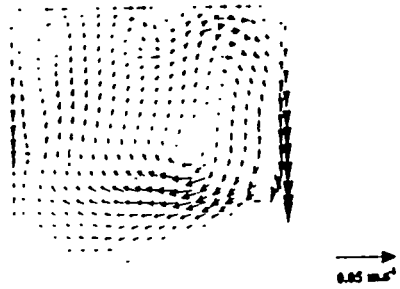


Fig. 3: COPO, velocity field calculated with Nusselt numbers derived from the experiment.

The second calculation shows that with adapted correlations, the TOLBIAC code is able to simulate the natural convection in a volume. However, the general trend in the upper part of the vessel is still somewhat different from the experiments, because the Nusselt numbers used are mean values derived from several tests, on one hand. On the other hand, the exact geometry and experimental devices (thermal losses, thermal resistances) are not exacly known. A perfect fitting is probably not reachable.
In addition figures 2 and 3 present the calculated temperature and velocity fields. The main roll is perturbated by secondary rolls generated by the top heat exchange.

8. Failure of a pressure vessel

Presentation

This calculation has to be understood as a demonstration of the code abilities, since many of the code models are not yet assessed. In our simulation, the initial temperature of the metal phase is high, and consequently the wall ablation occurs within a short time. The code user has to answer to the main following questions: what is the corium composition, what are the metal and oxide temperature, what is the level of the residual power? The ame of the TOLBIAC code is not to address these questions.
At the beginning of our simulation, a stratified liquid corium made of 94.10^3 kg oxides and 39.10^3 kg metals at 2700 K is within a steel pressure vessel (0.20 m thick, initial temperature 373 K). Radiation at the free surface is taken into account, and a wall external heat exchange (coefficient 1000 $W.m^{-2}.K^{-1}$, external temperature 293 K) is supposed. The residual power is 1.6 $MW.m^{-3}$. A 20x20 meshing is used.

Results

Crusts appear along the wall in the oxide phase located in the bottom of the stratified corium pool, and grow, whereas no metal crust appears along the upper part of the pressure vessel wall (fig. 4). Consequently the wall heat transfer in the oxide phase is low and no ablation takes place in the bottom. On the contrary, the metal to wall heat transfer is very high, and ablation occurs, with a fast melting of the wall thickness (fig. 5-6). Due to the high value of the metal to wall heat flux, the major part of the heat transfered to the wall is used to melt the wall. Conduction is low, and becomes notice able only when the wall thickness becomes low (fig. 7). Due to the low oxide to wall heat transfer, the oxide flow is more depending from the metal-oxide heat and momentum transfers than from the oxide wall exchange: the natural convection flow in the metal phase induces the oxide phase flow (fig. 8). The temperature in the oxide phase is rather homogeneous, whereas high differences exist in the metal phase (fig. 9).

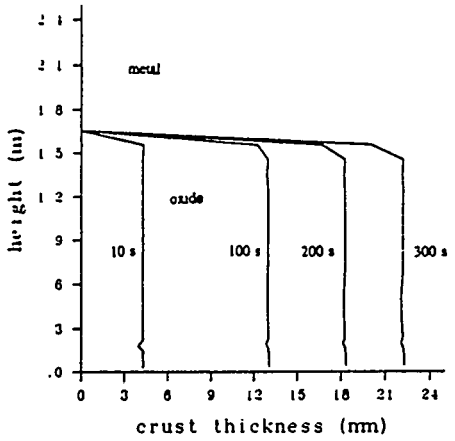


Fig. 4: Pressure vessel, wall crust thickness (mm) versus height (m) along the wall, at different times.

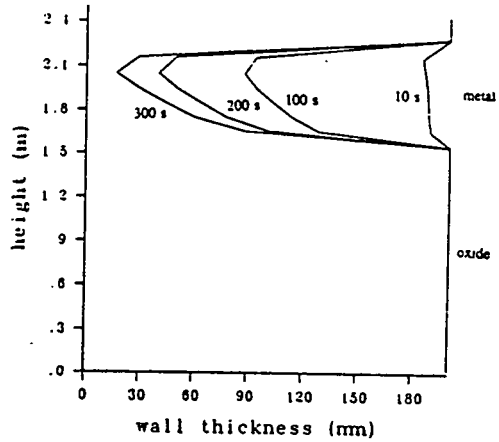


Fig. 5: Pressure vessel, wall thickness (m) versus height (m) at different times.

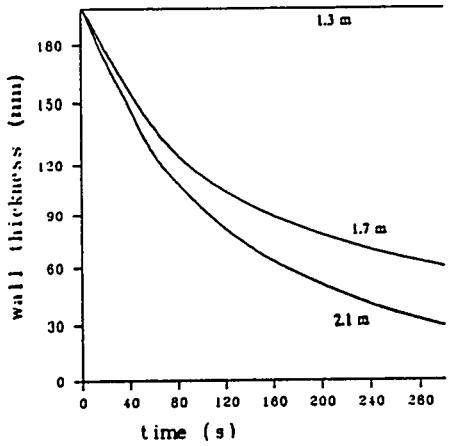


Fig. 6: Pressure vessel, wall thickness (m) versus time (s), at different heights.

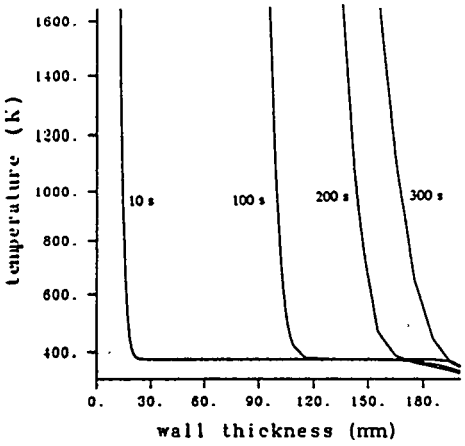


Fig. 7: Pressure vessel, temperature (K) profile in the wall at height 1.9 m, at different times.

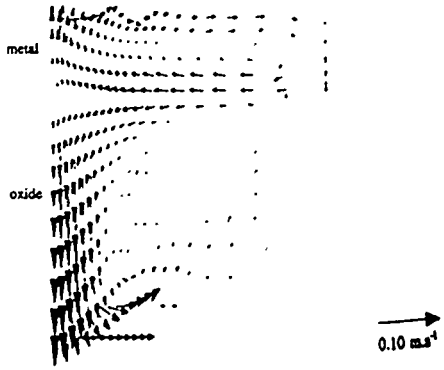


Fig. 8: Pressure vessel, velocity field at 200 s.

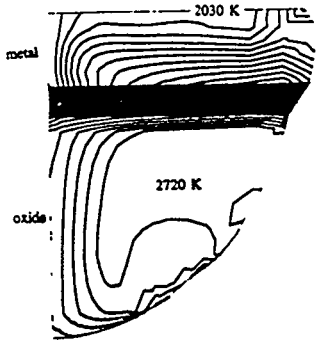


Fig. 9: Pressure vessel, temperature field at 200 s. Temperature difference between two curves: 10K.

9. Conclusion

TOLBIAC is a simulation code developed in order to describe the behavior of a molten core within a structure. A three dimensions three components model is used. The first results show the ability of the code to simulate natural convection on one hand, ablation and crust formation on the other hand.

NOMENCLATURE

variables					
Cp	specific heat	T	temperature	b	corium
e	crust thickness	β	thermal expansion coefficient	c	crust
g	gravity	Γ	mass transfer	D	oxide
h	heat exchange coefficient	ΔT	temperature difference	ext	external
H	enthalpy	λ	conductivity	g	gas
H_{LS}	solidification heat	μ	viscosity	q	power
L	length scale	ρ	density	sol	solidification
Q	volumetric power			sur	surface
t	time	indices		X	light oxide
		A	metal	w	wall

ACKNOWLEDGEMENTS

This work is performed within the frame of cooperative task between CEA, EDF and Framatome.

REFERENCES

[1] BRUN B., PARENT, M., SPINDLER, B., Three-Dimensional Two-Phase Flow Module of the Code CATHARE 2, International Topical Meeting on Advances in Mathematics, Computations and Reactor Physics, Pittsburgh, April 28-May 1, 1991.

[2] CHEVALIER, P.Y., CENERINO, G., Thermodynamic Data Bases and Calculation Code Adapted to the Modelling of Molten Core Concrete Interaction Phenomena Developed Jointly by THERMODATA and the Institut de Protection et de Sûreté Nucléaire (France), 2nd OECD (NEA) CSNI Specialist Meeting on Molten Core Debris-Concrete Interactions, Karlsruhe, Germany, 1-3 April 1992.

[3] GONZALES, L., Some Physical Properties of the Melt; CORCON-WECHSL Comparison, ACE TAC Meeting, Palo Alto, November 1991.

[4] HABERSTROH, J.K., REINDERS, R.D., Conduction Sheet Model for natural Convection through a Density Stratified Interface, Int. J. Heat Transfer, 17, 307, 1974.

[5] CHAWLA, T.C., CHAN, S.H., Heat Transfer from Vertical/Inclined Boundaries of Heat-Generating Boiling Pools, J. of Heat Transfer, 104, 465-473, 1982.

[6] STEINBERNER U., REINEKE, H.-H., Turbulent Buoyancy Convection Heat Transfer with Internal Heat Sources, Proc. Sixth International Heat Transfer Conf., Toronto, Canada, Aug. 1978.

[7] KYMALAINEN, O.,HONGISTO, O., ANTMAN, J., TUOMISTO, H., THEOFANOUS, T.G., COPO: Experiments for Heat Flux Distribution from a Volumetrically Heated Corium Pool, private communication, 1992. See also: Heat Flux Distribution from a Volumetrically Heated Pool with High Rayleigh Number, KYMALAINEN, O., TUOMISTO, H., HONGISTO, O., THEOFANOUS, T.G., Proceedings of the 6th Topical Meeting on Nuclear reactor Thermal Hydraulics (NURETH 6), Grenoble, France, October 5-8, 1993, vol 1, pp 47-53.

RESUME

SIMULATION DU COMPORTEMENT THERMOHYDRAULIQUE D'UN COEUR FONDU DANS UNE STRUCTURE, AVEC LE CODE A TROIS DIMENSIONS ET TROIS COMPOSANTS TOLBIAC

Le code TOLBIAC a pour objet la simulation du comportement d'un coeur de réacteur fondu dans une structure (fond de cuve ou récupérateur), en tenant compte de la position relative des composants, de l'ablation de la paroi et de la formation de croûtes. On présente une brève description du code: modèle 3D, propriétés physiques et lois constitutives, ablation des parois et formation de croûtes. Deux résultats sont présentés: la simulation de l'expérience COPO (convection naturelle en eau dans une cuve elliptique à l'échelle 1/2), et la simulation du comportement d'un corium dans un fond de cuve REP, avec formation de croûte et ablation.

The Modeling of Core Melting and In-Vessel Corium Relocation in the *APRIL* Code

S.W. Kim, M.Z. Podowski, R.T. Lahey, Jr. and N. Kurul

Rensselaer Polytechnic Institute
Troy, NY 12180-3590, USA

ABSTRACT

This paper is concerned with the modeling of severe accident phenomena in boiling water reactors (BWR). New models of core melting and in-vessel corium debris relocation are presented, developed for implementation in the APRIL computer code. The results of model testing and validations are given, including comparisons against available experimental data and parametric/sensitivity studies. Also, the application of these models, as parts of the APRIL code, is presented to simulate accident progression in a typical BWR reactor.

1. INTRODUCTION

This paper presents the results of the recent work of thermal-hydraulic models of phenomena governing the progression of hypothetical severe accidents in boiling water nuclear reactors (BWRs). These new models have been developed for, and implemented in, the new interactive version of the APRIL computer code, APRIL.MOD3X. A description of the modeling concepts in APRIL is given, encompassing phenomena from the inception of an accident to the advanced phase of core meltdown, and including the in-vessel/ex-vessel thermal-hydraulics and fission product transport. The new models which are discussed in detail are those of core heatup, degradation & meltdown, and melt relocation into the lower plenum. The results of model testing and validations are given, including comparisons against the available experimental data and parametric/sensitivity studies. Also, the application of these models, as parts of the APRIL code, is presented to simulate accident progression in a typical BWR.

2. OVERVIEW OF THE APRIL CODE

APRIL is a severe accident analysis code which has been developed at Rensselaer Polytechnic Institute under the sponsorship of Oak Ridge National Laboratory and the Empire State Electric Energy Research Corporation (ESEERCO). A summary of the modeling principles used in APRIL is given in this section. A detailed description of the models developed for, and implemented in, the APRIL code can be found in Refs. 1 and 2.

The APRIL code consists of mechanistic models pertaining to the reactor core, pressure vessel, and the primary and secondary containments. The simulations can start from the fully covered core conditions and continue into the core dryout, core degradation and melting, breach of vessel, primary containment and secondary containment. The most recent version of APRIL, APRIL.MOD3X is intended for use in accident management, and its major components are outlined below.

The core model in APRIL uses a two-dimensional (in axial and radial directions) nodalization scheme. In each node, the following core structures are accounted for: fuel, cladding, canister, and control rod. The specific in-core phenomena modeled include: 2-D heat transfer between individ-

ual core components as well as between the core and surrounding structures; heat convection to the coolant in both the covered and uncovered portions of the core; oxidation of the fuel cladding, channel wall, and control blade; fuel buckling (used as a criterion for rubble bed formation); slumping of the canisters and control blades; melting of individual core components; formation of an eutectic mixture of fuel and molten Zircaloy; molten material relocation and refreezing; channel blockage; and the resultant flow redistribution. The effect of B_4C and stainless steel (SS) eutectic is accounted for by appropriately lowering the control rod melting temperature. A similar approach can be used for the SS/Zircaloy interaction.

The core model is coupled with a model of in-vessel thermal-hydraulics. Various flow configurations inside the vessel are accounted for, including the formation of a natural circulation loop between the hot core and the relatively cool downcomer region after the core and jet pump discharge get fully uncovered. The in-vessel model provides the core model with boundary conditions such as gas/steam mixture inflow temperature, system pressure, and temperature of surrounding structures.

The gas pressure and temperatures in the primary containment are calculated using a multi-compartment natural circulation model. The primary containment module accounts for the events following corium release from the vessel, namely, concrete ablation and the resultant gas release, debris cool-down/solidification in contact with the concrete and due to the radiative and convective heat losses, corium/water interaction in the pressure suppression pool (PSP), and others.

The fission products are collected into several groups according to their physical properties. Following the release of each group from the core, their concentration and deposition are tracked in the vessel compartments, and in primary and secondary containments, using mechanistic aerosol transport models.

The APRIL code is written in FORTRAN, and has been used on a variety of platforms, including 486 PC, Unix computers, VAX VMS, etc. Its speed is up to five times faster than the real time on an IBM RS6000-7012. The APRIL code has user-friendly input and output formats for stand-alone usage. It can also be used in conjunction with its graphical user interface (GUI) on Unix workstations equipped with X-windows environment. One of the screens of the APRIL-GUI is shown in Fig. 1. This screen includes most of the operator controls. In addition, main parameters can be viewed in the form of dynamic plots. Fission product concentrations, temperatures and pressures in the primary containment can be monitored on other screens. The active screen can be switched on at any time during the run.

The Graphical User Interface of APRIL has been developed using the Computer Visualization System (CVS) and the graphical libraries of the Nuclear Plant Analyzer obtained from EG&G Idaho. The APRIL engine and the GUI run in parallel, communicating over a unix pipe. This architecture has several advantages, mainly, better performance due to a more uniform usage of the computer resources, suitability for platforms with multiple CPUs, and an easier code maintenance. Among other code characteristics, the restart/playback feature can be particularly useful for performing analyses. During a run, the current status can be saved at several check-points; the results can be played backward and forward without re-running the code. The calculations can be resumed starting from any of the check points if the user wishes to modify some of the operating parameters.

3. MODELING CORE HEATUP AND MELTING

3.1. Model description

This section presents some of several new and/or improved models for heat transfer inside the

degraded core and between the core and the surrounding structures. The development of such models was stimulated by the modifications in the original core model of APRIL which were required in order to compare this model against the data obtained in the SANDIA DF-4 experiments [3] and the CORA experiments [4] performed at KfK (Germany). The validation of the APRIL model against the above-mentioned experiments was very helpful in identifying areas where improvements were needed concerning the various heat transfer models and the specific modeling assumptions used.

The new models and modifications of the reactor core model included: (a) adding new experiment-specific structures to the original core model, such as a multi-node model of the multi-layer shroud, including the ZrO_2 fiber insulator and dense ZrO_2 tube, employed in the DF4 experiments and models of similar structures in the CORA experiments, and separate models of the unheated UO_2 rods used only in the CORA experiments; (b) the modeling of physical phenomena of core heatup and degradation (all applicable to actual BWRs), such as: steam-induced oxidation of zircaloy and stainless steel, possible B_4C liquefaction, eutectic interactions between UO_2 & Zircaloy and other core materials, convective heat transfer under developing-flow conditions, and heat transfer between fuel elements, channel boxes, control rods and steam/gas flow in the uncovered portions of the core. The latter model is summarized below.

Nodal Equations in the Uncovered Core Region

The nodal governing equations of the gas mixture in the uncovered region of the reactor core refer to the system pressure calculated in the in-vessel thermal-hydraulic model of APRIL [2]. Based on this assumption, the nodal flow rates and temperatures of the gas mixture are calculated. Fig. 2 illustrates the modeling of heat and mass (steam consumption and hydrogen production due to oxidation) transfer in a node in the uncovered region of the core, between wall k (where the index, k, refers to one of the following structures: cladding, canister, and control blade) and the gas (steam and hydrogen) mixture. The governing continuity and energy equations of the gas mixture become, respectively

$$V_i \frac{d\rho_i^m}{dt} = w_{i-1}^m - w_i^m + \sum_k \left(w_{Hp,i}^k - w_{sc,i}^k \right) \tag{1}$$

$$\rho_i^m c_{pm} V_i \frac{dT_i}{dt} = w_{i-1}^m c_{pm} (T_{i-1} - T_i) + \sum_k \left(w_{Hp,i}^k c_{pH} + A_{w,i}^k H_i \right) \left(T_{w,i}^k - T_i \right) + V_i \frac{dp}{dt} \tag{2}$$

where

$$w_i^m = w_{s,i} + w_{H,i} \tag{3}$$

$$\rho_i^m = \rho_{s,i} + \rho_{H,i} \tag{4}$$

Here, $w_{s,i}$ and $w_{H,i}$ are the flow rate of steam and hydrogen from the i-th node, $\rho_{s,i}$ and $\rho_{H,i}$ are the density of steam and hydrogen, respectively, $w_{sc,i}^k$ is the steam consumption rate on the k-th wall, $w_{Hp,i}^k$ is the hydrogen generation rate from the k-th wall in node i, c_{pm} and c_{pH} are the specific heat of the gas mixture and hydrogen, respectively, $A_{w,i}^k$ and $T_{w,i}^k$ are the heat transfer area and temperature of the k-th wall in node i, H_i is the heat transfer coefficient, and p is the pressure.

By using the ideal gas assumption, Eq. (1) becomes

$$w_{i-1}^m - w_i^m + \sum_k \left(w_{Hp,i}^k - w_{sc,i}^k \right) = -\frac{\rho_i^m V_i}{T_i} \frac{dT_i}{dt} + \frac{\rho_i^m V_i}{p_i} \frac{dp}{dt} \tag{5}$$

Eqs. (2) and (5) are solved to evaluate the nodal temperature, T_i, and the flow rate of the gas mixture, w_i. Then, the flow rate of each gas component can be calculated according to its local mass fraction.

Radiation Heat Transfer Between Structures

Radiation heat transfer is one of the most important modes of heat transfer during and after core uncovering. In order to improve the predictive capabilities of the degraded core model in APRIL, the structural radiation heat transfer model has been replaced by a new model. This improved model takes into account the geometrical configuration of the core to evaluate the view factors and the emissivities of core materials.

In this model the radiation heat transfer in the main channels and in the bypass are modeled separately. In the nodal configuration of APRIL (see Fig. 3), the fuel rods in a node in the main channel are surrounded by two channel walls. It is assumed that there is no radiation heat transfer between channel wall-1 and channel wall-2, since the surface area of channel wall-1 facing channel wall-2 is negligible compared to the area facing the fuel rods.

Unlike in the main channel, there is radiation heat transfer in the bypass region between channel wall-2 in radial node i and channel wall-1 in radial node $(i+1)$ (See Fig. 3). The radiation heat transfer between the structures accounts for the axial position of the control rods in each radial zone.

Naturally, the radiative heat transfer mode is combined with heat convection, as indicated in Eq.(2). In addition to heat radiation between internal core structures, the present model also accounts for radiative heat losses between the core and the surrounding structures.

3.2. Model Validation and Testing.

The models described in the previous section have been implemented in the APRIL code and extensively tested and validated against experiments. Specifically, the degraded core model in APRIL has been used to simulate the experimental conditions of five different BWR severe fuel damage experiments: the DF-4 experiment performed at Sandia National Laboratory (SNL), and the CORA-16, CORA-17, CORA-28, and CORA-31 experiments performed at Kernforschungszentrum (KfK), Germany.

In all these experiments the key structural elements of the BWR core were included, such as fuel rods, canisters, and control blades. A common purpose of the DF-4 and CORA-16 experiments was to investigate the phenomena associated with failure of, and interactions between, the fuel rods, canisters and control blades in a BWR core. The specific purpose of the CORA-17 test was to observe the effect of quenching following a heat-up phase similar to the CORA-16 experiment. In the CORA-31 experiment, the influence of slow initial heat-up (0.3 K/s compared to 1.0 K/s in other experiments) was investigated. The objective of the CORA-28 experiment was to investigate the effect of preoxidation [6]. A brief overview of those experiments is given in Table 1.

Since the results of APRIL predictions of the DF-4 experiment were presented before [5], the results given below are focused on the APRIL predictions of the four CORA experiments listed in Table 1. As mentioned before, because the APRIL code has been designed for the analysis of severe accidents in BWRs, new models for the experiment-specific structures had to be implemented for the purpose of CORA simulations, including a test bundle insulator and unheated rods. A simplified geometry of the CORA test section and the related APRIL representation are shown in Fig. 4. With these modifications, each experiment was simulated using the same model, combined with appropriate geometrical input data and initial/boundary conditions.

Several APRIL-calculated parameters were compared against the CORA experimental data, such

Table 1. Overview of the simulated experiments

Experiment	Objective	Heating	Heatup Rate	Gas Injected	Cooling
DF-4	Investigate the behavior of BWR core geometry under severe accident conditions	Fission	0.3 K/s ~1.2K/s	steam	Slow gas
CORA-16	Influence of B_4C/SS absorber material on the Zircaloy channel walls	Electric	1 K/s	steam+Ar	Slow gas
CORA-17	Additional damage progression during quenching	Electric	1 K/s	steam+Ar	Water quench
CORA-28	Influence of pre-oxidation	Electric	1 K/s	steam+Ar	Slow gas
CORA-31	Influence of slow initial heatup (0.3K/s)	Electric	0.3 K/s	steam+Ar	Slow gas

as: the structural temperatures at various locations along the test section in each experiment, the amount of hydrogen generated due to oxidation and the deformation of the test bundle flow area due to structural melting and melt relocation. Typical comparisons between the calculations and the data for all four experiments at the same location near the exit of the heated section are shown in Figs. 5 through 8. A typical result for the hydrogen generation rate is shown in Fig. 9 for CORA-31.

Generally, very good agreement has been observed between the APRIL predictions and the experimental data. The analysis of the obtained results also revealed several factors which may cause differences between the measured and predicted data, including both modeling assumptions and experimental methods, thus helping to understand the fundamentals of degraded core phenomena. Concerning the former issue, i.e. the modeling simplifications and limitations, the following seem to be the most important ones: the lumped parameter approach to heat transfer and system nodalization, uncertainties in the modeling of melt relocation, and uncertainties in the parameters used in the calculation of heat transfer following a significant structural deformation caused by melting and melt relocation. The discrepancies in the comparisons may have been caused by apparent limitations of the technique used in these complicated experiments in the measurements of the accumulated mass of hydrogen (specifically, a delaying effect of gas mixing) in the CORA experiments.

4. A MODEL OF CORIUM RELEASE INTO LOWER PLENUM

4.1. Modeling Concept

The present model evaluates a variety of phenomena occurring in the reactor pressure vessel (RPV) lower plenum following the release of molten corium debris from the core. This new model replaces the simplified lower plenum model developed for the original version of APRIL. The models of specific phenomena associated with melt/structure interaction in the lower plenum include the heat transfer and phase change between the melt, solid structures and any water which may be present, and the RPV failure mechanisms and the resultant release of the molten corium into the reactor containment. The lower plenum model also accounts for the heatup and remelting of the quenched debris beds. The lower plenum internal structures considered here include the control rod drive (CRD) tubes, the instrument guide (IG) tubes, and the lower head. The entire lower plenum volume is divided into a user-specified number of vertical nodes. The parameters

calculated in each node include the temperature and mass of solid and molten materials. The molten debris model assumes corium stratification into two main regions: a molten metallic pool on the top and a heavier oxidic pool at the bottom. In contact with cold solid structures and water in the lower plenum, the molten materials in each pool may gradually freeze and simultaneously ablate these structures. The frozen metallic material freezing on the walls (i.e. metallic crust) is added to the structures in the respective nodes. In particular, a solidified metallic layer is typically formed on the bottom of the lower head as a result of the initial melting of stainless steel and melt release into the lower plenum. The frozen oxidic material (crust) in the nodes containing molten oxidic pool is always treated separately from the RPV structures. Following crust formation on the surface, the structure can be heated up to the point that the heat from the crust ablates the structural surface, and the molten metal combines with the metallic pool. The modeling concept described above uses mass and energy conservation equations for each material, including heat conduction in solids and heat convection between the molten pools and surrounding structures.

The internal lower plenum structures are nodalized in such a way that each node contains a section of vessel wall, CRD tubes, IG tubes, and debris crust. A lumped parameter approach is used to evaluate the temperatures and masses of the structures. Heat transfer mechanisms considered here include: convective heat transfer to the water in the lower plenum, and to the water/steam inside the tubes, axial heat conduction, heat transfer from the crust or molten corium pool, and the heat and mass transfer associated with phase change. Considering these mechanisms, the lumped parameter governing equations become:

Mass Conservation

$$\frac{dM^{j}_{ik}}{dt} = \dot{M}^{j}_{fz,\,ik} - \dot{M}^{j}_{ab,\,ik} \tag{6}$$

where, k denotes the structure (i.e. the lower head, CRD tubes and IG tubes), i is the node number, j is the material identification number, $\dot{M}^{j}_{fz,\,ik}$ is the rate of solidification of the j-th material on the k-th structure in the i-th node, and $\dot{M}^{j}_{ab,\,ik}$ is the rate of ablation. Since a node can be in contact with the crust and the metallic melt at the same time, both the ablation and freezing rates are accounted for in Eq. (6).

Energy Conservation

$$\frac{d\,[Mu]_{i,k}}{dt} = Q_{c,\,ik} - Q_{lin,\,ik} - Q_{lout,\,ik} + Q_{fz,\,ik} - Q_{ab,\,ik} + Q_{ax,\,ik} + Q_{mp,\,ik} \tag{7}$$

where, M and u are the total mass and internal energy of the k-th structure in the i-th node, $Q_{c,\,ik}$ is the heat transfer from the crust to the structure, $Q_{lin,\,ik}$ and $Q_{lout,\,ik}$ are the heat transfer to the gas/water in the lower plenum and the heat loss to outside, $Q_{fz,\,ik}$ is the energy carried by the frozen material, $Q_{ab,\,ik}$ is the energy carried by the ablated structure, $Q_{ax,\,ik}$ is the axial heat conduction, and $Q_{mp,\,ik}$ is the heat from the metallic pool. Since a given structure may contain more than one material, the properties of the structure are established as composition-dependent average values.

As the molten oxidic material containing UO_2 and ZrO_2 freezes on the cold structural surfaces, a crust is formed. This crust is modeled separately in each node. The lumped crust mass and energy conservation equations are used in each node separately.

Mass Conservation

$$\frac{dM^{j}_{c,\,i}}{dt} = \sum_{k} \dot{M}^{j}_{fc,\,ik} \tag{8}$$

where, $M^j_{c,i}$ is the mass of the j-th material (j=1 for UO_2, j=2 for ZrO_2) in the crust in node-i, and $\dot{M}^j_{fc,ik}$ is the rate of solidification of the j-th material on the surface of the k-th structure in node-i.

Energy Conservation

$$\frac{d[M_c u_c]_i}{dt} = Q_{cint,i} - \sum_k Q_{c,ik} + \sum_k Q_{fc,ik} + Q_{pc,i} + Q_{axc,i} - Q_{cw,i} \tag{9}$$

where, $Q_{cint,i}$ is the internal heat generation (decay heat) in the crust, $Q_{fc,ik}$ is the energy associated with phase change, $Q_{pc,i}$ is the heat transfer from the oxidic pool to the crust, $Q_{axc,i}$ is the axial heat conduction, $Q_{cw,i}$ is the heat loss to water/gas in the lower plenum if the crust is exposed to the water/gas environment, and $Q_{c,ik}$ is the heat transfer from crust to the wall. Like the structure model, the properties of the crust are composition-dependent, and are evaluated as mass-weighted average values.

The oxidic pool model accounts for phenomena such as: phase change, corium inflow, and corium discharge to the containment, the conservation equations for this pool become:

Mass Conservation

$$\frac{dM^j_{cp}}{dt} = \sum_j W_{j,in} - \sum_i \sum_k \sum_j \dot{M}^j_{fc,ik} - \sum_j W_{j,out} \tag{10}$$

where, $W_{j,in}$ is the flow rate of the j-th material of the oxidic material from the reactor core, and $W_{j,out}$ is the discharge rate of the j-th material into the containment after RPV failure.

Energy Conservation

$$\frac{d[M_{cp}u_{cp}]}{dt} = \sum_j W_{j,in}h_{j,in} - \sum_j W_{j,out}h_{j,cp} - \sum_i \sum_k Q_{fc,ik} + Q_{cp,int} - Q_{pc,i} - Q_{cpm} - Q_{cpw} \tag{11}$$

where, $h_{j,in}$ is the enthalpy of the j-th material of corium inflow, $h_{j,cp}$ is the enthalpy of the j-th material in the oxidic pool at the pool average temperature, $Q_{cp,int}$ is the internal heat generation rate in the pool, Q_{cpm} is the heat transfer between the oxidic pool and the metallic pool, and Q_{cpw} is the heat loss to the water/steam in the lower plenum. $Q_{fc,ik}$ and $Q_{pc,i}$ are the same as in Eq. (9).

As in the modeling of the molten oxidic pool, the inflow from the core, discharge of molten metal into the containment, solidification on the wall surface, and heat loss to the water are considered in the modeling of the metallic pool. The governing conservation equations are similar to Eqs. (10) and (11).

The remaining water in the lower plenum serves as a heat sink for the reactor vessel wall and the internal lower vessel structures, thus preventing, or delaying, the process of lower head melting and failure in contact with the corium debris. At the same time, a substantial amount of steam can be produced during the debris cooldown. This, in turn, may result in considerable pressure buildup in the RPV and rapid oxidation of the remaining metallic zircaloy in the core. The present model accounts for such phenomena as heat convection between molten/solid debris pool and water, and the resultant steam generation.

Two possible modes of heat transfer between the debris and water in the lower plenum are considered. One is the heat transfer from free falling debris through the water pool inside the lower plenum, and the other is the heat transfer from the debris pool. Adding the two heat sources, the

evaporation rate of water inside the lower plenum is calculated.

4.2. Corium Solidification

An important part of the overall model is concerned with the phase change phenomena in the corium pool and in lower plenum structures. As mentioned before, the molten corium, both metallic and oxidic, may freeze in contact with cold lower plenum internal structures, and heat up the structures to cause RPV failure. Since only molten materials are likely to be discharged into the containment after the RPV failure, it is important to predict the amount of molten material in the lower plenum at the time of RPV failure.

Whereas a lumped parameter approach has been used to model the molten corium pool, in order to model phenomena such as localized freezing of melt at the structural surface, an approximate analytical solution of a one-dimensional problem of heat conduction with solidification [8] is used. Consider the case where molten material "1"(corium) is suddenly brought in contact with solid material "2"(structural wall), as shown in Fig 10. The melting and initial temperatures of material-1 are assumed to be higher than those of material-2. In this situation, the interface temperature of these two materials can either be lower than the melting temperature of material 2 or reach this melting temperature. In the former case only material-1 undergoes phase change at the interface. In the latter case, both materials will undergo phase change. Both cases are considered, as discussed below.

(a) Solidification of the melt without wall ablation

In this case the interface temperature T_i is below the melting temperature of material-2, T_{2m}. Using one-dimensional semi-infinite thickness conduction models for three regions, i.e. molten material-1, solidified material-1, and material-2, the following expression has been derived for the rate of crust growth,

$$\delta_c(t) = 2\Omega_c\sqrt{\alpha_1 t} \tag{12}$$

where, Ω_c is the root of the following transcendental equation,

$$(T_{1m}-T_i)\frac{exp\left(-\Omega_c^2\right)}{erf(\Omega_c)} - (T_{1\infty}-T_{1m})\frac{exp\left(-\Omega_c^2\right)}{erfc(\Omega_c)} = \sqrt{\pi}\frac{\lambda_1}{c_{p1}}\Omega_c\,, \tag{13}$$

where T_i is the time dependent interface temperature, which is evaluated by coupling the crust model with the wall model as discussed later.

(b) Solidification of the melt with wall ablation

If the interface temperature is greater than the melting temperature of the wall, Wall ablation will occur immediately. In the case where molten layer of the wall material is present between the crust and wall, it is assumed that the molten wall material can escape from the interface immediately. This assumption is based on the experimental observation [7] that the molten material-2 percolates upward through cracks in the crust to the debris pool surface when the density of material-2 is lower than that of material-1. This means that the interface temperature will stay at the wall melting temperature as long as phase change continues on the wall surface. Thus, the solution for the melt and the crust is similar to the one obtained for the case without ablation, but with T_i replaced by T_{2m}. The values of Ω_c have been calculated for various interface temperatures and melt superheats for both cases, and the calculated values have been implemented in the APRIL as a look-up table.

Using the analytical solution described above, the functional dependence of the heat flux from the

crust to the wall surface can be deduced. The heat flux into the wall can be obtained from the temperature distribution inside the crust as

$$q''_i = \frac{2}{\sqrt{\pi}} \frac{\Omega_c}{\int_0^1 erf(\Omega_c y)\, dy} \frac{k_1}{\delta_c} (T_c - T_i) \tag{14}$$

where the average temperature of the crust is,

$$T_c = \frac{1}{\delta_c} \int_0^{\delta_c} T_c(t,x)\, dx = T_i + (T_{1m} - T_i) \int_0^1 \frac{erf(\Omega_c y)}{erf(\Omega_c)} dy \tag{15}$$

Therefore, considering the finite geometry, it is assumed that the heat flux from the crust to the wall can be approximated by

$$q''_i = f_c \frac{2}{\sqrt{\pi}} \frac{\Omega_c}{\int_0^1 erf(\Omega_c y)\, dy} \frac{k_c}{\delta_c} (T_c - T_i) \tag{16}$$

where, f_c is the correction factor for finite geometry and multi-dimensional effects.

4.3. Wall Heatup and Ablation

As indicated before, the solidification rate of the oxidic melt is a direct function of the interface temperature. After the interface temperature reaches the melting temperature of steel, the wall surface heat flux is needed to evaluate the wall ablation rate. These variables can be readily determined if the temperature profile across the wall is known. In the present model, the wall is represented by a finite (possibly, time-dependent) thickness slab, and the temperature distribution at time t is used as an initial condition in the calculations of the new temperature profile at time $t + \Delta t$. A cubic profile is assumed across the wall,

$$T(\eta) = a(t)\eta^3 + b(t)\eta^2 + c(t)\eta + d \tag{17}$$

where, a, b, c, and d are the coefficients of the profile which is to be determined at each time step of calculation, and $\eta = x/\delta$, where, x is the distance from the outer surface of the wall, and δ is the wall thickness. Fig. 11 shows the definition of the coordinate and the conditions at the boundaries. In this study, two cases are considered, one is the case without ablation and the other is that with ablation.

Without wall ablation

In this case, the heat fluxes at both sides of the wall can be used as boundary conditions for the time-dependent one-dimensional heat conduction equation across the slab. Since Eq.(17) contains four time-dependent coefficients, these boundary conditions must be complemented by two additional conditions. These conditions can be obtained by integrating the governing heat conduction equation, first directly and then after multiplying both sides by x (or, in other words, taking the "zeroth-order" and "first-order" moments over the slab thickness). This approach yields a system of ordinary differential equations for $a(t)$, $b(t)$, $c(t)$ and $d(t)$. At each time step these four coefficients are used to evaluate the interface temperature,

$$T_i = a + b + c + d \tag{18}$$

The initiation of wall ablation can be determined by comparing T_i with the melting temperature of the wall.

With wall ablation

After the interface temperature reaches the melting temperature of the wall, T_{wm}, the wall surface may be ablated by the continuous heat addition at the interface. Since it is assumed that the ablated material is immediately removed from the interface, the interface temperature remains at the wall melting temperature while wall ablation occurs. Therefore, the boundary conditions at the wall interface become,

$$T_i = a + b + c + d = T_{wm} \tag{19}$$

$$\lambda_w \rho_w \frac{d\delta_w}{dt} = q''_i - k\frac{dT}{dx}\bigg|_{x=\delta} \tag{20}$$

where q''_i is the interfacial heat flux from the corium crust. Using the integral moments method similar as in the case without ablation, the time dependent coefficients, $a(t)$, $b(t)$, $c(t)$ and $d(t)$ can be calculated and used to obtain the heat flux at the inner wall surface,

$$q''_{wi} = k\frac{dT}{dx}\bigg|_{x=\delta} = \frac{k}{\delta}(3a + 2b + c) \tag{21}$$

The model described above was tested in a stand-alone fashion for the case of a steel slab 21.5 cm thick in contact with corium on one side. The other surface was exposed to air at a temperature of 285 °C. The heat transfer coefficient between the slab and the air was assumed to be 170 W/m^2-K (30 Btu/hr-ft^2-F). The initial temperature of the slab was 285 °C. The initial contact temperature between the corium and the wall was 1125 C. A constant heat flux, 2.2×10^5 W/m^2, was assumed between the corium and the wall. The assumed value of the heat flux was an average heat flux from the crust to the wall surface calculated by Eq. (16). The calculated temperature profiles across the slab at various time instants are shown in Fig. 12. As can be seen, the interface temperature increases until it reaches the melting temperature of steel (at 1240 s). A continuous supply of heat to the interface after 1240 s causes wall ablation. The ablation of the slab is represented as the movement of the boundary to the left side in Fig. 12. Throughout the transient, the temperature of the outer wall continues to increase. The rate of increase is a result of the net heatup due to the heat conduction from inside being higher that the heat loss to the ambient.

4.4. Modeling of debris-pool-to-interface heat flux

The evaluation of the debris pool-to-interface heat flux is considered for two cases. In the first case, molten corium pool still exists, and the convective heat transfer plays a dominant role. In the other case, after all debris has solidified, only heat conduction between the solidified debris pool and crust is considered.

When a molten corium pool exists, an experimental correlation for the heat transfer coefficient due to natural convection in the pool is used to estimate the pool-to-solid interface heat flux. This correlation is given by,

$$Nu_m = 0.68 + 0.67\frac{Ra^{0.25}}{\left[1 + (0.492/\mathrm{Pr})^{9/16}\right]^{4/9}} \tag{22}$$

where, $Ra = \left[g\beta\,(T_c - T_{cm})\,L^3\right]/(\nu\alpha)$ is the Rayleigh number and Pr is the Prandtl number.

As can be seen in Eq. (22), the heat transfer coefficient is dependent on the pool superheat and the pool height for a given material. Several values of heat fluxes for different corium superheats and geometries have been calculated for molten UO_2 and stainless steel, and implemented in the APRIL code in tabular form.

When the debris gets completely solidified, the solid debris temperature is calculated from the energy balance which accounts for: heat conduction between the various debris materials and lower plenum structures, heat convection/radiation to the water/gas and/or upper structures in the lower plenum, and internal decay heat generation.

4.5. Modeling of Lower Plenum Failure

There are more than 200 reactor vessel bottom head penetrations in the lower plenum of a BWR. These penetrations include CRD tubes, IG tubes and possibly a drain line. Thus, it is possible that the initial lower plenum failure after the corium attack may occur through those penetrations. Two types of failure of tube penetrations are considered in this study. One is an ex-vessel tube failure, and the other is a tube ejection failure.

In the ex-vessel tube failure, melt-through of the tube inside the lower plenum due to the interaction between the corium and the tube wall causes a spill of corium into the tube. The downward relocation and freezing of the corium inside the tube can result in tube failure outside the lower head. The failure mechanism would be creep-rupture of the tube wall. This failure mechanism illustrated in Fig. 13 applies to CRD tubes, IG tubes and the drain line. Because the CRD tube internal cross section is almost completely blocked by the movable index tube (only a 0.6 mm annular flow gap exists there), the ex-vessel tube failure is less likely to occur in the CRD tubes than in the IG tubes and/or the drain line both having a relatively large open cross section.

In the case of tube ejection failure, the heatup of welds holding the tube penetrations in place may cause failure or melting of the welds. Then, the pressure difference between inside and outside the lower plenum can cause the ejection of the tubes. Since BWRs are required to have a structure beneath the lower head that would limit the downward movement of any control rod assembly to about 3 cm in the event of failure of its stub tube weld, this type of failure is considered only for the IG tubes.

A continuous heatup or ablation of the lower head by corium may cause gross failure of the entire lower head. However, considering the thickness of the lower head (~20 cm), this type of failure is expected to occur much later than the potential penetration failure. Nevertheless, the gross failure mode is also considered in the present model.

The models for each bottom head failure mode are discussed below.

Following the melt-through of some of the tubes inside the lower plenum, the molten corium must reach the tube region outside the lower head to cause melt release. Therefore, it is necessary to estimate the penetration distance the corium inside the tube will travel for the possibility of ex-vessel tube failure. This distance is evaluated by using the conduction layer model [9] and the bulk freezing model [10]. Both models are illustrated in Fig. 14. Existing experimental data indicate that the distance reached by the melt is bounded by the values predicted by these two models [11].

The bulk freezing model assumes that turbulence in the flowing melt prevents stable crust from forming at the channel wall. The plug solidification distance in the bulk freezing model is given as [10],

$$X_p = \frac{1}{2}\frac{D_e}{f}\frac{[\lambda_c + c_c(T_c - T_{cm})]}{c_c(T_c - T_w)} \tag{23}$$

where, D_e is the equivalent diameter of the tube, f is the friction coefficient, λ_c is the heat of fusion of corium, c_c is the specific heat of corium, T_c is the temperature of corium, T_{cm} is the melting temperature of corium, and T_w is the initial wall temperature.

The conduction layer model involves the growth of a stable frozen layer at the channel wall. Once the frozen layer closes at the channel center, flow ceases and the remaining melt inside the channel freezes. The model also assumes a constant penetration melt velocity into the channel.

The distance predicted by the conduction layer model is given by,

$$X_p = \frac{D_e^2 v}{16\Omega_c \alpha_c} \tag{24}$$

where, v is the inlet velocity of corium, Ω_c is the solidification constant, and α_c is the thermal diffusivity of corium. The solidification constant, Ω_c can be estimated from Eq.(13). Typical values are between 0.8 and 1.1). The melt velocity of corium, v, at the point where melt exits the vessel lower head is given by,

$$v = \sqrt{\frac{2(p_1 - p_2)/\rho_c + 2gl_t}{4fl_t/D_e + K + 1}} \tag{25}$$

where, p_1 and p_2 are the pressure at point 1 and 2 in Fig. 13, ρ_c is the corium density, f is the friction coefficient, l_t is the distance the melt travels before exiting the lower head, and K is the entrance loss coefficient at the failed tube.

As mentioned before, the two models give bounding values of the distance traveled by the corium. However, both models have predicted that melt would travel to distances below the vessel outer surface in all BWR penetrations for depressurized conditions, regardless of melt composition (metallic or oxidic) [11]. Both models have been implemented in the code, and either can be chosen by user input.

After the molten corium fills the ex-vessel tubes, the heat-up of tube wall is modeled using a one-dimensional lumped parameter model (see Fig. 15). The temperature of the tube wall is used to determine a possible tube failure due to creep rupture. The Larson-Miller correlation [1] is used to estimate the failure time of the tube.

This model is used to determine the ex-vessel tube failure of the IG tubes, CRD tubes, and the drain line. Unlike IG and CRD tubes, the drain line has no internal structures, and is directly accessible to the molten/solidifying corium materials delivered into the lower plenum. If a large amount of molten corium is delivered over a short time, the drain line will be filled with the corium, and may fail. However, if the rate of delivery of corium is low, so that the molten corium solidifies around the drain line causing a complete blockage of the entrance to the drain line, this failure mode will be unlikely to occur. Therefore, a selection for the failure of drain line is made based on the delivery rate of corium, i.e., if the delivery rate of corium is less than a certain value, the failure of the drain line is not considered. The threshold value of the delivery rate of corium is determined by user input.

As mentioned before, tube ejection failure map for the IG tubes. also developed by Rempe, et al [11], is used to express the tube ejection conditions in terms of the RPV pressure and the lower

head inner temperature.

The lower head can fail mechanically at temperatures well below its melting point because of high vessel pressure and the combined mass of the debris and of the lower head itself. The failure mechanism would be creep-rupture. In this study, the creep-rupture curves [13] for the SA533B1 carbon steel of the BWR reactor vessel are used to estimate the failure time of the lower head. Since the creep-rupture curves are not applicable to the temperature range above 1373 K, the Larson-Miller parameter correlation [1] is used in this range. The stress used in the determination of the time to failure is calculated by considering the system pressure, the mass of the debris, and the mass of the lower head.

4.6. Corium Discharge Outside the Vessel

Following the penetration failure of the lower head, the corium discharge into the containment will be governed by the RPV pressure and corium pool height. For the modeling purposes, it has been assumed that the initial size of the opening made through the lower head is equal to the cross-sectional area of the tube originally penetrating the lower head. The modeling concept is shown in Fig. 16. When the penetration failure occurs, failure of N tube penetrations is assumed. The number of failed tubes, N, is controlled by user input.

The mass flow rate of corium through the openings can be calculated by,

$$w_d = A(t)\,\rho_c v(t) \tag{26}$$

where, ρ_c is the corium density, $v(t)$ is the corium velocity obtained from an equation similar to Eq.(25), $A(t) = \pi r_m^2(t) N$ is the opening area, and $r_m(t)$ is the radius of tube penetration calculated by [1],

$$\frac{dr_m}{dt} = \varepsilon \frac{H_c (T_c - T_{ms})}{\rho_s [\lambda_s + c_{ps}(T_{ms} - T_s)]} \tag{27}$$

where T_{ms} and T_s are the melting and current temperatures of the lower head, T_s is the lower head temperature, ρ_s, λ_s, c_{ps} are the density, heat of fusion, and specific heat of steel, H_c is the heat transfer coefficient between the corium and the lower head, and ε is a correction factor.

4.7. Testing and Validation of the Lower Plenum Model

Two series of tests for the stand-alone lower plenum model have been performed. In one of them the effects of melt composition and delivery rate & duration on the timing and mode of local penetration failure have been investigated. In the other series, the long term lower head heatup and gross failure have been studied for various melt delivery scenarios.

After the molten corium relocates into the lower plenum, the initial lower plenum failure is likely to occur through the tube penetrations. The failure of the penetrations depends on the composition and the temperature of corium. Normally, molten metals are released first, followed by oxidic debris. The molten corium would interact with the drain line first (especially for high delivery rates) since it is located at the bottom of the lower plenum. Then, the interactions with other tubes (IG and CRD tubes) would follow. The penetration failure modes discussed in Section 4.5 have been tested for various conditions of corium delivery into the lower plenum: different material composition (metallic and oxidic) have been used in the individual test cases; the temperature of the incoming corium has been varied; and the order of the material delivery has been changed with the metallic and oxidic corium delivered sequentially into the lower plenum. The effect of system pressure on the penetration failure has also been tested. It has been assumed that the drywell atmosphere is air at 200 °C and the pressure is 1 atm. in all test cases. Table 2 shows the con-

ditions for the various test cases. A total of six cases were run in this series. In all tests, the rate of delivery has been assumed to remain constant during the time of delivery. The predicted timings of the ex-vessel tube failure for all the cases are summarized in Table 3. The results of these tests indicate that the important parameters which affect the ex-vessel tube failure are: the material properties of corium (oxidic or metallic), the superheat of molten corium, the pressure inside the reactor vessel, and the sequence of corium delivery into the lower plenum.

Table 2. Summary of test conditions

	Material delivered	Rate of delivery (Kg/s)	Duration of delivery	Temperature (C)	System Pressure (atm.)
CASE 1	UO_2	200	0 ~ 300 s	2760	1
CASE 2	UO_2	200	0 ~ 300 s	2760	68
CASE 3	SS	100	0 ~ 200 s	1370	1
CASE 4	SS	100	0 ~ 200 s	1570	1
CASE 5	UO_2	200	0 ~ 300 s	2760	1
	SS	100	0 ~ 300 s	1370	
CASE 6	UO_2	200	200 ~ 500 s	2760	1
	SS	100	0 ~ 300 s	1370	

Table 3. Summary of test results

Case No.	Timing of failure (s)		
	Drain line	IG tube inside LP	IG tube outside LP
CASE 1	130	210	440
CASE 2	87	210	370
CASE 3	no failure	no failure	no failure
CASE 4	76	120	no failure
CASE 5	130	120	340
CASE 6	no failure	240	450

When the penetration failure occurs, the long-term lower head heatup will be due to the solidified corium in the lower plenum. Since in this case almost all molten corium has already left the lower plenum, the heatup of lower head will be slow, and the global failure of lower head, if any, will occur long after the penetration failure. If the penetration failure did not occur, the only possible mode of failure would be the global rupture of the lower head. In order to identify the important parameters which affect the gross failure of the lower head, the thermal and mechanical responses of the lower head without penetration failure have been tested for various situations. The test conditions for each case, including different specified parameters such as: corium superheat, corium

flow rate, material composition of corium and system pressure, are summarized in Table 4. In all the cases, it was assumed that the initial mass of water in the lower plenum was 30,000 kg. Also, the decay heat power was assumed to be at 1.5 MW/m^3.

The time of gross failure of the lower head is also shown in Table 4. From the results of these tests, it can be concluded that the gross failure of the lower head can be affected by the system pressure, the corium release rate, the presence of water in the lower plenum, and the history of corium release.

Table 4. Summary of conditions in the testing of lower head failure

	Material Delivered	Rate of Delivery (Kg/s)	Duration of Delivery (s)	Temperature (C)	System Pressure (atm.)	Global Lower Head Failure Time (s)
CASE 1	UO_2	50	0 ~ 1000	2760	68	6360
	SS	0	-	-		
CASE 2	UO_2	50	0 ~ 1000	2960	68	6240
	SS	0	-	-		
CASE 3	UO_2	5	0 ~ 10000	2760	68	9840
	SS	0	-	-		
CASE 4	UO_2	50	0 ~ 1000	2760	1	13980
	SS	0	-	-		
CASE 5	UO_2	0	-	-	68	No failure
	SS	50	0 ~ 1000	1671		
CASE 6	UO_2	50	0 ~ 1000	2760	68	6900
	SS	25	0 ~ 1000	1371		
CASE 7	UO_2	5	1000 ~ 11000	2760	68	14820
	SS	25	0 ~ 1000	1371		

5. MODEL APPLICATION TO SIMULATE SEVERE ACCIDENTS IN BWRs

The models discussed in Sections 3 and 4 have been implemented in the APRIL code and used to simulate a hypothetical station blackout accident in a typical BWR. The definition of 'station blackout' includes both the loss of offsite power as an initiating event and, subsequently, the loss of emergency AC power. In the analysis, it was assumed that the station blackout is due to equipment failures at the emergency buses or 115 kV supplies, and the situation is not recoverable. Similarly, the emergency diesels are not available. Thus, all coolant injection systems fail to supply emergency cooling to the reactor core. In order to delay the core heatup, the automatic depressurization system (ADS) was manually activated at 5000 s into the accident.

The station blackout accident causes a loss of feed water to the RPV, and the reactor system pressure to rise rapidly to the safety relief valves (SRV) setpoint. The SRVs open in response to high

vessel pressure. Since no emergency core cooling system (ECCS) water was injected, the water level in the core begins to decrease due to decay heat. When the core is partially uncovered, the ADS is activated (at 4000 s as shown in Fig. 17). This action results in flashing of water in RPV, and provides temporary cooling of the uncovered region of the core. After the RPV depressurization, the water level drops below the lower core plate. The change in the water level is shown in Figure 18. Thereafter, the core becomes completely uncovered and is heated up by the combined decay heat and the heat from the oxidation reactions. Figure 19 shows the temperature of fuel rods in the central zone of the core.

A continuous heating of the core results in melting of in-core structures, such as control blades, channel boxes, cladding and, finally, fuel pellets. As core melting is in progress, the molten materials released from the degraded core eventually reach the lower core plate. The predicted timing of the first arrival of the melt at the core plate is about 6,420 s (114 min). A continuous relocation of the melt to the core plate will cause heatup and, possibly, failure of the core plate. The predicted timing of the lower core plate failure is 7,460 s (126 min).

Following the failure of the lower core plate, the molten materials relocate into the lower plenum. Figure 20 shows the amount of corium released into the lower plenum. As can be seen, at the time of the lower core plate failure, molten steel was the first material relocated into the lower plenum.

As molten fuel (UO_2) relocates into the lower plenum, the heatup of the lower plenum structures is accelerated. The IG tubes inside the lower plenum are predicted to fail at 13020 s (217 min). At 13295 s. (221.5 min) the CRD tubes inside the vessel also started to fail. This was followed by the failure of the ex-vessel portion of the IG tubes tube at 13835 s (230.5 min). Then, the molten corium and the water are released into the primary containment. Figure 21 shows the amount of corium released on the drywell floor.

Even after the penetration failure, the structures in the lower plenum continue to be heated by the solidified corium. Fig. 22 shows nodal temperatures of the lower head.

6. CONCLUSIONS

Several new models of severe accident thermal-hydraulics have been presented. These models have been extensively tested and validated. The results shown in this paper demonstrate the consistency of both the physical modeling assumptions and numerical methods used in the analysis. The above conclusions have also been confirmed by applying the new models, after their implementation into the APRIL.MOD3X code, to simulate a station blackout accident in a typical BWR/4 reactor. Moreover, it appears that this code is well suited for BWR accident management.

ACKNOWLEDGEMENTS

The authors wish to acknowledge the financial support given this study by Empire State Electric Energy research Corporation (ESEERCO) and the helpful discussions with Dr. J.M. Burger.

REFERENCES

[1] S.H. Kim et al, "The Development of APRIL.MOD2-A Computer Code for Core Meltdown Accident Analysis of Boiling Water Nuclear Reactors", NUREG/CR-5157, ORNL/Sub/81-9089/3, 1988.

[2] Lahey, R. T. Jr. and M. Z. Podowski, "Degraded BWR core modeling. APRIL.MOD3 severe accident code", ESEERCO report, EP 84-4, 1990.

[3] R.O. Gauntt, "Summary of the ACRR DF-4 BWR Control Blade/Channel Box Experiment", CORA Workshop, KfK, Karlsruhe, FRG, September, 1989.

[4] S. Hagen et al, "Test Results of BWR Experiments, CORA-16 and CORA-17", International CORA Workshop '89, KfK, Karlsruhe, FRG, September, 1989.

[5] S.W. Kim, M.Z. Podowski and R.T. Lahey, Jr., "Numerical Simulation of DF-4 and CORA-16/17 Severe Fueld Damage Experiments Using APRIL.MOD3," Proc. Fifth International Topical Meeting on Reactor Thermal Hydraulics, Salt Lake City, UT, USA, 1992.

[6] L. J. Ott, "Posttest Analysis of the CORA-28 Preoxidized BWR Experiment," Letter Report, ORNL/NRC/LTR-93/26, 1993.

[7] M. Z. Podowski and R. T. Lahey, Jr., "Degraded BWR Core Modeling-Physical Simulation of Selected Components", ESEERCO Report EP 84-4, 1989.

[8] M. N. Ozisik, "Heat Conduction", John Wiley & Sons, Inc. 1980.

[9] M. Epstein, et al, "Transient Freezing of a Flowing Ceramic Fuel in a Steel Channel", Nucl. Sci. Eng., Vol. 61, 310-323, 1976.

[10] R. W. Ostensen, "Fuel Flow and Freezing in the Upper Subassembly Structure Following an LMFBR Disassembly" Trans. ASME, 18, 1974.

[11] J. L. Rempe, et al, "Lighter Water Reactor Lower Head Failure Analysis", NUREG/CR-5642, EGG-2618, 1992.

[12] F. R. Larson and J. Miller, "A Time-Temperature Relationship for Rupture and Creep Stresses", Trans. ASME, 765, July 1952.

[13] L. A. Stickler, et al., "Calculations to Estimate the Margin to Failure in the TMI-2 Vessel", NUREG/CR-6196, TMI V(93)EG01, EGG-2733, 1994.

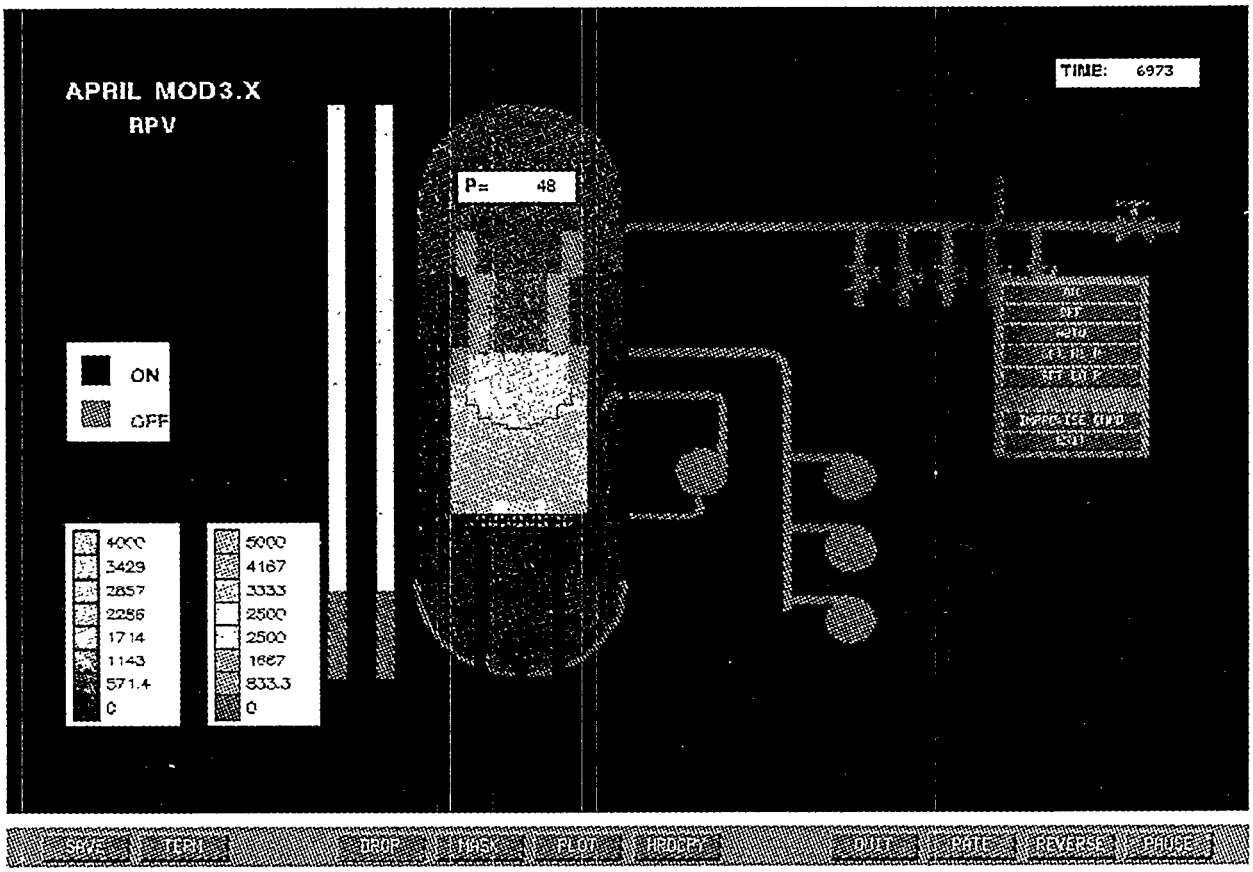


Figure 1 The initial screen of the APRIL.MOD3X Graphical User Interface

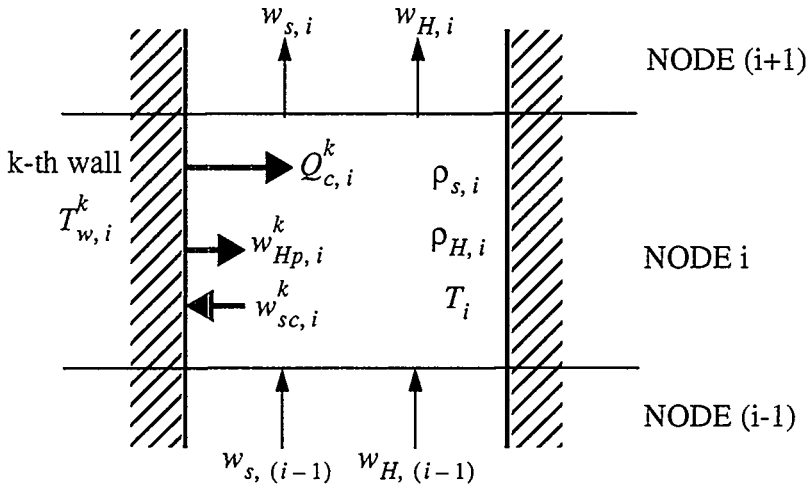
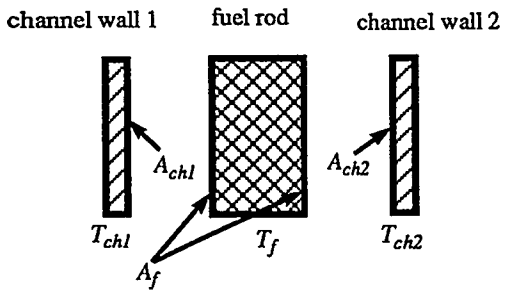
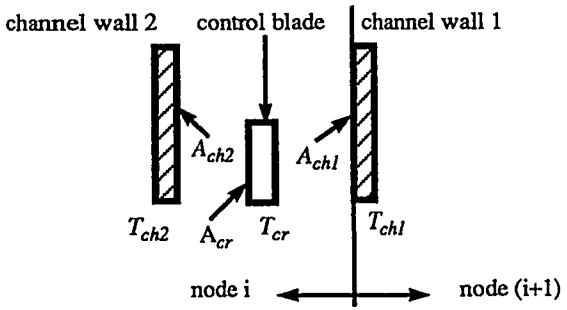


Figure 2 Schematic of the thermal-hydraulic model in the uncovered region of the core



(a) Fuel rod and channel walls in the main channel



(b) Control blade and channel wall in the bypass channel

Figure 3 Nodal configuration of core structures in APRIL

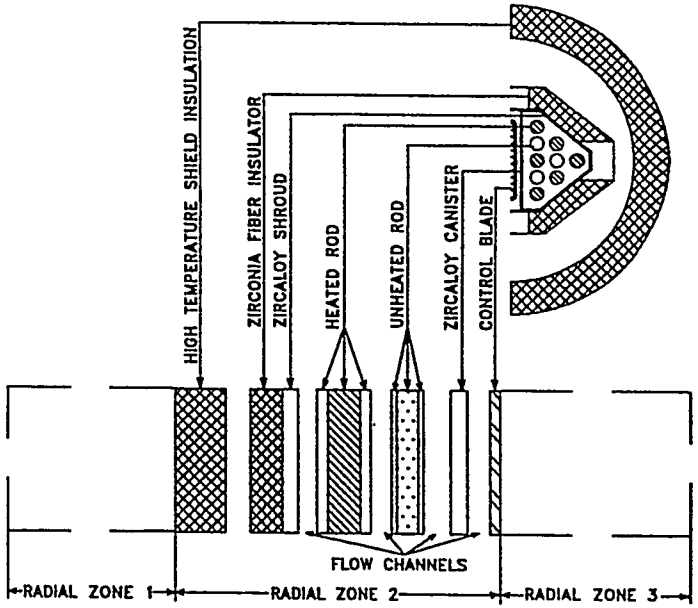
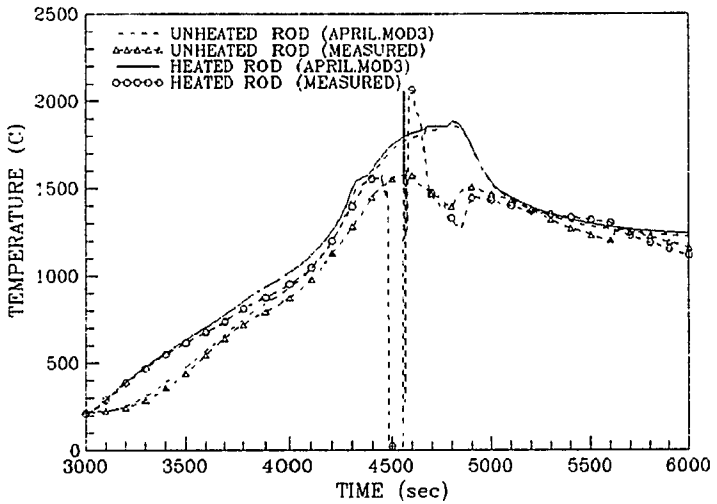
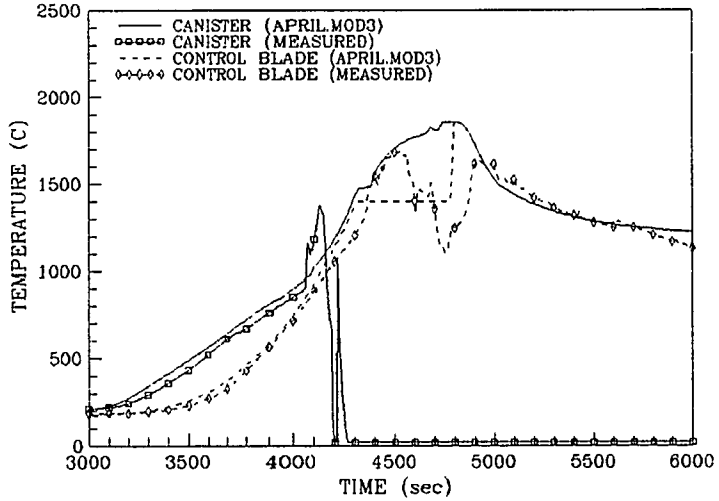


Figure 4 The configuration of the CORA test section and its representation used in APRIL based simulations.

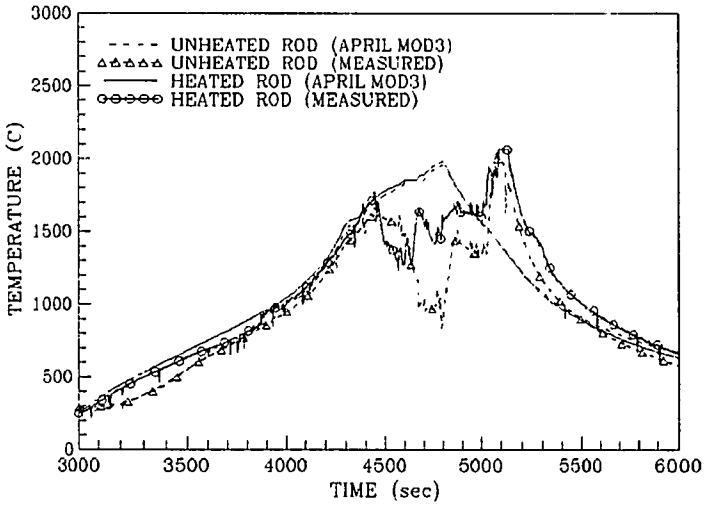


(a) Heated and Unheated rod

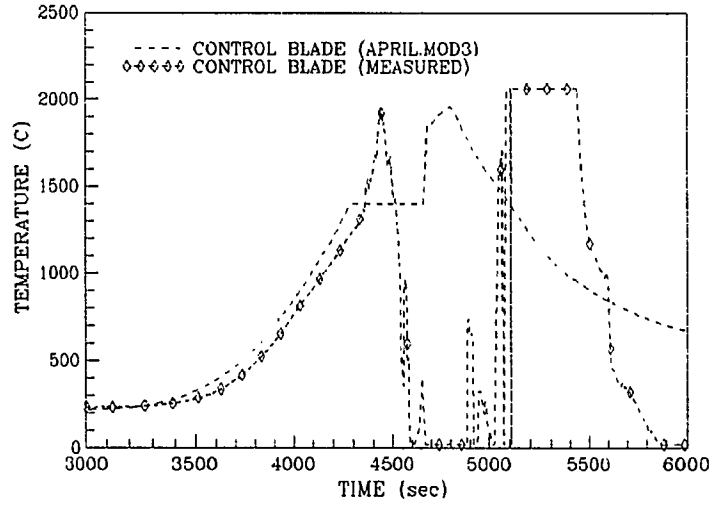


(b) Control Blade and Canister

Figure 5 Comparison of the measured and predicted structural temperatures at 950 mm plane in CORA-16

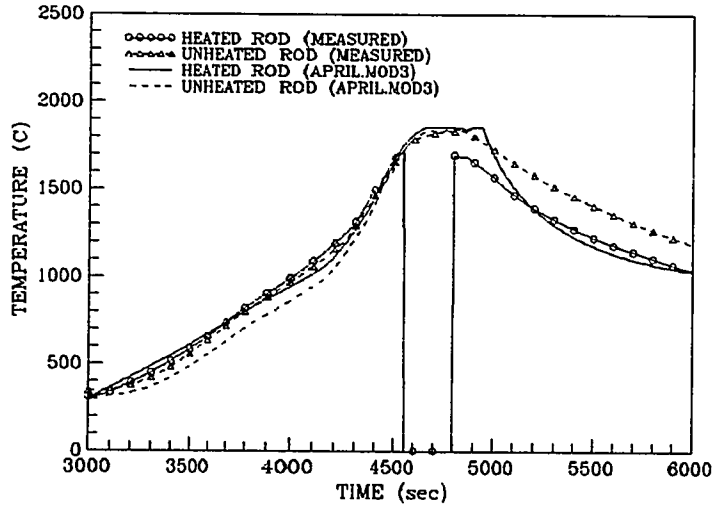


(a) Heated and Unheated rod

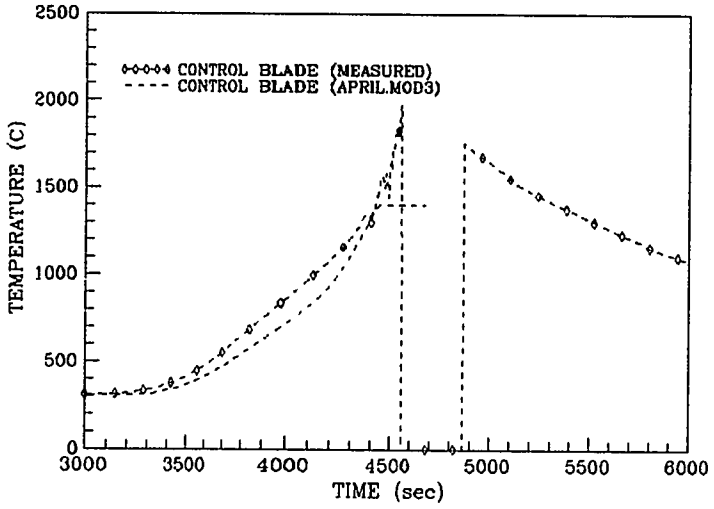


(b) Control blade

Figure 6 Comparison of the measured and predicted structural temperatures at 950 mm plane in CORA-17

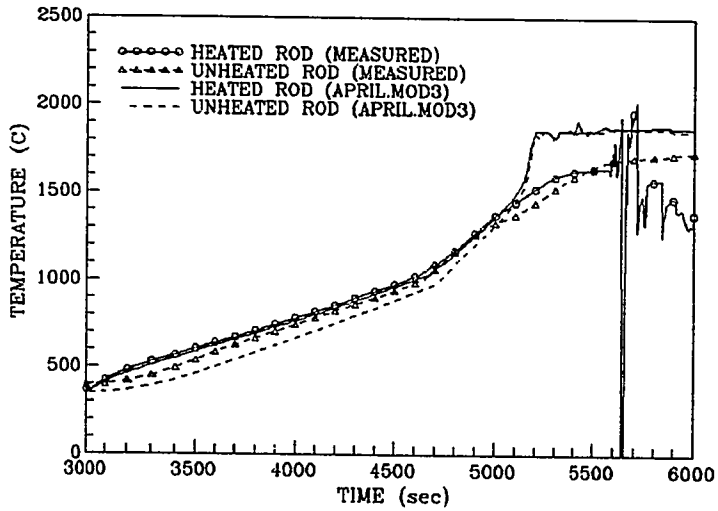


(a) Heated and Unheated rod

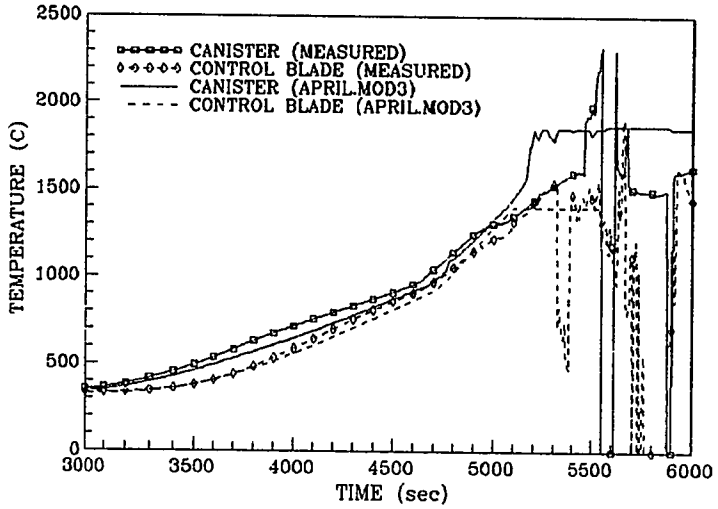


(b) Control blade

Figure 7 Comparison of the measured and predicted structural temperatures at 950 mm plane in CORA-28



(a) Heated and Unheated rod



(b) Control blade and canister

Figure 8 Comparison of the measured and predicted structural temperatures at 950 mm plane in CORA-31

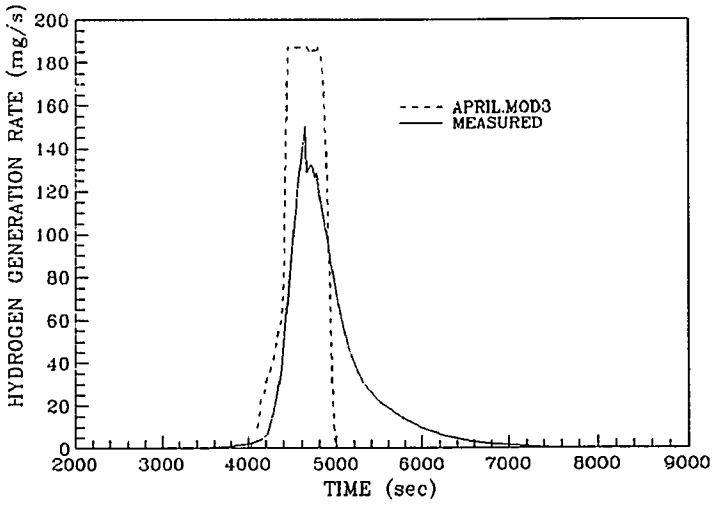


Figure 9 Hydrogen generation rate in CORA-28

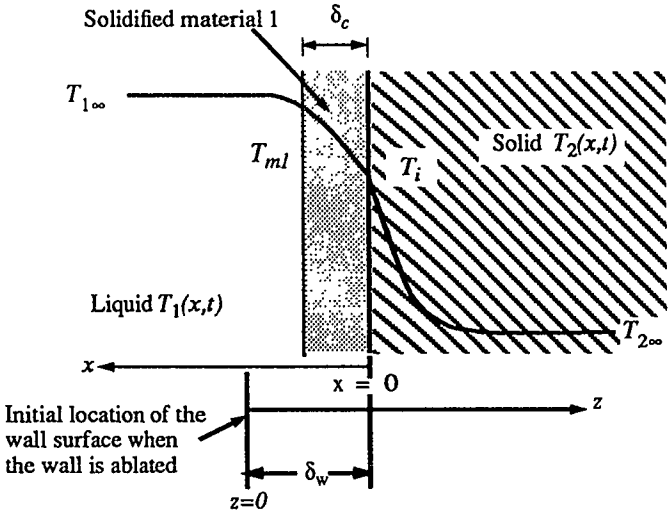


Figure 10 Interaction between molten corium and solid wall

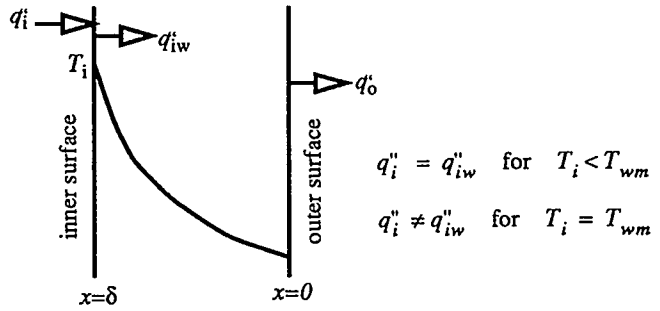


Figure 11 Temperature profile across the wall

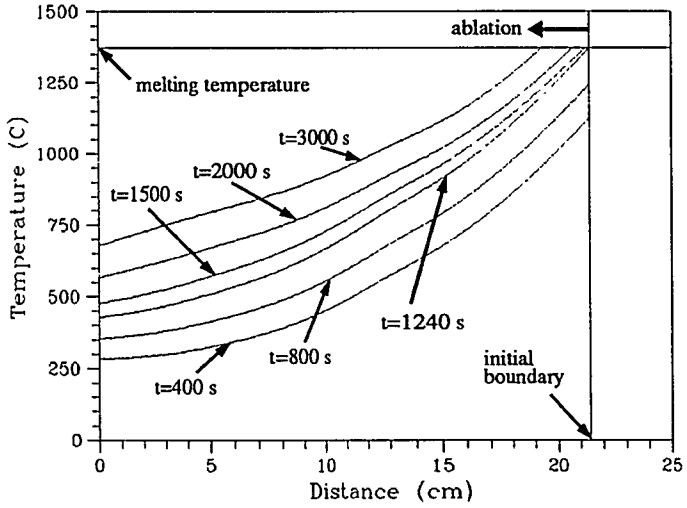


Figure 12 Test results of the wall ablation model

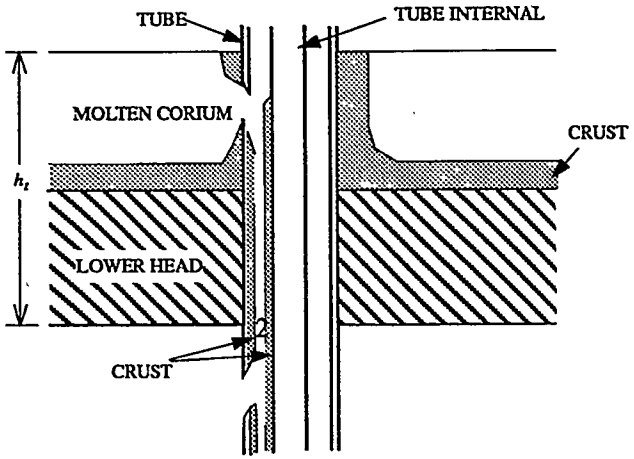


Figure 13 Illustration of ex-vessel tube failure

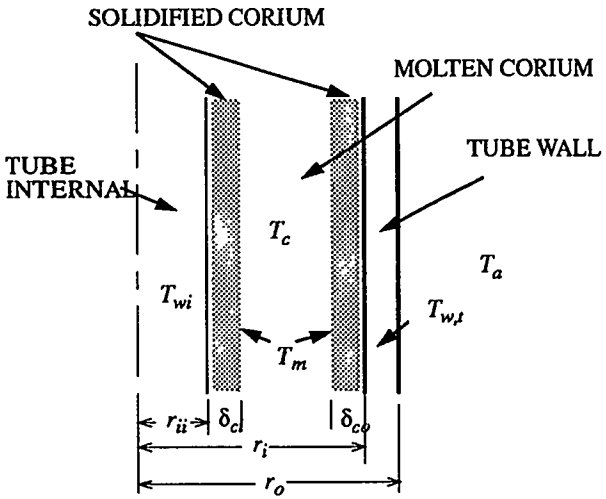


Figure 15 Interaction between the corium and ex-vessel tube

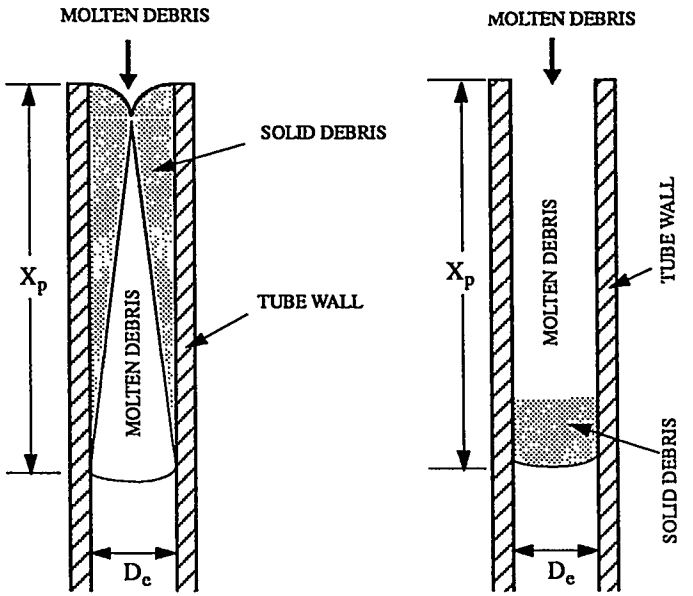


Figure 14 Illustration of the models for the evaluation of the melt penetration distance

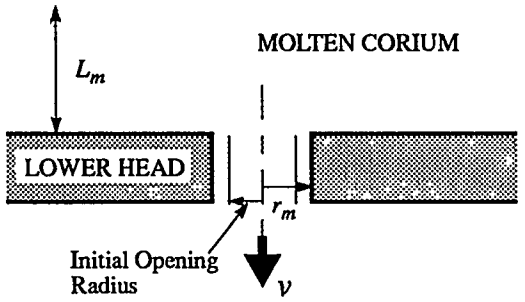


Figure 16 Schematic of corium discharge with wall ablation

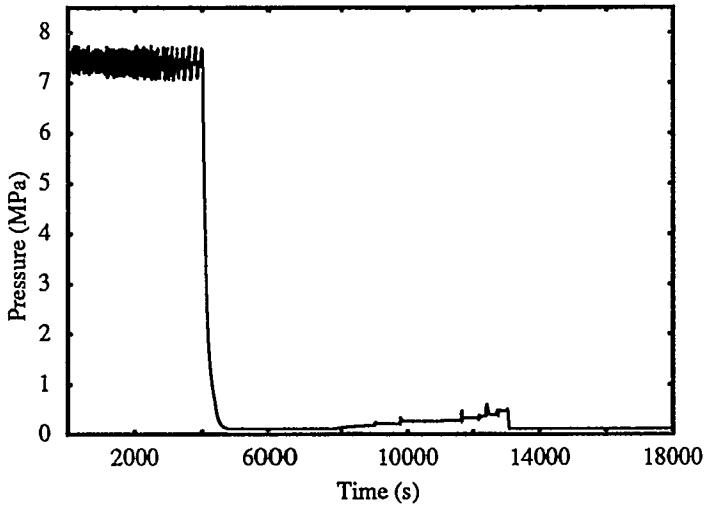


Figure 17 Predicted RPV pressure

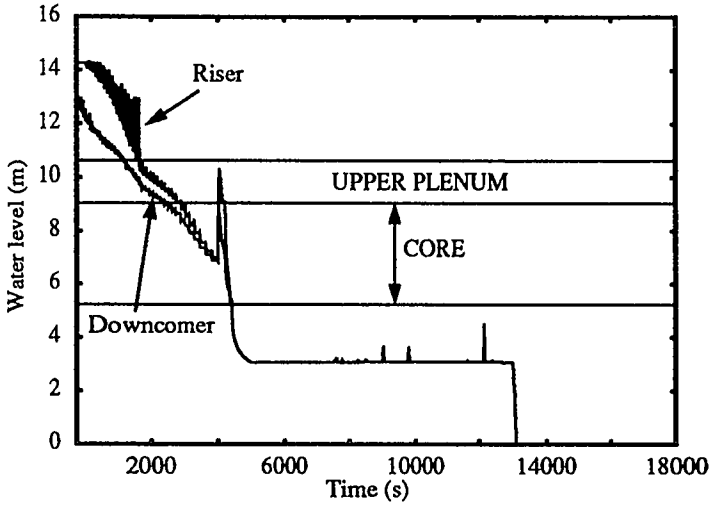


Figure 18 Predicted water level inside the RPV (referenced to the vessel bottom)

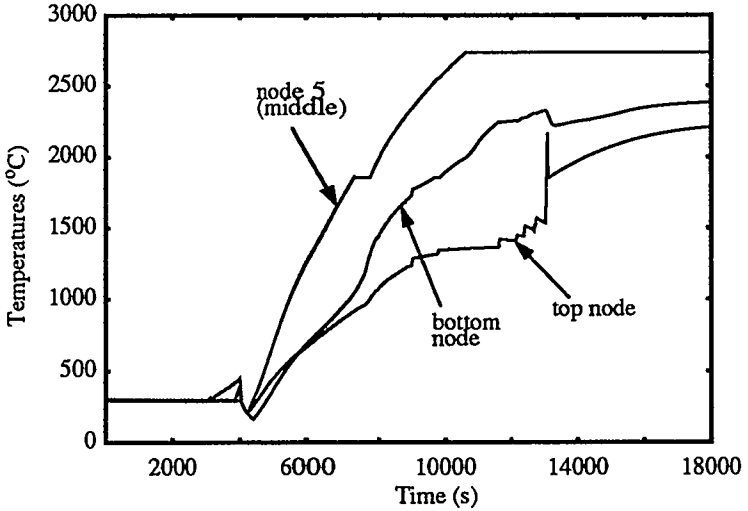


Figure 19 Temperatures of fuel rods in the central radial zone of the core.

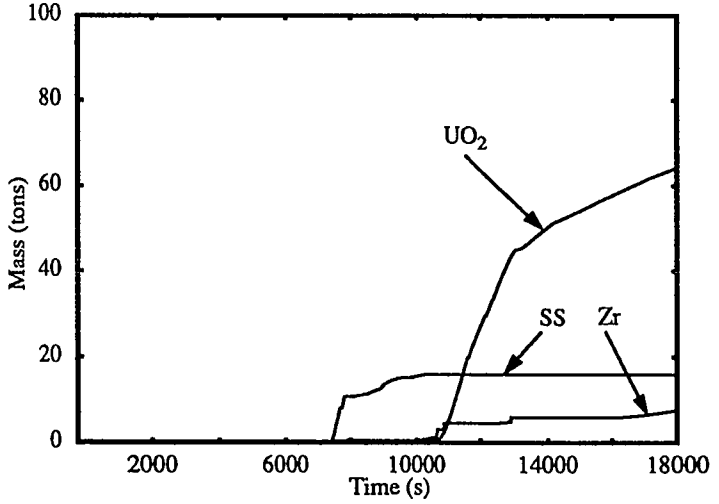


Figure 20 Mass of corium released into the lower plenum

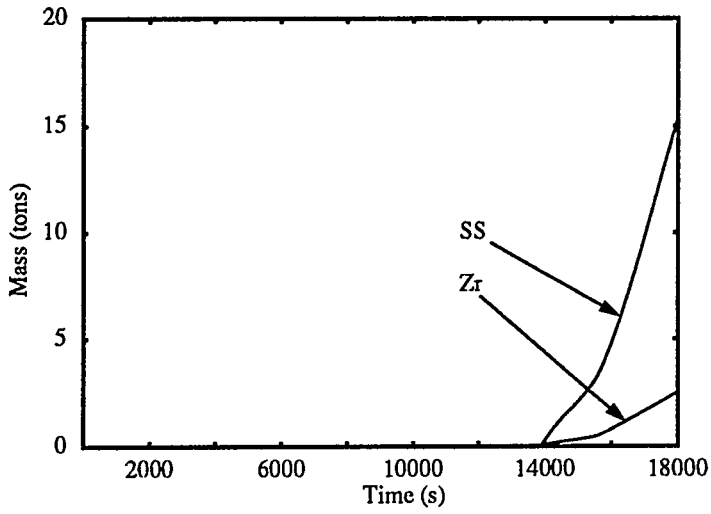


Figure 21 Mass of corium released from the lower plenum

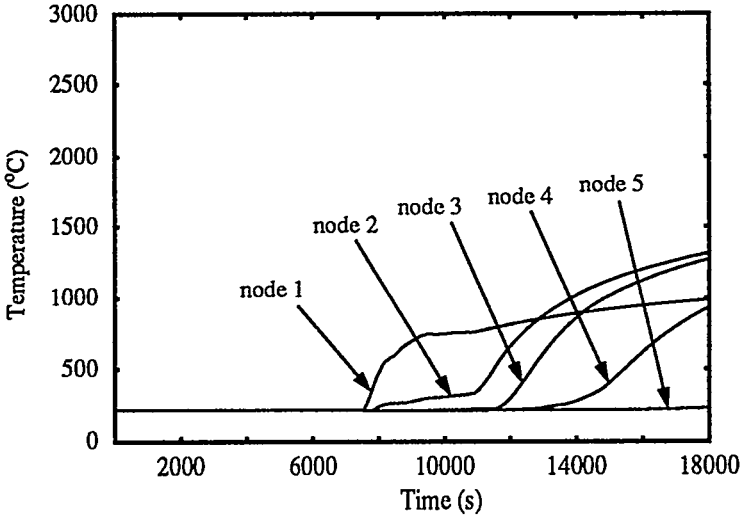


Figure 22 Vessel wall temperatures in the lower plenum

CODE PACKAGE "SVECHA": Modeling of Core Degradation Phenomena at Severe Accidents

M.S.Veshchunov, A.E.Kisselev, A.V.Palagin, A.V.Lemekha,
A.M.Volchek, N.V.Yamshchikov, A.V.Boldyrev, A.I.Deryugin,
Nuclear Safety Institute, Russian Academy of Sciences, Moscow.

Abstract

The code package SVECHA for the modeling of in-vessel core degradation (CD) phenomena in severe accidents is being developed in the Nuclear Safety Institute, Russian Academy of Sciences (NSI RAS). The code package presents a detailed mechanistic description of the phenomenology of severe accidents in a reactor core. The modules of the package were developed and validated on separate effect test data. These modules were then successfully implemented in the ICARE2 code and validated against a wide range of integral tests. Validation results have shown good agreement with separate effect tests data and with the integral tests CORA-W1/W2, CORA-13, PHEBUS-B9+.

1. Introduction

The code package SVECHA for the modeling of in-vessel core degradation (CD) phenomena in severe accidents is being developed in the Nuclear Safety Institute, Russian Academy of Sciences (NSI RAS). The code package SVECHA presents a new detailed mechanistic description of the phenomenology of severe accidents at nuclear power plants.

A recent OECD/CSNI state-of-the-art report (SOAR) [1] on in-vessel core degradation (status 1991) concluded that although the experimental data base and models are adequate in some areas, there are still substantial gaps. This was confirmed by the results of two recent OECD International Standard Problems: ISP 28 (PHEBUS B9+ test) and ISP 31 (CORA-13 test). Model inadequacies are quite common for the majority of existing codes and these inadequacies have been formulated for the SCDAP/RELAP5 code in the Independent Peer Review [2] and can be summarized as follows:

1) Mechanistic models are not included to account for effects of internal pressure, effects of oxidation in strengthening the cladding, effects of oxide cracks in oxidation kinetics, description of oxide-shell failure and mechanistic description of breach formation;

2) The Zr-U-O mixture relocation is based on a gravity driven mixture, slug-ring flow. Rivulet, rather than slug flow has been established experimentally;

3) The possibility of melt running down the inside of the balloon rather than forming a crust on the outer surface ("gap candling") is not considered;

4) There is no proper coupling between the models for the reactions between Zry/steam (outside of the cladding) and UO2/Zry (inside);

5) Additional Zr oxidation during Zr-U-O relocation is not modeled;

6) The current models for control rods and spacer grids material interactions are absent or oversimplified.

To avoid these discrepancies a more physically grounded approach for the description of CD phenomena is being developed in NSI RAS. The main features of this approach can be characterized as follows:

1) development of detailed physical theory of key processes for the analysis of experimental data;

2) investigation of qualitatively new physical phenomena occurring in accident conditions on the basis of the developed theory;

3) recommendations for arrangement of additional experiments (or examinations of existing samples) aimed at revealing of required details or data collections;

4) development of code modules on the basis of physically grounded simplifications of the theoretical models;

5) development of new mathematical methods which allow the implementation of these more sophisticated physical models in the codes;

6) verification of the modules against separate-effect tests;

7) implementation of the new modules in different integral codes;

8) benchmarking and sensitivity calculations against integral experiments and comparison with other code systems; analysis of the test results and improvement of the models and codes.

Such an approach increases the predictive power of the qualitative analysis of the complex system behavior and reduces the ambiguity gap in the quantitative results.

The following models are currently under investigation:

1. Fuel - Cladding Oxidation.
2. Dissolution of UO_2 by Molten Zircaloy.
3. Fuel - Cladding Deformation.
4. Relocation of Molten Materials (Candling).
5. Eutectic Interactions and Liquid Phase Formation.

On the basis of these models FORTRAN modules, ready for implementation in different CD codes, are being developed. Currently some of the developed modules have been implemented into ICARE2 code (France) [12] and have demonstrated satisfactory description of integral Severe Fuel Damage (SFD) tests. Implementation of the modules into the codes ATHLET (Germany) and SCDAP (USA) has been started recently

2. Fuel-Cladding Oxidation

The progress of a severe accident is strongly influenced by the Zr/steam and Zr/fuel reactions. The former produces significant additional heat and hydrogen. The temperature of the core may as result rise sufficiently for the remaining unoxidized Zr to melt. This liquefied cladding can dissolve a substantial quantity of UO_2 fuel, forming an eutectic, which may then relocate downwards.

Two different approaches for modeling of pellet-cladding oxidation were used previously

(i) simulation of the oxidation processes by the parabolic law for growth of different layers width;

(ii) physical modeling, using diffusion equations of oxygen in different layers and mass balance conditions on the interface boundaries.

An advantage of the first approach is its simplicity and quick calculation. However, it works well in the simplified isothermal conditions, and is valid for unlimited steam supply and a semi-infinite Zr substrate. Problems of physical consistency arise if the approach is used directly to model complete oxidation of finite-thickness fuel clad and under possible steam-starved conditions. Calculations demonstrate that in the transient temperature regime this approach fails.

The second approach (realized, for example in code PECLOX [3]) is more physically grounded and provides better agreement with experiment.

A serious disadvantage of this second approach is that numerical realization requires large computation time and memory consumption.

Physical model. The proposed model is free from the disadvantages of these two approaches. This model is based on the solution of the oxygen diffusion equation in the multilayered structure (7 and more layers) of different phases formed in the course of the UO_2/Zr/steam interactions. PDE describing real diffusion processes are reduced to ODE (this mathematical procedure is physically well grounded). The proposed model is accurate and simple, taking into account the following physical phenomena occurring in the course of UO_2/Zr/steam interactions and not accounted in the framework of the correlation approach:

- coupling of Zr/steam (outside) and Zr/UO_2 (inside) interactions;
- cladding internal oxidation;
- "chemical thinning" (or even complete disappearance) of the oxide layer in the conditions of limiting steam supply ("starvation");
- tetragonal-to-cubic phase transition in ZrO_2 at transient temperature regimes;
- formation of liquid metallic fractions due to the interaction of UO_2 with Zr(solid);
- oxidation of Zr-U-O mixture during relocation.

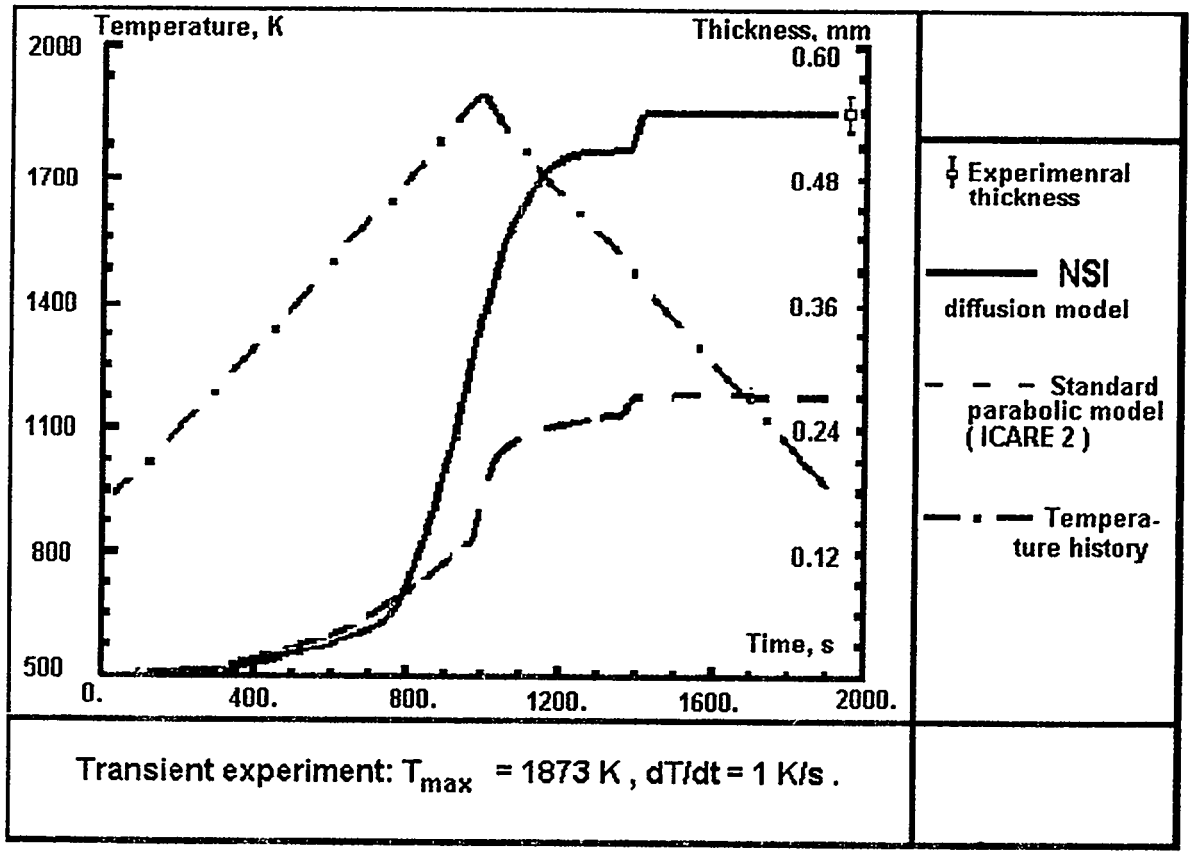


Figure 1. Comparison of the results of calculations by the developed diffusion model and standard parabolic model (Urbanic-Heidrick correlation) with experimental data for transient regime (Hofmann's experiment [3]).

Numerical module. On the basis of this model a FORTRAN module was developed [4]. The proposed mathematical procedure leads to a great simplification of calculations,

which become comparable (in computation time and memory consumption) with the empirical correlation approach. The accuracy of these calculations is high and comparable with the more sophisticated and time consuming methods (i.e. PECLOX code).

Data base formation. The P.Hofmann's, Urbanic-Heidrick and Olander experiments for isothermal and transient temperature conditions were used to complete the database for the module.

The simplicity, relatively high degree of accuracy and fast running speed of the developed module allows its implementation it in different code systems. The module has been implemented into the ICARE2 computer code (named UZRO in the code) and validated against the integral SFD tests CORA-13, CORA-W1,W2 and PHEBUS B9+. Currently, implementation of the module into codes ATHLET (GRS) and SCDAP (NRC USA) is in development.

In Fig.1 the results of calculations with the diffusion model and a standard parabolic model (Urbanic-Heidrick correlation) are compared with experimental data for the transient regime (Hofmann [3]).

3. Dissolution of UO_2 by Molten Zircaloy

Dissolution of UO_2 by molten Zircaloy is an important chemical process influencing many physico-chemical processes during core melt progression in severe accidents. When Zircaloy cladding starts to melt at about 1760°C, the interaction between solid UO_2 and molten Zr becomes more active and leads to a partial dissolution of fuel in the liquid phase. Therefore, liquefaction and relocation of UO_2 must be assumed about 1000°C below the melting point of the fuel (2850°C). This limits the possibility of stopping the high-temperature transient before an uncontrolled core meltdown occurs and has a strong impact on fission product release.

A theoretical study of this complicated phenomena has been carried out. It has been demonstrated that, depending on dimensions of the molten cladding, two different mass transfer mechanisms through the liquid phase can take place. Correspondingly, two different models for the dissolution process are proposed: diffusion and convection.

Diffusion model. The diffusion model describes dissolution kinetics on the basis of diffusion mass transfer equations in the phases that account for an appearance and growth of a two-phase (solid and liquid) region at the boundary between the solid UO_2 and liquid (Zr,U,O) phases. It is shown analytically [5] that diffusion mass transfer through this two-phase region can be described by an effective (temperature-dependent) diffusion coefficient. Its value, estimated from measurements, is several orders of magnitude smaller than the corresponding value in a pure liquid phase and, thus, determines the rate of dissolution process.

Convection model. The theoretical convection model [6], developed in cooperation with P.Hofmann (KfK, Germany), describes dissolution kinetics on the basis of a convective mass transfer equation in the liquid phase and a diffusion equation in the solid UO_2.

The results of different experiments (P.Hofmann, D.Olander, P.Hayward), performed in conditions of convective mixing of molten Zircaloy inside UO_2 crucibles, are rather controversial and do not allow an unambiguous choice of an empirical kinetic correlation which could be used in numerical simulations. The proposed convective model resolves the apparent discrepancy between the empirical results of different groups and provides practical recommendations for application of measured

correlations for fuel rods, resulting in a certain renormalization (by a factor 2.5 for Hofmann's correlation) of UO_2 dissolution rates, measured in crucibles.

The model self consistently describes both stages of the dissolution process, observed experimentally: incubation, or saturation (exponential rate), and post-incubation, or precipitation (parabolic rate). It shows that a rather quick saturation of the liquid phase due to UO_2 dissolution is reached at the first (incubation) stage, and after that, a more slow dissolution process, accompanied by precipitation of ceramic phase and described by parabolic time law takes place. It resolves the discrepancy of existing codes, in which Hofmann's or Olander's parabolic correlations are used for the description of the incubation stage, at which saturation is reached, instead of the post-incubation stage which should be described by a renormalized parabolic correlation.

Currently a general model for simultaneous dissolution of UO_2 and ZrO_2 by molten Zr in an oxidizing atmosphere is in development.

Numerical module. A FORTRAN module has been developed on the basis of the diffusion model. It is coupled with the Fuel-Cladding Oxidation module and describes simultaneous dissolution of UO_2 pellets and the ZrO_2 layer, which is competitive with the Zr oxidation process.

A FORTRAN module, where convective movement in the liquid will be taken into account, is currently in development.

Benchmarking calculations for the diffusion model were performed against D.Olander's measurements in special conditions (provided diffusion mass transfer through the liquid phase: experiment with UO_2 disk). These calculations have demonstrated satisfactory agreement with the experimental data.

The developed diffusion module is implemented in ICARE2 code and validation studies against integral tests are in development.

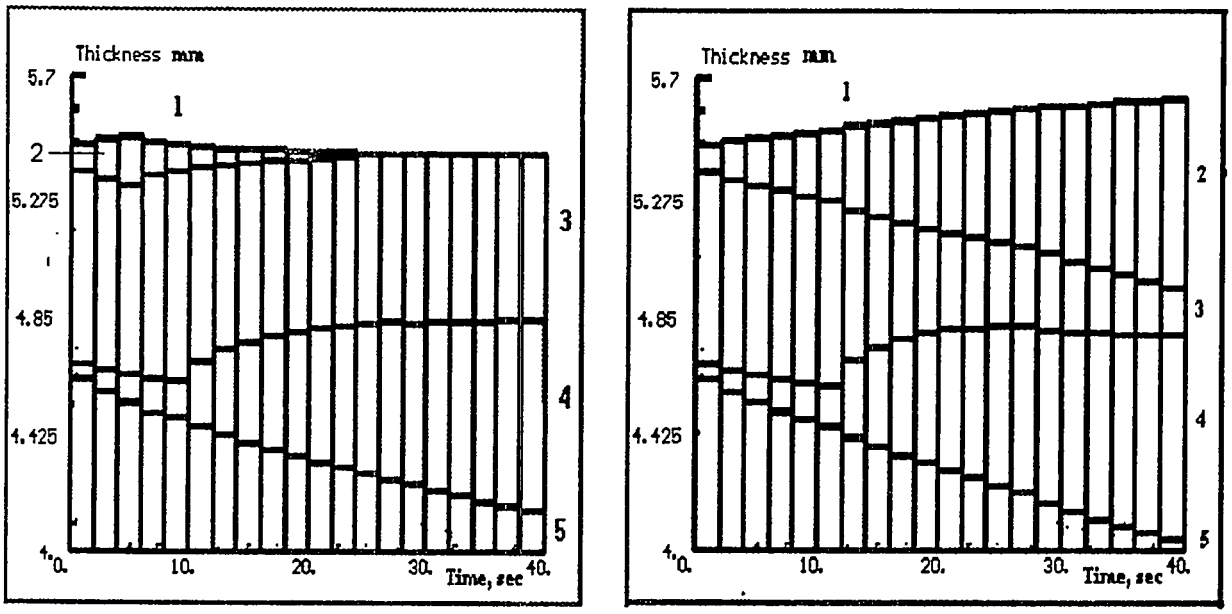


Figure 2. Results of calculations by the developed diffusion model of simultaneous dissolution of UO_2 (5) and ZrO_2 (2) by molten Zr (3) under the conditions of time-limited external oxygen (1) supply (left side - oxigen available for 8 s, right side - oxigen available for 100 s), accompanied by the growth of the two-phase region (4).

Fig.2 gives the temporal evolution of layers at T=2600 K for the case where two reactions of oxidation and dissolution goes simultaneously.

In the right picture (b) external oxygen supply from the cladding surface was unlimited during 100 seconds, in the left one (a)- only during 8 seconds. In the left picture the protected zirconia layer is totally dissolved after 20 seconds.

4. Fuel - Cladding Deformation.

The basic parameters controlling deformation and rupture of fuel rods are stress, strength and temperature. Clad ballooning occurs when tensile hoop strain induced by the pressure difference across the clad thickness exceeds the ultimate value. The fuel rod behavior in a temperature transient is strongly influenced by the spatial temperature distribution of the fuel element.

Once liquid U-Zr-O eutectic has formed, it is assumed to be held in place by the oxide crust until this crust fails. The position and timing of the oxide layer breach will depend on the thickness and mechanical properties of this layer together with the stress acting upon it. The existing rupture criterion: $T > T_{max}$, $\sigma > \sigma_{max}$, is very rough and depends significantly on the choice of the critical temperature. This assumption is most influential in terms of the peak temperatures attained and the extent of fuel dissolution and relocation.

Physical model. The model for the analysis of mechanical behavior of cladding [7] describes a deformation of a multilayer structure (α-Zr, β-Zr, α-Zr + β-Zr, ZrO_2) with an account of the dependence of physico-mechanical properties of cladding material on temperature, oxygen concentration, deformation rate and cracking of the ZrO_2 layer. The main considered factors which influence the deformation of cladding in the model are: internal and external pressure, the pressure due to expansion and extrusion of the liquefied eutectic into the fuel cavity, relative change of material volume due to the oxidation, and temperature. The model is based on the consideration of mutual viscoelastic deformation of different layers with an account of three-dimensional stress-strain state of each phase and influence of oxygen concentration on the creep rate of α-Zr. The ZrO_2 layer is proposed to be deformed elastically till the moment of failure. The maximal stresses due to a circumferential temperature distribution in the oxide layer are analyzed for the description of failure and breach formation by "flowering" mechanism.

The proposed model describes the:

- change of fuel cladding geometry and collapse of a gap between fuel and cladding;
- effects of oxidation in strengthening the cladding and reducing the strength due to cracking of oxide;
- effects of oxide cracks on the oxidation kinetics,
- the prediction of internal pressure drop due to the burst (ballooning) of the cladding;
- the prediction of oxide-shell failure due to "flowering", caused by a circumferential temperature gradient, and the beginning of U-Zr-O mixture relocation.

Numerical module. On the basis of this physical model, a computer program, in FORTRAN, was developed. This program is coupled with the Fuel-Cladding Oxidation module which allows the incorporation of the influence of cladding geometry change and oxide layer cracking on oxidation kinetics.

A number of verification tests were performed on the basis of S.Sagat's et al. (Chalk River Nuclear Laboratories, Canada), S.Leistikov's et al. (KfK, Germany) and REBEKA experiments (for isothermal and transient temperature conditions with oxidizing and inert environments). On Fig.3 the results of benchmarking calculations against the experiments of Sagat [8] are presented. There is reasonable agreement between the modeling of the phenomena and the experimental data.

The module was implemented in the ICARE2 computer code (named CROX in the code) and validated against the integral SFD tests CORA-13 and PHEBUS B9+.

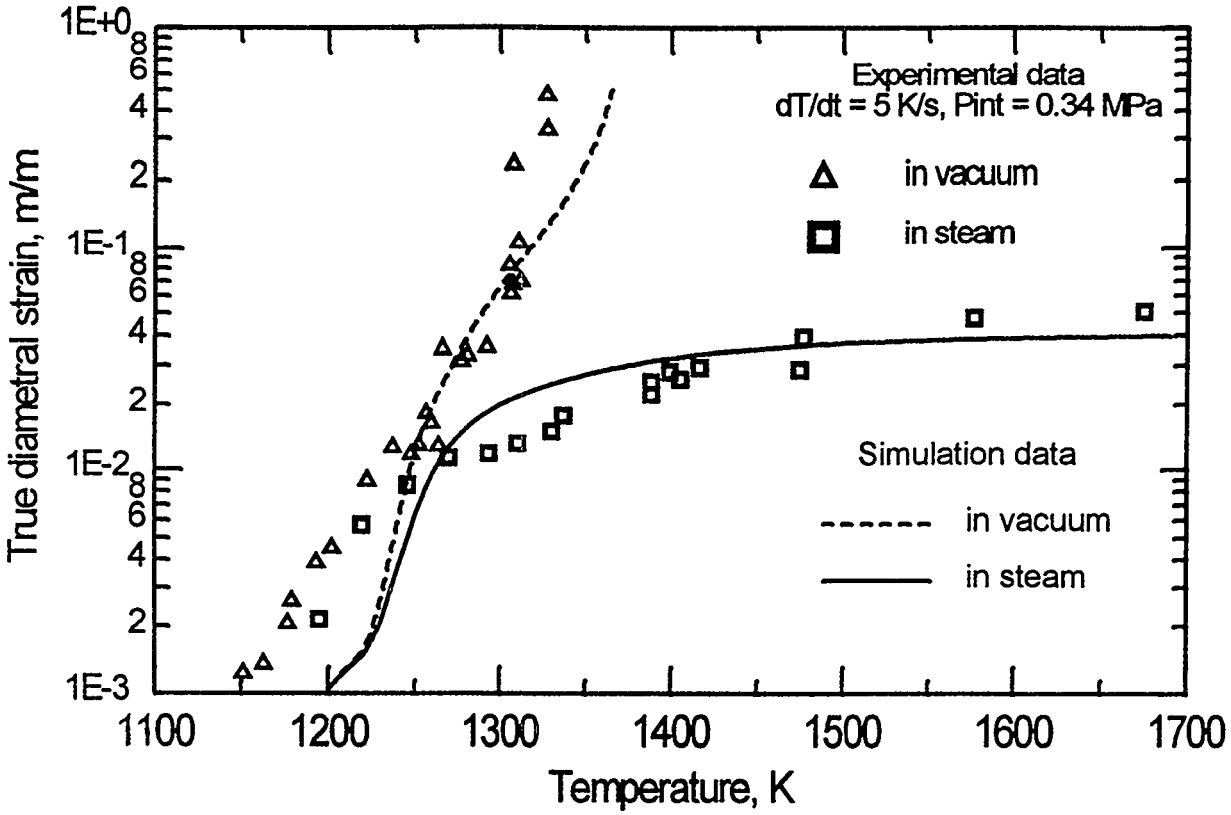


Figure 3. The simulation results of Sagat's experiments [8] performed by the developed fuel-cladding deformation module demonstrating the effect of oxidation in strengthening of the cladding. The diametral strains of Zircaloy-4 fuel cladding (15.25 mm in diameter, 0.45 mm wall thickness) under overpressure of 0.34 MPa and heat rate of 5K/s in steam and vacuum are plotted.

5. Relocation of Molten Materials (Candling)

Once the clad oxide is breached, the process of relocation of materials (downward flow of ceramic melts and liquefied eutectic mixtures) begins. As the mixture flows, it will affect the heat transfer, possibly causing the formation of a frozen track. The influence of this process upon the global core behavior during the accident is conditioned by the fact that it results in a change of flow cross sections or a blockage of the cooling channels, further fuel rod heatup and extended core degradation.

In existing codes the description of the candling process is usually based on the assumption of a one-dimensional axysimmetrical flowing film. This assumption clearly has an important influence on the flow of the mixture and heat transfer to the clad. It can lead to incorrect determination of blockage formation.

Physical model. The model [9, 10] is based on the system of differential equations obtained by the integration of the hydrodynamic equations over the volume of the moving liquid element, taking into account boundary conditions on the liquid-solid and liquid-gas interfaces.

The model allows to take into account:

- capillary effects (contact angle hysteresis, contact line resistance to displacement, wetting of the fuel rod surface) and the introduction capillary scale;

- viscous effects (viscous drag force, laminar/turbulent regimes);
- heat exchange influence (melting/solidification process, temperature dependence of viscosity, surface tension, etc.).

The model also allows the description of:
- various types of flow (drops, rivulets of different length, films);
- transient processes (drop-rivulet transitions, liquid element disintegration due to viscous-gravitational interaction);
- nonstationary heat exchange of the liquid mixture with arbitrary temperature distribution along the fuel rod.

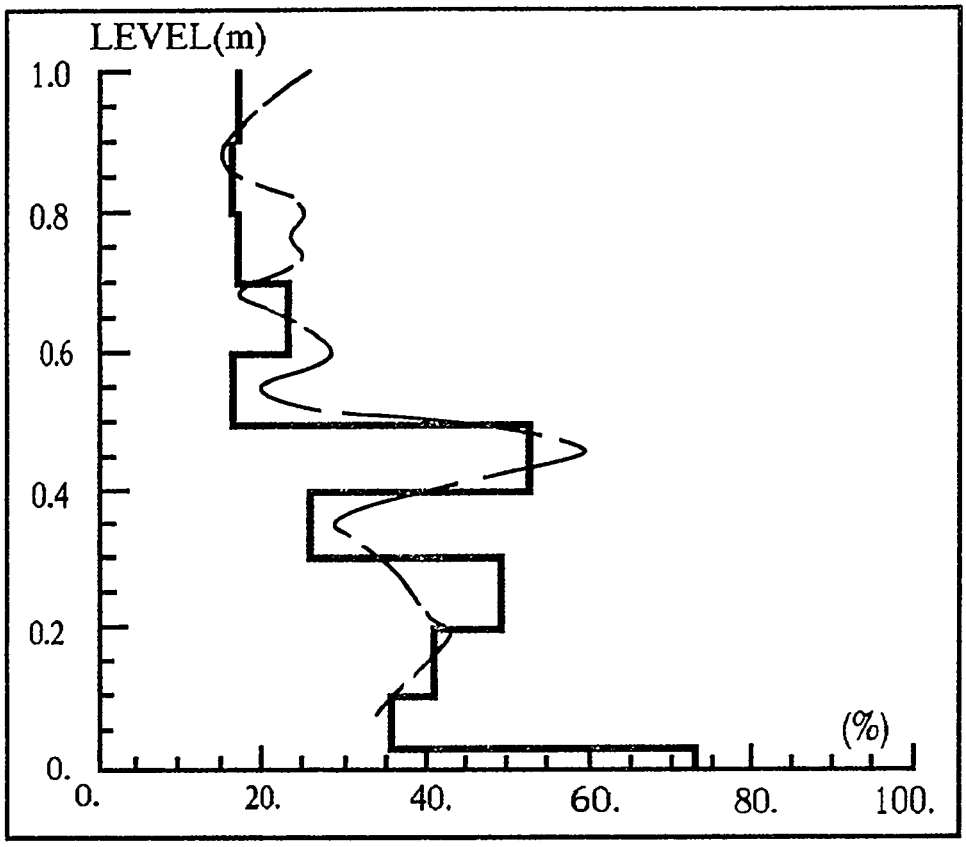


Figure 4. Post-experimental distribution of relative area blockage: dashed line - experimental results (CORA-13), solid line - calculation by ICARE2 code with the developed (NSI) candling model.

The model also describes the gap candling process - flow inside the gap formed by cylindrical structures (cladding/fuel pellet). The latter process is especially important in the case of the gap thickness increase, up to several mm, due to cladding deformation ("ballooning") or extended melting and may affect sufficiently the blockage mass distribution outside the cladding.

The process of the disintegration of the liquid element (drop formation) in accordance with capillary-viscous-gravitational interaction accounting for different regimes of this process (single drop formation, united liquid element flowing, mixed transient disintegration/confluence case) is involved in the model.

Numerical module. On the basis of this physical model, a computer program in FORTRAN was developed. A detailed physical consideration of the process of disintegration of the liquid element allows the determination of the characteristic size of the liquid elements and thus decreases the dependence of the results of the calculations on the nodalization scheme.

The module has been implemented into ICARE2 computer code (two different versions, named DROP and DROG in the code).

A number of verification tests performed on the integral SFD tests CORA-13 [11], CORA-W1/W2, PHEBUS shows good agreement with experimentally measured blockage distributions along the fuel rod (see Fig. 4).

6. Eutectic Interactions and Liquid Phase Formation.

Models for physico-chemical interactions between more important core components: - Zry/stainless steel (SS);

- Zry/(Ag,In,Cd);
- Zry/Inconel;
- Zry/B_4C;
- SS/B_4C;

are currently under investigation.

All of these reaction pairs have relatively low eutectic temperatures and, therefore, their interactions are of concern in a severe accident, since relocation of the resulting fragments or melts and formation of local blockages cause further heatup of the core. Separate-effect tests have been performed in different laboratories (KfK, Germany; JAERI, Japan; KI, Russia) in parallel with the integral out-of-pile and in-pile experiments and serve to explain the complex material interactions in the integral tests and the TMI-2 accident by the resulting multi-phase system at room temperature.

Physical models. New physical models have been developed for the description of interaction kinetics measured in these separate-effect tests. A new approach for theoretical study of diffusion processes in multi-component and multi-phase reaction zones, observed experimentally, has been developed (in cooperation with P.Hofmann, KfK). On the basis of the proposed theory, experimental data obtained by different groups are compared and revised. The models, being based on first-principle equations, are well physically grounded and, thus, can be used for the description of material interactions in complex transient (accident) conditions.

Numerical modules. FORTRAN modules based on the proposed model are currently in development.

7. Results of validation of new models against integral test data.

Validation on PHEBUS-B9+ experimental results. The main objectives of the PHEBUS-B9+ were to investigate the following phenomena occurring during a SFD accident:

- cladding oxidation;
- mechanical behavior of the cladding with ZrO_2 layer of variable thickness containing molten Zr;
- simultaneous dissolution of UO_2 and ZrO_2 by molten Zr;
- relocation of the resulting melts.

Practically all these objectives are the subject for the simulation with the newly developed modules UZRO, CROX, DROP/DROG.

The PHEBUS-SFD facility consists of several main parts:

- governing core which provides nuclear power for test bundle;
- SFD contour for modeling thermal hydraulic conditions in the bundle;
- pressurized water line (Pressure 8 MPa, temperature 528 K) for cooling of a test bundle.

The SFD contour consists of three inlet lines for steam and helium supply, test bundles and outlet line. The test bundle consists of 21 fuel rods placed in a rectangular matrix with a pitch of 12.6 mm. Fuel pellets with the diameter 8.19 mm (enrichment is equal to 2.6 %) are placed in Zircaloy cladding with an inner diameter of 8.36 mm and an outer diameter of 9.56. The total length of the fuel rods is 0.8 m. Two Inconel spacer grids are located at the levels 0.138 and 0.661 m. Rods are placed inside multilayer insulation which consists of Zircaloy pipe with a thickness of 0.6 mm and porous zirconium dioxide. Thermocouples allow the measurement of temperatures for the fuel, cladding, liquid and shroud on different elevations.

Scenario of the experiment can be divided into three phases:

- oxidation phase which was modeled by supply of steam with the rate of 2 g/s which lasted for 8370 s;
- helium phase (flow rate 0.5 g/s) when the temperature of 2750 K was obtained;
- final stage followed by decreasing of input power leading to the cooling of the bundle.

Three power steps allowed rod temperature to reach levels of 1000, 1350, 1600 K at the hottest level. A slower power increase followed and increased temperatures from 1600 K to about 1800 K. A subsequent power step allowed practically complete oxidation in the inner part of the bundle. The second heat up phase was performed in pure helium starting at 8366 s. A pressure of 1.9 MPa was maintained throughout this temperature phase. The fulfillment of five power steps led to a maximum rod temperature of about 2750 K. During the final phase, which began at 13860 s, step reductions in nuclear power enabled a slow cool down which kept the previous bundle geometry unchanged. The pressure was decreased to 0.4 MPa at 14135 s. During this phase the mean helium mass flow rate was 0.5 g/s with an inlet temperature of 528 K. It was maintained up to the end of the test (time of 18000 s).

The results of simulations performed with the ICARE2 code using new versions of developed modules UZRO and DROP are shown in Figures 5 and 6.

In Figure 5 the simulated temperatures are compared with experimentally measured data for the levels of 0.6 m and 0.7 m. A good agreement was observed. The temperature escalation after 8000 sec was correctly predicted as well as temporary temperature evolution. Final bundle state (Fig. 6) shows correct prediction of bundle melting and relocation. As observed in the experiment the cladding was damaged at elevations 0.4-0.48 m and the melt does not relocate below elevation 0.16 m. One can see the liner damage between the levels of 0.48 and 0.64 m. The melted parts of the liner relocated down to the levels 0.08 - 0.0 m.

Validation on CORA-W2/ISP36 experimental results. Experiment CORA-W2 was carried out in the CORA facility with the following main goals:

- analysis of heat up of the core;
- investigation of relocation processes;
- comparison of the experimental results with the code predictions.

The following physical processes were studied during the experiment:

- temperature behavior of fuel and control rods;
- oxidation of cladding and hydrogen generation;
- melting of spacer grids;

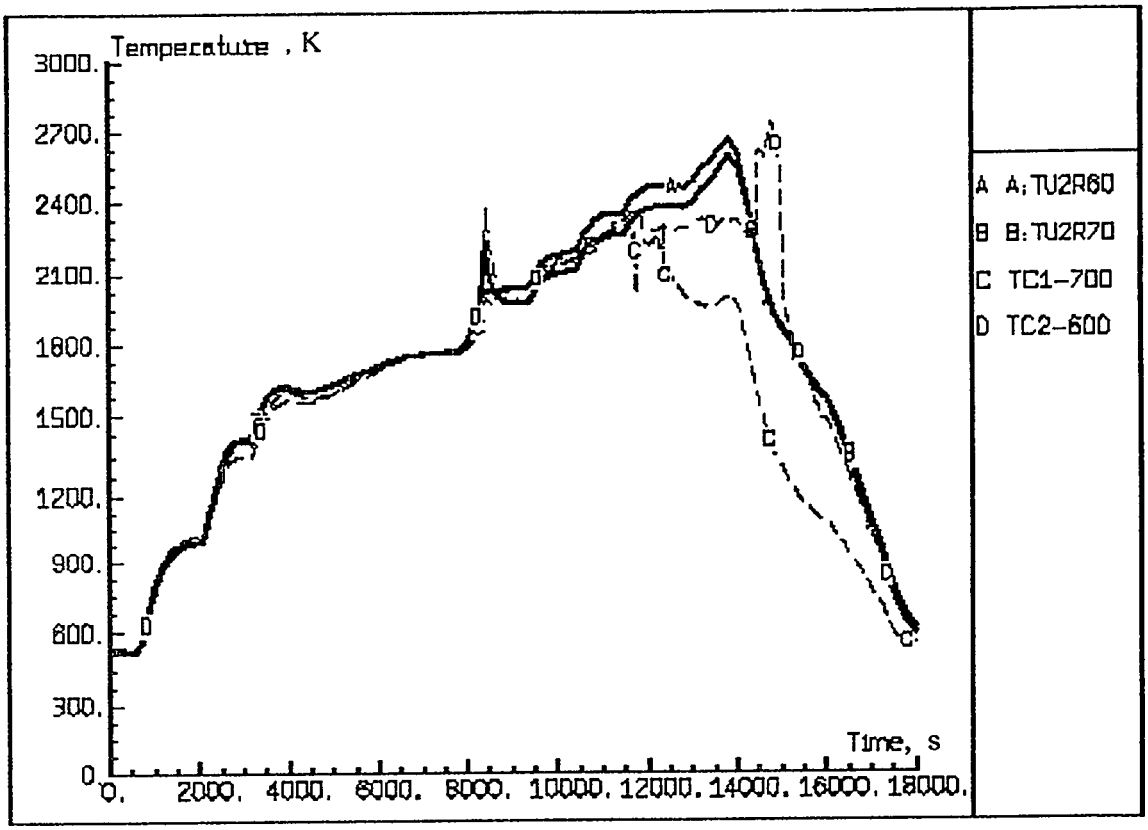


Figure 5. PHEBUS B9+. Fuel temperature evolution v.s. time in comparison with measured data.

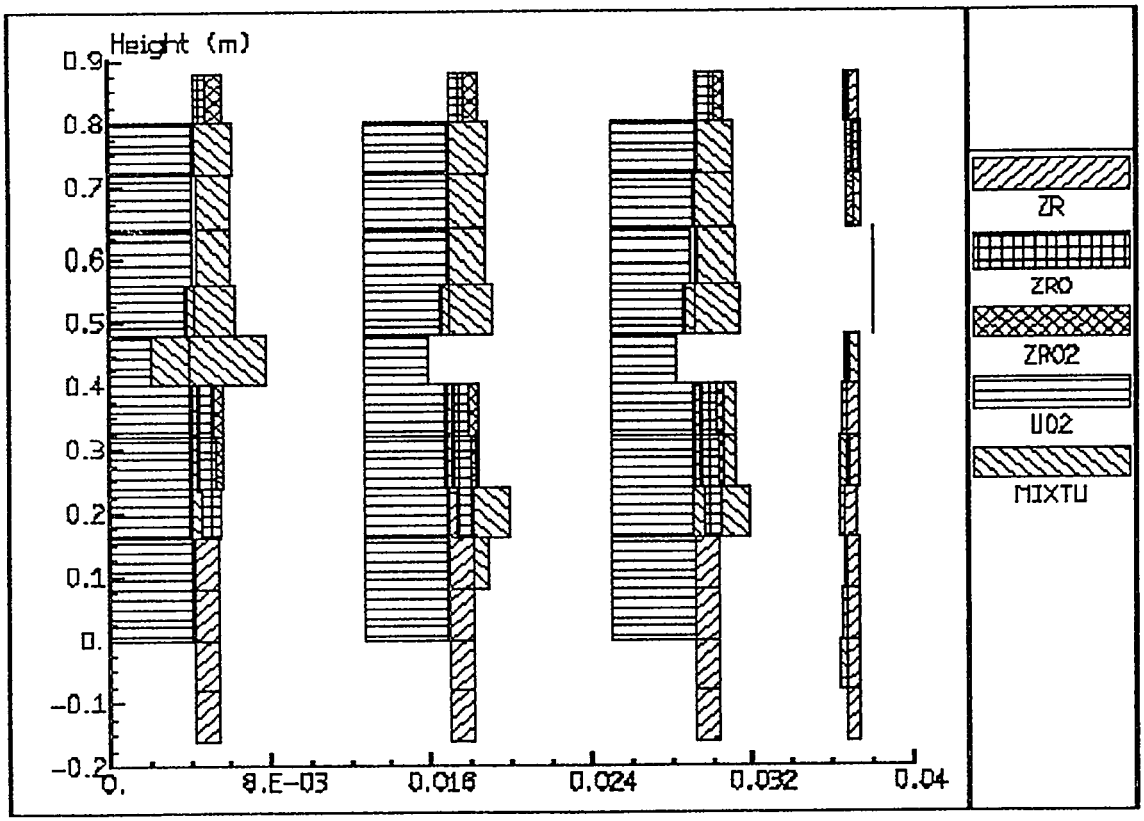


Figure 6. PHEBUS B9+. Final state of bundle. 1,2,3 - ring's rod and liner. Time 18000 s.

- dissolution of UO_2 and ZrO_2 by molten Zr;
- mechanical damage of the cladding;
- relocation of materials and formation of blockages.

The test bundle contained almost all materials used for WWER-400/1000 reactor cores, thus the interaction and relocation of real materials were considered. Decay heat was modeled by electric heating. The central part of the CORA facility is a test bundle placed in porous insulator made of zirconium dioxide. Argon and superheated steam flow through an inlet nozzle on the level 0 m. The CORA-W2 test scenario was divided into three phases

- 0 - 3000 s is the preheating phase;
- 3000 - 4500 s is a transient phase;
- 4500 - 5000 s is a cooling down phase (electrical power reduced to 0.52 kW).

During the first phase of heating the electrical power was constant and was equal to 0.52-1.65 kW. The flow rate of heated argon was 8 g/s.

During the transient phase the rate of the temperature increase was defined by a linear increase of the electrical power up to 14.3 kW. At 3300 s, steam with a flow rate of 4 g/s was supplied to test bundle. During the first two phases the pressure in the system was 0.22 MPa. Instrumentation of the test bundle allowed the measurement of temperature profiles, hydrogen generation rate and etc.

The modified ICARE2 code (with modules UZRO, DROP, CROX) simulation results are presented in Figs 7-10.

In Fig. 7 the simulated and measured cumulative hydrogen production data are compared. One can see that up to the time 4500 s good agreement exists between both sets of values. The agreement occurs due to correct simulations of total bundle temperature behaviour during the second phase of experiment (including oxidation during melt relocation). After instant 4500 s in the calculations the amount of hydrogen produced is slightly lower than the experimental one. The explanation of this discrepancy may be the following. At 4500 s, the injection of the steam to the test bundle was turned off. That resulted in steam starvation and total suppression of the oxidation reaction. Experimentally, oxidation was observed practically up to the end of experiment. Apparently, a residual flux of steam existed in the experiment (evaporation from the quench cylinder) and to improve the simulation data for that phase of the experiment more exact information about the residual steam fluxes is needed.

The temperature behaviour for elevations 35, 55 and 95 cm are presented on Fig. 8 and 9. One can see well agreement at the times for the temperature escalation, start of melt relocation as well as dynamics of melt movement at lower parts of the bundle.

In Fig.10 the simulated final state of the bundle is presented for different types of the rods (1, 2, absorber, 3, 4 rings). In agreement with the experiment the absorber rod practically totally destroyed on elevation higher 20 cm. Melted pares of rods not penetrate lower when 10 cm, in accordance with experimental data. Position of channel blockage is well predicted (20 cm.).

The usage of the modified ICARE2 code allows the correct prediction of the main physical phenomena observed during the CORA-W2 experiment: oxidation, temperature escalation, movement of the melt, blockages formation.

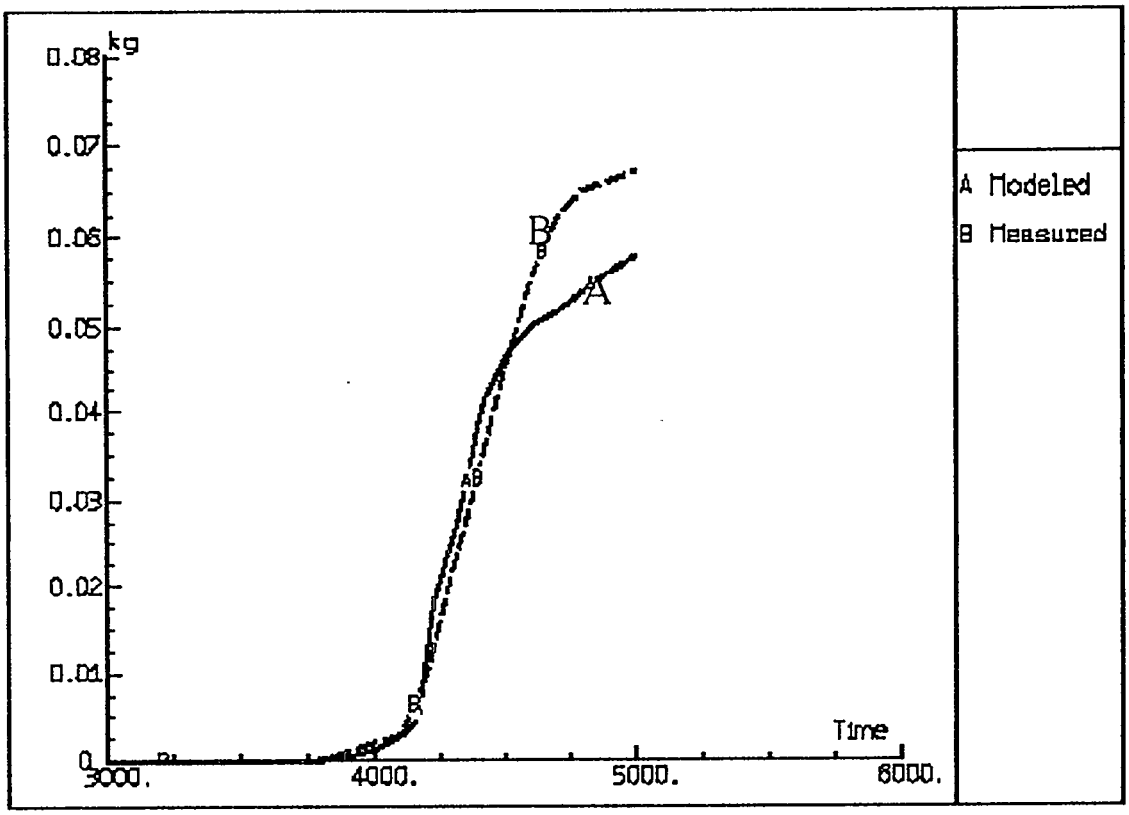


Figure 7. CORA-W2. Cumulated hydrogen production by all oxidation reactions.

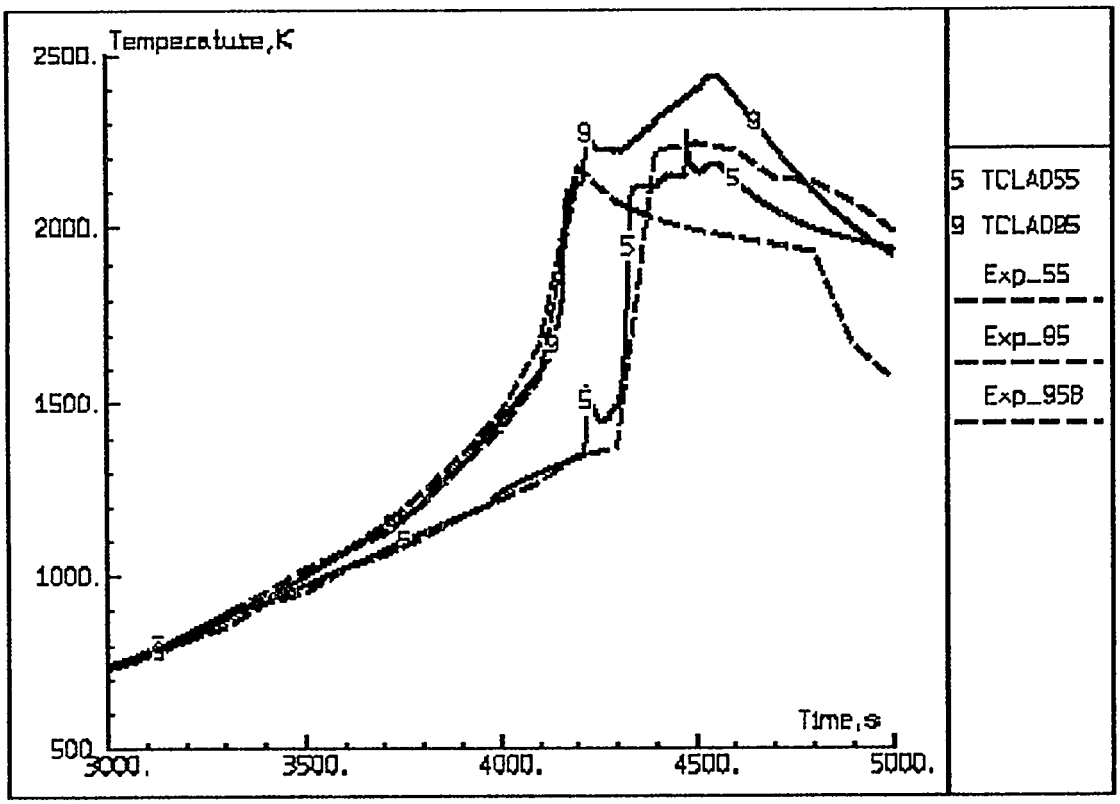


Figure 8. Cladding temperature evolution of central rod for elevations 95 (9 and Exp_95) and 55 (5 and Exp_55) cm.
Solid lines - result of simulation, dotted - experimentally measured.

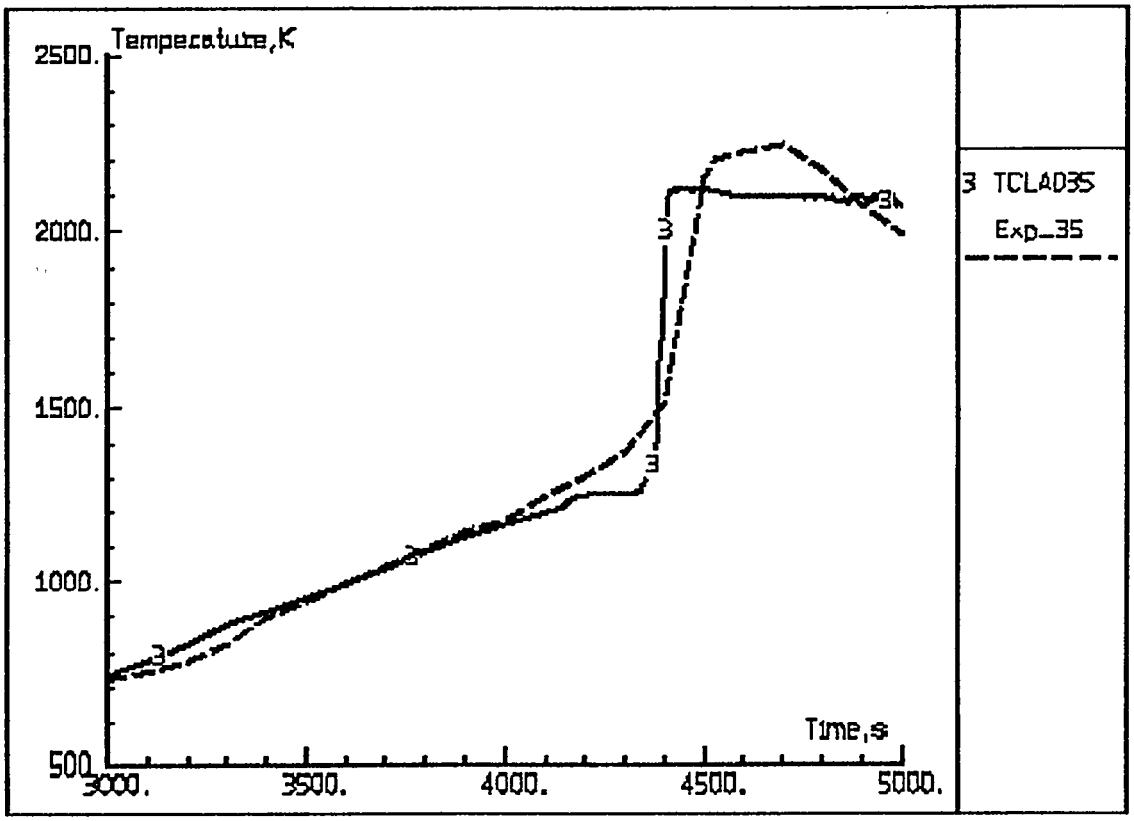


Figure 9. CORA-W2. Cladding temperature evolution of central rod for elevations 35 (3 and Exp_35) cm. Solid lines - result of simulation, dotted - experimentally measured.

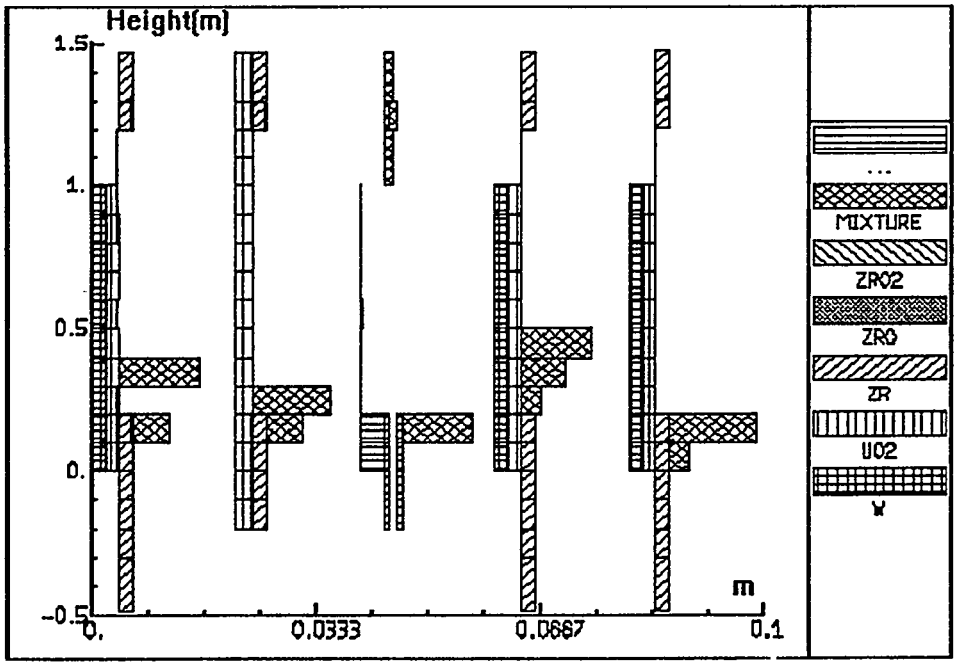


Figure 10. Final state of CORA-W2 bundle.

8. Conclusions

1. The modules in the package "SVECHA" modules were developed and validated on separate effect test data in the current scope of work. They include the following:
-a module for the mechanical behavior of the cladding under severe accident conditions;
-the diffusion module for cladding oxidation, dissolution of UO_2 pellet by solid and liquid Zr;
-the module for description of candling on surfaces of solid components and candling in gaps with mechanism of drops formation.

2. Modules were successfully implemented in ICARE2 code and validated against a wide range of integral tests.

3. The use of the new modules does not cause to a significant increase of consumed CPU time. (This value is about 1.5 times greater than the old one.)

4. Validation results have shown good agreement with the separate effect tests data as well as with the integral tests CORA-W1/W2, CORA-13, PHEBUS-B9+.

5. Use of modules, developed in NSI allow to improved simulations for the description of the following phenomena:
-destruction of fuel rod cladding under inert and oxidizing conditions;
-simulation of fuel rod cladding oxidation in transient regimes;
-melt relocation and oxidation during melt relocation.

Acknowledgments:

Authors are very grateful to Drs. A.Porracchia and R. Gonzalez (IPSN, Cadarache, France) for fruitful discussions of the new models and their great help and guidance in the implementation of models into the code ICARE2; to Dr.P.Hofmann (KfK, Karlsruhe, Germany) for fruitful cooperation in the development of some of the new models and valuable discussions of the results of his experiments; to Prof. L.A.Bolshov, Drs. R.Arutyunyan and V.Strizhov (NSI, Russia) for their permanent interest and support of this work.

References:

[1]. In-Vessel Core Degradation in LWR Severe Accidents: A State of the Art Report to CSNI, January 1991, NEA/CSNI/R(91)12.
[2]. SCDAP/RELAP5 Independent Peer Review, 1994, Los Alamos National Laboratory, LA-12481.
[3]. *P.Hofmann, H.J.Neitzel, E.A.Garcia*, Chemical interactions of Zircaloy-4 Tubing with UO2 Fuel at Temperatures Between 900 and 2000 C, KfK-4422, 1988.
[4]. *A.M.Voltchek, A.E.Kisselev.* "On the Modeling of the Pellet/Cladding/Steam Interactions in the Framework of the Oxygen Diffusion Theory." Proc. of ARS'94 Int. Topical Meeting on Advanced Reactors Safety, Pittsburgh, PA, April 17-21, pp.583-590.
[5]. *M.S.Veshchunov and A.M. Voltchek.* "On the Kinetics of UO_2 Interaction with Molten Zircaloy at High Temperatures. J.Nuc.Mat., 188 (1992), pp. 177-182.
[6]. *M.S.Veshchunov, P.Hofmann*, "Dissolution of solid UO_2 by molten Zircaloy", J.Nucl.Mater., 196 (1994), pp. 207-221

[7]. *A.Boldyrev, N.Yamshchicov, V.Shestak*, "Fuel cladding deformation behavior module (CROX)", Preprint NSI-SARR-05-94, Nuclear Safety Institute, Moscow, 1994
[8]. Deformation and Failure of Zircaloy Fuel Sheaths Under LOCA Condition. Sagat S., Sills H. E., and Wolsworth J. A., Zirconium in the Nuclear Industry: Sixth International Symposium, ASTM STP 824, D. G. Franklin and R. B. Adamson, Eds., American Society for Testing and Materials, 1984, pp. 709-733.
[9]. *A.V.Palagin*, "On the flowing down the fuel rod of Zr-U-O liquefied mixture during severe accident at nuclear power plant", Preprint NSI-1-93, Nuclear Safety Institute, Moscow, 1993
[10]. *A.V.Palagin, M.S.Veshchunov*, "Relocation of molten materials during core degradation (Candling)", Preprint NSI-SARR-04-94, Nuclear Safety Institute, Moscow, 1994
[11] *A.V.Palagin*, "Application of ICARE2 V2 mod2 code to CORA-13: sensitivity studies on the candling DROG Module", Note Technique SEMAR 94/110, IPSN, France, 1994.
[12]. *R.Gonzalez. P.Chatelard, F.Jacq* "ICARE2 - A Computer Program for Severe Core Damage Analysis in LWRs", Note Techhnique SEMAR 93/33, IPSN, France, 1993.

EXPERIMENTAL SIMULATION OF THE WATER COOLING OF CORIUM SPREAD OVER THE FLOOR OF A BWR CONTAINMENT

F. Moraga, R.T. Lahey, Jr. and M.Z. Podowski
Rensselaer Polytechnic Institute
Troy, NY 12180-3590, USA

ABSTRACT

This paper is concerned with an experimental investigation of the cooling effect of water collected on the surface of corium released onto the floor of a BWR drywell. In the present experiments, the actual reactor materials were replaced by simulant materials. Specifically, the results are shown for Freon-11 film boiling over liquid Wood's metal spread above a solid porous surface through which argon gas was injected. An analysis of the obtained experimental data revealed that the actual film boiling heat transfer between a molten pool of corium and the water above the pool should be more efficient than predicted by using standard correlations for boiling over solid surfaces. This effect will be further augmented by the gas released due to the ablation of concrete floor beneath the corium and percolating towards its upper surface and into through the water layer above.

1. INTRODUCTION

Containment integrity is an important safety issue for boiling water nuclear reactors (BWR), especially for those having Mark-I containment's. In this type of containment early failure could occur because of molten corium attack of the steel liner. Significantly, if sufficient energy is removed from the corium by film boiling heat transfer to an overlying water pool, the spreading rate of the corium would gradually slow down and eventually stop, preventing liner attack.

Chemical reactions induced by the high temperatures involved will occur between the materials present in the concrete floor and the corium. The noncondensible gases released in these reactions will bubble through the corium/water interface and may enhance the heat transfer. Thus, in order to asses the consequences of severe accidents with gross core melting, it is necessary to study the film boiling heat transfer of layered liquids above a solid surface through which noncondensible gases are bubbling.

It has been assumed that when no gas flow is present and the heavier liquid's top surface is quiet, film boiling over a solid surface will occur. Greene's [1] experiments with Freon-11 and bismuth support this hypothesis, however the experiments of Henry et al.[2] for Freon-11 and mercury and Freon-22 and water show that the minimum superheat and the minimum heat flux can be drastically different.

A model for gas-sparging-enhanced melt/water film boiling heat transfer has been developed and implemented into the MELTSPREAD-I computer code [3], [4]. This model

assumed that Taylor instability theory, on which the predictions of film boiling heat transfer are based, can be modified to take into account the flow of the noncondensable gases. Using this model, and the experimental results of Greene [5], these authors conclude that the most important effect of gas bubbling is to augment the net area available for film boiling heat transfer due to deformation of the surface of the heavier liquid. Thus, the heat flux was assumed to increase linearly with the superficial gas velocity of the noncondensable gases.

Duignan and Greene [6] measured the effect of a gas flow on the heat transfer of water film boiling over a solid surface. The gas passed through small holes arranged in a square pattern. The data were fitted by the equation

$$\frac{q''}{q''_{Be}} = (1 + 2.086 j_g)^{1/4} \tag{1}$$

where j_g is expressed in cm/s and q''_{Be} is the Berenson film boiling correlation [7].

For the purpose of future reference the heat transfer coefficient (H_{film}) predicted by Berenson [7] and the predictions of Zuber [8] using Taylor instability theory for q''_{min}, respectively are given below,

$$H_{film} = 0.425 \left\{ \frac{(k_{f11}^3 \rho_v (\rho_L - \rho_v) L' g)}{\mu_v \Delta T [\sigma / g (\rho_L - \rho_v)]^{1/2}} \right\}^{1/4} \tag{2}$$

$$q''_{min} = \left(\frac{0.4\pi\sqrt{2}}{3^{0.25}} \right) \left(\frac{\pi L' \rho_v}{24} \right) \left[\frac{\sigma g (\rho_L - \rho_v)}{(\rho_L - \rho_v)^2} \right]^{1/4} \tag{3}$$

The fluid properties in Eqs. (2) and (3) are evaluated at the average temperature in the vapor film. Eq. (2) is reliable when radiation is not important but the surface temperature is significantly higher than the Leindenfrost point.

It is the purpose of this paper to report results obtained for Freon-11 film boiling over liquid Wood's metal spread above a solid porous surface through which argon gas was injected.

II. EXPERIMENTAL SETUP

An experiment was designed to measure the stationary film boiling of Freon-11 over a layer of liquid Wood's metal with a noncondensible, non-reactive gas, argon, passing

through the liquid metal and the vapor film. For the purpose of comparison, experiments on Freon-11 film boiling over a solid porous surface with gas flowing through it were also carried out. The experimental setup is shown in Figure 1 and details of the test section are shown in Figure 2.

The test section consisted of a bronze porous plate (Figure 3) silver soldered to the top of a hollow copper cylinder (99.9% pure copper). Eight radial grooves on top of the copper cylinder allowed the Argon gas to reach the top of the porous plate with a uniform distribution.

A cylindrical electric heater, which was silver soldered to the copper cylinder, provided the required power. The wall heat flux was measured using six thermocouples (T_6 to T_{11} in Figure 2). Since the thermal conductivity of copper was known and the two groups of thermocouples used to measure the copper temperature were at a given distance (60 mm) apart, the heat flux along the cylinder could be determined quite accurately.

The copper cylinder was insulated using three concentric Teflon cylinders, which are not shown for simplicity. An approximately 3 mm air gap prevented any direct contact between the metal and the Teflon, except at the top where a Teflon piece provided a seal and insulation simultaneously. This use of Teflon was very important because it prevented direct contact between the enclosing flange and the liquid, diminishing heat losses and, when only Freon was used, helped to stabilize the film boiling regime.

On top of the Teflon piece, a 50.8 mm ID glass tube was placed. On top of this tube there was an aluminum upper plenum. An exit at the top of this plenum led to a condensing system used to recover Freon-11. An auxiliary condensing coil was also installed inside the aluminum plenum to help with the condensation process when necessary.

Freon-11 was fed to the aluminum plenum from a supply tank. When necessary, the incoming Freon was preheated to maintain saturation conditions. An aluminum cylinder inside the plenum helped to reduce the kinetic energy of Freon delivered onto the boiling surface. This effect was particularly important during the initial phase of Freon pouring over a hot surface, when an undesired transition to nucleate boiling could occur. The total level of Freon was controlled visually and more Freon was added when necessary.

The porous plate used in the experiments was a 50.8 mm ID by 12.7 mm thick bronze sintered disk of grade 23 (150 microns). This coarse grade was selected to prevent liquid silver solder from filling-in the pores during the soldering operation and, consequently, obstructing the argon gas flow.

The amount of silver solder used was carefully controlled, so as to ensure good thermal contact between the copper and the porous plate on the one hand, and, on the other hand, to prevent the pores above the grooves, or the hole in the cylinder, from filling in.

After soldering the test assembly, argon gas was bubbled through liquid Wood's metal pool to verify the uniformity of argon distribution across the plate.

In order to determine the minimum thickness of the porous plate required to have a flat temperature profile at the top, numerical simulations were performed using the PHOE-

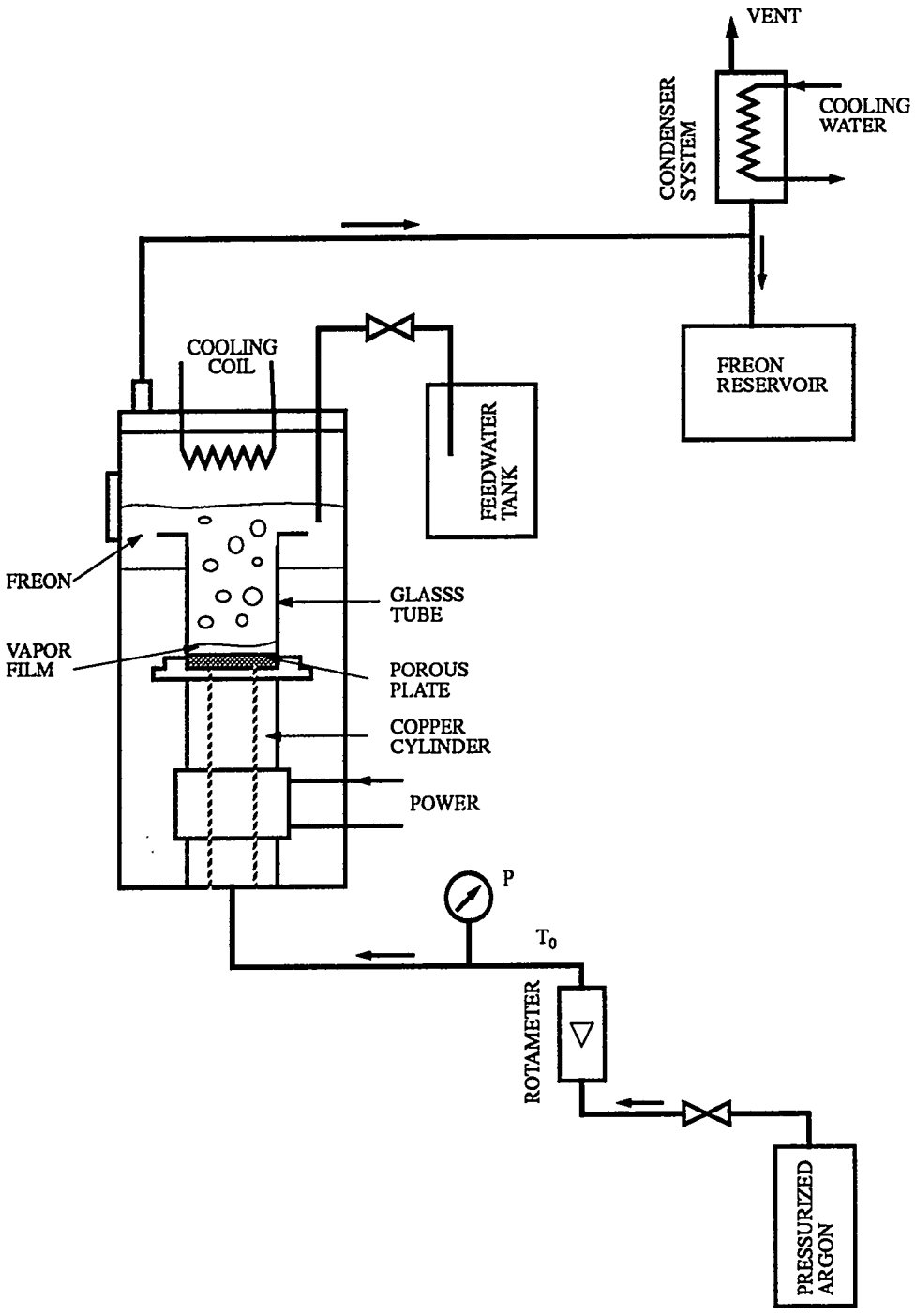


Figure 1 A schematic of the test facility

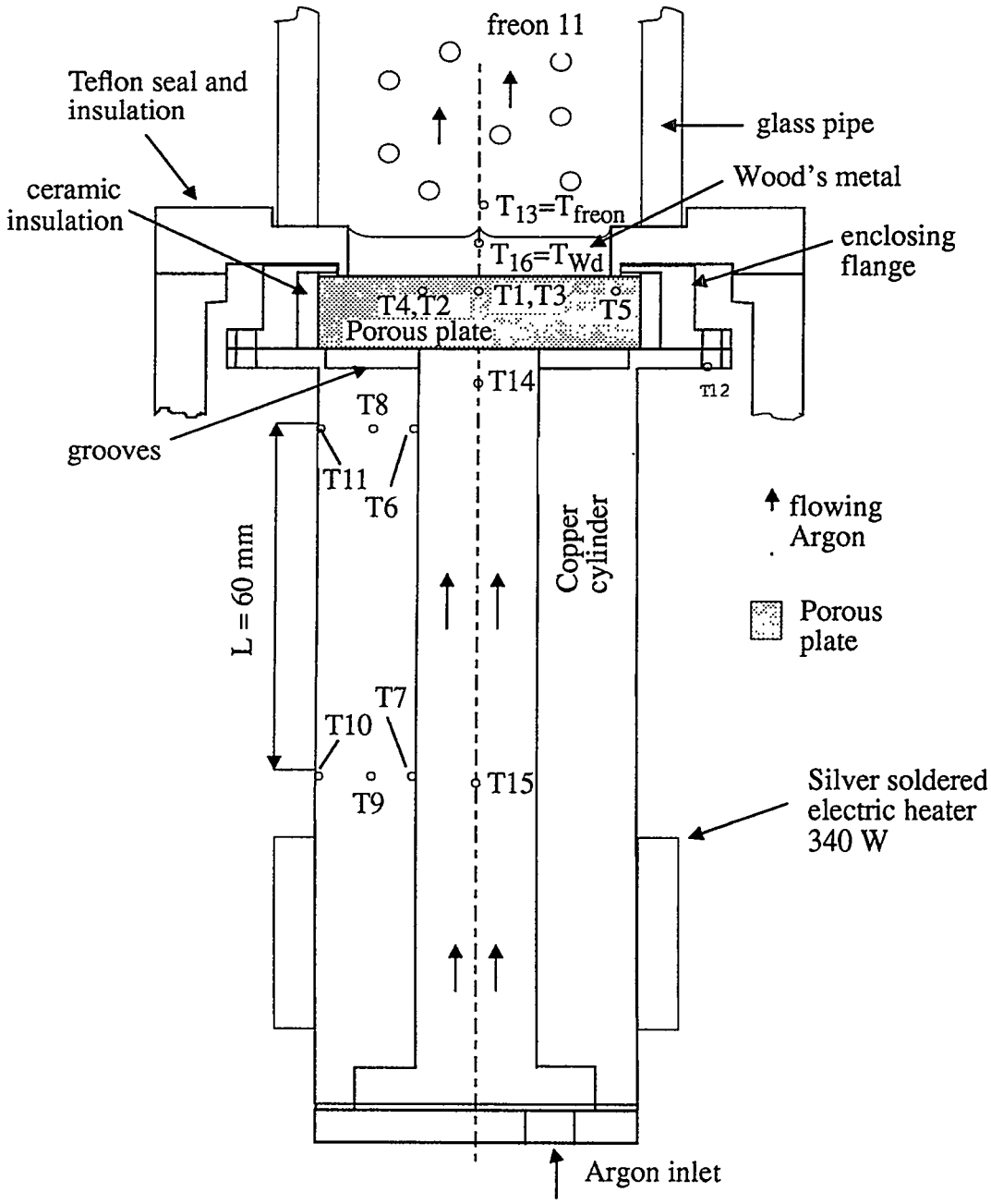
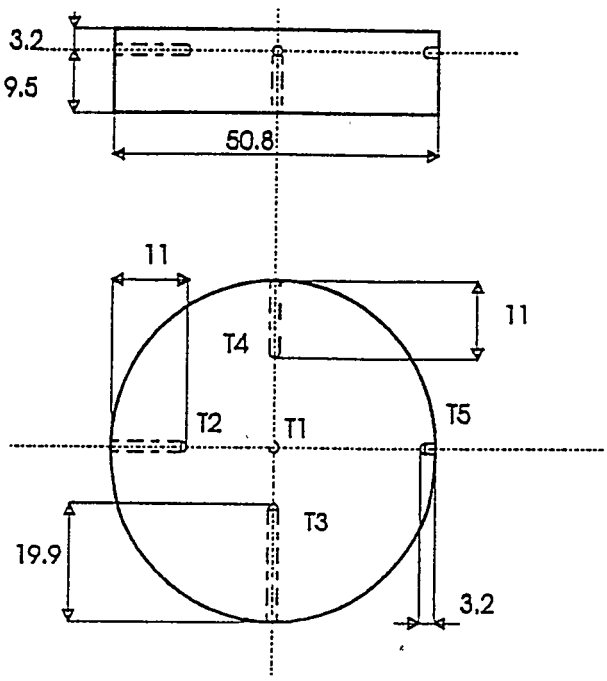
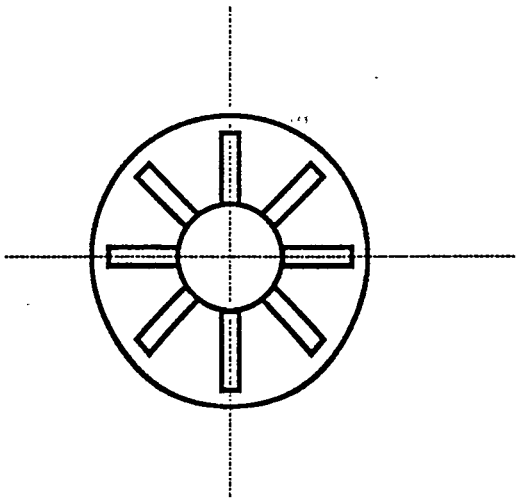


Figure 2 Test section



ALL MEASUREMENTS I N mm.

(a) Location of thermocouples



(b) Grooves

Figure 3 Location of thermocouples and details of the grooves in the copper cylinder.

NICS code. The temperature profiles at the surface and at the plane where the thermocouples were located can be seen in Figure 4. Good agreement between the simulations and the data has been obtained. The simulations were also useful to evaluate any necessary corrections in the wall temperature.

The thermal conductivity used in these simulations was given by,

$$k = k_b (1 - \alpha_b) \tag{4}$$

where k_b is the thermal conductivity of bronze and α_b is the volumetric void fraction of the porous bronze plate. The latter parameter was determined by weighting several similar porous plates and using the density of bronze provided by the manufacturer.

The available surface for heat transfer at the top of the porous plate was a disk 41.3 mm in diameter. The remaining area of the porous plate was used to accommodate o-rings and to insulate the porous plate. Kesselring et. al. [9] showed that when the smallest horizontal dimension of a flat heat transfer surface is larger than 25.4 mm, the film boiling of Freon-113 or Freon-11 is not affected by the boundary effects. Klimenko [10] proposed that when the surface dimension is greater than 2.8 λ_d, the surface is large enough. Both above-mentioned criteria have been satisfied in the present experiments.

The noncondensible gas flow system consisted of a pressurized tank of argon and a flow regulator. The flow rate of argon and the inlet pressure were measured during the experiments using a rotameter and a manometer, respectively.

The argon was routed into the bottom of the copper cylinder and its temperature increased while flowing along the cylinder. The argon temperature was measured at the exit of the rotameter (T_0 in Figure 1) and was always close to room temperature. The argon temperature was also measured at the bottom of the portion of the copper cylinder used to measure the heat flux (T_{15} in Figure 2), and at the bottom of the porous plate (T_{14} in Figure 2). The sheaths of thermocouples, T_{14} and T_{15} were carefully insulated with a ceramic to eliminate systematic errors due to the conduction along the sheath.

The temperatures of argon at the outlet of the rotameter and at the bottom of the porous plate were used to determine a correction factor to account for the thermal expansion of argon. Since the specific heat of argon is very low, the error introduced in the heat flux measurement by the argon cooling of the interior walls of the cylinder was found to be negligible. This fact was verified by the measured temperature increment (T_{14} - T_{15}) of argon in the portion of the cylinder used to evaluate the heat flux.

The manometer indicated that the argon pressure before the inlet to the copper cylinder was never higher than 5 mm Hg gauge. Thus, for the purpose of properties determination, the entire system was considered to be at atmospheric pressure.

Seventeen copper-constantan (i.e,T-type) thermocouples were used. Most of them (T_1 through T_9, T_{13}, T_{14} and T_{15}) were Inconel sheathed thermocouples 1/16" O.D.

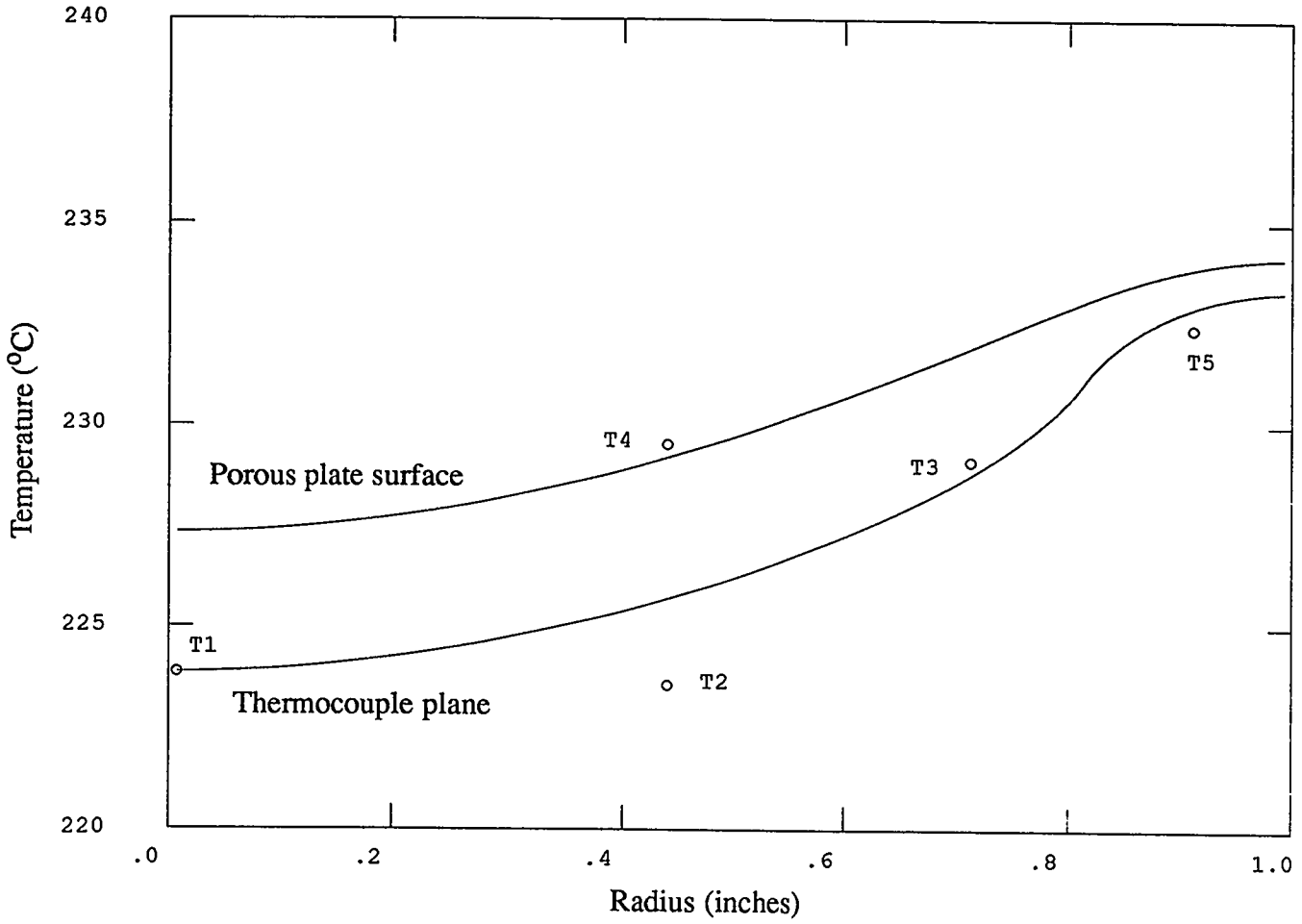


Figure 4 Temperature profile in the porous plate. Comparison between the measured values and PHOENICS calculations.

Three thermocouples, (T_{10}, T_{11} and T_{12}) were bolted onto the copper cylinder. T_{12} was used mainly to ensure that heat losses in the radial direction were negligible.

Five thermocouples were located at the porous plate (Figure 3) and four of them were placed radially (T_2 through T_5). Since temperature gradients are more important in the axial direction, this way of locating thermocouples allowed for accurate measurements.

Thermocouples T_2 and T_4 were located at the same radial distance from the center in order to check for symmetry. There was a systematic difference between the readings of these two thermocouples. Typical values can be seen in Figure 4. In order to be sure that this difference came from asymmetries in the porous plate and not from the data acquisition system, the connection of the thermocouples to it were swapped. From this procedure it was concluded that the difference responds to a small asymmetry in the porous plate properties, presumably due to inhomogeneities in the silver solder distribution between the porous plate and the copper cylinder. However, it should be stressed that the error introduced was small, as discussed in the following sections.

The Wood's metal temperature was measured by a thermocouple (T_{16}) placed as close to the Freon-Wood's metal interface as was possible, yet always submerged in the Wood's metal. Furthermore, instead of Inconel sheathed thermocouples, a naked tip Teflon insulated thermocouple was also used to determine the Wood's metal temperature. No difference was found between the readings of these two thermocouples. Thus, the possibility of a systematic error in the Wood's metal temperature due to heat conduction through the thermocouple sheaths was eliminated.

Another thermocouple (T_{13}) was used to check that the Freon was at saturation temperature.

A personal computer was used with an Exp-16 Keithley temperature acquisition card having an electronic cold junction compensation. The power supplied to the electric heater was measured using a watt meter. However, this information was used only as a check because most of the heat losses occurred at the bottom of the copper cylinder. The reasons for this are explained below.

The copper cylinder was connected from above to the bottom of the aluminum plenum. This setup had an advantage that heat losses through structural materials did not introduce measurement errors, but also a disadvantage that the elements immediately below the copper cylinder had to provide both mechanical support and thermal insulation. The purpose of the mechanical support was two fold, since besides providing the required stability, it provided the alignment necessary for the seals of the glass pipe. To satisfy these requirements, a combination of ceramic and Teflon elements was chosen. To prevent Teflon melting or deformation, a steep temperature gradient was used. The "price paid" was that the electric power could not be used to calculate heat losses.

The entire thermocouple acquisition system was carefully calibrated prior to running the experiments.

III. EXPERIMENTAL PROCEDURE

Once the liquid Wood's metal (or the porous plate for experiments without Wood's metal) reached a temperature slightly above 300 °C, Freon was poured over the hot surface. Simultaneously, an argon flow was supplied. It was visually checked that the Wood's metal stayed liquid during the measurements. Entrainment of liquid Wood's metal into the Freon region was noticed to occur only during a short time interval just after the Freon was introduced. For the case without argon flow, the Wood's metal surface was quiescent. For other cases, some agitation at the surface was observed. The height of the liquid Wood's metal without gas bubbling was 7 mm for every run. No Wood's metal oxidation was evident during or after the experiments.

It was found that the film boiling regime could not be maintained when Freon was boiling directly over the porous plate for porous plate temperatures lower than 180°C. This result was independent of the superficial gas velocity of argon.

Moreover, since the pores were large, it was not possible to reduce the gas flow rate to zero when there was no Wood's metal, because the Freon would penetrate the plate. This limitation is intrinsic to this type of experiments and has been noted before by Duignan et al. [6].

The basis of the experimental design was the needed accuracy of the heat flux measurements. To accomplish this, temperature gradients must be unidimensional along the test section used in the measurements. Moreover, this section has to be long enough to obtain the required accuracy of the temperature gradient. The disadvantage of this approach is that the required large amount of copper introduces thermal inertia and, consequently, the porous plate and/or Wood's metal temperatures can be controlled only over broad ranges and large time spans. For this reason, most measurements were made using the same initial electric power, adjusting it only to prevent transition to nucleate boiling and/or an overheat that could damage the Teflon piece above the enclosing flange (T_1 well above 300°C). Furthermore, the electric power was adjusted during the transient phase of experiments in order to reduce the time required to reach steady-state, but only if the final heat flux and porous plate temperature were approximately known from a previous shorter run.

A couple of hours were usually required to reach steady-state conditions. Only the temperature values measured at steady-state were considered useful. The final values for each temperature measurement come from averaging over an interval of at least eight minutes. Since each temperature was measured once every 0.78 s., a sample of at least 61 measurements was used to calculate the final values. The case of boiling over Wood's metal with no gas flow was measured twice. Although the results are very much the same for both measurements, only the values obtained for the longer run were used.

The superficial argon velocity, j_g, defined as the volumetric flow rate of argon through the porous plate divided by the area of the test section, was the variable chosen to quantify the effect of the argon gas flow.

Due to the heat losses from the combined copper cylinder/porous plate system (estimated as less than 10% of the total heat supply) the measured temperatures differences along the copper cylinder varied with the radial position. Hence, the average heat flux into the porous plate was calculated using the following formula,

$$q'' = \frac{k_{Cu}}{L}\left[a_1 (T_{10} - T_{11}) + a_2 (T_9 - T_8) + a_3 (T_7 - T_6)\right] \tag{5}$$

where $k_{Cu} = 3.84\ W/cm - {}^{o}C$ is the copper thermal conductivity, L = 60.3 mm is the distance between the thermocouples in the measurement section of the copper cylinder, and a_i are the area weighting factors. These weighing factors were obtained by dividing the cross section of the copper cylinder into two concentric rings of the same "radial length" and using the measured temperatures to obtain an average axial temperature difference for each ring. The resultant values of are:

$$a_1 = 0.307$$

$$a_2 = 0.50$$

$$a_3 = 0.193$$

Since the dominant factor contributing to the overall error was concerned with the thermocouples' readings, the error in the heat flux was estimated from,

$$\delta|\Delta q''| = \frac{k_{Cu}}{L}\left[a_1|\delta (T_9 - T_8)| + a_2|\delta (T_{10} - T_{11})| + a_3|\delta (T_7 - T_6)|\right] \tag{6}$$

where $|\delta (T_i - T_{i-1})| = |\delta T_i| + |\delta T_{i-1}| = 0.8^{o}C$ (i=7,9,10) is the statistical fluctuation of the measured temperature difference.

The film boiling heat transfer coefficient at the surface between the Wood's metal pool (or porous plate in the experiments w/o Wood's metal) and the liquid/boiling freon above was obtained from,

$$H = \frac{q''}{T_s - T_{13}} \tag{7}$$

where (see Fig. 2) T_{13} is the freon temperature and T_s is the reference heat source temperature ($T_s = T_{16}$ for the experiments with Wood's metal and $T_s = T_1$ when only the porous plate was used).

The porous plate temperature was always considered to be T_1. The error in the porous plate temperature was taken to be T_5 - T_1 (a conservative estimate).

Since only one thermocouple was used to measure the temperature of the liquid Wood's metal, and the statistical fluctuations observed in this temperature were substantial, the error for the Wood's metal temperature, typically about 1°C, came from the standard deviation in the time interval being considered.

IV. EXPERIMENTAL RESULTS

The results of measurements are shown in Table 1 and in Figures 5 to 7. The porous plate and Wood's metal temperatures are referred to the Freon-11 saturation temperature, $T_{sat} = 23.7°C$,

$$\Delta T_{pp} = T_1 - T_{sat} \tag{8}$$

$$\Delta T_{Wd} = T_{16} - T_{sat} \tag{9}$$

As mentioned before, the experiments without Wood's metal, i.e. where Freon boiling occurred directly on the porous plate surface, were always accompanied by flowing argon. The results in Figs. 5 through 7 indicate only a small effect of the superficial velocity of argon on the measured parameters. Regarding the film boiling heat transfer coefficient, a slight decreasing trend can be observed in Fig. 7 if the gas flow rate increases.

Table 1. Freon-11 film boiling over porous solid surface.

j_g cm/s	$T_1 - T_{sat}$ °C	q'' W/m^2	$\Delta q''/q''$ %	q''_{plate} W/m^2	H W/m^2 °C	$\Delta H/H$ %
2.61	200	1.49 10^5	4	3.2 10^4	740	8
3.01	210	1.40 10^5	4	3.3 10^4	670	7
3.96	219	1.57 10^5	4	3.5 10^4	720	8
4.56	226	1.59 10^5	4	3.6 10^4	700	8
5.59	271	1.58 10^5	3	4.3 10^4	580	5
4.37	202	1.44 10^5	3	3.2 10^4	710	7

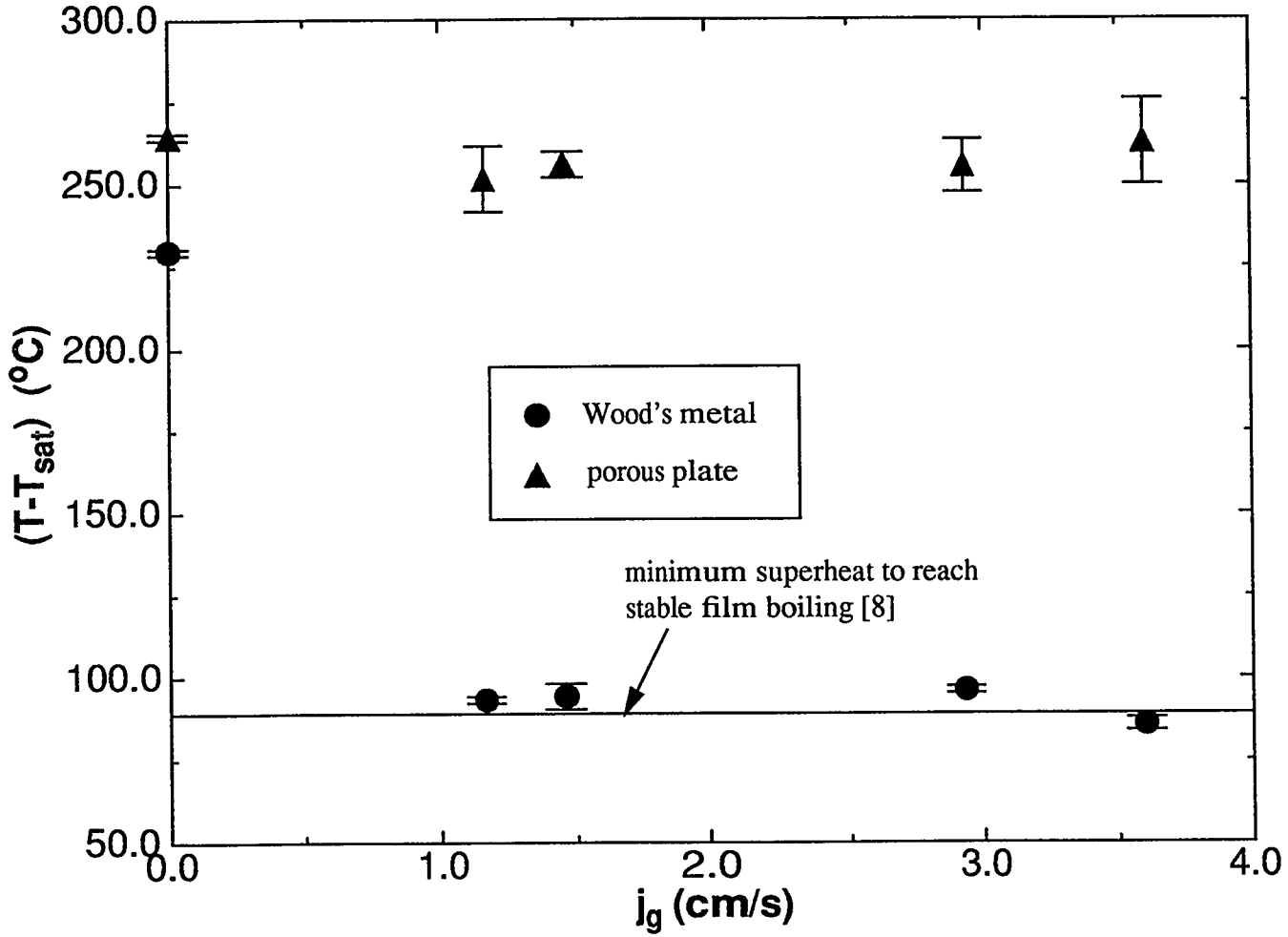


Figure 5 Measured temperatures for film boiling of Freon-11 over liquid Wood's metal

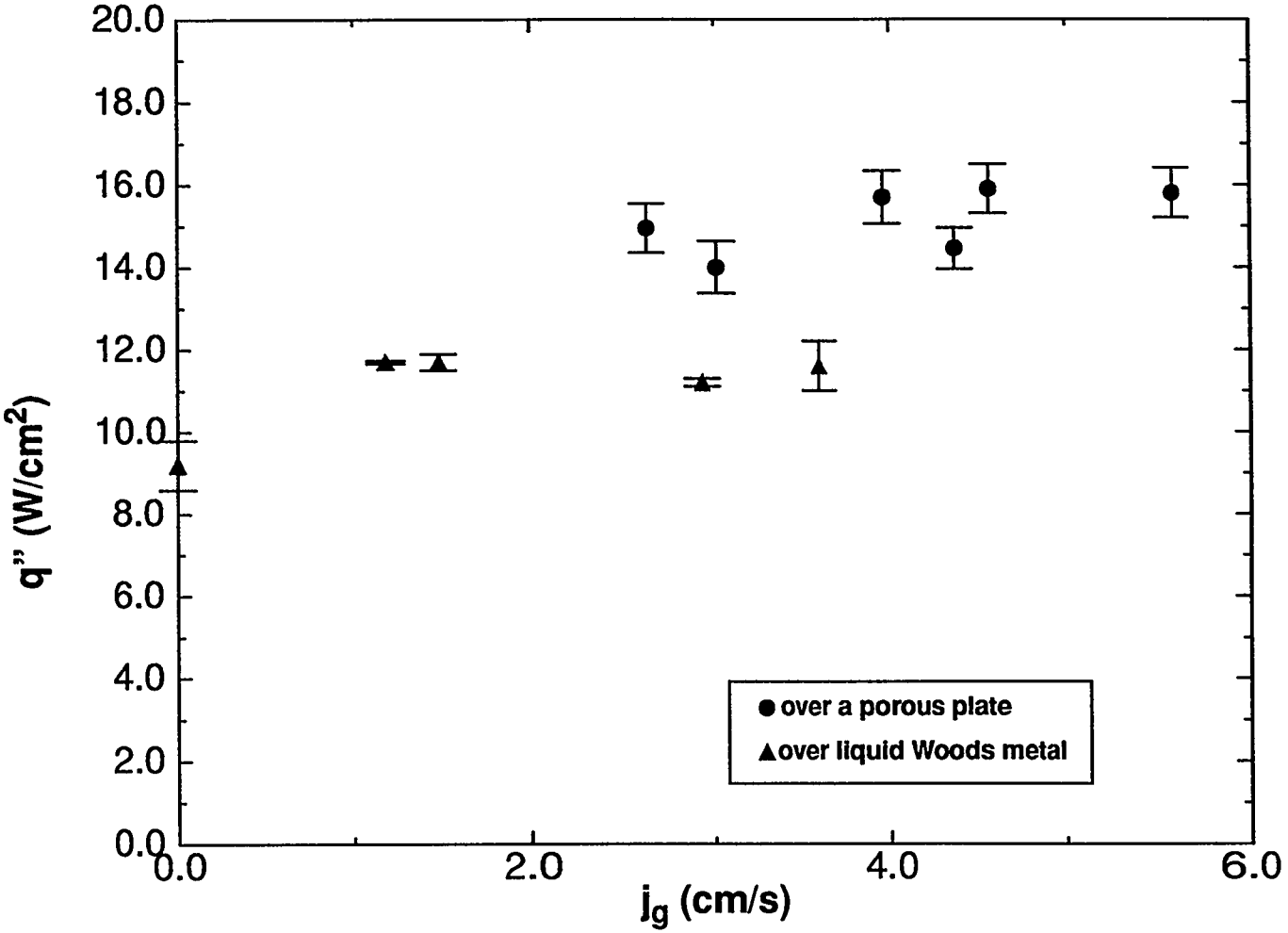


Figure 6 Measured temperatures for film boiling of Freon-11 over different surfaces

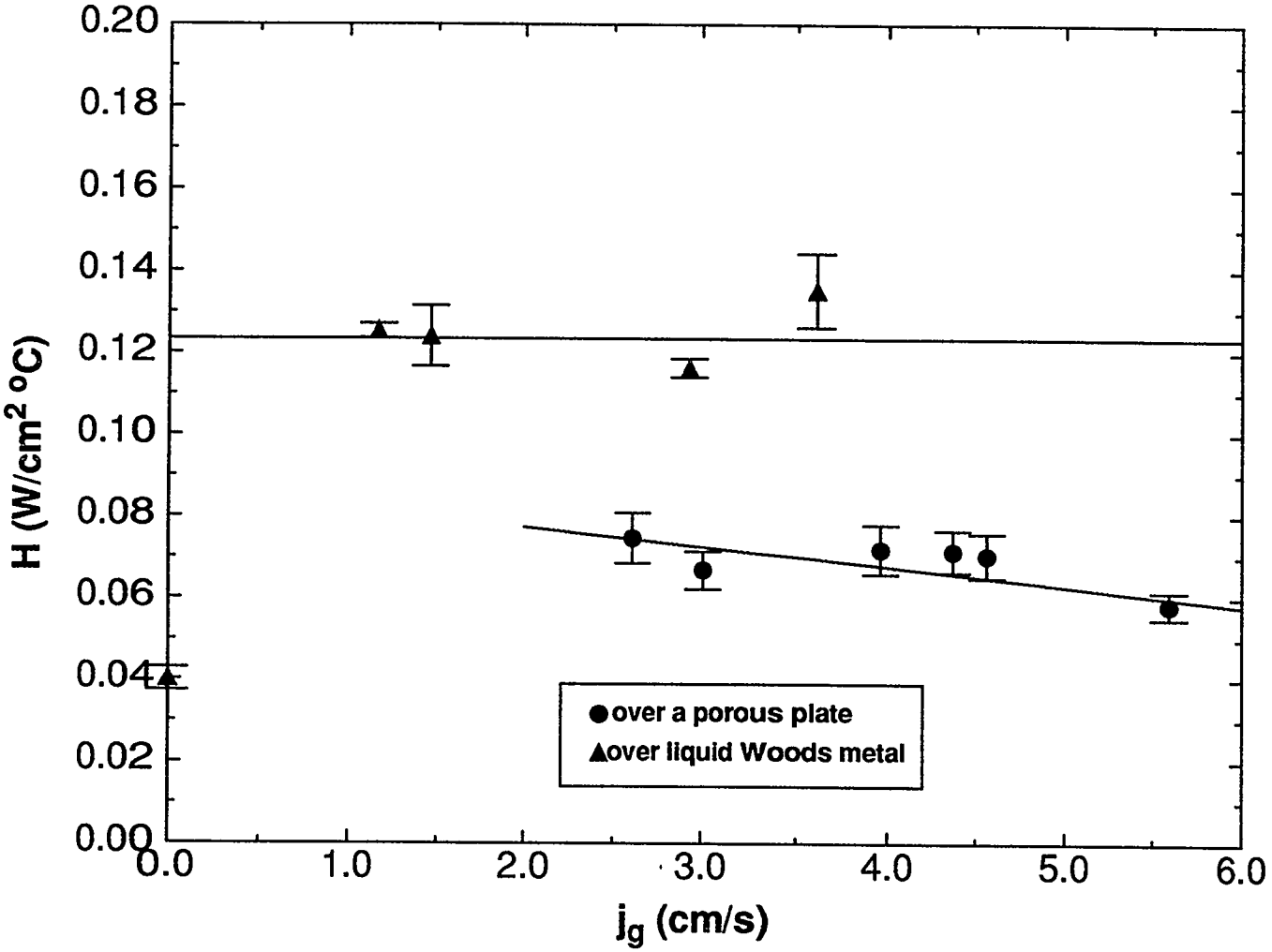


Figure 7 Freon-11 film boiling heat transfer coefficient.

Table 2 Freon-11 film boiling over liquid Wood's metal

j_g cm/s	$T_1 - T_{sat}$ °C	$T_{13} - T_{sat}$ °C	q'' W/m^2	$\Delta q''/q''$ %	q''_{plate} W/m^2	H W/m^2 °C	$\Delta H/H$ %
0	265	229	$9.2\ 10^4$	7	$3.7\ 10^4$	400	8
1.17	252	93	$1.17\ 10^5$	0.4	$1.8\ 10^4$	1250	8
1.46	256	94	$1.17\ 10^5$	2	$1.8\ 10^4$	1240	6
2.93	256	96	$1.12\ 10^5$	1	$1.9\ 10^4$	1200	8
3.60	263	86	$1.10\ 10^5$	5	$1.8\ 10^4$	1350	7

The data for film boiling of Freon on the Wood's metal surface show a significant difference between the cases without and with gas flow. Specifically, Fig. 7 and Table 2 indicate that even a small gas flow rate increases the net film boiling heat transfer coefficient by a factor of 3. On the other hand, this heat transfer coefficient stays almost constant over the entire range of superficial velocities of argon used in the experiments.

The current results have been compared against typical existing data for pool film boiling over a horizontal plate, such as those obtained by Hozler and Westwater [7] for film boiling of Freon-11 over a solid plate. It has been found that the results for boiling over a porous plate (q''_{plate}) give an increase by a factor of about 4 compared to the case of boiling over a smooth solid plate. In order to explain this difference, let us calculate/ estimate the vapor film thickness from,

$$\delta = \frac{k_{f11}}{H} \tag{10}$$

The present data indicate that the film thickness is about 10μm to 15 μm. Since the porous plate is made of bronze beads approximately 150 μm in diameter, the film thickness is only about 10% of the bead size. Hence, it is clear that the geometry factor, due to the fact that the actual contact area between the surface and the Freon is substantially higher than the projected area, must be taken into account. A rough estimate indicates that replacing the area of hemisphere ($2\pi r^2$) by its projected area (πr^2) gives a 100% increase. Now, the effect of gas flow in Eq.(1) gives an increase rate between 1.6 and 1.8 for the range of superficial gas velocities used in the experiments, compared to the case without

gas flow. A superposition of these two effects yields the same augmentation as that present results and the data of Hasler and Westwater [6].

It is interesting to mention that the effect of increasing gas flow through the pores may result in a reduction in the effective area between the Freon and the surface, thus reducing the net heat transfer coefficient. Since this effect competes against the increasing rate of gas/vapor removal rate from the surface, the net anticipated impact should be small, as shown in Fig. 7.

V. CONCLUSIONS AND SUMMARY

Examining the results for Freon boiling over liquid Wood's metal yields two major conclusions. First, and most importantly, film boiling over a liquid surface is much more efficient (i.e 250%) than a similar film boiling situation over a solid plate. There are several reasons for this. In particular, the effect of surface wettability and local motion of the liquid metal may result in a thinner film of vapor. Also, the evaporation of the coolant and of the hot metal mixed with the gas coming from the solid surface (i.e. argon), leads to the formation of a binary mixture in the vapor film. It is well known [11], [12] that even a slight amount of volatile and trinary elements coming from the evaporating liquid metal pool can dramatically change the film thickness and, consequently, the effective heat transfer coefficient. Secondly, the effect of gas percolating through the metal layer and into the film agitates the gas/vapor mixture and further reduces the effective film thickness and increases the heat transfer coefficient. The observed qualitative effect of the latter phenomenon is similar to (or even higher than that) indicated by Eq. (1).

In summary, applying the experimental data presented in this section to severe accident phenomena, one concludes that the actual film boiling heat transfer between a molten pool of corium and the water above the pool should be more efficient than predicted by using standard correlations for boiling over solid surfaces. This effect will be further augmented by the gas released due to the ablation of concrete floor beneath the corium and percolating towards its upper surface and into through the water layer above.

ACKNOWLEDGEMENTS

The authors wish to acknowledge the financial support given this study by Empire State Electric Energy research Corporation (ESEERCO) and the helpful discussions with Dr. J.M. Burger.

NOMENCLATURE

a_i	area weight factors used for text flux calculation (i = 1,..,3)
C_V	heat capacity of freon vapor
g	acceleration of gravity.
H	measured heat transfer coefficient
h_{lv}	enthalpy change of vaporization
j_g	superficial argon velocity
k	thermal conductivity used for numerical simulation of conduction in porous plate
k_b	bronze thermal conductivity
k_{Cu}	copper thermal conductivity
k_{f11}	thermal conductivity of gas Freon-11
k_{wd}	thermal conductivity of Woods metal
L	distance used to calculate heat fluxes (see Figure-2)
L'	enthalpy change of vaporization plus sensible heat of vapor.
q"	measured heat flux
$q"_{Be}$	heat flux predicted using Berenson correlation
$q"_{f11}$	best fit of exponential results for film boiling of Freon-11 over a non porous solid "large" surface as reported by Hosler and Westwater (1962).
$q"_{min}$	minimum heat flux for which stable film boiling is possible.
$q"_{plate}$	heat flux for film boiling over a porous plate (without Woods metal).
T_i	temperature measured by thermocouple i (i = 0,1,....,15)
ΔT	Superheat (Temperature minus saturation temperature)
ΔT_{min}	Minimum superheat for which stable film boiling is observed.
ΔT_{pp}	temperature of the porous plate, (T_1) - Freon saturation temperature (23.7°C)
ΔT_{wd}	temperature of the Woods metal, (T_{13}) - Freon saturation temperature
α_b	void fraction in the porous plate
δ	vapor film thickness
λ_d	most critical wavelength in film boiling
μ_V	viscosity of vapor
ρ_V	vapor density
ρ_L	liquid density
σ	surface tension

REFERENCES

[1] G.A. Greene et. al., "Liquid-Liquid Film Boiling of Freon 11 on Liquid Metal", Trans. Am. Nuc. Soc., 45, 1983, pp.446.

[2] R.E. Henry, D. J. Quinn and E. A. Spleha, "An Experimental Study of the Minimum Film Boiling Point for Liquid-Liquid Systems", Proceedings of the Fifth International Heat Transfer Conf., Tokyo, 1974.

[3] M.T. Farmer, J.J. Sienicki and B.W. Spencer, "CORQUENCH : "A Model for Gas Sparging-Enhanced Melt-Water Film-Boiling Heat Transfer", Trans. Am, Nucl. Soc., 62, 1990, pp.646.

[4] M.T.Farmer, J.J. Sienicki and B.W. Spencer, "The MELTSPREAD-1 Computer Code for the Analysis of Transient Spreading and Cooling of High Temperature Melts", Code Manual, ANL, 1991.

[5] G.A.Greene, "Gas Bubbling-Enhanced Film boiling of Freon 11 on Liquid-Metal Pools", Trans. Am. Nucl. Soc., 49, 1985, pp.249.

[6] M.R. Duignan, G. A. Greene and T. F. Irvine Jr., "The Effect of Surface Gas Injection on Film Boiling Heat Transfer", J. Heat Transfer, Transactions of the ASME, 115, 1993, pp. 986-992.

[7] P.J. Berenson, "Film-Boiling Heat Transfer from a Horizontal Surface", J. Heat Transfer, 83, 351, 1961.

[8] E.R. Hosler and J.W. Westwater, "Film Boiling on a Horizontal Plate", ARS J., 32, 1962, pp. 553-558.

[9] R.C. Kesselring, P.H. Ropsche and S.G. Bankoff, "Transition and Film Boiling From Horizontal Strips", AIChe J. 13, (4), 1967, pp.669-675.

[10] V.V. Klimenko, "Film Boiling on a Horizontal Plate - New Correlation", Int. J. Heat Mass Transfer, 24, 1981, pp.69-79.

[11] D.E. Kautzky and J.W. Westwater, "Film Boiling of a Mixture on a Horizontal Plate", Int. J. Heat Mass Transfer, 10, 1967, pp.253-256.

[12] R.A.W. Shock, "Boiling in Multicomponent Fluids", in *Multiphase Science and Technology*, Hemisphere Press, 1982.

NURETH7 Conference
Saratoga Springs, NY, USA, Sept. 10-15, 1995

SULTAN TEST FACILITY
LARGE SCALE VESSEL COOLABILITY IN NATURAL CONVECTION AT LOW PRESSURE

S. Rougé

Commissariat à l'Energie Atomique
Direction des Réacteurs Nucléaires/Département de Thermohydraulique et de Physique
Service de Thermohydraulique des Réacteurs
Centres d'Etudes Nucléaires de Grenoble
17 rue des Martyrs-38054 GRENOBLE CEDEX 9 (France)
Fax: (33) 76.88.52.51

ABSTRACT

The SULTAN facility (France/CEA/CENG) was designed to study large scale structures coolability by water in boiling natural convection.

The objectives are to measure the main characteristics of 2D two-phase flow, in order to evaluate the recirculation mass flow in large systems, and the limits of critical heat flux, on a wide range of thermohydraulic (Pressure: 0.1-0.5 MPa, Inlet temperature: 50-150°C, Mass flow velocity: 5-4400 kg/s/m², flux: 100-1000 kW/m²) and geometric (gap: 3-15 cm, inclination: 0-90°) parameters.

This paper makes available the experimental data obtained during the first two campaigns (90°, 3 cm) and (10°, 15 cm): pressure drops DP = f(G), CHF limits, local profiles of temperature and void fraction in the gap, visualisations.

Other campaigns should confirm these first results indicating a favorable possibility of coolability of large surfaces under natural convection.

INTRODUCTION

In case of a severe accident in a PWR leading to core melt-down, different corium retention concepts may be emphasized among which retention of debris within the lower head, or within core catchers placed under the vessel. In both cases, external surface of the retaining structure would be cooled by boiling water in natural convection.

Considering the expected heat flux levels (0.2 to 1.5 MW/m²) film boiling should be avoided, and the coolability limits will be the limits corresponding to "critical heat flux" (CHF) [1].

Hundreds of experiments in the past show that the critical heat flux depends strongly on the thermohydraulic conditions (mainly: pressure, inlet temperature, mass flow rate) and on the geometric conditions (as hydraulic diameter, inclination of heating surface) [2], [3].

But, if the particular conditions of our problem, low pressure, low flowrates, large hydraulic diameters, inclined surfaces of large dimensions, are taken into account, the experimental data reduce to nearly none, if we except the very recent experiments such as ULPU and CYBL (USA) [4], [5].

Moreover, the standard approach for CHF correlations, based on average local thermohydraulic conditions in the test section, is not applicable to large test sections, where the vapour generated by boiling can remain confined within a two-phase boundary layer along the heating surface.

Another problem is that CHF is very dependent on the local mass flow rate induced by natural convection, itself very dependent on the geometrical characteristics of the two-phase flow path, channels and restrictions. Therefore, the two aspects, system behaviour under natural convection and CHF are highly connected, and a full-scale experimental approach representing correctly the heating surface, but not the whole system itself, could lead to unrealistic data.

Considering these different points, and taking also into account that the final reactor concept (flooded lower head or core catcher, different possible designs of core catchers...) was not yet chosen in France, the SULTAN facility was designed in a spirit of an analytical approach, with a great emphasis on two phase flow measurements and code validation.

In a first approach, the system effect is not represented, and the range of mass flow rates, estimated by pre-calculation, is varied by forced convection.

The test section itself is full scale dimensioned but represents only schematically the heating structure.

The influence of the main thermohydraulic and geometric parameters is then systematically tested over a wide range of parameters.

Main characteristics of the two-phase flow, pressure drop, void fraction distributions, temperatures distributions, are measured, and will help to validate 3D codes such as CATHARE code.

The general behaviour of the two-phase water system can then be predicted, and even optimised.

The CHF results will be gathered in a data bank covering most of the situations involved.

In a second step, some realistic and heating structure and optimized two-phase water flow path will be tested together.

The purpose of this paper is to make available the experimental data obtained on SULTAN facility during the first two campaigns.

The SULTAN program is realised at Grenoble Nuclear Research Centre (France/CEA/CENG) and is supported by CEA (Commissariat à l'Energie Atomique), EdF (Electricité de France) and FRAMATOME.

SULTAN was designed in 1992, built and tested in 1993, the tests started in 1994 and should last up to 1996 [6].

I - CHARACTERISTICS OF THE SULTAN FACILITY

SULTAN facility is a demineralised and degassed water loop. It is possible to perform tests under forced convection or free convection configurations (figure 1).

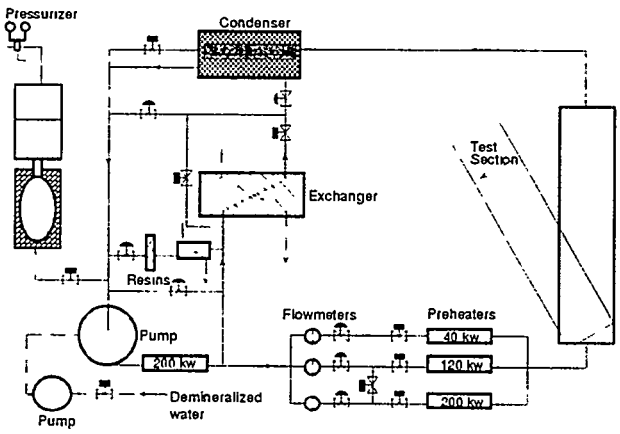


Figure 1 : SULTAN forced convection

Actually, the forced convection configuration is used, with the following characteristics:

- outlet absolute pressure: 0.1 → 1 MPa (P)
- inlet temperature: 50 → 180 °C (Te)
- mass flow velocity: 5 → 5000 kg/s/m² (G_{se})
- heat flux: 0.1 → 1 MW/m² (ϕ_{se})

II - THE TEST SECTION

Description

The test section itself simulates schematically a slice of the vessel (lower head or core catcher).

A rectangular flat stainless steel plate 4 × 0.15 m² is heated electrically by direct Joule effect, and cooled on one side in a rectangular channel (figure 2). The section of the channel can vary from 0.15 × 0.03 m² to 0.15 × 0.15 m², the distance between the heating plate and the opposite wall or "gap" is one of the geometric parameters of tests.

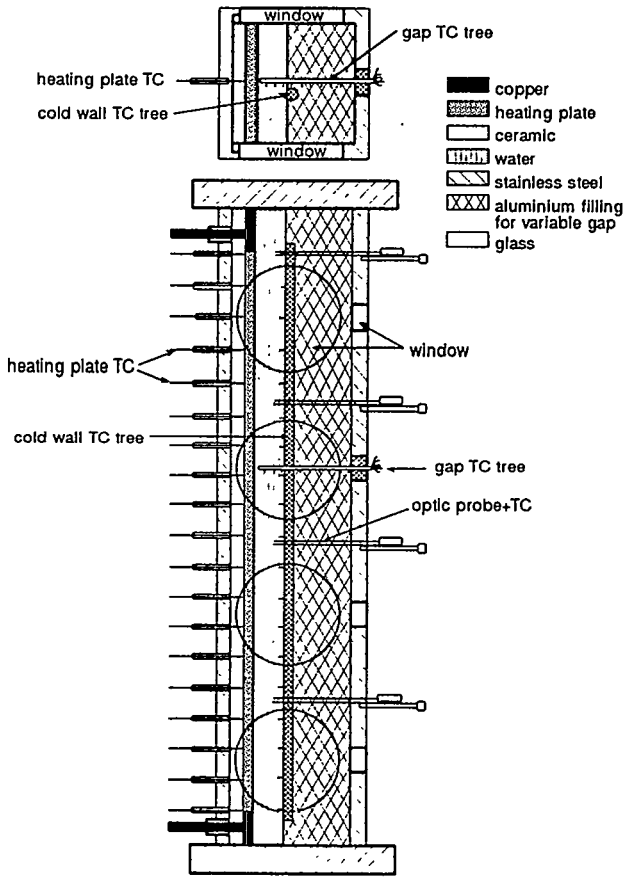


Figure 2 : SULTAN test section

The test section can also be put from the vertical position to the horizontal position with heating plate above water, to simulate the effect of inclination.

The plate is electrically insulated from the rest of the test section by ceramics. It is maintained every 10 cm to prevent local deformations by thermal stress, but can expand freely.

The heating plate is 1.5 mm thick, its uniform thickness is controlled before tests to guarantee for a uniform heat flux.

Of course, this thin plate has small thermal inertia compared to the inertia of a reactor lower head wall with a residual thickness of, say, 4 cm. For comparison based on avoiding melting, at 1 MW/m², the maximum permanent allowed dry patch should be about D = 4 cm for the vessel and only D = 1.5 cm for the thin plate. If we consider intermittent big dry patches, durations of 80 s are allowed for the vessel, and only 7 s for the thin wall.

Another inconvenience is that the tests are more difficult to perform and can easily lead to the destruction of the plate.

But, on another hand, we can insure that the limits of CHF measured on SULTAN are conservative with regard to reality.

Instrumentation

The test section is instrumented, as well as the pipe at its outlet (figure 3).

For the test section itself:

- inlet absolute pressure
- outlet absolute pressure
- inlet mass flowrate: 3 nozzles
- inlet fluid temperature: 3 Pt probes
- outlet fluid temperature: 3 Pt probes
- electrical voltage and current. Use × Ise
- pressure drop: 14 DP transducers giving 1 DP every 1 meter
- axial profile of fluid temperature: "Cold Wall TC tree" made of 20 type K TC
- radial profile of fluid temperature : "Gap TC tree" made of 10 type K TC
- axial profile of heating plate temperature: 38 non isolated type K TC welded on the back of the plate
- 1 radial profile of local void fraction and of local fluid temperature every 1 m: a moving table (15 cm displacement) supports a type K TC and an optic fiber probe
- visualisation: 4 sets of 3 windows every 1 m to make visual observations and video films.

For the outlet pipe:

- outlet absolute pressure
- outlet fluid temperature: 1 Pt probe
- pressure drop: 4 DP transducers

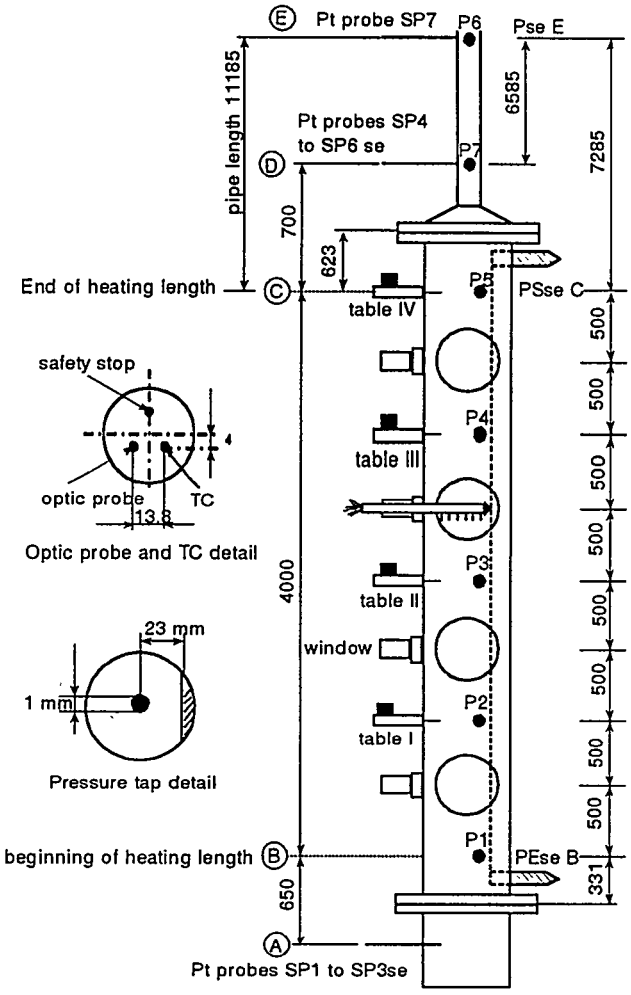


Figure 3 : SULTAN test section instrumentation

The data acquisition is made with a Hewlett Packard 3852 system every 10 s, the data are averaged on 5 to 15 acquisitions and stored, so that a complete recording of each test is retained.

For the void fraction measurement, the acquisition is made every 1 s as long as necessary to tend towards an average. Generally, data acquisition during 1 to 3 mn is necessary.

The data are measured with the following accuracy:

- Absolute and differential pressure: ± 1%
- fluid temperature with Pt probes: ± 0.25°C
- fluid temperature with TC: ± 0.5°C
- heating wall temperature: ± 15°C

These thermocouples are not insulated and the error due to the voltage of the plate must be compensated.

Their role is mainly to detect the limit of boiling crisis.

- mass flow rate: ± 2% relative
- electrical flux: ± 1% relative
- void fraction: no precision estimate
- relative position in gap: ± 0.01 mm
- absolute position in gap: ± 1 mm

These precisions are only valid for steady state conditions and can be degraded in pulsated flows, or when shocks due to condensation occur.

The tests are performed in quasi steady state conditions only.

III - TEST CAMPAIGNS AND OPERATING PROCEDURES

Each test campaign corresponds to a geometric configuration of the test section:

- 1 gap
- 1 inclination

Inside a campaign, two kinds of tests are perfomed, the first one aims to determine the internal characteristics DP = f(Gse) of the test section, and the limits of critical heat flux, the second to measure profiles of temperatures and void fractions.

For the first kind of tests, the outlet pressure and the inlet temperature are held constant, the flowrate is decreased very slowly with a constant ratio $\Delta Q/Q$ of about 2% per mn for different levels of heat fluxes up to the CHF limit or to the minimal flowrate available. A complete test can last 1 week.

For the second kind of tests, all the parameters are held constant, and measurements are made at different positions inside the gap. It takes about one hour to achieve a profile.

The limits of critical heat flux are determined by a sharp increase of the temperature of the plate above a given level set at Tsat + 100°C. Small oscillations of thermocouples (up to 40°C), very often observed, are not taken into account.

Electrical power is then automatically reduced by 15%, or even switched off . Dry patches are sometimes difficult to rewet when the detection thermocouples are not exactly located on the dry spot.

The whole experimental program made in 1994 is summarised below:

	Gap (m)	Inclination (° from horizontal)
1st campaign	0.03	90° (vertical)
2nd campaign	0.15	10°

Each campaign includes:

First campaign:

Cover pressure (MPa)	Inlet temperature (°C)	Heat flux levels (kW/m²)	Flow rate (kg/s/m²)
0.1	50	100 → 1000	20 → 4400
0.5	100	100 → 1000	20 → 4400
0.1	99	100 → 1000	20 → 4400
0.5	150	100 → 1000	20 → 4400

Measurements:

- Internal characteristics DP = f(Gse)
- CHF limits
- Axial profile of fluid temperature (cold wall)

Second campaign:

Cover pressure (MPa)	Inlet temperature (°C)	Heat flux levels (kW/m²)	Flow rate (kg/s/m²)
0.1	50	100 → 1000	5 → 1800
0.5	100	100 → 1000	5 → 1800
0.1	99	100 → 1000	5 → 1800
0.5	150	100 → 1000	5 → 1800

Measurements:

- Internal characteristics DP = f(Gse)
- CHF limits
- Axial profile of fluid temperature (cold wall)
- Radial profiles of fluid temperature and void fraction
- Visual observations and video films

IV - RESULTS OF THE FIRST CAMPAIGN AND INTERPRETATION

The first campaign of tests, (vertical position and 3 cm gap) is presented and analysed: an evaluation of the recirculation mass flow rate in a free convection system is simply predicted, the levels of critical heat flux are given.

In two-phase flow recirculation, different types of instabilities may occur: static and dynamic instabilities.

Static instabilities concern the mean mass flow rate which may decrease to very low values and induce CHF.

Dynamic instabilities are periodic flow oscillations around a mean value of the mass flowrate,

they may also lead to periodic dry out and rewetting of the heating surface. In this case, thermal inertia of the wall and mechanisms of rewetting are very important.

SULTAN forced convection tests only deal with static instabilities, and give the general behaviour of the system, natural convection tests in the future will have to study the effects related to the dynamic instabilities.

Static instabilities are studied with the well known approach of External and Internal Characteristics (EC and IC).

Of course, this approach is limited to systems where a clear water circuit may be identified, and where no predominant 3D effects exist.

The whole flow path is separated into two parts, the hot leg in two-phase flow and the cold leg in single phase flow. Each circuit is defined by its "Characteristic", that is the variation of pressure drop versus the mass velocity flowing through this part $\boxed{\Delta P = f(G)}$ for given thermohydraulic conditions.

The "Internal" Characteristic is attributed to the hot leg, the "External" Characteristic to the cold leg.

The determination of the Internal and External Characteristics will provide:

- the recirculation mass flowrate at the intersection of both Characteristics (Working Point)
- the stability of the Working Point: a static instability develops if the LEDINEGG criterion $(DP/DQ)_{int} > (DP/DQ)_{ext}$ is not fulfilled. Dynamic instabilities can also, to some extend, be predicted as they are related to the slope differences of both Characteristics.

Classical EC and IC for channel with small hydraulic diameters are given as an example on figure 4.

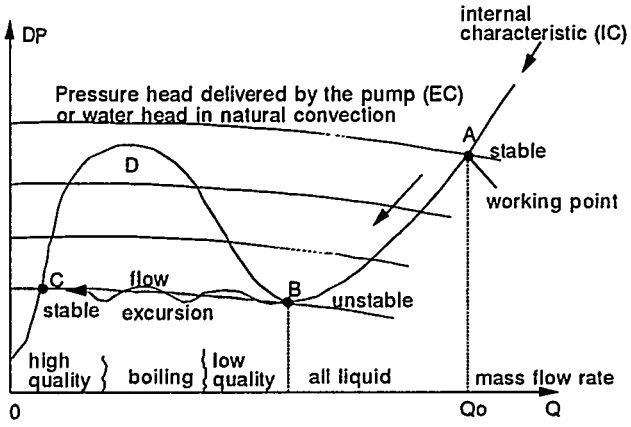


Figure 4 : Internal and external characteristics (classical shapes)

In the case of larger hydraulic diameters (Dh > 2 cm), calculations predict that the Internal Characteristics are continuously increasing. In that case, no static instabilities can develop.

That important point was confirmed by SULTAN first campaign: the pressure drop over the test section DP15se (IC) decreases continuously with the decrease of the mass flowrate, for any conditions of pressure, inlet temperature or heat flux tested (figures 5, 6).

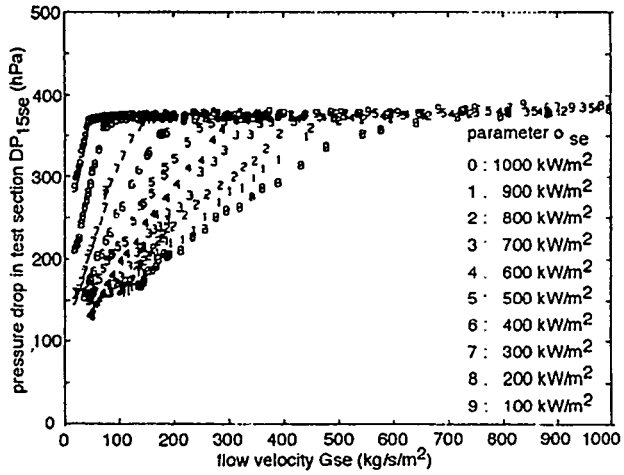


Figure 5: Internal characteristics of test section 1st campaign (90°, 3 cm) P = 0.5 MPa Te = 100°C

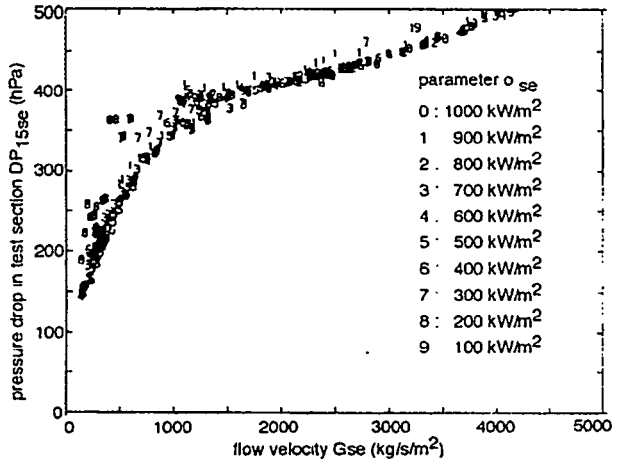


Figure 6: Internal characteristics of test section 1st campaign (90°, 3 cm) P = 0.1 MPa Te = 99°C

If the cold circuit is optimised, with little pressure drop due to restrictions and friction, the recirculation flow may be rather high.

A nonheating pipe with two-phase flow above the heating length (test section + outletpipe) may even

provide a chimney effect and increase this flowrate (figure 7).

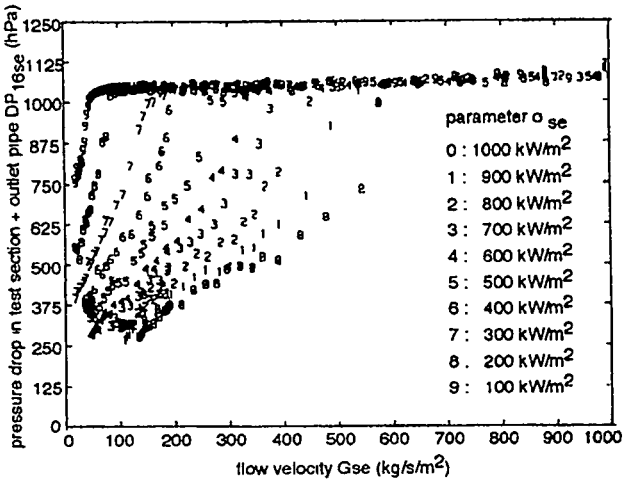


Figure 7: Internal characteristics of test section + Outlet pipe
1st campaign (90°, 3 cm) P = 0.5 MPa Te = 100°C

At a given heat flux, the slope of the Internal Characteristic is rather flat at high mass flowrate and becomes steeper after average saturation (thermodynamic outlet quality Xth = 0) is reached (figure 8).

The CHF points are always located in regions where Xth > 0.

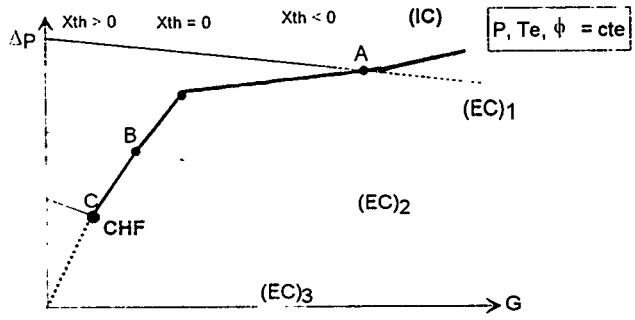


Figure 8: Internal and External Characteristics (large hydraulic diameters shapes)

Working point A could lead to large dynamic flow oscillations, since the slopes of IC and EC are quite closed, but with no real danger of dry out as CHF point is very far.

Point B is more stable, since the IC and EC slopes are quite different, but the flowrate is lower and CHF limit is not so far away.

Point C leads to the destruction of the plate.

In natural convection, in so far as the cold leg (EC) is optimised and a good chimney effect is provided, the working point could easily be located between points A and B.

In that case, coolability for vertical surfaces of large dimensions can be assumed for any conditions of cover pressure and inlet temperature in the range of P = 0.1 - 0.5 MPa ; Te = 50 - 150°C ; and for heat fluxes up to 1 MW/m².

Of course, this analysis has to be confirmed on a demonstrative test section with real geometry tested under natural convection.

CHF generally occurs within the last meter of the heated plate and under some circumstances even at lower levels.

Dry patches are generally rather small, about 2 to 6 cm². When CHF is detected lately, dry patches expand towards the bottom of the plate with an oblong shape, but their surface never exceeds 50 cm², since the thin plate melts rapidly.

The CHF results are reported on figure 9.

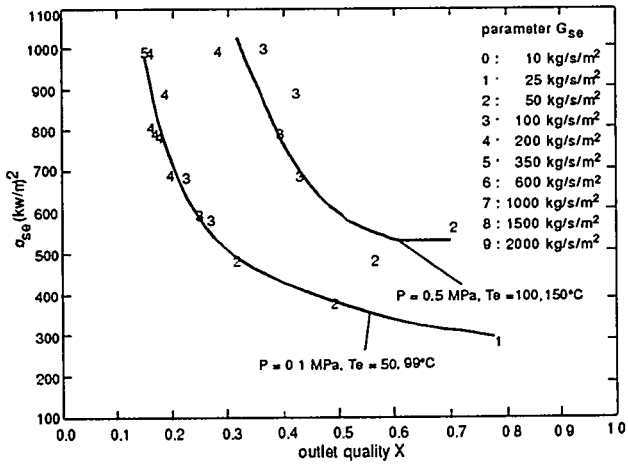


Figure 9: CHF limits : Heat flux versus outlet quality
1st campaign (90°, 3 cm)

The CHF limit increases when the pressure or the mass velocity increases. There is no influence of the inlet temperature if the points are compared at outlet average conditions, which is rather normal as CHF is always observed to occur for saturated conditions (Xth > 0).

These results have been compared with Groeneveld's Data Table [Ref. 3], with the maximal correction for hydraulic diameter (K = 0.79) recommended.

This comparison reveals a great discrepancy between the table and the experimental results. Groeneveld's table overestimates CHF by nearly a factor of 2 at low quality (Xth < 0.2) and underestimates CHF by about 20% at high quality (Xth > 0.6).

This is not surprising since the test conditions in SULTAN are very far from the validity conditions of Groeneveld's Data.

V - SECOND CAMPAIGN (10° INCLINATION FROM HORIZONTAL, GAP 15 CM) PRELIMINARY RESULTS

Pressure drop measurements, CHF limits, visualisations through windows, video films and radial profiles of local fluid temperatures and void fractions have been performed.

Visualisations show that the flow is highly 2D, with a two-phase flow boundary layer localized near to the heating plate.

The interface between the two-phase and liquid regions is quite well defined, but becomes very weavy when quality increases. The flow can even come to a SLUG type flow at low heat fluxes 100-300 kW/m² and low mass velocities 5-50 kg/s/m², with periodic rewetting of the plate (period ≈ a few seconds).

Visualisation is not sufficient for a good understanding of the two-phase flow. Local measurements prove that, for rather high void fraction near the plate, the fluid can remain highly subcooled (figure 10).

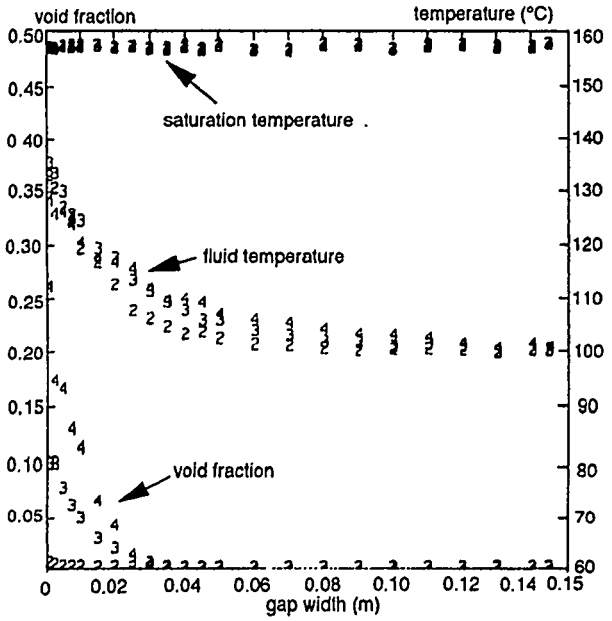


Figure 10: Profiles of void fraction and liquid temperature in gap at +2 m (2), +3 m (3) and +4 m (4) in test section
2nd campaign (10°, 15 cm). P = 0.5 MPa, Te = 100°C, G_{se} = 700 kg/s/m², φ_{se} = 1000 kW/m²

The pressure drop measurements show the same tendancies when compared with the first campaign, but with a significative difference : if we consider natural convection with a liquid head corresponding only to the elevation of the inclined test section, it would be possible to avoid CHF only for low heat fluxes (φ < 300 kW/m²) - figure 11).

It is important to notice that, for the particular geometry of the second campaign, natural convection mass flow rates would be much greater if we take into account the test section + the outlet pipe (DP16se) (figure 12).

This last point is very important, as it confirms that, in natural convection tests, a whole system and not only the heating part must be represented in order to provide a good evaluation of the CHF limits.

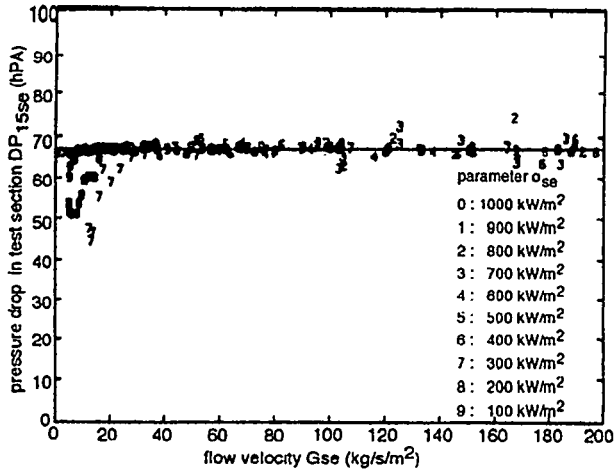


FIGURE 11: Interal characteristics of test section 2nd campaign (10°, 15 cm). P = 0.1 MPa, Te = 50°C

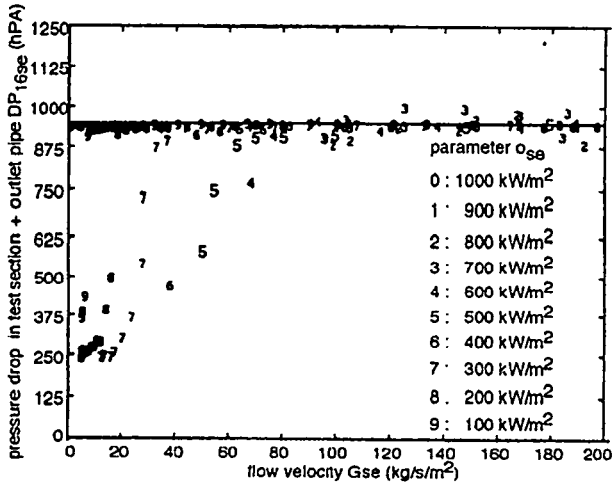


FIGURE 12: Interal characteristics of test section + outlet pipe
2nd campaign (10°, 15 cm)
P = 0.1 MPa, Te = 50°C

The CHF results are gathered on figure 13 and figure 14.

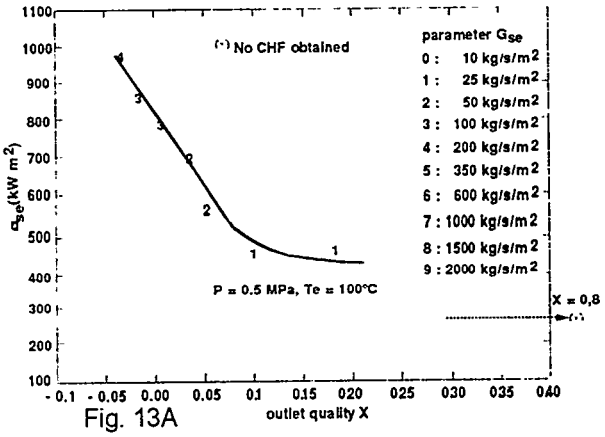


Fig. 13A

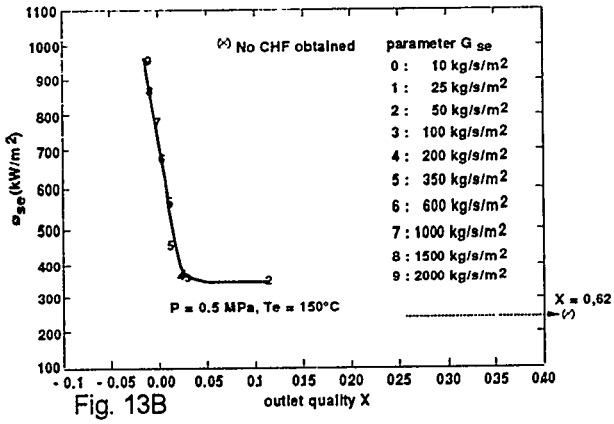


Fig. 13B

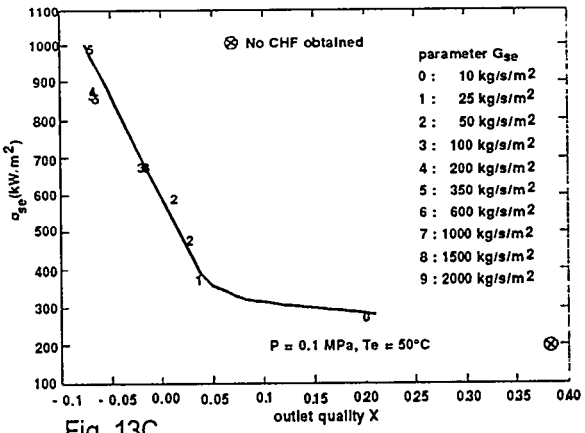


Fig. 13C

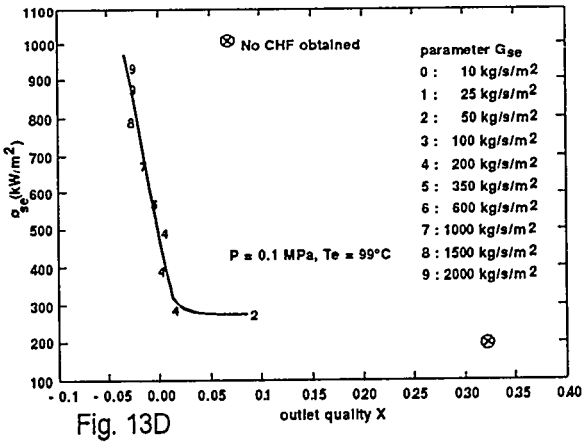


Fig. 13D

Figure 13: CHF limits : Heat flux versus outlet quality. 2nd campaign (10°, 15 cm) Influence of pressure and subcooling

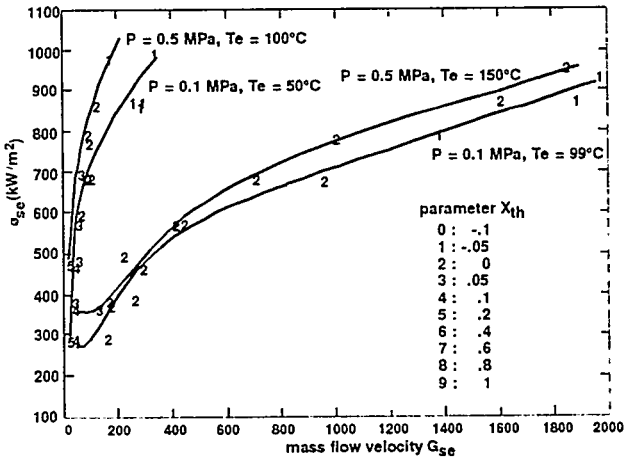


Figure14: CHF limits : Heat flux versus mass flow velocity. 2nd campaign (10°, 15 cm) Influence of pressure and subcooling

As for the 1st campaign, there is a small influence of the pressure.

The influence of subcooling is much more important than for the 1st campaign.

For near saturation inlet conditions, the influence of mass velocity on CHF becomes predominant.

At low mass velocities, CHF curves tend towards an asymptotic limits (φ > 200 kW/m² at 0.1 MPa, φ > 300 kW/m² at 0.5 MPa).

Visualisation allows to explain this phenomenon: at low heat flux and low mass velocity, we observe a type of SLUG flow, with rewetting of the plate every 2 to 3 seconds. A film of water remains on the plate and tends to evaporate but has no time enough to dry out before next water reflooding. This particular regime can be maintened for hours without occurence of CHF. Local measurements give then average void fractions up to 95% with two-phase boundary layers thicker than 10 cm.

At higher heat fluxes, this particular wetting mecanism cannot persit any more and CHF occurs before reaching SLUG flow regime.

CONCLUSION

Other campaigns with different inclinations and gaps will be performed on the SULTAN facility. The pressure drop measurements and CHF results will help to optimize a circuit in natural convection. Local measurements are very important in large sections, as the flow is very 2D, with vapour staying near by the heating surface, and SULTAN will help to validate the 3D two-phase CATHARE code.

The results of the first two campaigns indicate favorable possibilities of coolability of large surfaces under natural convection, especially the first one which indicates clearly that heat fluxes larger than 1 MW/m² may be removed under natural water circulation conditions, provided that the water circuit is well designed and optimized.

The results obtained on the SULTAN facility are in agreement with the results obtained on other existing large scale experiments (ULPU at UCSB). Furthermore the influence of pressure mass flow rates, inlet subcooling, channel width and inclination are separately characterized.

BIBLIOGRAPHY

1. ROUGÉ S., SEILER J.M., Core debris cooling with flooded vessel or core catcher. Heat exchange coefficients under natural convection. CSNI-PWG-4 (June 1994)
2. COLLIER J.G., Convective boiling and condensation, McGraw-Hill Book Co. (1981)
3. HEWITT G.F., DELHAYE J.M., ZUBER N., Multiphase Science and Technology, volume 2, Hemisphere Publishing Corp. (1986)
4. T.G. THEOFANOUS et al., Critical heat flux through curved, downward facing, thick walls. OECD/CSNI/NEA Workshop on Large Molten Pool Heat Transfer, Grenoble (France) , 9-11 march 1994
5. T.Y. CHU et al., Large scale boiling experiments of the flooded cavity concepts for In-Vessel core retention, OECD/CSNI/NEA Workshop on Large Molten Pool Heat Transfer, Grenoble (France) , 9-11 march 1994
6. BONNET J.M., ROUGÉ S., SEILER J.M., Large scale experiments for core melt retention - BALI : corium pool thermalhydraulics - SULTAN : boiling under natural convection, OECD/CSNI/NEA Workshop on Large Molten Pool Heat Transfer, Grenoble (France) , 9-11 march 1994

RESUME (EN FRANÇAIS)

L'installation SULTAN (France/CEA/CENG) a été conçue pour étudier le refroidissement externe en convection naturelle de la cuve d'un REP, ou d'un récupérateur de corium, en cas d'accident grave.

Les résultats dans deux configurations géométriques extrêmes (90°, 3 cm et 10°, 15 cm) sont présentés : les débits de convection naturelle sont évalués par la méthode des caractéristiques internes et externes, les points de crise d'ébullition sont donnés sur la gamme 0.1-0.5 MPa, 50-150°C, 5-4400 kg/s/m², 100-1000 kW/m².

Les premières mesures de profil de température et de taux de vide caractérisant l'écoulement fortement 2D sont fournies.

Ces premiers résultats tendent à confirmer la possibilité de refroidissement en convection naturelle.

AN INTEGRAL MODEL FOR THE CALCULATION OF HEAT FLUX DISTRIBUTION IN A POOL WITH INTERNAL HEAT GENERATION

J.M. Bonnet
Commissariat à l'Energie Atomique C.E.N.G[i]
DRN/DTP Service de Thermohydraulique des Réacteurs[ii]
17 rue des Martyrs - 38054 GRENOBLE CEDEX 9 (France)
(33) 76.88.97.17

ABSTRACT

A simplified model of heat transfer from a volume heated pool has been developed on behalf of IPSN[iii] for use in reactor accident codes. These codes have to handle many physical phenomena and cannot describe the internal pool thermohydraulics with great details as could be done with sophisticated codes. For the description of corium pools, the needs concern mainly the knowledge of the heat flux distribution at the boundaries as a function of the geometry. The model is restricted to pool situations corresponding to high Rayleigh numbers (10^{+15} or higher), so for turbulent boundary layer flows; this is the case of concern for reactor situations. The model also treats homogeneous pools. A constant temperature is considered as the boundary condition for the bottom heat transfer calculation and different boundary conditions may be considered for upward heat transfer (crust or liquid surface with radiation). The model predictions are compared with results obtained for different geometries (BAFOND, COPO, ..) The simplified approach will allow in a second step to take into account geometry evolution during the propagation of a corium pool in the core or in a debris bed.

I. FORMULATION OF THE MODEL

A. General overview

The model assumes that the lower part of the pool can be divided into a bulk central region and an external boundary layer. Due to the natural convection flow, the heated liquid rises in the bulk central region and releases sensible heat by flowing down at the boundary layer (b.l.).
A pool formed by only one volumetrically heated oxidic component is considered.

If the pool is also cooled from the top, the presence of a cold boundary leads to the formation of an unstable upper layer. Periodically the cold fluid returns to the bulk as cold tongues. As a result, the well mixed upper layer is assumed to be at a uniform temperature. Furthermore, this temperature will be the maximum temperature of the pool.

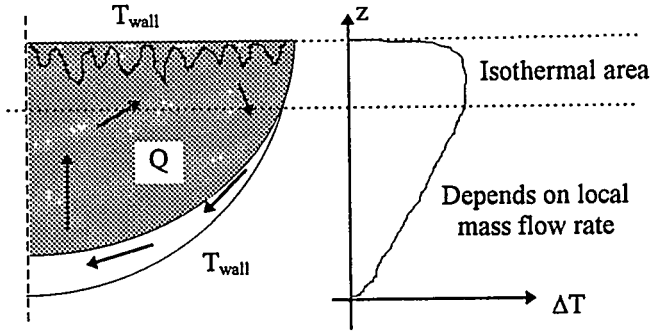


Figure 1 : Description of the assumed flow

The general modeling principle is based on the determination of the heat flux distribution using the temperature profile along the center line and a local heat transfer correlation.

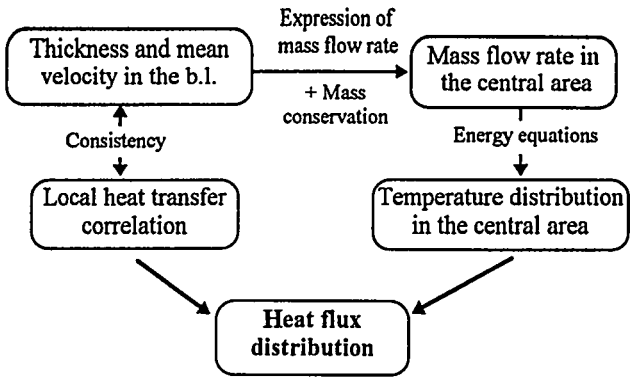


Figure 2 : General overview of the model

B. Energy equations in the central area.

In our 1D model, the pool is axially divided into slices of thickness dz with a central area and a boundary layer area.

To calculate the enthalpy transfer between the boundary layer and the bulk central area, we assume uniform radial temperature distribution for each region. It is physically justified for the central region in which the radial temperature profile is expected to be quite flat and it is a necessary simplification for the boundary layer. Heat conduction and viscous dissipation terms are neglected.

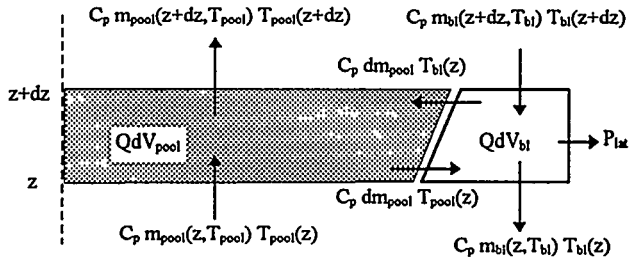


Figure 3 : Power balance on a slice of thickness dz

If we consider only the central area we obtain the following equations:

- For a mass transfer from pool to boundary layer :

$$QdV_{pool} - C_p \frac{dm_{pool} T_{pool}}{dz} dz = -C_p T_{pool} \frac{dm_{pool}}{dz} dz \qquad (1a)$$

- For a mass transfer from boundary layer to pool :

$$QdV_{pool} - C_p \frac{dm_{pool} T_{pool}}{dz} dz = -C_p T_{bl} \frac{dm_{pool}}{dz} dz \qquad (1b)$$

If the mass transfer occurs from boundary layer to the central part of the pool, the boundary layer temperature T_{bl} has to be known. To reach this objective we have three possibilities : 1) to write a power balance in the boundary layer area and solve both equations 2) to use a temperature profile in the boundary layer to calculate the mean temperature. (such as $T_{bl}=1/8T_{wall}+7/8T_{pool}$ for Eckert's temperature profile) and 3) to assume that the recirculation occurs at a temperature equal to T_{pool}. (In relation to the second way the error is less than 12.5 %)

Due to the fact that recirculation from boundary layer to pool is significant only in a few meshes in the lower part of the pool and also to keep the approach as simple as possible, we choose the easiest way to express T_{bl} by assuming $T_{bl} = T_{pool}$.

In that case the equations (1a) and (1b) reduce to :

$$\frac{dT_{pool}}{dz} = \frac{Q dV_{pool}}{C_p m_{pool} dz} \qquad (2)$$

C. Coupling with the upper layer

In our model we consider that the well mixed upper area is globally isothermal at T_{max} and bounded in its lower part by a virtual adiabatic plane ($\frac{dT_{pool}}{dz} = 0$).

We assume that the enthalpy rate which goes through this virtual plane is entirely redistributed to the boundary layer. Thus we consider that all the volumetric power generated in the top layer (excluding the volume of the boundary layer) is removed from the upper surface.

The lateral heat flux is calculated on the same basis as in the lower part of the pool. (Heat transfer correlation and temperature difference T_{pool}-T_{wall}).

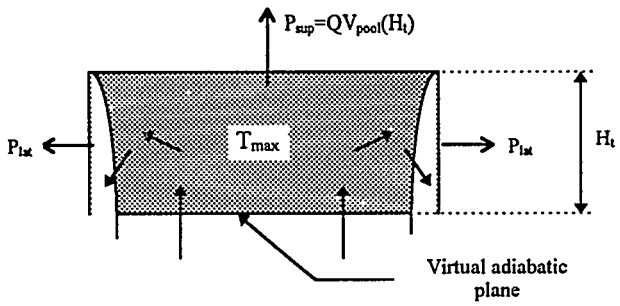


Figure 4 : Unstable upper layer

The relation between the maximum temperature difference and the height of the unstable upper layer is determined using Kulacki's heat transfer correlation.[3]

$$Nu = 0.345\, Ra^{0.226} \text{ avec } Ra = \frac{g\beta Q H_t^5}{\lambda \nu \alpha} \text{ et } Nu = \frac{\varphi H_t}{\lambda \Delta T}$$

This correlation was established for rectangular slice, volumetrically heated and cooled only through the upper surface. Validity range : $2.10^{+04} < Ra < 4.4\ 10^{+12}$, $2.75 < Pr < 6.85$ and $0.025 < H_t/D < 0.50$.

We choose Kulacki's correlation because it's application conditions are close to our model approach excepted for the fact that there is no rigid adiabatic plane. Even if the range for Rayleigh numbers is not high enough, the advantage of this correlation is to allow independent treatment of the upper layer for different pool geometries. We obtain a relation between ΔT_{max} and H_t.

$$\Delta T_{max} = \frac{H_t^{-0.13}\, V_{pool}(H_t)\, Q^{0.774}}{0.345\lambda \left(\frac{g\beta}{\lambda \nu \alpha}\right)^{0.226} S_{pool}} \qquad (3)$$

With this expression, the coupling with the upper layer is ensured. For each elevation the local temperature is compared to the maximum difference given by expression (3).

In case of radiative transfer from the upper surface, the coupling is made also by iteration on the temperature of the free surface.

D. Calculation of heat flux profile

The global balance in the pool is calculated by integration of local heat flux distribution along the upperward, sideward and downward walls.

The local heat flux is calculated from a local heat transfer correlation depending on the local inclination and on the local temperature difference between the centre line of the pool and the wall.

$$\varphi = h(\alpha, \Delta T)(T_{pool} - T_{wall})$$

The heat transfer coefficient is supposed to be given by Chawla's correlation : [2]

$$h(\alpha, \Delta T) = F(\mathrm{Pr})\lambda\left(\frac{g(\alpha)\beta\Delta T}{\upsilon^2}\right)^{1/4}$$

This correlation corresponds to the case of a turbulent boundary layer along a vertical or an inclined plate (up to 30° from the vertical line).

The expression of Nussselt as a function of $Gr^{1/3}$ implies that the heat transfer coefficient depends only on the local temperature difference and on the local gravity (inclination).

For the bottom of cylindrical geometry we have to use different correlations (Steinberner correlation for example).[8] Nevertheless, most of time the heat transfer from the bottom is negligible and in a first step it is not taken into account.

E. Mean flow rate in the boundary layer

The starting point of the model is the analytical expression of the mean flow rate in the boundary layer and the expression of heat transfer law which have to be consistant.

In order to calculate the mean flow rate our first approach was based on the semi-theoretical work by Eckert and Jackson which opens the way to establish velocity and temperature profiles analytically in a turbulent boundary layer.[1] Their work is based on an integral model (developped for Pr = 0,7), supported by a number of assumptions with respect to the velocity profiles, the temperature profiles, the friction equation and the heat transfer equation.

Velocity profile in b.l. : $$\frac{u}{u^*} = \left(\frac{y}{\delta}\right)^{\frac{1}{7}}\left(1 - \frac{y}{\delta}\right)^4$$

Temperature profile in the b.l. : $$\theta = \frac{T_{pool} - T}{T_{pool} - T_{wall}} = \left(1 - \left(\frac{y}{\delta}\right)^{1/4}\right)$$

These authors used the following definitions for the characteristic velocity and the thickness of the boundary layer:

$$u^* = \sqrt{g\beta\Delta T x}$$

$$\delta = 0.6 \times Gr^{-0.1}$$

Nevertheless, the use of these correlations tends to overpredict the mass flow rate by a factor of about 3 (as shown by the interpretation of the BAFOND experiments), consequently the temperature profile and thus the heat flux distribution are not well predicted. This discrepancy was attributed to a limitation of the validity of Eckert's laws. In particular, the influence of Prandtl number is not taken into account. As it is the case in laminar regime, we may assume that such a dependency also exists in turbulent regime.[5]

We attempted to express this dependency by determining a characteristic velocity and a characteristic thickness for the boundary layer by introducing corrections factors f_1 and f_2:

$$u^* = f_1(Pr)\sqrt{g\beta\Delta Tx}$$

$$\delta = f_2(Pr) \times Gr^{-0.1}$$

The integration of momentum and energy equations in the boundary layer allowed us to determine expressions for f_1 and f_2. In the same time with this integral model we ensure consistency between heat transfer law and expression of mean velocity or thickness in the boundary layer.

Following assumptions are made:

1 It is assumed that the thickness of the thermal boundary layer is equal to the thickness of the momentum boundary layer. ($Pr_t \sim 1$)
2 It is assumed that u* takes the form of a constant times x^p (ΔT constant: semi-infinite medium)
3 It is assumed that δ takes the form of a constant times x^q(ΔT constant: semi-infinite medium)
4 An expression is consedered for the Nusselt number of the form : $Nu = F(\mathrm{Pr})\, Gr^n$
5 The expression of the friction term has been determined on the basis of Colburn's analogy (forced convection).
6 We have neglected the volumetric heat generation in the boundary layer.

The integration of momentum and energy equation in the boundary layer using the Chawla correlation for the heat transfer (this calculation is not detailed here) leads to the following expressions for u* and δ.

Characteristic velocity :

$$u^* = \left(8\left(7.84\,10^{-2} + 3.66\,10^{-2}\,\mathrm{Pr}^{3/4}\right)\right)^{-1/2}\sqrt{g\beta(T_{pool} - T_{wall})x}$$

$$u^* = f_1(\mathrm{Pr})\sqrt{g\beta(T_{pool} - T_{wall})x}$$

Boundary layer thickness :

$$\delta = \frac{\left(8\left(7.84\,10^{-2} + 3.66\,10^{-2}\,\mathrm{Pr}^{3/4}\right)\right)^{1/2} F(\mathrm{Pr})}{3.66\,10^{-2}\,\mathrm{Pr}} x Gr^{-1/4}$$

$$\delta = f_2(\mathrm{Pr}) x Gr^{-1/4}$$

with $$F(\mathrm{Pr}) = \frac{0.15\,\mathrm{Pr}^{1/4}}{\left(1 + \left(\frac{0.492}{\mathrm{Pr}}\right)^{9/16}\right)^{16/27}}$$

The mean flow rate in the boundary layer is derived from these expressions, as a function of the curvilinear abscissa and local temperature difference.

In the expression of boundary layer thickness we observe that the exponent affecting the Grashof number, (-1/6) is not the same as in Eckert's relations. We would have obtained an exponent (-1/10) if we had considered a Nusselt law expressed as a function of Gr at the power 2/5.

It is now possible to derive the functions f_1 and f_2 and determine their effect on the characteristic thickness and velocity in the boundary layer.

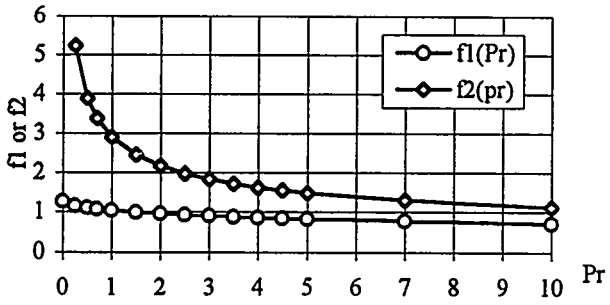


Figure 5 : Variation of f_1 and f_2

The factors f_1 and f_2 decrease with the Prandtl number, but the effect is more significant for f_2, i.e. on the thickness of the boundary layer. f_1 remains, in all cases, close to unity and so the effect on the velocity is less important.

It is now possible to explain a reduction of the recirculating mass flow rate (and thus on the axial temperature distribution) observed for BAFOND (Pr number around 7) with original Eckert's expression (Pr number around 0.7).

More detailed justification of the model would need analysis of other experimental results (not available in the open litterature) in order to obtain independent validation for the analytic expressions of mean velocity and boundary layer thickness for fully developped turbulent boundary layers.

II. VALIDATION

A. Validation on BAFOND experimental results.

The BAFOND experimental program has been developped in the CENG CEA on behalf of IPSN, to study natural convection in volumetrically heated liquid pool. This experiment was applied to FBR assembly.[7]

The facility consists in a cylindrical water pool, heated by Joule effect (upper and lower disks form electrodes) and cooled at constant temperature through upper, lateral and lower surfaces. Measurements included: 1) temperature profiles on the axis of the pool, 2) temperature profiles in the boundary layers and 3) velocities on the axis of the pool.

For the validation of FLUXBAIN we choose a high Rayleigh number experiment, and a large H/D aspect ratio, in order to get a turbulent regime over a great height in the boundary layer.

Characteristics.

- Cylindrical geometry: $R = 0.18$ cm $H = 1.08$ m
- Dissipated power $P = 8$ kW
- Uniform wall temperature $T_{wall} = 20°C$
- Internal Rayleigh number $Ra = 2.54\ 10^{+15}$ (Water physical properties at 20°C)

Temperature profile

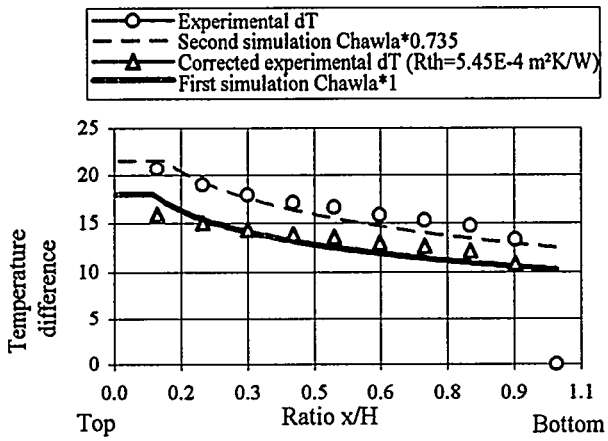


Figure 6 : Tpool-Twall in BAFOND test n°74

Two calculations was carried out. The first was made without any adjustment and the second by a modification of the lateral heat transfer correlation (multiplied by about 0.7).

A thorough analysis of the experimental results showed that these adjustments are physically justified: a supplementary thermal resistance has to be taken into account due to the presence of a thin varnish layer deposited on the lateral surfaces to ensure electrical insulation. This insulation layer can be taken into account either through an additionnal thermal resistance ($5.4\ 10^{-4}$ m²K/W) or through a decrease of the lateral heat transfer (factor 0.7). If this correction is taken into account, a satisfactory agreement between experiment and calculation is obtained.

Velocity profile on axis

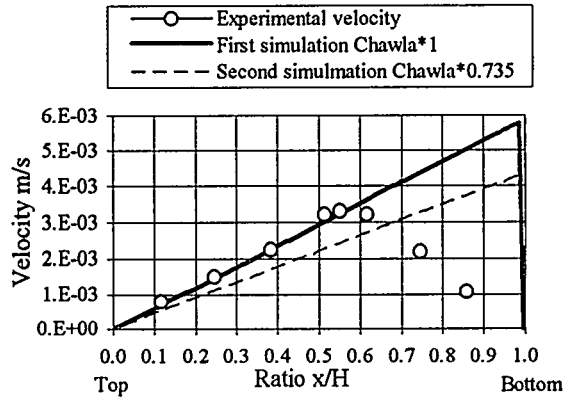


Figure 7 : Velocity profile on axis BAFOND test n°74

In the calculation, at mid-height, a velocity of 3 mm/s is calculated which is comparable with the experimental value of about 3.2 mm/s.

In the frame of our assumptions, it is not possible to describe the bottom effect which gradually induces a decrease of the boundary layer flow (2D effect). So it is not surprising that the description of the lower zone is incorrect. Nevertheless the effect on the whole temperature profile is limited.

B. Validation on COPO experimental results. [4]

The COPO facility has been constructed for the study of the heat transfer from a molten corium pool. The geometry reproduces the lower head of a VVER-440 reactor at scale 1:2.

The corium pool consists of a two-dimensional slice heated by Joule effect. The simulant fluid is water with zinc sulphate addition to adjust the electrical conductivity.

Several runs, with different power levels, are available. Our numerical calculations are based on run fh2 for which the power level and so the Rayleigh number are the highest. [4]

Characteristics and hypotheses.

- Elliptic bottom $2a = 0.8$ m, $2b = 1.77$ m
- Dissipated power $P = 5.2$ kW
- Uniform wall temperature $T_{wall} = 63.7°C$
- Liquid height $H = 0.8$ m
- Internal Rayleigh number $Ra = 1.5\ 10^{+15}$

The power balance otained from the integration of measured heat fluxes does not agree with the total dissipated power P. It is assumed that the difference about 16.7% represents the thermal losses through front and back faces or the measurement uncertainties.

Two calculations were carried out. The first was made without any adjustment and the second with two adjustments: one on the lateral heat transfer law (factor 0.6) and the second on the upward heat transfer law (factor 2.2).

The correction factor affecting the lateral heat transfer may have the same justification as for the BAFOND experiments: the cooling units of the COPO facility are insulated by means of a thin (0,1 mm) Teflon layer. The thermal resistance associated to this insulation layer corresponds to a reduction of the lateral heat transfer by about 30%.

The correction factor on the upward heat transfer law is more puzzling. The differences observed with Kulacki's correlation are greater than those obtained with Steinberner's correlation. In the analysis of the COPO runs presented at Nureth 6, it appears that for Rayleigh numbers lower than $5\ 10^{+14}$ the comparison shows a good aggreement between experimental results and Steinberner's correlation but for Rayleigh numbers higher than 10^{+15} Steinberner's correlation also underpredicts the experimental results by a factor of about 40%. [9] There is a difference of liquid height in the pool between these different runs. Is this behaviour due to a transition in the mechanism of heat transfer around Rayleigh 10^{+15} or is there an effect of the aspect ratio for a particular geometry ? At this time we have no explanation to this behaviour.

Power distribution

	Upward	Sideward	Downward
Experimental heat flux	18.5 kW/m²	5.8 kW/m²	2.6 kW/m²
Experimental evacuated Power	75.6%	13.5%	10.9 %
First calculation	44.5%	34.5%	20.1 %
Second calculation	76.0%	13.9 %	9.7 %

In the first calculation, without any adjustment, the power distribution is not well reproduced. The power evacuated to the upper boundary represents only 44.5% of the total dissipated power.

In the second calculation described below, a good agreement is obtained for the power distribution between each zone.

Sideward heat flux

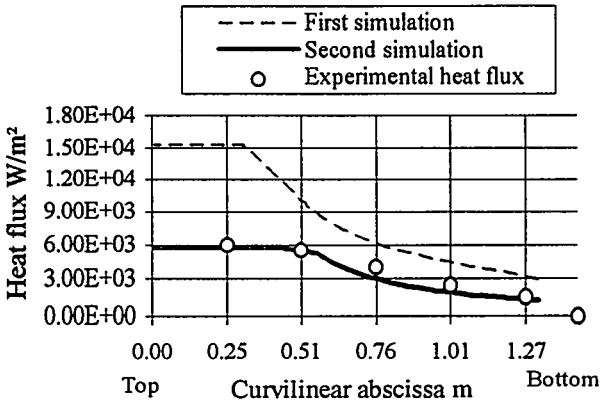


Figure 8 : Sideward heat flux COPO fh2

In the first calculation the sideward heat flux is over-estimated and the unstable upper zone is incorrectly reproduced. The low upward heat transfer induces an increase of pool temperature and also higher sideward heat fluxes.

In the second calculation the heat flux profile is in good agreement with the experimental results.

In the first calculation the maximum temperature is too high and the height of the isothermal upper zone represents only 31.5 cm. The upward heat flux is only about 10.9 kW/m².

The adjustments in the second calculation lead to a good agreement with the experimental data. The upper zone is about 55 cm thick and the maximum temperature difference reaches 12.6°. The calculated upward heat flux reaches 18.6 kW/m².

Temperature on the axis of the pool

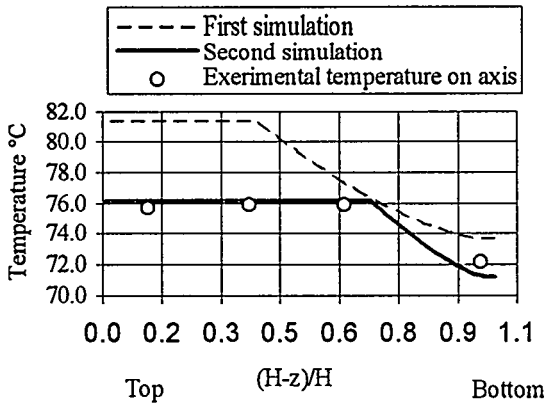


Figure 9 : Temperature on the axis of the pool

C. Validation on TRIO-VF numerical results.

In the absence of experimental data available for hemispherical geometry and for high Rayleigh numbers, a comparison has been made with existing TRIO-VF results for a PWR lower head. We do not presume about the physical validity of these results.

Some TRIO-VF results for this case have been presented at the Workshop on Large Molten Pool Heat Transfer (Grenoble 9-11 Mars 1994) and have been used.[6]

Due to the large radius of a vessel, the meshes are too large for a self description of heat transfer in the boundary layer and TRIO-VF code also used heat transfer correlations at boundaries.

Characteristics and hypotheses.

- Hemispherical geometry : R = 2 m, H = 2.12 m

- Dissipated power : 32 MW

- The molten corium is surrounded by a thin crust of oxide. So a uniform boundary temperature of 2700 K is considered except at the free surface.

- For the radiative heat transfer the steel upper structures are assumed to be at their melting point 1658K. The emissivities are assumed to be $\varepsilon_{cor} = 1$ for corium upper surface and $\varepsilon_{steel} = 0.2$ for steel.

For our calculation we have taken the same characteristics and hypothesis, furthermore the calculation was made without any correction factors.

Power distribution

Power extracted in the upper zone	8.5 MW	26.5 %
Power extracted from the side wall	23.4 MW	73 %

Sideward heat flux

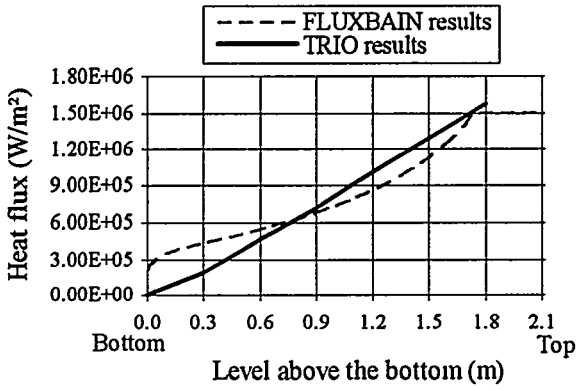


Figure 10 : Heat flux at the wall of the vessel lower head

The tendencies are quite similar for the two calculations. Differences can be explained by expressions of heat transfer coefficient which are different for the two calculations.

Both calculations use the Chawla's correlation to express the sidewards heat transfer coefficient, but do not consider the same dependency laws : 1) for the TRIO-VF calculation, the heat transfer coefficient varies with the local temperature difference between wall and the first mesh. The effect of inclination is taken into account by a sin α multiplier 2) for the FLUXBAIN calculation, the heat transfer coefficient varies with local temperature between the bulk and the wall and the effect of inclination is represented by $(\sin \alpha)^{1/3}$.

Upper zone

Both calculations are in agreement: - the free surface temperature is about 2863K. There is no crust of oxide in the upper zone - the height of top cooling zone is about 38cm. In this upper zone the temperature is maximum and uniform $T_{max.}$=3213K

III. CONCLUSION

The model presented in the paper is aimed to calculate the heat flux distribution at the boundaries of a pool on the basis of a simplified, fast running, model which is able to take into account geometry evolutions during the propagation of a corium pool in the core or a debris bed . A simplified model cannot describe the reality with details similar to what may be obtained with sophisticated codes. The analysis of what is important to describe and what is less important showed that the lateral (or downward) heat flux distribution is strongly connected to the temperature distribution in the central part of the pool itself strongly connected to the recirculation flow rate in the boundary layers. Therefore a specific effort was made for the approximate description of the boundary layer flow.

Validation of the model on BAFOND experiment has shown that it was necessary to develop a specific analytical expression of the mean flow rate in a turbulent boundary layer including Pr dependency. With this expression we obtain good agreement with BAFOND or with TRIO-VF results. The correction factor for BAFOND is clearly justified and takes account for the thermal resistance due to the electrical insulation.

The comparison with the results from COPO showed that, in addition to the correction taking into account the effect of an electrical insulation layer, we have to add a correction factor on upward heat transfer correlation in order to reach a good agreement with experimental results. For Rayleigh numbers higher than 10^{+15} the Kulacki's correlation but also Steinberner's correlation are not appropriate. It is concluded that complementary specific efforts would be necessary to understand the physical phenomena which control the heat transfer in the upper unstable layer.

Also basic experiments concerning boundary layer thicknesses and velocity profiles for fully turbulent layers under natural circulation are needed.

NOMENCLATURE

Physical properties of the pool

β	Dilatation coefficient (1/K)
C_p	Specific heat (J/kg K)
λ	Thermal conductivity (W/mK)
μ	Dynamic viscosity (Pa.s)
ν	Kinematic viscosity (m^2/s)
ρ	Density (kg/m^3)
$g(\alpha)$	Gravity m/s^2

Non-dimensional numbers

$Gr = \frac{g\beta\Delta Tx^3}{\nu^2}$ Grashof number

$Nu = \frac{hx}{\lambda}$ Nusselt number

$Pr = \frac{Cp\mu}{\lambda}$ Prandtl number

$Ra = \frac{g\beta QH^5}{\lambda\upsilon\alpha}$ Internal Rayleigh number

Boundary layer

x	Abscissa parallel to the wall or curvilinear abscissa (origin at free surface) (m)
y	Normal coordinate on the wall (m)
δ	Boundary layer thickness (m)
u	Boundary layer velocity (m/s)
u*	Boundary layer characteristic velocity (m/s)
T_{bl}	Boundary layer temperature (K)
m_{pool}	Mass flow rate in the boundary layer
T_{wall}	Wall temperature (K)
ΔT	Temperature difference T_{pool}-T_{wall}
dV_{bl}	Elementary boundary layer volume of thickness dZ (m^3)
P_{lat}	Power extracted from side wall (W)

Pool

m_{pool}	Mass flow rate along the centre line of the pool (kg/s)
T_{pool}	Temperature along the centre line of the pool (K)
dV_{pool}	Elementary pool volume of thickness dZ (m^3)
V_{pool} (H_t)	Volume of the unstable upper layer (m^3)
S_{pool}	Upper pool surface (m^2)
D	Diameter of S_{pool} (m)
Q	Power dissipated in the pool (W/m^3)
H_t	Thickness of the upper layer (m)
z	Level above the bottom (m)
H	Liquid height (m)

REFERENCES

1. E.R.G. Eckert and T.W. Jackson, ''Analysis of Turbulent Free-Convection Boundary Layer on a Flat Plate'', *NACA TN* 2207, 1950.

2. T.C. Chawla and S.H. Chan, ''Heat Transfer from Vertical/Inclined Boundaries of Heat-Generating Boiling Pools'', *J. Heat Transfer* 104, 465 (1982)

3. A.A. Emara and F.A. Kulacki, ''Hight Rayleigh Number Convection in Enclosed Fluid Layers with Internal Heat Sources'', *NEUREG-75/065*

4. O.Kymäläinen, O.Hongisto, J.Antman, H.Tuomisto and T.G.Theofanous ''COPO: Experiments for Heat Flux Distribution from a Volumetrically Heated Corium Pool'', Imatran Voima Oy (IVO) P.O. Box 112, 01601 Vantaa, Finland

5. Y. Jaluria, Basics of Natural Convection Ch 12 Handbook of single-phase convective heat transfer S. Kakaç, R.K. Shah, W. Aung Wiley Intersscience

6. S. Pigny, ''Thermal Hydraulic Study of a Corium Molten Pool''. *Proceedings of the Workshop on Large Molten Pool Heat Transfer* O.E.C.D N.E.A Grenoble Mars 94

7. JM. Seiler, ''Cooling of Molten Liquid Pool Correlations'', *Proceedings of International Conference Avignon 88* France

8. U. Steinberner, H.-H. Reineke, ''Turbulent Buoyancy Convection Heat Transfer with Internal Heat Sources''. *Proceeding of Sixth International Heat Transfer Conference*. Toronto, Canada. August 7-11, 1978.

9. O.Kymäläinen, H.Tuomisto, O.Hongisto, and T.G.Theofanous, ''Heat Flux Distribution from a Volumetrically Heated Pool with High Rayleigh Number'' *Proceedings, NURETH-6*, Grenoble, October 5-8, 1993.

RESUME

Un modèle simplifié de calcul de transfert de chaleur aux frontières d'un bain chauffé en volume a été développé au STR-CEA, avec le soutien de l'IPSN, en vue d'une utilisation dans les codes d'accident grave. Ces codes qui doivent prendre en compte de nombreux phénomènes physiques ne peuvent pas décrire de manière détaillée la thermohydraulique du bain comme cela se fait avec des codes plus sophistiqués. Pour la description des bains de corium les besoins sont axés principalement sur la détermination de la distribution du flux de chaleur aux frontières en fonction de la géométrie.

Le modèle se limite aux bains correspondant à des nombres de Rayleigh élevé (10^{15} ou plus) c'est à dire à des écoulements de couche limite turbulents. Ces situations sont représentatives des cas réacteur. Le modèle considère un bain homogène. Une température constante est imposée aux frontières pour calculer le transfert de chaleur vers le bas. Différentes conditions aux limites peuvent être imposées pour le transfert de chaleur vers le haut (croûte ou surface liquide avec échange radiatif).

Les prévisions du modèle sont comparées à des résultats obtenus pour différentes géométries (BAFOND, COPO,...)

L'approche simplifiée permettra dans un deuxième temps de prendre en compte l'évolution de la géométrie durant la phase de propagation d'un bain de corium dans le coeur ou d'un lit de débris.

---

[i] C.E.N.G Centre d'Etude Nucléaire de Grenoble

[ii] DRN Direction des Réacteurs Nucléaires
DTP Département de Thermohydraulique et de Physique
STR Service de Thermohydraulique des Réacteurs

[iii] IPSN Institut de Protection et de Sûreté Nucléaire

Numerical Simulation of Stratified Shear Flow using a Higher Order Taylor Series Expansion Method

Kengo Iwashige and Takashi Ikeda
Power and Industrial Systems R & D Division, Hitachi, Ltd.
7-2-1 Omika-cho, Hitachi-shi Ibaraki-ken, 319-12 Japan.

ABSTRACT

A higher order Taylor series expansion method is applied to two-dimensional numerical simulation of stratified shear flow. In the present study, central difference scheme-like method is adopted for an even expansion order, and upwind difference scheme-like method is adopted for an odd order, and the expansion order is variable. To evaluate the effects of expansion order upon the numerical results, a stratified shear flow test in a rectangular channel (Reynolds number=1.7×10^4) is carried out, and the numerical velocity and temperature fields are compared with experimental results measured by laser Doppler velocimetry and thermocouples. The results confirm that the higher and odd order methods can simulate mean velocity distributions, root-mean-square velocity fluctuations, Reynolds stress, temperature distributions, and root-mean-square temperature fluctuations.

I. INTRODUCTION

The present thermal-hydraulic design of liquid metal fast breeder reactors (LMFBRs) is made with many experimental test results considering conservative safety margins rigorously. Advanced numerical analysis methods should, however, be developed to optimize the design and to enable further reduction of the construction costs. In the thermal-hydraulic design, it is important to study mixing phenomena of sodium coolant in the reactor vessel and the primary loops. For example, thermal stratification of sodium coolant occurs in the upper plenum and primary pipes under reactor trip conditions, while thermal striping occurs in the core outlets under normal operation. In these phenomena, hot and cold sodium coolants commingle in mixing shear flows, so that temperature fluctuation occurs, which can cause thermal stress for internal structures. To evaluate the thermal stress, not only the averaged temperature difference, but also frequency of the change must be considered. Hence, it is necessary to estimate instantaneous velocity and temperature for the design. For this purpose, numerical simulation using higher order finite difference schemes, represented by the third-order upwind schemes[1]-[4], is a suitable one, and is simple to use for complex geometries and boundary conditions. Nishida et al.[5] and Kajishima[6], however, have compared direct simulation results of turbulent flow using spectral methods with higher order central difference schemes, and have showed that it took more than fourth-order calculations to obtain the same precision as by spectral methods. Rai et al.[7], [8] have showed the fifth-order upwind scheme was a good candidate for numerical simulations of turbulent flows. Although higher order upwind methods are superior in numerical stability for high Reynolds number flow, they have some artificial numerical errors. The applicability and precision of higher order upwind methods than third-order have not been studied sufficiently.

In this study, a higher order Taylor series expansion method is applied to two-dimensional numerical simulation of a stratified shear flow. The expansion order is adopted to variable, and third- to seventh-order methods are examined. To evaluate the effects of expansion order upon the numerical results, a stratified shear flow test in a rectangular channel is carried out, and the numerical velocity and temperature fields are compared with the experimental ones.

II. EXPERIMENTAL PROCEDURE

1. Experimental Apparatus

The test section for a stratified shear flow in a rectangular channel is shown in Fig. 1. The test section was 5m long, 0.1m wide and 0.3m high, and was made of transparent acrylic resin to allow laser beam measurements and visualization. The section entrance was divided into upper and lower regions by a flow separator.

The instantaneous local velocity was measured by laser Doppler velocimetry (LDV), which was an optical fiber and probe type two-dimensional system. The laser light source was a 4W argon gas laser. The probe was moved by a traversing system with precision $\pm 4\times10^{-3}$mm.

2. Experimental Conditions

The experimental conditions are shown in Fig. 2. The mean inlet velocities of the lower (cold) and the upper (hot) regions were set for $(1.20\pm0.06)\times10^{-1}$ m/s and $(3.30\pm0.17)\times10^{-2}$ m/s, respectively. The water depth h was set as (200±2) mm and temperature differences between the lower and upper regions ΔT were 0 and (7±0.5) K. Under these conditions, Reynolds number and Richardson number were defined as follows.

$$\mathrm{Re} = \frac{\Delta U\, h}{\nu} = 1.7\times10^{4} \tag{1}$$

$$\mathrm{Ri} = \frac{g\,\beta\,\Delta T\, h}{\Delta U^{2}} = 0 \text{ and } 0.4 \tag{2}$$

The three-dimensional coordinates were defined with their origin as the edge of the separator and the middle of the channel width, with x, y and z as the stream, channel width, and vertical directions. The vertical distributions of the velocities for x- and z-directions were measured at (x, y) = (0.45m, 0) and (0.9m, 0), where the mixing layer of the upper and lower fluids had just started to form and was fully developed, respectively.

The algebraic mean velocities $\bar{u}$, $\bar{w}$, the root-mean-square velocity fluctuations $\sqrt{\overline{u'^2}}$, $\sqrt{\overline{w'^2}}$, Reynolds stress $-\overline{u'w'}$, algebraic mean temperature $\bar{T}$, and the root-mean-square temperature fluctuations $\sqrt{\overline{T'^2}}$ were calculated from the measured instantaneous velocities and temperatures.

3. Measurement Errors

The measurement errors of the velocity and temperature were estimated for LDV and thermo-couples on the basis of the measurement uncertainty analysis method[9]. The results[10] for 95% coverage were as follows.

Uncertainty of the velocity: $\pm6.9\times10^{-4}$ m/s

Uncertainty of the temperature: ±0.1 K

III. NUMERICAL METHOD

The non-dimensional forms of the governing equations for the two-dimensional unsteady incompressible fluids are written as follows:

$$\frac{\partial\omega}{\partial t} + u\frac{\partial\omega}{\partial x} + w\frac{\partial\omega}{\partial z} = \frac{1}{\mathrm{Re}}\left(\frac{\partial^2\omega}{\partial x^2} + \frac{\partial^2\omega}{\partial z^2}\right) + \mathrm{Ri}\frac{\partial T}{\partial x}, \tag{3}$$

$$\frac{\partial T}{\partial t} + u\frac{\partial T}{\partial x} + w\frac{\partial T}{\partial z} = \frac{1}{\mathrm{Re\,Pr}}\left(\frac{\partial^2 T}{\partial x^2} + \frac{\partial^2 T}{\partial z^2}\right), \tag{4}$$

$$\left(\frac{\partial^2\psi}{\partial x^2} + \frac{\partial^2\psi}{\partial z^2}\right) = -\omega, \tag{5}$$

$$\frac{\partial \psi}{\partial z} = u, \quad \frac{\partial \psi}{\partial x} = -w. \tag{6}$$

A two-dimensional approximation was chosen according to the measured results that the mean velocity distributions and the root-mean-square velocity fluctuations showed two-dimensionalities at y=-0.03 to 0.03 m between x= 0 and 1.5 m.

In the numerical calculation of the governing equations, the spatial derivatives are obtained by a higher order Taylor series expansion method[11]. The nth-order Taylor series expansion of a function f(x) about a certain point $x_i+\Delta x_j$ is approximated by the following polynomial of $f(x_i)$:

$$f(x_i+\Delta x_j) \approx \sum_{r=0}^{n} \frac{1}{r!} \left(\Delta x_j \frac{\partial}{\partial x_j}\right)^r f(x_i) \quad . \tag{7}$$

Equation (7) represents first-order simultaneous equations by substituting n+1 quantities at a point x_i and n points near x_i for $f(x_i + \Delta x_j)$. These equations have n+1 unknowns about the 0th- to nth-order spatial derivatives of $f(x_i)$. The spatial derivatives can be obtained to solve the simultaneous equations of Eq. (7) numerically.

In the present study, a numerical analysis was carried out using the higher order Taylor series expansion methods from n=3 to 7. The spatial derivatives in Eq. (3), (4), (5) and (6) were obtained to solve the simultaneous equations of Eq. (7) by using the Gaussian elimination method. In the choice of n+1 spatial mesh points, a central finite difference scheme-like method was adopted for an even order, and a upwind finite difference[12] scheme-like method was adopted for an odd order, namely, one-point upstream biased. In these methods, both the first- and second-order derivatives of $f(x_i)$ can be calculated with nth-order accuracy using the even order ones. But, using the odd order ones, the first- and second-order derivatives are calculated with nth- and (n-1)th-order accuracies, respectively. Configurations of the spatial mesh points are shown in Fig. 3.

The third-order Adams-Bashforth method was used for integration of the time derivatives in Eqs. (3) and (4). The fast Fourier transformation method[13] was applied to solve the Poisson's equation (5).

The calculational region was 1.35m from the edge of the separator and 0.2m deep in the test section. This region was divided by two-dimensional meshes at 200×32 points. The mesh points were set so that the maximum wave number

$$k_{max} = \frac{2\pi}{\Delta x_i} \quad , \tag{8}$$

obtained from the spatial mesh interval, was enough larger than the energy containing range of this flow. The k_{max} was determined according to the experimental one-dimensional energy spectrum for the streamwise velocity component, illustrated in Fig. 4. Previously, the authors carried out numerical simulation of one-dimensional random waves[14] and two-dimensional isotropic turbulent flow[15] using the present method, and the numerical results were compared with theoretical solution and numerical solution of spectral method. The results on a succession of grids showed that the present higher and odd order methods (more than fifth) had a good applicability to the comparatively large scale fluctuations, corresponded to the low wave number less than about $k_{max}/4$, and higher wave number fluctuations were dissipated abruptly.

The boundary conditions at the upper free surface, bottom wall and outlet (x=1.35m) were slip, no-slip and free-outflow conditions, respectively. The inlet velocity distributions were given as the experimental ones, and the inlet velocity fluctuations were given using the Gaussian random numbers, which had the experimental root-mean-square ones as the center values.

The time integration step was selected as 2×10^{-3} seconds, and 40000 time steps were calculated in a case. The typical computing time was about 4 hours by using a Hewlett Packard Model 735 workstation.

IV. RESULTS AND DISCUSSION

1. Flow Fields

A flow visualization photograph from the test section at Ri=0.4 is shown in Photo.1. A laser light sheet and fluorescent dyes were used for the visualization. The dyes were injected from the inlet of the lower fluid. The dyes were mixed with water of the lower region. The photograph shows the mixing shear layer between the upper

and lower fluids has grown downstream due to the velocity difference. The interface of the upper and lower fl .ds fluctuated unstably.

Photo. 2 and 3 compare the instantaneous vorticity and temperature fields of the calculational results for n=3 and 5, respectively. With both n=3 and 5, the upper and lower fluids were mixed and vortices grew and were transferred downstream. Furthermore, the vorticity and temperature fields fluctuated unstably near the interface of the upper and lower fluids, the same as seen experimentally. Smaller vortices could be captured for n=5 than n=3.

2. Mean Velocity Distributions

Figure 5 shows experimental and calculational results for the vertical distributions of the non-dimensional mean velocities $\bar{u}/\Delta U$ and $\bar{w}/\Delta U$ at x=0.45m and Ri=0. The averaging time of the calculation was 10 seconds (5000 time steps), almost the same as the experimental time. In these figures, (a) and (b) were calculated by n=3 and 5 methods, respectively. With both n=3 and 5, the velocity $\bar{u}/\Delta U$ could simulate the experimental trends. But for both $\bar{u}/\Delta U$ and $\bar{w}/\Delta U$, the differences between the calculational results of n=3 and the experimental ones were larger than that of n=5 near z/h=0, which was the interface of the lower and upper fluids. The calculational results of n=3 were shifted a little downwards near z/h=0. The results of n=5 agreed with the experimental results with 95% coverage near the fluids interface. But the difference between the calculational and the experimental results for $\bar{w}/\Delta U$ was large near the bottom wall (z/h= -0.5 to -0.25). The authors considered that the generation and growth of wall turbulence could not be reproduced in the present calculation because of a lack of turbulent boundary layer resolution and the assumption of two-dimensionality.

In the present calculations, the results of n=7 were almost the same as 5, and further improvement of the precision could not be obtained. In the case of even orders (n= 4 and 6), numerical instabilities occurred.

3. Velocity Fluctuations

Figure 6 shows experimental and calculational results for the vertical distributions of the non-dimensional root-mean-square velocity fluctuations $\sqrt{\overline{u^2}}/\Delta U$ and $\sqrt{\overline{w^2}}/\Delta U$ at x=0.45m and Ri=0, respectively. For both n=3 and 5, the calculational results could simulate the experimental trends, the same as the velocity distributions. But for both $\sqrt{\overline{u^2}}/\Delta U$ and $\sqrt{\overline{w^2}}/\Delta U$, the differences between the calculational results of n=3 and the experimental ones were larger than those of n=5 at the interface of the lower and the upper fluids and near the bottom wall especially, where the shear stress worked strongly. The difference between the calculational and the experimental results was large near the bottom wall (z/h= -0.5 to -0.25) for the same reason as the velocity distribution of $\bar{w}/\Delta U$.

Figure 7 compares experimental and calculational results for the vertical distributions of the Reynolds stresses $-\overline{u'w'}/\Delta U^2$ at x=0.45, 0.9m and Ri=0. The experimental results showed that the Reynolds stress had a peak near z/h=0, where mixing of the upper and lower fluids was vigorous and the momentum of the faster region was transferred to the slower one. In the calculational results of n=3, the peak was shifted a little downwards. The results of n=5 had good agreement with the experimental ones. The authors considered that the results of n=3 corresponded to underestimation of the momentum transport near z/h=0.

4. Mean Temperature Distributions and Fluctuations

Figure 8 compares experimental and calculational results for the vertical distributions of the non-dimensional mean temperature $(\bar{T}-T_c)/\Delta T$ and fluctuations $\sqrt{\overline{T'^2}}/\Delta T$ at x=0.45, 0.9m and Ri=0.4. Both mean temperature distributions and fluctuations could be simulated by the method of n=5.

The present results showed that higher and odd order Taylor series expansion methods can be applied to direct simulation of stratified shear flow and can estimate mean velocities, temperature and their fluctuations with good precision. To evaluate the thermal stress on the internal structures of LMFBR, not only mean quantities but also the frequency must be considered. Clarification of the precision of the method for the frequency estimation must be done next.

V. CONCLUSION

A higher order Taylor series expansion method was applied to the numerical simulation of stratified shear flow in a rectangular channel with the Reynolds number 1.7×10^4. The numerical velocity and temperature fields were compared with experimental results measured by LDV and thermo-couples, and it was confirmed that the higher and odd order methods could simulate mean velocity distributions, root-mean-square velocity fluctuations, Reynolds stress, temperature distributions, and root-mean-square temperature fluctuations.

ACKNOWLEDGMENTS

The experimental facility of the University of Tsukuba was used for the experimental study. The authors wish to thank Prof. G. Matsui and Dr. H. Monzi of the University for their valuable comments and discussions on the experimental method and results.

NOMENCLATURE

g	Gravity acceleration (m/s^2)
h	Water depth (m)
n	Taylor series expansion order
Pr	Prandtl number
Re	Reynolds number
Ri	Richardson number
T	Temperature (K)
T_c	Cold water temperature (K)
u	x-direction velocity (m/s)
w	z-direction velocity (m/s)
x	Stream direction (m)
y	Channel width direction (m)
z	Vertical direction (m)

Greek symbols

β	Volume coefficient of expansion (K^{-1})
ΔT	Entrance temperature difference (K)
ΔU	Entrance velocity difference (m/s)
ν	Kinematic viscosity (m^2/s)
ω	Vorticity
ψ	Stream function

REFERENCES

[1] T. Kawamura and K. Kuwahara, "Computation of High reynolds Number Flow around a Circular Cylinder with Surface Roughness", AIAA Paper 84-0340 (1984).

[2] T. Kawamura and K. Kuwahara, "Direct Simulation of a Turbulent Inner Flow by Finite-Difference Method", AIAA Paper 85-0376 (1985).

[3] K. Ishii, K. Kuwahara, S. Ogawa, W.J. Chyu and T. Kawamura, "Computation of Flow around a Circular Cylinder in a Supercritical Regime", AIAA Paper 85-1660 (1985).

[4] S. Shirayama, "Construction of Modified Third-Order Upwind Schemes for Stretched Meshes", AIAA Journal Vol.30, No.5, 1237-1242 (1992).

[5] H. Nishida and N. Satofuka, "Large-Scale Direct Simulation of Two-Dimensional Homogeneous Isotropic

Turbulence Using a Higher-Order Method of Lines", Trans. Jpn. Soc. Mech. Eng. Vol.56,No.528 B, 2283-2290 (1990).
[6] T. Kajishima, "Numerical Accuracy of the Direct Simulation of Turbulent Flow", Trans. Jpn. Soc. Mech. Eng. Vol.57, No.544 B, 4080-4084 (1991).
[7] M. M. Rai and P. Moin, "Direct Simulations of Turbulent Flow Using Finite-Difference Schemes", J. Comp. Phys. 96, 15-53 (1991).
[8] M. M. Rai and P. Moin, "Direct Numerical Simulation of Transient and Turbulence in a Spatially Evolving Boundary Layer", J. Comp. Phys. 109, 169-192 (1993).
[9] ASME, Measurement Uncertainty, trans. by Jpn. Soc. Mech. Eng. (1987).
[10] K. Iwashige, G. Matsui, T. Sanagi, M. Yamakawa and H. Monji, "An Experimental Study of Turbulent Energy Spectra in Stably Stratified Shear Flow", Trans. Jpn. Soc. Mech. Eng. Vol.57, No.537 B, 1652- 1657 (1991).
[11] K. Iwashige and N. Yokota, "Numerical Simulation of Turbulent Shear Flow Using Higher Order Taylor Series Expansion method", J. Nucl. Sci. Technol. Vol.32, No.1, 30-41 (1995).
[12] P.J. Roache, Computational Fluid Dynamic, Hermosa Publishers, New Mexico (1976).
[13] R.C.L. Bail, "Use of Fast Fourier Transforms for Solving Partial Difference Equations in Physics", J. Comp. Phys. 9, 440-465 (1972).
[14] K. Iwashige and T. Ikeda, "Applicability of a Higher Order Taylor Series Expansion method for Random Wave Simulations", J. Nucl. Sci. Technol. Vol.32, No.3, 257-259 (1995).
[15] K. Iwashige, "Numerical Simulation of Two-Dimensional Isotropic Turbulent Flow Using a Variable-Order Finite Difference Method", Trans. Jpn. Soc. Mech. Eng. Vol.59, No.564 B, 2450-2454 (1993).

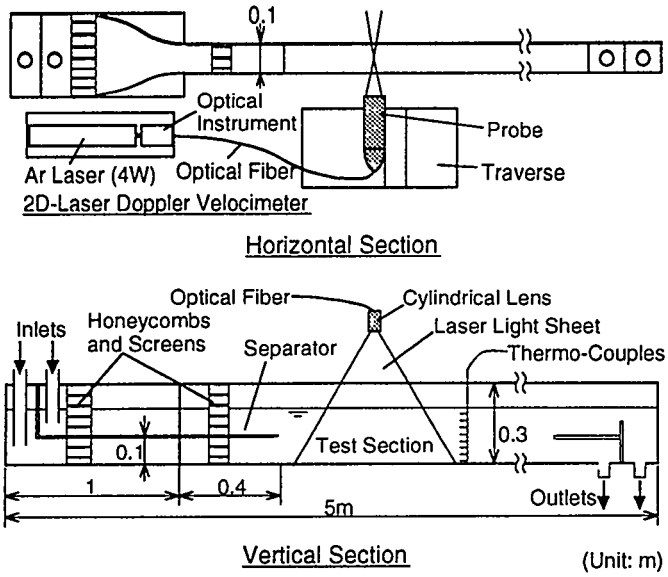


Fig.1 Schematic illustration of the test section

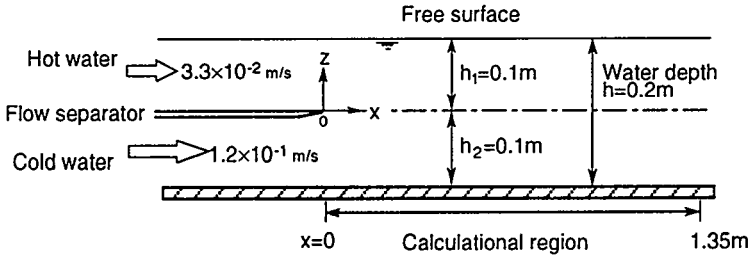


Fig. 2 Experimental conditions and coordinates

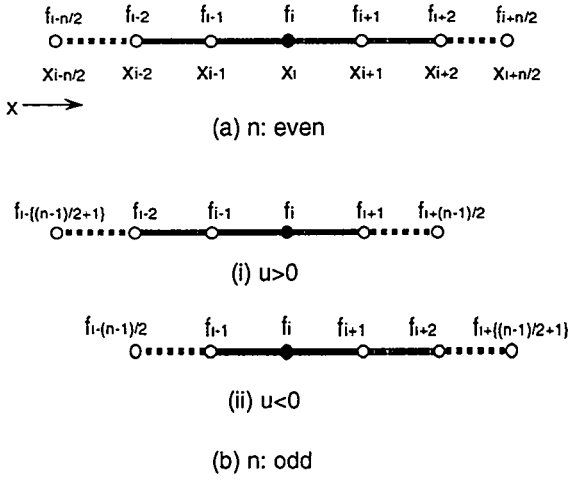


Fig. 3 Configurations of the mesh points for even and odd order methods

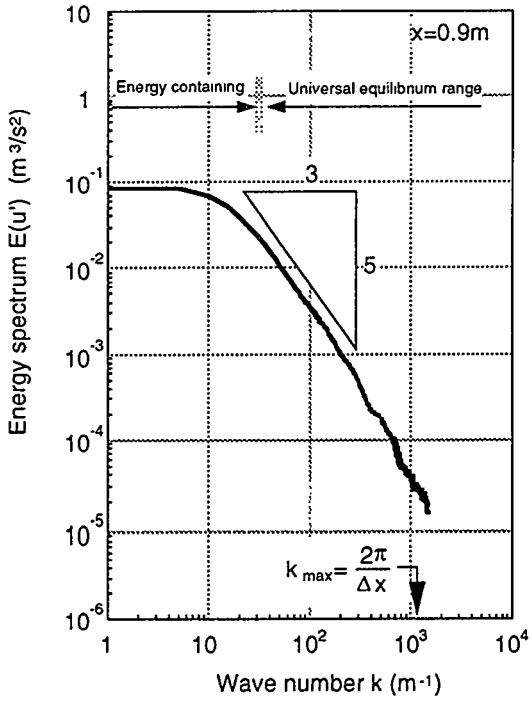
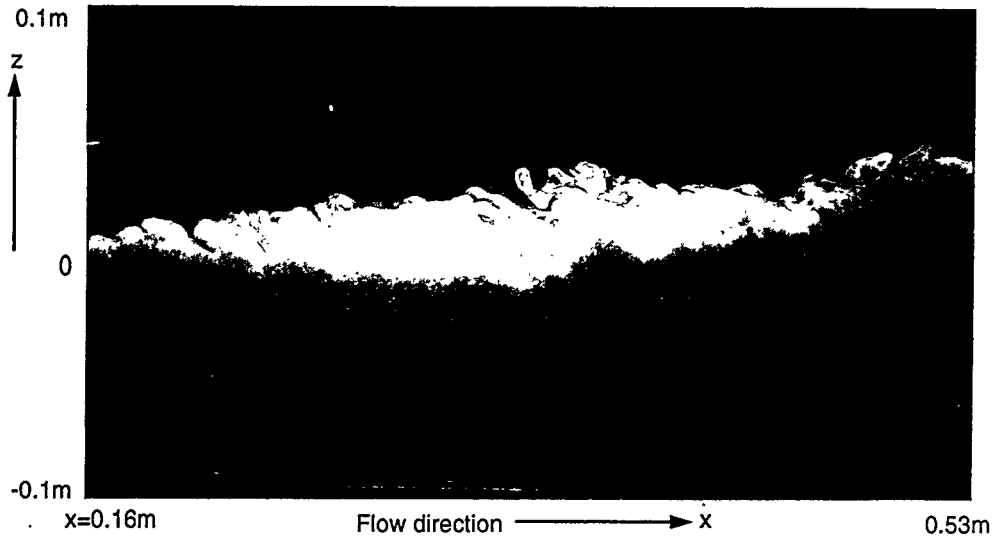


Fig. 4 Relation between the maximum wave number obtained from the minimum spatial mesh interval and the one-dimensional energy spectrum



Phot.1 Flow visualization photograph from the test section (Re=1.7 $\times 10^4$, Ri=0.4)

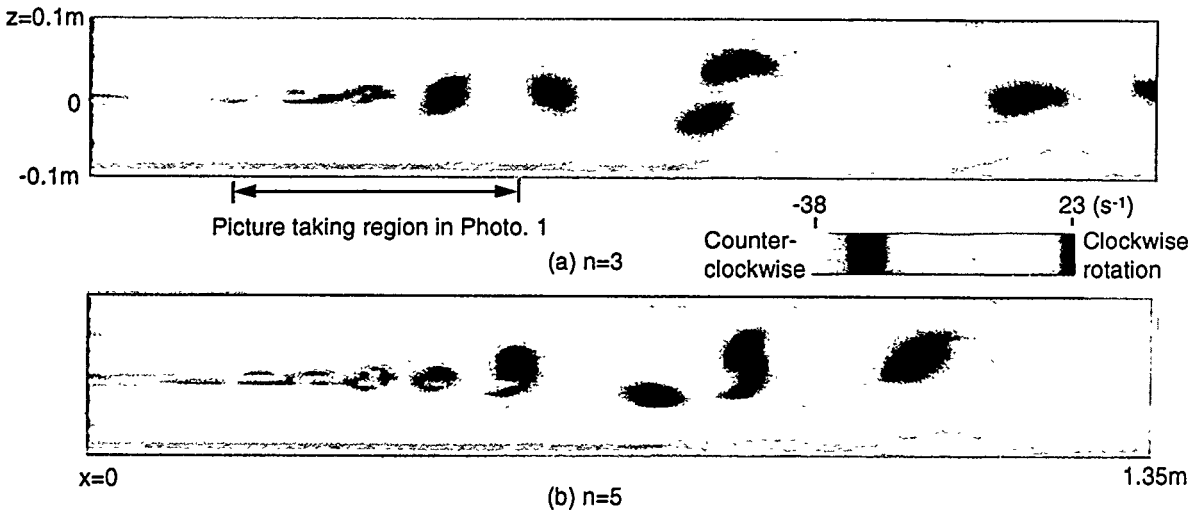


Photo. 2 Calculational results of vorticity distributions (Re=1.7 $\times 10^4$, Ri=0.4)

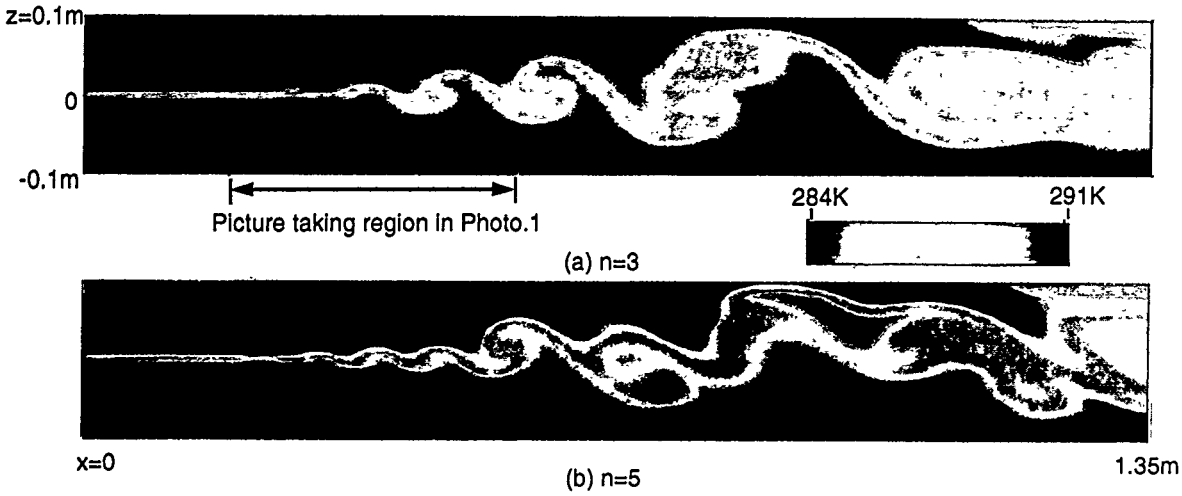


Photo. 3 Calculational results of temperature distributions (Re=1.7 $\times 10^4$, Ri=0.4)

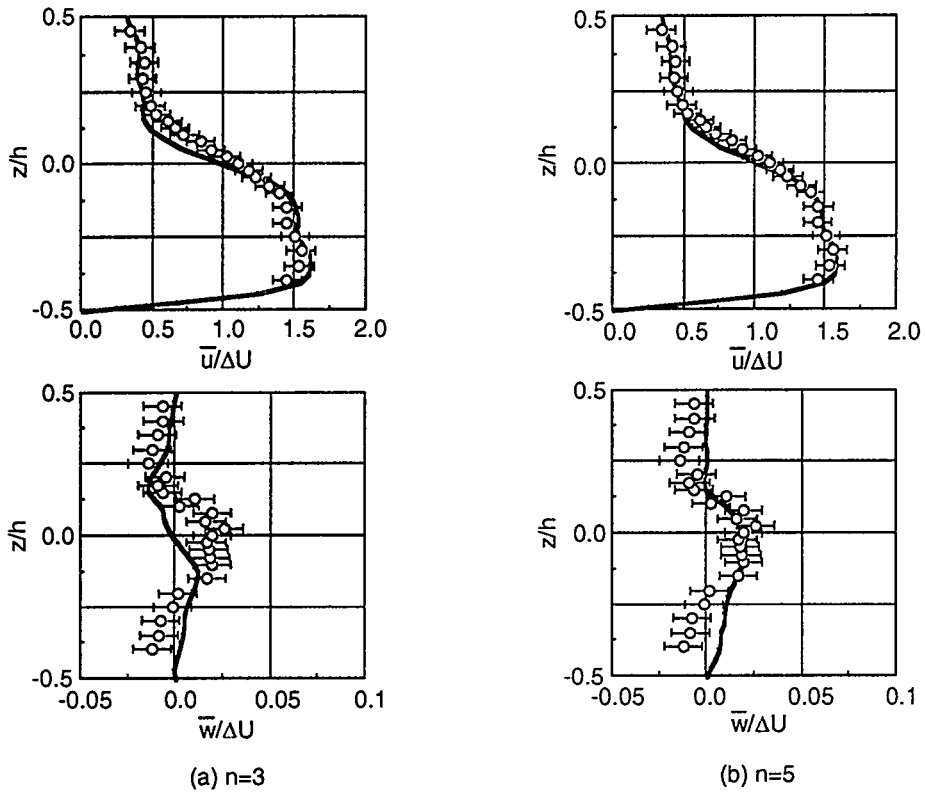


Fig. 5 Comparison between the experimental (circles: error bars show 95% confidence intervals) and calculational (solid lines) mean velocity distributions at x=0.45m, Re=1.7×10^4 and Ri=0.

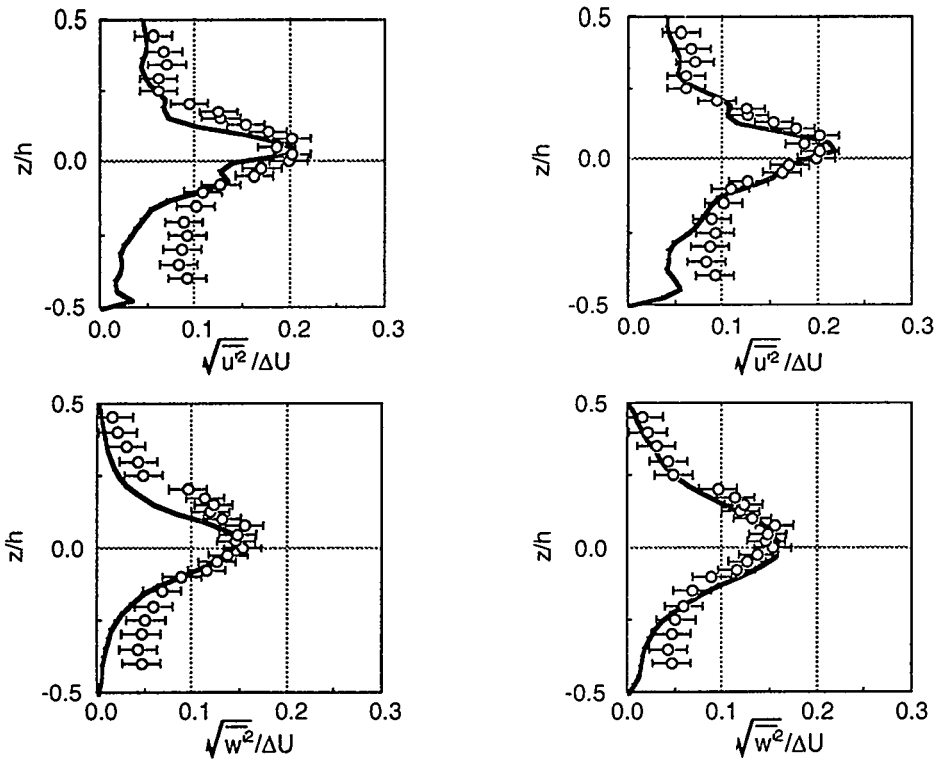


Fig. 6 Comparison between the experimental (circles: error bars show 95% confidence intervals) and calculational (solid lines) r.m.s. velocity fluctuations at x=0.45m, Re=1.7×10^4 and Ri=0.

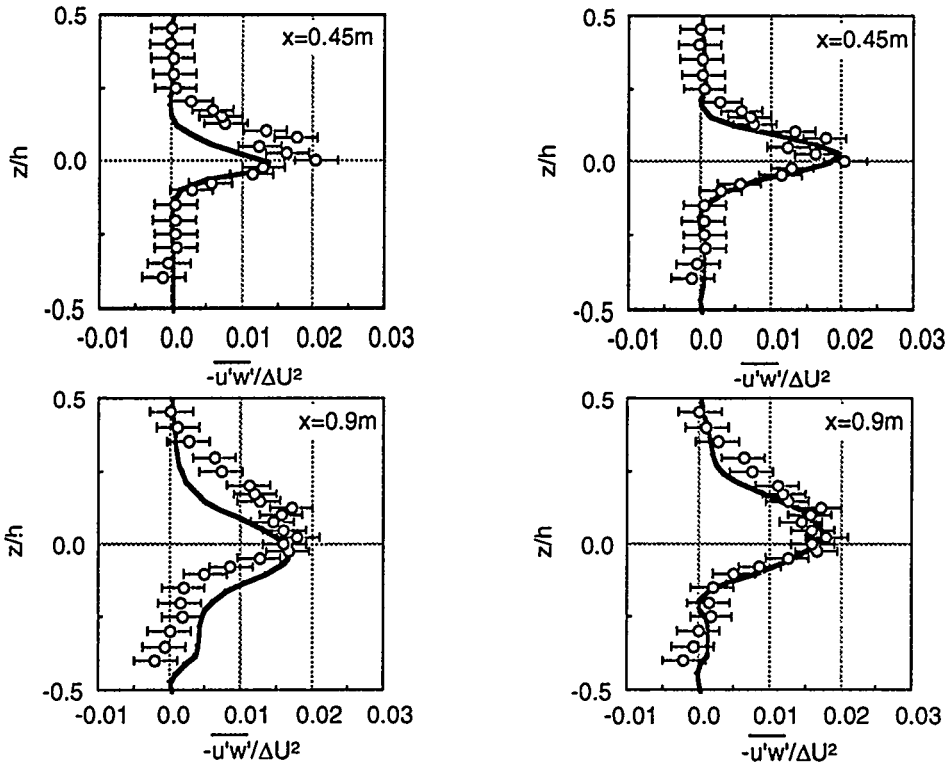


Fig. 7 Comparison between the experimental (circles:error bars show 95% confidence intervals) and calculational (solid lines) Reynolds stresses at Re=1.7 ×10⁴ and Ri=0.

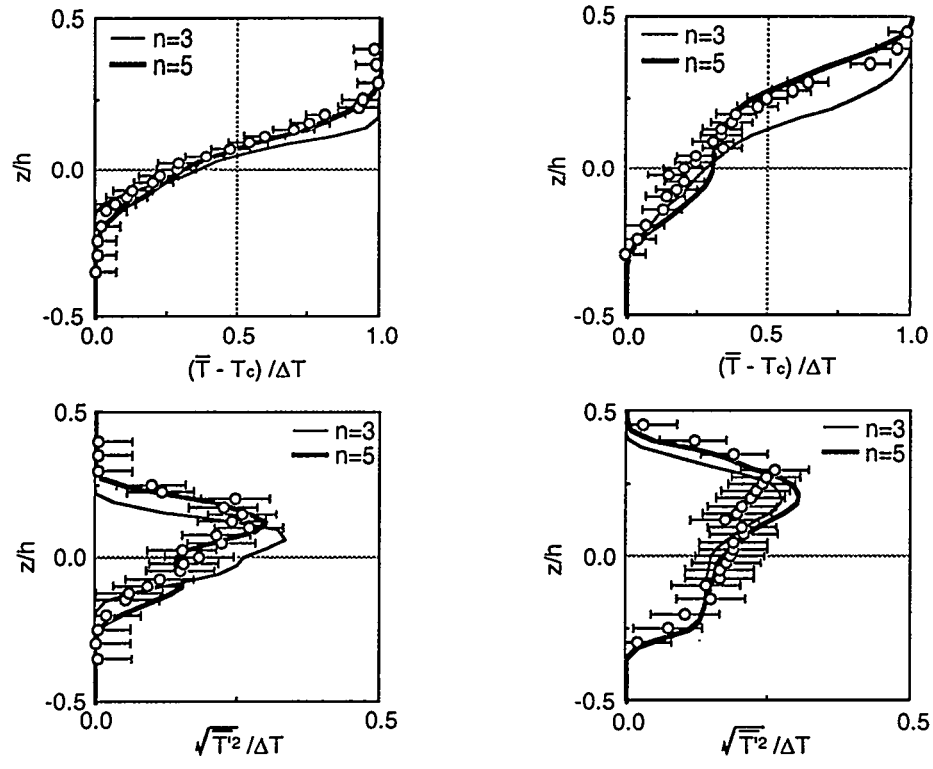


Fig. 8 Comparison between the experimental (circles: error bars show 95% confidence intervals) and calculational (solid lines) mean temperature distributions and fluctuations at Re=1.7×10⁴ and Ri=0.4.

Application of an Analytical Method for Solution of Thermal Hydraulic Conservation Equations

M. R. Fakory
Simulation, Systems & Services Technologies Company (S3 Technologies)
8930 Stanford Blvd
Columbia, MD 21045

Abstract

An analytical method has been developed and applied for solution of two-phase flow conservation equations.The test results for application of the model for simulation of BWR transients are presented and compared with the results obtained from application of the explicit method for integration of conservation equations. The test results show that with application of the analytical method for integration of conservation equations, the Courant limitation associated with explicit Euler method of integration was eliminated. The results obtained from application of the analytical method (with large time steps) agreed well with the results obtained from application of explicit method of integration (with time steps smaller than the size imposed by Courant limitation). The results demonstrate that application of the analytical approach significantly improves the numerical stability and computational efficiency.

Introduction

Training simulators require mathematical models with capabilities for faster than real time or near real time computation. Modern nuclear power plant simulators are designed for accurate simulation of full range of plant operation including unanticipated transients and abnormal operations or accidents. Thermal hydraulic and neutronic models with accurate numerical methods are required to design simulators which are now being used for engineering analysis of plant behavior (analytical simulators) as well as for training the reactor operators. The high fidelity simulators that are designed today use thermal hydraulic models which divide the simulated system into a number of nodes (fluid cells) and flow-paths or channels [1,2]. Thermal hydraulic conservation equations are integrated for each of these nodes to obtain local thermodynamic and thermal hydraulic parameters such as temperature, pressure, phasic flow rate, void fraction, etc., as a function of time step increments. Normally, a sufficient number of nodes provides detailed information about flow behavior and produces precise local parameters needed for simulation of response of the plant instruments (eg, in-core and ex-core neutron detectors, LPRMs, etc.). Most simulators employ four-equation or five-equation thermal hydraulic models but six-equation models have also been tried [3,4]. Reference [5] gives an overview of advantages and disadvantages of five-equation models versus six-equation models for real time simulators.

Models

Ideally, a high fidelity model may attempt to solve the conservation equations in a closed form both in space and time domains. However, due to complexity which arises from application of closed form solutions, the method application has been limited to special initial and boundary conditions [6]. The Method of Characteristics (MOC) which integrates differential equations along the characteristic lengths has provided closed form solutions for two-phase flow problems in some cases [eg, 7,8,9]. Closed form solutions have been obtained using method of lines (MOL) which assumes linear variation of parameters over the time step [10]. The well known thermal hydraulic codes such as TRAC [11] and RELAP5 [12] use finite differencing method in both time and space with donor cell (upwind) approach. Simulators also employ models which use nodalization and donor cell approach through division of the simulated system into a number of nodes (fluid cells). The governing thermal hydraulic conservation equations are integrated for each of these nodes to obtain local thermodynamic and thermal hydraulic parameters per increment of time. High fidelity simulators are required to employ, in addition to accurate two-phase flow models and closures, sufficient number of nodes to be able to calculate local phenomena associated with transients or oscillatory behavior of the reactor operation [13]. However, the extra number of nodes may require smaller integration time step which is associated with stability of explicit or semi-implicit numerical methods. On the other hand, the real time constraint requires that the integration time step (Δt) remain larger than or equal to the updating problem time increment, and therefore necessitates computers with fast CPUs. The time step requirement combined with the speed of computer CPU can limit the number of nodes which are employed to simulate a system and therefore may affect the simulator fidelity.

This paper is concerned with application of near analytical solution to conservation equations used for two-phase flow. This closed form solution is continuous in time but discrete in space. That is, the fluid system is divided into a number of nodes (fluid elements) and the closed form solution is applied to each element under the assumption that the thermal hydraulic and thermodynamic parameters remain uniform within each element but they may vary from an element to the next and as a function of the time. The results of application of the method for calculation of thermal hydraulic parameters during a fast transient in a BWR are presented and are compared against the results obtained from application of fully explicit solution for the same transient. The method has been applied under the assumption that the effects of acoustic wave propagation can be ignored. This assumption is well justified since the integration time step used for real time simulators is on the order of tenth of a second which is much higher than the time which is required for acoustic wave propagation across the simulated system (eg, the reactor pressure vessel). Therefore the code uses a five equation (two mass, two energy and one mixture momentum) two-phase model, and the mixture momentum conservation equation is solved separately from the mass and energy conservation equations. The method chooses liquid mass, gas mass, liquid energy and gas energy as the conserved quantities which also provides a possibility to avoid computational errors associated with low independence between the constituting conservation equations [14].

A general conservation equation for one-dimensional area averaged, time averaged, unsteady-state two-phase flow can be presented as [15].

$$\frac{\partial(\alpha_k * \rho_k * \psi_k)}{\partial t} + \frac{\partial(\alpha_k * \rho_k * u_k * \psi_k)}{\partial z} = F_k \qquad (1)$$

where we have assumed uniform flow area in the z direction, and α_k, ρ_k, u_k, are the volumetric fraction, density and velocity, respectively of phase-k (k=V for vapor, k=L for liquid), ψ_k is a general variable the physical meaning of which depends on the conservation principle under consideration, where its value is set equal to one for mass conservation, and for energy conservation ψ_k represents specific internal plus kinetic energy, and for momentum conservation ψ_k represents phasic velocities. F_k represents the source term or forcing function where for mass conservation it represents phase conversion (condensation or evaporation) as well as sink or source of mass. Then mass conservation for vapor phase implies,

$$\frac{\partial(A * \alpha_k * \rho_k)}{\partial t} + \frac{\partial(A * u_k * \alpha_k * \rho_k)}{\partial z} = A * \Gamma_k \qquad (2)$$

Assuming the average of product of properties is equal to product of the averages, and defining α as the volume averaged vapor void fraction,

$$\alpha = \int \alpha_v * dz \; / \; \Delta Z$$

then Equation (2) can be integrated along the z direction for the vapor phase of a fluid cell, i, to obtain,

$$\frac{d(A_i * \Delta Z_i * \alpha_i * \rho_{v_i})}{dt} + \int \left(\frac{d(A_i * u_{v_i} * \alpha_i * \rho_{v_i})}{dz} \right) dz = A_i * \Delta Z_i * \Gamma_i \qquad (3)$$

Where we have assumed the fluid properties within each element (fluid cell) remain spatially uniform (well mixed) and,

u_v : Vapor velocity

α : Vapor void fraction

ρ_v : Vapor density

ΔZ : Length of element, constant

A : Channel flow area

Γ : Rate of vapor generation per unit volume

i : Node number

Equation (3) can be applied to all fluid cells within the system to yield a set of coupled differential equations which in vectorized form can be presented as,

$$\frac{d[Y]}{dt} = [R]*\{Y\} + \{F\} \qquad (4)$$

Where:

$\{ Y \}$ = $\{ y_i, y_{i+1}, \ldots \}$; $i = 1, N$

y_i = $\alpha_i * \rho_{V,i}$

N : Number of fluid cells (nodes) in the system

[R] : A matrix of order N containing the coefficients which are function of fluid velocity

{ F } : A forcing vector with its elements in the absence of external source is defined as,

$$\{F\} = \{\Gamma_i\} \qquad (5)$$

The solution to the set of differential equations shown in form of Equation (4) at time $t = \Delta t$ is:

$$\{Y(\Delta t)\} = e^{([R]*\Delta t)}*\{Y_0\} + e^{([R]*\Delta t)} * \int_0^{\Delta t} e^{(-[R]*t)} *\{F\} * dt \qquad (6)$$

Where:

$\{ Y_0 \}$: A vector containing values of "y" at time zero which are obtained from previous time step

Δt : Integration time step

Performing the integration the following equation for Y is obtained:

$$\{ Y \} = e^{([R]*\Delta t)} * \{ Y_0 + [R]^{-1} * [I - e^{(-[R]*\Delta t)}] * \{ F \} \} \quad (7)$$

Where:

[I]: Identity matrix of order N

Equation (7) gives the exact solution for the set of equations given by Equation (4). The solution is valid for any chosen time step (Δt) as long as the forcing vector {F} and the coefficient matrix [R] remain constant for the duration of the time step. The rate of phase change (Γ) within a fluid cell (assumed constant here but could be a function of time) has been included in the forcing vector. Therefore, the phase change within one time step can not exceed the phasic mass inventory within the fluid cell. The forcing vector may also become a function of the rate of external input flow into the fluid cells. Therefore, the chosen time step cannot be larger than the time step which is used for calculation of the system's input flow or output flow.

Similar equations can be derived for liquid phase as well as for energy conservation and solved simultaneously. The model was implemented into RETACT®† [1] which is a five equation drift flux based thermal hydraulic code and has been widely used world wide for design of full scope nuclear power plant training simulators.

Results

The performance of the developed method has been tested by applying the model for simulation of boiling water reactors (BWRs) with various type of recirculation systems. Two sets of results, the first for a BWR with external recirculation pumps and the second set for a BWR with internal recirculation pumps, are presented here. For the case of the BWR with external pumps, the reactor core region was divided into 4 channels (one channel represents the bypass flow region and three channels represent the fuel region), but each channel was further divided into 6 axial nodes providing 24 nodes for calculation of thermal hydraulic parameters in the reactor core. Identical tests were performed with application of explicit Euler method of integration as well as with application of the analytical approach. The results show that for a configuration with 6 axial nodes (fluid cells) in the reactor core, the integration time step associated with the analytical method can be easily increased beyond the Courant limitation. For the case of this test the time step was set equal to 0.25 sec (4 cycles per second), where the material Courant number, defined as ($u * \Delta t / \Delta z$), can exceed one (for the case of this test it passed two in the reactor core region) without affecting the numerical stabilities. For comparison, the same nodalization required a time step smaller or equal to 0.083 sec (at least 12 cycles per second) with the explicit method. For comparison, the same nodalization required a time step smaller or equal to 0.083 sec (at least 12 cycles per second) with the explicit method.

†RETACT® is a registered trademark of Simulation, Systems & Services Technologies Company.

The test results for a few sample parameters are shown in Figures 2 through 5. For this test, the feedwater flow rate and enthalpy as well as the main steam line pressure downstream of the discharged flow from the steam dome were kept constant around their values corresponding to 100% normal condition. As shown in Figure-1, the test was started from 100% normal condition but the fuel power generation was suddenly dropped to the decay power level and then was increased back to 100% normal level in a single step mode after the void in the reactor core region had collapsed. Figure-2 compares the results for pressure in the steam dome region, and Figure-3 shows the results for the discharge flow rate from the steam dome. Figure-4 provides a comparison for the system mass calculated from the two different approaches, and Figure-5 shows the calculated results for void fraction in the steam dome. The comparison shows that the results obtained from the analytical method (executed with time step Δt=0.25 seconds) and the results obtained from explicit Euler method of calculation (executed with time step Δt= 0.083 seconds) are the same, although the required computer CPU time associated with the two methods are substantially different. For example, on a SGI-320 computer, the analytical model required 448 msecs per one second of real time simulation while for the same nodalization, the explicit method required 1032 msecs per one second of real time simulation.

The second test presented here deals with power excursion in a BWR with 10 internal recirculation pumps. For this case, the reactor core region was divided into 6 channels and each channel was further subdivided to 6 axial nodes (fluid cells) providing a total of 36 nodes within the reactor core region. The test was started from normal 100% condition, reactor power generation was suddenly dropped to the decay power level and then was set to the normal 100% power level after all the voids in the system had collapsed. Identical test conditions, except for the size of integration time steps, were imposed for the case of the analytical approach as well as for the case of the explicit Euler approach. The integration time step for the case of the analytical approach were set to Δt=0.1 second (10 cycles per second), while for the case of the explicit integration, a time step of Δt= 0.0417 second (24 cycles per second) was imposed due to numerical stability associated with the Courant limitation. On a SGI-Challenge computer, the analytical model required about 320 msecs per one second of real time simulation while for the same nodalization, the explicit method required 610 msecs per one second of real time simulation. Figure-6 compares the results for reactor vessel mass inventory calculated during the test through application of the two approaches. Figure-7 compares the test results for steam dome void fraction which are calculated through application of the two approaches. As can be seen, the calculated results from the two approaches agree well with each other although the time steps used for application of the two methods are significantly different. The code performance with the explicit method of integration has been previously compared and validated against data from test facilities and actual power plant data for various types of power plants and transients [eg, 16, 17]. The good agreement between performance of the code upon application of the analytical method (with relatively large time steps) in comparison with the code performance upon application of the explicit method of integration (with small time steps) shows that the analytical method improves computational efficiency as well as numerical stability. Consequently, the analytical method provides facilities for implementation of large integration time steps. On the other hand, with fixed CPU time and computer speed, the analytical approach provides opportunities for implementation of larger numbers of nodes. Thus, thermal hydraulic parameters can be calculated in detail for accurate simulation of response of measurement instruments.

Conclusion

Use of analytical methods for solution of two-phase flow conservation equations can significantly improve the numerical stability and computation efficiency for real time applications. The analytical approach can eliminate the material Courant limit associated with the size of a node. Therefore, the approach provides an opportunity to increase the number of nodes employed for simulation of a system and consequently can improve the simulation fidelity.

References:

1. Fabic, S. et al., "Advanced Thermohydraulic Modeling for Power Plant Simulators, Proc. of the Institute of Nuclear Engineers Conference on Simulation for Nuclear Reactor Technology, Cambridge, England (1984).

2. Fakory, M. R., "Component Flow-Path Thermal Hydraulic Model For Real-Time Simulation of Natural Circulation Steam Generators," ASME National Heat transfer Conference, 85-HT-63 (1985).

3. Anderson, J. G. M.,and Shaug, J. C., "TRACS Best Estimate Simulation in Real Time," Proceedings of the SCS Eastern Simulation Multiconference, Vol 22, No. 2 (1990).

4. Grimaldi, Delerue, J. and Agator, J. M., "Simulator for Post Accident Simulations," Proceedings of Specialist Meeting on Operator Aids for Severe Accidents Management and Training, OECD Halden, Norway (1993).

5. Podowski, M. Z. and Fakory M. R., "Two-Phase Flow Modeling For Next Generation Nuclear Power Plant Simulators," ASME/JSME Nuclear Engineering Conference, Vol. 1, pp 201-207 (1993).

6. Wulff, W., "Computational Methods For Multiphase Flow," Multiphase Science and Technology, edited by G. F. Hewitt, J. M. Delhaye, N. Zuber, Hemisphere Publishing (1990).

7. Gonzalez-Santalo, J. M. and Lahey, R. T. Jr., "An Exact Solution for Flow Transients in Two-Phase Systems by the Method of Characteristics," J. Heat transfer, Vol. 95, (1973).

8. Fakory, M. R. and Lahey, R. T., Jr., "An Analytical Model For The Prediction of Two-Phase Level During The Bottom Reflood of a BWR Channel," Proceedings of The Third International Topical Meeting on Reactor Thermal Hydraulics, Newport, Rhode Island (1985).

9. Hancox, W. T. and Banerjee, S., "Numerical Standards for Flow Boiling Analysis," Nuclear Science and Eng., 64, p. 106 (1977).

10. Agee, L. J., " An Analytical Method of Integrating The Thermal Hydraulic Conservation Equations," Journal of Nuclear Engineering and Design, Vol 42, pp 195-208 (1977).

11. Mahaffy, J. H., etal, "TRAC-PD2 An Advanced Best Estimate Computer program for Pressurized Water Reactor Loss of Coolant Accident Analysis," NUREG/CR-2054 (1981).

12. Ransom, V. H., etal, "RELAP5/MOD2 Code Manual," NUREG/CR-4312 (1985).

13. Rosa, M. P. and Podowski, M. Z., "Neutronically-Coupled Two-Phase Flow Modeling and Numerical Solution for Application in Boiling Water Nuclear Reactor," Proceedings of ASME/JSME Nuclear Engineering Conference, Vol 1, pp 209-220 (1993).

14. Ohkawa, T. and Tomiyama, A., "Effects of Mass Equations For Two-Phase Flow Analysis on Numerical Solutions," ASME/JSME Nuclear Engineering Conference, Vol. 1, pp 23-29 (1993).

15. Drew, A. D., "Analytical Modeling of Multiphase Flows," Boiling Heat Transfer, Modern Development and Advances, edited by R. T. Lahey, Jr., Elsevier Science Publishers (1992).

16. Fakory, M. R. and Olmos, J., "Simulation of SONGS Unit 2/3 NSSS with RETACT," Society for Computer Simulation, Simulation Series, Vol 24, No. 1, pp 201-212 (1991).

17. Fakory, M. R. and Meng, W. M., "Real-Time Simulation of Russian Designed VVER-440 Reactors With Horizontal Steam Generators," Proceedings of the Simulation Multiconference, pp 188-193 (1994).

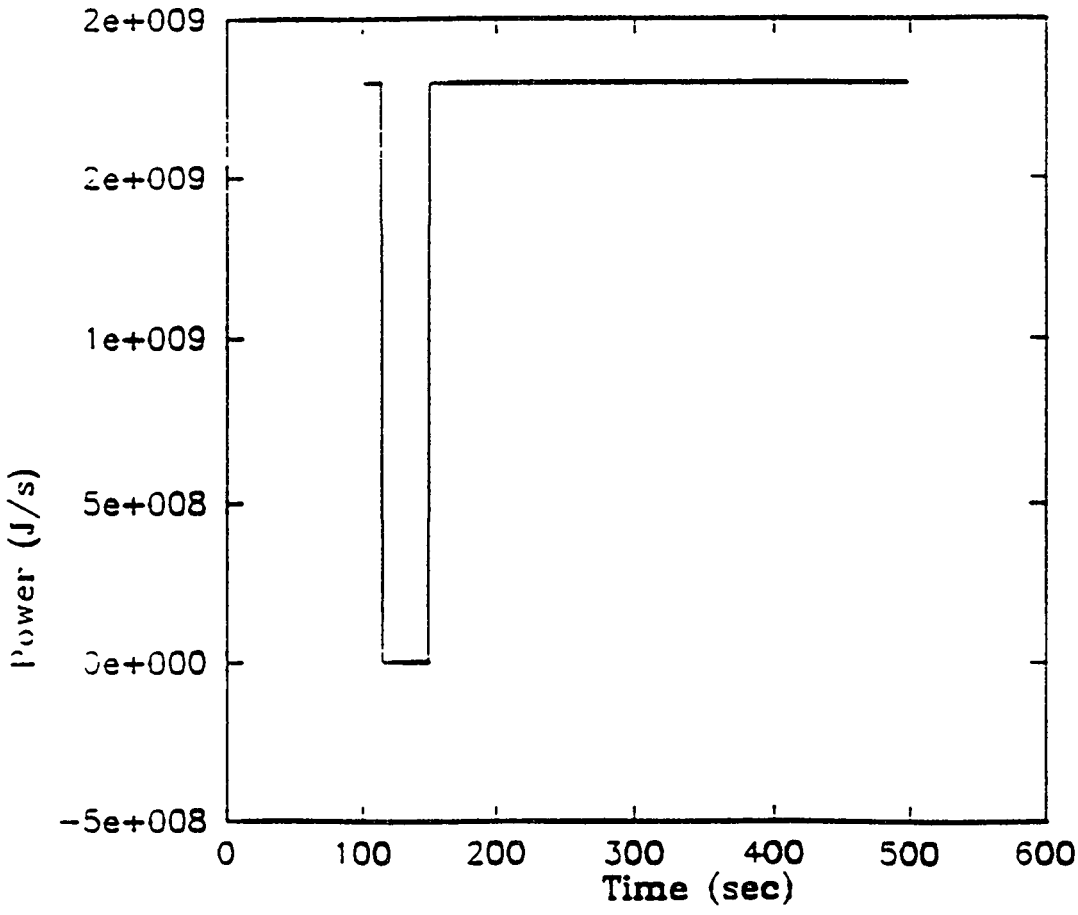
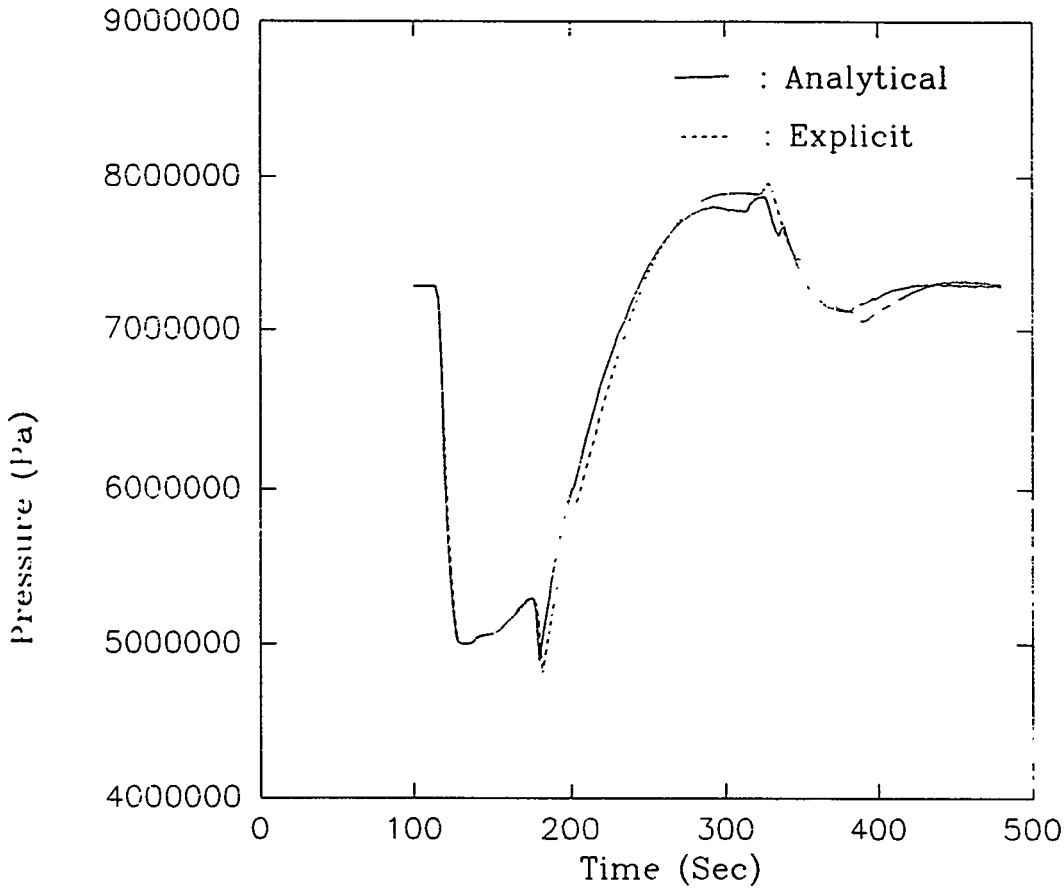


Figure-1, Power Generation Input During Power Excursion (Test #1)



Figure–2, Pressure In The Steam Dome Region (Test #1)

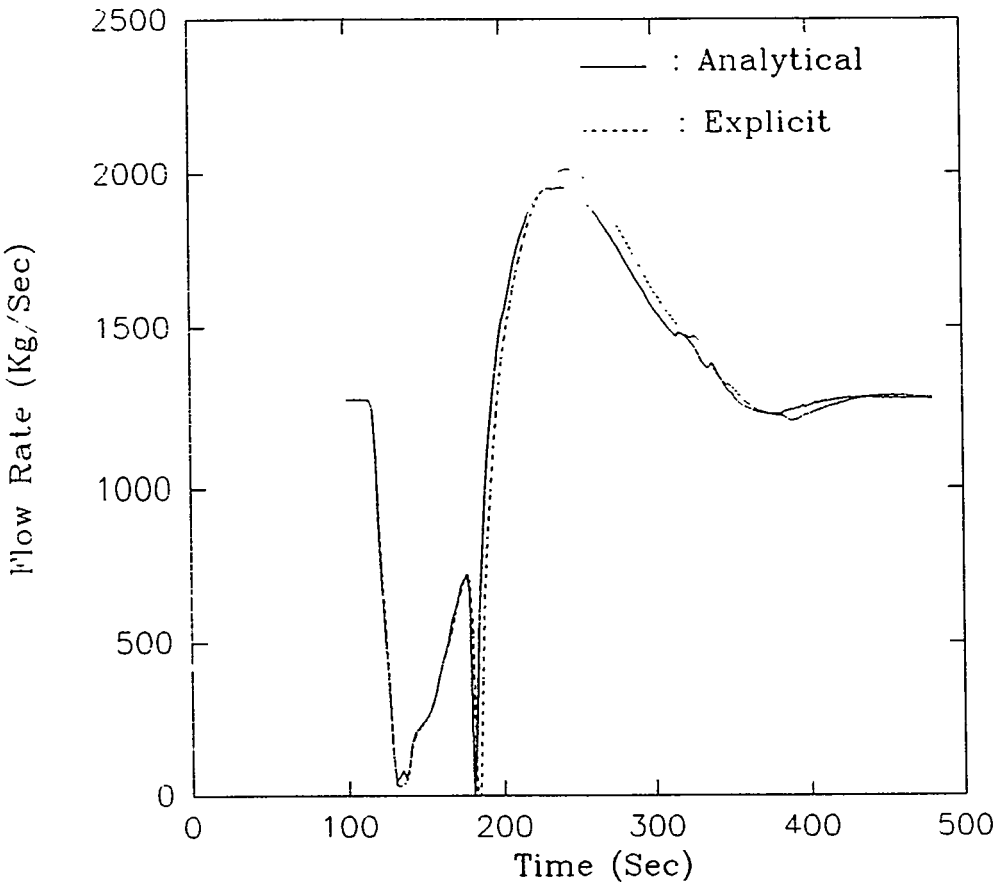


Figure-3, Steam Dome Discharge Flow Rate (Test #1)

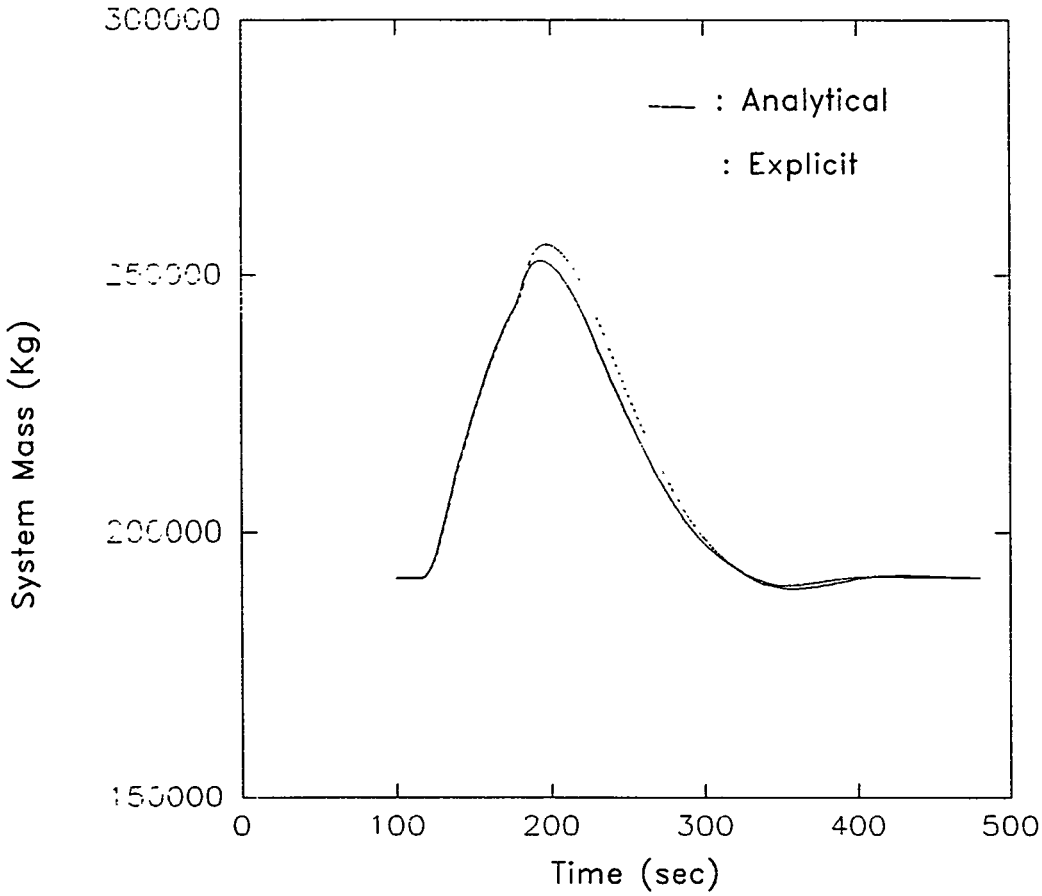


Figure-4 Total Fluid Mass In The Reactor Vessel

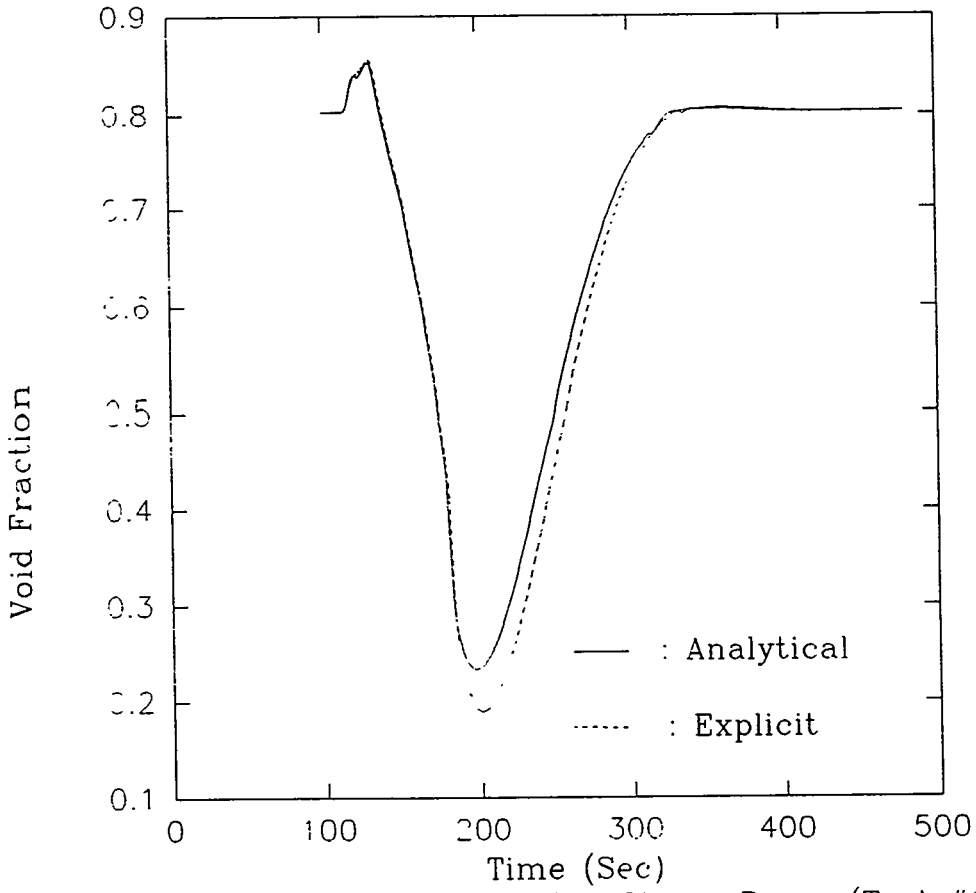


Figure-5, Void Fraction In The Steam Dome (Test #1)

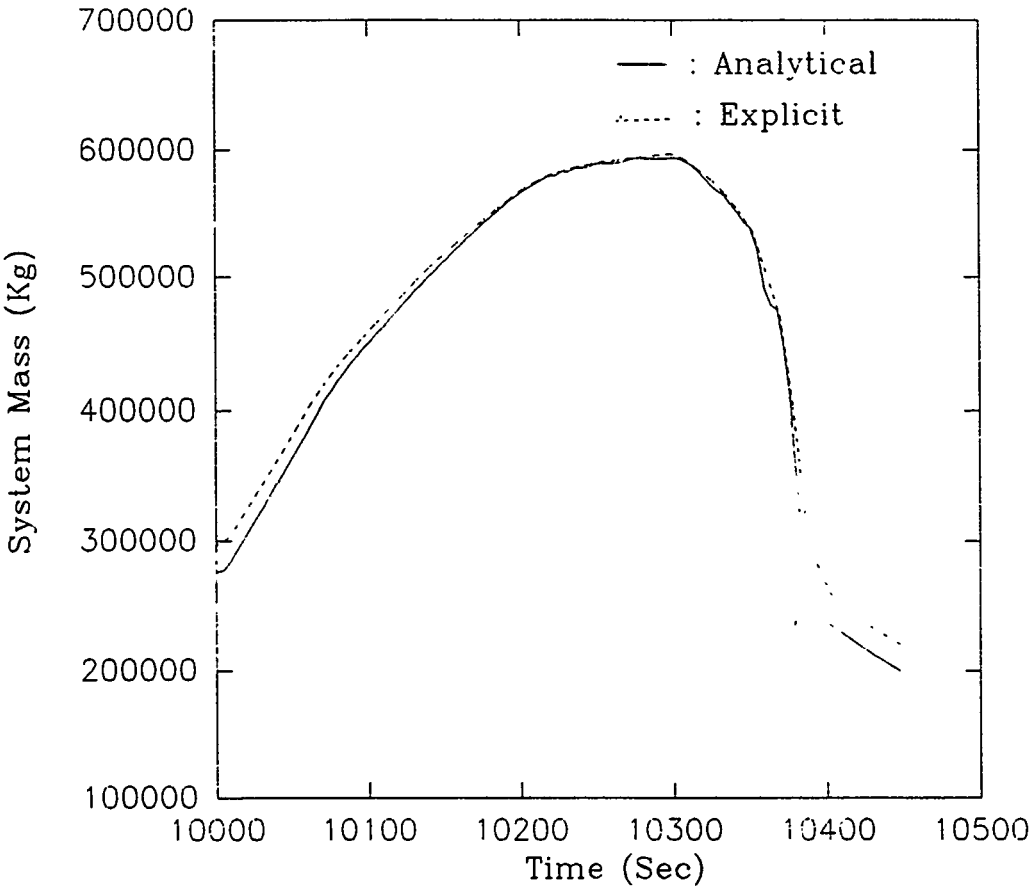


Figure-6, Coolant Mass In The Reactor Vessel (Test #2)

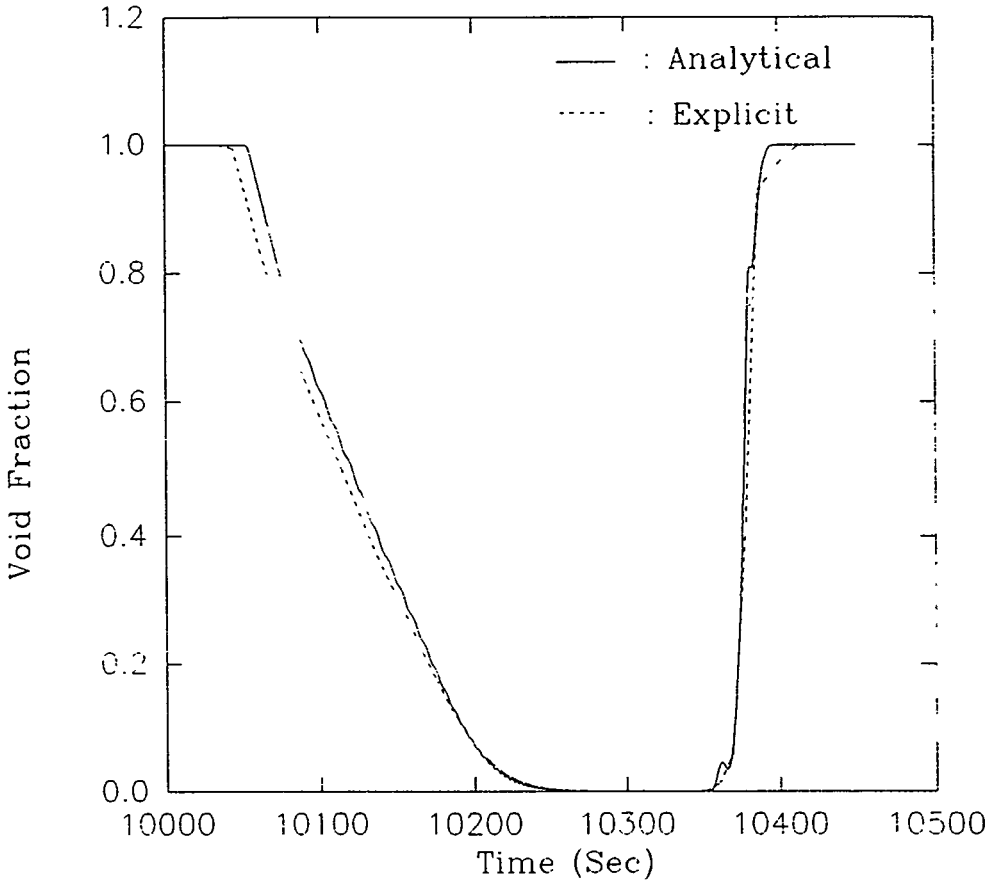


Figure-7, Void Fraction In The Steam Dome (Test #2)

NUMERICAL INVESTIGATION OF HEAT TRANSFER IN HIGH-TEMPERATURE GAS-COOLED REACTORS

Gary Chen and Samim Anghaie

Innovative Nuclear Space Power and Propulsion Institute
College of Engineering, University of Florida
Gainesville, FL 32611, U.S.A.

ABSTRACT

This paper proposes a computational model for analysis of flow and heat transfer in high-temperature gas-cooled reactors. The formulation of the problem is based on using the axisymmetric, thin layer Navier-Stokes equations. A hybrid implicit-explicit method based on finite volume approach is used to numerically solve the governing equations. A fast converging scheme is developed to accelerate the Gauss-Seidel iterative method for problems involving the wall heat flux boundary condition. Several cases are simulated and results of temperature and pressure distribution in the core are presented. Results of a parametric analysis for the assessment of the impact of power density on the convective heat transfer rate and wall temperature are discussed. A comparative analysis is conducted to identify the Nusselt number correlation that best fits the physical conditions of the high-temperature gas-cooled reactors.

I. INTRODUCTION

Over the past few decades, high temperature gas cooled reactors (HTGRs) have been considered and used for a wide range of applications. Compactness, high efficiency and very high temperature capability of these reactors are of great importance to power generation in space. Other applications of HTGRs include: terrestrial electric power generation, nuclear thermal propulsion and direct use of high temperature gas for a variety of industrial processes such as steel-making[1]. The technology of HTGRs for commercial power generation, as well as the computational methods for analysis of thermal fluid performance of these reactors are well developed. The majority of existing HTGR thermal fluid analysis methods use empirical correlation to resolve heat and momentum transfer at the fuel-coolant boundary. However for HTGR concepts with operating parameters beyond those of commercial HTGRs, the issue of the accuracy and applicability of empirical correlations are not fully resolved. In particular, energy transport in very compact space power reactor concepts may require flow at very high velocities and high Reynolds numbers. This paper presents a detailed non-correlation based computational thermal-fluid model for analysis of flow and heat transfer in HTGR cores. The computational model is used to assess the performance of several mechanistic correlations and 1-D approximation models for calculation of heat transfer and pressure drop in HTGR cores.

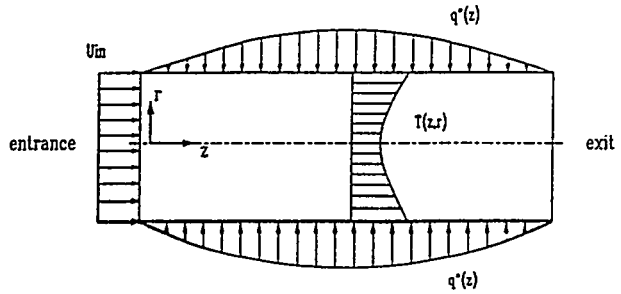


Fig. 1 Schematic of numerical modeling .

The numerical model solves the compressible thin layer Navier-Stokes equations for turbulent flow of a gas in a smooth tube which is shown in Figure 1. Viegas and Rubesin[2] have addressed the complexities of dealing with the numerical solution of Navier-Stokes equations for the prediction of heat transfer. In their treatment, they have used empirical relations for the turbulent boundary layer instead of near wall fine grids. Since mid 1970's the explicit techniques with highly stretched fine grids have been the dominant method for near wall heat transfer calculation. This approach lends itself to computational stability limitations and slow rate of convergence. To remove the time step limitation, a fully implicit numerical scheme has been introduced by Briley and McDonald[3]. Although the implicit procedure allows for large time step sizes, the factorization introduces an error proportional to the time step, which restricts the time step size. MacCormack[4,5] developed a hybrid implicit-explicit method using a finite volume method combined with the Gauss-Seidel and Newton iterative scheme to solve compressible Navier-Stokes equations. In this method an explicit scheme and flux splitting procedure are used to change a block matrix into a diagonally dominant matrix structure which is more amenable to the Gauss-Seidel row-iteration procedure.

The work presented in this paper utilizes the MacCormack hybrid method with the Baldwin and Lomax[6] algebraic turbulence model. To meet the requirements of the heat flux thermal boundary conditions in the HTGR cores, a new enthalpy-rebalancing scheme is developed to accelerate the rate of convergence. Real helium gas properties at high temperature are used. A variety of parameters for the HTGR coolant flow, such as core power and mass flux, are considered and

investigated. The Nusselt number correlation and pressure drop equation that best fits the physical conditions of helium cooled flow is identified.

II. MATHEMATICAL FORMULATION

2.1 Governing Equations

Compressible thin layer Navier-Stokes equations are used to simulate hydrogen or helium flow in a HTGR nuclear reactor. This model considers both convective and conductive heat fluxes. The radiative heat transfer in very narrow channels of HTGRs which are cooled by transparent gases is several orders of magnitude smaller than the conductive and convective heat transfer rates[7] and is not included in this model. At temperatures up to 3000°K the mean free path of the thermal radiation is many times larger than the transverse flow dimensions in HTGRs. Therefore the absorptivity of the thermal radiation is very small and can be ignored for this analysis. For HTGR cores with very high axial temperature gradient, the conductive and radiative heat transfer may prove to be significant. However, the analysis of wall-to-wall radiative heat transfer and conduction through the solid fuel is beyond the scope of this investigation and in not included in the model. The Navier-Stokes equations in strong conservative and axisymmetric form are given as

$$\frac{\partial \overline{U}}{\partial t}+\frac{\partial \overline{F}_i}{\partial z}+\frac{\partial \overline{G}_i}{\partial r}+\overline{H}_i=\frac{\partial \overline{G}_v}{\partial r}+\overline{H}_v \tag{1}$$

where

$$\overline{U}=\begin{bmatrix}\rho\\ \rho u\\ \rho v\\ e\end{bmatrix}\quad \overline{F}_i=\begin{bmatrix}\rho u\\ \rho u^2+P\\ \rho uv\\ (e+P)u\end{bmatrix}\quad \overline{G}_i=\begin{bmatrix}\rho v\\ \rho uv\\ \rho v^2+P\\ (e+P)v\end{bmatrix}\quad \overline{H}_i=\begin{bmatrix}\rho v\\ \rho uv\\ \rho v^2\\ (e+P)v\end{bmatrix} \tag{2}$$

and the viscous and thermal source terms are

$$\overline{G}_v=\begin{bmatrix}0\\ \mu_T\frac{\partial u}{\partial r}\\ 4\frac{\mu_T}{3}\frac{\partial v}{\partial r}-\frac{2}{3}\mu_T\frac{v}{r}\\ \mu_T u\frac{\partial u}{\partial r}+\frac{4}{3}\mu_T v\frac{\partial v}{\partial r}-q''_c\end{bmatrix} \tag{3}$$

$$\overline{H}_v=\frac{1}{r}\begin{bmatrix}0\\ \mu_T\frac{\partial u}{\partial r}\\ 2\mu_T(\frac{\partial v}{\partial r}-\frac{v}{r})\\ \mu_T u\frac{\partial u}{\partial r}+\frac{4}{3}\mu_T v\frac{\partial v}{\partial r}-q''_c\end{bmatrix} \tag{4}$$

In the above formulas, u and v are the velocity components in z and r directions respectively, ρ is the density, P is the pressure, μ_T is the total viscosity, q''_c is the conductive heat flux, and e is the total energy per unit volume which is related to the internal energy ε and kinetic energy.

$$e=\rho\left[\varepsilon+\frac{1}{2}(u^2+v^2)\right] \tag{5}$$

The thermal and transport property of helium are used for all cases considered in this study.

2.2 Turbulence Model

The turbulence modeling is the most important factor influencing the convergence of the Navier-Stokes equation solver. The turbulent models are classified according to the number of supplementary partial differential equations. This number ranges from zero (algebraic model) to two (κ-ε model). The turbulent shear stresses in the mean-momentum equations are replaced by product of an effective viscosity and a mean rate of strain. The zero-equation model relies on specifying velocity and length scales in terms of the mean flow, which has been used to yield faster convergence at reasonable accuracy in this study. The algebraic turbulence model used in this analysis is a two-layer algebraic eddy viscosity model[6] in which the effects of turbulence are simulated in terms of the eddy viscosity coefficient, μ_t. For the inner region, the Prandtl-Van Driest formulation for turbulent viscosity is used:

$$(\mu_t)_{inner}=\rho k^2 y^2[1-e^{(\frac{y^+}{A^+})}]^2|\omega| \tag{6}$$

For the outer region, the eddy viscosity is given by

$$(\mu_t)_{outer}=kC_{cp}\rho\ F_{wake}F_{kleb}(y) \tag{7}$$

$$F_{wake}=y_{\max}F_{\max} \tag{8}$$

where k is the Clauser constant, C_{cp} is an additional constant, F_{max} is the maximum value of F(y) in a radial profile and the function F_{kleb} (y) is the Klebanoff intermittency factor[6] given by

$$F_{kleb}(y)=\left[1+5.5\left(\frac{C_{kleb}y}{y_{\max}}\right)^6\right]^{-1} \tag{9}$$

The constants used for this model are A^+=26, C_{cp}=1.6, C_{wk} =0.25, C_{kleb} =0.3, k=0.4 and K=0.0168, and ω represents the vorticity.

This model has the advantage of avoiding the necessity for finding the edge of the boundary layer and exhibits good accuracy.

III. NUMERICAL PROCEDURE

In this study, MacCormack's hybrid implicit-explicit upwind approach with the line Gauss-Seidel and Newton iteration procedure is employed[8]. An algebraic grid clustering technique is used to obtain a high degree of accuracy within the limits of the second-order accurate solution scheme.

The discrete governing equations take the following form:

The predictor step

$$\Delta U^{n}_{i,j} = -\Delta\left[\frac{D_+\cdot F_i}{\Delta x}+\frac{D_+\cdot(G_i-G_v)}{\Delta r}-H\right]^{n}_{i,j}$$

$$\left[I+\Delta\left(\frac{D_+\cdot A_-}{\Delta x}+\frac{D_-\cdot A_+}{\Delta x}\right)+\Delta\left(\frac{D_+\cdot B_-}{\Delta r}+\frac{D_-\cdot B_+}{\Delta r}\right)-\frac{\Delta t}{\delta r}(\delta G_v)\right]^{n}_{i,j}\delta U^{n+1}_{i,j}=\Delta U^{n}_{i,j}+\Delta H^{n}_{i,j}$$

$$U^{n+1}_{i,j}=U^{n}_{i,j}+\delta U^{n+1}_{i,j} \tag{10}$$

The corrector step

$$\Delta U^{n+1}_{i,j} = -\Delta\left[\frac{D_-\cdot F_i}{\Delta x}+\frac{D_-\cdot(G_i-G_v)}{\Delta r}-H\right]^{n+1}_{i,j}$$

$$\left[I+\Delta\left(\frac{D_+\cdot A_-}{\Delta x}+\frac{D_-\cdot A_+}{\Delta x}\right)+\Delta\left(\frac{D_+\cdot B_-}{\Delta r}+\frac{D_-\cdot B_+}{\Delta r}\right)-\frac{\Delta t}{\delta r}(\delta G_v)\right]^{n+1}_{i,j}\delta U^{n+1}_{i,j}=\Delta U^{n+1}_{i,j}+\Delta H^{n}_{i,j}$$

$$U^{n+1}_{i,j}=\frac{1}{2}(U^{n}_{i,j}+U^{n+1}_{i,j}+\delta U^{n+1}_{i,j}) \tag{11}$$

where the difference operators D_+, D_- and δ represent forward, backward and central difference approximations. $A=\partial F/\partial U$ and $B=\partial G/\partial U$ are the Jacobians of F and G with respect of U. Using a flux splitting scheme[9] the implicit block matrix equations can be changed into a diagonal matrix of the following form

$$\begin{bmatrix} B_{jl} & A_{jl} & C_{jl} & & & & & \\ & \ddots & & & & & & \\ & & \ddots & & & & & \\ & & B_j & A_j & C_j & & & \\ & & & \ddots & & & & \\ & & & & \ddots & & & \\ & & & & B_2 & A_2 & C_2 & \\ & & & & & -E & I & \end{bmatrix}\begin{bmatrix} \delta U_{i,jl} \\ \vdots \\ \vdots \\ \delta U_{i,1} \\ \vdots \\ \vdots \\ \delta U_{i,2} \\ \delta U_{i,1} \end{bmatrix}=\begin{bmatrix} \Delta U_{i,jl}+\dots \\ \vdots \\ \vdots \\ \Delta U_{i,1}+\dots \\ \vdots \\ \vdots \\ \Delta U_{i,2}+\dots \\ 0 \end{bmatrix} \tag{12}$$

where A_j, B_j and C_j are block matrices in terms of u, v, ρ, T, Δx, Δr and Δt. The last equation in Equation (12) is used to set the boundary conditions. The hydraulic and thermal boundary conditions at the solid wall are set as the following:

$u_{i,1}=-u_{i,2}$ axial velocity condition (13)

$v_{i,1}=-v_{i,2}$ radial velocity condition (14)

$T_{i,1}=2T_{i,wall}-T_{i,2}$ uniform wall temperature condition (15)

$T_{i,1}=T_{i,2}+\frac{q^1}{k}(r_{i,2}-r_{i,1})$ heat flux boundary condition (16)

A simple sketch of finite volume mesh to express the boundary conditions is shown in Figure 2. The Gauss-Seidel row iteration method is used to solve diagonal metrics equation (12).

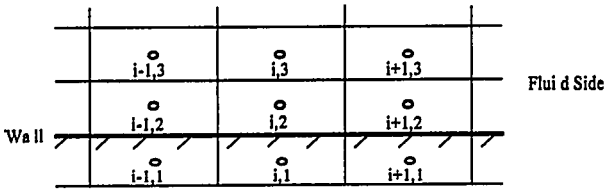


Fig. 2 Finite volume grid system.

3.2 Enthalpy-Rebalancing Scheme

In order to solve problems under an arbitrary heat flux boundary condition, a novel method of enthalpy-rebalancing at the transverse flow surface has been developed. This scheme is based on the fact that under steady conditions the gas enthalpy rise at each transverse flow surface is equal to the heat removal from the wall. Mathematically, it is written as follows:

$$(\Delta Q)_i = 2\pi R\Delta z q''_i \tag{17}$$

Equation (16) is explicitly solved to obtain the balancing bulk temperature $(T_b)_i$, that is

$$(T_b)_{i+1}=(T_b)_i+\frac{2\Delta z q''_i}{Cp_i(\rho u)_i R} \tag{18}$$

where T_b is the bulk temperature, and Cp_i is the local specific heat. In this section, $(T_b)_i$ is known, $(T_b)_{i+1}$ can be found from Equation (18) which is always true in the transient procedure based on the enthalpy-balancing principle. The bulk temperature $((T_b)_{i+1})_{num}$ is calculated from temperature fields under every iteration. Since these two bulk temperatures should be equal, their relation may be used as a convergence criterion as follows:

$$\delta=\frac{(T_b)_{i+1}}{((T_b)_{i+1})_{num}} \tag{19}$$

Before achieving the steady-state flow conditions, the mass flux, ρu, is always smaller than the final steady value. Therefore, during the transitory pre-steady state conditions the value of δ is greater than one. Whenever the mass flux, ρu, approaches its steady-state value, the convergence parameter δ approaches its asymptotic value which is one. At this moment, the wall boundary condition (16) is used to calculate the wall temperature. As soon as δ is equal to one, a thermal steady-state condition is achieved. At this point, the wall temperature is frozen to control the heat transfer through the solid wall until a global thermal convergence is achieved. This scheme has been proven successful when problems with heat flux boundary condition are to be solved.

IV. RESULTS AND DISCUSSION

A dual path cermet fuel fast spectrum reactor is used as a computational model to analyze the high-temperature gas-cooled reactor system. The core consists of 631 fuel rods and 37 holes per fuel rod which has flow equivalent diameter of 3.2 mm and heated length of 0.544 m. The system pressure of 6.5 MPa and the core power of 25 MW, 50 MW, 75 MW and 100 MW are used, respectively. The Reynolds number of the flow is in the range of 10^4 to 10^5.

The flow domain was divided into 54 radial and 54 axial control volumes spaced non-uniformly. A fine grid, defined by algebraic method, was used near the wall to ensure more than two grid points in the laminar sublayer which is used to control the heat flux near the wall. The convergence history in Figure 3 shows that the root-mean-squared residuals of velocity and temperature drop 5 and 4 orders of magnitude in about 1000

iterations or 300 minutes of CPU time using an IBM 486 computer. The Figure 4 shows the typical computational grids.

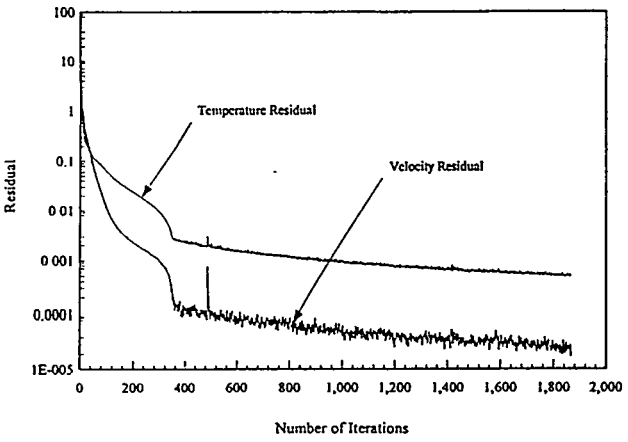


Fig. 3 Convergence history.

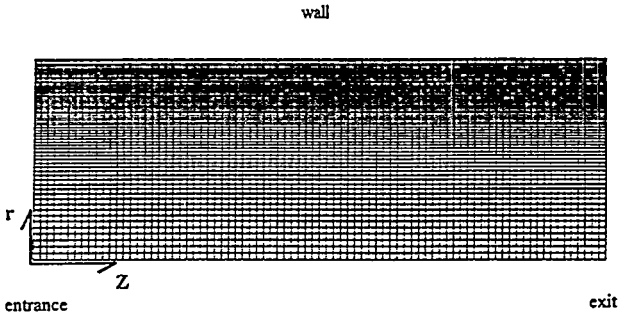


Fig. 4 Overall view of computational grid (84x54).

The maximum temperature in the HTGR reactor is strongly dependent on the power density. To demonstrate the influence of power density, a calculation was done with core power of 25 MW, 65 MW and 100 MW, which is shown in Figure 5. Because of high heat flux the derivative of temperature at wall is much higher than temperature at the center area. The temperature at Q=100 MW grows much faster than temperature at Q=65 MW.

Nusselt number correlations are of great importance to calculation of the heat transfer. However, almost all of these correlations are developed under fully developed and constant wall heat flux conditions. In some cases the heat flux used for the generation of the experimental data base is rather low. The low wall heat flux indicate small temperature gradient in the flow boundary layer. Therefore the changes in flow properties due to temperature gradient may not be important. Under flow, temperature and heat flux conditions of ultrahigh temperature and compact HTGRs, similar to those proposed for space power and propulsion applications, the flow is not fully developed, so the temperature gradient could be very large and the wall thermal boundary conditions may be different from what is used for the development of the experimental data base used for the derivation of the particular heat transfer empirical correlation. Thus, the detailed computational analysis developed in this work is used to evaluate the most common experimental correlations for wall heat transfer in HTGRs.

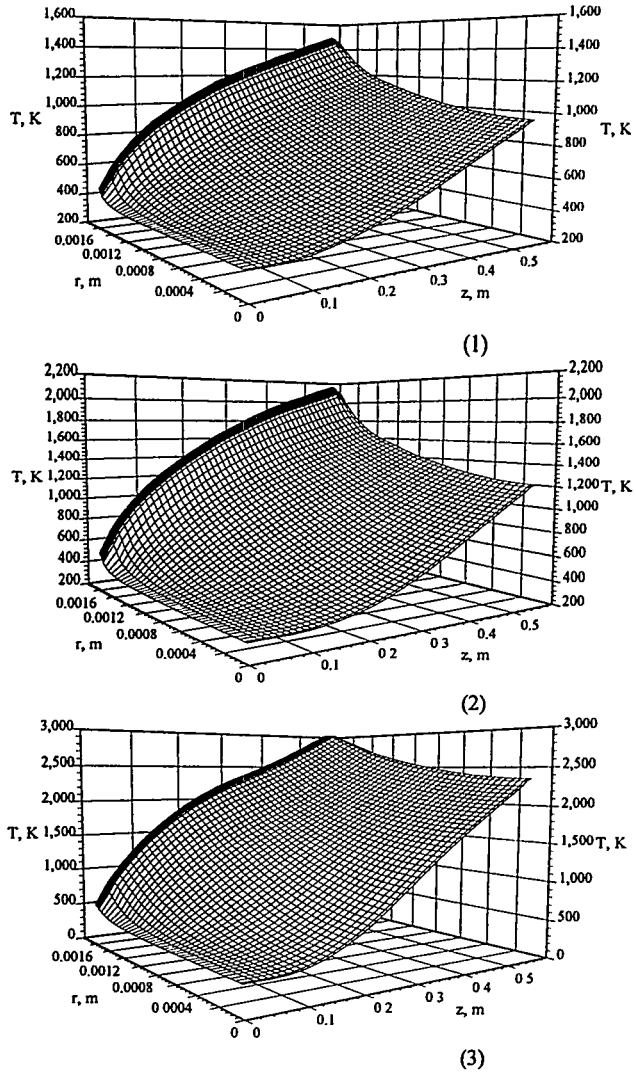


Fig. 5 Comparison of temperature distribution for different valued of core power: (1) Q=25 MW, (2) Q=65 MW, (3) Q=100 MW.

Among the long list of correlations for the Nusselt number, four correlations which seem to have more relevance to the heat transfer in a high-temperature gas-cooled reactor are chosen for this analysis. These correlations which have been developed by Colburn, Gnielinski, Karman-Boelter-Martinelli and Notter-Sleicher and the associated functions for variable property and axial distance corrections are as follows:

The Colburn correlation[10]

$$Nu = 0.023\,\mathrm{Re}^{0.8}\,\mathrm{Pr}^{\frac{1}{3}} \tag{20}$$

The Gnielinski correlation[10]

$$Nu = \frac{(\mathrm{Re}-1000)\,\mathrm{Pr}\left(\frac{f}{2}\right)}{1.07+12.7\left(\mathrm{Pr}^{\frac{2}{3}}-1\right)\sqrt{\frac{f}{2}}} \tag{21}$$

The Karman-Boelter-Martinelli correlation[11]

$$Nu = \frac{\mathrm{Re}\,\mathrm{Pr}\sqrt{\frac{f}{2}}}{0.833\left(5\mathrm{Pr}+5\ln(5\mathrm{Pr}+1)+2.5\ln\left(\mathrm{Re}\frac{\sqrt{\frac{f}{2}}}{60}\right)\right)}$$

$$f = 0.0014 + \frac{1}{8}\mathrm{Re}^{-0.32} \tag{22}$$

The Notter-Sleicher correlation[11]

$$Nu = 5 + 0.015\mathrm{Re}^{a}\,\mathrm{Pr}^{b}$$

$$a = 0.88 - \frac{0.24}{\mathrm{Pr}+4} \tag{23}$$

$$b = \frac{1}{3} + 0.5e^{-0.6\,\mathrm{Pr}}$$

The Perkins and Worsoe-Schmidt axial distance correction[11]

$$f_z = \left[1+\left(\frac{z}{D}\right)^{-0.7}\left(\frac{T_w}{T_b}\right)^{0.7}\right] \tag{24}$$

The Notter and Sleicher property correction[11]

$$f_p = \left(\frac{T_w}{T_b}\right)^{0.3-\left(\log_{10}\left(\frac{T_w}{T_b}\right)\right)^{0.25}} \tag{25}$$

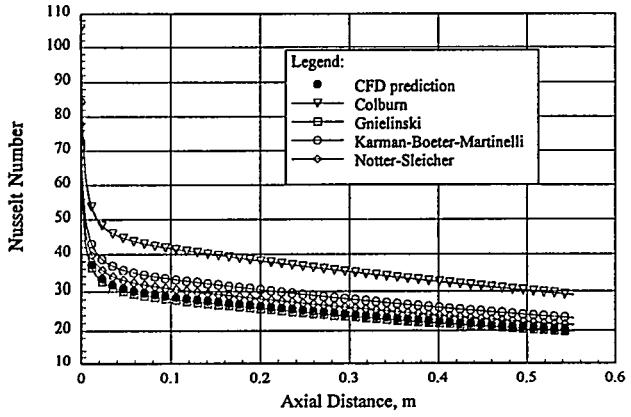


Fig. 6 Comparison of the numerically calculated Nusselt number with the empirical correlations.

Figure 6 compares results of detailed numerical calculations with Nusselt number correlations. The Gnielinski equation, when is combined by Perkins and Worsoe-Schmidt axial distance correction and Notter-Sleicher property correction shows the best agreement with the computationally calculated Nusselt number based on full compressible Navier-Stokes equations.

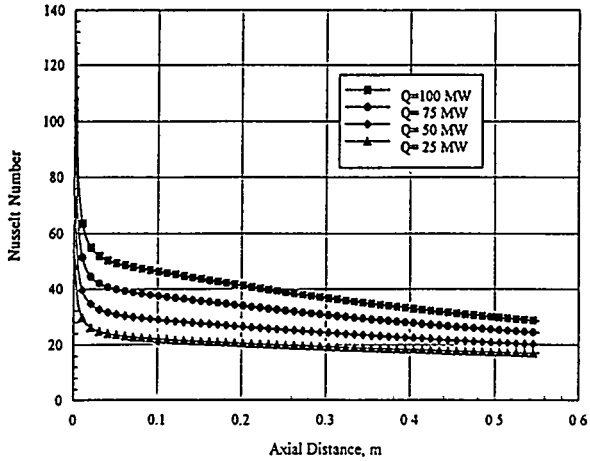


Fig. 7 Local Nusselt number variation (G=45kg/m^2.s).

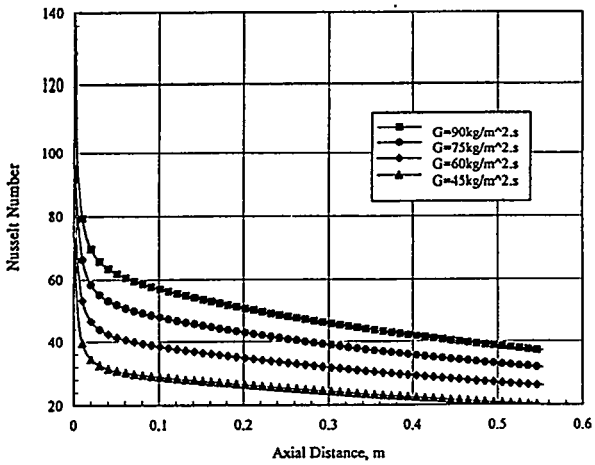


Fig. 8 Local Nusselt number variation (Q=50 MW).

Nusselt number variation along the tube length is shown in Figures 7 and 8. From the results of this study, the Nusselt number increases as the core power increases. The differences of the Nusselt number of core power of 25 MW, 50 MW, 75 MW and 100 MW at x=0.554 m are about 14% and differences of the Nusselt number of mass flux of 45, 60, 75 and 90 kg/m^2.s is about 29.5%. It is interesting to note that the core power and mass flux have similar effects to Nusselt number.

Similarly, simplified equations are used to calculate the pressure drop in heated channels of HTGRs. These equations may or may not be applicable to the flow and thermal conditions of ultrahigh-temperature gas-cooled reactors. An analysis is performed to evaluate the accuracy and validity of the pressure drop equations for HTGRs. Equations which are conveniently used to calculate the accelerational and frictional pressure drop in HTGR cores are:

$$\Delta P = \rho V^2\left[\left(\frac{T_2}{T_1}-1\right)+2f\frac{\Delta Z}{D}\left(\frac{T_1+T_2}{2T_1}\right)\right] \tag{26}$$

$$\Delta P = \frac{RG^2T_m}{P_m}\left(\ln\frac{\rho_1}{\rho_2}+2f\frac{\Delta Z}{D}\right) \tag{27}$$

$$\Delta P = G^2\left[\left(\frac{1}{\rho_2}-\frac{1}{\rho_1}\right)+2f\frac{\Delta Z}{D}\left(\frac{1}{\rho_m}\right)\right] \quad (28)$$

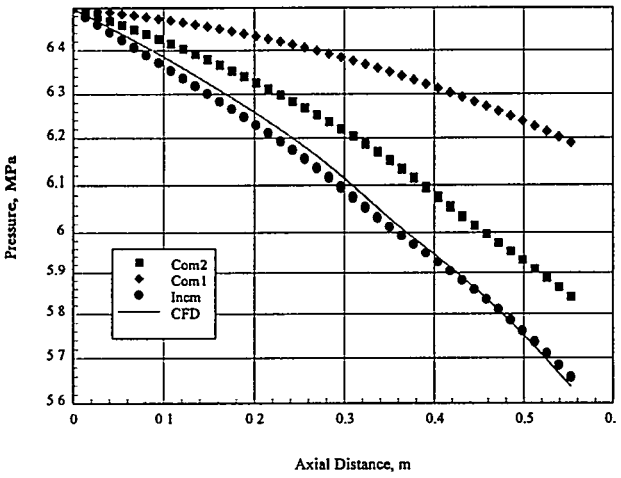


Fig. 9 Pressure drop correlation comparison.

Figure 9 shows the axial pressure distribution in the heated flow channel as calculated by the detailed Navier-stokes solver can also by Equations (26)-(28). The legend appearing in the Figure 9 is: Incm implies equation (26) which is found in Reference [12]. Com1 implies equation (27) and Com2 implies equation (28) which can be found in Reference [13]. From this analysis it is evident that the equation (26) provided the best agreement with the numerical results. This is mainly due to the fact that the thermal evolution of the flow is taken into account in the equation (26), which is much closer to the governing equation used for the CFD calculation.

V. CONCLUSIONS

In this paper, a convective numerical model is developed to simulate fluid flow and heat transfer in high temperature gas-cooled reactor. The real transport and thermal properties of helium gas are used. The axisymmetric, thin-layer Navier-Stokes equations are employed as the governing equations for this model. The results of this study indicate that HTGRs can be operated at power density ratings up to about 1000 W/cm^3. As power density increases, wall temperature and Nusselt number increases. In particular, the Gnielinski correlation with axial and property corrections provide the best agreement with numerical results.

ACKNOWLEDGMENT

This work was performed for the Department of Defense Ballistic Missile Defense Organization Innovative Science and Technology Office, under contract number NAS3-26314, managed by NASA Lewis Research Center.

REFERENCES

[1] S. B. Hosegood, "The high temperature reactor & process applications," Proceedings of the International Conference organized by British Nuclear Energy Society, 242-250 (1974).

[2] J. R. Viegas and M.W. Rubesin, "On the Use of Wall Function as a Boundary Conditions for Two-dimensional, Separated Compressible Flows," AIAA 23rd Aerospace Sciences Meeting, Reno, Nevada, AIAA 85-0180, 1-11 (1985).

[3] M. R. Briley and H. McDonald, "Solution of the Three-dimensional Compressible Navier-Stokes Equations by an Implicit Technique," Proceeding of 4th International Conference on Numerical Method in Fluid Dynamics, 35-38 (1975).

[4] R. W. MacCormack, "A Numerical Method for Solving the Equations of Compressible Viscous Flow," AIAA Journal, 20, 1275-1281 (1982).

[5] R. W. MacCormack, "Current Status of Numerical Solutions of the Navier-Stokes Equations," AIAA 23rd Aerospace Sciences Meeting, Reno, Nevada, AIAA 85-032, 1-21 (1985).

[6] B. S. Baldwin and H. Lomax, "Thin Layer Approximation and Algebraic Model for Separated Turbulent Flows," AIAA 16th Aerospace Sciences Meeting, Huntsville, Alabama, AIAA 78-257, 1-15 (1978).

[7] S. W. Chung and S. Anghaie, "A Computational Model for Determination of Wall Heat Transfer Rate Due to Flow of Very High Temperature, Optically Thick Gas," NURETH-5, Proc. Fifth International Topical Meeting on Reactor Thermal Hydraulics, Salt Lake City, UT, Septeber, 1992.

[8] D. A. Anderson, J. C. Tannehill, and R. H. Pletch, Computational Fluid Mechanics and Heat Transfer, Hemisphere Publishing Corporation, (1984).

[9] J. L. Steger and R.F.Warming, "Flux Vector Splitting of the Inviscid Gas Dynamic Equations with Application to Finite-Difference Methods," NASA TM D-78605, (1979).

[10] B. S. Petukhov, "Heat Transfer and Friction in Turbulent Pipe Flow with Variable Physical Properties," Advances in Heat Transfer, Academic, New York, pp. 503-564, (1970).

[11] R. K. Shah and R. S. Johnson, "Correlations for Fully Developed Turbulent Flow through Circular and Noncircular Channels," Proceedings of the 6th International Heat and Mass Transfer Conference, Madras, India, pp. 75-96, (1981).

[12] S. Anghaie, "reactor Thermal Hydraulics," Class Notes, University of Florida, Gainesville, Florida, (1992).

[13] W. M. Kays & H. C. Perkins, "Forced convection internal flow in Ducts," Handbook of Heat Transfer Fundamentals, 7, McGraw Hill, New York (1985).

Development of a Graphical User Interface for the TRAC Plant/Safety Analysis Code

Ann E. Kelly
Cynthia K. Harkins
Richard J. Smith
Knolls Atomic Power Laboratory (KAPL)

Abstract:

A graphical user interface (GUI) for the Transient Reactor Analysis Code (TRAC) has been developed at Knolls Atomic Power Laboratory. This X Window based GUI supports the design and analysis process, acting as a preprocessor, runtime editor, help system and post processor to TRAC-PF1/MOD2. TRAC was developed at the Los Alamos National Laboratory (LANL). The preprocessor is an icon-based interface which allows the user to create a TRAC model. When the model is complete, the runtime editor provides the capability to execute and monitor TRAC runs on the workstation or supercomputer. After runs are made, the output processor allows the user to extract and format data from the TRAC graphics file. The TRAC GUI is currently compatible with TRAC-PF1/MOD2 V5.3 and is available with documentation from George Niederauer, Section Leader of the Software Development Section, Group TSA-8, at LANL.

Users may become functional in creating, running, and interpreting results from TRAC without having to know Unix commands and the detailed format of any of the data files. This reduces model development and debug time and increases quality control. Integration with post-processing and visualization tools increases engineering effectiveness.

1.0 Introduction

The Transient Reactor Analysis Code (TRAC-PF1/MOD2) is a state-of-the-art, best-estimate thermal-hydraulic, reactor kinetics and plant analysis code that was developed at the Los Alamos National Laboratory (LANL)[1]. It is used for simulating the performance characteristics of pressurized water reactors as well as thermal-hydraulic test facilities. Because TRAC provides so many capabilities, creating a TRAC model is a complex and often error prone task. It is especially difficult for the user to keep track of the dependencies between input parameters. The goal of the TRAC GUI development team was to devise a graphical interface (Figure 1) that makes the creation of TRAC input files more intuitive and less prone to errors. One of the primary development requirements was to make the GUI easier to use than workstation text editors. This interface will minimize plant design and analysis process cycle time while maximizing quality control. The GUI must provide runtime control and access to the various output files of TRAC, such as the dump, restart and graphics files.

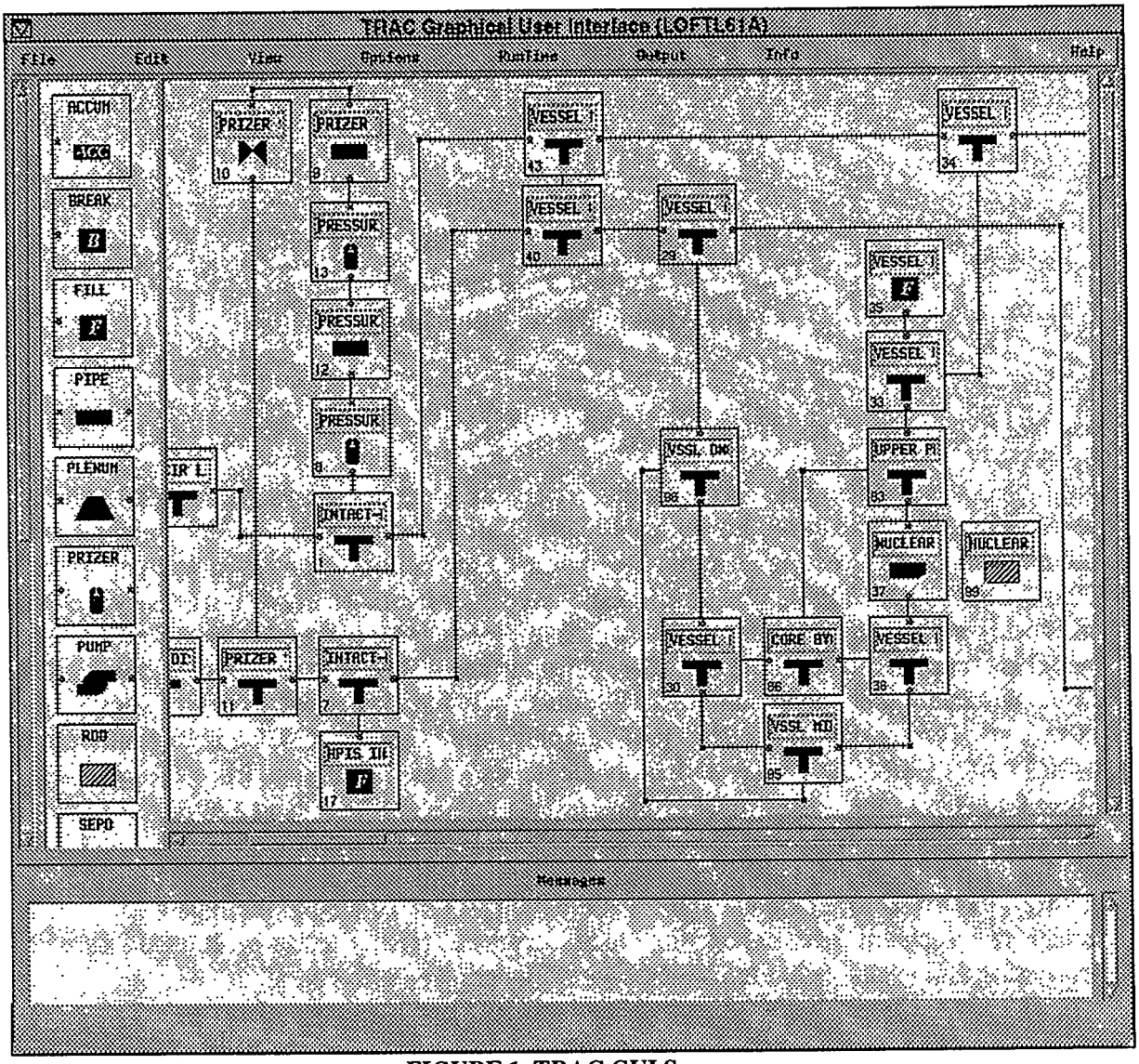


FIGURE 1. TRAC GUI Screen

The TRAC GUI was designed to support different levels of users. This includes beginners who have no experience with TRAC, advanced users who know the TRAC input format, and users who will be making many runs which are permutations of a base model. Novice users need a GUI to provide easier access to data, guidance in understanding the dependencies between input variables, and the generation of the TRAC input file (TRACIN) which is needed to run TRAC. They also need the interface to perform all system commands so that no knowledge of Unix or file transfer is needed. Expert users must be able to create models and modify existing models in an efficient manner, and have the software perform error checking during a model creation session. All levels of users must be able to submit many runs of the same base model from within a TRAC GUI session, access the graphics data generated from a run and load graphics data into post-processing tools. These capabilities must be provided without the user having to leave the TRAC GUI environment.

These goals were achieved by teaming expert TRAC users with user interface software design experts and involving the intended user community throughout the GUI development and design process. Early in the development cycle, a user interface functional requirements document was created to serve as a road map throughout the GUI design. Changes from the original functional requirements were allowed to occur as the GUI was tested by users and as new software development tools became available.

This paper presents an overview of the TRAC GUI design and implementation. The model shown in the TRAC GUI in Figure 1 is the LOFT test facility model [2], which is one of the TRAC assessment problems. The LOFT model is shown in all the GUI displays throughout this paper.

2.0 TRAC GUI System Summary

This section describes the software tools used to develop the TRAC GUI, the modules that make up the system, and the flow of data through the system.

2.1 System Description

The TRAC GUI uses the X Window System and Motif widgets to perform all graphical user interface capabilities. The GUI requires the X11R5 version of the X Window System and was implemented in the C programming language. It has been tested on both the Sun and SGI workstations.

The TRAC GUI consists of three main modules: Model Generator, Runtime Editor and Output Processor. Figure 2 shows the interaction between the three modules and the data flow between these modules.

2.1.1 Model Generator

TRAC is an input intensive code, requiring a great deal of information to describe system configuration, geometry, initial fluid state, specialized component inputs (e.g. - pumps, reactor kinetics, valves, etc.), and reactor plant control system inputs. The Model Generator [3] facilitates rapid model construction through an intuitive user interface.

The Model Generator capability in the TRAC GUI allows a power plant analyst to interactively create a plant schematic using TRAC components which are supplied in a component library. This process entails "dragging" a component icon to an infinite work area where the model schematic is being created. When added to the model, the components are automatically named and numbered (although component names and numbers can be modified). After the components are dragged into the work area, they can be connected together through point and click operations using the mouse. The TRAC junction array (or connectivity array) is automatically numbered when the user clicks on the component icon connectors, which can be seen in Figure 1.

Components are initially populated with default data (where applicable) which the user can modify through input panels accessed through the component representation in the schematic (Figure 3). Data entered through these panels are checked for consistency and type, eliminating

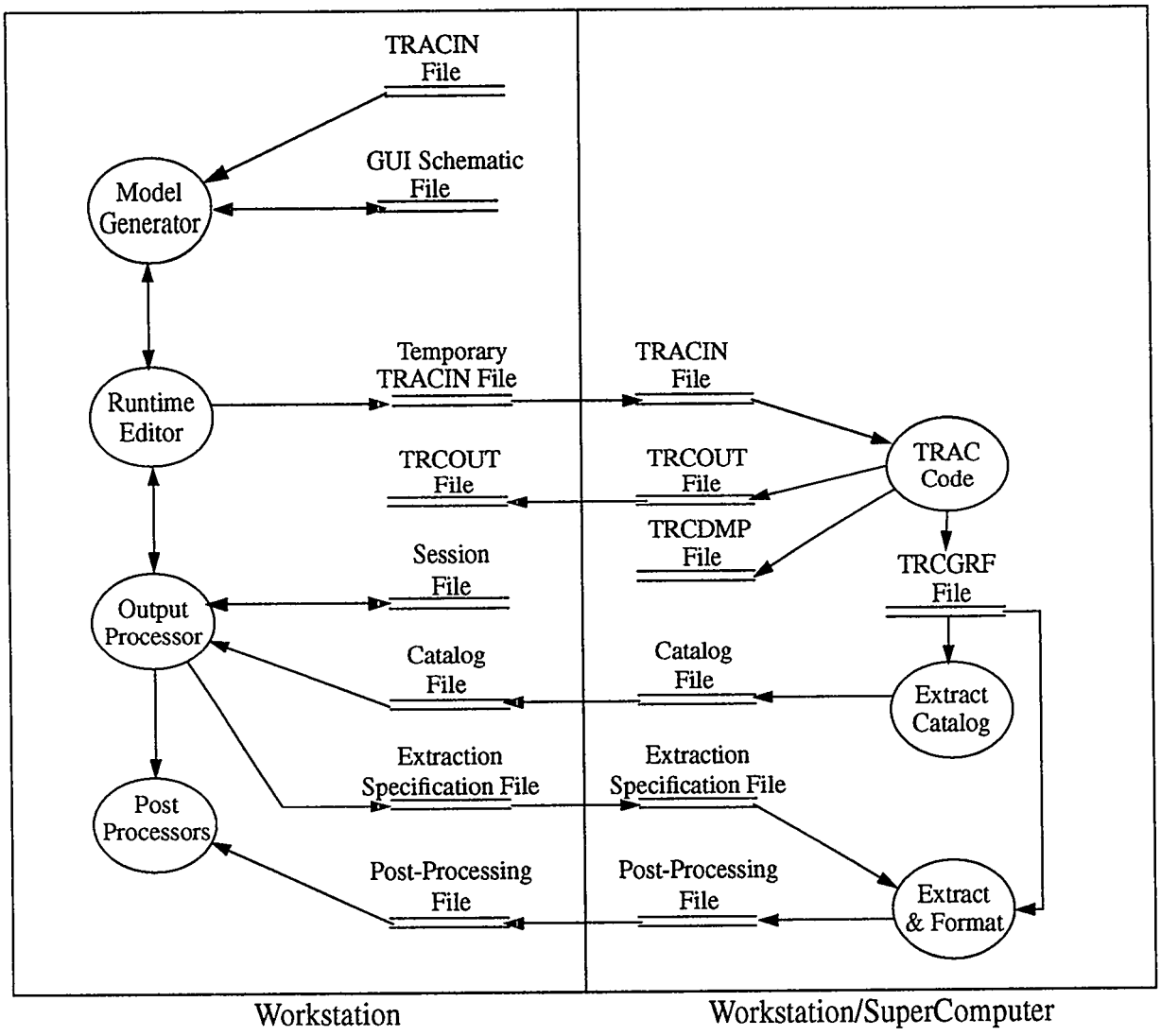


FIGURE 2. TRAC GUI Data Flow

errors due to data format. Input arrays are initialized to "no data" so that as array sizes change, default data is not used. Arrays are checked for "no data" before a TRAC model is run so that the TRAC input file does not contain array data which was not specifically set by the user.

The TRAC GUI also performs logic checking of data entered by the user and updates array sizes when the dimension parameter is modified. The interface incorporates interdependencies of TRAC input data by automating the TRAC user manual logic, thereby aiding the user during model creation and reducing modeling errors. Data which are not needed are desensitized ("grayed out") so the user receives a visual queue that this data is not required and will not be used.

A plant designer may create a TRAC model from scratch or read in an existing TRAC input file for TRAC-PF1/ MOD2 (Version 5.3). When starting from a TRACIN file, the user must still create the schematic for that model. Once a schematic has been created, the model may be read into the TRAC GUI as a Model Generator file.

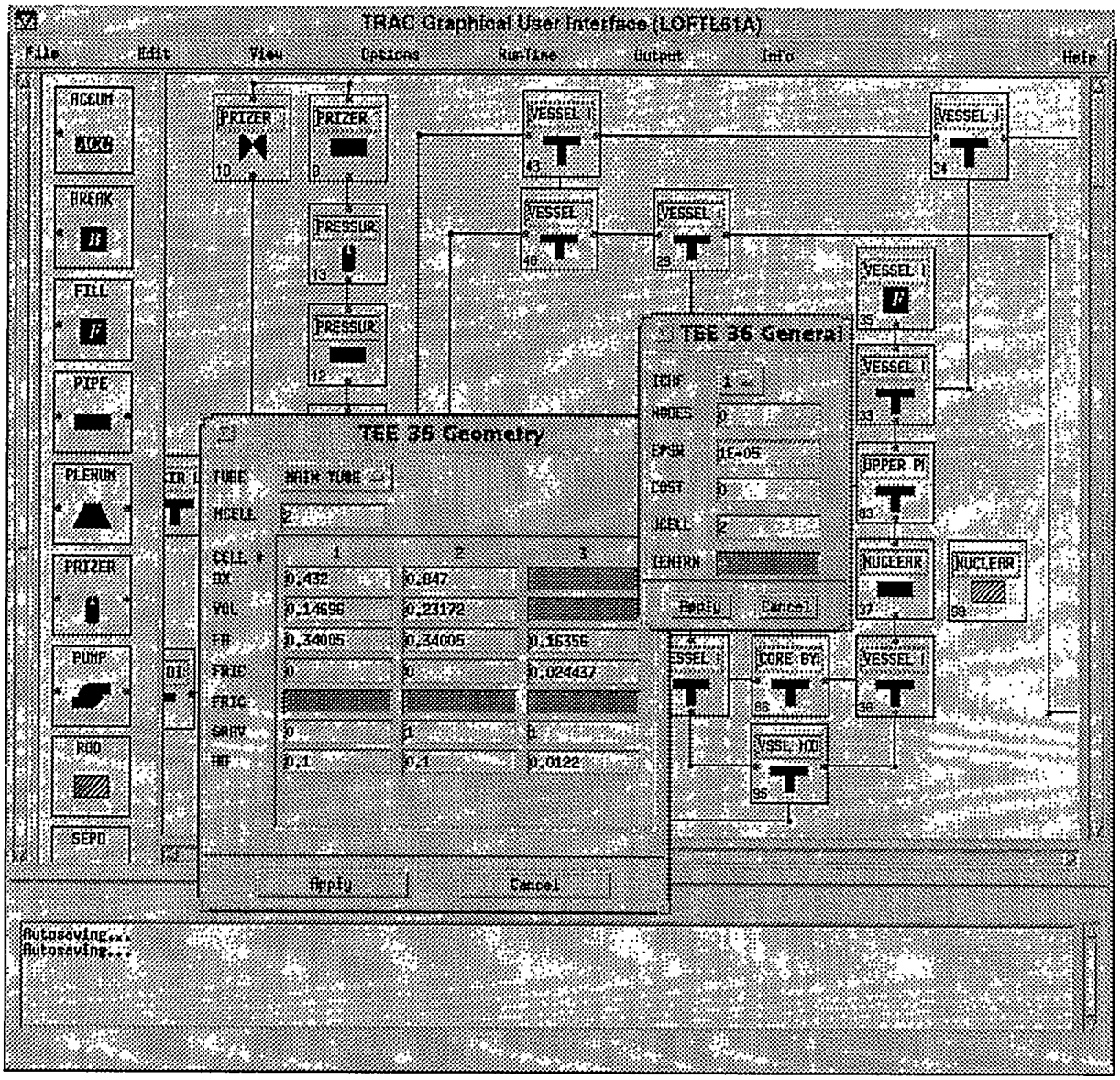


FIGURE 3. TRAC GUI Screen

The user interface contains a connection to on-line help through a Help menu. This allows users to access a specific section of the TRAC manual. If the exact section is not known, a Table of Contents may be accessed which contains hypertext links to the correct portion (or page) of the manual. Any text processor may be linked into the user interface as a way of obtaining help, assuming the help files are formatted for that text processor.

Along with user manuals, connections to documentation on the status of TRAC development items and user interface information have also been incorporated.

2.1.2 Runtime Editor

TRAC is currently used in a batch-oriented environment. When a model is complete, the TRAC GUI generates a TRAC input file (TRACIN) and provides the capability to execute TRAC on the workstation or super-computer and monitor runs. The user may specify TRAC run parameters

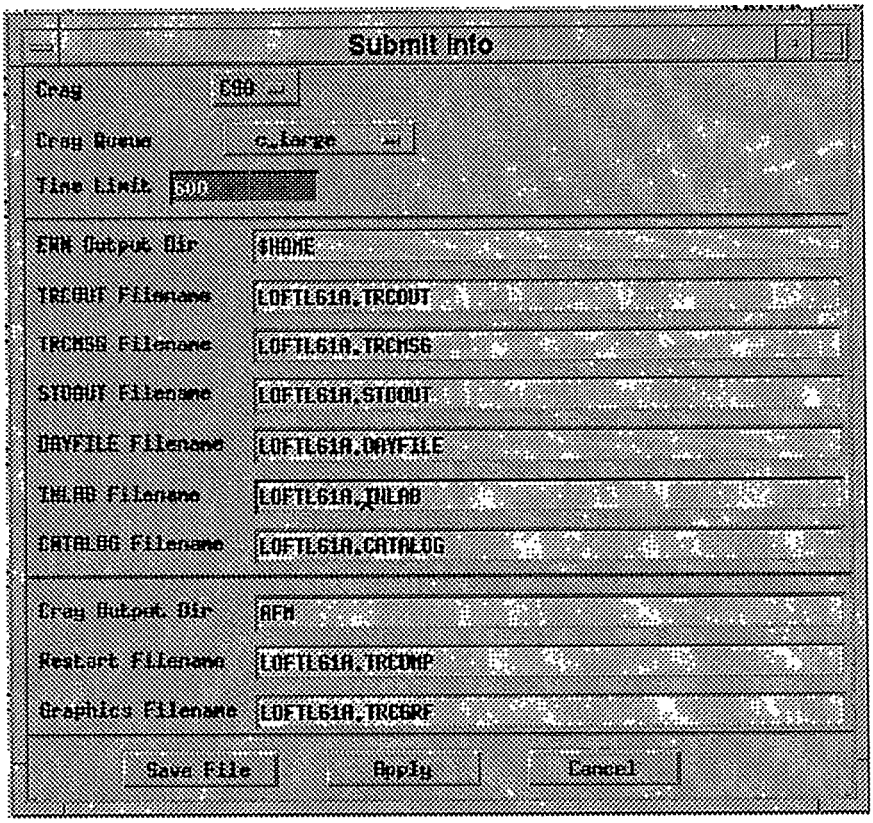


FIGURE 4. Runtime Editor

such as which machine to run on, memory required, and time limits. The user also specifies where to save all of the possible output files. The TRAC run is submitted from the interface without the user needing to know the details of Unix or how to submit runs. Figure 4 shows the method used to submit a TRAC run to the supercomputer. Once a run is submitted, the user may monitor that run from within the interface.

2.1.3 Output Processor

Once a model is run, the engineer needs to evaluate the results and make decisions based on these results. In most cases, visualization techniques provide the fastest means of understanding output. There are currently many excellent commercial visualization and analysis packages available. Rather than reinvent the functionality provided by these packages, the TRAC GUI provides the user with the means for easily utilizing TRAC run data within these tools. One challenge involved in meeting this goal is that each visualization and analysis tool has its own data format. A second challenge is that the TRAC graphics file (TRCGRF) is currently a machine specific binary file. TRCGRF contains output parameter data at each timestep as well as a catalog of what data are available in the graphics file. This file may reside on a different machine than the visualization software. In order to use this data, it must first be extracted from the binary data file, formatted appropriately and then moved to the machine where the visualization software resides.

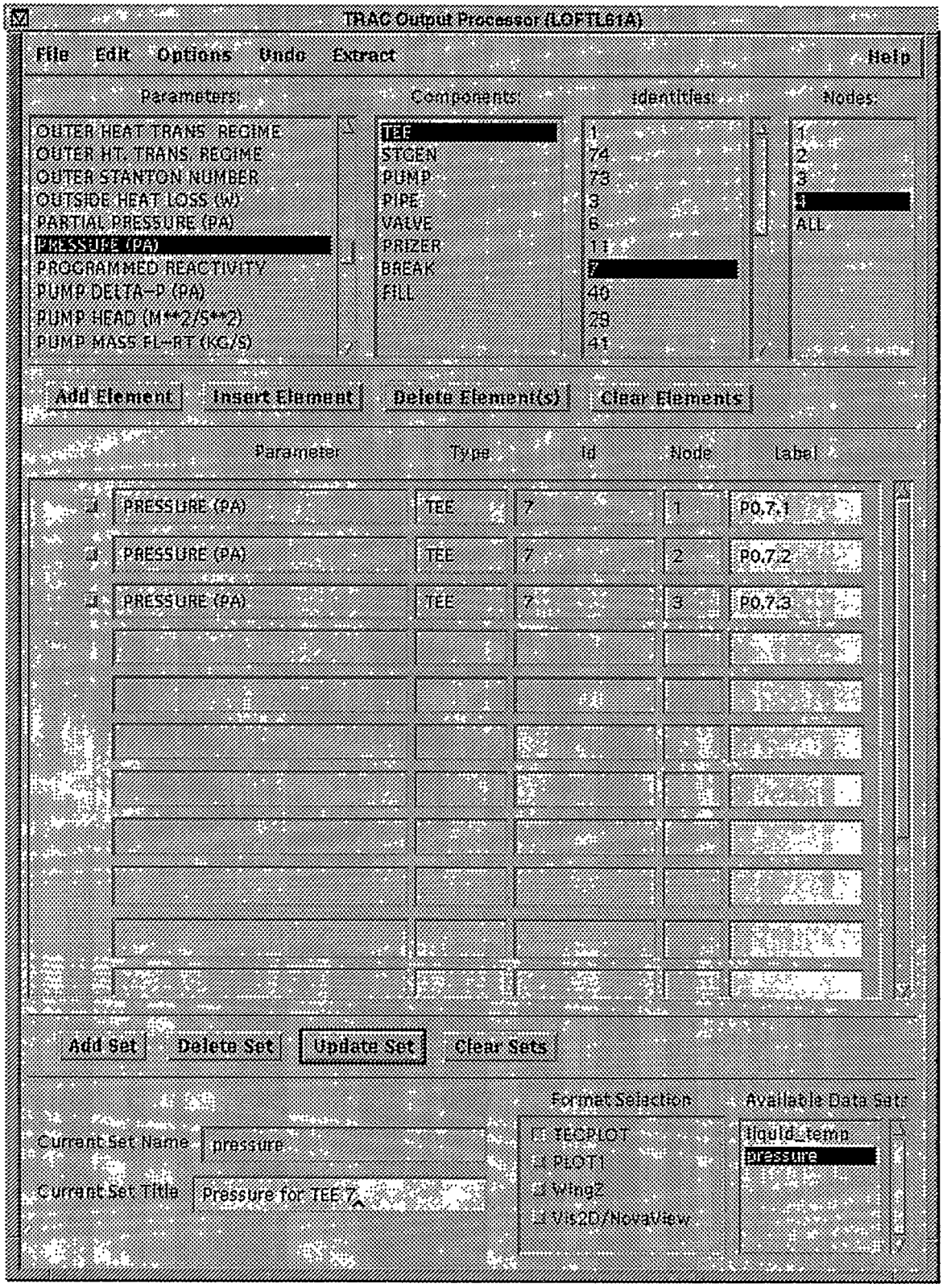


FIGURE 5. Output Processor GUI

To handle this data formatting and extraction process, the TRAC GUI provides an Output Processor. The Output Processor is a window-based tool that allows engineers to specify what data they want to look at and for which tools the data should be formatted

Figure 5 shows the output processing GUI. At the top of the window is a set of scrolled windows used to display the data catalog. The data catalog is a list of what data are available from a specific TRAC run (the available data may vary between TRAC runs). The Output Processor automates the process of extracting the data catalog from a specific TRAC graphics file and transferring it back to the workstation. Using the data catalog display, the engineer selects the parameters to be extracted and model locations at which to extract those parameters. For each set of parameters selected, the user may select one or more formats to output the extracted data in. After the user has defined the data to be extracted, the Extract option may be invoked. This option extracts data from the TRCGRF file and formats it as specified by the user. The Output Processor handles the data transfer between the machine where the data resides and the machine on which the user is working. The Output Processor also provides a tool for loading this data into the appropriate visualization tools so that the user appears to never leave the GUI even when using a separate data processing tool.

3.0 Summary and Conclusions

The TRAC GUI provides a flexible, robust means for creating and quality checking TRAC models, controlling the analyses, and processing the output information all from a single, intuitive user environment.

Users are able to create TRAC models without detailed knowledge of the TRAC input format, the operating system, or the connection between the workstation and the supercomputer for submitting runs. Both new and experienced TRAC users are able to more rapidly construct hydraulic system models and perform analyses using the TRAC GUI than with a traditional text editor.

ACKNOWLEDGMENTS

This work was performed at Knolls Atomic Power Laboratory, operated for the U.S. Department of Energy by the Lockheed Martin Company under Contract No. DE-AC12-76SN00052.

REFERENCES

[1] N.M. Schnurr, et al., TRAC-PF1/MOD2 Code Manual User's Guide, Los Alamos National Laboratory, Los Alamos, New Mexico (1992).

[2] J.C. Lin, V Martinez, J.W. Spore, TRAC-PF1/Mod2 Developmental Assessment Manual, Los Alamos National Laboratory, Los Alamos, New Mexico (1993).

[3] A.E. Kelly, "Development of an Interactive Model Generator for the TRAC Plant Safety Analysis Code," Transactions of the American Nuclear Society, 71, 554-558 (1994).

A COMPARISON OF THE EFFECT OF THE FIRST AND SECOND UPWIND SCHEMES ON THE PREDICTIONS OF THE MODIFIED RELAP5/MOD3

G. Th. Analytis

Laboratory for Thermal Hydraulics,
Paul Scherrer Institute (PSI),
CH-5232 Villigen PSI, Switzerland
Tel: 56-99-21-11 / Fax: 56-99-21-99

ABSTRACT

As is well-known, both TRAC-BF1 and TRAC-PF are using the first upwind scheme when finite-differencing the phasic momentum equations. In contrast, RELAP5 uses the second upwind which is less diffusive. In this work, we shall assess the differences between the two schemes with our modified version of RELAP5/MOD3 by analyzing some transients of interest. These will include the LOFT LP-LB-1 and LOBI small break LOCA (SB-LOCA) BL34 tests, and a commercial PWR 200% hypothetical large break LOCA (LB-LOCA). In particular, we shall show that for some of these transients, the employment of the first upwind scheme results in significantly different code predictions than the ones obtained when the second upwind scheme is used.

1. INTRODUCTION

All transient analysis thermal-hydraulic analysis system codes are employing a staggered-mesh solution scheme for the solutions of the finite-differenced phasic equations. As far as the phasic momentum equations are concerned, the phasic velocities are computed at the edges of the computational cells by using an upwind scheme [1]. Both TRAC-BF1 [2] and TRAC-PF are using the **first upwind**, while RELAP5 [3] uses the **second upwind** scheme which is less diffusive [1].

One can ask the question to what extent (if any) these two schemes may lead to different results within the framework of the same code and, furthermore, should the two schemes really lead to different code predictions, are these differences large enough to justify a more in-depth investigation of the problem. It is the aim of this work to try to give an answer to these questions.

This work is organized as follows. In section 2, we shall outline the way that the phasic momentum equations are finite-differenced in RELAP5/MOD3 (henceforth to be referred to as R5M3) by using the second upwind scheme while we shall also outline the first upwind scheme, which is the one used when finite-differencing the momentum equations in the TRAC codes. Subsequently, by using standard techniques, we shall demonstrate that the former scheme is less diffusive than the latter. Furthermore, we shall briefly describe a Crank-Nicolson type scheme [4] for the convective terms in the framework of the semi-implicit first-upwind solution scheme, which improves the accuracy (in the temporal direction) and is in fact the one we implemented in the code. In section 3, we shall present some comparisons of code predictions calculated by using the two schemes and we shall discuss any differences between the two. In this work, we used our modified version of RELAP5/MOD3 which

we have extensively assessed and qualified in the past with a number of separate-effect and integral test experiments [5-7] (reflooding, LB-LOCA and SB-LOCA tests).

2. THE TWO UPWIND SCHEMES

In RELAP5, one uses the sum and the difference phasic momentum equations. The vapour momentum equations can be written as [3]

$$\begin{aligned} \alpha_g\,\rho_g\,\frac{\partial V_g}{\partial t} \;+\; \frac{1}{2}\,\alpha_g\,\rho_g\,\frac{\partial (V_g^2)}{\partial z} \;=\; &-\alpha_g\,\frac{\partial P}{\partial z} \;+\; \alpha_g\,\rho_g\,B_x \\ &-\;(\alpha_g\,\rho_g)\,f_{w,g}(V_g) \;+\; \Gamma_g\,(V_{g,I} \;-\; V_g) \\ &-\;(\alpha_g\,\rho_g)\,f_{i,g}\,(C_1\,V_g \;-\; C_0\,V_l) \\ &+\;f_{\tau g}\,|V_g|\,V_g \;-\; f_{\tau l}\,|V_l|\,V_l \;+\; F_{vm,g} \end{aligned} \tag{2.1}$$

where all the symbols have their usual meaning. A similar equation can be written down for the liquid phase. The last term in eq. (2.1) is the virtual mass force $F_{vm,g}$. The finite-differenced difference phasic momentum equations for example are generally written as follows

$$\begin{aligned} V_{l,j}^{n+1} \;-\; V_{g,j}^{n+1} \;+\; \ldots \;=\; &V_{l,j}^{n} \;-\; V_{g,j}^{n} \;+\; \ldots\ldots\ldots \\ &-\;(R_l^{n+1}\,\mathbf{CONV}_l^{n+1} \;-\; R_g^{n+1}\,\mathbf{CONV}_g^{n+1})\,\Delta t \;+\; \ldots \end{aligned} \tag{2.2}$$

where we shall define R_l^{n+1} and R_g^{n+1} in due course, while $\mathbf{CONV}_l^{n+1}$ and $\mathbf{CONV}_g^{n+1}$ are the convective terms. In the nearly-implicit scheme, one assumes

$$R_l^{n+1}\,\mathbf{CONV}_l^{n+1} \;=\; R_l^{n}\,\mathbf{CONV}_l^{n} \tag{2.3a}$$

and

$$R_g^{n+1}\,\mathbf{CONV}_g^{n+1} \;=\; R_g^{n}\,\mathbf{CONV}_l^{n} \tag{2.3b}$$

RELAP5 uses the second-upwind scheme for the convective terms which is more accurate than the first upwind scheme, since it maintains something of the second-order accuracy of the convective terms possessed by the central difference schemes [1]. For the vapour momentum equation for example, after integrating the equation from the centre **L** of the down-stream volume of the junction **j**, to the centre **K** of the up-steam volume, the convective term in the semi-implicit scheme is written at time-step **n** as follows

$$\frac{1}{2}\left(\frac{\partial (V_g^2)}{\partial z}\right)^{n}\Bigg|_K^L \;=\; \mathbf{CONV}_g^{n} \;=\; \frac{(V_{g,L}^{n}\,\tilde{V}_{g,L}^{n} \;-\; V_{g,K}^{n}\,\tilde{V}_{g,K}^{n})}{2\,\Delta z_j} \tag{2.4}$$

where Δz_j is the length of the hydraulic volume around the junction **j** (from **K** to **L**). In RELAP5, the donored phasic velocities are defined as follows (here for the vapour phase):

$$\tilde{V}^{n}_{g,K} = V^{n}_{g,K} + 0.5 \frac{|V^{n}_{g,K}|}{V^{n}_{g,K}} (V^{n}_{g,j-1} - V^{n}_{g,j}) \tag{2.5a}$$

and

$$\tilde{V}^{n}_{g,L} = V^{n}_{g,L} + 0.5 \frac{|V^{n}_{g,L}|}{V^{n}_{g,L}} (V^{n}_{g,j} - V^{n}_{g,j+1}), \tag{2.5b}$$

while the volume-centre velocities $V^{n}_{g,K}$ and $V^{n}_{g,L}$ are defined by

$$V^{n}_{g,K} = 0.5 (V^{n}_{g,j-1} + V^{n}_{g,j}) \tag{2.6a}$$

and

$$V^{n}_{g,L} = 0.5 (V^{n}_{g,j} + V^{n}_{g,j+1}). \tag{2.6b}$$

Finally, the convective term given by eq. (2.4) is written as follows:

$$\left(\mathbf{CONV}^{n}_{g} \right) = \frac{1}{2\Delta z_j} \left((V^{n}_{g,L})^2 - (V^{n}_{g,K})^2 + \mathbf{VISC}^{n}_{g} \right) \tag{2.7a}$$

where

$$\mathbf{VISC}^{n}_{g} = 0.5 \left(|V^{n}_{g,L}| (V^{n}_{g,j} - V^{n}_{g,j+1}) - |V^{n}_{g,K}| (V^{n}_{g,j-1} - V^{n}_{g,j}) \right) \tag{2.7b}$$

is the **numerical viscosity** term.

In this formulation, it can readily be seen from the above equations that the products $V^{n}_{g,K} \tilde{V}^{n}_{g,K}$ and $V^{n}_{g,L} \tilde{V}^{n}_{g,L}$ appearing in the convective term are explicitly defined by

$$V^{n}_{g,K} \tilde{V}^{n}_{g,K} = \begin{cases} V^{n}_{g,K} V^{n}_{g,j-1} & V^{n}_{g,K} \geq 0 \\ V^{n}_{g,K} V^{n}_{g,j} & V^{n}_{g,K} < 0 \end{cases} \tag{2.8}$$

and

$$V^{n}_{g,L} \tilde{V}^{n}_{g,L} = \begin{cases} V^{n}_{g,L} V^{n}_{g,j} & V^{n}_{g,L} > 0 \\ V^{n}_{g,L} V^{n}_{g,j+1} & V^{n}_{g,L} \leq 0 \end{cases} \tag{2.9}$$

The convective term $\mathbf{CONV}_l^n$ of the liquid momentum equation is defined in the same way.

As can readily be seen from eq. (2.1), in R5M3, the vapour convective term enters the difference phasic momentum equations in the form [3]

$$\frac{1}{2}\left(\frac{\alpha_g\ \rho_g}{\alpha_g\ \rho_g}\right)\left(\frac{\partial(V_g^2)}{\partial z}\right)^n\Bigg|_K^L = \frac{(V_{g,L}^n\ \tilde{V}_{g,L}^n\ -\ V_{g,K}^n\ \tilde{V}_{g,K}^n)}{\Delta z_j}\left(\frac{0.5\ \tilde{\alpha}_{g,j}^n\ \tilde{\rho}_{g,j}^n}{\bar{\alpha}_{g,j}^n\ \bar{\rho}_{g,j}^n}\right) \tag{2.10}$$

The factor in the large brackets multiplying the $(\mathbf{CONV}_g^n)$ would be equal to 1 if one had cancelled the product $(\alpha_g\ \rho_g)$ from the original equations. Though, due to the donor-cell differencing of the convective terms, one has to assume that, provided the up-stream or down-stream volumes are not time-dependent volumes, this ratio is not equal to 1 and if one assumes this, a number of transients terminate with minimum time-step or water-property error. In RELAP5, this term is modelled as follows:

$$\begin{aligned}(\mathrm{R_g^n}) &= \left(\frac{0.5\ \tilde{\alpha}_{g,j}^n\ \tilde{\rho}_{g,j}^n}{\bar{\alpha}_{g,j}^n\ \bar{\rho}_{g,j}^n}\right) \\ &= \frac{1}{\bar{\alpha}_{g,j}^n\ \bar{\rho}_{g,j}^n}\max(5.\ 10^{-16},(\mathrm{R1_g^n}\ \rho_{g,L}^n\ \alpha_{g,L}^n\ +\ (0.5\ -\ \mathrm{R1_g^n})\ \rho_{g,K}^n\ \alpha_{g,K}^n)\end{aligned} \tag{2.11}$$

where

$$\mathrm{R1_g^n}\ =\ \min(\max((\mathbf{CONV}_g^n\ +\ 10^{-5})\ 2.5\ 10^4\ ,\ 0)\ ,\ 0.5). \tag{2.12}$$

There is no justification given by the code developers for the aforementioned functional form of R_g^n and the same form was also used in RELAP5/MOD2. A tilde over a variable indicates that the variable is an **upwinded** quantity, while a **bar** ($\bar{\alpha}_{g,j}^n$ and $\bar{\rho}_{g,j}^n$) indicates that they are cell-length averaged. From the above definitions it is clear that $R1_g^n\ =\ 0.5$ as long as $(\mathbf{CONV})_g^n\ \geq\ 10^{-5}$; if $(\mathbf{CONV})_g^n\ =\ 0$, $R1_g^n\ =\ 0.25$ and if $(\mathbf{CONV})_g^n\ <\ -10^{-5}$, $R1_g^n\ =\ 0$. In exactly the same way, one defines the term (R_l^n) multiplying the convective term $\mathbf{CONV}_l^n$ of the liquid momentum equation.

The first upwind scheme and the way we implemented is in R5M3 can be outlined as follows. The convective term of the vapour momentum equation in the TRAC codes is finite-differenced in the following way:

$$\begin{aligned}&\frac{1}{2}\left(\frac{\partial(V_g^2)}{\partial z}\right)^n\Bigg|_K^L = \left(V_g\ \frac{\partial V_g}{\partial z}\right)^n\Bigg|_K^L = \\ &\frac{1}{\Delta z_j}\ (V_{g,j}^n\ (V_{g,j}^n\ -\ V_{g,j-1}^n)\ (WV)\ +\ V_{g,j}^n\ (V_{g,j+1}^n\ -\ V_{g,j}^n)\ (1\ -\ WV))\ = \\ &\frac{1}{\Delta z_j}\ (V_{g,j}^n\ \delta V_{g,(j,j-1)}^n\ (WV)\ +\ V_{g,j}^n\ \delta V_{g,(j+1,j)}^n\ (1\ -\ WV)),\end{aligned} \tag{2.13}$$

where

$$(WV) = (WV)_j^n = \begin{cases} 1 & V_{g,j}^n > 0. \\ 0 & V_{g,j}^n \leq 0. \end{cases} \tag{2.14a}$$

Before proceeding any further, we shall first show that the first upwind scheme is more diffusive than the second upwind one which is used in R5M3. To show this, we shall first consider as an example the general form of the (spatially discretized) steam momentum equation: it is written as

$$\frac{\partial V_{g,j}}{\partial t} = \mathbf{CONV}_g^n + \ldots\ldots\ldots \tag{2.15}$$

where all the symbols have their usual meaning. We shall now use standard techniques [1] and investigate the truncation error introduced by the two different discretization schemes. We shall assume that the velocity direction is from the cell **K** to the cell **L** and let us first introduce in the above equation eqs. (2.7a) and (2.7b) (second upwind scheme). Finally, we shall use the following Taylor expansions around $V_{g,j}$ for the velocities at the junctions

$$V_{g,j-1} = V_{g,j} - \Delta z \frac{\partial V_{g,j}}{\partial z} + \frac{1}{2}(\Delta z)^2 \frac{\partial^2 V_{g,j}}{\partial z^2} + \ldots\ldots \tag{2.16a}$$

$$V_{g,j+1} = V_{g,j} + \Delta z \frac{\partial V_{g,j}}{\partial z} + \frac{1}{2}(\Delta z)^2 \frac{\partial^2 V_{g,j}}{\partial z^2} + \ldots\ldots \tag{2.16b}$$

where Δz is the mesh-length. If we now take into account eqs. (2.6a) and (2.6b), it can readily be shown that eq. (2.15) can be written as (after dropping the subscript j)

$$\frac{\partial V_g}{\partial t} + V_g \frac{\partial V_g}{\partial z} = \frac{1}{4}\Delta z \left(V_g \frac{\partial^2 V_g}{\partial z^2} \right) + \frac{1}{4}\Delta z \left(\frac{\partial V_g}{\partial z} \right)^2 + \ldots\ldots\ldots \tag{2.17}$$

This is the original steam momentum equation and the terms on the right-hand side are the truncation errors: The first term is the numerical diffusion, while it can readily be seen that the second term modifies the convection term itself (and decreases as the mesh-size Δz decreases). If we now follow the same procedure for the first upwind method, one can readily show that the steam momentum equation corresponding to (2.17) will be

$$\frac{\partial V_g}{\partial t} + V_g \frac{\partial V_g}{\partial z} = \frac{1}{2}\Delta z \left(V_g \frac{\partial^2 V_g}{\partial z^2} \right) + \ldots\ldots\ldots \tag{2.18}$$

Clearly, the numerical diffusion of the first upwind scheme is twice as high as the on of the second upwind.

We have implemented the first upwind scheme in R5M3 but in a slightly modified form than used in the TRAC codes. In particular, we used a Crank-Nicolson (in time) type treatment of the convective terms of the phasic momentum equations by evaluating them at half the

time-step, which results in a more "implicit" evaluation of these terms; after some lengthy algebra, one can show that the difference phasic momentum equations can be written as

$$V_{l,j}^{n+1}\left(1+\frac{1}{2}\Delta t\left(R_l^n\left(\delta V_{l,(j,j-1)}^n\,(WL)+\delta V_{l,(j+1,j)}^n\,(1-WL)\right)\right)\right)-$$
$$V_{g,j}^{n+1}\left(1+\frac{1}{2}\Delta t\left(R_g^n\left(\delta V_{g,(j,j-1)}^n\,(WV)+\delta V_{g,(j+1,j)}^n\,(1-WV)\right)\right)\right)+\ldots..$$
$$=V_{l,j}^n-V_{g,j}^n+\ldots....-$$
$$\frac{1}{2}\Big(R_l^n\left(V_{l,j}^n\,\delta V_{l,(j,j-1)}^n\,(WL)+V_{l,j}^n\,\delta V_{l,(j+1,j)}^n\,(1-WL)\right)-$$
$$R_g^n\left(V_{g,j}^n\,\delta V_{g,(j,j-1)}^n\,(WV)+V_{g,j}^n\,\delta V_{g,(j+1,j)}^n\,(1-WV)\right)\Big)\Delta t+\ldots. \qquad (2.19)$$

where all the quantities $\delta V_{g,(j,k)}^n$ etc are defined as in eq. (2.13).

3. NUMERICAL EXAMPLES

In this section, we shall compare the predictions of R5M3 when using the second and the first upwind methods for finite-differencing the convective terms of the momentum equations. As basis for our analysis, we shall use modified version of the code [5-7] since as we have shown in a series of previous investigations, the frozen version leads to erroneous results for almost all separate- effect and integral test experiments analyzed. In this section, we shall analyze the following three transients: **The LOFT LP-LB-1 [8] and the LOBI SB-LOCA BL34 [9] tests and a hypothetical 200% LB-LOCA calculation for a two-loop commercial PWR [10].** We shall show that the code predictions (here, we shall mainly concentrate our attention to the rod surface temperature (RST) histories) are depending on the upwind scheme used in the solution of the momentum equations, although the extent of this dependence varies depending on the transient under consideration. We shall perform all the calculations with a fixed spatial nodalization since the aim of this work is to assess the importance of two different discretization schemes of the convective terms of the momentum equations rather than study the effect of node size on the code predictions. Furthermore, we should point out that simple, separate-effect type calculations (reflooding in a heater rod bundle etc) have been performed with both versions of the code and the results were for all practical purposes identical and indistinguishable from each other. Hence, the differences between the predictions obtained by using the two different schemes are mainly showing up in large system calculations rather than in separate-effect tests.

(a) The LOFT LP-LB-1 test.

For this analysis, the input deck of Ref. 8 was utilized, and the RST histories at the peak axial power level predicted by the two versions of the code are shown in Fig. 1. Clearly, for this case, the predictions obtained are not so sensitive to the finite-differencing scheme used in the phasic momentum equations. Notice that since the aim of this work is to assess the possible differences due to the two different discrtetization schemes rather than investigate possible deficiencies of physical models, we are not showing the measured values in this figure. The interested reader is referred to Ref. 7, where the predictions of our modified code for the same LOFT test are compared

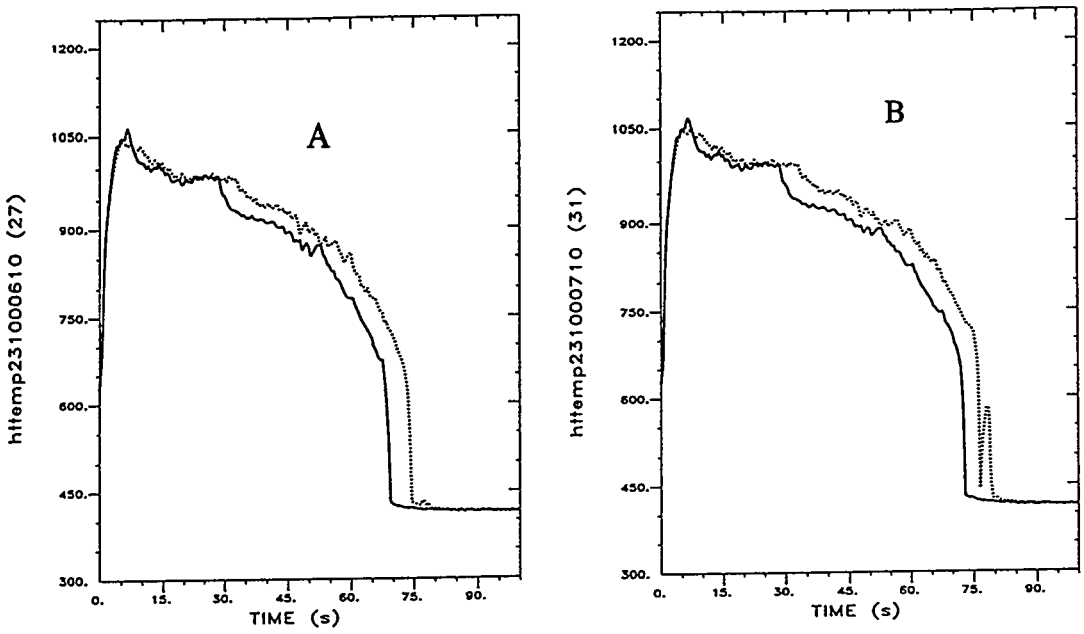


Fig. 1 LOFT LP-LB-1 Test. Predicted RST histories at axial elevations of 27 (A) and 31 (B) inches with the modified R5M3: (——): second upwind; (.....): first upwind.

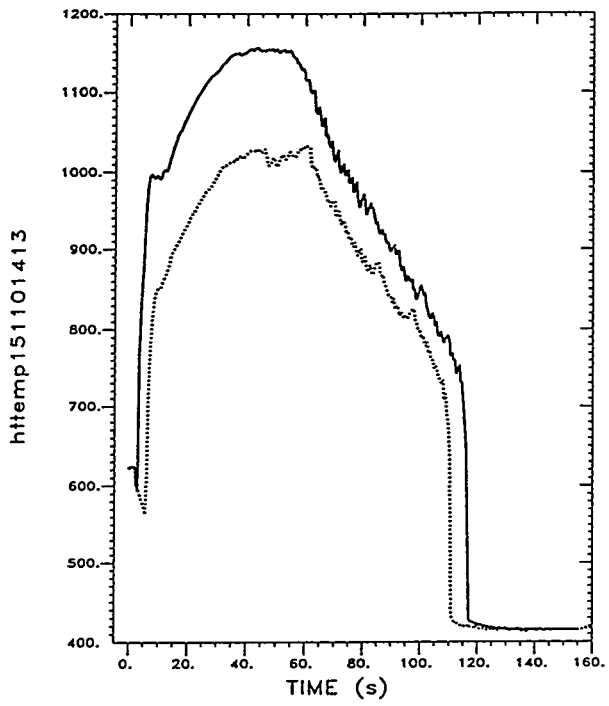


Fig. 2 Predicted peak RSTs (K) for a hypothetical LB-LOCA in a Commercial PWR calculated with the modified R5M3: (——): second upwind; (.....): first upwind.

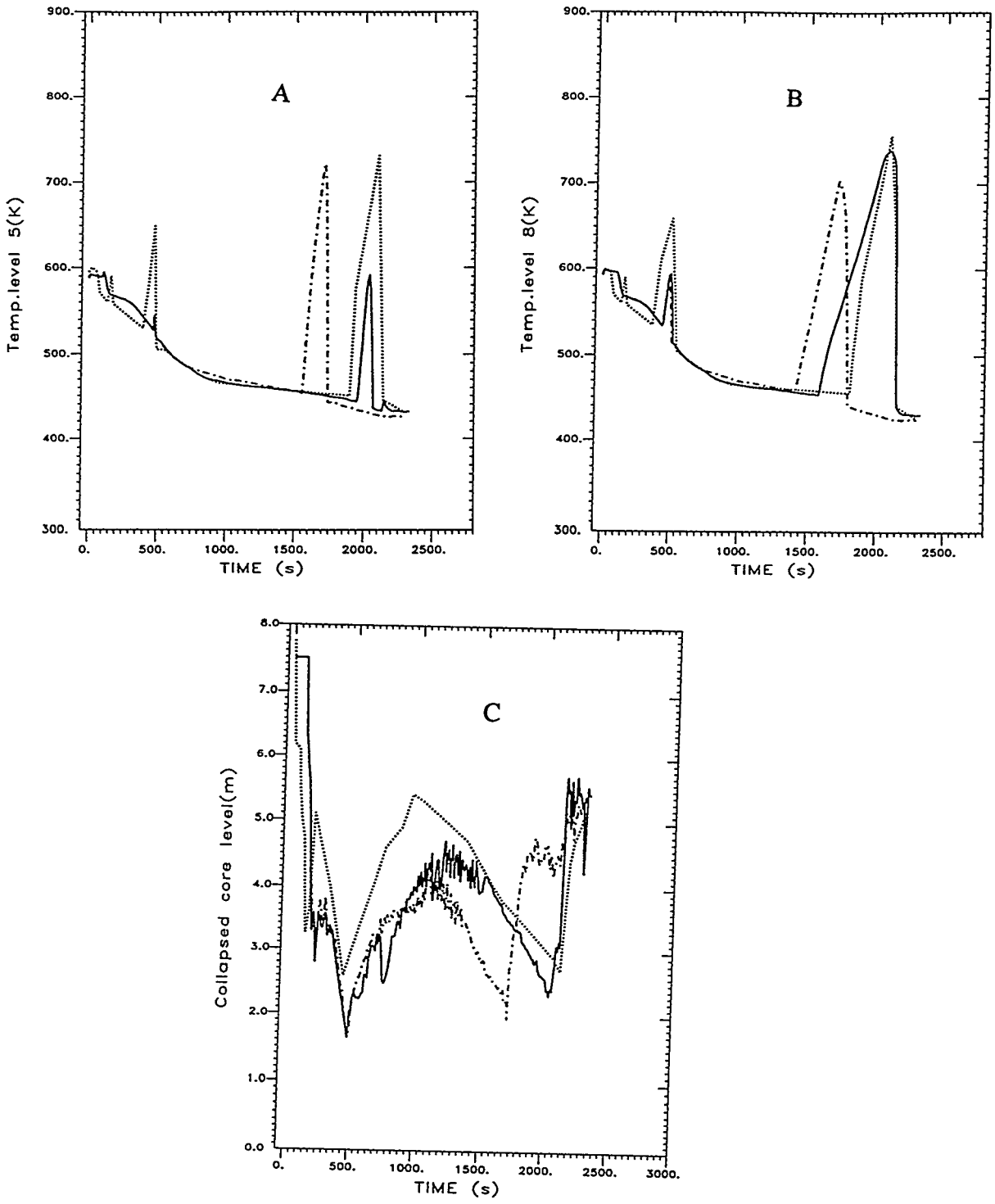


Fig. 3 LOBI BL34 SB-LOCA test. Predicted RST histories at two axial levels (A and B) and collapsed level in the core (C) with the modified R5M3: (———): second upwind; (-.-.-.-.): first upwind; (.....): measurements.

both to the ones of the frozen version and to the measurements. An other important point which we would like to notice here is that the differences between the predictions obtained by using the two different discretization schemes are also depending on the actual physical models in the code and in particular, the different interfacial shear models. This we have shown by analyzing the same LOFT test with these two schemes, but by using the option of our code version which activates the Andersen drift-flux wet-wall interfacial shear correlations for pipes as in TRAC-BF1 [2,5,7]. For this case, the differences in predicted RSTs obtained by using the two schemes were much larger, indicating that there can be strong interactions between the numerics in the code and particular physical models. This complex interaction and inter-relation between the discretization scheme and the physical models and correlations used in the code is an additional evidence of the fact that qualifying code uncertainties in a rigorous and invariant fashion is not really an attainable goal.

(b) A hypothetical 200% LB-LOCA calculation for a two-loop commercial PWR plant.

For this case, we used the input deck of Ref. 10 which models a two-loop 1130 MW commercial PWR. In Fig. 2, we show the predicted RST histories at the peak axial power level. Here, one can see that the employment of the first upwind scheme for the convective terms in the momentum equations results in RSTs (for this particular axial elevation) which are approximately 150 K lower than the case in which the second upwind scheme was used. One of the reasons for this behaviour may be the fact that since the former scheme is more diffusive, during the blow-down phase, more water is held in the core; consequently, the RSTs start increasing a little later, leading to a lower maximum RST during the reflooding phase.

(c) The LOBI SB-LOCA BL34 test.

Finally, the LOBI SB-LOCA BL34 test [9] was analyzed with the two versions and in Fig. 3A and B, the predicted RST histories at two different axial elevations are compared to the measured ones. One can see that when the first upwind finite-differencing scheme is used, both the time that the third dry-out is predicted to occur and the predicted peak RSTs change significantly. A closer look at the results of this analysis reveals that as can be seen from Fig. 3C, this can be attributed to the fact that when the former scheme is used, the collapsed level in the core starts decreasing earlier, probably due to the larger numerical diffusion of the first upwind scheme.

4. CONCLUSIONS

In this work, we have tried to assess the effect of two finite-differencing schemes of the phasic momentum equations on the predictions of R5M3. In particular, we investigated the differences between the second upwind scheme used in the code, and a modified first-upwind scheme, similar to the one used in the TRAC codes. Our conclusions are that in general, due to the different truncation errors of the two schemes and the fact that the second upwind scheme is less diffusive than the first, the code predictions are to some extent influenced by the particular scheme. Consequently, care should be exercised when one tries to compare predictions obtained by two different codes, even if the physical models in them are identical (which is actually never the case). We saw that although the differences between the code predictions for the LOFT test LP-LB-1 were not very significant, this was not the case either for the LOBI SB-LOCA test BL34 or for the hypothetical LB-LOCA in a commercial PWR, both from the point of view of the predicted RST histories and the CLL. Additionally, when the same LOFT test was analyzed by our code version in which different wet-wall interfacial shear correlations were activated, there were also large differences in the RSTs predicted when the two different schemes were used. Clearly, there may be transients for which the two different schemes lead to significantly different predictions while for others, this may not be the case and in fact, these differences may be enhanced by the actual physical correlations used.

Concluding, we can say that there is really a large number of effects which have to be taken into account when one tries to estimate uncertainties in the predicting capabilities of the codes; certainly, although some of these effects can indeed (at least to some extent) be quantified [11], we do not believe that this can be achieved for the general case in any rigorous and invariant fashion.

Acknowledgements

The author would like to express his gratitude to Brian Smith with whom he had some illuminating discussions.

References

[1] P. J. ROACHE, Computational Fluid Dynamics, Hermosa Publishers (1972).

[2] D.D. TAYLOR et al., TRAC-BD1: An Advanced Best-Estimate Computer Program for Boiling Water Reactor Transient Analysis, NUREG/CR-3633 (1984).

[3] K.E. CARLSON et.al., RELAP5/MOD3 Code Manual Volume IV: Models and Correlations (Draft), (1990).

[4] B. SMITH, Private Communication (1993).

[5] G. TH. ANALYTIS, A summary of model changes and options in RELAP5/MOD3. Paper presented at the 2nd CAMP Meeting, May 10 - 13, 1993, Brussels, Belgium.

[6] G. TH. ANALYTIS, Development and assessment of a modified version of RELAP5/MOD3: A search for excellence, Invited paper presented at the RELAP5 International User's Seminar, Baltimore, Maryland, USA, August 29 - September 1, 1994

[7] G. TH. ANALYTIS, Development and assessment of a modified version of RELAP5/MOD3, To be presented at the NURETH-7 Conference, Saratoga Springs, NY, USA, September 10 - 15, 1995.

[8] D. LÜBBESMEYER, Post-Test-Analysis and Nodalization Studies of OECD LOFT Experiment LP-LB-1 with RELAP5/MOD2/CY36.02, PSI Report Nr.91 (1991).

[9] F. D'AURIA and G.M. GALASSI, Assessment of RELAP5/MOD2 code on the Basis of Experiments performed in LOBI Facility, *Nuclear Technology*, Vol 90, Nr. 3 (1990)

[10] D. LÜBBESMEYER, Private communication (1992).

[11] S. N. AKSAN and F. D'AURIA, Investigation of the User Effects for the Thermal-Hydraulic Transient Analysis Codes: Case Studies, Proceedings of the NURETH-5 Conference, Vol.II, pp 424 - 434, (1992).

Local Mesh Refinement for Incompressible Fluid Flow with Free Surfaces

H. Terasaka[1)], H. Kajiwara[1)], K. Ogura[1)], H. Ueda[2)], and A. Takizawa[2)]

1) Toshiba Corporation,
2) Tokyo Electric Power Company

ABSTRACT

A new local mesh refinement (LMR) technique has been developed and applied to incompressible fluid flows with free surface boundaries. The LMR method embeds patches of fine grid in arbitrary regions of interest. Hence, more accurate solutions can be obtained with a lower number of computational cells. This method is very suitable for the simulation of free surface movements because free surface flow problems generally require a finer computational grid to obtain adequate results. By using this technique, one can place finer grids only near the surfaces, and therefore greatly reduce the total number of cells and computational costs. This paper introduces LMR3D, a three-dimensional incompressible flow analysis code. Numerical examples calculated with the code demonstrate well the advantages of the LMR method.

1. Introduction

Local Mesh Refinement (LMR) is a kind of zone decomposition method. The basic idea of the technique is based on local adaptive mesh refinement (LAMR) developed by Berger et al.[1] to track shock wave propagation in compressible flow. LAMR uses a sequence of overlapping grids of increasing fineness. The grid is adaptively refined until the solution error estimate is below some desired level. This method makes it possible to use very fine mesh and is suitable to resolve detailed structure of complicated flow, such as burning flow with fast chemical reactions[2].

The main difficulty of this method is the need for data structures not usually found in numerical software. It makes programs highly complex. To adapt LAMR to incompressible flow analysis, the authors have converted it into LMR by neglecting the adaptiveness, but retaining the simple data structure used in conventional flow analysis programs. LMR embeds grid patches with an arbitrary level of fineness in arbitrary regions of interest. Although the grid patches are "frozen," so that the computational grid system does not change, the fine mesh regions are confined within the patches and the increase in the number of cells is restrained unlike in the conventional program. As a result, more accurate solutions can be obtained with lower computation costs.

The LMR technique is extended to solve free surface flow problems in this study. Several methods, such as the height function method[3], MAC method[4], ALE method[5] and so on, have previously been used to approximate free surfaces in finite difference numerical simulations. From among the methods, the volume of fluid (VOF) method[6] is chosen for this study because of its flexibility and wide applicability. A special interpolation scheme is needed to redistribute the fluid volume fraction in coarser cells into finer cells contained within the coarser cells. This

interpolation scheme is very important to maintain the mass conservation of the fluid. A program, LMR3D, has been developed to investigate performance of the LMR method. It is a three-dimensional code for incompressible flow with free surface boundaries and can solve a wide range of free surface problems in Cartesian or cylindrical coordinate systems with the LMR grid. Several numerical examples are solved to verify the code. The results clearly demonstrate the advantages of the LMR method.

2. Outline of LMR3D

LMR3D is a three-dimensional code for incompressible viscous flow with free surface boundaries. The free surfaces are treated by the VOF method. VOF is used in a lot of general purpose fluid analysis codes because of its flexibility and applicability to a wide range of free surface problems. The following is an outline of LMR3D.

(1) Basic equations

The incompressible viscous flows are governed by the following set of nonlinear partial differential equations:

$$\frac{\partial u_j}{\partial x_j} = 0$$

$$\frac{\partial u_i}{\partial t} + \frac{\partial}{\partial x_j}\left(u_i u_j\right) = -\frac{1}{\rho}\frac{\partial p}{\partial x_i} + \frac{\partial}{\partial x_j}\left\{\nu\left(\frac{\partial u_i}{\partial x_j} + \frac{\partial u_j}{\partial x_i}\right)\right\} + g_i . \qquad (1)$$

$$\frac{\partial F}{\partial t} + \frac{\partial (u_j F)}{\partial x_j} = 0$$

The third equation is a kinematic equation governing a volume-fraction function, F, which specifies the fraction of volume containing fluid per unit volume. This cell-centered function assumes a value of unity in cells full of fluid, a value of zero in empty cells, and intermediate values in surface cells. The surface is located at F=0.5. The kinematic equation is usually solved by a donor-acceptor method[6].

(2) Grid system

The grid system of LMR is the same as that of LAMR. It is composed by a sequence of nested, logically rectangular meshes on which the basic equations are discretized. Differences between the two grid systems are:

i) The LMR grid system is not adaptive, and so all the refined regions must be fixed before calculation.
ii) Fine grid must be contained in only one coarser level grid in LMR.
iii) LMR employs the same staggered mesh arrangement as the traditional incompressible flow analysis programs instead of the regular mesh employed by LAMR.
iv) In the LMR grid system, only the outer boundary cells are overlapping to connect physical quantities smoothly.

The above restrictions make LMR less flexible but highly effective and easy to implement.

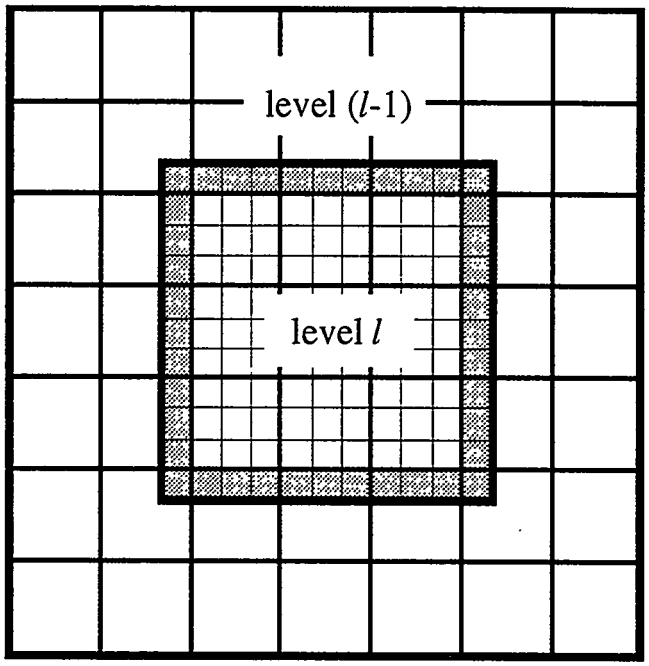


Figure 1. An example of grid system used in LMR3D. Overlapping cells of the level l grid are indicated by shading.They are treated as the fictional cells.

Calculation of a number of geometrical quantities, such as metrics and index list vectors, that are frequently needed in later work is required only one time. Error estimation and grid refinement in each time step are not required.

LMR3D uses a staggered mesh arrangement in which all the vector components, u, v, and w, are defined at the center of cell faces and all the scalar variables, p and F, are located at the cell center. This is the best way to prevent the checker-board pressure oscillations. To connect the patches of different fineness level smoothly, an overlapping grid system is employed. Level l patches are also presupposed to exist in the next-coarser grid patches, level (l-1), for simplification. As shown in Figure 1, the outer boundary cells of a level l grid patch are overlapped with a level (l-1) patch. Boundary values of all the variables for the level l grid are set at the overlapped cells by interpolation, and fixed during each time cycle. The highest grid level available in LMR3D is 2, although this is not essential and extension to a higher level is straightforward. The refinement ratio, $r = \frac{\Delta x_{l-1}}{\Delta x_l}$, is set to 3 because this is suitable for a staggered mesh arrangement. Then, a cell in a level (l-1) grid is divided into 3x3x3 sub-cells of level l. The variable mesh approximation is also used on the level zero grid.

(3) Redistribution of fluid volume fraction

One of the important problems to be solved is the redistribution of fluid contained in coarser cells to sub-cells. This is directly related to mass conservation. LMR3D employs a special interpolation scheme for this fluid redistribution which assures adequate fluid transfer between the different fineness grids.

Figure 2 illustrates this interpolation method. Let the fluid in a cell (i,j,k) of level (l-1) be redistributed into sub-cells of level l, and assume the surface boundary near the cell can be approximated by a plane cutting through the cell. Then, the height of the surface above the bottom face of the surface cell is defined at each location. After interpolating the surface heights corresponding to the sub-cells, the fluid volume fractions of the sub-cells are obtained as follows.

$$F^{l}_{1,j+\beta,k+\gamma} = \max\left[0,\ \min\left\{3\left(h^{l}_{j+\beta} - (1+\frac{\gamma}{3})\right),\ 1\right\}\right], \qquad (2)$$

where, $h^{l}_{j+\beta}$ is the surface height and $F^{l}_{1,j+\beta,k+\gamma}$ is the fluid volume fraction to be redistributed to the sub-cell, (1,j+β,k+γ), as shown in the figure. For fluid mass conservation,

$$F^{l-1}_{i,j,k} = \frac{1}{27}\sum_{\alpha=0}^{2}\sum_{\beta=0}^{2}\sum_{\gamma=0}^{2} F^{l}_{i+\alpha,j+\beta,k+\gamma}\ , \qquad (3)$$

should hold.

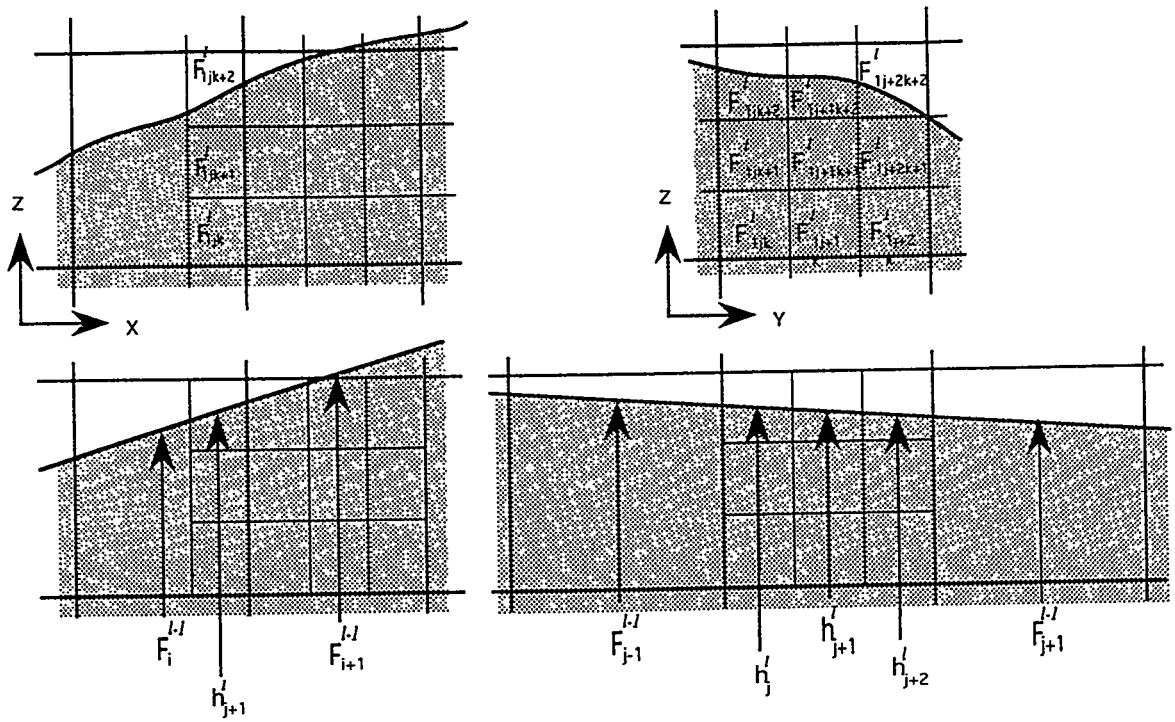


Figure 2 Illustration for the fluid re-distrubution into sub-cells

(4) Numerical procedure

LMR3D is based on a finite-volume formulation. The finite-volume equations are derived by integrating the governing equations, Eq.(1), over a control volume. In this formulation, the unsteady terms are discretized by the 1st-order Euler scheme and the convection terms in the momentum conservation equations are discretized by the 1st-order upwind scheme or QUICK scheme. Other terms, such as pressure and diffusion terms, are discretized by the 2nd-order central difference method.

LMR3D performed fluid dynamic calculations by marching in time using a fully implicit scheme, SIMPLEST[7]. A steady-state solution is obtained from calculation starts with an initial guess and continues the marching-in-time process until the values of the dependent variables stop varying with time. SIMPLEST secures unconditional numerical stability, so that the time-step size is not limited by the Courant number criterion when fixed boundary problems are solved. Hence, one can get a steady-state solution rapidly by marching with very large time-step, e.g. 10^{10} second. In the case of free surface calculation, however, the time-step size is limited by the Courant criterion because the donor-acceptor scheme for VOF equation is essentially explicit. The SIMPLEST scheme is still useful to enhance the numerical stability.

If there are no refined regions, then LMR3D solves Eq.(1) just the same way as the conventional

programs do on a single grid. With multiple grids, each grid is separately defined and has its own solution, so that a grid can be advanced independently of other grids, except for the determination of its boundary values. This feature would match well with parallel processing computers. The present version of LMR3D is tuned up for vector computers, so that the time advancement is performed from the lowest level grid to the highest level grid by using boundary values at the previous cycle, say m, and the values of the independent variables at cycle m+1 are calculated. Then the boundary values of each grid are updated from the highest to the lowest level. When this iterative process is considered converged, the last iterated values are used for the advanced time variable values. The main structure of the computer program can be seen in Figure 3.

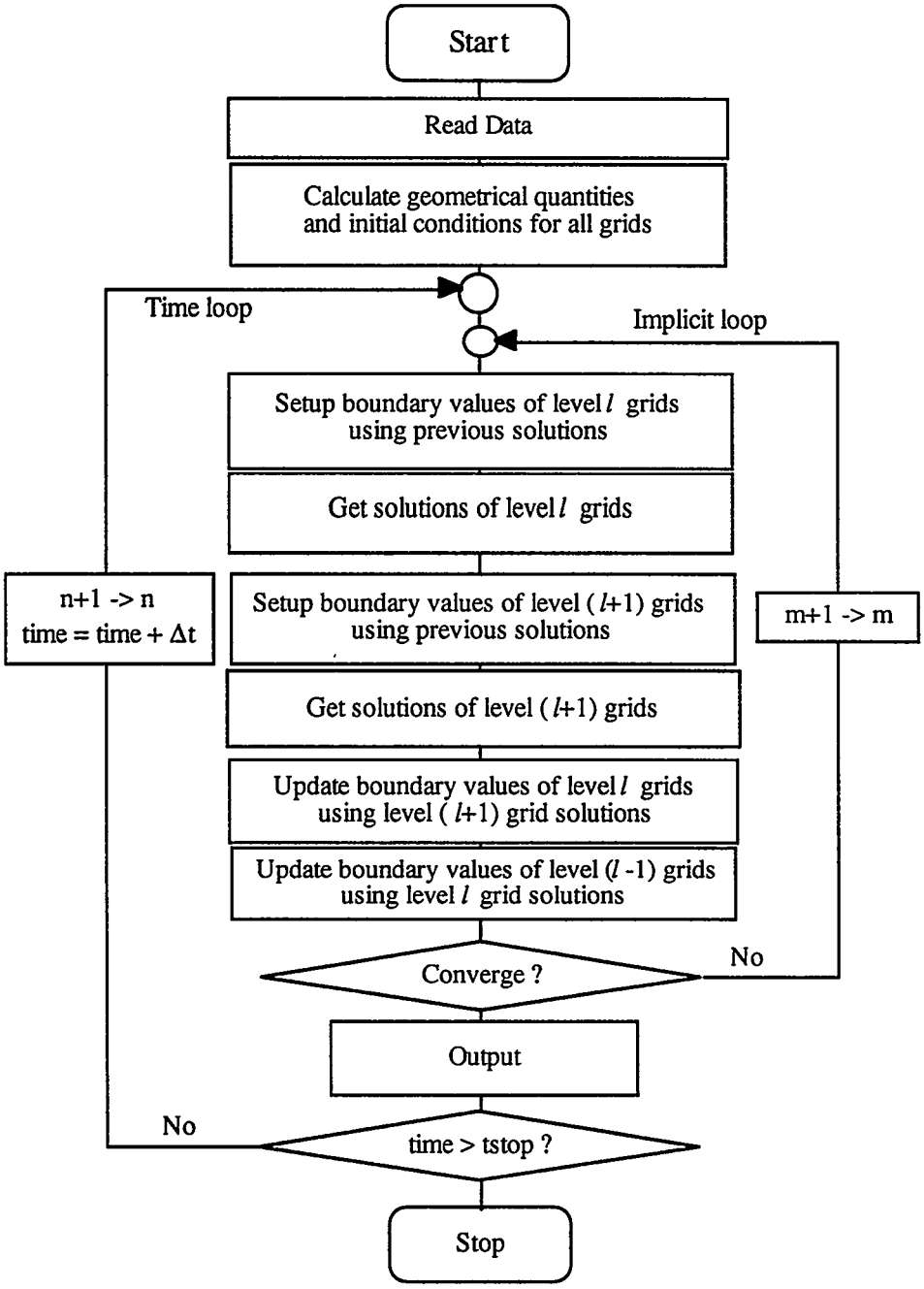


Figure 3. Main structure of LMR3D

3. Numerical examples

(1) Flow around a rectangular column

A three-dimensional flow around a rectangular column without free surfaces is solved to verify LMR3D. A schematic diagram of the flow is shown in Figure 4(a). Three calculations, listed in Table 1, are made to compare accuracy and computing time. The total number of cells in the coarse grid (Case A) is 1,800, in the LMR grid (Case B) 10,548, and in the finer grid (Case C) 48,600, respectively. Figure 4(b) shows the flow vector distribution on the horizontal plane, and Figure 4(c) shows that on the vertical plane of each case. Figures 4(d) and 4(e) compare velocity and pressure profiles, respectively. Although the refined grid region is not very large, excellent results are obtained from the LMR calculation. The computing time of each case is also summarized in Table 1. It shows that by using the LMR technique, almost the same results are obtained with about 1/8 of the computing effort.

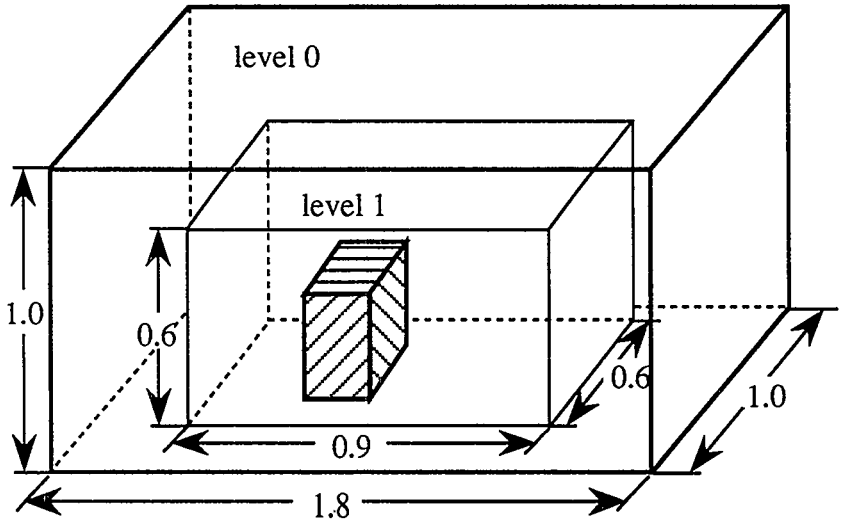


Figure 4(a) Configuration of the flow around a rectangular column

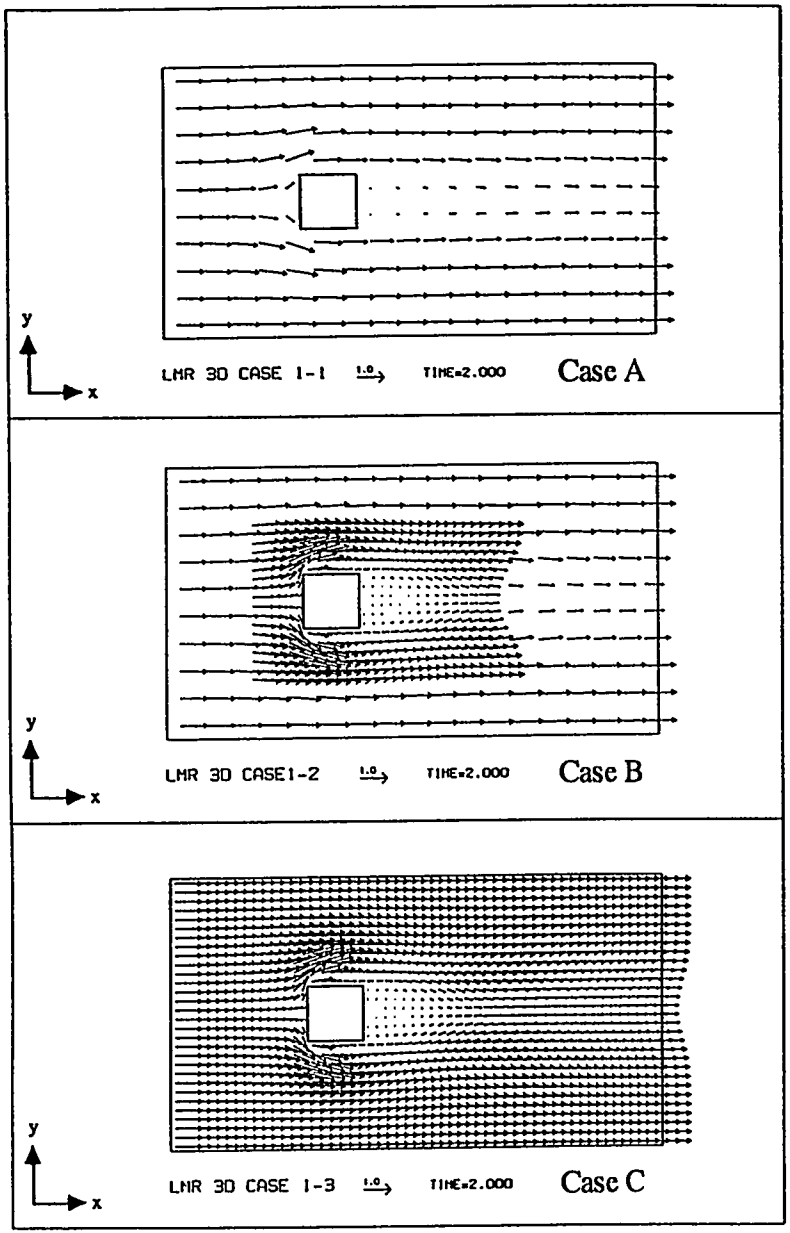
Table 1. Numerical conditions and CPU times

Case	Number of cells	CPU time ratio
A (level 0 only)	1,800	0.07
B (level 0 and 1)	10,548	1.00
C (level 1 only)	48,600	7.74

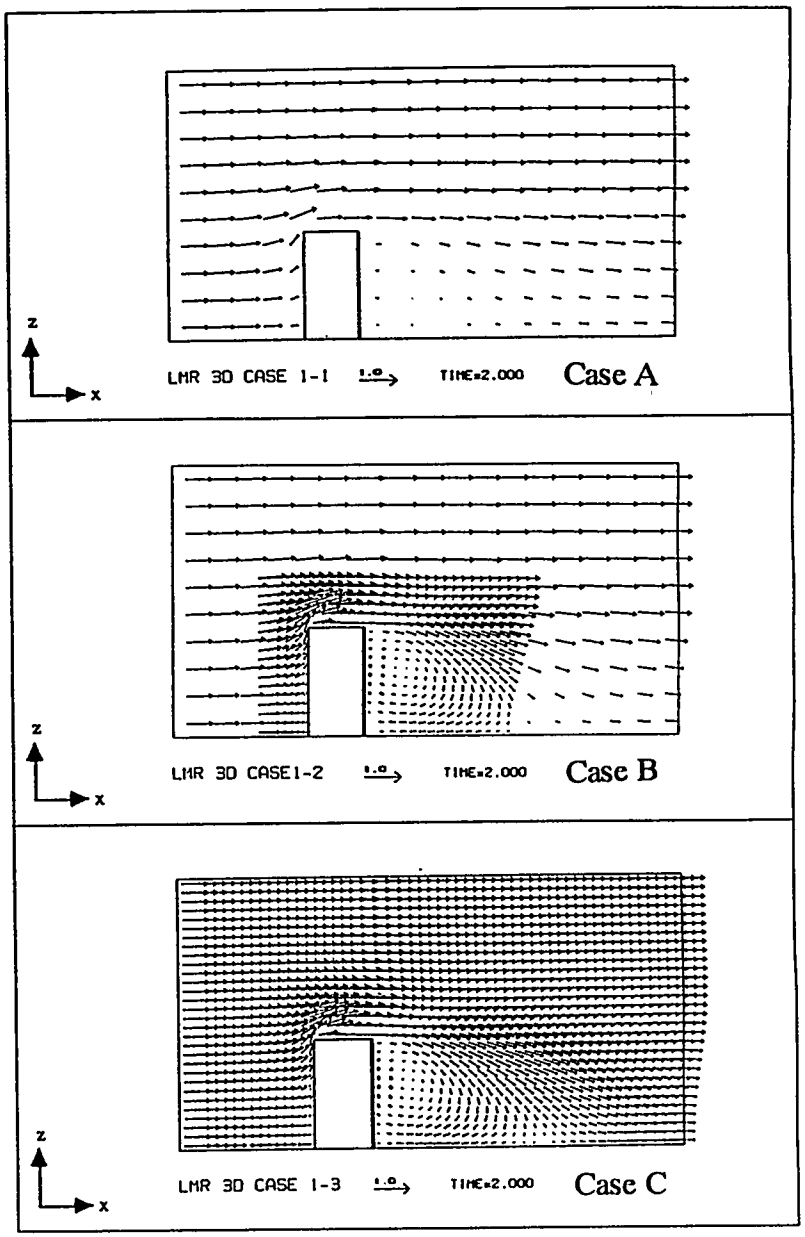
The CPU times are measured from the 2-second simulations.

(2) Free surface flow around a rectangular column

Free surface movement when a column suddenly takes up motion at constant speed is calculated using LMR3D. This is a good test to verify the fluid redistribution scheme of Eqs.(2)and (3). Figure 5(a) is a schematic diagram of the problem, and Figures 5(b), 5(c) and 5(d) show the instantaneous velocity vectors around the column when the time is 0.2 second. These figures

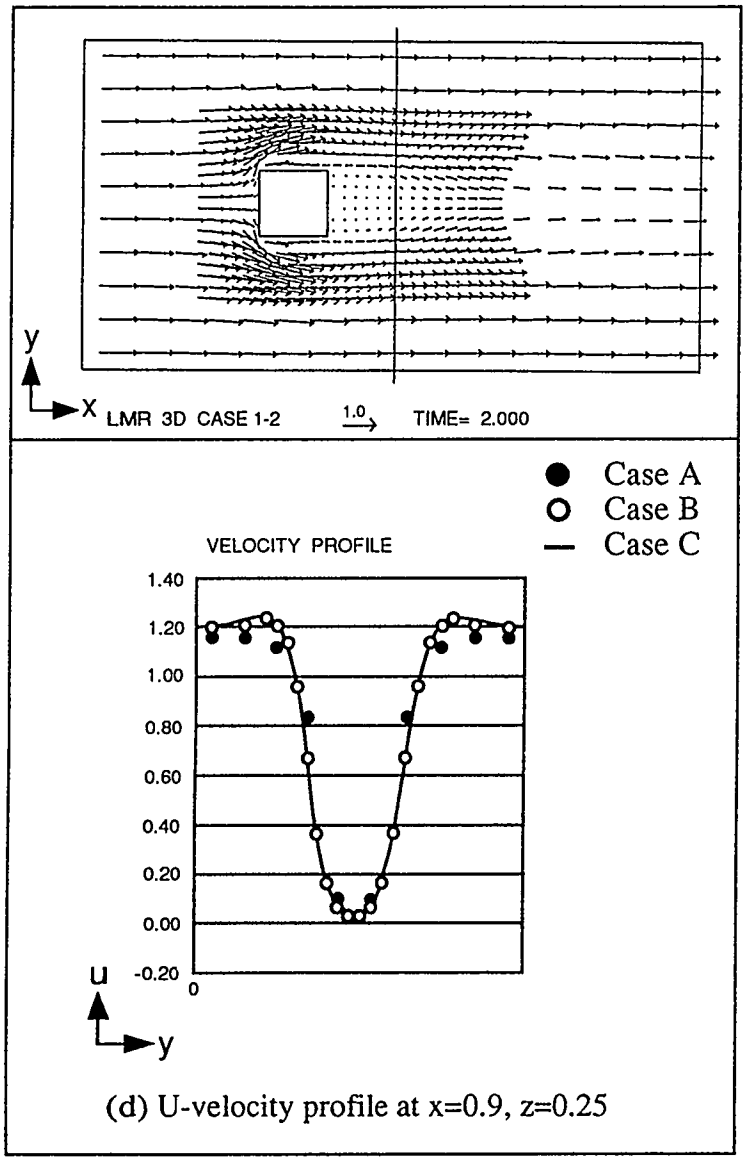


(b) Horizontal view at time=2.0, z=0.25

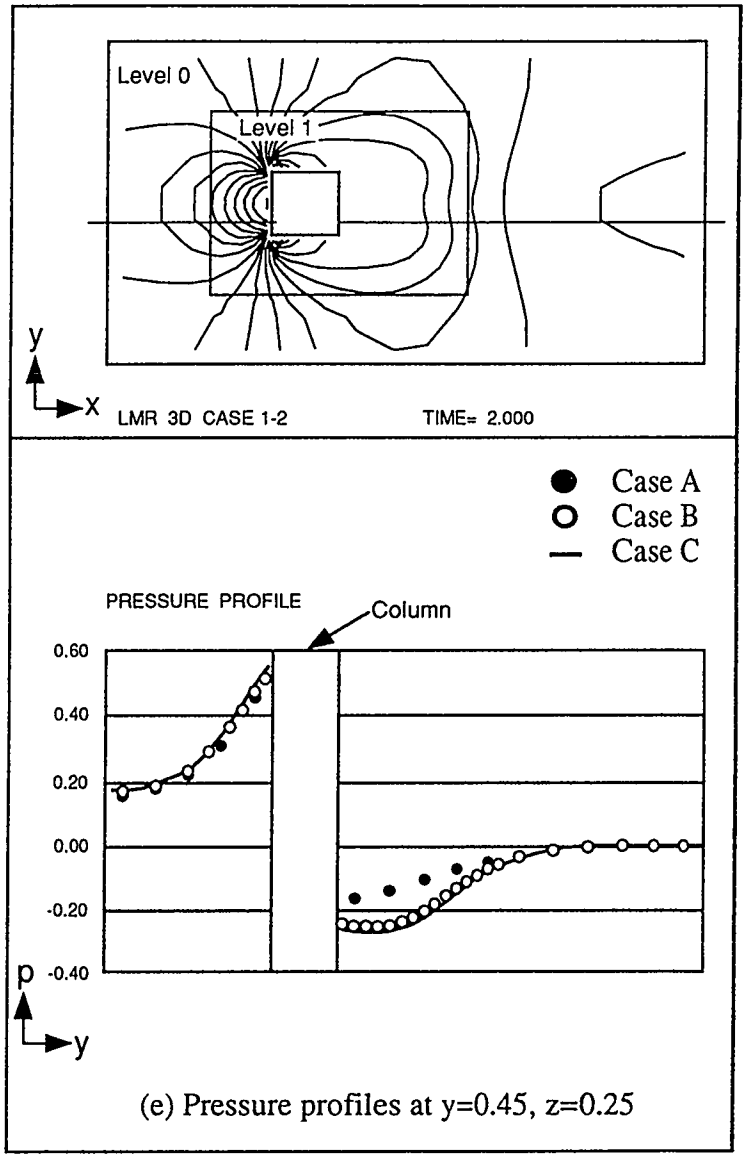


(c) Vertical view at time=2.0, y=0.45

Figure 4(b) and (c) Velocity vectors for horizontal and vertical views



(d) U-velocity profile at x=0.9, z=0.25



(e) Pressure profiles at y=0.45, z=0.25

Figure 4(d) and (c). Comparison of velocity and pressure profiles at time=2.0

demonstrate the adequacy of the redistribution scheme. The total number of cells for the LMR calculation is 10,801 and that for the fine grid is 41,580. The computing time for LMR is less than 1/3.2 that consumed by the fine grid calculation. The reduction in computing time for these problems is approximately in proportion to the ratio of total number of cells.

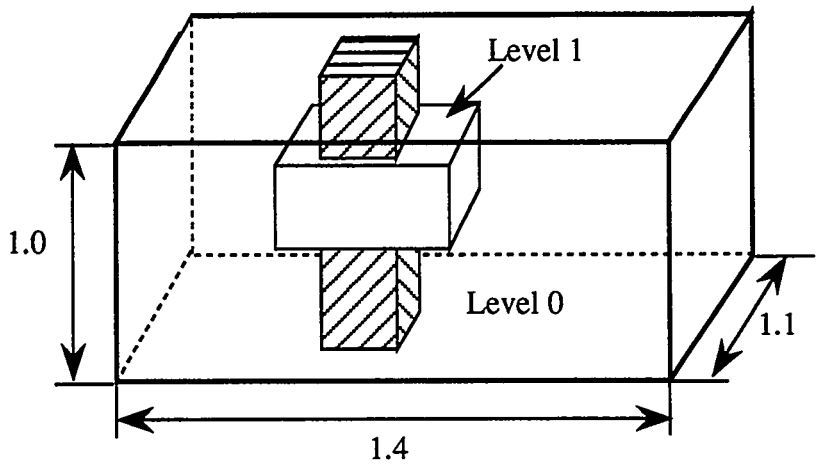


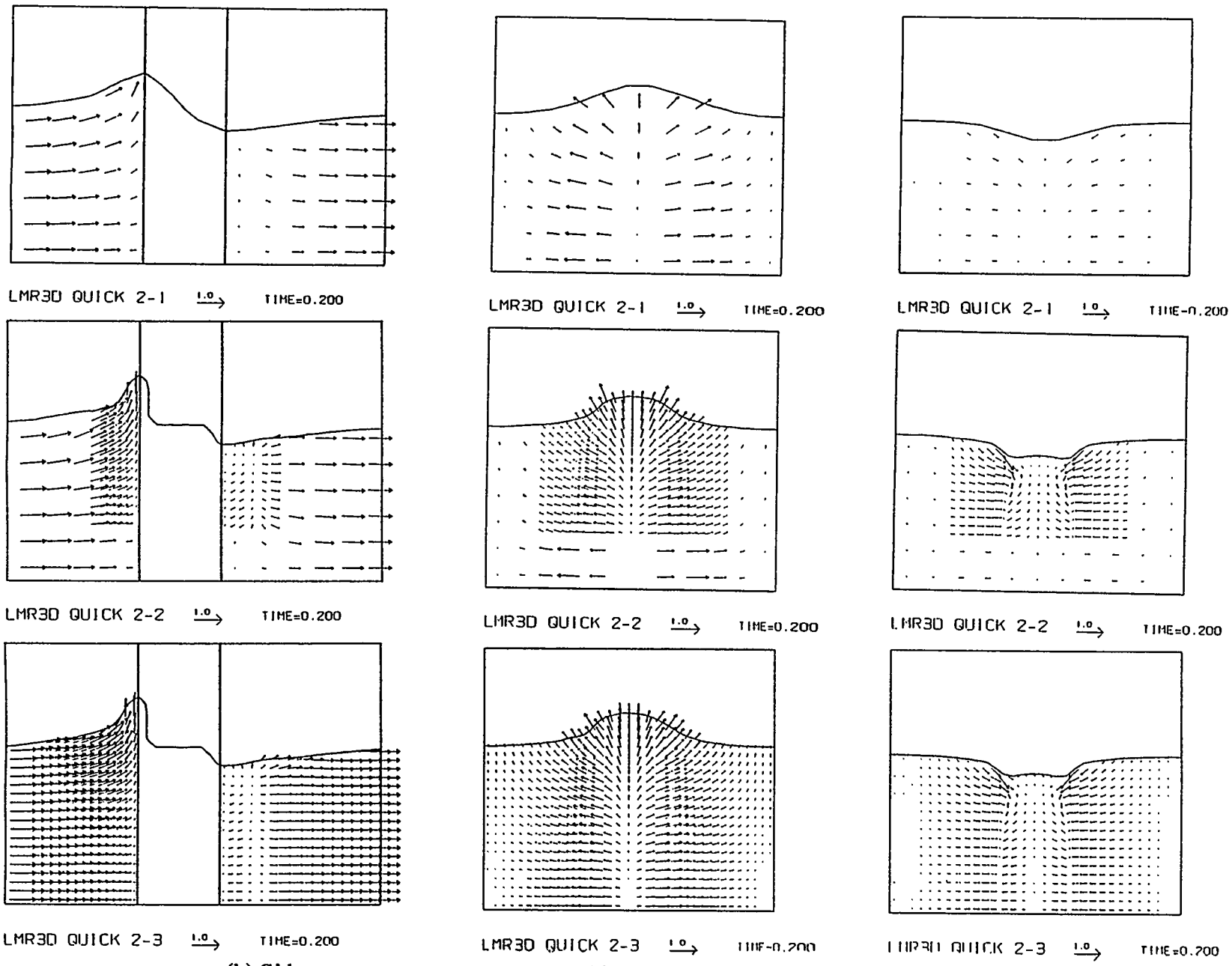
Figure 5(a) Schematic diagram of the free surface flow

(3) Large recirculating flow with free surface

Gas entrainment tests were conducted at Abiko Research Laboratory in Central Research Institute of Electric Power Industry[8]. In these tests, five models with geometrical similitude but with different scales were used to examine the scale effects. LMR3D qualification is done against data obtained from the large size model test and the time-averaged surface profile is compared with the experimental one measured by wave gauges. The test section for the L-size model is shown in Figure 6(a). The major analysis conditions are:

i) initial water level	150 cm
ii) flow rate	0.3 m^3/s (inlet velocity is about 2.0m/s)
iii) grids	20x1x15 (level 0)
	45x3x12 (level 1)
	18x9x15 (level 2)
iv) difference scheme	QUICK

Figure 6(b) shows the grid system. In this analysis, non-uniform mesh is applied for the coarsest grid, i.e. level 0, as shown in the figure. The level 1 grid is located around the water surface, and level 2 grid is located at the upper right corner where the vortex induced gas entrainment intermittently appears. The instantaneous velocity vectors together with water surface profile at 30 second are shown in Figure 6(c). The calculated flow pattern is very similar to the observed one. The velocities, pressures and surface profile are varying during the simulation, as in the experiments. Figure 6(d) is a time history of surface height at x=5cm, and represents this surface fluctuation. The fluctuation becomes periodic after 10 seconds, and so the time averaged surface profile is obtained by averaging the profile from time at 10 to 30 second. The comparison result is shown in Figure 6(e). The solid line shows the calculated profile and dots show the averaged surface height measured at each location. Good agreement is observed from the figure.



(b) Side (c) Front (d) Back

Figure 5(b),(c) and (d) Velocity vectors and sueface profiles around the column at time=0.2

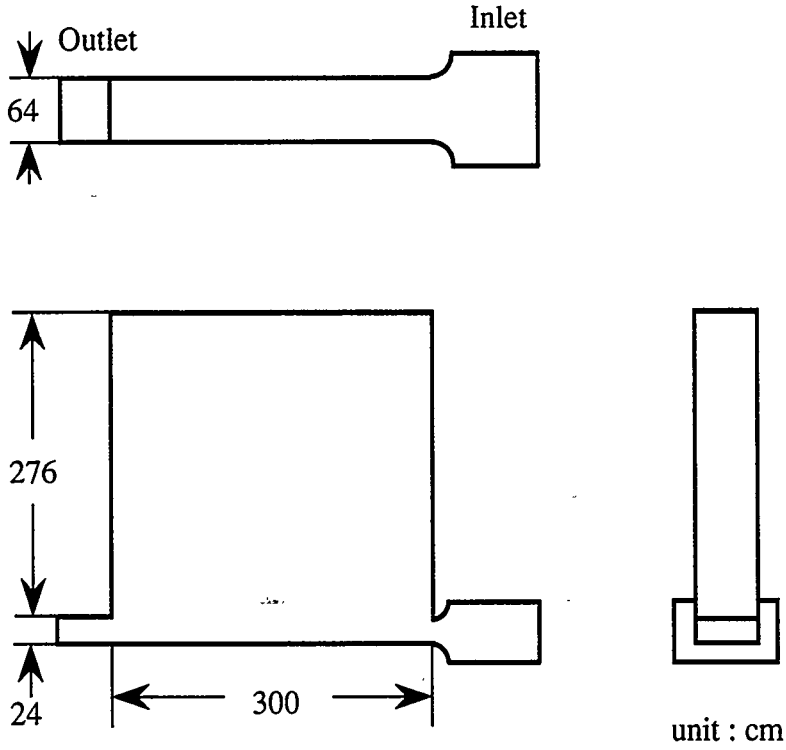


Figure 6(a) L-size test section

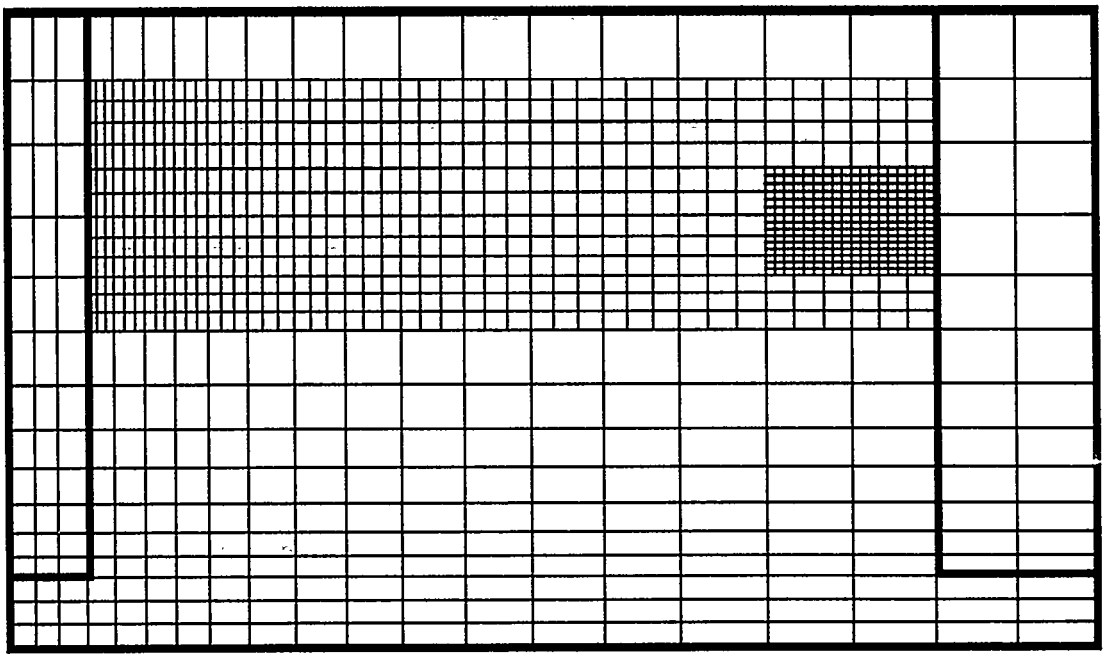


Figure 6(b) Grid system for recirculating flow

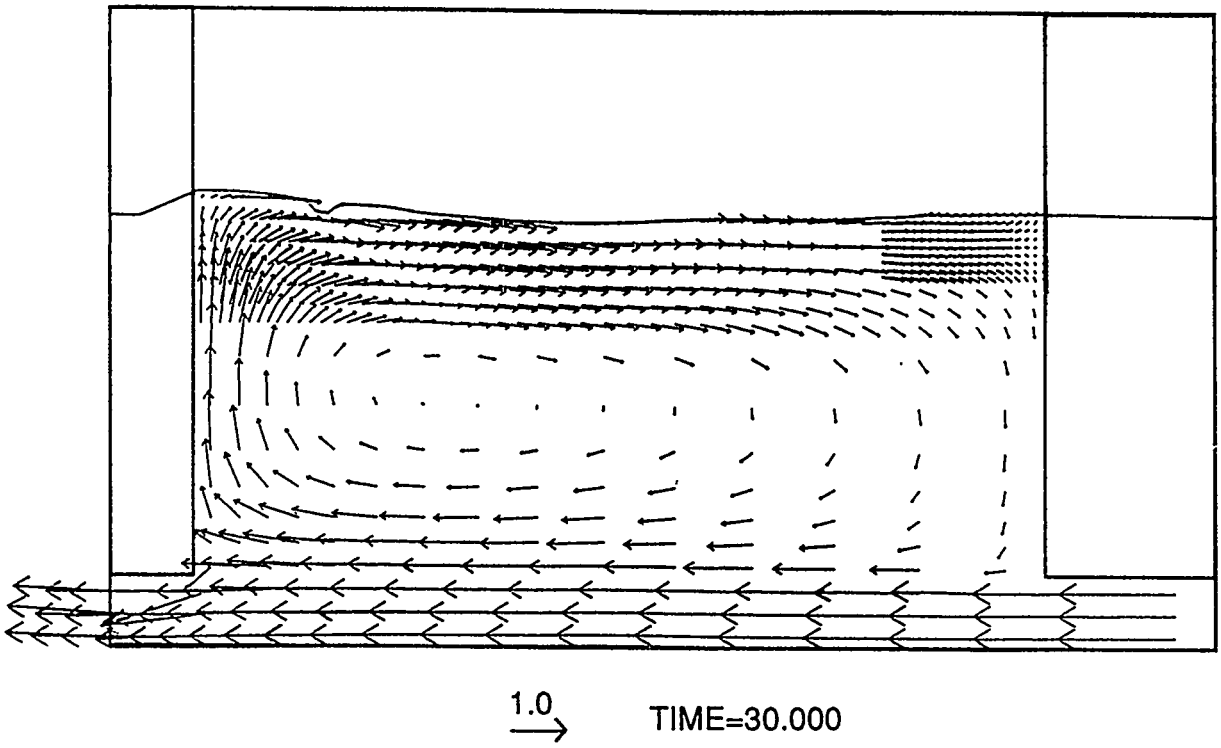


Figure 6(c) Velocity vectors at time=30 sec.

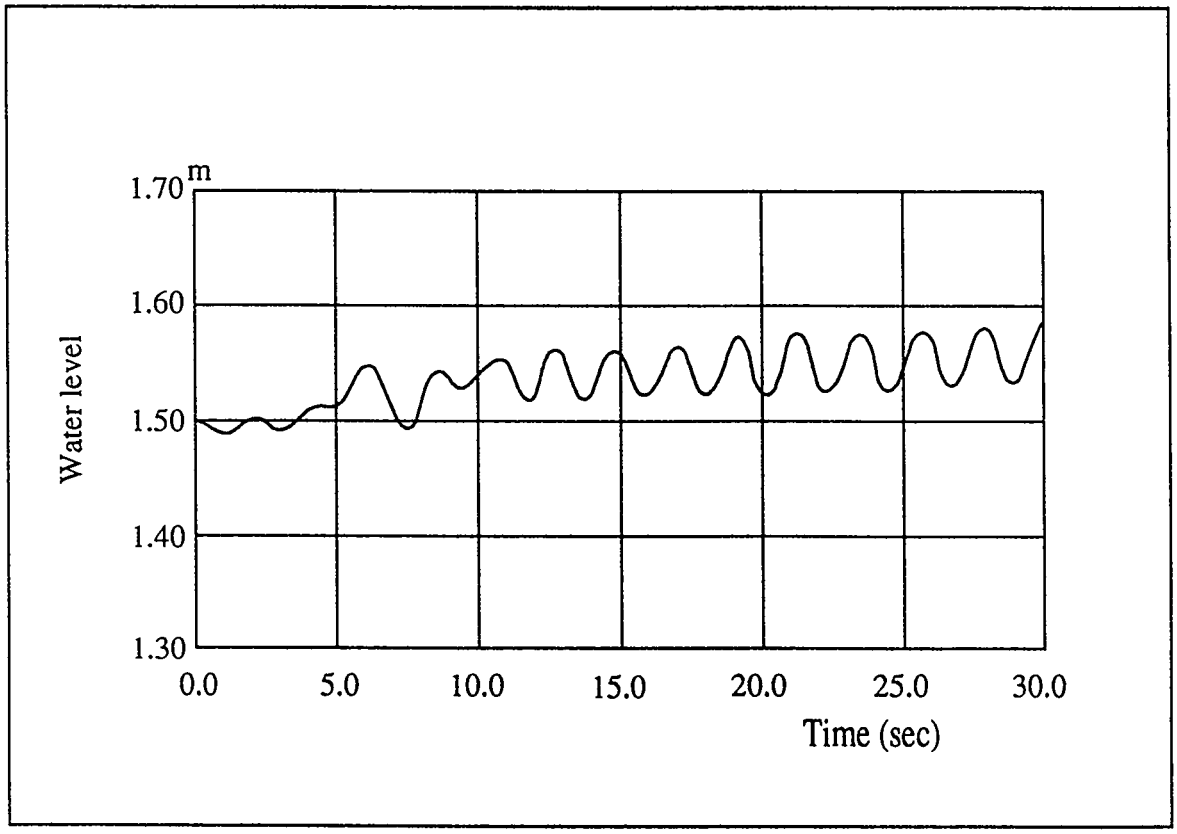


Figure 6(d) Time history of serface fluctuation at x=5cm.

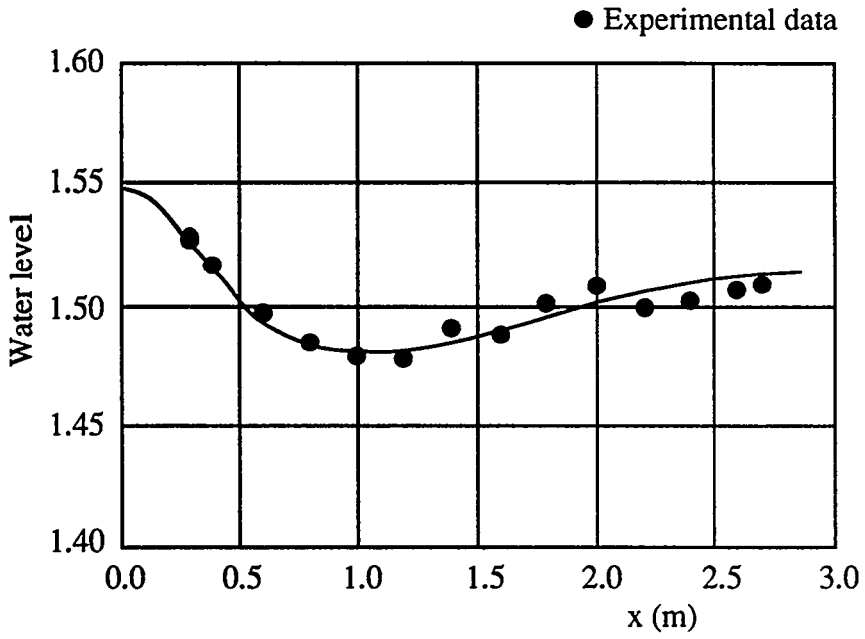


Figure 6(e) Comparison of surface profile between experiment and calculation

4. Conclusion

This paper presents a local mesh refinement (LMR) technique and describes its applications for incompressible flows with free surfaces. Although the idea of LMR is based on a local adaptive mesh refinement (LAMR) method developed for compressible flow analysis, it is converted into a zone decomposition method. The LMR method is more flexible in the composition of computational grid systems than usual zonal methods. It can place an arbitrary number of patches with arbitrary levels of fineness in any regions of interest. This flexibility enables us to use a high-resolution grid system with a reduced number of cells in total. Therefore, more accurate solutions are obtained at less computational cost. The LMR method can, furthermore, be extended to free surface flow problems. A special interpolation scheme for the redistribution of fluid in coarser cells into finer sub-cells is developed to achieve this extension. Several numerical examples are presented. These examples demonstrate well the advantages of LMR.

REFERENCES

[1] M.J. Berger and P. Colella, "Local adaptive mesh refinement for shock hydrodynamics," Journal of Computational Physics, 82: 64-84, 1989.

[2] S. Taki, "Solution-adaptive multilevel grig refinement method for numerical calculations of high-speed burning flow," The proceeding of the 3rd Computational Fluid Dynamics Symposium, 431-434, 1989 (in Japanese).

[3] C.W. Hirt, B.D. Nichols, and N.C. Romero, "SOLA - A numerical solution algorithm for transient fluid flows," Los Alamos Scientific Laboratory report LA-5852, 1975

[4] J.E. Welch, F.H. Harlow, J.P. Shannon and B.J. Daly, "The MAC method: A computing technique for solving viscous incompressible, transient fluid flow problem involving free surfaces," Los Alamos Scientific Laboratory report LA-3425, 1966.

[5] C.W. Hirt, A.A. Amsden and J.L.Cook, "An arbitrary Lagrangian-Eulerian computing for all flow speed," Journal of Computational Physics, 14, 227-254, 1974.

[6] C.W. Hirt and B.D. Nichols, "Volume of fluid (VOF) method for the dynamics of free boundaries," Journal of Computational Physics, 39: 201-225, 1981.
[7] H.M. Domanus, R.C. Schmitt, W.T. Sha, and V.L. Shah, "A new implicit numerical solution scheme in the COMMIX-1A computer program," Argonne National Laboratory report ANL-83-64, 1983.
[8] Y. Eguchi, "Scale effects on gas entrainment phenomena at free surface," Central Research Institute of Electric Power Industry, Abiko Research Laboratory Report U91005, 1991.

Level Tracking in Detailed Reactor Simulations

Birol Aktas and John H. Mahaffy

The Pennsylvania State University
Department of Nuclear Engineering
University Park, PA 16802

We introduce a useful test problem for judging the performance of reactor safety codes in situations where moving two-phase mixture levels are present. The test problem tracks a two-phase liquid level as it rises and then falls back to its original position. Pure air exists above the level, and a low void air-water mixture is below the level. Conditions are subcooled and isothermal to remove complications resulting from failures of interfacial heat transfer packages to properly account for the level. Comparisons are made between the performance of current versions of CATHARE, RELAP5, TRAC-BF1, and TRAC-PF1. These system codes are based on finite-difference methods with a fixed, Eulerian staggered grid in space. When a partially filled cell with a mixture level discontinuity becomes the donor cell, the sharp changes in fluid properties across the interface results in numerical oscillations of various terms. Furthermore, the cell-to-cell convection of mass, momentum and energy are inaccurately predicted nearby a mixture level.

To adequately model moving mixture levels, an efficient discontinuity tracking method for the finite-difference Eulerian approximations is described. This model had been implemented in the TRAC-BWR code for the two-phase mixture level tracking since the TRAC-BD1 Version (released April 1984). The result of the test problem run by the current version of TRAC-BF1/MOD1 with the mixture level tracking model shows some peculiar behavior of the variables such as velocities, pressures and interfacial terms. A systematic approach to improving performance of the tracking method is described. Implementing this approach in TRAC-BF1/MOD1 has shown a major improvement in the results.

1. Introduction

Tracking of distinct water levels has always been an issue for simulations of Boiling Water Reactor (BWR) vessel behavior. Although it has been less important in Pressurized Water Reactor (PWR) simulations, situations do exist where the ability to accurately model moving levels would be desirable. Since the interfacial heat transfer in the two-fluid codes of our interest is tied to the flow regime map through the void fraction of the mesh cell, distinguishing the annular/drop flow above and bubbly/churn flow below the two-phase level requires the knowledge of void fractions above and below the level. Otherwise, for the mesh cells partially filled with two-phase mixture, the interfacial heat transfer is inaccurately predicted.[1] Since the interfacial heat transfer around two-phase level is based on the cell average void fraction, reactor safety codes can not accurately predict the rate of pressurization or depressurization of systems. Boyer et al.[2] compared major U.S. safety codes for a BWR/4 main steam isolation valve (MSIV) closure transient where smearing of void fraction front reduced the pressure quenching effect. In the same study, tracking the two phase level and accurately predicting the interfacial heat transfer helped to simulate the pressure quenching more accurately when cold feedwater was sprayed into pure steam above the sharp void fraction front.

For simulations of advanced passive reactor designs, an accurate level tracking is even more important. Since system behavior of passive designs is dependent on the delicate pressure balances of natural circulation, anomalous pressure behavior due to the presence of two-phase levels can seriously degrade the quality of advanced reactor simulations. In principal, the flow problems associated with two-phase level interfaces can be handled numerically by working with the governing equations in *integral* form and constitutive relationships that hold across the discontinuities. In practice, however, their application is severely limited. Away from these interfaces, where the solution is smooth, the integral equations can be well approximated by partial differential equations (PDEs). Most fluid models in reactor safety usually approximate these PDEs by finite difference methods. For the finite-difference

numerical methods to be accurate near discontinuities, where the PDEs fail to approximate the integral equations, they must treat the discontinuity specially. Otherwise, the sharp changes in flow quantities such as void fraction and phasic velocities across the discontinuous interface will result in peculiar behavior of pressure, phasic velocities and void fraction.

Although flow problems involving motion of pure liquid into a voided region are useful, they miss some important phenomena related to the interface between two phase mixture and single phase regions that occur in full reactor transients. Therefore, we have designed a test problem including a two-phase mixture below the level to provide more understanding of these situations. Our problem involves an isothermal air and water mixture. Thus, the solution of this problem is only sensitive to how the two phase interface is handled by the conservation equations for mass, momentum and their constitutive equations. With this test problem, we have compared the performance of current versions of major nuclear safety codes CATHARE, RELAP5, TRAC-BF1 and TRAC-PF1. The comparison of codes has shown that problems with the treatment of interfacial shear and inertial densities result in poor simulation of pressure behavior for the mesh cells around the two phase boundary.

As we shall see, the results from test runs indicate a common gap in the two-fluid models of major safety codes when dealing with moving two phase levels. Akimoto et al.[3] studied the numerical pressure spikes associated with a quasi-stable water surface in the initial stage of reflood phase after a PWR-LOCA. They rigorously showed that upwind-difference scheme approximating the gradient of liquid velocity across a liquid front, resulted in numerical pressure excursions. Unlike pressure spikes due to water packing that is a well known phenomenum[4], these numerically induced pressure oscillations resulting from level motion are often overlooked when judging calculations. In general, to deal with flows containing sharp fronts, the *tracking* methods have been very popular, where additional computational elements are introduced to explicitly keep track of the front. These methods have been developed for various interfaces that commonly occur in many fluid flow problems such as detonations, flame fronts and multiphase flows.[5,6] Among these methods, the so-called volume-tracking methods offer region following schemes where the problem domain is a union of fluid regions divided by interfaces. Because of their simplicity, they are widely applied to various multi-phase interface problems including reactor safety applications.[7] In 1980s, the General Electric (GE) developed a level tracking model for TRAC-BWR to curtail the numerical diffusion of void fraction, a tracking model that shares common features with other volume-tracking methods. Later, the developmental assessment at the Idaho National Engineering Laboratory (INEL) demonstrated several deficiencies in the model which could lead to spurious computational results.[8] Despite the changes made by INEL to improve the level tracking model, it has failed to properly simulate the moving mixture level in our test problem. In this study, we also suggest a systematic approach to improving performance of the TRAC-BF1 level tracking model.

In the next section, we will introduce our test problem for judging the performance of reactor safety codes in situations where moving two-phase mixture levels are present, and the following section will compare the results from recent versions of CATHARE, RELAP5, TRAC-BF1, and TRAC-PF1. Later in the paper, we will review the TRAC-BF1 level tracking model and show the test run results when level tracking is activated that clearly illustrate the nature of the problems encountered. Further, an improved approach to the level tracking will be described, and we will provide the results obtained implementing the improved level tracking in TRAC-BF1.

2. Moving Mixture Level Test Problem

Given our experience with level tracking problems in BWR simulations, we found it necessary to introduce a new, simple problem to test our method. A schematic of the test problem is shown in Figure 1. The model consists of a vertical pipe with 0.1 m^2 axial flow area and 1.0 m height, that is made of 10 equal volume cells. A *T* branch is connected to the bottom of the test pipe, through which an air flow maintains the air and water mixture at 0.13 void fraction and 50 °C equilibrium temperature. A mixture level is initially maintained in cell *2* of the test pipe with 37 kg total liquid inventory. Below the mixture level, the air bubbles form and rise at a terminal velocity. Due to differences in interfacial shear models of the codes being tested, equal air mass flows result in different mixture void fractions. We have adjusted the flow of air in each code to match the below level mean void fractions for a better comparison. From the *T* branch, the liquid water is first injected and then withdrawn to create a moving mixture level. The injection at 5 kg/sec into the test pipe creates a *rising* level that moves a distance approximately one-half grid spacing per second for the first 5 seconds. Similarly, the liquid water is withdrawn at the same rate to create a *falling* mixture level for another 5 seconds.

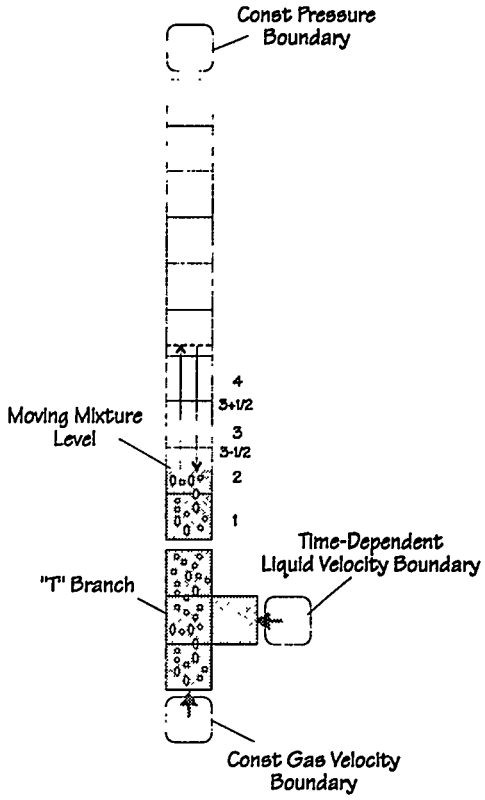


Figure 1. Schematic of the test problem

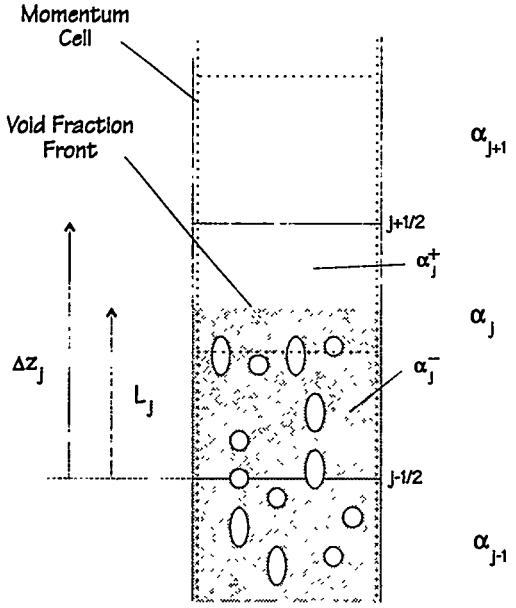


Figure 2. A flow cell with the mixture level

Conditions are subcooled and isothermal to remove complications resulting from failures of interfacial heat transfer packages to properly account for the level. Hence, the solution depends only on the conservation equations for liquid and gas *mass* and the conservation equations for liquid and gas *momentum*. Gravity and the interfacial shear between air bubbles and liquid water are the only forces that act on the fluid. The wall friction is suppressed in the calculations, so that pressures below the level solely result from the hydrostatic gravity head. Moreover, the isothermal and subcooled conditions at 1.01 x10^5 Pascal force all interfacial mass transfer terms to zero. The safety codes then effectively solve Equations (1),(2),(3) and (4) that govern the fluid flow of *moving mixture level test problem.*

$$\frac{\partial}{\partial t}(\alpha\rho_g) + \frac{\partial}{\partial z}(\alpha\rho_g V_g) = 0 \tag{1}$$

$$\frac{\partial}{\partial t}[(1-\alpha)\rho_\ell] + \frac{\partial}{\partial z}[(1-\alpha)\rho_\ell V_\ell] = 0 \tag{2}$$

$$\frac{\partial V_g}{\partial t} + V_g\frac{\partial}{\partial z}V_g = -\frac{1}{\rho_g}\frac{\partial P}{\partial z} - \frac{1}{\alpha\rho_g}F_{\ell g} + g \tag{3}$$

$$\frac{\partial V_\ell}{\partial t} + V_\ell\frac{\partial}{\partial z}V_\ell = -\frac{1}{\rho_\ell}\frac{\partial P}{\partial z} + \frac{1}{(1-\alpha)\rho_\ell}F_{\ell g} + g \tag{4}$$

where $F_{\ell g}$ is the interfacial shear at the face interface.

3. Comparison of Reactor Safety Codes

In order to judge the performance of codes, we have selected a set of common variables for comparison. The state variables are defined at the cell centers, whereas dynamic variables are at the cell faces. We then present pressures in cells *2,3,4* of test pipe shown in Figure 1. However, we only compare the void fraction in cell *3* and phasic velocities at cell face *3+½* of the test pipe.

The pressures as the mixture level rises and falls are depicted in Figures 3,4,5 and 6. We observe pressure spiking in various degrees during the transient while the mixture level rises. In order to understand the underlying mechanism that results in pressure spikes, we solve the momentum equations (3) and (4) for the pressure gradient. Multiplying Equations (3) and (4) by macroscopic densities and rearranging, we have

$$\alpha \frac{\partial P}{\partial z} = -(\alpha \rho_g)\frac{D_g V_g}{Dt} - F_{lg} + \alpha \rho_g g \quad , \tag{5}$$

$$(1-\alpha)\frac{\partial P}{\partial z} = -[(1-\alpha)\rho_l]\frac{D_l V_l}{Dt} + F_{lg} + (1-\alpha)\rho_l g \quad . \tag{6}$$

where D_g/Dt and D_l/Dt are the substantial derivatives along the gas and liquid flow respectively. Away from the two-phase interface, summing Equations (5) and (6) gives the pressure gradient proportional to the hydrostatic gravity head, provided that the acceleration terms on the right hand sides vanish. In all the safety codes being tested except TRAC-BF1, interfacial shear is modified to strongly couple the liquid field to the gas when the flow is single phase gas (codes assume $1-\alpha=10^{-5}$ or 10^{-6}) as can be seen in Figure 7. In contrast, a *rising* mixture level that partially fills mesh cell *j*, reduces the cell average void fraction convected across cell face *j+½*, and therefore weakens the interfacial drag. When combined with the upward gas flow, this results in negative liquid velocity at *j+½*. As the void fraction front rises in cell *j*, the void fraction convected at *j+½* decreases, which in turn, continuously changes the force balance between interfacial drag and gravity acting on the dispersed droplets. When finally the two-phase mixture fills up cell *j*, the liquid velocity at *j+½* suddenly becomes positive and resulting high liquid acceleration term in Equation (6), inducing a pressure peak.

It is important to note that the water packing options are in effect for RELAP5, TRAC-BF1 and TRAC-PF1. Although spiking due to water packing is suppressed by an ad hoc procedure setting the compressibility artificially to zero when a cell nears the filling point,[4] in our test run, this procedure has not suppressed the pressure spikes. CATHARE has no special water packing treatment. On the other hand, a method proposed by Akimoto et al.[3] avoids high acceleration pressure losses associated with liquid velocity reversals in TRAC-PF1 (their method is not implemented in our version). As seen from Figure 7, while the mixture level fills up cell *3*, the liquid velocity above the void fraction front, predicted by RELAP5, TRAC-BF1 and TRAC-PF1 changes very rapidly. When the mixture level is between *j* and *j-½*, pressure at *j* is overpredicted since the flow is assumed uniform in cell *j*, although it is really not.

The void fraction in cell *3* predicted by all codes are compared in Figure 8. When the mixture level fills up cell *3*, TRAC-PF1 and RELAP5 predict 0.0 void fraction. That is smaller than the donor cell mixture void fraction. Although the TRAC-PF1 void fraction returns to more reasonable values, RELAP5 retains a lower void fraction than predicted by the others and as a result, RELAP5 propagates the mixture level to cell *2* later than predicted by the others. For *falling* mixture level, while the void fraction of cell *3* convected across cell face *3-½* changes from 0.13 to 1.0, the flow regime shifts from bubbly to annular droplet. During this transition, the codes interpolate between the interfacial drag coefficients based on these flow regimes. We observe that the rate of downward liquid flow then becomes smaller as the liquid mass in cell *3* decreases. Here, the comparison between the asymptotic approach to 1.0 of computed void fraction from Figure 8 and the straight line that could be theoretically predicted for the level motion, gives us a measure for the numerical diffusion of void fraction. The safety codes selected the time step size based on their numerical method and time step selection algorithm.

We have only considered the maximum time step size of 0.1 seconds in comparing the safety codes. Only TRAC-BF1 did not achieve this step size, running at about 0.05 seconds. This allows at least 20 time steps to fill each cell. Our test results of codes certainly indicate a need for explicitly keeping track of void fraction front. Otherwise, inadequate modeling of moving mixture levels will decrease the accuracy and degrade the quality of our analyses.

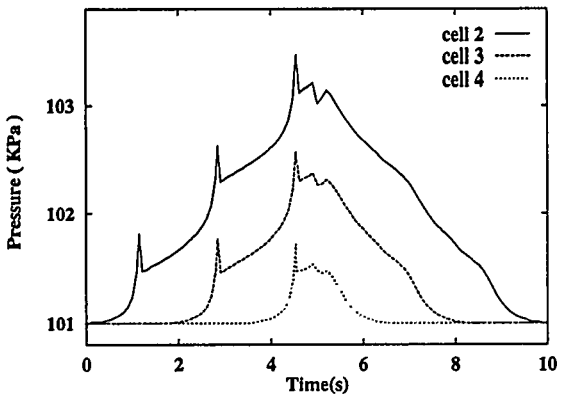


Figure 3. Pressures from CATHARE

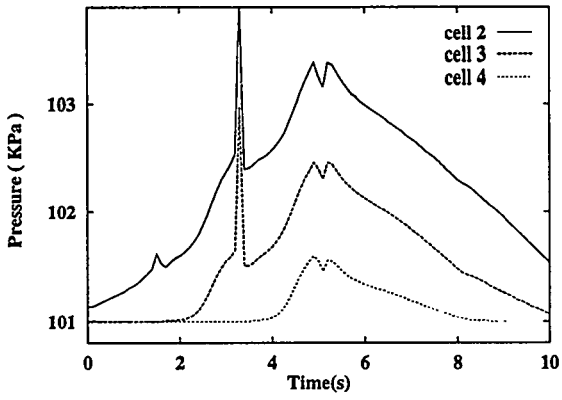


Figure 4. Pressures from RELAP5

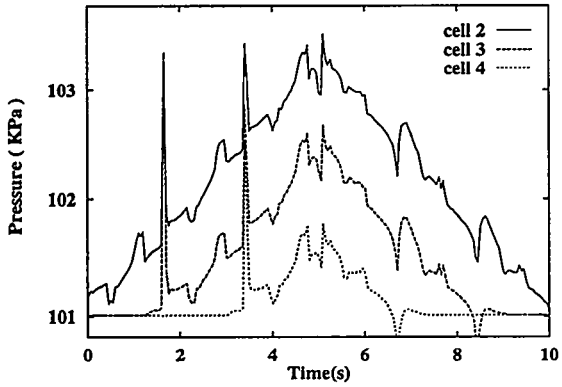


Figure 5. Pressures from TRAC-BF1

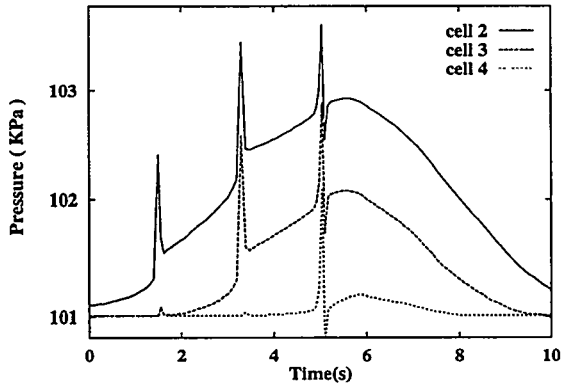


Figure 6. Pressures from TRAC-PF1

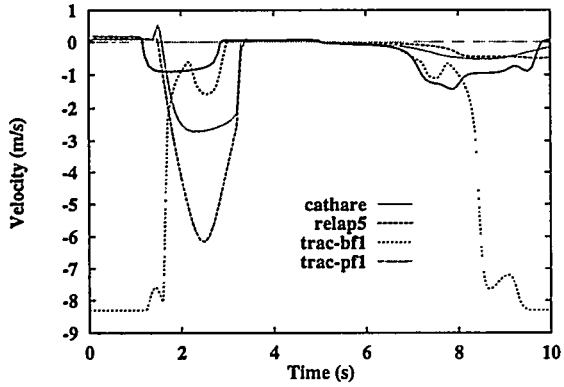


Figure 7. Liquid Velocity at cell face *3+1/2*

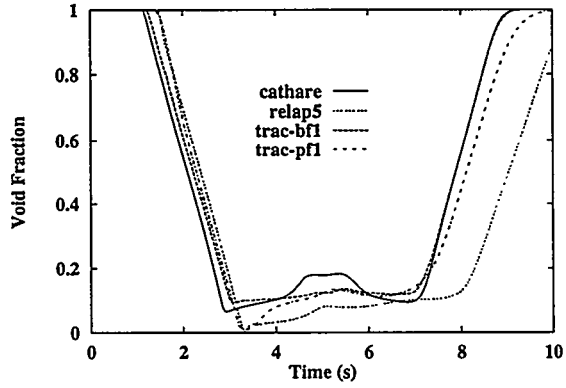


Figure 8. Void Fraction in cell *3*

4. Mixture Level Tracking

As we pointed out in our introduction, a level tracking model was implemented in TRAC-BF1 primarily to have more accurate interfacial heat transfer description for partially filled mesh cells. Several assessments following the model development indicated deficiencies which could lead to spurious results. Before we introduce our new approach to level tracking in reactor safety two-phase flow, we feel that it is important to learn more about TRAC-BF1 level tracking. In this section, we briefly describe how TRAC-BF1 level tracking works and then present the results of TRAC-BF1 test run when the two-phase level tracking is activated.

For each vertically oriented cell, the level tracking model first searches for the presence of a two-phase mixture level from criteria based on the axial void profile around that particular cell. This logic developed by GE to test for the level in a computational cell is based on certain BWR experimental test data and numerical experiments.[9] The initial step in detecting a void fraction front is to evaluate the axial void profile around a particular hydrodynamic cell. In general, a level is assumed to exist in cell j if the calculated cell centered void distribution satisfies the following criteria:

$$\alpha_{j+1} - \alpha_j > 0.2 \text{ or } \alpha_j - \alpha_{j-1} > 0.2 \quad \text{and} \quad \alpha_{j+1} > 0.7 \tag{7}$$

provided that no level exists in cell $j+1$ or cell $j-1$ (Figure 2). When a level is detected in cell j, its position is calculated in terms of computed mean cell and non-cell centered void fractions according to Equation (8)

$$L_j = \Delta z_j \frac{\alpha_j^+ - \alpha_j}{\alpha_j^+ - \alpha_j^-} \tag{8}$$

where α^+ represents the void fraction above the level and is equal to the void fraction in cell $j+1$; α^- represents the void fraction below the level and is equal to the void fraction in cell $j-1$. For example, in the first time step of our test problem a mixture level is initially detected in cell 2 where the void fractions in cells 1, 2 and 3 are α_1=0.12, α_2=0.69 and α_3=1.0. An existing level in cell j is propagated to $j+1$, if the projected position based on the level velocity is in cell $j+1$ or the mean void fraction α_j becomes less than the mixture void fraction α^-. Similarly, the level is propagated to $j-1$, if the projected position based on the level velocity is in cell $j-1$ or the mean void fraction α_j becomes equal to the above level void fraction α^+.

When there is no mixture level in the momentum cell $j+½$, TRAC-BF1 linearly interpolates between above and below cell macroscopic densities based on the lengths of cells on either side of the cell edge under consideration in order to determine inertial macroscopic densities in the staggered momentum cell. If a mixture level exists, TRAC-BF1 interpolates non cell-centered void fractions based on the relative position of the level in the space between the cell center and the cell edge and determines *an average void fraction* for the half of momentum cell in which the level exists. The mass and energy equations then convect the non cell-centered macroscopic quantities across the cell face.

For the TRAC-BF1 test run when the level tracking is activated, pressures in cells 2,3 and 4 are depicted in Figure 9. We have no doubt that the TRAC-BF1 level tracking has failed in our moving mixture level test. Figure 10 further indicates that the interfacial drag between dispersed bubbles and liquid does not remain constant. Whereas, bubbles should rise at a terminal velocity based on a constant balance of drag and buoyancy forces and resulting pressure gradient at the phase interface.

Conventionally, the safety codes assume an average flow regime and evaluate the coefficients of momentum equations in terms of densities, void fraction and known velocities either defined at $j+½$ or interpolated between j and $j+1$, which are also assumed uniform. We have found it necessary to take greater care in this area of modeling, and have introduced several new corrections to the basic finite difference equations.

If a void fraction front exists, the level tracking model provides void fractions which are uniform in regions between the void fraction front and the edges of staggered cell. The regions above and below the void fraction front then have two distinct flow regimes based on these non cell-centered void fractions. Since the velocities convect the fluid either from above or below the void fraction front, inertial macroscopic densities and interfacial drag must be evaluated in terms of the non cell-centered void fraction in theregion which occupies cell face $j+½$.[10] Therefore, we define the inertial macroscopic densities that prevail at $j+½$ as follow when a void fraction front exists between $j+½$ and j,

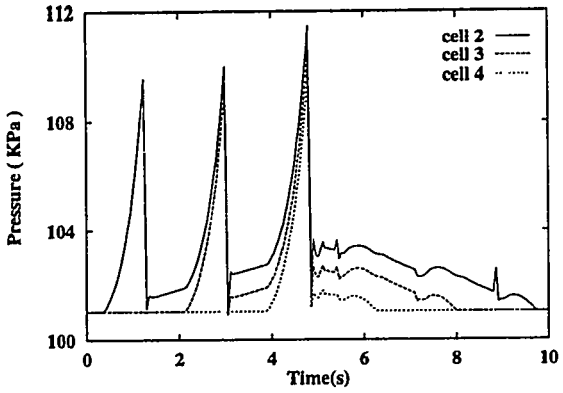


Figure 9. Pressures from TRAC-BF1 When Level Tracking is activated

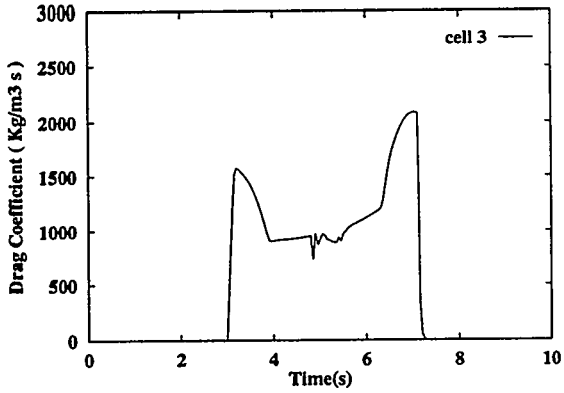


Figure 10. Interfacial Drag from TRAC-BF1 When Level Tracking is activated

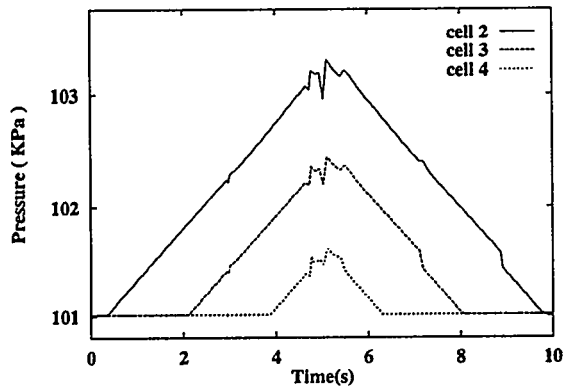


Figure 11. Pressures After Level Tracking is Improved

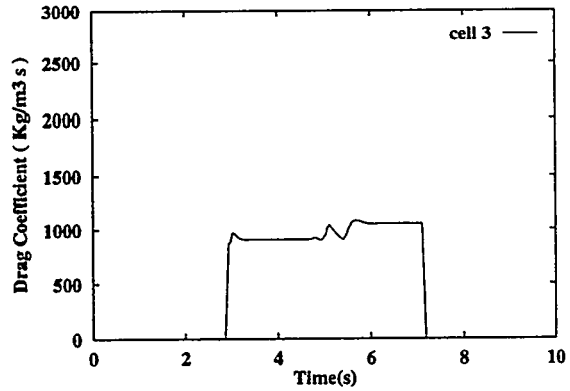


Figure 12 Interfacial Drag at *3+1/2* After Tracking is Improved

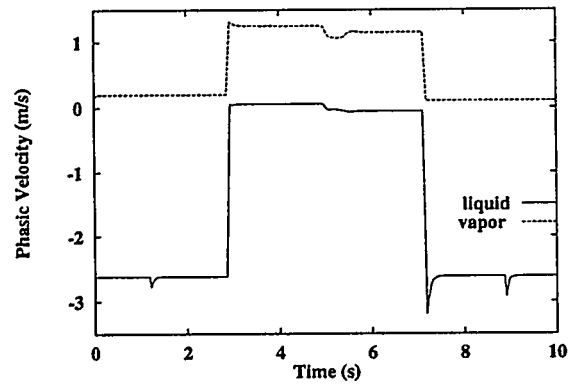


Figure 13. Velocities at *3+1/2* After Tracking is Improved

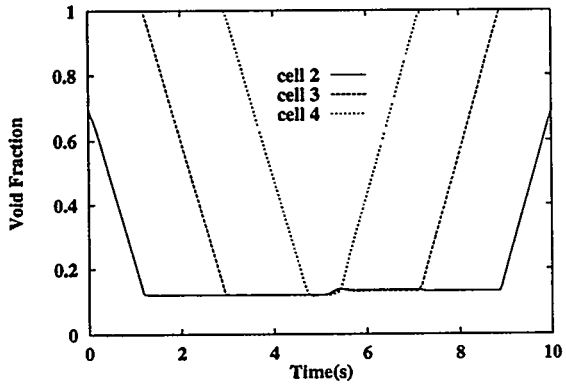


Figure 14. Void Fractions After Level Tracking is Improved

$$(\alpha\rho)_{j+1/2} = \frac{(L_j - \Delta z_j/2)\alpha_j^{+}\rho_j + (\Delta z_{j+1}/2)\alpha_{j+1}\rho_{j+1}}{(L_j - \Delta z_j/2) + \Delta z_{j+1}/2}\ , \tag{9}$$

or if a void fraction front exists between $j+½$ and $j+1$, then

$$(\alpha\rho)_{j+1/2} = \frac{(\Delta z_j/2)\alpha_j\rho_j + (\Delta z_{j+1}/2 - L_{j+1})\alpha_{j+1}^{-}\rho_{j+1}}{\Delta z_j/2 + (\Delta z_{j+1}/2 - L_{j+1})}\ . \tag{10}$$

where the void fraction and density are defined for liquid and gas phases accordingly.

Obviously, the resulting pressure gradient at cell face $j+½$ will not yield an accurate pressure drop between points j and $j+1$ when multiplied by $\Delta z_{j+½}$, since there are really two distinct pressure gradients in each region above and below the void fraction front. Therefore, the pressure gradient must be corrected for the hydrostatic head of mixture level in order to give the pressure drop across the momentum cell when multiplied by the cell length.

$$\left.\frac{\partial P}{\partial z}\right|_{j+1/2} = \frac{P_{j+1} - (P_j - P_{hydro})}{\Delta z_{j+1/2}} \tag{11}$$

The pressure drop correction given by Equation (11) is vital, since the velocities in the implicit finite-difference equations for the conservation of *mass* and *energy* are linearly expressed in terms of the pressure drop across the momentum cell. If a mixture level exists below cell face $j+½$, the pressure gradient at $j+½$ must be the gradient between the void fraction front and $j+1$ when corrected by

$$P_{hydro} = (L_j - \Delta z_j/2)\, g\, \left[\alpha^{-}\rho_g + (1-\alpha^{-})\rho_\ell\right]_j\ , \tag{12}$$

and similarly if a mixture level exists above cell face $j+½$, it becomes the gradient between the void fraction front and j when corrected by

$$P_{hydro} = -(\Delta z_{j+1}/2 - L_{j+1})\, g\, \left[\alpha^{-}\rho_g + (1-\alpha^{-})\rho_\ell\right]_{j+1}\ . \tag{13}$$

We also experienced very short-lived pressure and velocity excursions as the void fraction front was propagated across the cell faces. For smooth changes in *relative* velocity, a first-order Taylor series expansion in time provides a simple method to evaluate the *new time* interfacial shear. As soon as discontinuities appear when the void fraction front is propogated across the cell face, the information for the new time step provided by Taylor series expansion is destroyed. Reevaluating the old time level interfacial shear for the flow pattern behind the void fraction front stabilized the solution.[10]

The corrections implemented to TRAC-BF1 showed major improvement in the results for the moving mixture level test. As can be seen from Figure 11, the pressures in cells *2,3* and *4* accurately follow the hydrostatic pressure of moving two-phase mixture level. The comparison of void fractions between Figure 8 and Figure 14, gives us a measure for the numerical diffusion of void fraction when there is no level tracking. As seen from Figure 13, the liquid and gas velocities display a sharp transition after the void fraction front moves across the cell edge. Moreover, the interfacial drag at the cell edge remains constant throughout distinct regions above and below the void fraction front and shows a stable rapid transition in Figure 12 as the void fraction front is propagated across the cell edge. When finally the motion of void fraction is adequately modelled, we can now observe the small increase in mixture void fraction (Figure 14) and decrease in bubble rise velocity (Figure 13) when the flow is counter-current.

5. Conclusions

Based on our experience with TRAC codes, we think that pressures, void fractions and velocities must be carefully considered when judging the results of benchmark problems. These variables are especially important during down flow in testing safety codes. To demonstrate this approach, we designed a test problem which simulated a moving void fraction front in a vertical tube. We then compared the performance of current versions of CATHARE, RELAP5, TRAC-BF1 and TRAC-PF1. Our test results indicate that CATHARE is the best performing of the current releases of these reactor safety codes. The results of RELAP5 and TRAC-PF1 has shown some peculiar pressure and void fraction behavior. Based on the results presented, we have concluded that TRAC-

BF1 is the worst performing code in our moving mixture level test. We have further demonstrated that relatively simple corrections can make radical improvements in even the worst performing code. After corrected, the level tracking has helped TRAC-BF1 to produce the most accurate results for our moving mixture level test problem.

We only considered the mixture levels moving with constant velocity in our test problem. We recognize that the detailed strategy presented here does not function nearly as well when strong accelerations are present. Current research is addressing this issue.

Nomenclature

P	Pressure
P_{hydro}	Hydrostatic pressure between the void fraction front and the cell bottom edge
$F_{\ell g}$	Interfacial drag at the phase interface
V	Phasic velocity
α	Void fraction
ρ	Density
g	Gravity vector
Δz	Cell length
Subscripts	
ℓ	Liquid phase
g	Gas phase
j	Cell center index
j+1/2	Index for the cell edge in positive flow direction
j-1/2	Index for the cell edge in negative flow direction
Superscripts	
+	Fluid region above the void fraction front
-	Fluid region below the void fraction front

References

1. K.H. Chu, J.G.M. Andersen, Y.K. Cheung, J.C. Shaug, "BWR Full Integral Simulation Test (FIST) Program TRAC-BWR Model Development.", **Vol 2** , NUREG/CR-4127

2. B.D.Boyer, J.W. Hartzel, S. Lider, G.E. Robinson and A.J. Baratta, "Modeling Condensation Steam Quenching Effects in an MSIV Closure Transient Using RETRAN-02-MOD002 With And Without Nonequilibrium Pressurizer Model Option And TRAC-BF1", *Nuclear Technology*, **102**, 206 (August 1993)

3. Y. Abe, H. Akimoto, H. Kamo and Y. Murao, "Elimination of Numerical Pressure Spikes Induced by Two-Fluid Model", *Journal of Nuclear Science and Technology*, **30** (December 1993)

4. R.J. Pryor, D.R. Liles and J.H. Mahaffy, *Trans. Amer. Nuclear Soc.* **30** (1978)

5. A.J. Chorin, "Flame Advection and Propagation Algorithms", *Journal of Computational Physics* **35** (1980)

6. J.M. Hyman, "Numerical Methods for Tracking Interfaces", *Physica* **12D**

7. C.W. Hirt and B.D. Nichols, "Volume of Fluid (VOF) Method for the Dynamics of Free Boundaries", *Journal of Computational Physics* **30**, (1981)

8. D. Taylor, *Improvements to GE Level Tracking Model for 3-D Components*, EG&G Idaho, Inc. Internal Technical Report, WR-NSMD-83-007

9. J.A. Borkowski, N.L. Wade, S.Z. Rouhani, R.W. Shumway, W.L. Weaver, W.H. Rettig, C.L. Kullberg, "TRAC-BF1/MOD1 Models and Correlations", **Vol 3**, *NUREG*/CR-4391 (August 1992)

10. B. Aktas, "Improvements to the Two-Phase Water Level Tracking Model of A Transient Reactor Analysis Code", *M.S. Thesis Submitted to The Pennsylvania State University*, August 1994

7th International Meeting On Nuclear Reactor Thermal-hydraulics
NURETH-7
Saratoga Springs, NY USA -Sept 10-15, 1995

THE SENSITIVITY ANALYSIS BY ADJOINT METHOD FOR THE UNCERTAINTY EVALUATION OF THE CATHARE 2 CODE

F. Barré, A. de Crécy, C. Perret
French Atomic Energy Commission (CEA)
85X 38041 Grenoble Cedex, France
Tel : (33) 76 88 49 04, Fax : (33) 76 88 51 77

SUMMARY

This paper presents the application of the DASM (Discrete Adjoint Sensitivity Method) to CATHARE 2 thermal- hydraulics code.

In a first part, the basis of this method is presented. The mathematical model of the CATHARE 2 code is based on the two fluid six equation model. It is discretized using implicit time discretization and it is relatively easy to implement this method in the code. The DASM is the ASM directly applied to the algebraic system of the discretized code equations which has been demonstrated to be the only solution of the mathematical model. The ASM is an integral part of the new version 1.4 of CATHARE. It acts as a post-processing module. It has been qualified by comparison with the "brute force" technique.

In a second part, an application of the DASM in CATHARE 2 is presented. It deals with the determination of the uncertainties of the constitutive relationships, which is a compulsory step for calculating the final uncertainty of a given response.
First, the general principles of the method are explained: the constitutive relationships are represented by several parameters and the aim is to calculate the variance-covariance matrix of these parameters. The experimental results of the separate effect tests used to establish the correlation are considered. The variance of the corresponding results calculated by CATHARE are estimated by comparing experiment and calculation. A DASM calculation is carried out to provide the derivatives of the responses. The final covariance matrix is obtained by combination of the variance of the responses and those derivatives.
Then, the application of this method to a simple case - the blowdown Canon experiment - is presented. This application has been successfully performed.

In short, this paper can be seen as an interesting contribution to the general problem of uncertainty analysis.

INTRODUCTION

CATHARE is the safety code developed by EdF (the French utility), Framatome (the French vendor) and the safety authority (CEA-IPSN). It is based on a six-equation two-fluid model with 4 additional equations for non-condensable gases [1]. Additional equations can also be used for transportation of boron and activity. Additional models are present in the code to take into account thermal conduction in the heat structures, mechanics in the fuel pins, neutronics and reflooding. Several hy-

draulical models are available:
*A one-dimensional model, with fully implicit time discretization
*A three-dimensional model, with a multistep method for time discretization, ensuring implicit behaviour
*A tee model, boundary conditions, source, sinks, pump model and various components useful to describe an industrial device

The coupling between thermal-hydraulics models and heat structures is implicit.

The code is used for safety analysis, accident management, definition of plant operating procedure and research and development. It is also used to quantify the conservative analysis margin and for licensing by EdF. This last point led EdF and IPSN to develop rules and methodology for the application of best estimate codes. One of the major points is to develop tools for uncertainty analysis.

The aim of this paper is to present, in a first part, a powerful tool for uncertainty analysis: the discrete adjoint sensitivity method (DASM), which provides an economical answer - in terms of CPU time and man hours - to the following question: *how sensitive is the response of a code to any parameter?* The origins of this method are the works of Oblow [2] and Parks [3] about the adjoint sensitivity method (ASM). Its application to a code, where the equations are discretized, has been developed by Ounsy and al.[4]. It has been implemented in the new version of Cathare 2.

In a second part, an application of the DASM is presented: it permits to calculate the range of variation of the constitutive relationships of the code. The general methodology is defined and is then applied to a simple case: the uncertainty of the interfacial friction from the results of the Vertical Canon experiment [5].

To sum up, the purpose of this paper, unlike the CSAU [6 and 7] for example, is not the definition of a general methodology for the uncertainty analysis. It only presents an important contribution to such an analysis. Problems like the combination of the individual uncertainties or the uncertainties due to the scaling effect are not considered.

PART 1: PRESENTATION AND QUALIFICATION OF THE DASM METHOD FOR THE CATHARE 2 CODE

1.1. The ASM method

1.1.1 . The problem to be solved

The problem to be solved is an engineering problem. It can be formulated in the following way. Let **R** be a response of the code; it can be, for instance, a physical quantity (as mass inventory, cladding temperature, break flow rate, heat flux, etc.) or the timing of an event, etc .
Let ε_k be any parameter of the code: physical quantity (pressure, temperature, etc.), steam-water physical properties, constitutive relationships (interfacial friction, wall friction, mass and energy transfer between phases, etc.), initial or boundary conditions, etc.

The first question to answer is: what will be the change $\delta\mathbf{R}$ of the response **R**, due to a modification $\delta\varepsilon_k$ of the parameter ε_k? It needs to be able to calculate the sensitivity profile:

$\frac{\varepsilon_k}{R} \cdot \frac{dR}{d\varepsilon_k}$ which is the percentage of change of the response **R** for one percent of change of the parameter ε_k.

The second question is to determine the uncertainty $\Delta\mathbf{R}$ on $\mathbf{R}$.

The initial physical problem (i.e. the set of equations resolved in the **CATHARE** code) is modelized by a partial differential system: $A(X_\varepsilon,\varepsilon)=0$, where X_ε is the solution of the equation, $\varepsilon=(\varepsilon_1,\varepsilon_2,...\varepsilon_d)$ is the parameter vector and **A** is a **non-linear function** of both X and ε. In this paper, it is called the "direct" problem. A response of the code is a real function **R** which could be considered as a function of the vector of parameters ε: $\mathbf{R}(\varepsilon)=F(X_\varepsilon)$. The sensitivity evaluation consists in calculating the derivatives of **R**:

$$D_\varepsilon \cdot R(\varepsilon) = [\frac{dR}{d\varepsilon_1}, ..., \frac{dR}{d\varepsilon_d}] \qquad (1)$$

Several methods are used to calculate this derivative vector.

1.1.2 . The brute force.

The most commonly used and easiest method is the one referred to as "brute force". To evaluate the sensitivity of **R** with respect to the parameter ε_k, one calculation is performed using the standard set of parameters $\varepsilon=(\varepsilon_1,\varepsilon_2,...,\varepsilon_k,...,\varepsilon_d)$, and one calculation with $\varepsilon=(\varepsilon_1,\varepsilon_2,...,\varepsilon_k+\Delta\varepsilon_k,...,\varepsilon_d)$.The derivatives are numerically evaluated:

$$\frac{dR}{d\varepsilon_k} = \frac{R(X_{\varepsilon+\Delta\varepsilon_k}) - R(X_\varepsilon)}{\Delta\varepsilon_k} \quad (2)$$

The advantage of this method is that the sensitivity of the code is obtained. The drawbacks are that one CATHARE computation is needed for each $\varepsilon_1,\varepsilon_2,...\varepsilon_d$ parameter. This results in a heavy computing cost for reactor computation dealing with a large range of parameters. Another drawback is the difficulty to choose appropriate $\Delta\varepsilon_k$ increments.

This method will be used in this study to qualify the ASM.

1.1.3 . The direct sensitivity method.

Another method, which is often used, is the direct sensitivity method, which consists in resolving the derived equations of the initial system:

$$\frac{dA}{dX}\cdot\frac{dX}{d\varepsilon_k} = -\frac{dA}{d\varepsilon_k} \quad (3)$$

The main drawback is that the computation time of each derivative is of the same order of magnitude as the computation time for the solution.

1.1.4 . The adjoint sensitivity method.

The proposed method is the Adjoint Sensitivity Method (ASM).

If (X,ε) is a solution of the system, another solution around (X,ε) is $(X+\Delta X,\varepsilon+\Delta\varepsilon)$. At the first order,

$$D_X A(X,\varepsilon)\Delta X + D_\varepsilon A(X,\varepsilon)\Delta\varepsilon + O^2(I\Delta\varepsilon) = 0 \quad (4)$$

where D_X and D_ε are differential operators. The change of the response R of the code, due to the change in ε parameter vector can be evaluated:

$$\Delta R = \langle \nabla_X F(X) | \Delta X \rangle + O^2(I\Delta\varepsilon) \quad (5)$$

The sensitivity profile vector can be written: $D_\varepsilon R(\varepsilon) = \langle \nabla_X F | D_\varepsilon X \rangle$ (6)

As, $D_\varepsilon X = -D_X^{-1}(X_\varepsilon, \varepsilon) \cdot D_\varepsilon A(X,\varepsilon)$ (7), then, it can be written:

$$D_\varepsilon R(\varepsilon) = \langle {}^t\left(-D_X^{-1}(X_\varepsilon,\varepsilon)\right) \bullet \nabla_X F | D_\varepsilon A(X,\varepsilon) \rangle \quad (8)$$

$$D_\varepsilon R(\varepsilon) = \langle {}^t\Phi | D_\varepsilon A(X,\varepsilon) \rangle \quad (9)$$

where ${}^t\Phi$ is the adjoint vector, which is the solution of the adjoint equation:

$${}^t(-D_X A(X,\varepsilon)) \cdot {}^t\Phi = \nabla_X F(X) \quad (10)$$

The advantage of this method is that only one linear adjoint equation for each response **R** is needed after calculation of one direct problem. In addition, it is very easy to introduce new parameters ε_k. There are two methods for applying the ASM.

The first one, the Continuous Adjoint Sensitivity Method (**CASM**) (Figure 1), involves writing the adjoint system of the initial direct problem and then discretizing it. In this way, two problems arise: the first one is how to choose the boundary conditions of the adjoint problem and the second one is how to be sure that the discretization of the adjoint problem is consistent with the discretization of the direct problem. The sensitivity calculated using this method is not the sensitivity of the initial code.

The second method, the Discrete Adjoint Sensitivity Method (**DASM**) (Figure 2), is to derive the adjoint problem from the discretized direct problem. From a mathematical point of view, Ounsy and al. [4] have demonstrated that this approach is correct and that the calculated sensitivity is really the sensitivity of the initial code.

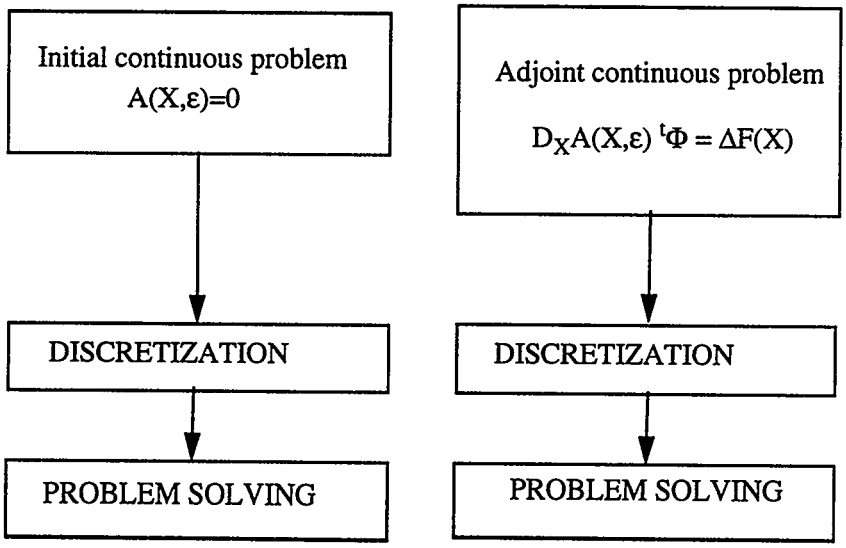


FIGURE 1
CONTINUOUS ADJOINT SENSITIVITY METHOD

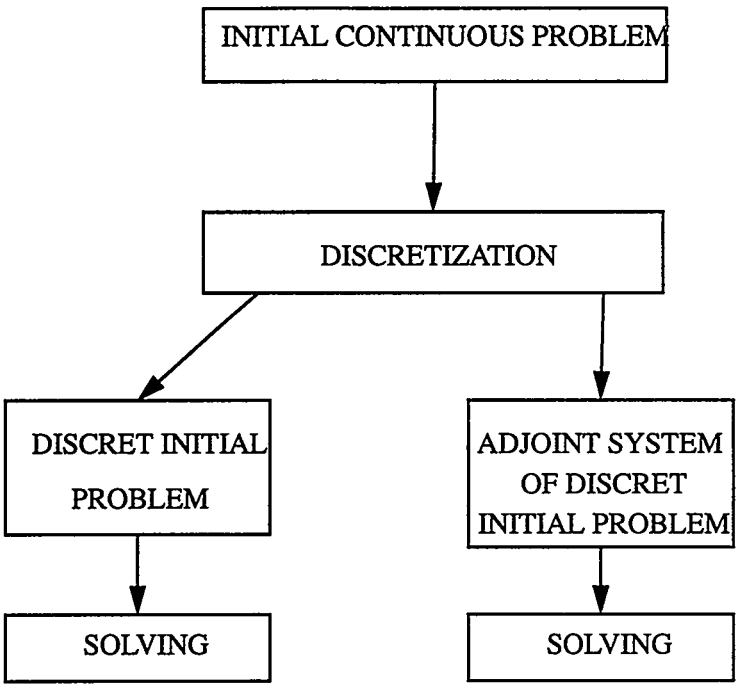


FIGURE 2
DISCRETE ADJOINT SENSITIVITY METHOD

1.2. Implementation of the DASM in the Cathare 2 code.

1.2.1 . Method of implementation

As a physical problem is computed with the CATHARE code, the system of equations is resolved at each time step.
first time step: $A^0(X_\varepsilon^0,\varepsilon) = 0$ (11)

n-th time step: $A^n(X_\varepsilon^{n-1},X_\varepsilon^n, \varepsilon) = 0$, for n=1,N (12)

To simplify the notation in this section, $\frac{\partial A}{\partial X} = D_X A$ and $\frac{\partial R}{\partial X} = \nabla_X F(X)$.

Each time step is resolved, using a Newton-Raphson method, as the system is non-linear. As the discretization is fully- or nearly- implicit, a Jacobian matrix has to be calculated at each iteration, p, of a given time-step to evaluate X_ε^n from X_ε^{n-1}:

$$A^{n,p} = A^{n,p-1} + \left(\frac{\partial A}{\partial X}\right)^{n,p-1} \cdot \left(X^{n,p} - X^{n,p-1}\right) = O \quad (13) \text{ for } p>1 \text{ and } X^{n,1}=X^{n-1}$$

$\left(\frac{\partial A}{\partial X}\right)^{n,p-1}$ is the Jacobian matrix, re-evaluated at each iteration p of the n-th time step.

The time step has converged when $X^{n,p} - X^{n,p-1}$ is small enough and the converged values of

the main variables are $X^n = X^{n,p}$. This implicit behaviour of the CATHARE code makes implementation of the DASM very easy. For a given response **R**, the adjoint system can be written (where the left matrix is the transposition of the matrix of the initial direct system):

$$\begin{bmatrix} {}^t\left(\frac{\partial A^0}{\partial X^0}\right) & {}^t\left(\frac{\partial A^1}{\partial X^0}\right) & 0 & \dots & \dots & 0 & 0 \\ 0 & {}^t\left(\frac{\partial A^1}{\partial X^1}\right) & {}^t\left(\frac{\partial A^2}{\partial X^1}\right) & \dots & \dots & 0 & 0 \\ \dots & \dots & \dots & \dots & \dots & \dots & \dots \\ 0 & 0 & 0 & \dots & \dots & {}^t\left(\frac{\partial A^{N-1}}{\partial X^{N-1}}\right) & {}^t\left(\frac{\partial A^N}{\partial X^{N-1}}\right) \\ 0 & 0 & 0 & \dots & \dots & 0 & {}^t\left(\frac{\partial A^N}{\partial X^N}\right) \end{bmatrix} \begin{bmatrix} \Phi^0 \\ \Phi^1 \\ \dots \\ \Phi^{N-1} \\ \Phi^N \end{bmatrix} = \begin{bmatrix} -\frac{\partial R}{\partial X^0} \\ -\frac{\partial R}{\partial X^1} \\ \dots \\ -\frac{\partial R}{\partial X^{N-1}} \\ -\frac{\partial R}{\partial X^N} \end{bmatrix} \quad (14)$$

To resolve this system, it is necessary to start at the last time step and to go up to the first time step, as can be seen on the equation (14).

Initial condition (last time step of the direct calculation): $${}^t\left(\frac{\partial A^N}{\partial X^N}\right) \cdot \Phi^N = -\frac{\partial R}{\partial X^N} \quad (15)$$

n-th time-step: $${}^t\left(\frac{\partial A^n}{\partial X^n}\right) \cdot \Phi^n = -\frac{\partial R}{\partial X^n} - \left({}^t\left(\frac{\partial A^{n+1}}{\partial X^n}\right) \cdot \Phi^{n+1}\right) \quad (16)$$

It is apparent that in the adjoint system, derivatives with respect to explicit variables are necessary. As in CATHARE discretization is fully or nearly implicit, the additional calculations needed to write the explicit Jacobian matrix is reduced.

Another interesting point is that the equation (16) is linear and then very cheap in cpu cost.

The sensitivity calculation is therefore performed in the code in three stages:

1) CATHARE computation: only one computation for the sensitivity study where the Jacobian matrix and the main variables of the calculation have to be saved: $\frac{\partial A^n}{\partial X^n}(X_\varepsilon^{n-1}, X_\varepsilon^n, \varepsilon), X_\varepsilon^n$

2) Resolution of one LINEAR adjoint equation for a given response **R** :

* Computation of the derivatives of R : $\frac{\partial R}{\partial X^n}$

* Computation of the derivatives with respect to the explicit variables of the direct code: ${}^t\frac{\partial A^{n+1}}{\partial X^n}$

* Computation of the Equation (16), then storage of the adjoint flux Φ.

3) For each parameter ε_k, computation of the sensitivity profile: $\frac{dR}{d\varepsilon_k} = \langle \Phi | \frac{\partial A}{\partial \varepsilon_k} \rangle$ (17), which is only a simple vector product.

This sequence of calculation is summarized in figure 3. Thus, for each sensitivity study, one direct CATHARE calculation is needed, one CATHARE adjoint calculation is needed for every response R, and only one vector product per ε_k parameter.

1.2.2 . Implementation in the CATHARE 2 code.

In the new version of CATHARE 2 (version 1.4), the adjoint calculation has been implemented. For each hydraulical module (1-D,volume,Tee and boundary conditions), the heat conduction module and the fuel thermo-mechanical module, it is possible to perform an adjoint calculation. For the reflooding module and the 3D module development is still underway.

The adjoint modules use, from a coding point of view, all the elementary subroutines of the CATHARE code. Then it ensures that exactly the same equations, the same discretization, the same physics are used for the adjoint calculation. Additionnal subroutines have been added to calculate the derivatives of the terms which are explicit in the direct code and the derivatives of the response.

When a CATHARE 2 calculation is performed, the sensitivity calculations are used as a **post-processing module**.

1.3. Qualification of the DASM in the Cathare 2 code.

1.3.1 . Method of qualification

The method of qualification of the DASM is to compute a large number of analytical tests with CATHARE 2 and to compare the results of DASM with the brute force technique. This work has been started using the qualification matrix of CATHARE 2 and the first results indicate that for very simple sensitivity studies the results of both methods must be exactly the same. To reach this quality of results, considerable attention has been paid to the debugging process. This was also of considerable value for the CATHARE code itself because some errors were found.

Two examples of calculations are presented here: a very simple CANON experiment [5] and a more complex blowdown experiment in a reactor Large Break LOCA condition (OMEGA EXPERIMENT) [5].

1.3.2 . Adiabatic blowdown.

The Vertical Canon blowdown tests were conducted in Grenoble. The test section consists of a vertical straight pipe of 0.100 m inner diameter. The total length is 4.483 m. The void fraction is measured at several elevations. The bottom end of the test section is closed. The upper head is surmounted by a 7 degree converging nozzle. The nozzle is followed by a 4mm long straight pipe with the desired break inside diameter and the rupture disc. The pipe is initially pressurized at 13.3MPa. The top break is open and the fluid depressurizes very quickly. This experiment is very suitable for qualifying momentum and heat exchange between phases.

A CATHARE calculation is performed for a test with a 5mm break. The sensitivity of three responses to different parameters is evaluated with the DASM and with the brute force technique.

1.3.2.1 First response: mass inventory at the end of the experiment.

The chosen parameters are: initial pressure and temperature, interfacial friction and energy transfer between liquid and interface.

The results are on table 1 and show a good agreement between both methods.

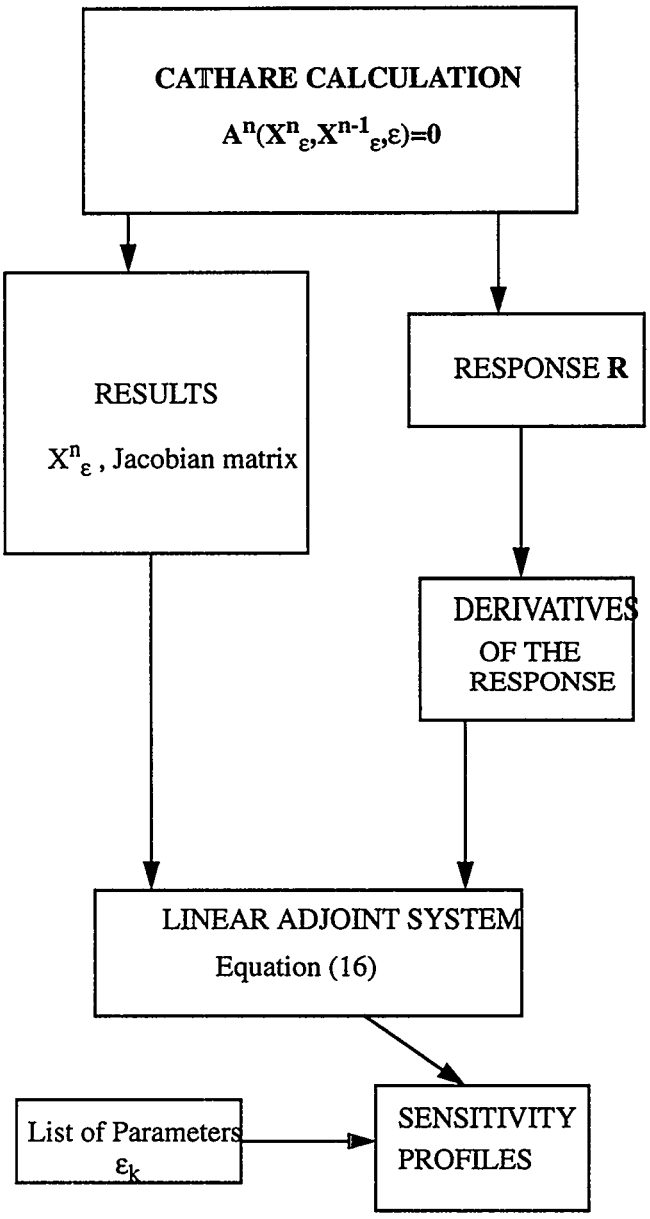


FIGURE 3
METHOD OF SENSITIVITY CALCULATION IN THE CATHARE 2 CODE

PARAMETERS ε_k	$dR/d\varepsilon_k$	ΔR (DASM)	ΔR (brute force)	Sensitivity profile %
initial temperature	$-1.07\ 10^{-5}$	-1.943	-1.953	-2.242
Initial pressure	$2.567\ 10^{-8}$	$2.567\ 10^{-2}$	$2.578\ 10^{-2}$	0.032
Interfacial friction	-1.475	-0.148	-0.149	-0.137
energy transfer between liquid and interface	-4.310^{-2}	-0.004	-0.005	-0.004

Table 1: Comparison between DASM and brute force in a blowdown calculation. Sensitivity of the final mass inventory for one percent of change of the parameters.

1.3.2.2 Second response: maximum break flow rate during the transient

The chosen parameters are those of the previous test: initial pressure and temperature, interfacial friction and energy transfer between liquid and interface.

The results are on table 2 and show good agreement between both methods.

PARAMETERS ε_k	$dR/d\varepsilon_k$	ΔR (DASM)	ΔR (brute force)	Sensitivity profile %
initial temperature	$-1.07\ 10^{-5}$	-1.07	-1.07	-1.291
Initial pressure	$6.36\ 10^{-7}$	0.636	0.629	0.824
Interfacial friction	$-2.127\ 10^{-5}$	-0.002	-0.002	$2.027\ 10^{-5}$
energy transfer between liquid and interface	-0.452	-0.045	-0.041	-0.044

Table 2: Comparison between DASM and brute force in a blowdown calculation.Sensitivity of the maximum break flow rate for one percent of change of the parameters.

1.3.2.3 Third response: wall temperature

The chosen parameters are those of the previous test: energy transfer between liquid and interface and wall material specific mass.

The results are on table 3 and show good agreement between both methods.

PARAMETERS ε_k	$dR/d\varepsilon_k$	ΔR (DASM)	ΔR (brute force)	Sensitivity profile %
Energy transfer between liquid and interface	2.44	0.25	0.25	0.75
Wall material specific mass	25.6	2.7	2.7	1.68

Table 3: Comparison between DASM and brute force in a blowdown calculation.Sensitivity of the maximum break flow rate for one percent of change of the parameters.

1.3.3 . Blowdown in a heated pipe.

The OMEGA bundle test section consists of a rod bundle connected upstream and downstream to spherical plena. The connection pipes support spool pieces. The rod bundle simulates a reactor core. It consists of 36 rods arranged in a 6x6 array on a 12.6mm square pitch with a 3.656m heated length. The thickness of the rods varies in order to obtain a cosine axial heat flux with a peak factor of 1.34. Two spherical plena simulate the primary circuit water volume, respectively downstream and upstream from the core. Break nozzles can be connected either to one of the spheres or to both, in order to simulate small or large break LOCA.

A test representative of a double ended break was chosen in order to analyse the peak cladding temperature due to flow stagnation during the blowdown phase of a large break LOCA.

The chosen response is the maximum cladding temperature. The parameters are: the forced liquid convection heat transfer, the nucleate boiling heat transfer, the interfacial friction, the energy transfer between liquid and interface, the wall conductibility and the power generated in the wall.

PARAMETERS ε_k	$dR/d\varepsilon_k$	ΔR (DASM)	ΔR (brute force)	Sensitivity profile %
forced liquid convection heat transfer	-5.72	-0.572	-0.582	-0.015
the nucleate boiling heat transfer	2.16	0.216	0.221	0.006
the interfacial friction	88.	8.8	8.8	0.231
energy transfer between liquid and interface	-24.4	-2.44	-2.45	0.064
wall conductibility-mass	51.23	5.12	5.14	0.135

Table 4: Comparison between DASM and brute force in a blowdown calculation.Sensitivity of the maximum break flow rate for one percent of change of the parameters.

PART 2: AN APPLICATION OF THE DASM IN THE CATHARE 2 CODE: THE CALCULATION OF THE UNCERTAINTIES OF THE CONSTITUTIVE RELATIONSHIPS.

2.1. Presentation of the method.

2.1.1 . Introduction : sensitive parameters and relevant parameters

The DASM provides the derivatives of the responses with respect to the parameters. The most natural idea is to compare, for a given response R, the different derivatives with respect to the ε_k parameters, i.e. $dR/d\varepsilon_k$. The largest derivatives would correspond with the most *sensitive* parameters, for the considered response. Nevertheless, this information is not very interesting. In fact, there is an immediate problem of units: there is no sense in comparing derivatives if the parameters are expressed in different units.

Moreover, the notion of *relevant* parameters is more interesting than that of *sensitive* parameters. At the first order, the relevant parameters are those corresponding to the largest values of the square of the product $(dR/d\varepsilon_k)\times \delta\varepsilon_k$, where $dR/d\varepsilon_k$ is given by the DASM and where $\delta\varepsilon_k$ is the range of the ε_k parameter. This approach is theoretically limited to small ranges $\delta\varepsilon_k$, where the first order approximation is valid. Nevertheless its use for larger ranges gives interesting results, as shown below.

So the *relevant* parameters are those having the greatest influence on the response. They are the ones selected to set up the calculational test matrix leading to the calculation of the response surface in a methodology like the CSAU one [6 and 7]. But in this methodology or in others [8 and 9], the determination of the *relevant* parameters - the ranking of the parameters, in other words - comes from expert judgement. In this paper, this notion has a mathematical definition.

However using this notion involves knowing the $\delta\varepsilon_k$ range of the parameters. Its knowledge is also useful for determining the variations to be given to the parameters when establishing the calculational test matrix.

2.1.2 . Purpose of the study

Knowing the range of parameters is fairly easy for parameters which describe the conditions of the plant (such as initial power or geometrical data) or for parameters describing thermophysical data (such as thermal conductivity of UO_2). It is more difficult for parameters relative to the constitutive relationships.

This is the purpose of this part of the paper. A methodology was developed, which calculates the variance-covariance matrix of the parameters relative to the constitutive relationships of the code (chapter 2.1). As shown below, this methodology needs the results of the DASM.

The methodology is general: theoretically, it can be applied to all the constitutive relationships of the code. But, in this paper, it is only applied to a simple case (chapter 2.2): the relevant parameters of the Vertical Canon experiment. It is proved that the methodology works in this case. Its extension to other parameters and other experiments is planed in the future, as explained in chapter 2.3.

2.1.3 . Overview of the methodology for determining the uncertainties of the constitutive relationships

To this end, the results of the Separate Effects Tests (SET) useful for establishing or assessing these constitutive relationships are used, as well as their experimental uncertainties. The corresponding results calculated by the code are also used, and denoted R_i.

The general idea is to calculate the variance-covariance matrix of the parameters relative to the constitutive relationships from an estimation of the variance of the R_i responses. The following equation (19), written for one response and valid at the first order, is used:

$$\mathrm{var}\left(R_i\right) = \frac{{}^t dR_i}{d\varepsilon} \times C_\varepsilon \times \frac{dR_i}{d\varepsilon} \quad (19)$$

where, supposing there are d parameters:

- $\mathrm{var}(R_i)$ is the variance of the R_i response. Only an estimation of it, denoted $\widehat{\mathrm{var}}\left(R_i\right)$ can be obtained. This estimation is a combination of the experimental uncertainty and of the code-experiment difference.
- C_ε is the variance-covariance matrix of the parameters. It is unknown. More precisely, it is a d×d symmetrical matrix, so there are d(d+1)/2 unknowns.
- $\frac{{}^t dR_i}{d\varepsilon} = \left(\frac{dR_i}{d\varepsilon_1}, \frac{dR_i}{d\varepsilon_2}, \ldots \frac{dR_i}{d\varepsilon_d}\right)$ is the transposed d-dimension vector of the d derivatives of the response R_i with respect to the d parameters. It is given by a DASM calculation of the SET facility. Equation (19) is the basis for the calculation of the variance-covariance matrix of the parameters. The rest of the study only deals with its use and the necessary developments.

Consider now the set of responses of a SET facility, or even of several SET facilities treated together. The minimum of the following sum S (equation (20)) with respect to the terms of C_ε (the unknowns) has to be found:

$$S = \sum_{i=1}^{n} \left(\widehat{\mathrm{var}}\left(R_i\right) - \frac{{}^t dR_i}{d\varepsilon} \times C_\varepsilon \times \frac{dR_i}{d\varepsilon} \right)^2 \quad (20)$$

where n is the number of considered responses.

A linear system of d(d+1)/2 equations in d(d+1)/2 unknowns is obtained. Its solution amounts to the inversion of a matrix, called inertia matrix . If this one can be inverted, which is generally the case, the problem has a single solution. The main issue is to know if this solution is satisfactory. For that, two conditions are obviously compulsory. The condition number of the inertia matrix (i.e. the ratio of the highest eigenvalue to the lowest one) must be not too high. And the solution matrix C_ε must be a variance-covariance matrix, i.e. with greater than or equal to 0 eigenvalues. Other conditions must be met. They will be explained later.

Having established the overall principles of the methodology, its application was checked in a simple case.

2.2. Calculation of the uncertainties of the constitutive relationships: application in a simple case

2.2.1 . Framework of the application

- Only one experiment, namely Vertical Canon [5], is considered. Four tests are considered for the application (table 5). This program was conducted to establish the constitutive relationship of the interfacial friction in a pipe, in slug-bubble flow, denoted in this paper as τ_i. So it is - a priori - a

relevant parameter (expert judgement).

n° test	break diameter (mm)	initial pressure (MPa)	initial temperature (°C)
27	3	10.8	300
22	5	5.7	232
23	5	14.9	320
24	5	13.4	300

table 5: list and main features of the Vertical Canon tests used

• A large number of responses R_i was chosen. They must meet the following criteria:

- the responses must be sensitive to interfacial friction: the remaining masses and the void fractions were selected.

- the responses must be independent. That is to say they have derivatives with respect to the interfacial friction which are significantly different. For example, two remaining masses at two close times can not be selected together.

- the responses must all represent the different ranges of pressures and void fractions in a similar manner. For example, the fact that a remaining mass, taken at a time *t*, integrates the effects of the pressures between the beginning until the time *t*, must be taken into account.

A total of 34 responses for the 4 tests is thus obtained: 17 remaining masses at different times and 17 void fractions at different times and elevations.

• At the beginning, a large number of parameters is considered. As described in paragraph 2.2.3, only the relevant parameters will be considered later for the calculation of matrix C_ε: an algorithm was developed for selecting them mathematically. Among the starting parameters, the following ones can be found:

- wall-fluid heat exchange coefficients
- liquid-interface heat exchange coefficients
- vapour-interface heat exchange coefficients
- thermal conductivity and heat capacity of the wall material
- wall-liquid and vapour friction
- interfacial friction (bubbly, slug ang churn flows)

.....

In fact, two parameters were defined for interfacial friction τ_i. The general form of τ_i is [10]:

$$\tau_i = \frac{K_l\rho_l + K_g\rho_g}{L}\alpha(1-\alpha)^{3,6}\left(V_l - V_g\right)^2$$

where K_g being multiplied by the ρ_g gas density takes into account the pressure effect.
Both paremeters ε_1 and ε_2 are defined as follows:

$$\tau_i = \varepsilon_1\frac{K_l\rho_l + \varepsilon_2 K_g\rho_g}{L}\alpha(1-\alpha)^{3,6}\left(V_l - V_g\right)^2$$

ε_1 is a multiplicative parameter of τ_i. Its nominal value is 1. Its variance and thus its stan-

dard deviation will be calculated. By misuse, ε_1 is denoted as τ_i.

ε_2 is introduced to take into account the eventual pressure effect. Its nominal value is also 1. By misuse, ε_2 is denoted as $P\tau_i$.

The combination of the variances of ε_1 and ε_2 will permit to calculate the variance of τ_i, depending on the hydraulic variables.

The other correlations are only represented by one multiplicative parameter, like ε_1 for τ_i.

• The study carried out with this test case consists of two parts:

i) systematic selection of the relevant parameters. It leads to several possible sets of relevant parameters, the corresponding matrix C_ε being calculated at each time. This step is not compulsory, but has the advantage of making sure that none of the relevant parameters included in the code are forgotten.

ii) setting up of criteria for estimating the quality of the different C_ε matrices found in i). This is the answer to the issue raised at the end of paragraph 2.1.3 (a solution is always possible but it must be also correct). Finally, the parameters corresponding to the best C_ε matrix are selected.

All in all, the C_ε matrix of the relevant parameters of Vertical Canon is established with sufficient reliability.

2.2.2 . Estimation of the variance of each response $\widehat{var}\left(R_i\right)$

This step is necessary before each calculation of the C_ε matrix.

• For each response R_i, the estimation of its variance can be written as follows: $\widehat{var}\left(R_i\right) = \widehat{var}\left(R_{i,\,code} - R_{i,\,true}\right)$

$R_{i,true}$ being the true response, that the user tries to measure (experiment) or calculate (code). It is unknown but it is not a random variable.

Assuming that the two amounts $(R_{i,code}\text{-}R_{i,measured})$ and $(R_{i,measured}\text{-}R_{i,true})$ are two independent random variables, the equation (21) is obtained:

$$\widehat{var}\left(R_i\right) = \widehat{var}\left(R_{i,\,code} - R_{i,\,measured}\right) + \widehat{var}\left(R_{i,\,measured} - R_{i,\,true}\right) \qquad (21)$$

• The estimation of the variance of $(R_{i,code}\text{-}R_{i,measured})$ depends on the quality of the results of the code with respect to the results of the experiment. Only one variance is considered for each type of response (remaining mass or void fraction), which is written, for example for any remaining mass:

$$\widehat{var}\left(Mr_{i,\,code} - Mr_{i,\,measured}\right) = \sum_{i=1}^{n_{Mr}} \frac{\left(Mr_{i,\,code} - Mr_{i,\,measured}\right)^2}{n_{Mr}} \qquad (22)$$

n_{Mr} being the number of remaining mass type responses.

• The estimation of the variance of $(R_{i,measured}\text{-}R_{i,true})$ depends on the quality of the measurements of the experiment and is given in [5].

• Finally the variances have to be normalized depending on whether they are relative to a remaining mass or a void fraction. Weights w_i are introduced in sum S (defined in (20)) as follows:

$$S = \sum_{i=1}^{n} \left[\frac{1}{w_i} \times \left(\widehat{var}\left(R_i\right) - \frac{{}^{t}dR_i}{d\varepsilon} \times C_\varepsilon \times \frac{dR_i}{d\varepsilon} \right) \right]^2 \quad (23)$$

n being the total number of responses (remaining masses and void fractions)

There are two kinds of weights, depending on whether they are relative to a remaining mass or a void fraction. For example, for the remaining mass type R_i responses, all the weights are equal

$$\text{to : } w_i = \frac{\sum_{i=1}^{n_{Mr}} \widehat{var}\left(R_i\right)}{n_{Mr}}$$

n_{Mr} being the number of remaining mass type responses.

2.2.3 . Systematic research of relevant parameters

2.2.3.1 . The principle

As pointed out in paragraph 2.1.1, a parameter ε_k is relevant with respect to a response R_i if the square of the product $(dR_i/d\varepsilon_k)\times \sigma_{\varepsilon k}$ is high, in comparison to the other parameters.

For the set of responses, the number R^2 lying between 0 and 1, and referred to as the square of the total correlation coefficient, is defined as follows:

$$R^2 = 1 - \frac{S}{\sum_{i=1}^{n} \widehat{var}\left(R_i\right)^2} \quad (24)$$

S is the sum to minimize defined in (20) and depends on the calculated matrix C_ε, and so on the considered parameters. In S, the squares of the products $(dR_i/d\varepsilon_k)\times \sigma_{\varepsilon k}$ arise. S is all the closer to 0 (and R^2 close to 1) because the latter are high. Consequently, having R^2 close to 1 means that the considered parameters are relevant.

On that basis, the following process is proposed. It is taken from the stepwise regression .

- The parameters are considered one by one:

For each parameter, matrix C_ε is calculated. It is reduced to the scalar $var(\varepsilon_k)$. A first set E_1 of parameters having the highest numbers R^2 is selected.

- The parameters are considered two by two, being limited to the pairs of $E_1 \times E_1$: the C_ε matrix relative to two parameters ε_k and ε_l takes the form: $\begin{bmatrix} var\left(\varepsilon_k\right) & cov\left(\varepsilon_k, \varepsilon_l\right) \\ cov\left(\varepsilon_k, \varepsilon_l\right) & var\left(\varepsilon_l\right) \end{bmatrix}$ $cov(\varepsilon_k, \varepsilon_l)$ being the covariance of the parameters ε_k and ε_l. A subset E_2 of $E_1 \times E_1$ is selected. It contains the pairs of $E_1 \times E_1$ for which the gain in R^2 is significant with respect to the maximum R^2 of E_1.

- the triplets of $E_2 \times E_1$ are tested in the same way. The process is continued until there is no more significant gain in R^2 .

2.2.3.2 . Application to Vertical Canon

• Considering the parameters one by one, the results below (table 6) are obtained. They are classified by descending order of R^2 .The other parameters present less than 0.20 coefficients R^2. The two apparently most relevant parameters are both relative to interfacial friction, which confirms the expert judgement. After them, the vapour interface heat exchange q_{ve} is found. The derivatives with respect to q_{ve} are average, but as its standard deviation is high, the coefficient R^2 is rather high. The large value of the standard deviation means that q_{ve} is poorly determined in Vertical Canon. The following parameters do not present large enough R^2 coefficients, to have any meaning and are not kept. To sum up, the set E_1 consists of { τ_i , $P\tau_i$, q_{ve} }, $P\tau_i$ being the parameter representing the pressure effect on interfacial friction τ_i.

parameter	standard deviation	R^2
interfacial friction τ_i	0.65	0.67
pressure effect in τ_i	1.11	0.65
vapour interface heat exchange qve	38.85	0.58
wall conductivity	4.82	0.45
wall vapour friction	42.34	0.44
nucleated ebullition heat coefficient	31.28	0.44
wall liquid friction	4.94	0.39
wall heat capacity	1.22	0.22

table 6: Vertical Canon, classification according to R^2 of the parameters taken one by one

• Considering the parameters two by two, the results below (table 7) are obtained. The matrix C_ε obtained for the pair of parameters ($P\tau_i$, q_{ve}) is negative. This solution must be rejected.

pair of parameters	standard deviation of 1st parameter	standard deviation of 2nd parameter	correlation coefficient	R^2
(τ_i , $P\tau_i$)	1.25	2.29	-0.89	0.73
(τ_i , q_{ve})	0.70	33.50	0.47	0.68

table 7: Vertical Canon, classification according to R^2 of the parameters taken two by two

N.B.: do not confuse the correlation coefficient with the *total* correlation coefficient R^2. The correlation coefficient of 2 parameters ε_k and ε_l, often denoted ρ_{kl}, is the ratio of the product of the standard deviations to the covariance of the two parameters.

• Considering the parameters three by three, amounts to calculating C_ε for the triplet { τ_i, $P\tau_i$, q_{ve} }. The matrix C_ε obtained is also negative, that is with less than zero eigenvalues.

Finally, this process leads to the selection of two possible pairs of relevant parameters (τ_i, $P\tau_i$) and (τ_i, q_{ve}). The total correlation coefficient is a little higher for the (τ_i, $P\tau_i$) pair, but not enough to permit a choice between the two pairs of parameters.

2.2.4 . Measurement of the quality of a result: study of its convergence

The two results are satisfactory with respect to the three following criteria: a correct condition number for the inertia matrix, a positive C_ε matrix and a high enough R^2 total correlation coefficient . A fourth criterion has to be added to them: do the results converge in relation to the number of responses? The answer to this question can be given with two ways.

2.2.4.1 . Influence of the sampling of responses

The first way consists in estimating the influence of the sampling of the responses. For that, two entirely different samples are taken and the results are compared. But, with 34 responses, it was difficult to find a really different sample of responses. So it seemed better to divide the 34 responses in two subsets of 17 responses and to compare the results. This separation is arbitrary. Nevertheless, in each subset of 17 responses, there are as many remaining masses (8 or 9) as void fractions (9 or 8). The second subset is a little different from the first one, as it takes into account responses for slightly higher time values.

The results found for the two subsets of 17 responses are summarized in the tables 8 and 9 , for comparison with table 7. The same process as the one described in paragraph 2.2.3 for the selection of the relevant parameters was applied.

In each case, the same parameters τ_i , $P\tau_i$, q_{ve} are found. The results are close, except for the ($P\tau_i$, q_{ve}) pair, which will be explained in the next paragraph.

2.2.4.2 . Convergence of the results in relation to the number of responses

The second way consists in checking the convergence with respect to the 34 responses by eliminating the responses step by step. More precisely:

• with the n selected responses, one C_ε matrix is obtained for a given set of parameter

pair of parameters	standard deviation of 1st parameter	standard deviation of 2nd parameter	correlation coefficient	R^2
(τ_i , $P\tau_i$)	1.30	2.26	-0.88	0.72
(τ_i , q_{ve})	1.13	102.16	0.85	0.83
($P\tau_i$, q_{ve})	0.48	41.92	-0.75	0.85

table 8: Vertical Canon, results with the first subset of responses

pair of parameters	standard deviation of 1st parameter	standard deviation of 2nd parameter	correlation coefficient	R^2
(τ_i , $P\tau_i$)	1.37	2.71	-0.92	0.77
(τ_i , q_{ve})	1.04	53.24	0.83	0.69
($P\tau_i$, q_{ve})	1.85	54.11	0.83	0.73

table 9: Vertical Canon, results with the second subset of responses

In each case, the same parameters τ_i , $P\tau_i$, q_{ve} are found. The results are close, except for the ($P\tau_i$, q_{ve}) pair, which will be explained in the next paragraph.

2.2.4.2 . Convergence of the results in relation to the number of responses

The second way consists in checking the convergence with respect to the 34 responses by eliminating the responses step by step. More precisely:

- with the n selected responses, one C_ε matrix is obtained for a given set of parameters.
- the responses are eliminated one by one. There are n possible combinations and as many $C_{\varepsilon,i}$ matrices, obtained by eliminating the response R_i. The average and the standard deviation of each term of $C_{\varepsilon,i}$ matrices are calculated. The averages must be close to the terms of C_ε : there is no drift. The standard deviations must be weak: there is no dispersion.
- the process is repeated by eliminating the responses two by two. n(n-1)/2 matrices $C_{\varepsilon,i,j}$ are obtained, which correspond to the elimination of the responses R_i and R_j. The averages and the standard deviations of the terms of the matrices $C_{\varepsilon,i,j}$ are calculated and compared with the terms of C_ε.:

	eliminating the responses 1 by 1			eliminating the responses 2 by 2		
	var (τ_i)	var ($P\tau_i$)	cov(τ_i , $P\tau_i$)	var (τ_i)	var ($P\tau_i$)	cov(τ_i , $P\tau_i$)
drift	1.07%	1.12%	1.24%	2.32%	2.39%	2.65%
dispersion	10.4%	11.6%	12.2%	16.0%	17.2%	18.3%

table 10:Vertical Canon, study of the convergence of the results relative to the (τ_i , $P\tau_i$) pair

A similar table (table 11) is get for the second pair of parameters (τ_i , q_{ve}):

	eliminating the responses 1 by 1			eliminating the responses 2 by 2		
	var (τ_i)	var (q_{ve})	cov(τ_i , q_{ve})	var (τ_i)	var (q_{ve})	cov(τ_i , q_{ve})
drift	0.33%	1.59%	1.56%	0.64%	3.19%	3.08%
dispersion	15.2%	35.0%	49.0%	21.4%	48.5%	67.8%

table 11:Vertical Canon, study of the convergence of the results relative to the (τ_i , q_{ve}) pair

When applied to the first pair of selected parameters, i.e. (τ_i , $P\tau_i$), the following results are obtained (table 10) .

The drift for both pairs of parameters is slight. But the dispersion of the results is high for the (τ_i , q_{ve}) pair: the results have not really converged for this pair.

All in all, the (τ_i , $P\tau_i$) pair will be kept.

Comment: the same process applied to the two subsets of 17 responses shows that the results have not at all converged for the ($P\tau_i$, q_{ve}) pair. It is particularly true for the results relative to the variance of $P\tau_i$. This explains the difference of the results for this pair when considering the two subsets of responses.

2.3. Future uses of the DASM

2.3.1 . Extension of the methodology of the calculation of the uncertainties of the constitutive relationships

The study achieved about Vertical Canon must be extended to several SET facilities treated together. To begin with, three experiments will be considered. Each of them is conducted with different pressure and hydraulic diameter conditions. However, i nterfacial friction is an apparently relevant parameter in all of them. Besides, other parameters are apparently relevant, but in one experiment at one time. The aim is to calculate only one C_ε matrix for the set of parameters relevant in one , two or three experiments.

When this preliminary study has been completed, the method will be applied to the set of all the correlations of the code by using the set of SET facilities used to establish these correlations. The variance covariance matrix for the set of all the correlations will be then known.

2.3.2 . Bias calculation

Up to now , the whole work presented in this paper deals with *frozen* code. Indeed, the existence of biases can be suspected, if there is a systematic shift of the code responses with respect to the experiment ones. The occurence of biases increases the standard deviations of the parameters of the constitutive relationships, as shown in figure 4. One can observe that the calculated standard deviation σ_ε includes the bias.

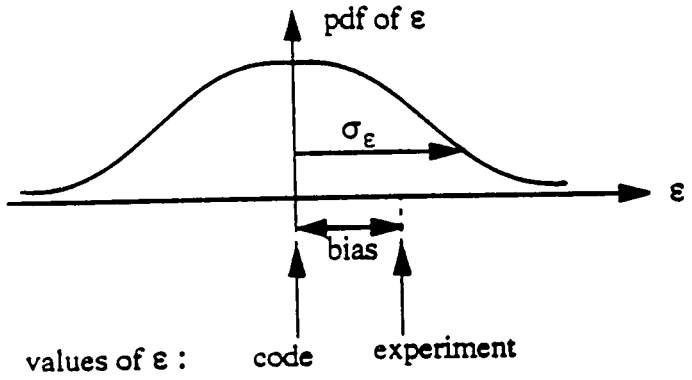


figure 4 : comparison of the standard deviation deviation σ_ε and of the bias

N. B. : pdf = probability distribution function

Thus, another interesting line of research might be the calculation of biases, if modifying the code is authorized. It is possible by using a relationship at the first order (equation 25) equivalent to equation (19) and also using the DASM results: $$R_{i,\,exp} - R_{i,\,code} = \sum_{j=1}^{d} \frac{dR_i}{d\varepsilon_j} b_j \quad (25)$$

where

- d is the number of parameters which are considered as influencing the response R_i.
- b_j is the bias associated to the parameter ε_j. The different b_j are the unknowns.

Like in paragraph 2.1.3, a sum S_b equivalent to the sum S (equation 20) is defined and must be minimized with respect to the unknowns b_j (equation 26):

$$S_b = \sum_{i=1}^{n} \left(R_{i,\,exp} - R_{i,\,code} - \sum_{j=1}^{d} \frac{dR_i}{d\varepsilon_j} b_j \right)^2 \quad (26)$$

which leads to a linear system of d equations in d unknowns.

A first estimation of the biases is thus obtained, which is denoted $b_j^{(1)}$.

The direct calculations are performed a second time while introducing the biases in the correlations. New code responses, denoted $R_{i,code}^{(2)}$ are thus obtained. New DASM calculations also provide new derivatives $dR_i/d\varepsilon_j^{(2)}$. By minimizing $S_b^{(2)}$ defined by (equation 27):

$$S_b^{(2)} = \sum_{i=1}^{n} \left(R_{i,\,exp} - R_{i,\,code}^{(2)} - \sum_{j=1}^{d} \frac{dR_i}{d\varepsilon_j}^{(2)} b_j^{(2)} \right)^2 \quad (27)$$

new biases $b_j^{(2)}$ are obtained, which must be added to the previous ones $b_j^{(1)}$.

The iterative process is restarted until the biases are insignificant.

This methodology was applied to Vertical Canon with encouraging initial results.

CONCLUSION

-1- The DASM has been successfully implemented in the CATHARE code. It has been demonstrated that it is a powerful sensitivity method, easy to use, and with a low CPU cost.

-2- The DASM has been qualified against the classical brute force method, using separate effect tests from the qualification matrix of CATHARE. The robustness of the method has been proved.

-3- An application of the method has been presented which deals with the determination of the uncertainty of the constitutive relationships. The general methodology is presented: it calculates the variance-covariance matrix of the parameters relative to these constitutive relationships. Its application to a simple case has been successfully performed: the Vertical Canon experiment. In this case, the relevant parameters have been determined, the variance-covariance matrix relative to these parameters has been calculated, and the quality of this matrix has been also estimated.

-4- Other applications of the DASM can be considered. Especially, it seems possible to calculate the biases relative to the constitutive relationships.

-5- This methodology will be included in the methodology developed by CEA and EdF defined for the use of best estimate code for safety studies and licensing.

List of symbols of part 2:

b_j : bias of parameter ε_j
C_ε : variance-covariance matrix of the parameters
$C_{\varepsilon,i}$: matrix C_ε obtained by eliminating the response R_i
$C_{\varepsilon,i,j}$: matrix C_ε obtained by eliminating the responses R_i and R_j
cov (ε_k ,ε_l) : covariance of the parameters ε_k and ε_l
d : number of considered parameters
n : number of considered responses
n_{Mr} : number of remaining mass type responses
$P\tau_i$: pressure effect in interfacial friction τ_i
R : response (generally speaking)
R_i : response number i
R^2 : square of the total correlation coefficient
q_{ve} : vapour interface heat exchange
S : sum to minimize for finding C_ε
S_b : sum to minimize for finding the biases of the parameters
w_i : weight given to response R_i
var (ε_k) : variance of parameter ε_k
var (R_i) : variance of response R_i
$\widehat{var}\left(R_i\right)$: estimation of the variance of response R_i
$\delta\varepsilon_k$: range of parameter k
ε : parameter (generally speaking)
ε_k : parameter number k
σ_ε : standard deviation of a parameter ε
τ_i : interfacial friction

REFERENCES

[1] F. BARRE and al.: New developments in the CATHARE 2 code.NURETH 6, Grenoble, France, October 5-8, 1993.

[2] E. OBLOW: Sensitivity Theory for Reactor Thermal-Hydraulics Problems, Nucl. Sci. Engrg. 68 (1978), 322-337.

[3] C.V. PARKS: Adjoint Based Sensitivity Analysis for Reactor Safety Applications, ORNL/CSD/TM-231, August, 1986.

[4] A. OUNSY, F. de CRECY, B. BRUN: The adjoint sensitivity method; a contribution to the code uncertainty evaluation, Nucl. Engrg. Des. 149 (September 1994) 357-364.

[5] F. BARRE, M. BERNARD: The CATHARE code strategy and assessment, Nucl. Engrg. Des. 124 (1990) 257-284.

[6] W. WULFF: Quantifying reactor safety margins - part 3: assessment and ranging of parameters, Nucl. Engrg. Des. 119 (1990) 33-65.
[7] G. S. LELLOUCHE and S. LEVY: Quantifying reactor safety margins - part 4: uncertainty evaluation of LB-LOCA analysis based on TRAC-PF1/MOD 1, Nucl. Engrg. Des. 119 (1990) 67-95.
[8] A. J. WICKLETT: «A review of LOCA uncertainty studies in AEA», AEA RS 5522 (Winfrith, UK, June 1993).
[9] H. GLAESER, E. HOFER, M. KLOOS, T. SKOREK (GRS): «Uncertainty and Sensitivity Analysis of a Post-Experiment Calculation in Thermal Hydraulics» in «Report on special workshop on uncertainty analysis methods», by A. J. Wicklett and G. Yadigaroglu, report n° : AEA CS 16401569.002, June 1994.
[10] D. BESTION:The physical closure laws in the Cathare code, Nucl. Engrg. Des. 124 (1990) 229-245.

DEVELOPMENT AND ASSESSMENT OF A MODIFIED VERSION OF RELAP5/MOD3

G. Th. Analytis

Laboratory for Thermal Hydraulics,
Paul Scherrer Institute (PSI),
CH-5232 Villigen PSI, Switzerland
Tel: 56-99-21-11 / Fax: 56-99-21-99

ABSTRACT

A summary of a number of modifications introduced in RELAP5/MOD3 is presented. These include implementation of different heat transfer packages for different processes, modification of the low mass-flux Groeneveld CHF look-up table and of the dispersed flow interfacial area (and shear) as well as of the criterion for transition into and out from this regime, elimination of the under-relaxation schemes of the interfacial closure coefficients etc. The modified code is assessed against a number of separate-effect and integral test experiments and in contrast to the frozen version, is shown to result in physically sound predictions which are close to the measurements.

1. INTRODUCTION

During the last few years, extensive assessment [1-4] of the transient thermal hydraulics code RELAP5/MOD3 [5,6] (to be referred to as R5M3) has been pursued at the Thermal Hydraulics Laboratory at PSI and a number of model deficiencies and problem areas have been identified, the most striking one being the inability of the code to even remotely capture the physics of reflooding due to a number of reasons on which we have extensively elaborated elsewhere [1,7]. As a result of this, a rather broad developmental program has been undertaken, and a number of improvements covering a rather extensive area have been made [1,7].

In this work, we shall report on the final model changes and code modifications introduced into R5M3. These will be summarized in section 2 and include the implementation of two different wall-to-liquid heat transfer packages and removal of the package of the frozen version (which has been shown to be unphysical and problematic), modification of the low mass-flux limit of the Groeneveld CHF look-up table, modification of the minimum allowed droplet diameter (and hence, the interfacial shear) in dispersed flow and the criterion for transition to this regime, re-activation of the modified Bestion bubbly/slug interfacial shear correlation for bundles at low pressures and almost complete elimination of the under-relaxation schemes of the interfacial closure coefficients. In section 3, we shall compare the predictions of the modified code with the ones of the frozen version as well as with measurements for a number of separate-effect and integral test experiments and wherever possible, we shall discuss the origin of the differences in predictions. Finally, we shall conclude this work in section 4 with some recommendations.

2. SUMMARY OF MODIFICATIONS IN R5M3

In this section, we shall briefly outline the code modifications and model changes we found necessary to make in R5M3.

(a) The modified Bestion interfacial shear correlation for bubbly/slug flow was re-activated and used for pressures less than 10 bar. It reads [7-9]

$$f_i = \frac{65\ \alpha\ (1\ -\ \alpha)^3\ \rho_g}{D_H}\ (C_1 V_g\ -\ C_o V_l)^2 \tag{2.1}$$

where ρ_g and D_H are the steam density and hydraulic diameter, respectively, while the value of the distribution parameter C_o is set equal to 1.2. For pressures greater than 20 bar, the EPRI interfacial shear correlation [5] already in the code is used, and a linear interpolation is used between these two pressures. There is a number of reasons for re-activating the modified Bestion correlation, one of them being that as has already been shown in Ref. 5, it results in very good predictions for low pressures. Additionally, recent work has shown that the highly complex EPRI correlation, due to its dependence on a large number of local variables which are usually oscillating in a transient calculation, may induce a number of other problems, one of them being an unacceptably large mass-error. Hence, although the EPRI correlation, due to the fact that it is actually a fit to a large number of data points, is bound to result, in general, in better predictions than other correlations, we would generally recommend employing a simpler bubbly/slug interfacial shear correlation for pipes similar to the one used in codes like TRAC-BF1 [10].

(b) In order to avoid vapour de-superheating, the average droplet diameter $D_o^{'}$ defined via the Weber number (We) was increased in R5M3 by the code developers by first increasing (We) to 12 (in RELAP5/MOD2.5, it had the value of 3). Furthermore, the minimum allowed droplet diameter D'_m in the post-dryout regime is defined (ad-hoc) as a function of the pressure p as follows:

$$\left.\begin{aligned} &D'_m\ =\ 0.0025\ \text{ for } \tilde{p}\ \leq\ 0.025, \\ &D'_m\ =\ 0.0025\ - \\ &4.444\ (0.0025\ -\ 0.0002)\ (\tilde{p}\ -\ 0.025), \\ &\text{for } 0.025\ <\ \tilde{p}\ <\ 0.25, \\ &D'_m\ =\ 0.0002\ \text{ for } \tilde{p}\ \geq\ 0.25 \end{aligned}\right\} \tag{2.2}$$

$\tilde{p}\ =\ p/p_{cr}$, p is the pressure and p_{cr} is the critical pressure. Finally, th average droplet diameter D_o used is defined by

$$D_o\ =\ \min\left\{D_H, \max\left(D'_m, D'_o\right)\right\} \tag{2.3}$$

where D'_m is defined by eq.(2.2). Hence, as can be seen from eq. (2.3), for $p < 5.4$ bar, D_o is not allowed to be less than 0.0025 m. Subsequently, the droplet interfacial area per unit volume S_{dr} is defined by [5,6]

$$S_{dr}\ =\ \frac{3.6\ (1-\alpha)}{D_o}. \tag{2.4}$$

In R5M3, the interfacial shear is proportional to S_{dr} and since the droplets are large (small interfacial area), in a number of situations, they cannot be "lifted" by the vapour. Hence, we re-set the Weber number to 3 and assumed a minimum D_o of 0.0015m. Here, we should clearly state that in a 2-fluid model code one cannot "rigorously" define an average droplet diameter since there is only one liquid field. The assumed value of 0.0015m (which in itself may also be relatively high since the average droplet diameters measured in FLECHT did not exceed 0.001m) is based on a compromise and engineering judgement rather than on a rigorous argument.

(c) The logic for selecting the pre- or the post-CHF interfacial closure laws in R5M3 is as follows: One defines

$$P \geq 1 \tag{2.5}$$

where

$$P = \max(0, \min(1, P'(0.4 - \alpha_B)10)). \tag{2.6a}$$

Now P' is defined by

$$P' = \min(1, P_{wind}\, T_{gs}) \tag{2.6b}$$

where

$$\left.\begin{aligned} P_{wind} &= 0.06667 \text{ for } \tilde{p} \leq 0.025, \\ P_{wind} &= 0.016667 \text{for } \tilde{p} \geq 0.25, \\ P_{wind} &= \text{Interp. for } 0.025 < \tilde{p} < 0.25, \end{aligned}\right\} \tag{2.6c}$$

and

$$T_{gs} = T_g - T_s - 1. \tag{2.6d}$$

α_B is the void fraction for transition from bubbly to slug flow and T_g and T_s are the vapour and saturation temperatures, respectively. If (2.5) is satisfied, the code selects the post-dry out closure laws. The reason for this "indirect" selection logic is that the interfacial closure laws subroutines are not actually "communicating" with the ones for the wall heat transfer and one would like to have some consistency between the two (which, by the aforementioned indirect procedure, is not always possible). We found that the definition of P' given by (2.6b) with P_{wind} given by (2.6c) is too restrictive. Hence, we modified equation (2.6b) to read (as it was defined in RELAP5/MOD2.5 [9])

$$P' = 1.0000454\,(1 - e^{-0.5\,T_{gs}}) \tag{2.7a}$$

where now (as we modified it in the past in RELAP5/MOD2.5 [9]), if the component in question is a bundle,

$$T_{gs} = T_g - T_s - 29 \tag{2.7b}$$

otherwise, T_{gs} is given by eq. (2.6d). This modification has a surprisingly large effect on a number of predictions. At this point, we should say that the selection of the value 29 in the above equation was made based on inspection of a number of predicted void fraction profiles during reflooding which with the original formulation, were exhibiting discontinuities near the quench front (QF) as in the case of RELAP5/MOD2.5 [9]. Conceptually, decrease (resp. increase) of this value results in employing the post-CHF interfacial closure laws at a lower (resp. higher) vapour temperature.

(d) During reflooding, if the wall heat flux is exceeding the CHF, we implemented in the code a special heat transfer package based on the **empirical** CATHARE film-boiling, wall - to - liquid HTC and modified the heat transfer logic in the same way we modified it for TRAC-BF1 [11]. Hence, for the post-CHF wall heat transfer regime, we first define

$$\tilde{h}_{wl(\mathrm{FB})} = \max\Big\{(f_1 - f_2\,\Delta z_{\mathrm{QF}})\,\min\,(1 - \alpha,\,0.5),\,0\Big\} + h_{\mathrm{BR}}\,\sqrt{1 - \alpha} \tag{2.8a}$$

where f_1 = 1400, f_2 = 1880, Δz_{QF} is the distance from the QF and h_{BR} is the original Bromley correlation. Subsequently, we define

$$h_{wl(FB)} = \max\Big\{h_{wl(FB,CAT)}, h_{FR}\Big\} \tag{2.8b}$$

where now h_{FR} is the Forslund-Rohsenow wall-to-droplets contact HTC [9]. Finally, we define the wall - to - liquid post-CHF HTC by

$$h_{wl} = \max\Big\{h_{wl(FB)}, h_{wl(TB)}\Big\} \tag{2.8c}$$

where $h_{wl(TB)}$ is the Weismann transition boiling correlation given by

$$h_{wl(TB)} = h_m e^{-\xi\Delta T} + 4500\Big(\frac{G}{G_R}\Big)^{0.2} e^{-0.012\Delta T}. \tag{2.9a}$$

We have chosen for the constant ξ = 0.03 and [9]

$$h_m = \frac{q_{CHF}}{T_{CHF} - T_s} \tag{2.9b}$$

$$\Delta T = T_w - T_{CHF} \tag{2.9c}$$

where T_{CHF} and T_s are the wall temperature at CHF and saturation temperature, respectively, G is the total mass-flux and G_R = 67.8 kg/m^2/s. No T_{MIN} is used in this formalism. Furthermore, we ramped the Weismann correlation linearly to 0 for distances between 0.1 m and 0.2 m from the quench front, ie

$$h_{wl(TB)} = \begin{cases} h_{wl(TB)} & \Delta z_{QF} \leqq 0.1m \\ 0 & \Delta z_{QF} \geqq 0.2m \\ \text{Interp.} & 0.1m < \Delta z_{QF} < 0.2m. \end{cases} \tag{2.9d}$$

The reason for this is that we want to avoid "spurious" quenching of a node (eg due to a high value attained by eq. (2.9a)) if the quench front is not in the vicinity of this node. This model should be applicable if the flooding velocities are not exceeding $0.2 - 0.3\ m/sec$. The author should take into account the fact that in conjunction with the aforementioned approach, one should in principle utilize a QF velocity correlation, and this is precisely the approach followed in CATHARE. Since one of our aims is to improve the physical models in the code without (at least for the time being) introducing radical changes to its basic structure and philosophy, we did not try to utilize such a QF velocity correlation.

(e) If the reflooding trip is not active, we implemented a different wall - to - liquid heat transfer package, which is similar to the one of TRAC-BF1 [10]. For this case, we define the wall-to-liquid film boiling HTC h_{wl} by

$$h_{wl} = h_{wl(BR)}\,(1 - \alpha) \tag{2.10a}$$

where $h_{wl(BR)}$ is the modified Bromley correlation. Additionally, we define a T_{MIN} and the transition boiling wall-to-liquid HTC (if $T_w < T_{MIN}$) by the Bjornard quadratic interpolation between the CHF point and the film-boiling wall-to-liquid HTC $h_{wl(FB)}$ ($= h_{wl(BR)} (1 - \alpha)$) in the usual way [10,11]

$$h_{wl(TB)} = (1 - \Gamma) h_{wl(FB)} + \Gamma \frac{q_{CHF}}{T_w - T_l} \tag{2.10b}$$

where

$$\Gamma = \left(\frac{T_w - T_{MIN}}{T_{CHF} - T_{MIN}} \right)^2. \tag{2.10c}$$

and all the symbols have their usual meaning. For the time being, we use a constant T_{MIN} equal to 710 K. Here, we should say that one of the concerns of the code developers when moving from RELAP5/MOD2 to R5M3 and unifying the two wall heat transfer packages was that the employment of two different packages was resulting in discontinuities when the reflooding trip was activated. In the framework of R5M3 and our model, we did not notice such a behaviour since the reflooding package is usually activated when the core is empty and discontinuities would generally arise from the different wall-to-liquid HTCs. In any case, even if such discontinuities exist, this is no reason for not accepting that since reflooding is a special process, it cannot be modelled by conventional means and requires a special heat transfer package.

(f) It has been shown [1,2,7] that during transients, for low $|G|$, the Groeneveld look-up table CHF exhibits oscillations which are fed-back into the HTC, hence adversely affecting the predicted rod surface temperature (RST) histories. For this reason, for low mass-fluxes $|G|$, we have modified the CHF in the code as follows:

$$\left.\begin{aligned} q_{CHF} &= q_{Zu} \quad \text{for } |G| < 50 \text{ kg/m}^2\text{/s}, \\ q_{CHF} &= q_{Gr} \quad \text{for } |G| > 150 \text{ kg/m}^2\text{/s}, \\ q_{CHF} &: \text{Interp., for } 50 \leq |G| \leq 150 \end{aligned}\right\} \tag{2.11}$$

where q_{CHF}, q_{Zu} and q_{Gr} are the critical heat flux, the modified Zuber CHF, and the CHF predicted from the Groeneveld tables, respectively.

(g) For the post-dry-out droplets (this includes low pressure reflooding), the interfacial shear coefficient c_{dr} is restricted in the code by the following (**wrong**) condition:

$$c_{dr} = \min (c_{dr}, 0.45). \tag{2.12a}$$

This condition severely limits the value that the coefficient c_{dr} can attain [12] since, even for very large Reynold's numbers, c_{dr} rarely becomes less than 0.45. The correct form of this condition reads

$$c_{dr} = \max (c_{dr}, 0.45). \tag{2.12b}$$

(h) The interfacial closure coefficients are "old-time averaged" (under-relaxed) in order to smooth largely different values obtained during flow-regime transitions [5]. The scheme used for under-relaxing the interfacial shear and heat transfer coefficients can be summarized as follows: The new-time under-relaxed coefficient f_i^{n+1} is defined by

$$f_i^{n+1} = f_i' \left(\frac{f_i^n}{f_i'} \right)^R \tag{2.13}$$

where f_i' is the explicitly evaluated interfacial coefficient, and the exponent R is generally defined by

$$R = f(\Delta t, \Delta t_{Cour}, \tau', C, V_g, V_l ...), \tag{2.14}$$

where R's are now complicated functions of the phasic velocities, time-step, Courant limit, different constants C's, relaxation time-constants τ's etc. We have shown that these schemes may lead to time-step dependent code predictions [1]. Hence, as an option, we almost completely eliminated the under-relaxation schemes by setting $R = 0$ in Eq. (2.13), except the one for the liquid interface-to-liquid heat transfer which we kept as is in the code if $f_i' > f_i^n$. We should warn the reader that there may be cases for which this elimination of the under-relaxation schemes may give problems and this may well be the case with transients which are using relatively large time-steps and hence, this procedure may not always be practical.

(i) We have implemented (also as an option) a linearization procedure for the interfacial shear terms in the momentum equations (both for the semi- and nearly-implicit hydro-dynamic solution schemes; subroutines **vexplt** and **vimplt**, respectively and also **jchoke**). Briefly, in the code, the new-time (superscript $n+1$) phasic velocities $V_{g,j+\frac{1}{2}}^{n+1}$ and $V_{l,j+\frac{1}{2}}^{n+1}$ at the junctions $j+\frac{1}{2}$ are solved in terms of, among other variables, the old-time velocities (superscript n) $V_{g,j+\frac{1}{2}}^{n}$ and $V_{l,j+\frac{1}{2}}^{n}$. Though, the interfacial shear term $f_{i,j+\frac{1}{2}}^{n+1}$ is at time-step $n+1$ and is given by (in general)

$$f_{i,j+\frac{1}{2}}^{n+1} = C_{IO} \left(C_1 V_g^{n+1} - C_o V_l^{n+1} \right)_{j+\frac{1}{2}}^{q} = C_{IO} (V_{R,j+\frac{1}{2}}^{n+1})^q \tag{2.15a}$$

where

$$C_1 = \frac{1 - \alpha C_o}{1 - \alpha}. \tag{2.15b}$$

q is an integer (in the case of RELAP5, $q = 2$), and C_o and C_{IO} are flow-regime dependent coefficients. Hence, to be able to express the new-time velocities in terms of the old-time ones, one has either to use a simple approximation for eq. (2.15a), eg

$$f_{i,j+\frac{1}{2}}^{n+1} \simeq C_{IO}(V_{R,j+\frac{1}{2}}^{n+1}) \, (V_{R,j+\frac{1}{2}}^{n})^{q-1} \tag{2.16}$$

(and this is the assumption made both in R5M2.5 and in R5M3), or one can use a second order linearization scheme as in TRAC-BF1 [10]. Eq. (2.16) is a good approximation provided

$$RA = | (V_{R,j+\frac{1}{2}}^{n+1} - V_{R,j+\frac{1}{2}}^{n}) / V_{R,j+\frac{1}{2}}^{n} | = \left| \frac{\delta V_{R,j+\frac{1}{2}}}{V_{R,j+\frac{1}{2}}^{n}} \right| \ll 1 \tag{2.17}$$

where $\delta V_{R,j+\frac{1}{2}}$ is the change in $V_{R,j+\frac{1}{2}}$ during one time-step. Hence, we shall adopt the more general linearization scheme and we shall linearize the interfacial shear term $f_{i,j+\frac{1}{2}}^{n+1}$ to second order as follows:

$$(V^{n+1}_{R,j+\frac{1}{2}})^q \simeq -(q-1)\,(V^n_{R,j+\frac{1}{2}})^q \;+\; q(V^n_{R,j+\frac{1}{2}})^{q-1}\,(V^{n+1}_{R,j+\frac{1}{2}}). \qquad (2.18)$$

Clearly, in contrast to the approximation given by eq. (2.16) which is valid provided $(RA) \ll 1$ (where (RA) is defined by eq. (2.17), one can readily show that the approximation given by eq. (2.18) is valid for $(RA)^2 \ll 1$ and hence, much larger changes of the phasic velocities between two successive time-steps are allowed without the danger of exciting numerical instabilities. This modification is bound to improve the numerical robustness of the code, either when the nearly-implicit solution scheme is used, or when the semi-implicit method is used with relatively large allowed time-steps.

(j) A number of additional **options** have been introduced in the code like the Andersen's drift-flux-based interfacial shear correlations (as in TRAC-BF1 [10]), the implementation of the first upwind scheme in the momentum equations and the inclusion of the spatial derivatives in the virtual mass term in the phasic momentum equations. We shall not comment on these different options in this work.

3. COMPARISON OF CODE PREDICTIONS

In this section, we shall compare the predictions of the frozen and modified version of the code with measurements from separate-effect and integral test experiments. We shall present and discuss four different cases: A simple constant inlet liquid velocity bottom flooding test in a heater rod bundle at PSI, the LOFT LP-LB-1 experiment [14], the LOBI SB-LOCA BL34 experiment and a two loop commercial PWR LB-LOCA calculation [16].

We shall start by discussing the low flooding rate NEPTUN experiment Nr. 5036 (P = 4.1 bar, ΔT_s = 10 K, V_{IN} = 0.015 m/s) [13]. We should say that other reflooding experiments have also been analyzed with both versions of the codes, and the interested reader is referred to Ref. 1. In Fig. 1, we show the measured and predicted RST histories and the predicted total HTC at axial elevations of 0.714 and 0.946 m. Clearly, our modified version predicts the RST history very well, while the frozen version of the code predicts a totally unrealistic and unphysical RST history. The main reason for this is the unphysical modeling of the HTC during reflooding, as well a number of other reasons related to the droplets interfacial shear. This can be seen in the highly oscillatory total HTC predicted by the frozen version.

We shall now present some results from the LOFT LP-LB-1 experiment by using the input deck of Ref. 16. In Fig. 2, we show the measured and predicted RST histories at axial elevations of 27 and 31 inches. Also here, one sees that although the RST histories predicted by the code are still below the measurements, there is a considerable improvement over the predictions of the frozen version. Additionally, in order to show the sensitivity of the results to the assumed interfacial shear correlations, we show the RST histories predicted by the code when the wet-wall interfacial shear correlations of Andersen [10] are used if the component is a pipe. One sees that the RSTs are now closer to the measured ones.

Next, we shall present some results from the LOBI SB-LOCA BL34 experiment [16] for which the reflooding option is not activated. In Fig. 3, we show measured and predicted RST histories at two axial elevations, as well as the collapsed level in the core. Neither our modified code nor the frozen version predict the first dry-out; though, the modified version predicts the RSTs significantly better than the frozen version.

As a final test of our fully modified version of R5M3, we run a two-loop commercial PWR 200 % LB-LOCA case, with an input deck supplied to us by Lübbesmeyer [16]. In Fig. 4, we compare the RST predictions of the modified and frozen versions [16] for the hot rod in the high power channel at axial elevations of 2.37m (peak axial power level). One can see that the predictions of the frozen version exhibit a sharp RST decrease at approximately 7.5s

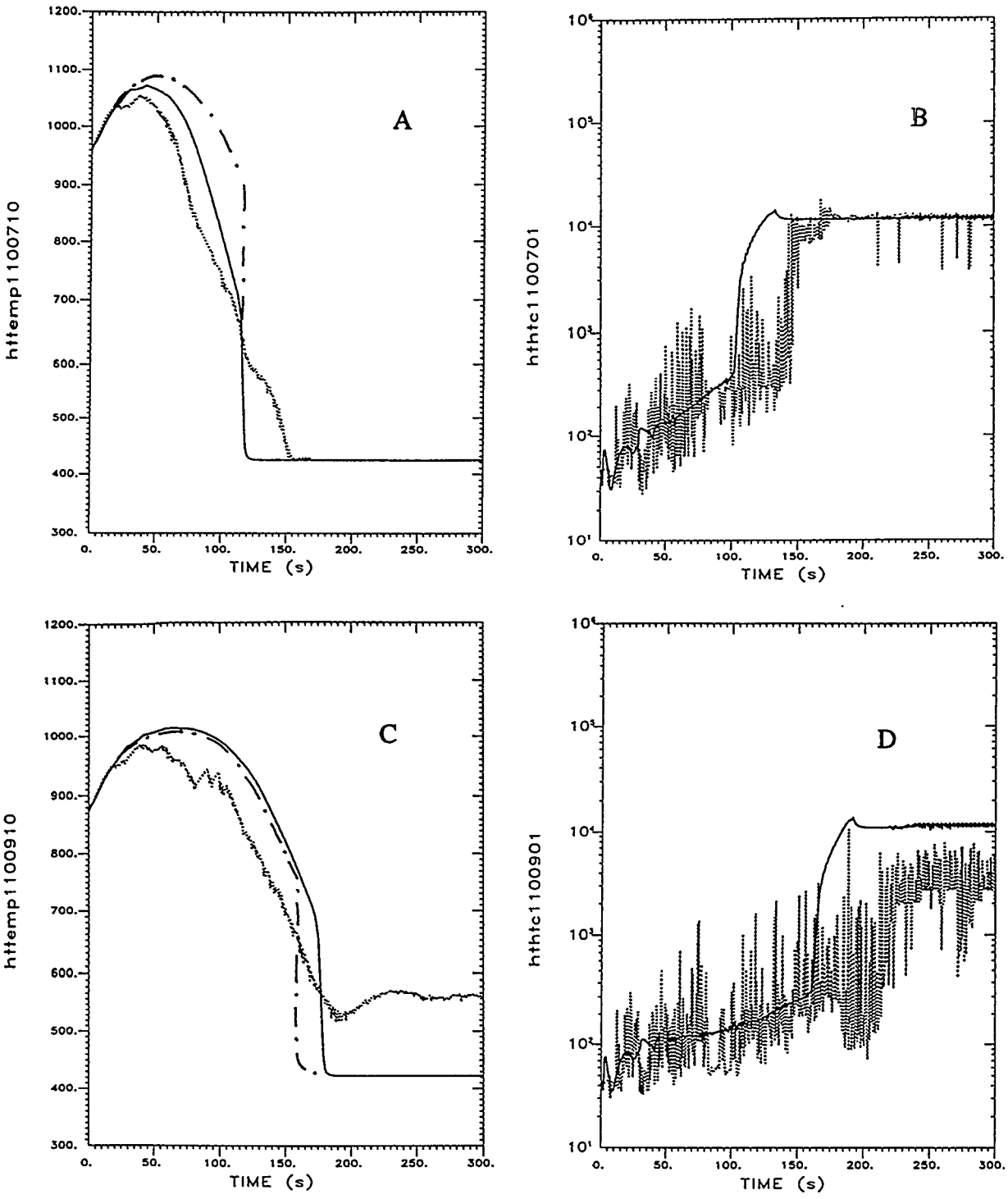


Fig. 1 NEPTUN bootom flooding exp. Nr. 5036. RST (K) and HTC (W/m^2/K) at axial elevation 0.714 m (A, B) and 0.946 m (C, D). (——): Modified R5M3; (.....): R5M3 frozen version; (-.-.-): measurements.

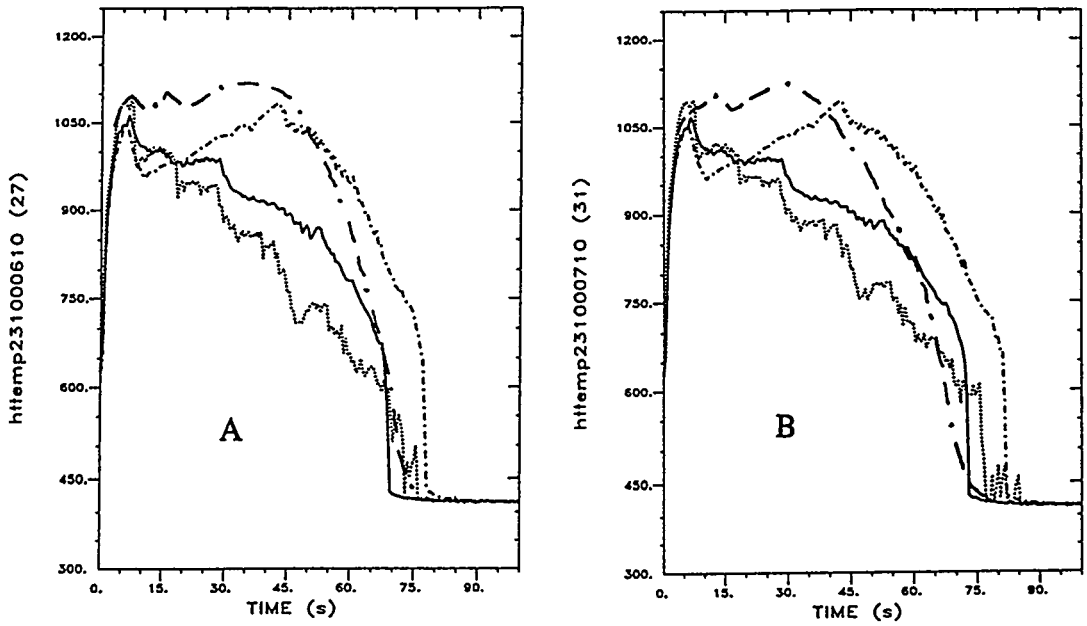


Fig. 2 LOFT LP-LB-1 Test. Predicted RST (K) histories at axial elevations of 27 (A) and 31 (B) inches. (——): modified R5M3; (.....): R5M3 frozen version; (-.-.-.): modified R5M3 + Andersen's wet wall shear for pipes; (- -.- -.): measurements.

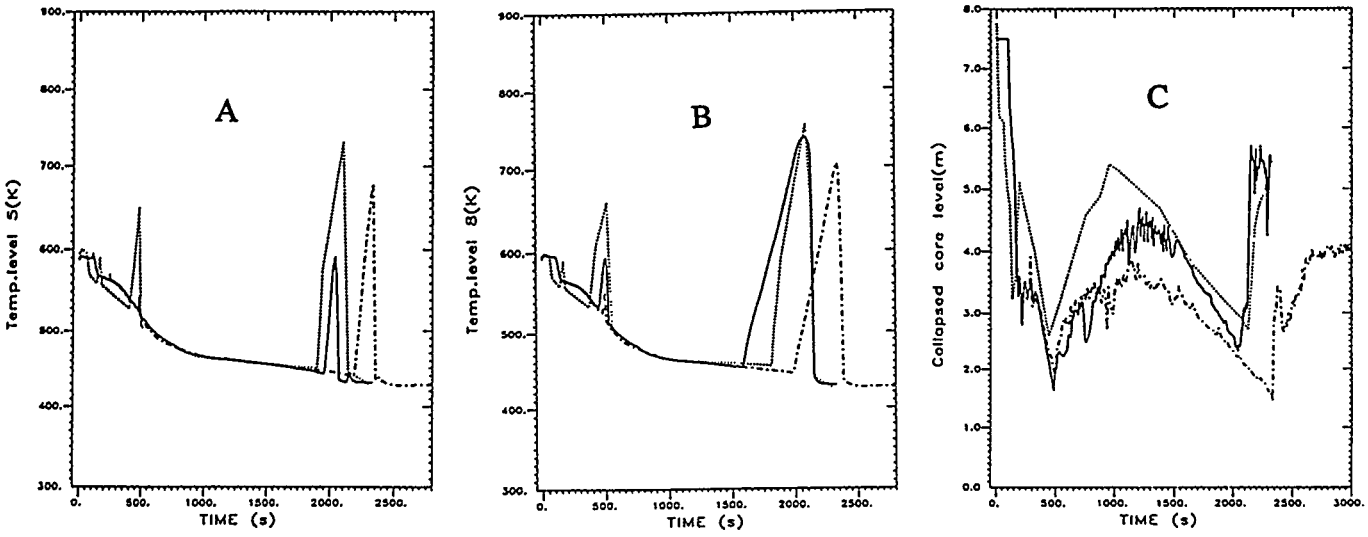


Fig. 3 LOBI BL34 SB-LOCA test. Predicted RST histories at two axial levels (A and B) and collapsed level in the core (C). (——-): modified R5M3; (-.-.-.-.): R5M3 frozen version; (.....): measurements.

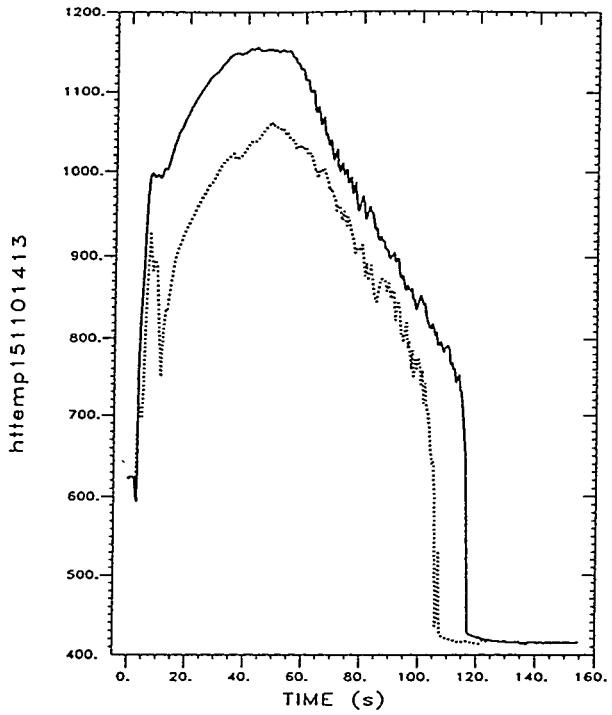


Fig. 4 Predicted peak RSTs for a hypothetical LB-LOCA in a Commercial PWR. (——): modified R5M3; (.....): R5M3 frozen version.

after the break opens, due to the problematic Chen transition/film boiling correlation which attains a very high value at $|G|$ = 271 kg/m^2/s and when later $|G|$ decreases, the RSTs start increasing again. A consequence of this is that the peak RSTs predicted by the frozen version of the code are much lower than the ones predicted by the modified version(s) since with the former code, a large amount of stored energy is removed during the first 12s of the transient. Sensitivity studies have shown that the peak RSTs are strongly dependent on the assumed interfacial shear during the first few seconds of the transient, but also on the assumed value of the T_{MIN}. Clearly, a detailed investigation and qualification of all these effects and their incorporation into an "uncertainty analysis methodology" matrix would be a horrendous job.

4. CONCLUDING DISCUSSIONS

In this work, we have outlined a number of modifications and model changes introduced in R5M3 which result in better and more physically sound code predictions. Some of the main code deficiencies we identified were in the modeling of the wall-to-liquid post-CHF heat transfer coefficient, the adverse effects of the oscillatory behaviour of the CHF predicted from the Groeneveld look-up table (mainly for low mass-fluxes), the unphysically small interfacial shear at lower pressures (which greatly affects the code predictions during reflooding), the effect of the under-relaxation schemes of the interfacial closure coefficients (particularly in the presence of numerical oscillations), as well as a number of other minor points which can show-up and become important under certain conditions.

A number of separate-effect and integral test experiments were analyzed with the modified code, and the predictions were compared with the ones obtained by the frozen version and (when possible) with the measurements. Without exception, the predictions of the modified code were closer to the measurements, in many cases free of unphysical oscillations, and

always more physically sound than the ones of the frozen version. These tests included reflooding in a heater rod bundle, the LOFT LB-LOCA LP-LB-1, the LOBI 6% SB-LOCA BL34 and a hypothetical 200% LB-LOCA in a two-loop commercial PWR. Clearly, a wider assessment of this version with a number of different transients is required before one can make general and definite statements about its improved predicting capabilities.

Acknowledgements

We would like to thank Dirk Lübbesmeyer for making available to us his PWR and LOFT LP-LB-1 input decks. We are also grateful to the University of Pisa, Italy, and in particular, to F. D'Auria for providing us with the LOBI input deck.

References

[1] G. TH. ANALYTIS, A summary of model changes and options in RELAP5/MOD3. Paper presented at the 2nd CAMP Meeting, May 10 - 13, 1993, Brussels, Belgium.

[2] G.TH. ANALYTIS, The effect of CHF modeling on some numerical oscillations of RELAP5/MOD3 during reflooding, paper presented at the International Working Group Meeting on CHF Fundamentals, March 3 - 4, 1993, University of Braunschweig, Germany.

[3] M.SENCAR and S.N.AKSAN, Evaluation of reflooding models in RELAP5/MOD2.5, RELAP5/MOD3/v5m5 and RELAP5/MOD3/v7j codes by using Lehigh University and PSI-NEPTUN bundle reflooding experiments, **TM-42-92-19**, PSI Internal Report, presented at the 2nd CAMP Meeting, Brussels, Belgium, 10 - 13 May, 1993.

[4] M.SENCAR and S.N.AKSAN, Evaluation of reflooding models in RELAP5/MOD2.5, RELAP5/MOD3/v5m5 and RELAP5/MOD3/v7j codes by using Lehigh University and PSI-NEPTUN bundle experimental data, to be presented at the NURETH-7 Conference, 10-15/9/1995, Saratoga Springs, NY, USA.

[5] K.E. CARLSON et al., RELAP5/MOD3 Code Manual Volume IV: Models and correlations (Draft), June 1990.

[6] V.H. RANSOM et.al., RELAP5/MOD2 Code Manual Volume 1: Code Structure, System Models and Solution Methods, NUREG/CR- 4312, (1985).

[7] G. TH. ANALYTIS, Development and assessment of a modified version of RELAP5/MOD3: A search for excellence, Invited paper presented at the RELAP5 International User's Seminar, Baltimore, Maryland, USA, August 29 - September 1, 1994

[8] G.TH. ANALYTIS and M. RICHNER, *Trans. Amer. Nucl. Soc.*, **53**, 540 (1986).

[9] G. TH. ANALYTIS, M. RICHNER and S. N. AKSAN, Assessment of Interfacial Shear and Heat Transfer of RELAP5/MOD2/36.02 During reflooding, **EIR Report Nr. 624**, 1987.

[10] D.D. TAYLOR et al., TRAC-BD1: An Advanced Best-Estimate Computer Program for Boiling Water Reactor Transient Analysis, NUREG/CR-3633 (1984).

[11] G. TH. ANALYTIS, Developmental Assessment of TRAC-BF1 with Separate-Effect and Integral Reflooding Experiments. NURETH-5 Conference, 21-24/9/1992, Salt-Lake City, Utah, U.S.A, Vol. I, pp 287 - 293.

[12] M. ANDREANI, Private Communication (1993).

[13] H. GRÜTER, F. STIERLI, S.N. AKSAN and G. VARADI, NEPTUN Bundle reflooding experiments: Test Facility description, EIR Report Nr.386 (1980).

[14] D. LÜBBESMEYER, Post-Test-Analysis and Nodalization Studies of OECD LOFT Experiment LP-LB-1 with RELAP5/MOD2/CY36.02, PSI Report Nr.91 (1991).

[15] F. D'AURIA and G.M. GALASSI, Assessment of RELAP5/MOD2 code on the Basis of Experiments performed in LOBI Facility, *Nuclear Technology*, Vol 90, Nr. 3 (1990)

[16] D. LÜBBESMEYER, Private communications (1992).

A STUDY OF THE DISPERSED FLOW INTERFACIAL HEAT TRANSFER MODEL OF RELAP5/MOD2.5 AND RELAP5/MOD3

M. Andreani*, G.Th. Analytis+ and S.N. Aksan+

*Nuclear Engineering Laboratory
Swiss Federal Institute of Technology
ETH-Zentrum, CH-8092 Zurich
Switzerland

+Thermal-Hydraulics Laboratory
Paul Scherrer Institute
CH-5232 Villigen PSI
Switzerland

Abstract

The model of interfacial heat transfer for the dispersed flow regime used in the RELAP5 computer codes is investigated in the present paper. Short-transient calculations of two low flooding rate tube reflooding experiments have been performed, where the hydraulic conditions and the heat input to the vapour in the post-dryout region were controlled for the predetermined position of the quench front.

Both RELAP5/MOD2.5 and RELAP5/MOD3 substantially underpredicted the exit vapour temperature. The mass flow rate and quality, however, were correct and the heat input to the vapour was larger than the actual one. As the vapour superheat at the tube exit depends on the balance between the heat input from the wall and the heat exchange with the droplets, the discrepancy between the calculated and the measured exit vapour temperature suggested that the inability of both codes to predict the vapour superheat in the dispersed flow region is due to the overprediction of the interfacial heat transfer rate.

1 Introduction

An extensive program of assessment, development and application of the RELAP5 and TRAC/B reactor safety computer programs has been underway for some time in the Thermal-Hydraulics Laboratory of the Paul Scherrer Institute (PSI).

One of the reactor safety issues to which the research has been specially addressed is the reflooding phase of the LOCA. The main results of this research and the contributions to the code development in the areas of wall heat transfer, interfacial drag, and numerical techniques have been fully documented [1][2][3]. For several reflooding experiments, it has been observed that both the trend and the values of the calculated results (wall and vapour temperatures, entrainment, collapsed liquid level, etc.) obtained by the 'frozen' version of the codes were very different from the measured experimental data. These discrepancies were noticeably large, especially for low flooding rate conditions. Low flooding rate experiments are characterized by very high void fractions all over the region above the Quench Front (QF), for long time periods. In this zone droplets are dispersed in a stream of superheated vapour, and the so-called Dispersed Flow Film Boiling (DFFB)

heat transfer regime controls the wall cooling rate. The incorrect calculation of either the vapour superheat or the wall heat transfer coefficient resulted in the poor predictions of the 'frozen' versions of the codes.

The implementation of more consistent packages of correlations for wall heat transfer and interfacial shear (for both the wet and dry wall regions), the accurate selection of several empirical constants entering in the various models on the base of sensitivity studies, and the modification of interpolation schemes lead to improved versions of the programs, which successfully simulate most experiments with *bundles* (references above).

Modifications to the closure laws (droplet size, interfacial heat transfer) related to the dispersed flow regime above the QF have also played a role in the achievement of good results. However, since only a few quantities (average temperatures, entrainment rate, quench front velocity, etc.) are measured and therefore used for the assessment, the adequacy of the closure laws used for the individual submodels can seldom be demonstrated.

In the present paper, a different approach to the analysis of the reflooding process is presented, which is more suitable for evaluating the capabilities of one of the submodels used in the codes, namely that for interfacial heat transfer in the dispersed flow region.

This study on the interfacial heat transfer model for the dispersed droplet regime in the RELAP5 computer codes was motivated by a previous general investigation [4][5] on the validity of the 1-D models usually adopted for calculating DFFB. The 1-D approach used for calculating the heat exchange between the vapour and the droplets in the dispersed flow region above a QF was shown to be questionable for conditions of low quality at the QF, and low mass flux. An extensive steady-state analysis of the heat transfer processes above the QF was performed for such conditions using the 1-D capabilities of a 3-D computer program developed for that purpose [5][6]. This study revealed that the vapour superheat was strongly underpredicted when the multi-dimensional effects were neglected, independently of the choice (within reasonable limits) of the droplet diameter [5]. The reason for the limitations of the 1-D approach was found to be the overprediction of the interfacial heat transfer. On the other hand, the 3-D model, accounting for the liquid droplets distribution, predicted vapour temperatures much closer to the measured values [5]. It was thus inferred that the reason for the failure of the 1-D approach is its inability to account for the accumulation of liquid around the centre where the driving temperature difference for interfacial heat transfer is low [5][7].

The present analysis using RELAP5 is, therefore, aiming at verification of such a general statement by a specific application of the 1-D approach. In this respect, the most interesting variable for judging the capability of the model is the vapour temperature at the exit of the test section, and this will be the main theme of the discussion of results. For this purpose, it is convenient to assess the codes against data obtained in single-tube experiments which avoid 'spurious' effects due to the presence of the grids on, for example, the droplet size. The results of two low flooding rate tube reflooding tests [8] were used in the present analyses.

The complete transient runs were carried out first [9]. However, while the aim of these codes is to analyze the transient behaviour of a complex system, much deeper insight in the influence of the interfacial heat transfer on the mixture evolution is made possible by considering 'snapshots' at different times during the transient. The values of several variables are considered constant over a short time period, and the analysis is referred to such a 'frozen' picture. The rationale for the consequent 'short-transient analysis' is briefly outlined here, and discussed in more depth in §4. This analysis is intended to approximate a quasi steady-state analysis, which cannot be performed by means of transient codes such as RELAP5. For forcing a 'short transient' to approach a quasi steady-state calculation the conditions above the QF must be assumed constant over a short time, and the wall heat flux over the tube length above the QF must be given as input. If good predictions

for both liquid and vapour mass flow rates are obtained, the resulting vapour temperature at the tube exit (which depends on the total heat exchanged with the droplets) will give a direct estimate of the adequacy of the interfacial heat transfer closure law used in the code. Indeed, the uniform heat flux which characterizes the single-tube experiments leads to slowly-changing axial wall temperature distributions and allows a sufficiently good estimate of the local heat flux at all elevations. This, in turn, allows a rather accurate evaluation of the total power input to the mixture above the QF (on which the vapour superheat strongly depends) to be made at any selected time, so that one of the unknowns which complicates the interpretation of the results of the transient analyses, namely the instantaneous 'actual' power input, can be eliminated.

Therefore, the present work focuses on a short-transient analysis of two low flooding rate tube reflooding experiments for the time of the mid-height quench.

2 Test Cases Used For The Assessment

Well documented experimental results for the reflooding of a non-insulated tube (3.66 m length and 14.25 mm inside diameter) were obtained at the University of California at Berkeley [8]. Two low mass flux tube reflooding experiments were analyzed: run 3051 at 2 bar and run 3053 at 3 bar. For both experiments, the initial wall temperature was 812 K and the inlet liquid velocity and subcooling were 2.5 cm/s and 80 K, respectively. These experiments were chosen because the separate steady-state analyses [5][7], showed severe limitations of the 1-D approach.

During many tests, the wall temperatures at some distance from the QF displayed nearly constant values for long times, with the heat input balanced by the heat losses and the heat transfer to the fluid. In the present investigation, the 'short-transient' analyses are chosen to begin at the earliest time such a quasi-steady condition (the quality at the QF being positive) for the wall temperatures at the higher elevations is attained.

The equilibrium quality immediately above the quench front x_{QF} is calculated by adding the quality immediately below the quench front x^- (as calculated by an energy balance over the wet region) to the quality change across the QF due to the intense vaporization caused by the release of the heat stored in the tube wall. The net heat flux q''_{in} at each elevation is obtained by subtracting from the inside-wall 'imposed' heat flux (the total power input to the test section, divided by the internal surface area), the heat losses (referred to the inside-wall surface area) and the sensible heat stored in the wall. The total heat input to the fluid in the dry region above the quench front P_{dry} is calculated by integrating q''_{in} over the wall heat exchange area. Values for the several variables required for the 'short-transient' analyses are given by Andreani et al. [9].

3 Transient Analysis

A transient analysis of run 3051 has been performed [9] with the 'frozen' versions of both RELAP5/MOD2.5 [10] and RELAP5/MOD3 [11]. The reflooding wall heat transfer package was then utilized in the calculation with RELAP5/MOD2.5; this option does not affect the correlations used by RELAP5/MOD3 as a unique wall heat transfer package is used for all conditions. Here, the results [9] are summarized:

- The calculated mass accumulated inside the tube, the collapsed liquid level, the vapour flowing out of the test section and the total liquid carry-out were all well predicted. One may therefore conclude that both code versions predicted the 'average' hydraulic behaviour of the system fairly well.

- The quench front progression, however, was substantially overpredicted by both codes. The test section quenched completely in about 550 s, while both codes predict complete quench within 160 s.

- The calculated vapour temperature in the uppermost node decreased early close to the saturation temperature whereas in the experiment remained for a long time around 600 K.

The fast desuperheating of the vapour at the tube exit is thus in accordance with the hypothesis that the interfacial heat transfer rate is overpredicted by the 1-D models. However, in the present calculation, the low vapour temperature was probably driven by the early rewetting of the wall, caused by inadequacies in the wall heat transfer package [3].

Therefore, with respect to the main goal of the present work, namely the assessment of the interfacial heat transfer model for Dispersed Flow, it appears that little can be concluded from the transient analysis; hence, the analysis of experiment 3053 (for which results similar to those obtained for test 3051 are expected) was not carried out.

4 Short-transient Analyses

4.1 Formulation

The basic idea behind the short-transient analysis has already been introduced in §1; here the mathematical formulation of this approach, as well as the conditions which must be fulfilled in order to arrive at the evaluation of the capabilities of the interfacial heat transfer model using only the experimental vapour temperature at the tube exit, are discussed.

When the quenching process progresses slowly, and at constant rate, as is usual when the quality at the QF is positive, the thermal-hydraulic conditions at any point in the channel downstream from the QF (wall and fluid temperatures, mass flows, qualities, etc.) vary slowly as well. The quasi steady-state condition is thus realized if the time necessary for the QF to move a significant distance (e.g., the distance between the centres of the volumes above and below the 'nominal' position of the QF) is larger than the residence time of the droplet in the post-CHF region. If this prerequisite is satisfied, any slow variation of the QF position (and quality) will lead to slow variations of the hydrodynamic variables downstream and the evolution of the mixture can be described by the usual conservation equations, dropping the time-derivatives.

The steady-state forms of the vapour continuity and energy equations can be written for a straight tube of cross-sectional area A as:

$$\frac{d}{dz}(< \alpha_g >< \rho_g > U_g) = \frac{dG_g}{dz} =< \Gamma > \tag{1}$$

$$< \alpha_g >< \rho_g > U_g \frac{dH_b}{dz} = G_g \frac{dH_b}{dz} = Q_{wg} + < Q_{ig} > - < \Gamma > (H_b - H_{g,s}) \tag{2}$$

where U_g, H_b, G_g, Q_{wg} and $< Q_{ig} >$ are the (averaged) axial vapour velocity, the bulk vapour enthalpy, the vapour mass flux, the phasic wall heat transfer rate per unit volume and the cross-sectionally-averaged interfacial heat transfer rate per unit volume, respectively. These are similar to those used in the RELAP5 codes, except that dissipation is neglected and the enthalpy is used instead of the internal energy.

By integrating between the QF elevation z_{QF} and the tube exit elevation z^T Eq. (2) Multiplying Eq. (2) by the tube flow area A and integrating between the QF elevation z_{QF} and the tube exit elevation z^T one obtains:

$$\int_{z_{QF}}^{z^T} AG_g \frac{dH_b}{dz} dz = \int_{z_{QF}}^{z^T} Q_{wg} A dz + \int_{z_{QF}}^{z^T} < Q_{ig} > A dz - \int_{z_{QF}}^{z^T} \Gamma(H_b - H_{g,s}) A dz$$

and, integrating by parts the first term in the left hand side of the equation,

$$\begin{aligned} AG_g^T H_b^T - AG_{g,QF} H_{g,QF} - \int_{z_{QF}}^{z^T} AH_b \frac{dG_g}{dz} dz \;=\; & \int_{z_{QF}}^{z^T} Q_{wg} A dz + \\ & \int_{z_{QF}}^{z^T} < Q_{ig} > A dz + \\ & - \int_{z_{QF}}^{z^T} \Gamma(H_b - H_{g,s}) A dz \end{aligned}$$

Using the continuity equation (1), and replacing $G_g A$ by the vapour mass flow rate $\dot{M}_g$, it follows that:

$$\begin{aligned} \dot{M}_g^T H_b^T - \dot{M}_{g,QF} H_{b,QF} \;=\; & \int_{z_{QF}}^{z^T} Q_{wg} A dz + \int_{z_{QF}}^{z^T} < Q_{ig} > A dz + \int_{z_{QF}}^{z^T} \Gamma H_b A dz \\ & - \int_{z_{QF}}^{z^T} \Gamma(H_b - H_{g,s}) A dz \end{aligned}$$

Observing that:

$$\int_{z_{QF}}^{z^T} \Gamma A dz = \dot{M}_g^T - \dot{M}_{g,QF}$$

one can write, assuming saturated vapour at the QF:

$$\dot{M}_g^T H_b^T = \dot{M}_{g,QF} H_{b,QF} + P_{g,dry} + \int_{z_{QF}}^{z^T} < Q_{ig} > A dz + (\dot{M}_g^T - \dot{M}_{g,QF}) H_{g,s} \tag{3}$$

where $P_{g,dry}$ is the total heat transfer rate to the vapour alone in the dry-wall region. If all the droplet population is represented by an average diameter d, the average interfacial heat transfer rate per unit volume is:

$$< Q_{ig} >= \frac{6h_i}{d} < (1 - \alpha_g)(T_b - T_s) > \tag{4}$$

where h_i is the interfacial heat transfer coefficient.

Since, in a 1-D model, the droplet concentration is assumed uniform over the cross section and the distribution coefficient is taken equal to unity, the relation:

$$< (1 - \alpha_g)(T_b - T_s) > \equiv < (1 - \alpha_g) >< (T_b - T_s) > \tag{5}$$

leads to:

$$< Q_{ig} >= \frac{6h_i}{d} < (1 - \alpha_g) >< (T_b - T_s) > \tag{6}$$

In both RELAP5/MOD2.5 and RELAP5/MOD3 a modified Lee and Ryley correlation is used for calculating h_i:

$$h_i = \frac{k_g}{d}(2 + 0.5\,Re^{0.5}) \tag{7}$$

where Re is the droplet Reynolds number. The other two variables which affect the calculation of Q_{ig} directly, namely $< \alpha_g >$ and d, are mainly influenced by the interfacial drag and by the maximum stable droplet diameter, respectively. The correlations for calculating these variables have practically the same form in both codes [10][11]: the differences between the two codes will be briefly outlined in §4.2.2, where their effects on the different results obtained will also be discussed.

Equation (6) is the relation that, under low mass flux and low quality conditions, will lead to the overprediction of the interfacial heat transfer, and the underprediction of the vapour temperature [5][7]. It is the aim of the present analysis to show that, by assuming Eq. (6) to be always valid, the Q_{ig} in RELAP5 is overestimated. In the present investigation, the validity of Eq. (7) will not be discussed, as an extensive analysis [12] of DFFB has shown that the predictions of the interfacial heat transfer cannot be improved by simply choosing a different correlation for h_i. Poor prediction were obtained for several low mass flux experiments also using the correlation which yields the lowest values for h_i [5][12].

From Eq. (3) one easily realizes that if the gas mass flow rate at the QF and the tube exit calculated by the computer code are (approximately) equal to the experimental ones, and the total wall-to-vapour heat transfer is the same as in the experiment, any deviation of the exit enthalpy (temperature) can be attributed to the incorrect prediction of the interfacial heat transfer. This estimation can be done irrespective of the wall-to-liquid heat transfer, and the consequent vapour production at the wall.

Therefore, to make the short-transient to approach a quasi steady-state condition, four conditions (Fig. 1) must be fulfilled in the calculation:

1. The time needed by the QF to advance a substantial length from the 'reference' QF position is much longer than the droplet residence time t_r ($\equiv (z^T - z_{QF})/\bar{U}_l$, $\bar{U}_l$ being the axially averaged drop velocity). The average values of the variables during this time (which we will call the 'averaging period' t_{av}) can be compared with the values obtained by a steady-state analysis.

2. The same (approximately) x_{QF} ($\dot{M}_{g,QF}$) to be adopted as in the experiment during the averaging period t_{av}.

3. The total heat input to the vapour to equal to the experimental value.

4. The same $\dot{M}_g^T$ as in the experiment.

The first two conditions can be satisfied by restricting the analysis to a section of the tube including the region downstream of the 'nominal' position of the QF, and a short length upstream of it. The fluid injected at the bottom of this 'reduced' length section is a mixture with quality close to that inferred from the experiment. The QF progresses from the inlet of the section up to the nominal location of the QF (and the quality at the QF changes accordingly), for which the tube exit vapour temperature must be compared with the experimental value. From this time on, and until the time the first node above z_{QF} quenches, the values of the various variables of interest are considered.

With respect to the third condition, the heat input to the vapour can only be approximated, as the total heat flux to the mixture is known only at the measurement stations. In order to prove

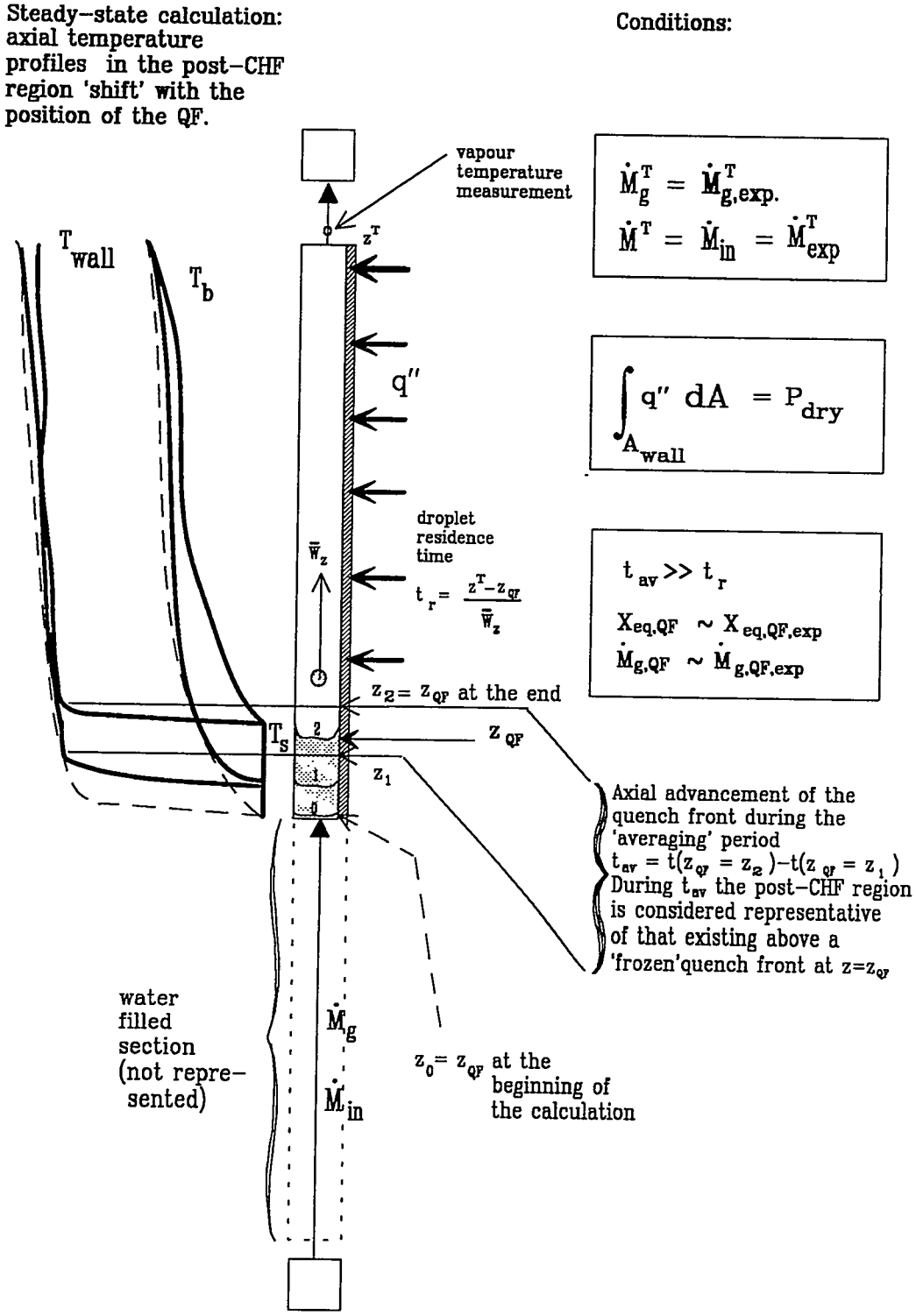


Figure 1: Prerequisites for the 'short-transient' analysis to approach a quasi steady-state representation of the zone above a slowly advancing quench front (under these conditions the interfacial heat transfer model can be assessed).

that the low vapour temperatures are due to the overprediction in the interfacial heat transfer, the calculations will use upper bounds for the wall heat transfer rates.

With regard to the fourth condition one can only assume that the computer program predicts liquid and vapour carry-out flow rates close to the experimental ones at the time of the mid-height quench. This expectation is confirmed by the results of the transient analysis above, where both calculated liquid and vapour carry-out were in excellent agreement with measured values. For the purpose of testing the interfacial heat transfer model, lower vapour mass flows than measured in the experiment can also be accepted, as the calculated vapour superheat is enhanced by a reduced vapour mass flow. Similarly, the liquid carry-out must be approximately equal to or lower than the experimental value. A calculated liquid mass flow much higher than in the experiment would imply a large concentration of liquid at high elevation: the consequent vapour desuperheating effect could not be related to the 1-D approach for the interfacial heat transfer.

In order to avoid misunderstandings, it is appropriate to repeat here that, since RELAP5 is a transient code, our 'short-transient' analysis consists in running the program over the short time period needed by the QF to advance from the inlet of the tube to the node immediately above the elevation z_{QF}, chosen for the analysis.

In summary: the analysis will be restricted to a shorter tube length, its inlet being a few cm below the QF. The quench front moves from the inlet to a certain predetermined elevation above z_{QF}. From the time the QF is close to z_{QF}, the quality immediately above must be close to x_{QF}, and the power input to the vapour in the dry region must be equal to $P_{g,dry}$; this last condition can be approximated by imposing the condition that the total heat transfer rate to the mixture is equal to or larger than the experimental P_{dry}. The mass flows at the tube exit will be monitored; if these are in close agreement with the experimental data (obtained by differentiating the experimental water and vapour carry-out), the vapour temperature at the tube exit will be compared with the experimental data.

4.2 Short-transient analysis of run 3051

4.2.1 Calculation with RELAP5/MOD2.5

The nodalization used for the short-transient analysis with the MOD2.5 version is shown in Fig. 2 and consists of ten short (0.03 m) cells below z_{QF}, and nine cells representing the above-QF region. The total mass flow rate was imposed. The inlet quality x_{in} was estimated by checking the value of x_{QF} at the end of the transient, as calculated from an energy balance performed by means of a control variable. This gave x_{in} at about 6%. The need for this procedure is due to the oscillations in the calculation of the mass flows immediately above the QF, which render a direct estimation of the quality impossible. The imposed value of x_{in} led to x_{QF} slightly higher than in the experiment (Fig. 3). The entrained liquid flow rate was, consequently, a little lower.

The axial heat flux distribution at the wall was initially imposed according to the experimental profile [9]. Unfortunately, the calculation stopped after a few seconds because a very large amount of heat was transferred directly to the vapour (in spite of the fact that a bubbly flow regime was predicted), and this led to vapour temperatures as high as 3000 K. It was realized that RELAP5, for imposed heat flux conditions, calculates the heat fluxes to the two phases by splitting the total heat input into two *equal* parts, irrespective of the flow regime.

It was thus necessary to change our approach of imposing the heat flux, and the following boundary conditions were used instead:

- Imposed power generation;

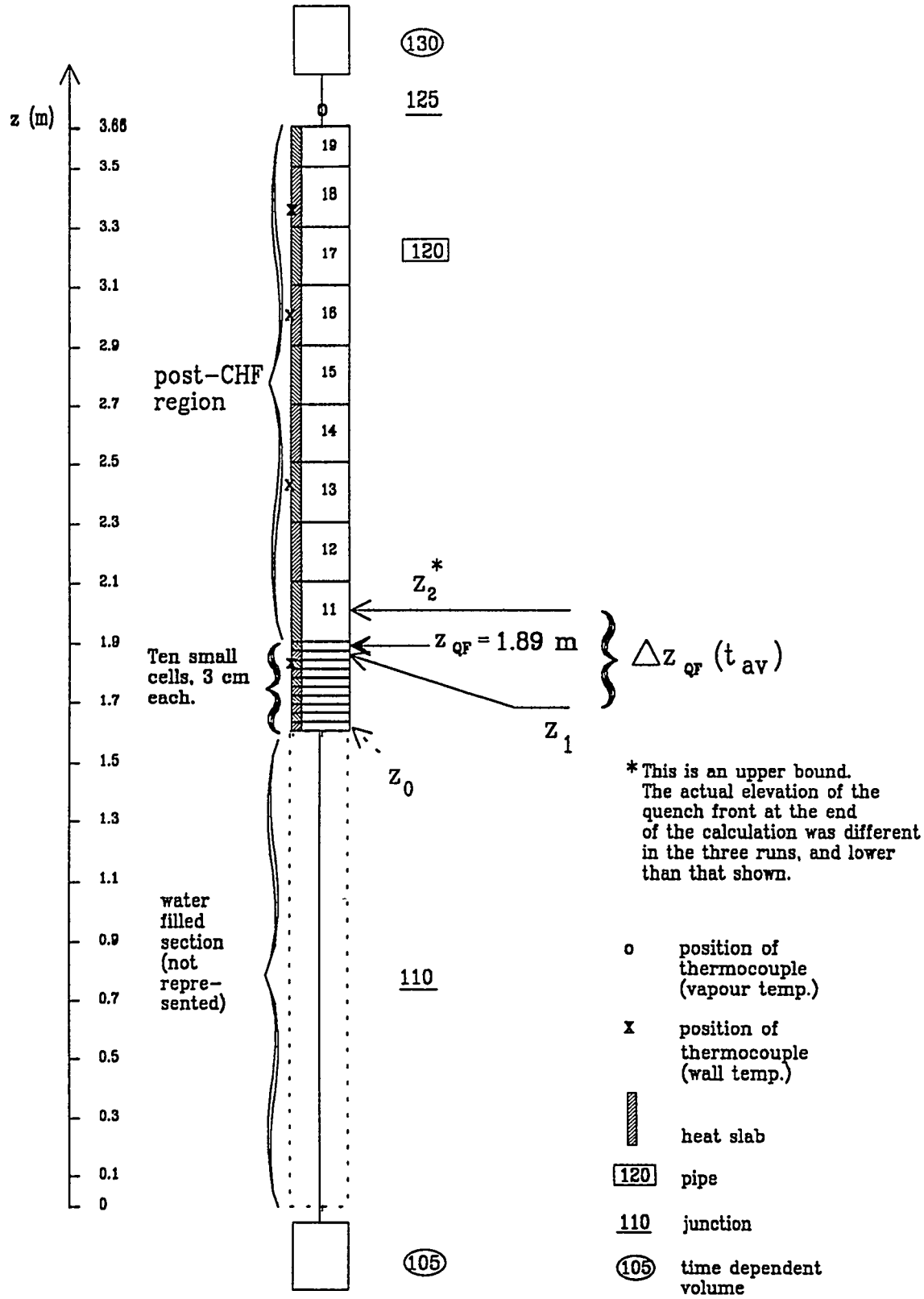


Figure 2: Nodalization used for the short-transient analysis of run 3051 by RELAP5/MOD2.5.

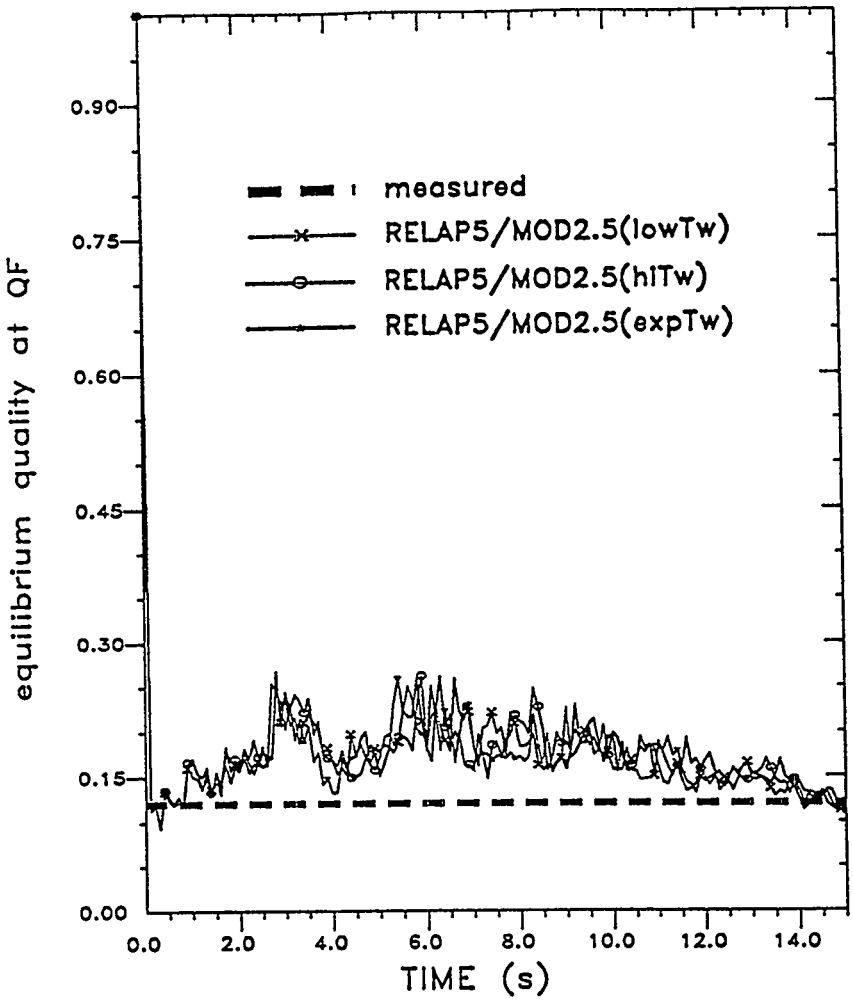


Figure 3: Equilibrium quality immediately above the QF calculated using the three different initial wall temperature distributions (Fig. 4). Inlet quality $x_{in} = 0.06$.

- Imposed experimental heat losses at the time selected for the beginning of the short-transient (t=150 s);
- Imposed axial temperature profile. As the heat flux is then calculated by the reflooding heat transfer package, the total heat input to vapour is not controlled, but varies during the short period of time of the short-transient analysis, and depends mainly on the initial wall temperature. Therefore, three different axial wall temperature profiles are imposed, and the resulting heat input to the vapour is calculated. The three axial wall temperature profiles, shown in Fig. 4, are:

  1. **exp**: experimental wall temperature distribution.
  2. **low**: temperatures decreasing with the distance from the QF. These values have been found (by trial and error) to yield (approximately) the desired axial heat flux distribution (Fig. 5).
  3. **high**: temperatures higher than those experimentally observed.

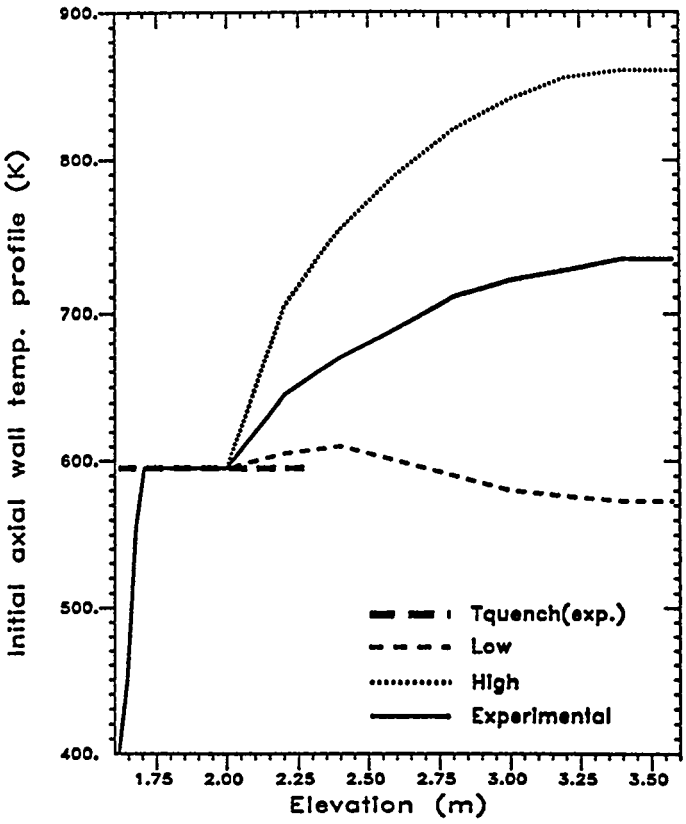


Figure 4: Initial axial wall temperature distributions used for the short-transient analysis of test 3051 at the time of the mid-height quench.

The resulting wall heat fluxes averaged over the last 5 s of the calculations are given in Fig. 5.

The transient for the three cases was set to 15 s. The temperature histories showed: 1) the wall temperatures at some distance from the QF ($z \geq 2.2$ m) are practically constant during the calculation time, and 2) in the time period between 10 and 15 s the QF lies somewhere between 1.855 m and 2.0 m. The time needed for the QF to advance from 1.855 m to 2.0 m was found to be larger than the droplet residence time t_r ($\simeq$ 1-2 s), so that the first requirement for the 'short-transient' analysis were satisfied.

The equilibrium quality at the QF oscillated during the transient, but was close to the experimental value, at least for times larger than 10 s.

The vapour mass flow rate at the tube exit was also in close agreement with the experimental value. However, the liquid mass flow rate exhibited large oscillations: their, amplitude, however, did not exceed 30% of the measured average flow rate. The fact that the average values (between 10 and 15 s) of the total mass flow rate and exit quality were quite close to the experimental values suggests that the hydraulic behaviour is, in general, well predicted.

The total power input to the vapour (Fig. 6) was, in all cases, at least as high as the total (experimental) heat input to the mixture, so that also the thermal boundary condition on the vapour superheat evolution is also satisfied in all cases.

Under the conditions mentioned above, the average values of the several quantities of interest for our analysis during the time period from 10 to 15 s are thus comparable with those obtained from a steady-state analysis for the QF 'frozen' at 1.89 m. Thus, it does make sense to compare the

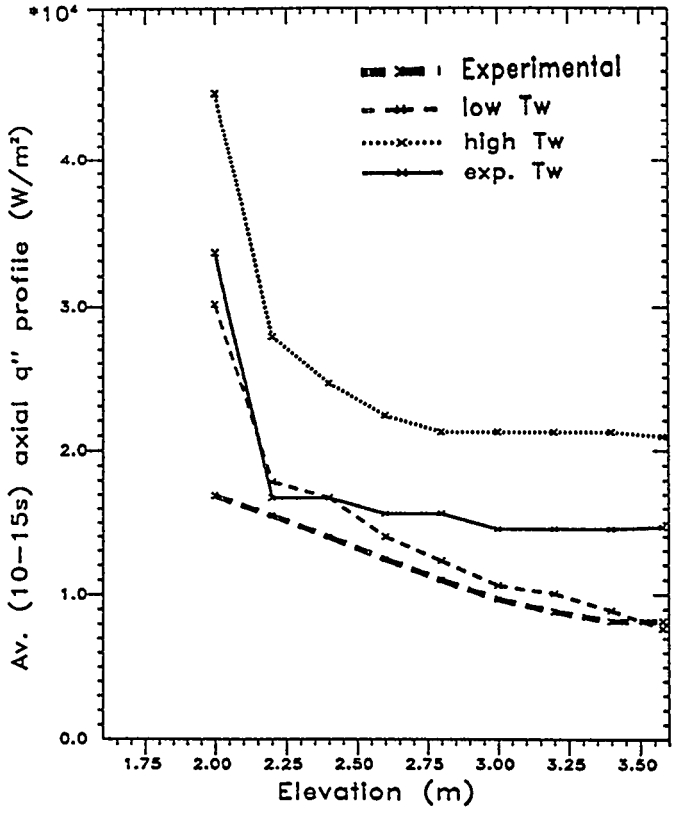


Figure 5: Average axial wall heat flux distributions during the time span 10-15 s for the three initial axial wall temperature distributions shown in Fig. 4.

calculated vapour temperature with the measured value. In Fig. 7, it can be observed that after 10 s the vapour temperature (while being unstable) is always underpredicted by at least 50 K, even when the power input to the vapour is twice as much as the experimental total heat transfer rate to the mixture (Fig. 6). The large underprediction (150 K) of the vapour temperature observed for the initial wall temperature (lowTw) distribution, which yields a value of P_{dry} close to experiment is in fairly good agreement with that expected on the basis of the steady-state separate model [7].

From the RELAP5/MOD2.5 calculations, we can thus conclude that the interfacial heat transfer must be overpredicted. The possible sources contributing to the overprediction are:

1. The liquid fraction may have been overestimated. This, however, can almost be excluded because of the imposed entrainment and the fairly good prediction of the liquid carry-out. A correct estimate of the axial liquid distribution can thus be supposed.

2. The correlation for the interfacial heat transfer coefficient h_i yields too high values. This is probably true. However, calculations by means of a separate steady-state program [6] showed that the 1-D approach underpredicted the vapour temperature even when a correlation yielding much lower values of h_i was used [7].

3. The interfacial heat transfer coefficient (h_i) is possibly overpredicted because of a large average value of the phase velocity difference. Indeed, one can suspect that large oscillations in the liquid velocity (leading even to negative velocities) can still be compatible with a correct average value of the liquid mass flow, but yield (because of the non-linear dependence of the

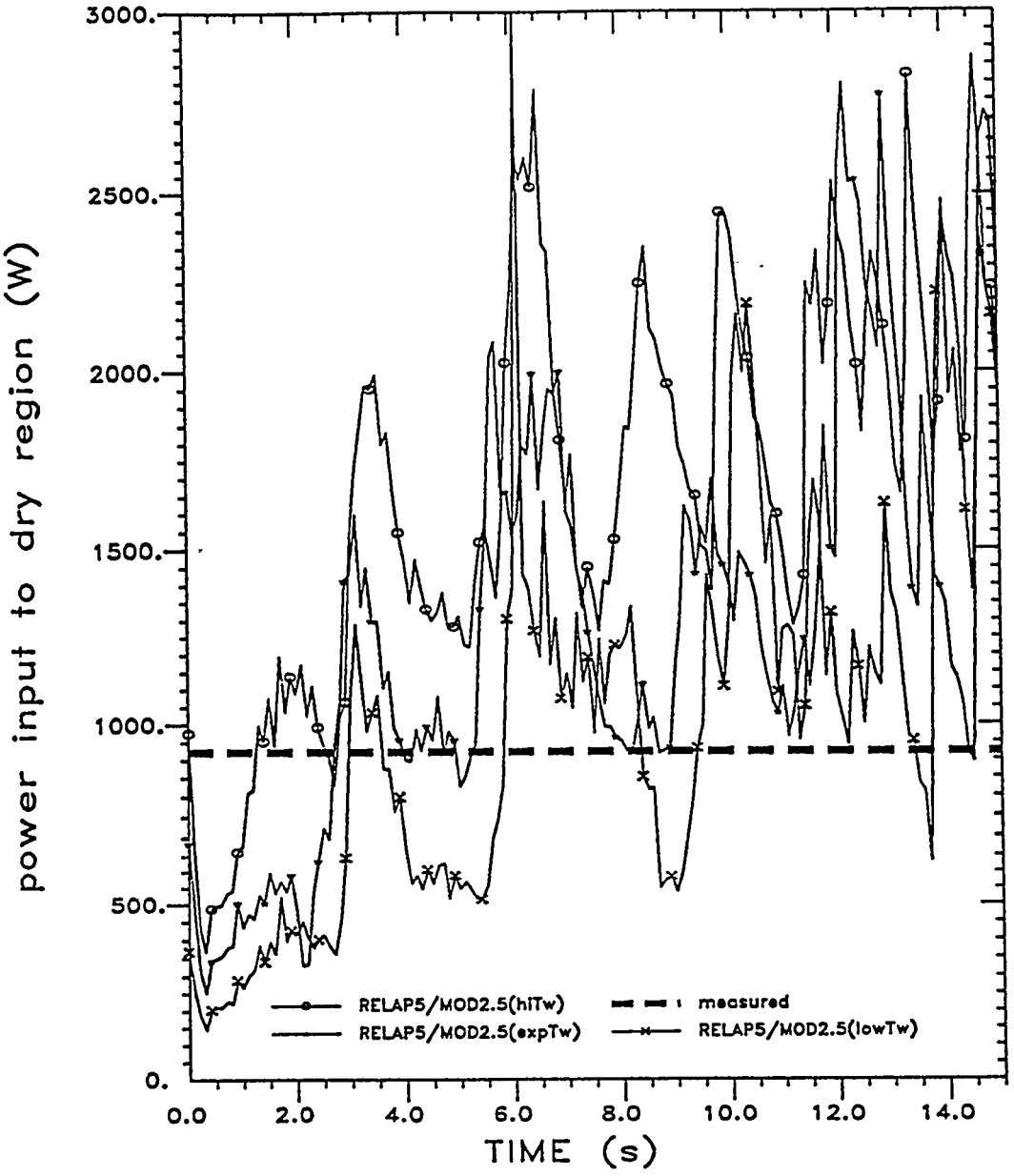


Figure 6: Comparison of the heat transfer rate to vapour with the total power input to the mixture measured in the experiment (run 3051).

heat transfer coefficient on the phase velocity difference $(U_g - U_l)$) large values of h_i. This can be also excluded as it was observed that the velocity difference at two elevations was quite stable.

4. The interfacial heat transfer coefficient used by the code might be inadequate because it neglects the effect of interactions between the droplets. No data, however, substantiate the suspicion that interaction effects at high void fraction can reduce the interfacial heat transfer rates to the extent necessary to reconcile calculations and experiments.

5. The droplet diameter may be underpredicted. The separate, steady-state analyses [5][7]

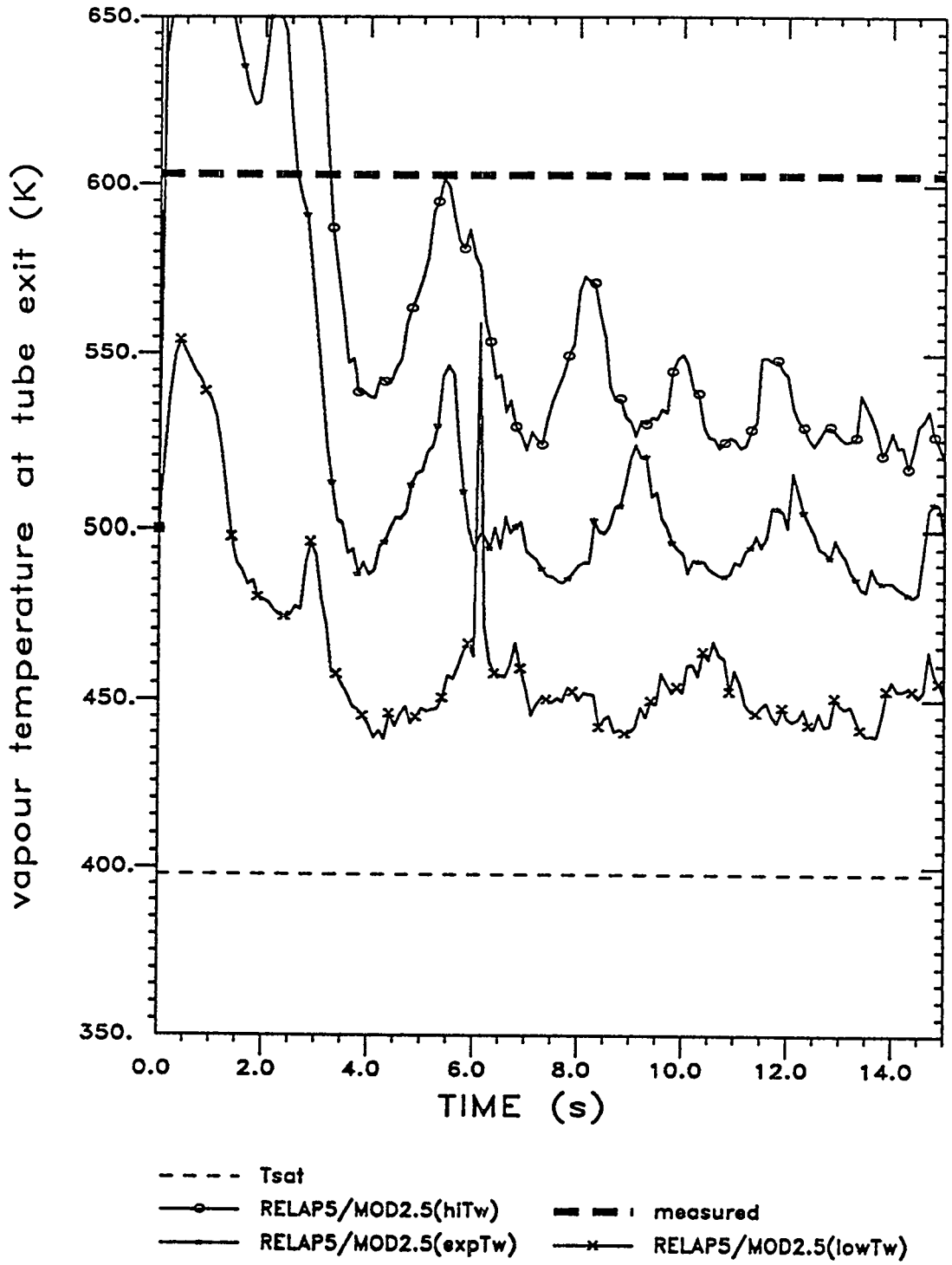


Figure 7: Comparison of the calculated vapour temperature at the tube exit with the experimental value at the time of the mid-height quench (run 3051).

showed, however, that for a wide range of droplet diameters the results are very similar to those obtained using the RELAP5/MOD2.5 criterion.

6. The only possibility left is, therefore, that the interfacial heat transfer rate (Eq. 6) is based on the wrong assumption of uniform distribution of the heat sinks (droplets) over the cross section.

Other calculations (not shown) have been carried-out using the normal (blowdown) heat transfer package, and slowing down the propagation of the QF by increasing the thickness of the heat slabs in the region below it. The vapour temperature at the tube exit was still underpredicted by at least 100 K.

In addition, a version of the code was generated in which the wall-to-liquid heat transfer was forced to zero within 30 cm from QF. The axial wall temperature profile was imposed in such a way as to preserve the total experimental power input to the dry region (P_{dry}), so that the heat transfer rate to the vapour ($P_{g,dry}$) was practically equal to the total measured value. Even under these conditions, the calculated vapour temperature was still much lower than in the experiment.

4.2.2 Calculation with RELAP5/MOD3

For the analysis with RELAP5/MOD3, the nodalization had to be slightly modified. This was due to the fact that the first calculation showed that the QF was progressing much faster than in the corresponding RELAP5/MOD2.5 calculation. Under these circumstances, the time necessary for the QF to propagate from the node below z_{QF} to the node above it (time t_{av} over which the thermal-hydraulic conditions of the post-CHF region can be considered approximately insensitive to the actual location of the QF around the imposed z_{QF}) became comparable with the droplet transit time: the averaging of the variables over the time period t_{av} was consequently becoming of dubious meaning. Therefore, larger nodes (50 mm instead of 30 mm) were used for the section below z_{QF} and for the node including z_{QF}. Moreover, the time over which the average values of the variables discussed above are calculated is made dependent on the transient, i.e., the averaging period is between the time the wall temperature in the cell below z_{QF} falls below the quench temperature (580 K) and the time this happens to the first node in the 'dry' zone. When the wall temperature in the node above the QF falls below 580 K the transient is thus terminated.

The first calculation, performed by using initial wall temperatures equal to the experimental values, also showed a very high heat transfer rate in the dry zone, nearly double that measured in the experiment, and a much larger vapour mass flow, resulting from the large evaporation rates caused by the high wall-to-liquid heat transfer. Hence, the low axial wall temperature distribution (Fig. 4) was used for the subsequent calculations. During the time 8 to 12 s, the QF was between 1.825 and 2.0 m and the equilibrium quality at the QF, though oscillating, was close to the experimental value.

The vapour temperature at the tube exit (Fig. 8) was predicted quite well, but it was realized from the negligible liquid carry-out that this was due to the deficiency of liquid in the region far away from the QF. In fact, the water accumulated in the region immediately downstream from the QF (notice the high void fractions at high elevations in Fig. 9), so that no heat sink was available to the steam further up. It was originally believed that one of the reasons for the insufficient liquid carry-over could be the larger value of the critical Weber number (We_{cr}=12) used in MOD3 with respect to that used in MOD2.5 (We_{cr}=3), which results in the calculation of quite large droplets in the mist-flow region, which cannot be lifted by the drag force.

It was then decided to perform the calculation with a modified version of the code developed at PSI (version bb) which, among other features, uses the same We_{cr} as in MOD2.5. This modified

version has been described by Analytis [3] and no details are given here: it suffices to say that better numerical stability is achieved and several unphysical effects (like the void fraction passing through a minimum immediately below the QF) are eliminated by the utilization of more physical correlations. The use of this improved version of the program, resulted in a little higher carry-out, but still much lower than in the experiment.

In order to understand the reasons why the utilization of the same criterion for the droplet size yields different results in RELAP5/MOD2.5 and in RELAP5/MOD3, the overall calculation scheme of the interfacial drag in RELAP5/MOD3 was reviewed. It was realized that, for reflooding calculations, the droplet diameter was bound by a lower limit of 2.5 mm. This value appears arbitrary, and for sensitivity analysis purposes it was changed to 1.25 mm in a new version of the code, which was called UPX. Moreover, it has been found out that the drag coefficient for droplets is defined as:

$$C_D = \min\{C_{D,v}, 0.45\} \tag{8}$$

where the drag coefficient for the viscous regime $C_{D,v}$ is given by:

$$C_{D,v} = \frac{24}{Re}(1 + 0.1\,Re^{0.75}) \tag{9}$$

It is clear from Eqs. (8,9) that for large Re (large droplets) the drag coefficient attains very low values. However, the drag coefficient for a solid sphere is asymptotically approaching the value 0.45 for $Re > 1000$ (Newton regime), being *higher* for lower values of Re (Ishii and Mishima [13]). The value of C_D for fluid particles is even higher, as they get distorted. Equation (8) is then basically incorrect and even if one wants to consider the droplets as solid spheres, it must be replaced by the usual criterion:

$$C_D = \max\{C_{D,v}, 0.45\} \tag{10}$$

Equation (10) was then implemented in the version UPX.

The liquid carry-out was larger than in the previous calculations, but it was still too low. The axial void fraction distribution showed a larger presence of liquid at the higher elevations (Fig. 9), and this determined the lower vapour temperature (Fig. 8).

It was also observed that the calculated heat transfer rate to the mixture was higher than in the experiment, but the heat transfer rate to the vapour was about 30% lower. However, radiation from wall-to-droplets can account for a significant portion of the wall heat transfer [7][12], so that the actual heat transfer rate to vapour $P_{g,dry}$ is likely to be predicted realistically.

Further attempts to modify the code in order to get the correct liquid mass flow were not performed. As a trend, it has been already established that, for decreasing values of the droplet diameter, more and more liquid can be carried over, and increasing underprediction of the vapour temperature results.

These results are thus in agreement with those obtained by RELAP5/MOD2.5 and by the steady-state analyses performed by a separate program [5][7].

4.3 Short-transient analysis of run 3053 by RELAP5/MOD2.5

Experiment 3053 was practically the same as 3051, the only difference being the higher pressure (3 bar instead of 2). The analysis has been performed only by RELAP5/MOD2.5, because of the difficulties in the prediction of the liquid carry-out by MOD3, which render the interpretation of the results more difficult. Two axial wall temperature distributions have been tested, only.

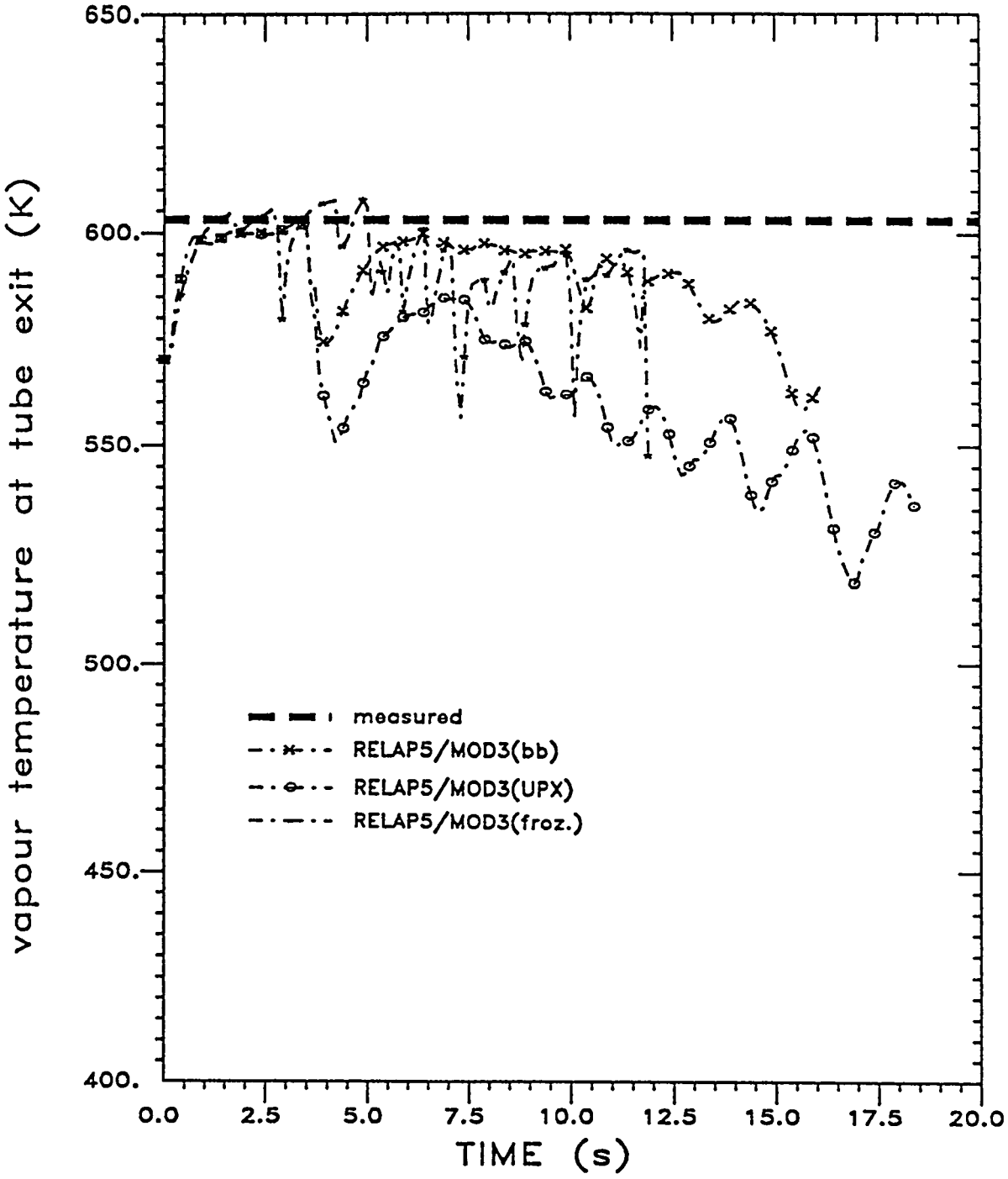


Figure 8: Vapour temperature at the tube exit calculated by the frozen RELAP5/MOD3 (– · – · –), by a version (bb) including the PSI updates (– · ✕ · – : Analytis [2]) and an 'ad hoc' modification (version UPX) of the RELAP5/MOD3(bb) using a reduced value for the minimum droplet diameter and the correct drag coefficient for droplets (– · ⊖ · –).

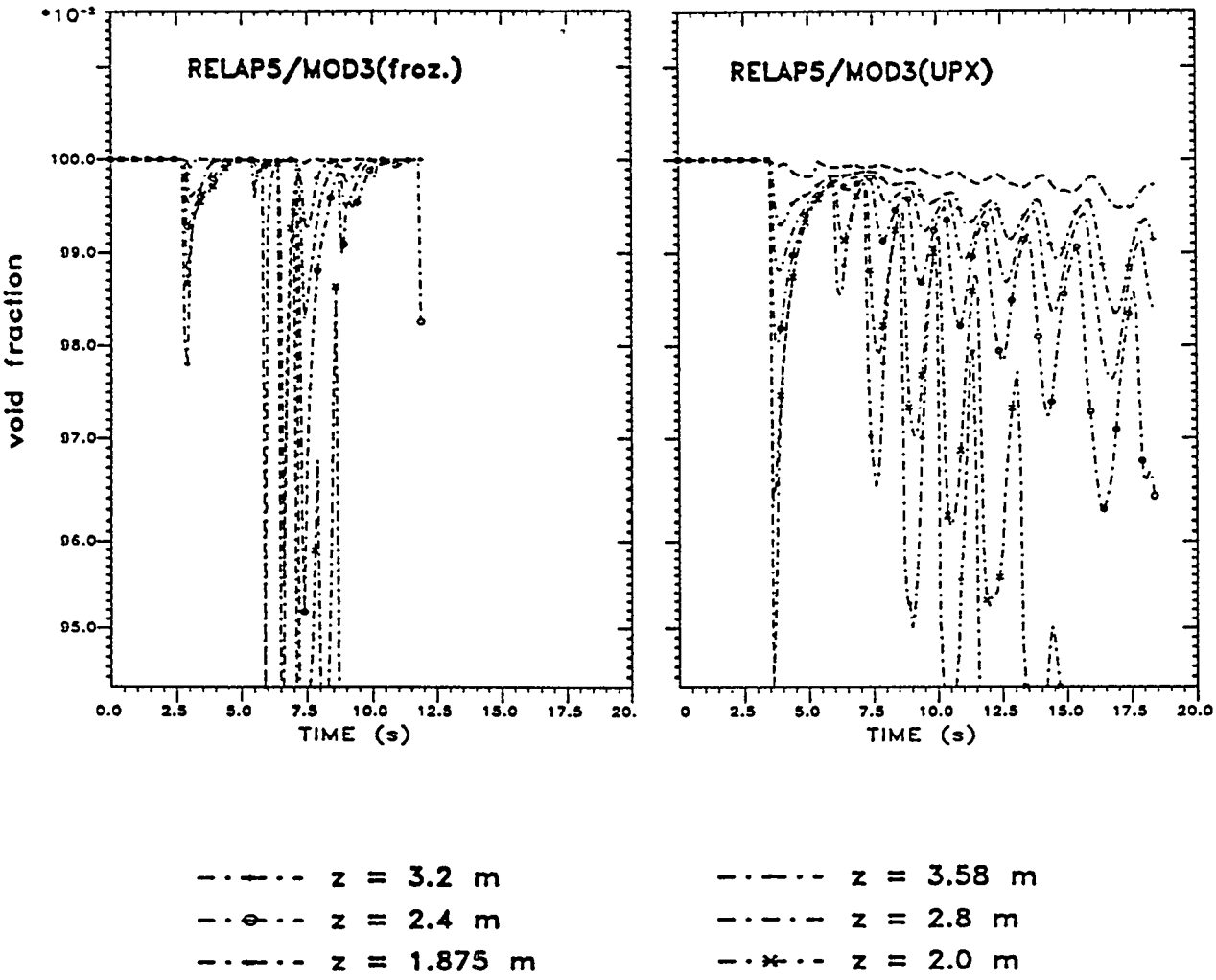


Figure 9: Void fractions at various elevations calculated for run 3051 by the frozen version of RELAP5/MOD3 (left) and by the modified version UPX (right).

The calculation time was 14 s, since the node above the 'nominal' value of z_{QF} quenches at that time. The time span over which the results are representative of a steady QF at 2.05 m (QF between 2.055 m and 2.2 m) is 8 to 14 s.

The quality at the QF was correctly obtained and the heat transfer to the vapour alone was much larger than the experimental *total* power input (Fig. 10). The calculated liquid carry-out and the total mass flow at the exit decreased during the averaging period to values lower than in the experiment. The calculated vapour carry-out was, however, always larger than in the experiment, due to an excessive evaporation in the tube. Therefore, one necessary condition for a fully-meaningful comparison between calculated and experimental vapour temperature was not satisfied (see §4). We note, however, two circumstances: 1) the experimental total mass flow was

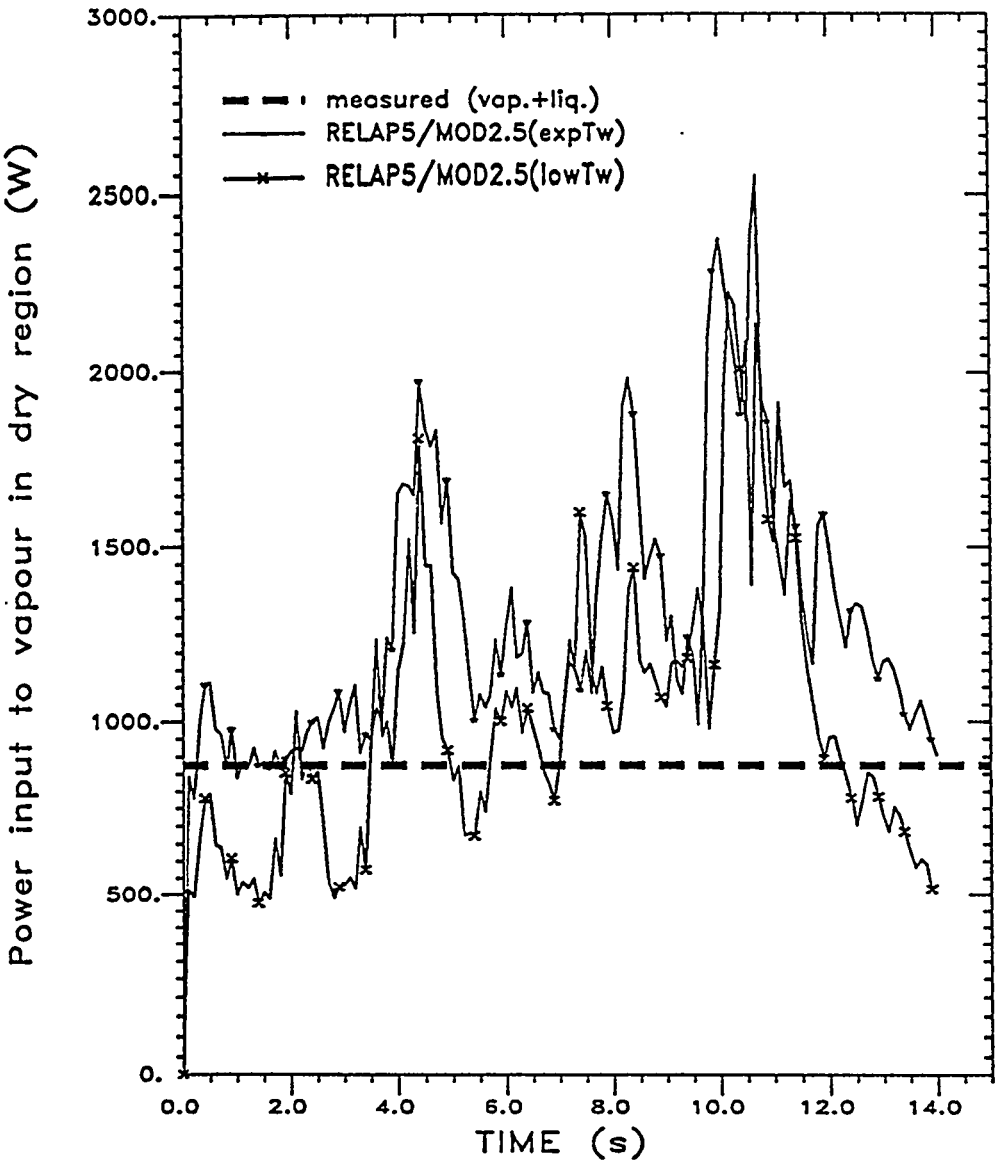


Figure 10: Heat Transfer rate to the vapour in the post-dryout region for two initial wall temperature distributions (run 3053).

probably larger than that measured in the test, as a certain error in the mass balance was found [9]; and 2) the heat input per unit volume of the flowing vapour is at least as large as in the experiment, since $P_{g,dry}$ was substantially larger than the total experimental heat flux.

It is thus possible to state that the large underprediction of the vapour temperature at the tube exit (Fig. 11) was again due to the overprediction of the interfacial heat transfer, and not to an overprediction of the vapour mass flow.

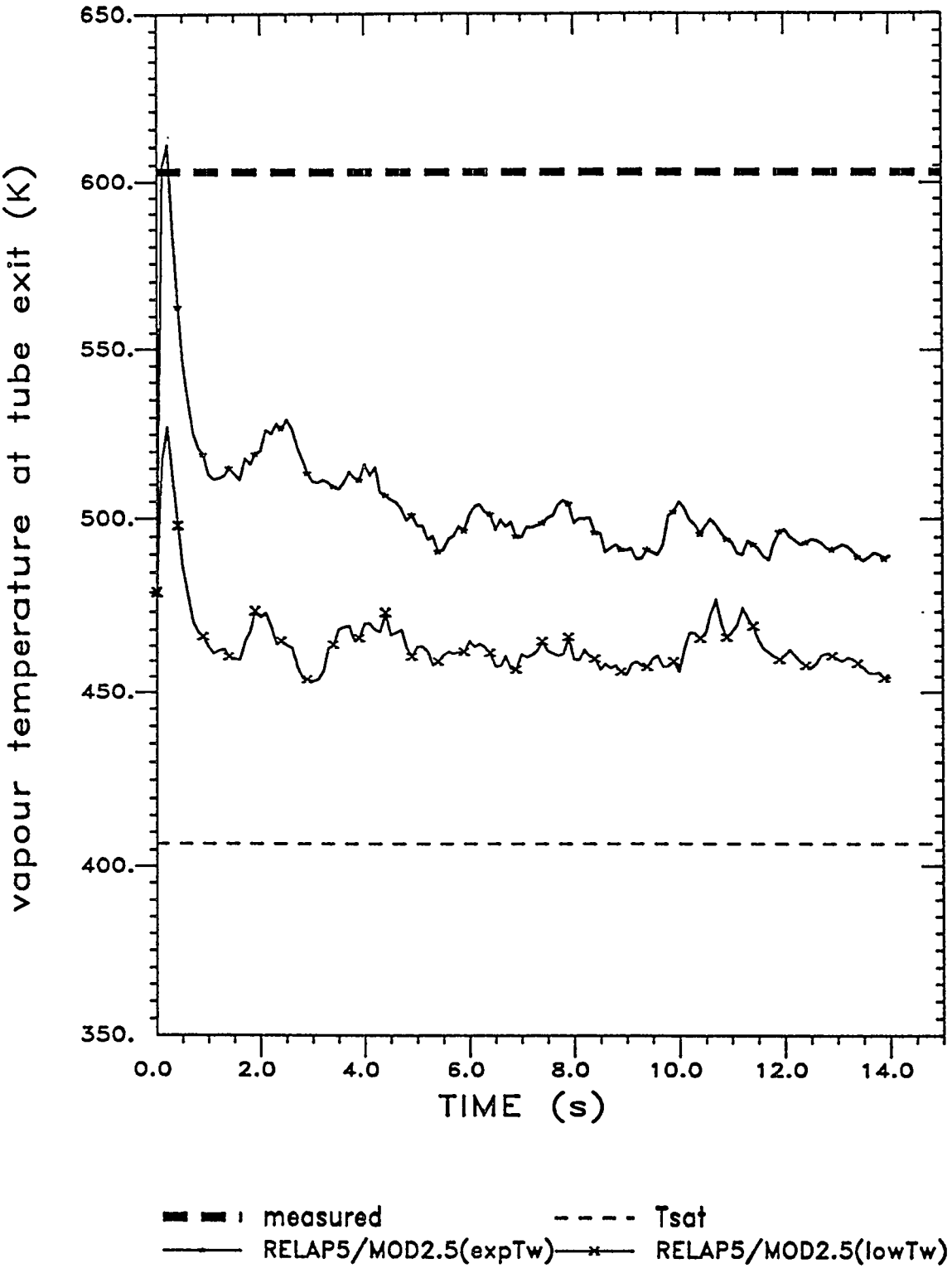


Figure 11: Vapour temperature at the tube exit calculated by RELAP5/MOD2.5 for two initial wall temperature distributions (run 3053).

5 Conclusions

The main goal of the present work was the assessment of the interfacial heat transfer model for the Dispersed Flow Film Boiling region above a quench front as implemented in a well established, 1-D computer code.

The transient analysis of a low flooding experiment by means of RELAP5/MOD2.5 and RELAP5/MOD3 has shown that both codes overpredict quench front propagation rates: this can be attributed to an inadequate modelling of the heat transfer phenomena in the vicinity of the QF and confirms other similar analyses. The vapour temperature at the tube exit dropped to the saturation value much earlier than in the experiment, but it could not be conclusively stated whether a too high interfacial heat transfer contributed to the poor predictions.

A short-transient analysis has thus been performed. A short transient was run, during which the quench front was allowed to advance a short distance from the position of interest, and imposing (approximately) the quality at the quench front. The power input to the mixture could be controlled, to a certain extent, by setting the initial wall temperature distribution above the quench front.

The RELAP5/MOD2.5 code calculated correctly the total carry-out but overpredicted the total heat transfer to the vapour. In spite of this, the vapour temperature was substantially underpredicted. It could be concluded therefore that the interfacial heat transfer was overpredicted.

RELAP5/MOD3 showed a large underprediction of the liquid carry-out, and this led to a good prediction of the vapour temperature. However, when the calculation was repeated using two other versions of the code, where the closure laws affecting the droplet dynamics were modified in a way to allow a larger carry-out (though still lower than experiment), the vapour temperature was again underpredicted.

The short-transient analysis of a second experiment at 3 bar was also performed by RELAP5/MOD2.5, and results similar to those obtained for the test at 2 bar were obtained.

It can be concluded that, as expected from the separate steady-state analysis, computer codes such as RELAP5 overpredict the desuperheating effect of the liquid, and hence underpredict the vapour temperature at large distances from the quench front. Taking into consideration Eq. (6), one can suspect various reasons for the overprediction of the interfacial heat transfer. These have been discussed in §4.2.1. There, it was shown that the most likely source of error is the cross-sectional averaging process used in 1-D codes (such as RELAP5), which neglect the actual cross-sectional droplet distribution. The present calculations confirmed the statement that the 1-D Dispersed Flow Film Boiling approaches are inadequate under low mass flux and low quality conditions. No attempt was made, however, to improve the results by reducing the interfacial heat transfer rate, since no information on any possible reduction factor is available. Even though the effects of the cross-sectional distribution of the liquid could yield such a reduction, no proof exists that this is the actual mechanism producing the necessary reduction in the interfacial heat transfer rate; only experiments can provide us with such evidence.

It is thus recommended that specific experiments for measuring the cross-sectional liquid fraction distribution are carried out, to test the hypothesis that the liquid accumulation in the centre does take place. If this phenomenon will be confirmed experimentally, the root to an improved interfacial heat transfer model for codes like RELAP5 can be the development of a correlation for a correction factor of the interfacial heat transfer rate per unit volume, trying to account for the 3-D effects.

Nomenclature

A	cross-sectional flow area
C_D	drag coefficient
d	droplet diameter
G_g	vapour mass flux
h_i	interfacial heat transfer coefficient
H_b	bulk vapour enthalpy
$H_{g,s}$	vapour saturation enthalpy
$\dot{M}_g^T$	vapour mass flow rate at the tube exit
$\dot{M}_{g,QF}$	vapour mass flow rate at the quench front
q''_{in}	wall heat flux
Q_{wg}	wall heat transfer rate to the vapour per unit volume
Q_{ig}	interfacial heat transfer rate per unit volume
P_{dry}	heat input to the mixture above the QF
$P_{g,dry}$	heat input to the vapour above the QF
QF	Quench Front
Re	droplet Reynolds number ($Re \equiv \rho_g(U_g - U_l)d/\mu_g$)
t_r	droplet residence time
T_b	vapour bulk temperature
T_s	saturation temperature
U_g	axial vapour velocity
U_l	axial droplet velocity
$\bar{U}_l$	axially averaged droplet velocity
x^-	quality below QF
x_{QF}	quality above QF
We	Weber number $= \rho_g(U_z - U_l)^2 d/\sigma$
z_{QF}	quench front elevation (nominal position)
z^T	tube exit elevation
α_g	void fraction
Γ	vapour generation rate
ρ_g	vapour density
σ	surface tension

References

[1] S.N.Aksan, G.Th.Analytis and D.Lübbesmeyer, "Switzerland's Code Assessment in support of the International Code Assessment and Application Program (ICAP)," Proc. 16th Water Reactor Safety Information Meeting, NUREG/CP-0097, 4, 245-273 (1989).

[2] G.Th.Analytis, "A Comparative Study of the Post-CHF Wall Heat Transfer Packages of the RELAP5 codes and Preliminary Assessment of Model Changes in RELAP5/MOD3/v7j," Paper presented at the 1st Code Assessment and Maintenance Program (CAMP) Meeting, Villigen, PSI, Switzerland (1992).

[3] G.Th.Analytis, "A Summary of Model Changes and Options in RELAP5/MOD3," Paper presented at the 2nd Code Assessment and Maintenance Program (CAMP) Meeting, Brussels, Belgium (1993).

[4] M.Andreani and G.Yadigaroglu, "Dispersed Flow Film Boiling. An Investigation of the possibility to improve the models implemented in the NRC computer codes for the reflooding phase of the LOCA," NUREG/IA-0042 (1992).

[5] M.Andreani and G.Yadigaroglu, "Effect of the Cross-Sectional Droplet Distribution in Dispersed Flow Film Boiling at Low Mass Flux," Proc. 5th International Topical Meeting on Nuclear Reactor Thermal-Hydraulics (NURETH-5), 3, 823-831 (1992).

[6] M.Andreani and G.Yadigaroglu, "A 3-D Eulerian-Lagrangian Model of dispersed Flow Film Boiling Including a Mechanistic Description of the Droplet Spectrum Evolution. Part I: The Thermal-Hydraulic Model," (forthcoming) accepted for publication in the International Journal of Heat and Mass Transfer.

[7] M.Andreani and G.Yadigaroglu, "A 3-D Eulerian-Lagrangian Model of Dispersed Flow Film Boiling. Part II: Assessment using Quasi-Steady State Data and Comparison with the Results of 1-D Analyses-Hydraulic Model," (forthcoming) accepted for publication in the International Journal of Heat and Mass Transfer.

[8] R.A.Seban, "Reflooding of a Vertical Tube at 1,2 and 3 Atmospheres," EPRI Report, EPRI NP-3191 (1983).

[9] M.Andreani, G.Th.Analytis and S.N.Aksan, "A Study of the Dispersed Flow Interfacial Heat Transfer Model of RELAP5/MOD2.5 and RELAP5/MOD3," Paul Scherrer Institute (PSI) Internal Report, TM-42-94-06 Villigen, Switzerland (1994).

[10] V.H.Ransom, "RELAP5/MOD2 Code Manual," NUREG/CR-4312, Rev. 1 (1987).

[11] K.E.Carlson et al., "RELAP5/MOD3 Code Manual," Vol. 1, 2, 3, and 4, Draft, NUREG/CR-5535 (1990).

[12] M.Andreani, "Studies of Dispersed Flow Film Boiling with 3-D Lagrangian Hydrodynamics and a 2-D Eulerian Vapour Field," Doctoral Dissertation, Swiss Federal Institute of Technology (ETHZ), Zurich (1992).

[13] M.Ishii and K.Mishima, "Two-Fluid Models and Hydrodynamic Constitutive Relations," Nucl. Eng. and Des. 82, 107-126 (1984).

ASSESSMENT OF COMPUTER CODES FOR VVER-440/213-TYPE NUCLEAR POWER PLANTS

L. Szabados, Gy. Ézsöl, L. Perneczky

KFKI Atomic Energy Research Institute
H-1525 Budapest, P.O.Box 49, Hungary

ABSTRACT

Nuclear power plants of VVER-440/213-type designed by the former USSR have a number of special features. As a consequence of these features the transient behaviour of such a reactor system should be different from the PWR system behaviour.

To study the transient behaviour of the Hungarian Paks Nuclear Power Plant of VVER-440/213-type both analytical and experimental activities have been performed. The experimental basis of the research is the PMK-2 integral-type test facility, which is a scaled down model of the plant. Experiments performed on this facility have been used to assess thermal-hydraulic system codes. Four tests were selected for "Standard Problem Exercises" of the International Atomic Energy Agency. Results of the 4th Exercise, of high international interest, are presented in the paper, focusing on the essential findings of the assessment of computer codes.

INTRODUCTION

The aim of the Standard Problem Exercises (SPE) of the International Atomic Energy Agency (IAEA) is to assess the modelling capabilities of thermal-hydraulic codes for VVER systems. Until now four IAEA-SPEs have been performed in the framework of projects between the IAEA and the KFKI Atomic Energy Research Institute (AEKI) in the time interval of 1985 to 1994. Results of the first three Exercises are published in Refs. [1], [2], [3].

The experimental basis of the IAEA-SPEs was the PMK-2 integral-type test facility which is a scaled down model of the Paks Nuclear Power Plant equipped with VVER-440/213-type reactors of Soviet design. Such reactors are different from PWRs of usual design and have a number of special features, viz.: 6-loop primary circuit, horizontal steamgenerator (SG), loop seal in both hot and cold legs; safety injection tanks (SIT) inject coolant directly to the reactor vessel and their set-point pressure is higher than secondary pressure.

The objectives of this work are summarized as follows: to give a short description of the PMK-2, to describe the test for SPE-4, to provide selected test findings, to show the results of code assessment, to offer conclusions.

FACILITY AND TEST DESCRIPTION

Facility Description

A detailed description of the facility is given in Refs. [1 to 4]. A short description is given here to facilitate the understanding of the results included in the report.

As shown in Fig. 1, the six loops of the plant are modelled by a single active loop. The pump is accomodated in a by-pass line. The hydroaccumulators (SIT) are modelled by two vessels. Both the low and high pressure systems are modelled (LPIS and HPIS). On the secondary side the feedwater and steam systems, as well as the emergency feedwater system are modelled. The control system of the facility provides any intervention to model the reactor protection system. The data acquisition system has 125 measurement channels with appropriate software to get the results in the desired format necessary for code validation. The core model consists of a 19-rod bundle with axially and radially uniform power distribution. The core model is presented in Fig. 2.

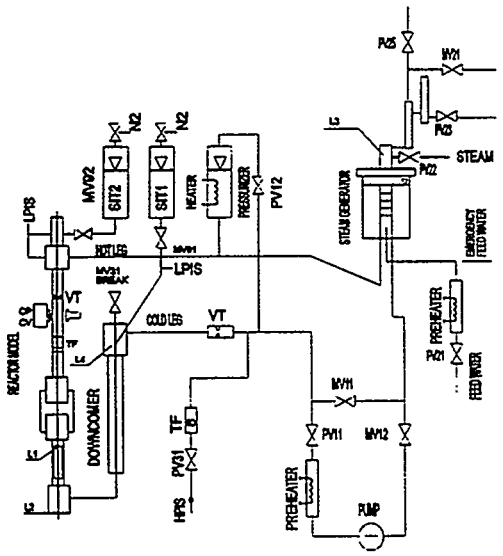
Test Description

The test for the IAEA SPE-4 can be characterized as follows [4]:

- Cold leg break, modelling a 7,4 % (∅ $135 \cdot 10^{-3}$ m) break in the VVER-440/213
- Starting from full power
- With injection from SITs
- Without injection from high pressure injection systems (HPIS)
- With injection from low pressure injection systems (LPIS)
- With secondary side bleed and feed.

The lack of HPI systems leads to a beyond design basis accident To reduce the pressure, secondary side bleed and feed is applied.

The initial steady state conditions and the sequence of events for the experiment and as they are calculated by AEKI using RELAP5/MOD3.1, are given in Tables 1 and 2. The comparison is an example, sequence of events for other codes is given in [5].



Abbreviations:

PV	- pneumatic control valve
MV	- motor valve
VT	- flow measurement device
TF	- flow measurement device
CP	- density measurement device
CV	- density measurement device
SIT-1	- connected to downcomer
SIT-2	- connected to upper plenum
HPIS	- high pressure injection system
LPIS	- low pressure injection system

Fig. 1 Flow diagram of PMK-2 facility

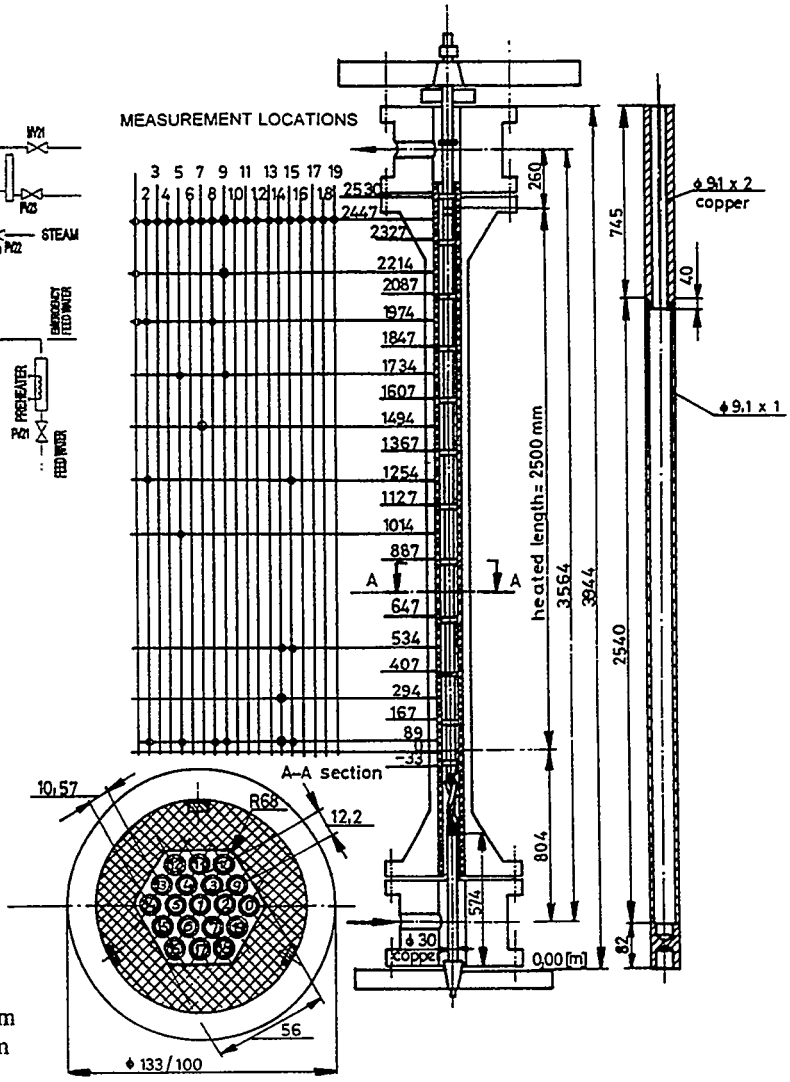


Fig. 2 Core model

The main characteristics are as follows:

- Scaling for power and volume: 1:2070
- Elevation ratio: 1:1
- Pressure: 16 MPa
- Core inlet temperature: 540 K
- Core nominal power: 664 kW
- Nominal flow rate: 4.5 kg/s
- 19 heater rods, with 2.5 m length
- Loop piping: $46 \cdot 10^{-3}$ m ID
- Pressure on the secondary side: 4.6 MPa
- Feed water temperature: 493 K
- Nominal steam mass flow: 0.36 kg/s

Table 1. Initial steady state conditions

Parameter	Units	Experiment	RELAP5/MOD3.1
Pressure in upper plenum	MPa	12.33	12.33
Loop flow	kg/s	4.91	4.91
Core inlet temperature	K	540.1	539.33
Core power	kW	665.12	665.12
Coolant level in pressurizer	m	9.38	9.26
SIT-1 pressure	MPa	6.05	6.05
SIT-2 pressure	MPa	6.04	6.04
Pressure in SG secondary	MPa	4.56	4.56
Feed water flow	kg/s	0.35	0.35
Feed water temperature	K	494.2	494.2

Table 2. Sequence of events

Event	Experiment [s]	RELAP5/MOD3.1 [s]
Break valve starts to open	0	0
Valves PV21 and PV22 start to close	0	0
Transient for power initiated	4	3
Pump cost down initiated	10	12
SIT-1 and SIT-2 actuated	27	34
SIT-1 and SIT-2 emptied (MV91 and MV92 are closed)	388	304
Pump coast down ended	160	162
Secondary bleed initiated	160	-
Dryout	1127	1112
Secondary feed initiated	1427	-
LPIS starts	1381	1427
Test/calculation terminated	1800	2000

ASSESSMENT ACTIVITY IN SPE-4

Participants and Codes

Countries participated in the 4th Exercise are as follows [5]: China, Croatia, Finland, France, Germany, Italy, Russia, Slovakia, Slovenia, Spain, Ukraine, United Kingdom, United States of America and Hungary, as the host country. The total number of organizations is 17.

Thermal-hydraulic system codes currently applied to safety analysis were used in the 4th Exercise as: ATHLET, CATHARE2 V1.3E, RELAP5-MOD2.5, -MOD3, -MOD3.1, and TRAC-PWR. Information on codes and experience on their application are given in [5].

Results of post-test analysis are presented for selected parameters provided by 6 participants as listed in Table 3. By this selection computer codes applied to the SPE-4 are included.

Table 3. Countries, organizations and codes

Item	Country	Organization	Code
1	France	Institute de Protection et de Surete Nucleaire	CATHARE2 V1.3E
2	Germany	SIEMENS AG	RELAP5/MOD2.5/V251
3	Germany	Forschungszentrum Rossendorf	ATHLET
4	Hungary	KFKI-AEKI	RELAP5/MOD3.1
5	Spain	TECNATOM, S.A.	TRAC-PWR
6	USA	Texas A & M University	RELAP5/MOD3.1

Legend in Figs. 4 to 11 are: Item 1: France - IPSN; Item 2: Germany - SIE; Item 3: Germany - ROS; Item 4: Hungary - AEKI; Item 5: Spain - TEC; Item 6: USA - TEXAS.

Computer Code Modelling Aspects

As shown in Table 3, five different computer codes were applied to the calculations. Due to the limitations of the paper, nodalization schemes cannot be included. Data for the nodalizations are given in Table 4. A short description of the modelling aspects is given below.

One of the most important modelling aspect is the right prediction of the pressure on the secondary side of SG, because it strongly affects the pressure decrease in the primary circuit. Another important aspect is the modelling of the break flow, as well as the prediction of the coolant distribution in the primary circuit, especially the coolant level in the core. In the

experiment dryout occurs in the core, when the core is significantly uncovered. Therefore, the prediction of the dryout strongly depends on the prediction of the level and coolant distribution and conditions in the core model.

Table 4. Data for nodalizations

Item	Code	Number of		
		Volumes	Junctions	Slabs
1	CATHARE	326 (total)		
2	RELAP5/MOD2.5/V251	157	162	158
3	ATHLET	97	104	116
4	RELAP5/MOD3.1	108	117	82
5	TRAC-PWR	164	44	25
6	RELAP5/MOD3.1	99	104	96

RESULTS OF ANALYSES

In IAEA-SPE-4 33 parameters were selected for comparison. However, due to the limitations of the paper, 4 parameters are chosen, which are the most representative parameters. They are given in Table 5.

Table 5. Selected parameters

Identification	Elevation [m]	Measurement accuracy (less than ±)	Unit
TE15	3.441	2 K	K
LE11	0.190/9.22	$5 \cdot 10^{-2}$ m	m
PR81	11.21	0.02 MPa	MPa
MA01	-	1.0 kg	kg

The TE15 is the heater rod surface temperature at the outlet of the core model. The Le11 is the coolant level in the reactor model. The PR81 is the pressure on the SG secondary side, while the MA01 is the integrated break mass flow. The locations of sensors are presented in Fig. 1 as L1, L2, L3 and L4.

In accordance with Table 3, two groups of results are presented in Figs. 3 to 10 for parameters given in Table 5. In both groups results of analyses are compared to the experimental results as a function of transient time.

Figs. 3 and 7 present the pressure on the SG secondary side. As shown, the pressure is underpredicted after about 400 s of the transient time which is a consequence of the overprediction of the secondary side bleed. It affects the pressure in the primary circuit resulting in errors in the predicted timing of the pressure actuated events.

Figs. 4 and 8 show the integrated mass flow. Again, predictions are fairly good until 400 s. After that, however, the single phase steam flow through the break is underpredicted except for AEKI and SIEMENS AG.

As shown in Figs. 5 and 9, there are problems in the prediction of the coolant distribution in the loop and especially in the prediction of coolant collapsed level in the reactor model. This discrepancy was identified in Ref. [6]. It is in connection with the cold leg loop seal clearing which has a large effect on the reactor water level. Codes fail to describe correctly the level increase after the clearance which takes place at about 200 s. As a consequence, the coolant level in the core and the timing of the minimum level are underpredicted. This group of phenomena leads to discrepances in the prediction of the dryout in the core (Figs. 6 and 10).

CONCLUSIONS

Sophysticated thermal-hydraulic computer codes were used to model an SBLOCA initiated event with secondary side bleed and feed at the PMK-2 test facility representing a VVER-440/213-type nuclear power plant. The general trend of the predictions is acceptable. Some of the weaknesses of the predictions are as follows:

- In most of the predictions the secondary side bleed is overpredicted resulting in the underprediction of the secondary and consequently the primary system pressure, especially late in the transient.

- The codes fail to predict correctly the cold leg loop seal clearance resulting in some discrepances in the correct prediction of the primary mass inventory distribution, especially the prediction of the coolant level in the reactor model.

- In most of the calculations the dryout in the core is predicted, but at a lower coolant level in the core and with different timing.

In conclusion, the RELAP5/MOD2.5, MOD3.1, CATHARE V1.3E, ATHLET and TRAC-PWR have demonstrated their applicability to model the phenomena during a SBLOCA of this type. The weaknesses, however, show that more analyses are needed to improve the results of these analyses.

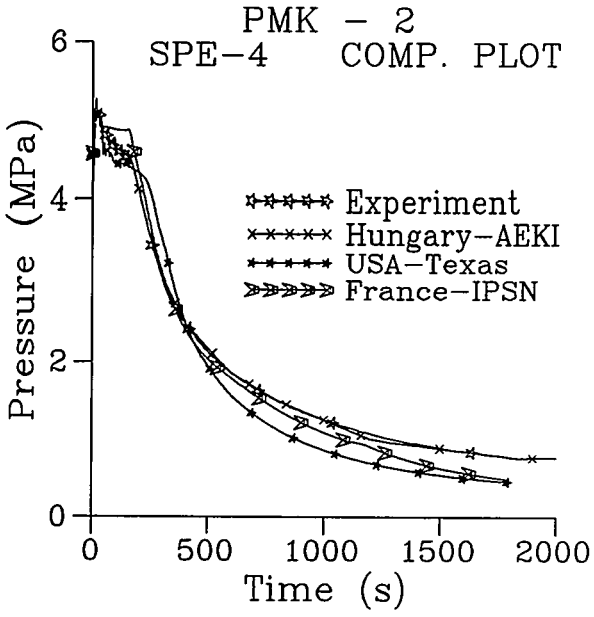


Fig. 3 Pressure in SG secondary

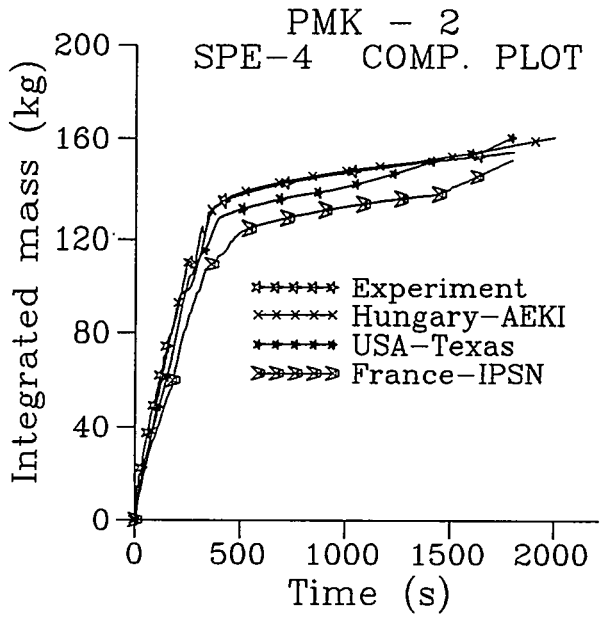


Fig. 4 Integrated mass flow

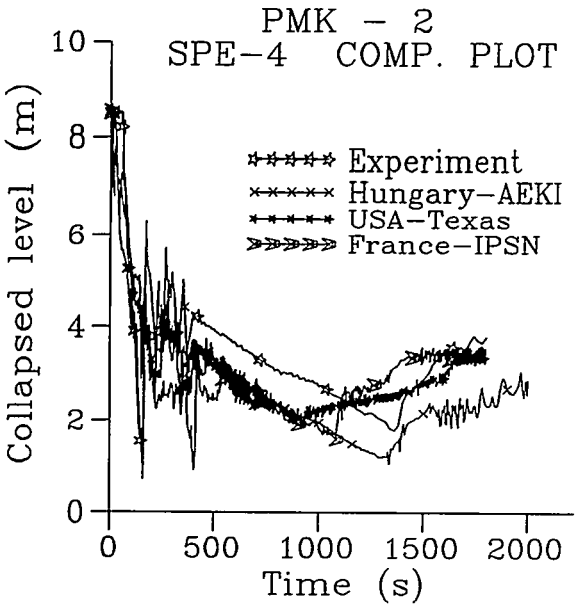


Fig. 5 Reactor model level

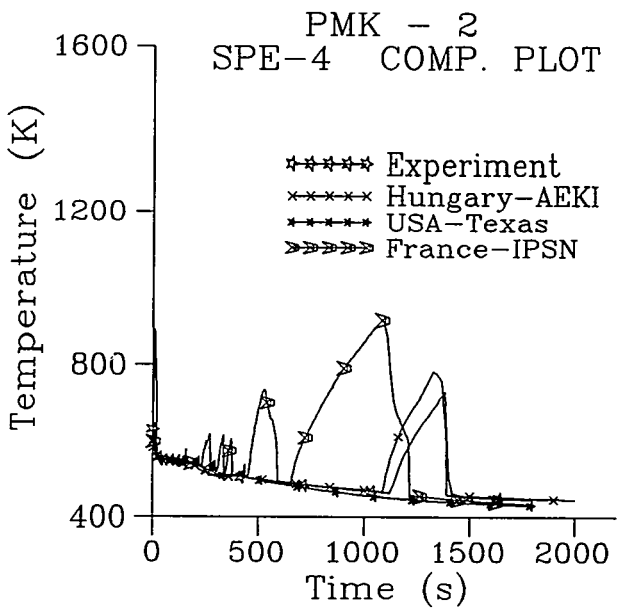


Fig. 6 Heater rod temperature

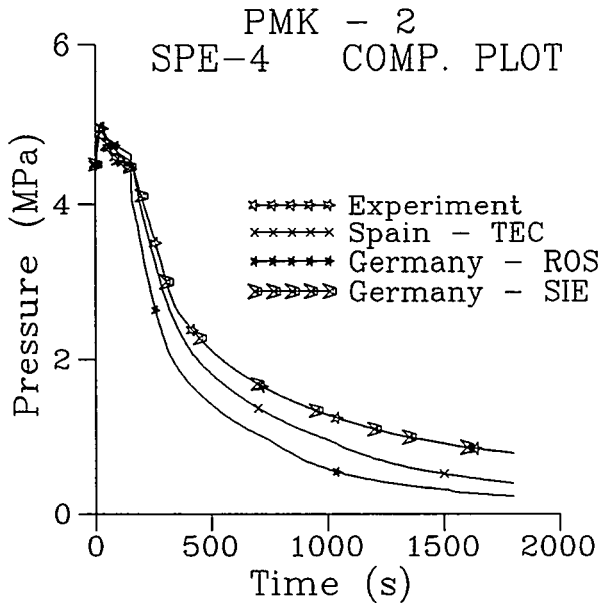


Fig. 7 Pressure in SG secondary

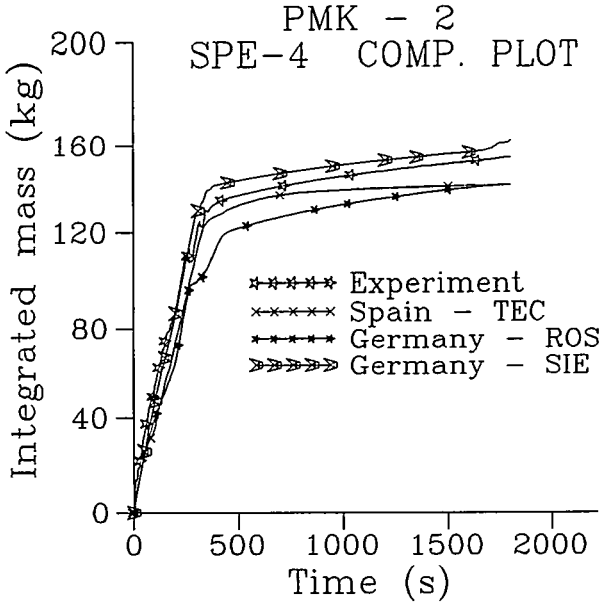


Fig. 8 Integrated mass flow

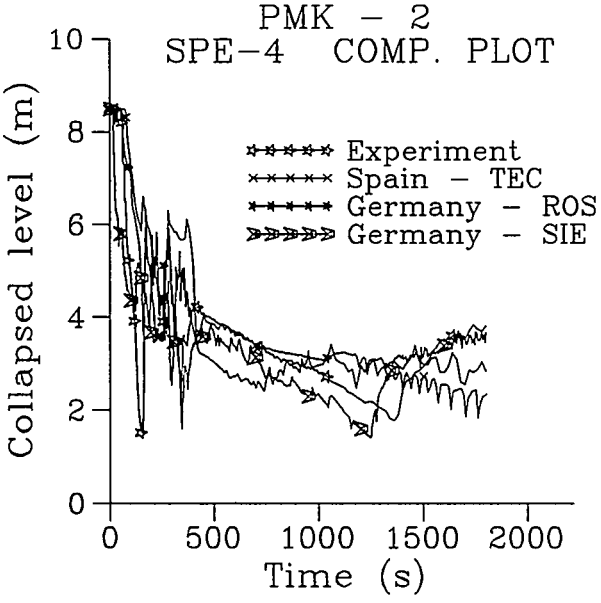


Fig. 9 Reactor model level

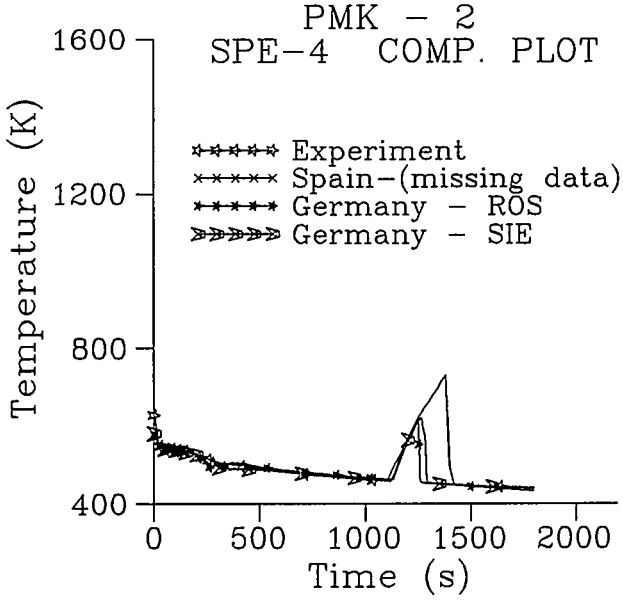


Fig.10 Heater rod temperature

REFERENCES

[1] Simulation of a Loss of Coolant Accident. Results of a Standard Problem Exercise on the Simulation of a LOCA. IAEA-TECDOC-425, Vienna, 1987.

[2] Simulation of a Loss of Coolant Accident with Hydroaccumulator Injection. Results of the Second Standard Problem Exercise on the Simulation of a LOCA. IAEA-TECDOC-477, Vienna, 1988.

[3] Simulation of a Loss of Coolant Accident with a Leak on the Hot Collector of the Steam Generator. Results of the Third Standard Problem Exercise. IAEA-TECDOC-586, Vienna, 1991.

[4] L. Szabados et al.: IAEA-SPE-4, Specification for the Fourth IAEA Standard Problem Exercise. KFKI Atomic Energy Research Institute, Budapest, Hungary 1993.

[5] Simulation of a Beyond Design Basis Accident with Bleed and Feed Preventive Measures (To be published as an IAEA TECDOC).

[6] P.P. Cebull and Y.A. Hassan: Simulation of the IAEA's Fourth Standard Problem Exercise Small Break Loss of Coolant Accident Using RELAP5/MOD3.1. Nuclear Technology, Vol. 19, March 1995.

VIPRE MODELING OF VVER-1000 REACTOR CORE FOR DNB ANALYSES

Y. Sung, T. Q. Nguyen
Westinghouse Electric Corporation
P.O. Box 598
Pittsburgh, PA 15230-0598

J. Cizek
Nuclear Research Institute, REZ
Prague, Czech Republic

Abstract

Based on the one-pass modeling approach, the hot channels and the VVER-1000 reactor core can be modeled in 30 channels for DNB analyses using the VIPRE-01/MOD02 (VIPRE) code (VIPRE is owned by Electric Power Research Institute, Palo Alto, California). The VIPRE one-pass model does not compromise any accuracy in the hot channel local fluid conditions. Extensive qualifications have been performed on the VIPRE modeling. The model qualifications include sensitivity studies of radial noding and crossflow parameters and comparisons with the results from THINC and CALOPEA subchannel codes. The qualifications confirm that the VIPRE code with the Westinghouse modeling method provides good computational performance and accuracy for VVER-1000 DNB analyses.

I. Introduction

Similar to other Pressurized Water Reactors (PWR), one of the design objectives of Russian-designed VVER-1000 reactors is to prevent reactor core from reaching departure from nucleate boiling (DNB) or boiling crisis. In the reactor design, DNB margin is evaluated based on local fluid conditions in the most thermal limiting subchannels (i.e., hot channels) predicted by a subchannel thermal-hydraulic (T/H) computer code coupled with a DNB correlation. Westinghouse uses VIPRE-01/MOD02 code (VIPRE) developed by Stewart et al. [1] for the T/H design of the Temelin VVER-1000 reactors in the Czech Republic. The VIPRE code is suitable for one-pass or one-stage modeling of the reactor core, which models hot channels and the reactor core in one simulation. The VIPRE modeling of the VVER-1000 core and model qualifications are discussed in the subsequent sections.

II. VVER-1000 Reactor and VIPRE Code

VVER-1000 is a four-loop PWR with a rated thermal power of 3000 MW. A VVER-1000 fuel assembly contains 312 fuel rods, 18 guide thimble tubes and one instrument tube in the center. The locations of guide thimble tubes are in rotational symmetry in every one-sixth section of the assembly. A one-sixth section of the fuel assembly is shown in Figure 1a. The reactor core contains 163 fuel assemblies as shown in Figure 1b.

The Temelin VVER-1000 reactors will be loaded with Westinghouse VVANTAGE6 fuel assemblies. The VVANTAGE6 fuel design is compatible with the original VVER-1000 fuel. However, the VVANTAGE6 fuel adapts many features of Westinghouse PWR fuel products to improve fuel economics, design and operational flexibility, performance margin, and reliability for VVER-1000 reactors. For example, the structural grids of the VVANTAGE6 fuel assembly at the axial region of high heat flux have mixing vanes to improve DNB margin of the reactor.

Like many other subchannel codes, VIPRE solves the finite-difference equations for mass, energy and momentum conservation for an interconnected array of channels assuming incompressible and thermal expandable homogeneous flow. Although the formulation is homogeneous, empirical models have been incorporated into the VIPRE code to account for subcooled boiling and vapor/liquid slip in two-phase flow. VIPRE has been approved by the U.S. Nuclear Regulatory Commission (NRC) for referencing in PWR licensing applications [2].

III. VVER-1000 Core Modeling

VIPRE modeling of the VVER-1000 core is based on the one-pass modeling approach. The one-pass modeling technique was first introduced by Moreno et al. [3] and has been widely used for PWR square-lattice core DNB analyses. In the one-pass modeling, hot channels and their adjacent region are modeled in detail, while the rest of the core is modeled simultaneously on a relatively coarse mesh. A reactor core can be modeled in a few channels while maintaining sufficient detail and accuracy around the hot channels.

In the VVER-1000 triangular lattice, a subchannel can be the flow area surrounded by three fuel rods (typical cell) or two rods with an instrument or thimble tube (thimble cell). By selecting a radial power and an inlet flow distributions symmetric to the core center, the reactor core can be represented by a one-sixth section with the hot assembly located in

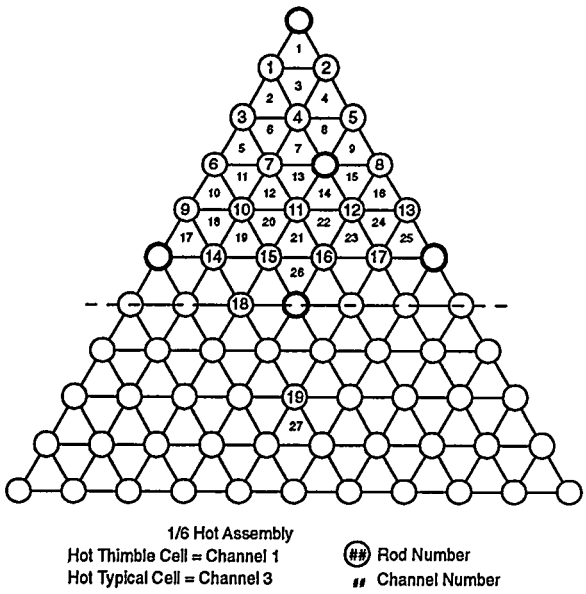


Figure 1a: VIPRE Modeling of VVER-1000 Core: 1/6th Hot Assembly

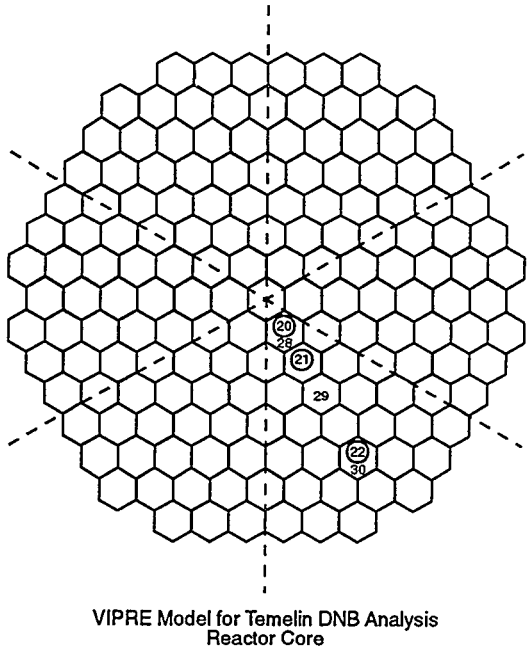


Figure 1b: VIPRE Modeling of VVER-1000 Core: Reactor Core

the center. The one-sixth core can be modeled in 30 channels, as shown in Figure 1. The 30-channel model covers the limiting subchannels in the VVER-1000 core, including hot typical cell and hot thimble cell with either an instrument tube or a guide thimble tube. Depending on reactor power distributions and fuel design, the hot channels can be Channels 1, 3, and 7 in Figure 1a. The hot channels are completely surrounded by at least two rows of subchannels to provide solution details of the flow field in the vicinity of the hot channels. The rotational symmetry in the VVER-1000 fuel assembly is simulated by connecting the peripheral subchannels (e.g., Channel 2 linked to Channel 4 in Figure 1a). A row of subchannels is lumped into one channel for transition to larger flow channels. The rest of the one-sixth hot assembly and the reactor core are modeled in four channels with increasingly larger channel size. In order to obtain correct crossflow for the lumped channels, parameters such as crossflow area and crossflow resistance are redefined for the VIPRE lateral momentum equation. Channel lumping for the VVER-1000 core is in general consistent with the lumping for a square lattice core described by Stewart et al. in Reference 1.

The 30-channel model meets the NRC's requirements for PWR one-pass modeling in Reference 2. It is possible to reduce number of subchannels in the 30-channel model for some VVER-1000 design applications. However, sensitivity studies have shown that further reduction in subchannels does not significantly improve computing speed with VIPRE running on a Hewlett Packard 735 workstation. The 30-channel model seems to yield better numerical stability for VVER-1000 applications.

The empirical models selected for VVER-1000 applications are consistent with the models used in the NRC-approved THINC code by Chelemer et al. [4]. For example, the turbulent mixing model in the VIPRE energy equation is based on the model proposed by Cadek [5]:

$$Q_m/\Delta x = - w'\Delta h$$

$$w' = \beta_m S G_{ave}$$

where

Q_m = thermal mixing energy, W (Btu/hr)
Δx = axial nodal length, m (ft)
w' = turbulent crossflow, kg/m-s (lbm/ft-s)
Δh = enthalpy difference between subchannel control volumes, J/kg (Btu/lbm)
β_m = thermal diffusion coefficient
S = channel gap width, m (ft)
G_{ave} = average axial mass flux in the adjacent channels, kg/m^2-s (lbm/ft^2-hr).

The turbulent mixing model accounts for the energy exchange between subchannels. The thermal diffusion coefficient for the VVER-1000 VVANTAGE6 fuel is verified with experimental data from bundle mixing test. The Levy model [6] is used for predicting subcooled void in the coolant. The homogeneous model is used for predicting bulk boiling and two-phase flow pressure drop. The crossflow resistance in subchannels is determined using the Lokshin-Formina correlation [7]. The Lokshin-Formina correlation predicts crossflow resistance in a triangular pitch from rod pitch and diameter and Reynolds number based on lateral flow velocity.

IV. Model Qualifications

Extensive qualifications were performed on the VIPRE modeling of VVER-1000 core. The model qualifications include parametric sensitivity studies and comparisons with THINC and the CALOPEA subchannel code developed by Kostalek et al. [8]. The sensitivity studies confirm the adequacy of the VIPRE modeling. The comparisons with THINC verify that the empirical models selected are equivalent to the THINC code for PWR square-lattice core applications. The comparisons with CALOPEA demonstrate that the simplified VIPRE model has the same accuracy for VVER-1000 design applications.

IV. a) Model Sensitivity Studies

Sensitivity studies were performed with different radial noding configurations of VVER-1000 core. The configurations considered in the studies include the following: 1) a one-sixth core model with the one-sixth hot assembly being modeled completely as subchannels, 2) a one-sixth core model containing one less row of subchannels as compared to the 30-channel model, and 3) a whole core model with the 30-channel model extended to the whole core. The results of sensitivity studies show that the maximum difference in DNB Ratio (DNBR) was less than 1% under various VVER-1000 design conditions. Figure 2 illustrates a comparison of the minimum DNBR values between the 30-channel model and the one-sixth core model with the complete one-sixth hot assembly modeled as subchannels, and the DNBR range considered in the sensitivity studies.

Sensitivity studies were also performed on parameters that affect the crossflow calculations, including the channel centroid distance and crossflow loss coefficient. VIPRE control volume for the lateral momentum equation is defined by channel gap width, centroid distance and axial nodal length. In the VIPRE model the centroid distance is approximated as the geometric centroid distance between the channels. In the sensitivity studies, subchannel and

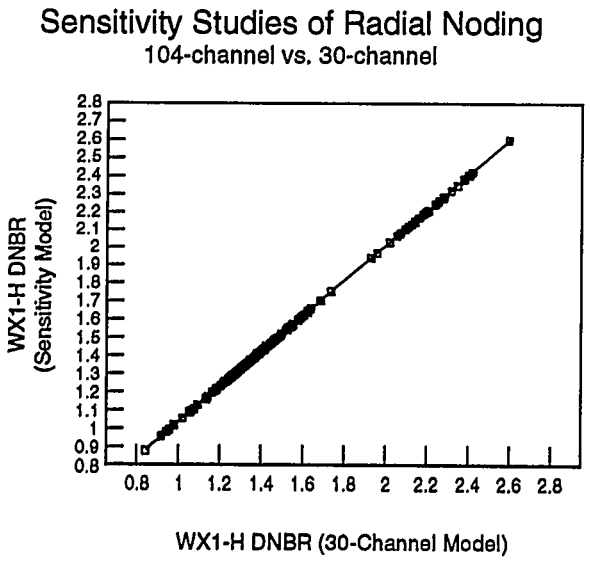


Figure 2: VIPRE Geometric Model Sensitivity Study

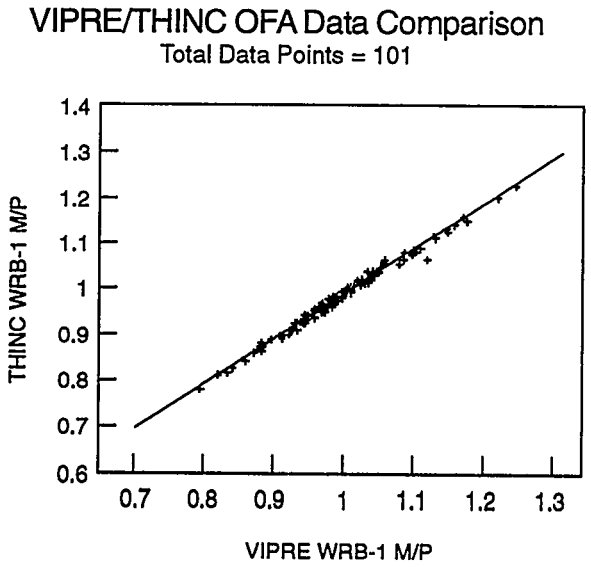


Figure 3: VIPRE/THINC Comparison for OFA DNB Data

lumped-channel centroid distances and crossflow loss coefficients were varied by 50% from the base value. The resultant DNBR changes were rather insensitive (<2%) considering the magnitude of variations in the parameters.

IV. b) Comparisons with THINC code

VIPRE and THINC benchmark calculations were performed for the DNB data from test sections that simulate Westinghouse 17x17 square-lattice Optimized Fuel Assembly (OFA) design [9]. The VIPRE analysis of the DNB data used the same empirical models as for VVER-1000 applications, including the two-phase flow model and the turbulent mixing model. Accuracy of DNB prediction was measured as the ratio of measured CHF to predicted CHF (M/P). The VIPRE predictions are in very good agreement with the THINC results. The comparison between VIPRE and THINC M/P values for 101 OFA DNB data points is shown in Figure 3. The difference in the M/P mean values is less than 1%.

IV. c) Comparisons with CALOPEA

To demonstrate the accuracy of the VIPRE one-pass model, the hot channel conditions predicted by the VIPRE model were also compared with the CALOPEA code for a VVER-1000 core with the original fuel design. CALOPEA is a subchannel code developed for VVER-440 and VVER-1000 design analyses, based on the COBRA-IIIC code developed by Rowe [10]. For VVER-1000 DNB analysis, CALOPEA models the entire fuel assembly in 666 channels as shown in Figure 4. For the purpose of code comparison, VIPRE calculations were performed for the hot assembly only, using the 27 channels in Figure 1a, with the mixing and two phase flow models same as the CALOPEA code. The code comparisons show that the VIPRE hot

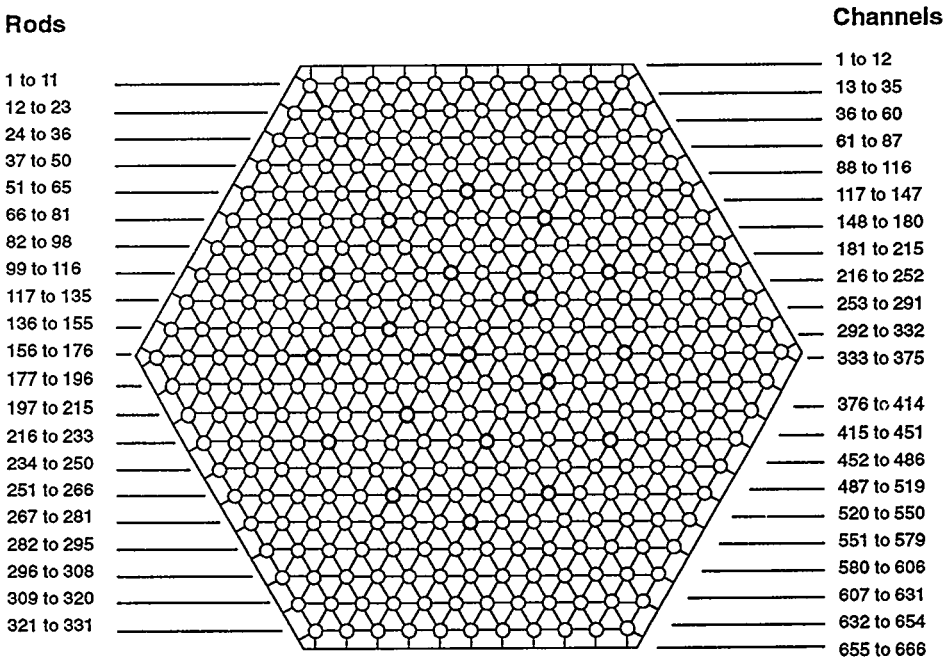


Figure 4: CALOPEA Modeling of VVER-1000 Fuel Assembly

channel conditions are in very good agreement with the CALOPEA predictions. The comparisons of local flow rate and local equilibrium quality in the hot channels at the DNB limiting time step of a postulated VVER-1000 4-loop loss of forced coolant flow accident are illustrated in Figures 5 and 6, respectively. The local flow rate and the local quality are the subchannel parameters used by most CHF correlations for reactor DNB margin predictions.

V. Conclusion

Based on the one-pass modeling approach, the VVER-1000 core can be modeled in 30 channels for DNB analyses. The VIPRE model has been qualified with sensitivity studies and comparisons with THINC and CALOPEA subchannel codes. The VIPRE code with the Westinghouse modeling method provides good computational performance and accuracy for VVER-1000 DNB analyses.

VI. References

[1] C.W. Stewart, et al., "VIPRE-01: A Thermal Hydraulic Code for Reactor Cores", Volumes 1-5, Revision 3, NP-2511-CCM-A, Electric Power Research Institute (1989).

[2] NRC Safety Evaluation Report, "Acceptance for Referencing of Licensing Topical Report, EPRI-NP-2511-CCM, 'VIPRE-01: A Thermal-Hydraulic Analysis Code for Reactor Cores",' Volumes 1, 2, 3 and 4" (1986).

[3] P. Moreno, et al., "Steady State Thermal Analysis of PWRs by a Single-Pass Procedure Using a Simplified Nodal Layout", Nuclear Engineering & Design, Volume 47, 35-48 (1978).

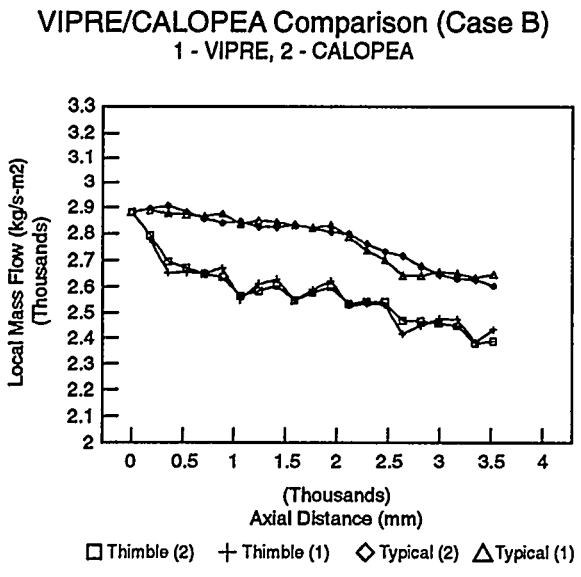


Figure 5: VIPRE/CALOPEA Comparison: Local Mass Flow

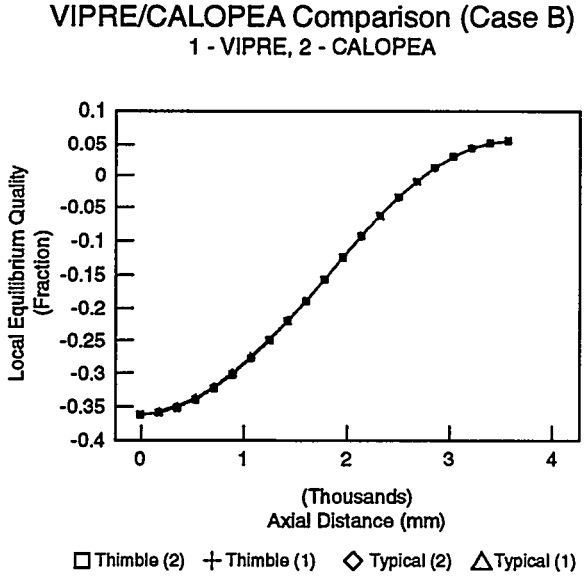


Figure 6: VIPRE/CALOPEA Comparison: Local Quality

[4] H. Chelemer, et al., "THINC-IV - An Improved Program for Thermal-Hydraulic Analysis of Rod Bundle Cores"., WCAP-7956-A, Westinghouse Electric Corporation (1989).

[5] F.F. Cadek, "Topical Report Interchannel Thermal Mixing with Mixing Vane Grids", WCAP-7755-A, Westinghouse Electric Corporation (1975).

[6] S. Levy, "Forced Convection Subcooled Boiling - Prediction of Vapor Volumetric Fraction", International Journal of Heat & Mass Transfer, Vol. 10, 951-965 (1967).

[7] I.E. Idelchik, "Handbook of Hydraulic Resistance", Second Edition, Hemisphere Publishing Corporation, 575,608 (1986).

[8] J. Kostalek, et al., "CALOPEA Program Description and User's Manual", ZJS-12/91, SKODA (1991).

[9] S.L. Davidson et al., "Verification testing and Analyses of the 17x17 Optimized Fuel Assembly", WCAP-9402-A, Westinghouse Electric Corporation (1979).

[10] D.S. Rowe, "COBRA-IIIC: A Digital Computer Program for Steady-State and Transient Thermal-Hydraulic Analysis of Rod Bundle Nuclear Fuel Elements", BNWL-1695, Pacific Northwest Laboratory (1973).

CATHARE2 CALCULATION OF SPE4 TEST

SMALL BREAK LOCA ON PMK FACILITY

E. LAUGIER, J. RADET

Institut de Protection et de Sûreté Nucléaire
Centre d'Etude de CADARACHE
FRANCE

ABSTRACT

Blind and post test calculations with CATHARE2 have been performed concerning the SPE-4 exercise organized under the auspices of IAEA on the hungarian PMK-2 facility, a one loop scaled model of VVER 440/213 Nuclear Power Plant.
The SPE-4 test is a cold leg SBLOCA associated to a "bleed and feed" procedure applied in the secondary circuit.
The present paper is devoted to the analysis of the post test calculation.

For the first part of the transient (until the end of the SIT activations), the primary and secondary pressures are rather well predicted, leading to a good agreement with the experimental trips, as scram, flow coast down, SIT beginning and end of activation. Nevertheless, some discrepancy with the experiment may be due to an over prediction of the thermal exchanges from the primary to the secondary circuits.
For the second part of the transient, the predicted primary circuit repressurization is shifted after the SITs are off, while in the experiment this event immediately follows the end of SIT activation. The delay in the calculation leads to underpredict primary and secondary pressures, thus anticipating the timing of events, such as LPIS and emergency feedwater activation.

1. BACKGROUND

In the framework of an IPSN (Institut de Protection et de Sûreté Nucléaire) Working Group, thermal-hydraulic calculations with the CATHARE2 code are performed, in order to verify the ability of the code to predict the behaviour of VVERs under accidental conditions.
Former calculations have been performed with CATHARE2 concerning the Standard Problem Exercises SPE1 & SPE2, realized under the auspices of IAEA, on the PMK hungarian facility [1].
This paper presents the analysis of the SPE4 test with the CATHARE2 code. It is focused on the additional post-test calculation performed with CATHARE2 V1.3 U in

order to improve the former results presented during the second SPE4 workshop held in Budapest on May 1994 [2].

2. FACILITY DESCRIPTION

The PMK-NVH integral facility is located at the KFKI Atomic Energy Research Institute (AERI), Budapest, Hungary.
The facility is a single loop full pressure, 1/2070 volume scaled model of the PAKS NPP and is designed mainly to investigate the processes following small and medium size breaks in the primary circuit and to study the natural circulation behaviour of VVER-440 type PWRs.
These reactors slightly differ from PWRs of western design and have a number of special features such as :

. horizontal steam generators,
. loop seal in hot and cold legs,
. safety injection tanks (SIT) connected to hot and cold legs.

The PMK-2 is an upgraded version of PMK-NVH, intended to extend the capability of the facility to the simulation of transient processes including accident sequences in support of accident management procedures.

3. STANDARD PROBLEM TEST

3.1 Test definition

The experiment selected is a small break loss of coolant accident (SBLOCA) in the cold leg with the unavailability of the high pressure injection system (HPIS), leading to a beyond design basis accident scenario. For the prevention of core damage, the secondary side " bleed and feed " procedure is applied [3].
The figure 1 shows the flow diagram of the PMK-2 facility.
The break in the cold leg is 3.2 mm diameter (simulating a 7.4 % break in NPP). It is located in the top of the downcomer, and activated by opening the valve MV31.
The pump of the PMK-2 facility is only used for establishing nominal operating conditions. During the steady state operation at a power level corresponding to full power in the reactor, the valve MV11 is closed and circulation takes place through the pump line. Since the pump is not designed to represent the main circulating pump of the NPP, pump trip is simulated during the transient. This is achieved by controlling the pump flow rate by PV11 in the pump line. When the flow rate decreases up to the prescribed flow rate, PV11 is closed and MV11 is opened simultaneously, thus establishing natural circulation in the cold leg. The pump is then switched off and the pump line valved off from the loop by closing MV12.

There are injections from the hydroaccumulators connected to the facility, SIT1 to top of downcomer (MV91), SIT2 to core upper plenum (MV92).

The low pressure injection system (LPIS) injects water only into the cold region of the facility (line of SIT1).

The feedwater line is connected to the secondary side of steam generator by the valve PV11. The outlet steam line is connected to PV22. These two valves are closed for simulating the secondary side isolation of SG.

PV23 has two functions : during a first period, it is used as a secondary relief valve, opening when the secondary pressure exceeds 5.3 MPa and closing at 4.9 PMa ; during a second period, it simulates the bleed procedure, the flow being limited by an orifice of 6 mm diameter and 15 mm length.

3.2. Test scenario

The scenario consists of different events tripped at particular values of the primary and secondary pressures. The sequence of these events is indicated in Table 1.

events	trip signals
start of break valve opening (MV31)	0 s
full opening of break valve	0.1 s
secondary side isolation	0 s
SCRAM at primary pressure	11.15 MPa
initiation of flow coast down at primary pressure	9.21 MPa
activation of SIT1 & SIT2 at primary pressure	5.9 MPa
SIT1 empty at relative level	.245 m
SIT2 empty at relative level	1.035 m
secondary bleed initiated at primary pressure + delay	9.21 MPa + 150 s
EFW initiated at secondary pressure	.93 MPa
LPIS initiated at primary pressure	1.04 MPa

Table 1 - Scenario of the test

3.3 Test results

At the beginning of the transient, the break in the primary circuit is opened and the secondary circuit is isolated.
In consequence, the primary circuit depressurization starts (figure-2), leading to the following trips : scram, pump trip, activation of SITs and initiation of bleed procedure in the secondary circuit.
After the end of SIT activations at 310 s, a temporary repressurization immediately takes place. It is due to the arrival at the break of liquid water following the climb of the downcomer collapsed level (figure-3). It is followed by a new depressurization until the end of the transient, eventually leading to LPIS activation at 1380 s.

In the secondary side, due to the secondary circuit isolation, the pressure increases and reaches a maximum value of 5.1 MPa (figure-2). Then a slow depressurization occurs, dropping the pressure to 4.5 MPa. The bleed procedure, initiated at 160 s, accelerates the depressurization until the end of the transient, leading to the initiation of the emergency feed water.

On figure 4, one can observe three core collapsed level depletions associated with core uncovery and heatup (figure-5). For the first and the second heatups, the temperature excursion remains very limited (15 K and 3 K). Each time, the core is recovered due to loop seal clearings in the hot leg at 165 and 345 s (table-3). The last heatup is very significant with a temperature excursion of 270 K, leading to 730 K as maximum clad temperature. The associated core recovery is due to coolant water arrival when LPIS activation occurs at 1380 s (table-3).

It is observed that core heatup takes place when the collapsed level drops below 61% of the heated length (figure-4).

4. CALCULATION RESULTS

4.1. CATHARE2 code [4]

The CATHARE2 code version V1.3 U used for this calculation is a French code jointly developed by CEA, EDF & Framatome. It is based on a two-fluid model leading to a 6 equations system in 1-D elements. Mass, momentum and energy equations are written for each phase. The numerical scheme is a finite difference method using staggered meshing and first order upwind differencing. Time discretisation is fully implicit.

Several modules are available to represent the different components of a circuit. The basic module is the 1-D pipe module. The so-called "volume module" is a two node volume with a moving mixture level. It allows the description of vertical stratification and phase separation effects at junctions with pipes. The "tee module" allows to connect a branch to a main pipe. It is a single node module provided with specific phase separation correlations.
The constitutive relations in the CATHARE2 code are either taken from the literature or original models developed from the analysis of a large experimental program associated to the code. For example, wall friction models are original and depend on the flow pattern : stratified or non stratified, with or without droplet entrainment. The stratification criterion takes account of the Kelvin-Helmholtz instability and liquid turbulence effects. The condensation model used for SG tubes is derived from the Shah correlation. Convective heat transfers in single-phase use the classical Colburn correlation.

The calculations were performed on a HP 735 workstation with 160 MBytes RAM.

4.2. PMK-2 nodalization

Figure 6 presents the nodalization of the primary circuit.
The 1-D pipe module is used for the hot leg, the surge line, 6 horizontal SG tubes (corresponding to 82 real tubes), the intermediate leg, the cold leg, the downcomer, the core, the link lines to SITs and the break line.
The volume module is used for the upper and the lower plena, the hot and cold collectors, the top of downcomer and the pressurizer.
The tee module is used for the connection of the hot leg to the surge line of the pressurizer and the pump line to the main cold leg.

Figure 7 represents the nodalization of the secondary circuit.
The 1-D pipe module is used for the exchange zone with the primary circuit, connection lines to steam volumes, the steam outlet (connected to PV22) and secondary break (PV23/1).
The volume module is used for steam dome and steam volumes.
The feedwater inlet is connected to the exchange zone by two points, PV21/1 (necessary upstream junction for the 1 D pipe) and PV21/2, specific arrival of VVER feedwater. The steam outlet is PV22.

During a first period (until the bleed procedure initiation), the secondary relief valve is represented by PV23/2, since PV23/1 is blocked up. Then, during a second period, (from bleed initiation to the end of the calculation), PV23/2 becomes blocked up and the secondary break is located at PV23/1.

4.3. Steady state calculation

For obtaining steady state at nominal conditions, several regulations have been used for :

. adjusting the secondary level by means of a couple "source-sink" located at the bottom of the steam dome volume.

. adjusting the inlet flow temperature of the core by fitting the fouling of the steam generator exchange.

. setting the feedwater flow rate equal to the outlet steam flow rate by controlling the inlet flow at PV21/2.

The steady state conditions are indicated in Table 2. From the experiment, they are given by [3] and [5].

Nominal condition	Experimental value	Calculation result
pressure in upper plenum (MPa)	12.33	12.33
loop flow (kg/s)	4.91	4.901
core inlet temperature (K)	540.1	539.6
core power (kW)	666.4	666.5
coolant level in pressurizer (m)	1.37	1.37
SIT-1 pressure (MPa)	6.05	6.05
SIT-2 pressure (MPa)	6.04	6.04
SIT-1 level (m	1.465	1.465
SIT-2 level (m)	1.855	1.855
total primary heat losses (kW)	23.4	23.4
coolant temp. at top of upper plenum (K)	534.2	533.5

Table 2 - Nominal conditions at steady state

4.4. Transient calculation and comparison with the experiment

General features.

The transient can be divided into three phases. The first corresponds to the period from the primary break opening until the initiation of the secondary bleed ; the second from the bleed initiation to the end of the SIT activation ; the last phase from the end of SIT activation to the end of the transient.

The primary and secondary pressures are generally underestimated by the code (figures-8 and 9). The loss of coolant through the primary break is underestimated until the LPIS initiation takes place at 1380 s. From this instant, the LPIS coolant participates to the break flow, thus increasing the integrated mass flow (figure-10).

Several depletions of the collapsed core level are calculated, leading to core heatups (figures-11 and 12). The predicted cladding temperature excursions are more pronounced and frequent than in the experiment.

These general trends are analyzed in more details in the following.

The occurrence of the main events are indicated in Table 3.

Reference	Occurrences	Timing (s) EXP	Timing (s) CALC
0	break valve opens	0	0
1	pressurizer is empty	23	18
2	first dryout occurs	138	195
3	two-phase flow at the break	44	50
4	hot leg loop seal cleared (LE31)	165 / 345	326 / 600
5	cold leg loop seal cleared (LE46)	250	364
6	reactor collapsed level drops to hot leg elevation	78	96
7	collapsed level reaches the top of the core	125	196
8	SIT-1 flow begins	26	27
9	SIT-2 flow begins	26	27
10	SIT-1 flow terminates	310	307
11	SIT-2 flow terminates	310	313
12	SG secondary pressure ≤ .8 MPa	1720	1080
13	heater rod surface temperature ≥ 873 K	no	no
14	LPIS starts	1380	950

Table 3 - Main occurrences

First phase (from break opening at 0 s to bleed procedure at 160 s)

The primary depressurization is rapid, leading to the different trips, scram, flow coast down and SIT activation, predicted in good agreement with the corresponding experimental events. During this period, the secondary circuit is isolated, the predicted secondary pressure increases, reaching the value of the secondary safety valve opening (figures-9 and 13). After a short secondary pressurization, stopped by the opening of the secondary safety valve, the calculated secondary pressure remains almost constant, whereas the experimental one continuously decreases. As a result, the primary pressure is underpredicted, while the secondary pressure is overpredicted. This behaviour may correspond to an over prediction of the thermal exchanges from the primary to the secondary circuits.
In order to explain this particular behaviour, especially the continuous decrease of the secondary experimental pressure, we make the hypothesis that the secondary safety valve could have been opened until the bleed initiation.
The over prediction of the thermal exchanges from the primary to the secondary circuits is probably due to the non calculation by the code of the recirculation in the horizontal tubes of the SG which takes place in the experiment. The indication of this experimental event is the reversal of the temperature gradient (hot collector temperature less than cold collector temperature during this period).
The consequence of the primary pressure under prediction is to stop the SITs before the initiation of the secondary bleed procedure (figure-14). As the SITs are off, the temperature of the liquid in the top of the downcomer increases, reaching the saturation temperature (figure-15). Two-phase appears at this location, swelling the level (figure-16). Thus, liquid reaches the break, leading to the prediction of a partial and slight primary repressurization. The experimental results show that the break remains uncovered during this period, associated to a continuous depressurization (figure-17).

Second phase (from bleed initiation at 160 s to SIT end of activation at 310 s)

The secondary bleed initiation produces a sharp decrease of the secondary pressure, involving a sharp decrease of the primary pressure (driven by the secondary pressure), leading to the reactivation of the SITs (figures-9, 8 and 14). As a consequence the liquid in the top of the downcomer becomes immediately undersaturated (figure-15). The double phase disappears in this region and the swelled level collapses, thus uncovering the break. This phenomenon also participates to intensify the primary depressurization.
During this period, the code predicts a depletion of the collapsed level of the core ("1" in figure-11), which produces a heatup when the level drops under 90 % of the heated length.
The SITs become off on their minimum elevation criterion.

Third phase (from the SIT end of activation at 310 s to the end of the transient)

At the end of the SIT activation, the temperature of the liquid at the top of the downcomer increases up to the saturation temperature (figure-15). The occurrence of the first loop seal clearing in the hot leg (figure-18) cools the liquid at this location, temporarily stopping the temperature increase. After the loop seal clearing end, the temperature increase goes on, reaching the saturation temperature, and again the same phenomenon occurs : swelling of the level (figure-16), leading to a partial and slight repressurization. This predicted repressurization is delayed compared to the experiment, due to the predicted clearing of the loop seal in the hot leg.
This delay of the calculated repressurization allows the primary pressure to decrease much more than in the experiment, leading to an under prediction of the primary and secondary pressures. This under prediction involves the anticipation of the following trips : LPIS activation and emergency feedwater.
During this period, several depletions of the core collapsed level occur, dropping under 90 % of the heated length ('2', '3', '4', '5' in figure-11), leading to heatup ('2', '3','4','5' in figures-12), whereas in the experiment such heatups appear for a level drop of about 61 %.
The second and the fourth calculated heatups are stopped by two loop seal clearings in the hot leg (figure-18).
The last temperature excursion is very important, 310 K , leading to reach 780 k as maximum clad temperature. It is stopped by core refilling (figure-11), due to LPIS activation (flow rate on SIT1 line in figure-14), as in the experiment.
In figure 18, we can observe that the first experimental loop seal clearing in the hot leg occurs at 165 s (table-3). Nevertheless, the calculated collapsed level of the hot leg loop seal perfectly follows the experimental evolution but does not drop as in the experiment, up to the minimum elevation necessary to involve the clearing.

6. CONCLUSIONS

The general trends of CATHARE2 calculation results on SPE-4 are in good agreement with the experiment.
The good prediction of the primary pressure during a first period (from the transientinitiation up to the end of SIT activations) leads to a good prediction of trips, as scram, flow coastdown, SIT beginnings and end of activations.

The overprediction of the thermal exchanges from the primary to the secondary circuits could be due to the non simulation by the code of the recirculation in the horizontal tubes of the SG, as well as the opening of the secondary safety valve until the start of the bleed procedure. Additional calculations will be performed in order to verify these assumptions.

The primary circuit repressurization following the SITs switch off is calculated with a slight delay compared to the experiment. This involves the underprediction of the primary and the secondary pressures leading to anticipate trips, as LPIS and emergency feedwater.

Nevertheless, the main features of the experiment, core uncovery, heatup, and core refilling are qualitatively rather well predicted by the code. These good results illustrate the capability of the CATHARE2 code in describing such kind of accidental sequence on VVERs.

REFERENCES

[1] M. Belliard and E. Laugier, "Cathare2 v1.3e post-test computations of SPE1 and SPE2 experiments at PMK-NVH facility," Proc. New trends in nuclear system thermohydraulics, Int. Conf. Pisa (1994).

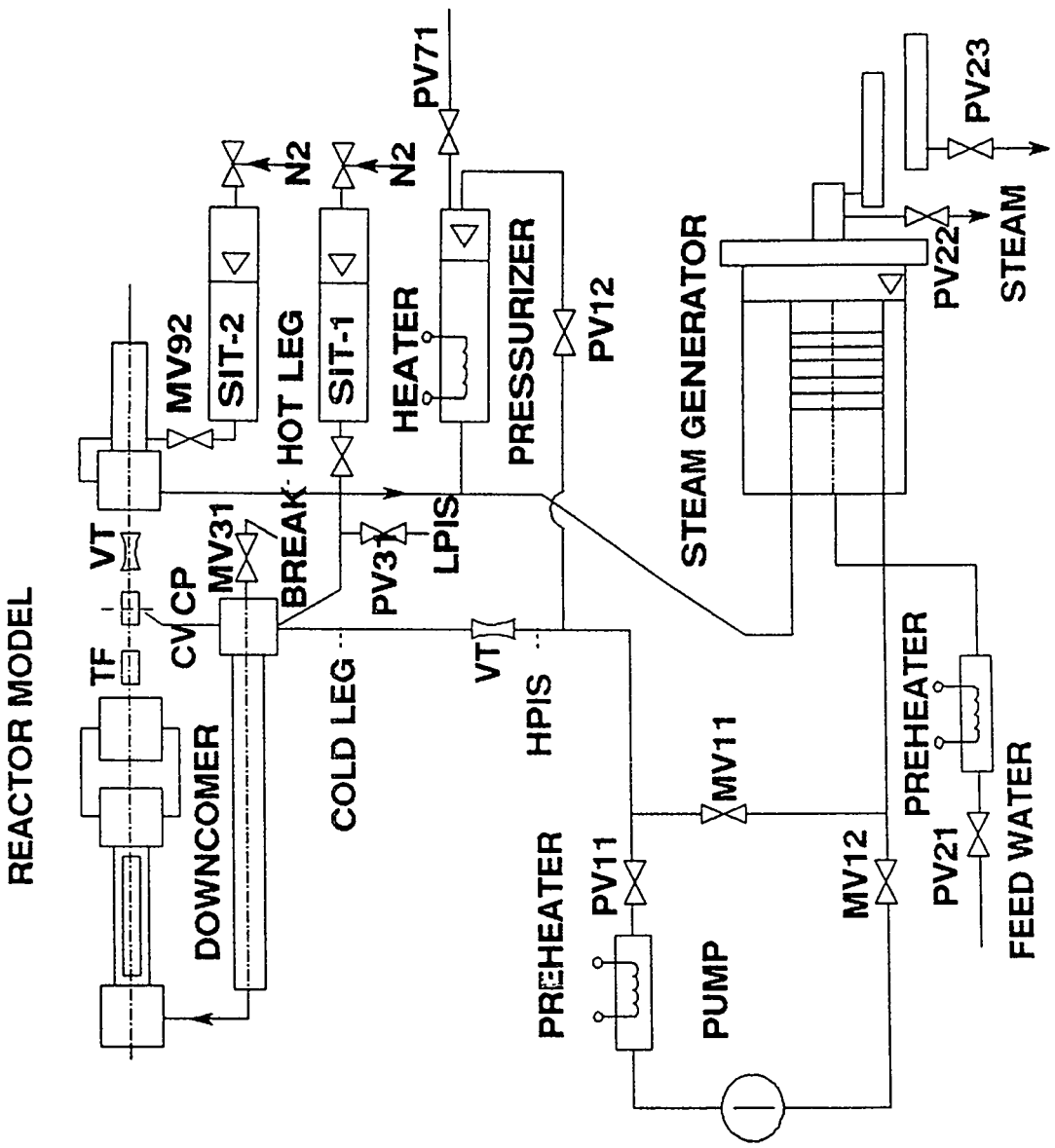
[2] E. Laugier, J. Radet, "SPE4 Post- test calculation", IPSN./.DRS Report, CE Cadarache, France, June 1994.

[3] L. Szabados et al, "Specification for the fourth IAEA Standard Problem Exercise," KFKI / AERI Report, Budapest, Hungary 1993.

[4] D. Bestion, "The physical closure laws in the Cathare code," Nucl. Engrg. 124, 229-245 (1990)

[5] L. Szabados et al, "Measured initial conditions for the fourth IAEA PMK-2 Standard Problem Test," KFKI/AERI Report, Budapest, Hungary July 1993.

ELFPML2



Abbreviations are:

PV	: pneumatic control valve
MV	: motor valve
VT	: flow measurement device
TF	: flow measurement device
CP	: density measurement device
CV	: density measurement device
SIT-1	: hydroaccumulators
SIT-2	: hydroaccumulators
HPIS	: high pressure injection system
LPIS	: low pressure injection system

Figure 1 : Flow diagram of PMK-2 facility

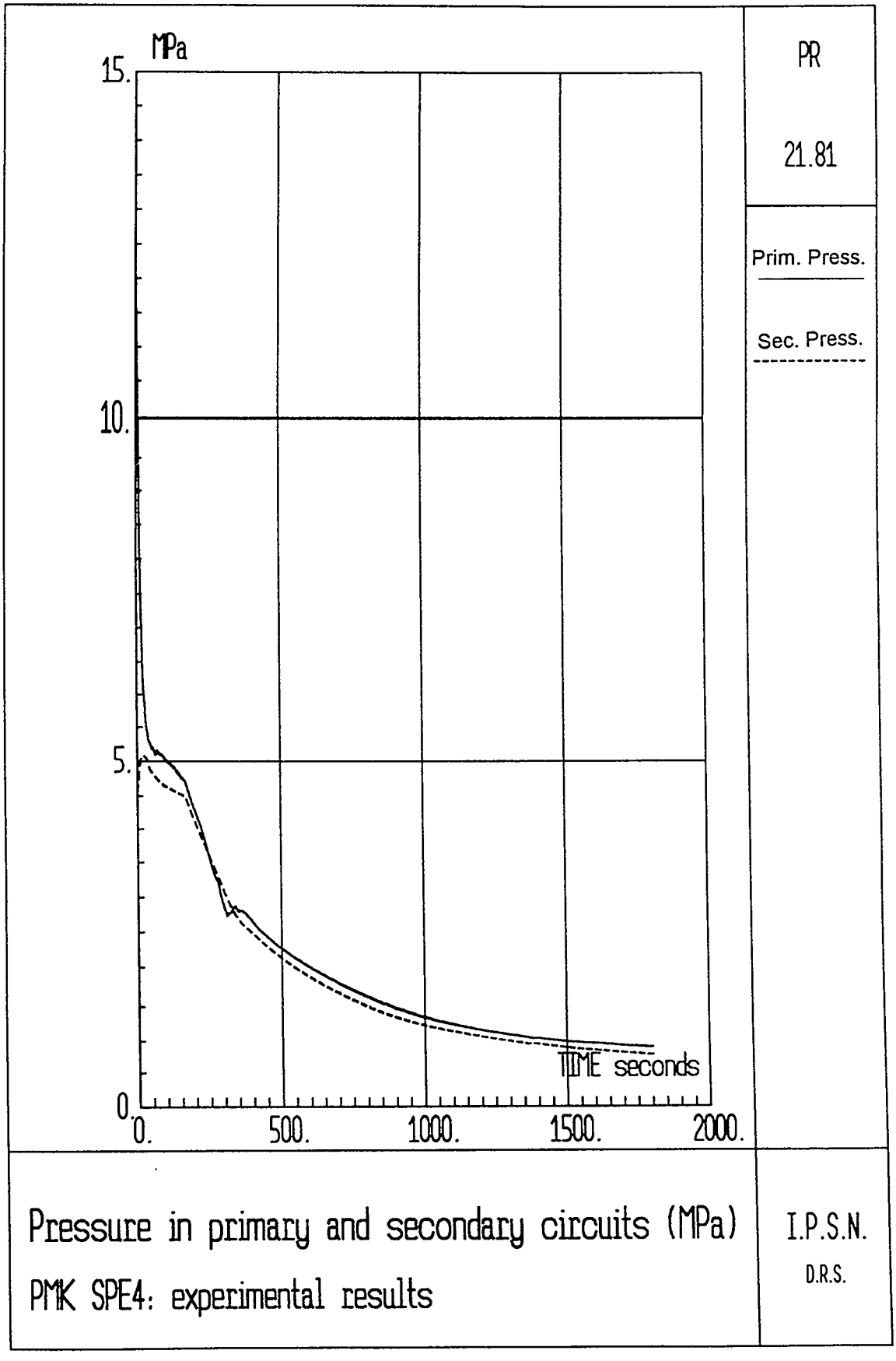


Figure 2: Primary and secondary pressures (MPa)

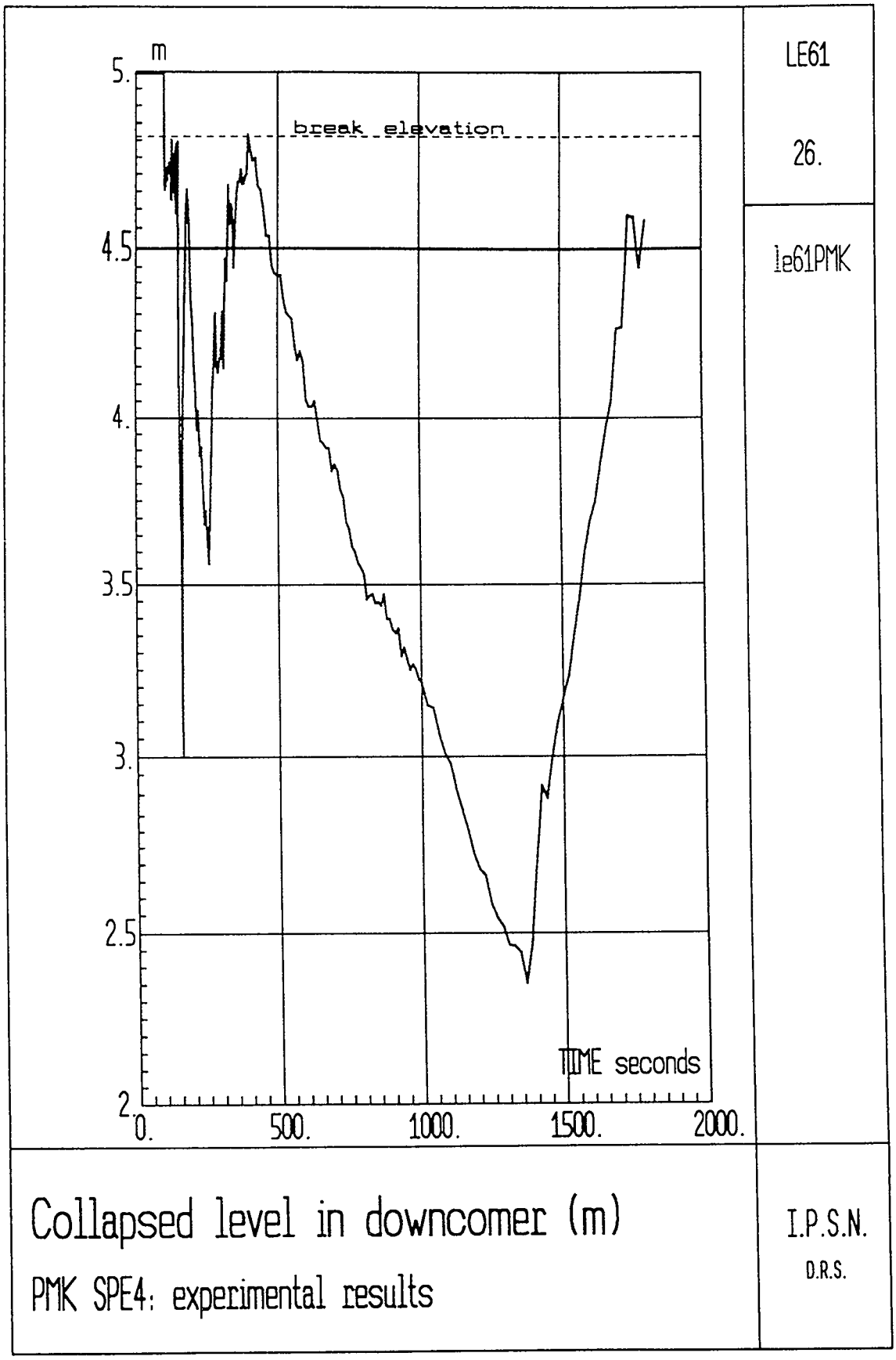


Figure 3: Collapsed level of downcomer (m)

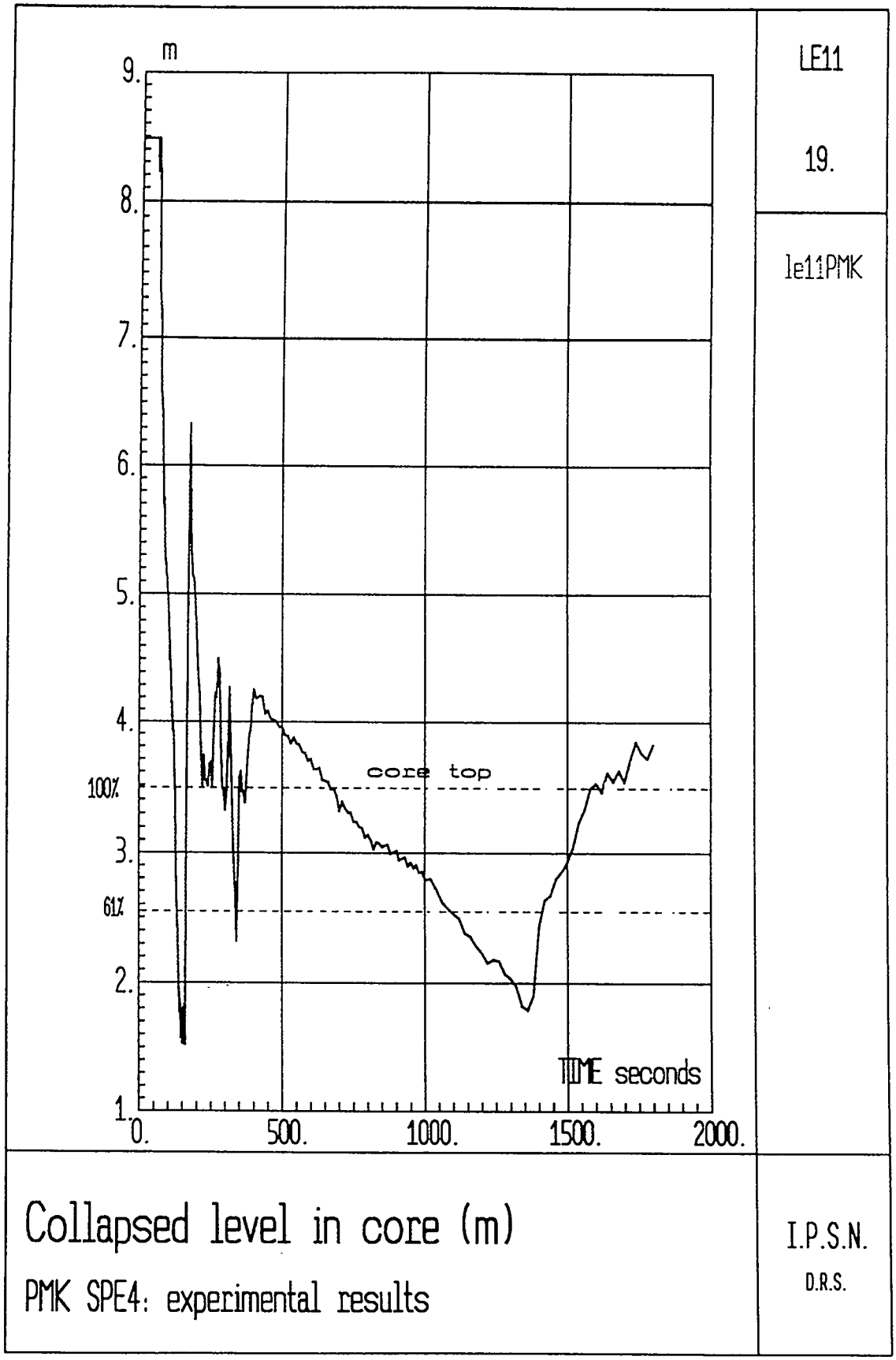


Figure 4: Collapsed level of core (m)

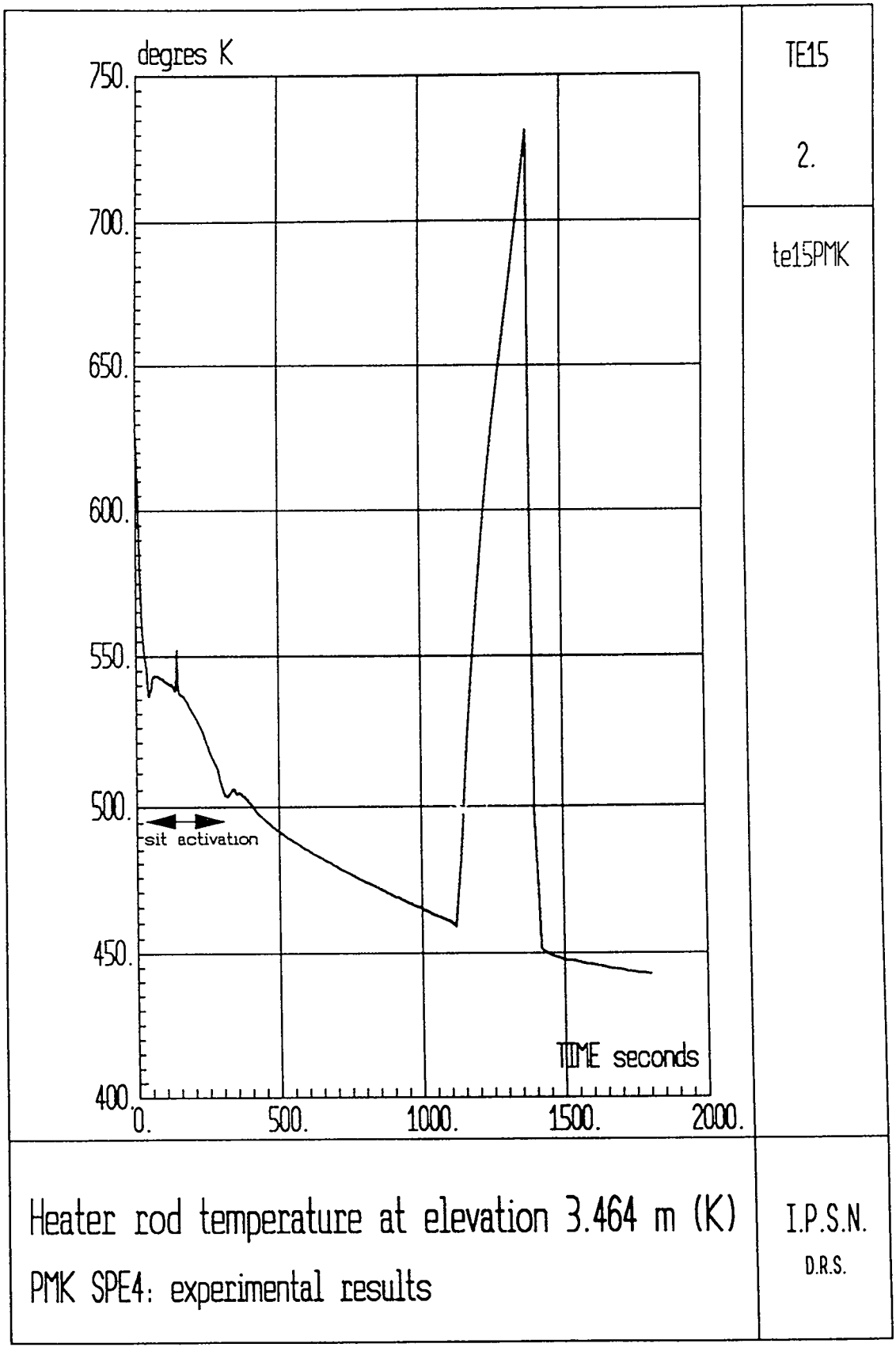
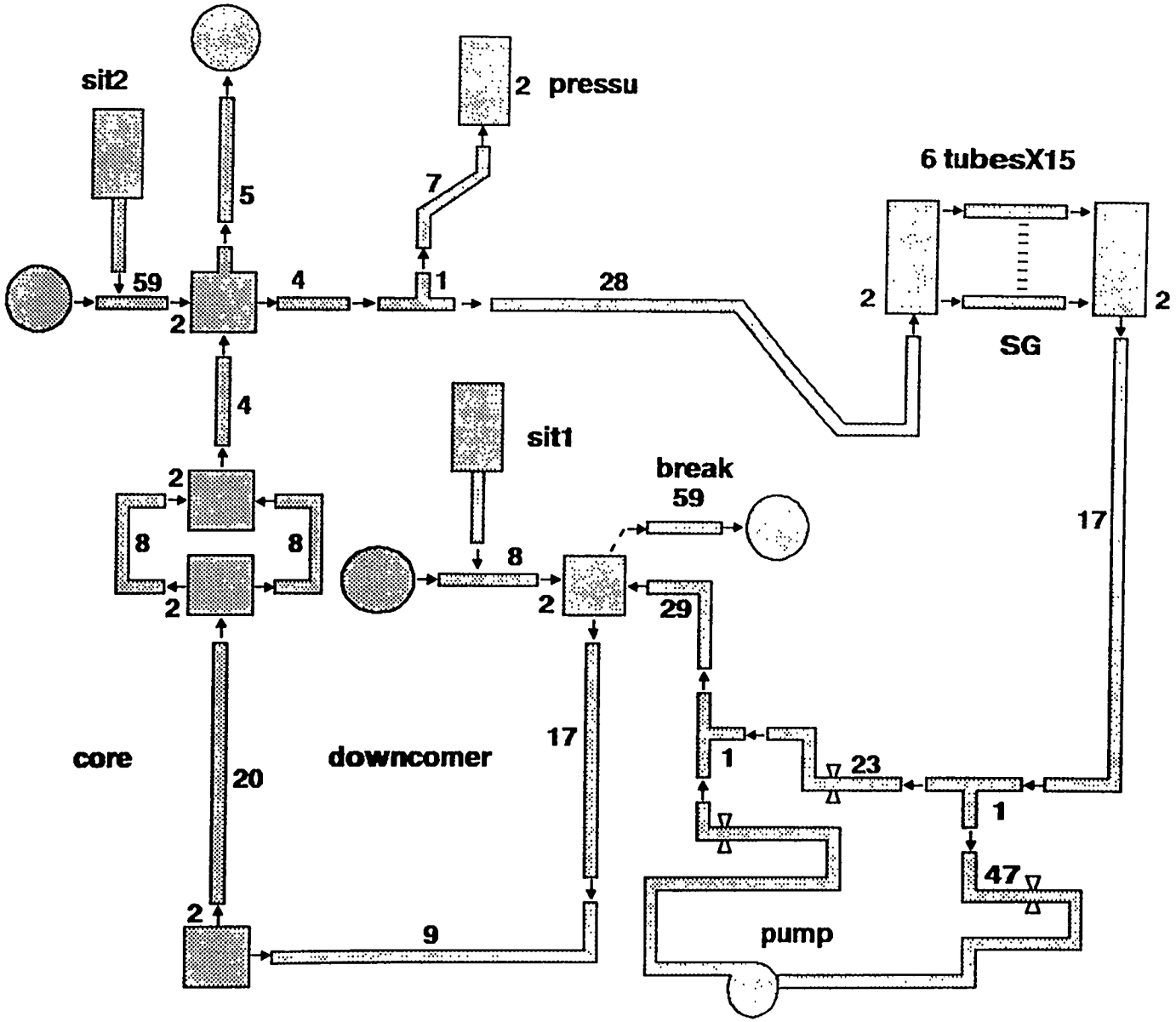
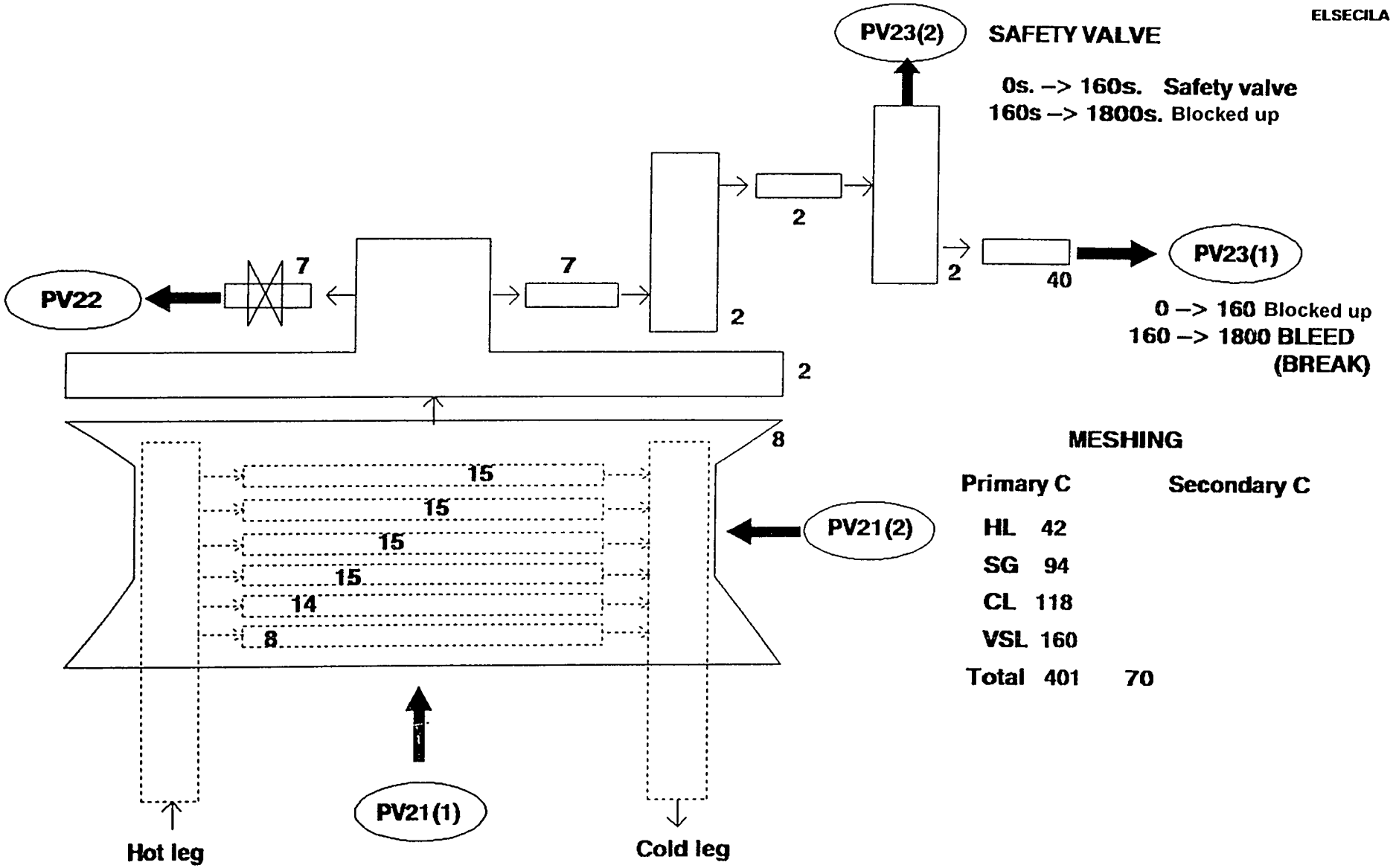


Figure 5: Core clad temperature (K)



Meshing	
Hot leg	42
S.G.	94
Cold leg	118
Vessel	160
Total	401

Figure 6 : Nodalization of the primary circuit.



2134

Figure 7 : Nodalization of the secondary circuit.

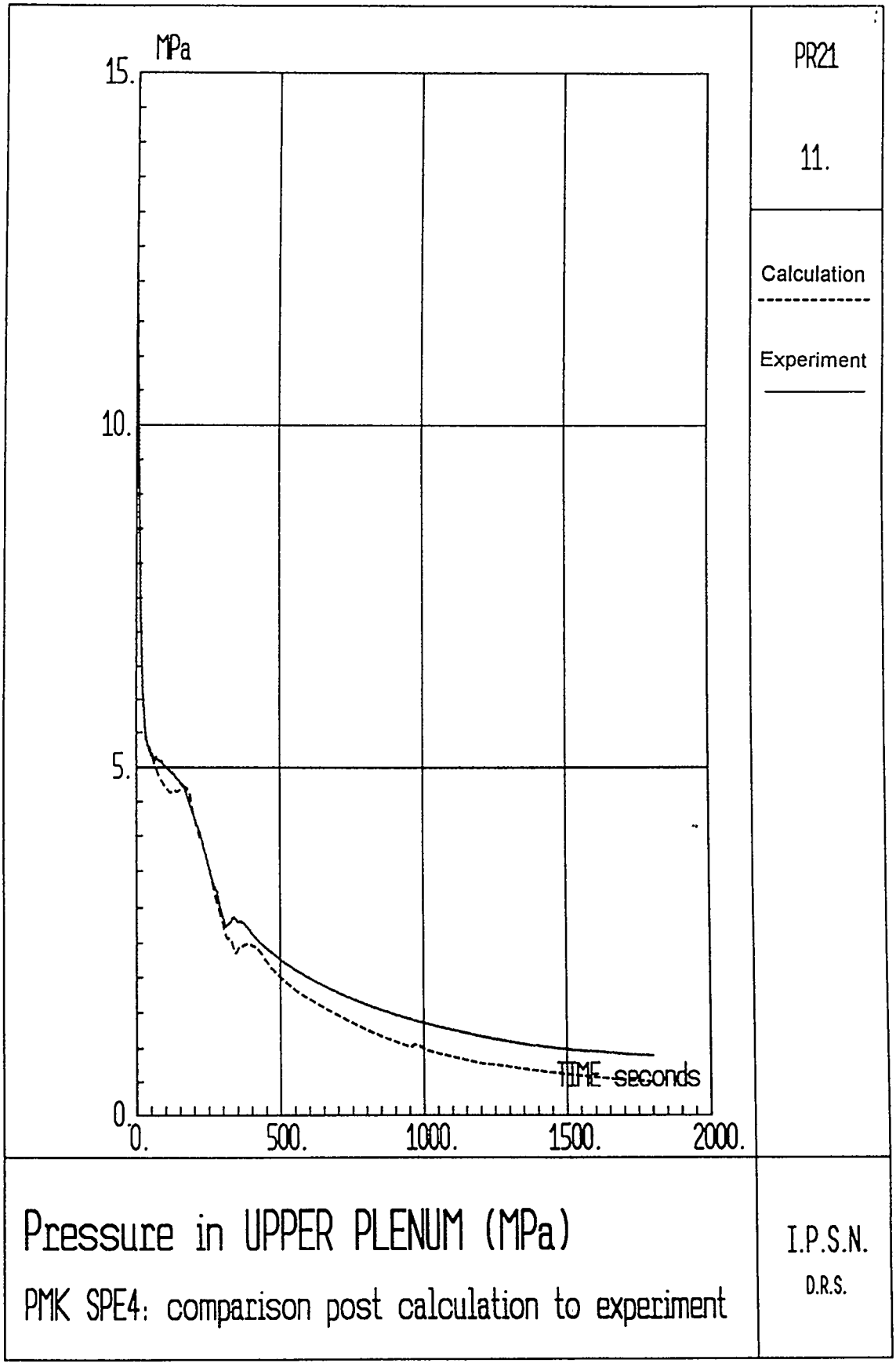


Figure 8: Primary and secondary pressures (MPa)

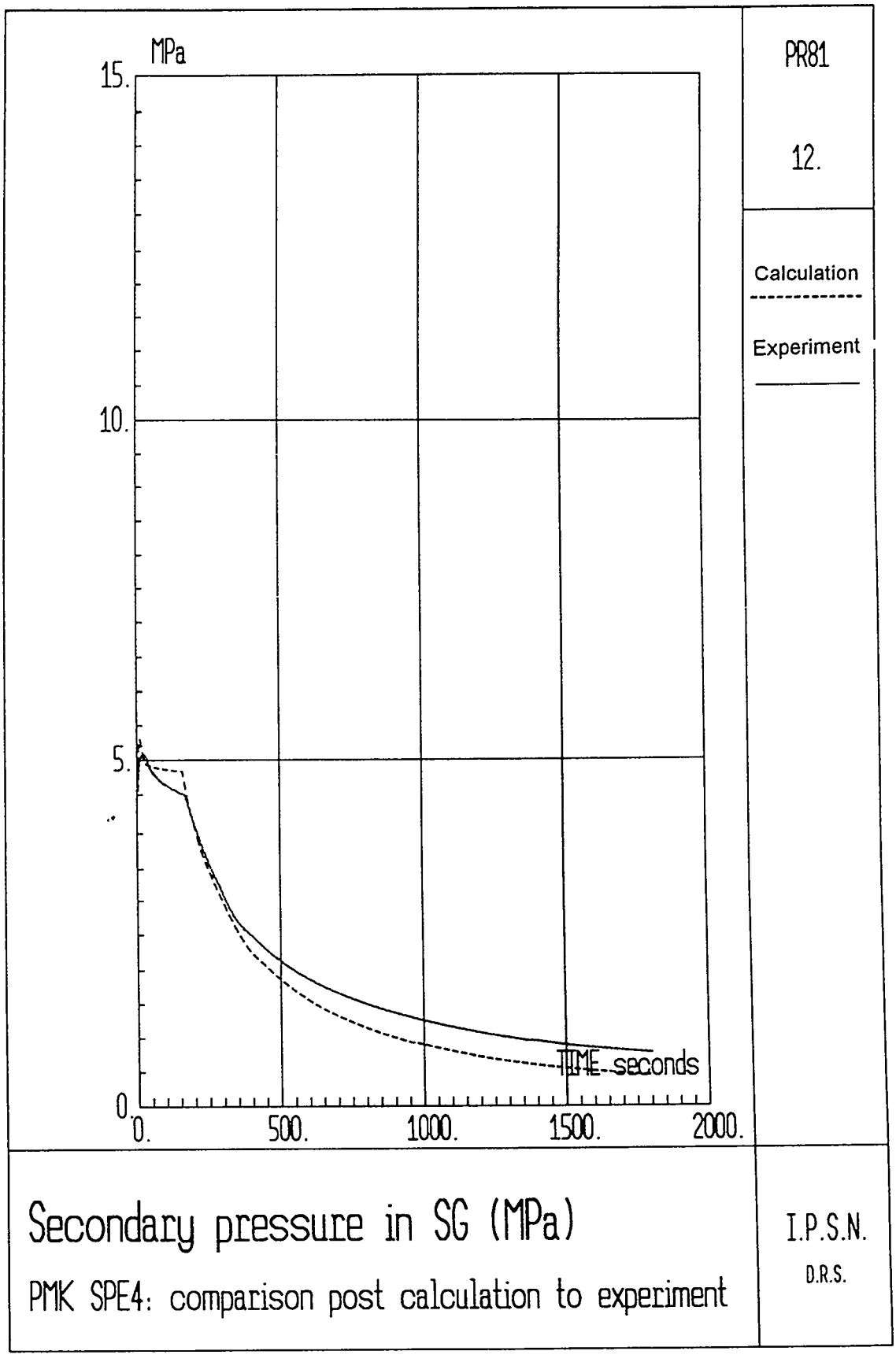


Figure 9: Secondary pressure (MPa)

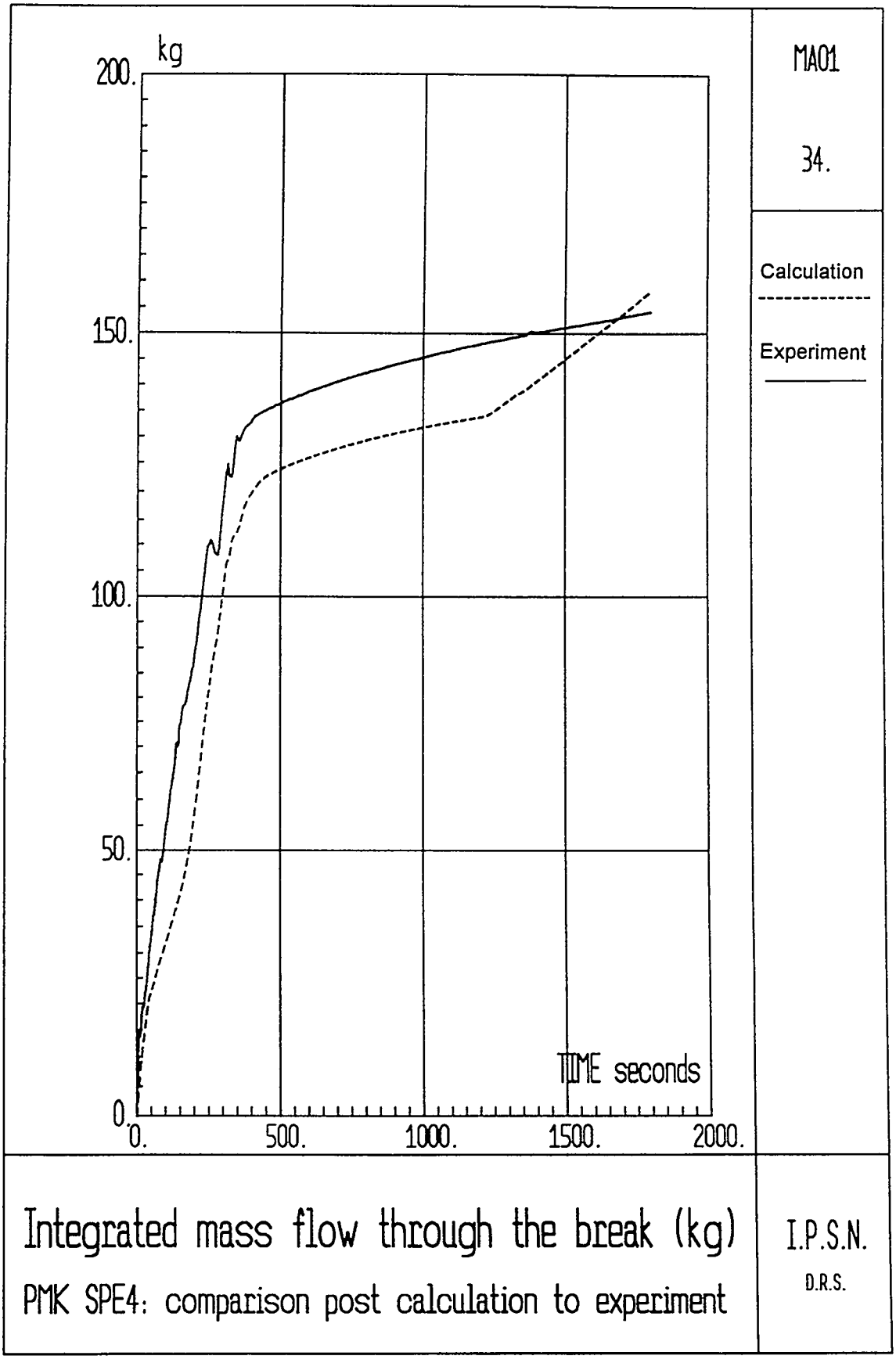


Figure 10: Integrated mass flow through the break (kg)

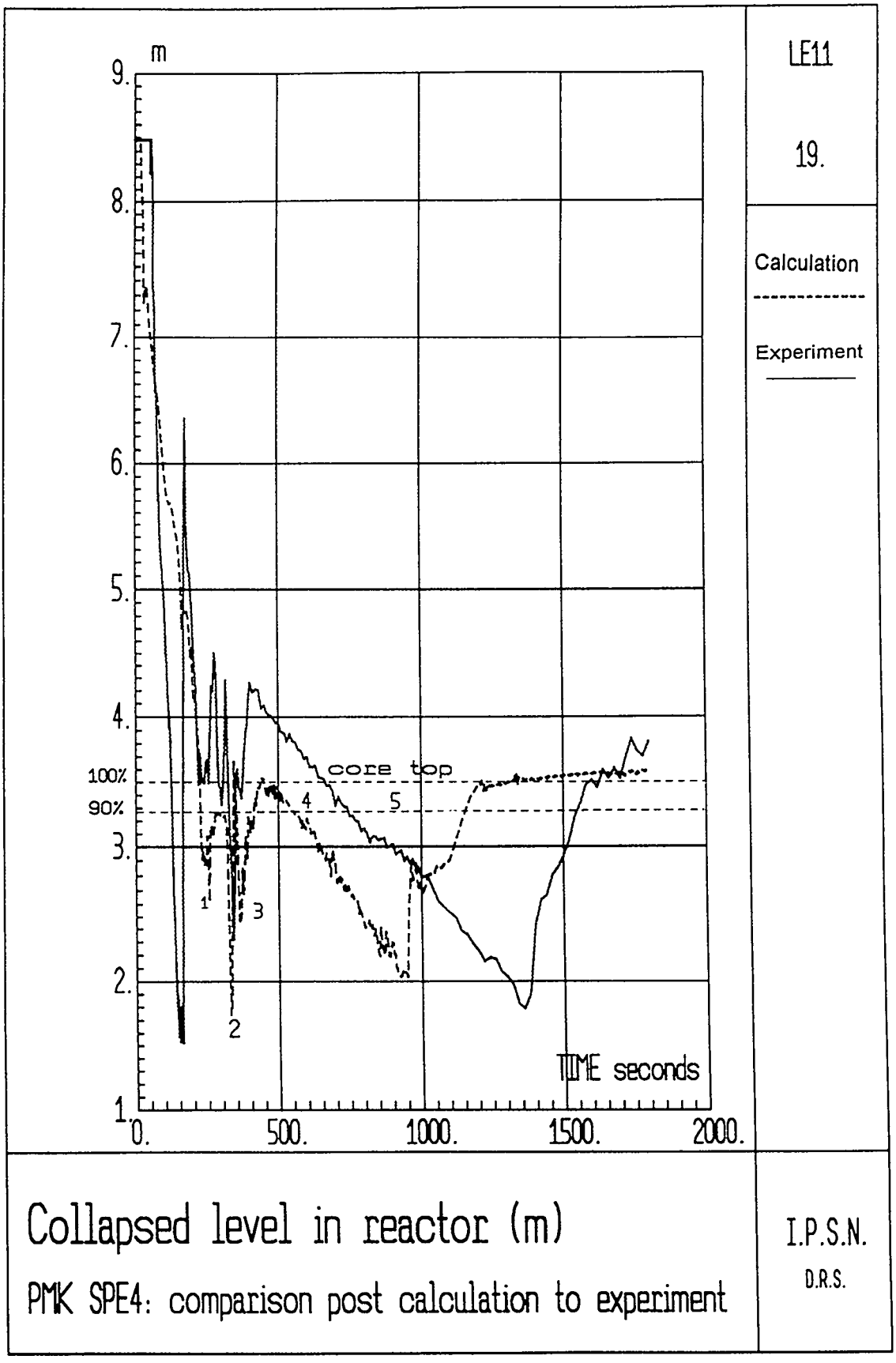


Figure 11: collapsed level of core (m)

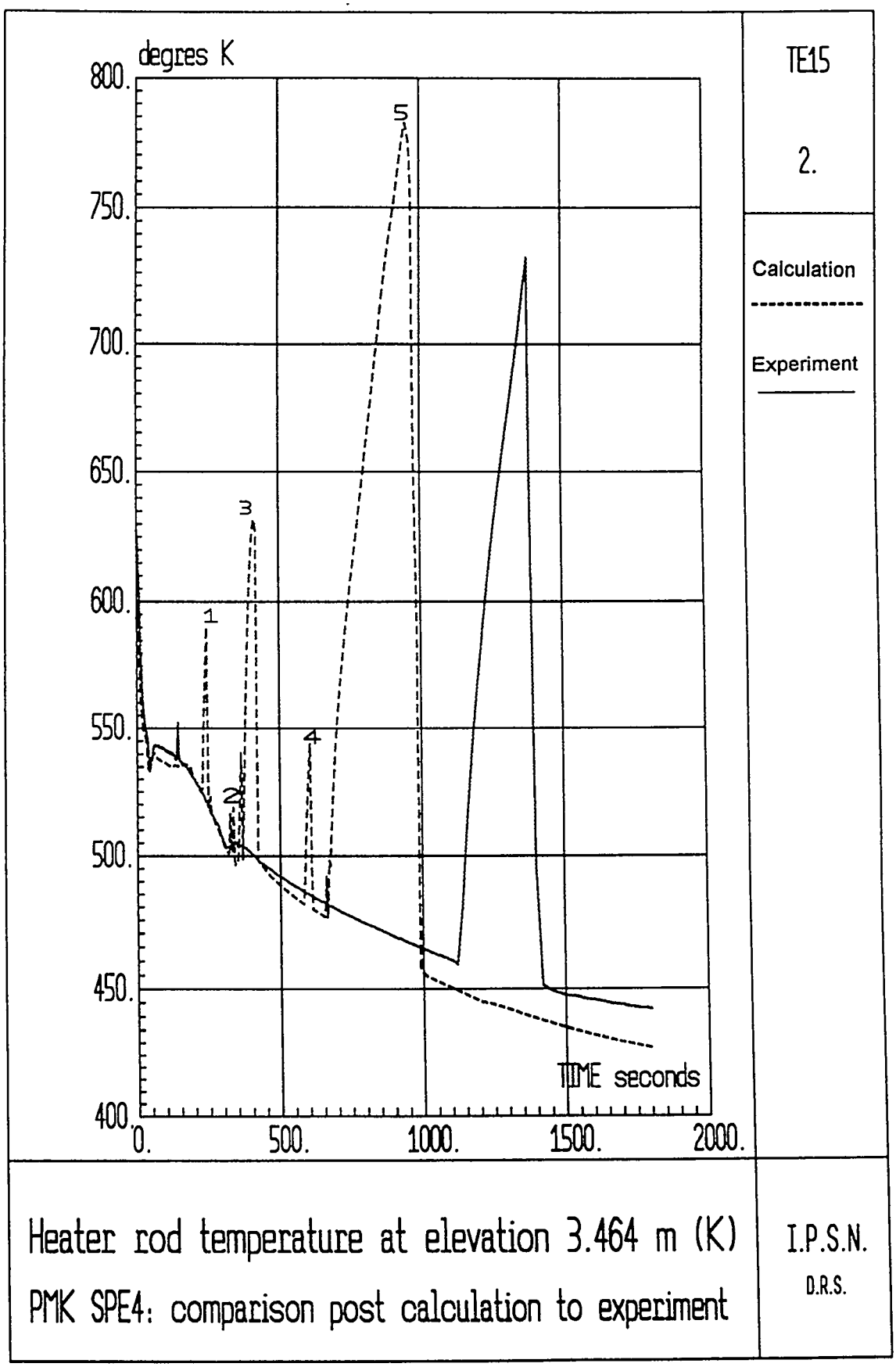


Figure 12: Core clad temperature (K)

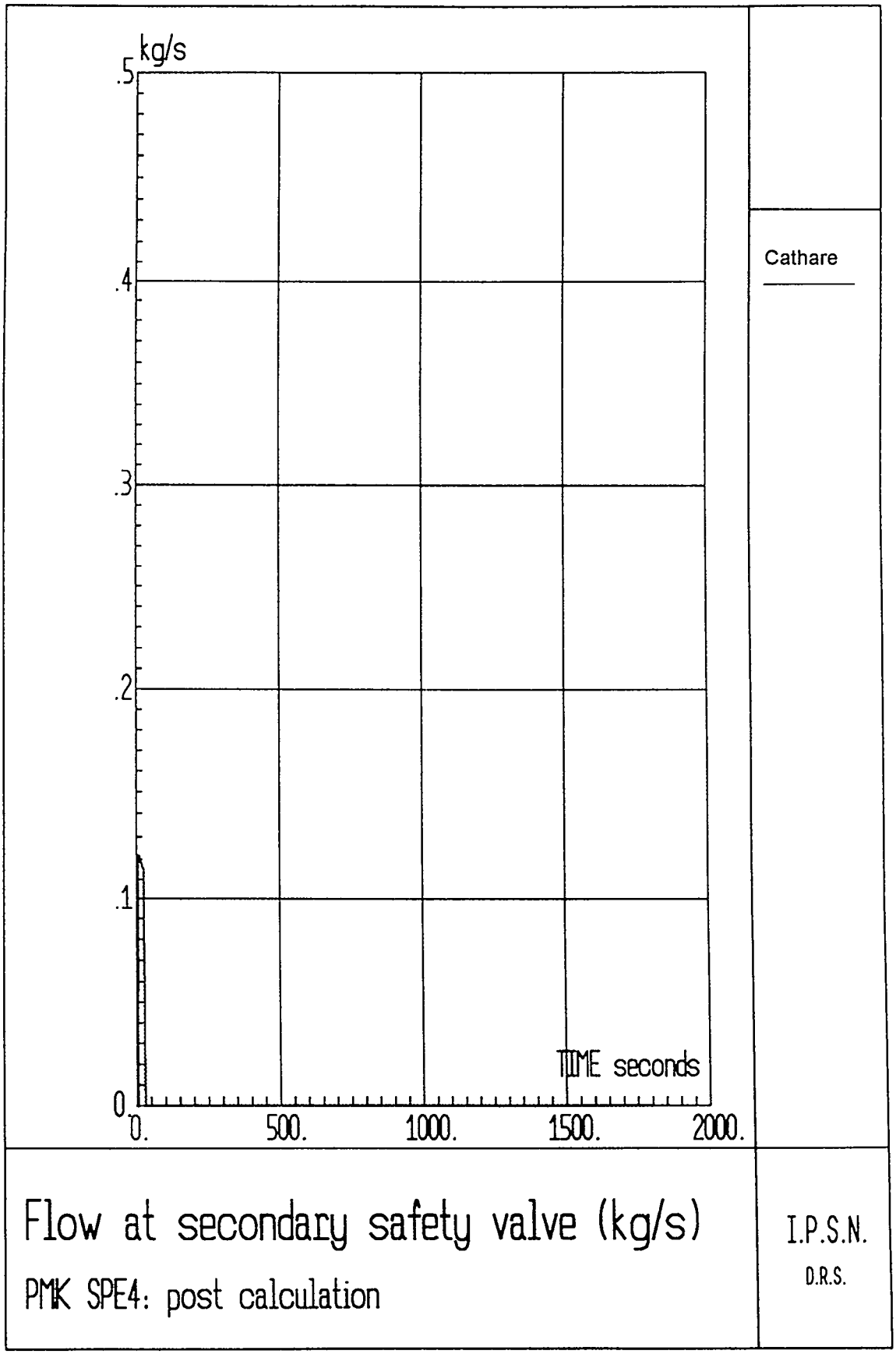


Figure 13: Flow at secondary safety valve (kg/s)

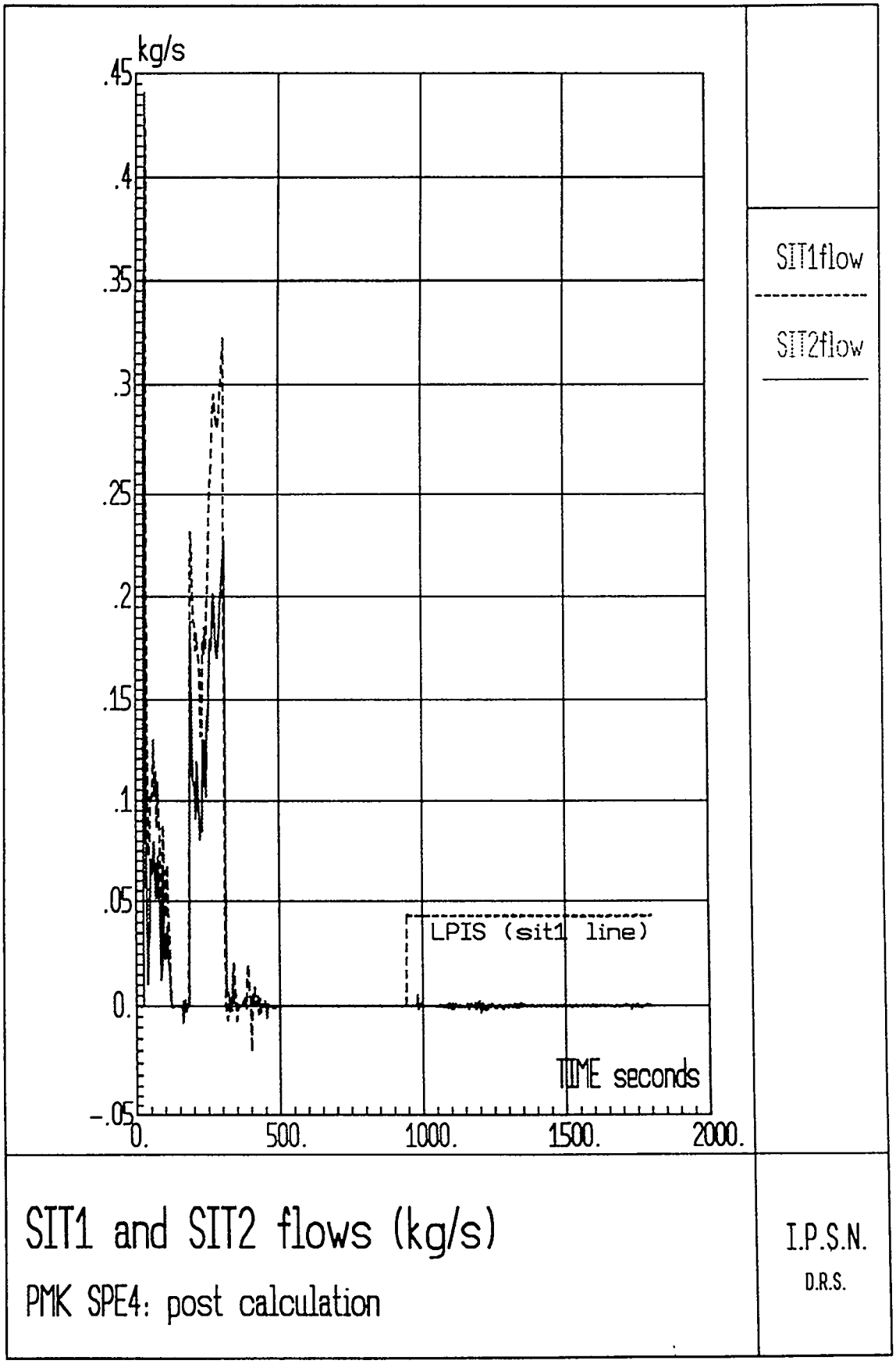


Figure 14: Sit1 and Sit2 flows (kg/s)

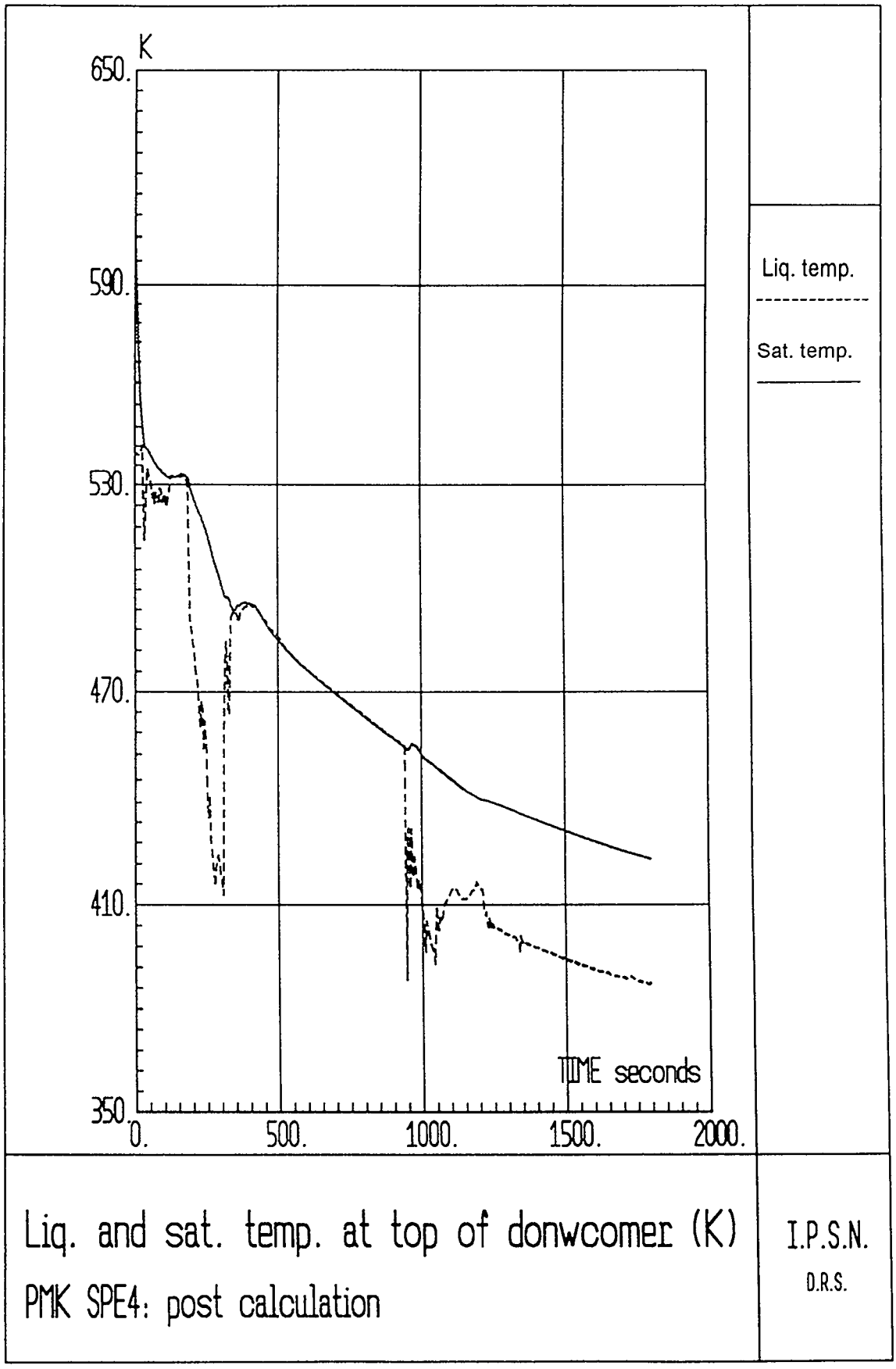


Figure 15: Liq. and sat. temp. at top of downcomer (K)

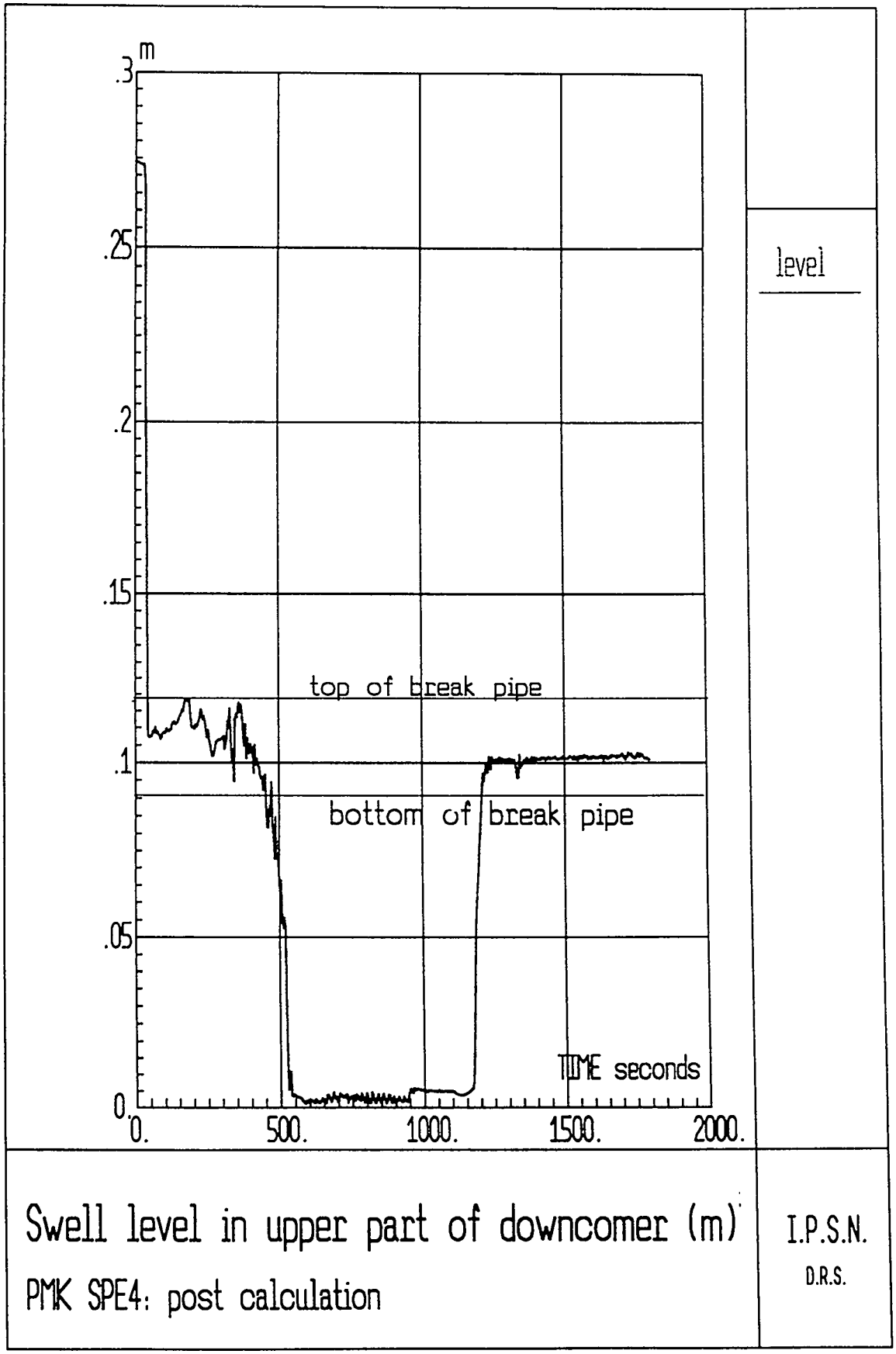


Figure 16: swell level of downcomer upper part (m)

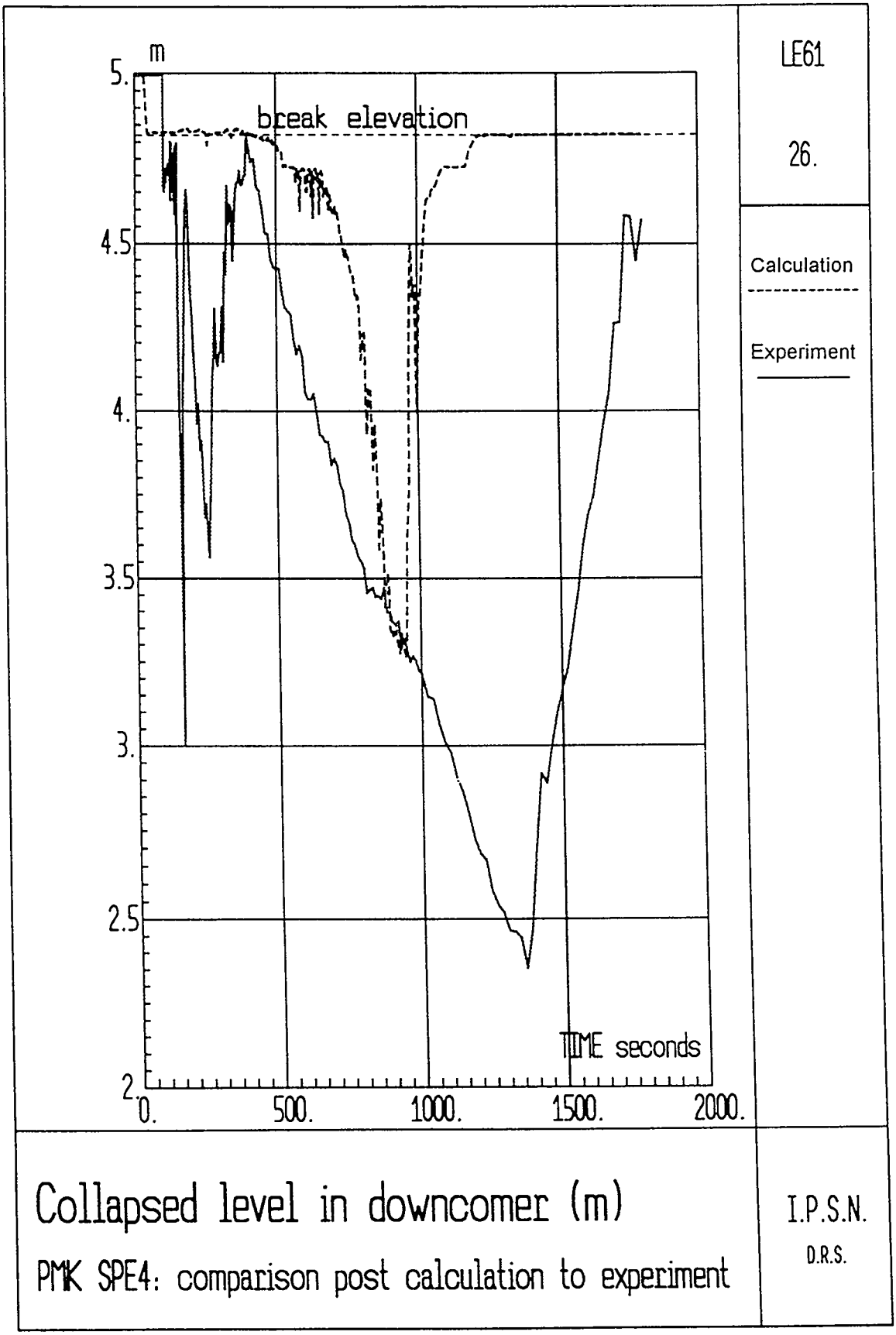


Figure 17: Collapsed level of downcomer (m)

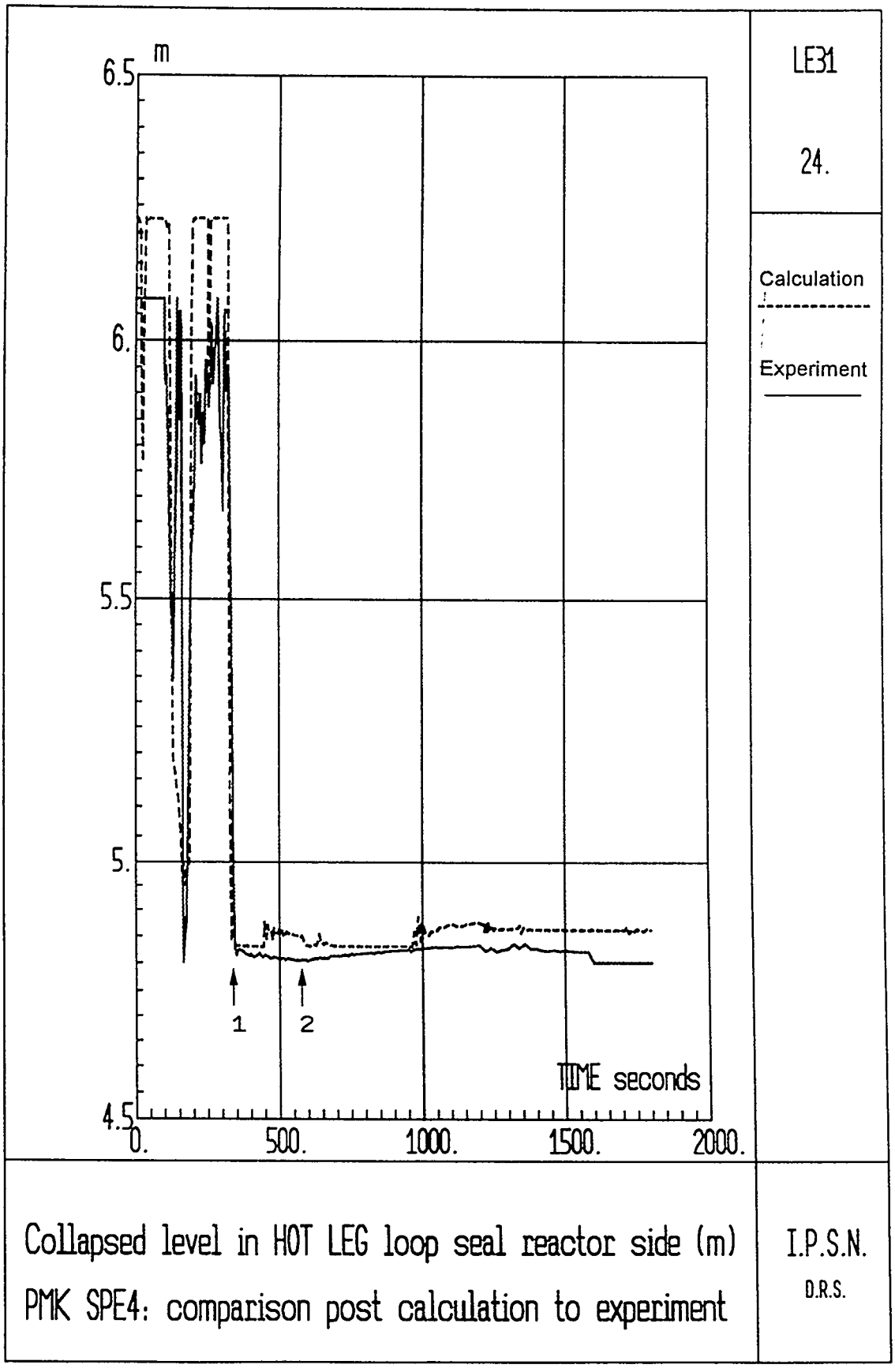


Figure 18: Collapsed level in hot leg loop seal (m)

QUANTITATIVE CODE ACCURACY EVALUATION OF ISP33

H. Kalli[1], A. Miettinen[1], H. Purhonen[2]
F.D'Auria[3], M. Frogheri[3], M. Leonardi[3]

[1]Lappeenranta University of Technology
P.O.B. 20, FIN 53851 Lappeenranta, Finland

[2]VTT Energy
P.O.B. 20, FIN 53851 Lappeenranta, Finland

[3]Dipartimento di Costruzioni Meccaniche e Nucleari
Facoltà di Ingegneria - Università di Pisa
Via Diotisalvi, 2, 56126 Pisa, Italy

ABSTRACT

Aiming at quantifying code accuracy, a methodology based on the Fast Fourier Transform has been developed at the University of Pisa, Italy. The paper deals with a short presentation of the methodology and its application to pre-test and post-test calculations submitted to the International Standard Problem ISP33. This was a double-blind natural circulation exercise with a stepwise reduced primary coolant inventory, performed in PACTEL facility in Finland. PACTEL is a 1/305 volumetrically scaled, full-height simulator of the Russian type VVER-440 pressurized water reactor, with horizontal steam generators and loop seals in both cold and hot legs. Fifteen foreign organizations participated in ISP33, with 21 blind calculations and 20 post-test calculations, altogether 10 different thermal hydraulic codes and code versions were used. The results of the application of the methodology to nine selected measured quantities are summarized.

1. INTRODUCTION

The assessment process of large thermal hydraulic computer codes aims principally at verifying the goodness of code predictions against experimental data gained mainly by tests performed in plant simulators. The reliability of these predictions, adopted for safety analyses of Nuclear Power Plants (NPPs), depends on many factors involving code features and user experience. The OECD/CSNI International Standard Problem (ISP) program was settled to investigate validity and the accuracy (i.e. the capability to predict correctly the observed scenario of tests performed in scaled facilities) of used computer codes and to increase the general confidence in their utilization.

A methodology suitable to quantify code accuracy has been developed at the University of Pisa, Dipartimento di Costruzioni Meccaniche e Nucleari (DCMN). It is an integral method using the Fast Fourier Transform (FFT) in order to represent the code discrepancies in the frequency domain. Preliminary applications of this method have been already carried out in the calculation analyses of other tests (e.g., ISP21, [1], ISP22, [2], ISP27, [3]). This paper deals with a new application of the

FFT methodology to the pre-test and post-test calculations submitted for the ISP33, [4],[5], in PACTEL facility, [6]. The facility was constructed and it is run by VTT Energy in co-operation with the Lappeenranta University of Technology, Finland. ISP33 was approved by the CSNI in 1991 as a double-blind standard problem, the experiments and the corresponding calculations were performed during the years 1992-1993.

As the objective of this paper is to present the application of the FFT method in the ISP33 case, Chapter 2 will contain only a short description of the method. Ref. [3] is recommended to readers interested in the details of the method; ref. [7] deals with a comparison of FFT based and other methods.

2. DESCRIPTION OF THE FFT METHOD

When using functions sampled in digital form, the FFT can be used, i.e. an algorithm that computes rapidly the discrete Fourier Transform. To apply this algorithm, functions must be identified by a number of values which is a power of 2. Thus, if the number of points defining the function in the time domain is $N=2^{m+1}$, the FFT gives the transformed function defined in the frequency domain by 2^m+1 values associated to the frequencies $f_n=n/T$, $(n=0, 1,...,2^m)$, where T is the time duration of the sampled signal. The accuracy quantification of a code calculation is based on the evaluation of the amplitude of the FFT of the experimental signal and of the difference between the calculated signal and the experimental one. The accuracy of a single parameter is characterized by means of a dimensionless average amplitude and a weighted frequency of the transformed quantities:

- a dimensionless average amplitude

$$AA=\frac{\sum_{n=0}^{2^m} |\widetilde{\Delta F}(f_n)|}{\sum_{n=0}^{2^m} |\widetilde{F}_{exp}(f_n)|}$$

- a weighted frequency

$$WF=\frac{\sum_{n=0}^{2^m} |\widetilde{\Delta F}(f_n)| \cdot (f_n)}{\sum_{n=0}^{2^m} |\widetilde{\Delta F}(f_n)|}$$

where the symbols with a tilde ($\sim$) denote Fourier transformed quantities, e.g., $\widetilde{\Delta F}(f_n)$ denotes the FFT of the difference $\Delta F(t)$ between the calculated signal $F_{calc}(t)$ and the experimental signal $F_{exp}(t)$.

The most significant information is given by AA, which represents the relative magnitude of the discrepancy deriving from the comparison between the addressed calculation and the corresponding measurements (AA=1 means a calculation affected by a 100 % of error). The WF factor gives an indication of the frequency content of the experimental and calculated signals: owing to the nature of the considered thermal hydraulic phenomena, high frequency errors are more acceptable than low frequency errors. In other words, analysing thermal hydraulic transients, better accuracy is generally represented by low AA values at high WF values, [7]. Trying to give an overall picture of the

accuracy of a given calculation, average indexes of performance are obtained by defining:

$$(AA)_{tot} = \sum_{i=1}^{N_{var}} (AA)_i \cdot (w_f)_i$$

$$(WF)_{tot} = \sum_{i=1}^{N_{var}} (WF)_i \cdot (w_f)_i$$

with $$\sum_{i=1}^{N_{var}} (w_f)_i = 1$$

where N_{var} is the number of analysed parameters and $(w_f)_i$ are weighting factors introduced to take into account the different importance of each parameter from the viewpoint of safety analysis, [3], [8]. This introduces some degree of engineering judgement requiring the choice of thermal hydraulic parameters and the definition of the weighting factors.

In the present investigation the weighting factors have been calculated using the following equation:

$$(w_f)_i = \frac{(W_{exp})_i * (W_{saf})_i}{\sum_{i=1}^{N_{var}} (W_{exp})_i * (W_{saf_i})}$$

where $(w_{exp})_i$ is the relative weight due to the experimental accuracy of parameter i, and
$(w_{saf})_i$ is the relative weight due to the safety relevance of parameter i.

3. FACILITY AND PROBLEM DESCRIPTION

3.1 PACTEL facility

PACTEL is a 1/305 volumetrically scaled, full-height model of the Russian design VVER-440 pressurized water reactors. The facility simulates all the major components of the primary system of the reference reactor,[4], [6].

The reactor vessel is simulated with a U-tube construction including separate downcomer and core sections. The core consists of 144 full-length, electrically heated fuel rod simulators with a maximum total power output of 1 MW, 22 % of the scaled full power. Three double capacity coolant loops with horizontal steam generators are used to model the six loops of the reference power plant. The horizontal orientation of steam generators is one of the unique features of the VVER design. One

consequence of this geometry is a reduced driving head for natural circulation. Component elevations correspond to those of the full-scale reactor to match the natural circulation gravitational heads in the reference system. Especially, the hot and cold leg elevations have been maintained, including the loops seals in both hot and cold legs. The hot and cold legs are shorter than in the reference system. To preserve the scaling, the leg cross-sections have been increased. Consequently, the Froude number in the loop seals becomes close to that of the full-scale plant.

The facility includes a pressurizer, high and low pressure emergency core cooling systems and an accumulator. The primary pumps were installed after the ISP33 experiment in the beginning of 1993.

3.2 International standard problem ISP33

The main goal of ISP33 was to study natural circulation in the VVER primary circuit in various single-and two-phase modes. This was the first time that a VVER type reactor was investigated in a CSNI international standard problem.

During the experiment the primary coolant mass was reduced from the lower plenum in several steps, allowing the system to restabilize between the steps. The secondary side was maintained near the nominal full power conditions of the reference plant. As the inventory was reduced the primary flow changed from single-phase to two-phase flow and finally to a boiler-condenser mode. Stagnation periods of the flow with corresponding pressure peaks were observed when the swell level in the upper plenum fell below the hot leg nozzles. The experiment was terminated when the core temperatures began sharply to rise.

Fifteen foreign organizations participated in ISP33 calculations, with 21 blind calculations and 20 post-test calculations, altogether 10 different thermal hydraulic codes and code versions were used, Table I. A detailed description of ISP33 can be found in the recently published final report [4], see also [5] in this conference.

4. QUANTITATIVE ACCURACY EVALUATION

4.1 Considerations about the evaluation

In the quantitative evaluation nine thermal hydraulic parameters of Table II have been used. The parameters have been chosen with the objective of identifying the most representative ones with the attention to their importance to reactor safety. The parameters related to the asymmetric behavior of the primary loops have not been included in the analysis. It should be noted here that in the earlier FFT applications larger sets of thermal hydraulic parameters have been used (e.g., 25 parameters in ISP27 [3]). As the behavior of individual loops is not included into this investigation, nine relatively independent parameters are enough to characterize the general behavior of the facility during the experiment.

As described in Chapter 2, the overall indexes of performance are obtained by a weighted average over the individual parameter indexes. The set of values utilized here to derive the weighting factors is the same as used in the earlier code accuracy evaluation of ISP27 [3]. On the basis of thermal hydraulic events during the experiment the quantitative analysis has been performed for five time

windows: 0 - 1200 s, 0 -1400 s, 0 - 2100 s, 0 - 3200 s and 0 - 6600 s. The last two time windows can be regarded as the most interesting ones: the last time window 0 - 6600 s includes the overall transient with the final rise of the cladding temperatures, the window 0 - 3200 s includes the stagnation periods of natural circulation flow (around t = 2500 - 3000 s, see ref. [5]) that represents a peculiarity of the experiment and a challenging phenomenon for the codes.

4.2 Pre-test results

Fifteen out of 21 submitted blind calculations have been evaluated with the FFT method for all five time windows. (Three sets of results were omitted due to missing parameters, three calculations were analysed only for the first three time windows.)

In Figures 1, 2 and 3 the development of the $(AA)_{tot}$ factor for all the calculations in five time intervals are shown. The AA factor tends to increase with time in all the calculations. The values increase most in the fourth time window due to the time shifting of the thermal hydraulic phenomena in the calculations or due to the difficulties in calculating of the flow stagnations. The smallest AA values for the blind ISP in the last two time windows were obtained by IJS (Relap5/mod2 and Relap5/mod3) and STUDS (Relap5/mod3). Figure 4 shows certain results on (AA, 1/WF)-plane: The marked zones characterize the dispersion of the calculational results for each code, illustrating the uncertainty of the calculations.

Based on the experience gathered from the previous applications of the DCMN method, ref. [3] gives the value $(AA)_{tot} = 0.4$ as a threshold for identifying acceptable accuracy. This threshold represents a value coming from the evaluation of several tens of complete experimental scenarios and related calculations, see also ref. [9]. In all the ISP33 calculations analysed the overall AA values are below the value 0.4 indicating acceptable accuracy. Similar criteria can be used to evaluate the code capability in a single parameter prediction. Especially, the acceptability limit for the primary side pressure evaluation has been defined based on the vast experience gathered from the earlier applications: $(AA)_{pressure} < 0.1$. The ISP33 results analysed clearly show difficulties in calculating the pressure during the flow stagnation periods in the experiment. In the time window 0 - 3200 s the AA value for the pressure is larger than the acceptability limit 0.1 in all the calculations. In fifteen cases out of 19 the AA value is even larger than 0.2.

4.3 Post-test results

Sixteen results out of 20 submitted ones were chosen for the FFT analysis. (Some participants submitted more than one set of results, i.e., a sensitivity study; only one set per participant per code version was analysed. One result was omitted due to missing parameters.) Figures 5, 6 and 7 show the development of the $(AA)_{tot}$ values for all the calculations in five time intervals. The AA values again increase significantly in the fourth time window (0 - 3200 s). The smallest AA values in the last two time windows were obtained by NRI (Relap5/mod3), SIEMENS (Relap5/mod2.5) and GRS (Athlet). The uncertainty of the calculations is illustrated on (AA, 1/WF)-plane in Figure 8. Especially, Relap5/mod3 calculations seem to have a large scatter. Again the overall AA values are well below the threshold value 0.4. However, the difficulties in calculating the pressure during flow

stagnations still exist: in the time window 0 - 3200 s the AA value for the pressure is larger than the acceptability limit 0.1 in fourteen calculations out of 16 and in seven cases AA is even larger than 0.2.

5. DISCUSSION

In this paper, the pre-test and post-test calculation results submitted for ISP33 have been analysed in order to quantify the code accuracy by the method developed at DCMN of the University of Pisa. As far as the authors know, ISP33 is the first ISP where a quantitative evaluation of the quality of the participants submissions has been a part of the very ISP procedure.

It should be pointed out that the DCMN method contains in the selection of thermal hydraulic parameters and associated weights a certain degree of engineering judgement which may vary from one expert to another. In the evaluation of the global accuracy nine thermal hydraulic parameters have been used. This is less than in the earlier applications and, hence, a certain caution should be exercised when comparing the ISP33 accuracy results with the results obtained in the earlier applications. Especially, in this work the parameters related to the asymmetric behavior of the three primary loops have not been included in the evaluation.

With reference to the experience gathered from the previous applications of the DCMN method, ref. [3] gives the value $(AA)_{tot}$=0.4 as a threshold identifying acceptable accuracy. We can note (keeping the caution above in mind) that in both pre- and post-test calculations for ISP33 all the results analysed are below this threshold indicating acceptable accuracy. On the other hand, difficulties in the calculation of the primary pressure during the flow stagnation periods in the experiment lead generally to large values of AA for the pressure exceeding the acceptability limit proposed by the developers of the DCMN method. It seems that in the case of ISP33 the two acceptability limits ($(AA)_{tot}$ = 0.4 and $(AA)_{pressure}$ = 0.1) are not well in balance.

The dispersion in the results obtained by different participants either with a certain code or with different codes leads to a scatter in the values of the factors AA and WF of the DCMN method, (Figures 4 and 8). This scatter illustrates the uncertainty in the code predictions and prevents an order of superiority among the different codes and code versions from being derived. In a sense, the scatter among the results with a certain code reflects also the user effect, i.e., the fact that different users having the same code and the same information from the ISP organizers produce different results.

It may be worth noting that the post-test predictions are generally characterized by a better accuracy than the pre-test ones. Improvements in boundary conditions, changes in nodalization, sensitivity analyses, result in a better prediction of phenomena and their timing; this improvement in the accuracy can be quantified by the FFT method.

The ultimate goal of code uncertainty quantification is to provide the basis by which it may be judged that a code is sufficiently accurate to be used in the safety analysis of a nuclear power plant.

This goal is clearly beyond the scope of the present application to an ISP in a scaled facility. Yet, the FFT based method can be used and has been used as a tool in the evaluation of the uncertainty in the code predictions of nuclear power plants related transient scenarios; see references [9] and [10] on UMAE, Uncertainty Methodology based on Accuracy Extrapolation.

REFERENCES

[1] CSNI International Standard Problem N. 21 - Comparison Report, vols. 1 and 2. NEA/CSNI Report N. 162, Paris (1989).

[2] W. Ambrosini, M.P. Breghi, F. D'Auria, "Evaluation of code accuracy in the prediction of the OECD/CSNI ISP22". University of Pisa, DCMN Report, NT 176 (1991).

[3] F. D'Auria, M. Leonardi, R. Pochard, "Methodology for the evaluation of thermalhydraulic codes accuracy". Proc. Conf. on "New Trends in Nuclear System Thermohydraulics", Pisa, May 30 - June 2, 1994, pp. 467 - 477 (1994).

[4] H. Purhonen, J. Kouhia, H. Holmström, "ISP33 OECD/NEA/CSNI International Standard Problem No.33. PACTEL natural circulation stepwise coolant inventory reduction experiment". NEA/CSNI/R (1994) 24, vol I and II, Paris (1994).

[5] H. Purhonen, J. Kouhia, H. Kalli, "ISP33 standard problem on the PACTEL facility". Proc. of this conference.

[6] P. Raussi, R. Munther, H. Kalli, J. Kouhia, M. Puustinen, "Experimental VVER safety studies in Finland". Trans. of ENC '94, Int. Nuclear Congress, Lyon, October 2-6, 1994, Vol. II, pp. 222 - 225 (1994).

[7] W. Ambrosini, R. Bovalini, F. D'Auria, "Evaluation of accuracy of thermalhydraulic code calculations". J. Energia Nucl. 7, pp. 5 - 16 (1990).

[8] R. Bovalini, F. D'Auria, M. Leonardi, "Qualification of the Fast Fourier Transform based methodology for the quantification of thermal hydraulic code accuracy". University of Pisa, DCMN Report, NT 194 (1992).

[9] M. Leonardi, F. D'Auria, R. Pochard, "The FFT based method utilization in the frame of the UMAE". OECD-CSNI Spec. Workshop on Uncertainty Analysis Methods, London, March 1-4, 1994. NEA-CSNI R(94)20.

[10] F. D'Auria, N. Debrecin, G.M. Galassi, "Outline of the uncertainty methodology based on accuracy extrapolation". J. Nuclear Technology 109, Nr1, 21-38, (1995).

TABLE I. Participants of ISP 33.

Organization	Code	Pre-test	Post-test
BARC (Bombay, India)	ATHLET MOD1 D ATHLET MOD1 D RELAP4/MOD6	X X X	
CEA CENG/SEMAR/LEACS (Cadarache, France)	CATHARE 2 V1.3e	X	X
ECN (Netherland Energy Research)	RELAP5/MOD2.5	X	X
FRG/FZR (Rossendorf, Germany)	ATHLET MOD1.0 E	X	X
GRS (Germany) & RSC KI (Kurchatov I., Russia)	ATHLET MOD1.0 E	X	X
IJS (J. Stefan I., Slovenia)	RELAP5/MOD2/36.05 RELAP5/MOD3 5m5	X X	X X
JAERI (Japan)	RELAP5/MOD2		XX*
NPPRI (Slovakia)	RELAP5/MOD2/RMA RELAP5/MOD3/5m5	X	X X
NRI (Czech Republic)	RELAP5/MOD2.5/SRL RELAP5/MOD3/5m5	X	 X
OKB Gidropress (Russia)	DINAMIKA-5 TECH-M-4	X X	
PSI (Switzerland)	RELAP5/MOD2.5	X	X
RRC KI ST. (Kurchatov I., Russia)	RELAP5/MOD3	X	X
RCS KI A.N. (Kurchatov I., Russia)	SCDAP/RELAP5/MOD2	X	X
RCS KI DE. (Kurchatov I., Russia)	RELAP5/MOD3/5m5	X	X
SIEMENS (Germany)	RELAP5/MOD2.5		X
STUDS (Studsvik, Sweden)	RELAP5/MOD3/5m5	X	
TAEK (Turkey)	RELAP5/MOD3/5m5	X	XX*
THZ (Zittau/Görlitz, Germany)	ATHLET MOD1.0 E	X	X
UP-DCMN (Pisa, Italy)	CATHARE 2 V1.2E	X	X
VTT (Finland)	RELAP5/MOD3		X

* sensitivity study

TABLE II. List of selected parameters and their relative weighting factor components.

EXP	PARAMETER	w_{exp}	w_{saf}
P02PZ	Pressurizer pressure	1.0	1.0
FDC	Downcomer flow	0.5	0.8
DP24PZ	Differential pressure over pressurizer	0.7	0.7
DP18UP	Differential pressure over upper plenum	0.7	0.7
DP16CO	Differential pressure over core	0.7	0.7
TCA25H_2286	Cladding temperature of core level 2286 mm	0.9	1.0
TCA25H_0672	Cladding temperature of core level 672 mm	0.9	1.0
TFCOH_2800	Coolant temperature at elevation 2800 mm	0.8	0.8
TFACH_6150	Coolant temperature at elevation 6150 mm	0.8	0.8

w_{exp}: relative weight due to experimental accuracy
w_{saf}: relative weight due to safety relevance

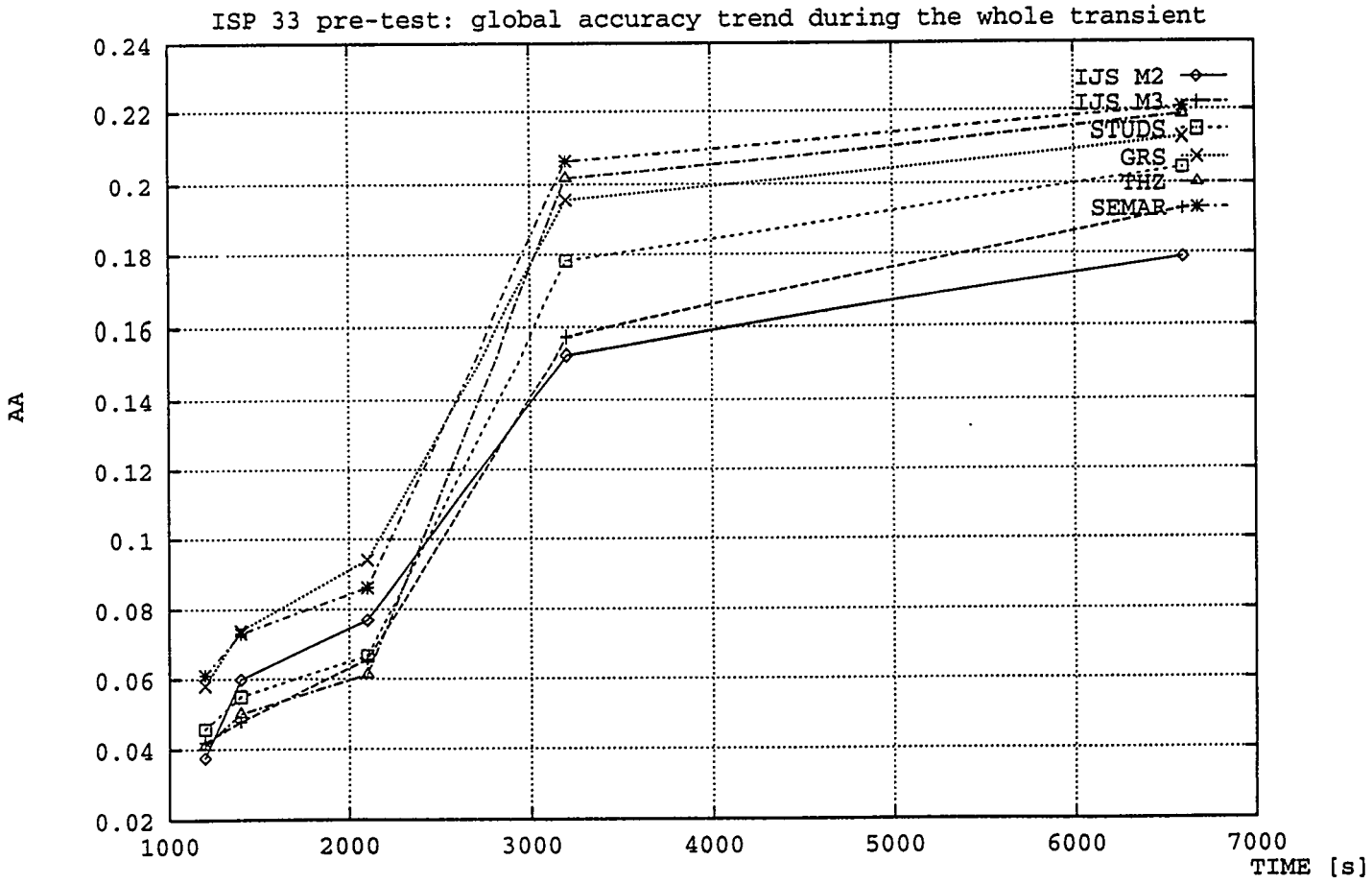


Figure 1. Pre-test results; AA factors in five time intervals.

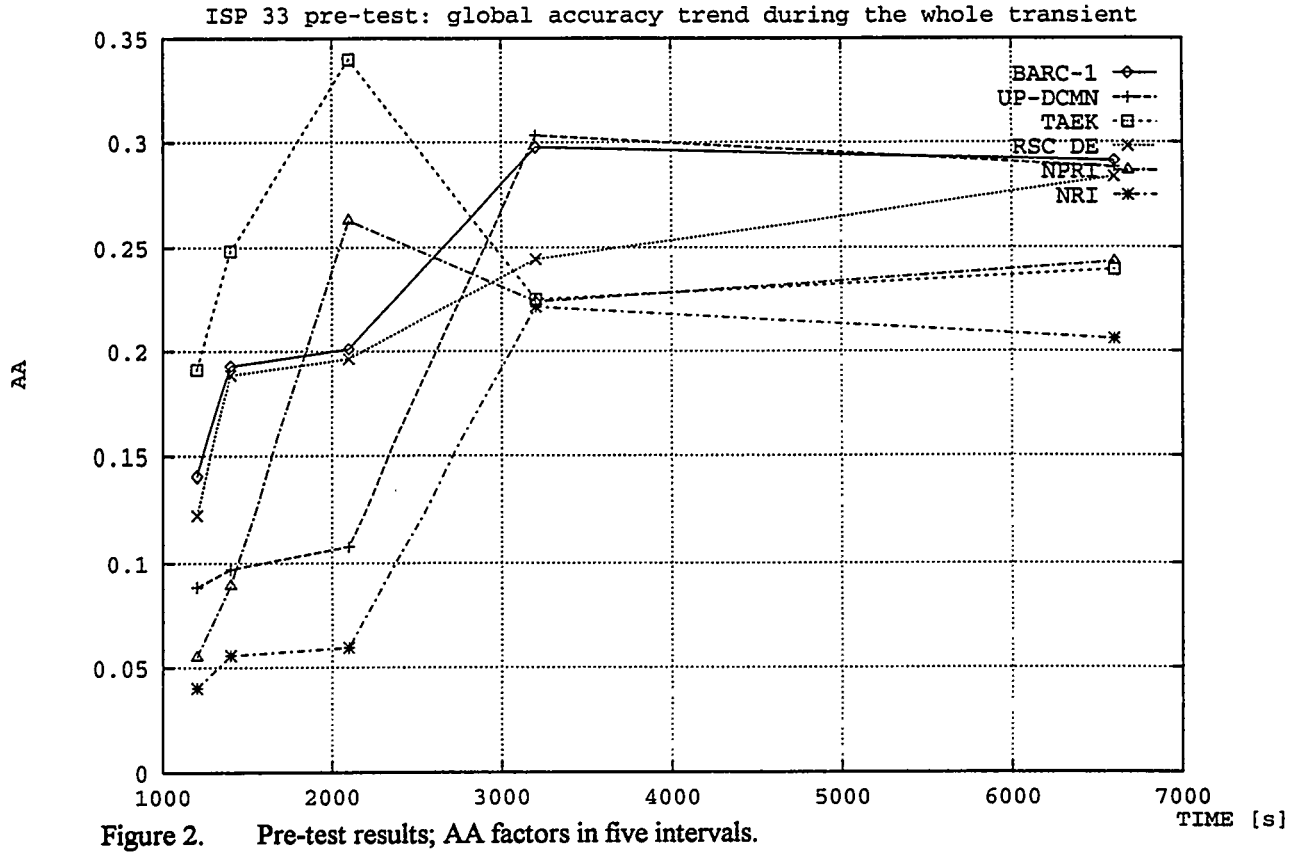


Figure 2. Pre-test results; AA factors in five intervals.

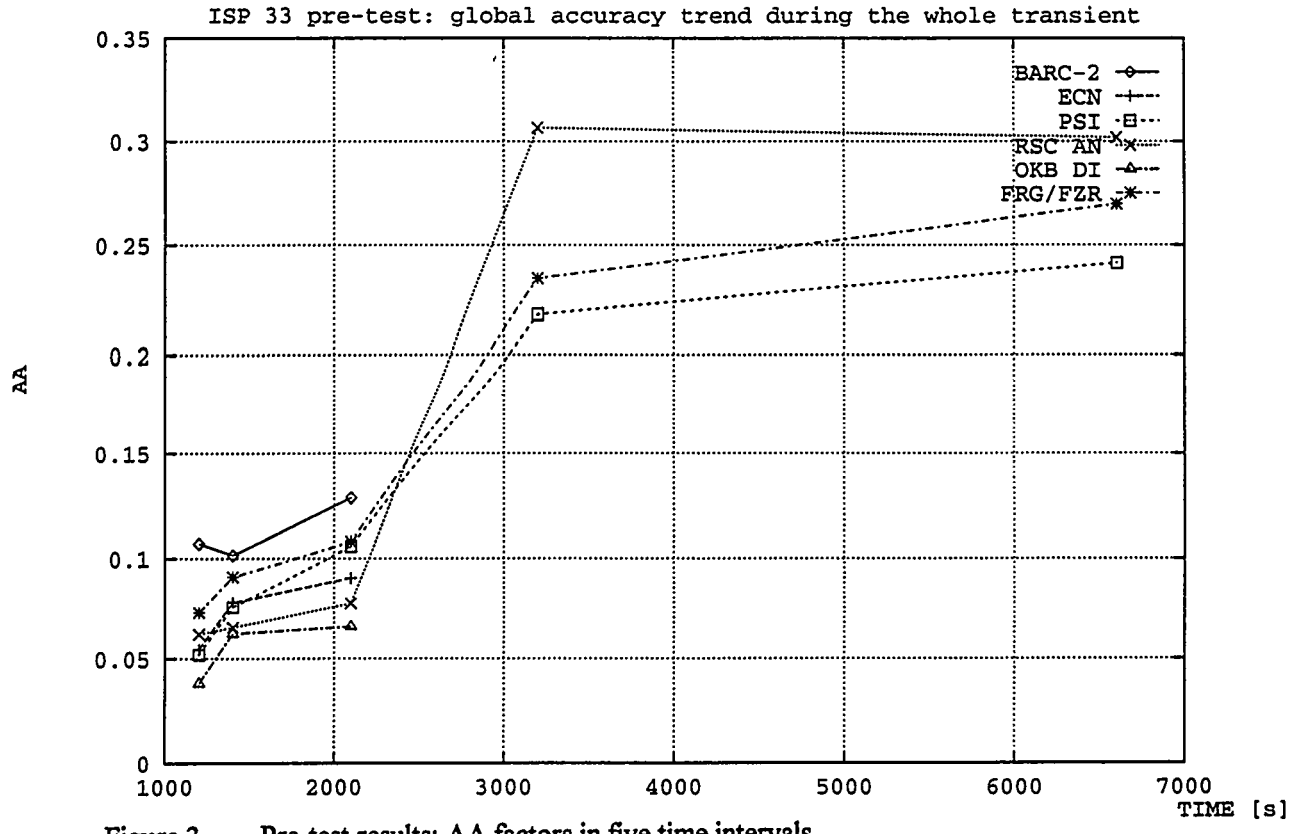


Figure 3. Pre-test results; AA factors in five time intervals.

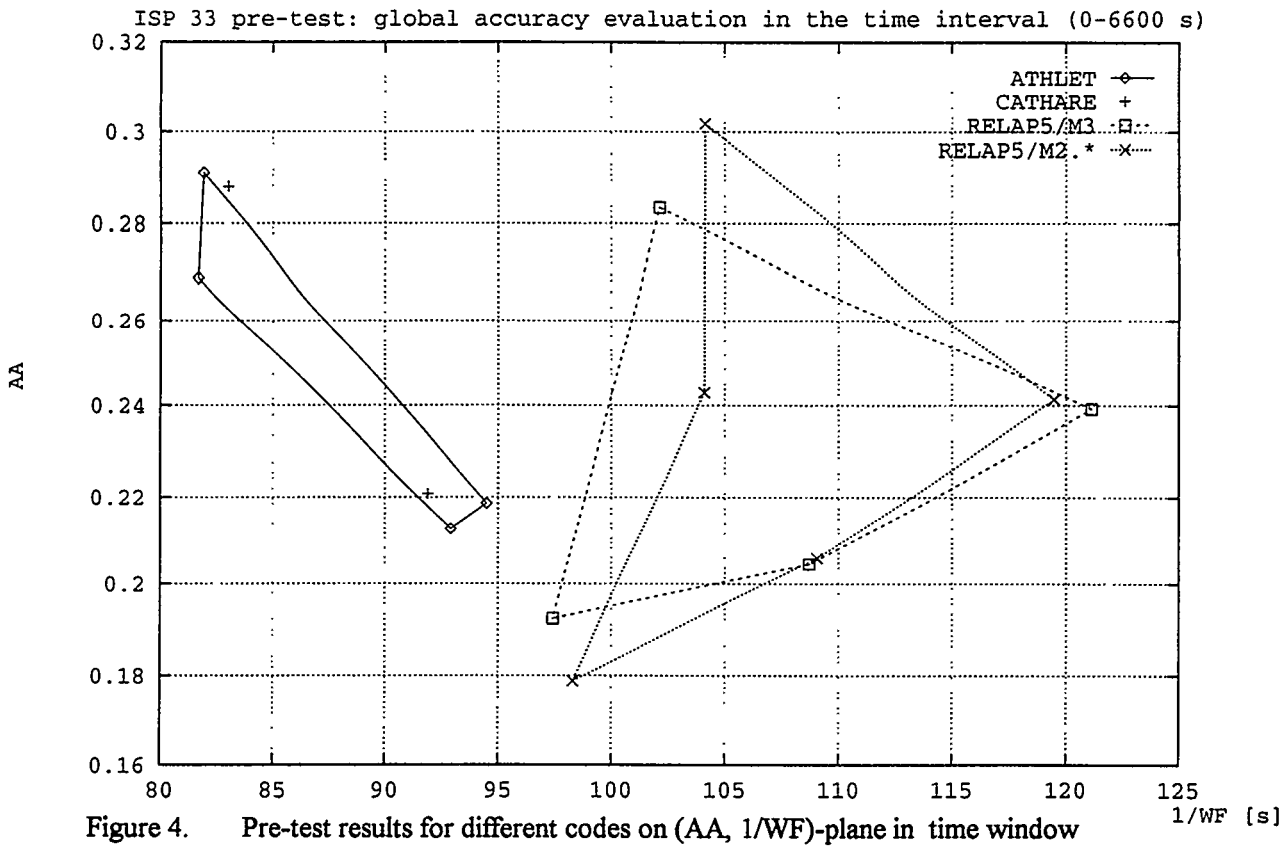


Figure 4. Pre-test results for different codes on (AA, 1/WF)-plane in time window (0 - 6600 s.).

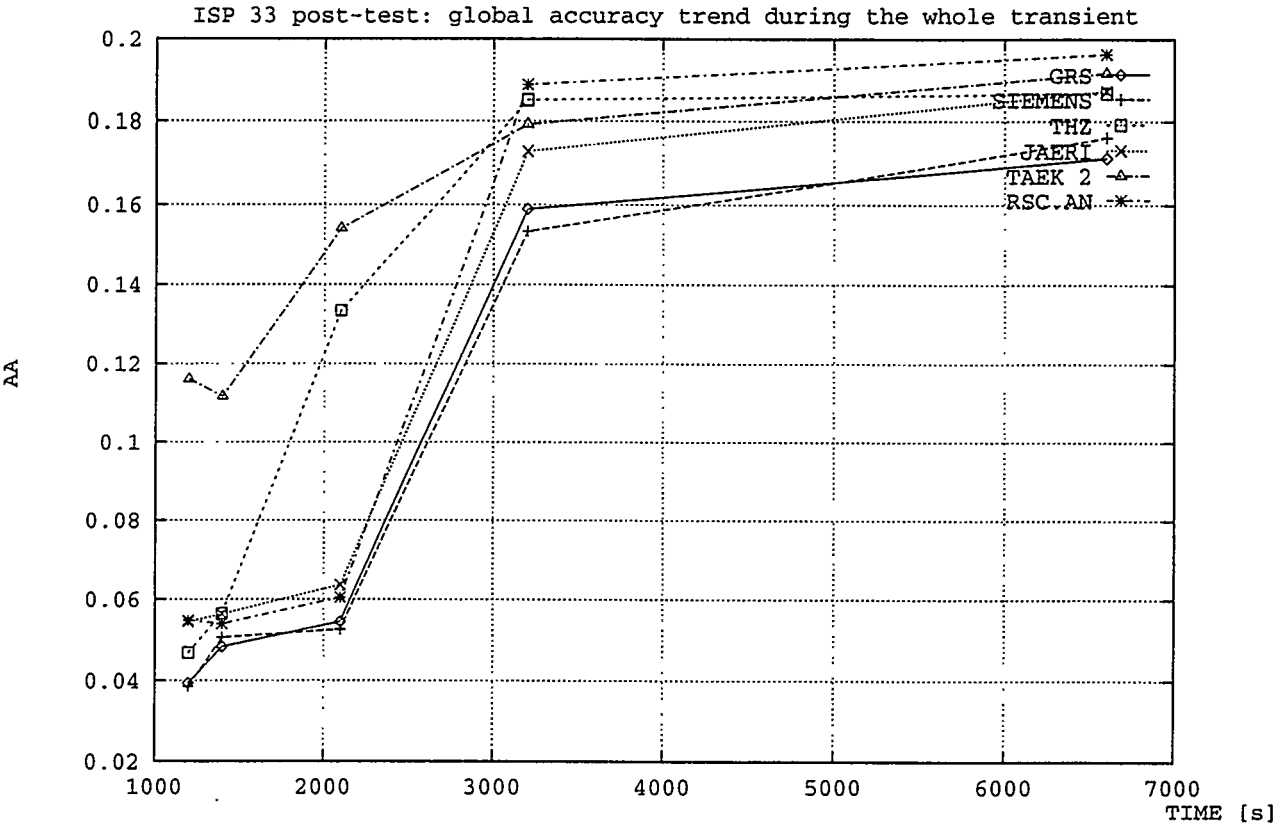


Figure 5. Post-test results; AA factors in five time intervals.

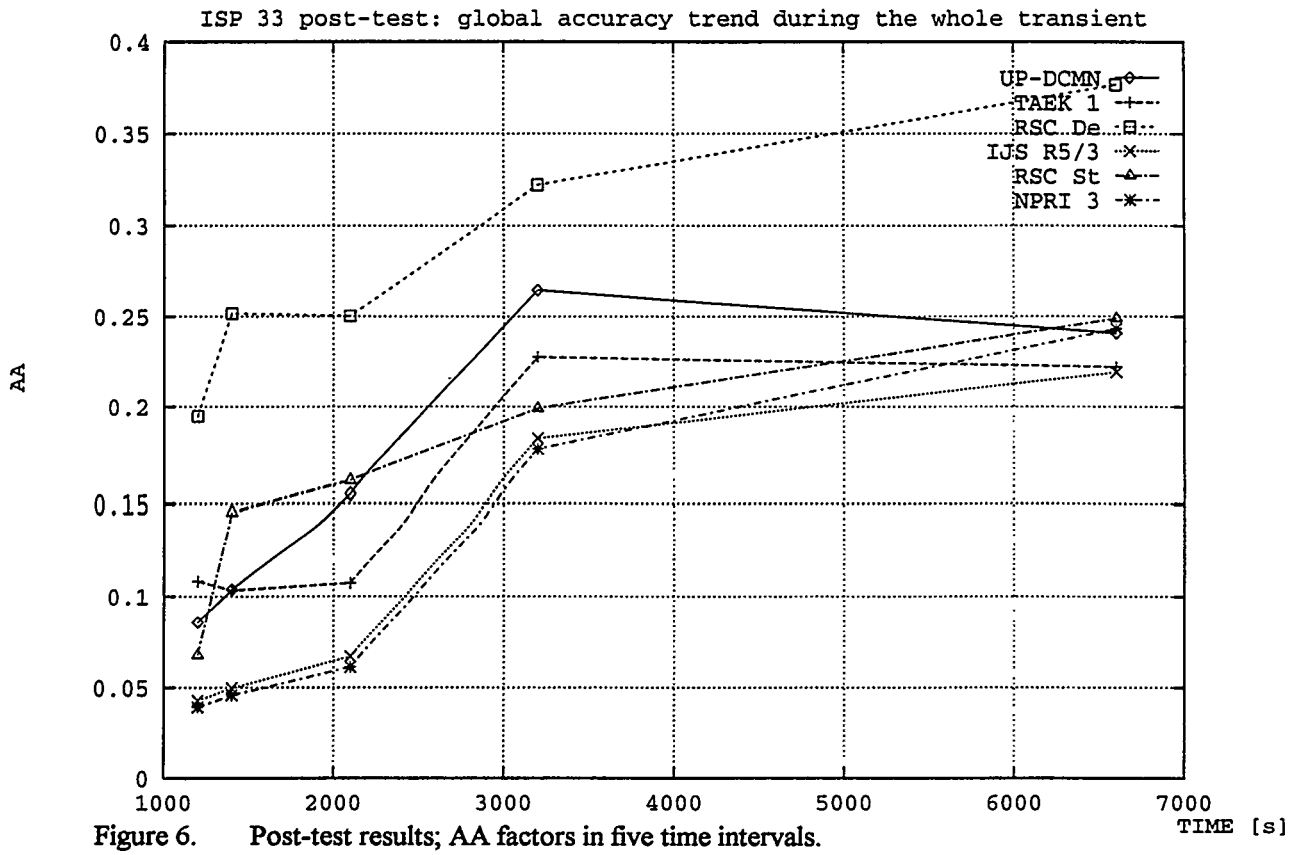


Figure 6. Post-test results; AA factors in five time intervals.

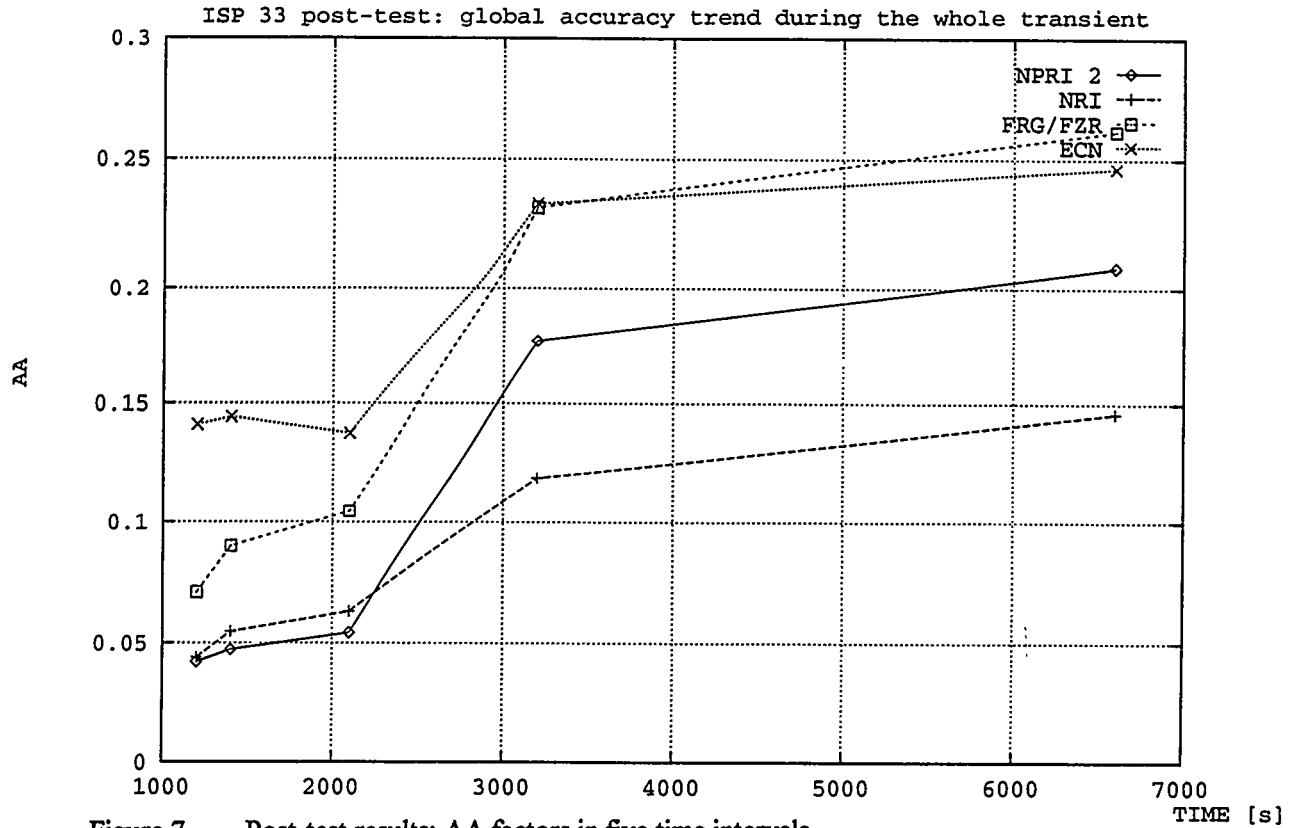


Figure 7. Post-test results; AA factors in five time intervals.

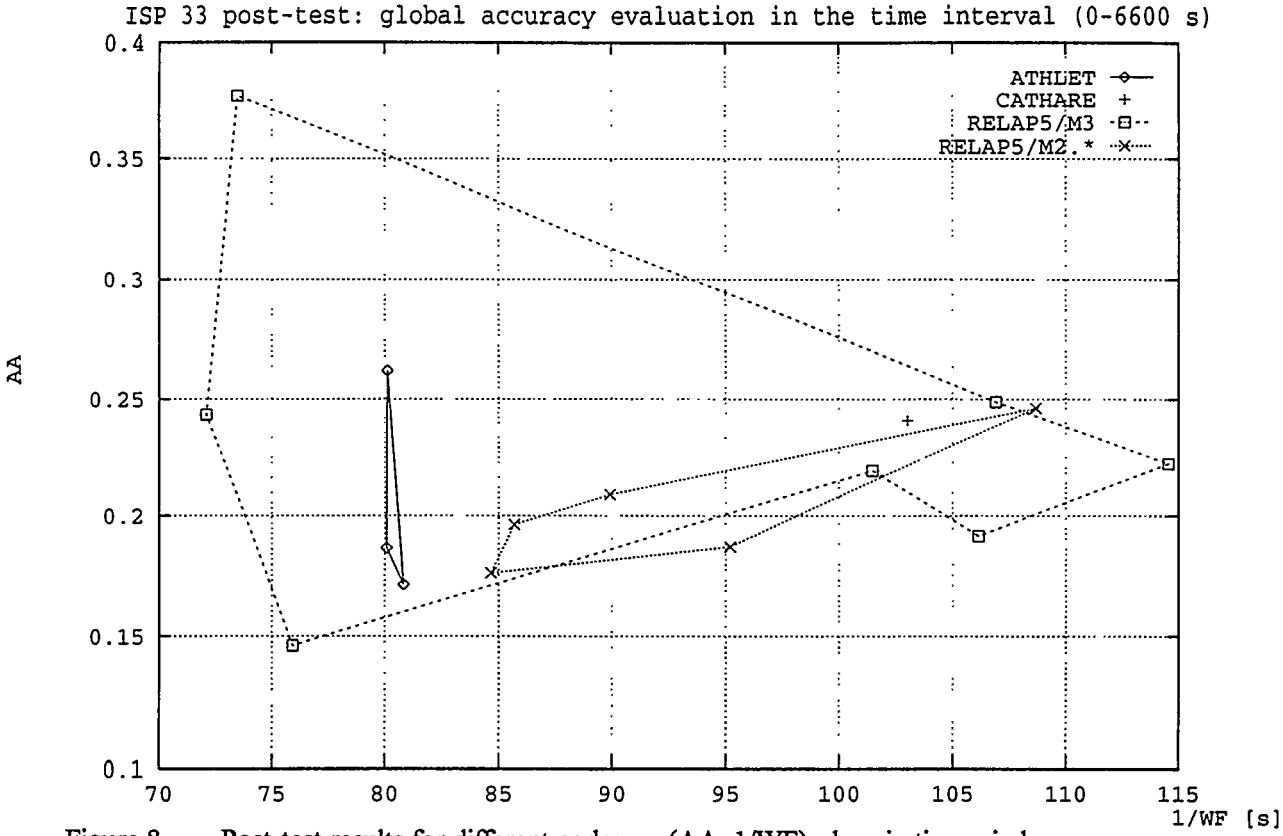


Figure 8. Post-test results for different codes on (AA, 1/WF)-plane in time window (0 - 6600 s.)

FARO Base Case Post-Test Analysis by COMETA Code

A. Annunziato, C. Addabbo
Joint Research Centre, Ispra Site
21020 Ispra (VA)
Italy

ABSTRACT

The paper analyzes the COMETA (Core Melt Thermal-Hydraulic Analysis) post test calculations of FARO Test L-11, the so-called Base Case Test. The FARO Facility, located at JRC Ispra, is used to simulate the consequences of Severe Accidents in Nuclear Power Plants under a variety of conditions. The COMETA Code has a 6 equations two phase flow field and a 3 phases corium field: the jet, the droplets and the fused-debris bed. The analysis shown that the code is able to pick-up all the major phenomena occurring during the fuel-coolant interaction pre-mixing phase.

1. INTRODUCTION

In a postulated severe accident in which the core melt-down has occurred jets of molten material are poured into the lower plenum through the core support plate. The presence of residual water in the lower plenum can determine a fragmentation of the melt leading to interaction of melt particles with the coolant. This thermal interaction, depending on the fragmentation degree and the fragments size, could lead to a strong vapor production that could eventually threaten the vessel integrity (steam explosion). On the other hand, if the melt reaches the bottom of the lower plenum unquenched potential exists for lower head penetration due to the residual power still produced in the debris bed.

In this context the FARO Program has been established in 1990 by the Commission of the European Communities in order to study the melt/water interaction. A first series of tests was proposed in collaboration with US Nuclear Regulatory Commission (NRC) and the Electric Power Research Institute (EPRI) [1].

The FARO tests concern the quenching of large masses of corium melt of realistic composition when poured into pressurized water at reactor scale depths. The test here analyzed was the first FARO test in which a large amount of melt material was released into the vessel. In the other tests at most 44 kg were introduced while in this case about 150 kg. In addition in this case the mixture contained about 6 kg of metallic Zr thus determining an additional energy input due to metal-water reaction.

The test has been analyzed by the COMETA computer code [2]. The primary objective of the COMETA code is the prediction of the thermal-hydraulic behavior of the FARO facility for design verification, definition of operational procedures and test interpretation. COMETA is composed of a two-phase flow field, which is described by 6+n equations (mass, momentum and energy for each phase and one mass conservation equation for each non condensable gas present in the considered problem) and a

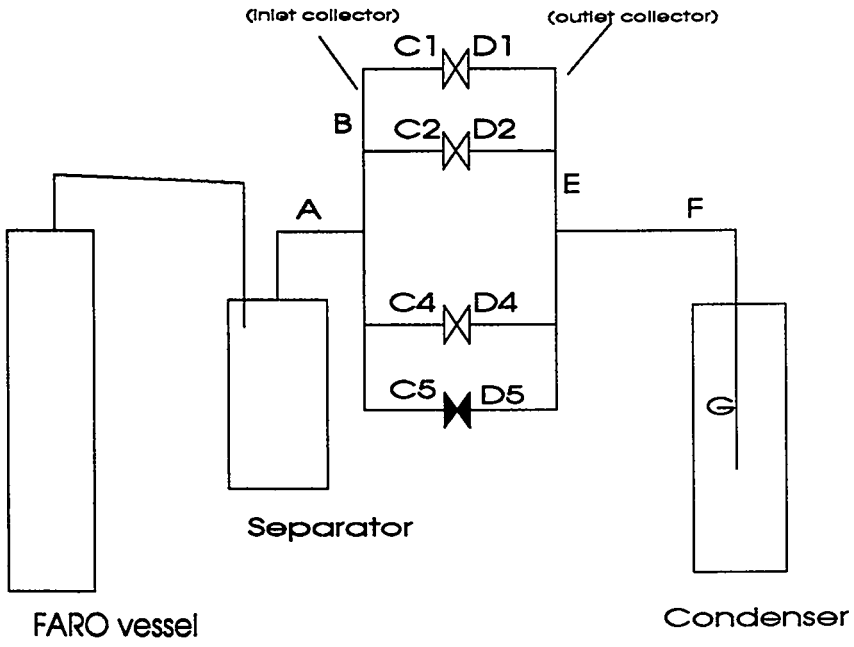


Fig. 2 - FARO discharge system scheme

corium field with 3 phases: the jet, the droplets and the debris. The two-phase field is described in Eulerian while the corium field in Lagrangian coordinates. The validation of the code is being performed by comparison with FARO tests as far as regards the fragmentation models and with LOBI tests for the thermal hydraulic models verification.

The code is actually used for the pre-test prediction of the FARO Tests in order to anticipate the prospected behavior and properly set-up the instrumentation and the experimental facility.

2. The FARO Base Case Test L-11

The table 1 summarizes the experimental conditions of the test L-11. This test, described in [3,4] was characterized by the injection of 151 kg of a mixture of UO_2 (76.7 w%), ZrO_2 (19.2 w%), and metallic Zr (4.1 w%) into a saturated environment of about 50 bar. The pressure history is presented in fig. 1. The pressure increased within 1.3 s up to the relief valves setpoint (93 bar) which started to open to control the system pressure. A maximum pressure of about 100 bar was reached in the test. In contrast to previous tests, the whole injected mass was completely fragmented, and this was attributed to the presence of the metallic Zr which enhanced the fragmentation due to the H_2 formation.

The knowledge of the real behavior of the control valves was retained important for the correct prediction of the transient. Therefore an analysis has been performed on the available experimental signals to determine the outlet mass flow rate [5]. This analysis allowed to obtain the following interpretations:

- valves 1 and 4 opened almost at the same time, 1.45 s;
- At 2.07 s the valve 2 opens determining the pressure decrease of the facility.

If therefore valve 5 did not open the pressure in this line can be considered as the outlet collector pressure and the quantities:

- ΔPv_1= PTSV1-PTSV5
- ΔPv_2= PTSV2-PTSV5
- ΔPv_4= PTSV4-PTSV5

show therefore the friction pressure drop between the valves outlet and the downstream common manifold (in Fig. 2: D_1-E, D_2-E, D_4-E, because $D_5 \approx$E). Taking this into account it was possible to estimate the mass flow rate through the valves (Fig. 8) by the evaluation of the lines discharge lines friction pressure drop.

3. COMETA Analysis

3.1 Initial and boundary conditions

Table I shows the test initial conditions compared with the values assumed in the calculations.

During the interaction phase, complicated flow patterns develop in the coolant, due to strong thermal gradients resulting from localized energy exchange with the molten corium. Therefore in the analysis of the FARO Base Case Test different nodalizations (1-d and 2-d) have been used in order to verify the influence of multidimensional phenomena on the calculated results. In the COMETA version used, in the 2-d case the melt (jet and droplets) are kept within the central radial cell and cannot get out of this zone. The dimension of this central zone (35 cm) has been selected based on the experimental evidence that the jet remained confined in about 30 cm within the center. Fig.s 3a and 3b show the two nodalizations adopted. In the calculations the hydrogen production has been calculated with a simple model which determined the gas production as a function of the local fragmented mass multiplied by a coefficient given in input which represents the reaction efficiency; the coefficient adopted for these calculations was 0.5.

In the COMETA code the fragmentation rate is controlled by jet break-up lenght correlations. The correlation adopted [2] is the Saito correlation in the water and the Epstein-Fauske correlation in the steam. In this case however a reducing factor has been adopted because this test, in contrast to the previous ones, presented a much higher fragmentation due to the presence of Hydrogen.

The temperature of the melt has been slightly increased, within the experimental uncertainty.

3.2 Results of the 1-d calculations

Table II indicates the comparison of the main quantities calculated by the code.

Tab. I - Initial Conditions of FARO Test L-11

		L-11	COMETA 1d	COMETA 2d
Melt Mass (kg)		151	151	151
Melt Composition	UO_2	76.7	=	=
	ZrO_2	19.2		
	Zr	4.1		
Temperature (K)		2823	2823.	2823.
Delivery time (s)		≈1	1.1	1.1
Outlet Orifice (m)		0.1	0.1	0.1
Water Mass (kg)		608	608	608
Water Height (m)		2	2	2
Water Temperature (K)		536.	536.	536.
Cover Gas Volume (m3)		1.28	1.28	1.28
Pressure (bar)		49.	49.	49.
Argon Partial Pressure (bar)		2	2	2

Tab. II - Results of FARO Test L-11

	L-11	COMETA 1d	COMETA 2d
Fragmented Mass (%)	100.	100.	100.
Maximum pressure (bar)	100.	95.	98.
Average Pressurization rate between 0. and 1.5 s (bar/s)	45	25.	45.
Melt Drops fragments mean diameter (mm)	3.5	4.2	3.6
Temperature increase (K):			
Gas Phase	44	38.	47.-64.
Water	27	44.	33.
Venting Phase:			
duration (s)	3.8	-	3.0
Water discharged (kg)	48		52.

The pressure calculated by the code is quite similar to the experimental curve (Fig. 4) up to 1. s. The pressurization rate after this time reduces and only a small valves opening occurs. At 2.5 s the pressure restarts to increase because saturation conditions are occurring in the vessel. This event is overpredicted because in the experiment the pressure re-increase occurs at 1.8 s. The reason for this can be identified by the temperature behavior. In the experiment thermocouples located in the central part of the vessel show a rapid increase to almost saturation conditions (Fig. 5), while the external ones grow slowly. On the contrary the calculation shows an intermediate behavior with a smooth increase. In a 1-d nodalization scheme part of the power released to the fluid is used for increasing the water temperature and part is used to create steam. The fraction used for temperature increase will be distributed over the whole surface area whereas in reality a temperature distribution is present, due to a

not-uniform heating, i.e.: the central zone is heated first while the external zone is heated by natural circulation. This phenomenon cannot be predicted with a 1-d nodalization. In addition, the fragmentation rate depends on the local steam and liquid velocities. In a 1-d nodalization the velocity is the average over the surface and therefore it is smaller than the velocity in the center, where the melt is travelling. The consequence is that the fragmentation rate is smaller. The behaviour could be improved by increasing the fragmentation rate correlations. In order to compare 1-d and 2-d cases this was not done.

3.3 Results of the 2d calculations

The subdivision of the area in multi-radial cells allows: a) greater heating of the central part while the external side of the pool is heated by natural convection; b) increase of the fragmentation rate due to higher local velocities. This determines an enhanced temperature and vapor generation rate and a better reproduction of the experimental data. Fig. 6 shows the behavior of the fluid temperature at elevation 400 mm. The temperature in the central part increases and then decreases. This was due to the fact that at the beginning the central part is heated; as well as the heating power reduces due to reduced heat transfer rate, the fluid in the external zones tends to re-enter in the central zone which is hotter thus causing a re-mixing by the natural circulation.

The pressure curve is also better reproduced because in this case the saturation occurs at 1.5 s with an enhancement of the vapor generation rate and an increase of the pressurization at 1.5 s (Fig. 7).

The valves mass flow rate is compared in Fig. 8. It is possible to see that the valves sequence is correctly predicted and also the amount of mass flow rate discharged by the relief valves.

The COMETA capabilities of tracking void fraction is shown in Fig. 9 where the situation at time 1.3 s is presented, just before valves opening. It is possible to see that the two phase mixture almost reached the top of the vessel. This caused entrainment of melt drops above the injection point. Also in the test this phenomenon occurred and 5 kg of small melt particles (diameter < 1mm) were found in the separator component.

4. Conclusions

The COMETA code has been used to perform the post test analysis of the FARO L-11 Test. This test was characterized by a strong interaction of the melt injected with the water, enhanced by the presence of Zr which determined a energy addition due to metal-water reaction. The code was able to predict the main phenomena occurring during the test even if the presence of Zr did change the fragmentation rate in relation to previous FARO tests.

Two nodalizations were used a 1d and a 2d one; it was pointed out that the 1-d nodalization allows a "fast" global evaluation of the test but that if a more detailed analysis is needed a 2-d scheme is necessary. With this nodalization it was infact

possible to predict the correct water temperature trend which affects the vapor generation rate and the pressure behaviour. The code has also been applied to give a description of the hydrogen distribution during the test.

References

[1] FASOLI STELLA P., HOHMANN '*Planning for FARO-LWR Experiments*' - CSARP Meeting, Washington, 1991

[2] A. Annunziato, C. Addabbo *'COMETA (Core Melt Thermal-hydraulic Analysis) a Computer Code for Melt Quenching Analysis'* - International Conference on New Trends in Nuclear System Thermohydraulics Pisa, 30.5.-2.6.1994

[3] A. Benuzzi, D. Magallon '*Quick Look Report on FARO Test L-11*' - JRC Technical Report n. I94.55

[4] D. Magallon, H. Hohmann - '*Experimental Investigation of 150 kg scale corium melt jet quenching in water*' - Paper submitted at the 7th Int. Mtg on Nuclear Reactor Thermal-hydraulics - NURETH 7

[5] A. Annunziato '*Evaluation of FARO L-11 Test Parameters Relevant to the Opimization of the COMETA Post Test Analysis*' JRC Technical Note I-94.100, June 1994

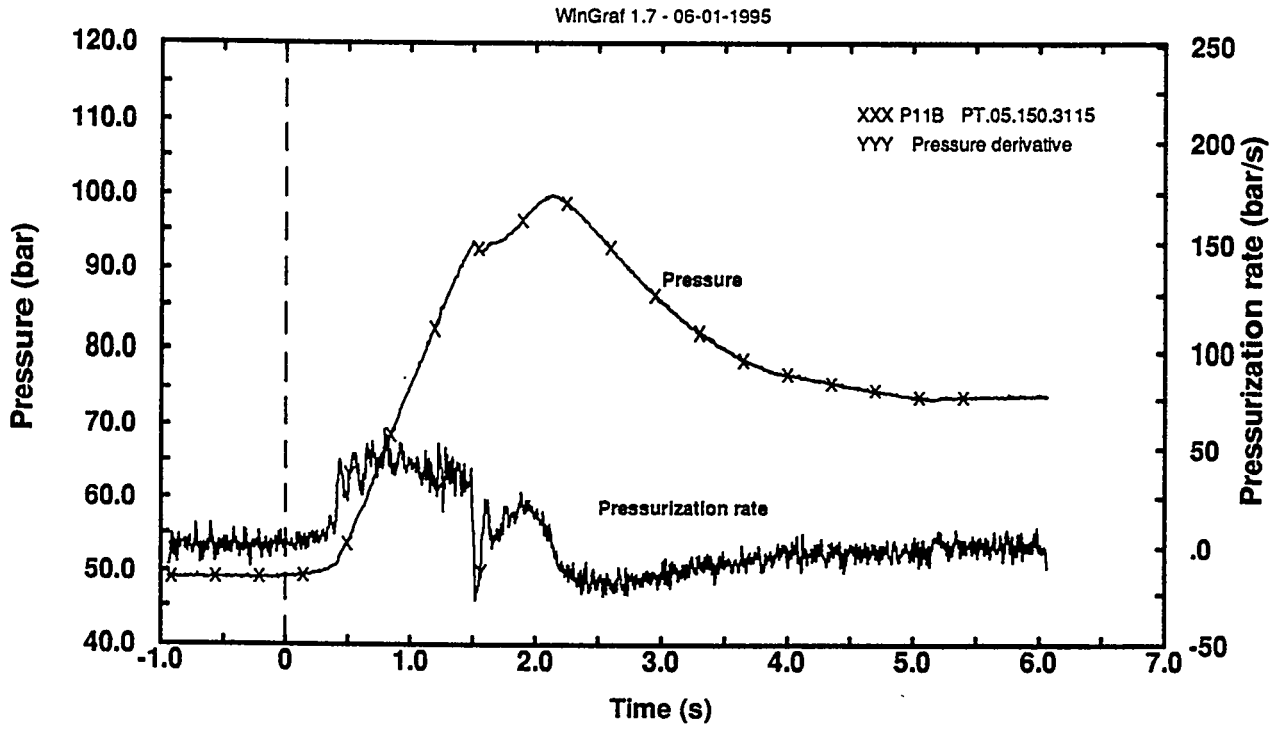
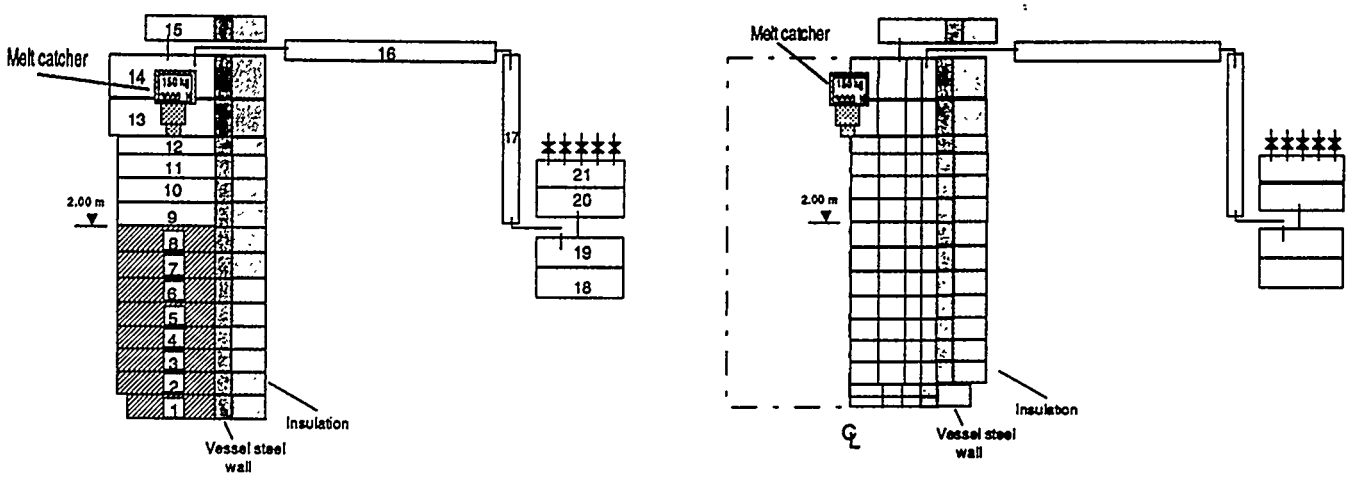


Fig. 1 - Pressure in the FARO Vessel in L-11 Test



a) 1-d Nodalization

b) 2-d Nodalization

Fig. 3 - COMETA Code Nodalizations

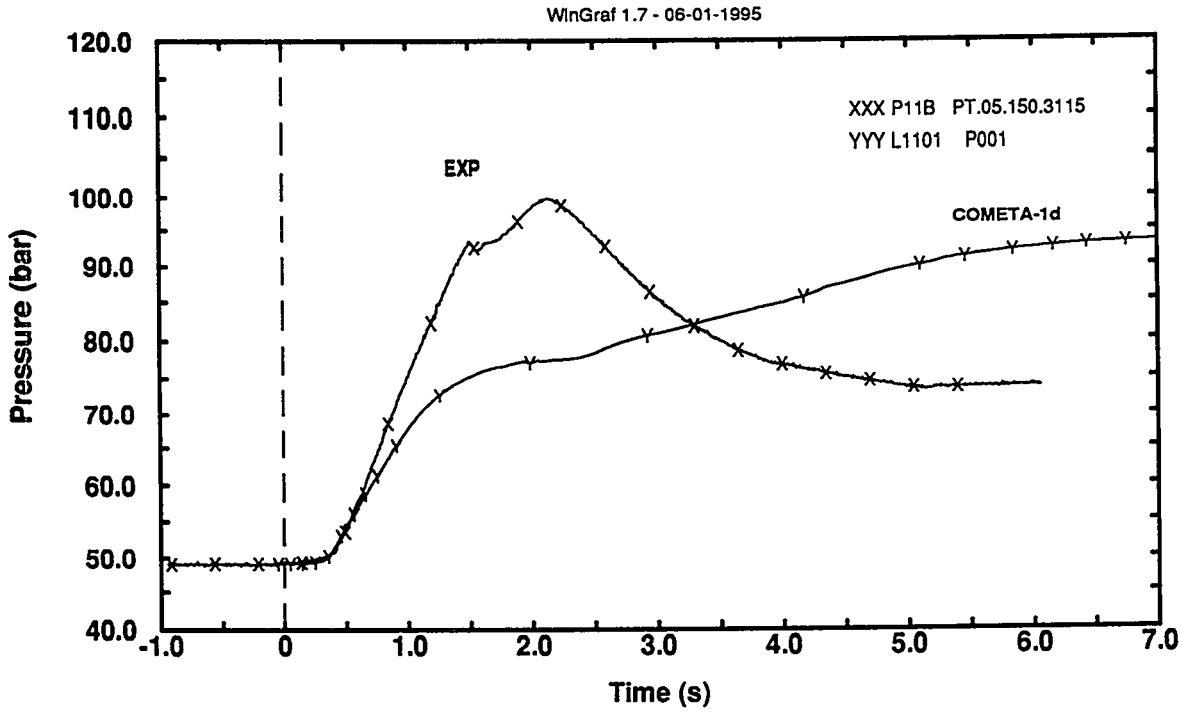


Fig. 4 - Pressure in the FARO Vessel in L-11 Test compared with the COMETA 1d calculation

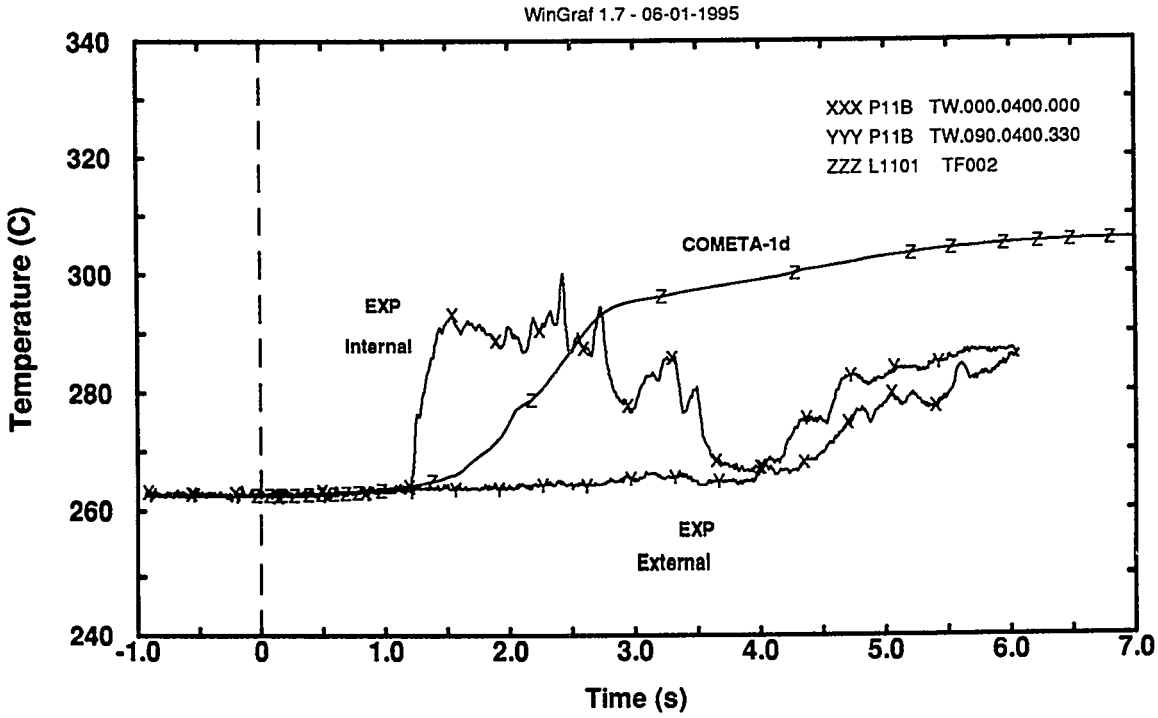


Fig. 5 - Temperature in the water in L-11 Test compared with the COMETA 1d calculation

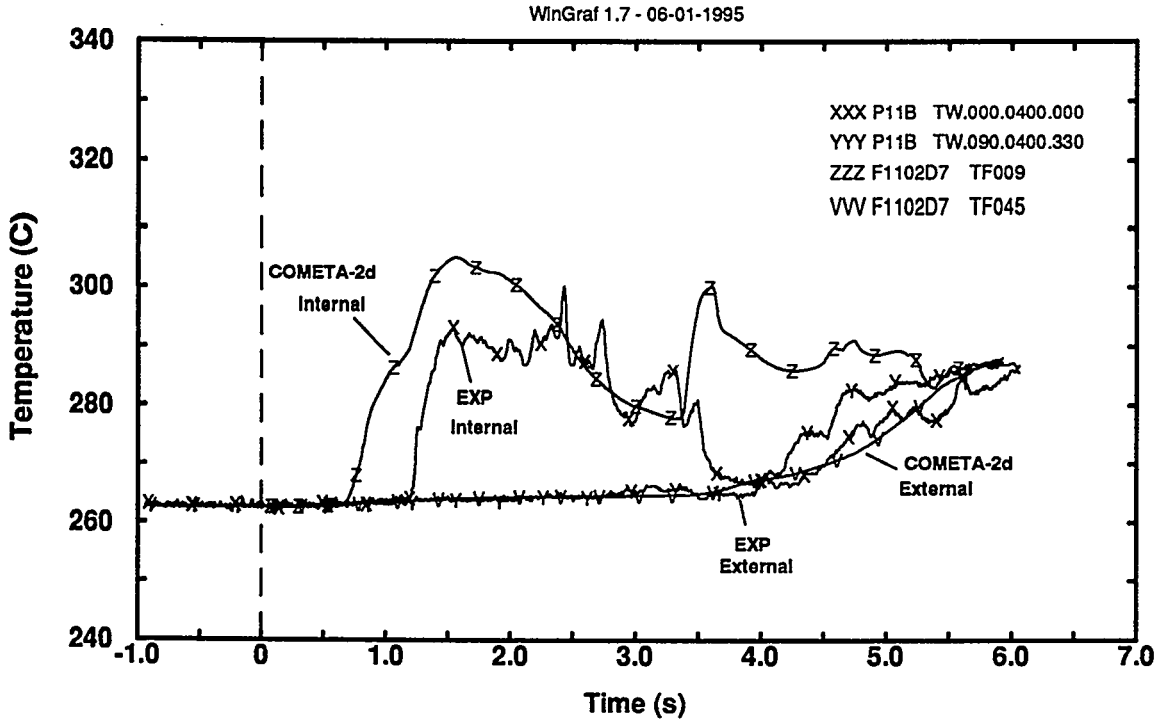


Fig. 6 - Temperature in the water in L-11 Test compared with the COMETA 2d calculation

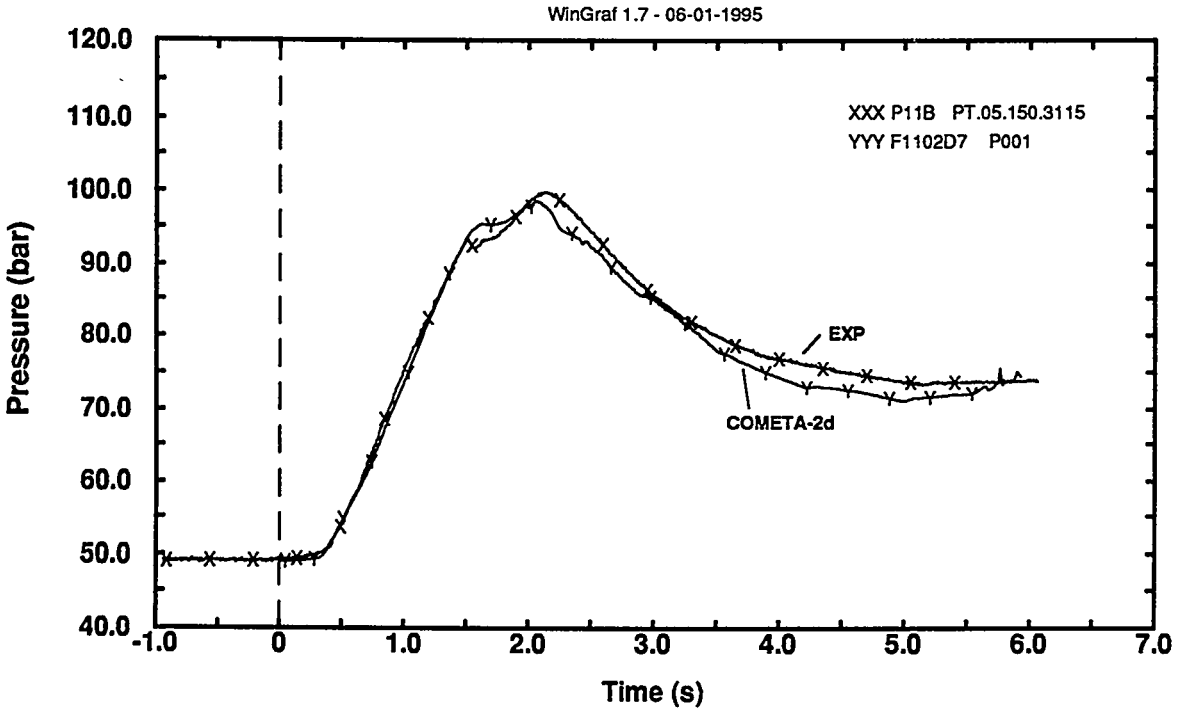


Fig. 7 - Pressure in the FARO Vessel in L-11 Test compared with the COMETA 2d calculation

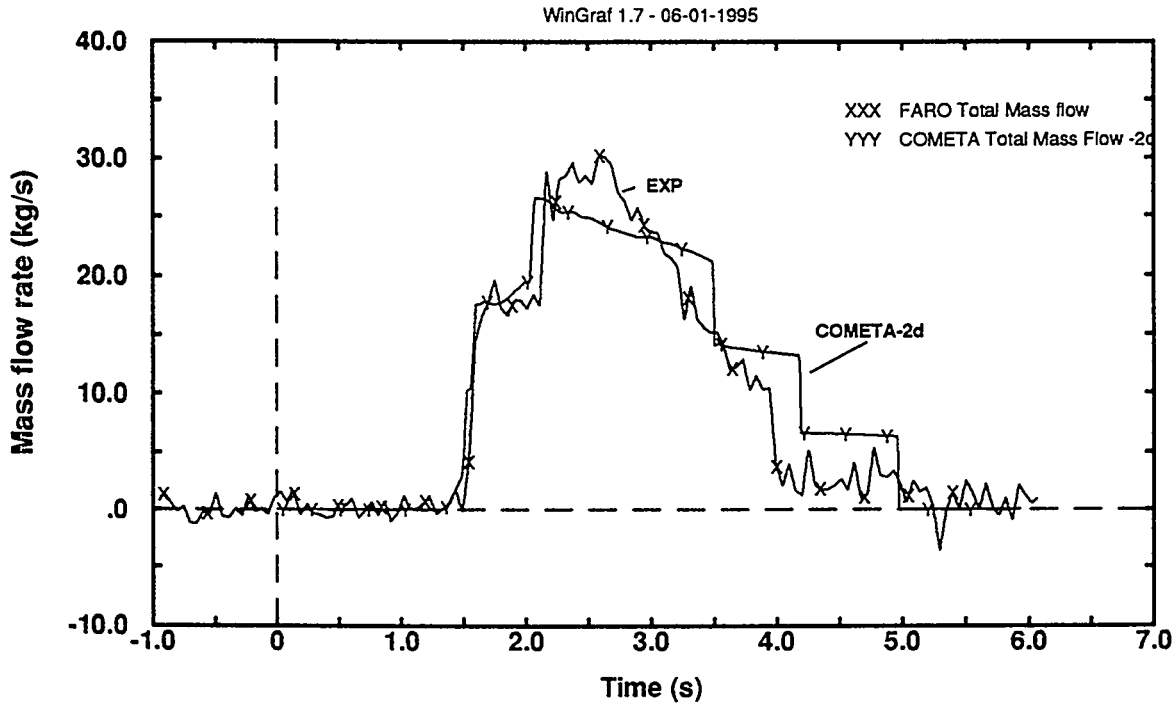


Fig. 8 - Relief valves mass flow rate

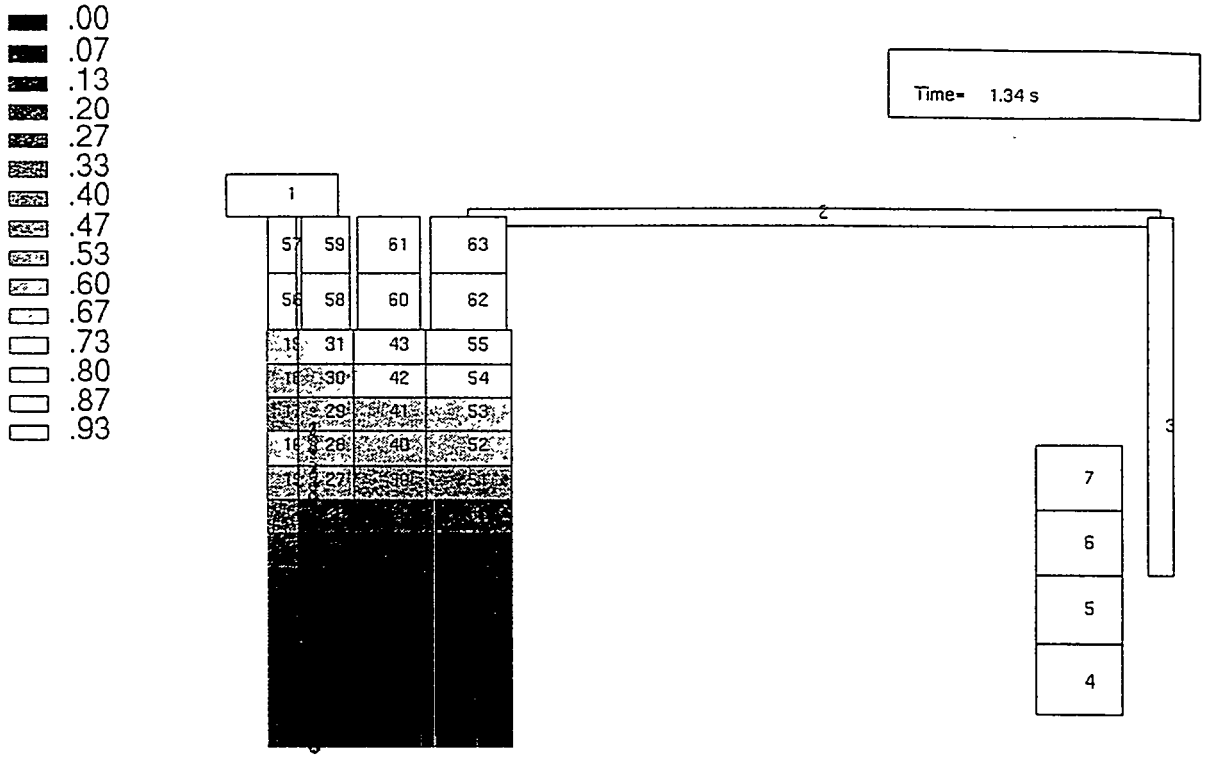


Fig. 9 - COMETA 2d Post test calculation of FARO L-11 Test:
Void fraction distribution prior to valves opening

THE ANALYSIS OF SCS RETURN MOMENTUM EFFECT ON THE RCS WATER LEVEL DURING MID-LOOP OPERATIONS

Jae Kwang Seo, Jae Young Yang, Sun Tack Hwang
Korea Atomic Energy Research Institute, Taejon, Korea

Goon Cherl Park
Seoul National University, Seoul, Korea

ABSTRACT

An accurate prediction of Reactor Coolant System (RCS) water levels is of importance in the determination of allowable operating range to ensure the safety during the mid-loop operations. However, complex hydraulic phenomena induced by Shutdown Cooling System (SCS) return momentum cause different water levels from those in the loop where the water level indicators are located. This was apparently observed at the pre-core cold hydro test of the Yonggwang Nuclear Unit 3 (YGN 3) in Korea. In this study, in order to analytically understand the effect of the SCS return momentum on the RCS water level and its general trend, a model using one-dimensional momentum equation, hydraulic jump, Bernoulli equation, flow resistance coefficient, and total water volume conservation has been developed to predict the RCS water levels at various RCS locations during the mid-loop conditions and the simulation results were compared with the test data. The analysis shows that the hydraulic jump in the operating cold legs in conjunction with the momentum loss throughout the RCS is the main cause creating the water level differences at various RCS locations. The prediction results provide good explanations for the test data and show the significant effect of the SCS return momentum on the RCS water levels.

I. INTRODUCTION

In order to perform the refueling and the steam generator (SG) maintenance activities simultaneously, SGs should be isolated from the radioactive reactor coolant by the SG nozzle dams. The RCS water level must be lowered below the lowest point of the nozzle dams to install the nozzle dams. In many pressurized water reactors (PWRs), the lowest point of the nozzle dams is lower than the top of the hot leg pipe. Therefore, during the nozzle dam installation the free surface of the reactor coolant remains in between the top and bottom of the hot legs : such an operation is called "Mid-Loop Operation". However, this operation involves certain risks to the plants decay heat removal (DHR) capability and loss of DHR (LODHR) accidents during nonpower operation (especially, during mid-loop operation) and its consequences have been of increasing concerns for years.

The most frequent reason for the LODHR accidents during the past fifteen years is the air binding of the DHR System or SCS pumps due to vortex formation near the junction of hot leg and SCS pump suction line resulting from insufficient RCS water level. In most cases, inappropriate indication of the level instruments followed by over drain of the RCS was the direct cause of the accident. The LODHR accident in the Diablo Canyon plant on April 10, 1987 [1], probably was the most serious one in this type, resulted in core uncovery, which prompted the issue of the US NRC Generic Letter (GL) 88-17 [2].

The GL required the holders of operating license and construction permits for PWRs to improve plant design, if necessary, to rectify the deficiencies in the areas of (1) prevention of accident initiation, (2) mitigation of accidents before they potentially progress to core damage, and (3) control of radioactive material if a core damage accident should occur. For (1) and (2) above, the GL emphasizes the importance of providing reliable level instruments by the discussions on the RCS level differences during the mid-loop operation. The GL indicated that the causes of the RCS level differences are the driving force necessary to accomplish the SCS flow and the SCS return water momentum. The GL also stated that these level differences will not be discovered if instrumentation is not independent nor will it be found by calibration between shutdown level instrumentation and the pressurizer level instrumentation.

Despite the importance of these phenomena to the safety in the mid-loop operation, efforts to analyze these phenomena have been circumvented due to the difficulties involved and lack of experimental data [3]. Previous works have been concentrated on developing experimental correlations to determine the critical water level incipient of vortex formation and air entrainment using downscaled experimental facilities [4,5,6]. However, their results showed large discrepancies so that their applications were not acceptable to some plants with narrow mid-loop operation bands. In addition, because (1) these experiments have been performed in downscaled facilities emulating only the portion of the operating hot leg and SCS suction line and (2) the level in the idle hot leg, where the level indicator is located, is expected to be higher than that in the operating hot leg, their applicability to the real plants is quite limited. As such, Palo Verde Nuclear Generating Station (PVNGS), Asea Brown Boveri-Combustion Engineering's (ABB-CE) System 80 type plants, has performed incipient air entrainment tests by measuring the RCS water level by differential pressure (DP) gauges and sight glasses to determine the acceptable mid-loop operation range. Such a test is prohibitive and must be performed with extreme care when the fuel is in the core. If, however, the test is performed without fuel in the core, applicability of the test data must be analyzed by considering the effect of the increase of flow resistance by the fuel and the reduction of the net RCS water volume by the RV upper structures. Therefore, it is important to develop an analytical tool to accurately assess the RCS water level distribution during mid-loop conditions with and without fuel in the reactor core. In order to prove the validity of the tool for the application to a real plant, it would be the best to be verified against the data obtained at the plants to be applied.

The Korea Electric Power Corporation (KEPCO) and the Korea Atomic Energy Research Institute (KAERI) jointly performed the RCS water level measurements at six different RCS locations of the YGN 3. The purpose of the test was to assess the operation range in conjunction with the measurements of incipient level of air entrainment for mid-loop operation. This paper (1) describes the test data of water levels at six legs obtained at the YGN 3, and (2) focuses on the analysis of the water level distribution during the mid-loop operation with a model developed in this study. The comparisons of the predicted results with the measured data are also provided and discussed.

II. OBJECTIVES

Through this effort, the authors intend to identify the important aspects of RCS water level distribution to be considered in assessing the allowable operating ranges for mid-loop operation. The objectives of this study are :

(1) to develop a model to predict the RCS water level distribution during the mid-loop conditions, (2) to validate the model by comparing the prediction with the test data, (3) to provide the phenomenological understanding of the effect of the SCS return momentum on the water level differences at various RCS locations, and (4) to provide a rudimentary basis for developing future design tool assessing the mid-loop operation bands.

III. DESCRIPTION OF THE TEST

A. The Plant

YGN 3 is a ABB-CE System 80 type PWR plant producing 1000 MWe consisting of two identical heat transfer loops (see Figure 1). Each loop is composed of one hot leg and two cold legs. SCS suction line is connected vertically on the bottom of each hot leg and SCS return lines (two per loop) are connected to the top of the cold legs with 60 degree inclination. Table 1 shows dimensions of components important for the analysis of the test data (the item numbers are correspondingly designated in Figure 1). The plant was at cold hydro test phase and the reactor core was not installed.

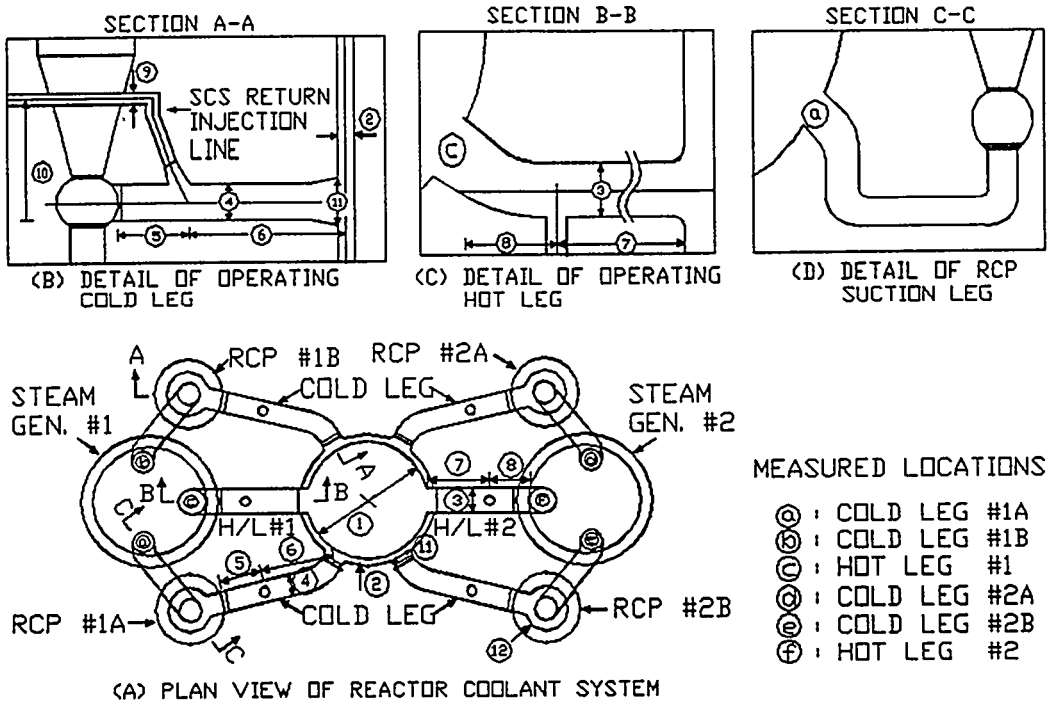


Figure 1. General Plan View with Major Components and Measured Locations

Table 1. Descriptions of YGN 3

Item	Major components related to the analysis	Dimensions (inches)
1	Reactor vessel core barrel inside diameter	140
2	Reactor vessel downcomer gap size	9
3	Hot leg inside diameter	42
4	Cold leg inside diameter	30
5	Distance from RCP casing to SCS return injection nozzle	73
6	Distance from SCS return injection nozzle to downcomer	154
7	Distance from SCS suction nozzle to downcomer	118
8	Distance from SCS suction nozzle to S/G plenum	22
9	SCS return injection pipe inside diameter	10
10	Height of SCS injection pipe relative to cold leg bottom	103
11	Cold leg nozzle exit diameter	35.5
12	RCP casing inside diameter (equivalent diameter considering internal structure)	30

Table 2. Test Conditions

Operating loop	Initial RWL (relative to hot leg center line, inches)	Flowrate (gpm)				
Loop 1	+ 2.9	2510	3038	3434	3963	4491
	0.0	2510	3038	3434	3963	4491
	- 2.0	2510	3038	3434	3963	4491
Loop 2	+ 2.0	2510	3038	3434	3963	4491
	0.0	2510	3038	3434	3963	4491
	- 2.0	2510	3038	3434	3963	(*)

* The level measurements could not be conducted due to the air entrainment to the SCS pump indicated by both the SCS pump current and vibration monitoring

B. Instrumentation

The level measurements were performed in the inlet and outlet nozzles of the SGs (ⓐ - ⓕ of Figure 1) by measuring the distance from the lowest pin hole for the nozzle dam installation to the surface of water by a ruler. A tygon tube and two differential pressure level transmitters with sensing taps located on each of the SCS suction lines respectively were used to determine the initial reference water levels (initial RWLs). SCS flowrates, SCS pump suction and discharge pressures, and SCS pump currents were also monitored and recorded from the main control room (MCR). SCS pump vibration was measured in the primary auxbuilding and were reported to the MCR by telephone. The RCS water behavior in the operating hot leg was recorded by using a video cassette recorder for later analysis.

C. Test Range

Three initial RWLs for each loop operation were selected. There were four SCS flowrates for each initial RWL, except for initial RWL of - 2 inches in the case of loop 2 operation, where the test was not conducted for 4491 gpm (see Table 2).

D. The Test Procedure

The RCS water level measurement test (RWLT) was performed in conjunction with the test to measure the incipient level of air entrainment (ILAT). The tests were performed using loop 1 SCS pump first and upon completion of RWLT and ILAT for the loop, repeat both tests by switching the SCS pump in loop 2. The test procedures were as follows:

(1) adjust the RCS level to a steady pre-determined initial RWL,
(2) start SCS pump at the preset lowest flowrate of 2510 gpm,
(3) wait to reach a steady state and measure/record the test parameters,
(4) raise the SCS flowrate and repeat (3) for all the flowrates in Table 2,
(5) repeat (1) through (4) for all the initial RWLs in Table 2.

Caution was given to the operator that the SCS pump current shall be continuously monitored and that if a sudden variation of pump current occurs or abnormally high pump vibration is reported, the pump shall be stopped immediately to protect the pump from being damaged by air entrainment and record the flowrate as the incipient flowrate of air entrainment for the level and terminate the RWLT.

IV. MODEL DEVELOPMENT

In order to predict the water level and understand the general trend of the level behavior during mid-loop conditions, modeling of hydraulic phenomena expected in the components composing the RCS is required. The review of the RCS pressure drop data indicated that the major source of level difference from the cold leg to the SCS outlet nozzle during mid-loop operation are 90° flow direction change at the RV inlet nozzle, flow area change and frictional pressure loss across the complex geometries of flow skirt, flow baffle and lower support structure of the lower RV plenum region and the flow area change at the RV outlet nozzle. To account for these, basic mass continuity equation, one-dimensional momentum equation, empirical head loss equation,

and Bernoulli equation are incorporated in the model. In addition, the hydraulic jump model is introduced to explain the overall water level trends. In part A of this section, equations and parameters with which the level profile of the flow in a horizontal pipe can be determined conveniently are derived and defined. Part B of this section describes the necessary equations and the calculational scheme to link these equations in the sequence of flow path.

A. General Method for Not Fully Filled Horizontal Pipe Flow

For general flow in pipe shown in Figure 2, 1-D momentum equation is written as

$$PA-(P+dP)(A+dA)-\tau_w P_e dx+\rho V^2 A-\rho VA(V+dV)=0. \tag{1}$$

Mass continuity equation for an incompressible flow is

$$VA=(V+dV)(A+dA). \tag{2}$$

By combining equation (1) and (2) and neglecting the terms of small order, we get:

$$-\frac{dP}{dx}-\frac{\tau_w P_e}{A}-\frac{(P-\rho V^2)}{A}\frac{dA}{dx}=0. \tag{3}$$

Since, the pressure at the faces of the control volume is essentially hydrostatic, the area-averaged pressure is given as:

$$P=k_c\rho g y, \tag{4}$$

where,

$$k_c=\frac{\left[-\theta\cos\theta+\sin\theta-\frac{\sin^3\theta}{3}\right]}{\left[(1-\cos\theta)(\theta-\sin\theta\cos\theta)\right]}. \tag{5}$$

The term $k_c y$ represents the distance from the free surface to the centroid of the water cross section, i.e. the centroid is located at $k_c y$ below the free surface.
Upon differentiation of equation (4) with respect to the axial coordinate, we get:

$$\frac{dP}{dx}=\rho g\frac{d(k_c y)}{dx}. \tag{6}$$

It can be shown that by substituting equations (4) and (6) into equation (3) and using the simplification method shown in Reference 8, equation (3) reduces to

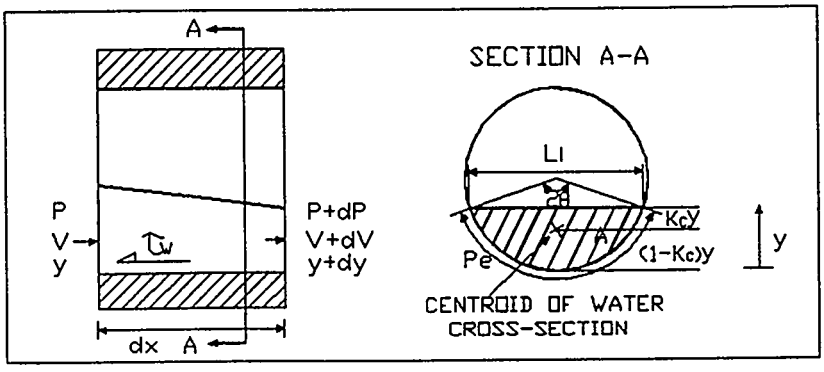


Figure 2. General Flow Geometry

$$\frac{dy}{dx} = \frac{-\tau_w P_e}{\rho g A - L_i \rho V^2} = \frac{-\tau_w P_e}{\rho g A} \frac{1}{(1-F_r^2)}, \tag{7}$$

where, F_r is Froude number and is defined by

$$F_r \equiv \sqrt{\frac{L_i V^2}{gA}}, \tag{8}$$

the shear stresses at the fluid-wall boundary, τ_W, is given by

$$\tau_W = f\frac{\rho V^2}{8}. \tag{9}$$

with geometrical parameters defined as:

$$\theta = \cos^{-1}(\frac{R-y}{R}), \tag{10}$$

$$P_e = 2\theta R, \tag{11}$$

$$L_i = 2\sqrt{R^2-(R-y)^2}, \text{and} \tag{12}$$

$$A = R^2\theta - \frac{1}{2}L_i(R-y). \tag{13}$$

If the friction loss term is negligible equation (1) reduces to

$$P_i A_i - P_{i+1}A_{i+1} = \rho Q(V_{i+1} - V_i). \tag{14}$$

Equations (7) and (14), in conjunction with other parameters defined above, are used to determine the water levels in the hot leg and cold leg, respectively.

B. The Model for the RCS Water Level Distribution

As indicated previously, the 90° turn of the fluid at the RV inlet nozzle impacts the level in the operating cold leg. In addition, the phenomenon of hydraulic jump needs to be considered. Hydraulic jump is a local nonuniform flow phenomenon which occurs when the supercritical flow decelerates to subcritical flow. It may be seen from equation (7) that when the Froude number of the fluid approaches to unity from a value greater than 1, the differential variation of fluid level in the direction of flow becomes infinity. The result, then, is a marked discontinuity in the surface, characterized by a steep upward slope of the profile. However, it has been a difficult topic to determine the location and the length of the jump in a rectangular channel [9, 10, 11, 12, 13, and 14]. Equation (7) must be solved to determine the location and the length of the jump. However, because the geometrical parameters of cylindrical channel are more complex than those of the rectangular channel, a further study is needed to solve equation (7) and to determine the location and the length of the jump. In order to model the hydraulic phenomena including the hydraulic jump as well as the effect of 90° turn of the flow direction at the RV inlet nozzle, the operating cold leg is divided into three control volumes as shown in Figure 3. The second control volume represents hydraulic jump. By noting that the water at the rear side of SCS injection nozzle is stagnant and all the x-momentum of flow is lost at the downcomer wall, and by assuming the friction loss is negligible we get

$$P_0 A_0 - P_{l_{UP}} A_{l_{UP}} = \rho Q(V_{l_{UP}} - V_{jsur}\cos 60), \tag{15}$$

$$P_{l_{UP}} A_{l_{UP}} - P_{l_{DN}} A_{l_{DN}} = \rho Q(V_{l_{DN}} - V_{l_{UP}}), \text{and} \tag{16}$$

$$P_{l_{DN}} A_{l_{DN}} - P_2 A_2 = \rho Q(-V_{l_{DN}}). \tag{17}$$

For a given downstream level, $y_{l_{DN}}$, equation (16) results in a quadratic equation with respect to the upstream water level, $y_{l_{UP}}$, hence, yields two different values for $y_{l_{UP}}$, which correspond to super- and subcritical levels.

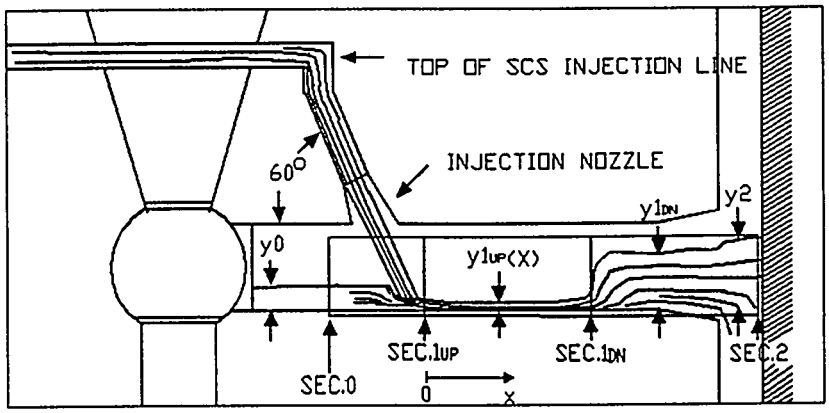


Figure 3. Three Control Volumes and Hydraulic Jump

V_{jsur} is the velocity of the SCS injection flow at the water surface, y_{sur}. Considering the gravity acceleration from the top of the SCS injection line, y_j, to y_{sur}, we get:

$$V_{jsur} = \sqrt{V_j^2 + 2g(y_j - y_{sur})}, \tag{18}$$

where V_j is the fluid velocity in the SCS injection line at y_j and y_{sur} is set equal to y_{1UP}. Considering the energy loss upon collision with the fluid in the cold leg and specific energy of the fluid after collision at x = 0, we get: The specific energy of the fluid at y_{sur} :

$$E_{1UP}(x=0) = y_{sur} + (1 - K_{COL})\frac{V_{jsur}^2}{2g}, \tag{19}$$

where K_{COL} is the energy loss coefficient and the value of 0.15, which corresponds to the loss coefficient of a 60° bend, is selected [7]. The specific energy of the fluid at the jump location is:

$$E_{1UP}(x=L_{jump}) = y_{1UP}(x=L_{jump}) + \frac{V^2(x=L_{jump})}{2g}. \tag{20}$$

$y_{1UP}(x=L_{jump})$ is obtained by solving equation (16) and $V(x=L_{jump})$ can be obtained from mass continuity equation for a given flowrate. While for supercritical flow region the excessive energy, $E_{1UP}(x=0) - E_{1UP}(x=L_{jump})$, is set equal to the energy dissipated by the wall friction, for subcritical region the energy dissipation is neglected. This approach is reasonable because the velocity of subcritical flow is negligibly small compared to that of supercritical flow.
Then, using Manning formula [9, 10], the location of the jump is determined by

$$L_{jump} = \frac{E_{1UP}(x=0) - E_{1UP}(x=L_{jump})}{S}, \tag{21}$$

where,

$$S = \left(\frac{n*V}{R_h^{2/3}}\right)^2. \tag{22}$$

S and R_h in equation (22) represent the slope of energy grade line and hydraulic radius of the flow channel, respectively and n is a constant in Manning formula. If the supercritical level yields the value of L_{jump} less than or equal to 0, the level is not physically acceptable, which means that the hydraulic jumps can not occur. Then, y_{1UP} is set equal to y_{1DN} and y_{sur} is set equal to the stagnant water level, y_0. As indicated above, the solution for upstream level, y_{1UP}, requires the knowledge

of downstream level, $y_{1_{DN}}$. In order to determine $y_{1_{DN}}$ using equation (17), the level at the exit of the cold leg should be known. In addition, to determine the water level in the idle cold leg, free surface profile must be known. If we consider H_{DC} as a Bernoulli constant of the fluid in the downcomer region, the water level at the exit of the operating cold leg is given by

$$y_2 = H_{DC} + K_p \frac{V_p^2}{2g}, \tag{23}$$

where K_p is defined in this analysis as the water level buildup factor and the value of 11.76 is chosen which best fits the overall trend of the RCS water level distribution.
At any location on the free surface in the downcomer the following equation holds:

$$H_{DC} = y_{DC}(x) + \frac{V_{FS}^2(x)}{2g}, \tag{24}$$

where $V_{FS}(x)$ is the velocity of the fluid at the free surface. In order to determine $V_{FS}(x)$ accurately a rigorous 3-dimensional analysis needs to be done.

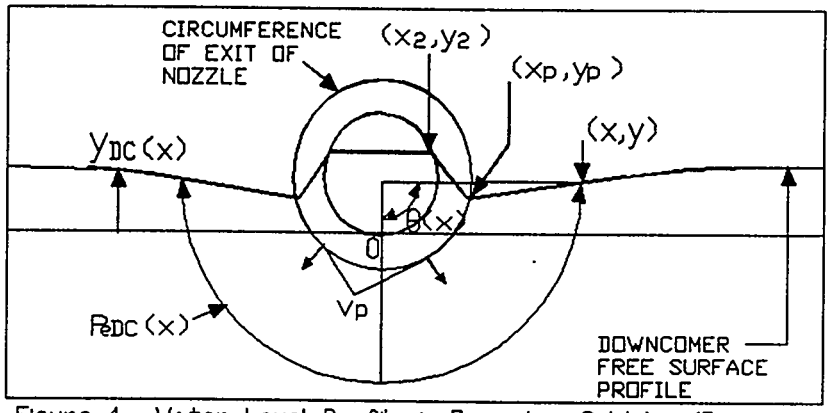


Figure 4. Water Level Profile in Operating Cold Leg/Downcomer

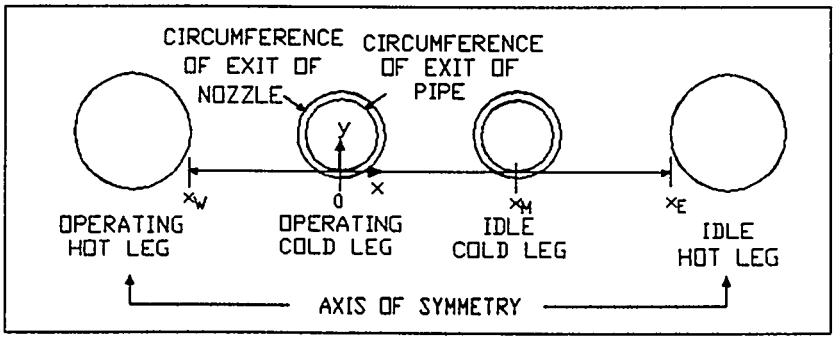


Figure 5. Half View of Flat Downcomer

However, for calculational simplicity, the velocity of the fluid at the free surface of the downcomer region is assumed to be inversely proportional to the length of the wetted circumference of the circle centered on the axis of the operating cold leg submerged in the water (see Figure 4), i.e.,

$$V_{FS}(x) = \frac{Q}{A_{DC}(x)}, \tag{25}$$

where $A_{DC}(x) = d_{DC}\, P_{e\,DC}(x)$, and d_{DC} is the downcomer gap size and $P_{e\,DC}(x) = 2 \times \theta(x)$.
The level profile based on this model is schematically shown in Figure 4. We can find the free-surface profile in the whole downcomer region by assuming a Bernoulli constant using equations (24) and (25). The correctness of the assumed H_{DC} can be checked by comparing the average water level of the downcomer region based on an assumed H_{DC} with the average water level necessary to overcome the resistance of the RV. If the level in the RV upper plenum, which is almost identical to that of idle hot leg, y_{iHL}, is known, the average water level in the downcomer region, $\overline{y_{DC}}$, can be obtained by

$$\overline{y_{DC}} = y_{iHL} + K_{DF}\frac{V^2}{2g}, \tag{26}$$

where K_{DF} is the flow resistance coefficient between the free surface of the downcomer and the RV upper plenum.

The average water level based on assumed Bernoulli constant, $\overline{y_{DCA}}$, is

$$\overline{y_{DCA}} = \frac{\int_{-x_w}^{-x_p} y_{DC}(x)\,dx + \int_{+x_p}^{x_E} y_{DC}(x)\,dx + 2x_p y_p + (x_p + x_2)(y_2 - y_p)}{x_W + x_E}. \tag{27}$$

If the calculated value of $\overline{y_{DCA}}$ falls within the convergence criteria about $\overline{y_{DC}}$, the assumed value of a Bernoulli constant is considered adequate.
At the entrance of the RV outlet nozzle (hot leg nozzle) water level drops due to the increase of dynamic head and entrance loss. If we define K_E as the entrance loss coefficient, the water level at the operating hot leg nozzle, y_E, can be expressed as

$$y_E = y_{iHL} - (1 + K_E)\frac{V_E^2}{2g}, \tag{28}$$

where y_E and V_E are water level and velocity at the hot leg nozzle, respectively.
In order to account for the level drop from the entrance of the hot leg pipe to the SCS suction nozzle, equation (7) is integrated over the flow path, i.e.,

$$y_{oHL} = y_E - \int_0^{L_{HL}} \frac{dy}{dx}\,dx, \tag{29}$$

where L_{HL} is the distance between the SCS suction nozzle to the end of the RV outlet nozzle.

It may be seen from the foregoing that if a level at any component in the RCS is known, all the levels can be determined successively. However, such information is not available. Hence, the solution should start with an assumed level. The appropriateness of the assumed level is checked by using water volume conservation before and after the SCS pump operation. The initial water volume in the RCS can be determined by using the measured initial RWL. If the relative error of the calculated total RCS water

volume, ε_{Vol}, defined as

$$\varepsilon_{Vol} \equiv \frac{\text{calculated total water volume} - \text{initial water volume}}{\text{initial water volume}} \tag{30}$$

falls within the convergence criteria the assumed level is considered adequate. In this study, the idle hot leg level is chosen as the independent variable to be assumed and a brief solution scheme is shown in Figure 6. In order to deal with the numerical instability perturbed by step function of the hydraulic jump, underrelaxation method was used in inner and outer loops shown in Figure 6. A summary of the values of the coefficients and factors used in this analysis is shown in Table 3.

Table 3. Values of Various Coefficients and Factors Used in the Analysis

Parameter	Description	Value
K_{DF}	Resistance coefficient of reactor vessel	15.21
K_P	Buildup factor at the exit of operating cold leg	11.76
K_{COL}	Collision loss coefficient of SCS Injection flow	0.15
K_e	Entrance loss coefficient at operating hot leg nozzle	0.25
n	Manning roughness coefficient	0.013
f	Friction factor in the wall of operating hot leg	0.0145

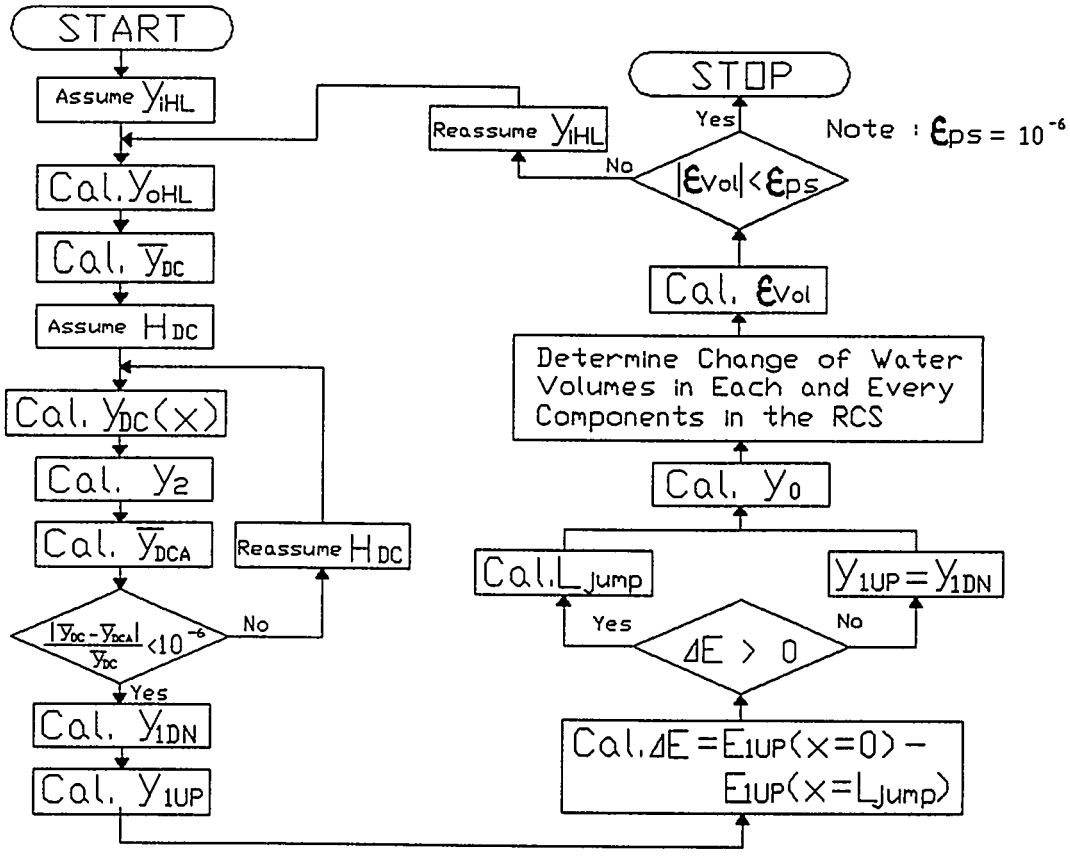


Figure 6. Solution Procedure

Table 4. Summary of Calculated Results

y_i	Q	y_0	$y_{1_{UP}}$	$y_{1_{DN}}$	y_2	y_{iCL}	y_{iHL}	y_{oHL}	E_j	E_{jL}	$E_{1_{UP}}$	$Fr_{1_{UP}}$	L_{jump}
inch	GPM	inch	inch	inch	inch	inch	inch	inch	inch	inch	inch		inch
2.90	2510.00	.38	4.03	4.03	4.33	2.87	3.20	2.96	92.67	.90	4.17	.13	.00
2.90	3038.00	.17	4.56	4.56	4.96	2.79	3.16	2.81	94.84	1.17	4.74	.15	.00
2.90	3434.00	.14	5.03	5.03	5.51	2.72	3.09	2.62	96.73	1.42	5.25	.16	.00
2.90	3963.00	.06	-12.43	5.97	6.54	2.88	3.21	2.59	99.63	1.81	75.73	10.06	13.26
2.90	4491.00	.54	-12.18	6.98	7.63	2.95	3.25	2.43	102.94	2.27	73.41	9.44	25.52
2.00	2510.00	-.72	3.21	3.21	3.54	1.97	2.32	2.06	92.67	.89	3.36	.14	.00
2.00	3038.00	-1.25	-12.88	3.84	4.27	1.96	2.35	1.95	94.84	1.16	77.70	11.23	1.86
2.00	3434.00	-1.07	-12.63	4.50	5.01	2.10	2.46	1.96	96.73	1.41	71.40	10.23	15.53
2.00	3963.00	-.68	-12.34	5.46	6.06	2.22	2.56	1.88	99.63	1.80	67.19	9.38	30.95
2.00	4491.00	-.16	-12.09	6.50	7.18	2.26	2.57	1.69	102.94	2.25	66.00	8.88	41.87
.00	2510.00	-3.03	-13.05	1.89	2.27	.52	.89	.57	92.67	.86	66.06	10.94	39.81
.00	3038.00	-3.15	-12.65	2.58	3.08	.50	.89	.42	94.84	1.12	54.51	9.18	43.98
.00	3434.00	-2.88	-12.41	3.32	3.89	.65	1.01	.41	96.73	1.37	51.89	8.55	59.03
.00	3963.00	-2.37	-12.13	4.38	5.05	.76	1.09	.28	99.63	1.76	51.06	8.04	74.01
.00	4491.00	-1.71	-11.88	5.50	6.25	.69	1.14	.07	102.94	2.22	52.21	7.77	84.27
-2.00	2510.00	-5.46	-12.76	.36	.83	-1.19	-.79	-1.19	92.67	.81	40.14	8.35	69.58
-2.00	3038.00	-5.24	-12.39	1.36	1.94	-.95	-.57	-1.14	94.84	1.08	36.97	7.46	94.19
-2.00	3434.00	-4.87	-12.16	2.17	2.84	-.82	-.45	-1.19	96.73	1.33	36.79	7.11	108.70
-2.00	3963.00	-4.19	-11.89	3.33	4.08	-.80	-.37	-1.37	99.63	1.73	38.19	6.87	121.59
-2.00	4491.00	-3.26	-11.68	4.59	5.42	-.98	-.39	-1.74	102.94	2.19	41.48	6.85	126.66

V. COMPARISON OF THE PREDICTED RESULTS WITH MEASURED DATA

A. Test Data Evaluation

The measured water levels are illustrated at the left-hand-sides of Figures 7 and 8 as functions of initial RWL and SCS flowrate. In these Figures, the level data are converted to the relative values with respect to the hot leg center line for convenience. The followings are the facts found in the evaluation of the test data.

(1) The levels in the operating cold legs are, in general, lower than those in other legs. For a given initial RWL, the level of the operating cold leg decreases as the RCS flow increases upto a certain point and further increase of the flowrate results in the increase of the level. The point where the minimum level occurs tends to move toward lower flowrates as the initial RWL decreases. (2) The level in the operating hot leg decreases as the SCS flowrate increases. For a given SCS flowrate, the levels in the operating hot leg are lower than those in the idle legs with the exceptions in several points at higher initial RWL and low SCS flowrate. The level differences increase with the SCS flowrate. (3) The levels in the idle loop increases with the increase of the SCS flowrate. (4) The scattering of the measured levels, especially the levels between the operating cold legs, is more pronounced at lower initial RWL and higher SCS flowrate. (5) In the case of initial RWL of 0.0 inch, the measured levels in the loop 2 during loop 1 operation are higher than those in the loop 1 during loop 2 operation.

B. Comparison of the Predicted Results with the Test Data

The water levels calculated from the suggested model are compared with measured data in Figures 7 and 8. Table 4 summarizes the analysis results. In this Table, the calculated level and the specific energy are converted to the relative values with respect to the hot leg center line for convenience. In the model, the cold leg level measurement points symmetric about the axis of hot legs are treated the same and only one value is given for a given flowrate for a given initial RWL. As can be seen in these figures, the trends as well as the calculated values of the RCS water levels are in good agreement with the measured data. Figure 9 illustrates the level predictions without hydraulic jump model. From these results the followings are found :

The trends of the RCS water level distribution described above are normally expected except the case of operating cold legs. Considering the driving force, the level in the operating cold leg should be higher than that in the idle hot leg. Therefore, it is concluded that the observed level depression occurs only in the rear side of the SCS injection nozzle and is caused by the drag of the SCS injection flow. However, if the level depression is caused only by the drag, the level of the operating cold leg should decrease monotonically with the SCS

flowrate. Hence, other hydrodynamic mechanism which results in a significant level buildup in the downstream of injection front thus, replenishes water to the rear side is expected to occur. It can be seen, upon summation of equations (15) to (17) that the level in the rear side of the injection front, y_0, is dependent only on the SCS return water momentum and the level at the downcomer wall, y_2. It should be noted here, however, that the value of y_2 is affected by the downstream levels and that because the downstream levels are influenced by the amount of water removed from the operating loop and added to the downstream, the amount of water removed from the operating loop will eventually influence the level, y_0. Based on the foregoing the authors felt it would be necessary to consider the hydraulic jump and the level buildup due to the momentum loss at the downcomer wall. The comparison of Figures 7 and 8 with Figure 9 indicates that even when the hydraulic jump is not considered the parabolic level behavior in the operating cold leg still exists but is less pronounced and the levels in all other legs are monotonically decreasing as the flowrate increases. Based on these, it may be concluded that both the hydraulic jump and the level buildup due to the momentum loss at the downcomer wall are important contributors in determining level profile in the operating cold leg. Further, a close review of Table 4 reveals that in most cases the energy of injection flow is large enough to make the flow in the operating cold leg supercritical and that the hydraulic jump occurs easily at lower initial RWL. The location of the jump increases with the SCS injection flowrate. Thus sweeping larger amount of water from the operating cold leg, resulting in higher water levels in the idle loop. This is consistent with what have been observed in the test. The foregoing clearly show that the overall behavior of the RCS water levels is strongly attributed by the hydraulic jump. The authors strongly believe that without the hydraulic jump, an accurate prediction of the RCS water levels during mid-loop conditions is not possible. Although the model suggested in this study incorporates several simplifying assumptions such as K_{COL} in equation (19), a constant n in equation (22), velocity profile in equation (25), preliminary sensitivity analyses indicate that the use of these assumptions has little impact on overall trends of the prediction. The differences in the measured levels between loop 1 and loop 2 operation in the case of initial RWL of 0.0 inch is not well understood. However, the comparison of the test data with the predicted results indicates that the water volume in the RCS during loop 2 operation is less than that during loop 1 operation. A possible explanation would be the replacement of voids in the SCS loop with water in the RCS. However, due to the lack of detail information of the SCS during the test, this cannot be confirmed. The level of the RV inside, which is a parameter directly influenced by the water volume transferred from the operating legs, strongly affects the change in the cross-sectional area of the flow at the entrance region of the hot leg nozzle, therefore the level profile in the operating hot leg is strongly influenced by the water volume transfer from the operating loop to the RV inside. However, the water level in the operating hot leg obtained from the test data is lower than that from the calculated result. This is partially due to the phenomenon of the local free fall and swirling at the entrance region of the SCS suction, which is not modeled in this analysis.

VI. CONCLUSION

The major factors affecting the RCS water level behavior during mid-loop operation are the SCS return water momentum, water level buildup at the RV inlet nozzle, water level drop at the operating hot leg, and water volume transfer from the operating loop to the RCS. Water volume transfer strongly affects the overall water level behavior. The locations of water volume transfer are the operating hot leg, the stagnant region in the operating cold leg, and the supercritical flow region in the operating cold legs. The volume removal swept by supercritical flow upstream of the operating cold legs is the strongest mechanism of the volume transfer. It is clear that the volume transfer effect in the post-core condition is stronger than that in the pre-core condition because of the reduction of net water volume in the RV. This, in conjunction with the increased flow resistance of the RV, limits the operational band of the mid-loop operation in the post-core condition.

ACKNOWLEDGEMENTS

The authors wish to acknowledge the Korea Electric Power Corporation's YGN 3 and 4 startup team members for their devotion in obtaining the test data with which this study deals.

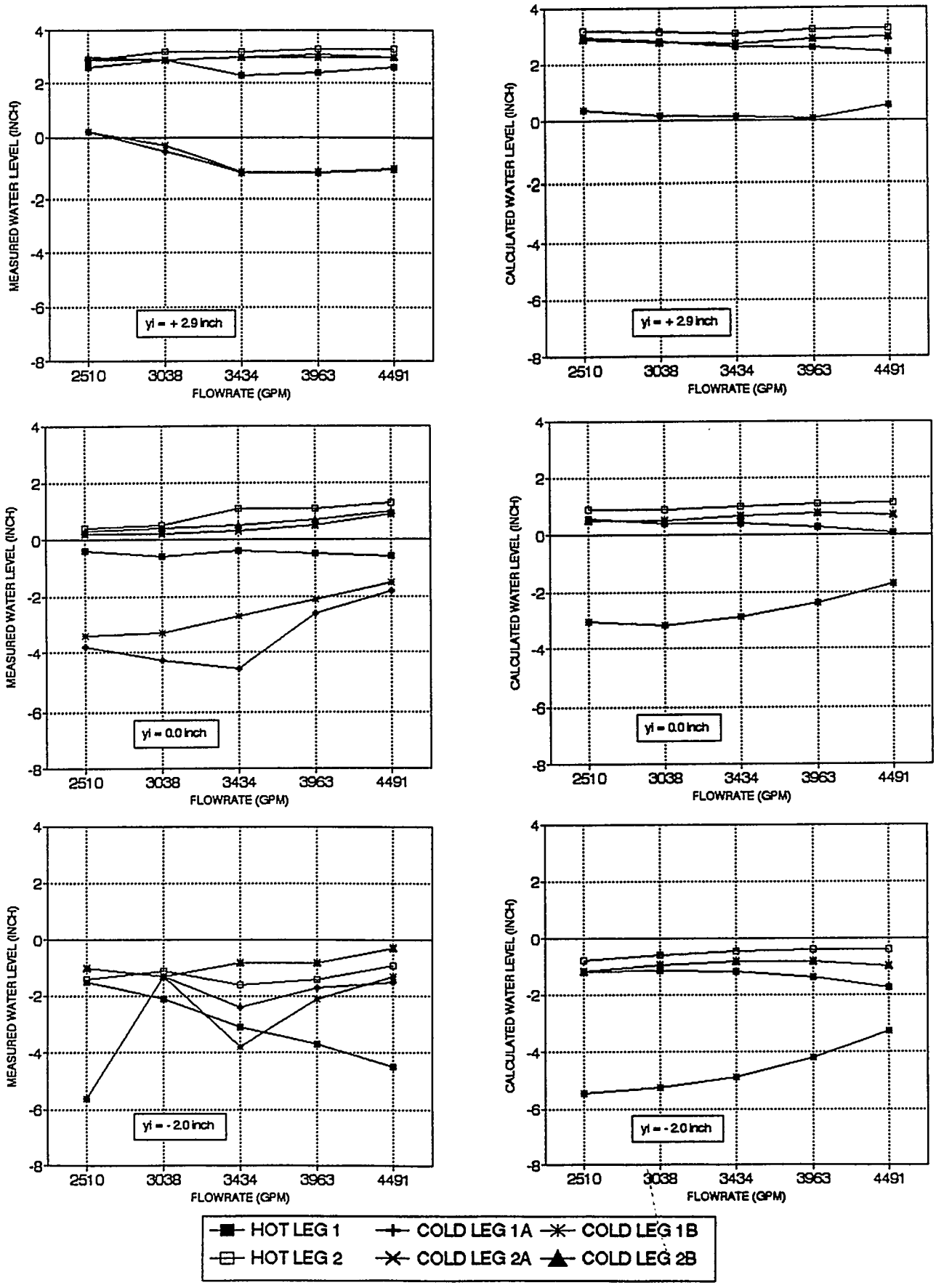


Figure 7. The Comparison of Test Data and Calculated Results for Loop 1 Operation

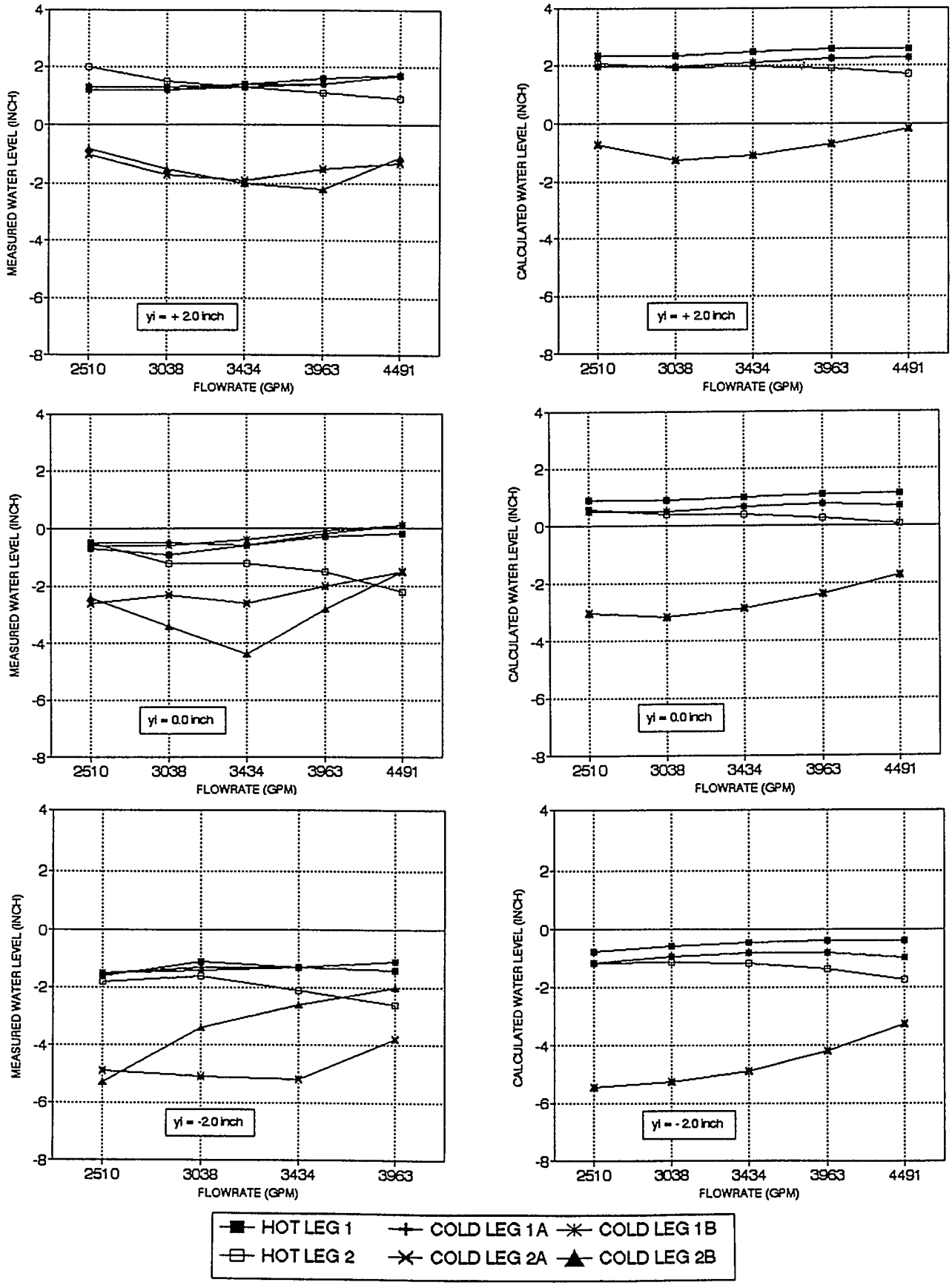


Figure 8. The Comparison of Test Data and Calculated Results for Loop 2 Operation

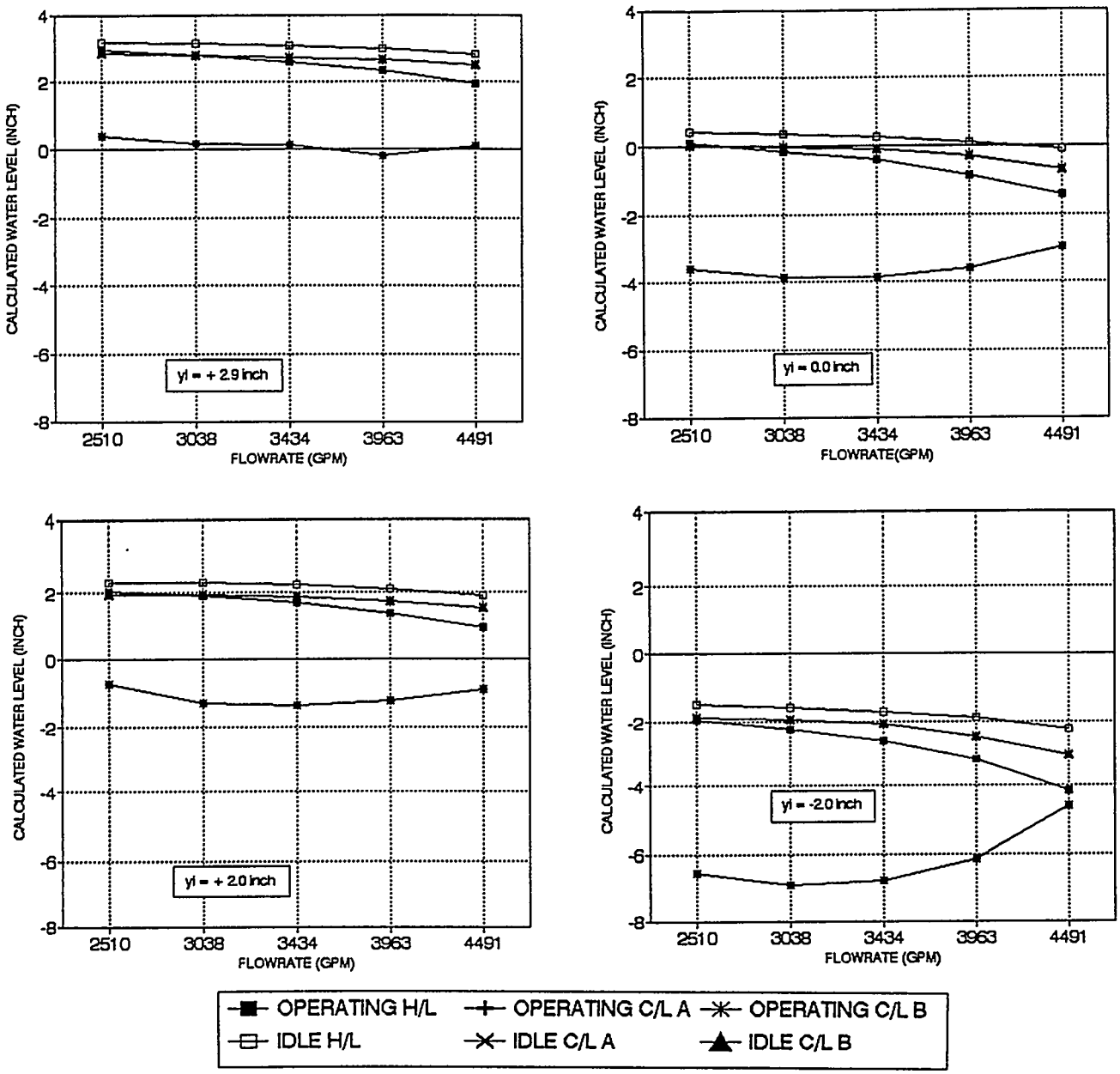


Figure 9. The Calculated Results Without Hydraulic Jump Model

Nomenclature

A : Area of water cross section
D : Diameter
E_j : Specific energy of the SCS return injection water
E_{jL} : Energy loss of injection fluid due to the collision to the water surface
H : Bernoulli constant
g: gravity acceleration, 9.8 m/sec^2
K: Flow resistance coefficient
L_{jump} : Distance from the SCS injection point to the location of hydraulic jump
P_e : Wetted Perimeter of water cross section in the pipe
Q : Volumetric flow rate
R : Radius

V: Average velocity

x : Axial coordinate in the pipe or x-coordinate of the free surface in the downco region

x_p : x-coordinate of the wetted circumference of the exit nozzle of the operating leg

y : y-coordinate of the water level in the pipe from the bottom of the cold leg.

y_i : Initial RCS reference water level (= initial RWL)

y_p : y-coordinate of the wetted circumference of the exit nozzle of the operating cold leg

ρ : Water density, 1000 kg/m^3

Subscripts :

CL : Cold leg

COL : Collision of the flow to the water surface

DC : Downcomer

DF : Driving force

DN : Downstream section of control volume

FS : Free surface of water in the downcomer region

HL : Hot leg

iCL : Idle cold leg

iHL : Idle hot leg

j : At the top of the SCS return injection line

oCL : Operating cold leg

oHL : Operating hot leg

p : Wetted Perimeter

RV : Reactor vessel

SUR : Water surface

UP : Upstream section of control volume

0,1,2 : Numbers of sections of control volume

References

[1] US NRC, "Loss of Residual Heat Removal System, Diablo Canyon, Unit 2, April 10, 1987," NUREG-1269 (1987).

[2] D.M. Crutchfield, "Loss of Decay Heat Removal," Generic Letter 88-17, USNRC (1988).

[3] R.A. Newton, "Westinghouse Owners Group Mid-Loop Operations Concerns," Letter to W. Hodges, NRC, from Chairman of Westinghouse Owners Group, OG-88-24 (1988).

[4] Y.K. Oh, "A Study of Vortex Formation on the Free Surface in a Pipe," Ph.D Dissertation, Kyunghee Univ., Seoul, Korea, (1991).

[5] T.S. Andreychek et al, "Loss of RHRS cooling while the RCS is partially filled," WCAP-11916, Rev.0, Westinghouse Electric Co., (1988).

[6] M.K. Chung et al, "Experiments on Air Entrainment into SCS by Vortex Formation during Mid-Loop Operation," KAERI/TR-357/93, Korea Atomic Energy Research Inst., (1993).

[7] Flow of Fluids Through Valves, Fittings, and Pipe, Technical Paper No. 410, Crane Co.(1975).

[8] M. Sadatomi, M. Kawaji, C.M. Lorencez, and T. Chang, "Prediction of Liquid Level Distribution in Horizontal Gas-Liquid Stratified Flows with Interfacial Level Gradient," Int. J. Multiphase Flow Vol. 19. No. 6, 987-997 (1993).

[9] R.L. Daugherty, J.B. Franzini, and E.J. Finnemore, Fluid Mechanics with Engineering Application, McGraw-Hill Book Company, Singapore (1989).

[10] F.M. White, Fluid Mechanics, 2nd ed., McGraw-Hill Book Company, New York (1986).

[11] A. M. Gharangik et al, "Numerical Simulation of Hydraulic Jump," Journal of Hydraulic Engineering, Vol. 117, No. 9, September, (1991).

[12] Chow, V.T., Open Channel Hydraulics, McGraw-Hill Book Co., Inc., New York (1959).

[13] McCowan, A.D., "The range of application of Boussinesq type numerical short wave models," IAHR XXII Congress, Int. Assoc. of Hydro. Res., 378 - 384 (1985).

[14] Basco, D.R., "Introduction to rapidly-varied unsteady, free-surface flow computation," USGS, Water Resour. Invest. Report No. 83-4284, U.S. Geological Service, Reston, Va (1983).

An Assessment of RELAP5 MOD3.1.1 Condensation Heat Transfer Modeling with GIRAFFE Heat Transfer Tests

Brian D. Boyer, Yüksel Parlatan, Gregory C. Slovik, and Upendra S. Rohatgi, Brookhaven National Laboratory

ABSTRACT

RELAP5 MOD3.1.1 is being used to simulate Loss of Coolant Accidents (LOCA) for the Simplified Boiling Water Reactor (SBWR) being proposed by General Electric (GE). One of the major components associated with the SBWR is the Passive Containment Cooling System (PCCS) which provides the long-term heat sink to reject decay heat [1]. The RELAP5 MOD3.1.1 code [2] is being assessed for its ability to represent accurately the PCCS. Data from the Phase 1, Step 1 Heat Transfer Tests performed at Toshiba's Gravity-Driven Integral Full-Height Test for Passive Heat Removal (GIRAFFE) facility [3] will be used for assessing the ability of RELAP5 to model condensation in the presence of noncondensables.

The RELAP5 MOD3.1.1 condensation model uses the University of California at Berkeley (UCB) correlation developed by Vierow and Schrock [4]. The RELAP5 code uses this heat transfer coefficient with the gas velocity effect multiplier being limited to 2 [5,6]. This heat transfer option was used to analyze the condensation heat transfer in the GIRAFFE PCCS heat exchanger tubes in the Phase 1, Step 1 Heat Transfer Tests which were at a pressure of 3 bar and had a range of nitrogen partial pressure fractions from 0.0 to 0.10.

The results of a set of RELAP5 calculations at these conditions were compared with the GIRAFFE data. The effects of PCCS cell nodings on the heat transfer process were also studied. The UCB correlation, as implemented in RELAP5, predicted the heat transfer to ±5% of the data with a three-node model. The three-node model has a large cell in the entrance region which smeared out the entrance effects on the heat transfer, which tend to overpredict the condensation. Hence, the UCB correlation predicts condensation heat transfer in the presence of noncondensable gases with only a coarse mesh. The cell length term in the condensation heat transfer correlation implemented in the code must be removed to allow for accurate calculations with smaller cell sizes.

INTRODUCTION

The PCCS is a new and unique safety feature for Advanced Light Water Reactors (ALWR). Figure 1 shows the containment and passive heat removal systems of an ALWR called the SBWR. By condensing the steam vented into the drywell from the Depressurization Valves (DPVs), a steam line break, or any line break in the reactor coolant system, the SBWR can prevent the drywell pressure from increasing to unacceptable levels during a LOCA. Because the drywell is inerted with nitrogen gas to prevent hydrogen explosions and fires, the PCCS will have to condense the steam in the presence of noncondensable gases. As the steam condenses in the tubes of the PCCS, the heat is transferred to a pool of saturated water containing the PCCS unit. The condensate from the PCCS drains to the Gravity-Driven Cooling System (GDCS) tank to be returned to the Reactor Pressure Vessel (RPV). Eventually, the nitrogen gas that accumulates in the PCCS is purged to the Suppression Chamber (S/C) through a vent tube

submerged in the Suppression Pool (S/P). Purging occurs when the pressure drop between the drywell and the S/C is sufficient to overcome the static head of the submergence of the vent tube, which is about 7 kPa.

It is necessary to remove nitrogen from the PCCS to enable the heat transfer rate to be high enough to remove enough energy from containment to reduce containment pressure. The nitrogen purging process in the PCCS will be an oscillatory process which will affect the heat removal rate in the PCCS. As the steam condenses, the nitrogen gas will tend to build up in the PCCS tubes. This nitrogen will gradually blanket large amounts of the liquid condensate film that has condensed on the tube surface. This increasing nitrogen layer will degrade the condensation process reducing the flow through the PCCS tubes and increasing the pressure difference between the drywell and the S/C.

As the pressure difference between the drywell and the S/C rises high enough to overcome the static head in the bottom of the nitrogen vent tube, the accumulated nitrogen will be purged out of the PCCS and into the S/C. The vapor flow into the PCCS will increase and purge the nitrogen out of the PCCS. Since the PCCS nitrogen concentration was made lower by the purging process, the condensing process can begin again. As condensation resumes, the pressure differential between the drywell and the S/C decreases forcing the venting process to terminate. As the steam condenses, the nitrogen gas will be stripped off the steam and will build up in the PCCS tubes to start the cycle over again.

The test program for the PCCS developed by Toshiba, for GE, is known as the Gravity-Driven Integral Full-Height Test for Passive Heat Removal (GIRAFFE) [1,3]. GIRAFFE demonstrates the ability of the PCCS to operate in the long-term heat rejection period of a SBWR LOCA. In the Phase 1, Step 1 test series various steady-state vapor flow rates, system pressures, and nitrogen concentrations were used in a separate effects test to examine the performance of the PCCS component. These flow rates and nitrogen concentrations are in the expected ranges for the long-term cooling period of an SBWR LOCA. The GIRAFFE Phase 1, Step 1 test results were also used to assess the ability of RELAP5 to predict condensation of steam in the presence of noncondensables and to model the venting of noncondensable gases to the S/C. Since the vent line tube was not submerged in the S/P water, the venting and heat transfer were steady-state processes in these tests. The effect of various cell nodings of the PCCS tubes was also investigated.

GIRAFFE FACILITY DESCRIPTION

GIRAFFE is a full-height test facility scaled 1/400 by volume and power. Toshiba designed GIRAFFE to preserve elevations and local pressure losses to capture data demonstrating the passive heat removal system [1,3]. The radial dimensions are scaled 1/20 while all the relative elevations of the SBWR have been preserved to achieve natural circulation flows typical of the SBWR. The GIRAFFE facility attempts to maintain (1) the gravity-driven circulation paths throughout the containment for liquid and vapor phases; (2) the nitrogen partial pressure in each volume; (3) the nitrogen transfer rate from one volume to another; and the (4) nitrogen accumulation in the PCCS condenser tubes. Hence, GIRAFFE's ability to represent the gravity forces, nitrogen gas concentrations, and the small pressure differences in the SBWR is important for the data collected at the GIRAFFE test facility.

The GIRAFFE Phase 1, Step 1 configuration is shown in Figure 2. The test facility included components for the reactor pressure vessel (RPV), the suppression chamber (S/C), and the isolation condenser pool containing the PCCS heat exchanger unit. The PCCS heat exchanger consists of an upper plenum (steam box) to represent the steam injection, three heat exchanger tubes, and a lower plenum (water box) which collects the liquid. The condensate drains out the water box to the RPV and the noncondensable gas vents to the S/C. As stated previously, in the latest version of the SBWR, the condensate will no longer drain directly to the RPV from the PCCS but will drain to the GDCS tank. However, the GIRAFFE Phase 1, Step 1 configuration will not distort the heat transfer and fluid flow phenomena being investigated.

The data from the Phase 1, Step 1 series of tests was used to assess RELAP5. In the Phase 1, Step 1 tests, steam and nitrogen were injected as boundary conditions at various nitrogen partial pressures into the PCCS. The steady-state condensation rates and temperature profiles were examined in this test. This test provided data on the steady-state behavior of the PCCS with prototypical flow, pressure, and nitrogen concentration conditions likely to be seen in a SBWR LOCA.

RELAP5 Heat Transfer Package

RELAP5 has been used to model the GIRAFFE Phase 1, Step 1 Heat Transfer Tests. The RELAP5 noncondensable heat transfer package is based on the UCB correlation by Vierow and Schrock [4,5,6]. The RELAP5 MOD 3.1.1 implementation of the correlation is:

$$h_{exp} = f_1 \, f_2 \, h_t \tag{1}$$

$$h_t = 3.185811 \left| \frac{\Delta Z_c \, D_h}{L_c^2} \right| h_{cond} \tag{2}$$

$$h_{cond} = 0.296 \left[\frac{\rho_f \left(\rho_f - \rho_g\right) g \, h_{fg} \, k_f^3}{D_h \mu_f \left(T_{gi} - T_w\right)} \right]^{1/4} \tag{3}$$

$$f_1 = \min[2, 1 + 2.88 \, (10^{-5}) \, Re_g^{1.118}] \tag{4}$$

$$f_2 = 1 - C * M_a^b \tag{5}$$

with h_{cond} being a laminar film condensation heat transfer coefficient derived by Chato [7] for horizontal pipes. C and b are factors that take into account the effect of gas mass fraction in the following fashion:

C= 10,	b=1.0	for	$M_a < 0.063$
C= 0.938,	b=0.13	for	$0.063 < M_a < 0.60$
C= 1.0,	b=0.22	for	$M_a > 0.60$

for different gas mass fractions. It should be noted that in the entrance region of a pipe where condensation is occurring the gas Reynolds number will be at its highest value. As the liquid condenses out of the vapor, the vapor velocity drops and the gas Reynolds number decreases. Hence, the dependence on gas Reynolds number can increase the gas velocity effect by a large amount in the entrance region.

Schrock has recommended that a limit of 2 be placed on the gas velocity effect factor, f_1, to avoid overpredicting the heat transfer in the entrance region. In a study of approaches to modeling condensation phenomena in the PCCS, Tills [8] found that the multiple linear regression technique for analyzing the heat transfer data produced a correlation that appears to predict heat transfer well over the wide range of data points. However, the wayward scattered points may not be random scatter. Points that are far from the calculated curve may be correlated to each other by their position in the tube. Lumping all the data together ignored local phenomena such as the entrance effect on the heat transfer coefficient.

RELAP5 PHASE 1, STEP 1 MODEL

A RELAP5 MOD3.1.1 model of the GIRAFFE test facility (Figure 2) for the Phase 1, Step 1 Heat Transfer tests is shown in Figures 3 and 4. It has components representing the PCCS, the RPV, and the S/C. In GIRAFFE, the steam and noncondensable gases were injected into the PCCS at constant flow rates. The RELAP5 model simulated this behavior by using a time-dependent volume and a time-dependent junction to specify flow and pressure boundary conditions. In GIRAFFE, the nitrogen purged to the S/C. During normal operation of the PCCS, uncondensed steam and nitrogen being purged to the S/P will cause condensation chugging and flow oscillations. As in the GIRAFFE tests, the S/C was kept empty of liquid to avoid oscillatory flow and heat transfer phenomena. The liquid drained out of the PCCS to the RPV which functioned as a collection tank. The RPV had a small amount of water at the tank bottom as its initial condition. Toshiba ran a line from the RPV to the S/C to equalize pressure between these two vessels. The pressure in the condensate collection tank and the purging tank were identical to avoid having a pressure gradient develop between the RPV and S/C that would cause gas flow to the RPV, liquid flow to the S/C, or even reverse flow from the S/C or the RPV to the PCCS. A valve on the S/C opened to vent out the purged gases at the rate that they were accumulating in the S/C [9]. A RELAP5 VALVE component simulated the vent valve by opening when pressure exceeded the nominal system pressure and by closing when the pressure dropped below the nominal system pressure.

The pool that the PCCS resides in was not explicitly modeled. RELAP5 being a one-dimensional fluid flow code could not simulate the two-dimensional nature of the natural convection pool boiling occurring in the pool. Therefore, a

table of heat transfer correlations for pool boiling, shown in Table 1, was developed from literature [10-14] to use for GIRAFFE and SBWR modeling.

Models have been developed to predict four Phase 1, Step 1 tests that have a system pressure of 3 bar and a steam flow rate of 0.03 kg/s. The nitrogen partial pressure fraction was varied in the four cases by keeping the steam flow rate at 0.03 kg/s and adding nitrogen to the inlet flow to reach the proper nitrogen concentration (nitrogen partial pressure fractions = 0.0, 0.02, 0.05, and 0.10). The heat transfer coefficients, overall heat transfer, and gas volume temperatures were calculated. The gas volume temperatures were compared to the temperatures obtained from six thermocouple positions in the GIRAFFE test [3]. The RELAP5 PCCS model used 5 different nodings of evenly spaced cells (3, 6, 12, 18, and 24 cells) to explore the effects of cell noding on the heat transfer calculations.

PHASE 1, STEP 1 TEST ASSESSMENT WITH UCB CORRELATION - RELAP5 RESULTS

Figures 5 through 8 show the RELAP5 predicted heat transfer coefficients for Phase 1, Step 1 and Figures 9 through 12 show the gas temperatures in the tube calculated by RELAP5 and the bulk tube temperatures from GIRAFFE test data for the Phase 1, Step 1 tests with nitrogen partial pressure fractions of 0.0, 0.02, 0.05, and 0.10, respectively. The RELAP5 flow and pressure input derived from GIRAFFE data is assumed to have an accuracy of ±2% corresponding to the accuracy of the flow and pressure instrumentation in the GIRAFFE facility [9]. The heat transfer coefficients and gas temperatures from the RELAP5 calculations are plotted in Figures 5 through 12 on the x-axis at the point corresponding to the mesh cell center. The origin is the top of the 2.4 m PCCS tubes. The GIRAFFE temperature test data were obtained from a bulk temperature probe located in the center of one of the three PCCS tubes. The x-axis locations for the test data are the positions of the thermocouples on the bulk temperature probe.

As shown in Table 2, the pool-side heat transfer coefficients are of the same order of magnitude as the tube-side heat transfer coefficients. The pool-side heat transfer coefficients are larger than the tube-side heat transfer coefficients except in the entrance region of the GIRAFFE test with pure steam. Hence, except in the entrance region of the GIRAFFE test with pure steam, the limiting resistance to heat transfer lies in the PCCS tubes.

The predicted heat transfer coefficients show the effects of the cell length dependence, as expected from the $\Delta Z_c / L_c^2$ term in Equation 2. As the number of nodes increased, the heat transfer coefficient increased. A comparison of Figures 5 through 8 illustrates the effect. With increasing nitrogen concentration the effect is more dramatic. The heat transfer coefficient increases to its greatest value at the tube entrance. Figure 5 shows that the cell length dependence on the gas velocity effect allows a higher maximum heat transfer coefficient with increasing cell numbers. Furthermore, this limit of two still appears to be high, especially for the cases with steam and nitrogen mixed.

As shown by Equation 4, the plateau in the heat transfer coefficients in Figure 5 is created by the high gas velocities near the tube entrance in the tests with pure steam cases. The high gas Reynolds number push the gas velocity effect number, f_2, to the maximum of two where the plateau occurs. Since the vertical film condensation heat transfer coefficient, h_t, should be nearly constant and the noncondensable gas degradation factor, f_2, is equal

to one in a pure steam environment, when f_1 is equal to two the condensation heat transfer coefficient will remain a constant. When Re_g falls below 11,518, the condensation heat transfer coefficient will drop below the plateau.

The temperatures in Figures 9 through 12 provide a direct comparison of RELAP5 calculations to GIRAFFE data (contains error bars of ±1°C). It can be seen that the three-cell and six-cell nodings predict the temperature profiles within 1-2°C of the GIRAFFE data in the two cases with the lowest nitrogen concentrations. The 12-,18-, and 24-cell node cases show up to 10°C deviation from the data by the exit of the PCCS in the two cases with the lowest nitrogen concentrations. In the two cases with the highest nitrogen concentrations, the RELAP5 entrance temperatures are 3°C greater than the GIRAFFE data and the data shows a temperature rise from the first thermocouple to the second thermocouple. The RELAP5 temperatures are consistent with the saturation temperatures for the partial pressures of steam for the two highest nitrogen concentration cases. Therefore, there may be experimental errors in the GIRAFFE bulk temperatures or pressure drops in the feed lines to the PCCS that are not included in the RELAP5 model. As in the two cases with the lowest nitrogen concentrations, the RELAP5 three-cell noding and the six-cell noding results show agreement within 1-2°C of the data. However, the twelve-cell noding also shows agreement of 1-2°C with the data and the runs with 18 and 24 cells are not appreciably different than the data.

As seen in Figure 9, the test with pure steam had a temperature plateau not seen in the tests with nitrogen present (Figures 10 through 12). Since the pressure drop in the PCCS tubes is small, the temperature stays at a constant saturation temperature until full condensation occurs and subcooling occurs. On the other hand, in the tests with nitrogen present, the saturation temperature drops as the partial pressure of steam decreases as the nitrogen content of the vapor mixture increases.

Since the tube exit temperatures decreases in all cases with increasing cell numbers, increasing the number of cells resulted in higher heat transfer. To get an idea of how much the cell noding affected heat transfer, the total heat transfer, as shown in Figure 13, must be examined. When nitrogen is added to the vapor mixture the total heat transfer calculated by RELAP5 is around 10% too high when compared to the GIRAFFE data for the cases with 6 cells. It is up to 20 to 33% too high when compared to the GIRAFFE data for the cases with 12, 18, and 24 cells. The three-cell noding calculated heat transfer that was at most ±5% off the GIRAFFE data.

The increase in heat transfer caused by increasing cell noding is more pronounced with increasing concentrations of noncondensable gases. In the test with pure steam, the condensation length is less than the total tube length. Therefore, as cell nodes increase in pure steam flow, condensation length decreases. However, the cell noding effect on sensible heat removal is nearly negligible and the total heat transfer is affected by only 2% by increasing cell nodes from 3 to 24. As noncondensable gas is added to steam, the heat transfer is degraded enough to prevent total condensation of the steam within the PCCS tube length and the cell noding effect on heat transfer is felt over the entire length of the tube causing a 20% to 33% increase in heat transfer as seen in Figure 13.

Since the UCB correlation overpredicts the heat transfer in the entrance region of a condensing tube [8], numerical homogenizing of the void fractions, air mass fractions, and gas and liquid velocities with decreasing cell nodes can reduce the entrance effect. Hence, the three-cell noding most closely reproduces both the GIRAFFE heat transfer (Figure 13) and temperature profiles. However, the code user must be aware that this effect is a product of the approach taken to implement the UCB heat transfer correlation in RELAP5 MOD3.1.1.

CONCLUSION

This study showed that the RELAP5 MOD3.1.1 implementation of the UCB correlation has a tendency to overpredict the heat transfer in the entrance region of the tube. Furthermore, and that increasing the noding in RELAP5 MOD3.1.1 has a profound effect on the heat transfer coefficient. The RELAP5 MOD3.1.1 implementation of the UCB correlation does overpredict heat transfer in the entrance region of a tube but the use of three large cells in the RELAP5 PCCS model will smooth out the effect and produce satisfactory agreement with the data. However, it is recommended that this version of RELAP5 should remove the cell length term in the condensation heat transfer correlation to avoid its effect on the heat transfer caused from using different cell sizes. If this change is implemented, another noding study should be conducted and the recommendation of using three cells reevaluated.

ACKNOWLEDGEMENT

The authors would like to acknowledge the support of the United States Nuclear Regulatory Commission in funding this research.

REFERENCES

[1] Shiralkar, B., et al., "SBWR Test and Analysis Program Description," NEDO-32391, Rev. A, General Electric Company (1994).

[2] Carlson, K.E., et al., "RELAP5/MOD3 Code Manual," NUREG/CR-5535 (1990).

[3] Nagasaka, H., et al., "Heat Removal Tests of Isolation Condenser Applied as a Passive Containment System", Proceedings of the 1st JSME/ASME Joint International Conference on Nuclear Engineering (ICONE-1), 265-271 (1991).

[4] Vierow, K.M., and Schrock, V.E., "Condensation in a Natural Circulation Loop with Noncondensable Gas Present, Part I Heat Transfer," Japan-US Seminar on Two-Phase Flow Dynamics, Berkeley, CA (1992).

[5] Shumway, R.W., "Condensation Models for SBWR," INEL Draft Report, (1992).

[6] Shumway, R.W., "Wall Condensation Improvements in RELAP5/MOD3.1," INEL Draft Report, (1993).

[7] Chato, J.C., "Laminar Condensation Inside Horizontal and Inclined Tubes," ASHRAE, 4, 52-60 (1969).

[8] Tills, J., "Letter Report on PCCS Modeling for SBWR," Containment Modeling Department, Sandia National Laboratory, Albuquerque, NM (1994).

[9] Arai, K., Personal Communication (1994).

[10] Kakaç, S., et al., editors, Handbook of Single-Phase Convective Heat Transfer, John Wiley & Son,12-24 (1987).

[11] Nishikawa, K., et al., "Effect of Heating Surface Orientation on Nucleate Boiling Heat Transfer," Proc. ASME-JSME Thermal Eng. Joint Conf., (1983).

[12] Carey, V.P., Liquid-Vapor Phase-Change Phenomena: An Introduction to the Thermophysics of Vaporization and Condensation Processes in Heat Transfer Equipment, Hemisphere Publishing Corporation, Washington, 238-243 (1992).

[13] Bui, T.D. and Dhir, V.K., "Transition Boiling Heat Transfer on a Vertical Surface," J. Heat Transfer, 107, 756-763 (1985).

[14] Bui, T.D. and Dhir, V.K., "Film Boiling Heat Transfer on an Isothermal Vertical Surface," J. Heat Transfer, 107, 764-771 (1985).

TABLE OF NOMENCLATURE

D_h = hydraulic diameter for heat transfer, m

ΔZ_c = RELAP5 cell change in elevation, m

f_1 = gas velocity factor

f_2 = noncondensable gas degradation factor

g = acceleration of gravity, m/s^2 = 9.81 m/s^2

G_g = gas mass velocity, kg/m^2-sec

h_{cond} = laminar film condensation heat transfer coefficient, W/m^2-K

h_{exp} = UCB heat transfer coefficient, W/m^2-K

h_{fg} = latent heat of vaporization, kJ/kg

h_t = vertical film condensation heat transfer coefficient, W/m^2-K

k_f = liquid conductivity, W/m-K

L_c = RELAP5 cell length, m

M_a = gas mass fraction

Re_g = $G_g D_h/\mu_g$ = gas Reynolds number

T_{gi} = interfacial temperature, K

T_w = wall temperature, K

δ_l = liquid film thickness, m

μ_g = gas viscosity, N-sec/m^2

μ_f = liquid viscosity, N-sec/m^2

ρ_g = density of gas, kg/m^3

ρ_f = density of liquid, kg/m^3 .

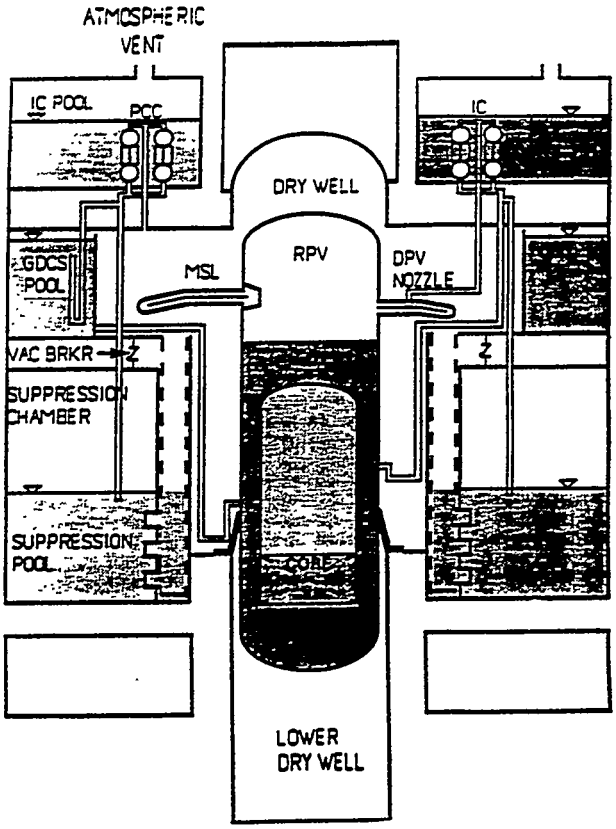


Figure 1: SBWR

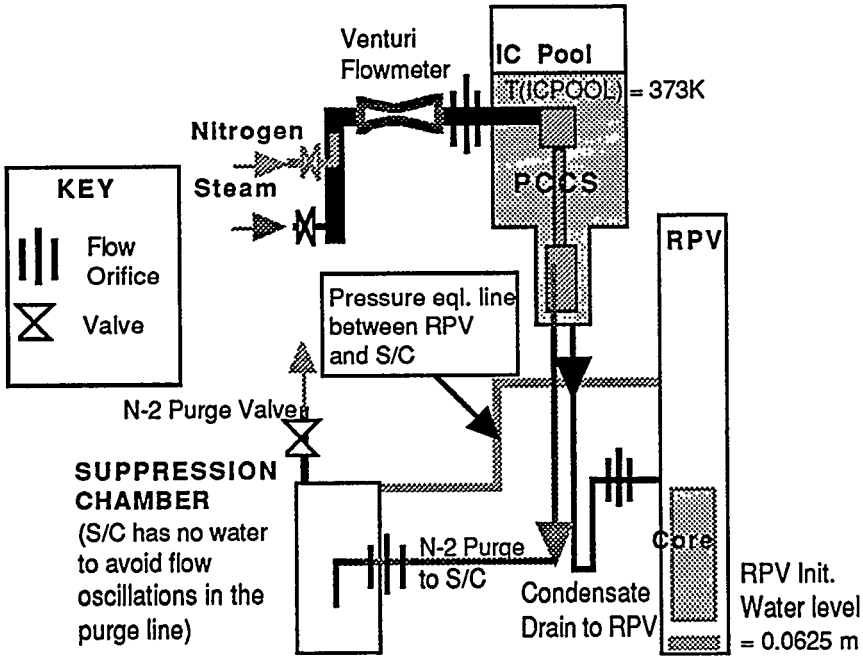


Figure 2: Phase 1, Step 1 Configuration

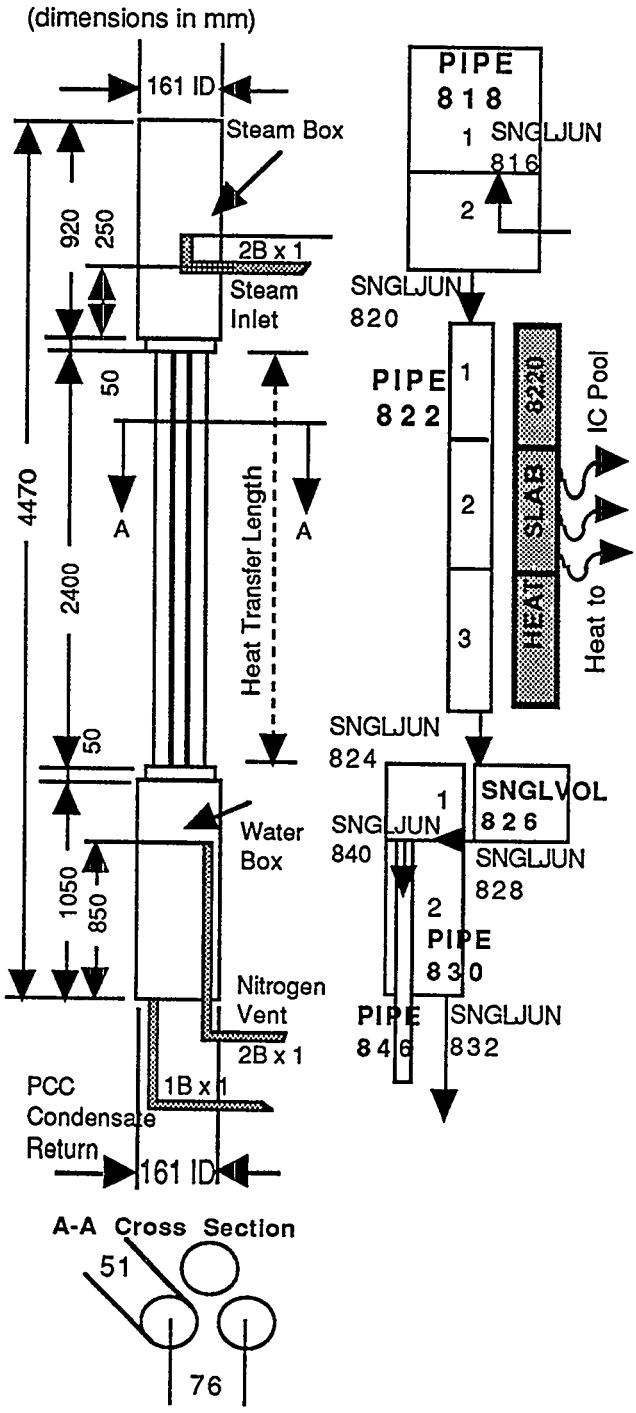


Figure 3: Phase 1, Step 1 PCCS Configuration With RELAP5 3-Cell PCCS Model

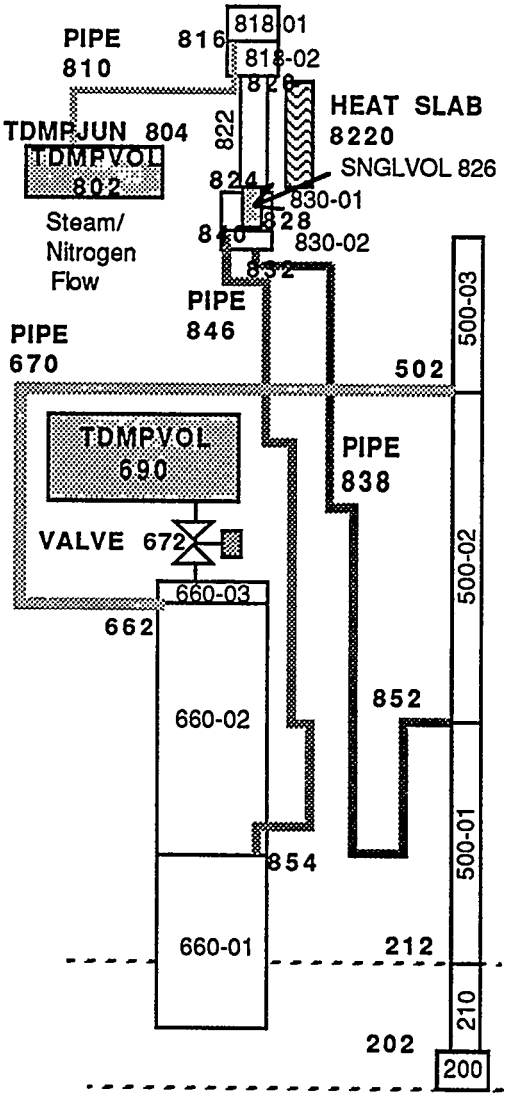


Figure 4: Phase 1, Step 1 BNL RELAP5 Model

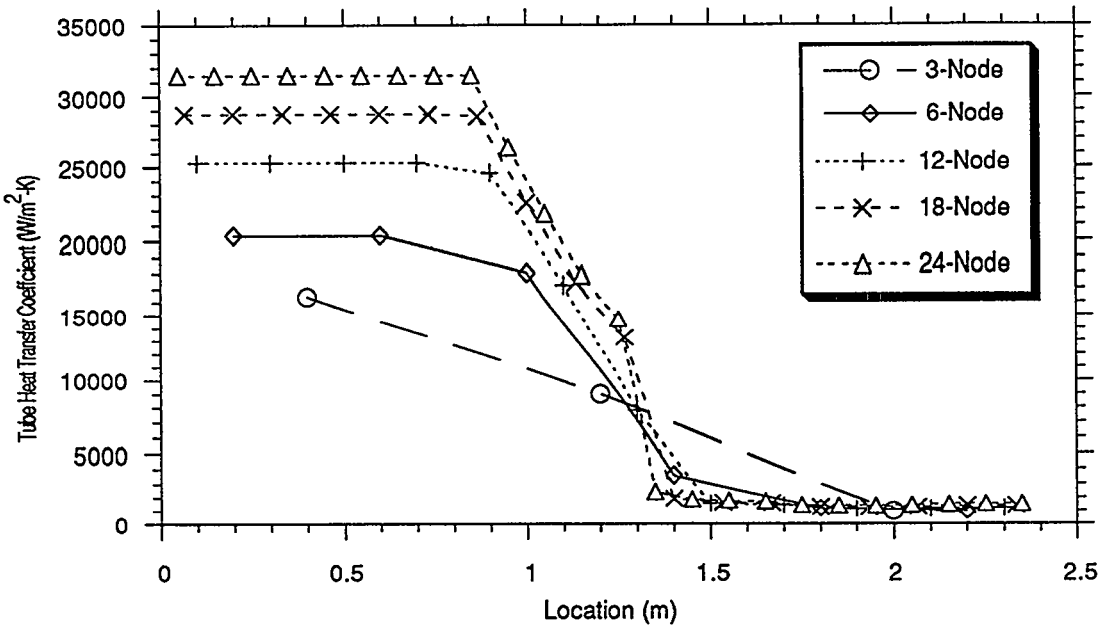


Figure 5: GIRAFFE - Phase 1, Step 1 Test - P_{N2}/P_{total} = 0.0 - Heat Transfer Coefficients

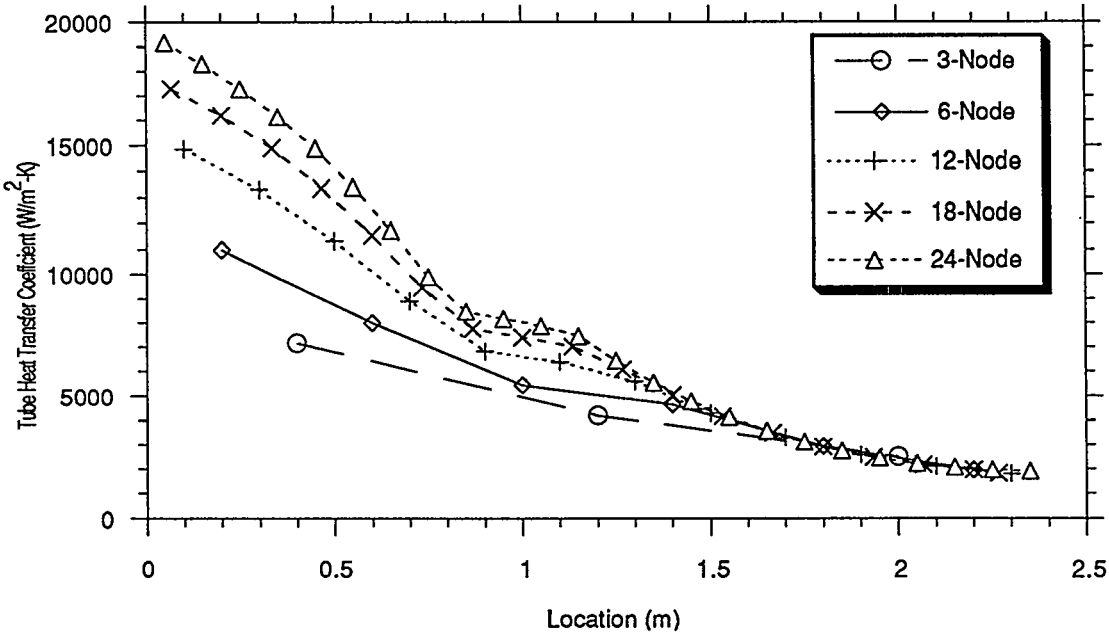


Figure 6: GIRAFFE - Phase 1, Step 1 Test - P_{N2}/P_{total} = 0.02 - Heat Transfer Coefficients

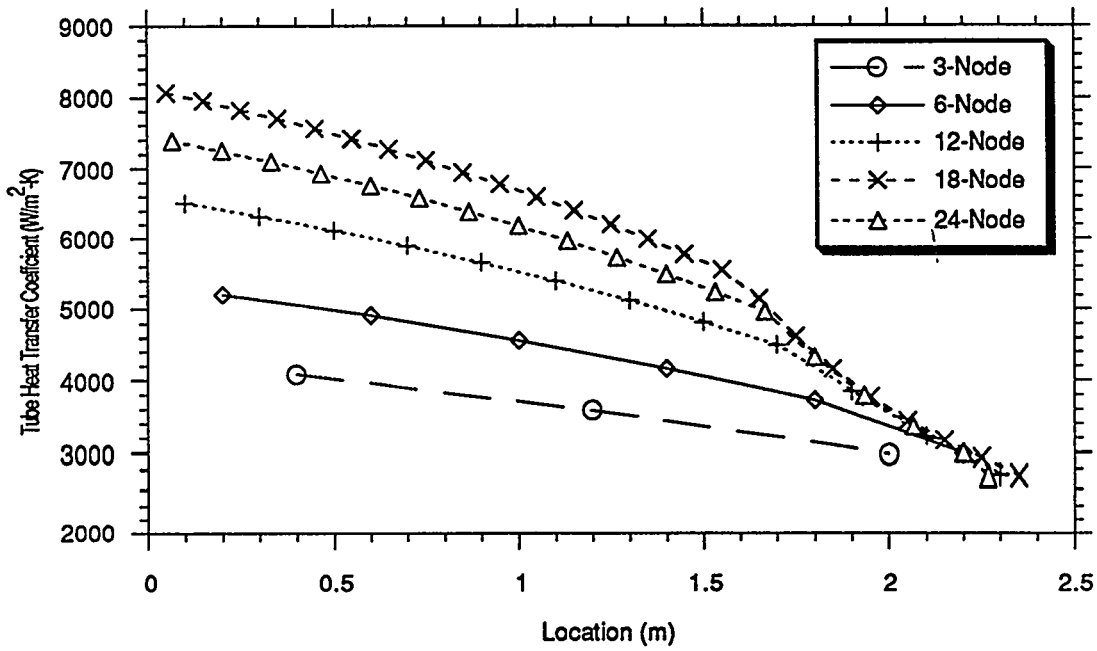


Figure 7: GIRAFFE - Phase 1, Step 1 Test - P_{N2}/P_{total} = 0.05 - Heat Transfer Coefficients

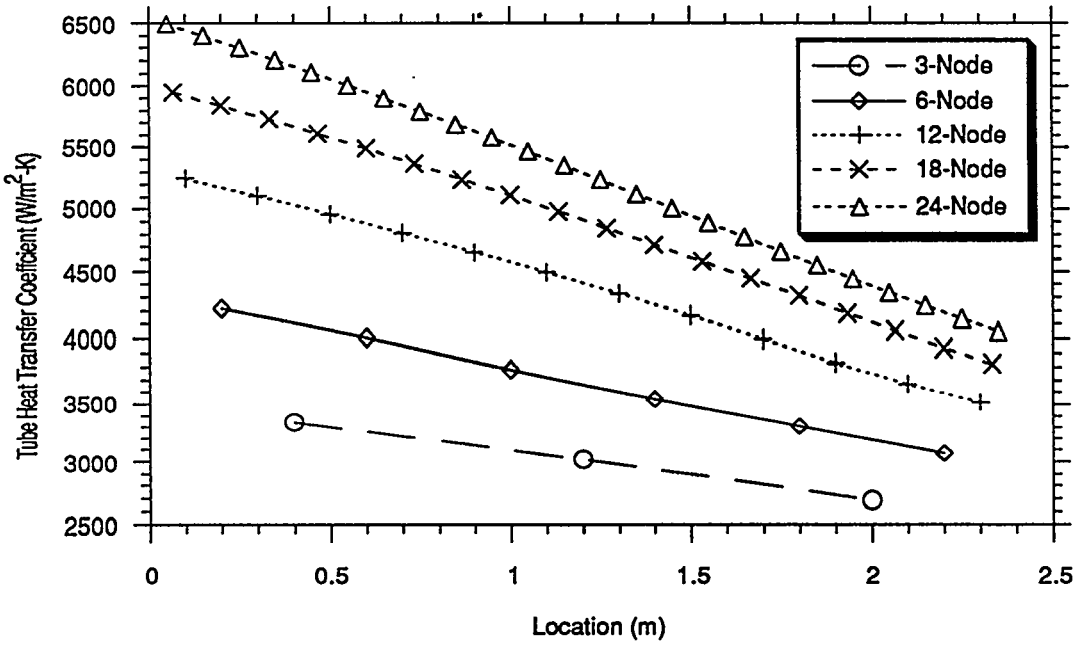


Figure 8: GIRAFFE - Phase 1, Step 1 Test - P_{N2}/P_{total} = 0.10 - Heat Transfer Coefficients

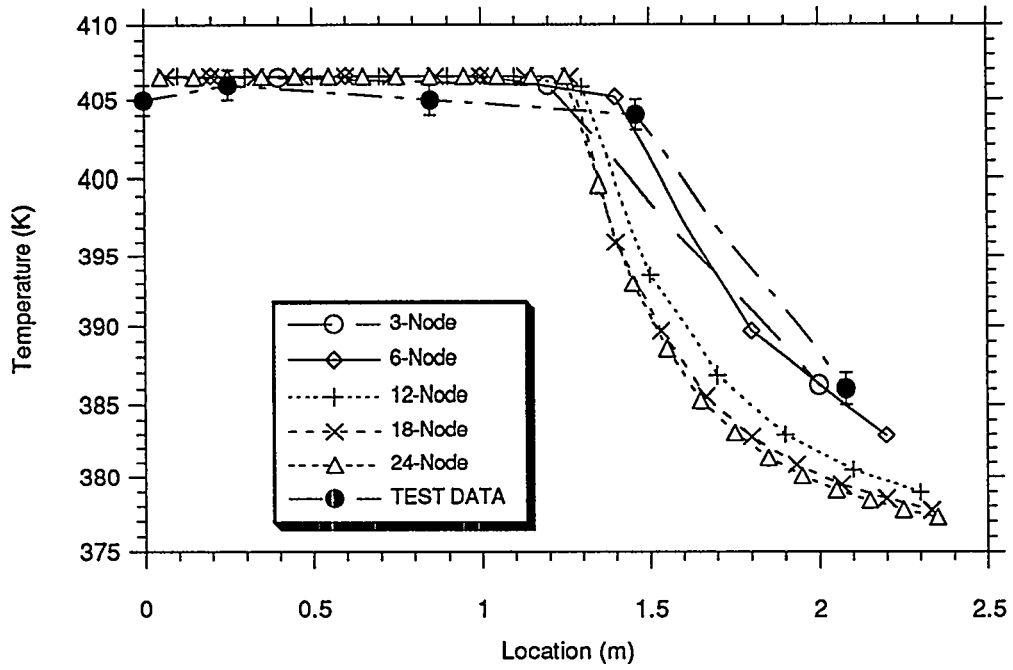


Figure 9: GIRAFFE - Phase 1, Step 1 Test- P_{N2}/P_{total} = 0.0 - Temperatures

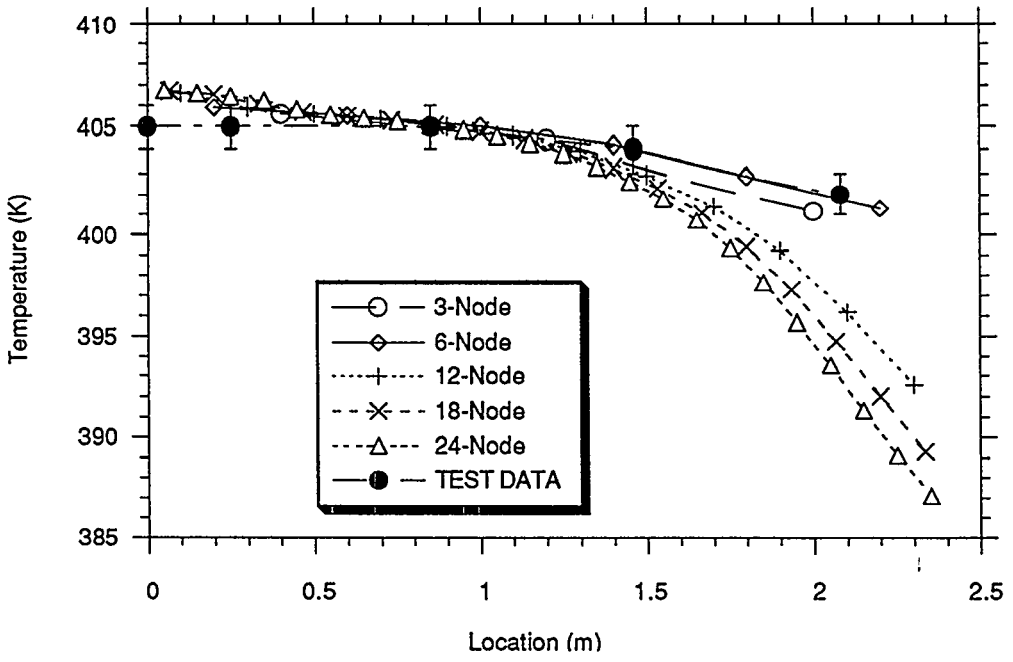


Figure 10: GIRAFFE - Phase 1, Step 1 Test - P_{N2}/P_{total} = 0.02 - Temperatures

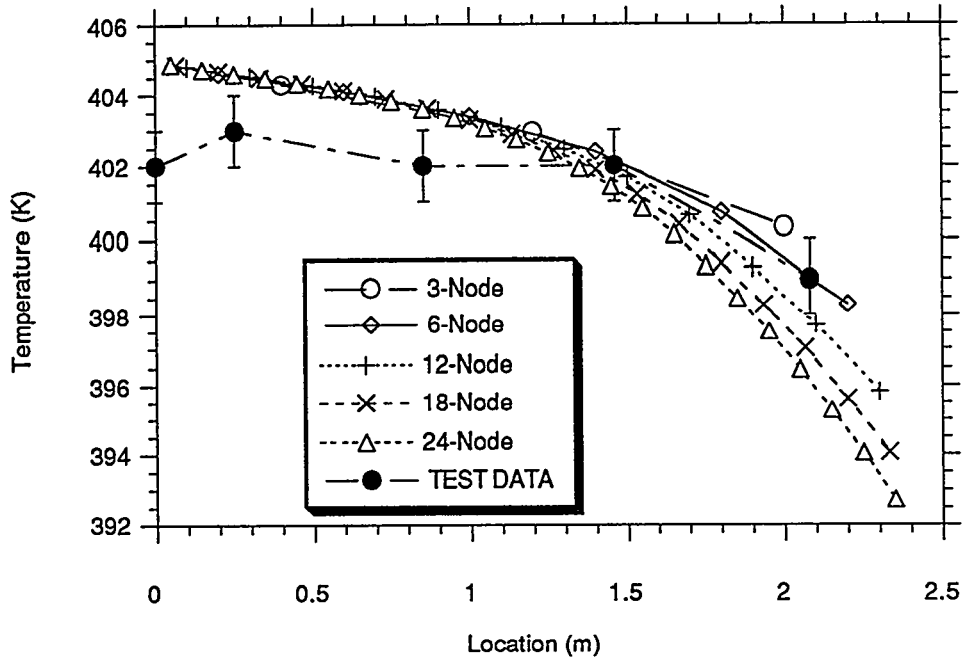


Figure 11: GIRAFFE - Phase 1, Step 1 Test - P_{N2}/P_{total} = 0.05 - Temperatures

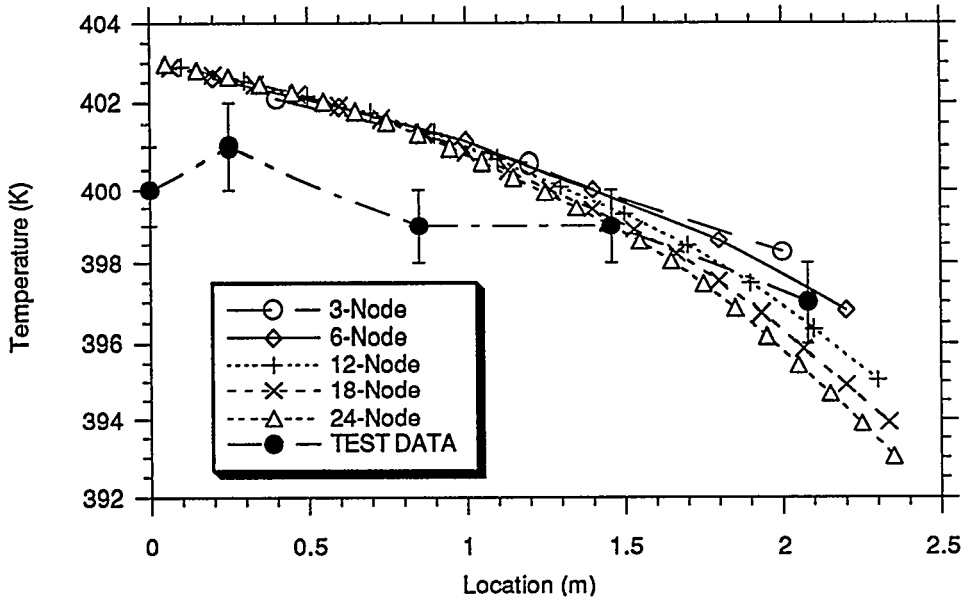


Figure 12: GIRAFFE - Phase 1, Step 1 Test - P_{N2}/P_{total} = 0.10 - Temperatures

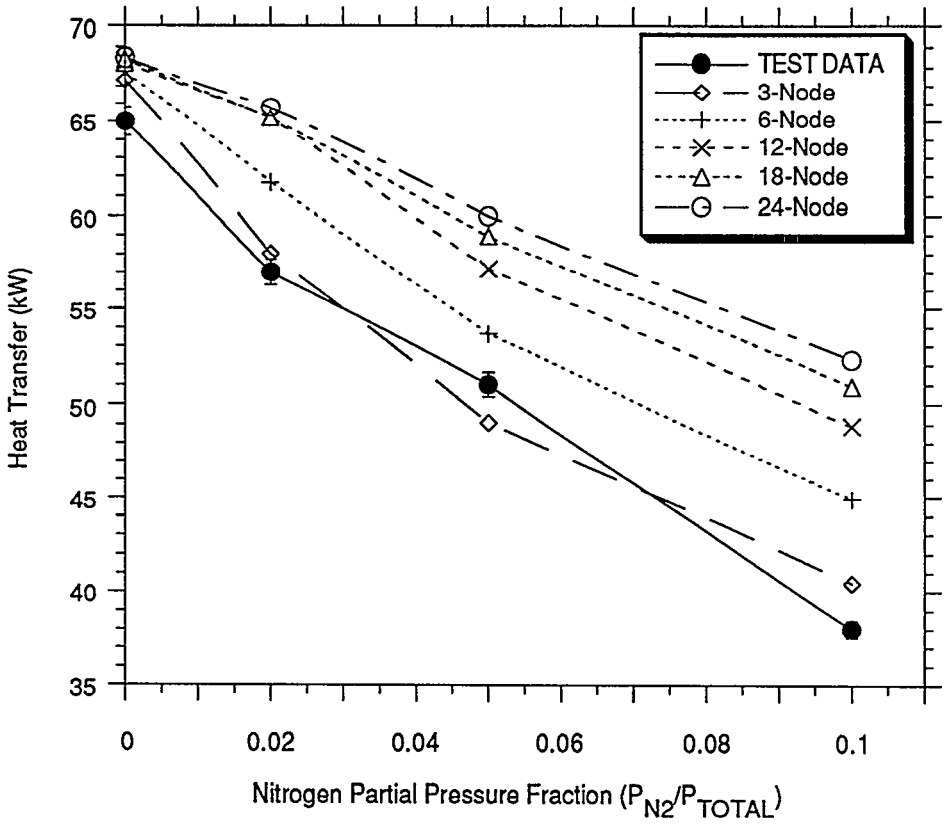


Figure 13: GIRAFFE - Phase 1, Step 1 Test - Heat Transfer Rates

Table 1: RELAP5 Pool Boiling Curve

Temperature (K)	Heat Transfer Coefficient (W/m^2-K)
373.25	169.0
373.65	290.0
374.15	365.0
375.15	460.0
376.15	526.0
376.65	554.0
376.83	1380.0
377.59	1480.0
377.77	1650.0
378.13	1810.0
379.15	2370.0
380.15	3250.0
381.15	4280.0
382.15	5460.0
383.15	6780.0
384.15	8250.0
385.15	9860.0
386.15	11600.0
387.15	13500.0
388.15	15600.0
389.15	17800.0
390.15	20200.0
391.15	22700.0
392.15	25400.0
393.15	28200.0
394.15	31200.0
395.15	34300.0
396.15	34300.0
397.15	34300.0
398.15	34300.0
399.15	34300.0
401.15	25900.0
403.15	18700.0
407.15	10400.0
411.15	6160.0
415.15	3850.0
419.15	2510.0
423.15	1700.0
427.15	1180.0
431.15	845.0
435.15	617.0
439.15	460.0
443.15	349.0
445.15	306.0
453.15	300.0
463.15	278.0
473.15	260.0
483.15	255.0
493.15	250.0

Table 2: RELAP5 Tube-Side and Pool-Side Heat Transfer Coefficients

GIRAFFE Test P_{N2}/P_{total}	Tube Pos. (m)	Tube-Side Heat Transfer Coefficient (W/m^2-K)	Pool-Side Heat Transfer Coefficient (W/m^2-K)
0.0	0.4	16418	8991.6
0.0	1.2	8996.9	7832.8
0.0	2.0	973.50	1586.5
0.02	0.4	7151.0	7281.9
0.02	1.2	4195.3	5960.4
0.02	2.0	2515.5	4428.8
0.05	0.4	4082.9	5874.4
0.05	1.2	3582.7	5391.3
0.05	2.0	2981.5	4636.7
0.10	0.4	3338.4	5130.9
0.10	1.2	3017.8	4704.5
0.10	2.0	2684.2	4151.7

ATHLET Validation Using Accident Management Experiments

V. Teschendorff, H. Glaeser and F. Steinhoff

Gesellschaft für Anlagen– und Reaktorsicherheit (GRS) mbH
Forschungsgelände, D–85748 Garching, Germany

Abstract

The computer code ATHLET is being developed by the GRS as an advanced best–estimate code for the simulation of leaks and transients in PWRs and BWRs including beyond design basis accidents. The code has features that are of special interest for applications to small leaks and transients with accident management, e.g. initialisation by a steady–state calculation, full–range drift–flux model, and dynamic mixture level tracking. The General Control Simulation Module of ATHLET is a flexible tool for the simulation of the balance–of–plant and control systems including the various operator actions in the course of accident sequences with AM measures.

The systematic validation of ATHLET is based on a well balanced set of integral and separate effect tests derived from the CSNI proposal emphasising, however, the German combined ECC injection system which was investigated in the UPTF, PKL and LOBI test facilities.

PKL–III test B 2.1 simulates a cool–down procedure during an emergency power case with three steam generators isolated. Natural circulation under these conditions was investigated in detail in a pressure range of 4 to 2 MPa. The transient was calculated over 22000 s with complicated boundary conditions including manual control actions. The calculation is in good agreement with the data and demonstrates the code's capability to model the following processes successfully:

- variation of the natural circulation caused by steam generator isolation,
- vapour formation in the U–tubes of the isolated steam generators,
- break–down of circulation in the loop containing the isolated steam generator following controlled cool–down of the secondary side,

- accumulation of vapour in the pressure vessel dome.

One conclusion with respect to the suitability of experiments simulating AM procedures for code validation purposes is that complete documentation of control actions during the experiment must be available. Special attention should be given to the documentation of operator actions in the course of the experiment.

1 Introduction

Large thermal–hydraulic system codes have been developed and verified in several countries during the past two decades. The aim of this development has shifted during this period from conservative calculations for design basis accidents to realistic analyses of loss–of–coolant accidents (LOCA) and transients.

With the planning and implementation of accident management (AM) procedures in the existing nuclear power plants a new field of application was opened for which the codes were not originally intended and for which assessment is not yet completed.

For the design and evaluation of safety systems, the specification of operator actions and for operator training, reliable and thoroughly validated thermal–hydraulic system codes are required, which describe the reactor system response under off–normal and accident conditions. Although AM involves many more subjects besides thermal–hydraulics it can be clearly stated from actual practice in Germany that thermal–hydraulic codes are valuable tools to support planning and assessment of specific AM procedures.

It is the objective of this paper to point out specific needs and conditions to be observed during the validation process necessary for applying thermal–hydraulic codes to AM procedures. This is exemplified by the post–test calculation of an integral experiment in the PKL–III facility.

2 Calculations For Preventive Accident Management

In Germany, investigations of possible AM measures were started several years ago [1]. The meaning of the term "Accident Management" is not exactly the same in all countries. Therefore, we shall use here the definition from a report jointly prepared by the IPSN and the GRS [2]:

"Accident management" includes all measures to prevent core damage and retain the core within the reactor vessel, maintain containment integrity and minimize off–site releases.

The above definition goes on making a distinction between prevention and mitigation. This paper will be confined to some aspects of thermal–hydraulic code validation for preventive AM measures.

A considerable number of accident sequences were analyzed by the GRS that begin with different initiating events and include AM measures [4], [5]. The most important ones for PWR's are:

- AM measures on the secondary side
  - Total loss of feed water
  - Station black–out
- AM measures on the primary side
  - Loss of secondary heat removal
  - Primary leaks with loss of secondary heat removal or failure of High Pressure Safety Injection (HPSI)
  - SG–tube ruptures with failure of pressurizer spraying

The analyses were performed, for a large part, to evaluate the risk reduction potential of AM–measures in the German Risk Study, Phase B [3]. Detailed analyses for selected transients are being performed presently to support planning and assessment of specific AM procedures.

Several leaks and transients involving AM–measures were analyzed also for German BWR's [4], [7]. Recently, the GRS has completed a probabilistic safety study for a 1300 MW_{el} BWR [5]. Additional AM sequences are analyzed for this study. Since 1989, all calculations are being performed with ATHLET, using best–estimate models.

3 The ATHLET Code

The computer program ATHLET (Analyses of Thermal–Hydraulics for Leaks and Transients) is being developed by the GRS for the whole spectrum of leaks and transients in PWRs an BWRs [6,7]. The code is based on a five–equation system (mixture momentum equation with drift) and is now being extended to a full six–equation two–fluid model including non–condensible gases. A four–equation system (only mass equations separated) is available as an option that users still prefer for operational transients. The reactor coolant system is modeled by a network of one–dimensional components (objects), allowing for cross flow between parallel channels. The time integration method is fully implicit.

The following features of ATHLET are of special interest for applications to small leaks and transients with AM measures.

- Steady–state capability:
  A steady–state, i.e. a time independent solution, is calculated to establish the initial conditions.

- Critical discharge model:
  The critical two–phase flow rates for a given geometry are calculated in a pre–processor step as a function of the upstream conditions and stored for use during the transient run.

- Full–range drift–flux model:
  A model for the relative velocity between the two phases was developed, based on experimental data for counter–current flow limitation in various geometries [8]. The model comprises options for vertical, horizontal and inclined channels as well as rod bundles and annuli.

- Dynamic mixture level tracking:
  In a user defined vertical stack of cells, a two phase level with bubble rise below and droplet entrainment above is calculated and dynamically traced across cell boundaries.

- General Control Simulation Module (GCSM):
  A high level simulation language allows via input control to model protection and other balance–of–plant (BOP) systems. Control circuits or even simplified fluid systems are convenient to model this way. GCSM has a general interface for user provided external BOP models.

- Integrated Mass and Momentum Balance (IMMB):
  This simplified treatment of the mixture momentum equation (one dynamic pressure for a whole loop) is a fast running option especially valuable for long transients. This technique has been extended to permit local flow reversal.

- Plant Analyzer:
  The code can be run in an interactive mode in the frame of an engineering plant analyzer.

A version ATHLET–CD (Core Degradation) is being developed [9]. The thermo–fluid–dynamic module is closely coupled with modules for core melt, fission product release and fission product transport in the primary system.

4 Validation of ATHLET for AM–Transients

4.1 General validation strategy

In 1987, the OECD/NEA/CSNI issued a report [10] compiled by the Task Group on the Status and Assessment of Codes for Transients and ECC. It contained proposed validation matrices for LOCA and transients, selected according to the dominating phenomena and the available test facilities. Meanwhile, the Task Group on Thermal–Hydraulic System Behaviour is in the process of updating the integral test matrices [12] and extended their work also to separate effect tests [11].

The systematic validation of the ATHLET code is based on a well balanced set of integral and separate effect tests derived from the CSNI proposal emphasising, however, the German combined ECC injection system which was investigated in the UPTF, PKL and LOBI facilities [13, 14, 15]. The ATHLET validation matrices actually comprise 94 integral and 91 separate effect tests, including only a few VVER–specific tests until now. The ATHLET matrices consist of a matrix for large breaks in PWRs, small and intermediate breaks in PWRs, small and intermediate breaks in PWRs with once–through steam generators, AM for a non–degraded core in PWRs, transients in PWRs, transients in shutdown conditions in PWRs, LOCA in BWRs and transients in BWRs. Table 1 shows the validation matrix for integral experiments with the number of tests in each category. The specific selection of tests is based on the intention to cover each relevant thermal–hydraulic phenomenon and each test type in the matrices by at least three facilities of different scales, if available. A total of approximately 30 test types results in about 90 integral tests for code validation. Validation work is shared between the GRS and independent organisations. By the end of 1994, 51 integral tests and 71 separate tests were calculated.

Facility or Plant	Scale	Pressurized Water Reactors *)				Boiling Water Reactors	
		Large Breaks	Small Leaks Intermediate Leaks	Transients	AM	LOCA's	Transients
UPTF/TRAM	1:1	4	2		3		
CCTF	1:25	2					
LOFT	1:50	1	4	1			
LSTF	1:50		2	2			
BETHSY	1:100		7	3	5		
PKL	1:134	3	6	5	5		
ROSA–III	1:424					5	1
FIST	1:642					2	1
LOBI	1:712	2	7	6	2		
GERDA	1:1686		1				
German Konvoi				3			
Brokdorf				1			
Gundremmingen							3
Krümmel							2
Total		**12**	**29**	**21**	**15**	**7**	**7**

*) Experiments for VVER reactors not included

Table 1: ATHLET Assessment Matrix (No. of Integral Experiments)

4.2 Validation for accident management phenomena

A large spectrum of small break and transient scenarios include the unavailability of safety systems, like high pressure injection system, and auxiliary feedwater system. Core heat–up and degradation would occur if no operator action would be taken. These actions constitute preventive accident management (AM) procedures. The OECD/NEA/CSNI "Task Group on Thermal–Hydraulic System Behaviour" will include a section on proposed experiments related to the validation of computer codes in the update of the integral test validation report [12]. The validation matrix for AM transients proposed in that publication comprises a list of 27 relevant phenomena. The PKL III test B 2.1 is selected as an example to validate the ATHLET code. The experimental

conditions of the test will be discussed later. The following list contains less than 27 phenomena since not all of them are adressed by this PKL test. For the remaining 13 phenomena, however, test B 2.1 is suitable for validating the code or has a limited suitablility at least:

1.	Natural circulation in 1–phase flow, primary side	suitable
2.	Natural circulation in 2–phase flow, primary side	suitable
3.	Asymmetric loop behaviour	suitable
4.	Phase separation without mixture level formation	suitable
5.	Mixture level and entrainment in SG secondary side	suitable
6.	Stratification in horizontal pipes	limited suitability
7.	ECC–mixing and condensation	limited suitability
8.	Heat transfer in covered core	suitable
9.	Heat transfer in SG primary side	suitable
10.	Heat transfer in SG secondary side	suitable
11.	Pressurizer thermal–hydraulics	limited suitability
12.	Surgeline hydraulics	limited suitability
13.	Structural heat and heat losses	limited suitability

The main subjects of investigation in the PKL III test B 2.1 are closely related to the first four phenomena of the above list:

- Variation of natural circulation in the different loops with active or isolated steam generator,
- Vapour formation in the U–tubes of the isolated steam generators,
- Break–down of circulation in the loops with isolated steam generator following controlled cool–down of the secondary side,
- Formation of a vapour bubble in the pressure vessel upper head.

The calculation of this PKL test is discussed in the following sections.

5 Calculation of a PKL–III Test with ATHLET

5.1 The PKL–III test facility

Within the scope of German reactor safety research, extensive experiments covering the thermal hydraulic behaviour of a PWR under accident conditions have been performed in the integral test facility PKL–III operated by Siemens/KWU in Erlangen [13]. The PKL test facility simulates a 4–loop, 1300 MW_{el} KWU–designed PWR with a volumetric and power scaling factor of 1:145 (Fig. 1). The elevations and the primary circuit pressure losses are scaled 1:1.

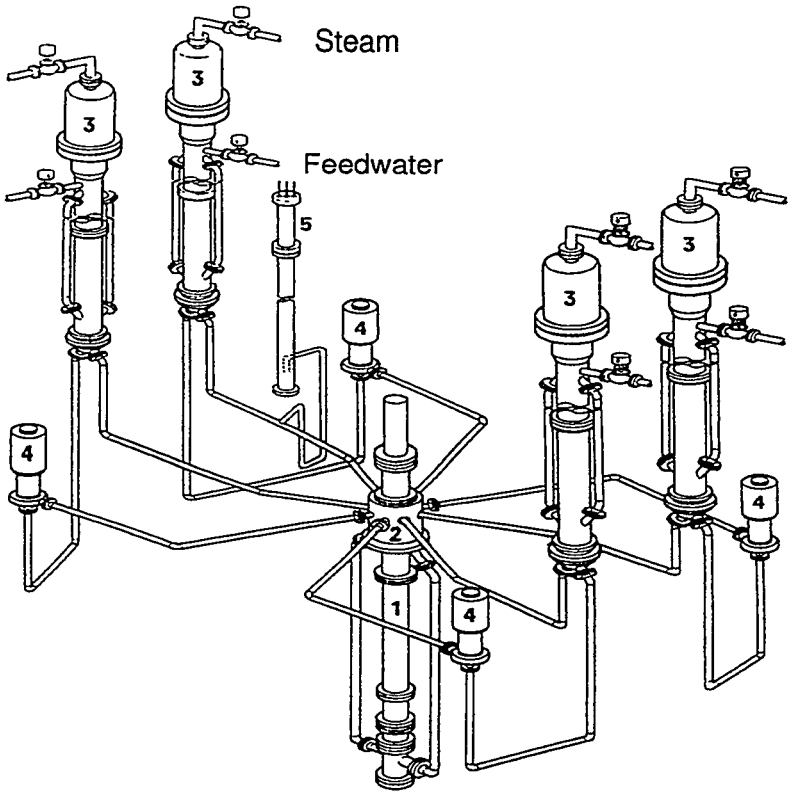


Fig. 1: PKL III test facility

The four loops of the test facility are symmetrically arranged around the pressure vessel, which consists of the lower plenum, core with bypass, upper plenum and upper head. The downcomer is modelled as an annulus in the upper mixing region which is connected to the lower plenum by two external pipes. Each of the four loops contains a hot leg, a steam generator and a cold leg with a main coolant pump. As in the PWR one of the loops is connected to the pressurizer by a surge line. The core is simulated by a bundle of 314 electrically heated rods with a total power of 2.5 MW which corresponds to 10% of the scaled nominal power. The primary pressure is limited to 4.5 MPa.

On the primary side, the test facility is equipped with all important engineered safety and auxiliary systems. These include the high–pressure safety injection system, accumulators, low pressure injection system, residual heat removal system, volume control system and pressurizer heating and spraying control system. Each of the four steam generators is equipped with 28 U–tubes which are the same as in a PWR with respect to length, inner diameter (19.6 mm), tube wall thickness, differing elevations (1.5 m) and material.

The secondary side of the steam generator and the systems connected were simulated as closely as possible to the reference plant. This includes the correct volume in the bundle region, water and steam dome volumes above the tube bundle, the resistance of the steam dryer, the flow limiter of the steam outlet, the main–steam lines with all control features of the original system, the simulation of the downcomer by two stand pipes, and the feedwater and emergency feedwater system. The test facility is equipped with extensive instrumentation which is divided into the PKL test (860), the PWR–identical (60), and the PKL operational instrumentation (150).

5.2 Objectives of test B 2.1

Test B 2.1 simulates a PWR cool–down procedure for a loss of preferred power event. The special feature of the procedure investigated here consists in the isolation of three steam generators, i.e. feed water line and main steam line of these steam generators are shut off by valves. Heat removal from the primary system has to rely in this case on the fourth steam generator alone whose secondary side is cooled down with a gradient of 50 K/h.

Although the cool–down process investigated in test B 2.1 is formally not an AM procedure this test was chosen for detailed presentation here because it exhibits phenomena and code requirements that are typical for this field of application, e. g.

- Small driving heads and mass flow rates (natural circulation),
- Complete phase separation and liquid level movement in vertical components,
- Long problem time (> 8 h),
- Decisive influence of facility specific boundary conditions on major results (e. g. heat losses),
- Variation of boundary conditions during the transient depending on the course of the transient itself (manual control actions).

5.3 ATHLET model for the PKL calculation

The post–test calculation was performed with ATHLET 1.0 Cycle E on a CONVEX 3840 computer at the GRS. In this code version the four equation thermo–fluid model was chosen, be-

cause the assumption that either the vapour or water phase is saturated should be appropriate for this type of transient.

The facility was modelled by 70 thermo–fluid objects (pipes, branches) comprising a total of 245 volumes and a larger number of junctions.

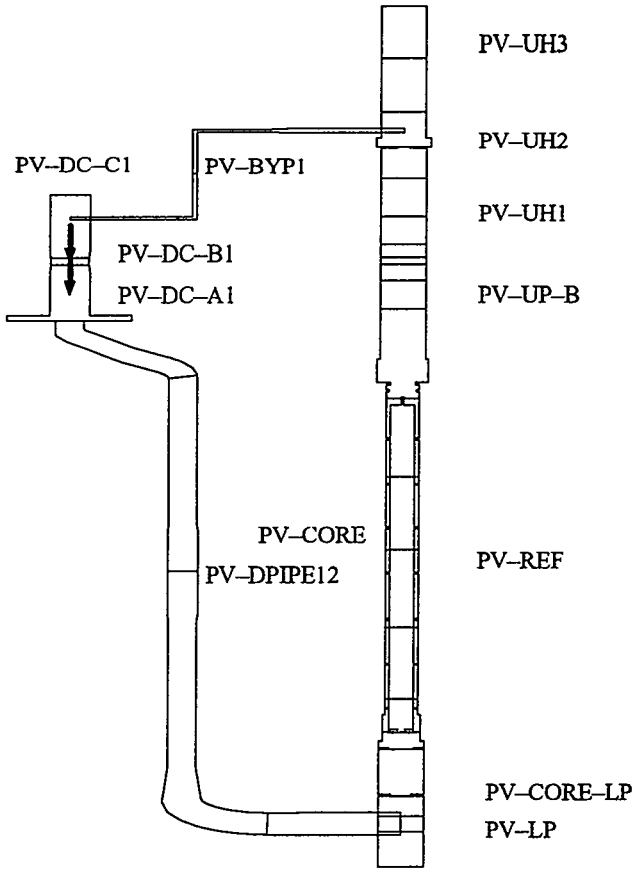


Fig. 2: Nodalization of PKL test vessel and downcomer

Figure 2 shows the nodalization for the pressure vessel and the downcomer. The two external downcomer pipes of the facility were modelled as one pipe. In the pressure vessel, the core bypass is visible around the heated rod bundle. This picture was drawn by a graphical tool using the ATHLET input data. Thermofluid objects are identified by user defined names. The ATHLET data set comprised three loops, while the facility has four loops. Loops 2 and 4 of the facility are simulated as one double loop in the calculation since the SGs in these loops were isolated at the same time. In order to follow the vapour formation and phase separation in the upper parts of the system with sufficient accuracy it was necessary to use a finer nodalization there than in our PKL deck used for previous calculations.

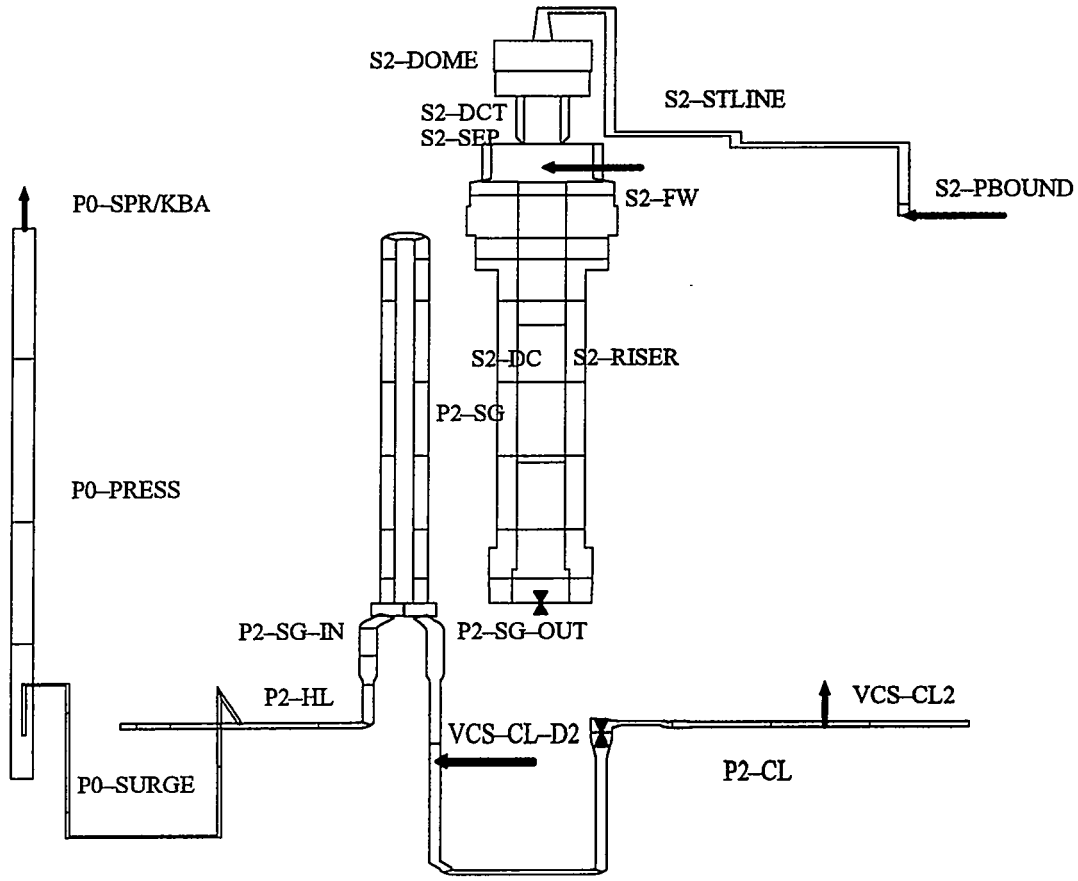


Fig. 3: Nodalization of loop no. 2, with pressurizer and steam generator secondary side

Figure 3 shows the nodalization for this loop including pressurizer and surge line. The SG secondary side with the steam line is off-set to the right of the SG tube bundle in the picture. The secondary side of the cooling system was modelled as an open system. Heat conductor objects were used to model heat losses through pipe and vessel wall. The GCSM Module was applied to model control systems, e. g. pressurizer level control, etc.

5.4 Initial conditions

At the time when the SGs in loops 2 and 4 were isolated (origin of time axis in plots), the following main parameters prevailed in the test:

Bundle power	425 kW (1.7%)
Primary pressure	4.0 MPa
Secondary pressure	2.6 MPa
Mass flow	1.1 kg/s per loop
Subcooling in primary system	ca. 5 K

Pressurizer level	4.2 m
SG heating (compensation of heat losses)	12 kW per SG

The main coolant pumps were not running.

ATHLET matched these conditions with sufficient accuracy after running from its automatic steady state initialization through a zero–transient phase of 1000 s. During this phase the control models, especially for pressurizer level control, were adjusted to the control characteristics of the facility.

5.5 Transient test phase

The transient was initiated by the isolation of two steam generators (SGs 2 and 4). In the stabilizing phase until 4500 s the core power was removed through the two remaining SGs 1 and 3 by an intentional depressurization of the secondary sides of these SGs. In this phase, the secondary side temperatures and the primary side outlet temperatures in SGs 2 and 4 were rising significantly while the primary side mass flow rates were decreasing (Fig. 9). In the active SGs 1 and 3 conditions were inverse, i. e. temperatures were falling while mass flow rates were increasing (Figs. 8 and 10).

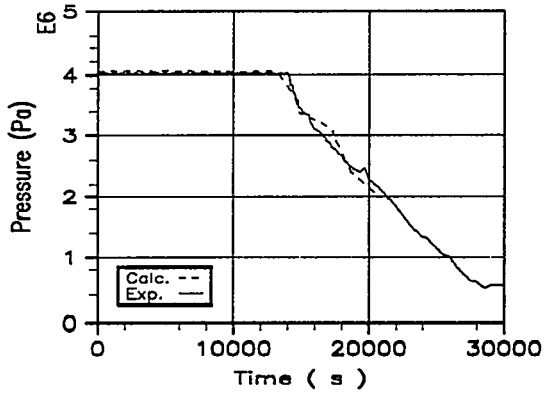


Fig. 4: Pressurizer pressure

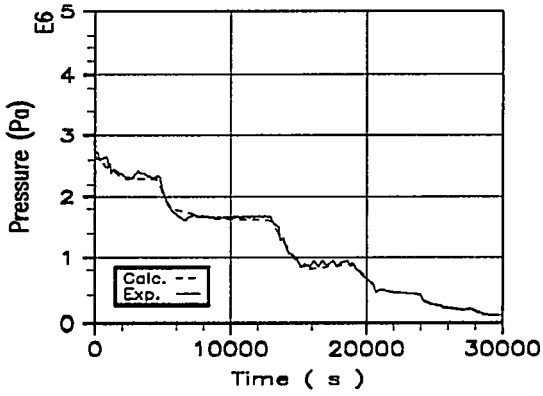


Fig. 5: Secondary pressure SG1

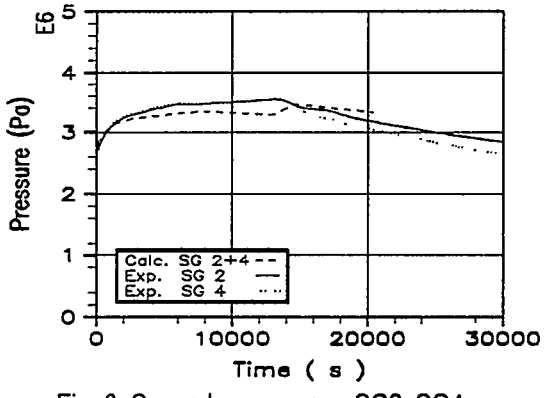


Fig. 6: Secondary pressure SG2, SG4

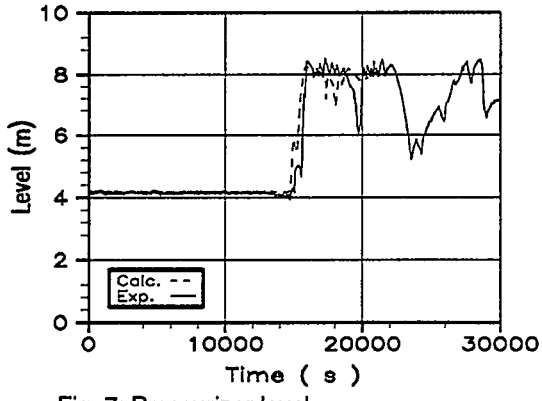


Fig. 7: Pressurizer level

At 4500 s, another steam generator (SG 3) was isolated and further depressurization of the secondary side of SG 1 was initiated. This caused a further temperature rise and mass flow decrease in SGs 2 and 4. Conditions in SG 3 (Fig. 10) rapidly approached those in SGs 2 and 4. After reaching stable conditions no further action was taken until 12900 s.

In the test phase until 12900 s primary pressure (Fig. 4) and pressurizer level (Fig. 7) could be kept almost constant in the test as well as in the calculation by means of controllers for the pressurizer heating and for the volume control system. For the stabilization of the subcooled fluid temperature in the upper plenum through the secondary side pressure and temperature, however, numerous manual control actions were taken in the experiment. Information on those actions was not sufficient to model them in the calculation with the necessary detail. Therefore, the measured secondary pressure in smoothed form was provided as a boundary condition for the calculation (Fig. 5).

At 12900 s, the manually controlled cool–down of the facility with a gradient of 50 K/h was initiated by means of the steam control valve of SG 1. Additional manual actions were taken in order to limit the expected rise of the pressurizer level to 8 m and to maintain a subcooling margin of 10 K in the upper plenum. These control actions involved the pressurizer spray and heating system ant the volume control system. Furthermore, the cool–down process was interrupted when necessary.

About 1500 s later, the primary side outlet temperature of the isolated SGs exceeded the inlet temperature causing complete flow stagnation there under single phase conditions when this temperature difference exceeded 8 K. In the test under consideration here, this process was supported by vapour formation causing end of flow through the isolated SGs at 2100 s after initiation of the cool–down (Figs. 9 and 10).

About 1800 s after initiation of the cool–down, vapour formation started in the vessel upper head (Fig. 11) and in the U–tubes of the isolated SGs (Figs. 12 and 13) pushing water into the pressurizer (Fig. 7).

At about 16000 s, the level of 8 m was reached in the pressurizer (Fig. 5). At 22000 s the vapour bubble completely occupied the vessel upper head (Fig. 9). The U–tubes of the three isolated SGs were completely filled with vapour (Figs. 10 and 11). After activation of the long term cooling system and the end of cool–down procedure the experiment was terminated at 31500 s.

The calculation was terminated at 22000 s when the upper parts of the primary system were completely occupied by vapour.

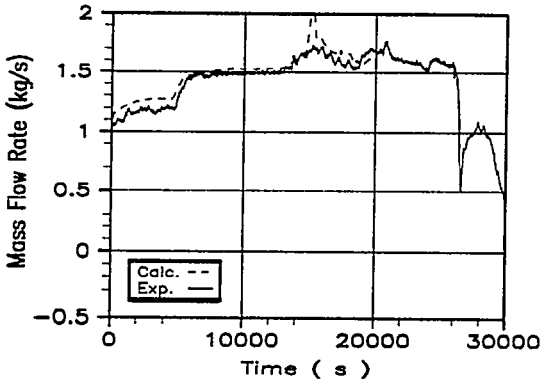


Fig. 8: Primary mass flow rate SG1

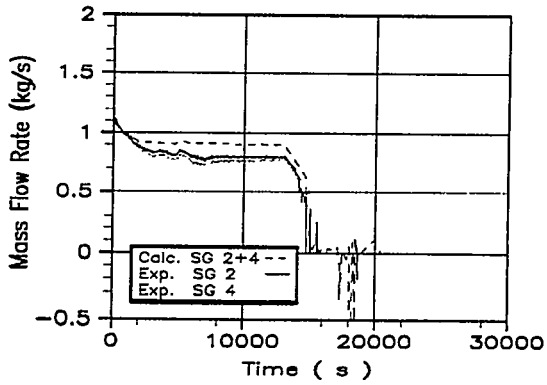


Fig. 9: Primary mass flow rate SG2, SG4

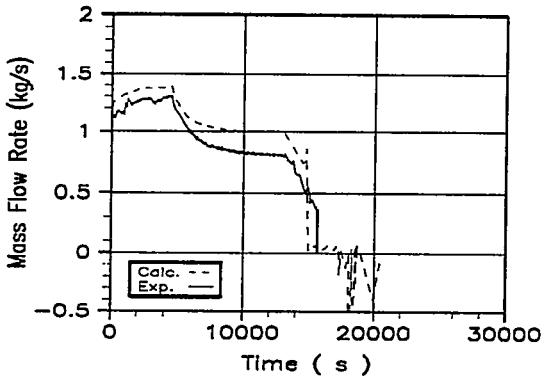


Fig. 10: Primary mass flow rate SG3

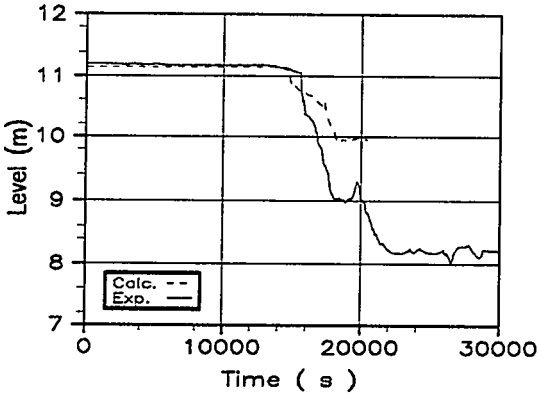


Fig. 11: Level in pressure vessel upper head

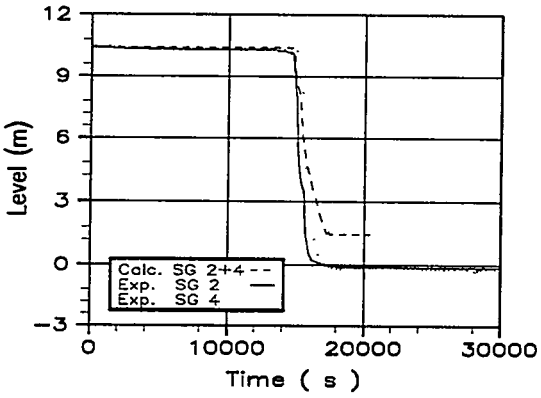


Fig. 12: Primary level in isolated SG2, SG4

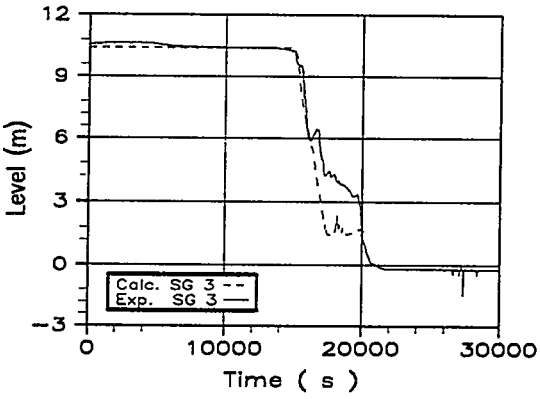


Fig. 13: Primary level in isolated SG3

5.6 Discussion of calculated results

The agreement of the calculated with the experimental data is good for the governing system parameters as pressure, fluid temperatures and pressurizer level. In the following, the results are discussed with respect to the four key phenomena that were dominating this experiment and that are expected to play a dominant role in PWR emergency procedures as well.

Variation of natural circulation in different loops

The initial mass flow rate of about 1.1 kg/s in each loop, decreased in loops 2 and 4 as a consequence of isolating the SG's secondary side in these loops, stabilizing at a constant mass flow of 0.8 kg/s. The calculation also shows this decrease (Fig. 9), stabilizing, however, at a 10% higher flow rate. During the same phase of the transient, the mass flow rates in loops 1 and 3 with the SG's remaining active increase to 1.3 and 1.4 kg/s respectively. Again, the calculation follows correctly the shape of this increase (Figs. 8 and 10), with the flow rates overpredicted by about 10%. It is concluded, that the transient variation of flow in the different loops during natural circulation is well predicted by the code.

Vapour formation in the U–tubes of the isolated steam generator

About 1800 s after initiating the controlled cool–down of SG 1, vapour formation was observed in the primary tubes of all isolated SGs. Figures 12 and 13 show a pronounced decrease of collapsed levels. Timing and gradient of that decrease are well predicted by the code.

Break–down of circulation in loops with isolated steam generator

Vapour formation in the isolated SG's was accompanied by a sharp decrease of mass flow rates (Figs. 9 and 10). At about 16000 s, the flow in loops 2, 3 and 4 dropped to zero, while a flow rate of 1.5 kg/s persisted in the active loop no. 1. The calculation predicted this event at the correct time.

Formation of a vapour bubble in the pressure vessel upper head

Vapour accumulation in the pressure vessel upper head started shortly after vapour formation in the U–tubes of the isolated SG's, i. e. about 1800 s after the initiation of secondary side cool–down of SG no. 1. Figure 9 shows the collapsed level in the pressure vessel. The level decreases slower in the calculation with a maximum deviation from the measured level of less than 1 m.

General observations

There was no tuning of physical models in the code version during this validation process. It should be mentioned, however, that a set of parametric runs was necessary for establishing

the initializing conditions as well as for the transient phase where controllers had to be adjusted in order to simulate boundary conditions of the test that were influenced by manual control actions in the experiment. Obviously, for transients of long duration where natural circulation depends in a most sensitive way on small variations in boundary conditions the quality of the calculation is dominated by the ability to model these boundary conditions. This means for the code validation using AM related experiments, that the ability of both the code and the user to model control actions and other test conditions in full detail is challenged more than the validity of specific physical models.

6 Conclusions

Best–estimate thermal–hydraulic calculations with comprehensive system modelling are required for planning and assessment of preventive accident management. Validation of these codes on integral experiments that simulate AM procedures is necessary to apply these codes with confidence in this extended range of application. In the validation matrix for ATHLET, tests addressing AM from all major experimental facilities are included. The code's capabilities to make reasonable predictions for AM related transients was demonstrated by a post–test calculation of PKL–III test B 2.1 where good agreement with the measured system parameters was achieved. It was especially observed that the results are very sensitive to boundary conditions that were varied during the transient by automatic controllers and as well as by manual control actions. The limited possibilities to reconstruct all manual control actions in full detail from the data recordings limits the accuracy to be expected from post–test calculations.

References

[1] Hicken, E.F., Erven, U., Kersting, E.,
"German Accident Management Program",
Proc. 15th Water Reactor Safety Information Meeting,
Gaithersburg, MD, Vol.6, pp. 133–148 (1987).

[2] Institut de Protection et de Sûreté Nucléaire (IPSN), Gesellschaft für Reaktorsicherheit (GRS) mbH,
"Accident Management in France and Germany",
Common Report IPSN/GRS No. 2, (1991).

[3] Gesellschaft für Reaktorsicherheit
"Deutsche Risikostudie Kernkraftwerke, Phase B"
Verlag TÜV Rheinland, Köln, (1990)

[4] Nolte, W., Burger, H., Kersting, E.,
"Accident Management Measures for BWR Plants–69",
CSNI Report 158, pp. 324–337, (1989).

[5] Kersting, E., et al,
"SWR–Sicherheitsanalyse, Abschlußbericht",
GRS–Report 102, (1993).

[6] Burwell, M.–J., Lerchl, G., Mirò, J., Teschendorff, V., Wolfert, K.,
"The Thermalhydraulic Code ATHLET for Analysis of PWR and BWR Systems"
Proc. 4th Intern. Topical Meeting on Nuclear Reactor
Thermal–Hydraulics (NURETH–4), Karlsruhe,
Vol. 2, pp. 1234–1239, (1989).

[7] Austregesilo, H., Frisch, W., Höppner, G., Mirò, J.E.,
"Analysis of Multiple Failure Transients in BWRs with the System Code ATHLET", Proc. Int. ENS/ANS Conf. on Thermal Reactor Safety (NUCSAFE 88),
Avignon, Vol.3, pp. 1093–1102, (1988).

[8] Sonnenburg, H.–G.,
"Full–Range Drift–Flux Model Based on the Combination of Drift–Flux Theory With Envelope Theory"
Proc. NURETH–4, Karlsruhe, Vol.2, pp. 1003–1009, (1989).

[9] Trambauer, K.,
"The Code ATHLET–CD for the Simulation of Severe Accidents in Light Water Reactors", Paper submitted to 5th Intern. Topical Meeting on Nuclear Reactor Thermal–Hydraulics (NURETH–5), Salt Lake City, (1992).

[10] OECD/NEA/CSNI, "CSNI Code Validation Matrix of Thermo–Hydraulic Codes for LWR LOCA and Transients", CSNI Report 132, (1987).

[11] Aksan, N., D'Auria, F., Glaeser, H., Pochard, R., Richards, C., Sjöberg, A.,
"OECD/NEA–CSNI Separate Effects Test Matrix for Thermal–Hydraulic Code Validation", Volume I: Phenomena Characterisation and Selection of Facilities and Tests, Volume II: Facility and Experiment Characteristics; NEA/CSNI/R(93)14 Part 1 and Part 2, Paris (1994).

[12] Annunziato, A., Glaeser, H., Lillington, J., Marsili, P. Renault, C., Sjöberg, A.,
"CSNI Integral Test Facility Validation Matrix For the Assessment of Thermal–Hydraulic codes for LWR LOCA and Transients; to be issued

[13] Weber, P., Umminger, K.J.,
"Accident Management Procedures on the Secondary and Primary Side for a PWR – Experimental Investigations in the PKL Test Facility –"
Proc. NURETH–6, Grenoble, Vol. 2, pp. 1100–1108, (1993).

[14] "LOBI Test Facility"
CSNI–SINDOC (83) 262 (1983)

[15] Weiss, P.,
"UPTF Experiment, Principal Full–Scale Test Results for Enhanced Knowledge of Large Break LOCA Scenarios in PWRs",
Proc. NURETH–4, Karlsruhe, Vol. 1, pp. 60–66, (1989).

Abbreviations

AM	Accident Management
BWR	Boiling Water Reactor
CSNI	Council on the Safety of Nuclear Installations
ECC	Emergency Core Cooling
GCSM	General Control
IPSN	Institut de Protection et de Surete Nucleaire
LOBI	LWR Off–normal Behaviour Investigations
LOCA	Loss–of–Coolant Accident
NEA	Nuclear Energy Agency
PKL	Primärkreislauf (Test Facility)
PWR	Pressurized Water Reactor
SG	Steam Generator
UPTF	Upper Plenum Test Facility
VVER	Water cooled Water moderated Reactor (Russian type)

Acknowledgement

Development and validation of the ATHLET code is sponsored by the
German Federal Ministry for Education, Science, Research and Technology (BMBF).

A Simple Modelling of Mass Diffusion Effects on Condensation with Noncondensable Gases for the Cathare Code

P. Coste & D. Bestion

Commissariat à l'Energie Atomique
CENG/DRN/DTP/STR/LML 17 rue des Martyrs
38054 GRENOBLE Cedex 09 FRANCE
Fax:76 88 51 77

ABSTRACT

This paper presents a simple modelling of mass diffusion effects on condensation. In presence of noncondensable gases, the mass diffusion near the interface is modelled using the heat and mass transfer analogy and requires normally an iterative procedure to calculate the interface temperature. Simplifications of the model and of the solution procedure are used without important degradation of the predictions. The model is assessed on experimental data for both film condensation in vertical tubes and direct contact condensation in horizontal tubes, including air-steam, Nitrogen-steam and Helium-steam data. It is implemented in the Cathare code, a french system code for nuclear reactor thermal hydraulics developed by CEA, EDF, and FRAMATOME.

INTRODUCTION

CATHARE [9] is a french system code for nuclear reactor thermal hydraulics developed by CEA (IPSN & DRN), EDF, and FRAMATOME. Within the range of accidental sequences, both direct contact condensation and condensation due to heat release from the walls are encountered and require a specific modelling. The first case was investigated [1,2,3] using experimental data from the COSI test facility which simulates the ECC injections and original correlations were derived. Also a critical review of the film condensation models [4] has shown that the Chen et al. [5] correlation was able to properly describe some available experimental data. More recently, attention was paid to the modelling of the effects of the presence of noncondensable gases on the condensation [6]. Nitrogen from the accumulators, Hydrogen from zircalloy clad oxidation or air in case of mid loop operation may be present in the primary circuit. It is known that it can reduce significantly the condensation rate. The diffusion layer near the interface requires a mass diffusion modelling. The heat and mass transfer analogy is used to write the interfacial steam diffusion mass flux. This model generally requires an iterative procedure for calculating the interface temperature.

As system codes for nuclear safety analysis like Cathare are industrial codes with many users, CPU cost must be also considered and some compromise between modeling choices and code efficiency is necessary. In this frame, a first attempt to simplify the modelling and the solution procedure for mass diffusion effects was proposed [6],but the data base for validation had to be extended. The present work presents a new set of simplifications with an extensive validation which includes direct contact condensation data (Cosi data [3]) and film condensation data (data of Nagasaka [7], data of Siddique [8]), with nitrogen/steam, air/steam, and Helium/steam.

THE CATHARE CODE

The Cathare code 1-D module uses the 2-fluid model with a mass momentum and energy equation for each phase. Mass balance equations may be added for each noncondensable gas. Closure terms related to condensation concern mainly mass and energy balance equations.

Mass balance equations:

$$A\frac{\partial \alpha_G \rho_G}{\partial t} + \frac{\partial A \alpha_G \rho_G V_G}{\partial Z} = A\Gamma$$

$$A\frac{\partial \alpha_L \rho_L}{\partial t} + \frac{\partial A \alpha_L \rho_L V_L}{\partial Z} = -A\Gamma$$

$$A\frac{\partial \alpha_G \rho_G X_n}{\partial t} + \frac{\partial A \alpha_G \rho_G X_n V_G}{\partial Z} = S_n$$

Energy equations:

$$A\frac{\partial \alpha_L \rho_L H_{TL}}{\partial t} + \frac{\partial A \alpha_L \rho_L V_L H_{TL}}{\partial Z} - A\alpha_L \frac{\partial P}{\partial t} = A\left(Q_{IL} - \Gamma H_{TL}\right) + \chi q_{WL} - A\alpha_L \rho_L V_L g$$

$$A\frac{\partial \alpha_G \rho_G H_{TG}}{\partial t} + \frac{\partial A \alpha_G \rho_G V_G H_{TG}}{\partial Z} - A\alpha_G \frac{\partial P}{\partial t} = A\left(Q_{IG} + \Gamma H_{TV}\right) + \chi q_{WG} - A\alpha_G \rho_G V_G g$$

An energy balance through the interface gives:

$$\frac{\Gamma}{A_I} = -\dot{m}_{cond} = \frac{q_{WI} - q_{IL} - q_{IG}}{H_{VL}} \qquad (1)$$

with: $H_{TK} = H_K + V_K^2/2$

$$Q_{IG} = A_I q_{IG} = A_I h_{IG}\left(T_I - T_G\right)$$

$$Q_{IL} = A_I q_{IL} = A_I h_{IL}\left(T_I - T_L\right)$$

Γ : interfacial steam flux per unit volume

Q_{IG} (Q_{IL}):interface to gas (interface to liquid) heat flux per unit volume

q_{IG} (q_{IL}):interface to gas (interface to liquid) heat flux

q_{WI} wall to interface heat flux (heat flux used for boiling or for condensation)

The closure laws are presented in [9].

MODELING OF CONDENSATION

The governing constitutive laws

According to eq. 1, the condensation rate may be controled by interfacial heat fluxes q_{IG} and q_{IL}, and by a wall to interface heat flux q_{WI} which is necessary for starting condensation in case of superheated steam and subcooled wall as it was necessary for subcooled boiling. In direct contact condensation, only interfacial heat fluxes play a role and q_{IL} is the governing term. When condensation is due to heat release from a wall, one can write in steady state conditions:

$$|q_W| = -q_{WL} = q_{IL} = \dot{m}_{cond} H_{VL} - q_{IG}$$

or, using quantities adapted to the condensation case:

$$q_{W,cond} = q_{LW} = q_{IL} = \dot{m}_{cond} H_{VL} + q_{GI}$$

$$q_{GI} = -q_{IG}$$

In the Cathare Version 1.3 Rev5, The Shah [10] model was used. However, it is not valid for high quality flows and the Chen model [5] was found more appropriate [4] for pure film condensation conditions. It uses a combination of three heat transfer correlations:

for laminar wavy regime:

$$Nu = \frac{h}{\lambda_L}\left(\frac{\nu_L}{g}\right)^{1/3} = 0.823\,Re_f^{-0.22} \qquad (2a)$$

for fully turbulent regime:

$$Nu = \frac{h}{\lambda_L}\left(\frac{\nu_L}{g}\right)^{1/3} = 0.00402\,Re_f^{0.4}\,Pr_L^{0.65} \qquad (2b)$$

for high interfacial shear stress regime:

$$Nu = 0.036\,Pr_L^{0.65}\,\tau_I^{*1/2} \text{ with } \tau_I^* = \frac{\tau_I}{\rho_L (g\nu_L)^{2/3}} \qquad (2c)$$

And: $$q_W = h(T_W - T_{sat})$$

This formulation includes a film momentum balance which eliminates the film thickness δ_f. This allows to predict the correct film thermal resistance even if the 2-Fluid model does not predict a correct δ_f. Both Shah and Chen correlations were developed for steam water conditions without presence of noncondensable gas. Only the total heat flux is given and the effect of a hypothetical steam superheating is not described. The separation between the contributions to steam cooling, condensation and liquid cooling can be done as follows:

$$q_{LW} = 2h(T_L - T_W) \quad ; q_{IL} = 2h(T_I - T_L)$$

with: $T_I = T_{sat}(P_V)$ for a pure steam gas phase.
This choice allows to predict a liquid temperature being the average of the wall and interface temperatures. Another heat transfer coefficient must be used for q_{GI} for superheated steam conditions. It also gives the possibility to use the same liquid to interface heat transfer coefficient in direct contact condensation without wall cooling. This is the method used for implementing the Chen correlation in the code. A similar approach was used for the Shah correlation.

Effects of non condensable gases.

The mass transfer through the diffusion layer near the interface must be modelled. In turbulent forced convection conditions, only the use of heat and mass transfer analogy is possible. But, depending on the authors, it may be used in different ways. From Bird [12] theory of film, the mass balance at the interface writes:

$$J_V = D_{vn} c_G \frac{\partial Y_V}{\partial y} + J_V Y_V$$

This can be put into different forms giving different Sherwood number definitions. If written with mass quantities rather than molar,

$$\dot{m}_{cond} = -D_{vn}\rho_G \frac{1}{X_n}\left(\frac{\partial X_n}{\partial y}\right)_I \qquad (3)$$

the following Sherwood number is defined:

$$\dot{m}_{cond} = D_{vn}\rho_G Sh_o \frac{1}{D_H}\frac{X_{n,I} - X_n}{X_{n,I}} \qquad (4)$$

If integrated over a laminar diffusion layer of thickness δ_M,

$$J_V = \frac{D_{vn} c_G}{\delta_M} \ln\left(\frac{Y_{n,I}}{Y_n}\right)$$

the Sherwood number is then defined as:

$$Sh = \frac{D_H}{\delta_M} \Rightarrow \dot{m}_{cond} = \frac{D_{vn} M_v c_G}{D_H} Sh \ln\left(\frac{Y_{n,I}}{Y_n}\right) \qquad (5)$$

The definition of eq. 5 is used by Kageyama [12] whereas the form of eq. 4 was recommended by Vernier [13] for turbulent forced convection and is used by Siddique [14,15]. Eq 4 will also be used in this work with a classical correction factor for boundary layer suction effects: $Sh = \theta_d\, Sh_o$

$$\theta_d = \frac{\ln(1+R)}{R} \quad \text{with } R = \frac{X_n - X_{n,I}}{X_{n,I}}$$

Then: $\dot{m}_{cond} = D_{vn}\rho_G Sh \frac{1}{D_H} \ln\frac{X_{n,I}}{X_n}$ (6)

Or $q_{cond} = \dot{m}_{cond} H_{VL} = D_{vn} \rho_G Sh \frac{H_{VL}}{D_H} \ln \frac{X_{n,I}}{X_n}$ (7)

and: $Sh = C\, Re_G^r\, Sc_G^s$ (8)

Now eq.1 and 7 must be solved iteratively to find T_I.

Simplifying physical assumptions:

(a) - q_{IG} will be considered as negligible compared to q_{IL} in eq 1 when calculating T_I. Then:

$$q_{IL} = h_{IL}(T_I - T_L) \cong q_{cond} \quad (9)$$

(b) - the gas is considered as an ideal gas mixture when calculating T_I

Eq 7 and 9 can be plotted as heat flux functions of T_I (See Fig 1). The intersection of the two functions gives the solution.

(c) - q_{GI} will be simply calculated, without boudary layer suction effect as:

$$q_{GI} = h_{GI}\left[T_G - T_{sat}(P_V)\right]$$

Taking T_{sat} instead of T_I simplifies the calculation procedure and is not so bad as this term plays only a significant role on total heat transfer for very high gas superheating.

Simplified solution procedure:

(d) - Eq. 7 is approximated by a linear function of Ti:

$$q_{cond} = \varphi'_I\left[T_{sat}(Pv) - T_I\right] \quad (10)$$

The intersection of eq.9 and 10 gives:

$$q_{cond} = q_{IL} = \frac{h_{IL}}{1 + h_{IL}/\varphi'_I}\left[T_{sat}(Pv) - T_L\right] \quad (11)$$

$$T_I = T_L + \frac{T_{sat}(P_V) - T_L}{1 + h_{IL}/\varphi'_I} \quad (12)$$

where the denominator gives the only correction factor to the pure steam formulation of q_{IL}.

The first approximation to determine φ'_I is derived from a linearization of eq.7:

$$\varphi'_{I,1} = \left(\partial q_{cond}/\partial T\right)_{Tsat(Pv)} \quad (13)$$

This is illustrated in fig. 1 and was tested in [6].Further iterations are possible to approach the exact solution:

$$\varphi'_{I,j+1} = \frac{q_{cond}(T_{I,j})}{T_{sat}(P_V) - T_{I,j}} \qquad (14)$$

$q_{cond}(T_I)$ is calculated using eq.7 with:

$$X_n = \frac{1 - Y_V}{1 - Y_V\left(1 - {}^{M_V}/_{M_n}\right)}; Y_V = \frac{P_V}{P}; P_{V,I} = P_{sat}(T_I)$$

Then calculations will be performed with successive levels of approximations for T_I and q_W: $T_{I,j}$ and $q_{w,j}$

The zeroth order approximation is by definition:

$T_{I,0} = T_{sat}(P_V)$

Case of several noncondensable gases

When several noncondensable gases are present in the gas phase, the model may still be used. A mass balance equation is written for each noncondensable gas component. As for closure laws related to condensation and mass diffusion effects, the mixture of all noncondensable gas can be considered as an equivalent gas the properties of which are:

$$X_{n,eq} = \sum_{n=1}^{k} X_n = 1 - X_v$$

$$M_{n,eq} = \frac{X_{n,eq}}{\sum_{n=1}^{k} \frac{X_n}{M_n}}$$

$$D_{vn,eq} = \frac{\sum_{n=1}^{k} Y_n}{\sum_{n=1}^{k} \frac{Y_n}{D_{vn}}}$$

Each binary diffusivity D_{vn} is calculated using the Fuller et al model (See Reid [16])

Implementation in the Cathare code

The closure laws defined here above are used according to the following logic:

Equation 1 is used in every case for expressing the interfacial mass flux as function of the interfacial heat fluxes and wall to interface heat flux:

-1- when $a > 1\text{-}10^{-5}$ and $T_W < T_{sat}(P_v)$

This case corresponds to the *beginning of the film condensation* process. q_{WL} and q_{IL} cannot be used as there may not be any liquid present yet.

$q_{WL} = q_{LI} = 0$

$$q_{WI} = \frac{h_{Chen}}{1 + h_{Chen}/\varphi'_I}\left[T_{sat}(Pv) - T_W\right]$$

$$q_{GI} = h_{GI}\left[T_G - T_{sat}(P_V)\right]$$

-2- when $\alpha < 1\text{-}10^{-5}$ and $T_W < T_{sat}(P_v)$

This case corresponds to an *established film condensation* where the convective and condensation heat fluxes (q_{GI} and $\dot{m}_{cond}H_{VL}$) are first passing from interface to liquid then from liquid to wall.

$$q_{WI} = 0$$

$$q_{WL} = 2h_{Chen}\left[T_W - T_L\right]$$

$$q_{IL} = \frac{2h_{Chen}}{1 + 2h_{Chen}/\varphi'_I}\left[T_{sat}(Pv) - T_L\right]$$

$$q_{GI} = h_{GI}\left[T_G - T_{sat}(P_V)\right]$$

As was mentioned above, the Shah correlation may be used for lower quality flows (X < 0.8) instead of Chen correlation which can only be used for pure annular flows. The exact criterion for using these two correlations must still be defined.

-3- *Direct contact condensation*

There is not any wall heat flux. Then:

$$q_{WI} = q_{WL} = q_{WG} = 0$$

$$q_{GI} = h_{GI}\left[T_G - T_{sat}(P_V)\right]$$

$$q_{IL} = \frac{h}{1 + h/\varphi'_I}\left[T_{sat}(Pv) - T_L\right]$$

where:

$h = 2\,h_{Chen}$ for annular flows

h uses specific correlations [2] for stratified flows

$h = 2\,h_{Shah}$ for other flow patterns

EXPERIMENTAL DATA

Data of Siddique

The experimental apparatus consists of an open cooling water circuit and an open noncondensable gas/steam loop with a boiler and the test section. The gas mixture

flows downwards in a vertical stainless steel tube, 2.54m in length, with a 46.mm inner diameter and a 50.8 outer diameter. A 62.7 mm inside diameter concentric pipe surrounds the condenser tube and the cooling water flows upwards through the annulus. The selected test conditions for assessment are presented in Table 1 for air-steam tests and table 2 for helium-steam tests. Measurements comprise cooling water temperatures along the annulus, inner wall temperatures and centerline temperatures along the condenser tube. The heat flux through the condenser tube wall is determined from the gradient of the cooling water axial temperature profile. The local slope of the temperature profile was determined from a least square polynomial fit. Local curve fitted values of the condenser tube inside wall were also determined.
Calculation are performed with the inside wall temperature as boundary conditions. The downstream pressure, inlet gas temperature, flowrate and noncondensable mass fraction are also imposed. This procedure is the most precise for qualifying the heat transfer modeling for film condensation as it is not affected by possible errors in the predictions of the other thermal resistances, within the tube wall and from wall to cooling fluid. It gives also the possibility to compare the local heat flux with experiment.

Data of Nagasaka
The experimental facility (gravity Driven Integral Full Height Test for Passive heat Removal), which belongs to the Toshiba corporation, investigates the film condensation in tubes with nitrogen in order to determine the design criteria of an Isolation Condenser for a Simplified Boiling Water Reactor. It consists of three vertical tubes (2.4m in length, 45.7mm inner diameter and 51mm outer diameter) located in a water pool kept at 373K. A saturated steam-nitrogen mixture flows downwards in steady state conditions with a steam flow of 30.g/s at 0.3 Mpa.
Calculation are performed with the cooling fluid temperature (373 K) as boundary conditions. The downstream pressure, inlet gas temperature, flowrate and noncondensable mass fraction are also imposed. This procedure is not so precise for qualifying the heat transfer modeling for film condensation as it is affected by possible errors in the predictions of the heat transfer coefficient from wall to cooling fluid. The calculations presented here used a simple uniform heat transfer coefficient from wall to cooling fluid of 4000 $W/m^2/K$.

Data of the Cosi experiment
The Cosi loop is a test facility to investigate direct contact condensation at ECC injections in a cold leg of a Pressurized Water reactor. The test section simulates a cold leg by a 118mm inner diameter horizontal pipe. A boiler provides steam and all types of ECCS are simulated. The downcomer is simulated by a vertical pipe connected to the cold leg and a water tank provided with a level regulation. A break is located downstream of the junction with the downcomer simulator to discharge the non condensed steam.A few tests were performed with addition of some nitrogen upstream of the test section (Table 4). Steady state tests are performed at about P = 2 MPa with an injected liquid flowrate $Q_{L,inj}$ of 0.2kg/s and measurements allow to determine the total condensed steam flowrate in the system Q_{cond}. The flow is stratified in the test section and interfacial heat transfer coefficients were derived in pure steam condition taking into account the local increased turbulence due to the injection jet.
Calculations are performed with imposed inlet gas and liquid flowrates, gas and liquid temperatures, noncondensable mass fraction and downstream pressure.

CALCULATION RESULTS

Film condensation

One can first notice (see fig 2) that the heat flux is generally underestimated at the top of the test section and overestimated at the bottom end. The entrance effects mentioned by Siddique are here neglected and this can explain the error at the top. Moreover the inside wall temperature data are fitted as well as the heat flux profile and

all fitting techniques are not so accurate for extreme points. It seems that at the bottom end, the two fittings are not consistent, the slope of the wall temperature suggesting a high heat flux whereas the heat flux is low.Sensitivity tests have shown that taking entrance effects into account has not a strong effect on the total power exchanged.

The gas outlet temperature is generally slightly overestimated probably because of assumption (c). However, the total effect of q_{GI} remains negligible compared to q_{LI} for all tests. Other local variables such as local condensation mass flux, steam saturation temperature and local bulk noncondensable mass fraction are not compared as it seems that the calculation of such quantities in the data report [8] may not be fully exact; the power due to film cooling seems to be neglected, resulting in an overestimation of the condensation.

The first approximation is not sufficiently accurate, but the second order approximations remains always very good compared to the exact solution of the physically simplified model (Table 5). It gives about 1.5% error compared to the solution with tenth order approximation and it would be recommended for implementation in the code.

All calculations are performed with a Sherwood number definition derived from Gilliland Nusselt number definition:

$$C = 0.023,\ r = 0.83,\ s = 0.44$$

Good results are obtained for all air-steam and nitrogen-steam data (Fig 3, 5 and Tables 1, 3). A general overestimation of the heat flux is obtained for Helium-steam data (Fig 4 and Table 2). Helium tests reach very soon laminar Reynolds numbers. The laminar value of 4.0 was taken as a minimum Sherwood number. Some sensitivity tests to coefficients C, r and s should be performed.

Direct contact condensation

The stratified flow Cosi tests are calculated using a different Sherwood number. The constant C = 0.023 has been multiplied by 4. to obtain good results (Fig 6 and Table 4). This could be attributed to a more agitated interface which enhances turbulent mixing in the gas and increases the condensing surface resulting in a lower interfacial mass flux and a lower resistance due to diffusion.

CONCLUSIONS

A modelling of noncondensable gases effects on condensation in pipes is proposed which is applicable for both film condensation and direct contact condensation in stratified flows.

Simplifying assumptions are applied to a classical heat and mass transfer analogy method. They concern both physical models and solution procedure.

From the physical assumptions, the liquid to interface and gas to interface heat fluxes can be written with temperature differences calculated at bulk conditions for phase temperatures and bulk saturation reference temperature. Only the liquid to interface heat transfer coefficient is modified by estimating an interface temperature which takes into account mass diffusion effects. Such assumptions are found reasonable as long as steam superheating is not too high.

The simplified solution procedure avoids long iterative calculations, reducing CPU costs for the code, and the quality of predictions is not affected.

The validation data base includes three noncondensable gases, annular flows and stratified flows, laminar and turbulent gas flows, direct contact condensation and wall cooling conditions.

The predictions are reasonably good for complex system codes like Cathare. They could probably be improved by some adjustment of the Sherwood number correlation.

Table 1: Data of Siddique
Air-Steam tests

Run	$T_{G,in}$ °C	P_{out} bar	$Q_{G,in}$ g/s	$X_{n,in}$	$Q_{tot,exp}$ kW	$Q_{tot,cal}$ kW
A-S 1	100	1.07	2.72	.087	6.67	6.28
A-S 2	100	1.12	2.87	.146	6.72	6.26
A-S 3	100	1.16	2.99	.185	6.50	6.15
A-S 4	100	1.21	3.36	.244	6.25	6.24
A-S 5	100	1.27	3.58	.292	6.22	6.11
A-S 6	100	1.32	3.78	.332	5.95	6.00
A-S 35	100	1.09	7.94	.114	14.22	15.35
A-S 36	100	1.13	8.79	.144	14.45	15.80
A-S 37	100	1.17	9.81	.189	14.51	15.70
A-S 38	100	1.23	10.1	.242	14.08	15.10
A-S 39	100	1.30	11.4	.299	14.03	14.40
A-S 40	100	1.36	12.3	.348	13.59	13.93
A-S 41	120	2.11	9.37	.099	18.66	19.10
A-S 42	120	2.19	10.1	.149	18.38	18.65
A-S 43	120	2.28	10.5	.199	17.64	17.62
A-S 44	120	2.37	11.0	.243	16.74	17.03
A-S 45	120	2.51	11.8	.306	15.92	16.06
A-S 46	120	2.61	12.5	.344	15.90	15.80
A-S 47	140	3.78	9.83	.098	21.55	21.00
A-S 48	140	3.97	10.4	.154	20.59	19.70
A-S 49	140	4.10	11.0	.196	19.70	19.40
A-S 50	140	4.32	11.7	.250	19.11	18.70
A-S 51	140	4.50	12.4	.296	18.80	18.13
A-S 52	140	4.78	13.4	.354	17.34	17.55

Table 2: Data of Siddique
Helium-Steam tests

Run	$T_{G,in}$ °C	P_{out} bar	$Q_{G,in}$ g/s	$X_{n,in}$	$Q_{tot,exp}$ kW	$Q_{tot,cal}$ kW
H-S 12	102	1.18	5.25	.020	11.59	12.04
H-S 13	103	1.33	5.27	.041	11.00	11.86
H-S 14	104	1.43	5.45	.053	10.71	11.80
H-S 15	104	1.56	6.01	.072	10.72	12.37
H-S 16	119	2.12	5.26	.021	10.86	12.57
H-S 17	120	2.50	5.49	.054	10.60	12.44
H-S 18	120	2.69	5.53	.073	10.03	11.92
H-S 19	120	2.91	5.53	.093	9.12	11.45
H-S 20	141	3.93	5.77	.016	13.51	14.35
H-S 21	141	4.31	5.88	.038	12.88	14.27
H-S 22	141	4.58	5.96	.054	12.51	13.80

Table 3: data of Nagasaka

Run	P_{out} bar	$Q_{v,in}$ g/s	$Y_{n,in}$	$X_{n,in}$	$Q_{tot,exp}$ kW	$Q_{tot,cal}$ kW
1	3.0	30.	0.	0.	65.0	68.4
2	3.0	30.	.01	.016	62.5	61.2
3	3.0	30.	.02	.031	59.0	58.0
4	3.0	30.	.05	.076	52.5	51.8
5	3.0	30.	.10	.147	38.5	44.8

Table 4: Cosi experiment data

Run	P_{out} bar	$Q_{G,in}$ g/s	$Q_{L,inj}$ g/s	$X_{n,in}$	$Q_{cond,exp}$ g/s	$Q_{cond,cal}$ g/s
1	23.3	170.	200.	0.	83.	84.
2	21.8	180.	199.	.094	72.	67.
3	20.5	217.	198.	.249	59.	58.
4	22.0	238.	199.	.319	57.	56.

Table 5: Effect of level of approximation
Siddique data and Nagasaka data

Run	$Q_{tot,exp}$ kW	$Q_{cal,10}$ kW	$Q_{cal,2}$ kW	$Q_{cal,1}$ kW	$Q_{cal,0}$ kW
A-S 41	18.66	19.10	19.40	20.9	21.3
A-S 42	18.38	18.65	19.03	21.0	21.8
A-S 43	17.64	17.62	17.99	20.2	21.3
A-S 44	16.74	17.03	17.34	19.8	21.1
A-S 45	15.92	16.06	16.35	19.0	20.7
A-S 46	15.90	15.80	16.13	18.9	20.8

Run	$Q_{tot,exp}$ kW	$Q_{cal,10}$ kW	$Q_{cal,2}$ kW	$Q_{cal,1}$ kW	$Q_{cal,0}$ kW
1	65.0	68.4	68.4	68.4	68.4
2	62.5	61.2	62.0	64.3	67.1
3	59.0	58.0	58.8	61.5	65.9
4	52.5	51.8	52.4	55.4	62.1
5	38.5	44.8	45.2	48.1	56.3

NOMENCLATURE

A	Tube cross section area (m^2)
Ai	Interfacial area per unit volume (m^{-1})
c	molar density ($mols/m^3$)
D_{vn}	mass diffusivity (m^2/s)
D_H	hydraulic diameter
g	gravity constant (m/s^2)
H	specific enthalpy (J/kg)
H_T	specific total enthalpy (J/kg)
H_{VL}	latent heat (J/kg)
h	heat transfer coefficient(J/m/s)
J	molar flux ($mole/s/m^2$)
$\dot{m}_{cond}$	interfacial condensation mass flux (kg/m^2)

Nu	Nusselt number
P	Pressure
Pr	Prandtl number
Pv	Bulk steam partial pressure
Q	heat flux per unit volume (W/m^3)
Q_G	gas mixture mass flowrate (kg/s)
q	heat flux (W/m^2)
Re	Reynolds number
Sc	Schmidt number
Sh	Sherwood number
Sn	Source term of noncondensable gas
t	time
X	mass fraction
Y	molar fraction
Z	tube abcissa

a	void fraction	
G	interfacial mass flux per unit volume	($kg/m^3/s$)
r	density (kg/m^3)	
l	heat conductivity	(W/m/K)
m	dynamic viscosity	(kg/m/s)
n	kinematic viscosity	(m^2/s)
c	heating (or friction) perimeter (m)	
q	correction coefficient for mass	transfer
t*	non dimensional friction	

Subscripts

f	film
I	relative to interface
G	relative to the gas mixture or gas phase
K	relative to phase K
L	relative to liquid phase
V	relative to vapour
W	relative to inside wall
n	relative to noncondensable gases
eq	equivalent
exp	experiment value
cal	calculated value
cond	relative to condensate
inj	injection
in	relative to pipe inlet
out	relative to pipe outlet
sat	at saturation conditions
,1	first approximation
,j	j th approximation

Note that bulk condition variables have no specific subscript as they correspond to averaged variables of the 1-D 2-Fluid model

REFERENCES

[1] A. Janicot and D. Bestion , "Condensation modelling for ECC injection", Nuclear Engineering and Design, 145 (1993) 37-45, 1993

[2] D. Bestion & L. Gros d'Aillon, Condensation tests analysis and correlation for the Cathare code, 4th NURETH meeting, Karlsruhe, 1989

[3] A. Janicot, Qualification Report Cathare version 1.3 revision 5: Cosi experiment (Vol. Q11), Rapport CEA, STR/LML/EM/93-152

[4] S. Belsito, D. Bestion and F. d'Auria, "Condensation heat transfer modelling" Proceedings of the First ISHMT-ASME Heat and Mass Transfer Conference, Jan 5-7, 1994, Bombay

[5] S. L. Chen, F. M. Gerner and C. L. Tien, General film condensation correlations , Int Comm. Heat & Mass Transfer, Vol 20, pp 265-277, 1993

[6] D. Bestion, P. Coste and S. Barsotti, "Study on condensation modelling in the CATHARE code with and without noncondensable gas", Proceedings of the International Conference on New Trends in Nuclear System Thermalhydraulics, May 30 - June 2nd, 1994, Pisa

[7] H. Nagasaka, K. Yamada, M. Katoh and S. Yokobori, Heat removal tests of isolation condenser applied as a passive containment cooling system, ICONE, November 4-7, Vol. 1

[8] M. Siddique, M.W. Golay and M.S. Kazimi, The Effects of noncondensable gases on steam condensation under forced convection conditions, Massachusetts Institute of Technology

[9] D. Bestion, The Physical Closure Laws in the CATHARE code, Nucl. Engrg. Des. 124 (1990) 229-245

[10] M. M. Shah, A general correlation for heat transfer during film condensation inside pipes, Int Journal of Heat & Mass Transfer, Vol 22, pp 547-555, 1979

[11] R. B. Bird, W. E. Stewart & E.N. Lightfoot, Transport Phenomena, John Wiley (1060)

[12] T. Kageyama, P. F. Peterson and V. E. Shrock, Diffusion layer modeling for condensation in vertical tubes with noncondensable gases, Nuclear Engineering and Design 141, (1993) 289-302

[13] P. J. Vernier & P. Solignac, A test of some condensation models in the presence of a noncondensable gas against the Ecotra axperiment, Nuclear Technology, Vol. 77 (1987), pp.82-91

[14] M. Siddique, M.W. Golay and M.S. Kazimi, Local heat transfer coefficients for forced convection condensation of steam in a vertical tube in the presence of air, HTD-Vol. 197, Two-Phase Flow and Heat Transfer, ASME 1992

[15] M. Siddique, M.W. Golay and M.S. Kazimi, Theoretical modeling of forced convection condensation of steam in a vertical tube in the presence of a noncondensable gas, Nuclear Technology Vol. 106 May 1994

[16] R.J. Reid, J.M. Prausnitz and B.E. Poling, The Properties of gases and liquids, Mc Graw-Hill Book Company

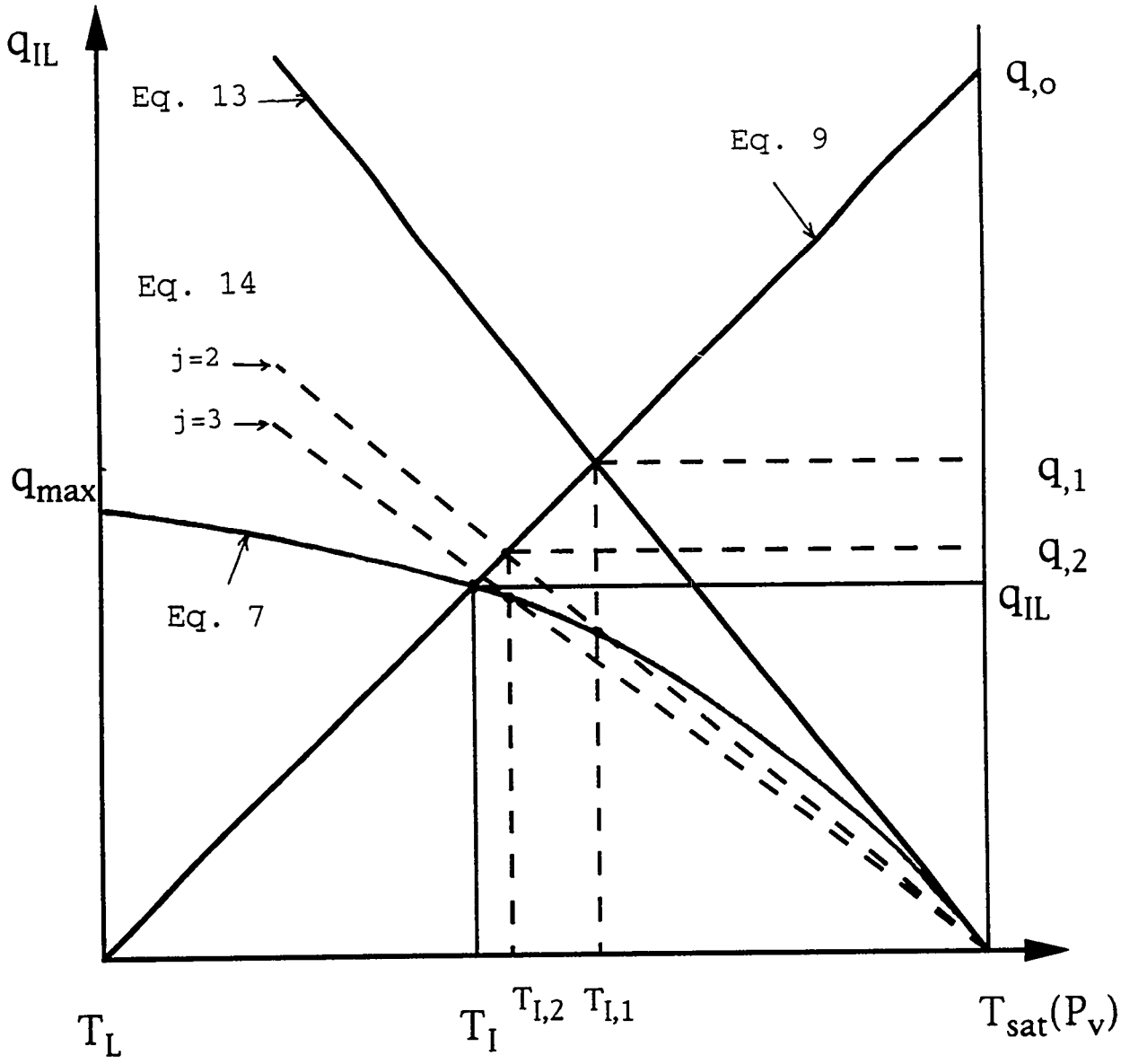


Fig. 1: Illustration of the solution procedure

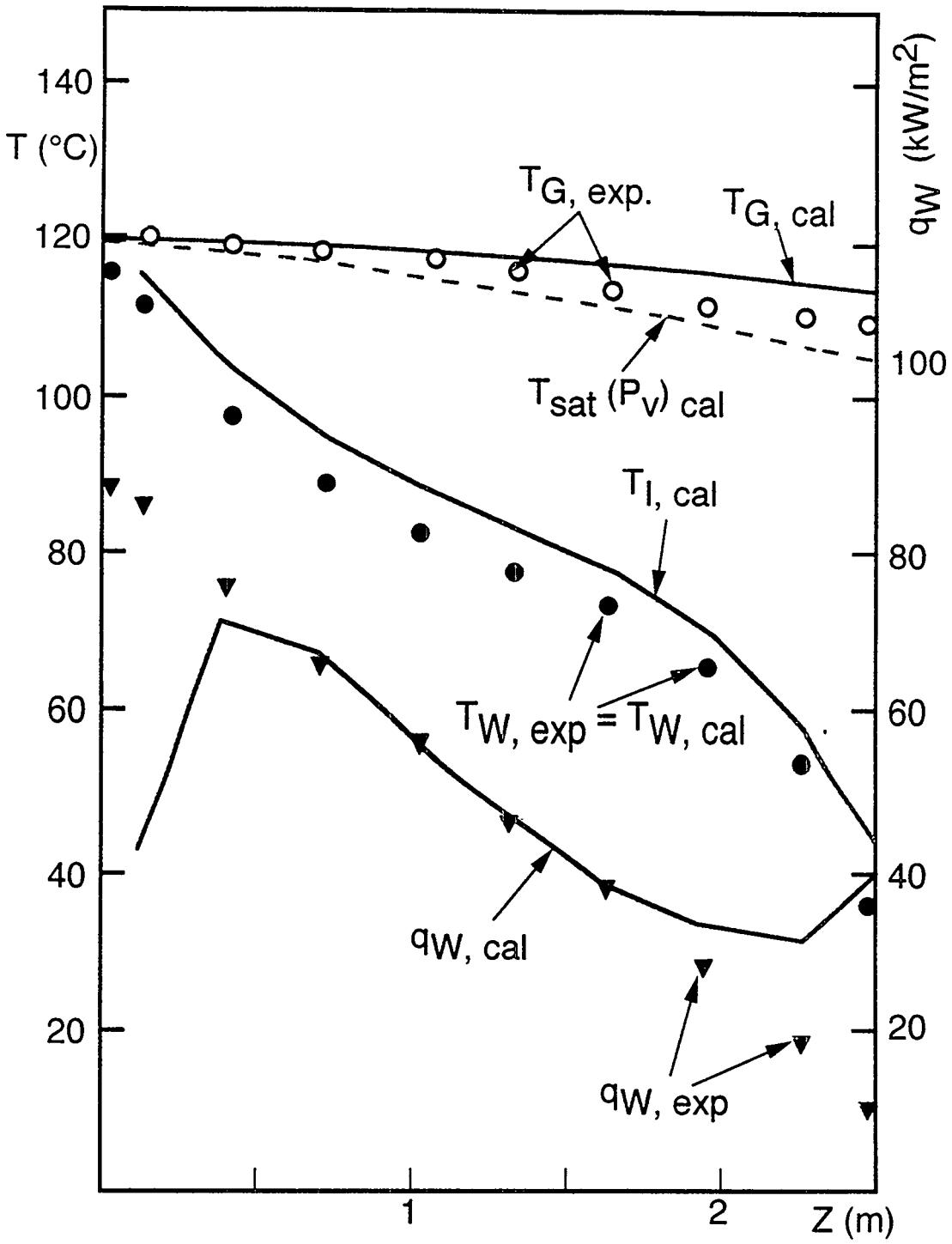


Fig. 2: Example of compared local parameters (test A-S 43)

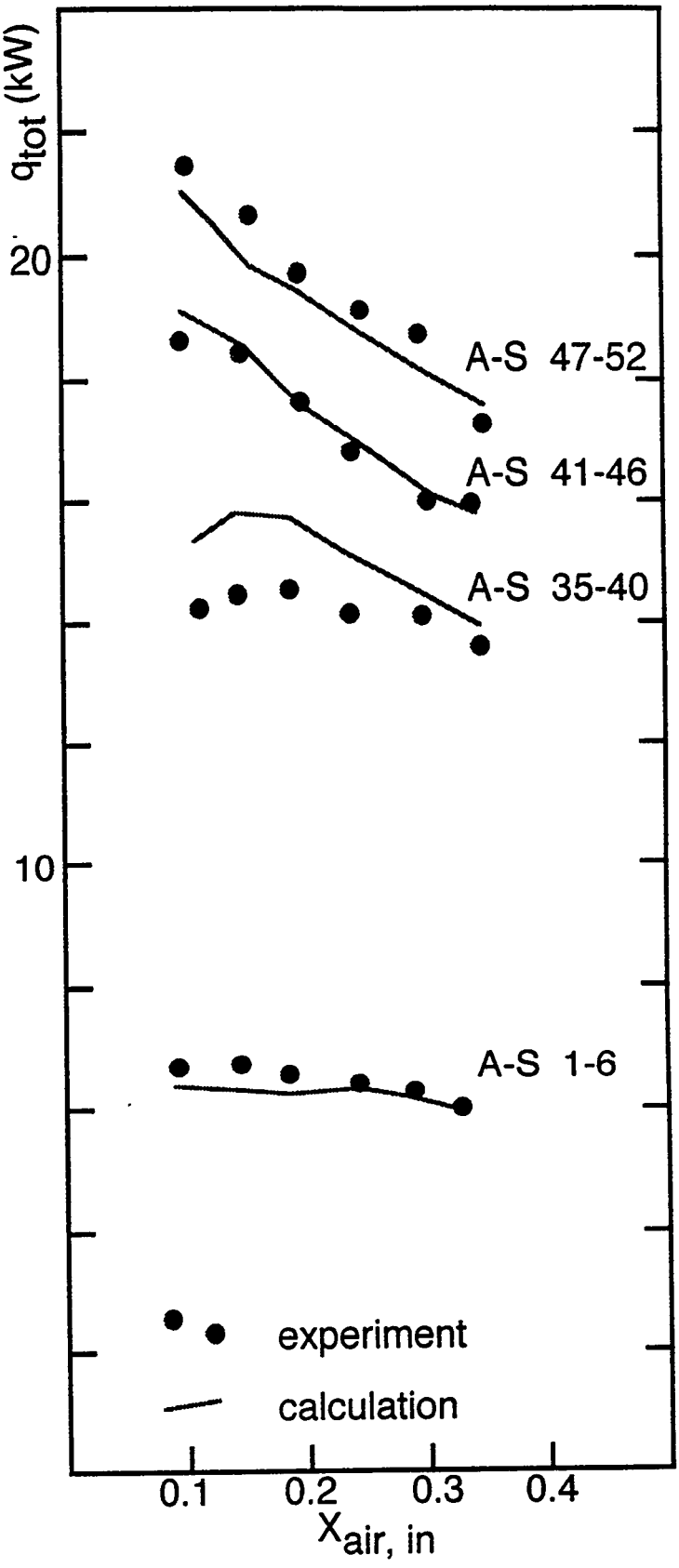


Fig. 3: Data of Siddique-air/steam tests
Total power versus air inlet fraction

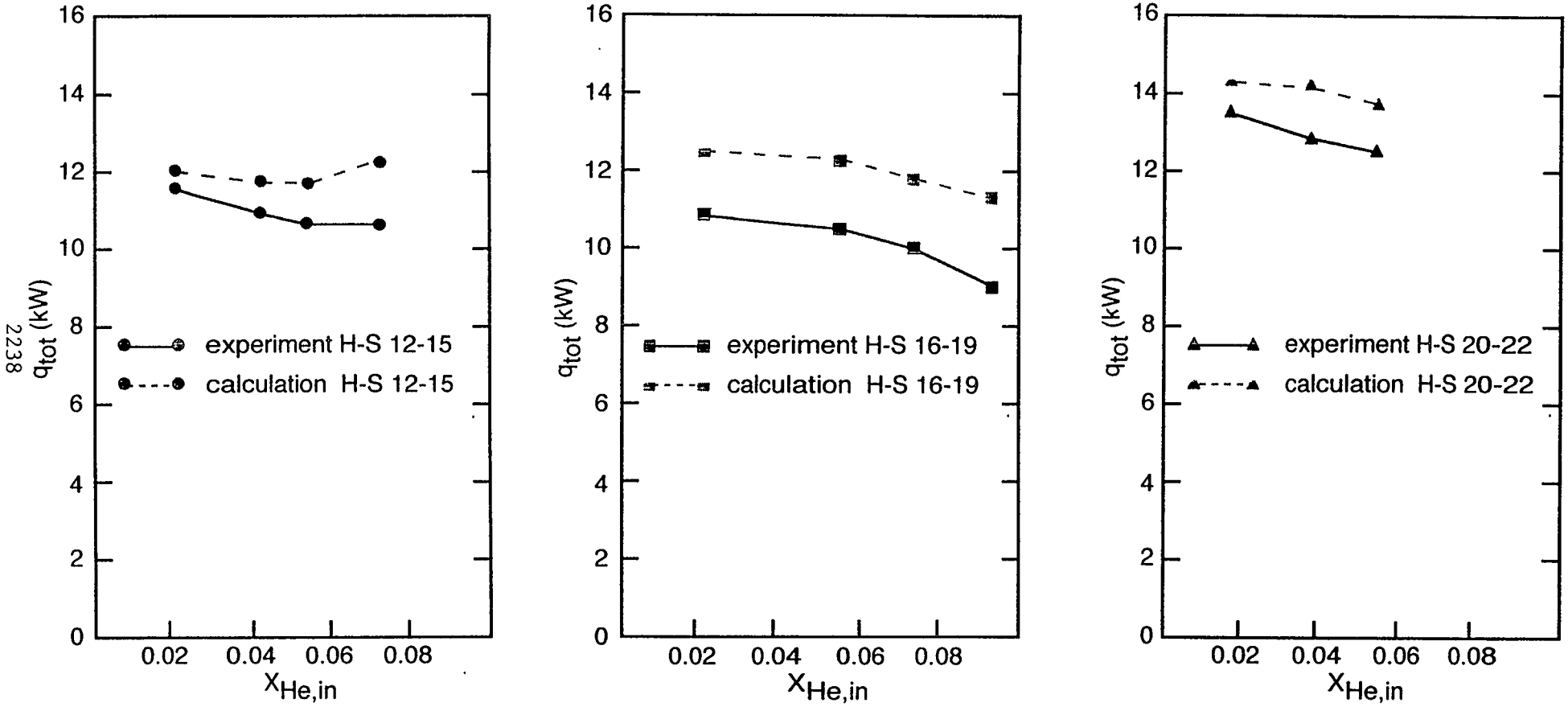


Fig. 4: Data of Siddique- Helium/steam tests
Total power versus air inlet fraction

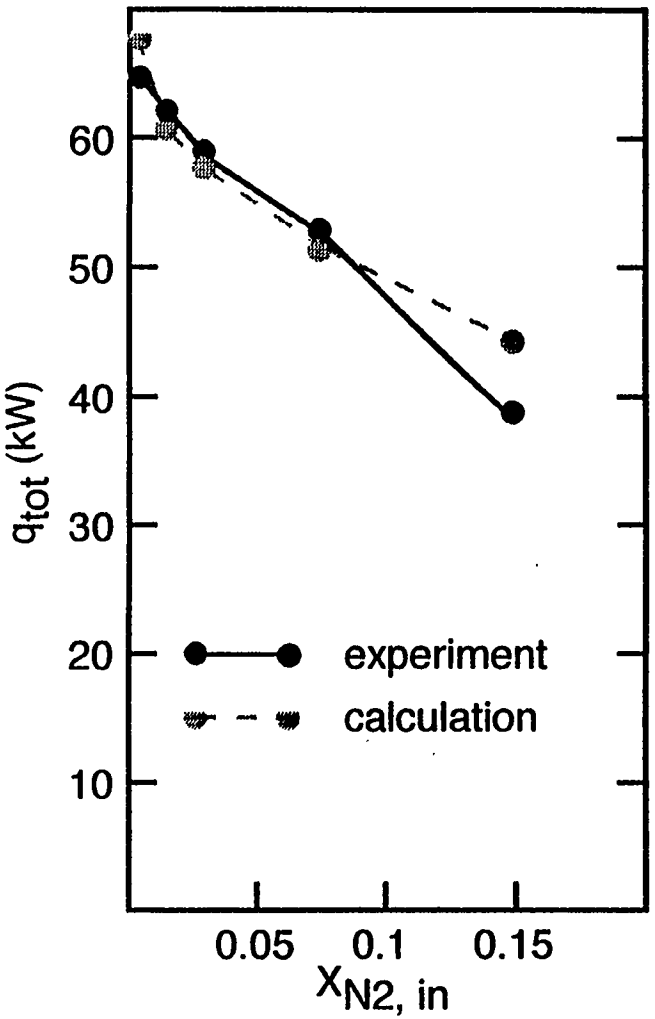


Fig. 5: Data of Nagasaka- Nitrogen/steam tests
Total power versus air inlet fraction

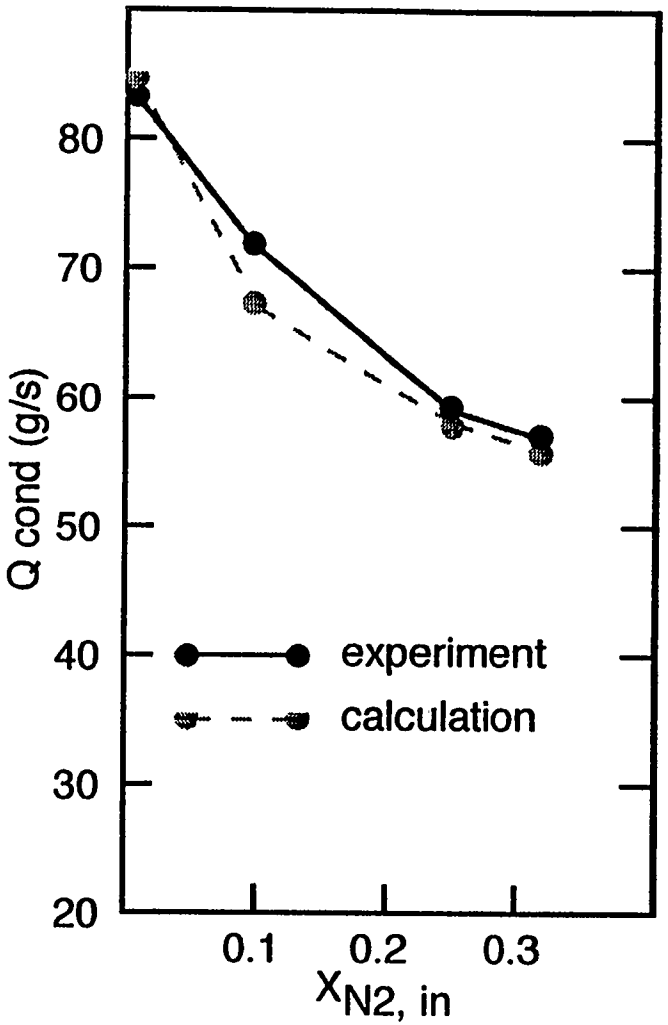


Fig. 6: Data of the COSI experiment - Nitrogen/steam tests
Total condensed flowrate versus air inlet fraction

INJECT and the Modeling of Waste Recycling Processes

Eric J. Gracyalny
Michael L. Corradini
Department of Nuclear Engineering
University of Wisconsin
Madison, WI 53706

Abstract

Enhancements were performed to the computer model CORCON to allow for more general energy and transport processes, thus creating a general equilibrium, chemistry tool for a liquid pool with fluid injection. The summation of these model modifications are referred to as INJECT. It is believed that with these enhancements, INJECT becomes a useful tool to study waste management technologies and materials processing. A demonstration of such was performed with a simulation of pyrolysis and materials extraction of ion exchange resins produced by pressurized water reactors. A 5 kg pool consisting of iron, carbon and alumina was injected with CO_2 and contaminated resin, commonly known as styrene. The injection rates varied from 0.2 - 1.0 $\frac{L}{min}$ for the CO_2 and 0.5 - 1.5 $\frac{g}{min}$ for the resin. Simulation results indicated that the cesium and zinc contaminants were released as gases, cobalt would be in the metallic phase, cerium remained in the oxidic phase and manganese was found in both the oxidic and metallic phases.

Introduction

With the substantial increase of environmental concerns, numerous reprocessing techniques and recycling technologies have been introduced to minimize the volume of radioactive waste streams. For several of these proposed processes, no comprehensive hydrodynamic and chemical models exists that will predict the responses of these techniques under expected operating conditions. The current research was aimed at developing a tool that can perform simulations for a multitude of chemical engineering processes. This new model, INJECT [1], is a superset of CORCON [2] in that it can perform any simulation that is within CORCON capabilities, namely molten pool ablation of surroundings, plus an entirely new set of simulations of condensed phase mass and energy processes involved in nuclear and chemical processing.

The specific enhancements made to produce INJECT lie in the areas of 1) an enhanced energy generation model for fission products that includes decay heat tables consistent with spent fuel; 2) a volatilization model in which volatilized fission products will now remove the appropriate amount of decay heat; 3) a more robust form of mass addition at the bottom

of the pool that can vary with time and contain oxides, metals and/or gases; 4) a modified heat transfer model for energy leaving the molten pool to the crucible. A vastly improved and simplified process to add species to the database is also introduced and is similar to that seen in SOLGASMIX [3]. At the core of these models is a model of a molten pool where hydrodynamic mixing due to gas, liquid and/or solid injection determines the mixing processes for the chemical reactions or the energy transferred. The summation of these improvements is contained in a computer model which can study several possible phenomena. These phenomena include, but are not limited to, molten core-concrete interactions, catalytic extraction, steelmaking, reprocessing of mixed chemical/radioactive waste, and simple equilibrium chemistry problems.

Of current interest is the catalytic extraction process being proposed by waste recycle industries [4]. This process could potentially be used to minimize waste streams ranging from pesticides, municipal waste and mixed chemical and radioactive waste from military or commercial fuel cycle systems. As a demonstration of the ability of INJECT, a simulation was performed on the catalytic extraction of radioactively contaminated ion exchange resins. The goal of this research is to successfully partition the contaminants into one of three phases (oxide, metal, gas) in a form that is easily separable from the product. This simulation was motivated by experiments in progress in association with radioactive waste reprocessing at Oak Ridge National Laboratory, Scientific Ecology Group and Molten Metal Technology, Inc.

CORCON Models

CORCON.Mod2 was originally developed by Cole et al at Sandia National Laboratories [2] as an improvement to the CORCON.Mod1 [5] model used to model the molten core-concrete interaction process (MCCI). The purpose of this section is to provide a review of the models present in CORCON.UW, which is a superset of CORCON.Mod2 that has been developed at the University of Wisconsin for reactor safety applications [6]. There are four major system components to be specified in a CORCON simulation; debris pool, surroundings, concrete (crucible) and atmosphere. The debris pool is the system that has undergone the majority of the enhancements through our research and will be described here.

The debris pool in the MCCI consists of the molten materials that result from a meltdown in a severe accident at a nuclear power plant. The melted reactor core, cladding material, control material and structural materials which have accumulated as the result of a severe accident can be modeled by CORCON in the debris pool. The debris pool could consist of five layers. In an unmixed geometry, the possible configuration is a heavy oxide layer, a metal layer, and a light oxide layer. If conditions are right these layers will mix hydrodynamically due to gas injection into the pool from concrete decomposition. When this occurs they will form either a heavy oxide-metal mixed layer or a light oxide-metal mixed layer. The threshold of mixing these layers is based upon experiments and associated models resulting in a correlation proposed by Casas [7].

Layer Stratification

Mixing was not modeled in the original CORCON, but the logic was included for the pool configuration to contain mixed layers given appropriate models. Casas [7] expanded on the experimental data for immiscible liquid layer mixing by gas injection collected by Gonzalez and developed a model, and implemented a mixing correlation. Casas' mixing correlation is based on experimental data for a liquid pool depth up to 40 cm. It was decided not to include the effect of pool depth on mixing, because the effect was found to be weak and the data was not comprehensive enough to allow for partially mixed layer configurations.

Casas assumes that the layer exists in one of two states, fully mixed or not mixed at all. There is no partial mixing of the layers, and the logic is as follows:

- The characteristic velocity is calculated from

$$V_{ch} = \left(\frac{\sigma_h (\rho_h - \rho_l) g}{\rho_l^2} \right)^{1/4} \tag{1}$$

- If $V_{ch} < 0.15 \frac{m}{s}$, then the liquids can fully mix in the bubbly regime. If V_{ch} is greater than this, mixing will occur only in the churn-turbulent regime.

- For bubbly flow conditions, there is a check to see if the layers were mixed in the previous time step. If the layers were mixed, there is a check for segregation. Segregation occurs when the superficial gas velocity is lower than the velocity for the onset of entrainment and mixing, $j_g \leq j_g^{oe}$ where

$$j_g^{oe} = 0.0751\, V_{ch} - 0.00271. \tag{2}$$

  If the layers were not mixed in the previous time step, mixing is checked. The test for mixing is when the superficial gas velocity is greater than the velocity for fully mixed layers, $j_g \geq j_g^{fm}$ where

$$j_g^{fm} = 0.2121\, V_{ch} - 0.01131. \tag{3}$$

- In the churn turbulent region, Casas never observed complete mixing for the materials he used at a mixing height of 40 cm as the arbitrary limit for the fully mixed state. Casas developed a correlation for mixing height based on the superficial gas velocity

$$e = 0.76 j_g - 11.37. \tag{4}$$

  The maximum mixed layer thickness attained in the churn turbulent region was 20 cm. For this height and a value of $e = 0$, we can calculate values of j_g and then use Equation 2 and Equation 3 to get values for j_g^{oe} and j_g^{fm}. In this case, the same logic can be applied as in bubbly flow.

Chemistry

CORCON performs an equilibrium chemistry calculation every time step for every layer present in the pool at that time step given an incoming mass flow. The method utilized for these calculations is a first order minimization of Gibbs free energy subject to mass conservation and non-negativity constraints based upon the method of Van Zeggeren and Storey [8]. Thermochemical data for the species considered can be found in a variety of sources [9, 10].

The original CORCON program distributed by Sandia only contemplated metal/gas reactions in the chemistry package due to the characteristics of a severe accident phenomena. In such an event, the core materials consist primarily of the chemically stable oxides UO_2, ZrO_2. The eroded reactor vessel is composed of steel, which contains the metallic elements iron, nickel and chromium. The ablating concrete consists of a variety of oxides, carbon dioxide, water vapor, and possibly some metallic rebar. Given the above circumstances, the gases released from the concrete will preferentially oxidize the available metals, while the existing oxides remain in their current state. The original CORCON contained only 38 chemical species.

Norkus initiated the introduction of several new species into CORCON [11], a process that has continued to the present day, bringing the total number of chemical species considered to over 230 (Table 1). With modifications made to the data structure during this work, this number can easily be increased based on the particular chemical process considered.

An area of concern is with the accuracy of the computational model utilized. When selecting a computer model to compute the chemical equilibrium calculations, two requirements were placed upon its performance. These are that highly accurate solutions are not required, however accurate stoichiometry is required. The first requirement implies that computational speed and the lack of high quality initial guesses have more priority than accuracy. Accurate stoichiometry essentially means that there is conservation of mass. In the original study of the computational method utilized [12] in CORCON.Mod2, the model satisfied stoichiometric constraints up to 1 part in 10^8, but was not very accurate for trace species at smaller concentrations. 'Trace species' as used here is on the order of parts per billion.

Energy Generation

Molten core-concrete interactions are driven by the heat generated in the pool due to radioactive decay and the chemical reactions as discussed above. In CORCON, there exists two options for describing the internal heat generation process. One option is for a user to input a power history to determine the energy deposited to the oxidic and/or metallic phases of the melt. This is most applicable in the modeling of experiments such as ACE, MACE, or the SURC tests where the experiments are run with a known power for the entire test phase [13].

The second method for providing an internal power source is by using a model that describes the generation of decay heat in the melt pool. The user inputs the core size, core operating power and the retention factors for fission products. The initial pool fission product inventory is determined from the core size, the given operating power, and multiplied by a given retention factor for each element in the melt. The retention factors account for the loss of the more volatile species early in the accident sequence. The mass of the decay heat contributor is then

multiplied by its specific decay heat concentration in order to determine energy generation.

INJECT Models

It is not feasible for us to describe in detail all of the enhancements made to produce INJECT. Therefore, only the conceptual picture will be described below. For a detailed examination of the models and methods used in INJECT the reader is encouraged to review the INJECT user manual [14]. This manual is also available online via the World Wide Web at `http://trans4.neep.wisc.edu/NSRC/inject/`.

Chemistry

Although no modifications were made to the chemistry model from Norkus' previous work, one restriction regarding the application of INJECT towards general chemical systems should be noted. That restriction is that the time constant for chemical equilibrium should be less than the time constant for bubble transport. In addition, a time step in INJECT should be greater than the time it takes for the gas bubbles to pass through a layer to invoke chemical equilibrium in that layer. This is seen in

$$\Delta t > \tau_{Bubble} > \tau_{Equil} \tag{5}$$

$$\tau_{Bubble} = \frac{\ell}{U_t} \tag{6}$$

where ℓ is the layer thickness and U_t is the bubble rise velocity. The reason behind this restriction is clear. The gas bubbles passing through the layer are the driving potential for the hydrodynamic stirring and associated chemical reaction. If these bubbles are not allowed to be well reacted with the layer, misleading simulations can result. For many of these condensed phase systems we consider the INJECT time-step is no smaller than about 10 seconds, while the gas bubble transport time is on the order of a second compared to a small fraction of a second for the time constant for chemical equilibrium.

Energy Generation

Several improvements were made to the energy generation model. A new ORIGEN [15] calculation was performed utilizing more recent cross section libraries to generate initial radionuclide compositions and associated decay power for the fission products. The crude volatilization model of the halogen and alkali metals were removed. The pseudo-fission product species were removed and replaced by individual fission product elements. Volatilization and aerosol generation of any fission product now removes energy from the pool, as opposed to the original model where only the volatilized alkali metals and halogens removed energy. Finally, the possibility was included for heat to be added to the system by both decay heat and external heating in the form of oxidic or metallic phase energy deposition.

One of the original intents for developing INJECT was to study the feasibility of reprocessing spent fuel by the removal of fission products through volatilization. This process was to be

assisted by the heat generation of the spent fuel itself. Since a vast quantity of spent fuel has been around for a period greater than ten years, the energy generated by spent fuel of that age was of interest. The empirical tables of heat generation, which were implemented in CORCON only extend out to a period of 10 days after final discharge from the reactor [16]. Hence there was a need to perform a new calculation of initial concentrations and decay heat associated with aging spent fuel. The empirical tables of heat generation now extend to 20 years after final discharge from the reactor.

Mass Addition

CORCON was limited in its mass addition abilities in that the composition of the incoming flow was constant over the duration of the simulation and had to be composed of materials found in concrete. CORCON would compute unreasonable results if non-concrete materials were added, especially gases. Therefore a new mass feed model was developed to provide INJECT with the needed flexibility.

During the mass addition sequence, several parameters vital to INJECT operation are incorporated. One is that the wall temperature, or the interface temperature between the pool and the crucible, is allowed to vary depending upon calculations performed during the previous time-steps energy balance. In order to calculate energy loss from the system to the boundaries, a user supplied heat transfer coefficient is required. Also included specifically for material injection is the definition of the mass flow and mass fraction of the injected phases. Both of the parameters above may vary with time. Not knowing exactly how these parameters might vary, two interpolation schemes were included to suit the user's needs. One is a step function from one table point to the next and the other is simple linear interpolation. All above mentioned parameters undergo this interpolation.

Vaporization Model

Experience with operating INJECT led to an obvious shortcoming when it came to vaporizing volatile chemical species. The original authors of CORCON realized this and incorporated a simplistic exponential volatilization model for only certain fission products. This method was not very robust and has been replaced by an equally transparent, but more robust, vaporization model.

In this model, chemical equilibrium is achieved in the normal way, after which a check is made to see if any of the products should in reality be gases at a given temperature and pressure. If such a species is identified and a matching gaseous species exists, the mass of the species that would normally have been in the condensed phase is added to the that of the gaseous phase and the latent heat of vaporization is extracted from the pool layer.

As an example, cesium has a boiling temperature of 950 °K at atmospheric pressure. In a system of only cesium at a temperature of 1000 °K, the results of the chemistry equilibrium routine would indicate products of both gaseous cesium (expected) and metallic cesium (unexpected). The vaporization model in INJECT redirects the mass of the metallic cesium to that of gaseous cesium as should be expected with the associated energy transport. This is allowable

because the properties of both species are identical at temperatures above 950 °K.

INJECT Uses

Possible Uses

There are a number of real world phenomena that INJECT can be applied to. First is the molten pool ablation of surroundings (MCCI). Since INJECT is a superset of CORCON, INJECT can perform MCCI simulations as CORCON does. The results will be the same with the exception of some minor output format differences. Modern steelmaking has a similar mass transfer mechanism as the MCCI. In steelmaking a flux of gas and scrap metals are added to a metallic converter. This converter becomes the steel, while a slag layer and off-gases are the byproducts. This layered phenomena is ideal for INJECT to model. INJECT can be used as a simple chemistry box, i.e. given some reactants, what are the products at $t = \infty$. Essentially a model similar SOLGASMIX [3], but one that has mass flows which can vary with time. Finally, INJECT was created with the intent to study reprocessing technologies. One such technology is the Catalytic Extraction Process (CEP) [4].

The CEP is a waste recycle and minimization technology first originated and being developed by Molten Metal Technology [4]. It takes a page from steelmaking in that wastes are added to a metal pool in which the waste decomposes into its constituent elements or simpler chemical species by oxidation/reduction reactions within a large molten metal pool (i.e., equilibrium chemistry). Vitreous products and off-gases are generated as a byproduct. The CEP could be used to minimize municipal waste, mixed waste, nuclear waste, or, as in the the demonstration below, low level waste in ion exchange resins from commercial nuclear power plants.

The reasons INJECT can be applied to a technology such as catalytic extraction are numerous. The mass transfer mechanisms are very similar. Arbitrary materials are fed into a metallic bath giving rise to chemical oxidation/reduction reactions and gas release. The INJECT chemistry species database can be easily adjusted to consider new materials as needed. Heat transfer in the CEP system should be nearly identical to that of MCCI. The only area in which INJECT needs improvement in simulating the CEP is in determination of the pool melting temperatures. Its current assumption is that the primary constituents of the melt would be iron, chromium and nickel in the metallic phase and urania, zirconia and molten calcite/siliceous slag in the oxidic phase. For this eventuality INJECT allows the user to input expected solidus and liquidus temperatures of the various phases.

INJECT Simulation of the CEP of Ion Exchange Resin

Pressurized water reactor power plants in the United States generate roughly 8000 tons of radioactively contaminated ion exchange resin annually. The primary radionuclides present in this resin are as listed in Table 2. These elements are generally found in an oxidic form. The resin itself is C_8H_8, commonly known as styrene.

An INJECT simulation of the CEP of the ion exchange resin was performed. The primary

objective of the simulation was to note how the radionuclides were partitioned after the process was finished. Ideally the radionuclides might be contained in the oxidic phase, however some of the isotopes are released in the off-gas stream. This simulation is the beginning step of a chemical reactor design to maximize retention of contaminants in the condensed phase.

Parameters of interest to this simulation are the initial pool masses, initial pool temperature, incoming feeds and flow rates and the heat added to the pool. The pool initially contained 4.6 kg of iron, 0.5 kg of Al_2O_3 and 0.1 kg of carbon at a temperature of 1500 °C. There were four injection strategies considered.

- 0.2 $\frac{L}{min}$ of CO_2 and 0.5 $\frac{g}{min}$ of resin (Lo-Lo).
- 0.2 $\frac{L}{min}$ of CO_2 and 1.5 $\frac{g}{min}$ of resin (Lo-Hi).
- 1.0 $\frac{L}{min}$ of CO_2 and 0.5 $\frac{g}{min}$ of resin (Hi-Lo).
- 1.0 $\frac{L}{min}$ of CO_2 and 1.5 $\frac{g}{min}$ of resin (Hi-Hi).

About 9 kW of heat is added to the melt to maintain the temperature at steady-state conditions. A note should be made in that the resin was modeled by CH, as styrene is not present in the species database. This was done because CH was already in the current database and styrene would naturally decompose to CH compounds quite quickly. The total molar amount of the resin injected remains identical.

The results from the simulations are summarized in Figures 2 - 5. These figures demonstrate the effect the injection rates of the resin and CO_2 gas have upon the final partitioning of the isotopes. As can be seen, the isotopes are predominately in one phase (metal,oxide,gas) or the other with the exception of manganese. Zinc and cesium are generally found in the gaseous phase, cobalt is metallic and cerium is in some oxidic state. None of these results are unexpected. The fluctuation in manganese is due to the fact that the Gibbs free energy of MnO is about that of carbon monoxide at these temperatures (Figure 6) and the temperature of each simulation were slightly different from one another. Since carbon monoxide is a primary product of the reaction, the equilibrium phase of the isotopes will be determined by whether or not the isotopes free energy is greater (isotope is metallic) or lower (isotope is oxidic) than the free energy of carbon monoxide. When comparing the INJECT results to the free energies in Figure 6 the INJECT results appear very reasonable.

Another figure of merit for the simulations are the primary off-gases (Figure 7). Over 99.99 percent of the gases released consist of hydrogen, water, carbon dioxide and carbon monoxide. Given the the Gibbs free energies seen in Figure 6, one would suspect much lower water vapor release than seen in the simulation results. This difference is due to the fact that Figure 6 does not incorporate considerations for the partial pressures of the available gases. The effect of variable partial pressure ratios is to rotate the equilibrium curve of a species about some axis. In the case of H_2O in this simulation, the curve is lowered due to the high $\frac{H_2}{H_2O}$ fraction of about 10^4. The actual free energy of water vapor is the adjusted value seen in Figure 6. Given this adjusted free energy, the off-gases released during the simulation appear quite reasonable.

On the whole, the INJECT simulation results are quite good. A more detailed and quantitative comparison could be performed in the future when Molten Metal Technology performs experiments under a given set of conditions.

Conclusions

The goal of this work was to develop a computer model to study a variety of energy/chemical reaction simulations when a molten metal/oxide pool is stirred by gas injection with associated liquid or solid injection. This was accomplished by modifying the existing model CORCON in areas of pool hydrodynamics, energy generation, mass addition, and heat loss. The newly created model is called INJECT due to the analogy of the addition of materials (gaseous, liquid, and solid) by injection into the bottom of a molten pool.

INJECT can be used to simulate molten core-concrete interactions, steelmaking, catalytic extraction or any process involving molten pools undergoing material injection. INJECT is ideally suited to study reprocessing of nuclear waste streams given its extensive database of both chemical species found in nuclear systems and nuclear decay heat models associated with spent fuel. INJECT is also suited to predict the effects the catalytic extraction process has upon waste streams as was demonstrated earlier. Catalytic extraction is an exciting new technology that could address a great number of waste problems facing this country.

Further enhancements to INJECT are currently be considered. INJECT will be updated with heat transfer models developed by Lee [17]. The removal of condensed species originally conceived in CORCON, but never modeled, will be completed and enhanced to allow INJECT to model continuous recycle processes. Species can be added to the database as the need arises. An application of particular interest is to use INJECT to model an MCCI event that cannot be handled by CORCON. In this phenomena, the MCCI occurs as normal, however coolant is injected into the bottom of the molten pool at some specified rate while simultaneously the concrete is eroded. This form of debris coolability is a unique concept that needs to be investigated. Simulations of the Catalytic Extraction Process will also continue as a benchmark for the reliability of INJECT.

References

[1] E.G. Gracyalny, "INJECT And the Modeling of Energy and Transport Processes in a Molten Pool," Masters Thesis, Department of Nuclear Engineering and Engineering Physics, University of Wisconsin, (1994).

[2] R.K. Cole Jr., D.P. Kelly, M.A. Ellis, "CORCON-MOD2: A Computer Program for Analysis of Molten-Core Concrete Interactions'," Sandia Report, NUREG/CR-3920, SAND84-1246, (1984).

[3] Theodore M. Besmann, "SOLGASMIX-PV, A Computer Program to Calculate Equilibrium Relationships in Complex Chemical Systems," ORNL/TM-5775, (1977).

[4] Christopher A. Herbst, Eric P. Loewen, Anna Protopapas, Claire A. Chanenchuk, and Esther W. Wong, "Quantum-CEP^{TM} Applications to Mixed and Radioactive Wastes," Molten Metal Technology, Inc., Waltham, MA, (1995).

[5] J.F. Muir, "CORCON-MOD1: An Improved Model For Molten-Core/Concrete Interactions," Sandia Report, SAND80-2415, (1981).

[6] Joan-Carles Casas, John Ptacek and Michael L. Corradini, "Analysis of the ACE Molten Core-Concrete Interaction Experiments Using the CORCON.UW Model," Proceedings of NURETH-5, Salt Lake City, Utah, (1992).

[7] J.C. Casas, M. Corradini, "Study of Void Fraction and Mixing of Immiscible Liquids in a Pool Configuration by an Upward Gas Flow," Nuclear Technology, 99, 104-119, (1992).

[8] F.H. Van Zeggeren and S.H. Storey, The Computation of Chemical Equilibrium, Cambridge University Press, Cambridge, Massachusetts, (1970).

[9] JANAF Thermochemical Tables, National Standard Reference Data Series, National Bureau of Standards, (1985).

[10] Thermochemical Properties of Inorganic Substances, Springer-Verlag, (1991).

[11] J.K. Norkus, "Modeling of Molten Core Concrete Interaction and Fission Product Release," PhD Thesis, Department of Nuclear Engineering and Engineering Physics, University of Wisconsin, (1988).

[12] "Light Water Reactor Safety Research Program Quarterly Report," Sandia Report, SAND79-2057, (1980).

[13] W.C.H. Kupferschmidt et al, "Final Report of the ACE/RTF Experiments," Whiteshell Nuclear Research Establishment Report, ACE-TR-B3, (1992).

[14] E.J. Gracyalny, R.M. Bilbao, B. Huxtable, J. Ptacek, J.C. Casas, J. Norkus and M.L. Corradini, "INJECT: A Multipurpose Computer Program For Analysis Of Molten Pool-Structural Interactions And Associated Recycling Technologies," University of Wisconsin, Nuclear Safety Research Center Report, UWRSR-80, (1995).

[15] "ORIGEN 2.1, Isotope Generation and Depletion Code," RSIC Computer Code Collection, CCC-371, (1991).

[16] D.R. Bradley, R.K. Cole and A.W. Shiver, "Memorandum: Second Correction Set for CORCON-MOD2," Sandia Report, (1986).

[17] M. Lee, "Modeling of Corium/Concrete Interaction," PhD Thesis, Department of Nuclear Engineering, Massachusetts Institute of Technology, (1985).

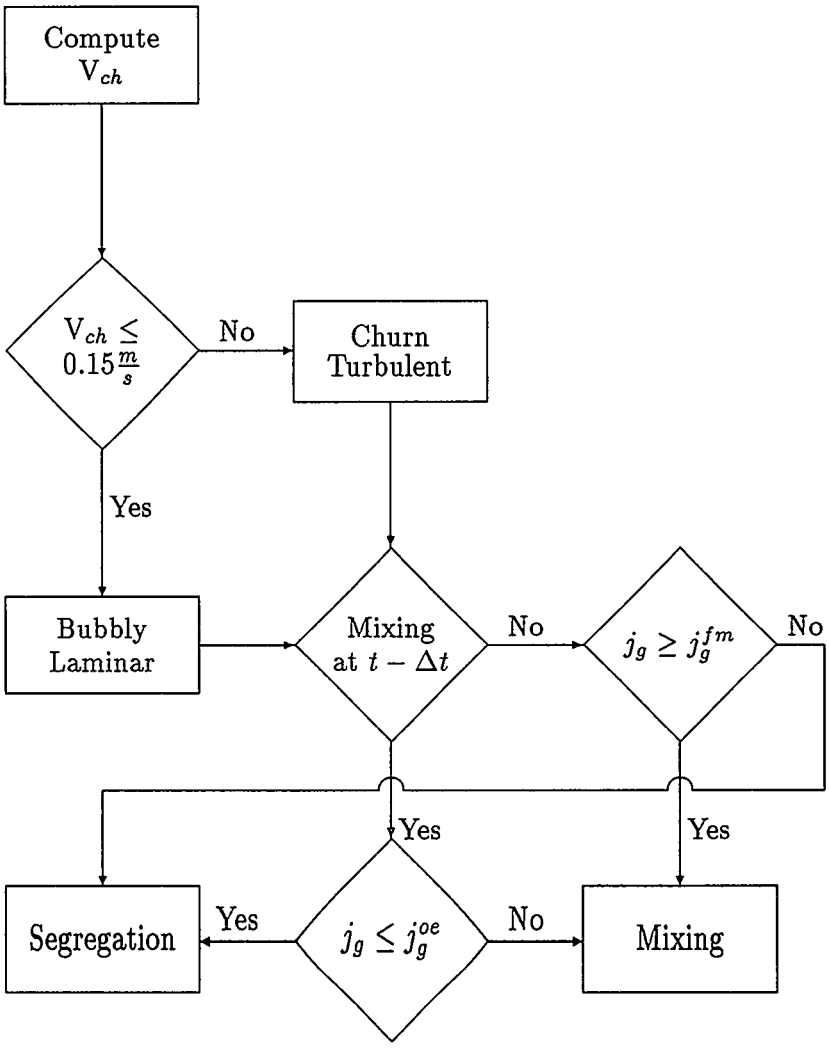


Figure 1: Casas' Mixing Logic

Oxides	Metals	Gases			
Al_2O_3	Ag	Ag	Ce	Ru	ZrO
B_2O_3	Al	AgO	CeO	RuO	ZrO_2
BaO	B	AgOH	CeOH	RuO_3	ZrOH
CaO	B_4C	$Ag(OH)_2$	$Ce(OH)_2$	RuO_4	Zr(OH)
CeO_2	Ba	Al_2O_2	CrO_3	RuOH	Micellaneous
Ce_2O_3	C(c)	Al_2O	Cs	$Ru(OH)_2$	
CoO	Ca	AlO	Cs_2	SiO	
Cr_2O_3	Ce	OAlH	CsI	Si	
CsO_2	CeB_6	Al(OH)	CsH	Si_2	H_2O_{Evap}
CsOH	Co	OAl(OH)	CsOH	Si_3	H_2O_{Chem}
Cs_2O	CoAl	AlO_2	$(CsOH)_2$	SiO_2	$CaCO_3$
Cu_2O	Cr	B	Cs_2O	SiOH	$Ca(OH)_2$
FeO	CrB	BH_2	Cu	$Si(OH)_2$	H_2O_{Cool}
Fe_2O_3	CrB_2	BH_3	Cu_2	SiH	
Fe_3O_4	Cs	HBO	CuO	SiH_2	
K_2O	Cu	BH	H	SiH_3	
La_2O_3	Fe	BO	H_2	SiH_4	
Li_2O	La	B_2	H_2O	Sn	
MgO	Mg	HBO_2	H_2Te	SnO	
MnO	Mn	$H_3B_3O_6$	I	SnOH	
Mn_3O_4	Na	B_5H_9	I_2	$Sn(OH)_2$	
Na_2O	Nb	$B_3H_3O_3$	La	SnTe	
NbO	Ni	B_2O	LaO	Sr	
NbO_2	Pu	B_2O_2	LaOH	SrI_2	
Nb_2O_5	Ru	B_2H_6	$La(OH)_2$	SrH	
NiO	Si	$B_2(OH)_4$	Mg	SrO	
RuO_2	SiC	$B(OH)_2$	Mg_2	SrOH	
PuO_2	Sn	H_3BO_3	MgO	$Sr(OH)_2$	
SiO_2	Sr	B_2O_3	MgOH	Te	
SrO	Te	BO_2	$Mg(OH)_2$	Te_2	
TeO_2	U	Ba	Mn	TeO_2	
TiO_2	UAl_2	BaH	N	TeO	
UO_2	UAl_3	BaO	NH_3	Te_2O_2	
U_3O_8	Zn	BaOH	N_2	TeOH	
ZnO	Zr	$Ba(OH)_2$	Nb	$Te(OH)_2$	
ZrO_2	$ZrTe_2$	C	NbO	U	
$KAlO_2$	FP_M	CO	NbO_2	UO	
$NaAl_2$	X	CO_2	NbOH	UO_2	
$BaAl_2O_4$		C_2H_2	$Nb(OH)_2$	UO_3	
$CaAl_2O_4$		CH	O	UOH	
$MgAl_2O_4$		CH_2	O_2	$U(OH)_2$	
$MnAl_2O_4$		CH_3	OH	Zn	
FP_{MO_2}		CH_4	Pu	Zr	
FP_{MO_3}		C_2H_4	PuO	ZrH	
FP_{O_x}		C_2H_6	PuO_2	ZrI_2	
FP_{AakMet}		CHO	PuOH		
FP_{Halogn}		CH_2O	$Pu(OH)_2$		

Table 1: INJECT Species List

Isotope	Compound	$\frac{mCi}{g_{resin}}$	Half Life (s)	$\frac{g_{isotope}}{g_{resin}}$
Ce^{141}	Ce_2O_3	2.41E(-4)	2.85E(6)	8.59E(-12)
Co^{58}	CoO	6.47E(-4)	6.16E(6)	2.05E(-11)
Co^{60}	CoO	1.32E(-2)	1.66E(8)	1.65E(-8)
Cs^{137}	CsO_2	2.26E(-3)	9.47E(8)	2.60E(-8)
Cs^{134}	CsO_2	6.11E(-3)	6.47E(7)	4.69E(-9)
Mn^{54}	MnO	4.58E(-3)	2.62E(7)	5.74E(-10)
Zn^{65}	ZnO	1.74E(-2)	2.11E(7)	2.11E(-9)

Table 2: Typical Ion Exchange Radioactive Contaminants

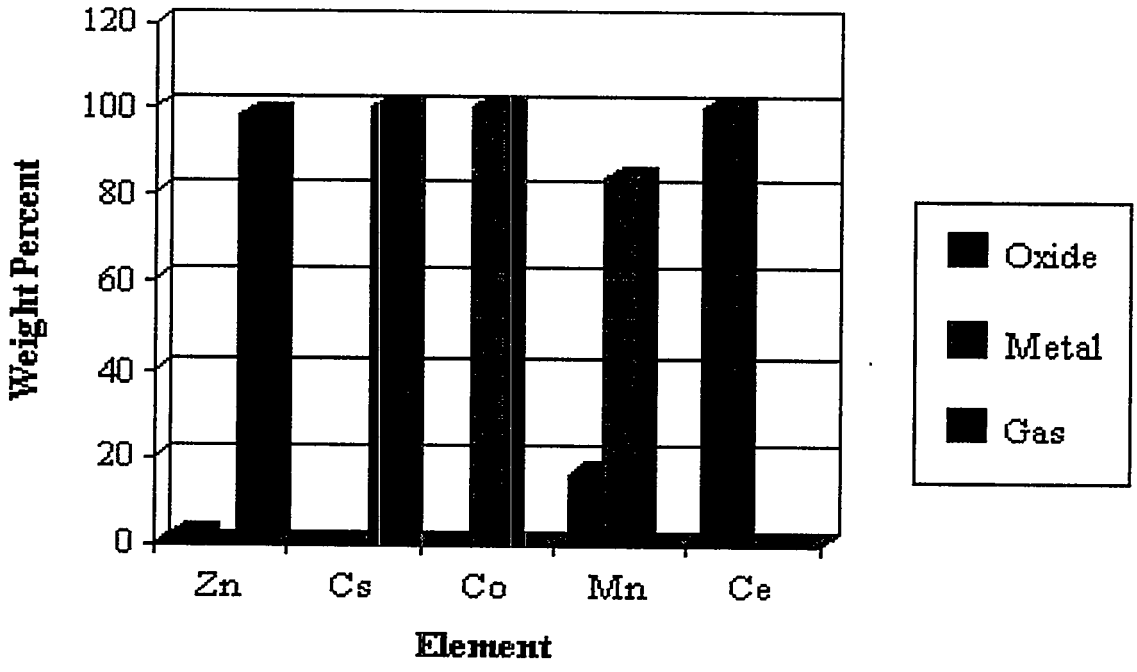


Figure 2: Radionuclide Partitioning for Low Gas and Low Resin Injection

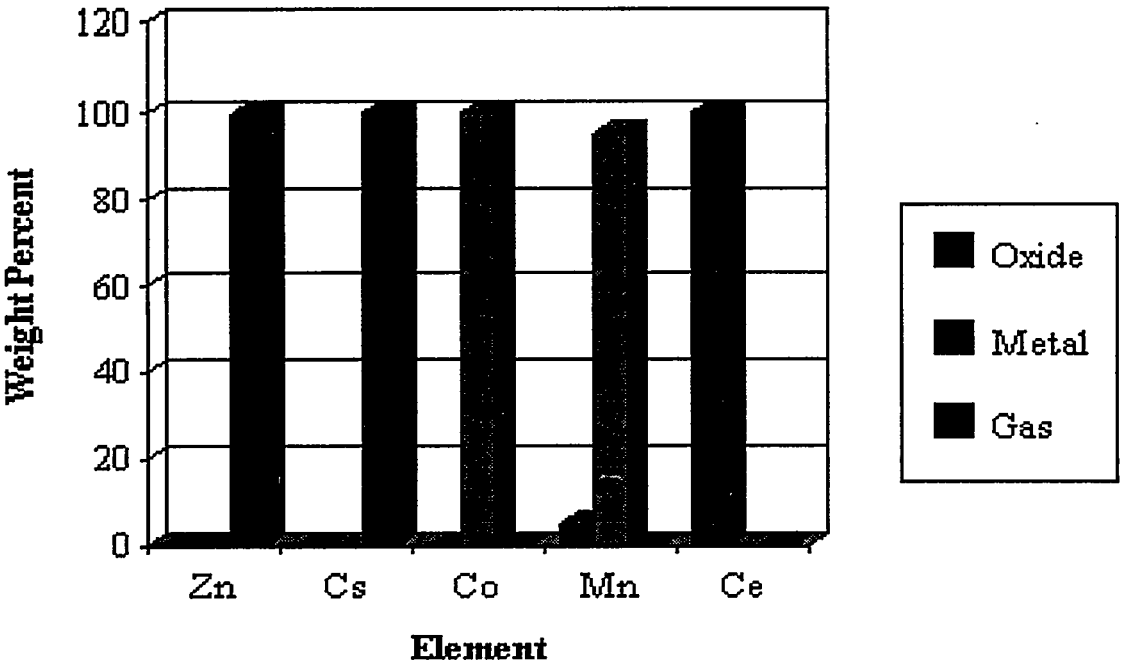


Figure 3: Radionuclide Partitioning for Low Gas and High Resin Injection

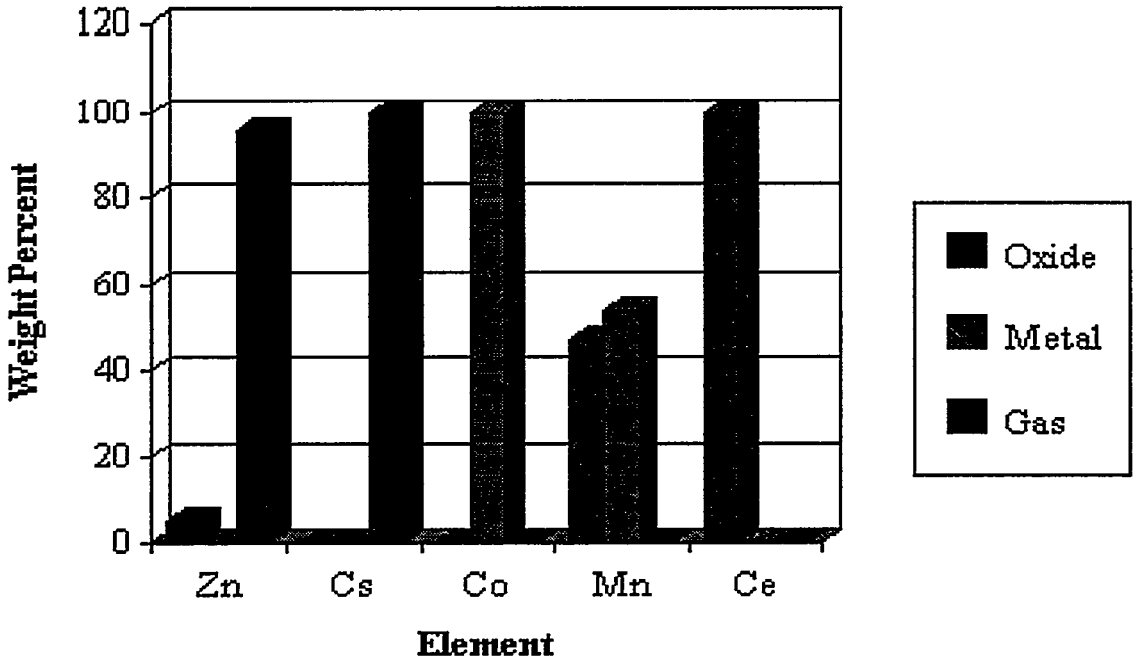


Figure 4: Radionuclide Partitioning for High Gas and Low Resin Injection

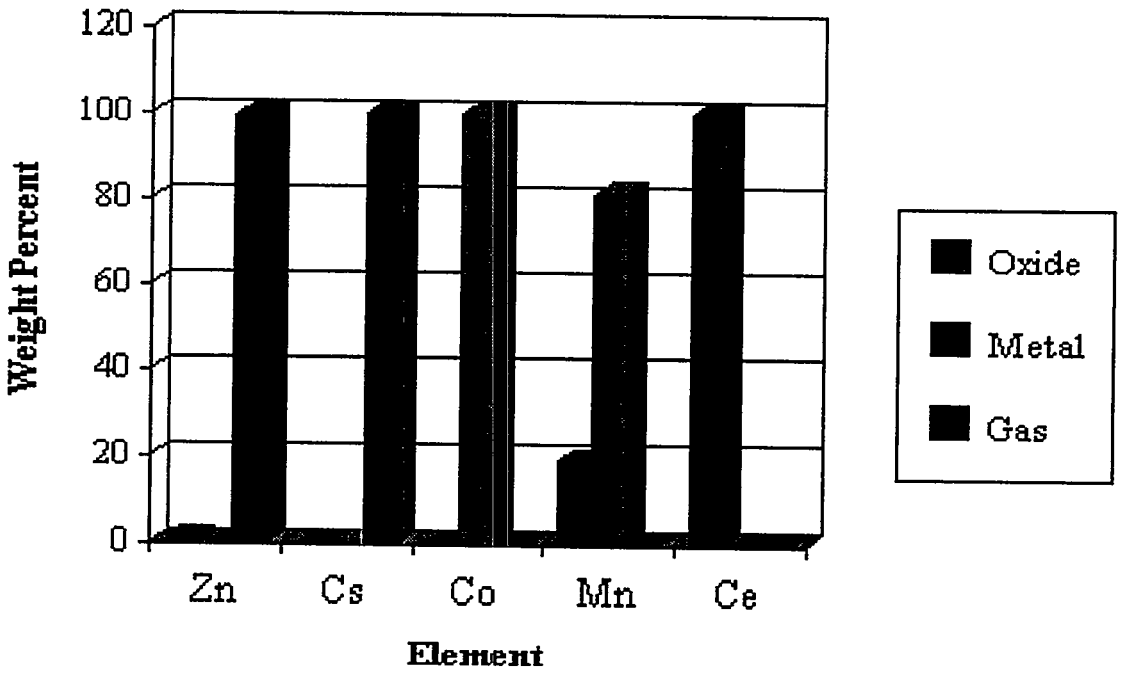


Figure 5: Radionuclide Partitioning for High Gas and High Resin Injection

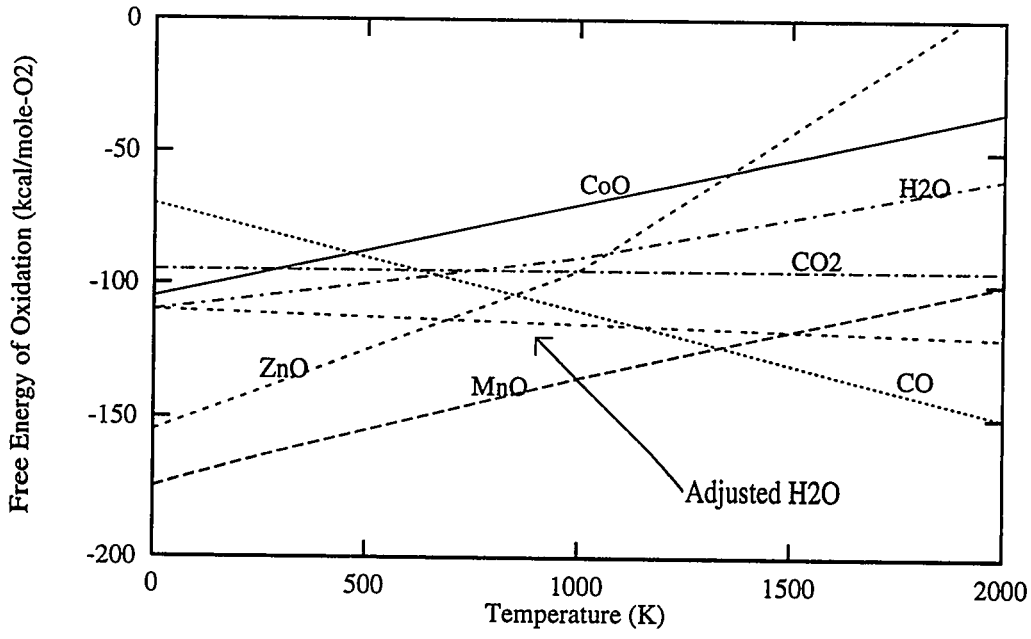


Figure 6: Free Energies of Relevant Oxides

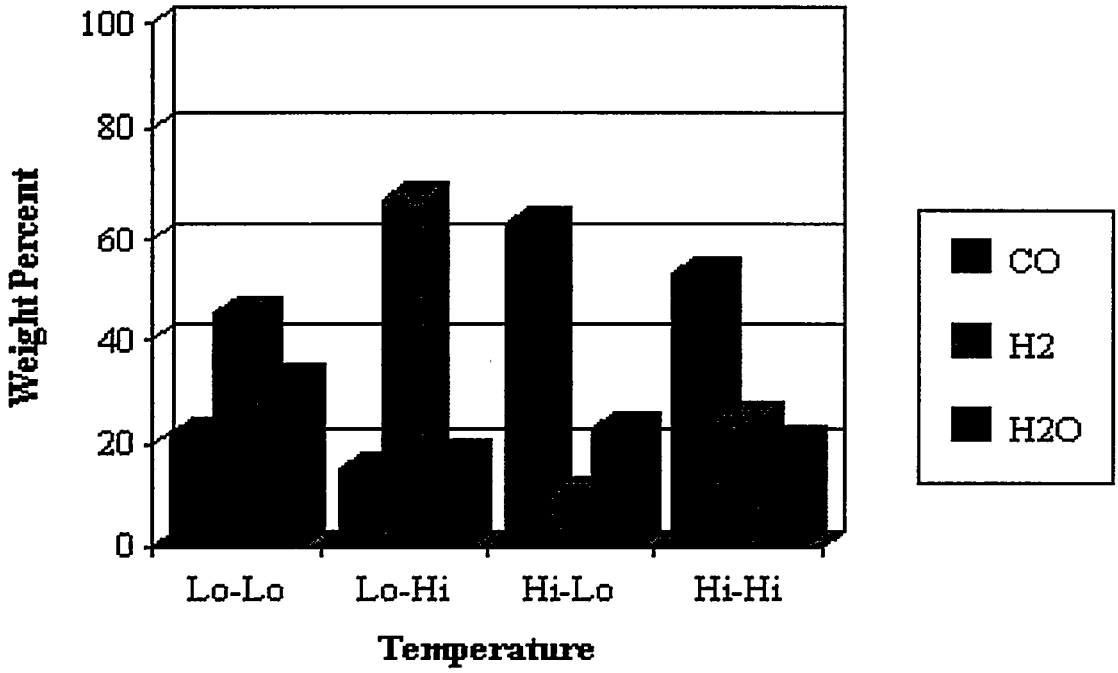


Figure 7: Primary Gases Released During CEP Resin Simulation

SOME THERMOHYDRAULICS OF CLOSURE HEAD ADAPTERS IN A 3 LOOPS PWR

F. Hofmann*, O. Daubert*, C. Bertrand**, M. Hecker*, F. Arnoux-Guisse* and O. Bonnin*.

*EDF/DER/National Hydraulics Laboratory.
6, Quai Watier - B.P. 49 - 78401 CHATOU Cédex 01 - FRANCE

**EDF/SEPTEN/MS/Théorie.
12-14, avenue Dutrièvoz, 69628 VILLEURBANNE Cédex - FRANCE

ABSTRACT

In 1993 a R&D action, based on numerical simulations and experiments on PWR's upper head was initiated. This paper presents the test facility TRAVERSIN (a scale model of a 900 MW PWR adapter) and the calculations performed on the geometry of different upper head sections with the Thermalhydraulic Finite Element Code N3S used for 2D and 3D computations.

The paper presents the method followed to bring the adapter and upper head study to a successful conclusion. Two complementary approaches are performed to obtain global results on complete fluid flow in the upper head and local results on the flow around the adapters of closure head. A validation test case of these experimental and numerical tools is also presented.

I. INTRODUCTION

The problem of cracks detected in a number of vessel closure heads led EDF to undertake a program of studies involving physical and numerical simulations. The one presented here is devoted to temperature evaluation inside adapters of control rod drive penetrations where these cracks have been located.

The mean temperature of the fluid in the upper head region was estimated by previous experimental studies (1978) allowing a classification into cold upper head and hot upper head plants, according to the amount of the flow rate of cold liquid injected under the closure through the nozzles located around the circumference.

Inside the adapters, the temperature may be different from this mean value because of the local flow configuration : as a hole is bored through the upper part of the thermal sleeve separating the adapter from the control rod drive, the two concentric channels on each side of the sleeve can communicate like a siphon (figure 1). The flow in these channels is driven by both hydraulic and thermal effects which have to be evaluated.

II. METHOD

Because of the difference between the closure head diameter (4 m) and the distance between the adapter and the thermal sleeve (3 mm), a global numerical simulation is unrealisable. So, the study was divided into 2 parts involving some numerical simulations with N3S code and a physical scale model.

The first part is a global approach of the flow into the closure head with 4 objects :

- to know the global flow in the upper head,
- to determine if there are upward flow rates from the upper internal plenum to the upper head,
- to design the local scale model,
- and to have the incident velocity profile on peripheral adapters, which is a boundary condition of local models.

The second part of the study is a local approach to determine the flow in the siphon. The hydraulic boundary conditions of this siphon are given by two computations and one scale model. The aim of the scale model is to validate the N3S code and the purpose of the numerical simulation is to calculate the both boundary conditions : at the base of the adapter, on one side, and at the end of the thermal sleeve, on the other.

A further development of a 1D numerical model (THERSIF) will determine the flow rate and the temperatures in the siphon. The diagram given on figure 2 shows the links between the different approaches.

III. THE N3S CODE

The FEM code N3S has been developed by the Research Branch of EDF for thermohydraulics studies in nuclear engineering design [1], taking advantage of our experience on 3D finite difference codes. N3S's development

starts in 1982 with the main feature of the use of unstructured meshes for complex geometries modelling. After intensive testing required by EDF Quality Assurance policy, it is now available for use as a general purpose tool which can be applied successfully to a wide variety of incompressible laminar or turbulent flows with or without heat transfer [1, 2, 3 and 4]. For code assessment, a wide range of computer program validation is made under a Quality Assurance procedure for every main release of N3S. Code results are compared with analytical solutions when available or with literature experiments. In addition, international numerical workshops provide further validation cases (See [4], for example).

Four steps are needed to perform a numerical study which will be briefly presented here. They are : the mesh generation, the boundary condition prescription, the solution of the equations and the post-processing. Each step use a particular program/tool, as follows.

For the meshing task, N3S uses the CAD softwares IDEAS™ marketed by SDRC or SIMAIL marketed by SIMULOG, specially the solid modeler for the geometry definition step and the finite element modeler for the unstructured mesh generation [3].

The pre-processor PREN3S checks the mesh and prescribes the boundary conditions and all the other data.

N3S solves the Reynolds averaged Navier-Stokes equations for an unsteady incompressible flow with, as a standard choice, k-ε turbulence model [4, 5 and 6]. The time discretization is based on a fractional step method. At each time step the code solves successively :

- an advection step, for the non-linear convection terms of the Navier-Stokes, k-ε and eventually temperature equations, by a characteristics method,
- a diffusion step for the remaining part of the k and ε equations : the finite element discretization leads to linear systems solved by a preconditioned conjugated gradient algorithm,
- a generalized Stokes problem for the velocity and the pressure, solved by a Chorin algorithm.

Assuming a logarithmic velocity profile, we use wall functions on the solid boundaries to compute the friction shear stress at each time step.

For the post-processing task, either GRAFN3S or MPGS/EnSight (marketed by CEI inc.) can be used ; these two softwares are very well suited for CFD visualisations. All specific functionalities were developed according to EDF specifications.

Table 1 give the characteristics of the different meshes used to the numerical simulations. They use a P1-isoP2 discretization on tetrahedra in 3D or triangles in 2D.

Name	COUV. 15°	COUV. 45°	TRAVERSIN	MANCHETTE
Dimension	3D	3D	3D	2D
Number of velocity nodes	84 000	207 000	116 000	12 000

Table 1 : Characteristics of the different numerical simulations.

IV. GLOBAL APPROACH

Numerical model COUVERCLE-15°

The first 3D computation named COUVERCLE-15° (mesh figure 3 left) takes into account a 15° upper head section with 1 inlet injection and 5 free outlets. The obstacles (adapters, thermal sleeves and guide tubes) are not represented and this section is bounded by 2 assumed symmetry planes. The outlets are located between the housing plates and the thermal sleeves.

Figure 4 shows the velocity profile of the wall jet at the location of a peripheral adapters. With this profile and the flow rate calculated, we can design the scale model TRAVERSIN.

Numerical model COUVERCLE-45°

The disposition of guide tubes and spray nozzles in 900 MW CPY upper heads allows to model only $1/8^{th}$ of the domain, with two symmetry planes. This 3D computation named COUVERCLE-45° (mesh figure 3 right) is more accurate than the previous one because the geometry is symmetrical and all guide tubes are represented. There are three peripheral nozzles where the inlet flow is prescribed. Outlets are located inside the 13 guide tubes and their boundary conditions are normal stresses calculated with pressures measured in a previous experimental study (1978) and including the pressure drops of the housing plates. This boundary condition allows to obtain the flow rate in each guide tube as a result.

So this model gives a good representation of the global flow in the upper head, as it can be seen on the figure 5. This result allows us to obtain a better incident velocity profile of the wall jets, as shown on the figure 4. This profile is used for the inlet condition of the scale model and the computation TRAVERSIN.

V. LOCAL APPROACH

Physical and numerical models TRAVERSIN

The TRAVERSIN scale model was designed in January 1994, using the flow rate evaluation given by COUVERCLE-15° computation. It represents a upper head section around a peripheral adapter and its thermal sleeve (figure 7). All parts are made of Perspex for flow fields visualisations an measurements like LDV and PIV.

The scale of the model is 1 for the length and the velocity, and $1/8^{th}$ for the Reynolds number, because of the water viscosity which is greater at room temperature than in the reactor. The inlet boundary condition is a velocity profile set by an adjustable guide flow followed by a honey comb which regularizes the profile at the entrance of the test section. The flow rate of the experimental loop is measured with a magnetic flow-meter ; it is limited to 240 l/s. 10 pressure sensors, will give dynamic pressure at the base of the adapter and around the thermal sleeve.

This scale model is used to validate the choice of the best available turbulence model in N3S code for the numerical simulations in the same geometry [7].

The mesh (figure 6) used for the numerical model TRAVERSIN reproduces exactly the test section of the scale model. This model has the advantage of being free of limitations on the flow rate and the velocity profile at the inlet, but the turbulence model used in the computation has to be tested. There are several choices in N3S and from previous test cases, we know that turbulence modeling is not obvious in this type of flow (impinging jet on a cylinder).

The comparison between experimental and numerical models is made with the following boundary conditions :

- a uniform velocity profile of 1m/s at the inlet, (i.e. flow rate of 87 l/s and parallel flow guide plates in the physical model),
- the outlet is free (i. e. uniform normal stress in the outlet plane of the numerical model),
- in the computation, the ceiling and the obstacles are treated with wall functions associated with the turbulence model, but the other walls are considered as free slip planes, because the boundary layers along them do not interact with the local flow around the adapter. So it is not necessary to refine the mesh there.

The figure 8 shows a visualisation of the flow around the thermal sleeve in both models : in the physical one, it is viewed with wool yarn representing the direction of the velocity vectors ; in the numerical one, there are particle traces calculated by the post-processor from the computed velocity field.

A further comparison of pressure and velocity fields is planned to validate more precisely the N3S code on this geometry. After that, another computation will be done on the same geometry, with the real Reynolds number of the plant and the inlet velocity profile given by the global computation COUVERCLE-45°.

The expected result is the first boundary condition of the siphon : over pressure value at the base of the adapter.

Numerical model MANCHETTE

The second boundary condition of the siphon is given by the last numerical simulation named MANCHETTE (mesh figure 9). This is a 2D axi-symmetric computation, which represents an adapter, a thermal sleeve, a rod drive and a guide tube. The hole bored though the upper part of the thermal sleeve is not represented because this hole is not axi-symmetric. So the mesh of the siphon is cut under the hole and both channels are artificially linked by two velocity boundary conditions calculated with the pressure drop law of the hole.

So the numerical model takes into account the flow rate through the siphon. For a given upward or downward flow rate in the guide tube, the model can calculate, taking into account the temperature or not, the pressure level at the base of the thermal sleeve, which is the last boundary condition of the siphon. The values of the flow rate in the guide tubes are picked up from the numerical simulation COUVERCLE-45°.

The figure 8 shows an upward and a downward flow rate in the guide tube. In fact with a downward flow, the pressure at the base of the thermal sleeve is nearly equal to the pressure in the upper head. Inversely, when the flow is upward, the over pressure is significant.

VI. CONCLUSION AND FURTHER DEVELOPMENTS

This study contributes to increase the knowledge of the flow in the upper head and around the adapters. In particular its results allow reducing the likelihood of a hot upward flow from the upper internal plenum to the upper head in the 900 MW CPY units.

The comparison between the experimental and numerical TRAVERSIN models will be continued with the flow and pressure fields comparaison.

All results of the study will be brought together in the THERSIF model to give more informations about the flow and the temperature in the siphons. The thermal aspects will be also developed with thermal numerical simulations on the COUVERCLE-45° and MANCHETTE models.

ACKNOWLEDGEMENT

The authors are grateful to N3S team (EDF) and Mr G. Barois (FRAMATOME) for their fruitful help and pertinent advices.

REFERENCES

[1] J.P. Chabard, B. Métivet, G. Pot, B. Thomas, "An Efficient Finite Element Method for the Computation of 3D Turbulent Incompressible Flows", Finite Element in Fluids, vol 8 Hemisphere Publishing Corp. Ed, (1992).

[2] J.F. Combes, E. Rieutord, "Numerical and experimental analysis of the flow in a centrifugal pump at nominal and partial flow rate", Int. ASME Gas Turbine and Aeroengine Congress and Exposition, Cologne, Germany June &-4 (1992).

[3] A. Caruso, N. Mechitoua, "Finite element computations of turbulent diffusion flame", Proc. 2nd Int. Conf in Advanced Computational Methods in Heat Transfer, Milan, Italy, july (1992).

[4] B. Delenne, D. Manzoni, G. Pot, "Modelling of the turbulent boundary layer implemented in CFD Code N3S and application to flows in heated and cooled rooms", Int. J. Num. Met. in Fluids, Vol 20, p 469-492 (95).

[5] J.P. Chabard, G. Pot, A. Martin, "Industrial applications of N3S finite element code", ASME Jour. of Mech, Eng (1993).

[6] G. Pot, O. Bonnin, V. Moulin, B. Thomas, "Improvement of finite element algorithms implementated in CFD code N3S for industrial turbulent applications", Proc of 8th International Conference on Numerical Methods in Laminar and Turbulent Flow, Swansea, U. K. (1993).

[7] D. Alvarez, A. Martin, J.P. Schneider, "Boron mixing transients in a 900 MW PWR vessel for a reactor start-up operation". Proc. of the NUTHOS 4th, Taipei, Taiwan (1994).

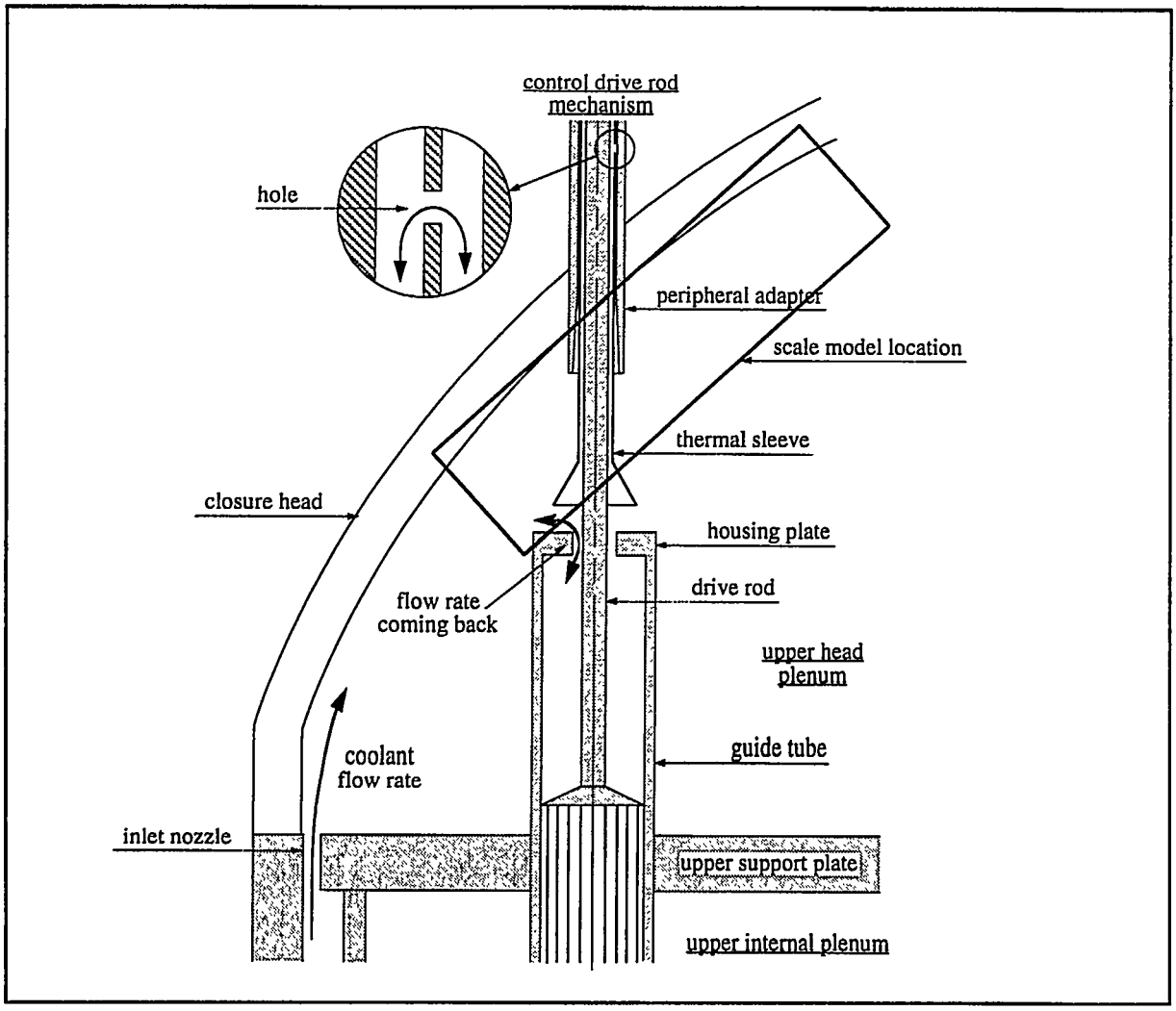


Figure 1 - Global view of the upper head geometry with one adapter.

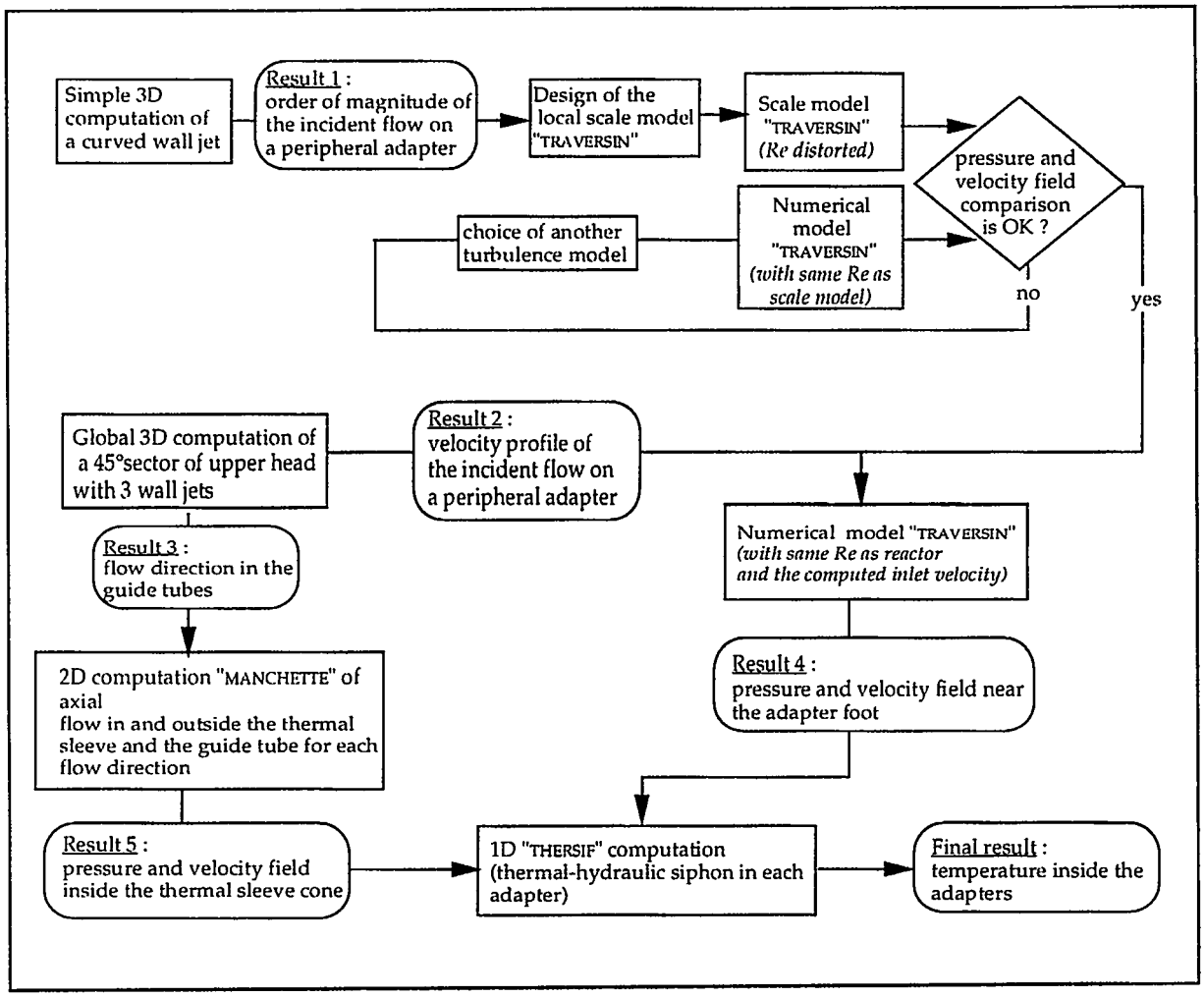


Figure 2 - Diagram showing the links between the different approaches.

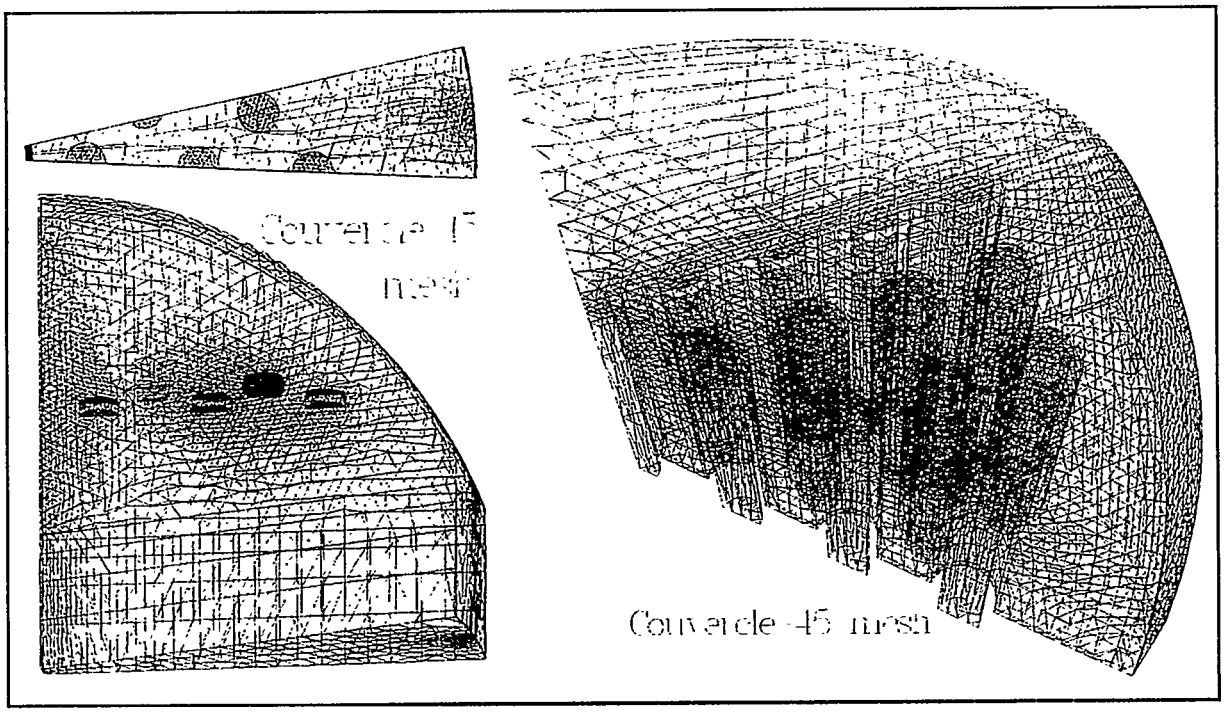


Figure 3 - Meshes of the computations COUVERCLE-15° and COUVERCLE-45°.

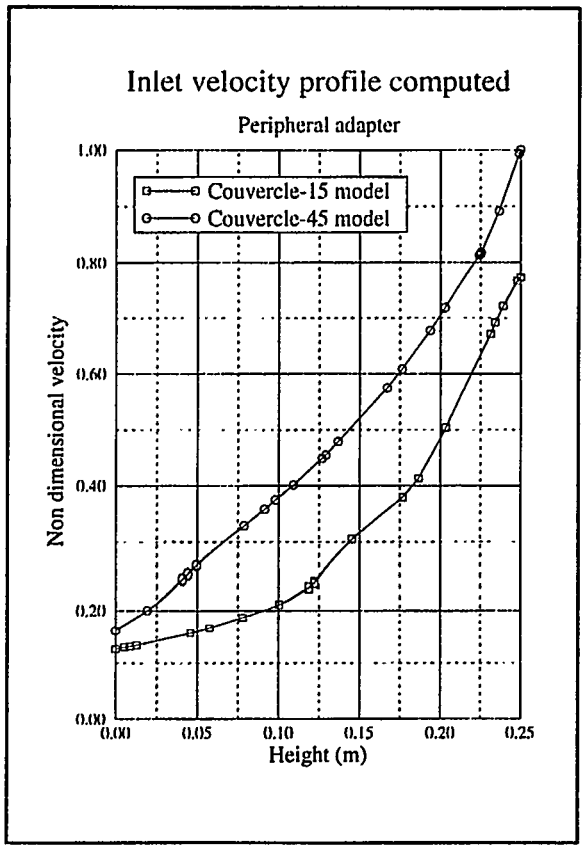


Figure 4 - Velocity profile at a peripheral adapter location calculated by COUVERCLE-15° and COUVERCLE-45° computations.

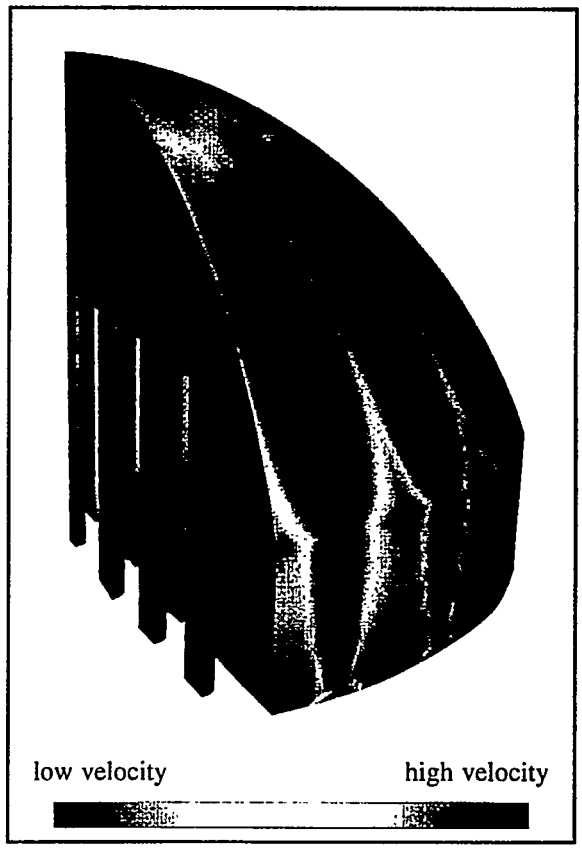


Figure 5 - Global flow in a 45° section of the upper head computed by the COUVERCLE-45° model.

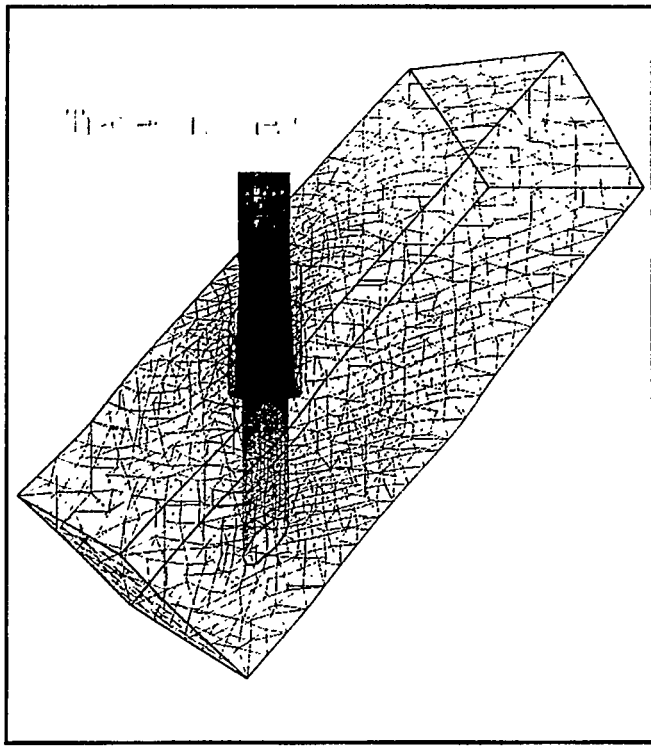


Figure 6 - Mesh of the TRAVERSIN model.

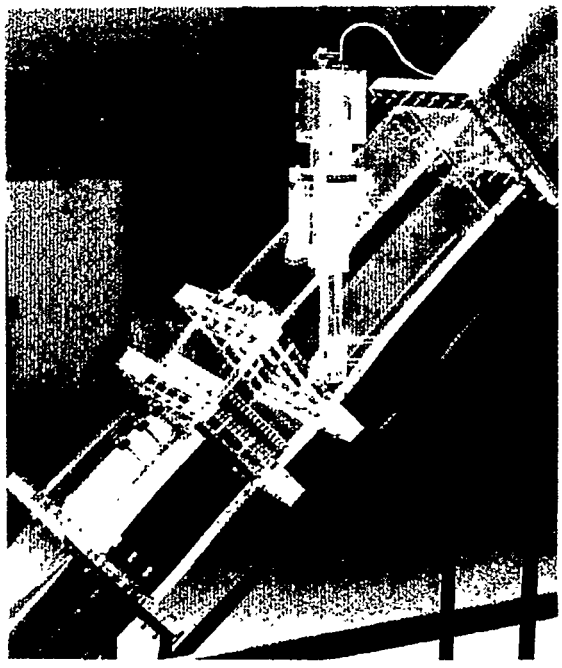


Figure 7 - View of the scale model TRAVERSIN

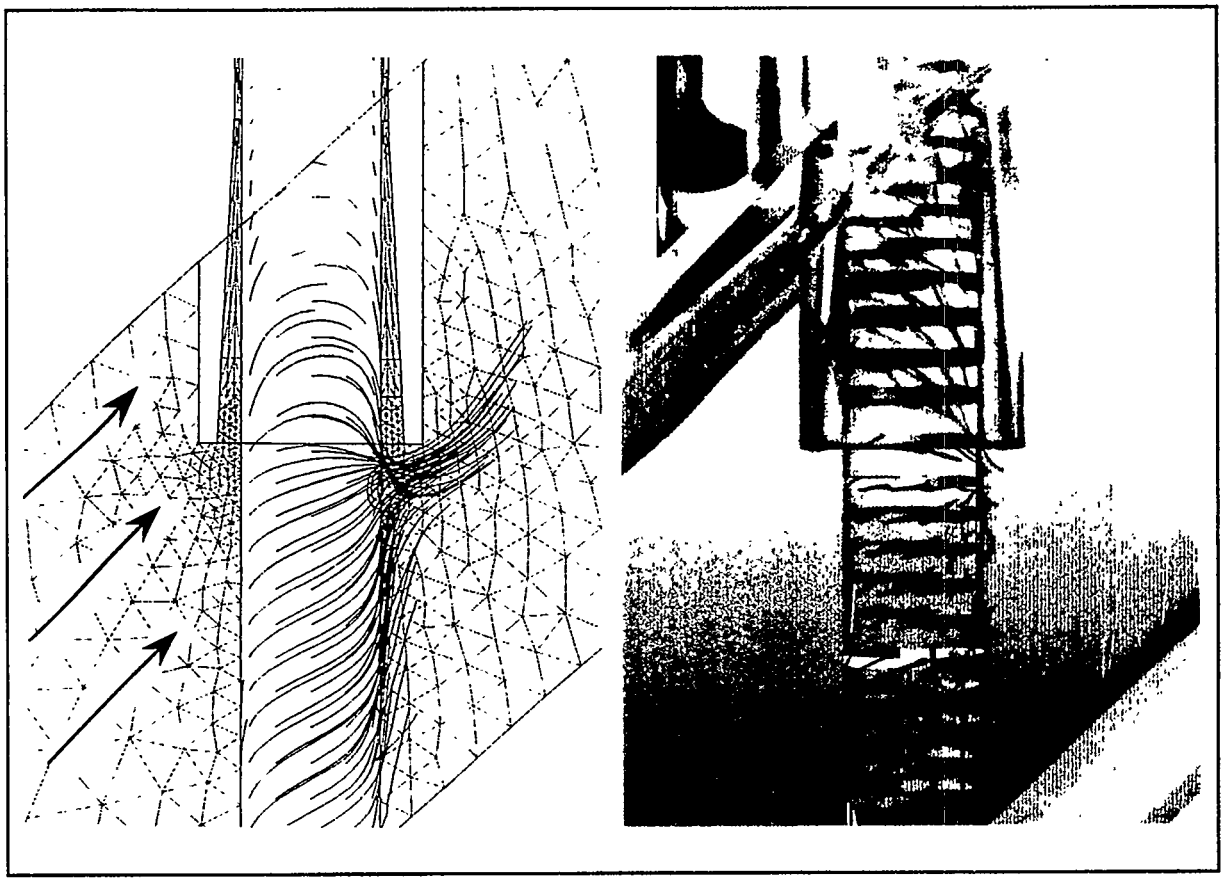


Figure 8 - Comparison between the experimental and numerical TRAVERSIN model.

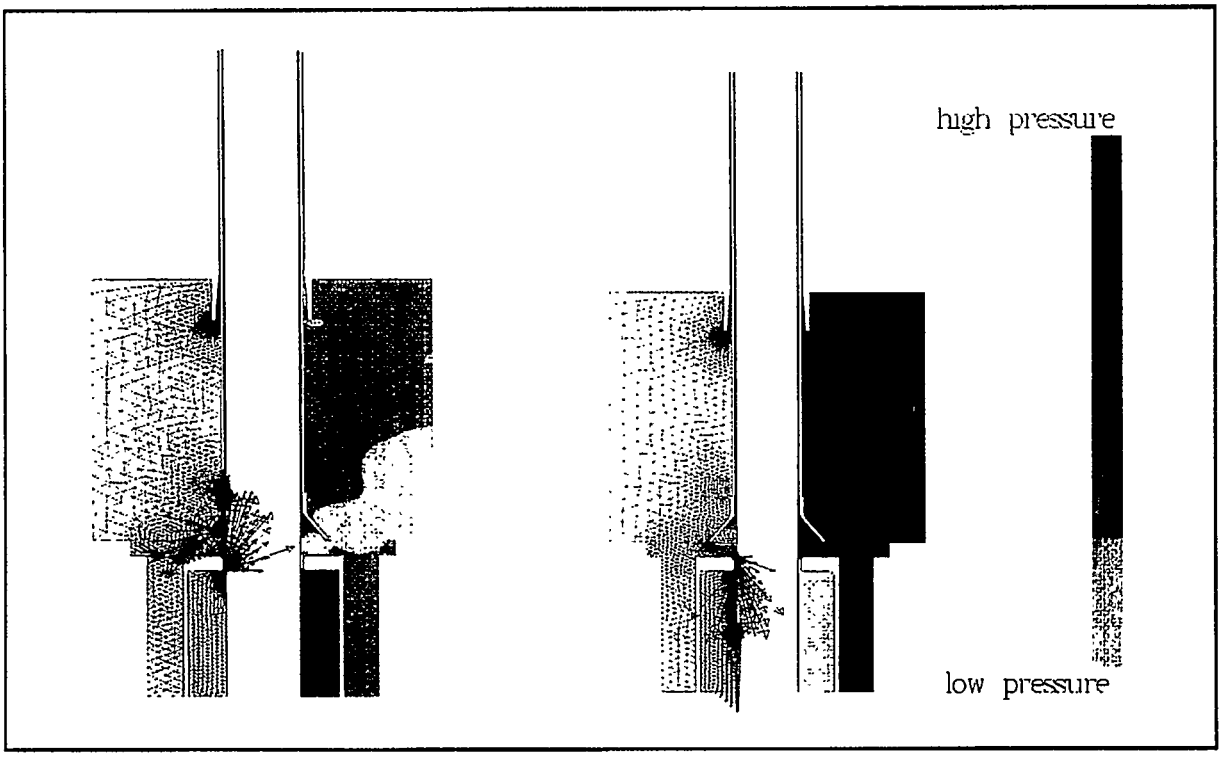


Figure 9 - Mesh, pressure and velocity fields of the MANCHETTE computation
(upward flow on the left and downward flow on the right).

Analysis of a Small Break Loss-Of-Coolant Accident of Pressurized Water Reactor by APROS

Sabah Al-Falahi[1] Markku Hänninen[2] Kari Porkholm[3]

[1] Department of Energy Engineering,
Helsinki University of Technology,
Otakaari 1, FIN-02150 Espoo, Finland
Telefax: 358-0-4565000

[2] VTT Energy,
Tekniikantie 4 C, Espoo,
P.O.Box 1604, FIN-02044 VTT,Finland
Telefax: 358-0-4565000

[3] IVO International Ltd,
Rajatorpantie 8, Vantaa,
FIN-01019 IVO, Finland
Telefax: 358-0-85613403

ABSTRACT

The purpose of this paper is to study the capability of APROS (Advanced PROcess Simulator) code to simulate the real plant thermal-hydraulic transient of a Small Break Loss-Of-Coolant Accident (SBLOCA) of Loss-Of-Fluid Test (LOFT) facility. The LOFT is a scaled model of a Pressurized Water Reactor (PWR). This work is a part of a larger validation of the APROS thermal-hydraulic models. The results of SBLOCA transient calculated by APROS showed a reasonable agreement with the measured data.

1. INTRODUCTION

APROS has been developed in a co-operation project between Imatran Voima (IVO) and the Technical Research Centre of Finland (VTT) (1). APROS has an efficient and user friendly graphical interface and it can be used in the process and automation design, safety analysis and training for the nuclear, fossil and chemical processes (2). APROS is a simulation program for the whole power plant. It includes the thermal-hydraulic models that are able to calculate the different type of LOCAs related phenomena. The program has been coded with Fortran 77. Some part of the graphical user interface utilizes with C language. The program is commercially available.

APROS contains the 3-, 5- and 6-equation one-dimensional thermal-hydraulic models. The calculation of the 3-equation model is based on the mass, momentum and energy conservation equations applied for mixture (3). In the 5-equation model the mass and energy conservation equations are calculated for the gas and liquid phases separately (4) and the momentum equation is calculated only for mixture. In the 6-equation model the separate mass, energy and momentum equations are used for gas and liquid phases (5). The transient presented in the

paper has been calculated with the APROS version 2.12 using both 5- and 6-equation thermal-hydraulic models.

The aim of this study was to test the APROS calculation capability of a SBLOCA of LOFT facility. The experiment LP-SB-3 was chosen to provide data on the thermal-hydraulic, nuclear and structural processes expected to occur during the transient of a small break in the cold leg.

LOFT experiment LP-SB-3 covers a large range of SBLOCA phenomena. In the experiment the leak mass flow changes gradually from subcooled to saturated two-phase and finally to one-phase steam flow. The total simulation time of the transient was 7000 seconds.

In the paper the APROS simulation results have been compared with the measured data. The calculations were carried out with the HP 9000/735 workstation. APROS has also been implemented on SUN, DEC, Alpha and SGI workstation, with UNIX operating system.

2. THERMAL HYDRAULICS OF APROS

APROS program includes three different one-dimensional flow and heat transfer models. All the models are based on the conservation equations for mass, energy and momentum (equations 1 to 3).

$$\frac{\partial \alpha_k \rho_k}{\partial t} + \frac{\partial \alpha_k \rho_k u_k}{\partial z} = \Gamma_k \qquad \text{(mass)} \qquad (1)$$

$$\frac{\partial \alpha_k \rho_k u_k}{\partial t} + \frac{\partial \alpha_k \rho_k u_k^2}{\partial z} + \alpha_k \frac{\partial p}{\partial z} = \Gamma_k u_{ik} + \alpha_k \rho \bar{g} + F_{wk} + F_{ik} + f_k \qquad \text{(momentum)} \qquad (2)$$

$$\frac{\partial \alpha_k \rho_k h_k}{\partial t} + \frac{\partial \alpha_k \rho_k u_k h_k}{\partial z} = \alpha_k \frac{\partial p}{\partial t} + \Gamma_k h_{ik} + q_{ik} + q_{wk} + F_{wk} u_k + F_{ik} u_{ik} + \alpha_k \rho_k u_k \bar{g} \qquad \text{(energy)} \qquad (3)$$

In equations 1 to 3 the subscript k refers to gas (g) or liquid (l) phases, i refers to the interface of the phases and w refers to the wall of a flow channel. The function of f takes into account the effect of valves, pumps and form losses.

The differential equations are discretized in respect to time and space. In the space discretization the staggered grid scheme is applied. In this scheme the state variables (pressures, enthalpies and densities) are calculated in the middle of the mesh (node) and the flows are calculated between nodes (branch). The nonlinear terms are linearized and the resulting linear equation groups for pressure, void fraction, liquid and steam enthalpies are solved (6).

3-equation model

The 3-equation model is mainly used in the calculation of the secondary circuit as it includes models for turbines, condensers and feed water system.

5-equation model

The 5-equation model is based on the conservation equations of mass and energy for liquid and

gas phases and the momentum equation for mixture of gas and liquid. The wall friction of mixture, wall heat transfer for liquid and gas separately, interfacial heat and mass transfer and phase separation by the drift flux phase separation need constitutive equations in addition to the basic conservation equations.

The discretized forms of the conservation equations are solved via a sparse matrix solution giving the pressure, the liquid enthalpy and the vapor enthalpy distribution in the nodes, the mixture velocity distribution in branches and the prediction for the new void fraction distribution in the nodes. The void fraction prediction includes the effect of the phase separation, which is calculated by a drift flux formula.

The pressure and mixture velocity distributions include an effect of the wall friction. The Blasius equation is applied for the turbulent flow area and a laminar approach is used for the low flow velocities.

The solution of the momentum conservation equation includes the limitation of the critical flow. The frozen sound speed of mixture has been used as a limitation for the mixture velocity.

The drift flux model has two parameters, the basic drift velocity and the radial void distribution factor for the fitting of the mathematical model into the physical data. These coefficients are derived by using the EPRI full range correlation. The correlation includes the effect of the counter current flow limitation, which is included as an additional limiter into the formulation.

The wall heat transfer correlation is selected on the basis of the wall temperature, the saturation temperature, the critical heat flux and the Leidenfrost temperature. The forced convection into the single phase liquid and gas is solved by the Dittus-Boelter correlation. Boiling occurs above the saturation temperature and Chen correlation has been used for this heat transfer regime. The critical heat flux model combines Zuber-Griffith, Biasi and Westinghouse correlations on their validity range. The additional heat transfer for the dry wall due to the inverted annular film boiling is calculated by Bromley correlation. The transient boiling heat transfer is calculated by the interpolation between the critical heat flux point and the minimum film boiling point. Additionally an effect of the wall condensation is calculated, when the wall temperature is below the saturation temperature and surrounded by steam. All the heat transfer correlations, except Dittus-Boelter are programmed as the multiparameter functions resulting the full range correlation over the whole expected parameter range.

The interfacial heat transfer includes the flashing of the superheated liquid and the steam condensation into the subcooled liquid. For the condensation two approaches are included: the low condensation rate through a water level and high condensation between droplets and gas (7).

6-equation model

In the 6-equation model the separate mass, energy and momentum equations are calculated for the gas and liquid phases. The wall friction, the interface friction, the wall heat transfer and the interface heat transfer need the constitutive equations.

In the use of the correlations the bubbly, annular, droplet and stratified two-phase flow regimes have been taken into account.

The factor λ for the friction between the wall and liquid/gas is calculated in laminar area with the formula $\lambda=64/Re$ and with the Blasius equation in the turbulent area. The distribution between

the liquid and gas frictions is made on the basis of the flow regimes.

The interfacial friction is calculated separately for the stratified and non-stratified flows. The non-stratified friction consists of the entrainment and non-entrainment part. In the calculation of the total interfacial friction the different frictions are summed up by using the weighing factors for the stratification and entrainment (8).

The wall heat transfer correlations are selected on the basis of the wall temperature, saturation temperature, minimum film boiling temperature and critical heat flux. When the wall is wet Dittus-Boelter or Gnielinski correlations for the forced convection and Thom correlation for the nucleate and saturated boiling are used. When the wall is dry Berenson correlation for the pool boiling, Dittus-Boelter for the forced convection, the power law equations for the natural convection are employed. The critical heat flux is computed with Biasi or Zuber-Griffith correlations. The minimum film boiling temperature is calculated with Groeneveld-Stewart correlation.

The interfacial heat transfer is calculated separately for gas and liquid (8). In case of the gas the heat transfer is calculated with Lee-Ryley correlation. The condensation heat transfer for liquid is obtained by Shah correlation. The liquid vaporization is computed with the exponent formula as a function of void fraction.

3. LOFT MODEL OF APROS

The LOFT facility is a scaled pressurized water reactor owned by Idaho National Engineering Laboratory. The LOFT facility is equipped with a nuclear core of 50 MW thermal power. The facility consists of a reactor vessel, an intact loop including a U-tube steam generator, a pressurizer and two primary pumps in parallel, a broken loop and an emergency core coolant system.

During the period 1976 ... 1990 seventy transients were performed by LOFT facility. The selected case LP-SB-3 is a small break LOCA. The experiment was conducted on 5th of March 1984.

The LOFT facility nodalization scheme used in the APROS calculations is shown in Figure 1. The input data of the model is based on the References (9) and (10). The LOFT facility model of APROS consists of pipes, pumps, valves, a pressurizer, a core and a steam generator. These components can be automatically divided into the desired amount of the nodes and branches on the calculation level. The total number of nodes in the model is 184.

The APROS model of the LOFT facility contains several control systems. The steam generator water level was controlled by the main feedwater valve. The secondary side pressure of the steam generator was controlled by two valves, - the Main Steam Control Valve (MSCV) and the Safety Relief Valve (SRV). The MSCV closes when the primary pressure is less than 14.19 MPa.

The core has been modelled with 12 nodes, the pressurizer with 10 nodes and the steam generator with 16 nodes - 4 nodes on the primary side and 12 nodes on the secondary side. The reactor vessel model (Figure 2) consists of the downcomer, the lower plenum, the core, the core bypass, the core support structure, the reactor bypass and the upper plenum.

The LOFT reactor pressure vessel has six different by-passes. In the APROS model six by-passes

were modelled with two lines - one core by-pass line and the other line from the hot leg inlet to the pressure vessel downcomer (Figure 2). The amount of the mass flow through the by-passes was about 5% of the intact loop flow at the steady-state condition.

The Emergency Core Coolant (ECC) system consists of an accumulator, a High-Pressure Injection System (HPIS) and a Low-Pressure Injection System (LPIS). The ECC system was modelled in APROS as an external node.

In Figure 3 the break nozzle and the nodalizations are shown. In order to get the better results for the break mass flow the different nodalizations of the break nozzle in the 6-equation model calculation were considered.

4. OVERVIEW OF THE TRANSIENT

The main parameters of the steady-state conditions in the experiment initial state were carefully adjusted to meet the measurement data as seen in Table 1.

Table 1: Steady-state parameters for experiment LP-SB-3.

Quantity	Measured	5-equation model	6-equation model
Primary circuit flow (kg/s)	482.6±2.6	483.2	483.7
Pressurizer primary (MPa)	15.26±0.1	15.22	15.22
Hot Leg temperature (°C)	303.6±1	302.8	303.6
Cold Leg temperature (°C)	283.6±1	283.5	284.3
ΔT over reactor vessel (°C)	20.0	19.3	19.3
Reactor thermal power (MW)	50.3±1.2	50.0	50.0
Secondary pressure (MPa)	5.58±.06	5.6	5.55
Secondary steam flow (kg/s)	26.67±.77	26.42	25.88
Pressurizer water level (m)	1.115±.06	1.121	1.105

The calculated ΔT over reactor vessel deviates 0.7 °C from the measured value. With the aid of the energy balance it was discovered that the measured temperature difference and the mass flow do not correspond to the measured reactor power. The measurement uncertainties are expected to be the reason for the deviation.

The primary circuit pumps were tripped at 1600 s. Thereafter, the break mass flow decreased to 0.5 kg/s. Later on both the primary and the secondary pressures started to decrease gradually. The break was isolated in the experiment when the maximum cladding temperature rose to 562 °C at 4742 seconds. In the calculation the lower limit for the break isolation was used because only the average core was simulated. The cladding temperature increase in the average core was estimated to be 75% of the cladding temperature increase in the high power core. After the isolation of the break the primary pressure showed some increase till the steam generator feed and bleed was initiated.

The reactor thermal power decreased as a function of the time as presented in Table 2. The

break occurred at 0 seconds. and the reactor scram took place at 9.2 seconds when the primary pressure decreased to 14.19 MPa.

Table 2: Reactor thermal power

Time s	Power (MW)	Power %
0 - x	50	100
20	2.3	4.6
32	1.85	3.7
70	1.5	3.0
170	1.2	2.4
2000	0.625	1.25
4000	0.46	0.92
5600	0.4	0.8
7000	0.35	0.7

x = time for reactor scram

5. RESULTS

A general view on the transient and the calculation results can be seen in the Table 3. In the table the main events of the transient have been presented and the APROS results have been compared to the measured data.

Table 3: Chronology of events for experiment LP-SB-3.

Event	Measured value (s)	APROS 5-eq. (s)	APROS 6-eq. (s)
Small break	0.0	0.0	0.0
Reactor scrammed (PP = 14.19 MPa)	9.21	12.2	14.5
Main feedwater shut off	9.41	12.2	14.5
MSCV start to close	9.5	12.2	14.5
Pressurizer water level below indication	67.0	70.0	78.0
First time MSCV open	87.5	75.0	70.0
Subcooled blowdown ended	98.5	178.0	155.0
Last time MSCV open	1030.	1060.	1133.
Primary coolant pumps tripped (PSI = 2800kg)	1600.	1594.	1603.
Core start heatup	3800. ±50	4240.	4497.
Break isolated (MCT = 562 °C)	4742.	4848.*	4910.*
Steam generator feed and bleed initiated (MCT = 712 °C)	5415.	5110.*	5152.*
Maximum cladding temperature	5422.	5110.	5166.
Accumulator injection initiated (PP = 2,79 MPa)	5558.	5360.	5327.
Low pressure injection initiated (PP = 1,03MPa)	6785.	6680.	6605.
Experiment terminated	6845.	6890.	6900.

PSI = Primary System Inventory
MCT = Maximum Cladding Temp.
PP = Primary Pressure
* = Average Cladding Temp. (ACT)

Because of the small leak the total simulation time was relatively long, about 7000 seconds. The computer process unit times are 2800 s for the 5-equation model and 55000 s for the 6-equation model (HP 9000/735). The maximum time step was limited to 0.05 seconds.

Primary and secondary pressure

The primary and secondary pressures have been presented in Figures 4 and 5. In the short term plot (Figure 4) two calculated curves of the 6-equation model have been shown. The letters (a and b) refer to the different nodalizations of the break nozzle in Figure 3. In Figure 5 the pressures for long term plot (0 ... 7000 s) are shown. The pressure behavior of the calculated by the 5-equation model was close to that of the 6-equation model.

The behavior of the secondary pressure from 0 to 2000 s is shown in Figure 6. The steam flow through MSCV and the decay heat removal from the primary circuit had a large effect on the secondary pressure. The MSCV opened when the secondary pressure increased to 7.09 MPa and closed when the pressure decreased to 6.5 MPa. The MSCV opened and closed during this experiment four times as shown in Figure 6. In addition the MSCV leaked even at the closed position although it was not mentioned in the experiment reports. The estimation for the leakage at different points was between 200-350 g/s.

In general the behavior of the primary and secondary pressures was predicted right by both APROS models. The primary pressure was too high during the first 100 seconds, because of the too low break mass flow. Better results for the primary pressure with the 6-equation model were obtained when the more accurate nodalization for the break nozzle was used.

Break mass flow

The break was initiated at 0 second in the intact loop cold leg. The break mass flow is presented in Figure 7. The maximum break mass flow was 6.7 kg/s in the experiment, while 6.3 kg/s in case of the 5-equation model and 5.4 kg/s in case of the 6-equation model.

In the parametric study it was found that the nodalization of the break nozzle has a large effect on the break mass flow. In this calculation the nodalization type (a) was considered. Later on the calculation of the first 175 seconds was repeated with a nodalization type (b) and the maximum break flow was then 6.7 kg/s. The results in case (b) were much closer to the measurement data.

In the first 100 seconds the flow was subcooled. The leak mass flow dropped to 2.5 kg/s within the first 200 seconds and thereafter a slight decrease occurred in the leak mass flow till the pumps were tripped. After that the leak mass flow consisted of almost pure steam and decreased to about 0.5 kg/s.

Primary system inventory

Figure 8 presents a comparison of the primary system mass inventories. At the steady-state the total mass inventory of the primary system was 5650 kg.

During the first 1000 seconds the calculated mass inventories were higher than the measured value, because the calculated break mass flows were too low. After the isolation of the break most of the water was in the lower node of the reactor vessel, in the loop seal of the primary circuit pumps and on the cold side of the steam generator.

The primary system inventory increased later on, which was due to the injected water from the

accumulator and the LPIS. As a whole the mass inventory was predicted by both models satisfactory.

Mixture density in the intact loop hot leg

In Figure 9 the measured and calculated mixture densities of the intact loop hot leg are compared. At the steady-state the mixture density was about 720 kg/m^3. It can be observed that the calculated densities are higher than the measured density during the first 1600 seconds.

After the stop of the primary circuit pumps a strong decreasing in the density was observed in the measurement and in the simulation results. Thereafter the density increased clearly in the measurement and in the case of 6-equation model. The reason for that was that the fluid was not able to flow thought the steam generator, but it stratified in the hot leg. At the same time the water started to flow from the broken loop hot leg to the intact loop hot leg. The measured density dropped to 20 kg/m^3 at 2300 seconds. The corresponding value was reached by the 5-equation model at 2800 seconds and by 6-equation model at about 3000 seconds.

At the end of the transient the density began to increase again in the hot leg of the intact loop. That was due to the accumulator and LPIS, which injected water into the intact loop cold leg.

Mixture density in the intact loop cold leg

The measured middle beam and calculated densities in the intact loop cold leg are shown in Figure 10. At the steady-state the density was about 757 kg/m^3.

When the break was initiated the density started to decrease slightly till the primary circuit pumps were tripped after 1600 seconds. Too high density was predicted during the running of the pumps. Just before the stopping of the pumps the measured density was 300 kg/m^3 and the calculated density about 480 kg/m^3. The densities decreased sharply after the stopping of the pumps. Thereafter the density increased somewhat, which was due to the drain of the water from the descending tubes of the steam generator into the loop seal.

The 6-equation model exaggerated the density increase while the 5-equation model underestimated the increase. Later on the density started to increase when the ECC system injected water into the cold leg of the intact loop. As a whole the trends of the intact loop cold leg densities are quite well predicted by both models of APROS.

Mass flow in the intact loop

Figure 11 illustrates the mass flow in the intact loop. It can be seen that the calculated mass flows were too high as long as the pumps were running.

In order to find out the reason to the too high mass flow two different pump curves were considered. In the first calculation the default pump curves were used. The default curves are calculated on the basis of the specific rotation speed. In the second case the LOFT pump data was employed, but almost no difference was detected in the calculations. The pump model seems not to be sufficient to treat two-phase flow even if the two-phase characteristics are used. One deficiency in the model is that only the state before and after the pump are used and not the state inside the pump.

Cladding temperature

The comparison of the cladding temperature at different heights in the core has been presented in Figures 12 and 13. The cladding temperatures were measured at the high power region, while APROS calculates the radially average cladding temperatures. Therefore the calculated

cladding temperature did not rise so early and high as it did in the experiment. The better results can be obtained if the core is divided into several parallel channels with different decay heat power.

6. CONCLUSION

The small size break was calculated with APROS using both 5- and 6-equation thermal-hydraulic one-dimensional models.

The most interesting parameters were the primary and secondary pressures, break mass flow, primary circuit mass inventory, intact loop hot and cold leg mixture densities, intact loop mass flow and cladding temperatures. The calculated parameters were compared to the real measurement data.

There is a strong dependence between the break mass flow rate and the primary circuit pressure. In the calculation the break mass flow was somewhat smaller at the beginning of the transient. Therefore the pressure was higher and as a consequence the reactor scram was delayed. Better results were obtained when the more accurate nodalization for the break nozzle was used.

The calculated density was greater than the measured density in the hot and cold legs of the intact loop as well as in the break pipe. That was probably due to too low break flow at the early phase of the transient, and later due to too high mass flow, which was caused by the pump model. The differences of the calculated results between the 5- and 6-equation models were not large. After the pump trip the 6-equation model predicted higher densities in the cold and hot legs than the 5-equation model. This was probably related to the drift-flux and interfacial friction correlations used in the models.

APROS showed a lower cladding temperature than the measured data. One reason to this was that the measurements were at the high power core region, while in the calculation the average values were was simulated.

The information of the transient presented on the plant facility document was not enough. Because of that the estimation was made on the steam leak through the closed MSCV. Also the average cladding temperature was estimated by the maximum cladding temperature. All these estimations had some effect on the calculated results.

APROS was capable to calculate the transient with both thermal-hydraulic models. The calculations showed a reasonable agreement with the measurement data in relation to primary and secondary pressures, break mass flow, intact loop mass flow, primary system inventory, cladding temperature and density.

7. ACKNOWLEDGMENT

The authors wish to thank Imatran Voima (IVO) for the financial support.

8. NOMENCLATURE

In the paper the following notations have been used.

A = flow area, m^2
h = specific enthalpy, J/kg
p = pressure, Pa
q = heat flow, W/m^3
u = velocity, m/s
ρ = density, kg/m^3
$\bar{g}$ = gravitational acceleration, m/s^2
α = void fraction
F = friction, N/m^3
Γ = evap. or condensing mass flow, $kg/s\ m^3$
λ = friction factor
Re = Reynolds number

9. REFERENCES

(1) E. Silvennoinen, K. Juslin, M. Hänninen, O. Tiihonen, J. Kurki, K. Porkholm, "The APROS software for process simulation and model development", Research report of Technical Research Centre of Finland, 106p. + app 19 p. ISBN 951-38-3463-8 (1989).

(2) E. Puska, M. Saarinen, K. Porkholm, "APROS nuclear plant analyzer", 2nd European Nuclear Simulation Symposium, Schliersee, 22-24 October 1990, Berlin/Heidelberg: ASIMUTH, Applied Simulation Technology GmbH. Pp. 193-204 (1990).

(3) M. Hänninen, "A solution of one-dimensional flow and heat transfer processes with difference method", Thesis for the degree of Licentiate of Technology in Lappeenranta University of Technology, Department of Energy Technology, 1989.

(4) A. Hämäläinen, J. Miettinen, "SMABRE system models and numerical methods", Technical Research Centre of Finland, Nuclear Engineering Laboratory, 30.3.1992.

(5) M. Hänninen, J. Ylijoki, "The one dimensional two-fluid model of APROS", technical report of Technical Research Centre of Finland, 75p. HOHTI-2/92 (1992).

(6) T. Siikonen, "Numerical method for one-dimensional two-phase flow", Numerical Heat Transfer, vol. 12, pp. 1-18, (1987).

(7) J. Miettinen, "Main feature of the SMABRE code, version 4.2", technical report of Technical Research Centre of Finland, report No: VAHTI-01/95, 20p, (1995).

(8) D. Bestion, "Physical closure laws in the CATHARE code", Nuclear Engineering and Design, and Resent Developments on Interfacial Friction Models, European two-phase group meeting, Varese 21-24 (1990).

(9) J. C. Birchley, "LOFT Input Dataset Reference Document for RELAP5 Validation Studies", Winfrith Technology Center, United Kingdom Atomic Energy Authority, Dorkchester, Doreset, DT2 8DH, UK, (NUREG/IA-0072 AEEW- R2454), (1992).

(10) Douglas L. Reeder, "LOFT system and test description", (5.5-FT Nuclear Core 1 LOCES), Idaho National Engineering Laboratory, Department of Energy, NUREG/CR-0247, TREE-1208 (1987).

(11) S. Guntay, "RELAP5/MOD2 Assessment, OECD-LOFT Small Break Experiment LP-SB-03", Paul Scherrer Institute, CH-5303 Wurenlingen, Switzerland, NUREG/IA-0018, (1990).

(12) M. D. Peters, M. Tanaka, P. Marsili, "Experiment specification summary for OECD LOFT experiment LP-SB-3", EG&G Idaho, Inc. Idaho Falls, Idaho 83415, OECD LOFT-T-3601 (1983).

(13) W. H. Grush, M. Tanaka, P.Marsili, "Best estimate prediction for the OECD LOFT project small cold leg break experiment LP-SB-3", EG&G Idaho, Inc. Idaho Fals, Idaho 83415, OECD LOFT-T-3603, (1984).

(14) M. Tanaka, W. H. Grush, P. Marsili, N. Newman, M. D. Peteras, "Quick-look report on OECD LOFT experiment LP-SB-3", EG&G Idaho, Inc. Idaho Falls, Idaho 83415, OECD LOFT-T-3604, (1984).

(15) A. Alemberti, "Experimental analysis and summary on OECD LOFT experiment LP-SB-3", Ansaldo S.p.A., Genova, Italy, OECD LOFT-T-3605, (1985).

(16) A. Alemberti, "Comparison report on OECD LOFT experiment LP-SB-3", Ansaldo S.p.A., Genova, Italy, OECD LOFT-T-3606, (1987).

(17) S. Al-Falahi, M. Hänninen, A. Jahkola, "Analysis of Medium Size Cold Leg Break in Pressurized Water Reactor by Using APROS", Proc 36th SIMS'94 Simulation Conference Stockholm, Sweden, pp.185-191 (1994).

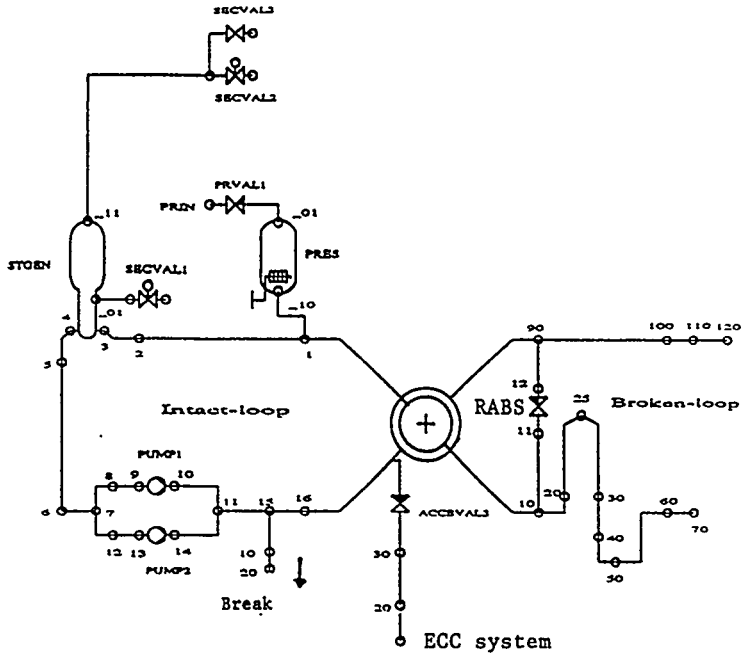


Figure 1: APROS scheme of the LOFT falcility.

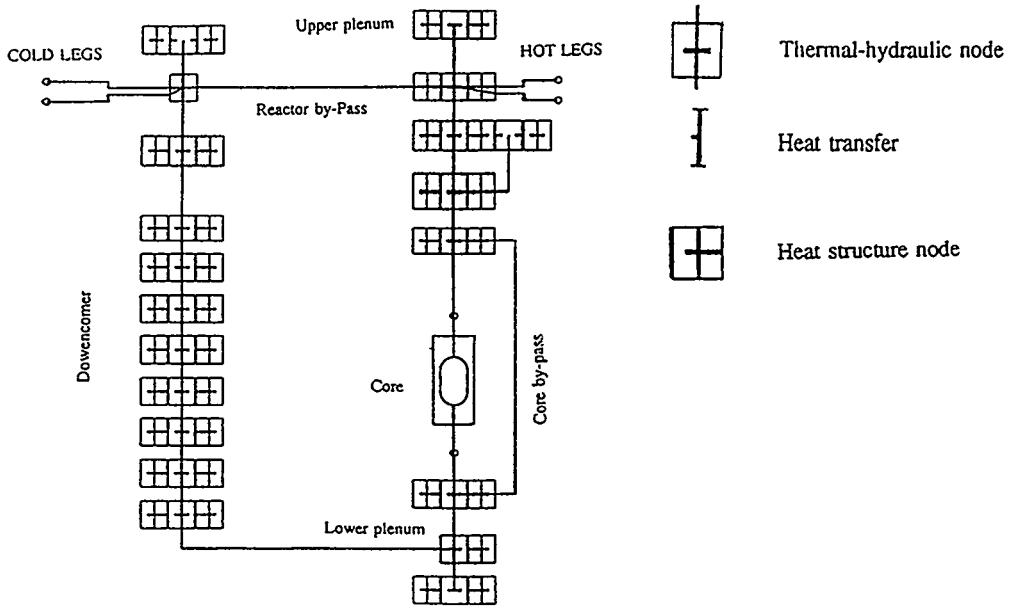


Figure 2: APROS nodalization for reactor vessel.

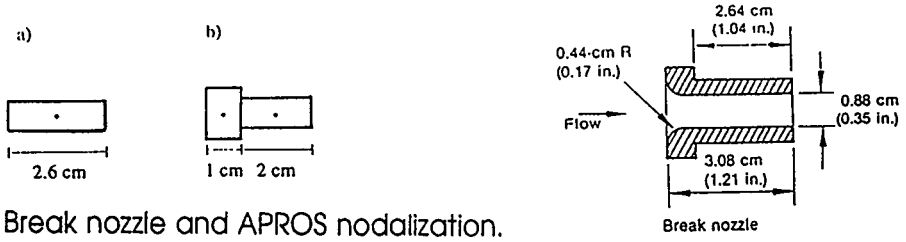


Figure 3: Break nozzle and APROS nodalization.

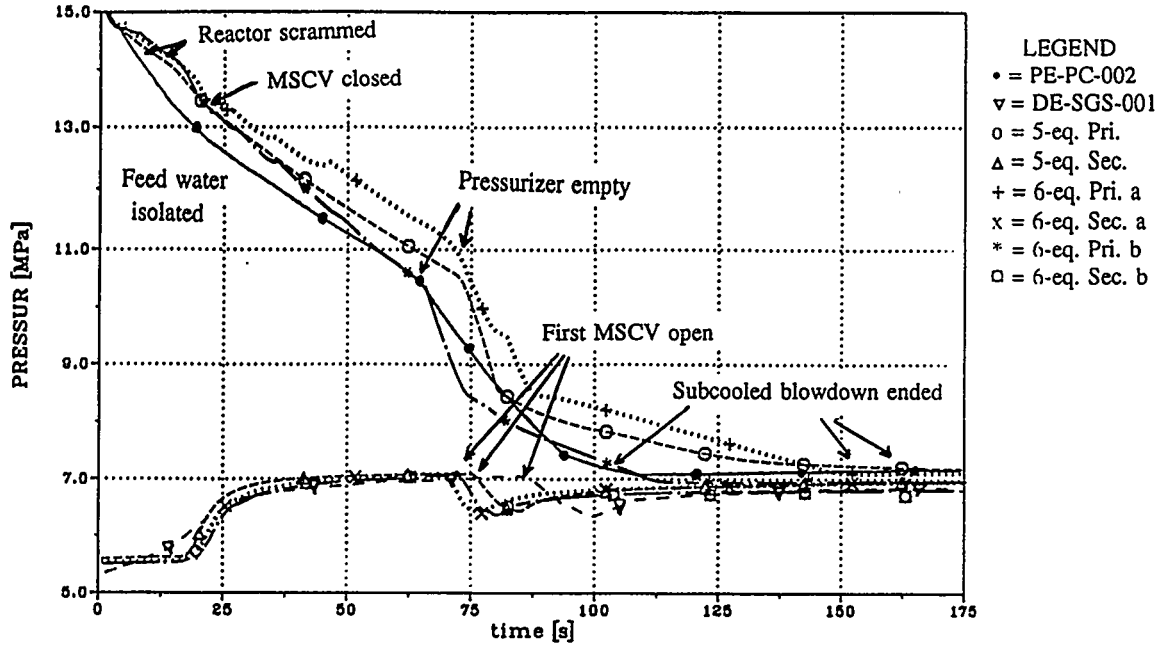


Figure 4: Primary and secondary pressures.

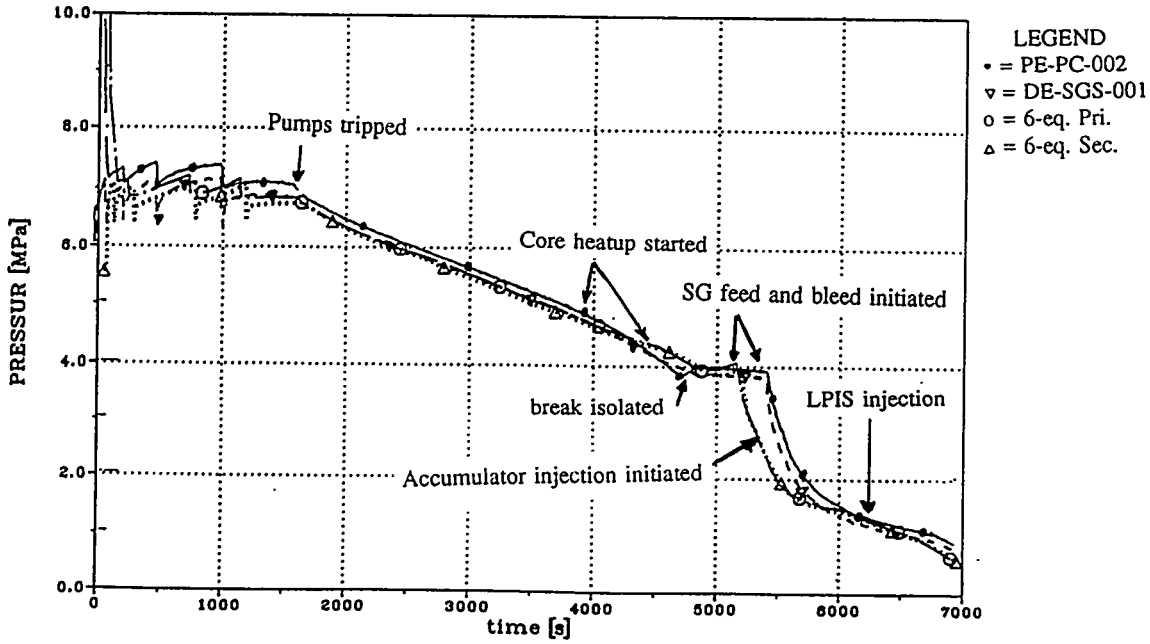


Figure 5: Primary and secondary pressures.

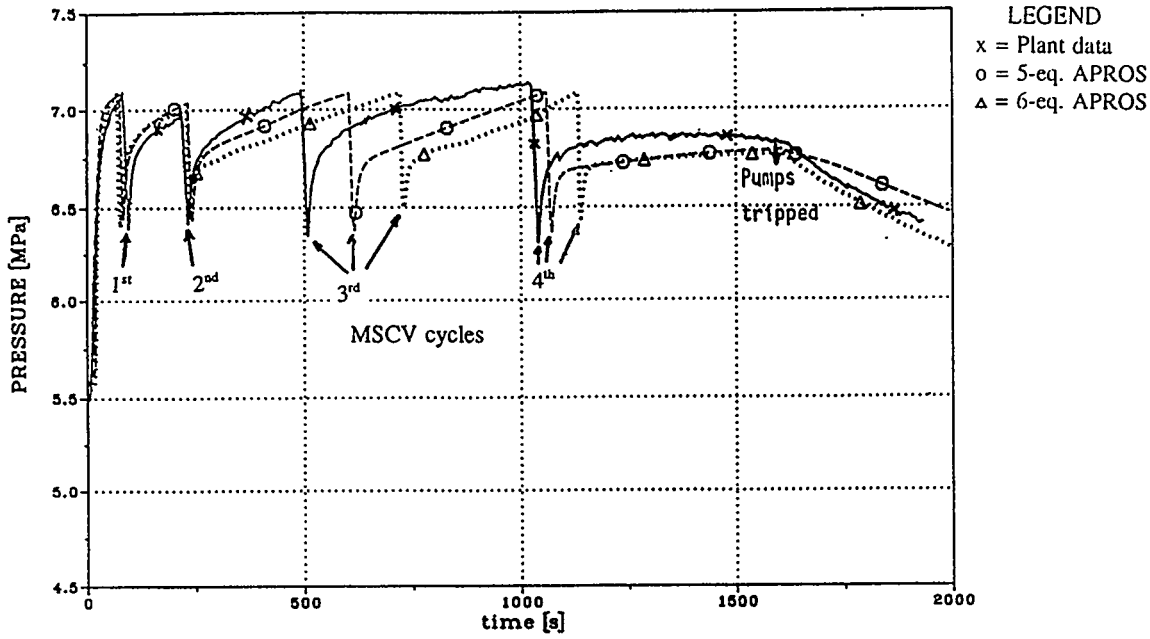


Figure 6: Secondary pressure.

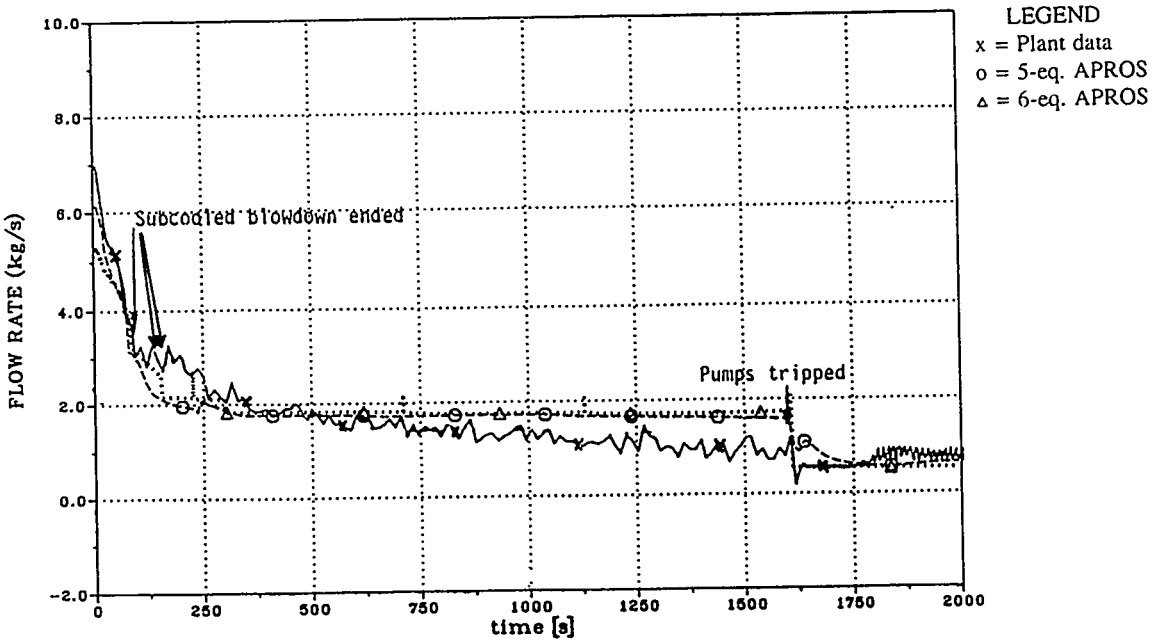


Figure 7: Break mass flow.

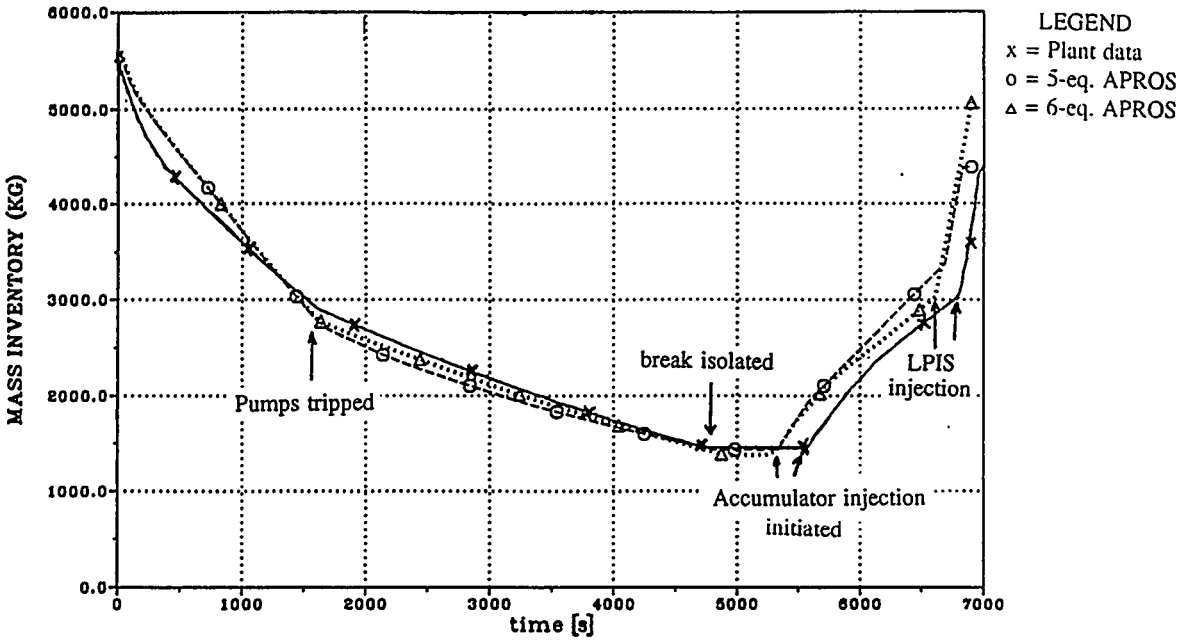


Figure 8: Primary system mass inventory.

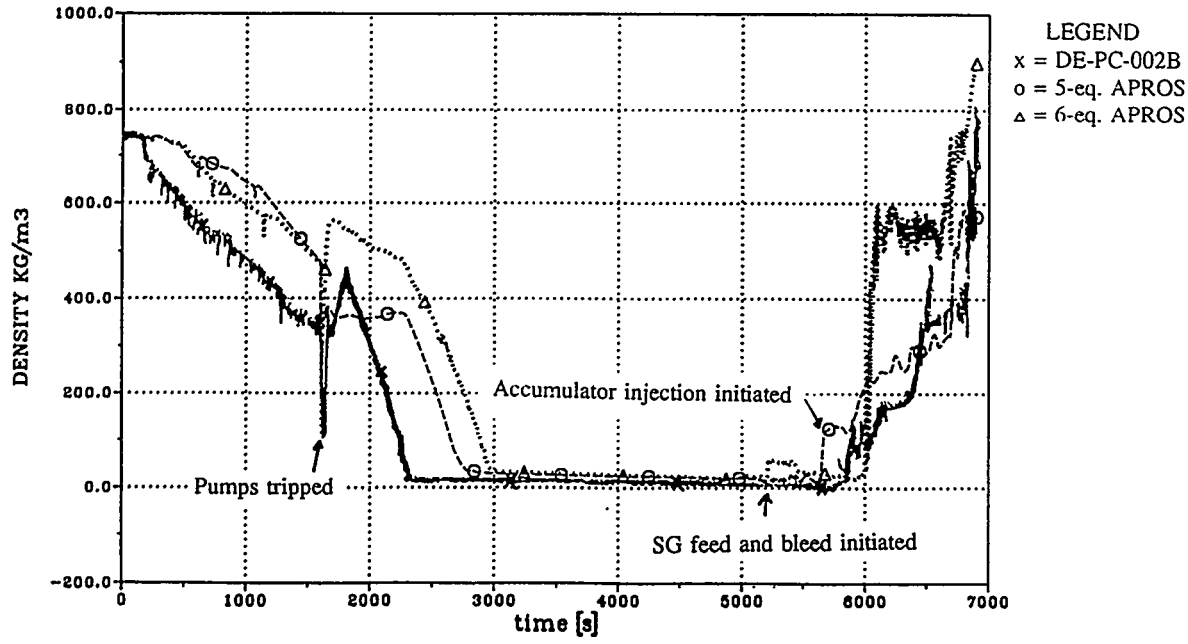


Figure 9: Mixture density in the intact loop hot leg.

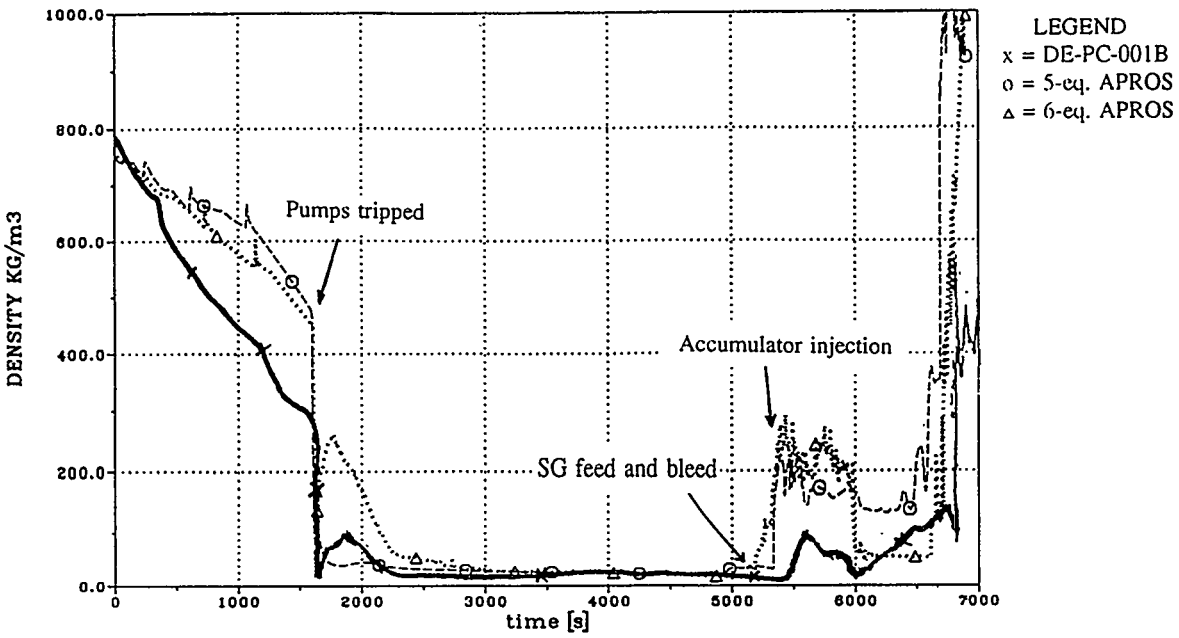


Figure 10: Mixture density in the intact loop cold leg.

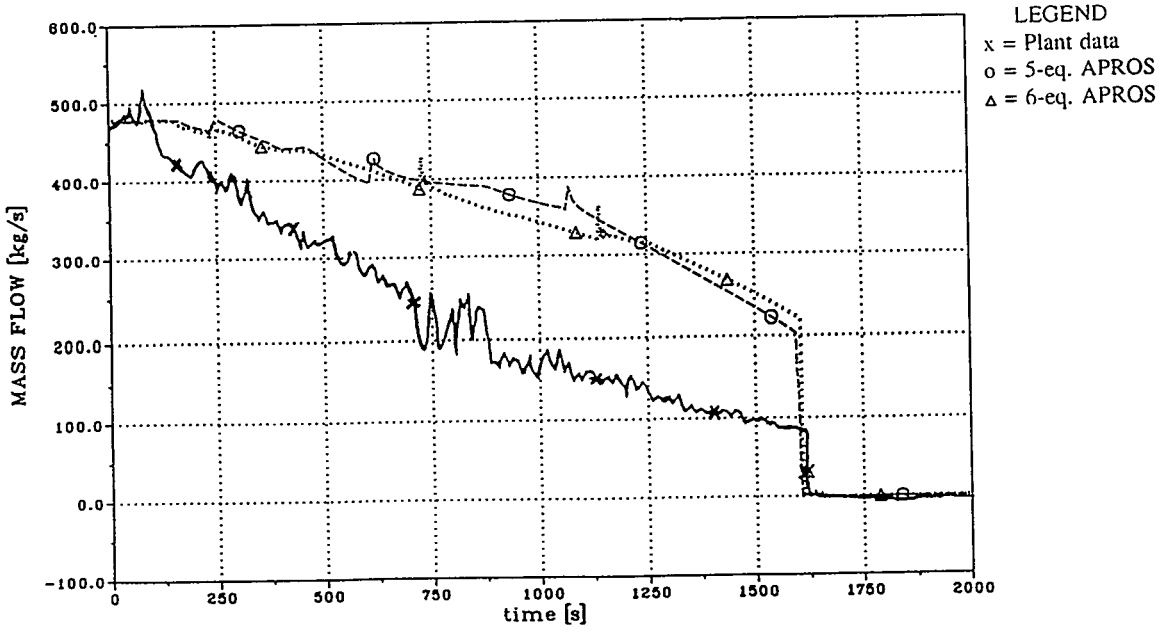


Figure 11: Mass flow in the intact loop.

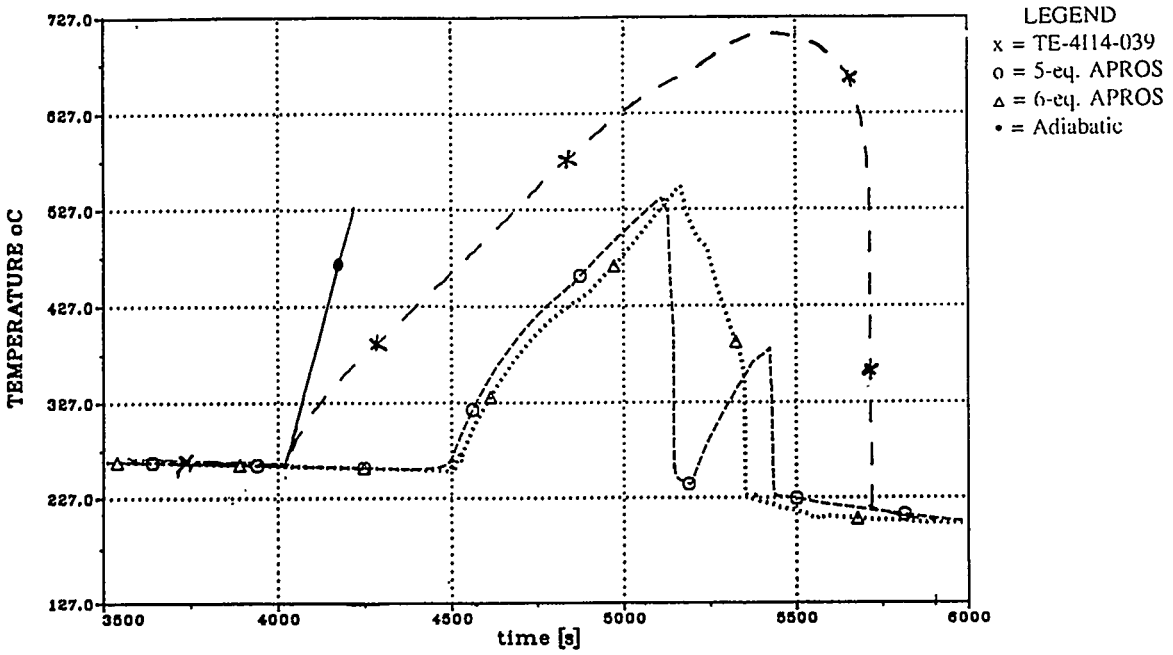


Figure 12: Cladding temperature at the 8th node = 102cm.

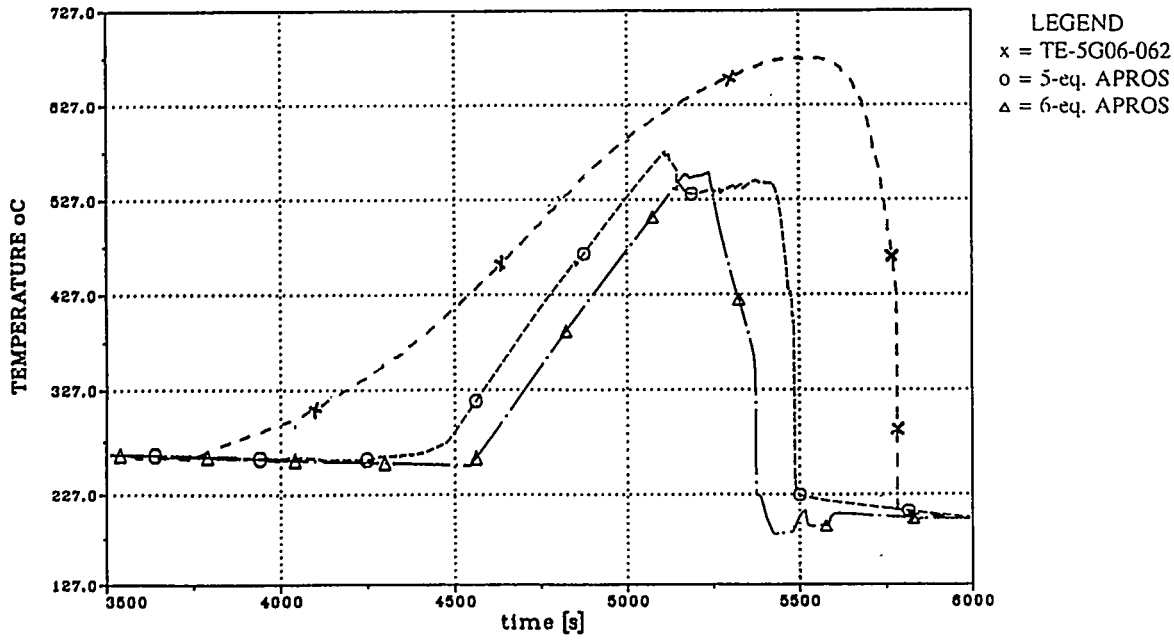


Figure 13: Cladding temperature at the 11th node = 157cm.

EVALUATION AND ASSESSMENT OF REFLOODING MODELS IN RELAP5/MOD2.5 AND RELAP5/MOD3 CODES USING LEHIGH UNIVERSITY AND PSI-NEPTUN BUNDLE EXPERIMENTAL DATA

M. Sencar* and N. Aksan

Paul Scherrer Institute (PSI),
Laboratory for Thermal-Hydraulics,
CH-5232 Villigen PSI,
Switzerland
* Presently at: COLENCO Power Consulting AG, 5405 Baden

ABSTRACT

An extensive analysis and assessment work on reflooding models of RELAP5/Mod2.5 and, RELAP5/Mod3/v5m5 and RELAP5/Mod3/v7j have been performed. Experimental data from Lehigh University and PSI-NEPTUN bundle reflooding experiments have been used for the assessment, since both of these tests cover a broad range of initial conditions. Within the range of these initial conditions, it was tried to identify their separate impacts on the calculated results. A total of six Lehigh University reflooding bundle tests and two PSI-NEPTUN tests with bounding initial conditions are selected for the analysis.

Detailed nodalisation studies both for hydraulic and conduction heat transfer were done. On the basis of the results obtained from these cases, a base nodalisation scheme was established. All the other analysis work was then performed by using this base nodalisation. RELAP5/Mod2.5 results do not change with renodalisation but RELAP5/Mod3 results are more sensitive to renodalisation.

The results of RELAP5/Mod2.5 calculations include the main hydraulic and heat transfer phenomena sequences for reflooding. Both of the RELAP5/Mod3 versions show very large deviations from the used experimental data. These results indicate that some of the phenomenology of the events occuring during the reflooding could not be identified. In the paper, detailed discussions on the main reasons of the deviations from the experimental data will be presented. Since, the results and findings of this study are meant to be a developmental aid, some recommendations have been drawn and some of these have already been implemented at PSI with promising results.

1 INTRODUCTION

This paper summarizes an extensive work performed at Laboratory for Thermohydraulics (LTH) of Paul Scherrer Institute (PSI) for code assessment purposes. This is a continuation of the previous code assessment work which was performed with RELAP5/MOD2 (ref. [1]) and some of the modifications, suggested in the cited reference, are included into the latest frozen version of RELAP5/MOD2, henceforth referenced as RELAP5/MOD2.5. A lot of verification work has already been performed with RELAP5/MOD2 at PSI and internationally. Based on these assessment works, some model changes have been introduced into RELAP5/MOD3 code and in its first released version v5m5 it was delivered to PSI in 1991. Some preliminary results obtained with this version were reported in [2]. Since then a new version of the code, v7j Beta Test version has been delivered. They both have been used for reflooding calculations of Lehigh University and PSI - NEPTUN tests and the results were compared to the experimental data and to the earlier calculations obtained by RELAP5/MOD2.5.

Among several experimental data available Lehigh University and PSI–NEPTUN reflooding experiments have been selected, they cover a broad range of initial conditions. Within the range of these initial conditions, it was tried to identify their separate impacts on the results.

The next sections provide some details of the code versions used, calculations and analysis of Lehigh University and NEPTUN bundle reflooding tests with evaluation of the results. Finally, conclusions drawn as a result of this work will be presented.

The results and findings of this work are meant to be a developmental aid, on the basis of which some recommendations for further development of the code can be done (and some have already been done, [4] and [5]) in terms of which models cause the main deviations from the experimental data and therefore main effort should be put on.

2 DESCRIPTION OF THE CODES USED FOR THE CALCULATIONS

All the calculations have been performed by the use of 3 codes: RELAP5/MOD2.5, RELAP5/MOD3/v5m5 and RELAP5/MOD3/v7j.

RELAP5/MOD2.5 is the latest frozen version of RELAP5/MOD2 cycle 36.05 which contains Bestion interfacial shear correlation for rod bundles. Its models are described in detail [6], [7] and [8].

RELAP5/MOD3/v5m5 is the first officially released version of RELAP5/MOD3 code which was delivered to PSI in the year 1991. Its internal models are different to RELAP5/MOD2, there is a single heat transfer package aimed at predicting all phases, including reflooding. There is no special reflooding heat transfer package, as in RELAP5/MOD2. A mathematical description of its models is given in [10] and explained in [11]. The first results obtained at PSI with this code were reported in [2].

RELAP5/MOD3/v7j is so called 'Beta Test version' of the code which was delivered to PSI in 1992. According to its authors a lot of coding errors of the previous versions were eliminated though there were no changes done in its internal models. A part of the results obtained by use of this code have been shown in [3]. This version of the code is very similar to RELAP5/Mod3.1 which is the latest available frozen version of the code to PSI, since october 1994.

3 DESCRIPTION OF LEHIGH UNIVERSITY EXPERIMENTS

Institute for Thermo-Fluid Engineering and Science of Lehigh University, USA, has designed and constructed a 9 rod bundle experimental facility for the purposes of thermohydrodynamic research. Its circuit is shown in figure 1. It enables three types of experiments: progressive quench front moving (reflooding), retreating quench front (boil-off) and stagnant quench front ('hot patch') experiments. The test section has been designed in a way to simulate the hydraulic conditions in a pressurized water reactor fuel bundle and the tests simulate its behaviour during different phases of a loss of coolant accident (LOCA). For the first two types of experiments only the test section needed, for the third type of experiments so called 'hot patch' is needed underneath the test section. This 'hot patch' consists of a large copper block around the housing and of 'hot rods' inside it, a continuation of test section heater rods with the same outer diameter as the test rods but different internal structure and higher power. This together enables stabilizing the quench front inside the 'hot patch' for the steady-state experiments. The test section is surrounded by a radiative shroud which compensates heat losses to the environment. At the top of the test section there is another heated ring, referenced as 'top patch' to prevent top-down quenching in the test section. The facility covers the following range of the inlet conditions ([11]):

Mass flux:	G:	0.1 - 26 $kg/m^2/s$	pressure:	p:	105 - 120 kPa
inlet quality:	x:	0. (40.K subcooled) - 0.4	heat flux:	Q:	5 - 43 kW/m^2

Although it is not typical for a reactor fuel, the axial power distribution is constant. The hydraulic conditions are very similar to those in a reactor core: rod outer diameter $d_{rod} = 9.5mm$, the solid heater rods are configured in a 3 X 3 square pitch of $12.6mm$ and their total heated length is $1.22m$. The test solid heater rods are internally heated by using a high resistance ribbon embedded in the test section at 0.762 m elevation of the heated bundle. The facility is described in detail in [11]. The range of initial conditions is limited to low pressure (approximately atmospheric pressure) and low flooding rate and these limitations have to be taken into account in the evaluation of the results with respect to the code internal models.

There were totally 144 experimental tests performed and reported in the documentation (ref. [11]) which means there were huge amounts of data and it was necessary to reduce them and maintain their representativity.

4 CALCULATION OF LEHIGH UNIVERSITY TESTS

4.1 Calculated test matrix

There are 50 cases of the progressing quench front movement type experiments (reflooding) reported in [11], from which six were selected for our calculations. The following table shows the range of initial and boundary conditions they cover. The numbering (#) corresponds to the test documentation.

Test nr.	**Initial conditions at bundle inlet**			**Heat source**	**Estimated initial clad temperature**	**Remark**
(#)	p [kPa]	T [K] coolant	G [kg/m^{2}s]	q *10^4 [W/m^2]	T [K]	
3	101.3	352.3	13.46	2.18	819.5	
9	101.2	367.3	7.23	1.57	848.5	
12	101.3	356.6	18.48	3.12	936.5	Base case
14	101.3	311.1	18.69	3.12	921.	
20	101.3	352.0	25.13	3.16	1016.5	
22	101.3	315.2	25.58	3.17	941.5	

Table 1: Test matrix of Lehigh University reflooding tests used for RELAP5/MOD2.5 and RELAP5/MOD3 calculations

Case #12 was selected as a representative base case at which none of the inlet conditions is an extreme one. This case was used for nodalization study and analysis of the effect of variation in the maximal number of subdivisions of the moving mesh during reflooding.

4.2 Description of the nodalization scheme used

The nodalization schemes used for the calculation are shown in the figure 2. The calculated reflooding tests only request a simple nodalization scheme of the test section without models of the 'hot patches'. The inlet thermalhydraulic conditions are defined in a time-dependent volume (TDV 105) which is located at the bottom of the test section. It is connected to the test section by a time-dependent junction (TDJ 110) which defines the inlet hydrodynamic conditions (inlet flow and velocities). The test section channel is modelled as a pipe component (PIPE 120), the test section heater rod is modelled as a heat structure (HT-STR 1120). Outlet of the test section is represented by a single junction component (SNGLJUN 125) which connects channel outlet with the mass sink, another time-dependent volume (TDV 130).

Apart from the mentioned components in the input deck, one finds the power table and some additional defined control variables, e.g. for unit conversions, calculating the collapsed liquid level, entrained flow and the entrained mass (time integral of the previous parameter) which can not be compared because they have not been reported in the experimental documentation ([11]).

4.3 Study of the nodalization and the number of moving meshes

Three nodalizations have been designed to model the test section. They only differ in the number of the axial nodes and their lengths, respectively. Nodalization 1 has 11 nodes with the axial lengths between $99.mm$ and $126.mm$, nodalization 2 has 18 nodes, their lengths lie between $60.mm$ and $80.mm$ and nodalization 3 has 25 nodes of $48.8mm$ length. Nodalization 1 is designed in a way which enables a direct comparison of the calculated quantities with the measured ones, i.e. the centers of the nodes 4, 6 and 9 correspond to the main instrumentation locations (vapour probes,...). Centers of the nodes of the nodalization 1 are henceforth referenced as levels. Consequently, in the nodalizations 2 and 3 the distances between the comparison levels and centers of the nearest nodes are minimized. Nodalizations 1 and 2 have variable node lengths, only nodalization 3 has uniform node length.

The nodalization changes influence the results, particularly those of RELAP5/MOD3 (both versions). RELAP5/MOD2.5 results do not change much with renodalization, sometimes they slightly improve, sometimes they deviate from the measurements. RELAP5/MOD3 results are more sensitive to renodalization, but all of them are so far from the measured data that one cannot judge which ones are better, which is illustrated by figure 3 (it should be noted that since the quenching temperatures of the heater rods were not measured in the Lehigh University tests, the expected quench behaviour have been shown as a region of horizontal lines in the temperature history diagrams, as in this figure and experimental data are provided as a bounding field). The largest effect is observed in increased CPU-time consumption. Therefore for all the other calculations nodalization 1 has been used.

Variation of the moving mesh number resulted in a very little change of the results. When it was increased from the usually used value 16 to 32 and 64, apart from a large increase in the CPU-time consumption, the results have remained practically the same. The lack of sensitivity to fine mesh renodalization indicates that the case considered is dominated by the hydraudynamics of the nodes. Consequently the value of 16 was chosen as the moving mesh number for further calculations.

4.4 Calculated results and discussion

Calculated results are presented in form of time diagrams. Rod temperature, vapour void fraction and heat transfer coefficient at level 6 for every calculated test are shown in the figures 4 - 6 and 8 - 10. For the base case #12, additional plots are provided to illustrate the collapsed liquid level, entrained mass from the test section and also the liquid velocity at the inlet into the level 6 (figure 7).

Generally RELAP5/MOD3 results show some unusual characteristics in relation to the reflooding phenomena.

First of all, the clad temperature shows an artificially strong decrease as if the node was intensively cooled in a continuous form, but there is no clear turn-around point - quench temperature. In some cases e.g. cases #14 and #22, temperature spikes are observed as if the node started to heat up again somewhere during the cooling phase due to the film boiling and quenching. This can be observed on the surface temperature history diagrams, for highly subcooled cases. On these plots, the measurements are shown as a field within which the temperature curve is expected and, since the quenching temperatures of the heater rods were not measured with the Lehigh University tests, the expected quench behaviour have been shown as a region of horizontal lines on the temperatur history diagrams. As it can be seen from these plots, RELAP5/MOD2.5 results are close to the boundaries of the fields of the experimental data and, they show the expected phenomena such as quench front progression.

Cases #3 and #9 are of extremely low flooding rates (table 1). They both show unstable spiky curves for the calculated temperature by RELAP5/MOD3 (figures 4 and 5) and a significant change of gradients with increasing height of the node (higher levels). This dependence on the level is not noticed in the RELAP5/MOD2.5 results.

Cases #12 and #14 differ mainly in the initial coolant subcooling. This higher subcooling in the case #14 causes RELAP5/MOD3 results to behave unrealistically in the sense that the temperature curve shows some little spikes, with sudden short phases of heat up during the cooling period. This is not observed in the low subcooled case #12, figures 6(a) and 8(a).

The same can be noticed by comparing the temperature plots of the cases #20 (low) and #22 (high subcooling; the other inlet conditions are close). The temperature curves of the case #22 show spiky behaviour during film boiling and quenching phases similar to those in the case #14 whereas the low subcooled case #20 does not show such a behaviour (figures 9 and 10). In the case #22, even some calculational troubles caused the calculation to stop due to water property error at about 110s. transient time. This did not happen in RELAP5/MOD3/v5m5 nor in the RELAP5/MOD2.5 calculations.

If one compares the results of the cases #12 and #20 which differ in the flooding rate and in the initial wall temperature, one can see a change in the derivatives, intensity of the cooling is much higher in the case #20 (figures 6(a) and 9(a)). This is a consequence of different initial rod surface temperatures in the referred cases. Also a comparison between cases #14 and #22 confirms the above situation, cases #14 and #22 differ in the flooding rate, but only minimally in the initial wall temperatures. The cladding temperature histories show just a parallel shift (figures 8(a) and 10(a)). However, this is true only if the flow rates are low (as they are in the Lehigh University tests).

Concerning vapour and liquid distribution, the results also show some characteristics. In RELAP5/MOD3, void fraction histories for all cases show a strong oscillatory behaviour at the beginning of the transient, i.e. shortly before the quench front is expected to approach. There is obviously a lot of liquid introduced into the node which causes a 'valley' in the void fraction history, more or less clearly seen in every calculated case (see diagram c in the figures 4 - 6 and 8 - 10. These 'valleys' occuring during quenching are clearly markable in extremely low flooding rate cases (#3 and #9). At higher flooding rate cases, the 'valley' is not so deep (cases #12 and #20). It almost disappears in highly subcooled cases (#14 and #22). So the 'valley' becomes less visible with increasing flooding rate and increasing inlet subcooling. Large oscillations in void faction histories were also observed during the aforementioned period (i.e. in the void fraction 'valley' during quenching process). The amplitude thereof is about 0.5 and it appears in any case (except in case #22 where it is larger, but then the calculation stops due to water property error). Generally these oscillations are larger in RELAP5/MOD3/v7j than in RELAP5/MOD3/v5m5 results. After this phase, the void fractions stabilize at (or undampedly oscillate around) a steady value, typically about 60% void fraction at level 6 for most cases.

RELAP5/MOD2.5 results show far less oscillations in void fraction histories than the RELAP5/MOD3 results, and the steady value at which they finally stabilize is higher than in RELAP5/MOD3 for every calculated

case. There are no experimental data available for void fraction in Lehigh University tests. There were delta P measurements. But the results of these measurements show fairly large oscillations so that the use of this data to estimate void fraction is highly uncertain. The reason for this is that the uncertainties in frictional pressure drop masks the static pressure drop for such flow regimes of low liquid volume fractions [11].

In RELAP5/MOD3 the critical Weber number is set very high (12; in RELAP5/MOD2.5 it is 3) and consequently liquid droplet diameter is artificially kept at very high values. One of the main reasons, why the calculated vapour temperatures are always too low, they oscillate strongly and finally drop under the values obtained by RELAP5/MOD2.5. The vapour temperatures calculated by RELAP5/MOD2.5 have been found to be always too low (ref. [1], [4]).

Another point of interest is to obtain the correct mass distribution in the bundle. It is observed that too much liquid is collected in the volume nodes. This is illustrated by the calculated collapsed liquid levels (as example in the figure 7(a)) which is in any case higher than obtained by RELAP5/MOD2.5, and entrained mass out of the test section (as example in the figure 7(c)) which is always lower compared to RELAP5/MOD2.5. In RELAP5/MOD3 the collapsed liquid level oscillations are larger and the trend is stagnating after a period of increase at the beginning, whereas the RELAP5/MOD2.5 show slow increase during all of the transient time.

Consistent with this peculiar 'valleys' in the void fraction curves (RELAP5/MOD3) the heat transfer coefficient is increased very much just after the liquid is introduced into the node. This peak is significantly higher than in RELAP5/MOD2.5, as well as, the value at which it stabilizes afterwards, diagrams (b) in the figures 4 - 6 and 8 - 10. This peak is natural, i.e. phenomenologically conditioned, it has to occur when the quench front crosses the volume node. The question remains how high it has to be. The earlier studies ref. [1] and the results presented for the NEPTUN cases, later in section 5, indicate that the problem can be separated into hydro effects and heat transfer. The results considered here support that the problem is more heat transfer driven. Therefore, it is necessary to analyze the heat transfer models in some detail. In RELAP5/MOD3, Chen correlation is used in transition boiling regime, in RELAP5/MOD2.5 - reflooding module - the Weismann correlation is used. It has been shown in the references [12] and [4] that Chen correlation has a strong dependence on mass flux and the initial wall temperature, both of which influence the calculation of the heat transfer coefficient in an incorrect way. For example, the heat transfer coefficient is increased enormously at and about mass flux $G = 250 kg/m^2/s$. The calculated mass fluxes fall into this region, as it can be seen from the liquid velocity diagram in the figure 7 (b). Therefore it is believed that the nodes from the beginning are overcooled in RELAP5/MOD3. Later on during the transient, the nodes are cooled all the time in a continuous way which is a consequence of large oscillations of the critical heat flux, as stated in the ref. [4]. The same reference shows even more pathological behaviour of the temperatures, if the used Groeneveld CHF tables (MOD3) are replaced by the correlation of RELAP5/MOD2.5: in that case the temperatures do not drop under a certain level to which they asymptotically approach and it is far above the experimentally obtained steady temperature (saturation temperature). This gives indication to a sort of compensating effects within the heat transfer package in RELAP5/MOD3. It should also be noted that some of the oscillations inherent in various versions of RELAP5/MOD3 may partly be coming from the way the closure relationships are time averaged or limited.

Apart from the fact that the results obtained by RELAP5/MOD3 (both versions) show phenomenologically unexpected behaviour quite different to the experimental results, the CPU-time consumptions were also higher than for RELAP5/MOD2.5 calculations, e.g., an increase in required CPU-time by 2 - 62% for RELAP5/MOD3/v5m5 and at least 80% for RELAP5/MOD3/v7j on CRAY-YMP.

5 CALCULATION OF PSI - NEPTUN TESTS

5.1 A brief description of NEPTUN facility and selected NEPTUN tests

The NEPTUN test facility was designed and constructed at PSI to perform reflooding studies in rod bundle geometry. It is a half-length simulator of PWR fuel bundle, with $1.68m$ of heated length. It is designed to enable an axial power profile of cosine shape with a peaking factor of 1.58 as in a PWR core. There are 33 specially designed solid heater rods in the bundle, together with 4 guide tubes, all with the outer diameter $10.7mm$ and $p/d = 1.33$, simulate the geometrical characteristics of the core. There are five fuel assembly spacer grids, axially located at equal distance. The facility is described in detail in the reference [14].

The following table shows the initial conditions for the two calculated tests, a low flooding rate and a high flooding rate one. The initial conditions for the low flooding rate case(No. 5036) are close to the Lehigh University tests, apart from the pressure which is higher. Still, this test is a low flooding rate and low pressure test.

Test number	**Initial conditions at bundle inlet**			**Rod power**	**Maximal initial clad temperature**
(#)	p [kPa]	$\Delta T_{subc.}$ [K]	v [cm/s]	P [kW]	T [K]
5036	410.	11.	1.5	2.45	1030.
5050	410.	78.	15.	2.45	1140.

Table 2: Test matrix of PSI - NEPTUN reflooding tests used for RELAP5/MOD2.5 and RELAP5/MOD3 calculations

5.2 Results and discussion

For the calculations, nodalization A with 18 volumes in figure 11 has been used, the other two of them have been analyzed in the reference [1]. They have not necessarily improved the agreement of the results but they required more CPU time.

The results of NEPTUN 5036 calculation show the same characteristics as the Lehigh University tests. The temperature histories (figure 12(a)) show quenching phenomena correctly, which is missing in the RELAP5/MOD3 results (of both versions). RELAP5/MOD2.5 shows the physics of the phenomenon, though it overpredicts the time of quenching, the experimental temperature drops earlier; the quench front progresses slower than in the measurements.

In the vapour void fraction histories, the same type of decrease (a 'valley') at the beginning of the transient is found in RELAP5/MOD3 results, figure 12(b). RELAP5/MOD2.5 gives a delay relative to the measurements. but both curves show the same trends, which is not true for RELAP5/MOD3 in both versions. They also show large oscillations with higher amplitudes in the version v7j than in v5m5. The main differences are assumed to be caused by the computed heat transfer coefficients. In RELAP5/MOD3, they oscillate much more and are generally higher than in RELAP5/MOD2.5.

The collapsed liquid levels follow the experimental one, after the time of 200.s RELAP5/MOD2.5 results follow the measured increase on the contrary to RELAP5/MOD3 (in both versions). Similarly, the entrained

mass from the test section (fig. 12(c)) was computed by RELAP5/MOD2.5 closer to the experiments than RELAP5/MOD3 (again in both versions). This gives an indication to the impact of pressure: in the Lehigh University tests (p = 1.bar) the levels were always computed lower and the entrained mass higher in the RELAP5/MOD2.5 relative to RELAP5/MOD3, whereas in the NEPTUN experiments (p = 4.bar) the opposite situation is observed.

The results of PSI-NEPTUN low flooding rate experiment calculations confirm the findings of Lehigh University test calculations, namely the unexpected temperature behaviour in RELAP5/MOD3 results (in both versions). One of the main reasons is the aforementioned use of the Chen transition boiling correlation which due to its dependence on mass flux and wall temperatures strongly overpredicts the heat transfer coefficient which causes the observed node to overcool and it prevents quenching. Another problem is high oscillations of the heat flux which are partly the consequence of critical heat flux oscillations due to its dependence on the local variables (ref. [15], [4]).

For illustration, the results of a high flooding rate PSI-NEPTUN test are shown, figure 13. The temperature history of RELAP5/MOD3 show, this time, quite a good agreement with the experimental data. The transient is so fast, that the vapour void fraction histories do not show the 'valley' at the beginning of the transient so clearly as in the previous cases but large oscillations can still be noticed. Heat transfer coefficients show similar behaviour in RELAP5/MOD2.5 and RELAP5/MOD3 (both versions), they differ mainly in a time shift, they all show a peak at the time when the node is expected to quench. Additionally, RELAP5/MOD3 calculations do not indicate any distinct quench behaviour. Comparison of RELAP5/MOD3 results and the experimental data seems to be very close to each other but the cooling behaviour during film boiling region is driven by different factors with different gradients.

6 CONCLUSIONS

From the above results and discussions some general concluding remarks can be drawn. Both versions of the RELAP5/MOD3 show unphysical behaviour such as continuous cooling of the nodes without clear turn-around temperature and no quenching phenomena can be recognized. This was not the case in RELAP5/MOD2.5 calculations. It has been identified that very high heat transfer coefficients are calculated for film boiling and transition boiling regimes.

Another general characteristics of RELAP5/MOD3 results is at low pressures, the calculated collapsed liquid levels are higher and consequently coolant entrainment is lower relative to RELAP5/MOD2.5 results, which also contributes to the previously mentioned unphysical cooling.

Apart from this unexpected mass distribution within the thermohydraulic system, it is observed with RELAP5/MOD3 calculations that the vapour void fraction histories demonstrate some peculiar void fraction decrease and consequently some 'valleys' at the beginning of the transient. Furthermore, oscillations in void fractions and collapsed liquid levels in various phases of transients characterize RELAP5/MOD3 results, and their amplitudes are larger in case of v7j version. This indicates that the new correlations, introduced into enlarged scheme of flow regimes in RELAP5/MOD3, have not solved the problems RELAP5/MOD2.5 had with too high interphase drag.

Another aspect of interest is the CPU - time requirement. A markable increase has been noticed: 2 - 62% in case of v5m5 and 80 - 187% in case of v7j version of RELAP5/MOD3 relative to RELAP5/MOD2.5, for the low flooding rate tests calculated. For high flooding rate tests the increase is even larger.

The effects of some inlet conditions have been identified in RELAP5/MOD3 results:

(a) Large inlet subcooling causes spiky unstable temperature behaviour with several changes of their time derivatives for both film boiling and quenching regions.

(b) Changes in flooding rate do not change the shape of temperature histories within the range of the calculated Lehigh University tests and NEPTUN low flooding rate ones. However, NEPTUN high flooding rate case shows influence on the shape of the temperature history.

(c) Initial wall temperature affects intensity of the cooling (average time derivative).

(d) Refined nodalization changes the surface temperature behaviour qualitatively, though the results are still far from the measured data.

Effects of above mentioned changes in the inlet conditions can not be generalized but they may give indication to the RELAP5/MOD3 heat transfer package deficiencies.

The above mentioned changes in the inlet condition cause minor changes in RELAP5/MOD2.5 results which can not be identified as being consequences of one particular inlet condition variation. They follow the experimental data much closer than RELAP5/MOD3 results. Renodalization causes only a slight parallel shift in RELAP5/MOD2.5 without much effecting the occurrence sequence of phenomena.

The above listed conclusions are not case nor facility dependent, they were obtained through the calculational analyses of eight experimental tests performed on two different facilities - Lehigh University and PSI-NEPTUN facility.

For the further development of RELAP5/MOD3 code in relation to reflooding, it can be suggested:

(a) Reintroduction of Bestion correlation for the interfacial shear in bundle geometries

(b) Reintroduction of a correlation for computation of the critical heat flux or the improvement of the CHF tables currently used to prevent large oscillations

(c) Removing Chen correlation for transition boiling and replacing it by another one in which quench front location is taken into account

(d) Close examination of the time averaging and limiting process of closure relationships in various versions of the code may be needed.

Some of this work has already been done with promising results as reported in the refs. [4] and [5].

References

[1] M. Richner, G. Th. Analytis, N. Aksan: Assessment of RELAP5/MOD2, Cycle 36.02, using NEPTUN Reflooding Experimental Data; NUREG/IA-0054 (and PSI Report No. 104), October 1991.

[2] M. Sencar and S.N.Aksan: Preliminary results on the assessment of RELAP5/MOD3 code reflooding models using PSI-NEPTUN and Lehigh University bundle reflooding tests; Presented at the 7th International Code Assessment and Application Program (ICAP) Meeting, Idaho Falls, Idaho, USA, 23-25/10/1991.

[3] M. Sencar and N. Aksan: Independent Assessment of RELAP5/MOD3/v7j Beta Test Version with Lehigh University and PSI - NEPTUN Reflooding Tests and Comparison to RELAP5/MOD3/v5m5 and RELAP5/MOD2.5; Presented at the 1st Code Assessment and Maintenance Program (CAMP) Meeting at PSI, Villigen, Switzerland, 24 - 26 June 1992.

[4] G. Th. Analytis: A comparative study of the post-CHF wall heat transfer packages of the RELAP5 codes and preliminary assessment of model changes in RELAP5/MOD3/v7j; Presented at the 1st Code Assessment and Maintenance Program (CAMP) Meeting at PSI, Villigen, Switzerland, 24 - 26 June 1992.

[5] G. Th. Analytis: Development and assessment a modified version of RELAP5/MOD3; Paper to be presented at the NURETH-7, Saratoga Springs, NY, USA, September 10 - 17, 1995.

[6] V. H. Ransom et al.: RELAP5/MOD2 Code Manual; Vol.1; NUREG/CR-4312 Rev.1, March 1987.

[7] R. A. Dimena et al.: RELAP5/MOD2 Models and Correlations; NUREG/CR-5194, 1988.

[8] R. A. Riemke: Report on CCFL and interphase drag models for RELAP5/MOD3; EGG-TFM-8012 (EG&G Idaho, internal report), February 1988.

[9] K. E. Carlson et al.: RELAP5/MOD3 Code Manual Vol.III: Developmental Assessment Problems (Draft); NUREG/CR-5535, June 1990.

[10] K. E. Carlson et al.: RELAP5/MOD3 Code Manual Volume IV: Models and correlations (Draft); NUREG/CR-5535, June 1990.

[11] K. Tuzla, C. Unal, O. Badr, S. Neti, J. C. Chen: Thermodynamic Nonequilibrium in Post-Critical-Heat-Flux Boiling in a Rod Bundle; NUREG/CR-5095, June 1988, Vol.1 - 3.

[12] G. Th. Analytis: Remarks on the Three Post-CHF Wall Heat Transfer Packages of RELAP5/MOD2 and RELAP5/MOD3, AN-42-91-19, October 1991.

[13] K. Tuzla , C. Unal , J. C. Chen: An experimental study of bottom rewetting in a rod bundle geometry; Nuclear Engineering and Design 125, pp. 189 - 200; 1991.

[14] H. Grüter, F. Stierli, S. N. Aksan and G. Varadi: NEPTUN Bundle reflooding experiments: Test Facility Description; EIR Report Nr.386, 1980.

[15] G. Th. Analytis: On the unphysical pseudo-enhancement of the post-CHF heat transfer coefficient of RELAP5/MOD3 during reflooding; TM-42-92-07, PSI, 1992.

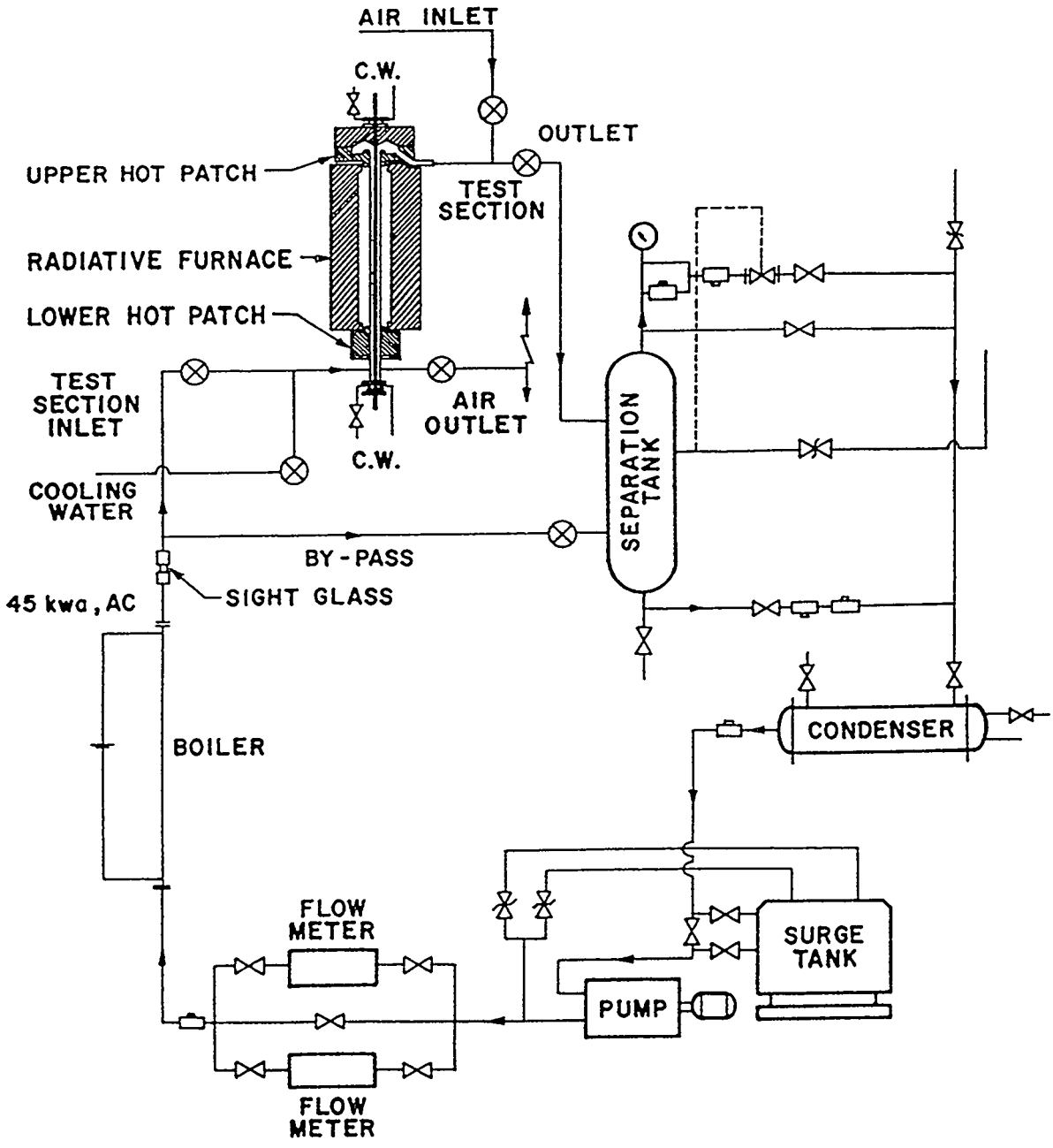


Figure 1: Lehigh University experimental device and its circuit

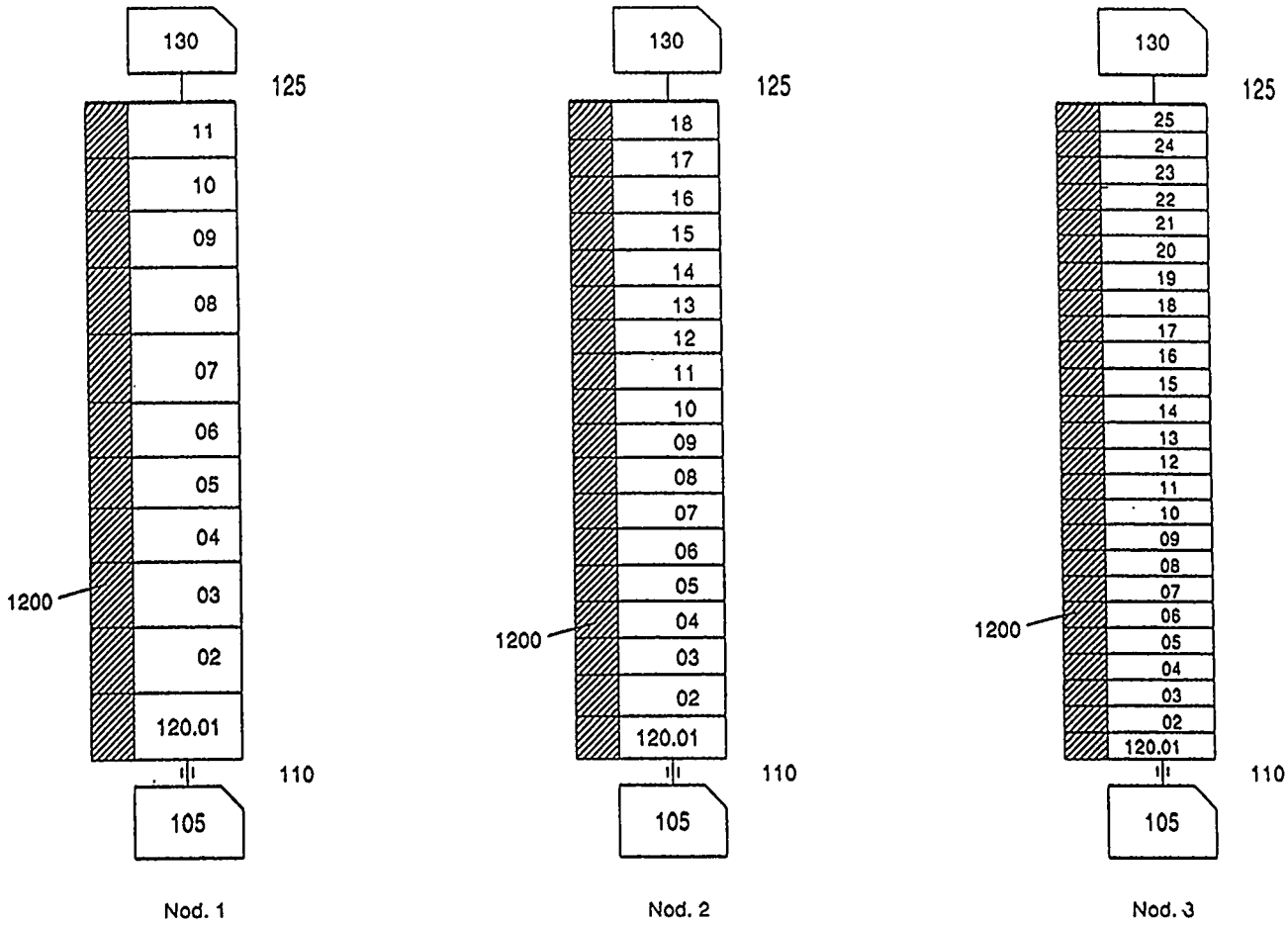
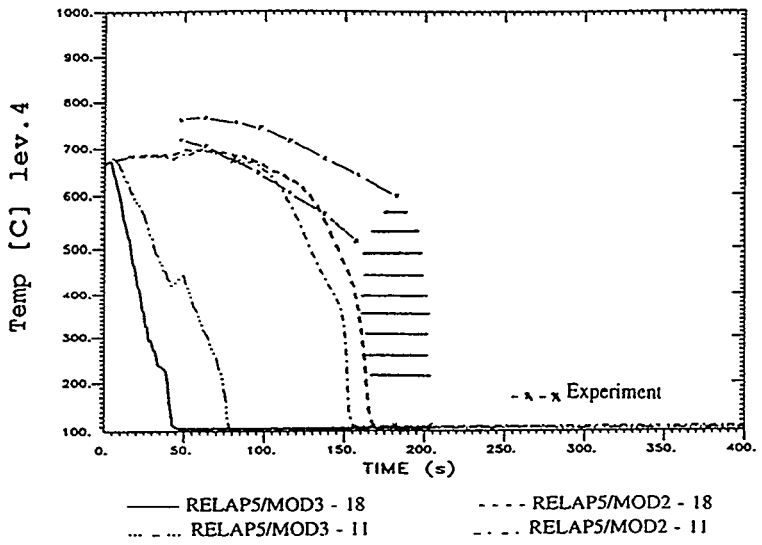
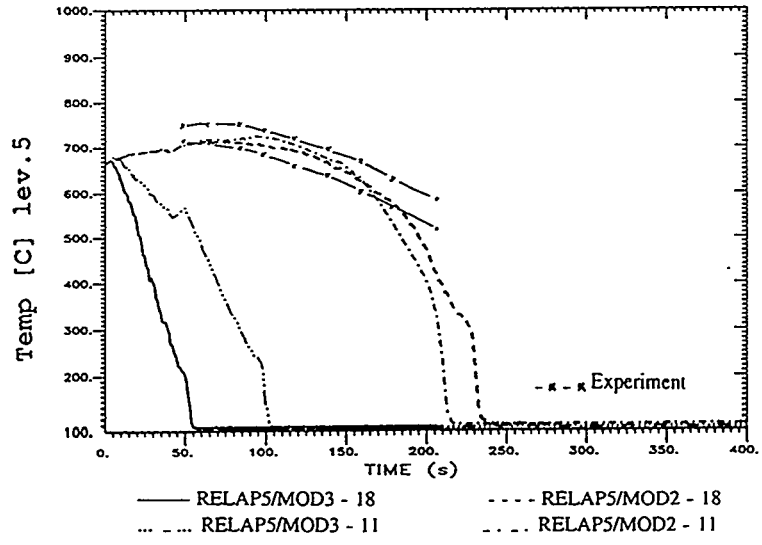


Figure 2: Nodalization schemes used for the calculations

a)



b)



c)

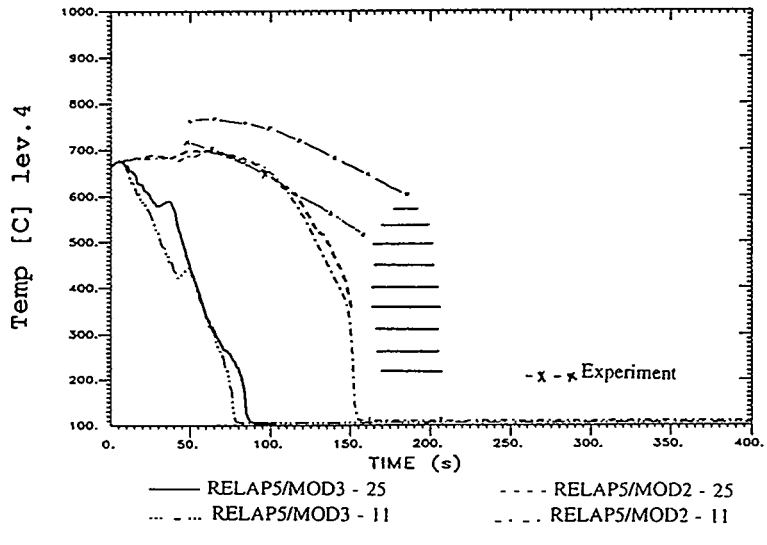


Figure 3: Nodalization study using test no. 12 (Base case)

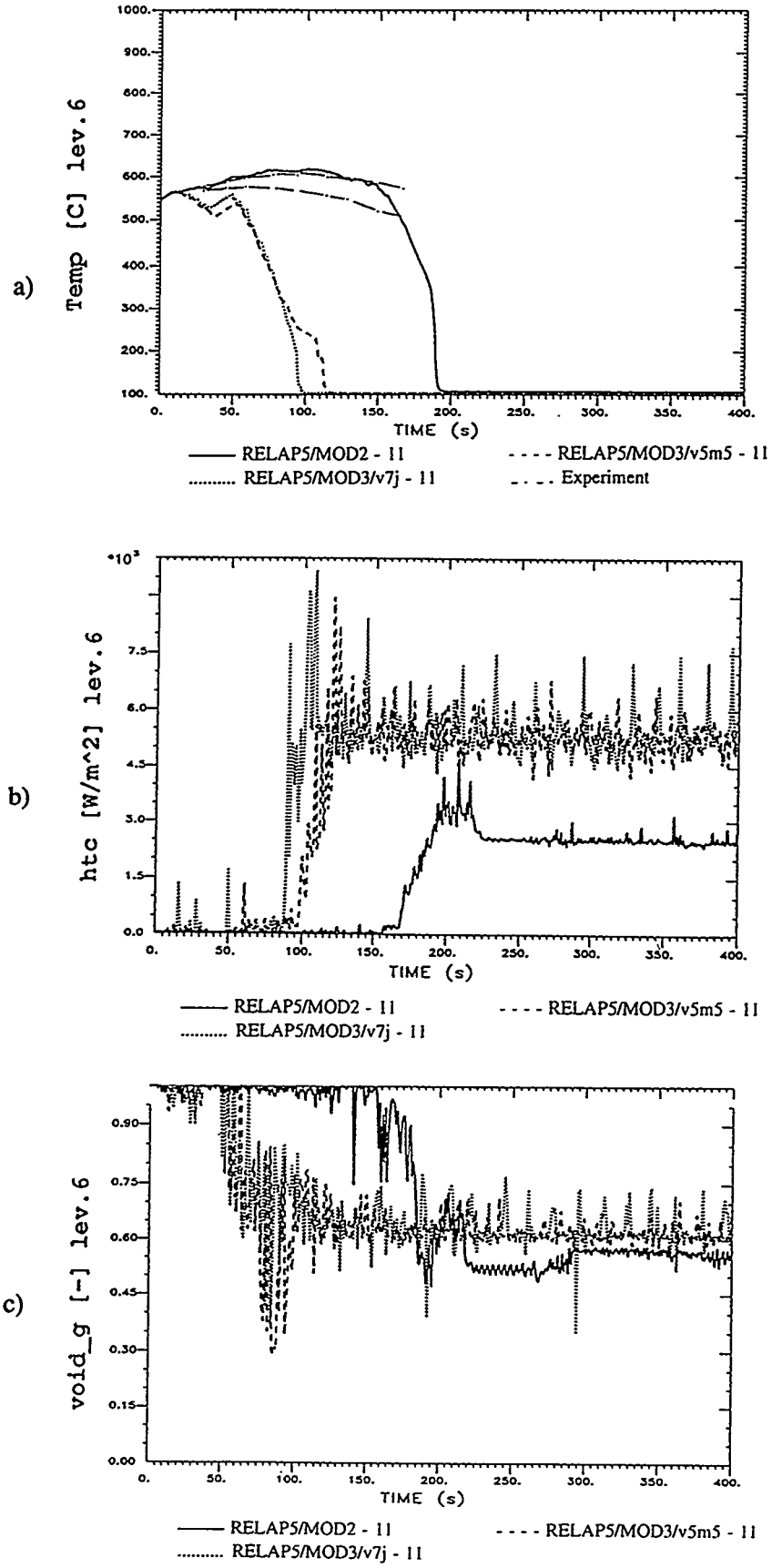
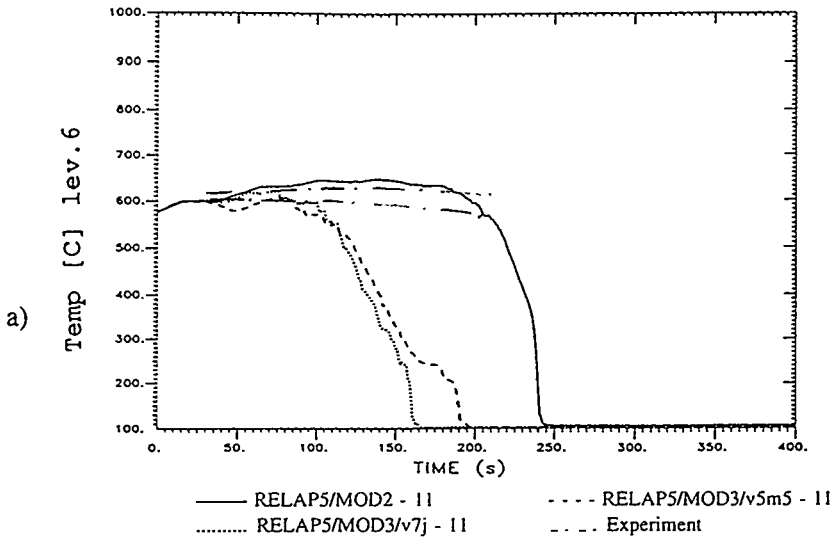
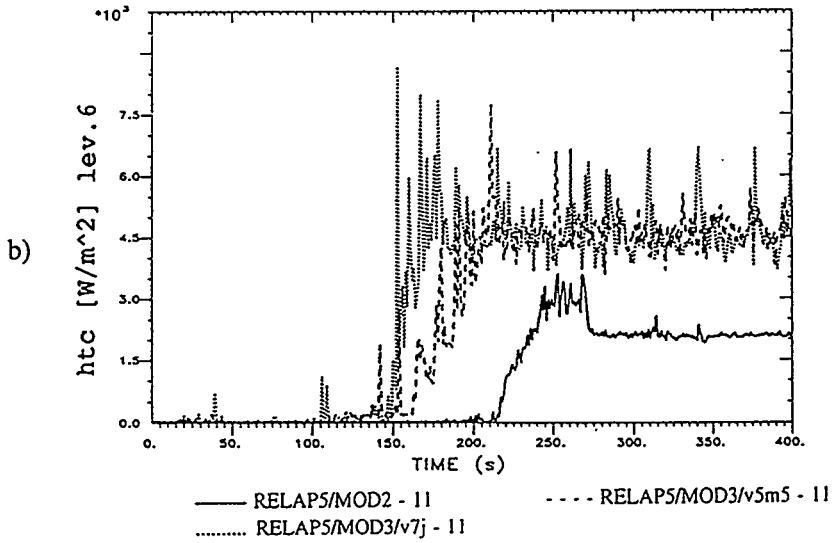


Figure 4: (a) Rod temperature, (b) heat transfer coefficient and, (c) vapour void fraction, at level 6, test #3





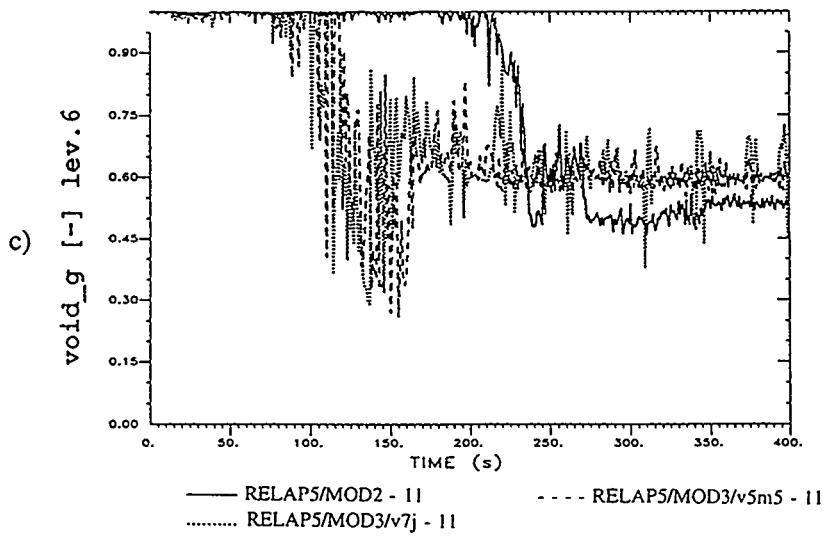
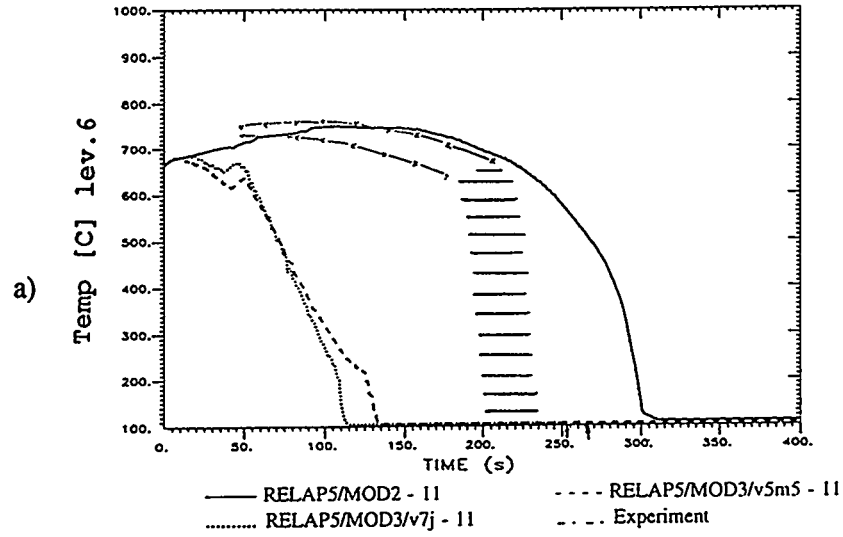
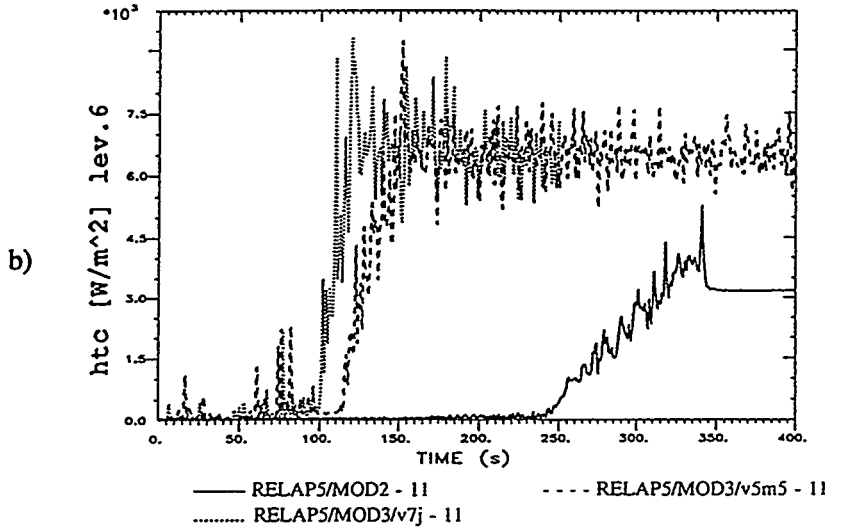


Figure 5: (a) Rod temperature, (b) heat transfer coefficient and, (c) vapour void fraction, at level 6, test #9





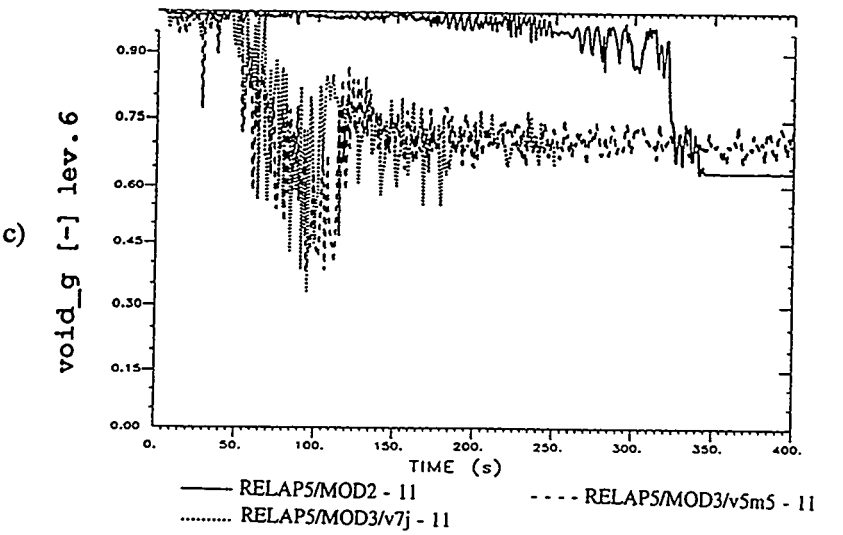


Figure 6: (a) Rod temperature, (b) heat transfer coefficient and, (c) vapour void fraction, at level 6, test #12

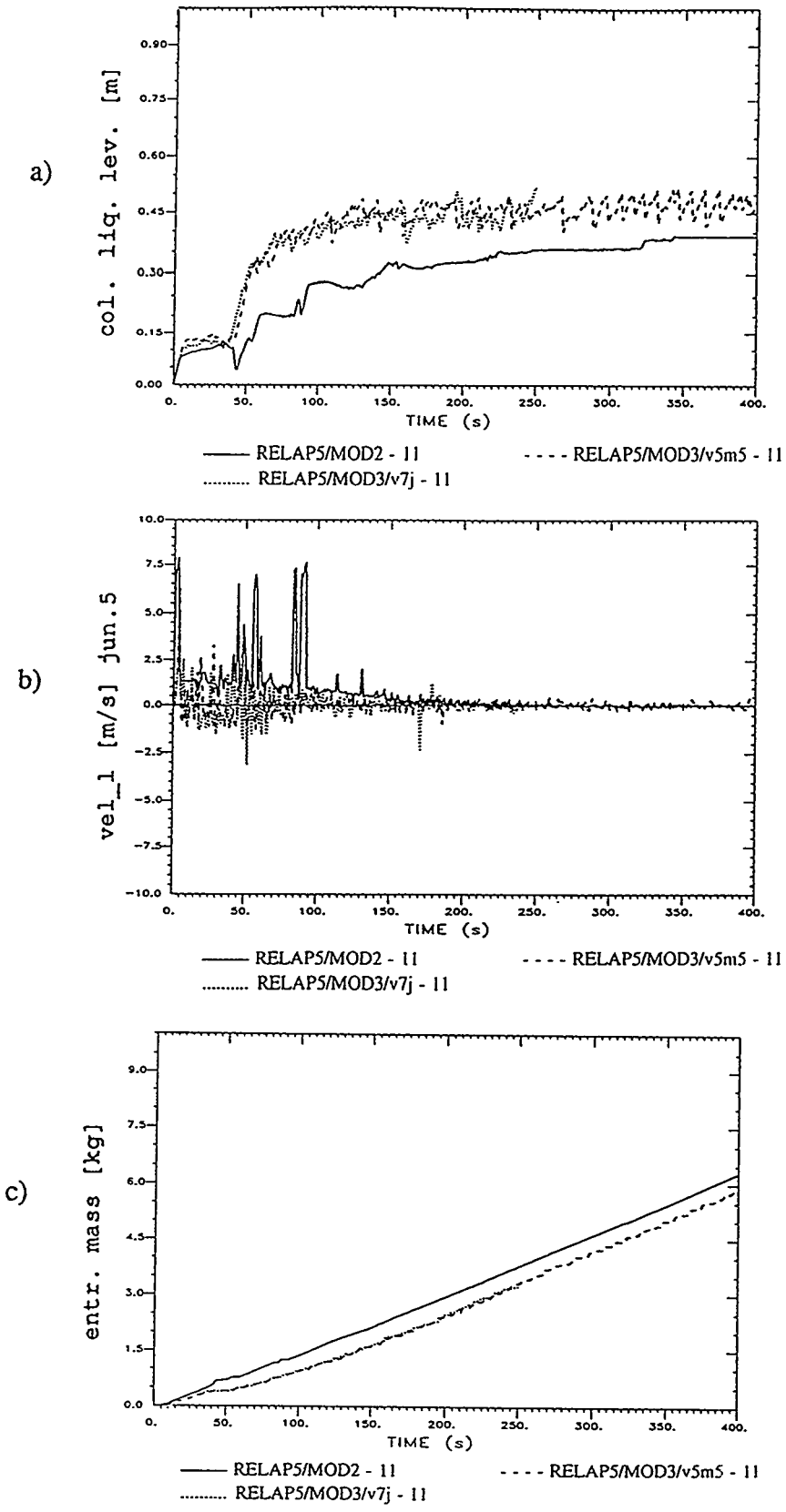
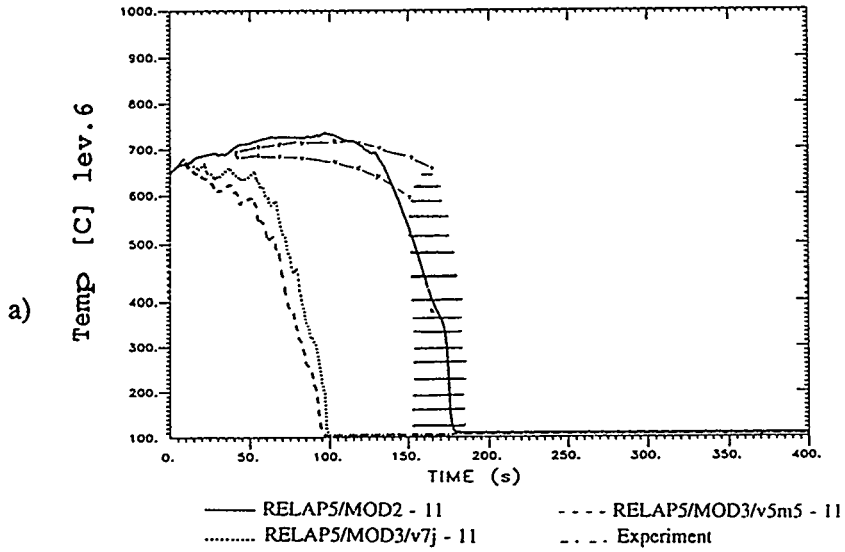
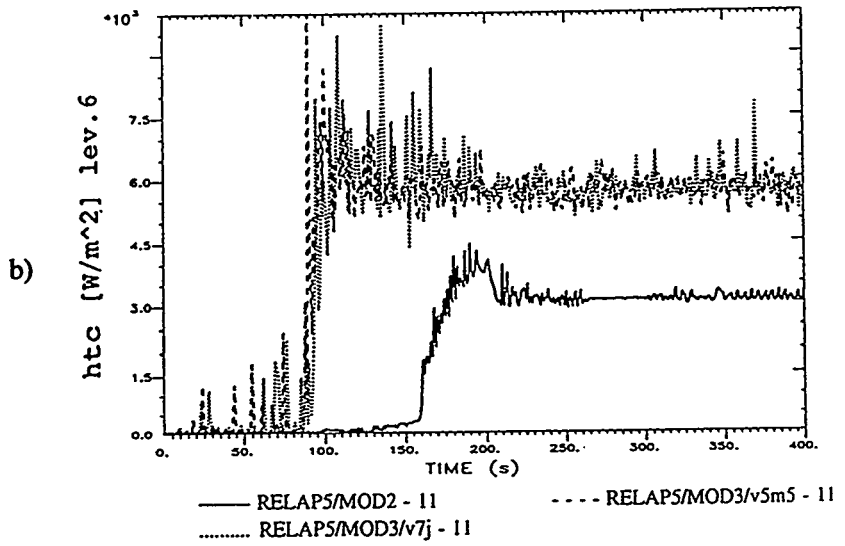


Figure 7: (a) Collapsed liquid level, (b) liquid velocity at level 6 and, (c) entrained mass from the test section, test #12





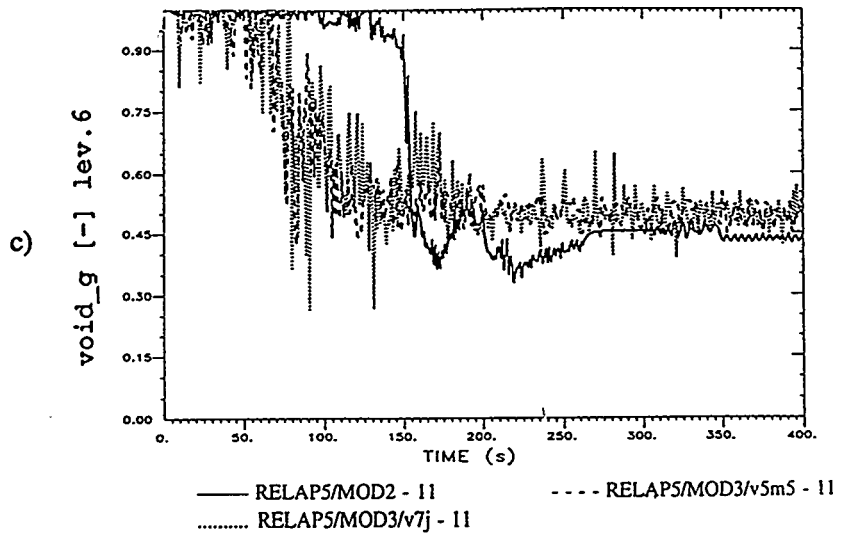


Figure 8: (a) Rod temperature, (b) heat transfer coefficient and, (c) vapour void fraction at level 6, test #14

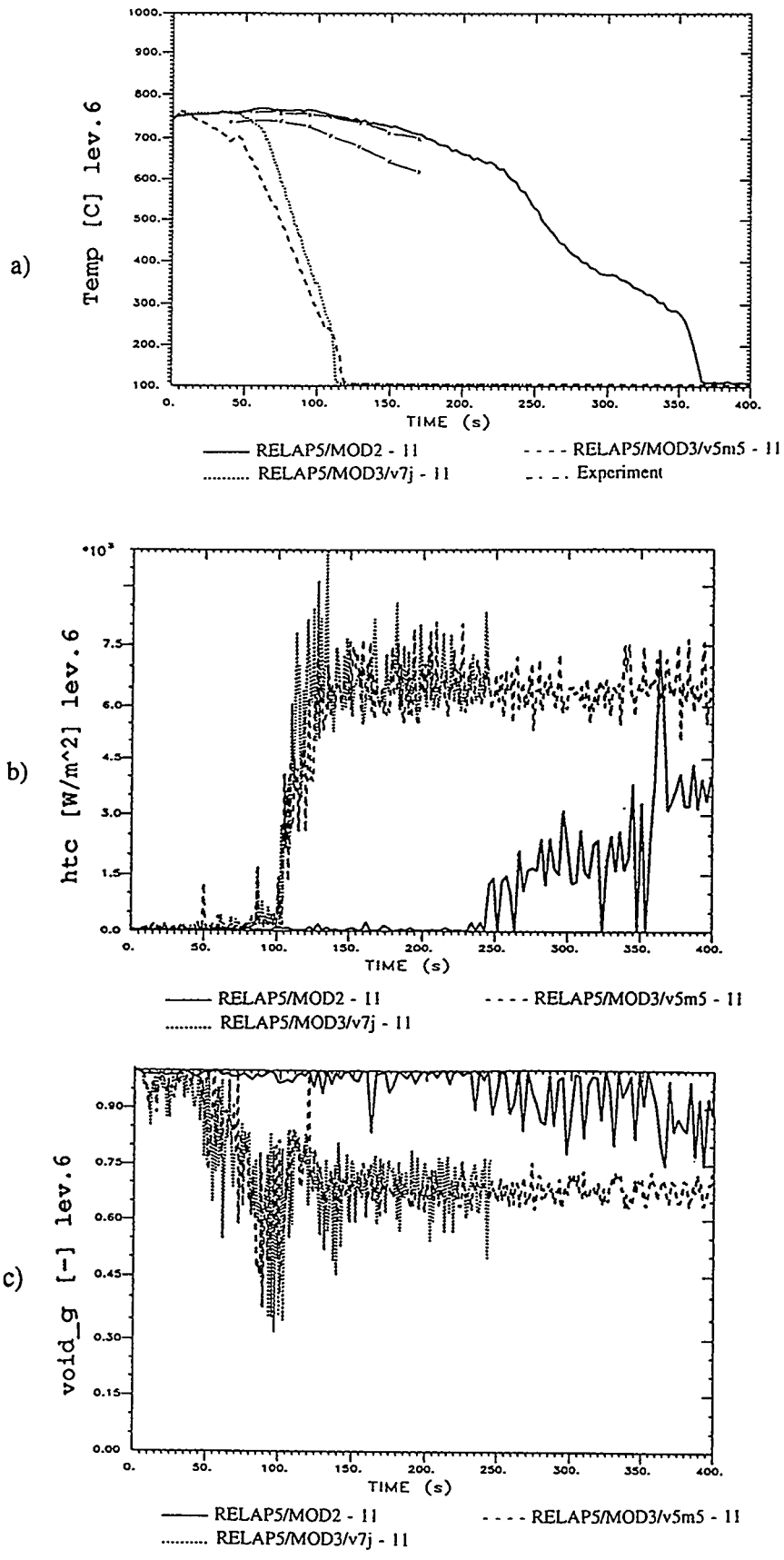


Figure 9: (a) Rod temperature, (b) heat transfer coefficient and, (c) vapour void fraction, at level 6, test #20

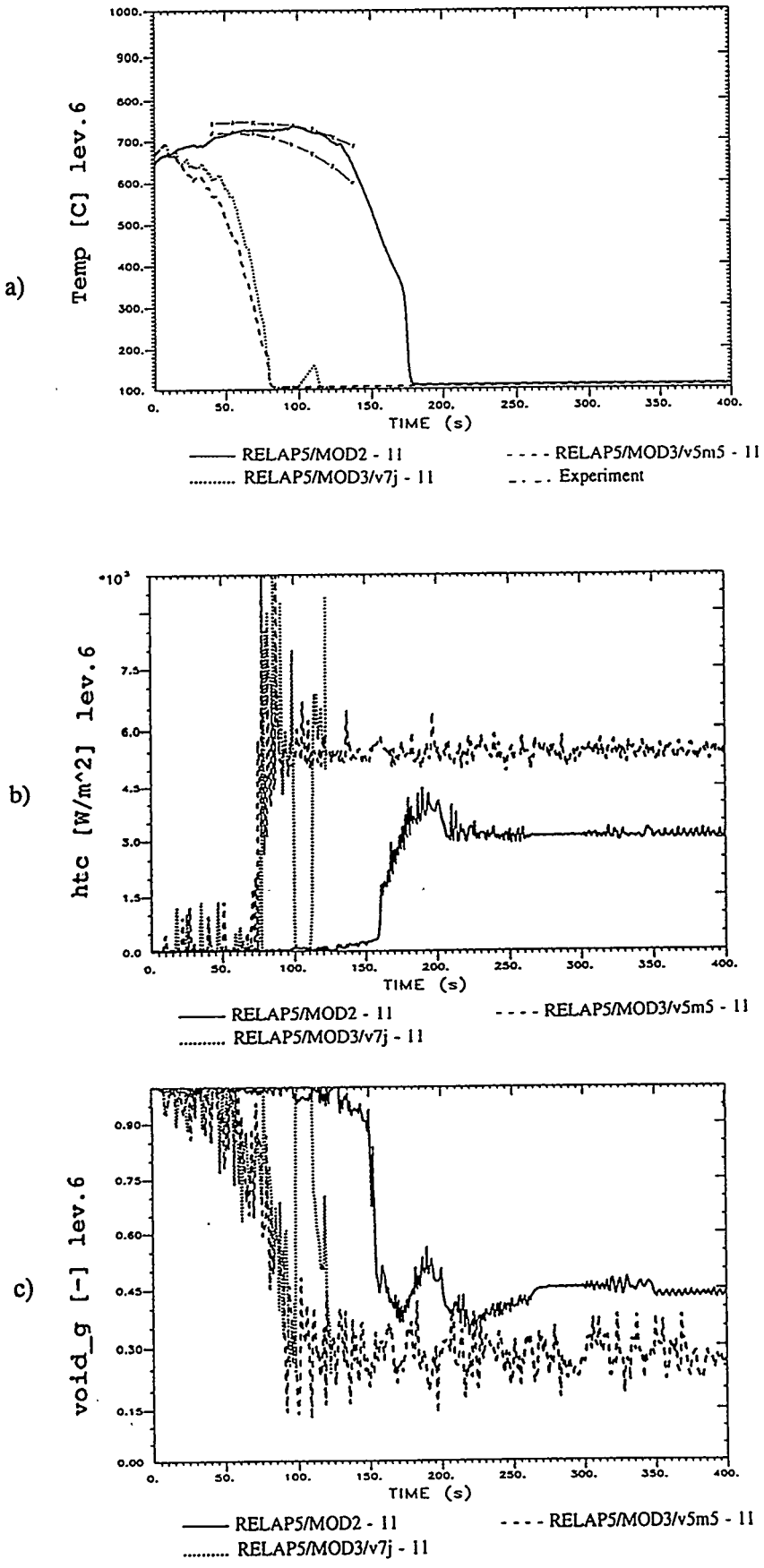


Figure 10: (a) Rod temperature, (b) heat transfer coefficient and, (c) vapour void fraction, at level 6, test #22

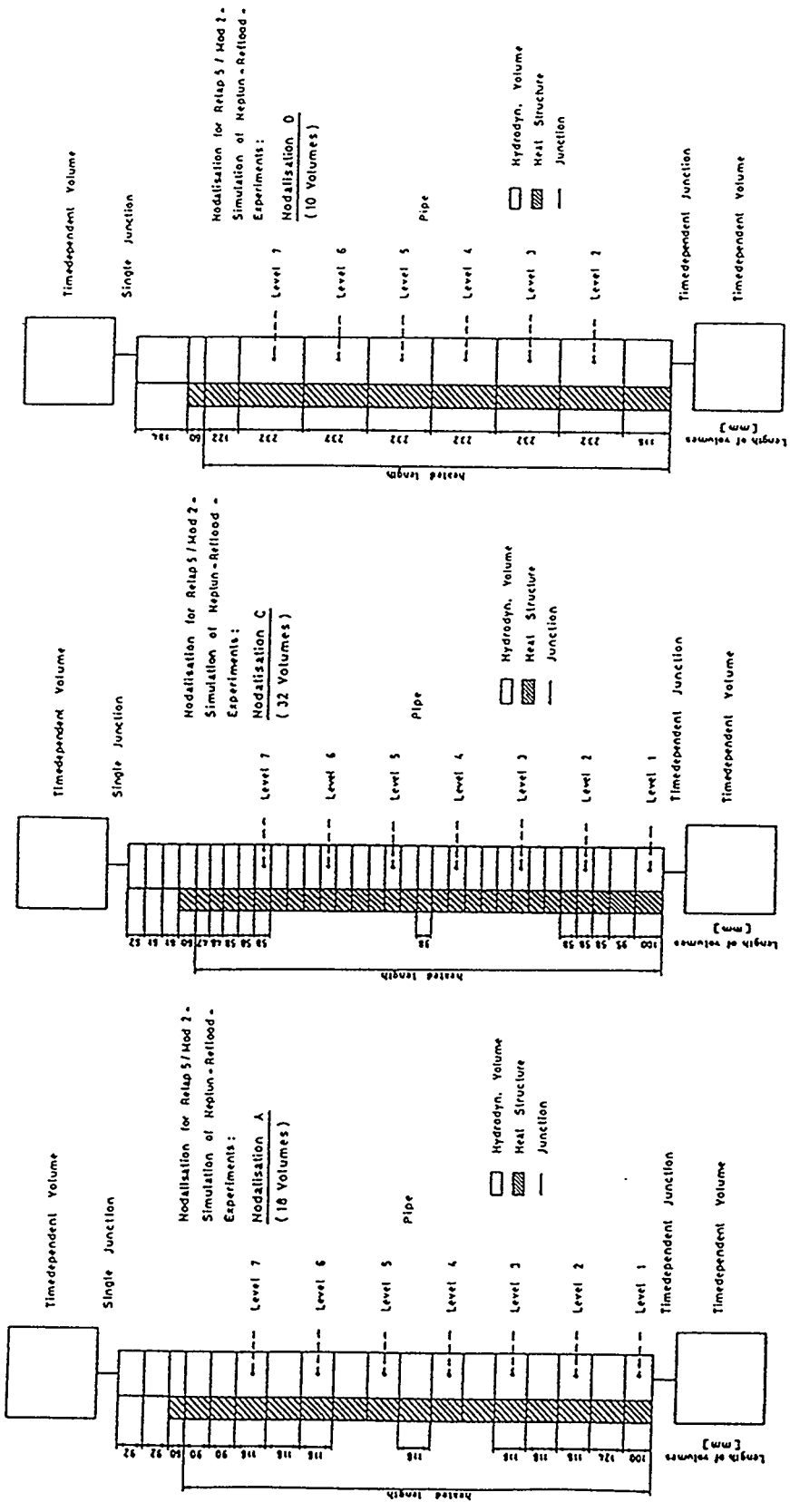


Figure 11: Nodalization schemes used for previous NEPTUN calculations, (ref. [1])

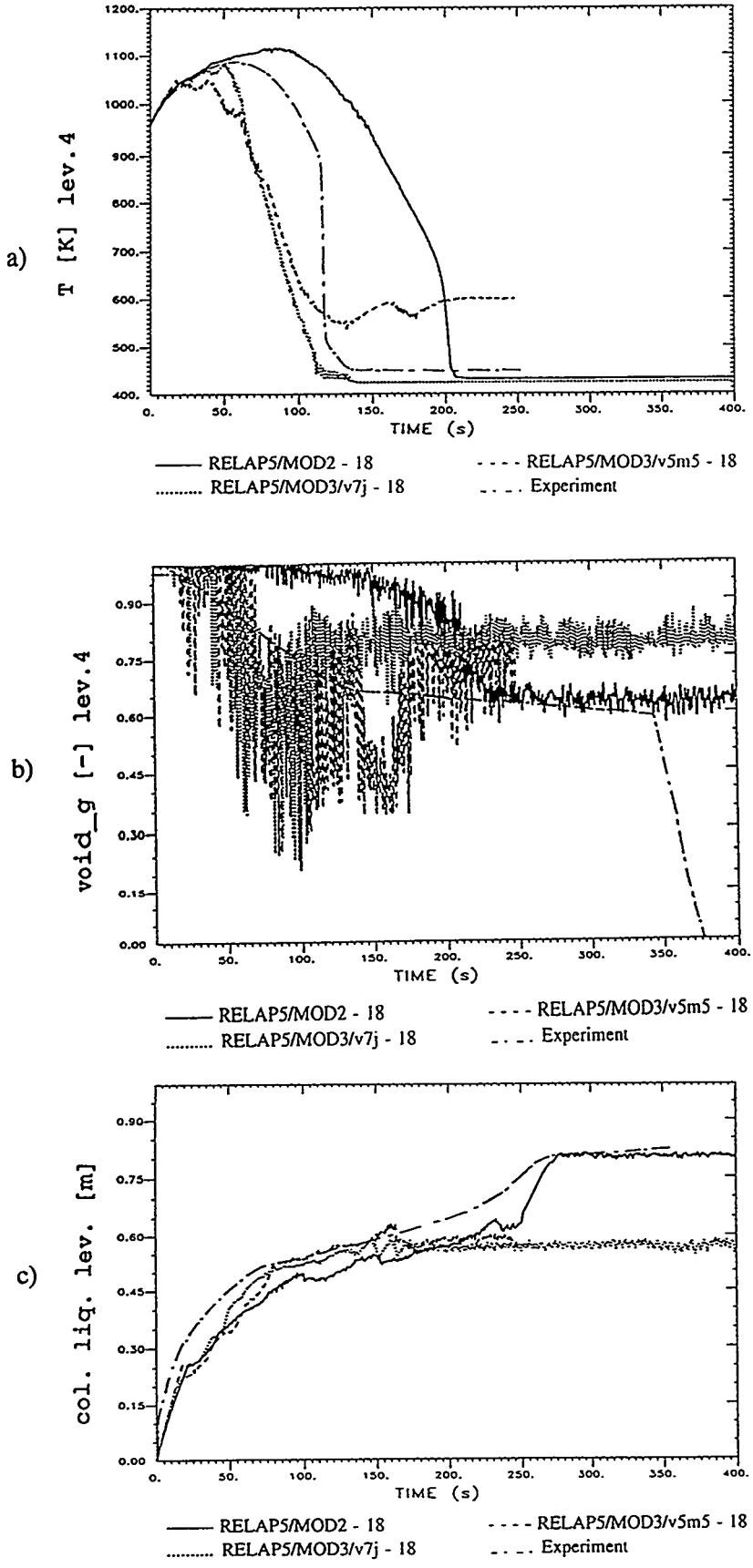
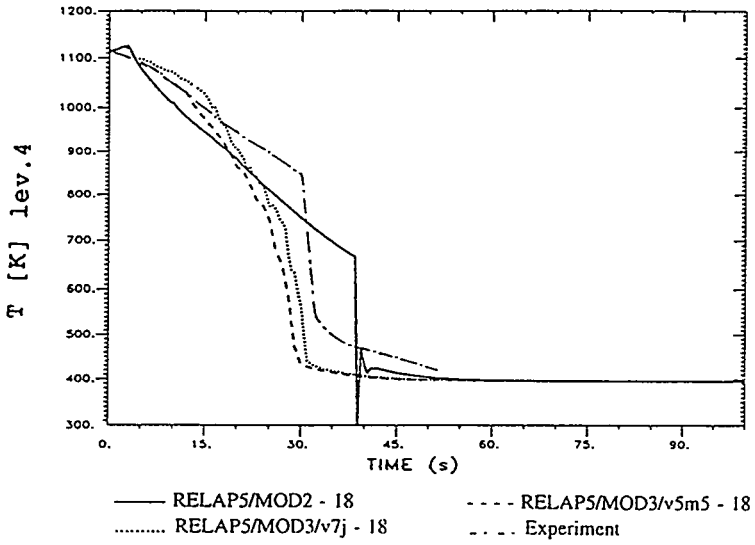
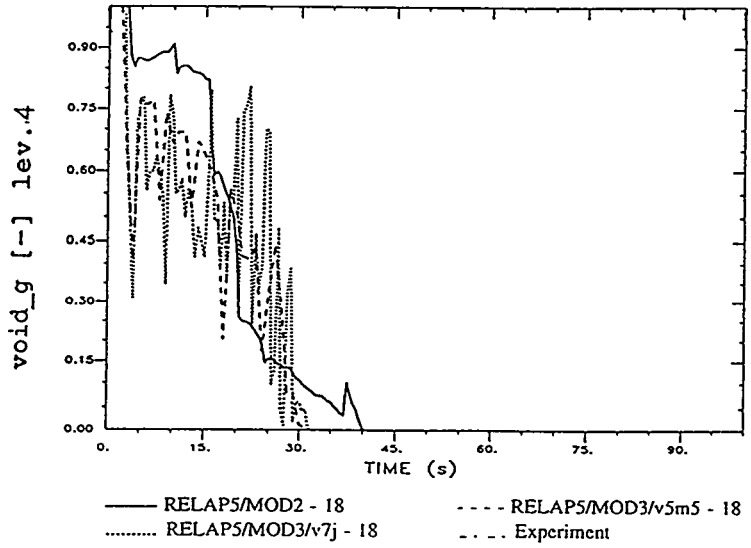


Figure 12: (a) Rod temperature, (b) vapour void fraction at node 7 and, (c) collapsed liquid level, PSI-NEPTUN 5036 test

a)



b)



c)

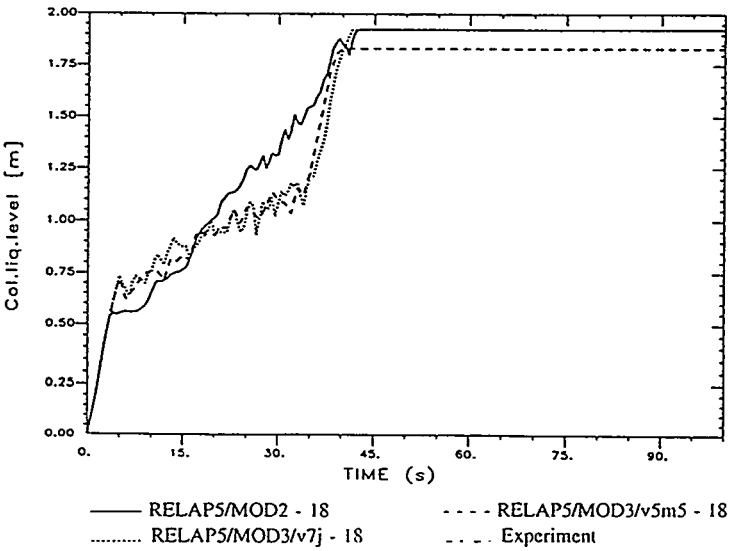


Figure 13: (a) Rod temperatures, (b) vapour void fractions at node 7 and, (c) collapsed liquid level, PSI-NEPTUN 5050 test

OVERVIEW OF CSNI SEPARATE EFFECTS TESTS VALIDATION MATRIX

N. Aksan[1], F. D'Auria[2], H. Glaeser[3], R. Pochard[4], C. Richards[5*] and A. Sjöberg[6]

[1]Paul Scherrer Institute (PSI), CH-5232 Villigen PSI, Switzerland
[2]University of Pisa, Dipartimento di Costruzione Meccaniche e Nucleari, Via Diotisalvi 2, 56100 Pisa, Italy
[3]Gesellschaft für Anlagen und Reaktorsicherheit (GRS), Forschungsgelände, 85748 Garching, Federal Republic of Germany
[4]Institut de Protection et de Surete Nucleaire, DPEI/SEAC, 92265 Fontenay-aux-Roses, France
[5]AEA Technology, Winfrith Technology Centre, Dorchester, Dorset DT2 8DH, United Kingdom
[6]Studsvik AB Safety and Ecology, 61182 Nykoping, Sweden

* Presently at: Bournemouth University, Computer Systems and Networking Centre, Talbot Campus, Fern Barrow Poole, Dorset BH 12 5BB, UK

ABSTRACT

An internationally agreed separate effects test (SET) Validation Matrix for thermal-hydraulic system codes has been established by a sub-group of the Task Group on Thermal Hydraulic System Behaviour as requested by the OECD/NEA Committee on Safety of Nuclear Installations (CSNI) Principal Working Group No. 2 on Coolant System Behaviour. The construction of such a Matrix is an attempt to collect together in a systematic way the best sets of openly available test data for code validation, assessment and improvement and also for quantitative code assessment with respect to quantification of uncertainties to the modelling of individual phenomena by the codes.

The methodology, that has been developed during the process of establishing CSNI-SET validation matrix, was an important outcome of the work on SET matrix. In the paper, the methodology developed will be discussed in detail, together with the examples from the SET matrix. In addition, all the choices which have been made from the 187 identified facilities covering the 67 phenomena will be investigated together with some discussions on the data base.

Facilities and phenomena have been cross-referenced in a separate effects test cross reference matrix, while the selected separate effects tests themselves are listed against the thermal-hydraulic phenomena for which they can provide validation data. As a preliminary to the classification of facilities and test data, it was necessary to identify a sufficiently complete list of relevant phenomena for LOCA and non-LOCA transient applications of PWRs and BWRs. The majority of these phenomena are also relevant to Advanced Water Cooled Reactors. To this end, 67 phenomena were identified for inclusion in the SET matrix and, in all, about 2094 tests are included in the SET matrix.

The SET matrix, as it stands, is representative of the major part of the experimental work which has been carried out in the LWR-safety thermal hydraulics field, covering a large number of phenomena within a large range of useful paramaters. The SET matrix also provides a basis for evaluating the existing data base and defining the main axes for further research in LWR-safety thermal hydraulics in relation to separate effects testing.

It is apparent from this work that the level of the state of knowledge related to the different phenomenon is far from uniform. Another important outcome is related to the large amount of work which is necessary to validate a computer code against the total number of phenomena which have been identified. Compared to existing code matrices the total number of selected tests is at least one order of magnitude more than has been utilised until now. The increasing power of available computers, however, makes the calculation of a larger number of tests more feasible now than in the past.

1. INTRODUCTION

Construction of a Separate Effect Tests (SET) validation matrix [1] is an attempt to collect together the best sets of openly available test data for code validation, assessment and improvement, from the wide range of experiments that have been carried out world-wide in the field of thermal-hydraulics. The objective of this paper is to provide an overview of the methodology developed and a brief summary of its application to the SET validation matrix [1a] [1b].[1]

The next section gives details on the background and the objectives of the CSNI-SET validation matrix. Further sections deal with the details of the methodology developed with an overview of the SET validation matrix and some conclusions drawn, as a result of this work.

2. BACKGROUND AND THE OBJECTIVES OF THE CSNI-SET VALIDATION MATRIX

As a result of intense activity over the last 20, years several large thermohydraulic codes now exist for simulating the behaviour of LWRs during transients and loss of coolant accidents (LOCAs), and these are supported by a wealth of experimental data. The state of the art in the modelling of LOCA and non-LOCA transients was recently reviewed in a CSNI State of the Art Report (SOAR), "Thermohydraulics of Emergency Core Cooling in Light Water Reactors" [2], also produced by the CSNI Task Group on Thermal Hydraulic System Behaviour. In order to assist the task of assessing and validating thermohydraulic codes, the OECD-CSNI Task Group on the Thermohydraulics of ECCS and LOCA, (the predecessor of the Task Group on Thermal Hydraulic System Behaviour), undertook to review the available test data and compile a validation matrix. The Task Group set up a specialist Writing Group to carry out this work.

In March 1987, the OECD/NEA Committee on the Safety of Nuclear Installations (CSNI) published a document that identified a set of tests which were considered to provide the best basis for the assessment of the performance of thermohydraulic codes, "CSNI Code Validation Matrix of Thermohydraulic Codes for LWR LOCA and Transients", [3], [4], and [5]. The set of tests was chosen to include examples of all phenomena expected to occur in plant transients and LOCA analyses. Tests were selected on the basis of the quality of the data, variety of scaling and geometry, and appropriateness of the range of conditions covered. A decision was made to bias the validation matrix towards integral tests in order that code models were exercised, and interacted, in situations as similar as possible to those of interest in LWR plant. This decision was taken on the assumption that sufficient comparison with separate effects tests data would be performed, and documented, by code development, that only very limited further assessment against separate effects test data would be necessary. This last expectation has proved unrealistic; it is now recognised that continued comparison of calculations with separate effects test data is necessary to underwrite particular applications of codes, especially where a quantitative assessment of prediction accuracy is required, as well as for code model improvement.

It has been decided to develop a distinct Separate Effects Test Matrix rather than extend the original CSNI Code Validation Matrix (CCVM), which consisted almost entirely of integral tests. Only in some specific cases where integral test facility data were not available, were separate effects tests used in the CCVM. The development of the separate effects test matrix was found to require an extension of the methodology employed for the CCVM both in the scope and definition of the thermal hydraulic phenomena and in the categorisation and description of facilities.

There are several reasons for the increased importance now placed on the comparison of codes with separate effects test data. Firstly, it has been recognised that the development of individual code models often requires some iteration, and that a model, however well conceived, may need refinement as the range of applications is widened. To establish a firm need for the modification or further development of a model it is usually necessary to compare predictions with separate effects data rather than rely on inferences from integral test comparisons.

Secondly, there is the question of uncertainties in predictions of plant behaviour. A key issue concerning the application of best estimate codes to LOCA and transient calculations is quantitative code assessment. Quantitative code assessment is intended to allow predictions of nuclear power plant behaviour to be made with a well defined uncertainty. Most schemes for achieving this quantification of uncertainty rely on assigning uncertainties to the modelling by the code of individual phenomena, for instance by the determination of reasonable ranges which key model parameters can cover and still produce results consistent with data. This interest has placed a new emphasis on separate effects tests over and above that originally envisaged for model development.

In the thermohydraulic codes, the physical processes are simulated by mechanistic models and by correlations. The prediction of particular phenomena, such as level swell or counter-current flow limitation, by a code are usually dominated by one, or perhaps a few, code models. Comparison of code predictions of basic phenomena with events observed in the relatively simple situations contrived in separate effects test facilities, often allows a better assessment

[1] CSNI-SET validation matrix reports can be obtained either applying to one of the authors of this paper or from: OECD Nuclear Energy Agency, Nuclear Safety Division, le Seine Saint Germain, 12 Boulevard des Iles, 92130 Issy les Moulineaux, France.

of the accuracy of code models than it is possible to make with data from integral tests. This may be, for instance, because steady state rather than transient observations are possible in the separate effects tests; or because in a separate effects test facility dedicated to the study of one particular phenomenon, the measurement instrumentation can be chosen more appropriately, with less need to compromise. The more highly controlled environment of the SET is likely to lead to a more systematic evaluation of the accuracy of a model across a wide range of conditions.

A further incentive to conduct separate effects tests, in addition to those carried out in integral facilities, is the difficulty encountered in scaling predictions of phenomena from integral test facilities (which of necessity are in some sense small scale) to plant applications. Where a phenomenon is known to be highly scale dependent and difficult to model mechanistically, there is a strong case for conducting separate effects tests at full scale. In general, it is desirable to have a considerable overlap of data from different facilities; successfully predicting data from different facilities provides some confirmation that a phenomenon is well understood. The main objective in producing the SET cross reference matrix is to identify the best available sets of data for the assessment, validation and, finally, the improvement of code predictions of the individual physical phenomena. While both integral test data and SET data are appropriate for code validation and assessment, for model development and improvement there should be a strong preference for SET data.

3. THE METHODOLOGY DEVELOPED

In the process of establishing the SET validation matrix, a methodology has been developed. This methodology helps to collect and present the data and information collected in a comprehensive and systematic manner. It is a general methodology and therefore, in principal, also applicable to the other type of validation matrices (e.g. on severe accidents). The methodology can be summarised as follows:

1. Identification of phenomena relevant to two-phase flow in relation to LOCAs and thermal-hydraulic transients in light water reactors (LWRs).
2. Characterisation of phenomena, in terms of a short description of each phenomenon, its relevance to nuclear reactor safety, information on measurement ability instrumentation and data base. In addition to these points, the present state of knowledge and the predictive capability of the codes is included in the characterisation of each phenomenon.
3. Setting up a catalogue of information sheets on the experimental facilities, as a basis for the selection of the facilities and specific tests.
4. Forming a separate effects test facility cross-reference matrix by the classification of the facilities in terms of the phenomena they address.
5. Identification of the relevant experimental parameter ranges in relation to each facility that addresses a phenomenon and selection of relevant facilities related to each phenomenon.
6. Establishing a matrix of experiments (the SET matrix) suitable for the developmental assessment of thermal-hydraulics transient system computer codes, by selecting individual tests from the selected facilities, relevant to each phenomenon.
   A brief description for each one of the steps of the methodology will be presented in a brief form in the following sub-sections.

3.1 Identification of Phenomena

The interactions of different correlations along with the conservation equations will constitute a code's capability to simulate important phenomena during the course of a LOCA or transient. It is essential to identify each relevant phenomenon and to ascertain that the specific phenomenon is adequately simulated by the code. This is usually done by comparing the code's results from simulations of well defined tests carried out in properly designed test facilities with the test data. In this context a distinction is made between integral tests and separate effects tests.

Integral tests are carried out in scaled test facilities and provide data on the overall behaviour of a simulated reactor system during a LOCA or transient. These tests are being used for code assessment purposes relating to overall reactor behaviour. A definition of sets of such tests (matrices) has been provided in refs. [3], [4] and [5]. These facilities have a complicated configuration. Compromises, for instance with respect to scaling to real plants, are inevitable. Also, the instrumentation for measurements of parameters governing different two-phase flow phenomena is limited. This makes the integral tests less suitable for detailed investigations of specific two-phase flow phenomena. As a consequence this also requires, in assessment analyses, that the code user is very confident of which phenomena

prevail during the course of a transient in order to avoid "good results but for the wrong reasons" (compensating errors).

Separate effects tests are employed not only to develop correlations of specific processes but also to investigate individual or localised two-phase phenomena which in most cases are dependent on several specific processes. These kinds of tests are also used to characterise the behaviour of single components such as pumps or steam separators.

As part of the definition of integral test matrices in refs.[3], [4], and [5] different phenomena were identified. In particular, phenomenological windows were distinguished in the case of

- Large break LOCAs in PWRs
- Small and intermediate break LOCAs and transients in PWRs
- LOCAs in BWRs
- Transients in BWRs

An expansion of that list covering different important LOCA and thermal hydraulics transients phenomena was presented for both BWR and PWR in ref. [2]. A weighting and appraisal of each phenomenon were also included. The main support for these phenomena was provided by a number of integral and separate effects tests. That list of phenomena is the basis for the one provided in this paper. Only minor modifications were introduced in the list. Apart from some rearrangement, a new group named "Basic Phenomena" has been added. These basic phenomena are not exostive list of fundamental thermalhydraulic aspects.They have been defined to minimize number of concepts but they govern all the fluid behaviour during an accident sequence and occur in one or another form in the listed system based phenomena. Each phenomenon in this group can be characterised as independent of other phenomena and is of a constitutive nature for the two-phase flow.

Those phenomena, such as the mechanical response of structures to the coolant behaviour, and pressurised thermal shock, which are outcomes of the system thermohydraulic behaviour, have been excluded. The propagation of pressure waves is noted in the list of phenomena, but because special facilities have been used to investigate this phenomenon, and specialised codes are used for its prediction, data for the validation of this aspect of the LOCA and transient codes is also considered outside the scope of the present exercise.

After the identification of the relevant two-phase flow phenomena is made, a short description of each phenomenon is provided as in the sub-section 3.2. A total of 67 phenomena are identified and the resulting phenomena list is given in Table 1. All representative phenomena occurring during a LOCA or transient are included, although several phenomena are combined under a general heading in some cases such as various instances of counter-current flow limitation, and of critical flow.

It should also be realised that some phenomena are dependent on each other, for instance spray effects and condensation. It will be seen that there are several different types of phenomena, varying from those such as interphase friction which is a very basic attribute of a two-phase flow, to those such as loop seal clearing, which is essentially a system phenomenon, localised in its occurrence but very dependent on events and conditions elsewhere in the loop. In such cases, the influences from the loop have to be provided as boundary conditions.

3.2 Characterisation of Phenomena

Most of the phenomena listed in above subsection are mentioned in [2] and some of these are discussed. That report, however, is organised under more general headings than the 67 set out above, and from the point of view of the current work the coverage of the phenomena it provides is rather uneven. Therefore, we have provided short summaries relevant to each phenomenon under the headings: Description of the phenomenon, Relevance to nuclear reactor safety, Measurement ability, instrumentation and data base, and Present state of knowledge - predictive capability

The scope of these summaries is outlined below.

Description of the phenomenon

A brief description of each phenomenon used in the SET matrix is given under this heading.

This indicates the interpretation that has been put on the phenomenon for the purposes of assessing suitable SET data. Thus, for example, it will be seen that the term horizontal stratified flow has been used to include the phenomenon of thermal stratification as well as aspects of two-phase stratified flow associated with the presence of a surface. The description also indicates where in a reactor system, and under what circumstances, the phenomenon is likely to occur. The discussion of the phenomenon should indicate features such as the degree of scale or geometry dependence, which affect the range of data likely to be necessary for code model validation.

Some groups of phenomena are linked. In this case an introductory description prefaces the group to avoid repetition of material. For instance counter-current flow limitation (CCFL) can occur at a variety of locations in a

LWR. CCFL is very geometry dependent and encompasses a wide range of situations, requiring data from different types of SET facilities. Nevertheless some aspects of CCFL are common to all these circumstances.

In some cases there is an apparent overlap of the phenomena description, since the same phenomenon occurs in combination with other phenomena. The details and specifics of overlaps and clarifications are provided in detail for each specific phenomena in ref.[1a].

Relevance to nuclear reactor safety

A brief discussion of the impact of the phenomenon (in as far as it is possible to isolate its effect from that of other phenomena) on nuclear reactor safety is presented.

In discussing the relevance of individual phenomena to reactor safety we have tried to be as specific as possible, since the "relevance rating" has a high significance in deciding whether poor data bases or weak modelling should be improved. The "relevance rating" was obtained by evaluating the question - how much influence does this individual phenomenon have on safety parameters such as pressure and clad temperature? The answer to this question has a strong influence on the opinions regarding the adequacy of database and modelling.

Measurement ability, instrumentation and data base

A summary of the data requirements and the degree to which they are satisfied by the available database are presented. This includes the discussion of the extent to which parameters required for model validation can be measured directly, the description of the accuracy and consistency of measurements, and the presentation of the range of conditions and scales covered.

In relation to instrumentation and measurement ability, two kinds of phenomena can be distinguished:

a) macroscopic phenomena like depressurisation rate, level decrease, loop seal clearing, etc.;

b) microscopic phenomena like formation of interfacial area, droplet coalescence, etc.

The first group of phenomena can be adequately characterised by the available instrumentation (e.g. pressure, level, temperature transducers); for the second group, in a few cases special techniques are available at the laboratory level to measure parameters which characterise them, but very seldom are these used in the facilities discussed in this study.

Additional phenomena like reflood and critical flow can also be assumed as part of the first group but retain some characteristics of macroscopic and microscopic phenomena. In the former, local (and discrete) measurements based on thermocouples are utilised to identify a three-dimensional situation; in the latter an average signal is provided in most cases that does not give indications about the local value of the reference quantity; the adequacy of the instrumentation system has to be addressed case by case.

The subsection includes a general comment on the adequacy of the database. In judging the adequacy of the database the following points have been taken into consideration:

- What are the experimental parameters needed to characterise the phenomenon?
- Can these parameters be measured directly?
- How extensive is the data base?
- How important is the phenomenon in terms of reactor safety?
- The conclusion that the database is not adequate implies that it should be improved.

Present state of knowledge - predictive capability

An assessment of the present state of knowledge and predictive capabilities are included in this section.

It is difficult to make entirely general statements about predictive capabilities, as the individual thermal-hydraulics codes sometimes use different levels of modelling of individual phenomena. For instance critical flow may be calculated by a "special process model" outside the main equation structure, or may optionally be evaluated using the basic six equation formulation of the main code. Pump models may contain different degrees of empiricism, and may embrace more or fewer of the observed parametric trends: for instance the change in two-phase head degradation with pressure. In general, the comments should apply to the best available models. Hence a comment in this section that the predictive capability is good or adequate, is not an automatic endorsement of all codes.

As with the comments on the database, the judgement on adequacy of the modelling takes into account the importance of the phenomenon in terms of reactor safety.

Detailed examples and discussions for the characterisation of phenomena are given in ref.[1a].

3.3 Catalog of Information sheets

As a preliminary to establishing a list of tests for code assessment and validation, a catalogue of the separate effects test facilities used within the OECD member nations was compiled.

In 1989 Members of the OECD-CSNI Task Group on Thermal Hydraulic System Behaviour wrote to various laboratories or organisations owning and/or operating test facilities or programmes known to them. Addressees were invited to supply information on:

- Objectives of the facility
- Geometry
- Experimental Conditions and Parameter Ranges
- Measurements
- Information concerning Documentation
- Use of Data
- Special Features of Experiments
- Phenomena investigated

To supplement the catalogue of facilities thus generated, members of the Writing Group provided information on other facilities described in the open literature but not volunteered by representative in the owning countries. As a result, a list of 187 SET facilities which are, or have been, in operation in 12 OECD member countries has been compiled.

The complete list of test facilities identified to the Writing Group is given in Table 2 as in ref [1b]. Those facilities for which sufficient information was supplied to produce an Information Sheet are indicated by "a" in the SET facility cross reference matrix. Only those facilities on which sufficient is known to produce an Information Sheet, (113 facilities), have been considered further in the process of selecting suitable test data.

The aim of the Information Sheets is to provide enough information to decide on the most appropriate test facility/programmes to select for code model validation/assessment with respect to particular phenomena.

This information was collected primarily to enable the selection of appropriate sets of test data for inclusion in the SET cross reference matrix. It would also form a starting point for anyone making use of the SET cross-reference matrix data for code validation purposes.

For each Facility, therefore, a standard brief Information Sheet has been prepared, describing the most important characteristics of that facility and its test programme. The Information Sheets are contained in Volume II of the SET Validation Matrix report [1b].

3.4 Forming a SET Cross-reference Matrix

The main objective in producing the Separate Effects Test Facility Cross Reference Matrix (SET CRM) is to identify the best available sets of data for the assessment, validation and, finally, the improvement of code predictions of the individual physical phenomena. While both integral test data and SET data are appropriate for code validation and assessment, for model development and improvement there should be a strong preference for SET data.

The thermohydraulic phenomena of interest in LWR LOCA and transients are listed in Table 1. A set of basic two-phase flow and heat transfer processes which are important for the thermohydraulic codes in the form of basic constitutive relations have been added explicitly to the list under the heading "Basic Phenomena". The scope of the SET Facility CRM has been restricted to those phenomena directly affecting the thermohydraulic behaviour in a transient or LOCA.

The resulting list of 67 thermohydraulic phenomena forms one axis of the SET Facility CRM. The second axis of the Matrix consists of the 187 facilities identified as potential sources of separate effects data. The test facilities in 12 OECD member countries are compiled according to the country in which they operate: Canada, Finland, France, Germany, Italy, Japan, Netherlands, Sweden, Switzerland, United Kingdom, USA, Norway. An example for SET facility CRM is shown in Table 2. The SET facility CRM tables for each country can be seen in ref.[1a]. For each test facility the phenomena addressed by the corresponding experimental research programme have been indicated in these Matrix tables, yielding the SET CRM for test facilities and thermohydraulic phenomena.

The correlation between phenomena and SET Facility is assigned to one of three levels:

- suitable for model validation, which means that a facility is designed in such a way as to simulate the phenomenon assumed to occur in a plant and is sufficiently instrumented (x);
- limited suitability for model validation: the same as above with problems due to imperfect scaling, different test fluids (e.g. Freon instead of water) or insufficient instrumentation (o);

- not suitable for model validation: obvious meaning, taking into account the two previous items (-).

This Matrix shows both the number of different phenomena covered by the experimental investigation with one test facility, and the number of different facilities in which an individual phenomenon has been investigated. The test facilities differ from each other in geometrical dimensions, geometrical configuration and operating capabilities or conditions. Therefore, the number of facilities relevant to an individual phenomenon provides some indication of the range of parameters within which a phenomenon has been investigated and experimental data generated. For instance, it is obvious from the SET CRM presented in ref.[1a] that heat transfer phenomena, especially post critical heat flux, departure from nucleate boiling/dryout and quench front propagation/rewet, were investigated in many SET facilities.

For the systematic evaluation of the capabilities of a thermohydraulic code, appropriate experiments have to be identified which provide data over the range of conditions of interest (as far as such data is available), for each phenomenon listed. The selection of facilities and relevant parameter ranges are the subject of the next two points in the methodology.

3.5 Selection of Facilities and Parameter Ranges

This item of the methodology deals with the identification of parameters relevant to each facility that characterise the phenomena

The 67 phenomena considered are assumed to cover the thermal hydraulic behaviour in nuclear power plants under normal and off-normal conditions. Thus the related ranges of parameters should be, especially with regard to geometry and fluid conditions, relevant to the plant conditions. Nevertheless, three main considerations suggested that the scope of the available experimental data base should primarily determine the ranges of variations of the main quantities:

a) the purpose of the data base to be constituted is computer code assessment;

b) in some cases the range of parameters in the plant is an order of magnitude away from the ranges of values investigated in the experiments;

c) a major requirement of qualified computer codes is that they should enable the extrapolation of phenomena to plant conditions: the consideration, for each phenomenon, of different rigs characterised by different scaling criteria and dimensions makes the attempt to achieve this objective more realistic.

Having this in mind, tables having the format shown in Table 3, as example, have been produced with reference to each phenomenon. The tables should be seen primarily as aiming at the selection of the facilities where the considered phenomenon has been investigated. The resulting information is utilised for the selection of experiments. As noted above, the reported ranges of parameters are only relevant to the specific facility.

Additional details related to each of the items included in the matrix format are as follows:

- PHENOMENON: each phenomenon of the facility cross reference matrix is considered including its numerical label;
- FACILITY IDENTIFICATION: an attempt is made to include at least three facilities for each phenomenon. Additional facilities are included depending upon the relevance of the phenomenon in terms of reactor safety and code assessment. In relation to the specific phenomenon, to be included in the list of selected facilities, the facility should be characterised by an "x" in the cross reference matrix, and the info sheet should be available ("a" in the matrix). If three facilities rated "x" are not available from the cross reference matrix, then facilities rated "o" with info sheet available have been considered. For a few phenomena these conditions are not fulfilled, and fewer facilities, or those without information sheets, are listed. The criteria for selection will be discussed later. In addition:
  - "No." is the facility number in Table 3 where the first digit identifies the country and the second one the facility;
  - "Status in the matrix" consists of two symbols: I) "x", "o" or "-", where the first two symbols are related to the cross reference matrix and the dash means that the facility was not considered relevant for the given phenomenon; II) "a" indicates that an info sheet is available.
  - "Name" is the label of the facility as reported in the cross reference matrix;
  - KEYWORDS: It appeared useful to characterise the facility or the overall scope of the experimental programme with 1 to 5 keywords that may give an idea of the dimension of the facility (e.g. full scale), the features of the hardware (e.g. glass facility), the type of experiment (e.g. blowdown), etc.;
  - RELEVANT PARAMETER RANGES: The range of parameters considered in each facility are included in this item. Facilities having quite different hardware characteristics can be utilised to investigate a given

phenomenon; furthermore, the available information is not consistent for the various facilities. For these reasons it must be recognised that the selected parameter ranges are specific to each facility and relevant to the given phenomenon.

- REASONS FOR SELECTION OR NOTES: Eight reasons have been identified for including a facility from the cross reference matrix in the following tables (these are self explanatory)

  1) Well known to the writing group;
  2) Well defined and clear boundary conditions;
  3) Good measurement and instrumentation (quality of data);
  4) Quality of documentation;
  5) Already used for code development;
  6) Suitable for independent assessment;
  7) To cover an important parameter range;
  8) To cover the effect of a specific parameter.

The above digits (up to five) are reported in this column. Furthermore, notes can be added to better characterise the status of the data.
For each table, a few additional optional comments are reported, essentially dealing with

- the relevance of the selected parameters as far as the characterisation of phenomena is concerned;
- the difference between the selected parameter ranges and the expected parameter ranges in the plant;
- reasons for the selection of the facility if this is not included in the items 1 to 8 above;
- the need for additional experimental activity in relation to the given phenomenon;
- available references;
- the evaluation of the possibility that the phenomenon can be addressed in any integral test facility

Finally, the facilities included in the CSNI integral test facility document [3], are noted in the following tables, even if the information sheet is not available.

The result of the activity outlined above consists of 67 tables (one per phenomenon) that give an idea of the quantity and the scope of experimental research carried out to investigate the phenomena with the aim of qualifying thermal-hydraulic system computer codes (Table 4, for example).

3.6 Establishing the Separate Effects Tests (SET) Matrix

For each of the 67 phenomena, a table presents the tests which have been identified as suitable for code validation with respect to that phenomenon, from the test facilities selected. The arguments for the selection of the facilities for a given phenomenon are already identified with, the previous step of the methodology.

In order to try to be practical, the number of facilities has been limited to 3 on the average, though in some special cases up to 5 are used. For heat transfer, a larger number was used, because of the large number of parameters affecting heat transfer and its high degree of importance. The total maximum number of tests has been fixed at up to 20 per phenomenon. Here a test is considered to be a set of data points involving one key parameter variation (e.g. a flooding curve at a single pressure and tube geometry). These numbers indicate the large amount of work which is necessary to assess a code.

It must be emphasised that tests have been chosen on the basis of available information: It is not always possible to determine how satisfactory data is for code validation until it is actually used (completeness of boundary condition information; measurement accuracy, internal consistency etc.) The situation of the various experimental programmes and chosen tests varies greatly in this respect.

The tests have been selected in order to cover the experimental data range as defined, knowing that the plant range is not always covered. Particular attention has been given to the geometric scaling problem and small, medium and large scale separate effect facilities have been integrated whenever possible.

As some facilities are useful with respect to several separate effects phenomena, a cross check and a tentative harmonisation of the selected tests have been made when possible, in order to try to minimise the number of input data needed for code validation.

In this matrix the selected tests are ordered following one arbitrary chosen main parameter (for example system pressure) with, optionally, additional parameters (for example, representative diameter). This will give the user an indication of the available range of data for code validation, and the possible need for additional tests.

At the bottom of the table the main references, if identified, are given for the chosen tests. The reader is supposed to have enough information in these references to be able to compute the test. Some examples of the SET matrix for selected number of phenomena are given in Tables 5 to 8. Further tables for each of the 67 phenomena are given in detail in ref.[1a].

Additional information related to the type of tests, or parameter ranges for instance are also provided in the listed references. This matrix has been published as a first attempt. It may be updated by new and additional input from the owners and by remarks from the users. Nevertheless, as it is, this separate effect test matrix covers a large number of phenomena within a large range of selected parameters. If a thermal-hydraulic code is to be used to cover a certain number of phenomena then calculation of the relevant identified tests in the matrix is considered to be a basic step toward the achievement of code qualification.

4. CONCLUSIONS

The present separate effects tests (SETs) validation matrix report [1a] contains the separate effects tests matrix requested by CSNI in support of thermal hydraulic code validation. The report and matrix can also be used for code development and for quantitative uncertainty analysis.

The construction of the present separate effects test matrix has represented a large effort. Much information has been collected, recorded and classified in three main areas:

- information on test facilities and test parameters
- state of the art knowledge with regard to a full range of thermal hydraulic phenomena (covering LOCA and transients in current designs of BWR and PWR)
- sources of data for validation of codes with respect to each specific individual phenomenon.

Facilities and phenomena have been cross-referenced in a separate effects test cross reference matrix, while the selected separate effects tests themselves are listed against the phenomena for which they can provide validation data.

Considerable efforts have been made to ensure that the cross reference matrix is as complete as possible and that the selected set of tests are as optimal as possible in range, usability and number. This report contains the most comprehensive compendium of tests and facilities brought together in one document. Nevertheless it is recognised that the work did not succeed in reaching all world data. Furthermore it has not been possible to date to prescribe particular suitable tests in certain areas, even when tests are known to exist, either because of the peculiarity of the particular area or because the data are currently proprietary.

It should be noted that in selecting tests and commenting on the completeness of the data base we have concentrated on the available experimental data ranges and considered the plant parameter range only in a limited way. It is up to the user, for his particular application, to solve the problem of the plant parameters range of the particular phenomenon and compare this to the available data range in the matrix. In order to facilitate this, the tests in the matrix are ordered following one relevant main parameter and possibly one or two subsidiary parameters.

An important outcome of our work is related to the methodology which has been developed during this project. This methodology has been summarised in some detail in this paper.

In the SET matrix, particular attention has been paid to the definition of each phenomenon, its relevance to nuclear safety, measurement capability, instrumentation and data base and the predictive capability of the code. This was done to meet some concerns resulting from the user feedback on the existing Integral Test Facility Matrix and dealt with questions raised about what is really meant by certain of the phenomena.

It is apparent from this work that the level of the state of knowledge related to the different phenomenon is far from uniform. For example the heat transfer process has been extensively studied in steady state conditions, whereas for non-condensable gas effects or boron mixing the data base is more limited. That indicates an absence of internationally co-ordinated work to provide more equal coverage of all the phenomena. On the contrary, there has been a tendency for particular phenomena to become the 'hot topic' and to be studied by everyone at certain periods of time. The positive side of this pattern is the large amount of international exchange and the large number of publications on a subject, though this is at the expense of interest in some other perhaps less obviously crucial phenomena.

Another important outcome is related to the large amount of work which is necessary to validate a computer code against the total number of phenomena which have been identified (67). Compared to existing code matrices the total number of selected tests is at least one order of magnitude more than has been utilised until now. The increasing

power of available computers, however, makes the calculation of a larger number of tests more feasible now than in the past.

It must be recognised by the users of this SET matrix that a detailed check of the selected tests and of the associated documentation was not possible on every single test. For some cases it was not possible to select particular tests. These open problems will, we hope, be solved in the future by feedback from the facilities owners and with the help of the users. So this matrix has to be considered as a living, evolving document. Nevertheless, even in its present form, this matrix is representative of the major part of the experimental work which has been carried out in the thermal hydraulics field, covering a large number of phenomena within a large range of useful parameters.

The first volume of the SET matrix report [1a] provides cross references between test facilities and thermal-hydraulic phenomena, and lists tests classified by phenomena. As a preliminary to the classification of facilities and test data, it was necessary to identify a sufficiently complete list of relevant phenomena for LOCA and non-LOCA transient applications of PWRs and BWRs. The majority of these phenomena are also relevant to Advanced Water Cooled Reactors. To this end, 67 phenomena were identified for inclusion in the SET matrix. Phenomena characterisation and the selection of facilities and tests for the SET matrix are included in volume I of the report [1a]. In all, about 2094 tests are included in the SET matrix.

The SET matrix, as it stands, is representative of the major part of the experimental work which has been carried out in the LWR-safety thermal hydraulics field, covering a large number of phenomena within a large range of useful parameters. The SET matrix also provides a basis for evaluating the existing data base and defining the main axes for further research in LWR-safety thermal hydraulics in relation to separate effects testing. Some evaluation of the CSNI-SET activity can be found in [6].

REFERENCES

[1] AKSAN N., D'AURIA F., GLAESER H., POCHARD R., RICHARDS C., SJOBERG A., *"Separate effects test matrix for thermal-hydraulic code validation"*
(a) Vol. I: Phenomena characterisation and selection of facilities and tests
(b) Vol. II: Facility and experiment characteristics
CSNI reports OECD/GD(94)82 and OECD/GD(94)83, respectively, September 1994

[2] LEWIS M.J., ET.AL. *"State of the art report (SOAR) on Thermalhydraulics of Emergency Core Cooling in Light Water .Reactors"*, OECD-NEA-CSNI report no. 161, October 1989

[3] *"CSNI Code Validation Matrix of Thermalhydraulic codes for LWR LOCA and transients"*, OECD-NEA-CSNI report no.132, March 1987

[4] WOLFERT K. AND BRITTAIN I., *"CSNI Validation Matrix for PWR and BWR Thermalhydraulic System Codes"* Nucl. Eng. and Design, Vol. 108, pp. 107-119, 1988

[5] WOLFERT K., GLAESER H., AKSAN N.: *"CSNI Validation Matrix for PWR and BWR Codes"* Proceedings of the CSNI-Specialist Meeting on Transient Two-Phase Flow Aix-en-Provence, France, edited by M. Reocreux and M.C. Rubinstein, NEA/CSNI/RL(92)/12, 1992

[6] D'AURIA F., AKSAN N., GLAESER H., SJOBERG A., POCHARD R., LILLINGTON J., "Further evaluation of the CSNI separate effect test activity", Paper to be presented at the 7th International Meeting on Nuclear Reactor Thermal-Hydraulics NURETH-7, Saratoga Springs, NY (USA), September 10-15, 1995

Table 1: LIST OF PHENOMENA

0	BASIC PHENOMENA	1	Evaporation due to Depressurisation
		2	Evaporation due to Heat Input
		3	Condensation due to Pressurisation
		4	Condensation due to Heat Removal
		5	Interfacial Friction in Vertical Flow
		6	Interfacial Friction in Horizontal Flow
		7	Wall to Fluid Friction
		8	Pressure Drops at Geometric Discontinuities
		9	Pressure Wave Propagation
1	CRITICAL FLOW	1	Breaks
		2	Valves
		3	Pipes
2	PHASE SEPARATION/VERTICAL FLOW WITH AND WITHOUT MIXTURE LEVEL	1	Pipes/Plena
		2	Core
		3	Downcomer
3	STRATIFICATION IN HORIZONTAL FLOW	1	Pipes
4	PHASE SEPARATION AT BRANCHES	1	Branches
5	ENTRAINMENT/DEENTRAINMENT	1	Core
		2	Upper Plenum
		3	Downcomer
		4	Steam Generator Tube
		5	Steam Generator Mixing Chamber (PWR)
		6	Hot Leg with ECCI (PWR)
6	LIQUID-VAPOUR MIXING WITH CONDENSATION	1	Core
		2	Downcomer
		3	Upper Plenum
		4	Lower Plenum
		5	Steam Generator Mixing Chamber (PWR)
		6	ECCI in Hot and Cold Leg (PWR)
7	CONDENSATION IN STRATIFIED CONDITIONS	1	Pressuriser (PWR)
		2	Steam Generator Primary Side (PWR)
		3	Steam Generator Secondary Side (PWR)
		4	Horizontal Pipes
8	SPRAY EFFECTS	1	Core (BWR)
		2	Pressuriser (PWR)
		3	Once-Through Steam Generator Secondary Side (PWR)
9	COUNTERCURRENT FLOW / COUNTERCURRENT FLOW LIMITATION	1	Upper Tie Plate
		2	Channel Inlet Orifices (BWR)
		3	Hot and Cold Leg
		4	Steam Generator Tube (PWR)
		5	Downcomer
		6	Surgeline (PWR)
10	GLOBAL MULTIDIMENSIONAL FLUID TEMPERATURE, VOID AND FLOW DISTRIBUTION	1	Upper Plenum
		2	Core
		3	Downcomer
		4	Steam Generator Secondary Side
11	HEAT TRANSFER:		
	NATURAL OR FORCED CONVECTION	1	Core, Steam Generator, Structures
	SUBCOOLED/NUCLEATE BOILING	2	Core, Steam Generator, Structures
	DNB/DRYOUT	3	Core, Steam Generator, Strucutres
	POST CRITICAL HEAT FLUX	4	Core, Steam Generator, Strucutres
	RADIATION	5	Core
	CONDENSATION	6	Steam Generator, Structures
12	QUENCH FRONT PROPAGATION/REWET	1	Fuel Rods
		2	Channel Walls and Water Rods (BWR)
13	LOWER PLENUM FLASHING		
14	GUIDE TUBE FLASHING (BWR)		
15	ONE AND TWO PHASE IMPELLER-PUMP BEHAVIOUR		
16	ONE AND TWO PHASE JET-PUMP BEHAVIOUR (BWR)		
17	SEPARATOR BEHAVIOUR		
18	STEAM DRYER BEHAVIOUR		
19	ACCUMULATOR BEHAVIOUR		
20	LOOP SEAL FILLING AND CLEARANCE (PWR)		
21	ECC BYPASS/DOWNCOMER PENETRATION		
22	PARALLEL CHANNEL INSTABILITIES (BWR)		
23	BORON MIXING AND TRANSPORT		
24	NONCONDENSABLE GAS EFFECT (PWR)		
25	LOWER PLENUM ENTRAINMENT		

Table 2: LIST OF FACILITIES

	info sheet	selected in the CCVM
1 - CANADA		
1.1 Elbow Flooding Rig	a	
1.2 CWIT (CANDU reactors)	a	
1.3 Pumps		
1.4 Header Test Facility (CANDU reactors)	a	
2 - FINLAND		
2.1 REWET-I	a	
2.2 REWET - II	a	x
2.3		
2.4 VEERA	a	
2.5		
2.6 IVO-CCFL (air:water)	a	x
2.7 IVO-Thermal Mixing	a	x
2.8 IVO-Loop Seal Facility (Air/Water)	a	x
3 - FRANCE		
3.1 MOBY-DICK	a	x
3.2 SUPER MOBY-DICK	a	x
3.3 CANON and SUPER CANON (Horiz)	a	x
3.4 VERTICAL CANON	a	
3.5		
3.6 TAPIOCA (Vertical)	a	x
3.7 DADINE (Vertical Tube, Inside)	a	x
3.8 PERICLES Rectangular	a	x
3.9 PERICLES Cylindrical	a	x
3.10 PATRICIA GV 1	a	x
3.11 PATRICIA GV 2	a	x
3.12 ERSEC Tube (Inside)	a	x
3.13 ERSEC Rod Bundle	a	x
3.14 OMEGA Tube (Inside)	a	x
3.15 OMEGA Rod Bundle	a	x
3.16 ECTHOR Loop Seal (Air/Water)	a	x
3.17 COSI	a	x
3.18 SUPER MOBY-DICK TEE	a	x
3.19 PIERO (Air/Water)	a	x
3.20 EPOPEE		
3.21 EVA	a	x
3.22 SEROPS		
3.23 BETHSY Pressuriser		
3.24 SUPER MOBY-DICK Horizontal		
3.25 REBECA	a	x
3.26 ECOTRA	a	x
4 - GERMANY		
4.1 UPTF	a	x
4.2 HDR Vessel	a	x
4.3 BATTELLE PWR RS 16	a	
4.4 BATTELLE BWR 150396	a	x
4.5 Blowdown Heat Transfer RS 37	a	x
4.6 Heat Transfer Refill/Reflood RS 36		
4.7 Steady state DNB Exp. RS 164		
4.8 Trans. Boil. Inst. Tube (Freon) RS 370	a	
4.9 Rewet RS 62/184	a	
4.10 Thermodyn. Nonequilibrium RS 77	a	x
4.11 LOCA Pump Behaviour RS 92	a	
4.12 Thermalhyd. UP-BBR RS 373	a	
4.13 Pressuriser-Valve RS 240, 347, 636		
4.14 Steam/Water Disch. Flow RS 93, 397	a	
4.15		
4.16 T-Junction Test Facility (KfK)	a	x
5 - ITALY		
5.1 Pressuriser (Vapore Plant) ENEA	a	x
5.2 Pressuriser Spray, TURIN	a	x
5.3 Pressuriser Flooding, CISE		
5.4 JETI-4 Fuel Channel SIET	a	x
5.5 Safety VALVE SIET	a	x
5.6 Gen 3x3 (Steam Generator), SIET	a	x
5.7 8x8 Bundle, CISE		
5.8 FREGENE (Steam Generator) ENEA		
5.9 ARAMIS (Separator) ENEA		
5.10 Jet Condensation, TURIN		
5.11 Jet Condensation, ENEA		
5.12 CHF, ENEA		
5.13 CCF, ENEA		
5.14 FOB Blowdown, ANSALDO		
5.15 GEST-SEP, SIET	a	x
5.16 GEST-GEN (20 M W SG), SIET		
5.17 PIPER (Blowdown), PISA	a	x
5.18 JF Blowdown, ENEA		
6 - JAPAN		
6.1 TPTF, JAERI	a	x
6.2 Air/Water Horiz. Flow Loop JAERI	a	
6.3 T-Break TF (Air/Water), JAERI	a	
6.4 Air/Water Rod Bundle TF, JAERI		
6.5 SG U-Tube TF, JAERI		
6.6. Single Pin Heat Transf. TF, JAERI	a	
6.7 SRTF (Reflood), Toshiba	a	
6.8 ESTA (18 Degree Sector), Toshiba		
6.9 ESTA-KP (KWU-PWR), Toshiba		
6.10 RRTF (Refill/Reflood), Toshiba		
6.11 SHTF (Spray Heat Transf.) Toshiba		
6.12 Guide Tube CCFL TF, Toshiba		
6.13 Swell Level Tests, Toshiba		
6.14 SCTF, JAERI	a	x
6.15 CCTF, JAERI	a	
6.16 HICOF (Hitachi Core and Fuel Tests)		
6.17		
6.18 Hot Leg CCFL Rig, JAERI	a	
7 - NETHERLANDS		
7.1 BCN Boiloff/Reflood Tests (36 rods)	a	
7.2		
7.3 NEPTUNUS	a	x
8 - SWEDEN		
8.1 GÖTA BWR ECC Tests	a	x
8.2 MARVIKEN	a	x
8.3 FRIGG/FRÖJA	a	x
8.4 120 bar Loop		
8.5 SIV		
8.6 SEPA		
9 - SWITZERLAND		
9.1 NEPTUN-I (Boiloff)	a	x
9.2 NEPTUN-I and II (Reflood)	a	x
9.3 PEANUT (Reflood Inside Tube)	a	
10 - UNITED KINGDOM		
10.1 ACHILLES Reflood Loop	a	x
10.2 THETIS Bundle	a	x
10.3 REFLEX Tube Reflood		
10.4 Post Dryout Ins. Tube (HP, Winfrith)	a	x
10.5 TITAN/9 MW Rigs	a	
10.6 High Pressure Rig	a	
10.7 Post Dryout Ins. Tube (LP, Harwell)	a	x
10.8 Air/Water Pipeline Fac. (Large Sc.)		
10.9 Hot Leg (Air/Water, Offt., Large Sc.)	a	
10.10		
10.11 Horiz. CCFL Rig (Air/Water, Small Sc.)	a	
10.12 Air/Water Rigs (Small Scale)		
10.13 LOTUS (Air/Water Ann. Flow in Tube)	a	x
10.14 Single Tube Level Swell (Harwell)	a	x
10.15 Single Tube Reflood (Harwell)	a	
10.16 Crossflow Two-Phase Wind Tunnel	a	
10.17 Loop Seal Air/Water Rig		
10.18 Hot Leg Co and CCF Rig		
10.19 Single tube Reflood (Leatherhead)	a	
10.20 Boiler Dynamics Rig	a	
10.21 Valve Blowdown Test Facility	a	x
10.22 Single Pin Reflood		
10.23 Multipin Cluster Rig		
10.24 Blowdown Rig		
10.25 ECCS Condensation Rig		
10.26 1/6th Sc. Broken Cold Leg Nozzle Rig	a	
10.27 1/10th Scale PWR Refill Strath Clyde		
10.28 R113 Vertical Forced Circul. Loop		
10.29 R113 Horiz. Forced Circul. Loop		
10.30 Vertical Flow Rigs		
10.31 High Press. Steam/Water Forced Circ.		
10.32 Low Pressure Boiling Fac. (Harwell)	a	

a : info sheet available in [1, volume 2] - *x : selected in the SETs matrix [1, volume 1, chapter 6]*

Table 2 (Cont.): LIST OF FACILITIES

	info sheet	selected in the CCVM
11 - U S A		
11.1 LTSF 1/6 Scale Jet Pump	a	x
11.2 Univ. California SB. LP BWR	a	x
11.3 THEF Post CHF Ins. Tube	a	x
11.4 Battle Columbus Laboratory		
11.5 Wyle Lab. Marshall Steam Station TF		
11.6 Miscellaneous Sources		
11.7 Univ. California SB. Vert. Tube		
11.8 Univ. California B. Tube Reflood	a	x
11.9 Univ. California Berkeley		
11.10 Columbia rod Bundle Blowdown HT	a	x
11.11 State Univ. New York at Buffalo		
11.12 State Univ. New York at Buffalo		
11.13 1/30, 1/5 + 1/5 VESSEL CREARE	a	x
11.14 1/5 DC + CL CREARE	a	
11.15 CDN DART Bubbly Flow Nozzles	a	
11.16 VERT TUBE PL/DART Annular CCF	a	x
11.17 TUBE + CHANNEL DART Air/Water		
11.18 SNTF DART BWR Spray Nozzle		
11.19 CE + MIT		
11.20 J-Loop Test Fac. Westinghouse		
11.21 HCNTL Univ. of Cincinnati		
11.22 Heat Transf. Loop Babcock and Wilcox		
11.23 FLECHT SEASET Westinghouse	a	x
11.24 Univ. California Los Angeles		
11.25 SCTF Univ. California LA		
11.26 Univ. California Santa Barbara		
11.27 Univ. California Berkeley		
11.28 HST, SSTF, VSF/GE Spray Tests	a	x
11.29 Four Loop Natural Circulation/SRI		
11.30 U-Tube SG Two-Loop Test Fac/SRI	a	
11.31 1/5 EPRI-CREARE Mixing Facility		
11.32 EPRI-SAI Thermal Mixing Test Fac.	a	
11.33 1/2 Scale Test Facility/CREARE	a	x
11.34 EPRI-Wyle Pipe Rupture Test Fac.		
11.35 TPFL/INEL Tee Critical Flow	a	x
11.36 EPRI-SAI Carryover Large Dim.		
11.37 PHSE/PURDUE 1/2 Scale Facility		
11.38 Thermal Hydr. Test Fac/ORNL		
11.39 INEL Pump Characterisation	a	x
11.40 Semiscale/INEL		
11.41 BWR-FLECHT/GE	a	x
11.42 LEHIGH Post CHF Heat Tr. Bundle	a	x
11.43 MIT Pressuriser	a	x
11.44 LS/GE Level Swell in Blowdown	a	
11.45 HOUSTON		
11.46 Cocurrent Hor. Flow/Northwest	a	x
11.47 ANL Power-Void Transf. Funct. BWR	a	x
11.48 Natural Circulation Boiling/ANL	a	
11.49 G2 Loop/Westinghouse		
11.50 Air/Water TF/B. Willamette Pump		
11.51 Univ. California Berkely		
11.52 MB-2 SG Transient/Westinghouse	a	x
11.53 Strat. Condens. Flow/Northwest	a	
11.54 Critical Flow Rig/GE	a	x
11.55 Reflux Rig/Univ. Cal. St. Barbara	a	x
11.56 LTSF Blowdown Quench/INEL	a	x
11.57 LEHIGH Post CHF Vertical Tube	a	x
12 - NORWAY		
12.1 HALDEN Reactor, Reflood Tests	a	x

a : info sheet available in [1, volume 2] - *x : selected in the SETs matrix [1, volume 1, chapter 6]*

Table 3: SEPARATE EFFECTS TEST FACILITY CROSS REFERENCE MATRIX

LEGEND

x suitable for model validation

o limited suitability for model validation

- not suitable for model validation

Phenomena		Separate Effects Test Facilities																				
						3. France																
		MOBY-DICK	SUPER MOBY-DICK	CANON and SUPER CANON (Horiz)	VERTICAL CANON		TAPIOCA (Vertical)	DADINE (Vertical Tube, Inside)	PERICLES Rectangular	PERICLES Cylindrical	PATRICIA GV 1	PATRICIA GV 2	ERSEC Tube (Inside)	ERSEC Rod Bundle	OMEGA Tube (Inside)	OMEGA Rod Bundle	ECTHOR Loop Seal (Air/Water)	COSI	SUPER MOBY-DICK TEE	PIERO (Air/Water)	EPOPEE	EVA
	Facility No.	1	2	3	4	5	6	7	8	9	10	11	12	13	14	15	16	17	18	19	20	21
	Info Sheet available	a	a	a	a		a	a	a	a	a	a	a	a	a	a	a	a	a	a		a
0 BASIC PHENOMENA	1 Evaporation due to Depressurisation	x	x	x	x		x	-	-	-	-	-	-	-	o	o	-	-	-	-	-	-
	2 Evaporation due to Heat Input	-	-	-	-		-	o	-	-	-	-	o	o	o	o	-	-	-	-	-	-
	3 Condensation due to Pressurisation	-	-	-	-		-	-	-	-	-	-	-	-	-	-	-	-	-	-	-	-
	4 Condensation due to Heat Removal	-	-	-	-		-	-	-	-	o	-	-	-	-	-	-	o	-	-	-	-
	5 Interfac. Frict. Vertic. Flow	-	-	-	o		o	x	-	-	-	o	-	-	o	o	o	-	-	-	-	-
	6 Interfac. Frict. Horiz. Flow	-	-	o	-		-	-	-	-	-	-	-	-	-	-	o	o	-	-	-	-
	7 Wall to Fluid Friction	x	x	x	-		-	-	-	-	-	-	-	-	-	-	-	-	x	-	-	-
	8 Press. Drops at Geometr. Discontinuities	-	x	-	o		o	-	-	-	-	-	-	-	-	-	-	-	x	-	-	-
	9 Pressure Wave Propagation																					
1 CRITICAL FLOW	1 Breaks	-	x	x	x		x	-	-	-	-	-	-	-	x	x	-	-	x	-	-	-
	2 Valves	-	-	-	-		-	-	-	-	-	-	-	-	-	-	-	-	-	-	-	-
	3 Pipes	x	x	-	-		-	-	-	-	-	-	-	-	-	-	-	-	-	-	-	-
2 PHASE SEPARATION/VERTICAL FLOW WITH AND WITHOUT MIXTURE LEVEL	1 Pipes/Plena	-	-	-	x		x	o	-	-	o	x	-	-	-	-	-	-	-	o	-	-
	2 Core	-	-	-	-		-	-	x	x	-	-	-	-	-	-	-	-	-	-	-	-
	3 Downcomer	-	-	-	-		-	-	-	-	-	-	-	-	-	-	-	-	-	-	-	-
3 STRATIFICATION IN HORIZ. FLOW	1 Pipes	-	-	-	-		-	-	-	-	-	-	-	-	-	-	o	o	x	-	-	-
4 PHASE SEPARATION AT BRANCHES	1 Branches	-	-	-	-		-	-	-	-	-	-	-	-	-	-	-	-	x	-	-	-
5 ENTRAINMENT/DEENTRAINMENT	1 Core	-	-	-	-		-	o	x	x	-	-	-	x	-	x	-	-	-	-	-	-
	2 Upper Plenum	-	-	-	-		-	-	o	x	-	-	-	-	-	-	-	-	-	-	-	-
	3 Downcomer	-	-	-	-		-	-	-	-	-	-	-	-	-	-	-	-	-	-	-	-
	4 SG-Tube	-	-	-	-		-	-	-	-	x	-	-	-	-	-	-	-	-	-	-	-
	5 SG-Mix. Chamber (PWR)	-	-	-	-		-	-	-	-	-	-	-	-	-	-	-	-	-	-	-	-
	6 Hot Leg with ECCI (PWR)	-	-	-	-		-	-	-	-	-	-	-	-	-	-	-	-	-	-	-	-
6 LIQUID-VAPOUR MIXING WITH CONDENSATION	1 Core	-	-	-	-		-	-	-	-	-	-	-	-	-	-	-	-	-	-	-	-
	2 Downcomer	-	-	-	-		-	-	-	-	-	-	-	-	-	-	-	-	-	-	-	-
	3 Upper Plenum	-	-	-	-		-	-	-	-	-	-	-	-	-	-	-	-	-	-	-	-
	4 Lower Plenum	-	-	-	-		-	-	-	-	-	-	-	-	-	-	-	-	-	-	-	-
	5 SG-Mix. Chamb. (PWR)	-	-	-	-		-	-	-	-	-	-	-	-	-	-	-	-	-	-	-	-
	6 ECCI in Hot and Cold Leg (PWR)	-	-	-	-		-	-	-	-	-	-	-	-	-	-	-	x	-	-	-	-
7 CONDENSATION IN STRATIFIED CONDITIONS	1 Pressuriser (PWR)	-	-	-	-		-	-	-	-	-	-	-	-	-	-	-	-	-	-	-	-
	2 SG-Primary Side (PWR)	-	-	-	-		-	-	-	-	x	-	-	-	-	-	-	-	-	-	-	-
	3 SG-Secondary Side (PWR)	-	-	-	-		-	-	-	-	-	x	-	-	-	-	-	-	-	-	-	-
	4 Horizontal Pipes	-	-	-	-		-	-	-	-	-	-	-	-	-	-	-	x	-	-	-	-
8 SPRAY EFFECTS	1 Core (BWR)	-	-	-	-		-	-	-	-	-	-	-	-	-	-	-	-	-	-	-	-
	2 Pressuriser (PWR)	-	-	-	-		-	-	-	-	-	-	-	-	-	-	-	-	-	-	-	-
	3 OTSG Second. Side (PWR)	-	-	-	-		-	-	-	-	-	-	-	-	-	-	-	-	-	-	-	-
9 CCF/CCFL	1 Upper Tie Plate	-	-	-	-		-	-	o	o	-	-	-	-	-	-	-	-	-	-	-	-
	2 Channel Inlet Orifices (BWR)	-	-	-	-		-	-	-	-	-	-	-	-	-	-	-	-	-	-	-	-
	3 Hot and Cold Leg	-	-	-	-		-	-	-	-	-	-	-	-	-	-	-	o	-	-	-	-
	4 SG-Tube (PWR)	-	-	-	-		-	-	-	-	x	-	-	-	-	-	-	-	-	-	-	-
	5 Downcomer	-	-	-	-		-	-	-	-	-	-	-	-	-	-	-	-	-	-	-	-
	6 Surgeline (PWR)	-	-	-	-		-	-	-	-	-	-	-	-	-	-	-	-	-	-	-	-
10 GLOBAL MULTIDIMENSIONAL FLUID TEMPERATURE, VOID AND FLOW DISTRIBUTION	1 Upper Plenum	-	-	-	-		-	-	o	-	-	-	-	-	-	-	-	-	-	-	-	-
	2 Core	-	-	-	-		-	-	x	-	-	-	-	-	-	-	-	-	-	-	-	-
	3 Downcomer	-	-	-	-		-	-	-	-	-	-	-	-	-	-	-	-	-	-	-	-
	4 SG-Secondary Side	-	-	-	-		-	-	-	-	-	-	-	-	-	-	-	-	-	-	-	-
11 HEAT TRANSF.: NAT. FORC. CONV.	1 Core, SG, Structures	-	-	-	-		-	x	-	-	-	-	-	-	-	-	-	-	-	-	-	-
SUBC./NUCL. BOIL.	2 Core, SG, Structures	-	-	-	-		-	x	-	-	-	-	-	-	-	-	-	-	-	-	-	-
DNB/DRYOUT	3 Core, SG, Structures	-	-	-	-		-	x	-	-	-	x	x	-	x	x	-	-	-	-	-	-
POST CHF	4 Core, SG, Structures	-	-	-	-		-	x	-	-	-	-	x	-	x	x	-	-	-	-	-	-
RADIATION	5 Core	-	-	-	-		-	-	-	-	-	-	-	-	-	-	-	-	-	-	-	-
CONDENSATION	6 SG, Structures	-	-	-	-		-	-	-	-	x	-	-	-	-	-	-	-	-	-	-	-
12 QUENCH FRONT PROPAG./REWET	1 Fuel Rods	-	-	-	-		-	-	x	x	-	-	o	x	-	-	-	-	-	-	-	-
	2 Channel Walls and Water Rods (BWR)	-	-	-	-		-	-	-	-	-	-	-	-	-	-	-	-	-	-	-	-
13 LOWER PLENUM FLASHING		-	-	-	-		o	-	-	-	-	-	-	-	x	x	-	-	-	-	-	-
14 GUIDE TUBE FLASHING (BWR)		-	-	-	-		-	-	-	-	-	-	-	-	-	-	-	-	-	-	-	-
15 ONE AND TWO PHASE IMPELLER-PUMP BEHAVIOUR		-	-	-	-		-	-	-	-	-	-	-	-	-	-	-	-	-	-	x	x
16 ONE AND TWO PHASE JET-PUMP BEHAVIOUR (BWR)		-	-	-	-		-	-	-	-	-	-	-	-	-	-	-	-	-	-	-	-
17 SEPARATOR BEHAVIOUR		-	-	-	-		-	-	-	-	-	-	-	-	-	-	-	-	-	-	-	-
18 STEAM DRYER BEHAVIOUR		-	-	-	-		-	-	-	-	-	-	-	-	-	-	-	-	-	-	-	-
19 ACCUMULATOR BEHAVIOUR		-	-	-	-		-	-	-	-	-	-	-	-	-	-	-	-	-	-	-	-
20 LOOP SEAL FILLING AND CLEARANCE (PWR)		-	-	-	-		-	-	-	-	-	-	-	-	-	-	x	-	-	-	-	-
21 ECC BYPASS/DC PENETRATION		-	-	-	-		-	-	-	-	-	-	-	-	-	-	-	-	-	-	-	-
22 PARALLEL CHANNEL INSTABILITIES (BWR)		-	-	-	-		-	-	-	-	-	-	-	-	-	-	-	-	-	-	-	-
23 BORON MIXING AND TRANSPORT		-	-	-	-		-	-	-	-	-	-	-	-	-	-	-	-	-	-	-	-
24 NONCONDENSABLE GAS EFFECT (PWR)		-	-	-	-		-	-	-	-	x	-	-	-	-	-	-	x	-	-	-	-
25 LOWER PLENUM ENTRAINMENT		-	-	-	-		-	-	-	-	-	-	-	-	-	-	-	-	-	x	-	-

Table 4: PHENOMENON No. 11.4 – HEAT TRANSFER: POST-CHF IN THE CORE, IN THE STEAM GENERATOR AND AT STRUCTURES (PART A)

FACILITY IDENTIFICATION			KEYWORDS	RELEVANT PARAMETERS RANGES			REASONS FOR SELECTION OR NOTES
No.	Status in the matrix	Name		Pressure (MPa)	Inlet mass flow (kg/m² s)	Heat flux (W/cm²)	
3.7	a x	DADINE (VERTICAL TUBE INSIDE)	Vertical tube, Steady-state, Boil-off	0.1-0.6	20-150	1-3	
3.12	a x	ERSEC TUBE (INSIDE)	Tube, reflooding	0.1-0.6	10-120	1-7	1 5 6
3.14	a x	OMEGA TUBE (INSIDE)	Blowdown	16	-	60-125	5 6 7
3.15	a x	OMEGA ROD BUNDLE	Blowdown	13-15	-	44-60	5 6 7
4.5	a x	BLOWDOWN HEAT TRANSFER RS 37	Blowdown Rod bundle	15-1.3	3828-3300	163-74	5 6 7
4.9	a x	REWET (RS 62/184)	Reflooding, tube, single rod	0.1-0.45	2-10 cm/s	2-6	5 6
5.6	a x	GEN 3x3 (STEAM GENERATOR) ENEA	SG Secondary, Steady-state, transient	3.5-8	200-600	-	
5.7	a x	8x8 BUNDLE CISE	BWR-6 Bundle, Steady state	7.1	125-1600	-	6 7
5.12	x	CHF ENEA					
6.1	a x	TPTF JAERI	Core heat transfer, Boil-off, Reflooding, BWR and PWR bundle	0.5-12	20-410	3-25	2 3 5 6
6.16	x	HICOF (HITACHI CORE AND FUEL TESTS)					
8.4	x	120 BAR LOOP					
9.1	a x	NEPTUN-I (BOILOFF)	Bundle	0.15	-	25-75 kW	2 3 5 6
10.3	x	REFLEX TUBE REFLOOD					
10.4	a x	POST DRYOUT INS. TUBE (HP, WINFRITH)	Hot patch	0.2-7	50-2000	1-30	2 3 5 6
10.7	a x	POST DRYOUT INS. TUBE (LP, HARWELL)		0.2-0.4	25-200		2 3 5 6
10.20	a x	BOILER DYNAMICS RIG	SG, transient boundary conditions	28	12 kg/s	12 MW	6 7
10.23	x	MULTIPIN CLUSTER RIG					
11.3	a x	THEF POST CHF INS. TUBE	Steady state, quasi-steady state	0.2-7	12-70	0.8-22.5	2 3 4 5 6
11.7	x	UNIV. CALIFORNIA B. TUBE REFLOOD					
11.8	a x	UNIV. CALIFORNIA B. TUBE REFLOOD	Reflooding	0.1-0.3	2.5-18 cm/s		1 5 6

Table 4 (Cont.): PHENOMENON No. 11.4 – HEAT TRANSFER: POST-CHF IN THE CORE, IN THE STEAM GENERATOR AND AT STRUCTURES (PART B)

FACILITY IDENTIFICATION			KEYWORDS	RELEVANT PARAMETERS RANGES			REASONS FOR SELECTION OR NOTES
No.	Status in the matrix	Name		Pressure (MPa)	Inlet mass flow (kg/m^2 s)	Heat flux (W/cm^2)	
11.9	x	UNIV. CALIFORNIA BERKELEY					
11.10	a x	COLUMBIA ROD BUNDLE BLOWDOWN HT	Post-CHF	13.8	3500	1.8 MW	Similar to OMEGA (rod bundle) 3.15
11.11	x	STATE UNIV. NEW YORK AT BUFFALO					
11.21	x	HCNTL UNIV. OF CINCINNATI					
11.23	a x	FLECHT SEASET WESTINGHOUSE	Reflooding, Unblocked and blocked bundle	0.14-0.4	1.5-15 cm/s	0.9-3.3 kw/s	1 2 3 5 6
11.25	x	SCTF UNIV. CALIFORNIA LA					
11.38	x	THERMAL HYDR. TEST FAC./ORNL					
11.40	x	SEMISCALE/INEL					
11.42	a x	LEHIGH POST CHF HEAT TR. BUNDLE	Bundle, hot patch, reflooding	0.1-1.	Up to 300	Up to 10	2 3 5 6
11.49	x	G2 LOOP / WESTINGHOUSE					
11.52	a x	MB-2 SG TRANSIENT/ WESTINGHOUSE	SG, transient conditions	7		6.7 MWt	6 7
11.56	a x	LTSF BLOWDOWN QUENCH/INEL	Single rod, bundle	0.1-7	0.4-6. m/s		2 5 6 7
11.57	a x	LEHIGH POST CHF VERTICAL TUBE	Hot patch	0.2-0.6	13-85	1.8-5.8	2 3 5 6
12.1	a x	HALDEN REACTOR, REFLOOD TESTS	Reflooding, fuel and heater rods	0.2-0.4	4-60 g/s	10-30 W/cm	5 6 7

Table 5: EVAPORATION DUE TO DEPRESSURIZATION (PHENOMENON No. 6.0.1)

FACILITIES IDENTIFIER		3.2	3.6	4.4	4.10	8.2
Main Parameters						
P (MPa)	D 10^{-3} m					
0.75					228	
2.59					239	
3		31B234C 33B234C 30B 9X				
5		48B234C			256	
	509					509 mm
	160					
6.37					88	
8.8				BWR steam line break 76 mm		
	76					
9.17					208	
11.58					168	
12		12R305 12R318 12R324 12ORSA 12OEB324				
	10		break 10 mm top lateral			
15			break 20 mm lateral			
	20					
		SELECTED TESTS				

References:

3.2 - B. Spinler, Reconstitution d'essais SUPER MOBY DICK avec le code TRAC PF1/MOD1, version 14.3, N. Technique CEA/DTE/SETh/LEML n° 88-134

3.6 - FRAMATOME report TP/CT/DC 494 June 1980

4.4 - System description, experimental procedures: BF-R64. 167-01, 1982 = (1) data reports: BF-R64.167-30-1 to 11 and (3.1)-(3.9) in (1)
B. Hoïzer et al.: Specification of OECD Standard Problem No. 6, GRS/Battelle Frankfurt, February 1977

4.10 - System description, experimental procedure: résults (plots): RS 77 Final Report, C.E.C. ISPRA 1976 to BMFT-Bonn

8.2 - The Marviken Full Scale Critical Flow Tests. Conclusions. Joint Reactor Safety Experiments in the marviken Power Station, Sweden. MXC-402. December 1979

Additional Information:

3.2 - Convergent inlet diameter 87.5 mm, outlet diameter 20 mm

4.10 - Liquid expansion experiment

Table 6: CRITICAL FLOW IN BREAKS (PHENOMENON No. 6.1.1)

FACILITIES IDENTIFIER		3.2	3.25	8.2	11.54
Main Parameters					
P (MPa)	Temp (K)				
0.3			3 B X 06 3 B X 20 3 B X 100		
0.5			5 B X 29 5 B X 100		
0.8			8 B X 40		
2.0	465	20 B 192			
2.0	477	20 B 204			
2.0	484	20 B 211			
4.0	501	40 B 227			
4.0	514	40 B 240			
4.0	522	40 B 249			
P, T_{sub} = 5.0,30	D, L/D = 0.2,3.0			13	
P, T_{sub} = 5.0,30	D, L/D = 0.3,1.0			6	
P, T_{sub} = 5.0,30	D, L/D = 0.3,3.0			12	
P, T_{sub} = 5.0,30	D, L/D = 0.3,3.7			18	
P, T_{sub} = 5.0,30	D, L/D = 0.5,0.3			24	
P, T_{sub} = 5.0,30	D, L/D = 0.5,1.5			21	
P, T_{sub} = 5.0,30	D, L/D = 0.5,3.6			22	
6.89	x_0 = 0.003				Nozzle 3
6.62	x_0 = - 0.002				Nozzle 3
8.0	567	80 B 293			
		SELECTED TESTS			

References:

3.2 -
- Report CEA/DRE/STT No. TT-163, July 1981.
- Note CEA/CDR/STT No. TT/SETRE/82-32, January 1983.
- Note CEA/DRE/STT No. TT/SETRE/71, September 1983.

3.25 - Note CEA, DRE/SETRE/LTA 784/612, July 1984.

8.2 - The Markiven Full Scale Critical Flow Test. MXC-301. Summary Report, December 1979

11.54 Sozzi G.L., Sutherland W.A.: Critical Flow of Saturated and Subcooled Water at High Preessure. General Electric Report NEDO-13418, May 1975.

Table 7: GLOBAL MULTIDIMENSIONAL FLUID TEMPERATURE, VOID AND FLOW DISTRIBUTION IN THE CORE (PHENOMENON No. 6.10.2)

FACILITIES IDENTIFIER	3.8	6.14	6.15	10.1	10.2	11.23
Main Parameters						
P (MPa)						
< 1.0 MPa	31B	S2-16/621 cold leg ECC inj.	C2-12/71 cold leg ECC inj.	Level swell, 0.2 MPa: A1L069 A1L070 A1L071		Boil off: 35.557 35.658 35.759
	32A 35	S3-11/715 combined ECC inj.	C2-20/80 combined ECC inj.	Voidage distribution: A3L040 A3L046 A3L049 BE reflood: A1B091 A1B099 A1B101 A1B112		Steam cooling: 32.753 36.160 36.261 36.262 36.463 36.564 36.766 36.867
0.5-4.0 MPa					7 tests, selected in Ref. 3.8/10.2	
	SELECTED TESTS					

References:

3.8 - R. Deruaz, P. Clement, J.M. Veteau: "Find Report - Study of Two Dimensional Effects in the Core of a Light Water Reactor During the Reflooding Phase of a LOCA." contract N.002 SRF

3.8/10.2 - A. Forge et al.: "Comparative Calculations on Selected Two-Phase Flow Phenomena Using Major PWR System Codes." CEC, EUR 12901 EN, 1990.

6.14 - Data Reports on Large Scale Reflood Tests for each SCTF-Test.

6.15 - Data Reports on Large Scale Reflood Tests for each CCTF-Test.

10.1 - Technical Reports to ACHILLES Steering Group: UK Nucl. Industry and CEGB Chairman for Experimental Program.

10.2 - C.A. Cooper, K.G. Pearson, D. Jowitt: Contract SR-030-UK.

G.L. Shires et al.: "The Thermal Performance of a Partially Water Filled Fuel Cluster, Part1: An Exploratory Experimental Study of Level Swell at Pressures from 2 to 40 bars." AEEW-R-1369, June 1980.

11.23 - S. Wong, L.E. Hochreiter: Analysis of the FLECHT-SEASET Unblocked Bundle Steam Cooling and Boil-off Tests; NUREG/CR-1533, May 1981

Table 8: HEAT TRANSFER: POST-CHF IN THE CORE, IN THE STEAM GENERATOR AND AT STRUCTURES (PHENOMENON No. 6.11.4) (5/7)

FACILITIES IDENTIFIER		11.8	11.23			
Main parameters						
P (MPa)	Inlet velocity (cm/s)					
0.1	7.5	3076				
0.3	7.5	3070				
0.3	12.5	3060				
0.2	2.5	3051				
0.3	7.5	3059				
	Mass Flux (kg/m^2s)					
0.1	74	6-3-70-1				
0.1	74	10-3-70-1				
0.1	74	6-3-150-1				
0.1	74	10-3-150-1				
0.4	74	6-3-150-4				
0.4	74	10-3-150-4				
0.4	26	6-1-150-4				
	Rod peak power (KW/m)					
0.28	1.6		33056	Steam cooling		
	0.16		36160			
	0.79		36262			
	0.039		36564			
	0.02		36867			
		SELECTED TESTS				

References:

11.8 - R. Seban: "Reflooding of a Vertical Tube at 1, 2 and 3 Atmospheres" EPRI-NP-3191, July 1981.

R. Seban, et al.: "Heat Transfer During Quench and Dryout in a Vertical Tube" EPRI-NP-4157, July 1985.

11.23 - S. Wong, L.E. Hochreiter: "Analysis of the FLECHT SEASET Unblocked Bundle Steam-Cooling and Boil-off Tests "NUREG/CR-1533, May 1981.
N. Lee, et al.: "PWR FLECHT SEASET Unblocked Bundle, forced and Gravity Reflood Task: Data Evaluation and Analysis report" NUREG/CR-2256, February 1982.

Table 8 (Cont.): HEAT TRANSFER: POST-CHF IN THE CORE, IN THE STEAM GENERATOR AND AT STRUCTURES (PHENOMENON No. 6.11.4) (6/7)

FACILITIES IDENTIFIER		11.23 (cont.)	11.42	11.49		
Main parameters						
P (MPa)	Rod peak power (KW/m)					
0.28	2.4	31504				
0.28	2.5	32114				
0.41	2.64	32013				
0.14	2.7	31922				
0.28	7.6	31302				
0.28	2.1	31805				
0.28	3.8	31203				
0.27	1.5	31701				
0.28	15	34006				
	Mass Flux (kg/m^2s)					
0.1	13.46		3			
	7.23		9			
	18.48		12			
	18.69		14			
	25.13		20			
	25.58		22			
.56				716		
.56				718		
.1				736		
		SELECTED TESTS				

References:

11.42 - K. Tuzla, et al.: "Thermodynamic Non-Equilibrium in Post-Critical Heat-Flux Boiling in a Rod Bundle "NUREG/CR-5095, June 1988, Vols. 1-3.

M. Sencar and N. Aksan: "Independent Assessment of RELAP5/Mod 3 with Lehigh University and PSI-NEPTUN Reflooding Tests" Code Assessment and Maintenance Program Meeting, PSI-Switzerland June 1992.

11.49 Heat Transfer Above the Two-Phase Mixture Level Under Core Uncovery Conditions In a 336-Rod Bundle: Vol. 1 - Westinghouse Electric Corp.
Vol..2 - T.S. Andreychek, Westinghouse Electric corp., Pittsburgh
EPRI-NP-1692, Vols. 1 and 2

H.C. Yeh et al., Westinghouse ELECTRIC Corp.,USA
Heat Transfer Above the Two-Phase Mixture Level Under Core Uncovery Conditions in a 336-Rod Bundle.

Table 8 (Cont.): HEAT TRANSFER: POST-CHF IN THE CORE, IN THE STEAM GENERATOR AND AT STRUCTURES (PHENOMENON No. 6.11.4) (7/7)

FACILITIES IDENTIFIER		11.56	11.57	12.1		
Main parameters						
P (MPa)	Inlet fluid velocity (m/s)					
6.86	3.7	12				
6.92	0.4	7				
	Mass Flux (kg/m^2s)					
0.378	14.8		100			
0.255	14.9		105			
0.409	20.7		112			
0.396	42.7		124			
0.39	29.5		130			
0.272	42.9		158			
0.302	60		174			
0.395	29.9		191			
	Reflood rate (cm/s)					
				IFA-511-2		
0.2-0.4	9.6			5236		
	5.6			5239		
	7.4			5247		
				IFA-511-3		
	9.6			5258		
	5.6			5261		
	7.4			5265		
	2.1			5266		
		SELECTED TESTS				

References:

11.56 N. Aksan: "Evaluation of Analytical Capability to predict cladding Quench" EGG-LOFT-5555, August 1982.

11.57 D.G. Evans, et al. "Measurement of Axially Varying Nonequilibrium in Post-Critical Heat-Flux Boiling in a Vertical Tube" NUREG/CR-3363, Vols. 1 and 2, June 1983.

12.1 C. Vitanza et al.: "Blowdown/reflood tests with Nuclear Heated Rods (IFA-511.2)" OECD Halden Reactor Project, HPR-248, May 1980.

T. Johnsen, C. Vitanza: "Blowdown/Reflood Tests with Semiscale Heaters (IFA-511.3)" OECD Halden Reactor Project HWR-17, May 1981.

RELAP5 ANALYSES OF TWO HYPOTHETICAL FLOW REVERSAL EVENTS FOR THE ADVANCED NEUTRON SOURCE REACTOR

N. C. J. Chen, M. W. Wendel, and G. L. Yoder, Jr.
Oak Ridge National Laboratory[1]
P.O. Box 2009
Oak Ridge, Tennessee 37831-8045
(615) 574-0753

ABSTRACT

This paper presents RELAP5 results of two hypothetical, low flow transients analyzed as part of the Advanced Neutron Source Reactor safety program. The reactor design features four independent coolant loops (three active and one in standby), each containing a main circulation pump (with battery powered pony motor), heat exchanger, an accumulator, and a check valve. The first transient assumes one of these pumps fails, and additionally, that the check valve in that loop remains stuck in the open position. This accident is considered extremely unlikely. Flow reverses in this loop, reducing the core flow because much of the coolant is diverted from the intact loops back through the failed loop. The second transient examines a 102-mm-diam instantaneous pipe break near the core inlet (the worst break location). A break is assumed to occur 90 s after a total loss-of-offsite power. Core flow reversal occurs because accumulator injection overpowers the diminishing pump flow.

Safety margins are evaluated against four thermal limits: $T_{wall} = T_{sat}$, incipient boiling, onset of significant void, and critical heat flux. For the first transient, the results show that these limits are not exceeded (at a 95% non-exceedance probability level) if the pony motor battery lasts 30 minutes (the present design value). For the second transient, the results show that the closest approach of the fuel surface temperature to the local saturation temperature during core flow reversal is about 39°C. Therefore the fuel remains cool during this transient. Although this work is done specifically for the ANSR geometry and operating conditions, the general conclusions may be applicable to other highly subcooled reactor systems.

INTRODUCTION

Currently in the advanced conceptual design stage, the Advanced Neutron Source Reactor (ANSR) [1] is a research reactor to be built at the Oak Ridge National Laboratory. It will provide the highest continuous neutron flux levels of any reactor in the world. The reactor is cooled and moderated by highly subcooled heavy water (D_2O). To accommodate the high core power density (4.5 MW/l), coolant flows upward through the core at a high velocity (25 m/s). In addition, the ANSR features a submerged primary coolant loop configuration and passive gas-pressurized accumulators to improve the depressurization behavior.

---

[1]The submitted manuscript has been authored by a contractor of the U.S. Government under contract DE-AC05-84OR21400. Accordingly, the U.S. Government retains a nonexclusive, royalty-free license to publish or reproduce the published form of this contribution, or allow others to do so, for U.S. Government purposes.

Managed by Martin Marietta Energy Systems, Inc., under contract DE-AC05-84OR21400 with the U.S. Department of Energy.

The conceptual safety analysis report (CSAR) [2] was completed and included pipe break [3-9], Loss-of-Offsite Power (LOSP) [10,11], and reactivity insertion accident calculations. Since the CSAR calculations were completed, several updates to the RELAP5 input model have been made:

1. The power distribution in the cores has been updated to an improved core design with a new U^{235} distribution.
2. A refined nodalization has been used to represent more accurately the propagation of expansion waves that immediately follow an instantaneous pipe break.
3. A total accumulator volume of 7.52 m^3 and 0.52-m^3 bubble size have been assumed for each accumulator, consistent with the current design.
4. The piping layout is now consistent with the Conceptual Design Report [12]. (The major difference between the assumed piping layout and the present one is the elevation of the main circulation pumps.
5. The main circulation pump was changed from a Byron Jackson [13] design to a Westinghouse design that maintains a higher flow rate at lower developed pump head.
6. The primary system pressure sensor location (used for initiating reactor scram and primary pump trip) was moved closer to the core to provide more rapid and sensitive low pressure detection. Also, a first-order time lag of 0.03 s was used for the pressure sensor response lag instead of a straight 0.03-s delay.

In the CSAR calculations, the Costa [14] correlation was used to predict the onset of significant void (OSV), while the Gambill/Weatherhead [15] correlation was used to predict the occurrence of critical heat flux (CHF). Three additional thermal limit criteria have since been included in the code. The first is a modification of the Saha-Zuber [16] OSV correlation. Unlike the Costa correlation, the modified Saha-Zuber correlation has a reasonable low-subcooling limit. The second limit is the $T_{wall} = T_{sat}$ criterion, which is exceeded if the fuel surface temperature (as predicted by the Petukhov [17] correlation at high flow or a constant-Nu correlation at low flow) exceeds the bulk saturation temperature in the coolant channel. The third additional limit is the Bergles-Rohsenow [18] correlation for incipient boiling.

The safety margin is measured by thermal limit ratios. The ratios are defined as the calculated limiting heat flux divided by the local fuel surface heat flux (including uncertainties). The thermal limit correlations were calculated using local fluid conditions. A minimum ratio greater than one indicates that the limit has not been exceeded, and no fuel damage would be expected; if the minimum ratio is less than one, the possibility of fuel damage exists.

The objective of this work is to determine the effects of flow reversal events on the ANSR thermal hydraulic performance. The most recent version of the RELAP5/MOD3/VERSION 1.1.1 input model (including post-CSAR updates) was used to simulate two hypothetical transients that lead to flow reversal. The events are defined and calculated results (with the derived safety margin) are presented and discussed. It is shown that neither of these flow-reversal events present a significant safety threat to the ANSR.

FACILITY DESCRIPTION

The ANSR core design features an axially split core cooled by upward flowing heavy water (see Fig. 1). Each core half is constructed with a series of involute fuel plates arranged in an annular array to provide spanwise uniform coolant gaps. Inner control and shutdown rods and outer shutdown rods are located in the central hole region and the reflector tank, respectively. The core assembly is contained within a double-walled aluminum core pressure boundary tube (CPBT) that separates the high pressure heavy water core coolant from the low pressure heavy water in the reflector tank that surrounds the entire core region.

A simplified reactor primary cooling system diagram is shown in Fig. 2. The system consists of four identical loops connected in parallel to the reactor vessel and to a common reactor outlet pipe. Each loop contains a

gas charged accumulator, a main heat exchanger, an emergency heat exchanger, a reactor coolant pump (each with an AC-powered main motor and a DC-powered pony motor), a strainer, isolation valves, connecting piping, and instrumentation. During normal, full power reactor operation, three of the four loops are in operation with the fourth loop in standby mode.

MODEL DESCRIPTION

An ANSR RELAP5 system model has been developed based on the advanced conceptual design. The model includes three major regions as shown in Fig. 3. The core model (region 1) consists of two core halves, core bypass channels, and a central control rod region. The core is surrounded by the CPBT, which separates the high-pressure primary system and the low-pressure moderator tank.

Core power is calculated using a point kinetics model with reactivity feedback based on coolant density and control rod position. Power is distributed among the various metal and fluid regions and is distributed axially within the fueled region based on a specific fuel loading design.

Each of the two fuel elements is modeled as an average channel (which incorporates all but two of the fuel plates) and two hot channels representing the most limiting axial relative power density profile in each element. For each fuel element, one of these hot channels reflects 95% non-exceedance probability uncertainty levels (for analysis of unlikely events), and one represents 99.9% non-exceedance probability uncertainty levels (for analysis of anticipated events). The purpose of the hot channels is to calculate the most severe axial bulk temperature profile within the core. Within each of these channels, correlations are compared at hot spot conditions. The characteristics of these spots are defined using uncertainties that affect local heat flux conditions, but do not affect bulk coolant conditions because they are so localized.

The loop model (region 2) contains three independent heat exchanger loops. Each loop consists of an isolation valve, a hot/cold leg, an accumulator, horizontal U-tube main and emergency heat exchangers, a centrifugal main circulating pump, and an inertial flow diode (a preferred flow direction device). Both heat exchanger models are calibrated to design specifications. The single-phase homologous curves defining the performance of the main circulation pumps were developed from three-quadrant Westinghouse design curves, and two-phase corrections were based on Semiscale data [19].

An open-loop representation of the letdown and pressurizing system (region 3) is included in the model. Letdown flow is extracted from the inlet plena of the three main heat exchangers. In the design, core outlet pressure is controlled through modulation of the letdown valves. This is modeled by establishing the nominal valve opening size required to allow a nominal flow during normal conditions and controlling about that point.

A main pressurizing pump provides injection flow through a makeup line at the hot leg distribution header. Injection flow is drawn from a constant temperature heavy-water source by the main pressurizing pump. Following letdown isolation, flow through the pressurizing pumps is assumed to continue until the integrated injected flow reaches the makeup tank capacity.

RELAP5 MODIFICATIONS FOR APPLICABILITY TO ANSR

Although the RELAP5 code was designed for pressurized water reactor and boiling water reactor applications, the applicability of the code has been improved for the ANSR-specific fuel plate geometry. Three specific changes were implemented. The first replaced the Dittus-Boelter [20] single-phase forced convection correlation by the Petukhov correlation. The second change incorporated the Gambill/Weatherhead CHF

correlation into the existing Groenveld et al. [21] look-up table. Modification three altered the interfacial drag in the slug flow regime to reflect the Griffith [22] drift flux behavior in narrow channels.

In the low flow regions two additional changes were implemented. The friction factor correlation used to determine the flow resistance in the core (about 80% of the total loop pressure drop) was changed from the laminar friction factor correlation for circular tubes (f = 64/Re) normally used by RELAP to one for long, thin rectangular channels (f = 96/Re). The second change replaced the laminar constant-Nu correlation for circular tubes (Nu = 4.36) by one for rectangular channels (Nu = 7.63). This value of 7.63 accounts for the correct aspect ratio and the nonuniform boundary condition. Although the heat transfer coefficients that are used to determine the fuel surface temperature do not influence OSV, they are important in establishing the $T_{wall} = T_{sat}$ criterion. Experience has shown that RELAP5 will switch from the turbulent Petukhov correlation to the laminar, constant-Nu correlation at a Reynolds number of about 1000. RELAP5 simply takes the maximum of the two heat transfer correlations.

DESCRIPTION OF THE TRANSIENTS

The first transient involved the failure of a single main circulation pump with a stuck-open check valve, leading to flow reversal in the failed loop. The following assumptions were made: (1) the motors (both main AC and pony DC) driving one of the main circulation pumps fail leading to pump coastdown, (2) the check valve in the tripped pump outlet pipe fails to close to prevent reverse flow, and (3) following reactor scram, the core outlet temperature falls sharply, shrinking the coolant and leading to a low-pressure trip of the remaining two functional main circulation pumps. (Here, to force a coolant pump trip, the setpoint was assumed to occur at a pressure 5% higher than the nominal trip setpoint.) This is an unlikely or an extremely unlikely event. Therefore, a 95% non-exceedance probability level was used for the thermal limit comparison.

The second transient considered is a 102-mm-diam instantaneous core inlet break into the reactor pool (at about 3 atmospheres). The break is assumed to occur after the reactor and main circulation pumps are shut down, but while the system is still at high pressure. This shutdown-prior-to-break sequence may occur during an earthquake or during a normal shutdown period. For instantaneous breaks [7,9] that occur before shutdown, the pressure expansion wave propagating from the break site into the fuel channels is the limiting phenomenon, because it significantly reduces the subcooling in the fuel channels, causing thermal limits to be challenged (the Costa OSV limiting heat flux is proportional to subcooling). However, here the pipe break occurs after scram so the core exit subcooling is much larger, and is therefore only slightly affected by the oscillations in saturation temperature caused by the pressure expansion wave. Such an accident, however, leads to diminished core flow and possibly even to a flow reversal, if the break is large enough. Flow reversal could occur if the main circulation pumps (running at 10% pony motor flow after shutdown) are unable to maintain upflow against the accumulator (located in the hot leg) discharge. The accumulators act to maintain higher core exit pressure, but the core inlet pressure is decreased due to the break flow. Parametric simulations have shown that the pipe-break time most likely to result in flow reversal is approximately 90 s after reactor and main circulation pump shutdown. This event is also considered an unlikely or extremely unlikely event. Therefore, all limits are evaluated at a 95% non-exceedance probability level.

RESULTS AND DISCUSSION

Results and discussion of the two flow reversal events calculated using the RELAP5/MOD3/VERSION 1.1.1 input model are presented here.

Single Pump Failure with a Stuck Open Check Valve (Loop Flow Reversal)

At time zero, a main circulating pump was assumed to lose power and began coasting down. The two remaining functional pumps were tripped on low primary system pressure at 13.72 s and then coasted down to pony motor speed. The pony motors continued running for 30 min (until the batteries expired) and then coasted down so that all forced flow was lost. Subsequently, natural circulation developed within the primary system removing the decay heat from the core.

The pressure response at the upper core inlet and exit is shown in Fig. 4 (the upper core is limiting for this transient). After the initial pump trip, the core inlet pressure declines due to the diminishing primary pump head and flow rate, and coolant shrinkage after reactor scram. The core exit pressure changes only slightly because it is controlled by closing the letdown valves in response to the depressurization. The core pressure drop decreases as the core flow decreases and stabilizes once natural circulation is established.

Pump flow and total core flow (sum of three pump flows) are shown in Fig. 5. As the failed pump coasts down, the discharge (core inlet) pressure decreases, causing the functional pump flows to increase. At 1.95 s the failed pump developed head becomes low enough that flow reverses in the failed loop. Flow reversal in the failed loop is possible only because the check valve is also assumed to fail. Much of the flow supplied by the two remaining functional pumps is thus diverted back through the failed loop, bypassing the core. After the functional pump main motors are tripped (13.72 s), the loop flows diminish, but the same flow configuration continues with backflow through the failed loop. After the pony motor batteries expire at 30 min, a free convection flow pattern is established with forward flow through all three loops.

Temperature and coolant velocity transients are shown in Fig. 6 for the 95% hot channel exit. Three minima in the fuel channel subcooling occur, corresponding to three coolant temperature maxima (the saturation temperature remains relatively constant). Initially, the coolant temperature rises with declining core flow. The first peak occurs at the time of reactor scram since the drop in power causes the bulk temperature to fall sharply. After the functional pump main motors are tripped, core flow declines again, causing another increase in the core exit bulk temperature. However, decay heat is also decreasing so that once the flow rate stabilizes, the core exit bulk temperature begins to decline; thus, the second peak is observed. The final peak in the bulk temperature occurs during the transition to natural circulation, again because of reduced core flow. These three subcooling minima are responsible for the three thermal limit ratio minima shown in Fig. 7. Throughout the transient, the fuel surface temperature stays below the saturation temperature, indicating no boiling at the hot spot.

Figure 7 shows a comparison of various thermal limit ratios in the upper (most limiting) core hot spot for a 95% non-exceedance probability level. The thermal limit ratio is the ratio between the thermal limit criterion (e.g. $T_{wall} = T_{sat}$, IB, Costa or Modified Saha-Zuber) and the hot spot heat flux. All three thermal limit ratio minima (other than the original and the modified Saha-Zuber) are greater than unity, indicating that none of the thermal limits are exceeded. As expected, the $T_{wall} = T_{sat}$ and the IB criteria are the most limiting. Before scram, Costa is the most limiting OSV correlation. Discontinuities in both the original and the modified Saha-Zuber thermal limit ratios occur when the velocity falls below 8 m/s. Discontinuities in those ratios again occur (this time the ratios plummet to zero) when the Peclet number falls below 70,000 (about 20 s in Fig. 7). These two sets of discontinuities are a direct consequence of the sudden increases in uncertainty that we are applying to the Saha-Zuber correlation as the velocity is decreasing (see Table 1). In addition, the modification of the Saha-Zuber correlation causes the modified version of the correlation to predict higher limits at low subcoolings and lower limits at higher subcoolings than the original version of the correlation. The Costa correlation, which is considerably more conservative than either the Saha-Zuber or modified Saha-Zuber correlation at high velocities, becomes less so as the velocities decrease. In these calculations, the uncertainties for the Costa correlation were kept constant over all of the velocity range, while changing those

of the modified Saha-Zuber and original Saha-Zuber correlations. Thus, the Costa correlation has a lower thermal limit ratio than the Saha-Zuber formulations early in the transient (at high velocities), and higher ratios at the end of the transient (at lower velocities). Since the absolute lower limit on boiling (and therefore OSV) is $T_{wall} = T_{sat}$, the OSV curves cannot fall below the $T_{wall} = T_{sat}$ curve. This transient would therefore not exceed any of the thermal limits that could lead to potential fuel damage.

Table 1. Peaking factors for hot spot heat fluxes.

Limit Model		95% Probability	99.9% Probability
$T_{wall} = T_{sat}$		1.16	1.25
Bergles-Rohsenow (IB)		1.30	1.59
Costa (OSV)		1.30	1.59
Saha-Zuber and Modified Saha-Zuber (OSV)	Peclet > 70000, Vel > 8 m/s	1.52	2.30
	Peclet > 70000, Vel < 8 m/s	2.08	**
	Peclet < 70000	**	**

** Presently the $T_{wall} = T_{sat}$ or IB limit is recommended- and is more conservative- for these conditions until the low flow correlation for the modified Saha-Zuber correlation can be better characterized.

102-mm-Diam Instantaneous Core Inlet Break after Shutdown (Core Flow Reversal)

The pipe break was assumed to occur 90 s after a shutdown of the reactor and AC pump motors (LOSP). The pony motors were assumed to be available to provide 10% of the nominal flow after the coastdown.

The core exit pressures, shown in Figs. 8 and 8a, drop sharply when the pipe break occurs at 90 s, then recover due to the accumulator injection which causes the flow reversal in the core. After the break flow equilibrates with the accumulator flow (Fig. 9), the primary system pressure declines steadily approaching the reactor pool pressure as the accumulators are drained.

Thermal limit ratios at the 95% lower core hot channel entrance (the entrance is used here since it is the limiting location after flow reversal) are shown in Fig. 10 and indicate two minima. The first minimum occurs immediately after reactor scram and the second minimum occurs during core flow reversal immediately following the pipe break. Again, the Saha-Zuber based correlations show very low thermal limit ratios under low flow conditions because of the uncertainties imposed upon them. Figure 10a shows a close-up of the remaining thermal limit ratios immediately following the break. The Costa limit is exceeded because as the velocity reaches zero, the Costa prediction of heat flux required to initiate voiding goes to zero. However, the $T_{wall} = T_{sat}$ limit is not exceeded even during the core flow reversal. The violation of the Costa limit should be disregarded because OSV cannot physically occur if T_{wall} stays below T_{sat}.

The limiting location in each fuel element changes with the changing pressure, coolant bulk temperature, and coolant flow direction. When a flow reversal occurs, the limiting location moves from the core exit to the core inlet (referenced to the normal coolant flow direction). The limiting locations in each fuel element, immediately following the pipe break for the $T_{wall} = T_{sat}$ criterion occurs at the lower element inlet and the

upper element exit (the absolute limit is at the upper element exit). Figure 11 shows temperature and velocity responses at the lower core 95% hot channel entrance with a peaking factor of 1.16 (this peaking factor includes an assumed normal distribution of the error in the heat transfer coefficient with a standard deviation of 3.3%). Pressure oscillations following the break cause small changes in the local saturation temperature. Diminishing core flow results in lower heat transfer in the core, thus causing the wall temperature to approach the saturation temperature within 71 °C. The wall temperature decreases as decay heat decreases and core flow stabilizes. Figure 12 shows the transition from the turbulent Petukhov correlation to the laminar constant Nu correlation for the heat transfer coefficient in the lower core hot channel during the flow reversal. Figure 13 shows the temperature responses at the upper core 95% hot channel exit. The same behavior is observed at this location as was noted in Fig. 11, however, the closest approach between T_{sat} and T_{wall} is lower (but still about 39 °C) due to the higher heat flux levels in the upper core.

CONCLUSIONS

Although this work is done specifically for the ANSR geometry and operating conditions, the general conclusions can be applied to other highly subcooled reactor systems. Similar trends in the thermal limit margin should be observed in other systems for the pipe break and the single pump failure with stuck open check valve events.

For the single pump failure assuming a stuck open check valve, the results show that the core should not exceed any thermal limit criteria if the pony motor battery lasts 30 minutes, at a 95% non-exceedance probability level (used for extremely unlikely events).

In the event of the pipe break, the results show that the worst time for a post-scram pipe break to occur is approximately 92 s after reactor and AC motor pump shutdown. Even this event, which causes a core flow reversal, the closest approach between the fuel surface temperature and the saturation temperature at the hot spot is about 39 °C (for 95% non-exceedance probability levels), indicating that no boiling should occur in the core.

During low core flow, the OSV correlations were not useful for judging the acceptability of these events. The Costa correlation is based on data obtained at higher flow rates, and the Saha-Zuber correlation has very large uncertainty at the low flows. Instead, it was shown that the fuel surface temperature, T_{wall}, would not exceed the saturation temperature in the hot channel, T_{sat}, during the periods of low flow, thus prohibiting the possibility of OSV.

REFERENCES

[1] Conceptual Safety Analysis Report, Chapter 4, "Reactor," ORNL/ANS/INT-33/V2, Martin Marietta Energy Systems, Inc., Oak Ridge Natl. Lab., June (1992).

[2] Conceptual Safety Analysis Report, Chapter 15, "Accident Analysis," ORNL/ANS/INT-33/V4, Martin Marietta Energy Systems, Inc., Oak Ridge Natl. Lab., June (1992).

[3] N. C. J. Chen et al., "Loss-of-Coolant Accident Analysis of the Advanced Neutron Source Reactor," pp. 64-68 in *Seventh Proceedings of Nuclear Thermal Hydraulics*, ANS 1991 Winter Meeting, San Francisco, November (1991).

[4] N. C. J. Chen et al., "Thermal Hydraulic Response of the Advanced Neutron Source Reactor to Piping Breaks near the Core Region," pp. 69.01-69.15 in *8th Power Plant Dynamics, Control & Testing Symposium Proceedings*, Vol. 2, Knoxville, Tenn., May (1992).

[5] N. C. J. Chen et al., "Loss-of-Coolant Accident Mitigation for the Advanced Neutron Source Reactor," pp. 253-259 in *ANS Proceedings*, 1993 National Heat Transfer Conference, Atlanta, GA, August (1993).

[6] N. C. J. Chen et al., *Validation and Verification of RELAP5 for Advanced Neutron Source Accident Analysis: Part 1, Comparisons to ANSDM and PRSDYN Codes*, ORNL/TM-12418/V1, Martin Marietta Energy Systems, Inc., Oak Ridge Natl. Lab., December (1993).

[7] N. C. J. Chen et al., "Conceptual Design Loss-of-Coolant Accident Analysis for the Advanced Neutron Source Reactor," *Nucl. Technol.* 105, (1), 104-122, January (1994).

[8] N. C. J. Chen et al., "Flow Excursion Margin Behavior during a Pipe Break in the Advanced Neutron Source Reactor," *Transactions*, pp. 433-434, Vol. 70, 1994 American Nuclear Society Annual Meeting, New Orleans, LA, June (1994).

[9] M. W. Wendel et al., "Updated Pipe Break Analysis for Advanced Neutron Source Reactor," pp. 1-9, HTD-Vol. 294 (Thermal Hydraulics of Advanced Nuclear Reactors, Ed. Y.A. Hassen and R.M. Singer,), 1994 ASME Winter Annual Meeting, Chicago, November (1994).

[10] C. D. Fletcher et al., "Conceptual Design Station Blackout and Loss-of-Flow Accident Analysis for the Advanced Neutron Source Reactor," *Nucl. Technol.* 106, 1, 31-45, April (1994).

[11] N. C. J. Chen et al., "Transition to Natural Circulation with and without Depressurization for the Advanced Neutron Source Reactor," pp. 11-17, HTD-Vol. 294 (Thermal Hydraulics of Advanced Nuclear Reactors, Ed. Y.A. Hassan and R.M. Singer), 1994 ASME Winter Annual Meeting, Chicago, November (1994).

[12] *Conceptual Design Report Summary,* ORNL/TM-12184, Martin Marietta Energy Systems, Inc., Oak Ridge Natl. Lab., June (1993).

[13] A.J. Stepanoff, *Centrifugal and Axial Flow Pumps*, 2nd., John Wiley & Sons, New York (1957).

[14] J. Costa, "Measurement of the Momentum Pressure Drop and Study of the Appearance of Vapor and Change in the Void Fraction in Subcooled Boiling at Low Pressure," presented at European Group Double-Phase Meeting, Winfrith, U.K., (1967); English translation, ORNL/TR-90/21, Martin Marietta Energy Systems Inc., Oak Ridge Natl. Lab. (1990).

[15] W.R. Gambill, " Generalized Prediction of Burnout Heat Flux for Flowing, Subcooled, Wetting Liquids," *Chem. Eng. Prog. Symp. Series*, Vol. 59, 41, 71-87 (1963).

[16] P. Saha and N. Zuber, "Point of Net Vapor Generation and Vapor Void Fraction in Subcooled Boiling," *Proc. of 5th Int. Heat Transfer Conf.*, Tokyo, Vol. IV, pp. 175-179 (1974).

[17] B. S. Petukhov and V. N. Popov, "Theoretical Calculation of Heat Exchange in Turbulent Flow in Tubes of an Incompressible Fluid with Variable Physical Properties," *High Temp.*, Vol. 1, No. 1, pp.69-83 (1963).

[18] A. E. Bergles and W. M. Rohsenow, *Forced-Convection Surface Boiling Heat Transfer and Burnout in Tubes of Small Diameter*, DSR Report No. 8767-21, Dept. of Mechanical Engineering, Massachusetts Institute of Technology (1962).

[19] D.B. Collins et al., "Pump Operation with Cavitation and Two-Phase Flow," *Proc. 4th Western Canadian Heat Transfer Conf.*, Winnipeg, Manitoba, May (1972).

[20] P. W. Dittus and L. M. K. Boelter, "Heat Transfer in Automobile Radiators of the Tubular Type," Univ. Calif. Pub. Eng., Vol. 2, No. 13, pp. 443-461, (1930); reprinted in Int. Comm. Heat Mass Transfer, Vol. 12, pp. 3-22 (1985).

[21] D. C. Groeneveld, et al., "1986 AECL-UO Critical Heat Flux Look-Up Table," *Heat Transfer Eng.*, 7, 1-2, 56 (1986).

[22] P. Griffith,"The Prediction of Low Quality Boiling Voids," *ASME Heat Trans.*, p.327, Aug. (1964).

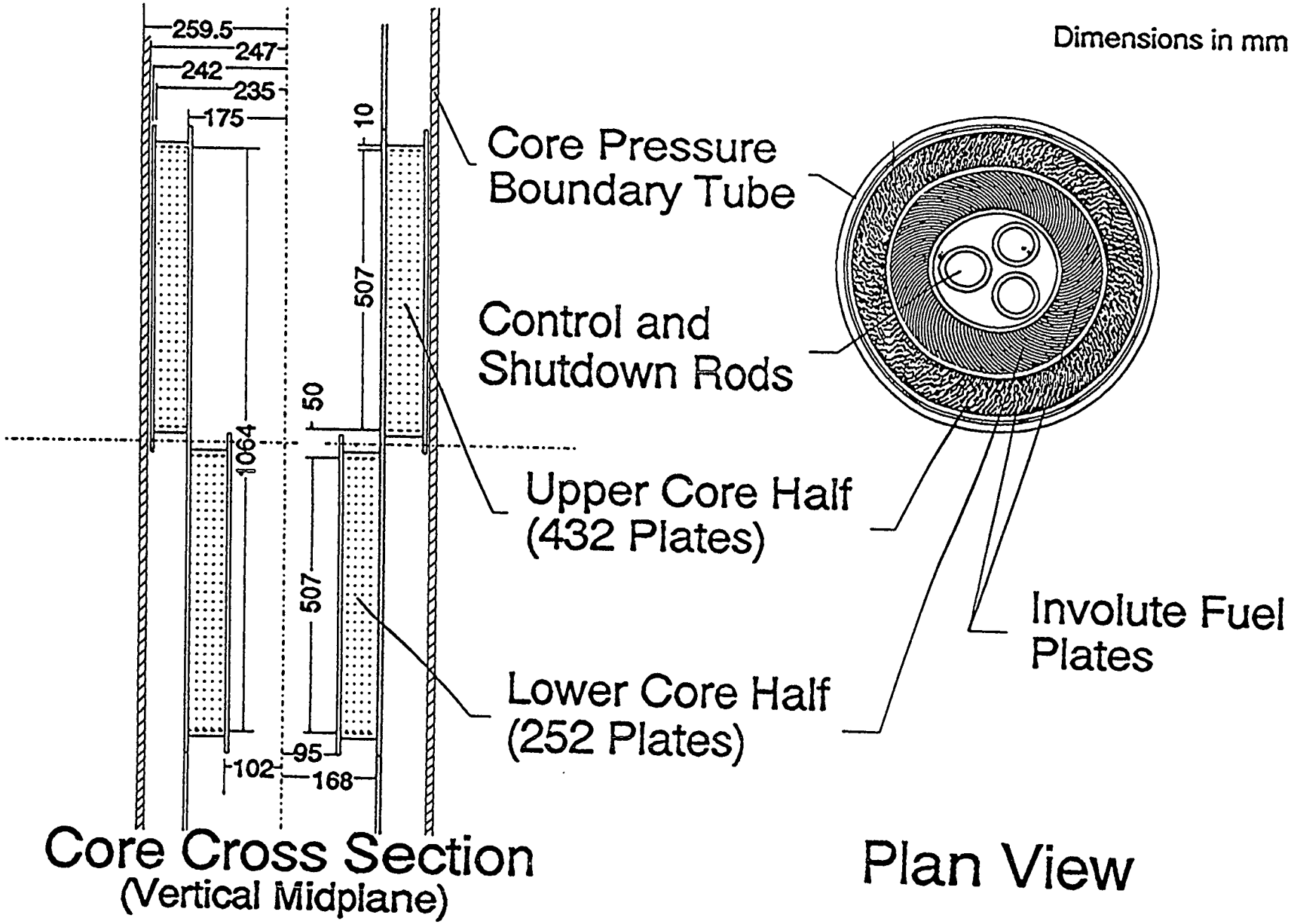


Fig. 1. Advanced Neutron Source Reactor core assembly and fuel plates arrangement.

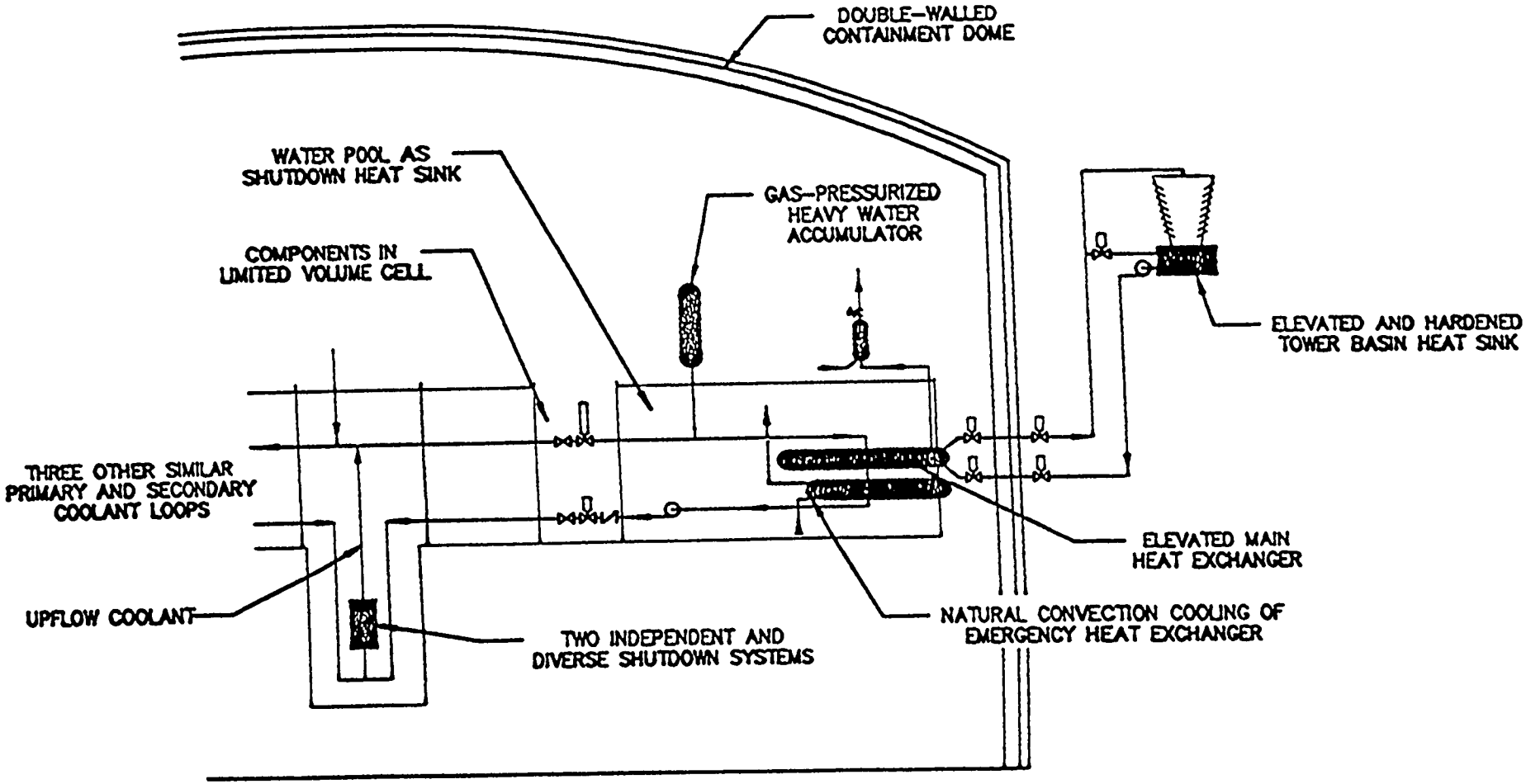


Fig. 2. ANSR system schematic showing general cooling system design characteristics.

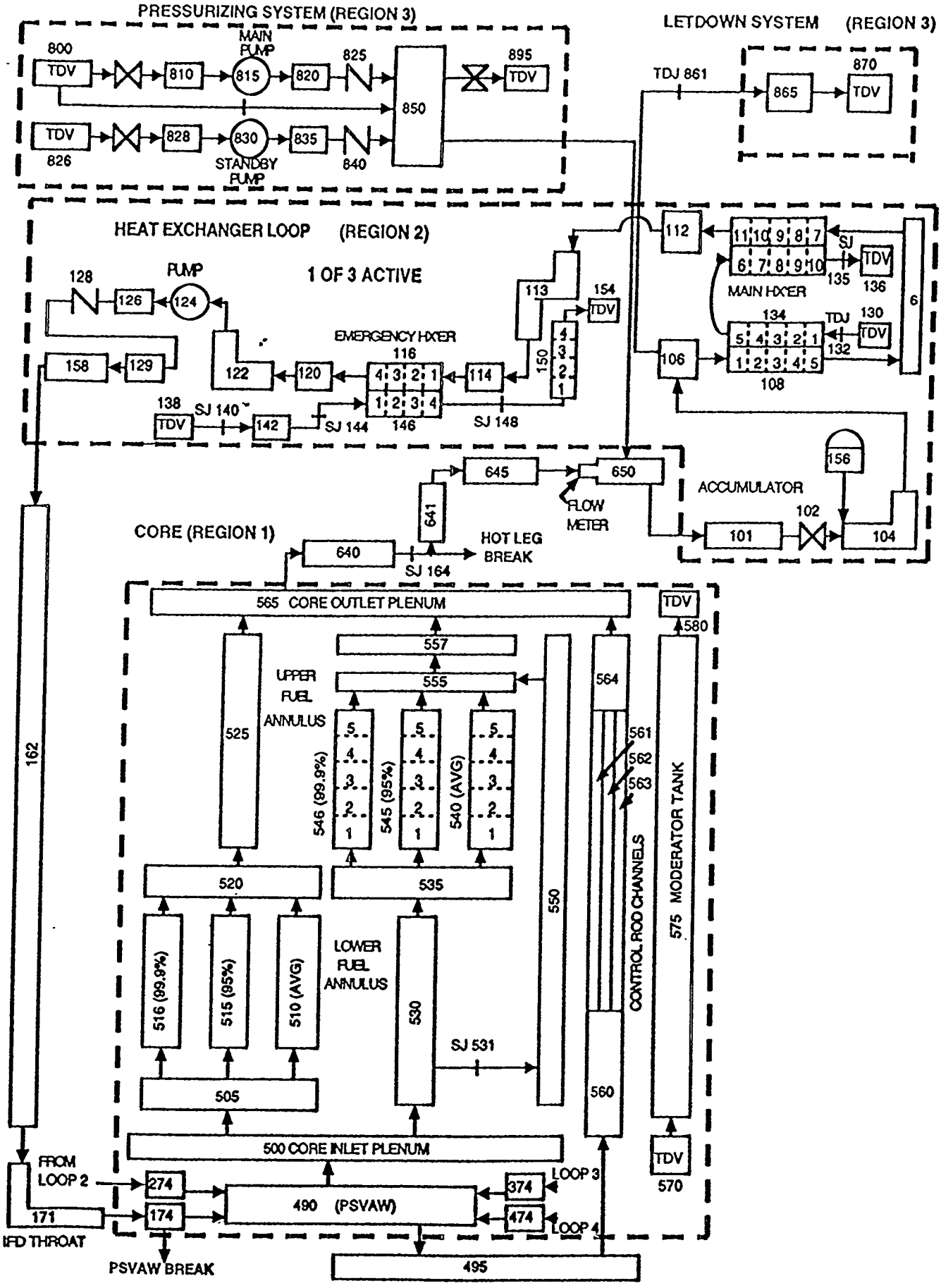


Fig. 3. Nodalization diagram of the ANSR RELAP5 thermal-hydraulic system model.

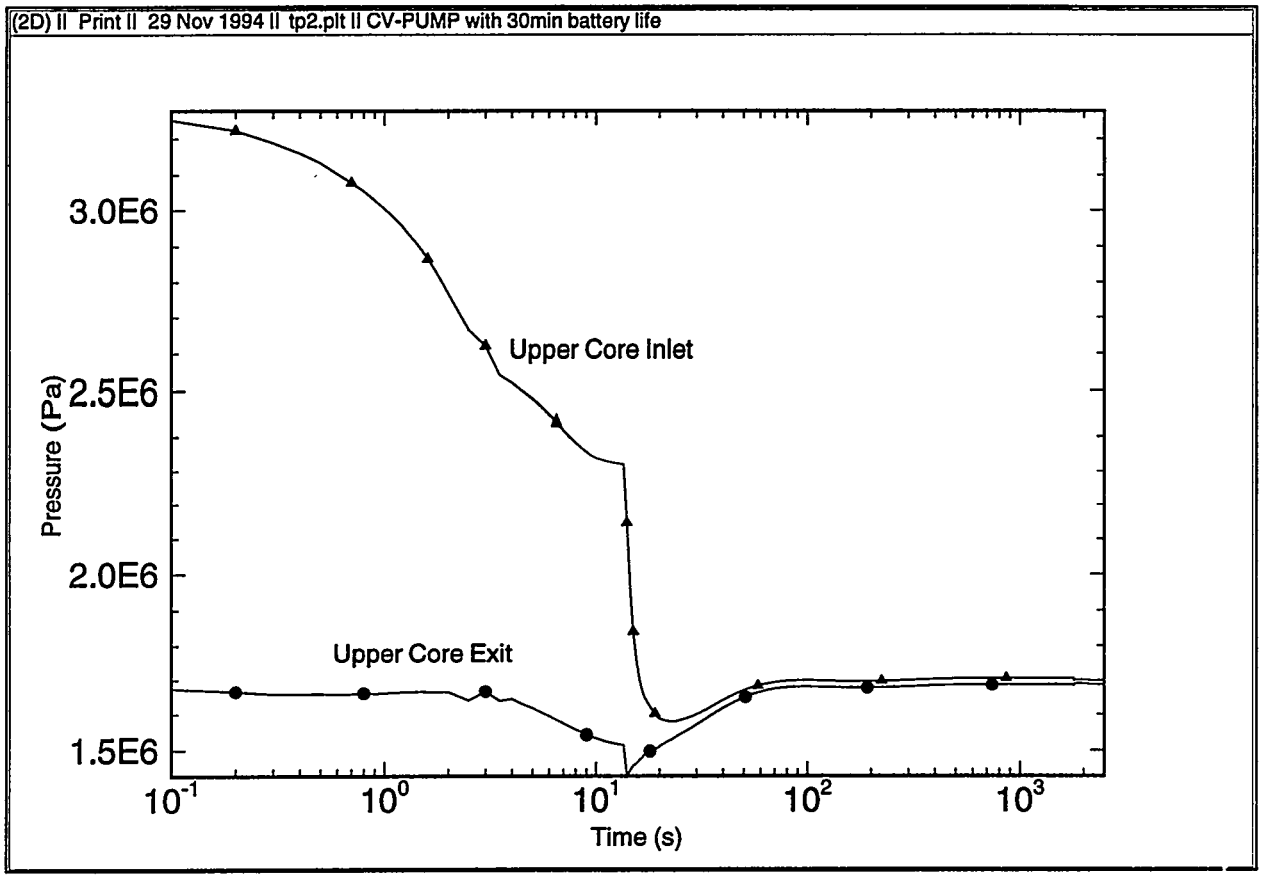


Fig. 4. Pressure traces at the upper core 95% hot channel inlet and exit during the single pump failure with stuck open check valve event.

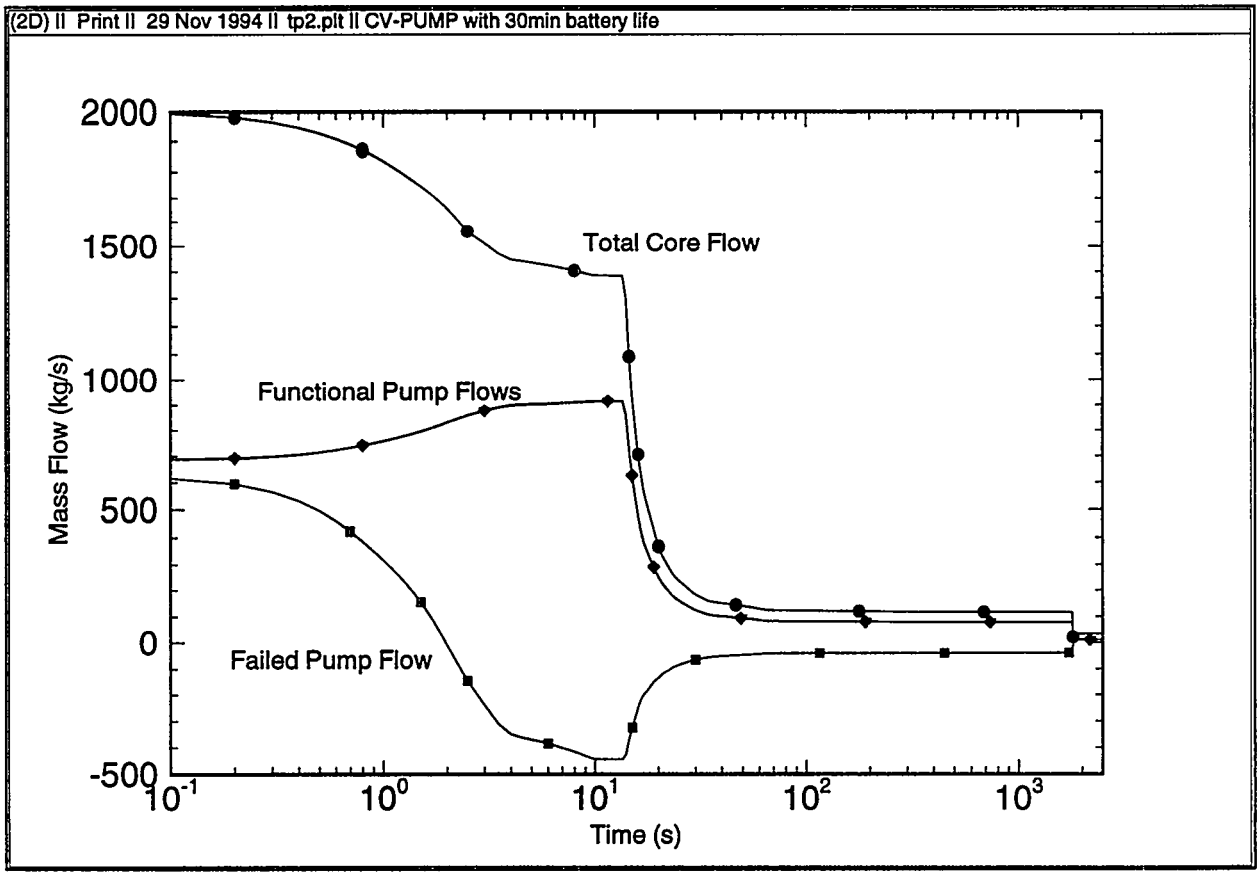


Fig. 5. Total core flow and pump flows during the single pump failure with stuck open check valve event.

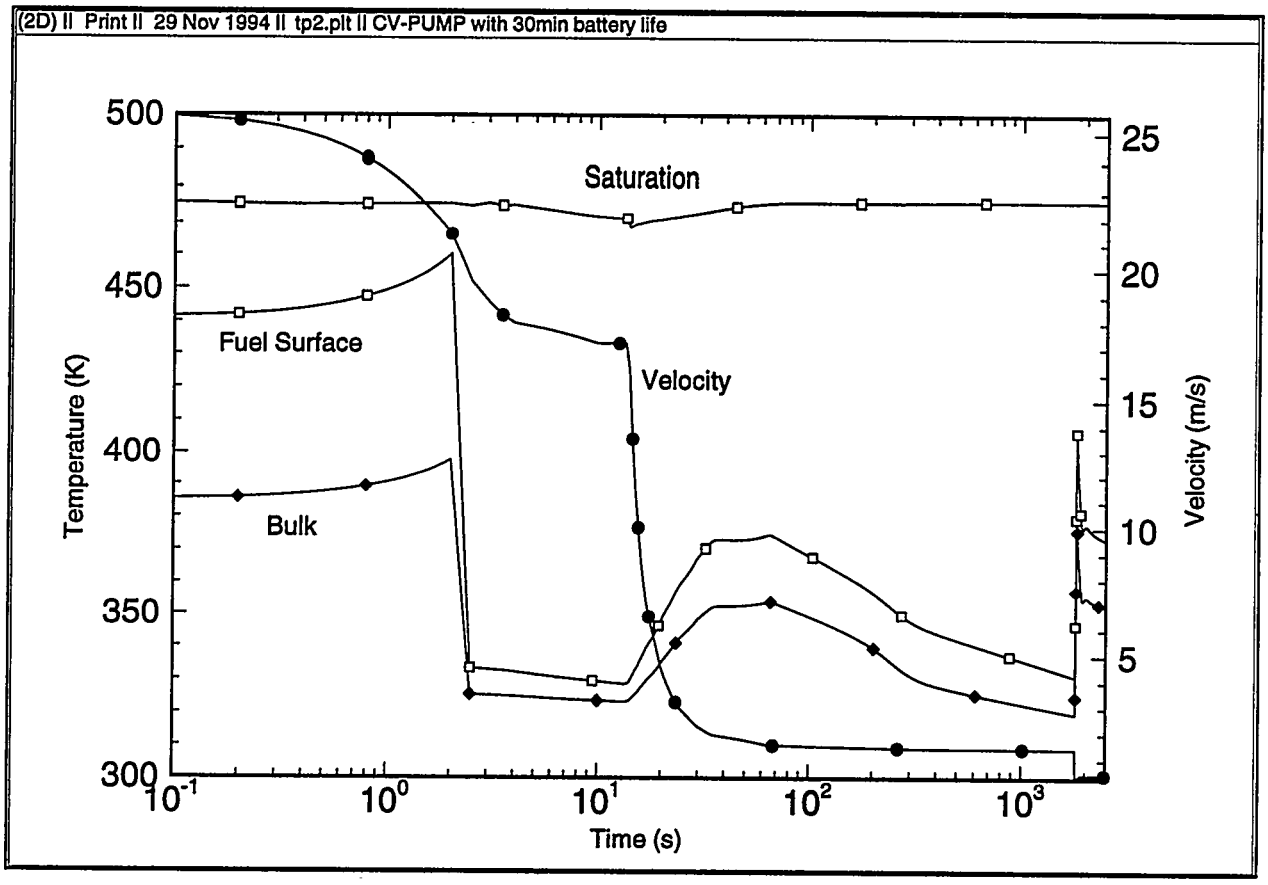


Fig. 6. Temperature and velocity transient at the upper core 95% hot channel exit during the single pump failure with stuck open check valve event.

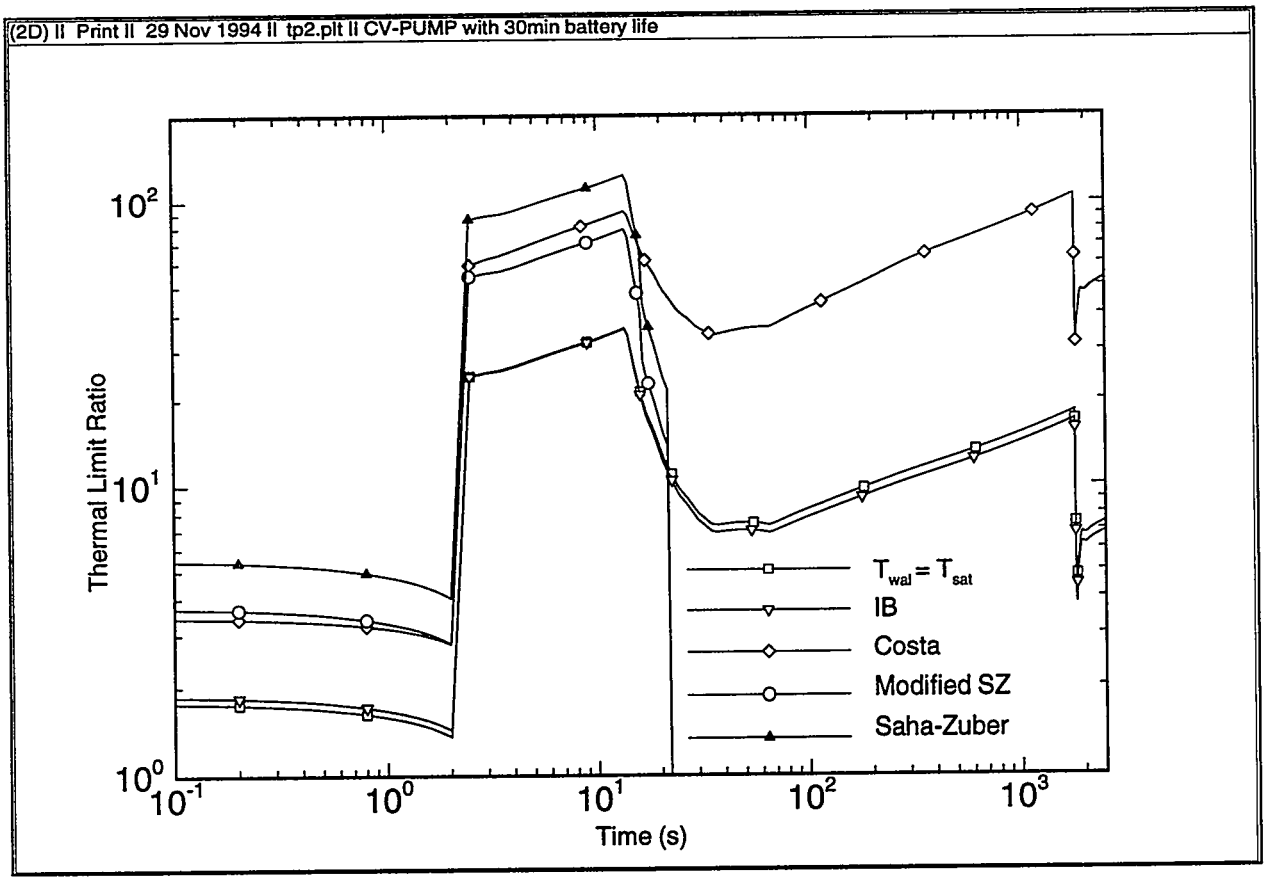


Fig. 7. Comparison in thermal limit ratio at upper core 95% hot channel exit during the single pump failure with stuck open check valve event.

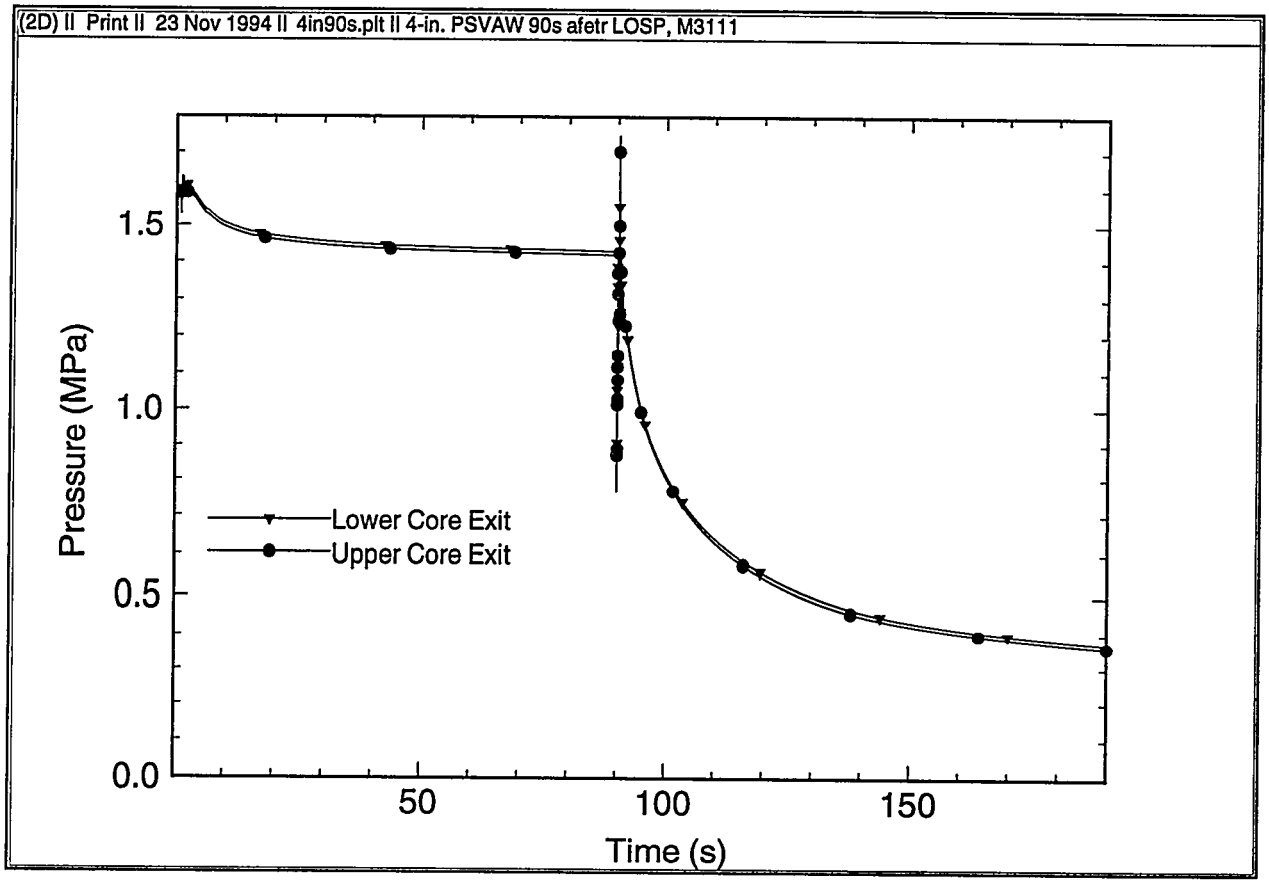


Fig. 8. Pressure traces at the lower and upper core 95% hot channel exit for the 102-mm-diam pipe break, 90 s after shutdown.

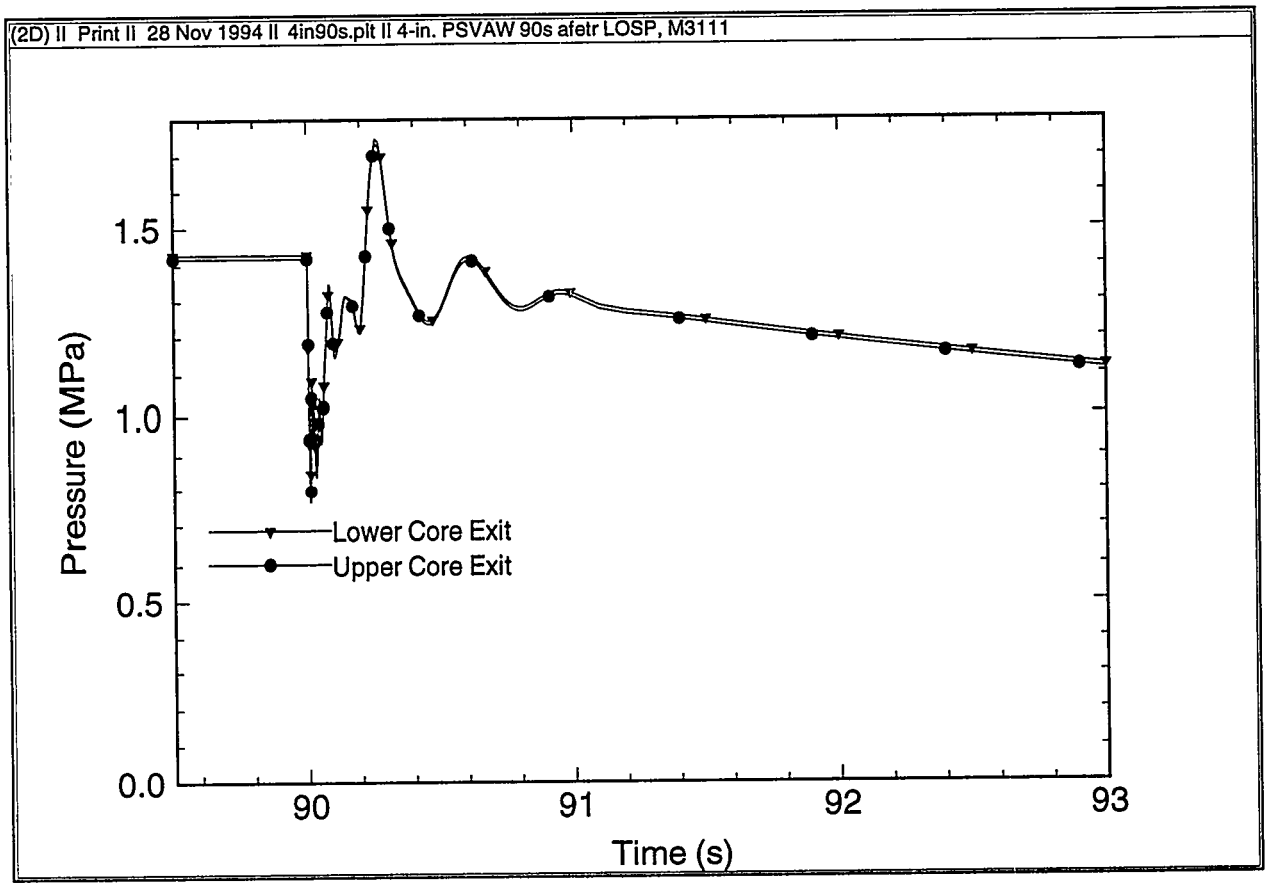


Fig. 8a. Close-up of pressure traces during core flow reversal for the 102-mm-diam pipe break, 90 s after shutdown.

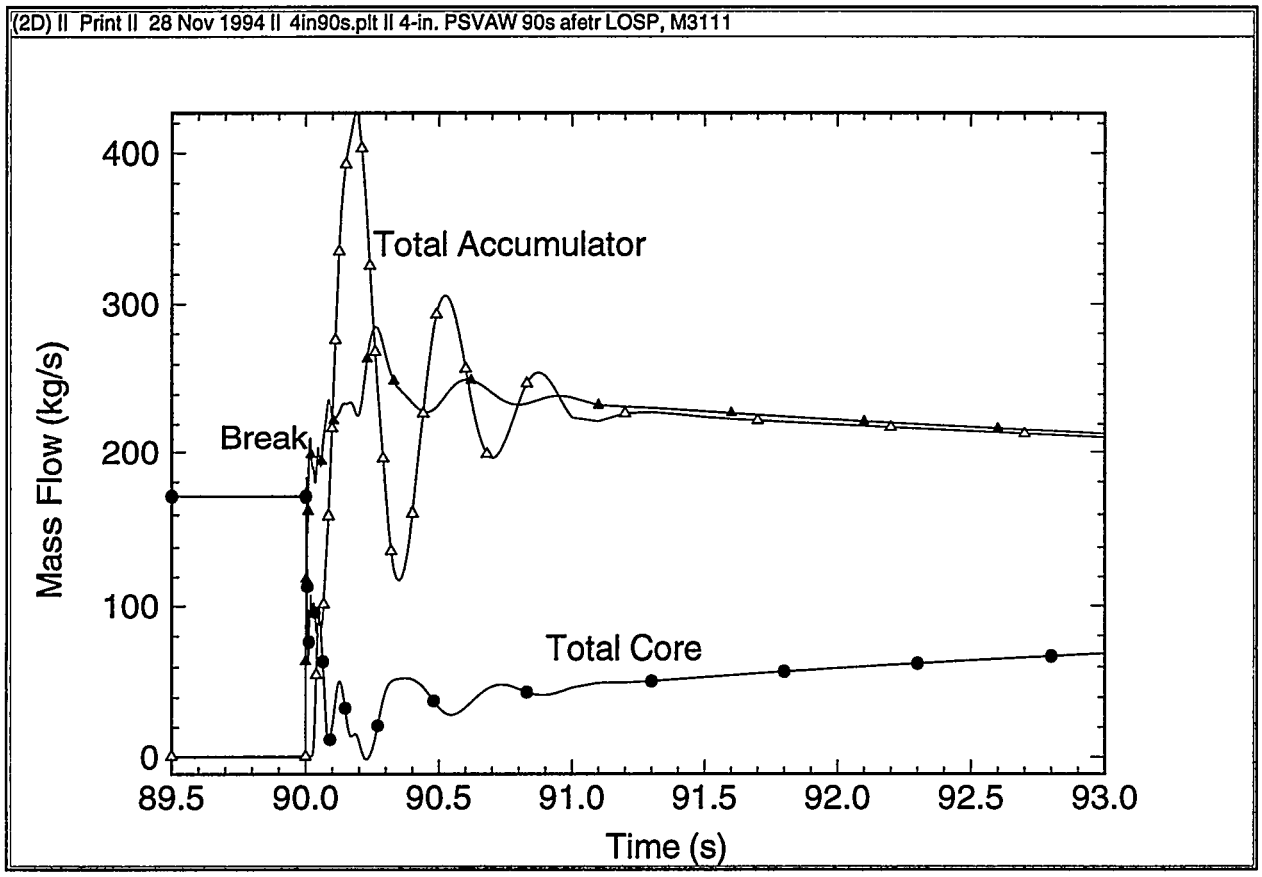


Fig. 9. Total core flow, accumulator flow, and break flow behavior for the 102-mm-diam pipe break, 90 s after shutdown.

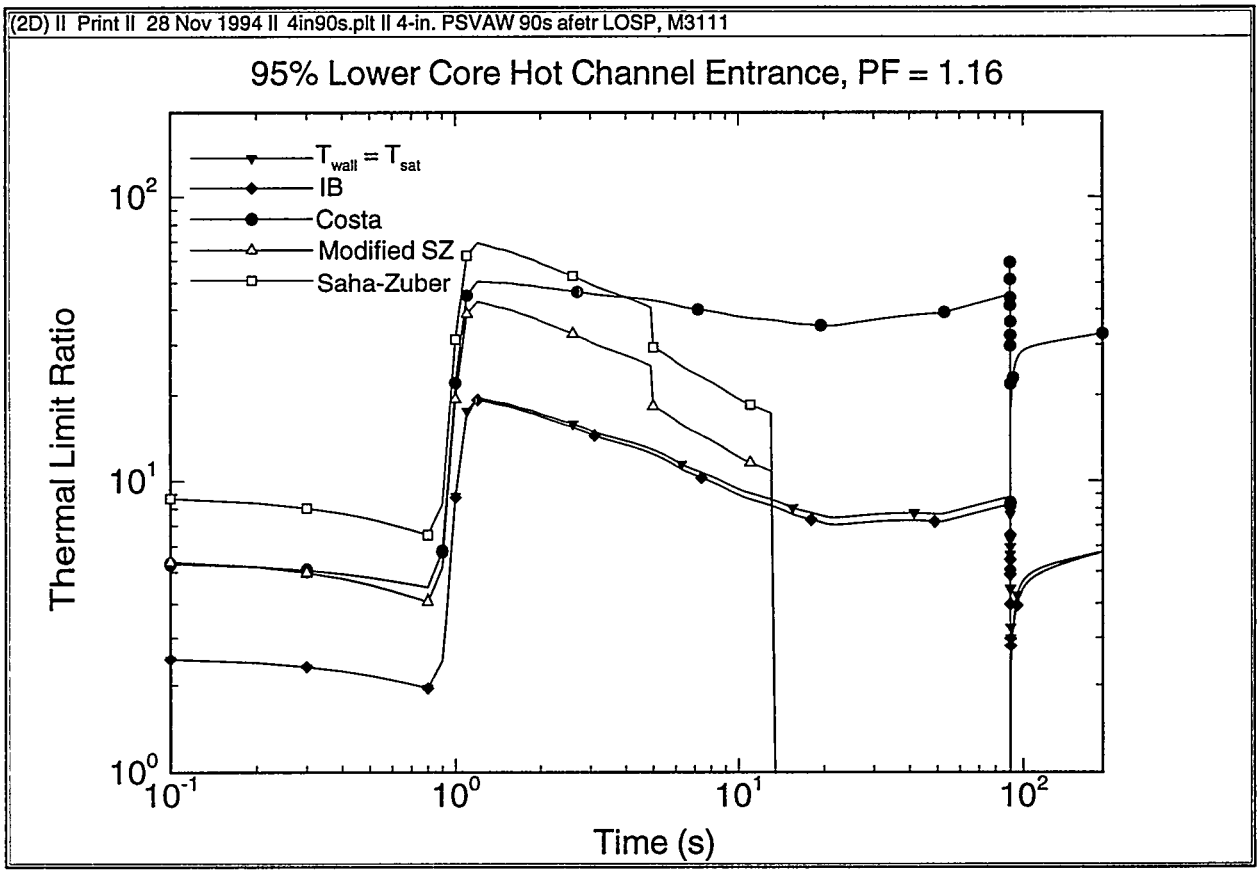


Fig. 10. Comparison in thermal limit ratio at the lower core 95% hot channel entrance for the 102-mm-diam pipe break, 90 s after shutdown.

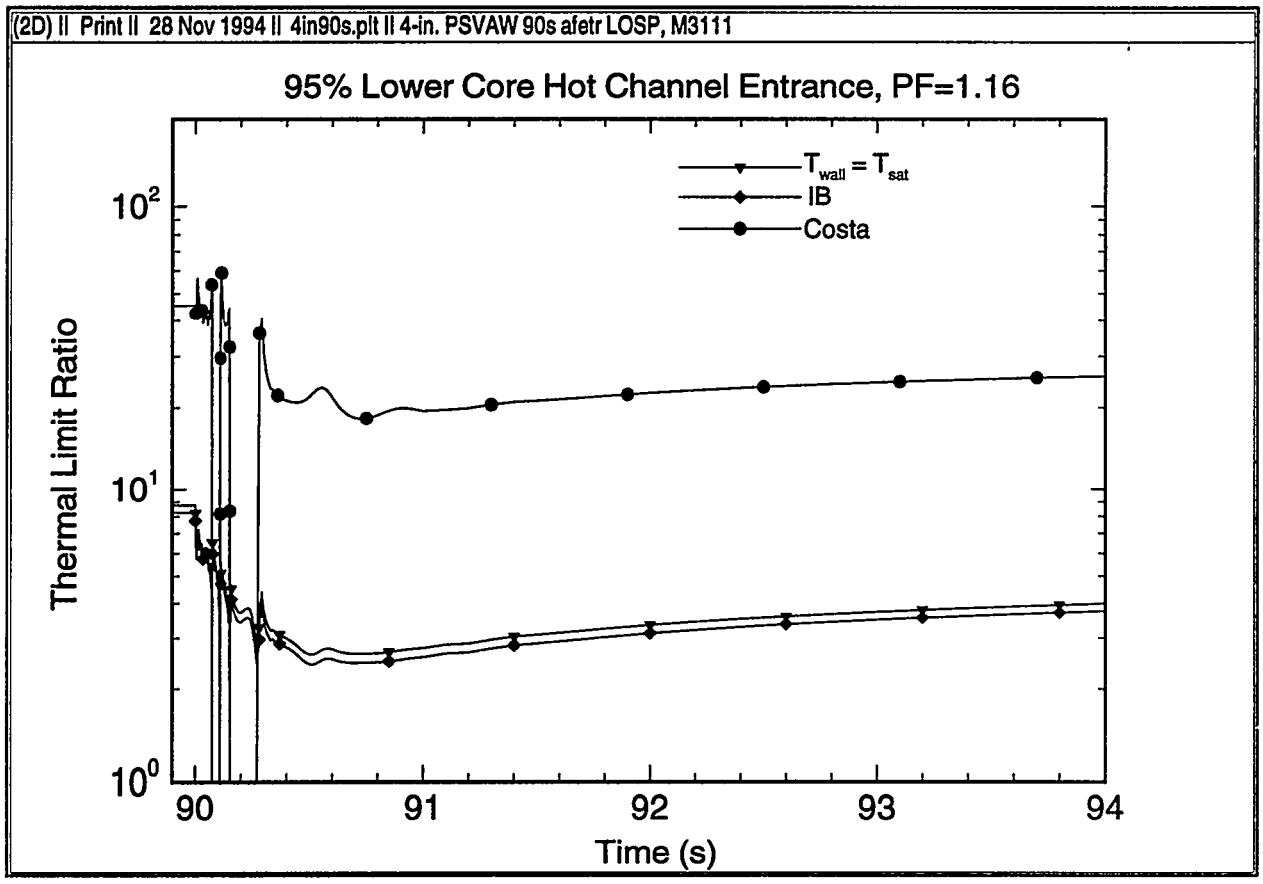


Fig. 10a. Close-up of thermal limit ratio comparison at the lower core 95% hot channel entrance for the 102-mm-diam pipe break, 90 s after shutdown.

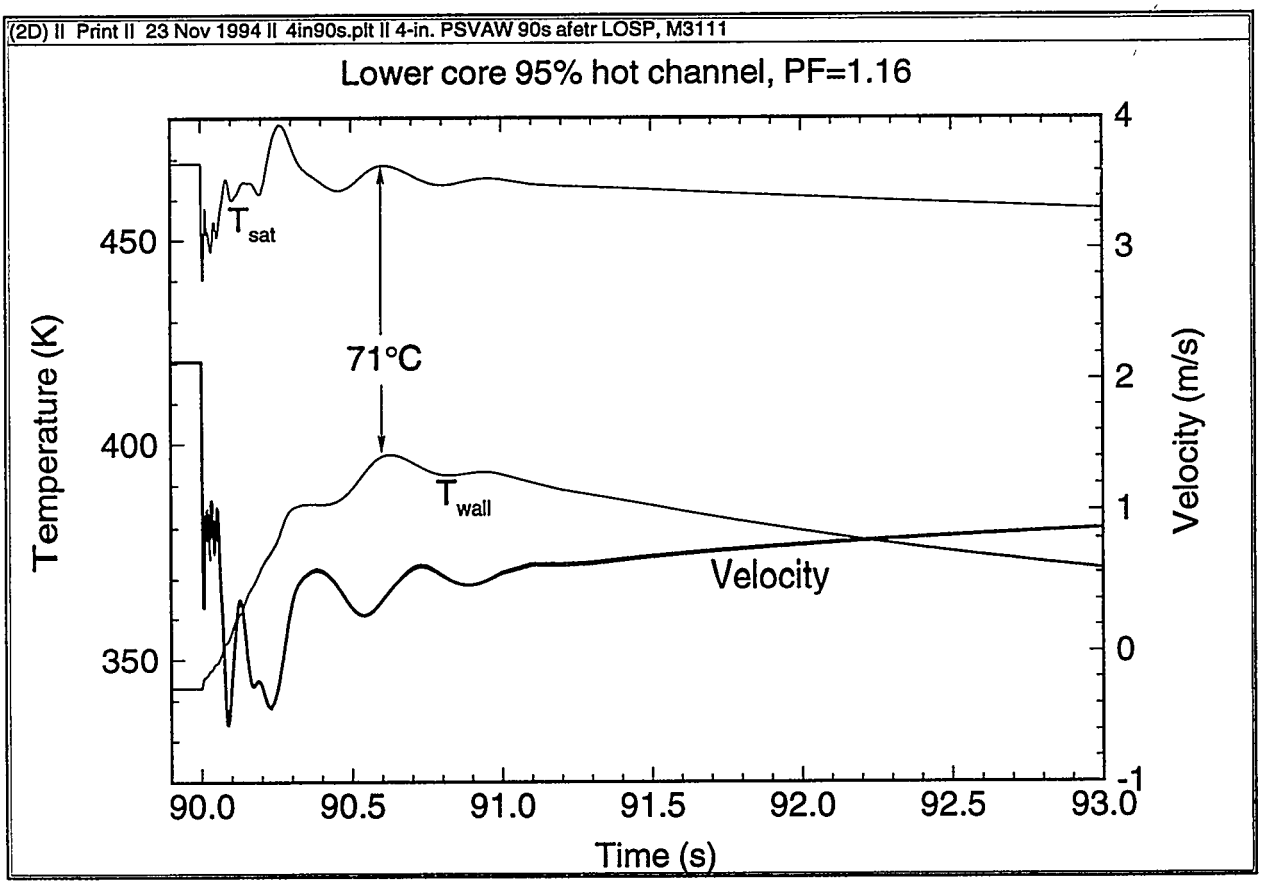


Fig. 11. Temperature and velocity response at the lower core 95% hot channel entrance for the 102-mm-diam pipe break 90 s after shutdown.

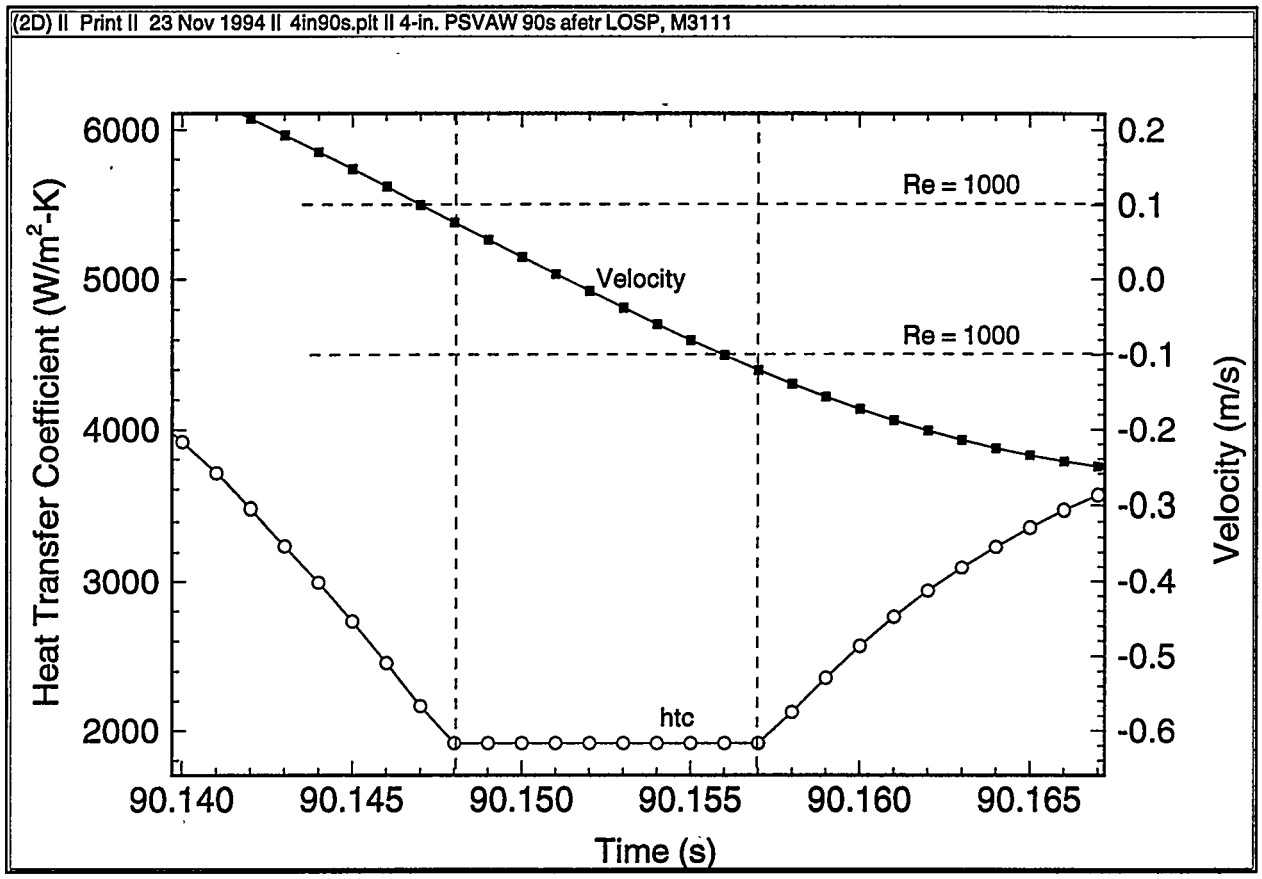


Fig. 12. Transition from the Petukhov turbulent correlation to the constant-Nu laminar in the lower core hot channel when Reynolds number declines to 1000 during core flow reversal for the 102-mm-diam pipe break, 90 s after shutdown.

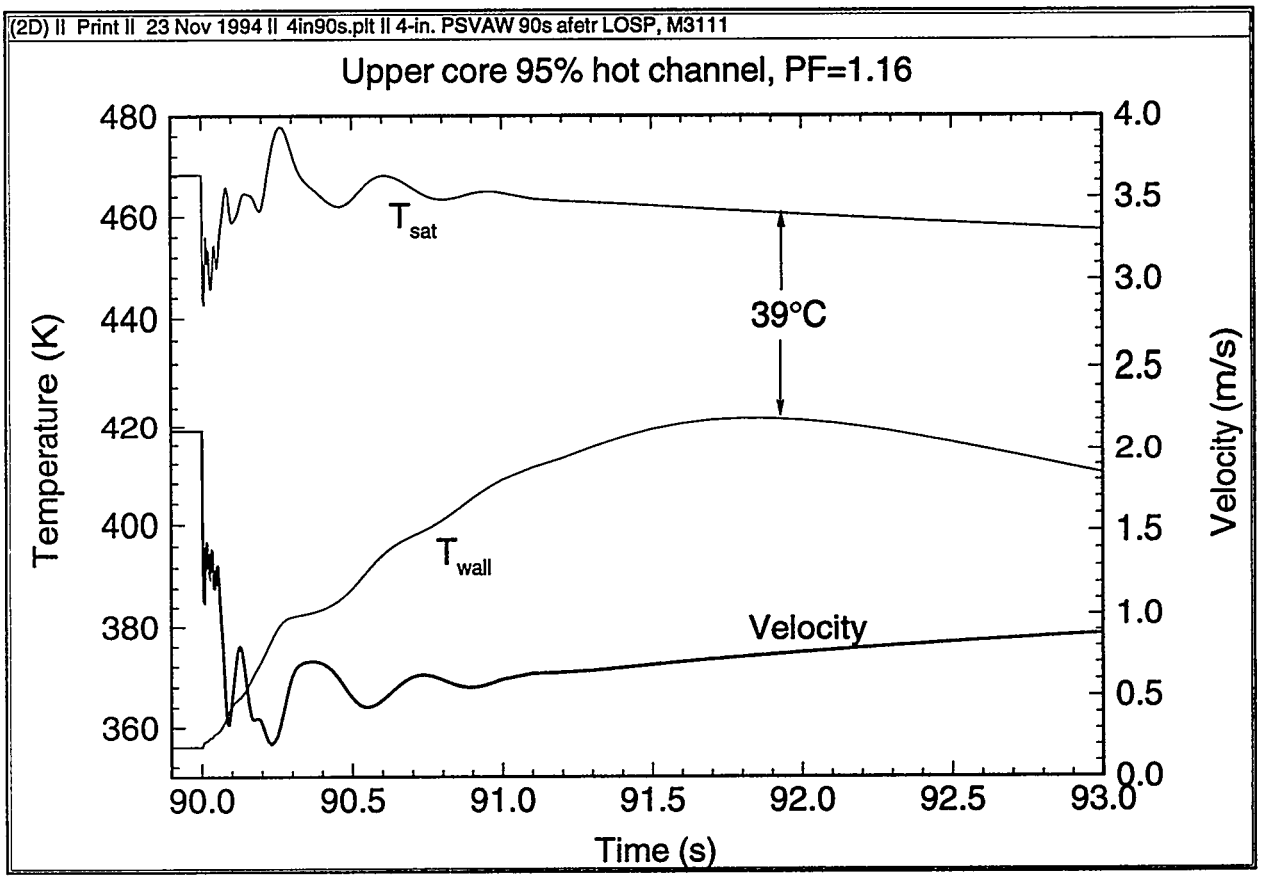


Fig. 13. Temperature and velocity response at the upper core 95% hot channel exit for the 102-mm-diam pipe break 90 s after shutdown.

MELCOR BENCHMARKING AGAINST INTEGRAL SEVERE FUEL DAMAGE TESTS[1]

I. K. Madni
Department of Advanced Technology, Brookhaven National Laboratory
Upton, NY 11973, USA

ABSTRACT

MELCOR is a fully integrated computer code that models all phases of the progression of severe accidents in light water reactor nuclear power plants, and is being developed for the U.S. Nuclear Regulatory Commission (NRC) by Sandia National Laboratories (SNL). Brookhaven National Laboratory (BNL) has a program with the NRC to provide independent assessment of MELCOR, and a very important part of this program is to benchmark MELCOR against experimental data from integral severe fuel damage tests and predictions of that data from more mechanistic codes such as SCDAP or SCDAP/RELAP5. Benchmarking analyses with MELCOR have been carried out at BNL for five integral severe fuel damage tests, namely, PBF SFD 1-1, SFD 1-4, and NRU FLHT-2, FLHT-4, and FLHT-5. This paper presents a summary of these analyses, and their role in identifying areas of modeling strengths and weaknesses in MELCOR.

INTRODUCTION

MELCOR is a fully integrated computer code that models all phases of the progression of severe accidents in light water reactor nuclear power plants [1]. It is being developed for the NRC by SNL as severe accident source term analysis tool to be used in Probabilistic Risk Assessment (PRA) studies. Severe accident phenomena that can be modeled in MELCOR include reactor coolant system and containment thermal/hydraulic response, core heatup, degradation and relocation, zircaloy and steel oxidation and hydrogen production, and fission product release and transport. However, the usefulness of MELCOR for risk assessment studies depends on its ability to provide validated models for the severe accident phenomena.

An area in MELCOR that has the largest uncertainty, and that requires the maximum assessment efforts, is in-vessel melt progression. Through the Cooperative Severe Accident Research Program (CSARP), the NRC has conducted several tests related to core degradation and melt progression during severe accident conditions in the Power Burst Facility (PBF) at Idaho National Engineering Laboratories (INEL), the Annular Core Research Reactor (ACRR) at SNL, and the National Research Universal (NRU) reactor at Chalk River Nuclear Laboratories (CRNL), and has been associated with the KfK work in NIELS and CORA out-of-pile facilities. Information on melt progression also became available from the TMI-2 post-test examinations and from the OECD LOFT project (Test FP-2).

BNL has a program with the NRC to provide independent assessment of MELCOR as a severe accident thermal-hydraulic/source term analysis tool, and a very important part of this program is to benchmark MELCOR against experimental data from integral severe fuel damage tests and predictions of that data from more mechanistic codes such as SCDAP or SCDAP/RELAP5. In accordance with a BNL study on experimental data alternatives for benchmarking MELCOR [2], which identified in-vessel phenomenology as an area in MELCOR that needed to be assessed, benchmarking analyses with MELCOR have been carried out at BNL for five integral severe fuel damage tests, namely, PBF SFD 1-1 [3], SFD 1-4 [4], and NRU FLHT-2 [5], FLHT-4 [6], and FLHT-5 [7].

The PBF SFD tests were a series of four integral severe fuel damage (SFD) experiments performed by INEL, to examine the meltdown behavior of a small region of a reactor core under loss of coolant accident conditions. These tests were performed with 0.9 meter long, 32-rod bundles of test fuel and at 68 bars test pressure. The final test, SFD 1-4, with high-burnup fuel, Ag-In-Cd control rods, and on-line aerosol diagnostics, was the most prototypical. These integral tests produced substantial data on core heatup, clad oxidation, fuel melting and relocation, and fission product release, for determining and modeling the early phase of severe accident conditions.

The NRU full-length, high-temperature (FLHT) experiments were a series of four severe damage tests, conducted by PNL, to characterize fuel bundle behavior, including fuel temperature history, hydrogen production, melting and relocation, and fission product release and transport, during the early phase of a severe accident. A stated objective of the tests also was to provide data for the validation of severe accident computer codes. The severity of peak conditions and their duartion increased from one FLHT test to the next, FLHT-5 being the most severe. The FLHT tests being performed with full-length PWR fuel rods, are important for code validation, particularly for clad oxidation and hydrogen generation where length scaling from the shorter PBF and ACRR data may cause some uncertainties.

[1]Work performed under the auspices of the U.S. Nuclear Regulatory Commission.

RESULTS AND COMPARISONS

In all tests, the fuel bundle was surrounded by an insulating shroud, to minimize radial heat losses. The shroud was multi-layered, consisting of zirconium oxide sandwiched between inner and outer zircaloy walls, and an inner zircaloy liner facing the fuel bundle. Bypass coolant flowed around the outer surface of the shroud. Bundle coolant entered the bundle inlet region and flowed up along the fuel rods. It was heated by fission power (representing decay heat in an actual plant), converted to steam, and reacted with the high-temperature zircaloy cladding and liner to form hydrogen. The boilaway transient began when inlet flow was reduced (coupled with a gradual increase in fission heat for tests SFD 1-1 and 1-4). The degraded cooling conditions led to rapid decrease in the bundle coolant inventory, fuel uncovery and dryout, heatup, cladding rupture, and rapid oxidation. With sustained fission power and heat from oxidation, temperatures continued to rise rapidly, resulting in melting and relocation of core material, and the release of hydrogen and fission products. More details on the individual tests can be obtained from the test results reports [8-12].

A typical MELCOR nodalization for the test simulations is shown in Figure 1 [5]. There are 4 control volumes (inlet, fuel bundle, plenum, and environment) and 3 flow paths interconnecting them. The environment is a contrived volume and is assumed very large, allowing the system pressure to stay nominally constant, as in the experiments. The fuel bundle active length is nodalized into several axial segments and 1 radial ring. The shroud is nodalized axially to match the core cells and radially into several layers. Note that for FLHT-5, the test bundle was modeled as a BWR geometry (see Figure 2), to allow the mass of zircaloy in the shroud liner and carriers to participate in oxidation with steam as a canister component [7].

The benchmarking calculations of integral severe fuel damage tests have helped to identify areas of modeling strengths and weaknesses in MELCOR; the most appropriate choices for input parameters; selection of axial nodalization for core cells and heat structures; and workarounds that extend the capabilities of MELCOR. These insights are explored in greater detail, with the help of selected results and comparisons from all five integral tests, as follows.

Temperature Comparisons

Comparisons between predicted and measured clad temperatures for all five tests are shown in Figures 3 to 7. The agreement between MELCOR and the test data appears to be very good in the heatup phase, prior to the onset of accelerated oxidation of zircaloy.

For the first four tests (Figures 3 to 6), MELCOR generally

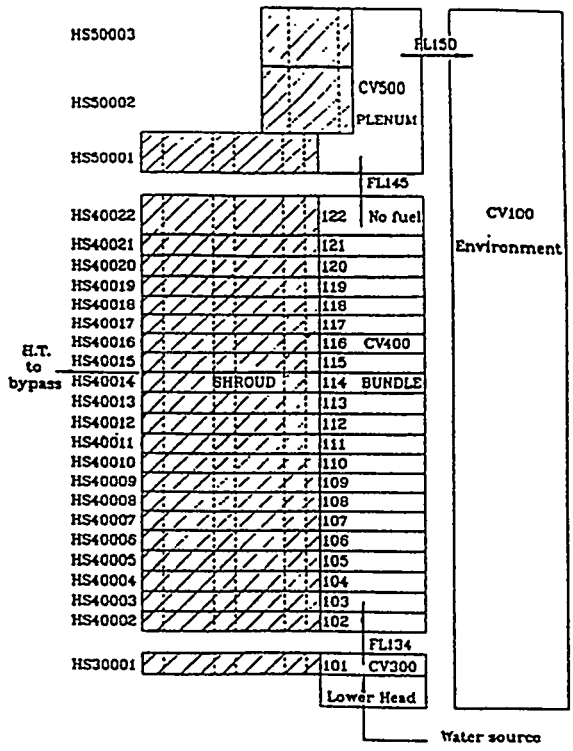


Figure 1. MELCOR Nodalization for the FLHT-2 Test

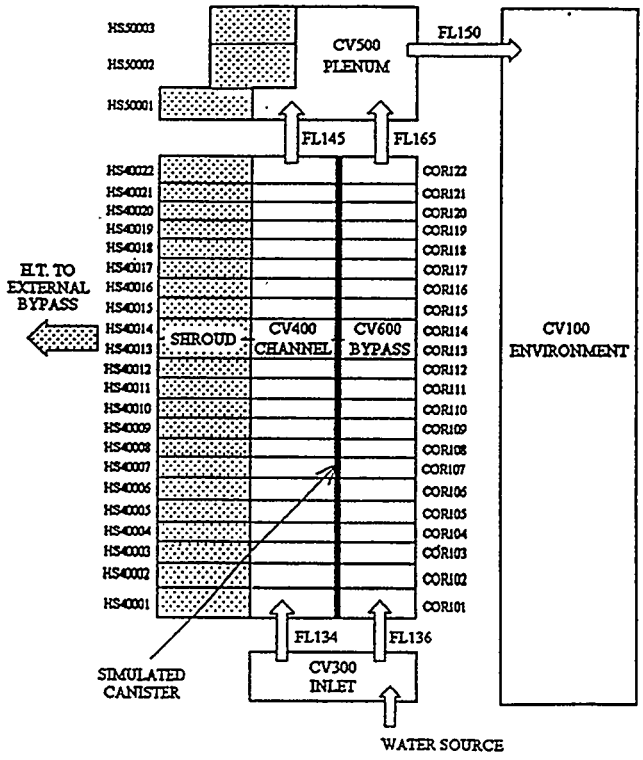


Figure 2. MELCOR Nodalization for the FLHT-5 Test

fails to achieve the measured steep temperature rise prior to thermocouple failure. This could be attributed to several causes. Firstly, following clad rupture, the inner clad surface also gets exposed to steam and hence subject to oxidation. This is not modeled in MELCOR. The effect may not be pronounced for steam-starved conditions, but there could nonetheless be local availability of steam close to the rupture opening. Secondly, the effect of clad ballooning (not modeled in MELCOR) could give rise to local flow reductions and temperature excursions. Finally, zircaloy present in the shroud inner liner, which can react with steam, was not allowed to oxidize in MELCOR as it was not a core component. This effect is not important for steam-starved conditions as in SFD 1-1. But where there is adequate steam supply, this may create divergence in predictions. For FLHT-5, the shroud liner was modeled as a canister of a BWR fuel bundle, and MELCOR predictions of both heatup and temperature escalation are very

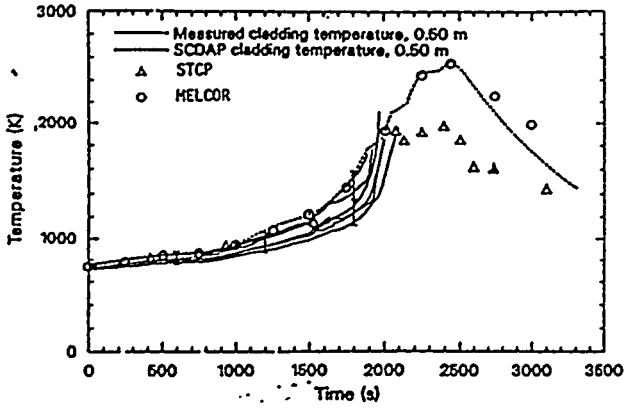


Figure 3. Comparison of measured and calculated clad temperatures, SFD 1-1

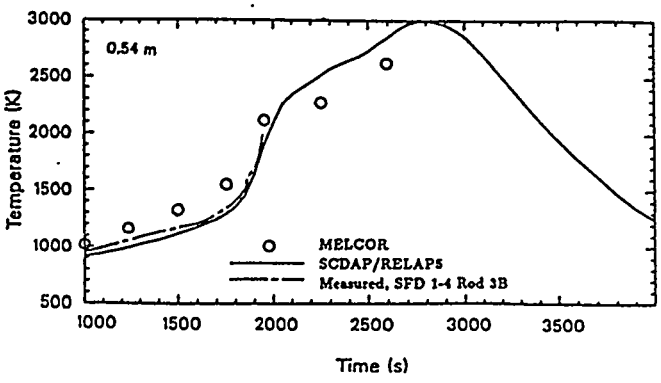


Figure 4. Comparison of measured and calculated clad temperatures, SFD 1-4

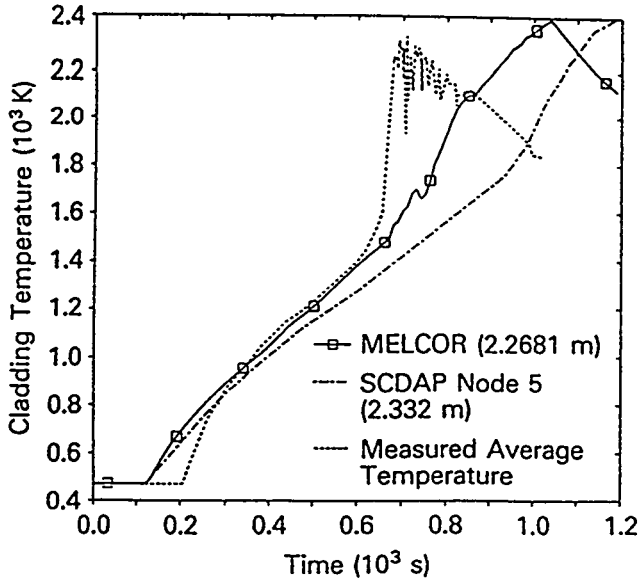


Figure 5. Comparison between calculated and measured temperatures, FLHT-2

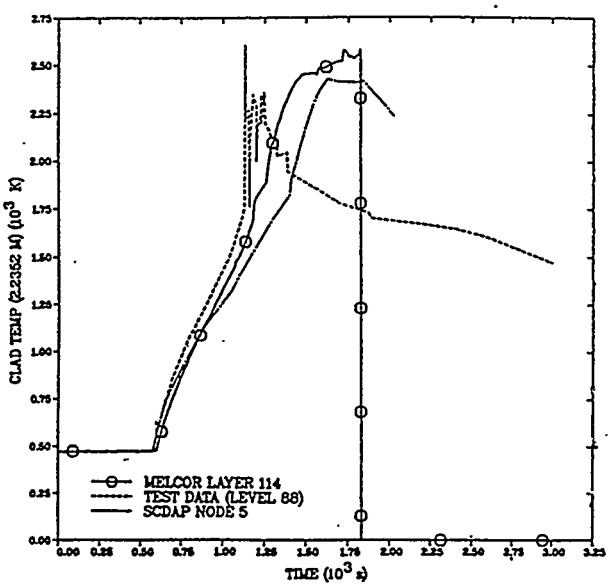


Figure 6. Comparison of calculated clad temperature with test data, FLHT-4

close to the measured values (see Figure 7). The sudden drop of MELCOR calculated cladding temperature in the figures represents clad melting and relocation downwards. SCDAP calculations [13] show temperatures rising to almost 3000K

before dropping. This is because the ZrO_2 holdup temperature in SCDAP was artificially specified to be 3000K, in order to minimize the predicted relocation, and increase the predicted hydrogen produced.

The difference between measured and predicted temperatures of the saddle, located outside the ZrO_2 insulation layer, is more significant and can be attributed in part to the difficulty in estimating the effective thermal conductivity of the shroud during the high temperature transient.

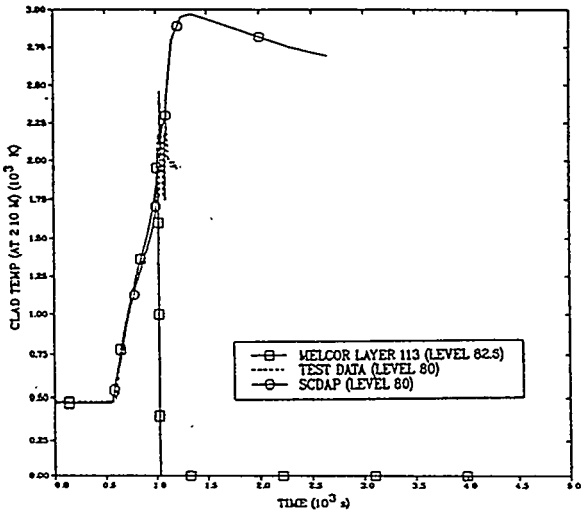


Figure 7. Measured and calculated clad temperatures, FLHT-5

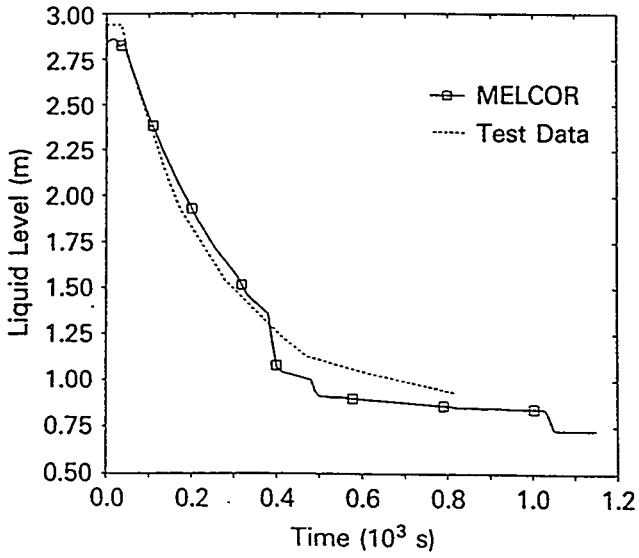


Figure 8. Comparison of calculated liquid level with test data, FLHT-2

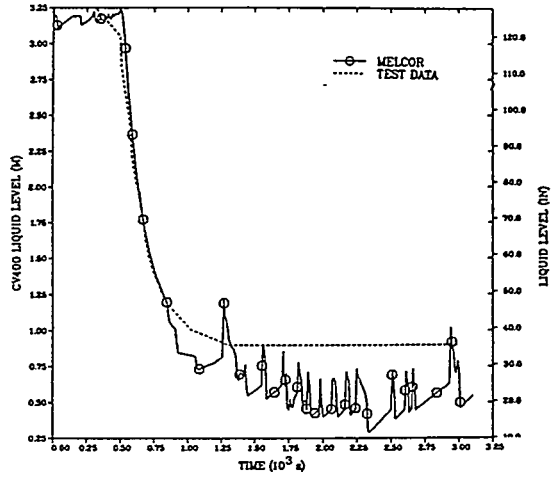


Figure 9. Comparison of calculated liquid level with test data, FLHT-4

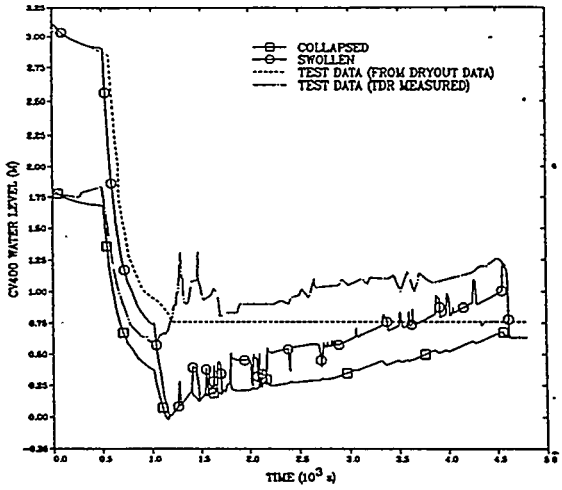


Figure 10. Comparison of calculated liquid level with test data, FLHT-5

The overall temperature behavior is strongly influenced by the calculated liquid level in the bundle region, and the converse is also true. Figures 8 - 10 show MELCOR-calculated liquid levels in the bundle region, compared with the measured levels, for tests FLHT-2, FLHT-4, and FLHT-5, respectively. A contributing factor to uncertainties in liquid level calculations

Table 1. Comparison of Calculated Total Hydrogen and Test Data

	HYDROGEN PRODUCED (g)			
	Experiment	MELCOR	SCDAP or SCDAP/RELAP5	STCP
PBF SFD 1-1	64 ± 7	67	89	60
PBF SFD 1-4	86 ± 12	86	87	--
FLHT-2	42 ± 2.5	43	39.7	--
FLHT-4	175 - 240	119	110/125	--
FLHT-5	220 - 340	158	168	--

Table 2. Comparison of Calculated Clad Rupture and Test Data for PBF SFD Test 1-1

	Criterion	Rupture Time(s)	Axial Location (m)
Experiment		1538 - 1632	0.30 - 0.69
MELCOR	T_{fail} = 1173K	1370	0.46 - 0.57
SCDAP	Mechanistic	1290	0.46 - 0.55
STCP	T_{fail} = 1173K	1755	

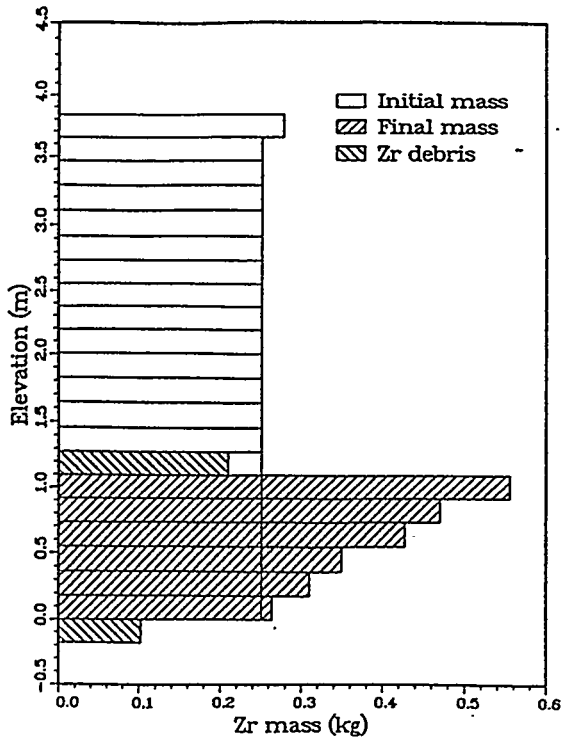


Figure 11. Fuel mass relocation calculated by MELCOR, FLHT-4

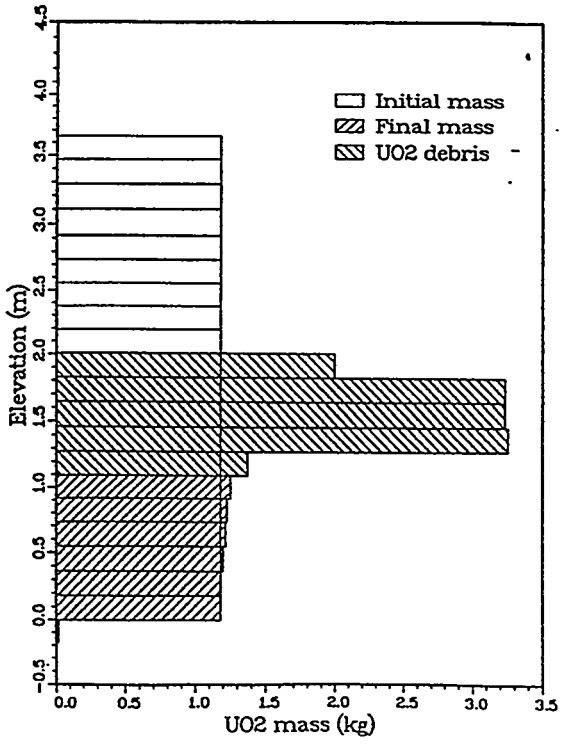


Figure 12. Zircaloy mass relocation calculated by MELCOR, FLHT-4

Table 3. Comparison of Measured and Calculated Release Fractions of Fission Products

Element	Experiment SFD 1-1	MELCOR (CORSOR)	SCDAP
Xe, Kr	0.06 ± 0.03	0.53	0.04
I	0.12 ± 0.02	0.53	
Cs	0.094 ± 0.014	0.53	
Element	**Experiment SFD 1-4**	**MELCOR (CORSOR)**	**FASTGRASS**
Noble Gas	0.23 - 0.52	0.57	0.63
I	0.24 ± 19%	0.57	
Cs	0.51 ± 15%	0.57	
Te	0.03	0.03	
Element	**Experiment FLHT-4**	**MELCOR (CORSOR)**	**SCDAP**
Noble Gas	0.25 - 0.55	0.67	0.12
Element	**Experiment FLHT-5**	**MELCOR (CORSOR)**	**SCDAP**
Noble Gas	Best estimate ~0.50	0.53	0.20

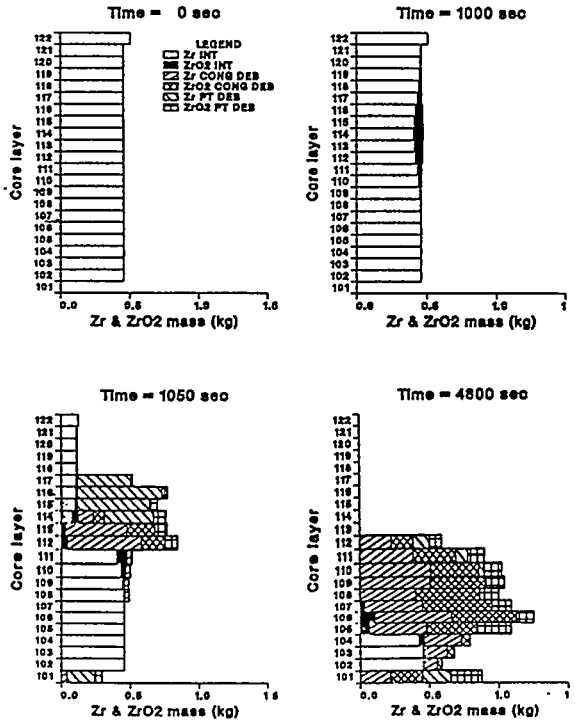


Figure 13. MELCOR-calculated relocation of Zr and ZrO_2, FLHT-5

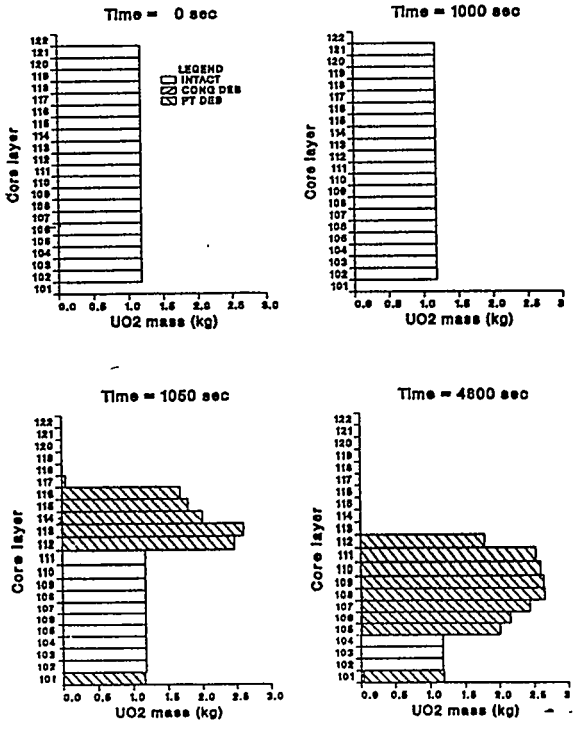


Figure 14. MELCOR-calculated relocation of UO_2, FLHT-5

is that the actual bundle flow was never constant, whereas MELCOR input (for convenience) assumed it to be constant.

Oxidation and Hydrogen Production

MELCOR calculates oxidation of both zircaloy and steel by solid-state diffusion through the oxide layer using standard parabolic kinetics, with appropriate rate constant expressions, and limited by steam availability. For zircaloy, the rate constant is evaluated from the correlation by Urbanic and Heidrick. The shift to rapid oxidation is modeled to occur at 1853K. This temperature can be changed via sensitivity coefficient, and was changed to 1700K based on experimental observations for FLHT-4 and FLHT-5.

Table 1 shows comparisons between experimental and calculated values of total hydrogen production for all five integral experiments. MELCOR calculations show good agreement with test data for PBF SFD1-1, SFD1-4, and FLHT-2, and poor agreement for FLHT-4 and FLHT-5. The poor agreement for the FLHT-4 test could be attributed to the following: (i) There was less zircaloy mass available for oxidation in MELCOR, since the liner, being a heat structure, was not allowed to oxidize; (ii) MELCOR does not model clad ballooning, and allows no oxidation on the inside of the clad after it fails, and (iii) MELCOR calculates more relocation than in the test, bringing zircaloy to cooler regions of the bundle, where oxidation is suppressed. For FLHT-5, the predictions were significantly improved (by about 55-60 %) by including the shroud liner as a canister component that could participate in oxidation. But the overprediction of relocation by MELCOR included significant relocation of the liner material, so that much less zircaloy from the liner was able to oxidize, as compared to the experiment. The better predictions for SFD1-1 and FLHT-2 tests can be partially attributed to less severe conditions in the tests resulting in almost no relocation, both observed and calculated. For SFD1-4, with a shorter length fuel bundle, and more severe conditions, there was significant relocation and the formation of blockages both calculated and observed in the test.

Changes in Bundle Geometry

The first indication of bundle geometry changes is clad ballooning. There is no explicit model for clad ballooning in MELCOR. Clad rupture is modeled to occur when the clad temperature at an axial cell exceeds a user-specified threshold temperature. This temperature has a default value of 1173K.

Table 2 [3] shows comparisons of measured (SFD 1-1) clad rupture times and location and MELCOR, SCDAP, and STCP predictions. Based on this comparison, the default value of 1173K, while not mechanistic, is adequate and need not be changed unless appropriate data is available for a given application.

For SFD1-4, MELCOR calculates 40 percent of fuel relocated during the transient [4]. This is a strong function of the assumed holdup temperature for the oxide shell in MELCOR (2600K in this case). An assumed holdup temperature of 2650K resulted in almost no relocation. The value of 2600K was selected based on observations of the SFD tests [14]. This sensitivity to user-input quantities clearly demonstrates the need for the user to be knowledgeable about the modeled phenomena.

During the FLHT-4 test, much of the fuel bundle metal components including the liner above 1.5m elevation was molten, but there was no indication of substantial relocation to lower bundle regions. In contrast, MELCOR calculated severe material relocation. Figures 11 and 12 [6] shown the UO_2 and zircaloy mass relocated, respectively, as calculated by MELCOR. The severe material relocation calculated by MELCOR could also be one of the reasons for the lower hydrogen production. For FLHT-5, MELCOR calculated severe material relocation (see Figures 13 and 14), area reduction, and also a period of 250 sec during which there was complete flow area blockage. The relocation caused early termination of oxidation, hence lower cumulative hydrogen produced. This deficiency also plagued the SCDAP code predictions of the test, in spite of artificially specifying a hold-up temperature of 3000K to minimize downward relocation of material.

Fission Product Release from Fuel

The release of fission products from fuel is modeled in MELCOR using either the original CORSOR or CORSOR-M formulation. Depending on user choice, these release rates can be modified to be a function of the surface-to-volume ratio (S/V) of the material compared to the ratio in the CORSOR experiments. Both models are based on the same experimental data using irradiated fuel. It can be expected, therefore, that agreement with data for fresh fuel will be poor and much better for irradiated fuel. This was confirmed by comparisons of MELCOR calculations using CORSOR and data for test SFD 1-1 which used fresh fuel and test SFD 1-4 that used irradiated fuel. These are shown in Table 3. In FLHT-2, there were no measurements of fission product release. For FLHT-4, MELCOR (1.8.1) somewhat overpredicts and SCDAP somewhat underpredicts the noble gas release. For FLHT-5, there is a large band of uncertainty in the measurements of noble gas release, with a best estimate of ~0.50. MELCOR (1.8.2) calculations using CORSOR are closer to the best-estimate values from the experiment than SCDAP.

MELCOR 1.8.2 also has two CORSOR-Booth models (for high-burnup and low-burnup fuels) available to the user [15]. Both these new models were used and found to predict much lower noble gas releases than measured data and the predictions from CORSOR.

Effect of Axial Nodalization

In the MELCOR core model, the bundle region is divided into concentric radial rings and axial segments that define core cells. Each cell may contain one or more components such as fuel pellets, cladding, etc.; and a lumped parameter approach is used for each component within a cell. For the FLHT-2 test simulation, besides the reference case with 20 axial segments in the bundle active region, three sensitivity cases with 5, 10, and 30 segments were also calculated. Comparisons of cladding temperatures are shown in Figure 15. Predicted values for hydrogen produced were 41g (20 segments), 27g (10 segments), and 26g (5 segments), compared to the measured value of 42g. The case with 20 segments appears to give predictions that are closer to experimental data, compared with the coarser nodalizations. The calculations with 30 segments gave results that were very close to the 20 segments case and are not shown here. Hence, the choice of 20 axial segments in the active length was justified for the reference case, and was retained for all subsequent test simulations.

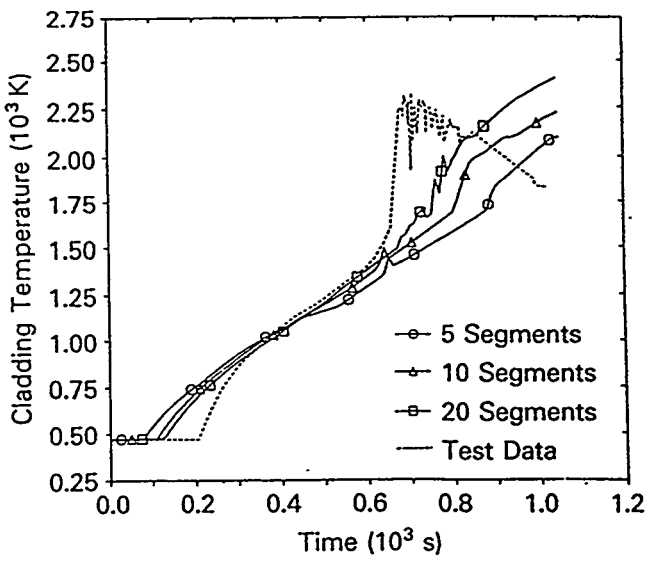


Figure 15. Impact of bundle nodalization on calculated clad temperatures, FLHT-2

Effect of Maximum Allowable Timestep

The maximum and minimum allowable timestep sizes are specified on MELCOR input. MELCOR calculates its system timestep based on directives from the various packages, but it cannot take timesteps greater than the maximum timestep or smaller than the minimum timestep. The selection of Δt_{max} and its impact on the calculational behavior of the code had been an area of lingering uncertainty in the use of earlier versions of MELCOR. For example, when the PBF SFD 1-1 calculation using MELCOR version 1.7.1 was performed with Δt_{max} = 10 s, 5 s, and 2 s, the results were seen to diverge rather than converge with the selection of Δt_{max} = 2 s [16]. In the FLHT-2 simulation using MELCOR version 1.8DN, the impact of Δt_{max} was found to be very small [5]. A similar exercise was attempted for the PBF SFD 1-4 test using version 1.8DN, but in each case, the calculation terminated due to a fatal code error. The impact of Δt_{max} was examined for the FLHT-4 simulation using MELCOR 1.8.1, by varying Δt_{max} from 0.5 s to 5.0 s. The case with 0.5 s gave the best clad temperature predictions, but earlier relocation, and less hydrogen and fission product release. The calculations appeared to converge with the selection of smaller Δt_{max}, prior to relocation. The FLHT-5 test was simulated using the recently released MELCOR version 1.8.2, which has corrections to mitigate numerical sensitivities. The effect of Δt_{max} was examined once again by varying Δt_{max} from 0.1 s to 5.0 s. The impact was insignificant for levels and clad temperatures. For hydrogen production, the maximum deviation was 8 % compared with 14 % for FLHT-4 using MELCOR 1.8.1. For noble gas releases, the maximum deviation was 10 %, compared to 16 % for FLHT-4 using MELCOR 1.8.1. While there was no convergence in going to a smaller Δt_{max}, there was a noticeable improvement in Δt_{max} sensitivity for MELCOR 1.8.2 [7].

Workarounds

Experience with the code has allowed the use of several innovative inputs or "workarounds" that were successful in extending the capabilities of MELCOR [16]. Most of them were used during MELCOR benchmarking analyses. For example, one can sometimes speed up a calculation if a problem control volume is eliminated without loss of physics. Initially, the MELCOR input model for the PBF SFD 1-1 test had a bypass volume, which received heat from the bundle region via the insulating shroud. During MELCOR simulation of the test, the timestep was severely restricted by Courant stability limitations. This problem was traced to the bypass volume which had very high flow through it. To improve timestep behavior, the bypass volume was replaced by a user-specified heat transfer coefficient (H_{ext}) on the outer surface of the shroud. The value of H_{ext} was selected based on actually calculated values of H_{ext} from the code. Sensitivity calculations showed the results to be insensitive to this parameter over a substantial range (5,000 - 15,000 W/m^2-K). That was expected, since the insulating shroud constitutes the largest resistance to heat transfer. This workaround increased the calculational Δt by more than a factor of 50. A similar effect was also achieved in integral plant calculations by eliminating unimportant control volumes.

Another more recent workaround was to model the FLHT-5 test

train as a BWR geometry, which allowed the mass of zircaloy in the shroud inner liner, carriers, and clad of one unfueled rod, to be modeled as a canister component and hence participate in oxidation with steam, as in the experiment. This was a modeling change from earlier simulations which treated the test train as a PWR geometry, in which the liner, being treated as a heat structure, could not participate in oxidation. The impact of this modeling change was to increase predicted cumulative hydrogen production by about 55-60%.

CONCLUSIONS

The benchmarking calculations of integral severe fuel damage tests performed by BNL have helped to identify areas of modeling strengths and weaknesses in MELCOR, the most appropriate choice of input parameters and nodalization, and workarounds that allow the analyst to extend the capabilities of MELCOR. Examples of workarounds include eliminating unimportant control volumes, without loss of physics, to speed up calculations, and representing heat structures surrounding the core as BWR canisters to enable them to oxidize as in the test. These and other insights were explored in the paper, with the help of selected results and comparisons with test data and other calculations, for all five integral tests.

The benchmarking analyses were performed for different tests using different versions of MELCOR. In general, the earlier versions of the code had a difficulty in adequately simulating the sharp temperature rise associated with the autocatalytic oxidation of zircaloy in steam. However, as the simulation of FLHT-5 has shown, using MELCOR 1.8.2 appears to have significantly reduced that deficiency.

The PBF SFD tests were operated under steam starved conditions, hence the inability of MELCOR to model oxidation of the inner liner did not cause any problem in the prediction of the oxidation and hydrogen production compared to the experiment, which was, in fact, quite good. However, for FLHT-4 and especially FLHT-5, the hydrogen production was severely underpredicted by both MELCOR and SCDAP. For FLHT-4, one of the reasons for the poor prediction by MELCOR was that there was less zircaloy available to oxidise in steam, since MELCOR does not model the oxidation of heat structures, and the zircaloy inner liner and hard-line carriers were modeled as heat structures. The other reason is that the relocation model in MELCOR is logical-based, rather than rate-equation based, and was found to overpredict the relocation of core material to cooler regions of the bundle where oxidation is predicted to stop. For FLHT-5, the first limitation of the code was removed via innovative input, that is, by modeling the liner and hard-line carriers as a canister component of a BWR reactor core. However, while this workaround improved hydrogen production significantly (by about 55-60 %), the hydrogen generation was predicted to terminate early and was hence still substantially underpredicted. This can be attributed to the code predicting early and severe relocation to cooler regions of the bundle, where oxidation is suppressed. The massive relocation predicted by MELCOR also led to complete blockage of the bundle flow area for a period of 250 s, during which no hydrogen was predicted to form. This is contrary to post-test visual examination of the test bundle which showed evidence of relocation over the bundle region, but no massive relocation and complete blockage anywhere.

Another observation from the FLHT-5 test simulation is that the relocated material in MELCOR included the liner, while the experiment showed oxidation of the liner but almost no relocation. The liner was predicted to relocate along with the core material because it was mmodeled as part of the core. Based on this, a strong recommendation is made to add the capability in MELCOR to model oxidation of heat structures, as in SCDAP. The other recommendation is that the relocation model in MELCOR may need to be examined closely for its adequacy, since the code predicts severe material relocation and significant blockage in the lowest regions of the bundle, which is contrary to the post irradiation examination of the FLHT-4 and FLHT-5 fuel bundles.

An evaluation of MELCOR improvement has shown that MELCOR 1.8.2 is a more robust code, with significant improvement in its numerical behavior. Based on results from the FLHT-5 analyses, the selection of the most appropriate timestep size appears to be less critical with the new code version. Several new models have been added to MELCOR 1.8.2, that have enhanced MELCOR's modeling capabilities.

REFERENCES

1 SUMMERS, R.M., ET AL. - *MELCOR 1.8.0: A Computer Code for Severe Nuclear Reactor Accident Source Term and Risk Assessment Analyses* - NUREG/CR-5331, SAND90-0364, Sandia National Laboratories (January 1991).

2 MADNI, I.K. - *Review of Experimental Data Alternatives for Benchmarking MELCOR* - Brookhaven National Laboratory Technical Report A-3281 (July 1988).

3 MADNI, I.K. - *MELCOR Simulation of the PBF Severe Fuel Damage Test 1-1* - Proc. 26th National Heat Transfer Conference, Philadelphia, PA, AIChE Symp. Ser., 85, 269 (1989).

4 MADNI, I.K. - *MELCOR Modeling of the PBF Severe Fuel Damage Test 1-4* - Proc. International Conference Probabilistic Safety Assessment and Management (PSAM), Beverly Hills, CA and Elsevier Science (1991).

5 MADNI, I.K., GUO, X.D. - *MELCOR Modeling of the*

NRU Full-Length High-Temperature 2 Experiment - Nuclear Technology, Vol. 99 (August 1992).

6 MADNI, I.K., GUO, X.D. - *MELCOR Simulation of the Full-Length High-Temperature 4 Experiment* - Brookhaven National Laboratory Draft Technical Report A-3281 (November 1991).

7 MADNI, I.K., GUO, X.D. - *MELCOR 1.8.2 Simulation of the Full-Length High-Temperature 5 Experiment* - Brookhaven National Laboratory Technical Report (October 1993).

8 MARTINSON, Z.R., PETTI, D.A., COOK, B.A., - *Volume 1: PBF Severe Fuel Damage Test 1-1 Test Results Report* - NUREG/CR-4684, EGG-2463, (October 1986).

9 PETTI, D.A., ET AL., - *Power Burst Facility (PBF) Severe Fuel Damage Test 1-4 Test Results Report* - NUREG/CR-5163, EGG-2541, (April 1989).

10 LOMBARDO, N.J., LANNING, D.D. - *Data Report, Full-Legth High- Temperature Experiment 2* - PNL-6551, (April 1988).

11 LOMBARDO, N.J., LANNING, D.D. - *Data Report, Full-Legth High- Temperature Experiment 4* - PNL-6368, (January 1988).

12 LANNING, D.D., ET AL. - *Data Report, Full-Legth High-Temperature Experiment 5* - PNL-6540, (April 1988).

13 LOMBARDO, N.J., LANNING, D.D., PANISKO, F.E. - *Full-Legth Fuel Rod Behavior Under Severe Accident Conditions* - NUREG/CR-5876, PNL-8023, (December 1992).

14 OSTEK, D.J. - *Results of the Four PBF Severe Fuel Damage Tests* - Transactions - 15th Water Reactor Safety Information Meeting, NUREG/CP-0090 (1987).

15 MELCOR 1.8.2 Users' Guide/Reference Manual, Sandia National Laboratories (February 1993).

16 MADNI, I.K. - *MELCOR Lessons Learned: A User Perspective* - Brookhaven National Laboratory Technical Report A-3281(January 1991).

Validation of the THIRMAL-1 Melt-Water Interaction Code

by

C. C. Chu, J. J. Sienicki, and B. W. Spencer
Argonne National Laboratory
9700 S. Cass Avenue
Argonne, Illinois 60439
(708) 252-6564

ABSTRACT

The THIRMAL-1 computer code has been used to calculate nonexplosive LWR melt-water interactions both in-vessel and ex-vessel. To support the application of the code and enhance its acceptability, THIRMAL-1 has been compared with available data from two of the ongoing FARO experiments at Ispra and two of the Corium Coolant Mixing (CCM) experiments performed at Argonne. THIRMAL-1 calculations for the FARO Scoping Test and Quenching Test 2 as well as the CCM-5 and -6 experiments were found to be in excellent agreement with the experiment results. This lends confidence to the modeling that has been incorporated in the code describing melt stream breakup due to the growth of both Kelvin-Helmholtz and large wave instabilities, the sizes of droplets formed, multiphase flow and heat transfer in the mixing zone surrounding and below the melt stream, as well as hydrogen generation due to oxidation of the melt metallic phase. As part of the analysis of the FARO tests, a mechanistic model was developed to calculate the prefragmentation as it may have occurred when melt relocated from the release vessel to the water surface and the model was compared with the relevant data from FARO.

1. INTRODUCTION

1.1 Background

The assessment of severe accident sequences in the light water reactors includes many situations in which molten core materials are released into water. In many instances the core materials enter the water in the form of a coherent melt stream. The THIRMAL-1 code has been developed at Argonne National Laboratory to provide an analysis tool for melt stream-water interactions in light water reactor severe accidents. The physical models and user's guide of THIRMAL-1 code have recently been comprehensively documented in a two-volume report prepared for the Electric Power Research Institute [1,2]. THIRMAL-1 is an outgrowth of an earlier code called THIRMAL-0 developed at Argonne [3]. In contrast to this earlier code, THIRMAL-1 incorporates significantly improved modeling and models for many additional processes. The THIRMAL-1 computer code is being used in the DOE Advanced Reactor Severe Accident Program and has been applied in studies of accident management for Swedish BWRs [4]. To support the

use of the code and assure its acceptability, it has been compared with available data from the FARO Scoping Test and Quenching Test 2 performed at elevated pressure and reported in the literature [5] as well as data from the Argonne Corium-Coolant Mixing (CCM) experiment at near atmospheric pressure conditions [6].

1.2 Brief Review of THIRMAL-1 Code

THIRMAL-1 was conceived and developed with a close connection to the behavior observed in and the understanding obtained from both simulant material and reactor material experiments. The simulant material tests of Spencer et. al. [7,8] showed the leading edge of the melt stream to be deformed and stripped after penetrating into the water pool and small melt droplets and ligaments to be stripped off of the melt stream column surface by the surrounding fluid. In the video and x-ray photographs from the simulant experiments of Schneider et. al. [9], an upward flowing vapor chimney can be observed surrounding the melt stream that undergoes sinuous or varicose deformation along its length while small drops and ligaments are observed to be stripped from the surface of the stream. Accordingly, THIRMAL-1 models erosion by stripping (i.e., small wave Kelvin-Helmholtz instabilities) from the stream surface, stripping from the leading edge surface, as well as breakup from large waves along the stream column. The mechanistic THIRMAL-1 approach thus reflects results from experiments with actual streams; this important aspect of the real premixing problem has instead been treated parametrically in the prefragmentation/cloud of spheres approach, an alternative premixing model [10]. Other modeling approaches on this subject have been developed. A description of the mechanism of the stripping at the stream column due to shear flow produced waves based on the Miles formulation of the instability has been given by Bürger et. al. [11]. Breakup of a melt stream due to Taylor instabilities alone at the leading edge of a melt stream has been described by Chu and Corradini [12].

THIRMAL-1 treats the case of a circular melt stream entering the water pool with a time varying diameter, velocity, temperature, and composition. Except for the initial transient penetration of the melt stream into the pool, the dominant fragmentation mechanism in the model is the erosion of molten droplets from the surface of the melt stream due to the formation of Kelvin-Helmholtz instabilities along the stream surface (Figures 1 and 2). Immediately behind the stream leading edge, the instabilities are driven by the upward flow of vapor inside a vapor film immediately surrounding the stream along part of its length. As the eroded fragments enter the surrounding water, heat transfer from the fragments gives rise to the local formation of steam which rises through the pool. This results in the formation of an interaction zone surrounding the stream containing melt droplets, melt particles, water, and steam. The radial extent of the interaction zone reflects the lateral migration of the droplets and particles and their temperatures that directly determine the vapor source.

Near the leading edge, the steam rises through water within the interaction zone in a bubbly flow regime. At increasing heights above the leading edge, the accumulation of steam increases the superficial vapor velocity through the interaction zone causing a transition to a churn turbulent flow regime. Dispersed flow typically develops in

the overlying part of the interaction zone. Here, melt droplets and particles together with water droplets are dispersed in the upward flowing steam. Heat transfer from the melt droplets and particles in the dispersed flow region typically produces superheated steam that exits the interaction zone at the elevation of the top of the pool.

Interactions of the upward flowing steam with the melt stream also result in the erosion of droplets from the stream surface through the Kelvin-Helmholtz instability mechanism. Heat transfer to the water droplets and the water at the outer boundary of the interaction zone can occur at such a high rate in the upper part of the dispersed flow region that local steam condensation is effectively eliminated. Depending upon the droplet/particle diameter and the vapor flow conditions, melt droplets and particles in the dispersed region may be swept up out of the pool or may settle downward through a continuous vapor flow before encountering the continuous liquid churn turbulent and bubbly flow regions near the stream leading edge.

In addition to Kelvin-Helmholtz instabilities, erosion of the melt stream leading edge due to boundary layer stripping is modeled as the stream initially penetrates downward rapidly through the water pool. Subsequently, the effects of erosion and acceleration of the melt stream cause the local stream diameter immediately behind at the leading edge to decrease to sizes so small that the stream column breaks up from capillary effects. In THIRMAL-1, this happens when the unstable large waves (i.e., varicose and sinuous wave growth) locally increase to about the melt stream radius. A number of relatively large melt fragments will be formed from the front part of the melt stream. Further breakup of the fragmented large segments is calculated according to a Weber number-based criterion.

2. COMPARISON WITH FARO EXPERIMENTS

2.1 General Description of FARO Tests

In the Scoping Test (ST) and Quenching Test 2 (QT2) (Table 1), 18 and 44 Kilograms, respectively, of an 80 wt % UO_2 - 20 wt % ZrO_2 melt were delivered under gravity through a 10 centimeter diameter nozzle into 0.87 and 1.0 meter depth pools, respectively, of slightly subcooled water [5]. It is noted that the Scoping Test is designated as L-06 and Quenching Test 2 as L-08 in recent publications. A feature of the FARO data is that the interaction vessel pressure increases before the onset of melt/water contact (MWC). According to the experimenters, the pressure increase observed in the Scoping Test during this period resulted from heating of the cover gas mixture above the water by the melt and from steam generation due to the "deequilibrium" at the time of pressure equilibration [5]. The Quenching Test 2 pressure increase is said to have been due only to gas heating [5]. Angelini, Yuen and Theofanous [10] claim that the pressurization rate of the gas before MWC in the Scoping Test can be explained by radiative heat transfer. As a test of this hypothesis, they note that breakup of the melt stream into drops of 1.2 centimeter diameter would afford sufficient additional surface area to provide the required heating.

TABLE 1. Comparison of the THIRMAL-1 Code with the Results of the FARO Scoping and Quenching Test 2

FARO Test Conditions	Scoping Test (ST)		Quenching Test 2 (QT2)	
Mass, Kg	18		44	
Melt composition, wt %	80% UO_2 + 20% ZrO_2		80% UO_2 + 20% ZrO_2	
Delivery nozzle, cm	10		10	
Free fall distance in cover gas, m	1.83		1.70	
Water pool depth, m Initial water temperature, K	0.87 539 (water surface) 503 (bottom plate)		1.0 536 (water surface) 528 (bottom plate)	
Gas Composition, mole %	91.5 steam + 8.5 Ar		84 steam + 16 Ar	
Gas volume, m^3	0.464		0.875	
Temperature at onset of melt release, K	543		536	
Pressure at onset of melt release, MPa	5.0		5.8	
Pressure at melt/water contact (MWC), MPa	5.4		6.1	
Summary of Prefragmentation Analysis	**Scoping Test**		**Quenching Test 2**	
Eroded melt mass before melt/water contact, Kg	4.9		9	
Total eroded melt mass before all melt in water, Kg	8.8		19.7	
Eroded melt droplet diameter, mm	5.5		3.83	
Melt stream velocity at water surface, m/s	6.2		6.67	
Melt stream diameter at water surface, cm	3.4		4.8	
Pressure at MWC, MPa	5.2		6.06	
Argon-steam mixture temperature at MWC, K	554		547	
Comparison of THIRMAL-1 Predictions and Experiment Results	**Experiment**	**Prediction**	**Experiment**	**Prediction**
Corium collection conditions, wt % particles/droplets/stream	67/0/33	50/17[a]/33	68/0/32	46/22[a]/32
Fragmented mass, Kg	12.0	12.0	30.0	30.0
Unfragmented mass, Kg	6.0	6.0	14.0	14.0
Particle size range, mm	0.4 to 6.0	0.7 to 5.5	0.4 to 6.0	0.7 to 3.8
Median particle size, mm	4.5	5.0	3.8	3.8
Melt and bottom plate contact after melt/water contact, s	0.370	0.370	0.270	0.288
Mean velocity of melt in water, m/s	2.3	2.3	3.7	3.5
Pressure increase from MWC to end of fragmentation, MPa	0.7	0.7	1.5	1.5
Peak pressure increase rate, MPa/s	1.6	1.7	3.3	3.4
Equilibrium gas space temperature, K	582	579	578	607

a) Includes partially frozen droplets.

The assumption of complete breakup of all the released melt into 1.2 centimeter diameter spheres prior to melt-water contact is, however, not the only possible interpretation of the early pressure increase. The FARO experiments do not provide for any visualization of the melt relocation and melt-water interactions. Consequently, the actual state of the released melt is not observed. In the present analysis, it is shown below that an alternative explanation of the data can be obtained with a mechanistic model that calculates partial fragmentation of the released melt stream in the cover gas space such that the melt enters the water mainly in the form of a reduced thickness stream surrounded by melt drops eroded from the stream. Thus, the model does not assume a prior complete breakup of the released melt into drops.

2.2 Analysis of Melt Prefragmentation in the FARO Tests

Using the measured melt stream fall time and the free fall distance through the cover gas space, the velocity of the melt stream exiting from the release vessel nozzle is estimated. The measured melt stream fall time, t_{fall}, is estimated from experimental determination of the mean melt velocity in the cover gas and the free fall distance in the cover gas. The released melt stream is assumed to have the configuration of a segment of a cone as illustrated in Figure 3.

The single feature of the FARO tests that most promotes prefragmentation is the high pressure that exceeds 5 Megapascals. The high pressures are accompanied by high densities in the cover gas space that result in significant interactions of the falling melt stream with the gas. At the high gas space density, the initial disturbances on the melt stream surface will grow to a critical wave magnitude due to the Kelvin-Helmholtz instability within a fraction of a second as the melt stream falls through the gas phase. Subsequently, melt on the stream surface will be eroded away and the melt stream diameter will decrease with time. The melt erosion rate can be represented by [1]

$$\dot{M}_E = \frac{A_J'}{3}\left(\frac{\alpha_{max}}{k_{max}}\right)\rho_m \tag{1}$$

where

$$k_{max} = \frac{2\,\rho_f\,U_J^2}{3\,\sigma_m}, \tag{2}$$

$$\alpha_{max} = \frac{2\,(\rho_f)^{3/2}\,U_J^3}{\sqrt{27}\,\rho_m^{1/2}\,\sigma_m}, \tag{3}$$

The erosion rate represented by Eqs. (1 through 3) assumes that the gas phase interacting with the melt stream has a density at the film temperature. The melt mass cumulatively eroded with time before MWC is given by the equation,

$$\Delta M_E = \frac{(\rho_f \rho_m)^{\frac{1}{2}}}{\sqrt{27}} \int_{t_o}^{t} \int_{x_o}^{x_1} D_J U_J \, dx \, dt. \tag{4}$$

In the current analysis, the melt stream velocity and diameter are approximated by representative average values to obtain

$$\Delta M_E = \frac{(\rho_f \rho_m)^{\frac{1}{2}}}{\sqrt{27}} \bar{U}_J \bar{D}_J \int_{t_o}^{t} (x_1 - x_0) \, dt. \tag{5}$$

If the fall distance at the trailing edge of the melt stream, x_2, is greater than x_0, then x_2 should be used instead of x_o in Eq. (5).

In THIRMAL-1, the droplet diameter resulting from Kelvin-Helmholtz instability-induced erosion is equal to 1.5 times the inverse wavenumber of the fastest growing wavelength. Therefore, the corresponding increase with time of the eroded melt droplet surface area is calculated from the equation,

$$A_p(t) = \int \dot{A}_p \, dt = \frac{4 \rho_f}{\sigma_m C_o \sqrt{27}} \left(\frac{\rho_f}{\rho_m} \right)^{\frac{1}{2}} \int_{t_o}^{t} \int_{x_o}^{x_1} D_J U_J^3 \, dx \, dt, \tag{6}$$

where C_o is a constant equal to 1.5. Using the representative average melt stream velocity and diameter, the melt surface area is calculated from

$$A_p(t) = \frac{6}{\sqrt{27} \bar{D}_p} \left(\frac{\rho_f}{\rho_m} \right)^{\frac{1}{2}} \bar{U}_J \bar{D}_J \int_{t_o}^{t} (x_1 - x_0) \, dt, \tag{7}$$

where

$$\bar{D}_p = \frac{3 C_o \sigma_m}{2 \rho_f \bar{U}_J^2}. \tag{8}$$

The inception of melt erosion due to Kelvin-Helmholtz instability occurs when the initial disturbance on the melt surface, η_o, grows to the critical unstable wave magnitude expressed by the equation,

$$\eta(t) = \eta_o e^{\alpha t_o} \geq \frac{\lambda_{max}}{4} = \frac{\pi}{2 k_{max}}, \tag{9}$$

where

$$\alpha t_o = \int_0^{t_o} \left(\frac{\rho_f k^2}{\rho_m} U_J^2 - \frac{\sigma_m}{\rho_m} k^3 \right)^{\frac{1}{2}} dt, \tag{10}$$

Combining Eqs. (9 and 10), the minimum melt stream velocity at which the initial disturbances will grow to the critical unstable wave magnitude is given by

$$\ln (a/r_o) + \ln \left(\frac{\pi}{2ka} \right) - \frac{k}{2g} \sqrt{\frac{\rho_f}{\rho_m}} \left[U_{J.min} \left(U_{J.min}^2 - \frac{\sigma_m}{\rho_f} k \right)^{\frac{1}{2}} \right.$$

$$\left. - \frac{\sigma_m}{\rho_f} \log \left(U_{J.min} + \left(U_{J.min}^2 - \frac{\sigma_m}{\rho_f} k \right)^{\frac{1}{2}} \right) \right]_0^{t_o} = 0. \tag{11}$$

In Ref. [13], a value of $\ln (a/r_o) = 6.0$ characterizing the magnitude of initial disturbance was evaluated both from the slope of the stream length curve at low velocities and by extrapolating the wave node amplitude back to the nozzle. This value is assumed here.

Heating of the steam-gas mixture in the gas space is mainly caused by radiative heat transfer from the melt stream plus both radiative and forced convection heat transfer from the melt droplets to the gas phase mixture. The melt droplet heat transfer rate is thus

$$Q_p'' = C_{rad} h_{rad} (T_m - T_{sat}) + h_{conv} (T_m - T_g), \tag{12}$$

and the melt stream heat transfer rate is

$$Q_J'' = C_{rad} h_{rad} (T_m - T_{sat}). \tag{13}$$

The melt stream prefragmentation model (Eqs. (1) through (11)) are applied until $x_2 = H_{fall}$ to provide the conditions (e.g., melt stream diameter, velocity, mass, eroded melt droplet diameter, velocity, and mass) with which melt enters the water pool in the following THIRMAL-1 calculations. The gas-steam space heatup model (Eqs. (12) and (13)) are only used to calculate heating of steam-gas mixture in the gas space before the melt stream contacts the water (i.e., $x_1 = H_{fall}$).

The cover gas heatup rate is dependent upon the fraction of the energy radiated from the melt that is absorbed by the gas-steam mixture instead of the surrounding wall. Transmission and absorption of thermal radiation were analyzed by Condiff [14] in conjunction with the direct containment heating problem for pressurized water reactors. Results for the percent absorption in an infinite steam atmosphere at a pressure of 0.3 Megapascal for UO_2 at various temperatures were calculated using the exponential band model of Tien [15]. Since absorption depends upon the quantity of steam that the thermal radiation passes through, Condiff [16] suggested that the results calculated can be used in the present analysis through the use of a scaling relationship that accounts for the effects of the differences in pressure and distance between FARO and the containment conditions of Ref. [14]. In particular, he suggested that a length in

the FARO system be multiplied by the ratio of the steam partial pressure in FARO to 0.3 Megapascal in order to determine the corresponding distance. In the FARO test vessel, radiation reaching the surrounding wall will be reflected from the wall. Part of the reflected radiation will be absorbed in the steam prior to reflecting off of the wall again and so on. It follows that the fraction absorbed in the steam is given by an infinite series of terms. A simple estimate for a one-dimensional long cylinder is

$$C_{rad} = 1 - \frac{\epsilon_w (1 - F)}{1 - (1 - F)^2 (1 - \epsilon_w)}. \quad (14)$$

Taking the absorbed fraction in an infinite medium to be 0.25 and assuming a wall emittance for steel of 0.3, it is found that about 60 percent of the radiation is absorbed in the steam. However, because this simple estimate neglects the effects of the multiple droplets/particles existing in the cover gas and radiation out the top and bottom of the cylindrical volume, it is assumed that a smaller portion of 40 percent is absorbed by the steam.

For the conditions of the cover gas region where steam-gas mixture and melt droplets/particles are present, the energy radiated from the melt and absorbed in the steam-gas/melt optical thickness can be expressed as [17]

$$F' = 1.0 - \exp[-(a_g + a_m)L_m]. \quad (15)$$

It is further assumed that the absorption fraction in an infinite medium gas-steam mixture is [17]

$$F = 1.0 - \exp[-a_g L_m] \quad (16)$$

Using F' instead of F in Eq. (14) and assuming 9 Kilograms of melt droplets/particles with a drop diameter of 5.5 millimeters existing in the cover gas, it is found that a higher fraction of 75 percent of the radiation is absorbed in the gas-steam/melt optical thickness, but a lower fraction of 45 percent of the radiation is absorbed in the gas-steam mixture only. This further supports the use of a 40 percent absorption fraction in the steam.

The radiant energy not absorbed by the gas-steam mixture is assumed to be absorbed by the water through the surface of the water pool and to generate steam if the water temperature at the water surface is equal to the saturation temperature. This assumption clearly overestimates the steam production from the mechanism since the absorption of energy by the steel wall is neglected.

The melt stream prefragmentation/gas-steam space heatup model was applied to both the Scoping Test and Quenching Test 2 (Table 1). For the Scoping Test, the calculated gas mixture temperature rises only from 543 to 544.5 degrees Kelvin during the first 0.3 second but rises quickly from 544.5 to 554 degrees Kelvin by 0.46 second (MWC). The distribution of the mixture temperature for Scoping Test is shown in Figure 8 of Reference 8. It is observed that the measured gas space temperatures don't increase during the first 0.3 second but begin to increase significantly as the melt stream approaches the water pool surface. It is also shown that the measured temperature is between 551 and 557 degrees Kelvin at a location 1.1 meters above the water pool surface and between 545 and 565 degrees Kelvin at a location 0.6 meter above the water pool surface at time of MWC. The pressure increases from 5 to 5.2 Megapascals just before MWC (Figure 4) and the corresponding pressurization rate increases to 1.8 Megapascal per second during the first 0.4 second and then decreases to 1.5 Megapascal per second just before MWC (Figure 5). At pressures below 5.16 Megapascals, the water temperature

near the pool upper surface exceeds the saturation temperature. Flashing of the superheated water is not modeled in the analysis. This is expected to lead to an underestimate of the pressurization rate and pressure rise. Vaporization of water resulting from the absorption of thermal radiation in the water pool is modeled, however; this source of steam is assumed present when the pressure is below 5.16 Megapascals. At higher pressures, thermal radiation penetrating into the water pool is assumed to raise the water temperature without producing steam. This is expected to further underestimate the pressurization rate and pressure rise as some vaporization could still be induced by the radiant flux. The prefragmentation analysis calculated pressurization rate of 1.74 Megapascal per second compares well with the measured gas pressurization rate of 1.65 Megapascal per second at the time of MWC (Figure 5) though the measured pressure of 5.4 Megapascals is higher than the calculated pressure of 5.2 Megapascals (Figure 4). As discussed above, the pressure predicted by the model is expected to be an underestimate due to neglect of flashing from the water pool surface as well as vaporization of subcooled water by incident radiant heating.

For the Quenching Test 2, the calculated mixture temperature increases slowly during the first 0.2 second and then rises quickly from 536 to 547 degrees Kelvin when the melt stream approaches the water pool surface. From the measured gas-steam mixture temperature for Quenching Test 2, the temperature is between 538 and 545 degrees Kelvin at a location about 0.765 meter above the water pool surface at MWC. The pressure increases from the initial value of 5.80 to 6.06 Megapascals before MWC (Figure 6). The pressurization rate increases significantly after melt erosion begins at a time of 0.105 second and reaches 3.0 Megapascals per second before MWC (Figure 7). The calculated pressurization rate of 3.0 Megapascals per second at MWC is higher than the measured pressurization rate of 1.7 Megapascals per second (Figure 7).

2.3 Comparison of THIRMAL-1 with the Scoping Test

As noted earlier, the comparison of the THIRMAL-1 calculations of melt-water interactions with experiment data from FARO is dependent upon what is assumed about the prefragmentation of melt as it falls from the melt catcher to the water pool. The results of the preceding analysis that mechanistically models the partial breakup of the melt stream are therefore used to determine the conditions with which melt enters the water pool. Significantly, melt enters the water both as a melt stream and a surrounding mass of eroded droplets. A representation of the melt stream column assumed in the calculation at the first instant of water entry and illustrating the eroded droplets is provided in Figure 3.

For the Scoping Test conditions, 67 percent of the melt is eroded away in the form of melt droplets. About 73 percent of the eroded melt droplets (48 percent of the total released mass) are eroded from the stream prior to entry into the water pool. Only 27 percent of the eroded droplets (19 percent of the total released mass) are eroded away as the melt stream penetrates through the water pool. The remaining 33 percent of the melt is calculated to arrive as large segments created by breakup of the melt stream. These segments collect upon the bottom plate of the THERMOS vessel in a molten state. About 75 percent of the eroded melt droplets (50 percent of the total released mass) solidifies completely to form particles prior to collecting on the interaction vessel base. All of the remaining eroded droplets (17 percent of the total mass) are calculated to arrive in a partially frozen state. In particular, 70 percent or more of the heat of fusion is calculated to be removed for each of the partially frozen droplets.

If the partially frozen droplets are assumed to subsequently freeze as particulate entities, then the material collection is predicted to consist of 33 percent

of the released mass in a molten state and 67 percent as particles. This prediction is in excellent agreement with the state of material found at the bottom of the vessel in the experiment together with other predictions that are also in excellent agreement with the data (Table 1).

The calculated cumulative particle size distribution is given in Figure 8 together with the measured particle size distribution. This information is provided for fully solidified particles only, i.e., 50 percent of the total released melt for the calculation and 67 percent of the released melt for the Scoping Test. This figure provides the cumulative distribution in which the percentage of mass having a size less than a given diameter is plotted against that diameter. In general, a distribution of sizes is calculated by THIRMAL-1 as opposed to a single diameter reflecting the spatial and temporal variation in the local mechanisms and conditions under which droplet erosion occurs from the melt stream. In contrast, the prefragmentation analysis made the simplifying assumption of a single representative droplet diameter that was calculated to equal 5.5 millimeters. This representative particle diameter is used for the droplets that enter the water together with the melt stream. Consequently, it makes a significant and sharp contribution to the distribution at 5.5 millimeters. The calculated particle diameters range in size from 0.7 to 5.5 millimeters with a median size of 5.0 millimeters which compares very well with the measured median particle size of 4.5 millimeters.

The available data on melt quenching and steam formation from the Scoping Test are the time dependent pressure and temperature measured in the gas space overlying the water pool. Comparisons of the pressure calculated with THIRMAL-1 versus that measured during the experiment corresponding to the first 1.4 second following melt release are shown in Figures 4 and 5. The curves show two phases of pressurization: (i) a prefragmentation phase lasting approximately 0.46 second as the melt falls 1.83 meters from the release vessel to the upper surface of the water pool; and (ii) a melt-water interaction phase lasting about 1.0 second as the melt falls through the 0.87 meter deep water pool and collects at the bottom of the water pool. The first phase shows the effects of heating of the argon-steam cover gas mixture associated with the melt relocation in the gas space while the second phase includes the effects of steam generation in the water pool and further heating of the argon-steam mixture in the gas space. THIRMAL-1 does not model the long-term quenching of melt that collects and spreads over the base. Thus, the pressures calculated account only for fall stage melt quenching as the melt relocates downward through the water. However, the low rate of pressurization observed in the experiment over a longer timescale of 10 seconds indicates that pressurization due to the effects of heat transfer off of collected debris and melt is relatively unimportant during the melt fall stage. The virtual attainment of the peak pressure of 5.9 Megapascals at 0.8 second after melt entry into the water pool thus corresponds to essentially complete settling out of particles and droplets from the water pool. Prior to this time, the THIRMAL-1 calculated pressure increases more rapidly during the first 0.7 second. The calculated pressure increase rate during this interval shows excellent agreement with the measured pressure increase rate. The oscillation of the calculated pressurization rate after MWC is due to the limited number of Lagrangian particle groups used in the THIRMAL-1 input for the prefragmented melt droplets in the gas space. Increasing the number of particle groups used to represent the prefragmented melt droplets would reduce the magnitude of the oscillations. The predicted pressure is less than that in the test. However, as discussed earlier, this difference mainly represents an underestimate of the pressure rise during the prefragmentation phase due to neglect of flashing off of the top surface of the water pool. During the melt-water interaction phase, the pressure predicted with THIRMAL-1 tracks the measurement more closely. Here the pressurization is due to steam

formation from the melt-water interaction and provides a test of the modeling incorporated in the THIRMAL-1 code.

A more delicate test of the THIRMAL-1 models is provided by comparing the calculated and measured pressurization rates. Excellent agreement is obtained after the THIRMAL-1 calculation is initiated at the time of MWC (0.0 seconds on the figures). Between 0.7 and 0.8 second after nearly all of the pressure rise has been attained, the calculated pressurization rate is lower than the measurement. This may be a result of the assumption of a shorter melt release time of 0.207 second compared with 0.260 second noted by the experimenter. Another effect possibly contributing to this difference is the approximation in THIRMAL-1 of neglecting heat transfer from the debris on the bottom.

Overall, the pressure increase calculated with THIRMAL-1 agrees well with the pressure increase measured during the melt-water interaction phase. Specifically, a pressure increase of 0.7 Megapascal is calculated versus 0.7 Megapascal determined from the data. Thus, THIRMAL-1 is in excellent agreement with the data insofar as steam formation from melt-water interaction.

It is calculated that a net steam mass of 0.78 Kilogram exits the pool upper surface as the result of melt fall stage quenching. The net steam formation represents the removal of 2.5 Megajoules of enthalpy from the melt. A peak steam formation rate of 1.63 Kilogram per second at 0.5 second following melt entry into the pool is calculated. A rise in the pool water temperature of 4.4 degrees Kelvin is calculated by THIRMAL-1 corresponding to the removal of an additional 2.5 Megajoules of enthalpy from the melt. The combined enthalpy removal of 5.0 Megajoules represents the removal of 72 percent of the difference between the initial release melt enthalpy (at 2923 degrees Kelvin) and the melt enthalpy at the solidus temperature of 2848 degrees Kelvin. A rise of the argon-steam mixture temperature from 554 degrees Kelvin at MWC to 579 degrees Kelvin at 1.0 second following MWC is calculated by THIRMAL-1 that treats the cover gas as a control volume having a single temperature. The measured steam temperatures at various locations in the cover gas space are not uniform, especially soon after the melt stream enters the water. However, the various temperatures come to equilibrium at a temperature of 582 degrees Kelvin at about 5 seconds following MWC. The predicted temperature rise of 36 degrees Kelvin is in good agreement with the rise of 39 degrees Kelvin corresponding to the measured equilibrium value. The heatup here reflects in part the modeling of superheating of steam exiting the water pool due to heat transfer from melt as well as heat transfer from the prefragmented melt falling to the water surface.

2.4 Comparison of THIRMAL-1 with the Quenching Test 2

Conditions assumed for Quenching Test 2 and results obtained are shown in Table 1. It is predicted that 68 percent of the melt is eroded away in the form of melt droplets. About 67 percent of the melt droplets (45 percent of the total released mass) are eroded away from the melt stream prior to entering the water pool. Only 33 percent of the droplets (23 percent of the total released mass) are created as the melt stream penetrates through the water pool. The remainder of the melt is calculated to impinge as a stream (9 percent of the released mass) or arrive as large segments formed by large wave breakup (23 percent of the released mass) to collect upon the bottom in an initially molten state. Similar to the Scoping Test, all of the partially frozen droplets arrive at the pool bottom with over 70 percent of the heat of fusion removed. Thus, the THIRMAL-1 prediction of the corium collection state is in excellent agreement with the test results.

The calculated particle size distribution collecting upon the bottom plate in Figure 9 is compared with the measured particle size data. This information is provided for fully solidified particles only, that is, 46 percent of the total released melt for the calculation and 68 percent of the released melt for the Quenching Test 2. The calculated particle diameter ranges in size from 0.7 to 3.8 millimeters with a median size of 3.8 millimeter which is identical to the measured median particle size of 3.8 millimeters. This is also the representative eroded droplet diameter in the prefragmentation analysis for Quenching Test 2.

Comparison of the pressure calculated with THIRMAL-1 versus the measurement is shown in Figure 6. Thus, the calculated pressure accounts for fall stage melt quenching only. The pressure increase prior to MWC at 0.0 seconds has been calculated in the prefragmentation analysis. The pressure increase after MWC is calculated with THIRMAL-1. The attainment of a peak pressure of 7.5 Megapascals at 0.6 second after MWC is calculated while a peak pressure of 7.6 Megapascals at 0.75 second after MWC was measured. The pressure rise here reflects mainly steam generation from melt/water interaction and, to a lesser extent, cover gas heatup during the prefragmentation phase. The calculated and measured peak pressure rises are in excellent agreement.

The calculated pressurization rate is compared with that determined from the data in Figure 7. The trends of the calculated and measured pressurization rates are consistent. The measured pressure rise rate is lower than the THIRMAL-1 results prior to 0.45 second and higher than the THIRMAL-1 results after 0.45 second. A peak pressurization rate of 3.4 Megapascal per second at 0.35 second after MWC is calculated in very good agreement with the measured maximum rate of 3.3 Megapascals per second. The shift in time in the pressurization rate may again be a result of the assumption of a shorter melt release time of 0.26 second relative to the measured melt release time of 0.38 second.

It is calculated that a net steam mass of 2.18 Kilograms exits the pool upper surface as the result of melt fall stage quenching. This net steam formation represents the removal of 8.15 Megajoules of enthalpy from the melt. A peak steam formation rate of 8.5 Kilograms per second and steam temperature of 763 degrees Kelvin are calculated at 0.45 second following melt entry versus 11.0 Kilograms per second determined from the data assuming an equilibrium steam temperature at 573 degrees Kelvin. A rise in the water pool temperature of 3.5 degrees Kelvin is calculated by THIRMAL-1 corresponding to the removal of an additional 5.5 Megajoules of enthalpy from the melt due to fall stage quenching. The combined enthalpy removal of 13.6 Megajoules represents the removal of 64 percent of the difference between the initial released melt specific enthalpy at a temperature of 3023 degrees Kelvin and the melt specific enthalpy at the solidus temperature of 2848 degrees Kelvin.

An increase in the argon-steam cover gas mixture temperature from 550 degrees Kelvin at MWC to 607 degrees Kelvin (i.e., a 57 degree Kelvin rise) at 1.0 second following melt entry is calculated by THIRMAL-1. This is higher than the equilibrium gas-space temperature of 578 degrees Kelvin (a 28 degree Kelvin rise) obtained from the data about 4 seconds after MWC when the measured pressure decreased from the peak pressure of 7.6 to 7.2 Megapascal. The calculated gas space temperature exceeds the measured equilibrium temperature of 578 degrees Kelvin about 0.2 second after melt entry into the water pool and increases to 590 degrees Kelvin when all of the melt has entered the water at 0.3 second. Then, the calculated argon-steam temperature begins to slowly increase to the 607 degrees Kelvin. It is possible to speculate on why the cover gas temperature rise is overpredicted. Specifically, heat transfer between water droplets swept out of the mixing zone with steam and argon in the cover gas region is not modeled in THIRMAL-1. Such a heat transfer mode would tend to reduce the gas temperature. On

the other hand, heating of the cover gas due to heat transfer from swept out melt droplets and particles as well as superheated steam exiting the mixing zone are modeled.

An energy balance calculation was performed to evaluate the effects of water droplets swept out of the mixing zone on the gas space temperature. A gas space temperature rise of 35 degrees Kelvin is obtained which is in much better agreement with the measured increase in the equilibrium temperature of 28 degrees Kelvin.

When the water droplets are swept out of the mixing zone into the gas space region, the temperature difference between the gas-steam mixture and the water droplets causes heat to flow to the droplets. Further assessment of the amount of energy estimated to be transferred to the water droplets according to heat transfer rate considerations is consistent with the amount from the energy balance that provides good agreement with the measured gas space equilibrium temperature.

3. COMPARISON OF THIRMAL-1 WITH CCM EXPERIMENTS

3.1 Description of CCM Experiments

The CCM experiments are a set of six reactor material experiments performed at Argonne to obtain data on melt stream breakup in water, melt quenching, hydrogen generation, and debris formation [6]. The experiments were motivated by a need to better understand the interactions of corium melt with water inside the Three Mile Island Unit 2 lower plenum when about 20 tonnes of melt relocated from a crust-encased molten core pool onto the lower head. Of the six experiments, two were selected for comparison with THIRMAL-1 at the present time. These are the CCM-5 and CCM-6 tests (Table 2) in which 12 Kilograms of a 60 wt % UO_2 - 16 wt % ZrO_2 - 24 wt % stainless steel mixture was delivered into 1.07 meter deep pools of water at 0.117 and 0.114 Megapascal pressure. In CCM-5, the water pool was subcooled by 49 degrees Kelvin while in CCM-6, the water was very nearly saturated.

Comparison of THIRMAL-1 with data from the CCM tests is strongly motivated by the fact that the tests differ from FARO in several respects. First, the CCM experiments were performed at low pressures as is the case for melt-water interactions in the SBWR and AP600 as opposed to the high pressures of 5.0 Megapascals or greater characteristic of FARO. Second, one of the experiments employed water with a significant subcooling whereas the FARO tests were all conducted at low subcooling/near saturation conditions. This enables the code's capabilities to handle subcooling to be tested. Third, the melt has a significant metal phase constituent that gives rise to chemical oxidation reactions and hydrogen generation. Fourth, the experiments furnish data on the penetration of the melt leading edge through the water pool that can be used to compare with THIRMAL-1 predictions of the penetration of the stream leading edge as well as the envelope of the droplets and particles formed. Comparable data is not available from the FARO tests.

3.2 Comparison of THIRMAL-1 with the CCM-5 Experiments

A major difference between the low pressure CCM experiments and high pressure FARO tests is that prefragmentation of the melt stream does not occur in the CCM experiments because of the lower density of the gas-steam mixture and the short fall height. There is negligible heating or pressurization of the cover gas mixture prior to melt/water contact. Thus the THIRMAL-1 calculations for the CCM experiments assume that all of the released melt enters the water as a circular melt stream.

TABLE 2. Comparison of the THIRMAL-1 Code with the Results of the CCM-5 and CCM-6 Experiments

CCM Test Conditions	CCM-5		CCM-6	
Water pool depth, m	1.07		1.07	
Initial water subcooling, K	49		2.5	
Gas composition, mole %	17 % Steam + 83%[a] Ar		96 % Steam + 4%[a] Ar	
Gas volume, m^3	0.46		1.14	
Gas temperature, K	363		404	
Pressure, MPa	0.117		0.114	
Melt composition, wt %	60% UO_2 + 16% ZrO_2 + 24% SS (67% Fe + 21% Cr + 12% Ni)			
Initial melt superheat, K	157		157	
Released melt mass, Kg	10.87		11.34	
Diameter at release vessel nozzle, cm	50.8		50.8	
Free Fall Distance in gas, cm	34		34	
Thermite vessel pressure at onset of melt release, MPa	0.117		0.202	
Comparison of THIRMAL-1 Predictions and Exp. Data	Experiment	Prediction	Experiment	Prediction
Corium collection conditions, wt% particles/droplets/stream	100/0/0	53/47[a]/0	100/0/0	50/48[a]/2
Fine fragments (<1.70 mm), Kg (wt%)	1.875 (17)	2.482 (23)	3.02 (27)	5.2 (46)
Intermediate-size fragments				
(1.7< <3.36 mm), Kg (wt %)	2.57 (24)	3.27 (30)	2.32 (21)	1.2 (10)
(3.36 < <6.35 mm), Kg (wt %)	2.088 (19)	2.05 (19)	2.36 (20)	1.10 (10)
Large fragments (> 6.35 mm), Kg (wt %)	4.347 (40)	3.08 (28)	3.7 (32)	3.9 (34)
Median particle size, mm	5.0	6.0	3.8	2.0
Melt and bottom plate contact after melt entry into water, s	0.95	0.81	0.29	0.27
Mean velocity of melt in water, m/s	1.1	1.3	3.7	4.0
Maximum pressure reached during fall stage quenching, MPa	0.246	0.256	0.354	0.304
Gas-steam temperature at time of maximum pressure occurrence, K	390	388	417	411
Hydrogen mass formed, g	24.7	28.4	47.2	56.7
Total steam generated, g	306	342	1423	1134

a) Includes partially frozen droplets.

The CCM-5 experiment was performed with subcooled water at an initial temperature of 328 degrees Kelvin equivalent to 49 degrees Kelvin of subcooling. The melt stream release and entry water pool conditions calculated for CCM-5 and 6 are summarized in Table 2 that also compares the THIRMAL-1 predictions with the experiment results.

Figure 10 shows the calculated time dependent penetration of the melt stream leading edge and the penetration front of the eroded droplets and particles together with the times of response indications of thermocouples located at various distances beneath the water surface in the path of the melt. The melt stream leading edge is calculated to penetrate to a depth of 0.24 meter during the first 0.1 second following entry into the water pool and then vary in an oscillatory manner from 0.1 second to 0.4 second. The oscillations are a result of breakup of the melt stream immediately behind the leading edge when the amplitude of unstable long waves along the stream column exceeds the size of the melt stream. At 0.4 second following entry into the water, the melt stream breakup distance is calculated to increase with time owing to an increase in the vapor volume fraction surrounding and below the melt stream. At 0.64 second following entry into the water (0.80 second after melt release), the melt stream leading edge has penetrated downward through approximately half the water pool depth. The melt stream breakup distance is calculated to decrease thereafter owing to a reduced melt stream entry velocity and diameter corresponding to the decreasing melt release rate. The location of the droplet/particle penetration front is calculated to first reach the base at 0.81 second following entry into the water. This corresponds to a mean melt velocity in the water pool of 1.3 meter per second.

As the corium penetrated through the water, it contacted thermocouples or was at least in close enough proximity to thermocouples to produce responses. Thermocouples that exceeded 1400 degrees Centigrade indicative of contact with corium are indicated by the shaded circles or squares. The axial centerline thermocouples clearly show a significant decrease in the melt penetration velocity after 0.1 second following melt entry into the water pool. This is indicative of a change in the melt configuration from a rapidly penetrating stream to slower penetrating droplets and particles implying breakup of the stream at a distance less than 0.31 meter. This distance is equivalent to 9 melt stream entry diameters.

Other thermocouples showed responses but these were significantly less than a rise to 1400 degrees Centigrade (representative of thermocouple melting) or more. For example, a rise of 100 or 200 degrees Kelvin would fall into this category. Such thermocouples are denoted with open circles on Figure 10. Responses of this nature are consistent with thermocouples being heated by heat transfer from droplets and particles as opposed to being engulfed by a melt stream. Finally, the squares correspond to thermocouples located on the base of the water pool at radii of 5.08 centimeters with shaded and open having the same meaning.

The predicted time dependent leading edge penetrations of the melt stream as well as eroded droplets and particles are both in excellent agreement with the stream and droplet front penetrations obtained from the thermocouple responses. Also the predicted time at which melt contacts the base is in very good agreement with the arrival times obtained from thermocouples on and near the base. The high temperatures measured at the base are consistent with material collection and agglomeration upon the base. The measured time of 0.95 second for corium to reach the thermocouples on the vessel bottom section is a little longer than the THIRMAL-1 calculated melt settling time of 0.81 second.

Seventy percent of the melt is calculated to be eroded in the form of melt droplets due to the effects of Kelvin-Helmholtz instability-induced stripping along the

melt stream column as well as droplet formation by boundary layer stripping from the rear of the leading edge of the melt stream. The remaining 30 percent of the melt is calculated to form large melt stream segments from breakup of the melt stream at the leading edge due to large wave instability. About 76 percent of the eroded melt droplets (53 percent of total released melt mass of 10.83 Kilograms) solidify completely to form particles prior to collecting on the bottom of experiment vessel. About 8 percent of the fully solidified particles (5 percent of the total released mass) is metallic melt. Nine percent of the eroded melt (6 percent of the total released mass) is calculated to arrive in a partially frozen state (above 70 percent heat of fusion removed). Thus, the material accumulating at the bottom is calculated to consist of solid particles, nearly solidified droplets, and 41 percent of the released melt mass that arrives in a molten state. About 19 percent of the total released melt mass arriving on the floor is metallic molten droplets. These results are included in Table 2. The THIRMAL-1 calculated debris size distribution collecting upon the base is shown in Figure 11 and compared with the measured particle size distribution. Upon posttest examination, melt arriving on the floor in a molten state was largely agglomerated together with solidified particles. The debris was sieved through 6350, 3360, and 1700 micron screens. Agglomeration effects raise the question of what portion of the debris was actually sized in arriving at the measured size distribution. For this reason, three different calculated size distributions representing different portions of the droplets and particles formed are plotted in Figure 11. The calculated diameter for the melt/droplet/segment distributions range in size from 0.7 to 16.0 millimeters with a median size of 2.8 millimeters. The calculated median diameter for fully solidified particles is 6.0 millimeters and the calculated median diameter for the 70 percent or greater solidified particle size distribution is 4.0 millimeters.

Data on transient melt quenching and steam formation behavior are the time dependent pressure and temperature measured in the gas space overlying the water pool. Comparison of the pressure calculated with THIRMAL-1 versus that measured in the experiment during the first 1.7 seconds following melt release is shown in Figure 12. For 0.16 second before melt/water contact as evidenced by thermocouple response, the data shows a small pressure rise. The pressure calculated with THIRMAL-1 accounts only for fall stage melt quenching as the melt relocates downward through the water pool. In addition, THIRMAL-1 does not model the long-term quenching of melt that collects and spreads over the water pool base. The virtual attainment of the peak pressure soon after melt entry into the water pool corresponds to essentially the complete settling out of particles and droplets from the water pool. The calculated pressure increases more slowly during the first 0.3 second after melt entry into the water pool than the CCM-5 data. THIRMAL-1 neglects heating of steam-gas mixture and steam generation associated with the melt stream relocation behavior as the melt stream falls through the gas space. The calculated pressure increase rate is slightly higher than the measured pressure increase rate between 0.4 and 0.85 second. This could reflect steam condensation on the dispersed subcooled liquid droplets swept away by the steam flow out of the mixing zone. This condensation process in the gas space is not modeled. The mixing zone regime flow become highly dispersed droplet flow at 0.3 seconds following melt entry into the water pool consistent with this latter conjecture. A peak pressure of 0.26 Megapascal (i.e., 0.14 Megapascal of pressure increase) is calculated versus a measured peak pressure 0.25 Megapascal (i.e., 0.13 Megapascal of pressure increase).

A peak steam formation rate of 0.35 Kilogram per second is calculated at 0.5 second following melt entry. The steam formation rate includes steam converted into hydrogen by oxidation of metal. The masses of steam and hydrogen generated and predicted by THIRMAL-1 are compared with those determined from the data in Table 2. The analysis of hydrogen generation is based upon mass spectrometry of gas samples

extracted shortly after the test. The investigation of the steam generation was focused on the short-term quenching of the corium, i.e., during the melt stream fall stage, rather than any long-term debris cooling stage. The steam generation during the melt stream fall stage is determined from the experiment vessel pressurization data in the test that were analyzed along with the amount of hydrogen generated. It is determined that a total hydrogen mass of 25 grams (or 12 gram-moles) was generated in the CCM-5 test. Therefore, a total steam mass of 306 grams is determined based on the maximum experiment vessel pressure of 0.246 Megapascal and the corresponding gas-steam mixture temperature of 390 degrees Kelvin. In the THIRMAL-1 analysis, a total steam mass of 342 grams and a hydrogen mass of 28 grams are calculated to exit the water pool surface as the result of melt fall stage quenching. These predictions are in good agreement with the experiment values. The time dependent gas-steam mixture temperature increases from 363 to 388 degrees Kelvin during the first 1.5 seconds following melt entry into the water pool. This calculated temperature increase compares well with the temperature increase measured by the thermocouple located 46 centimeters above the water surface which rose from 363 to 390 degrees Kelvin at the time of maximum pressure.

3.3 Comparison of THIRMAL-1 with the CCM-6 Experiment

The CCM-6 experiment was conducted with nearly saturated water at 374 degrees Kelvin (2.5 degrees Kelvin of subcooling). Figure 13 shows the calculated time dependent penetration of the melt stream leading edge and the melt droplet/particle penetration front as well as the thermocouple response indications. The melt stream leading edge is calculated to quickly penetrate to the base of the pool after only 0.27 second. Droplets and particles are calculated to first reach the base only slightly sooner. This corresponds to a mean melt penetration velocity through the water of 4.0 meters per second. Contact with the base was indicated by a thermocouple 5.08 centimeters away from the centerline at 0.29 second. The predicted leading edge penetration is in excellent agreement with the melt stream penetration inferred on the basis of major thermocouple responses (i.e., increases in temperature readings exceeding 1400 degrees Centigrade). The thermocouples also indicate a rapid penetration of the stream to at least 0.85 meter depth.

Sixty-six percent of the melt is calculated to be eroded as droplets due to Kelvin-Helmholtz instability-induced stripping along the melt stream column as well as droplet formation by boundary layer stripping from the rear of the leading edge. The remaining 34 percent of the melt is calculated to impinge as a stream (2 percent of the total released mass of 11.4 Kilograms) or arrive as large melt stream segments (32 percent of the total released mass) due to breakup of the melt stream upon the bottom plate of the experiment vessel. About 62 percent of the eroded melt droplets (41 percent of total released melt mass of 11.4 Kilograms) solidifies completely to form particles prior to collecting on the bottom of experiment vessel. Five percent of the eroded melt (3 percent of the total released mass) is calculated to arrive in a partially frozen state (above 70 percent heat of fusion removed). Twenty-eight percent of the large segments are calculated to arrive in a solidified state. Thus, the material accumulating at the bottom is calculated to consist of solid particles, nearly solidified droplets and 47 percent of the released melt mass that arrives in a molten state. These results are included in Table 2. Note that the large segments are included with droplets and particles in Table 2.

The calculated debris size distribution collecting upon the base is taken to be that for all droplets and particles formed either by Kelvin-Helmholtz-induced stripping, boundary layer stripping, or large wave breakup. The calculated diameters range in size from 0.6 to 27 millimeters with a median size of 2.0 millimeters which is below the measured median particle size of 3.8 millimeters. Distributions of fully solidified

particles of combined partially and fully solidified droplets and particles were not calculated.

Comparison of the pressure calculated with THIRMAL-1 versus that measured in the experiment during the first 1.6 seconds following melt release is shown in Figure 14. The calculated pressure increase is lower than the CCM-6 data during the first 0.2 second after melt release. The calculated pressure increase is comparable with the measured pressure increase thereafter. A peak pressure of 0.3 Megapascal (i.e., a 0.19 Megapascal pressure increase) is calculated versus a measured peak pressure of 0.35 Megapascal (i.e., 0.24 Megapascal of pressure increase).

A peak steam formation rate of 2.5 Kilograms per second at 0.28 second following melt entry into the water pool is calculated and a net steam generation rate of 2.3 Kilograms per second at 0.28 second following MWC. The net steam generation rate is approximately equal to the steam formation rate after 0.4 second. This is consistent with termination of the oxidation of metallic melt in the continuous vapor flow. The mass of steam and hydrogen predicted by THIRMAL-1 and those determined from the data are shown in Table 2.

In order to obtain the experiment steam generation during the fall stage, the experiment vessel pressurization data in the test was analyzed along with the amount of hydrogen generation determined from analysis of the gas samples. It was determined that a total hydrogen mass of 47 grams (or 23 gram-moles) was generated. Therefore, a net steam mass of 1014 grams (or a total of 1423 grams of steam formation) is estimated based on the maximum experiment vessel pressure of 0.354 Megapascal and the corresponding gas-steam mixture temperature of 417 degrees Kelvin. In the THIRMAL-1 analysis, a net steam mass of 625 grams (or a total steam mass formation of 1134 grams) and a hydrogen mass of 57 grams are calculated as the result of melt fall stage quenching.

The calculated time dependent gas-steam mixture temperature that increases from 404 to 411 degrees Kelvin during the melt fall stage. This calculated temperature increase is lower than the measured temperature rise from 404 to 417 degrees Kelvin at the time of maximum pressure.

4. SUMMARY OF FINDINGS

THIRMAL-1 calculations were found to be in excellent agreement with the results of the Ispra FARO Scoping Test and Quenching Test 2 as well as the ANL CCM-5 and CCM-6 experiments.

A mechanistic model for prefragmentation in the FARO apparatus was developed and applied to both the Scoping Test and Quenching Test 2. The melt configuration that is predicted to enter the water differs significantly from that assumed by Angelini, Yuen, and Theofanous [10]. In particular, the melt does not enter the water fully fragmented as a cloud of spheres. Instead, the melt is calculated to enter as a reduced diameter stream surrounded by melt droplets eroded from the stream surface by the growth of Kelvin-Helmholtz instabilities. Instability growth and erosion are effective in the FARO apparatus due to the high gas densities prevalent at the high pressures (e.g., 5.0 Megapascals) at which the FARO tests are carried out combined with the long fall heights from the melt release vessel to the water surface (about 1.8 meters). The eroded droplets heat up the cover gas above the water surface by thermal radiation and forced convection heat transfer. The calculated pressurization during the prefragmentation stage is in good agreement for the Quenching Test 2 but underpredicted for the Scoping Test. In the latter case, the difference may be attributed to flashing of steam off

of the surface of the water pool. Flashing in this manner would not be a factor in Quenching Test 2 or in advanced reactor systems. The results of the prefragmentation analysis are used to provide THIRMAL-1 with the conditions with which the reduced diameter stream and eroded droplets enter the surface of the water pool.

For both FARO tests, the calculated pressurization rate from steam formation is in excellent agreement with that determined from the data. The calculated time for melt to penetrate downward through the water pool is also in excellent agreement with that inferred from thermocouple responses indicative of interaction with melt near the top and bottom of the water pool. These results lend confidence to the modeling of melt stream penetration and breakup by various instability mechanisms that determine the amount and sizes of droplets formed as well as the modeling of multiphase heat transfer and flow inside the mixing zone that determine the net rate of steam formation. The predicted debris size distribution also agrees very well with that measured in posttest examination. This lends further confirmation to the modeling of melt breakup by Kelvin-Helmholtz instabilities that produces droplets of the observed sizes during both the prefragmentation and melt-water interaction phases.

The only notable discrepancy between the THIRMAL-1 calculations and the FARO data concerns the gas space temperature rise in Quenching Test 2 that is significantly overpredicted. The difference here was shown to correspond to the neglect in THIRMAL-1 of the cooling effects of water droplets swept out of the mixing zone into the overlying gas space. In particular, it was shown through a standalone energy balance analysis that the droplets constitute more than a sufficient heat sink to account for the discrepancy. Interaction with half of the swept out water mass would bring the calculated and measured gas space temperatures into agreement while the remaining half of the droplets deposit upon the walls and structures in the gas space. A separate standalone estimate of energy transfer rates from the gas space to the interacting water droplets further supports this explanation of the discrepancy. Thus, modeling for the interactions of swept out water droplets is identified as a worthwhile addition to THIRMAL-1 for future comparisons with the ongoing FARO tests.

For CCM-5 and CCM-6, the THIRMAL-1 predictions of the time dependent penetration of the melt stream leading edge and droplet/particle penetration front are in excellent agreement with the locations indicated by the timing of responses from thermocouples located along the experiment vessel centerline in the path of the melt or off the centerline on the base at the bottom of the water pool. This lends a high level of confidence to the modeling of melt stream breakup by three mechanisms: (i) Kelvin-Helmholtz (i.e., small wave) instabilities along the melt stream column, (ii) boundary layer stripping from the rear of the initial penetrating leading edge, and (iii) large wave breakup of the leading edge. For CCM-5, the code predicts an increase in the leading edge penetration when a large amount of vapor has been created in the mixing zone as observed in the penetration data confirming the instability modeling that depends upon the conditions in the surrounding medium. The very good agreement with the pressurization data from steam formation lends confidence to both the modeling of melt stream breakup and the sizes of droplets formed as well as multiphase flow and heat transfer in the mixing zone. The modeling approach here is further confirmed by the good agreement between the predicted and measured debris particle sizes. Very good agreement is obtained for the amount of hydrogen produced supporting the modeling of oxidation of droplets of the metallic constituent by interaction with flowing steam in the mixing zone.

ACKNOWLEDGEMENTS

This work was sponsored by the United States Department of Energy Advanced Reactor Severe Accident Program. The authors are indebted to S. W. Sorrell, ARSAP Program Manager and S. L. Additon (TENERA). The authors also appreciate the efforts of L. M. McUmber (ANL/RE) in providing original data from the CCM experiments. Argonne project management was provided by L. Baker, Jr. The manuscript was typed by L. J. Ondracek and J. A. Wozniak (ANL/RE).

NOMENCLATURE

A_J' = melt stream surface over which melt erosion occurs, m^2
a = melt stream radius, m
a_g = absorption coefficient of steam-gas mixture, 1/m
a_m = absorption coefficient of multiple melt droplets/particles, 1/m
= $1.5\ \epsilon_m\ \alpha_p / D_p$
C_{rad} = the fraction of radiation heat transfer absorbed by the gas-steam mixture, ~0.4
$\overline{D}_p$ = representative eroded melt droplet diameter, m
D_h = test vessel diameter, ~ 0.46 (ST) and 0.74 (QT2) meters
D_J = melt stream diameter, m
$\overline{D}_J$ = average melt stream diameter, $\approx \left(D_{J.0} + D_{J.e}\right)/2$, m
$D_{J.e}$ = melt stream diameter at the water pool surface, m
$D_{J.0}$ = melt stream diameter at the location where melt erosion begins, m
F = absorbed fraction in an infinite medium
f = subscript denoting properties evaluated at the film temperature, T_f
H_{fall} = melt stream fall distance before MWC, m
h_{conv} = force convection heat transfer coefficient, $W/(m^2 \cdot K)$
= $k_f / \overline{D}_p \left(2.0 + 0.6\ Re_p^{0.5}\ Pr_f^{0.3334}\right)$,
h_{rad} = radiation heat transfer coefficient, $W/(m^2 \cdot K)$
= $\epsilon_m\ \sigma_B \left(T_m^4 - T_{sat}^4\right) / \left(T_m - T_{sat}\right)$
k_{max} = wavenumber corresponding to the maximum wave growth rate, 1/m
L_m = mean free length, ~ 0.5 D_h, m
Pr_f = Prandtl number, $C_f\ \mu_f / k_f$
Re_p = melt droplet Reynolds number, $\overline{U}_J\ \overline{D}_p\ \rho_f / \mu_f$
T_f = film temperature, ½ $(T_g + T_m)$, K
T_g = gas-steam mixture temperature, K
T_m = melt temperature, K
t_o = time period corresponding to the melt stream fall distance, x_o, s
T_{sat} = saturation temperature, K
U_J = melt stream velocity, m/s
$U_{J.\,min}$ = minimum required stream velocity, m/s
$\overline{U}_J$ = average melt stream velocity for melt erosion, m/s
$\approx \left(H_{fall} - x_o\right) / \left(t_{fall} - t_o\right)$,
x_o = melt stream fall distance when the initial disturbance on the melt stream surface reaches the critical unstable wave magnitude, λ_{max}, and melt erosion begins, m
x_1 = free fall distance at the leading edge of melt stream, m
σ_m = melt surface tension, N/m
σ_B = Stefan-Boltzman constant, $5.67 \cdot 10^{-8}$ $W/(m^2 \cdot K)$
ρ_f = gas mixture density surrounding the melt stream evaluated at the film temperature, T_f, Kg/m^3
ρ_m = melt density, Kg/m^3

λ_{max} = wavelength corresponding to the maximum wave growth rate, m
η (t) = unstable wave magnitude at time t, m
η_o = initial disturbance magnitude, m
ϵ_m = melt emissivity
ϵ_w = steel wall emittance
α_p = melt droplet/particle volume fraction in the cover gas space
α_{max} = maximum wave growth rate due to Kelvin-Helmholtz (K-H) instability, 1/s

REFERENCES

[1] C. C. Chu, J. J. Sienicki, and B. W. Spencer, "The THIRMAL-1 Computer Code for Analysis of Interactions Between a Stream of Molten Corium and a Water Pool-Volume 1, Code Manual," EPRI Report, EPRI TR-103417-V1 (December 1993).

[2] C. C. Chu, J. J. Sienicki, and B. W. Spencer, "The THIRMAL-1 Computer Code for Analysis of Interactions Between a Stream of Molten Corium and a Water Pool-Volume 2, User's Manual," EPRI Report, EPRI TR-103417-V2 (December 1993).

[3] J. J. Sienicki, S. K. Wang, and B. W. Spencer, "Analysis of Melt Arrival Conditions on the Lower Head in U. S. LWR Configurations," NURETH-5, 2 (1992).

[4] J. J. Sienicki, C. C. Chu, B. W. Spencer, W. Frid, and G. Löwenhielm, "Ex-Vessel Melt Coolant Interactions in Deep Water Pool: Studies and Accident Management for Swedish BWRs," CSNI Specialists Meeting on Fuel-Coolant Interactions, Santa Barbara, CA, January 5-8, 1993, NUREG/CP-0127, NEA/CSNI/R(93)8, p. 37 (1994).

[5] D. Magallon and H. Hohmann, "High Pressure Corium Melt Quenching Tests in FARO," CSNI Specialists Meeting on Fuel-Coolant Interactions, Santa Barbara, CA, January 5-8, 1993, NUREG/CP-0127, NEA/CSNI/R(93)8, p. 1 (March 1994).

[6] B. W. Spencer, S. K. Wang, C. A. Blomquist, L. M. McUmber and J. P. Schneider, "Fragmentation and Quench Behavior of Corium Melt Streams in Water," NUREG/CR-6133, ANL-93/32 (February 1994).

[7] B. W. Spencer, J. D. Gabor, J. C. Cassulo, and D. J. Kilsdonk, "Results of Scoping Experiments on Melt Stream Breakup and Quench," International ANS/ENS Topical Meeting on Thermal Research Safety, 1, p. II.8-1 (1986).

[8] B. W. Spencer, J. D. Gabor and J. C. Cassulo, "Effect of Boiling Regime on Melt Stream Breakup in Water," Particulate Phenomena and Multiphase Transport, 3, ed. T. N. Veziroglu, Hemisphere Publishing Co. (1987).

[9] J. P. Schneider, M. Marciniak and B. G. Jones, "Breakup of Metal Jets Penetrating a Volatile Liquid," NURETH-5, 2, 437-449 (1992).

[10] S. Angelini, W. W. Yuen and T. G. Theofanous, "Premixing-Related Behavior of Steam Explosion," CSNI Specialists Meeting on Fuel-Coolant Interactions, Santa Barbara, CA, January 5-8, 1993, NUREG/CP-0127, NEA/CSNI/R(93)8, p. 99 (1994).

[11] M. Bürger, S. H. Cho, E. V. Berg, and A. Schatz, "Breakup of Melt Jets as Precondition for Premixing: Modeling and Experimental Verification," CSNI Specialists Meeting on Fuel-Coolant Interactions, Santa Barbara, CA, January 5-8, 1993, NUREG/CP-0127, NEA/CSNI/R(93)8, p. 54 (March 1994).

[12] C. C. Chu and M. L. Corradini, "One-Dimensional Transient Fluid Model for Fuel-Coolant Interaction Analysis," Nucl. Sci. and Eng. 101, 48-71 (1989).

[13] B. J. Meister and G. F. Scheele, "Prediction of Jet Length in Immiscible Liquid Systems," AICHE Journal 15, No. 5, p. 689 (1969).

[14] D. W. Condiff, D. H. Cho, and S. H. Chan, "Heat Radiation Through Steam in Direct Containment Heating," Trans. Am. Nucl. Soc., 53, p. 561 (1986).

[15] C. L. Tien, "Thermal Radiation Properties of Gases," Advances in Heat Transfer, 5, ed. T. F. Irvine, Jr. and J. P. Hartnett, Academic Press, New York (1968).

[16] D. W. Condiff, Private Communication, Argonne National Laboratory (January 1994).

[17] K. H. Sun, J. M. Gonzalez, C. L. Tien, "Calculations of Combined Radiation and Convective Heat Transfer in Rod Bundles Under Emergency Cooling Conditions," ASME Journal of Heat Transfer 98, p. 414 (1976).

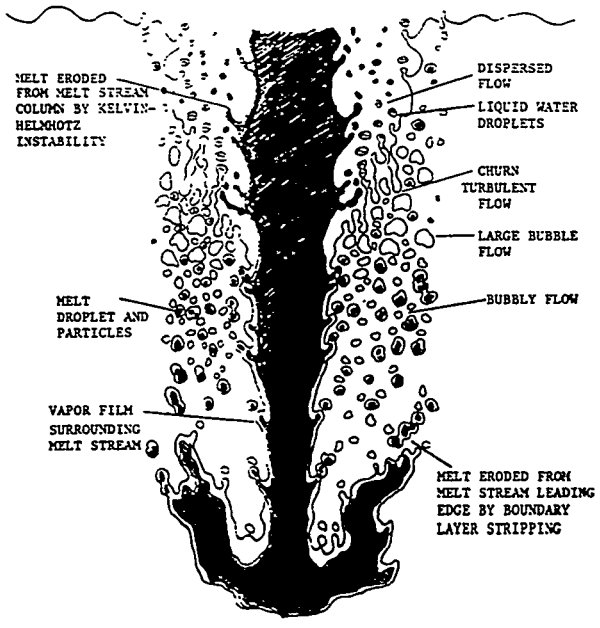


Figure 1. Depiction of melt stream penetrating through a water pool.

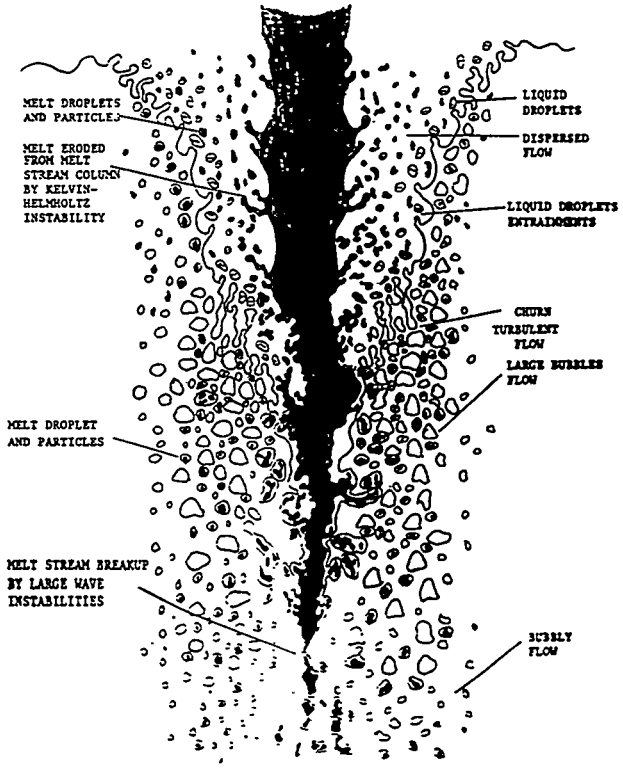


Figure 2. Depiction of erosion and breakup of melt stream in a water pool.

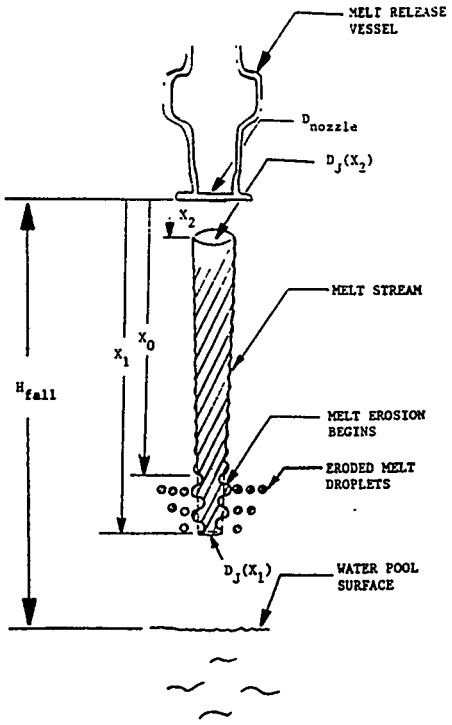


Figure 3. Depiction of prefragmentation analysis for the FARO Tests.

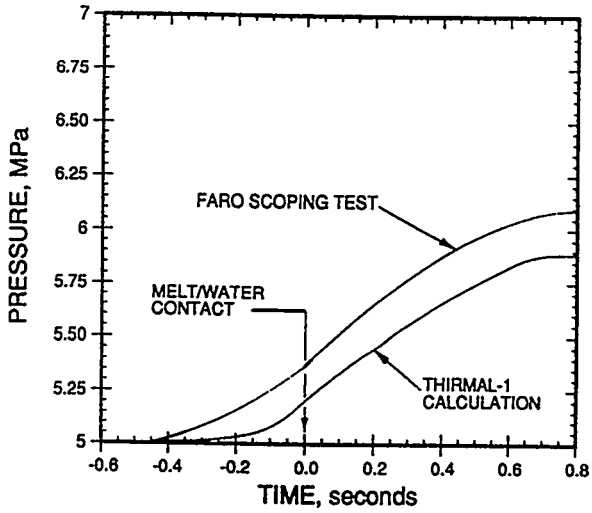


Figure 4. Vessel pressure increase for FARO Scoping Test.

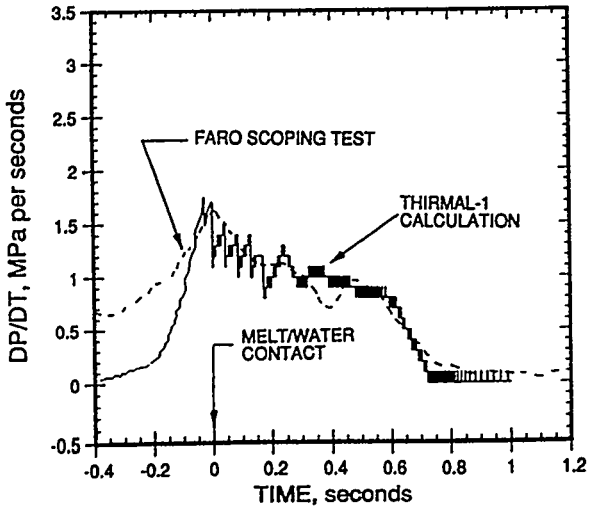


Figure 5. Vessel pressure increase rate for FARO Scoping Test.

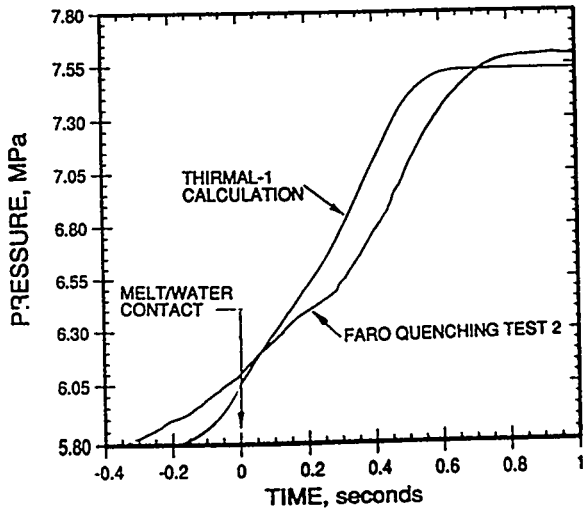


Figure 6. Vessel pressure increase for FARO Quenching Test 2.

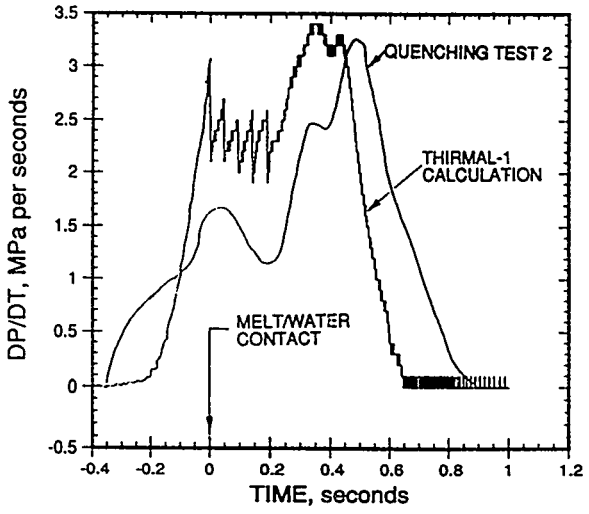


Figure 7. Vessel pressure increase rate for FARO Quenching Test 2.

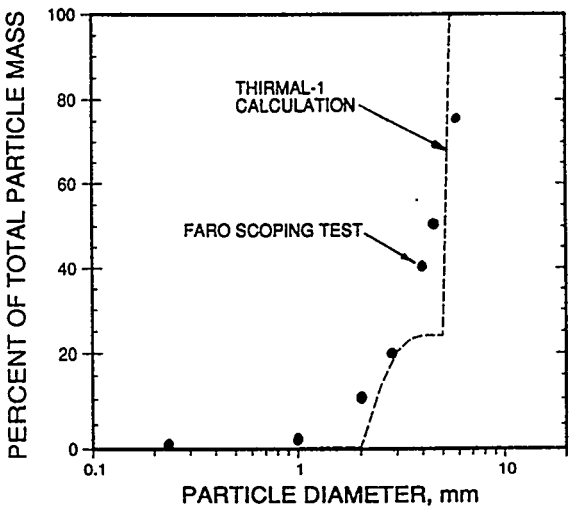


Figure 8. Cumulative particle size distribution for FARO Scoping Test.

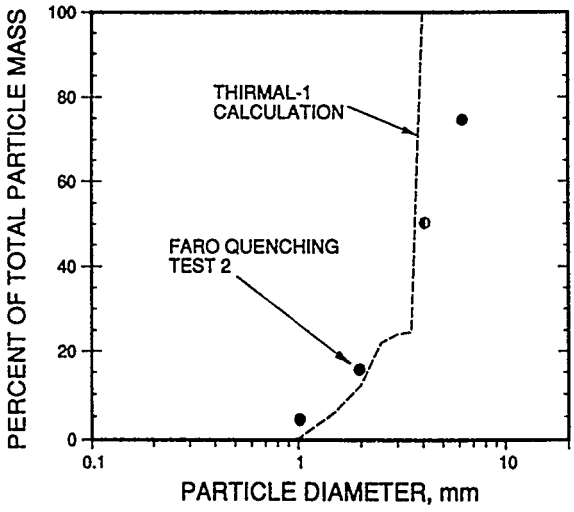


Figure 9. Cumulative particle size distribution for FARO Quenching Test 2.

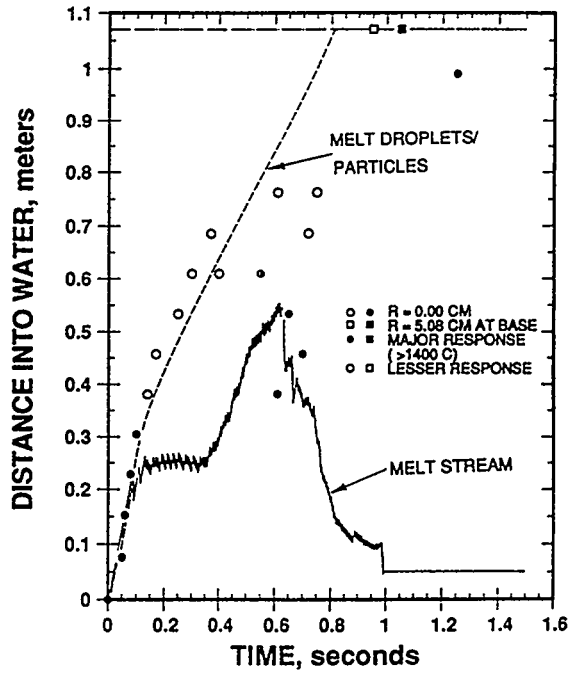


Figure 10. Comparison of THIRMAL-1 calculated penetration of melt stream and melt droplet/ particle leading edge with thermal responses of thermo-couples for CCM-5 experiment.

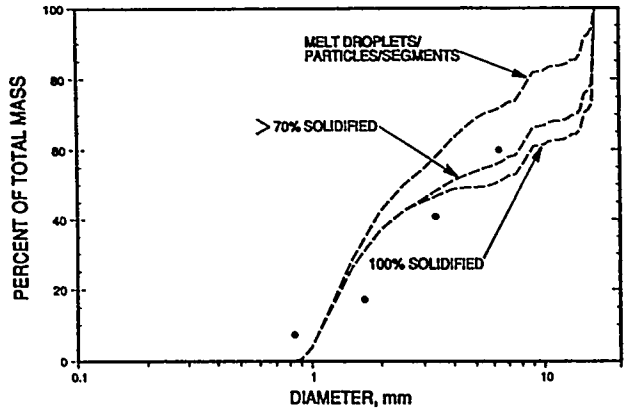


Figure 11. Comparison of THIRMAL-1 calculated cumulative particle size distribution with posttest debris size data for CCM-5.

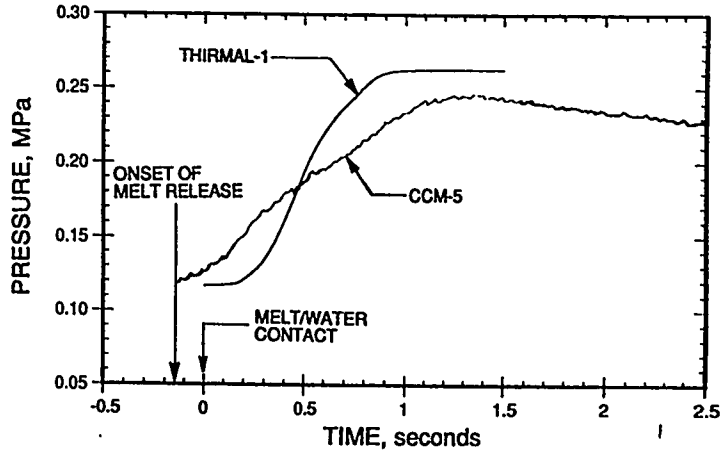


Figure 12. Comparison of THIRMAL-1 calculated experiment vessel pressure increase with measured pressure data for CCM-5 experiment.

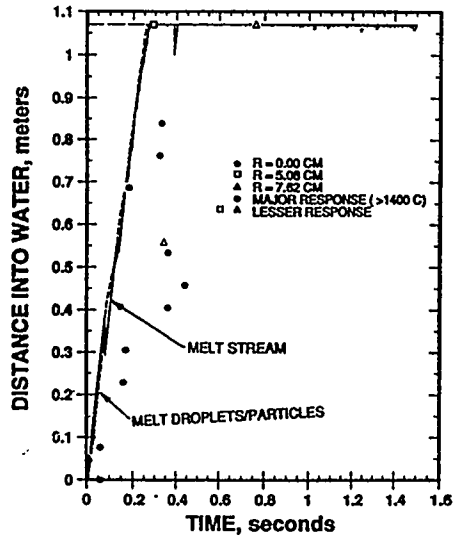


Figure 13. Comparison of THIRMAL-1 calculated penetration of melt stream and melt droplet/particle leading edge with thermal responses of thermocouples for CCM-6 experiment.

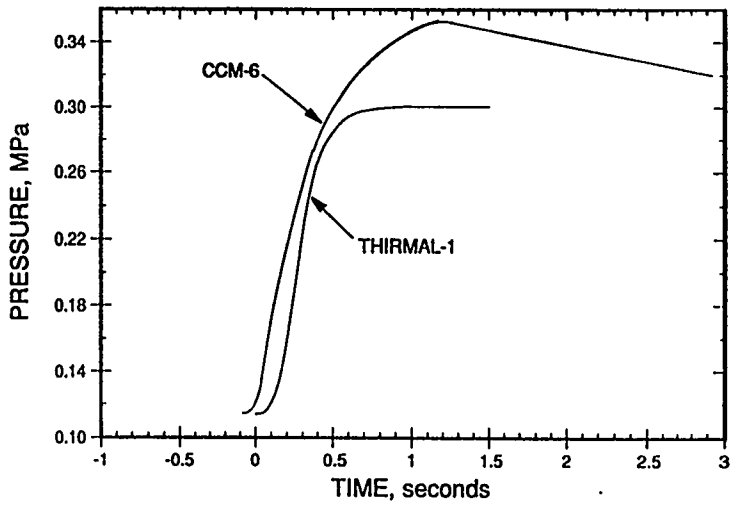


Figure 14. Comparison of THIRMAL-1 calculated experiment vessel pressure increase with measured pressure data for CCM-6 experiment.

EXPERIMENTAL ASSESSMENT OF COMPUTER CODES USED FOR SAFETY ANALYSIS OF INTEGRAL REACTORS

A.A. Falkov, V.S.Kuul, O.B.Samoilov, A.N.Lepekhin, G.N.Polyansky
OKB Mechanical Engineering, Nizhny Novgorod, Russia
Fax (8312) 418772

ABSTRACT

Peculiarities of integral reactor thermohydraulics in accidents are associated with presence of noncondensable gas in built-in pressurizer, absence of pumped ECCS, use of guard vessel for LOCAs localisation and passive RHRS through in-reactor HX's. These features defined the main trends in experimental investigations and verification efforts for computer codes applied. The paper reviews briefly the performed experimental investigation of thermohydraulics of AST-500, VPBER-600-type integral reactors. The characteristic of UROVEN/MB-3 code for LOCAs analysis in integral reactors and results of its verification are given. The assessment of RELAP5/mod3 applicability for accident analysis in integral reactor is presented.

1. INTRODUCTION

AST-500, VPBER-600-type integral reactors are advanced new generation reactors having the properties of enhanced safety due to their design features.

The major decisions on safety assurance that have been implemented in the nuclear district heating reactor AST-500 are being further developed in VPBER-600 design in framework of the concept relying upon the maximum use of passive safety principles. The integral layout of the primary circuit equipment with location of heat exchangers (steam generator) and pressurizer inside a reactor pressure vessel enabled to exclude large and medium size LOCAs (maximum leakage size < DN 50 mm). An additional passive confining barrier - the guard vessel (GV) encloses the reactor and primary circuit systems and ensures locking of the coolant leakage out of the reactor and keeping the core under coolant during LOCAs due to pressure equalization in the reactor-GV system. Passive residual heat removal system (RHRS) through in-reactor heat exchangers is envisaged for reactor cooling down in all classes of accidents including LOCAs.

Peculiarities of VPBER-600 and AST-500 reactor thermohydraulics in emergency conditions are associated with the distinctive features of an integral reactor, such as built-in steam-gas pressurizer, in-reactor heat exchangers for emergency residual heat removal, guard vessel [1]. Presence of noncondensable gas in built-in steam-gas pressurizer influences on dynamics of the pressurizer, on efficiency of heat removal by steam condensation on in-reactor HXs in LOCAs and on accidents sequences. The absence of pumped ECCS and use of GV and passive RHRS through in-reactor HXs affect the reactor plant behaviour in LOCAs and require accurate integrated description of reactor and GV behaviour in accidents. Simulation of natural effects and processes, such as natural circulation, leakages at small gravity-driving forces, non-condensable gas effects are essential for computer codes used for safety analysis of integral reactors. These features of integral reactor thermohydraulics determined the trends in experimental investigations and verification efforts for computer codes applied.

2. EXPERIMENTAL INVESTIGATIONS

Proceeding from integral reactors features at performing the experiments the main attention was paid to studying of the following effects and phenomena:

- thermohydraulics of the built-in steam-gas pressurizer;
- behaviour of non-condensable gas (gas transfer, gas distribution, dissolved gas in water);
- operation of the emergency heat removal HX under conditions of steam condensation from steam-gas mixture;
- the reactor-guard vessel system behaviour in LOCAs;
- passive safety systems actuation and functioning.

The list of experimental activities [2,3] included the investigation of the important separate effects and phenomena and the studying of the RP systems operation, as well as the integral experiments on the different scale reactor models-thermophysical rigs: 1385 (Fig.1.) and KMR-2 (Fig.2,3.) . The facilities represent electrically heated models of the integral reactor with natural circulation of coolant and built-in steam-gas pressurizer contain the GV model and enable to investigate all important

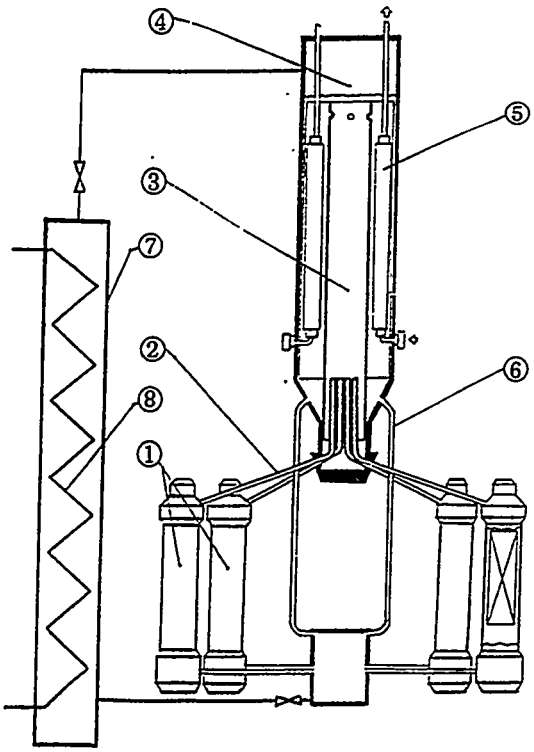


Fig.1. 1385 test facility. Model of integral reactor

1.- Heating columns
2.- Chimney tubes
3.- Riser
4.- Steam-gas pressurizer
5.- Heat exchanger
6.- Downcomer
7.- Guard vessel simulator
8.- GV heat exchanger

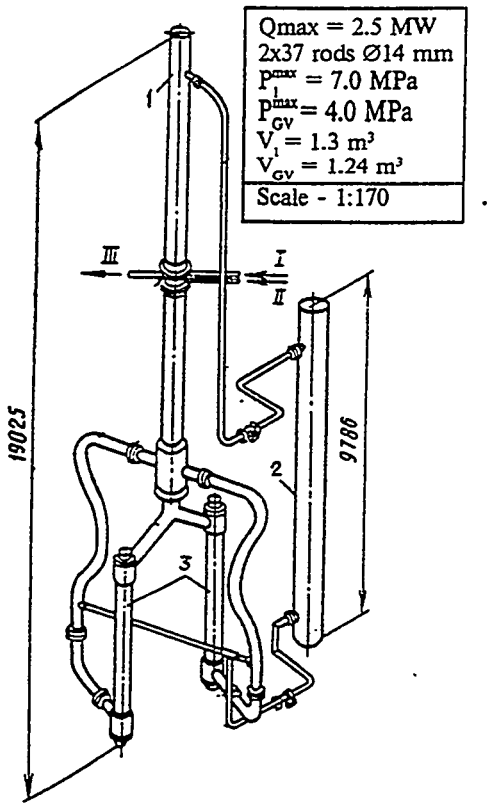


Fig.2. KMR-2 Test facility

1. Primary circuit model of integral reactor
2. Guard vessel simulator
3. Heating columns

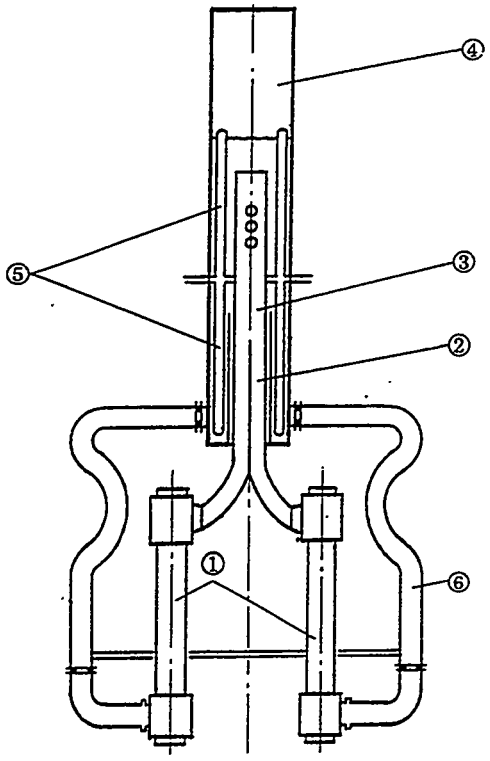


Fig.3. Natural circulation circuit of KMR-2 test facility

1.- Heating columns
2.- Chimney tubes
3.- Riser
4.- Steam-gas pressurizer
5.- Heat exchanger
6.- Downcomer

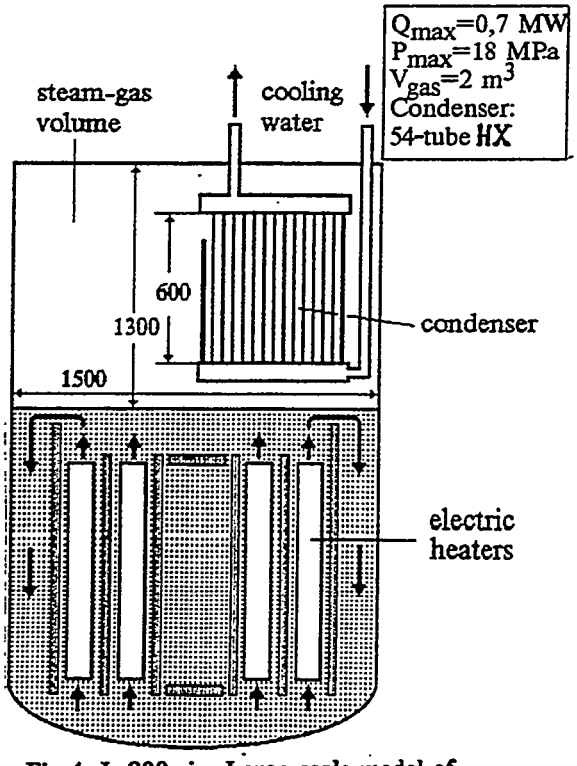


Fig.4. L-800 rig. Large scale model of steam-gas pressurizer with condenser located in steam-gas volume

thermohydraulical phenomena in the necessary range of parameters.

Investigations of LOCAs with coolant outflow into GV at different sizes and locations of openings imitating leaks at ruptures of pipelines in the pressurizer area and at loss of integrity in the RPV bottom, as well as experiments imitating loss of heat removal accident without scram were carried out at the test facilities.

Experimental data on the reactor - GV system behaviour in LOCAs were obtained that shown efficiency of guard vessel as a passive device for localisation and for core keeping under coolant. Normal cooling of heater rods was proved under the conditions of "waterfall" and steam-condensate circulation, taking place at considerable coolant losses from the primary circuit. Coolant subcooling value and natural circulation modes variations at small break LOCA experiment are shown in Fig.5.

Issues, such as non-condensable gas effects, heat-and mass transfer and gas distribution in the guard vessel model, temperature stratification in a water volume of the guard vessel model were investigated. Data on heat transfer coefficients at steam condensation on the guard vessel walls for wide range of steam-air mixture parameters (P=0.4-3.0 MPa; Pg/P=0.18-0.8) were obtained. They showed a considerable rise of a steam condensation intensity at pressure increase (Fig.7.). Investigation of effect of dissolved gas in water on evaporation and leak flowrate in LOCA experiment was carried out. It was obtained that dissolved gas (Cg=2600 ncm3/kg) did not influence noticeably on the course of small break LOCA. The effects of dissolved gas in water were in the range of experimental errors.

Experimental investigation of the steam condensation from steam-gas mixture were performed on the tube bundle models for the conditions of LOCAs accompanied by residual heat removal heat exchanger dryout. Experiments were carried out at L-800 test rig (Fig.4.) using multirow models of the AST-500 HX tube bundle. Investigation of gas influence on the intensity of steam condensation on the tube bundle of 1385 test rig heat exchanger were performed in the wider range of parameters. Data obtained at the rig L-800 on the influence of gas content in steam-gas plenum of the rig upon thermal power of the condenser are presented in Fig.6.

Together with the tasks of studying the thermohydraulical processes running under emergency conditions, and validation of operability and efficiency of the safety systems provided, the main objective of the experiments was to obtain the representative information for computer code verification.

3. UROVEN/MB-3 CODE VERIFICATION

3.1. CODE CHARACTERISTIC

UROVEN/MB-3 is a fast-running computer code, developed for the analysis of thermohydraulics of integral reactor with built-in steam-gas pressurizer during small break and medium size break LOCAs [4]. The code determines the change of reactor thermohydraulic parameters, of confining volume (guard vessel or containment), of secondary circuit at all stages of LOCAs, including the regimes with partial core dryout, fuel elements heating-up, reflooding.

Multielement one-dimensional model of reactor unit is used, basing on energy, mass, coolant motion equations. Reactor kinetics is described in the point model. At boiling the approximation of equilibrium steam-gas mixture with steam slipping on the basis of drift-flux model is used. Phases separation and change of mixture

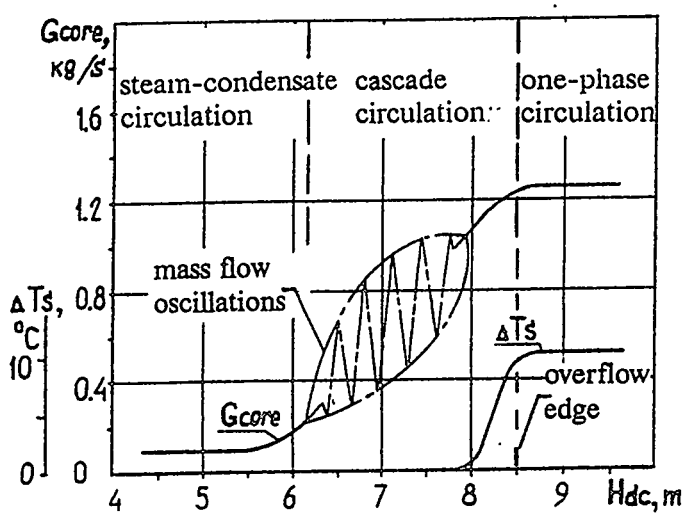


Fig 5. KMR-2. Natural circulation modes during small LOCA depending on water level in downcomer

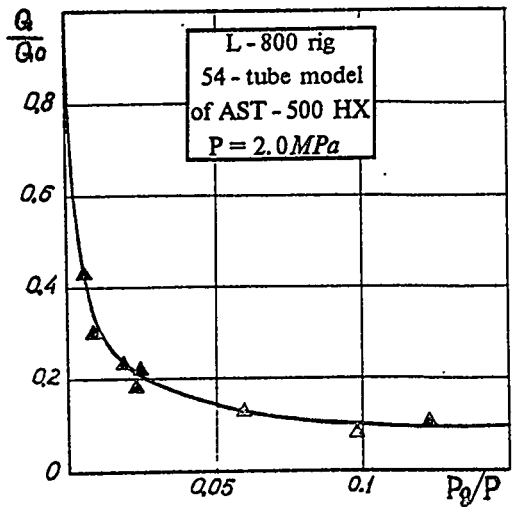


Fig6.Effect of gas content in pressurizer on relative condenser thermal power

level are described. The code describes different modes of natural circulation in primary circuit, characteristic of the processes with coolant loss - normal single-phase, "waterfall" (cascade), steam-condensate one.

The code takes into account the effects associated with the presence of noncondensable gases in the reactor and the confining volume. Gas distribution and gas transfer are calculated for four-component gas mixture (H_2, He,N_2,O_2) with account of gas dissolution and its release from water, radiolytic gases release and hydrogen generation due to steam-Zr reaction. Features of built-in steam-gas pressurizer dynamics and heat removal from reactor by steam condensation from steam-gas mixture in HXs uncovered during an accident are described. Heat-mass transfer in the guard vessel is described, steam non-equilibrium in steam-gas volume and effect of thermal stratification in the GV water volume are taken into account. The operation of safety systems - relief valves, emergency make-up means, residual heat removal systems is modelled. Steam slip, hydraulic resistance coefficients, heat and mass transfer coefficients are calculated by empirical relationships. Heat transfer correlations package covers the conditions of single phase medium, nucleate boiling, boiling crisis and beyond-crisis heat exchange regime.

UROVEN/MB-3 is widely used in the design calculations and at the safety analysis of AST-500, ATETS-150 and VPBER-600 reactor plants.

3.2. CODE ASSESSMENT

Extensive investigation has been carried out to verify the applicability of the code to integral reactors safety analysis [2,5]. Code assessment included analysis of separate effect tests as well as analysis of 12 integral experiments on the reactor models - KMR-2 and 1385 test facilities. The characteristic of experiments for UROVEN/MB-3 verification and list of processes and phenomena assessed are presented in Table 1. Some results of UROVEN/MB-3 experimental assessment are given below.

Steam condensation on guard vessel walls.

Peculiarities of heat and mass transfer in guard vessel are associated with enhanced GV pressure (P_{GV}=2-4 MPa) during LOCA's compared with emergency conditions in

UROVEN/MB-3 VERIFICATION

Table 1

Phenomenon	Experiment		
	Facility	Geometry	Parameters
Investigation of separate effects			
Condensation on tube bundle from steam-gas mixture	HX model L-800 rig	54 tubes H=0.6m	P=2.0 MPa Pg/P=0-0,15
	HX of 1385 rig	72 tubes H=2.1m	P=0.6-6 MPa Pg/P=0-0,8
Condensation on GV walls	GV model KMR-2 rig	V=1.24 m^3 H=10 m	P=0,4-3MPa Pg/P=0,15-0,8
Flow through leak restrictor	Model of AST-500 leak restrictor	Scale 1:1 DN 48 mm	P=1.-2. MPa
Evaporation and level swell due to depressurisation	GE level swell test [6] •leak DN9.5mm	V=0.3 m^3 H=4.3 m	P_o=7 MPa T_o=285°C
Heat up of rod bundle at partial uncovery • Boil of • Reflooding	37-rod bundle	d=10 mm H=3.5 m	P=1.2-4. MPa T_{max}=700°C
	NEPTUN[7] 33-rod bundle	d=10.7 mm H=1.7 m	P=0.5 MPa T_{max}=750°C
Integral Experiments			
Thermohydraulics of integral reactor at LOCA & ATWS-type experiments •leak flowrate •thermohydraulics of steam-gas pressurizer •NC modes at LOCAs •change of mixture level •noncondensable gas effects •reactor-GV system behaviour	**KMR-2** Large-scale model of AST-500 •Upper leaks DN 4, DN8 •Lower leaks DN 2, DN4, DN8 •Loss of heat removal	V1=1.3 m^3 V_{GV}=1.24m^3 Scale: Mv=1:170 MH=1:1	P_{1max}=7MPa Pg≤3MPa P_{GV}≤2 MPa
	1385 rig Integral reactor model •Upper leak DN 1,7 •Lower leak DN 1 •Loss of heat removal	V1=0.3m^3 V_{GV}=0.32m^3 Scale: Mv=1:1000 MH=1:2	P_{1max}=18MPa Pg≤8 MPa P_{GV}≤2 MPa

containment of existing reactors. The experimental data on intensity of condensation on GV walls obtained on GV model (V=1,24 m3, H=10 m, D=0,4 m) in final stage of LOCA experiment are presented in Fig.7. in comparison with UROVEN/MB-3 calculation results. It can be seen that experimental data are well described by UROVEN/MB-3 model based on the heat and mass transfer analogy for conditions of steam-gas mixture natural convection on a vertical wall. The known Uchida correlation [8] used at the description of a containment thermalhydraulics in some codes does not take into account the influence of thermophysical parameters and underestimates the value of heat transfer coefficient at increased pressure P> 0.3 MPa.

LOCA experiment DN8 mm on KMR-2 test facility.

Experiment with water outflow from downcomer lower part into the guard vessel model through orifice 8 mm in diameter is considered. The main parameters of test initial conditions are given in Table.

After 15 s from break opening the reduction of heater power to 151 kW is performed during Δt=35 s. Subsequently the power is held time-constant. Coolant parameters in HX secondary side do not change during experiment. The test is acompanied by depressurization and coolant level decrease in primary circuit, by pressure increase in GV vessel model. Coolant leakage causes natural circulation interruption in primary circuit in 75 s of experiment resulting from mixture level lowering below overflow edge. At this time the reverse of coolant flow through heater assemblies takes place due to leakage from lower part of primary circuit. Reliable heater rods cooling at negative flow rate through heater assemblies is provided. At coolant level decreasing in primary circuit the heat exchanger is uncovered and operate in steam condensation conditions. At the time of test termination the pressures in primary circuit and GV model are equalized at about of 2 MPa. The comparison of calculated main parameters of reactor and GV models with experimental data (Fig.8.) demonstrates satisfactory agreement between calculated and experimental results.

Heater power	698 kW
Primary circuit pressure	6,9 MPa
Gas partial pressure in pressurizer	3,2 MPa
Coolant flow rate	2,18 kg/s
Pressure in GV model	0,21 MPa
Temperature in GV model	32 °C

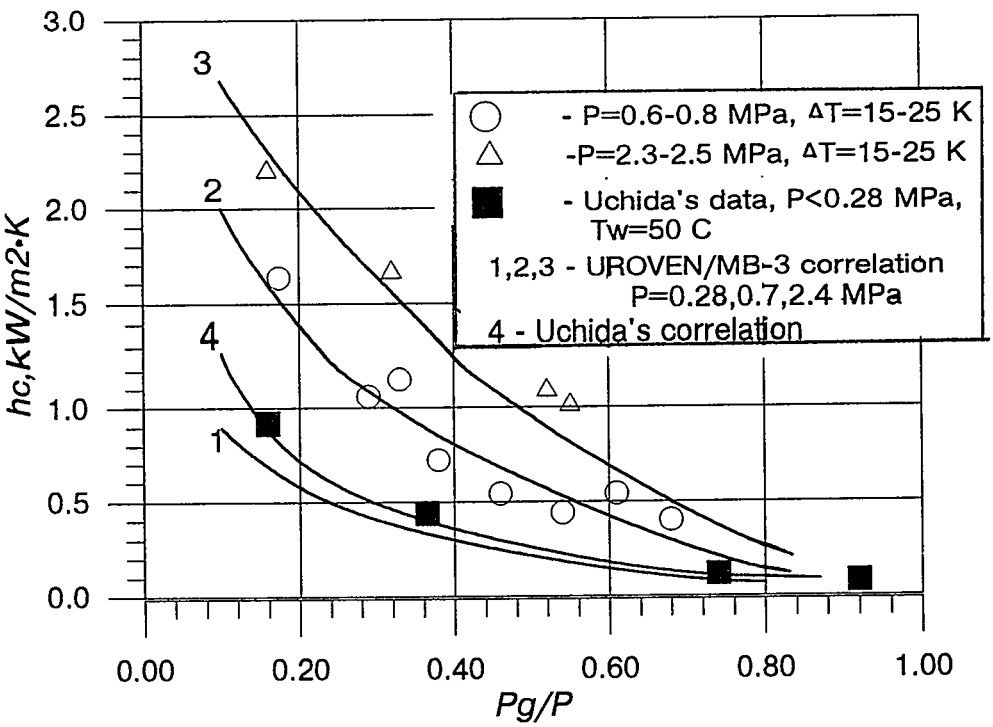


Fig.7 Heat transfer coefficients on guard vessel walls at steam condensation from steam-air mixture

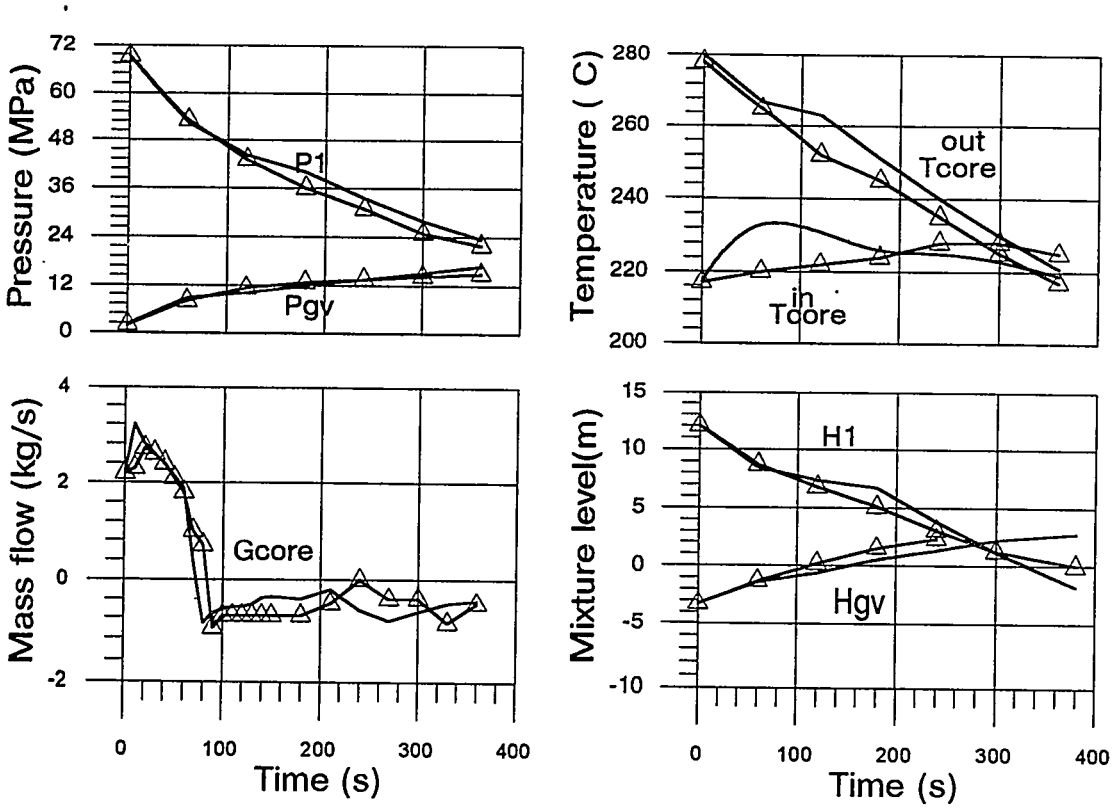


Fig.8 KMR-2 test facility. LOCA experiment DN 8 mm
——— UROWEN/MB-3 —△— experiment

4. EXPERIMENTAL ASSESSMENT OF RELAP5/MOD3 CODE

RELAP5/mod3 is used in OKBM for alternative analysis of VPBER, AST type reactors thermohydraulics under emergency conditions. Verification study is under way to estimate the code applicability for integral reactors. Proceeding from integral reactor features a focus was provided on investigation of code capabilities and limitations to simulate such characteristic processes as steam-gas pressurizer thermohydraulics, the coupled behaviour of reactor and GV, noncondensable gas effects. At present a lot of studies have been carried out together with specialists from RRC "Kurchatov Institute" [9-12]. The calculation analyses of LOCA and loss of heat removal experiments on the integral reactor models-KMR-2 and 1385 test facilities as well as tests with compression and expansion of steam-gas volume on large-scale pressurizer model - L-800 (Fig.4) were performed.

The results of RELAP5/mod3 calculations of two experiments on KMR-2 and 1385 facilities and discussion of code applicability for analysis of integral reactor accidents are presented below.

4.1. NODALIZATION SCHEME

The degree of detail of different components at experiments simulation was determined in accordance with character and dinamics of processes considered. RELAP nodalization of 1385 test facility consisting of 85 volumes, 91 junctions and 72 heat structures is shown in Fig. 9. Similar nodalization was used for KMR-2 test facility.

Core simulator includes 2 heater assemblies that are subdivided axially into 7 nodes. Steam generator (heat exchanger) is subdivided into 7 nodes in height. Secondary circuit is described by specifying of boundary conditions on inlet and outlet of SG. Pressurizer is modelled by pipe component with 10 volumes. Heat transfer with pressure vessel and steam-removing tubes of secondary circuit are taken into accout in pressurizer. Guard vessel simulator is modelled by pipe component with 7 volumes in height. In order to calculate the height of primary mixture level the special algorithm was developed basing on control system of RELAP5/mod3.

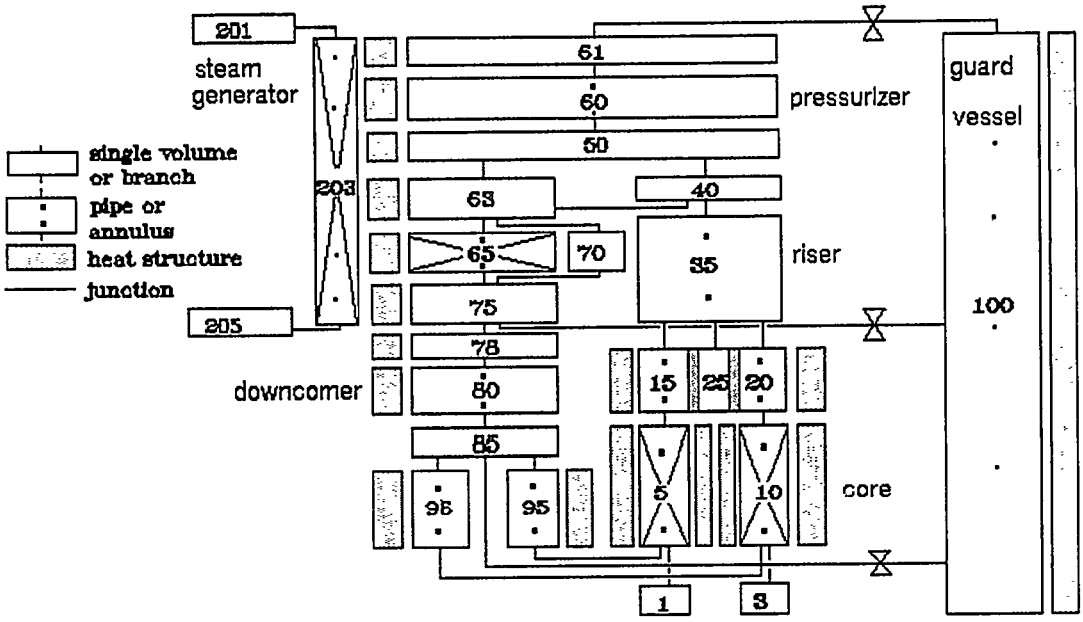


Fig.2. RELAP5/mod3 Nodalization of 1385 test facility

4.2. LOCA EXPERIMENT ON 1385 TEST FACILITY

The test scenario represents VPBER-600 accident with loss of integrity in the reactor vessel lower part. The initial conditions for the experiment are shown in the Table.

Heater power	753 kW
Primary circuit pressure	15.5 MPa
Gas (nitrogen) partial pressure in pressurizer	7.6 MPa
Coolant flow rate	1.153 kg/s
Pressure in guard vessel model	0.1 MPa
Temperature in guard vessel model	36 °C

The test started at a time t=0 s with opening of valve on pipeline communicating inlet collector in lower part of primary circuit with simulator of guard vessel. Leakage diameter was equal to 1.0 mm. At this time heating assemblies power is reduced to 100 kW during 80 s and mass flow of secondary coolant also is reduced to 0.074 kg/s. At the time t=500s the valve on pipeline joining pressurizer with upper part of GV model is opened (ND 1.7mm), that simulates the reactor depressurization system opening. Total duration of the experiment is 25 min. The results of calculation in comparison with some experimental data are shown on Fig. 10.

4.3. LOSS OF HEAT REMOVAL EXPERIMENT ON KMR-2 TEST FACILITY

The experiment imitates AST-500 beyond design accident with loss of heat removal from reactor and delay of scram. The parameters of test initial conditions are the following.

Heater power	1.52 MW
Primary circuit pressure	2.0 MPa
Gas (helium) partial pressure in pressurizer	0.78 MPa
Coolant flow rate	7.0 kg/s

The experiment starts at a time t-0s with stoppage of coolant flow rate in heat exhanger secondary side. Heater power is maintained time-constant during t=230 s, after that power is reduced to 0. Total time of experiment is 6 min. Calculations of main primary parameters history during the transient are presented in Fig. 11. compared with experimental data.

4.4. RESULTS OF RELAP5/MOD3 ASSESSMENT

The comparison with the experiments demonstrates satisfactory accuracy of description of integral reactor models behaviour by

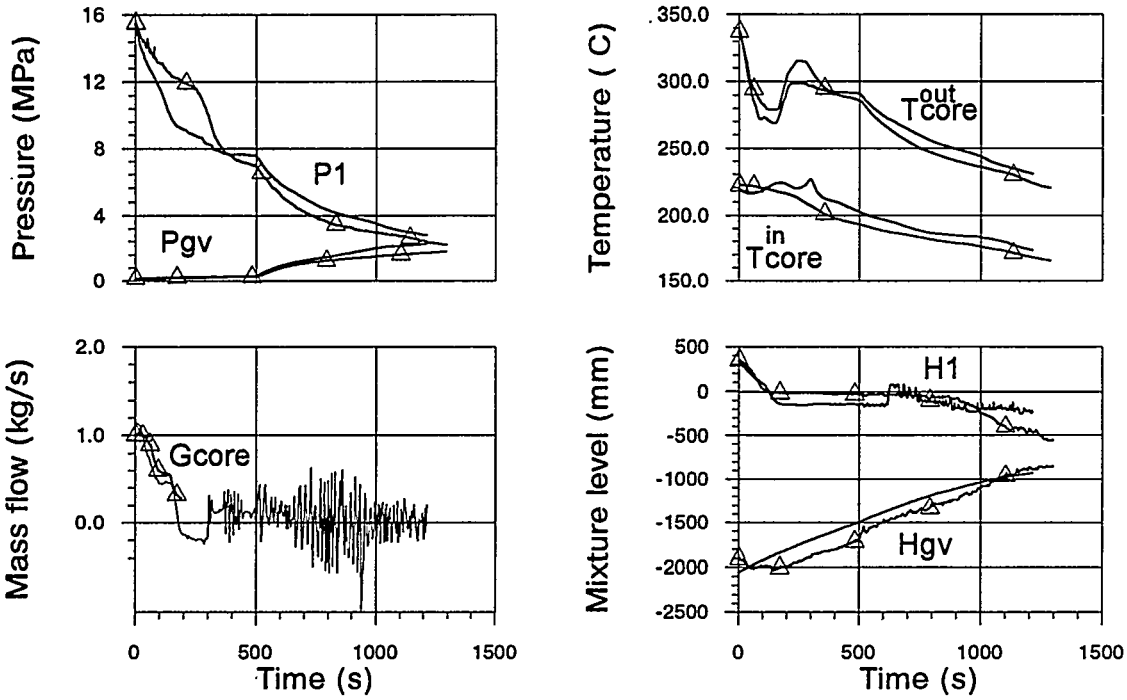


Fig. 10. 1385 test facility. LOCA experiment ND 1.03mm

—— RELAP5/mod3 —△— experiment

RELAP5/mod3 code. There are quantitative and qualitative agreement between calculated and experimental data.

GV behaviour and break flow rate simulation. The code predicts correctly the GV pressure history in LOCA experiments. A satisfactory correspondence between experiment and calculation on break flowrate of coolant with high content of dissolved gas (Cg=2600ncm^3/kg) was obtained.

Description of steam - gas pressuriser. The study of RELAP5/mod3 ability to simulate steam-gas pressurizer behaviour shows that main characteristics of pressurizer in accidents may be calculated by the code only using special nodalization. The pressurizer was devided into 10 nodes on height. Lower node was below coolant level, the next one contained steam-gas mixture at water temperature. The temperature of other nodes corresponded to volume-average gas partial pressure. More detail splitting of pressurizer volume took place in anticipated range of level change. Such approach of pressurizer nodalization allows to reduce errors attributed to an absence of interphase heat and mass transfer model for steam-gas pressurizer in RELAP5/mod3. The results of analyses of experiments on L-800 large-scale pressurizer model [10,12] confirm the code ability to predict main characteristics of steam-gas pressurizer.

Simulation of once-through steam generator. Comparison with experimental data on SG power in 1385rig shows that RELAP5/mod3 underestimates SG power by5-10% at full power condition. A possible explanation of this effect would be inaccurate simulation of interphase heat and mass transfer in steam-generating tubes that causes a droplet carry-over from SG and overprediction of steam superheating.

Noncondensable gas effect on HX heat transfer. The important issue of RELAP5/mod3 suitability for integral reactors LOCA analysis is simulation of heat transfer by steam condensation from steam-gas mixture on RHRS HX. RELAP5/mod3 models simulating heat and mass transfer by condensation in the presence of noncondensable gas are simplified [13] and overestimate the condensation intensity compared with experimental data. Yet, this limitation does not affect noticeably in case of ruptures of primary pipelines in upper part of RPV due to fast gas outflow from the reactor .

Code limitations. Limitations of RELAP5/mod3 suitability for integral reactors have been determined basing on the results of verification studies. Class of transients and accidents corresponding to the code limitations are the following:

1) Slowly developing quasi steady-state transients which need of correct description of interphase heat and mass transfer in steam-gas pressurizer.

2) Small break LOCAs with water outflow from lower part of RPV without depressurization where long term operation of RHRS HX in steam-gas mixture takes place.

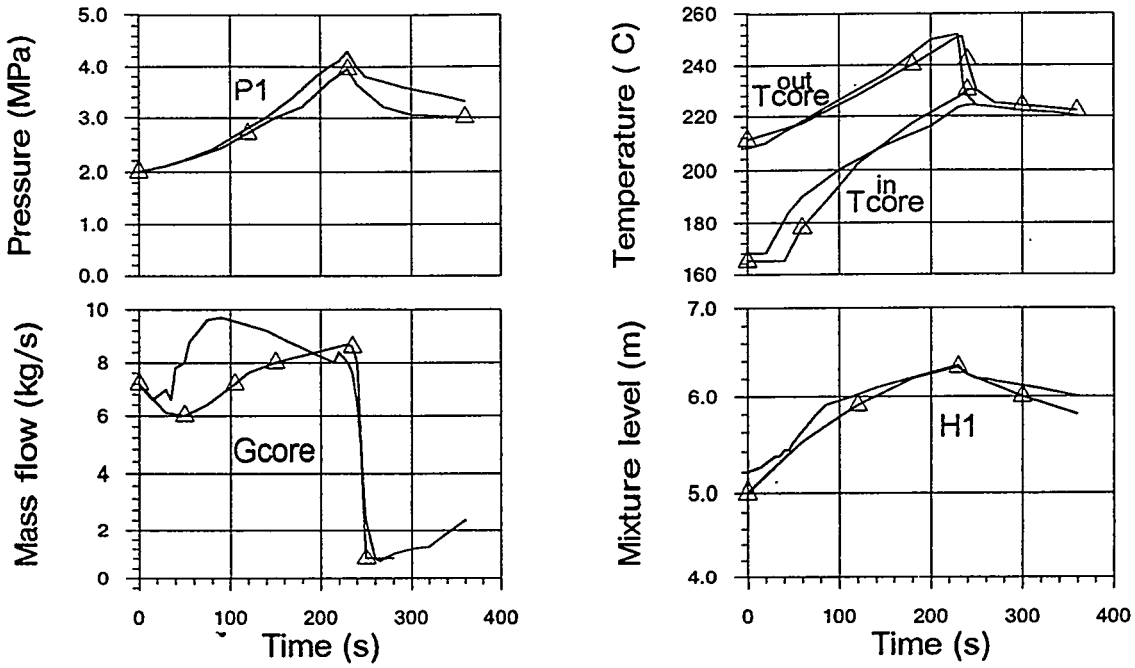


Fig. 11 KMR-2 test facility. Loss of heat removal experiment
—— RELAP5/mod3 —△— experiment

A new refined heat and mass transfer model in the presence of noncondensable gases is needed for RELAP5/mod3 to lift this limitations.

5. CONCLUSION

Peculiarities of integral reactor thermohydraulics in accidents are associated with presence of non-condensable gas in built-in pressurizer, absence of pumped ECCS, use of guard vessel for LOCAs localisation and passive RHRS through in-reactor HX's. These features defined the main trends in experimental investigations and verification efforts for computer codes applied.

Experimental information was used for verification of UROVEN/MB-3 code which is fast-running code for integral reactor LOCAs analysis offered to simulate the coupled behaviour of reactor and GV in long-duration accidents. Code assessment included calculation analysis of important separate effect tests as well as analysis of 12 integral experiments on the reactor models - KMR-2 and 1385 test facilities. Results of UROVEN/MB-3 assessment confirmed the code applicability for the analysis of LOCAs in integral reactors.

RELAP5/mod3 code is used in OKBM for alternative thermohydraulic analysis of accidents in VPBER, AST - type reactors. Verification study is under way to estimate the code applicability for integral reactors. RELAP3/mod3 assessment on the LOCAs and loss of heat removal experiments on two models of integral reactor shows the code ability to describe the plants behaviour in accidents. Class of transients and accidents corresponding to the range of RELAP5/mod3 code applicability for integral reactors has been determined basing on the results of verification studies: 1) fast-developing transients where interphase heat and mass transfer does not influence distincly on pressurizer dynamics; 2) LOCAs with outflow from upper part of primary circuit when there is no long operation of RHRS HX in the presence of noncondensable gas.

REFERENCES

1. V.S.Kuul, O.B.Samoilov, A.A.Falkov VPBER-600 Integral Reactor Thermohydraulics Study During LOCAs. Proc. NURETH-5, Salt Lake City, USA, Sept.21-24, 1992, v.2, p.325-330.

2. A.S.Babikin, B.F.Balunov, V.S.Kuul, A.A.Falkov et al., "Experimental validation of AST-500 reactor safety on large-scale reactor model", Atomnaya Energia, 73(1), p.37-44, 1992 (in Russian).

3. V.S.Kuul, O.B.Samoilov, A.A.Falkov, B.F.Balunov, - "Experimental investigations for validation of AST and VPBER integral reactors safety", NSI Conf. "Nuclear Energy and Human

Safety", June 28-July 2, 1993, N.Novgorod, Russia.
4. A.A.Falkov et al.,UROVEN/MB-3 Code. Analysis of Integral Reactor Thermohydraulics during LOCAs. Models and Applications Description, OKBM Report 2003э, Nizhny Novgorod, 1991 (in Russian).
5. A.A. Falkov, A.N.Lepekhin, G.N.Polyansky et al. Verification of UROVEN/MB-3 code for integral reactor LOCAs analysis. OKBM Report №787183, Nizhny Novgorod, 1993, (in Russian).
6. Leonard W. Ward. Application of drift flux to transient two-phase level swell. Nucl. Technol., vol.45, p.68-76,1979.
7. S.N.Aksan,F.Stierli,G.Th.Analytis. Boil-Off Experiments with the EIR-NEPTUN Facility: Analysis and Code Assessment Overview Report. NUREG/IA-0040, EIR-Bericht Nr.629, March 1992.
8. H.Uchida, A. Oyama, V. Togo, "Evaluation of Post-insident cooling systems of LWRs", Proc. Int. Conf. Peaceful Uses of Atomic Energy, IAEA, 13, p.93-102, 1965.
9. A.A.Falkov, G.N.Polyansky, RELAP5/mod3 assessment using results of VPBER-600 accidents experiments on the 1385 test facility. OKBM Report, N793813, N.Novgorod, 1994 (in Russian).
10. A.S.Devkin, E.D.Derbisher, RELAP5/mod3 calculation analysis of experiments on KMR-2 and L-800 test facilities. RRC "Kurchatov Institute" Report, Moscow, 1993 (in Russian).
11. A.S.Devkin, B.F.Balunov, RELAP5/mod3 assessment for depressurization processes at the test facility KMR-2 with gas-steam pressurizer. Proc. Int.Conf."New Trends in Nuclear System Thermohydraulics", Pisa, Italy, 1994, v.1, p.429-433.
12. A.V.Budnikov at al. Analysis of RELAP5/mod3 applicability to simulation of steam-gas pressurizer. OKBM Report 789013, N.Novgorod, 1994, (in Russian).
13. K.E.Carlson et.al. RELAP5/mod3 Code Manual. NUREG/GR-5535, Idaho Falls, 1990.

ASSESSMENT OF THE SE2-ANL CODE USING EBR-II TEMPERATURE MEASUREMENTS

W. S. Yang
Department of Nuclear Engineering
Chosun University
375 Scoseok-Dong, Dong-Gu, Kwangju
Republic of Korea

A. M. Yacout
Reactor Analysis Division
Argonne National Laboratory
Argonne, Illinois 60439

Abstract

The SE2-ANL code is a modified version of the SUPERENERGY-2 code [1]. This code is used at Argonne National Laboratory (ANL) to compute the core-wide temperature profiles in Liquid Metal Reactor (LMR) cores. The accuracy of this code has recently been tested by comparing the predicted temperatures with measured values in the Experimental Breeder Reactor II (EBR-II). The detailed temperature distributions in two experimental subassemblies and the mixed mean subassembly outlet temperatures were used in this validation study. The SE2-ANL predictions were found to agree well with measured values. It was also found that SE2-ANL yields results with accuracy comparable to the more detailed COBRA-WC [2] calculations at much lower computational cost.

I. Introduction

The SE2-ANL code is used at ANL to compute the core-wide temperature profiles in LMR core geometries for a given flow distribution and to determine the assembly flow rates yielding a desired (assembly-wise) peak temperature distribution. SE2-ANL is a modified version of the SUPERENERGY-2 thermal-hydraulic code, which is a multi-assembly, steady-state subchannel analysis code based on the simplified energy equation mixing model [3]. At Argonne, the SUPERENERGY-2 code was interfaced with ANL heating calculations [4]. Reactor hot spot analysis methods as well as fuel and cladding temperature calculation models were added to this code. An orificing scheme was also incorporated in SUPERENERGY-2 in order to determine the coolant flow rates that yield a desired peak temperature distribution. These modifications to the SUPERENERGY-2 code led to the SE2-ANL code.

The accuracy of the SE2-ANL code has recently been tested by comparing the predicted temperatures with measured values in EBR-II, which is a small sodium cooled fast reactor system with a nominal power rating of 62.5 MWt. The three-dimensional sodium temperature distributions within two experimental subassemblies were calculated and compared to the values measured by thermal expansion difference temperature monitors (TED's) installed in these subassemblies. The sodium temperature distributions predicted by SE2-ANL for the experimental subassemblies were also compared with the results obtained by the COBRA-WC code which includes more detailed thermal hydraulics models.

Subassembly outlet temperatures were also calculated for three reactor runs and compared with recorded plant data for 21 coolant outlet thermocouples installed in the upper plenum. The effects of interassembly heat transfer on the subassembly outlet temperatures were also studied by comparing the SE2-ANL results with the temperatures determined with an adiabatic treatment.

In this paper, the results of this validation study of the SE2-ANL code is presented. Sec. II briefly describes the main characteristics of the EBR-II. Sec. III discusses the overall computational procedures and methods. The comparisons between the predicted and the measured temperatures are made in Sec. IV. Finally, a summary of the work and conclusions are provided in the last section.

II. Characteristics of EBR-II

EBR-II is a small sodium cooled fast reactor system with a nominal power rating of 62.5 MWt. There are 637 subassemblies arranged in 16 rows of hexagonal rings within the reactor vessel. The core loadings in EBR-II are quite heterogeneous, consisting of various types of subassemblies with distinctly different hydraulic characteristics. As shown in Fig. 1 for a reactor cycle (Run 163A), a typical core loading consists mainly of drivers plus a few structural or experimental test subassemblies in the first seven rows, followed by three rows of stainless steel reflector subassemblies in Rows 8 through 10, which are surrounded by depleted uranium blanket subassemblies in Rows 11 through 16. Often a few stainless steel dummy subassemblies are also loaded in the blanket regions.

The subassembly positions within the reactor grid are designated by row, sector, and position within the row. The rows are numbered radially outward from the center. The grid is divided into six sectors which are identified as A through F as shown in Fig. 1. The position number in each sector of each row increases clockwise starting from the dividing line of each sector. The central position is identified as 1A1.

The pitch of each hexagonal subassembly is 2.32 inches and the effective core radius is approximately 12 inches. The active length of the cold, unirradiated driver fuel is 13.5 inches. There is a plenum directly above the core and a lower axial reflector directly below the core. An upper axial reflector is located above the plenum. The active length of the depleted uranium blanket is 55 inches. The stainless steel reflector subassembly consists of hexagonal prism stainless steel blocks and is 61.42 inches long.

The core contains two safety rods in Row 3 and eight to ten control rods in Row 5. All control rods are specially manufactured fuel subassemblies, and they reside in the core in normal reactor operating conditions. Control rods are withdrawn from the core to remove reactivity and shut down the reactor. In a typical core, there is only one "normal" control rod in Row 5; the other rods are High-Worth Control Rods (HWCRs). The HWCRs contain B_4C followers that are located above the core in the rods-inserted position.

The primary sodium is drawn from the primary tank and circulated through the system by two main centrifugal pumps. The discharge from each pump exits into a main pipe where it is divided into high and low-pressure streams. High-pressure sodium is piped from each pump outlet directly to the high-pressure inlets of the reactor grid plenum assembly, where it flows upward through the core region subassemblies in rows 1 through 7. The remaining sodium from each pump discharge is routed through a branch line equipped with a throttle valve, and this low-pressure coolant is then fed to the low-pressure plenum. From there, it flows upward through the subassemblies in rows 8 through 16. The high- and low-pressure streams merge in the outlet plenum as they come out of the top of the subassemblies. The mixed coolant exits from the reactor vessel through a 14-inch nozzle in the side near the top of the reactor vessel. It then flows through the electromagnetic auxiliary pump and enters the shell side of the heat exchanger, is cooled to $\sim 370°C$, and returns to the primary tank.

III. Computational Methods

For a given combination of mass flow rate, linear heat generation rate, and axial and radial power profiles for each assembly, SE2-ANL calculates detailed core-wide coolant temperature profiles based on the subchannel analysis method and the simplified energy equation mixing model [3]. Thus, coupled heating, flow, and temperature calculations need to be performed in order to compute the temperature distribution. This section briefly describes the computational methods and procedures of these coupled calculations.

A. Heating Calculation

The heating calculations were done with coupled neutron and gamma heating calculations [4] based on three-dimensional full core models which explicitly modeled each hexagonal subassembly through row 16. An additional row of hexagons (Row 17) was included in this model to represent the sodium pool. Each subassembly was radially homogenized into the following axial regions: lower axial reflector, lower grid plate, lower core, middle core, upper core, fission gas plenum, upper grid, and upper axial reflector. Using this reactor model, the neutron and photon fluxes were calculated by multigroup diffusion theory.

The coupled neutron and photon heating calculation is done in several steps. The neutron flux is first calculated using the finite difference triangular-z option of the DIF3D code [5]. This neutron flux is next used by the GAMSOR code to compute the photon source. The gamma flux is then calculated with this gamma source by using the finite difference triangular-z option of the DIF3D code once more. Using these neutron and gamma fluxes as well as the respective energy-

deposition conversion factors [4], the neutron, photon, and total heating rate densities are calculated.

Two different methods were used in calculating the pin power distributions within each subassembly for the sodium outlet temperature and the TED temperature calculations. For the sodium outlet temperature analysis, they were determined by the low-order polynomial interpolation scheme implemented in SE2-ANL. On the other hand, for the analyses of the spatially more detailed TED experiments, they were calculated with the RCT code [6] to take into account the different types of pins constituting a subassembly and the intra-assembly burnup gradients.

B. Flow Calculation

The flow rate of each subassembly was calculated using the EBRFLOW code [7]. This code is based on simple balances of flow rates and pressure drops in the EBR-II primary system, and on suitable input information from flow-modeling studies and engineering estimates of the leakage flow rates. The hydraulic characteristic of each subassembly is represented by a power-law relationship of the type $\Delta P = KQ^n$, where ΔP is the total pressure drop across the subassembly, Q is the flow rate through the subassembly, K is a dimensional constant, and n is a dimensionless exponent. The flow coefficients K and n are determined by calibrating the experimental data obtained from water and gas flow tests conducted on subassembly models or the actual subassemblies. The data from water and gas flow tests are scaled to sodium flow, at $427\,^{\circ}C$, through similarity principles.

The flow partition between the high- and low-pressure plenums are calculated by conserving the total flow rate and the total pressure drop through the two parallel flow paths between each pump discharge and the outlet plenum. The flow rates through the individual subassemblies are also determined with the equal pressure drop across each subassembly. In order to account for the radial pressure gradients existing in the high pressure inlet plenum, the experimentally determined effective pressure drop fractions are applied to the subassemblies in the high-pressure plenum [7].

C. Temperature Calculation

The SE2-ANL calculations were performed using the power distributions and subassembly flow rates determined by the above procedures. A full core model was used in these SE2-ANL calculations for the sodium outlet temperature analysis, whereas a seven subassembly model consisting of the subassembly of interest and its six neighboring subassemblies was employed for the analyses of TED experiments.

SE2-ANL calculates detailed core-wide coolant temperature profiles based on the subchannel analysis method and the simplified energy equation mixing model. The energy model is based on solving the energy equations for the coolant temperatures without explicitly solving the momentum and continuity equations. The momentum coupling between coolant channels is indirectly taken into account using enhanced eddy diffusivity and the swirl velocity ratio.[3] The derivation of the model starts by dividing the rod array of an LMR subassembly into two

predominant regions, the central and wall regions, and by assuming characteristic flows in each region. Energy transport equations are then derived based on four parameters: two axial velocities in the central and wall regions, one circumferential velocity in the wall region, and one enhanced eddy diffusivity for heat. The resulting equation for each subchannel accounts for axial convection, lateral heat exchange with neighboring subchannels due to conduction and wire-wrap sweeping flows (represented by an enhanced eddy diffusivity for heat), and volumetric heat source. For the subchannels in the wall region, two terms are added to the equation to account for the lateral convection due to circumferential swirl flow and the heat transfer from the duct wall.

In order to couple flow channels on either side of a duct wall, a one-dimensional resistance model is employed by ignoring axial and azimuthal conductions inside a duct wall. The bypass region of the double-ducted assembly is assumed to have no circumferential swirl flow, and inter nodal mixing within the bypass gap is assumed to occur by conduction only. The interassembly coupling is achieved by either a flowing interassembly gap or a resistance coupling.[1] In the flowing gap model, the interassembly gap flow is treated in a similar way as the bypass flow of double-ducted assembly, and the gap channels couple with the neighboring assemblies through the adjacent duct walls. In the resistance model, the interassembly gap sodium is considered to be stagnant, and a one-dimensional resistance model is used.

The four parameters involved in the energy equations are obtained based on experimentally determined correlations. For a particular total flow rate, the two axial velocities in the central and wall regions are obtained from the flow split correlations determined by hydraulic diameter flow analysis of Novendstern [8] and experimental data. The flow velocity split is correlated as a function of subchannel equivalent diameters. The circumferential swirl velocity in the wall region is also determined using a correlation for the ratio of the transverse swirl velocity to the average axial velocity. The enhanced eddy diffusivity for heat is obtained from a correlation for the dimensionless enhanced eddy diffusivity. Both the ratio of the transverse swirl velocity to the average axial velocity and the dimensionless enhanced eddy diffusivity are correlated as functions of subchannel geometry only. The correlation functions in Ref. 10 were employed in the analysis of TED experiments, while those in Ref. 9 were used in the sodium outlet temperature analysis.

IV. Comparison of Calculations with Measured Data

A. TED Experiments

The experimental subassemblies X494 and X495 were irradiated in the EBR-II during Run 152D. The subassemblies X494 and X495 were located in grid positions 4C2 and 6C4, respectively. Each of these subassemblies is a 61 pin driver subassembly that contains 11 dummy pins. The positions of these dummy pins in the subassembly are shown in Fig. 2 (the positions are the same for X494 and X495). The sodium temperature distributions within these subassemblies were measured using TED's mounted in the dummy pins.

Each TED consists of a stainless steel or Inconel capsule filled with sodium. As the sodium in the reactor passes around a TED, the sodium within the TED and its material expand. Since

the thermal expansion of the two materials is different, a permanent plastic deformation into the capsule's material will appear. This deformation is correlated with temperature, and gives an average value for the sodium temperature over the length of the TED. Fig. 3 shows a MK-III dummy element which is used in this study. Each dummy pin contains three 1-inch long TED's which are located at the center of core, the top of core, and the top of the fuel element. The measured temperature is the peak temperature that TED experiences during a reactor cycle.

Table I shows the temperatures collected from the two experiments. Each temperature represents the average value over the one inch length of a TED. Experience has demonstrated the TED's measurements to be accurate within $\pm 5°C$ [11]. The data for the pins 31 and 61 in X494 were not used in this study, since they showed unreasonably large deviations from their counterparts in X495 and from the other pins close to them. For example, the TED at the core center location of pin 31 in X494 has a temperature $\sim 60°C$ higher than the corresponding TED in X495, while the maximum difference between any other two corresponding TED's at the core center location is $\sim 21°C$.

SE2-ANL calculations were performed for the two experiments. The SE2-ANL results were compared with the measurements. The deviation between the calculated and measured temperatures are shown in Table II. The maximum deviation was $\sim 15°C$ for X494 and $\sim 20°C$ for X495. The root mean square deviation was $\sim 8°C$ for both subassemblies. The relative maximum deviation was ~3% for X494 and ~5% for X495, and the relative root mean square deviation was ~2% for both subassemblies.

The accuracy of the thermal hydraulics computational methods of SE2-ANL was also tested by repeating the same calculations using the COBRA-WC code [2] which includes more detailed thermal hydraulics models. The maximum difference between COBRA-WC predictions and measurements was $\sim 18°C$ for both subassemblies, and the root mean square difference was $\sim 8°C$ for X494 and $\sim 6°C$ for X495. The maximum difference between SE2-ANL and COBRA-WC predictions was $\sim 8°C$ for X494 and $\sim 13°C$ for X495, and the root mean square difference was $\sim 4°C$ for X494 and $\sim 6°C$ for X495 as shown in Table III. These comparison results show that the accuracy of SE2-ANL is comparable to that of the COBRA-WC code, which is about fifty times slower than SE2-ANL.

B. Subassembly Outlet Temperatures

In EBR-II, coolant outlet thermocouples are installed on the underside of the reactor vessel top cover. The thermocouple sensors are located one quarter inch above the subassembly outlet. They had initially been installed for 26 selected subassembly positions, but only 21 of them are currently functioning. These thermocouples monitor the sodium temperatures exiting from the subassemblies in the reactor. The mixed mean subassembly outlet temperatures were calculated for three reactor runs (Runs 163A, 164A, and 165A) by SE2-ANL and compared with the recorded plant data for these coolant outlet thermocouples.

Since SE2-ANL is applicable only to forced-convection turbulent flow conditions and the wire-wrapped pin bundle geometries, several modeling approximations were made in this analy-

sis. First, the axial heterogeneity of each subassembly was neglected by extending its pin geometry from the bottom to the top of the subassembly. Second, potential buoyancy effects in the stainless steel rod outer blankets were neglected. Finally, wire wraps of near zero (0.001 inch) diameter were artificially introduced to the subassemblies composed of bare rods. These approximations were tested by performing sensitivity studies and found to have little effect on computed values for the mixed mean subassembly outlet temperature.

Table IV shows the measured sodium outlet temperatures and the deviations of the SE2-ANL results from the measured values. The reported uncertainties in the measured temperatures are less than $2°C$ [12]. Excluding the four subassemblies in grid positions 2B1, 7A3, 7D4, and 16E9, the root mean square deviation between the calculated and measured temperatures was $\sim 6°C$, and the maximum deviation was $\sim 12°C$. The difference in the subassembly coolant temperature increment above inlet between SE2-ANL and measurement is thus within ~10% of the measured temperature increment. Considering ~10% uncertainties in subassembly power and flow rate, this deviation is well within 1-σ uncertainty of the calculated temperature increment.

The unreasonably large deviations between calculated and measured outlet temperatures observed in the aforementioned four subassemblies appear to be due to either biased thermocouple readings or pronounced flow mixing effects. The thermocouples for the subassemblies 2B1, 7A3, and 7D4 are believed to be biased based on the inconsistency of the thermocouple readings with the power-to-flow balances. As an example, consider the calculated and measured outlet temperatures, as well as the calculated power-to-flow ratios, shown in Fig. 4 for the subassembly in position 2B1 and its six surrounding subassemblies in Run 163A. The subassembly in position 2B1 is a nonfueled experimental subassembly, whereas its neighboring subassemblies are fueled ones. The calculated power-to-flow ratio of this subassembly is only 28 to 37% of the corresponding ratios of its neighboring subassemblies. Hence the outlet temperature of this subassembly is expected to be lower than the neighboring subassembly outlet temperatures, as predicted with SE2-ANL. However, the measured temperatures indicate that this subassembly is hotter than the neighboring ones. Similar results were obtained for Runs 164A and 165A. Consequently, these contradictory results suggest that the coolant outlet thermocouple for the subassembly position 2B1 is either malfunctioning or systematically biased.

The subassembly 16E9 is located in the part of the region where the flow baffle has its 90° opening. In this 90° opening region of the flow baffle, the coolant from the high pressure plenum region flows to the outer annulus between the inner and outer shells of the reactor vessel through the upper portion of the plenum, while the relatively low-temperature coolant from the low pressure plenum region exits to the outer annulus through the lower portion of the plenum. Hence it is very likely that the thermocouple for the subassembly position 16E9 is affected by the coolant flowing outward from the low pressure plenum region. In fact, the measured temperature for the subassembly in 16E9 are closer for each run to the calculated low pressure plenum average outlet temperatures than to the outlet temperature of the subassembly in 16E9 itself.

The effects of interassembly heat transfer on the subassembly outlet temperatures were also studied by comparing the SE2-ANL results with those determined with an adiabatic treatment. The SE2-ANL code generally gave better agreement with the measurement than adiabatic temperatures, especially for those subassemblies where interassembly heat transfer is relatively

important. The interassembly heat transfer considered in SE2-ANL calculations reduced the outlet temperature of the hottest subassembly in the core and blanket region by ~17 to 40°C. The structural subassemblies embedded in the core region showed the largest interassembly heat transfer effect. The outlet temperature underprediction in these structural subassemblies due to neglecting interassembly heat transfer was as large as 50°C. Most of the experimental subassemblies also showed a large discrepancy in subassembly outlet temperatures predicted by SE2-ANL and with an adiabatic treatment. The largest temperature difference in fueled experimental subassemblies was ~36°C. On the other hand, the interassembly heat transfer effects on the driver subassemblies were observed to be small, with the temperature overprediction in driver subassemblies due to neglecting interassembly heat transfer being at most 6°C.

V. Conclusions

Comparisons have been made between SE2-ANL estimates and measurements for the sodium temperature distributions within subassemblies and the mixed mean subassembly outlet temperatures. All the comparisons made in this study indicate reasonably good agreement between the SE2-ANL and the measurement. In addition, the code yields results with accuracy comparable to the more detailed COBRA-WC calculations at much lower computational cost. It was also observed that interassembly heat transfer needs to be considered even in computing the subassembly-average quantities such as mixed mean outlet temperatures. In conclusion, the validation studies summarized in this paper show that the SE2-ANL code can be used to perform accurate core-wide steady-state thermal hydraulics calculations with low computational cost.

Acknowledgment

The authors wish to thank J. F. Koenig and C. E. Lam for providing the TED's measurements and COBRA-WC results. This work was supported by the U.S. Department of Energy, Nuclear Energy Programs under contract W-31-109-ENG-38.

References

[1] K. L. Basehore and N. E. Todreas, "SUPERENERGY-2: A Multiassembly Steady-State Computer Code for LMFBR Core Thermal-Hydraulic Analysis," PNL-3379, Pacific Northwest Laboratory (August 1980).

[2] E. P. Coomes, et al., "User Manual CORBRA-WC: A version of COBRA for Single-Phase, Single and Multiassembly Thermal-Hydraulic Transient Analysis," PNL-4303, (May 1982).

[3] E. V. Kahn, W. M. Rohsenow, A. Sonin, and N. E. Todreas, "A Porous Body Model for Predicting Temperature Distributions in Wire Wrapped Fuel and Blanket Assemblies of an LMFBR," COO-2245-16TR, Massachusetts Institute of Technology (June 1975).

[4] R. Jacqmin, G. Palmiotti, and P. Finck, "Analysis of EBR-II Neutron and Photon Physics by Multidimensional Transport Theory Techniques," *Proc. Topl. Mtg. Advances in Reactor Physics*, Knoxville, Tennessee, April 11-15, 1994, Vol. I, p. 129, American Nuclear Society (1994).

[5] K. L. Derstine, "DIF3D: A Code to Solve One-, Two-, and Three-Dimensional Finite Difference Diffusion Theory Problems," ANL-82-64, Argonne National Laboratory (April 1984).

[6] W. S. Yang, P. J. Finck, and H. Khalil, "Reconstruction of Pin Power and Burnup Characteristics from Nodal Calculations in Hexagonal-Z Geometry," *Nucl. Sci. Eng.*, **111**, 21 (1992).

[7] A. Gopalakrishnan and J. L. Gillette, "EBRFLOW - A Computer Program for Predicting the Coolant Flow Distribution in the Experimental Breeder Reactor - II," *Nucl. Tech.*, **17**, 205 (1973).

[8] E. Novendstern, "Turbulent Flow Pressure Drop Model for Fuel Rod Assemblies Utilizing A Helical Wire-Wrap Spacer System," *Nucl. Eng. Design. 22*, 19-27 (1972).

[9] C. Chiu, W. M. Rohsenow, and N. E. Todreas, "Flow Split Model for LMFBR Wire Wrapped Assemblies," COO-2245-56TR, Massachusetts Institute of Technology (April 1978).

[10] S. K. Cheng and N. E. Todreas, "Hydrodynamic Models and Correlations for Bare and Wire-Wrapped Hexagonal Rod Bundles - Bundle Friction Factors, Subchannel Friction Factors and Mixing Parameters," *Nucl. Eng. Design.*, 92, 227-251 (1986).

[11] G. L. Batte', R. G. Pahl, and C. W. Wilkes, Argonne National Laboratory, personal communication (April 1990).

[12] J. F. Jensen, Argonne National Laboratory, personal communication (June 1993).

Table I. Measured Temperatures ($°C$) for Subassemblies X494 and X495

Pin No.	Subassembly X494			Subassembly X495		
	Core Center	Core Top	Element Top	Core Center	Core Top	Element Top
5	409	459	467	418	475	479
7	418	475	471	439	484	485
19	403	442	456	400	452	464
24	426	488	488	436	498	508
29	421	480	480	435	490	489
31	491	500	515	432	498	505
34	421	482	479	437	496	490
44	429	461	468	431	473	476
48	425	485	488	430	496	493
53	432	489	478	434	493	482
61	378	421	471	408	456	463

Table II. Deviations of SE2-ANL Computed Subchannel Sodium Temperatures ($°C$) from Measured Values

Row No.	Pin No.	Subassembly X494				Subassembly X495			
		Core Center	Core Top	Element Top	Row Average	Core Center	Core Top	Element Top	Row Average
1	31					1.8	-1.4	0.3	0.2
3	24	-0.8	-10.0	-5.4	-2.3	-4.5	-6.5	-11.0	-0.5
	29	5.8	-0.3	0.8		-0.1	6.1	7.8	
	48	1.9	-0.3	0.8		3.8	-2.0	2.1	
4	7	5.1	-4.4	1.1	-5.1	-9.0	0.2	0.3	-4.8
	34	1.0	-14.7	-11.3		-9.6	-17.7	-11.3	
	53	-5.9	-13.0	-3.8		-0.5	-1.8	6.5	
5	5	-1.7	-11.0	-9.1	-1.5	-6.3	-16.0	-7.7	1.5
	19	10.2	13.3	7.3		19.7	16.7	12.8	
	44	-14.5	-4.1	-4.2		-10.4	-4.6	-1.4	
	61					5.4	4.1	5.8	
Column Average		0.2	-5.5	-3.5		-0.9	-2.1	0.4	
Root Mean Square		7.8				8.5			

Table III. Deviations Between SE2-ANL and COBRA-WC Predictions of Subchannel Sodium Temperatures ($°C$)

Row No.	Pin No.	Subassembly X494			Subassembly X495		
		Core Center	Core Top	Element Top	Core Center	Core Top	Element Top
1	31				-2.1	-4.2	-1.4
3	24	-6.9	-6.1	-4.4	-5.6	-11.5	-8.2
	29	0.3	-2.0	-2.0	-5.7	-0.6	2.8
	48	-0.2	0.3	5.2	-1.2	-3.1	-0.7
4	7	-1.0	-2.7	0.5	-2.9	-6.5	-1.9
	34	-2.9	-5.8	-3.5	-6.3	-11.0	-8.5
	53	-0.9	-4.1	-2.1	1.7	1.7	2.6
5	5	2.7	5.7	0.3	-0.2	1.8	-3.3
	19	4.1	7.7	8.4	6.9	12.9	12.8
	44	3.3	2.6	0.2	0.7	7.1	4.2
	61				2.1	8.5	0.2
Root Mean Square		4.0			5.8		

Table IV. Deviations of SE2-ANL Computed Subassembly Mixed Mean Outlet Temperatures ($°C$) from Measured Values

Subassembly Position	Run 163A		Run 164A		Run 165A	
	SOT[a]	Diff.[b]	SOT[a]	Diff.[b]	SOT[a]	Diff.[b]
1A1	455.7	4.8	455.1	3.8	454.9	4.1
2A1	450.1	8.1	449.2	7.5	451.2	8.1
2B1	476.9	-35.1	486.8	-55.3	485.7	-52.9
2C1	442.7	8.9	443.0	7.3	449.7	11.3
2E1	458.5	-0.3	457.4	-0.7	458.4	-1.8
2F1	449.0	-7.8	447.6	-7.4	448.6	-7.1
3B1	475.0	0.1	474.4	-0.9	465.3	6.7
3C1	460.7	7.8	460.5	7.2	460.1	7.6
3F1	465.2	8.7	463.1	9.2	462.9	9.2
4B1	479.1	11.9	477.8	11.9	478.2	9.4
4C3	473.1	9.3	473.3	7.8	472.2	9.0
4E1	482.2	7.6	481.2	6.6	481.8	6.3
4F1	491.3	0.6	489.8	0.5	488.1	1.4
5A4	487.8	4.3	487.2	3.7	485.6	4.1
5C2	455.7	3.5	458.0	1.1	457.0	1.6
6C4	479.6	4.9	484.6	6.2	488.5	2.6
7A3	452.6	41.6	452.2	40.6	449.5	41.2
7D4	436.2	48.2	433.4	63.3	432.1	64.6
9E4	456.7	-4.2	462.6	-9.2	460.0	-6.1
12E6	518.1	-5.8	517.7	-4.5	519.7	-5.5
16E9	433.4	-48.1	430.5	-45.2	428.7	-43.3

[a] Measured Sodium Outlet Temperature
[b] Calculated Temperature - Measured Temperature

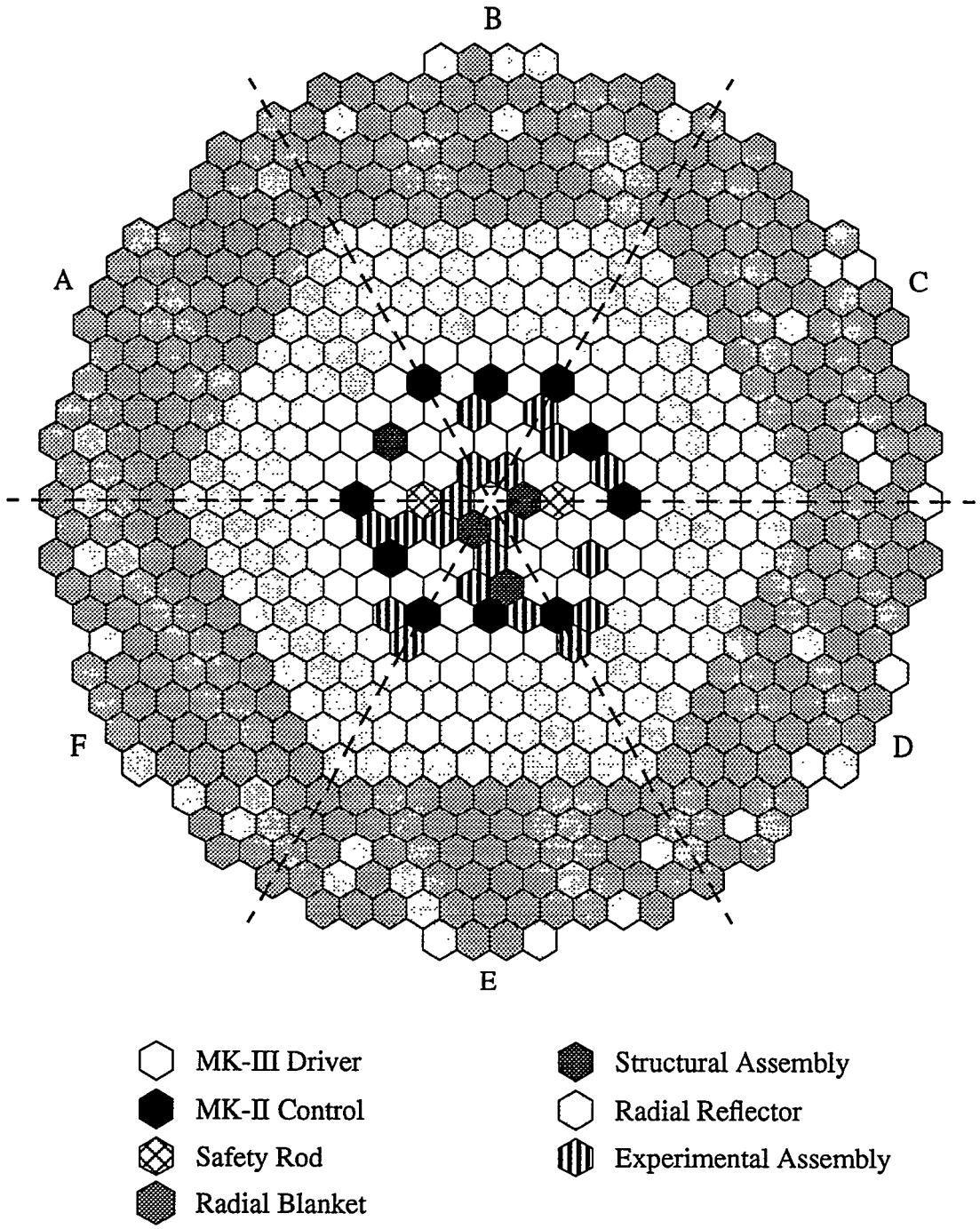


Fig. 1. Core Loading Diagram for EBR-II Run 163A

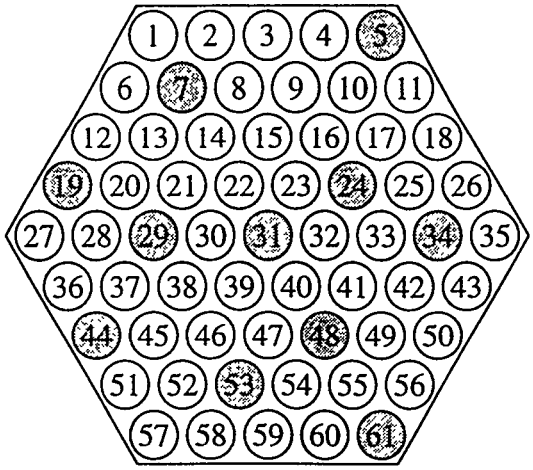


Fig. 2. Position of the 3 TED Dummy Elements in Subassemblies X494 and X495

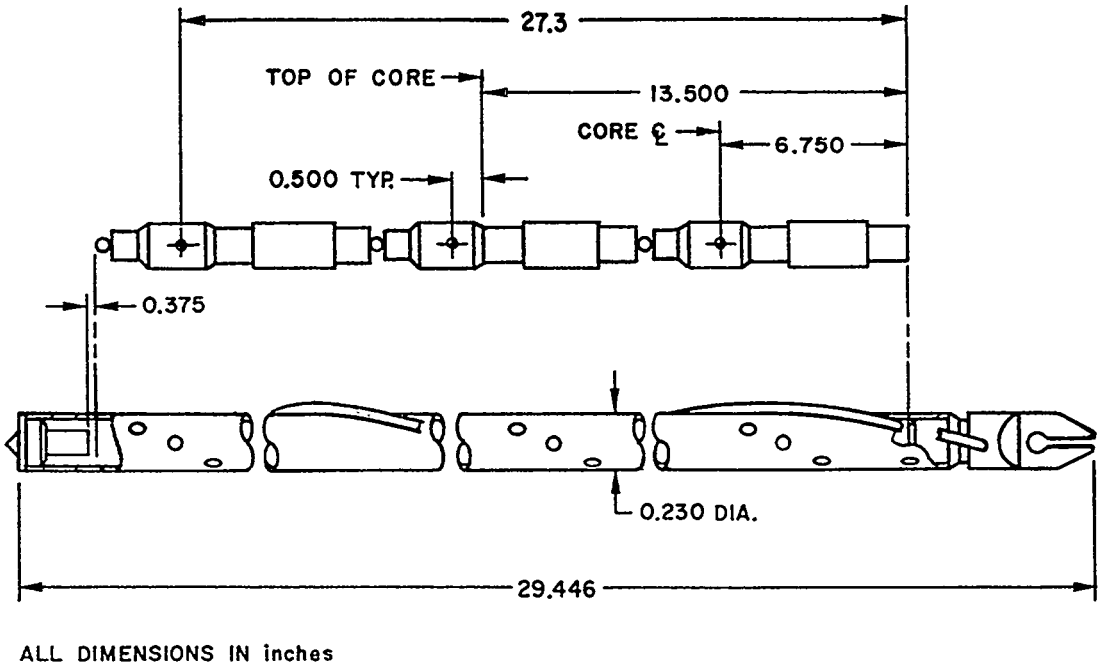


Fig. 3. MK-IIIA 3 TED Dummy Element Design

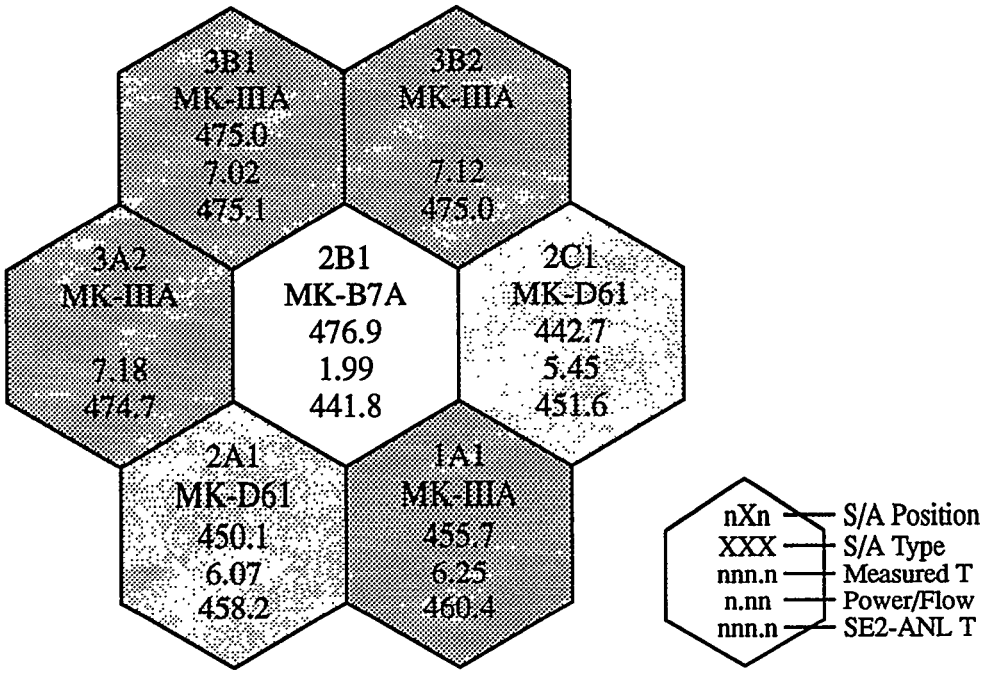


Fig. 4. Calculated and Measured Outlet Temperatures (^{o}C) of Subassembly 2B1 (Run 163A)

RELAP5 MODEL TO SIMULATE THE THERMAL-HYDRAULIC EFFECTS OF GRID SPACERS AND CLADDING RUPTURE DURING REFLOOD

C. K. Nithianandan, J. A. Klingenfus, and S. S. Reilly
B&W Nuclear Technologies, Lynchburg, Virginia 24506-0935
(804) - 832 - 2381

ABSTRACT

Droplet breakup at spacer grids and at cladding swelled and ruptured locations plays an important role in the cooling of nuclear fuel rods during the reflooding period of a loss-of-coolant accident (LOCA) in a pressurized water reactor (PWR). During the reflood phase, a spacer grid affects the thermal-hydraulic system behavior through increased turbulence, droplet breakup due to impact on grid straps, grid rewetting, and liquid holdup due to grid form losses. Recently, models to simulate spacer grid effects and blockage and rupture effects on system thermal hydraulics were added to the B&W Nuclear Technologies (BWNT) version of the RELAP5/MOD2 computer code. Several FLECHT-SEASET forced reflood tests, CCTF Tests C1-19 and C2-6, SCTF Test S3-15, and G2 Test 561 were simulated using RELAP5/MOD2-B&W to verify the grid model. The FLECHT-SEASET blockage Test 61607 and the REBEKA-6 test were simulated to verify the applicability of the model at the cladding swelled and rupture locations. The results demonstrate the importance of modeling the thermal-hydraulic effects due to grids, and clad swelling and rupture to correctly predict the clad temperature response during the reflood phase of large break LOCA. The RELAP5 models and the test results are described in this paper.

I. INTRODUCTION

Experiments, using separate effect test facilities in the U.S., France, Germany, and Japan, have been conducted to simulate PWR core thermal-hydraulic behavior during the reflood period of a large break loss-of-coolant accident (LOCA). These tests included electrically heated solid rods using simple or mixing-vane grids, electrically heated rods with metallic sleeves to simulate clad swelling and rupture effects, and electrically heated rods with a pressurized gap to model rupture during the transient. The results from these tests show a decrease in heater rod temperature downstream of a grid spacer. The REBEKA tests, using electrically heated rods with pressurized gaps, show that the formation and propagation of a second quench front from the rupture location is dominant in reducing the clad temperature downstream of the rupture location.

A. Studies on Droplet Breakup

Experiments conducted by Lee et al.[1,2], Yao, Hochreiter, and Cai[3], and Sugimoto and Murao[4] show that significant droplet breakup occurs when droplets impinge on spacer grid straps. The high surface area-to-volume ratios of these shattered micro-droplets cause them to evaporate rapidly in the superheated steam immediately downstream of the grid, resulting in the cooling of the fuel rod downstream of the grid spacer.

There are three controlling parameters for the droplet breakup process: the incoming droplet diameter (d_o), the droplet velocity (v_f), and the surface tension (σ). A generalized non-dimensional form to represent the controlling parameters is the incoming droplet impact Weber number:

$$We_l = \rho_f v_f^2 d_o/\sigma, \quad (1)$$

where ρ_f is the liquid density.

Wachters et al.[5,6] studied the effect of Weber number on droplet breakup when a droplet impacted normally upon a large heated plate. For small Weber numbers ($We_l < 30$), no droplet disintegration occurred, and the droplets simply rebounded from the surface. For Weber numbers between 30 and 80, the droplets did not shatter until they rebounded from the hot surface. The fluid sometimes became unstable, resulting in the ejection of one or two small droplets. For Weber numbers greater than 80, all droplets disintegrated upon impact at the surface.

Chiou et al. reviewed the droplet-shattering data of Watchers and the Carnegie Mellon experiments[7] to estimate the shattered droplet diameters as functions of the droplet impact Weber number. The resulting curve is shown in Figure 1.

Studies have been done on the dynamics of droplets impinging upon a thin hot strip and on an unheated grid spacer. Lee et al.[1,2] made detailed measurements of droplet diameters, using a laser Doppler anemometer, near an unheated spacer grid for air-water flow conditions. They observed that the area-to-density ratio of the small droplets downstream of the grid location increased by a factor of approximately ten over upstream values. This study clearly showed the effectiveness of grids in shattering large incoming droplets. In these studies, however, the effects of this process upon the heat transfer mechanisms observed in typical reflood conditions were not considered. Yao et al.[3] conducted experiments with water droplets impacting the edges of thin, heated steel strips. During the droplet-strip interaction, they observed a combination of cutting and splashing of droplets by the strip. Based on high-speed-movie observations of drop impingement on the metal strips, they suggested the droplet breakup process depicted in Figure 2.

Paik et al.[8] evaluated the data of Lee et al., Yao et al., and tests conducted by the Central Electricity Board (CEGB), England, and correlated the shattered droplet diameter as

$$d_e/d_o = 6.167\ We_l^{-0.53}, \quad (2)$$

where d_e is the shattered droplet diameter.

They incorporated this correlation in COBRA-TF along with a small droplet field model to calculate the vapor generation resulting from the rapid evaporation of the shattered micro-droplets. The production of micro-droplets at a grid location was calculated using the following equation:

$$G_{de} = \epsilon\, G_{do}\, \xi, \quad (3)$$

where

ϵ = grid blockage factor,
G_{de} = mass flux of micro-droplets produced,
G_{do} = incoming droplet mass flux, and
ξ = efficiency with which a droplet interaction with a grid spacer will generate a population of small drops. (A value of $\xi = 0.6$ was determined from Paik's studies.)

Sugimoto and Murao[4] conducted identical reflood tests in a 6x6 heater rod bundle by keeping the midplane grid spacer just below the measurement location in one case, and just above, in another. This way, the droplet spectra and cladding temperatures below and above the grid spacer could be measured. These tests showed that significant droplet breakup occurs when droplets impinge on grid spacer straps. Based on the assumption that when a droplet interacts with a grid, it splits into n droplets of equal size, Sugimoto and Murao derived a grid spacer atomization factor, η_{max}, which is defined as the ratio between the downstream and upstream droplet diameters. The factor is a function of n and the grid blockage factor, ϵ, and is defined as:

$$\eta_{max} = 1/\{1 + (n^{1/3} - 1)\epsilon\}. \quad (4)$$

It can be seen from the above equation that the droplet diameter at a location downstream of a grid decreases as the grid blockage ratio increases.

B. Grid Effects

The ERSEC reflood tests at Grenoble, France[9,10] examined the effects of different grid spacers on cladding temperature during reflooding. In these tests, three different grids were studied: (1) a simple, low-pressure drop grid; (2) a grid similar to PWR fuel assembly grids without mixing vanes; and (3) a grid with simulated mixing vanes. The results shown in Figure 3 demonstrate the decrease in rod temperature downstream of a spacer grid with increasing blockage ratio (ratio of grid projected area to channel flow area away from the grid).

In Germany, tests were conducted using the FEBA[11] test facility, under identical test conditions, with and without a midplane grid. The presence of the midplane grid resulted in improved cooling of the heater rod. Ihle and Rust[12] also evaluated grid effects using different rod materials and rods with gaps to simulate the gap between the fuel and clad.

The ERSEC, FEBA, and JAERI experimental results clearly showed that, during the reflood phase of a large break LOCA, the spacer grids improve downstream cooling mechanisms. During the reflood phase, a spacer grid affects the thermal-hydraulic system behavior through increased turbulence, droplet breakup (due to impact on grid straps), grid rewetting, and liquid holdup (due to grid form losses). Kelly and Kohrt[13] made detailed studies of these mechanisms using the COBRA-TF computer code and concluded that grid rewet has only a minor effect in predicting system behavior.

The Weber number effect on droplet breakup, shown in Figure 1, also explains why upper grids are observed to be more effective in breaking droplets than are lower grids, as shown in Figure 3. As the two-phase mixture moves upwards from the quench front, the vapor velocity increases due to droplet evaporation. This increase in vapor velocity causes the droplet velocity to increase with the higher interphase drag. As the liquid velocity increases, the drop impact Weber number increases, producing increased droplet shattering.

C. Blockage and Rupture Effects

During the refill and reflood phases of large break LOCA, the Zircaloy-clad fuel rods may reach high temperatures and have relatively high internal pressures compared with the pressure outside the fuel rods. This combination of high temperature and high pressure may cause the cladding to swell and burst. The resulting blockage may cause two opposite effects during reflood: (1) reduced coolant flow through the blocked channel, and (2) increased heat transfer due to increased turbulence and droplet breakup at the rupture location.

Various separate effects reflood experiments have been performed to examine the thermal-hydraulic effects of blocked rod arrays. The FLECHT-SEASET[14,15] and FEBA programs used solid electrically heated rods without gaps. The blockage and rupture effects in these tests were simulated using concentric and non-concentric stainless steel sleeves arranged in coplanar and noncoplanar fashion. The simulated fuel rod blockage was found to enhance the heat transfer and more than offset flow bypass effects. The important mechanism for the improved heat transfer is the shattering of entrained droplets in the non-equilibrium two-phase flow field.

The REBEKA program[16] examined the thermal-hydraulic effects of fuel rod swelling and rupture during reflood using electrically- heated rod simulators with a pressurized gap. The two-phase dispersed flow was found to quickly cool the cladding near the burst location, and a second quench front was formed and propagated axially from the rupture location. The propagation of this second quench front resulted in a substantial reduction in cladding temperature downstream of the rupture location. The REBEKA test program demonstrated that the formation and propagation of a second quench front from the rupture location is dominant in reducing the clad temperature downstream of the rupture location compared with other blockage effects.

II. RELAP5/MOD2-B&W CODE IMPROVEMENTS

The RELAP5/MOD2 computer program developed by EG&G has been extensively modified by B&W Nuclear Technologies (BWNT) to improve its predictive capabilities.[17,18] Models were added to predict the thermal-hydraulic behavior of a nuclear fuel rod during the reflood phase of a large break LOCA. These modifications include modeling to simulate spacer grid and blockage and rupture effects on the system thermal-hydraulics, a dynamic gap model to calculate gap heat transfer and to predict clad swelling and rupture, and a metal-water reaction model to calculate the Zircaloy-steam reaction. The U.S. Nuclear Regulatory Commission has reviewed and approved these models for licensing applications.

After several theoretical and experimental studies of droplet breakup near grid locations[1-7]were evaluated, a simple model was developed that could easily be incorporated into RELAP5. The droplet breakup model depends on the grid spacer atomization factor of Sugimoto and Murao[4] and a droplet breakup efficiency that depends on the droplet impact Weber number, given by Equation 1. The majority of the micro-droplets are generated by the shattering of large droplets in the vicinity of grids. These micro-droplets evaporate rapidly because of their large surface area-to-volume ratio. The area increase is assumed to be a function of the code-calculated interphase area, grid efficiency, and grid blockage. The formulation of these and other models is discussed in detail in References 17 and 18.

The BWNT model does not include grid rewet effects. The convective enhancement due to increased turbulence resulting from the presence of a grid is calculated using the Yao, Hochreiter, and Leech correlation:[19]

$$h(x)/h_o = 1 + 5.55\epsilon^2 e^{(-0.13X/De)}, \quad (5)$$

where

ϵ = grid blockage factor,
h_o = heat-transfer coefficient calculated using single-phase correlations,
X = distance from the downstream end of the grid spacer, and
De = hydraulic diameter.

In the current model, the dependency of the impact Weber number on the shattered droplet diameter, as shown in Figure 1, is defined in terms of a droplet breakup efficiency, θ, given by the following equation:

$$\theta = \begin{cases} 0.0 & We_l \leq 40 \\ (20^{\beta} - 1)/19 & 40 < We_l < 400 \\ 1.0 & We_l > 400, \end{cases} \quad (6)$$

where

$$\beta = \{(We_l - 40)/360\}^6.$$

The average reduction in droplet diameter due to droplet shattering is given by the atomization factor:

$$\eta = d_e/d_o = 1 - \theta(1 - \eta_{max}). \quad (7)$$

The maximum droplet breakup atomization factor, η_{max}, depends on geometric characteristics of the grid. It is determined using the Sugimoto and Murao[4] correlation, given by Equation 4.

The majority of the micro-droplets, generated by the shattering of large droplets by a grid, are assumed to be evaporated in the near vicinity downstream of the grid. The rapid evaporation of these droplets is due to the increased surface area. The increase in surface area can be assumed to be proportional to the grid efficiency, grid blockage factor, and droplet flux or reference surface area, a_{gf}, of the droplets after breakup. The surface area increase should also be inversely proportional to the control volume length, L, to preserve the total micro-droplet evaporation potential in grid volumes. Thus, the increase in surface area in the control volume containing the rupture is given by:

$$\Delta a_{gf} = C\,\theta\, a_{gf}\, \epsilon/L, \quad (8)$$

where C is the proportionality constant. The total surface area in the volume is:

$$a^*_{gf} = a_{gf}\,(1 + C\,\theta\,\epsilon/L\,). \quad (9)$$

In RELAP5/MOD2-B&W, the calculation of droplet diameter d_o depends on fluid conditions below the quench front. If the liquid below the quench front is subcooled, the flow regime near the quench front is inverted annular. In this case, droplets sheared from the liquid surface are small, and RELAP5 correlations are used to calculate the diameter, d_o. If the liquid is saturated below the quench front, the agglomeration of steam bubbles below the liquid surface and the burst of rising bubbles at the quench front results in the formation of droplets of diverse diameters. The average diameter of this population is expected to be substantially larger than for droplets sheared from an inverted annular liquid surface. The droplet size and the interphase drag calculated using RELAP5 correlations are adjusted to account for these considerations. The interphase drag is decreased, and the droplet size is increased to account for the larger droplets in the flow field as the boiling length, determined by the difference

between the quench to incipient boiling locations, increases. The average droplet interphase area a_{gf} is calculated using the RELAP5 correlations. The diameter d_e, given by Equation 7, is used in the a_{gf} calculation.

The droplet population in the downstream vicinity of a grid or a blockage can be divided into two groups: micro-droplets and droplets with diameter d_e. The micro-droplets evaporate within a short distance downstream of a grid or rupture location. The evaporation produces a local high source term of saturated vapor. Several reflood experiments[9-12] have shown a local depression of cladding temperatures downstream of the grids. Chiou et al.[7] added a shattered droplet field model to their reflood code to track the evaporation of the micro-droplets. From sensitivity studies, they concluded that only these micro-droplets have a localized high evaporation rate consistent with the cladding temperature data from these tests. In the present RELAP5/MOD2-B&W model, the high evaporation rate in a grid or rupture volume is accomplished by using the total droplet surface area, a''_{gf}, in the interphase heat transfer calculation. The micro-droplets influence the movement of average droplets indirectly, by increasing the local steam velocity which increases the drag force on the average droplets. Therefore, in a grid or rupture volume, the average droplet area, a_{gf}, is used in the interphase drag calculation. In other volumes, a_{gf} is used to calculate both interphase drag and interphase heat transfer.

Because the droplet shattering mechanisms at a grid and at a clad rupture location are similar, a model analogous to the grid model is used to calculate the rupture effect on the system thermal-hydraulics. The BWNT model does not yet include the effect of propagation of a second quench front from the rupture location. Additional REBEKA-type experiments would be required to develop an appropriately detailed model to simulate this phenomenon. Currently, the convective enhancement effect at the rupture location is also neglected.

RELAP5/MOD2-B&W (BEACH)[18] was benchmarked against several reflood tests. The selected tests and test conditions are given in Table 1. These tests included electrically-heated rods without gaps using simple or mixing vane grids, electrically heated rods with sleeves to simulate the clad swelling effect, and a REBEKA test. The range of test conditions and blockage factors benchmarked are:

Power	1.31 - 2.36 kW/m
Pressure	0.14 - 0.50 MPa
Clad Temperature	800 - 1166 K
Inlet Subcooling	2.8 - 80 K
Core Flooding Rate	1.5 - 16.5 cm/s
Grid Blockage Fraction	0.0 - 0.55 (-)
Rupture Blockage Fraction	0.0 - 0.51 (-)

The results of some of these benchmarks are discussed in the following sections.

III. FLECHT-SEASET REFLOOD TESTS

The FLECHT-SEASET tests selected for this study are forced reflood tests, done in the 161-rod bundle FLECHT-SEASET test facility.[20] The axial noding, power distribution, and location of grids are shown in Figure 4. The distance between grids was divided into three equal volumes. The bottom elevation of a grid coincided with the bottom elevation of the grid volume. The test inlet conditions were modeled using a time-dependent volume and a time-dependent junction. The test exit conditions were modeled using a single junction and a time-dependent volume. Grid parameters were calculated using a grid blockage ratio of 0.29.

The electrically heated rod was modeled using 21 heated slabs. The axial boundary of a heated slab coincided with the corresponding fluid volume. The cosine power shape was modeled using 21 power steps as shown in

Figure 4. The power to the rod was modeled using a power versus time table.

The measured and predicted quench front elevations and peak cladding temperatures (PCT) for Test 31504 are shown in Figures 5 and 6, respectively. From these figures, it can be seen that RELAP5 predicted the quench front propagation and the PCT variation well for Test 31504. Similar results were obtained for other tests.

IV. G-2 TEST 561

G-2 Test 561[21] was a forced reflood test, conducted in the 82-rod bundle G-2 test facility.[22] The rods were held together using mixing vane grids with approximately 50 percent projected flow area blockage. The RELAP5 input was generated using the same reasoning as that for the FLECHT-SEASET tests.

The measured and predicted quench front elevations and PCTs are shown in Figures 7 and 8, respectively. From these figures, it can be seen that RELAP5 predicted the quench front propagation and the PCT variation well.

V. CCTF TESTS

The Cylindrical Core Test Facility (CCTF)[23,24] is designed to simulate the thermal-hydraulic behavior in the primary system of a four-loop PWR during the refill and reflood phases of a LOCA. Two series of tests, CCTF-I and CCTF-II, were conducted using the facility. Two tests, one from each series, were selected to simulate using RELAP5/MOD2-B&W. Test C1-19[23] (Run 38), a CCTF-I test, had a controlled radial power shape of 1.299 for the central high-power zone, 1.092 for the middle zone, and 0.841 for the peripheral zone. The CCTF-II test C2-6[24] had a flat radial power profile.

In the present study, only the CCTF bundle region was modeled using RELAP5. The RELAP5 model for the CCTF core region is similar to the FLECHT-SEASET model shown in Figure 4. For C1-19 test simulation, the conditions were taken from Reference 23. In the test, the average core inlet flow could not be measured easily. Therefore, the JAERI-estimated average core inlet flow (using a mass balance technique) was used as the flooding rate for the RELAP5 simulation. Because the estimated flooding rate was based on the radially averaged core inlet flow, the rod simulated by RELAP5 had a radial peaking as close to the core average radial peaking as possible. For C2-6 test simulation, the test conditions were taken from Reference 24.

The measured and predicted quench front elevations and PCTs for Test C1-19 are shown in Figures 9 and 10, respectively. From Figure 9, it can be seen that RELAP5 predicted the quench front propagation well. From Figure 10, it can be seen that RELAP5 slightly overpredicted the PCTs in the lower portion of the bundle and significantly overpredicted the PCTs in the upper elevations. Similar results were obtained for Test C2-6.

VI. SCTF Test S3-15

The Slab Core Test Facility (SCTF)[25] is designed to simulate the reflooding phenomena of a full-scale PWR. The SCTF pressure vessel simulates a full radius slab section with the full height of a PWR. The simulated core consists of eight bundles arranged in a row with full radial width. Three series of tests, CORE-I, CORE-II, and CORE-III, were conducted using the facility. CORE-III Test S3-15[26] was selected to simulate using RELAP5/MOD2-B&W because of its inclined radial power distribution. For Test S3-15, the bundles had radial power factors that ranged from 1.36 in Bundle 1 to 0.76 in Bundle 8.

In the present study, only the SCTF bundle region was modeled using RELAP5. The RELAP5 input for Test S3-15 was generated using the same modeling rationale as that for the FLECHT-SEASET tests. Radially, the first bundle was the highest powered bundle and therefore was designated as the "hot channel." The remaining seven bundles were lumped into an "average channel." The hot and average channels were modeled independently; that is, the cross connections between the channels were not modelled.

The measured and predicted quench front progressions for the hot channel are shown in Figure 11. It can be seen that RELAP5 predicted a slower quench front advancement compared with the test. For the average channel, RELAP5 predicted appropriate quench front advancement in the lower portion of the bundle, and slightly faster quench front advancement in the upper portion of the bundle.

The measured and predicted PCTs for the hot channel are shown in Figure 12. It can be seen that RELAP5 slightly overpredicted the PCTs in the lower portion of the bundle and significantly overpredicted the PCTs in the upper elevations. Similar conclusions can also be made from the average channel results.

VII. FLECHT-SEASET BLOCKAGE TEST 61607

Test 61607 was a forced reflood test conducted in the 163-rod bundle FLECHT-SEASET test facility.[14] The fuel rod blockage due to ballooning of the cladding in the vicinity of the rupture location was simulated by installing long non-concentric stainless steel sleeves in two 21-rod bundle islands. The division of the test section into a blockage zone and a bypass zone allowed the effect of flow blockage on flow diversion from the blockage region to the bypass region to be studied. The axial locations of the center of the sleeves varied from 1.75 m to 1.91 m above the bottom of the heated section. The maximum blockage ratio in each blockage island was 0.4106, which occurred at 1.85 m above the bottom of the heated section. The RELAP5 model is similar to the model shown in Figure 4. The blockage parameters, calculated based on a blockage ratio of 0.4106, were added at Node 11 to simulate the blockage.

The measured and predicted quench front elevations and PCTs are shown in Figures 13 and 14, respectively. From these figures, it can be seen that RELAP5 predicted the quench front propagation and the PCT variation well. In Figure 14, the data obtained from the thermocouples located on the rods within the blockage and bypass zones are shown separately. In the vicinity of the blockage (1.67 to 1.98 m), the test results show a reduction in PCT. This indicates that the positive effects of blockage (liquid evaporation mainly by droplet breakup) dominate the effects of flow diversion. RELAP5, with blockage modeled, correctly predicted this behavior. It is to be noted that in this elevation range of the bypass zone, the test results show a reduction in PCT mainly due to flow diversion from the blockage zone.

VIII. REBEKA-6 TEST

The REBEKA-6 test[16] was conducted by Kernforschungszentrum Karlsruhe (KfK), Germany. The test bundle consisted of 48 electrically-heated fuel rod simulators arranged in a 7x7 configuration. An Inconel pipe, 10.75 mm in diameter, was located at the central fuel rod location. The rods were held in position using eight grid spacers of the original Kraftwerk Union (KWU)-PWR geometry with no mixing vanes.

The fuel rod consisted of an external Zircaloy (Zr_4) clad, alumina oxide (Al_2O_3) annular pellets, an Inconel heater rod clad, a boron nitrite insulator, an electrical Inconel heater, and a central magnesium oxide filler. The alumina annular pellets were separated from the internal Inconel heater rod shield and the external Zircaloy clad by 0.05 mm gaps filled with helium. A continuous, cosine-shaped power distribution, with axial peaking of 1.19,

was used to simulate the axial power shape in a nuclear fuel rod. Further details regarding the REBEKA test facility and the REBEKA-6 test are given in References 16 and 27, respectively.

The RELAP5 input was generated using the same modeling rationale as that for the FLECHT-SEASET tests. The transient was simulated using the present methodology selected for PWR analysis. At the predicted rupture time, parameters for the blockage model were added to the rupture node.

A comparison of measured and predicted parameters at the time of rupture is given below.

Parameter	Prediction	Test
Rupture Time (time after reflood initiation),s	25.6	20.0 - 42.0
Clad Rupture Temp.,K	1113.7	978 - 1089
Rupture Pin Pres., MPa	5.97	5.86 - 6.89
Rupture Elevation, m	2.01 - 2.19	1.92 - 2.10
Flow Blockage Fraction, -	0.6547	0.514

The test values given in the above table are for the inner 22 rods. The predicted rupture time, rupture elevation, and pin pressure at the time of rupture are within the scatter of the data. The predicted rupture temperature is slightly higher than the data range. The predicted flow blockage is higher than the measured value.

The measured and predicted PCTs are shown in Figure 15 as a function of elevation. RELAP5 correctly calculated the PCTs up to the rupture elevation (2.13 m). Above the rupture elevation, the code predicted highly conservative PCTs because the blockage and rupture models do not account for the formation and propagation of a second quench front from the rupture location. Additional REBEKA-type experiments would be required to develop appropriately detailed models to simulate this phenomenon.

The formation and propagation of a second quench front from the rupture location can be observed in the measured quench front elevation time history shown in Figure 16. When the rupture elevation (2.06 m) quenched, the primary quench front was at 1.22 m. By the time this quench front reached 1.83 m, the 1.83 to 2.44 m segment of the rod had already quenched. As a result, a shift in the quench front in the upper elevations can be observed that results in earlier quenching. Below the rupture elevation, the predicted quench front is lower than the data because RELAP5 overpredicted the liquid entrainment. Because the code does not model the second quench front, the differences between the data and the prediction continue to increase after rupture.

The thermal-hydraulic effects of grid and rupture models were evaluated by making two separate runs: one by removing the effect at the rupture location and another by removing both the grid and rupture effects. The following conclusions are made from these results. Near the rupture location, the rupture effect is dominant compared with the grid effect in reducing cladding temperature. The rupture effect diminishes as the distance from the rupture location increases. However, the grid effect increases as the distance of the grid from the bottom of the test section increases. This is due to the impact Weber Number effect discussed earlier. These results show that, for the REBEKA-6 test, the combined effect of the grid and rupture models is the reduction of cladding temperatures by as much as 70 K in the upper elevations. In PWR fuel assemblies with mixing vane grids, the magnitude of the temperature reduction will be higher than 70 K. This effect will be further amplified as the

cladding temperature reaches 1255 K (1800 F) where the metal-water reaction becomes significant. The predicted cladding temperatures could be further reduced by modeling the propagation of a second quench front from the rupture location.

IX. CONCLUSIONS

The RELAP5 code, with grid and blockage models, was benchmarked against several FLECHT-SEASET forced reflood tests, CCTF Tests C1-19 and C2-6, SCTF Test S3-15, G2 Test 561, the FLECHT-SEASET forced reflood blockage test 61607 and the REBEKA-6 test. The FLECHT-SEASET and G2 test benchmarks demonstrate that RELAP5/MOD2-B&W, with the grid model, will calculate the quench front propagation and the PCT variations well for forced reflood tests with simple and mixing vane grids. The CCTF and SCTF benchmarks show that RELAP5/MOD2-B&W will calculate proper quench front variations and conservative PCT variations for integral reflood tests. The FLECHT-SEASET test 61607 benchmark demonstrates that the blockage model added to RELAP5 correctly and conservatively calculates the blockage effects in a nuclear fuel rod, including flow diversion and droplet breakup.

The REBEKA-6 test shows that the occurrence of rupture enhances rather than inhibits core quenching during the reflooding phase of LOCA. For this test, RELAP5 correctly predicted cladding temperatures below the rupture location. Above the rupture location, the predicted temperatures were significantly higher than the data because the modeling does not account for the formation and propagation of the second quench front observed in the test. From a sensitivity of the grid and rupture models, it was found that for the REBEKA-6 test, these models account for a cladding temperature decrease by as much as 70 K. This value will be considerably higher in a PWR where mixing vane grids are used. This study has demonstrated the need to model the thermal-hydraulic effects due to grids and clad swelling and rupture to correctly predict the clad temperature response during the reflood phase of a large- break LOCA.

ACKNOWLEDGEMENT

The authors wish to thank Dr. F. E. Erbacher of KfK, Germany and Dr. K. H. Ardron of Nuclear Electric,PIC, UK for providing information related to the REBEKA program and the REBEKA-6 test.

REFERENCES

1. S. L. Lee, S. K. Cho, K. Rob, H. J. Sheen, and M. Aghile, "An LDA In Situ Study of Droplet Hydrodynamics Across Grid Spacers in PWR-LOCA Reflood," NUREG/CP-0041, pp. 253-274, January 1983.

2. S. L. Lee, S. K. Cho, and H. J. Sheen, "A Study of Droplet Hydrodynamics Across a Grid Spacer," NUREG/CR-4034, November 1984.

3. S. C. Yao, L. E. Hochreiter, and K. Y. Cai, "Dynamics of Droplets Impacting on Thin Heated Strips," paper presented at the National Heat Transfer Conference Held in Denver, Colorado on August 4-7, 1985.

4. J. Sugimoto and Y. Murao, "Effect of Grid Spacers on Reflood Heat Transfer in PWR LOCA," J. Nucl. Sci. Technol., pp. 103-114, February 1984.

5. L. H. J. Wachters and N. A. J. Westerling, "The Heat Transfer From a Hot Wall to Impinging Water Drops in the Spheroidal State," Chem. Eng. Sci., 21, pp. 1047-1056, 1966.

6. L. H. J. Wachters, L. Smulders, J. R. Vermeulen, and H. C. Kleiweg, "The Heat Transfer from a Hot Wall to Impinging Mist Droplets in the Spheroidal State," Chem. Eng. Sci., 21, pp. 1231-1238, 1966.

7. J. Chiou, L. E. Hochreiter, D. B. Utton, and M. Y. Young, "Spacer Grid Heat Transfer Effects during Reflood," NUREG/CP-0043, 1982.

8. C. Y. Paik, et al., Analysis of FLECHT-SEASET 163-Rod Blocked Bundle Data Using COBRA-TF, NRC/EPRI/Westinghouse Report No. 15, NUREG/CR-4166, October 1985.

9. P. Clement, R. Deruaz, and J. M. Veteau, "Reflooding of a PWR Bundle - Effect of Inlet Flowrate Oscillation and Spacer Grids," NUREG/CR-0027, pp. 1763-1770, February 1983.

10. J. M. Veteau, P. Clement, and R. Deruaz, "Reflooding of a PWR Bundle: Effect of Spacer Grids," NUREG/CP-0048, pp. 390-401, January 1984.

11. P. Ihle and K. Rust, "FEBA - Flooding Experiments With Blocked Arrays Evaluation Report," KfK 3657, March 1984.

12. P. Ihle and K. Rust, "Grid Spacer Effects on PWR Reflood Heat Transfer Measured in Bundle of 5x5 Rods With Zircaloy Cladding and Pellets," paper presented at the National Heat Transfer Conference held in Denver, Colorado on August 4-7, 1985.

13. J. M. Kelly and R. J. Kohrt, "COBRA-TF Flow Blockage Heat Transfer Programs," NUREG/CP-0048, pp. 211-232, January 1984.

14. M. J. Loftus, et al., PWR FLECHT-SEASET 163-Rod Bundle Flow Blockage, Task Data Report, NRC/EPRI/Westinghouse Report No. 13, NUREG/CR-3314, October 1983.

15. M. J. Loftus, et al., PWR FLECHT-SEASET 21-Rod Bundle Flow Blockage Task Data and Analysis Report, NUREG/CR-2444, September 1982.

16. K. Wiehr, REBEKA - "Bundelversuche Untersuchungen zur Wechselwirkung zwischen aufblahenden Zircaloyhullen und einsetzender Kernnotkuhlung," KfK 4407, May 1988.

17. RELAP5/MOD2-B&W: An Advanced Computer Program for Light Water Reactor LOCA and Non-LOCA Transient Analysis, BAW-10164, Babcock & Wilcox, Lynchburg, Virginia.

18. BEACH: A Computer Program for Reflood Heat Transfer During LOCA, BAW-10166, Babcock & Wilcox, Lynchburg, Virginia, April 1988.

19. S. C. Yao, L. E. Hochreiter, and W. J. Leech, "Heat Transfer Augmentation in Rod Bundles Near Grid Spacers," Trans. ASME, 104, pp. 76-81, February 1982.

20. M. J. Loftus, et al., PWR FLECHT SEASET Unblocked Bundle, Forced and Gravity Reflood Task: Data Report, Volume 1 and 2, NRC/EPRI/Westinghouse Report No. 7, NUREG/CR-1532, June 1980.

21. G. Collier, et al., BART-A1: A Computer Code for the Best Estimate Analysis of Reflood Transients, WCAP-9561, January 1980.

22. T. S. Andreychek, et al., Blowdown Experiments With Upper Head Injection in G-2 17x17 Rod Array Facility, WCAP-8642, 1976.

23. Y. Murao, et al., Evaluation report on CCTF Core-I Reflood Test C1-19 (Run 38) Experimental Assessment of the Evaluation Model for the Safety Analyses on the Reflood Phase of a PWR-LOCA, JAERI-M 83-029, February 1983.

24. H. Akimoto, et al., Evaluation Report on CCTF Core-II Reflood Test C2-6 (Run 64) Effect of Radial Power Profile, JAERI-M 85-027, March 1985.

25. H. Adachi, et al., Design of Slab Core Test Facility (SCTF) in Large Scale Reflood Test Program, Part III: Core-III, JAERI-memo 62,110, 1987.

26. T. Iwamura, et al., Evaluation Report on SCTF Core-III Tests S3-14, S3-15, and S3-16, JAERI-memo 62-329, 1987.

27. K. Wiehr, and U. Harten, Datenbericht REBEKA-6, KfK3986, March 1986.

Table 1. RELAP5 Benchmark Test Conditions.

Test Facility	Test No.	Flooding Rate mm/s	Pressure mPa	Rod Power kW/m	Clad Temp. K	Coolant Temp. K
FLECHT-SEASET	31504	24.0	0.28	2.3	1136.0	324.0
	31805	21.0	0.28	2.3	1114.0	324.0
	30817	38.6	0.27	2.3	804.0	326.0
	31302	76.5	0.28	2.3	1142.0	325.0
	32333	162.0-21.0*	0.28	2.3	1162.0	325.0
	34209	27.2	0.14	2.4	1162.0	305.0
	61607	21.0	0.28	2.3	1151.0	326.0
CCTF	C2-6	53.3-15.5*	0.29-0.2*	1.5	992.0	374.0-398.0*
	C1-19	33.5-17.5*	0.30-0.27*	2.3	1046.0	372.0-398.0*
SCTF	S3-15	Variable	0.20	1.9	1073.0	Variable
G-2	561	25.4	0.14	1.8	1033.0	316.0
REBEKA	6	30.0	0.41-0.50*	2.0	1038.0	Variable

* Variable

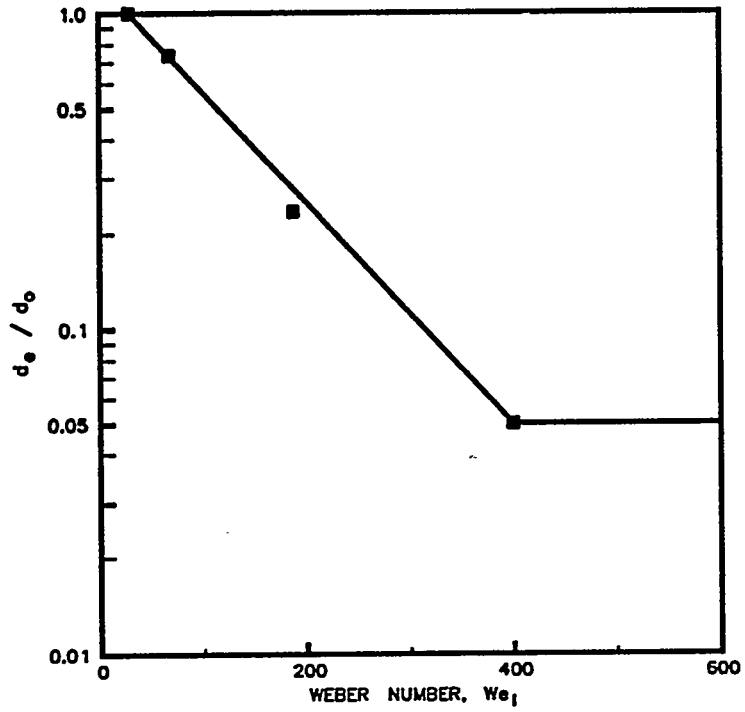


FIGURE 1. RATIO OF SHATTERED DROPLET DIAMETER TO ORIGINAL DROPLET DIAMETER AS A FUNCTION OF DROPLET WEBER NUMBER. [7]

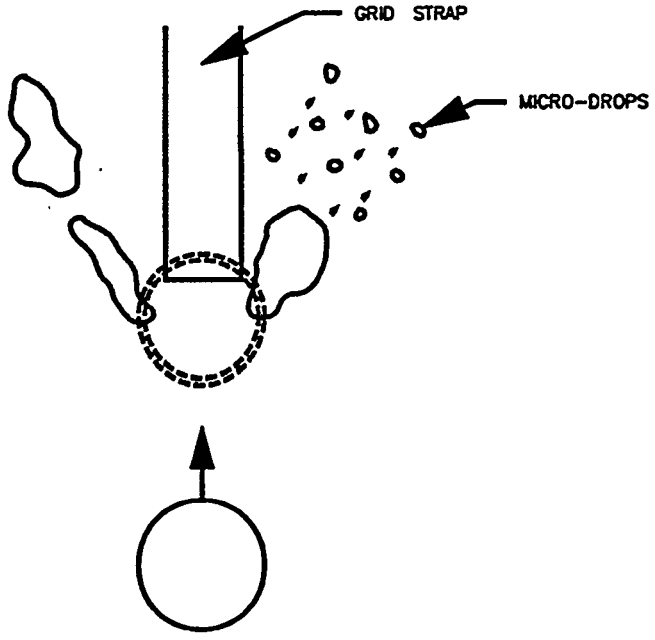


FIGURE 2. SCENARIO OF DROPLET BREAKUP ON A HEATED STRAP. [3]

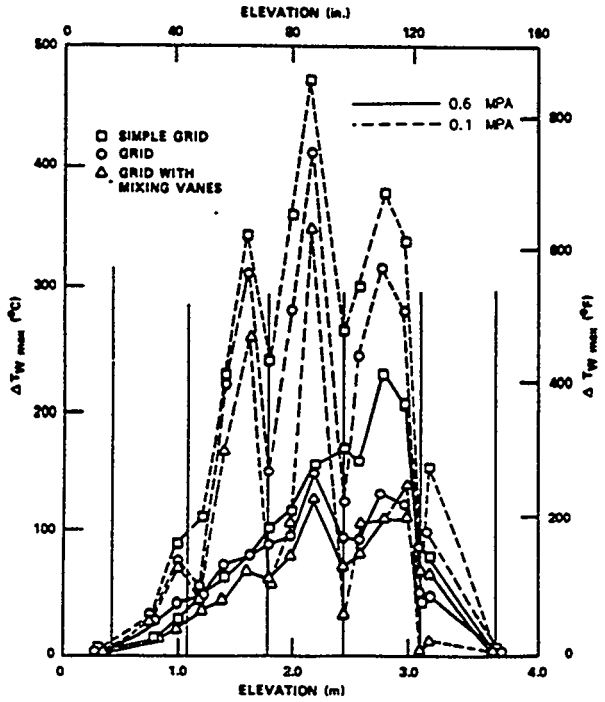


FIGURE 3. COMPARISON OF ΔT_{Wmax} FOR THREE TYPES OF SPACER GRIDS AT P = 0.1 AND 0.6 MPA IN ERSEC TESTS.[9]

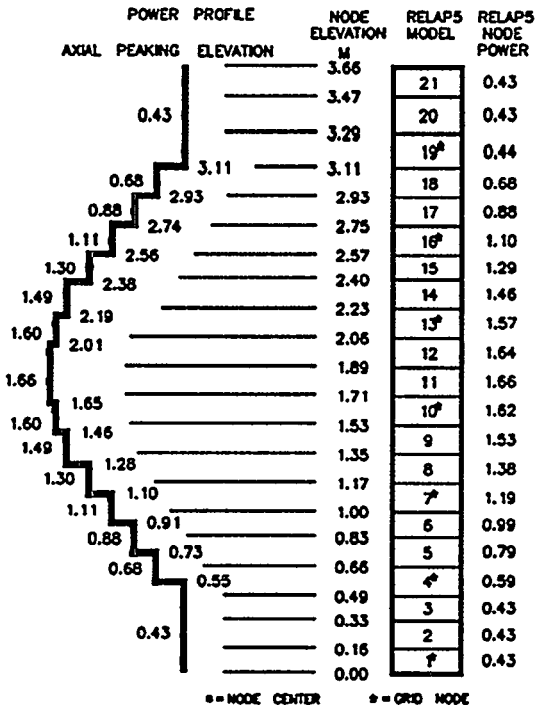


FIGURE 4. AXIAL NODING AND POWER DISTRIBUTION FOR FLECHT-SEASET TEST.

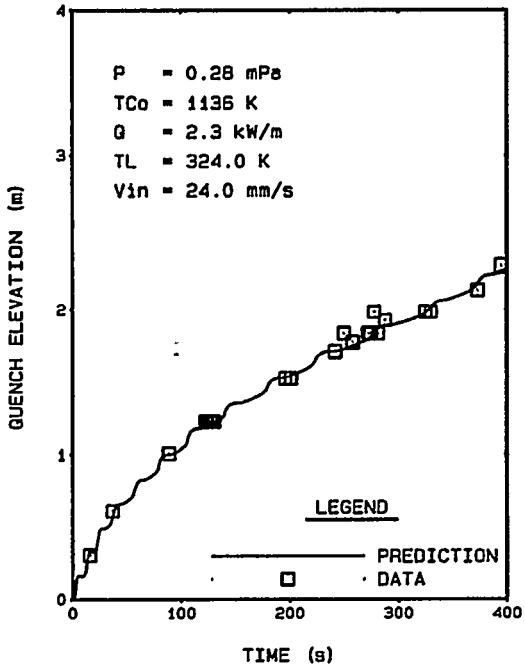


FIGURE 5. QUENCH FRONT - FLECHT-SEASET TEST 31504

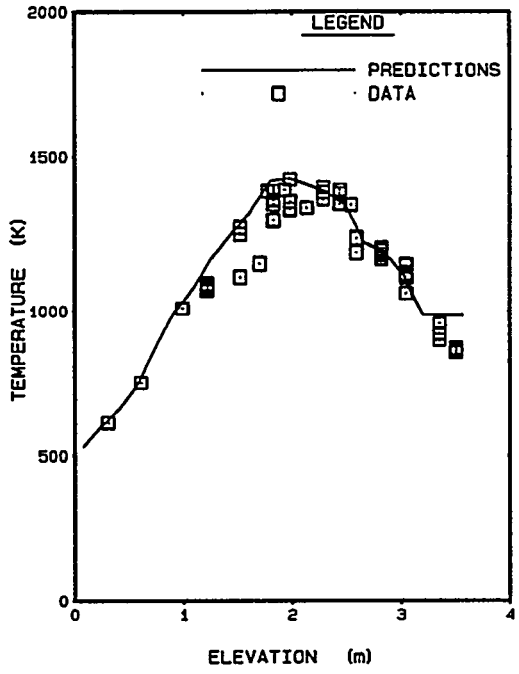


FIGURE 6. PEAK CLAD TEMPERATURE - FLECHT-SEASET TEST 31504

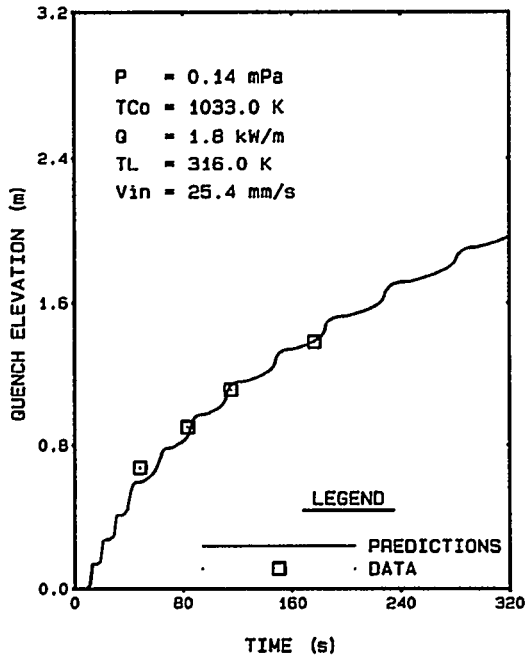


FIGURE 7. QUENCH FRONT - G-2 TEST 561.

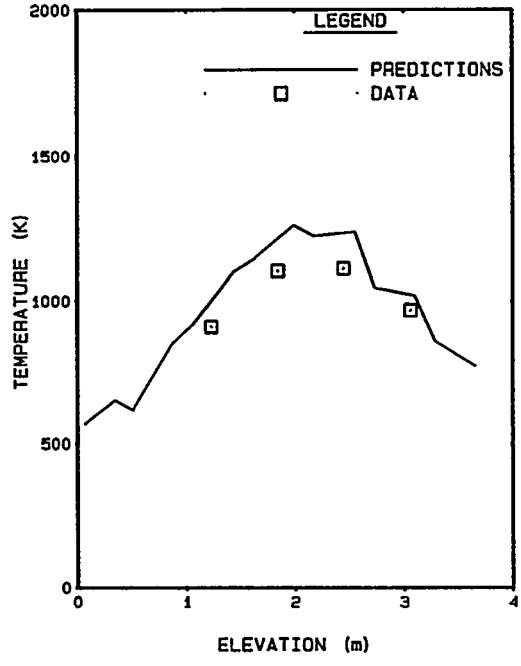


FIGURE 8. PEAK CLAD TEMPERATURE - G-2 TEST 561.

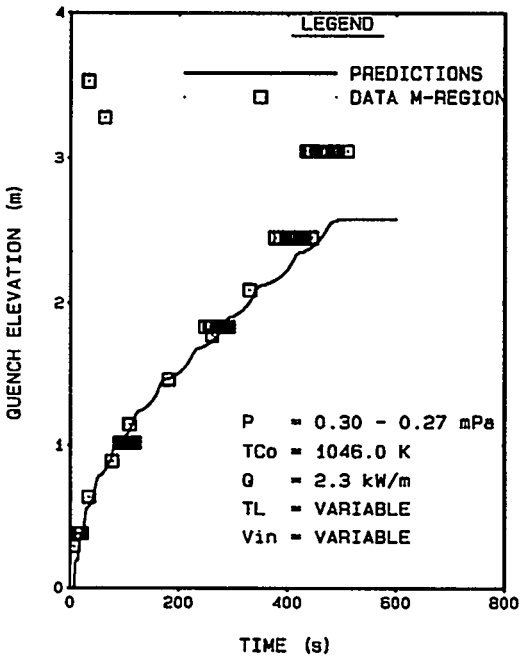


FIGURE 9. QUENCH FRONT - CCTF TEST C1-19.

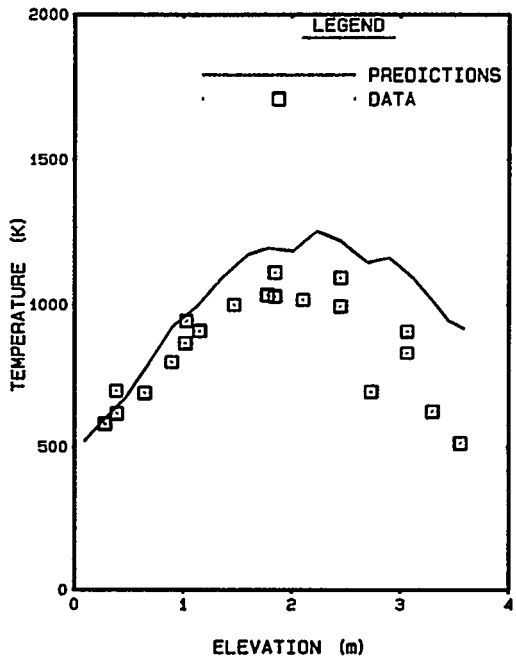


FIGURE 10. PEAK CLAD TEMPERATURE - CCTF TEST C1-19.

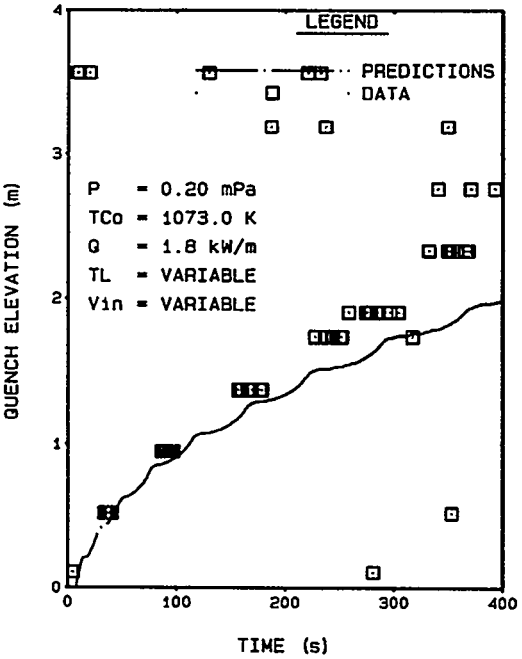


FIGURE 11. QUENCH FRONT - SCTF TEST S3-15.

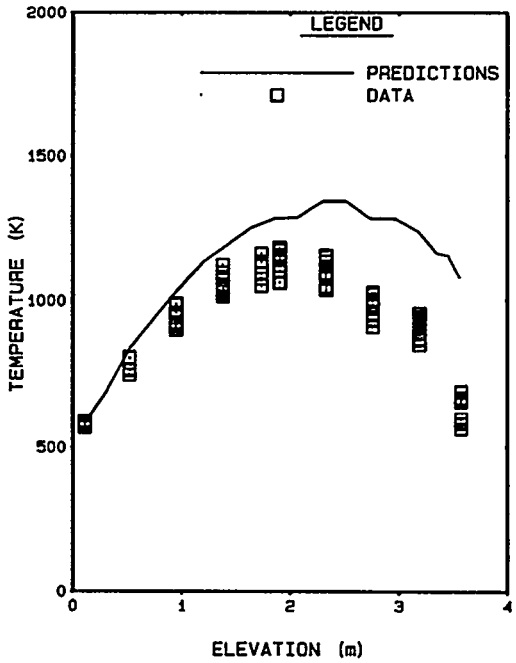


FIGURE 12. PEAK CLAD TEMPERATURE - SCTF TEST S3-15.

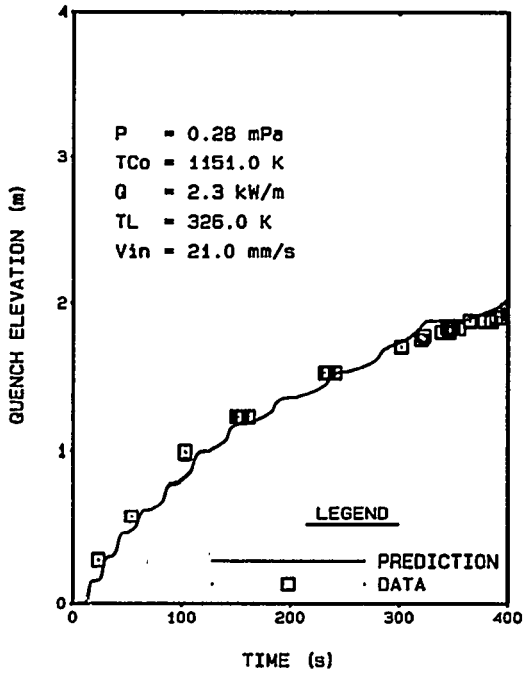


FIGURE 13. QUENCH FRONT - FLECHT-SEASET TEST 61607.

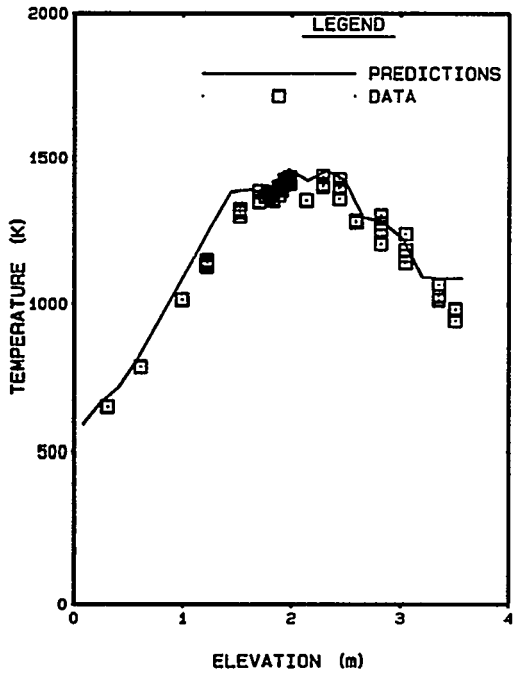


FIGURE 14. PEAK CLAD TEMPERATURE - FLECHT-SEASET TEST 61607.

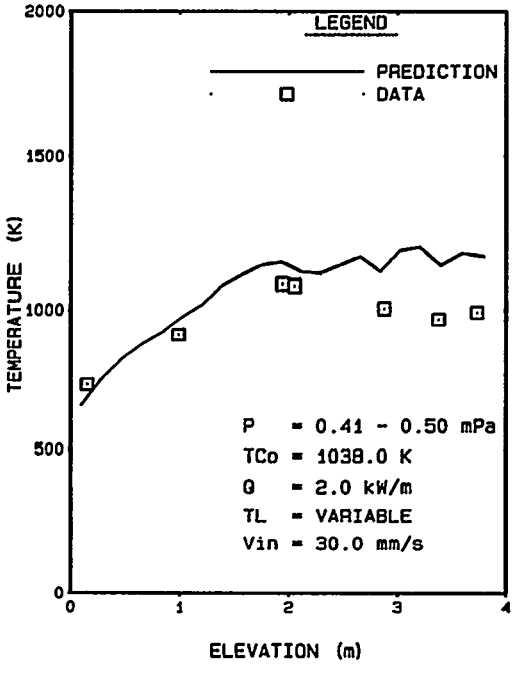


FIGURE 15. PEAK CLAD TEMPERATURE - REBEKA-6 TEST.

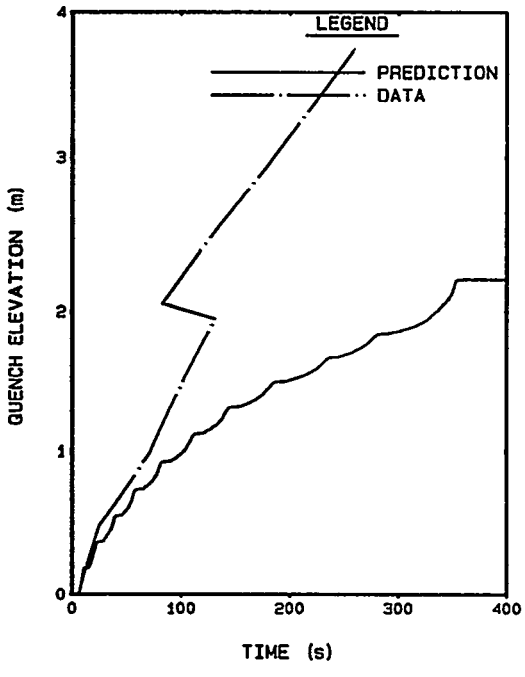


FIGURE 16. QUENCH FRONT - REBEKA-6 TEST.

VALIDATION OF ADVANCED NSSS SIMULATOR MODEL FOR LOSS-OF-COOLANT ACCIDENTS

by

S. P. Kao, S. K. Chang, H. C. Huang
Nuclear Training Branch, Northeast Utilities
Waterford, CT, U.S.A.
and
A. Chyra, J. Spalter
Safety Analysis Branch, Northeast Utilities
Berlin, CT, U.S.A.

ABSTRACT

The replacement of the NSSS (Nuclear Steam Supply System) model on the Millstone 2 full-scope simulator has significantly increased its fidelity to simulate adverse conditions in the RCS. The new simulator NSSS model is a real-time derivative of the Nuclear Plant Analyzer by ABB. The thermal-hydraulic model is a five-equation, non-homogeneous model for water, steam, and non-condensible gases. The neutronic model is a three-dimensional nodal diffusion model. In order to certify the new NSSS model for operator training, an extensive validation effort has been performed by benchmarking the model performance against RELAP5/MOD2. This paper presents the validation results for the cases of small- and large-break loss-of-coolant accidents (LOCA). Detailed comparisons in the phenomena of reflux-condensation, phase separation, and two-phase natural circulation are discussed.

1. INTRODUCTION

The staff at the Northeast Utilities' (NU) Nuclear Training Branch has upgraded the NSSS model on the Millstone 2 simulator in compliance with the ANSI 3.5 standards [1] for nuclear training simulators. Because NU plans to use the same NSSS model on all four PWR simulators operated by the utility, a rigorous benchmark/validation test program has been performed. The RELAP5/MOD2 [2] results obtained by the staff at the Safety Analysis Branch of NU are the basis for these benchmark tests.

The new simulator NSSS model is supplied by ABB's Plant Process Control division. The ABB/NSSS model is a real-time version of the Nuclear Plant Analyzer [3]. The thermal-hydraulic model for the Reactor Coolant System is a five-equation, non-homogeneous, non-equilibrium model for water, steam, and non-condensible gases. The conservation equations of water mass, total mixture mass,

steam/gas energy, total mixture energy, and the total mixture momentum for the RCS flowpath network are linearized and solved by an implicit algorithm using backward differentiation. The core neutronic model is based on space-time separation of the neutron kinetics equation in which the time-dependent amplitude function is solved axially and the spatial shape function is solved in the three-dimensional sense [4].

2. MODEL INPUT DATA CALCULATION

The input data of RELAP5/MOD2 model for Millstone 2 has been used to derive the plant parameters for the ABB/NSSS model. This is done in order to minimize discrepancies between the two models. The Millstone 2 control-volume diagrams for the ABB/NSSS and RELAP5 model input are shown in Figures 1 and 2, respectively. The nodalization for the ABB/NSSS model is more than three times coarser than that of RELAP5. In the ABB/NSSS nodalization scheme, the upper-plenum and core volumes are combined into one pressure node. The core region consists of 10 axial thermal nodes. The downcomer and lower plenum of the reactor vessel are combined into one control volume. The two suction legs in each RCS loop are lumped into one control volume. The coarse-nodal approach used in the ABB/NSSS model is necessary to meet the computational requirement for real-time simulation on a SUN SPARCstation. A control-volume collapsing scheme has been applied to derive the input data for the ABB/NSSS model using the RELAP5 input data. For example, the friction and loss factors are collapsed by averaging over the flowpath lengths. By lumping the core and upper plenum together as a single node, a well-defined level can be calculated for the water inventory inside the core shroud. The effect of using coarse-node approximation leads to averaging of mass and energy profiles within each node, thus, reducing the resolution of fluid property distributions within the RCS.

The neutronic input parameters for the ABB/NSSS model are determined by collapsing the results calculated by Siemen's XTG fuel reload analysis code. They include the three-dimensional nodal power and k-infinitive distribution profiles, control rod bank worth, boron, moderator, and fuel temperature coefficients. Neutronic parameters for three core burnup conditions have been calculated for the beginning, middle, and end of Cycle 12 of the Millstone 2 core [5].

3. INITIAL AND BOUNDARY CONDITIONS

A steady-state calculation has been performed to obtain a hot-full-power, middle-of-cycle initial condition for each model. During the process, the results of the ABB/NSSS model have been tuned to match those of RELAP5. The steady-state conditions established for both models are taken to be the initial conditions for all benchmark tests.

The boundary conditions for both models are controlled to match as closely as possible by using tables and control functions. Most of the RCS control systems have been disabled, except the pressurizer pressure control system. The turbine bypass and steam dump control functions have been implemented in both models. The steam generator feedwater flow is provided as a boundary condition. The HPSI, LPSI, and accumulator flows are calculated by linear interpolation of tables given as functions of RCS pressure. The containment pressure responses are determined via tables given as functions of time.

4. BENCHMARK TEST PROGRAM

The ABB/NSSS model benchmark test program is based on the simulator certification program designed to meet the ANSI 3.5 standards. The benchmark test program consists of ten transients and loss-of-coolant accidents as follows:

- Manual Reactor Trip,
- Trip of One Reactor Coolant Pump,
- Trip of All Reactor Coolant Pumps,
- Closure of All MSIVs,
- Main Steamline Break Outside Containment,
- Stuck-open Pressurizer PORV,
- Feed and Bleed,
- Steam Generator Tube Rupture,
- Small-break LOCA, and
- Large-break LOCA.

The test program begins with operational transients then makes transition to loss-of-coolant accidents. For each test case, several runs of the ABB/NSSS model have to be performed in order to closely match the boundary conditions, such as the initial break flow rate and the PORV discharge flow rate. While performing the LOCA tests, the ABB/NSSS model had to be tuned in order to match the RELAP5 predictions. Adjustments were made by changing the value of tuning factors for the core heat transfer coefficients, rate of condensation and flashing, and the transport admittance of non-condensible gases.

All of the above tests have been successfully completed. Only the test results from the small- and large-break LOCA cases are discussed in this paper.

5. SMALL-BREAK LOCA TEST RESULTS

The small-break LOCA case assumes that the break is two inches in diameter located in the Loop 2A cold leg and centered at the mid-plane. It is assumed that total loss-of-offsite-power occurs at the time of reactor trip, and that only one safety injection train is functional. The reactor trip is assumed to be caused by

the Thermal Margin/Low Pressure trip, which has been set at 1812 psia. Furthermore, it is assumed that there is no auxiliary feedwater flow to the steam generators.

At the onset of the break, the pressurizer pressure decreases rapidly as shown in Figure 3. At 46 seconds, the reactor is tripped. After the reactor trip, the pressurizer pressure drops precipitously to 1400 psia and then slowly stabilizes to around 1000 psia, the saturation pressure in the upper head. The slowing down in depressurization is a result of steam voiding in the reactor vessel upper head and upper plenum and the initiation of safety injection flow.

The results of the two models are in close agreement for the first 100 seconds of the transient. After that, the ABB/NSSS model deviates from RELAP5 such that the RCS repressurizes to about 1380 psia before stabilizing down to 1010 psia. During the same period, the RELAP5 results show a gradual and continuous depressurization.

During the period from 100 to 400 seconds, the RELAP5 calculation shows that the break flow exceeds the HPSI flow and the break flow removes enough stored energy and decay heat to prevent a repressurization of the RCS. This net loss of mass persists until the water level in the broken loop falls below the break elevation and steam begins to discharge through the break. At about 1200 seconds, an equilibrium condition is established in the RCS when the break flow is balanced by the HPSI flow. Then the RCS pressure is stabilized at the hot-leg saturation pressure around 1000 psia and decreases slowly.

The repressurization predicted by the ABB/NSSS model can be explained by two observations. First, the break flow averages about 20% less than RELAP5's prediction, as shown in Figure 4; hence, less energy is being removed from the RCS. Second, the natural circulation flow rate, as shown in Figure 5, is about 40% less than predicted by RELAP5. These two factors yield a higher hot-leg temperature, as shown in Figure 6, and result in a brief repressurization of the RCS in the ABB/ NSSS calculation.

At least four flow regimes can be identified during the course of this transient based on the calculations of both models. After all four RCPs are tripped, the forced single-phase flow coasts down to a stable, two-phase natural circulation flow. Voids in the RCS continue to build while the break flow exceeds the safety injection flow. The stable two-phase natural circulation lasts for about 600 seconds as calculated by RELAP5. Eventually, the two-phase natural circulation flow reduces to zero when steam binding occurs in both steam generator U-tubes. Then, the RCS loops exhibit an oscillatory flow pattern which resembles the reflux-condensation flow regime. After one half of the RCS loop seals are cleared, the flow in the RCS transforms to mostly single-phase-steam mixed convection.

In the ABB/NSSS calculation, a long period (600 seconds) of unstable, two-phase natural-circulation flow oscillation is observed before the reflux-condensation takes place. At 1500 seconds, the loop seal in the broken loop is cleared for steam passage, and the mostly-steam mixed convective flow is established.

For the small-break LOCA test case, the ABB/NSSS model yields a more conservative prediction than RELAP5. This is evident by a brief repressurization of the RCS, a higher hot-leg temperature, a longer time to clear the RCS loop seals, and a higher peak-clad-temperature (not shown) in the ABB/NSSS calculation. These are results of a lower two-phase natural circulation flow rate and a smaller break flow rate calculated by the model.

6. LARGE-BREAK LOCA TEST RESULTS

In the large-break LOCA case, the break is introduced in a ramped fashion rather than an instantaneous break assumed by the licensing analysis. Upon the inception of break, the break expands linearly from an initial area of 0.5 sq. ft. to a final area of 5.94 sq. ft. over 23 seconds. This method of introducing a large-break LOCA is applied because of the numerical instability imposed by the ABB's thermal-hydraulic model running with a fixed time-step-size of 0.1 seconds.

In RELAP5, the break flow is modeled as two flow junctions, each assumes one-half of the total break area. The break opening is simulated with two motor-operated valves with a stroke time of 23 seconds.

In this test case, it is postulated that the reactor is tripped at 0.5 seconds after the initiation of the break; loss of offsite power immediately follows the reactor trip, cutting AC power to all four RC pumps; and only one train of safety injection pumps is assumed operational. On the secondary side, it is assumed that the atmospheric steam dump valves and the condenser steam dump valves are not operable; the main feedwater flow is ramped down to zero after the reactor trip and the auxiliary feed flows never come on; and the containment pressure is given as a function of time.

The results from both models are recorded and analyzed for the first 120 seconds of the transient. The ramped break were milder than an instantaneous guillotine break in terms of rate of depressurization. According to RELAP5's calculation as shown in Figure 7, the RCS pressure decreases to 1600 psia within two seconds after the break is introduced. The depressurization then slows down to a rate of about 45 psi per second due to flashing of water to steam in the upper plenum and hot leg regions. The depressurization rate increases to about 85 psi per second when all four RCS loop seals are cleared occurred at 24 seconds, as shown in Figure 8. The RCS is completely depressurized in 32 seconds. The core

pressure actually decreases below the containment pressure for about six seconds. This is caused by excessive steam condensation inside the reactor vessel due to the safety injection flows.

The ABB/NSSS model calculates a slightly longer depressurization time, which lasts 35 seconds. This can be attributed to a smaller two-phase critical flow through the break calculated by the model.

The collapsed water level in the core calculated by RELAP5 is shown in Figure 9. (Note that the water level in the upper plenum calculated by RELAP5 is not shown.) Void in the core begins to form almost immediately at the break inception. At 29 seconds, the core is totally voided. Core reflood due to SI tank injection commences at 39 seconds. The water level reaches the top of core is at about fifty-one seconds, and then the core level is shown as a straight line at 12 feet.

The mixture level in the upper plenum and core region calculated by the ABB/NSSS model is plotted on the same figure (Fig. 9). The void starts to form in this region at 3 seconds. The mixture level decreases to below the top of core (12 feet) at 23 seconds, and the core is virtually voided at about 26 seconds. Core reflood commences at 45 seconds. The core is completely recovered at around 68 seconds. Then, the mixture level exhibits a small oscillatory behavior in the upper plenum region. This level oscillation is driven by a small pressure oscillation caused by steam condensation due to subcooled HPSI injection.

The predicted void fractions in the loop seal of the broken loop are shown in Figure 8. Both models predict that the loop seal is cleared at about 24 seconds, and it remains cleared for the initial 120 seconds. The same is true for the intact loop.

The fuel cladding surface temperature profiles at several core elevations are plotted in Figure 10. During the period of uncovered core, the cladding surface temperatures increase by more than 100 degree F at the upper and mid-core locations as calculated by ABB/NSSS, as compared to a 100-degree F increase by RELAP5. The propagation of quench front is evident by a sudden drop in the cladding surface temperatures. The core heatup predicted by the ABB/NSSS model is consistently higher than that of RELAP5 for all core elevations. It has been determined that the calculated post-DNB heat transfer coefficient of ABB/NSSS is consistently lower than that of RELAP5.

After recovery, the decay heat is removed through boiling. The boiled off water inventory in the core is amply replaced with the safety injection.

7. CONCLUSIONS

An advanced NSSS model for real-time simulation supplied by ABB has been benchmarked against the RELAP5 calculations for a wide range of transients including the small- and large-break LOCAs. The results of ABB/NSSS model in these tests closely matched those obtained by RELAP5 in most cases. For those instances where the two models deviated, the causes were explained and documented.

In the small-break LOCA case, both models predict flow regimes transition from forced single-phase-liquid flow to two-phase natural circulation flow, then to reflux-condensation, and finally, to steam mixed-convection.

In the large-break LOCA case, both models predict the same depressurization rate and time to clear loop seals. Both models also predict a core uncovering which lasts for about 50 seconds. The subsequent reflood quickly quenches the heatup in the core, thus maintains the integrity of the fuel.

However, the ABB/NSSS model consistently calculates a lower critical break flow rate than that of RELAP5 in both LOCA cases. In addition, the ABB/NSSS model exhibits a more pronounced RCS flow oscillation under the two-phase, natural circulation condition. This may be a result of coarse-node numerical scheme adopted by the ABB/NSSS model. Finally, the ABB/NSSS model gives a more conservative result which yields a higher peak-clad-temperatures than that of RELAP5/MOD2 in both the small- and large-break LOCA cases.

8. REFERENCES

[1] "Nuclear Power Plant Simulators for Use in Operator Training and Examinations," ANSI/ANS-3.5-1993.

[2] V. H. Ramsom, et al., "RELAP5/MOD2 Code Manual," NUREG/CR-4312, August 1985.

[3] R.J. Espinosa, S. Leichtberg, "First Principles Simulation of Events During Mid-Loop Operation of A PWR Using ABB's NPA," 1994 SCS Simulation Multiconference, San Diego, California, April 11-15, 1994.

[4] S.G. Wagner, A.T. Shesler, G. Lenhardt, and M.M. Tolmazin, "A Three Dimensional BWR Core Neutronics Model for Real-Time Simulation," XIV Spanish Nuclear Society Meeting, Marbella, Spain, 1988.

[5] "Millstone Unit 2, Cycle 12, Startup and Operations Report," Siemens Power Corp., Oct. 1992.

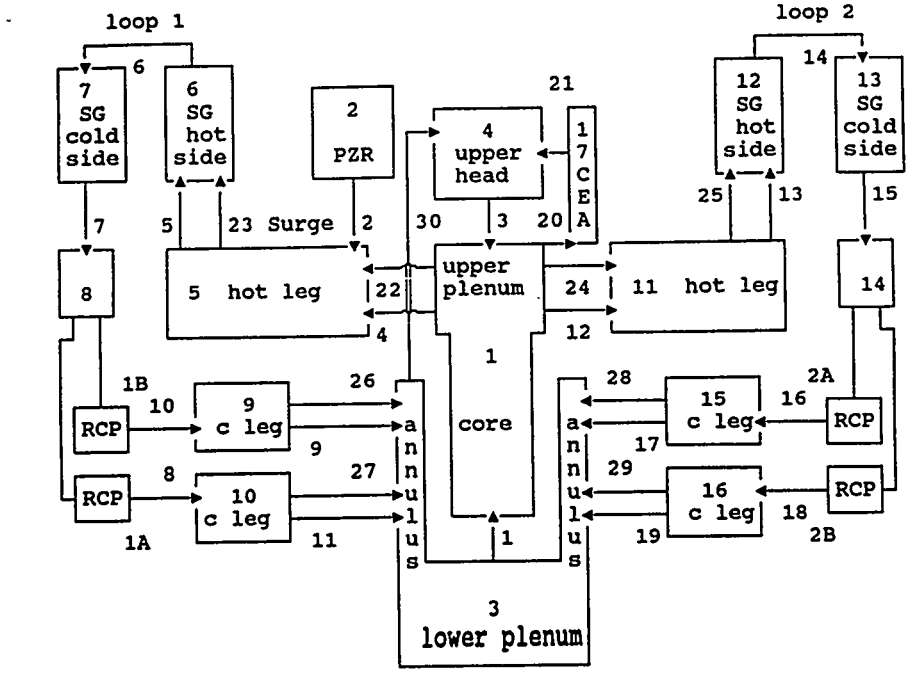


Figure 1 ABB/NSSS Noding Diagram for Millstone 2

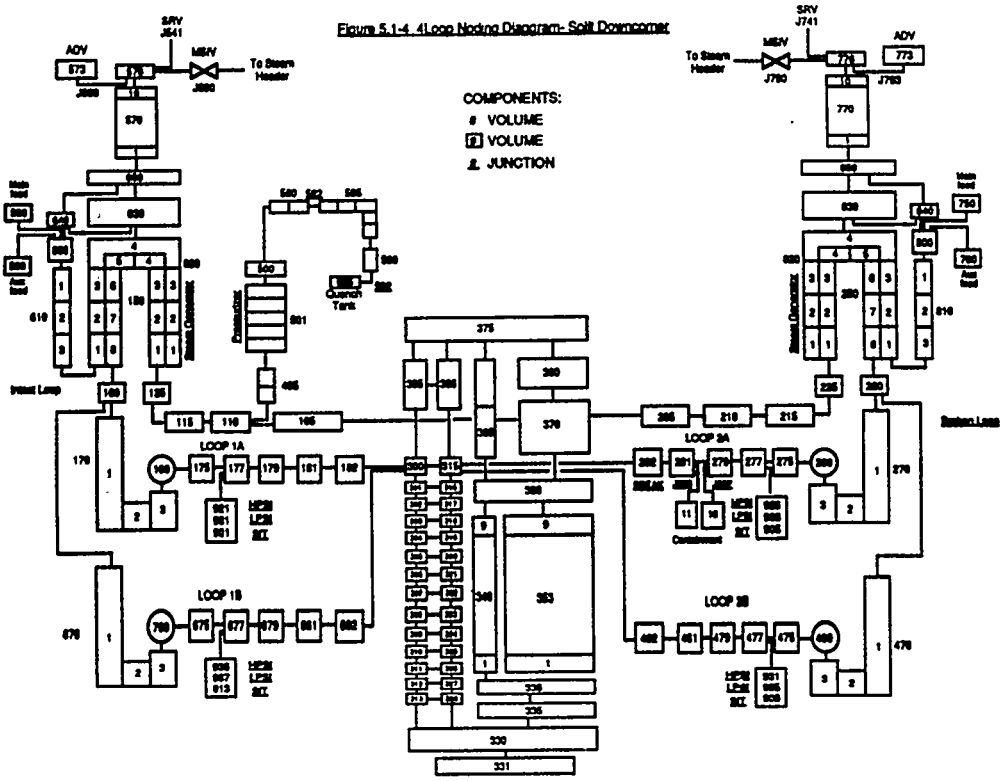


Figure 2 RELAP5/MOD2 Noding Diagram for Millstone 2

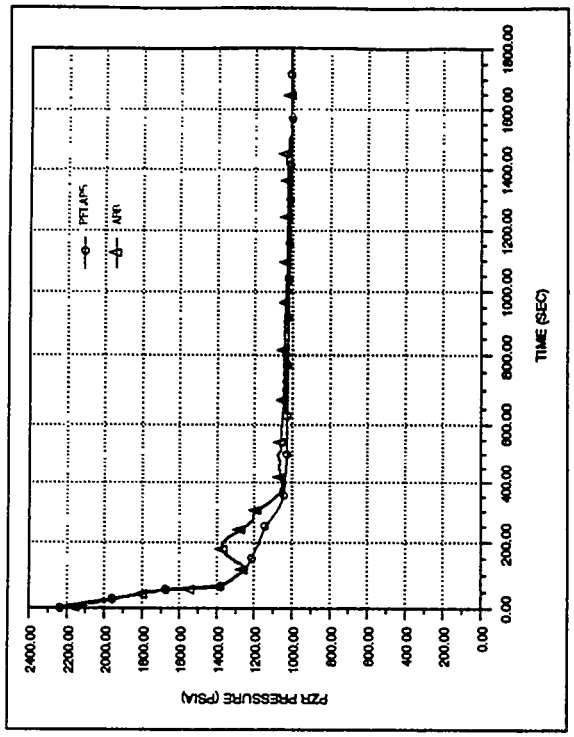


Figure 3 Small-break LOCA
Pressurizer Pressure (psia)

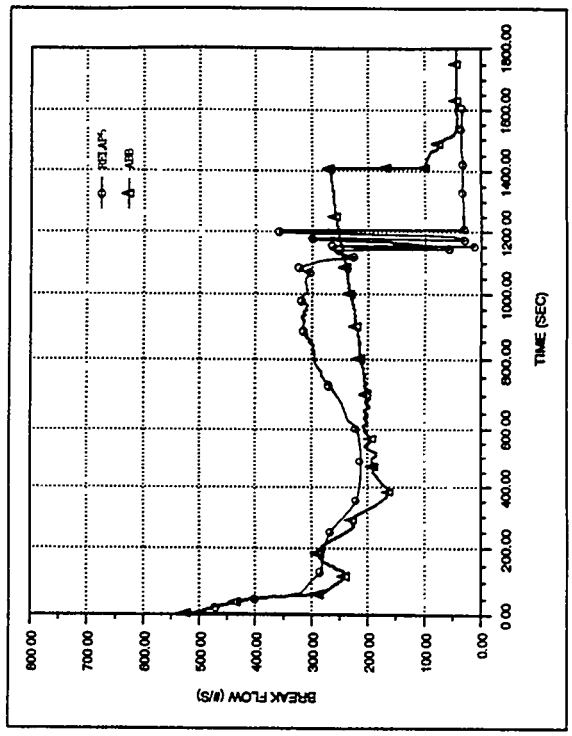


Figure 4 Small-break LOCA:
Break Flow Rate (lbm/s)

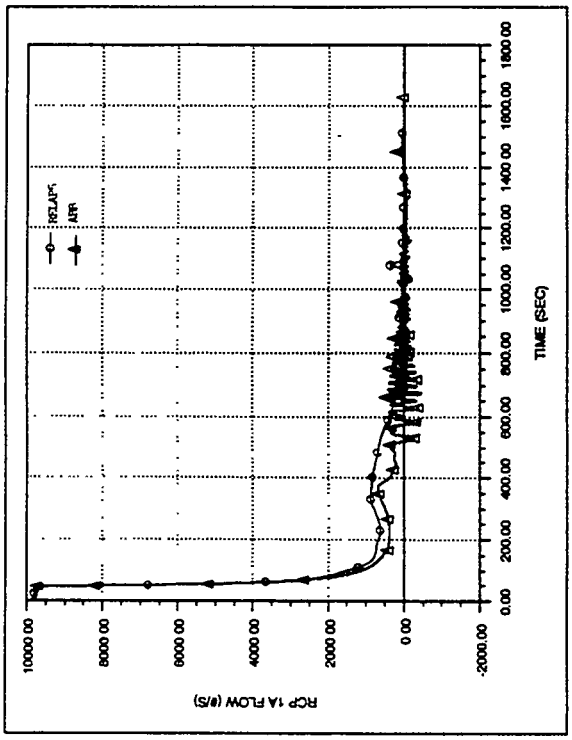


Figure 5 Small-break LOCA
Loop 1A Flow Rate (lbm/s)

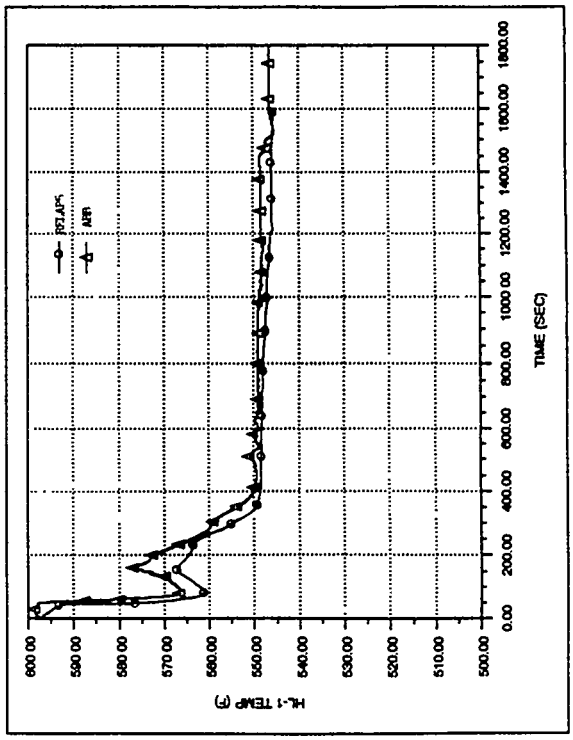


Figure 6 Small-break LOCA:
Hot-leg Temperature (F)

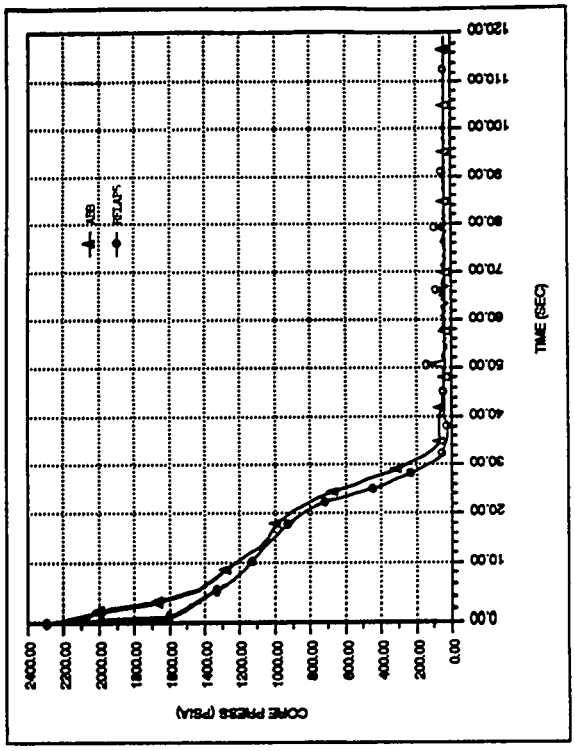


Figure 7 Large-break LOCA: Core Pressure (psia)

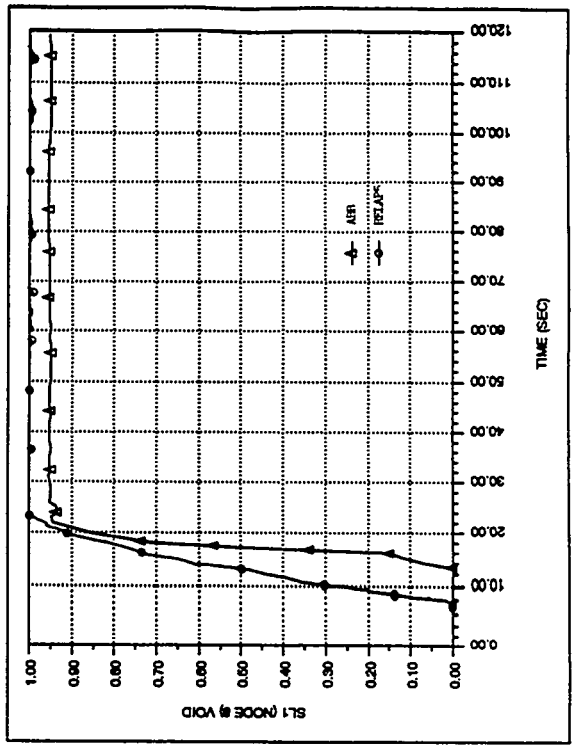


Figure 8 Large-break LOCA: Loop 1 Seal Void Fraction

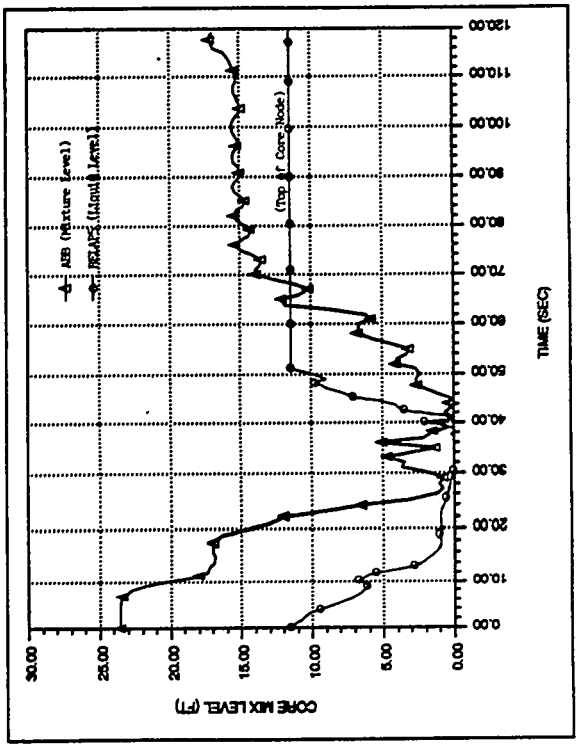


Figure 9 Large-break LOCA: Core Level (ft)

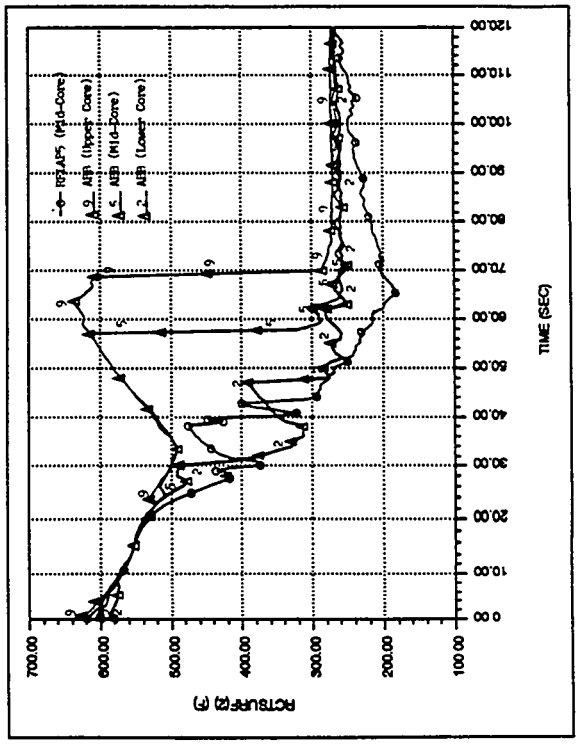


Figure 10 Large-break LOCA: Clad Surface Temp. (F)

Severe Accident Simulation at Olkiluoto

Heikki Tirkkonen and Tapio Saarenpää

Teollisuuden Voima Oy (TVO)
SF-27160 Olkiluoto
Finland

and

Li-Chi Cliff Po

Micro-Simulation Technology
10 Navajo Court
Montville, New Jersey 07045
U.S.A.

Abstract

A personal computer-based simulator was developed for the Olkiluoto nuclear plant in Finland for training in severe accident management. The generic software PCTRAN was expanded to model the plant-specific features of the ABB Atom designed BWR including its containment over-pressure protection and filtered vent systems. Scenarios including core heat-up, hydrogen generation, core melt and vessel penetration were developed in this work. Radiation leakage paths and dose rate distribution are presented graphically for operator use in diagnosis and mitigation of accidents. Operating on an 486 DX2-66, PCTRAN-TVO achieves a speed about 15 times faster than real-time. A convenient and user-friendly graphic interface allows full interactive control. In this paper a review of the component models and verification runs are presented.

1 Introduction

Following the Chernobyl accident in 1986, it became imperative that plans for managing events beyond the original design basis be implemented for all nuclear power plants. Teollisuuden Voima Oy (TVO) operates two boiling water reactor units, TVO I and II at Olkiluoto of Finland. They were designed by ABB Atom of Sweden and each is rated at 710 MWe.

Having conducted detailed probability safety analysis (PSA) for the plant, it was

noticed that two types of accident sequences, disregarding their low probability for occurrence, would challenge the containment integrity and public safety: a major loss of coolant accident (LOCA) with containment bypass, and a station blackout with extended loss of the Emergency Core Cooling System (ECCS). The first one leads to high steam pressure in the containment, and the second may result in core-melt and highly radioactive material release to the atmosphere.

As a counter-measure to these beyond-design basis events, two systems were installed at Olkiluoto: an Over-pressure Protection System 361 and a Filtered Venting System 362. The former prevents containment over-pressurization in case of a degraded pressure suppression during LOCA-conditions. It consists of a pipeline with shutoff valves and rupture disk in series to relieve high containment pressure. The latter is for the gradual rising of the containment pressure to a level, at which gases can be vented through a rupture disk. Radioactive gases will then be directed through a stainless steel wool filter submerged in a large water tank. It is capable of arresting 99.9% of the particle activity of the gas and 99% of the gaseous iodine.

Having the plant modification in place, TVO had developed plans for operator training, procedure development and related phases in its Severe Accident Management. In the training aspect the company's control room replica simulator did not incorporate the newly installed Systems 361 and 362 since degraded core conditions in a severe accident usually occur about five to ten hours after event initiation. In such a time frame real-time simulation becomes impractical for training purposes. It would also be too slow for the prediction of alternative consequences when various routes for mitigation are possible. On the other hand, the existing simulator models would have to be developed to include degraded core simulation. As a result, the need for a stand-alone, high-speed simulator designed specifically for severe accident management became apparent.

Instead of designing it from scratch, models available in the industry were evaluated. It was found that the personal computer-based software, PCTRAN[1,2], developed by Micro-Simulation Technology of U.S.A., was suitable for this task. It had been validated and verified [3] in the past 12 years against specific safety analysis reports and real-life events. In addition to the reactor nuclear steam supply system (NSSS) and containment models, it was recently expanded to model the Radiation Monitoring System (RMS) [4]. The company was contracted by TVO in March, 1993 to conduct the task. The core-melt model was developed by TVO and it was integrated into the PCTRAN-TVO model.

In the following sections the component models are briefly described. The design and operation of the graphical interface are explained. Finally, verification of the software by comparing against severe accident studies, conducted by TVO using the MAAP code [5] is described.

2. Background of the PCTRAN Software

Named as Personal Computer Transient Analyzer, PCTRAN was first introduced in 1985 [1]. Its scope was limited to the nuclear steam supply system. The first upgrade two years later expanded to include containment parameters [2]. Using a modern PC with SVGA graphics, design of the man-machine interface was recently upgraded using pull-down menu and mouse control.

For a light water reactor, even with the assumption of complete failure of the ECCS, it still takes hours to reach temperatures leading to core degradation. In order to analyze the consequences in a predictive manner for accident management, it is essential for the plant analyzer to accelerate the process. Running on a 486 DX2-66 machine, PCTRAN-TVO reaches a maximum speed of fifteen times faster than real-time. Other speeds can also be chosen for training purposes.

3 The Thermal-Hydraulics and Core Kinetics Models

The basic thermal hydraulics of PCTRAN are first principle in mass and energy balance, ensuring credible and realistic simulations. The water levels in the vessel downcomer and inside the core shroud use the drift flux model [6]. The fluid discharge rate from a break uses the Moody critical flow model [7]. A recirculation flow model has been constructed that reproduces the average core void fraction for BWRs. Feedwater flow is governed by the "three-element control" logic that considers the vessel water level, feedwater and steam flows. The turbine control valve is modeled for controlling the steam flow during power operation, and the bypass valves are used after a turbine trip.

PCTRAN uses a point-kinetics model with one delayed neutron group. Reactivity is controlled by rods and boron with feedback from voids and fuel temperature (Doppler). After reactor shutdown, a decay heat table based on standard ANS 5.1.1979 provides the heat input.

4 The Containment System

The pressure suppression containment system of the ABB Atom designed BWR is modeled by a drywell and a wetwell. The plant NSSS and containment systems were graphically displayed by a dynamic mimic (Figure 1). The drywell is separated into upper and lower compartments. There is a limited access between the two compartments. The upper drywell and the wetwell are connected by the pressure relieving vents and vacuum breakers. The containment spray system is modeled with four trains of pumps and valves with automatic initiation logic. The system may also be operated in the recirculation mode with water in the wetwell being recirculated through

the heat exchangers for containment cooling. A number of Safety Relief Valves (SRVs) can be operated in either (1) stand-by mode with fixed opening and closing setpoints, or (2) in pressure reduction mode with a constant 40℃/hr cooldown rate, or (3) in the forced de-pressurization mode.

5 Severe Accident Model

In order to simulate a severe accident with portions of the core exposed, a number of the plant's redundant safety systems have to be failed. Reduced heat transfer in the core leads to clad damage and hydrogen generation. Signs of core damage will show up in the elevated radiation readings. Release of the core inventory of iodine and noble gases constitutes the source term. Other fission product elements are not considered because they tend to be retained in the containment with little chances of being released.

The Radiation Monitoring System (RMS) of the containment, steam lines, condenser off-gas and stack is included in PCTRAN-TVO. The effects of iodine plate-out and attenuation by filters and/or initiation of the containment spray system are considered. For TVO I and II, which are equipped with the containment venting and filtration systems, their controlled release following a major accident provides the source term for off-site dose analysis. PCTRAN-TVO is successful in demonstrating the RMS's information in correlation with the reactor core and leakage pathways. Figure 2 is a display of the radiation monitors' readings and pathways through the turbine building and stack.

The Baker-Just Correlation [8] for metal-water reaction is used for calculating the amount of hydrogen generation. When the core materials are heated to their melting points, they are allowed to melt and flow into the degraded core. Core plate rupture and vessel penetration are also included in PCTRAN-TVO. The subsequent phenomena such as interaction with the containment concrete and corium are not included in PCTRAN.

6 The Graphic Man-Machine Interface

Figure 3 shows selection from a set of initial conditions (IC) corresponding to various power, flow, and time-of-life conditions before a run. Once simulation is started, the mimic displays the plant condition and the operator controls its operation using a mouse. The operator can also initiate malfunctions that cover all categories analyzed in the plant's FSAR and beyond. The malfunction list is shown in Figure 4. The severity, delay and ramp time of each malfunction is then entered. The status of every valve or pump in the mimic can be overridden by the operator to simulate a failed on/off situation. Partial failures at fractions of the full capacities are also possible. During execution, the operator can snap a new IC, freeze, back-track, and plot all simulated variables.

7 Verification Study

In order to verify the model, extensive studies have been conducted against the plant Final Safety Analysis Reports and established computer codes such as MAAP-3B [5]. Every malfunction in the malfunction list has been tested until reasonable agreement was obtained. TVO currently uses MAAP4 and will also use MELCOR 1.8.3 [9] in the future.

In order to evaluate the code's ability in analyzing severe accidents, two cases: a station blackout and a main steam line break without ECCS are presented below.

a. Station Blackout

The severe accident chosen is a station blackout (TB) and pedestal flooding at 3600 seconds. The MAAP-3B Analysis for TVO I and II was selected for PCTRAN-TVO benchmark.

The core consists of fuel assemblies of 101 tons UO_2. The mass of zirconium in cladding is 45 tons. The TB sequence is initiated with a total loss of AC power. It initiates a reactor trip, feedwater and steam isolation and failure of all emergency cooling systems.

The reactor pressure is maintained at 70 bar by the safety/relief valves. At one hour the drywell is flooded by opening the drain valve from the suppression pool (the pool is at a higher elevation than the drywell). Operators open six of the eight forced depressurization valves to depressurize the reactor vessel. The valves will be closed at pressure below 4 bar. The PCTRAN-TVO calculated reactor pressure, downcomer and shroud water levels, fuel average and maximum temperatures, and hydrogen generation are presented in Figures 5 to 8. Their trends are in general agreement with respect to the MAAP results. Allowing the portion of exposed core to heat up nearly adiabatically, PCTRAN-TVO calculated maximum fuel temperature takes a step increase as the core is uncovered. The average fuel temperature predicted by the two codes are very comparable.

If the containment pressure increases to 6 bar, the Containment Depressurization System initiates.

b. Steam Line Break and Loss of Core Cooling

The maximum steam line break size for TVO I and II is 560 cm^2. After the event initiation the feedwater is isolated. In addition, all Auxiliary Feed Pumps are disabled

by using the component malfunction feature. All Low Pressure Core Spray Pumps are also disabled before water is injected into the system.

Since there is no coolant makeup, reactor downcomer level falls to the ADS initiation level, at which all ADS valves open. The level drops continuously until total uncovery of the core. Anticipating melting of the core to be unavoidable, the operator opens the wetwell/drywell drain valves at about 1500 seconds to flood the lower drywell. Water flooding into the lower drywell also decreases the drywell pressure. Metal-water reaction starts at about 800 seconds and the containment hydrogen concentration reaches a maximum of about 25% by volume. PCTRAN-TVO uses a uniform containment non-condensible gas model so that the calculated concentration is an average for hydrogen in the upper drywell, lower drywell and wetwell. The calculated reactor pressure, levels, core temperatures and hydrogen production are presented in Figures 9 to 12. Their comparison with MAAP shows similar trends in general.

8 Summary and Conclusion

By conducting simulation at a speed many times faster than real-time, the strategy in accident mitigation, such as flooding the drywell, recirculation from the sump, use of external makeup (fire fighting) water, venting the containment and their respective impacts to the source term, can be analyzed. Plant specific models have been constructed and their verifications have been documented. They are being used in various phases of the severe accident management program of several power plants.

References

1. L. C. Po, 'A Personal Computer Transient Analysis Program', International Topical Meeting on Computer Application for Nuclear Power Plant Operation and Control, Pasco, Washington. September 8, 1985.

2. L. C. Po, "Containment Analyses using PCTRAN2", ANS Topical Meeting on Anticipated and Abnormal Transients, April 12, 1987, Atlanta.

3. L. C. Po, "Analysis of the Rancho Seco Overcooling Event Using PCTRAN", *Nuclear Science & Engineering*, 98, 154-161 (1988).

4. L. C. Po, "Extending PC-based Accident Simulation to Plant Radiation Monitors", *Nuclear Engineering International*, 36-37, April, 1993.

5. Proceedings: MAAP Thermal-Hydraulic Qualifications and Guidelines for Plant Application Workshop, EPRI NP-7515, pp. 10-1, October 1991.

6. R. T. Lahey, Jr. and F. J. Moody, "Thermal-Hydraulics of a Boiling Water Nuclear Reactor", ANS (1979). p. 202.

7. F. J. Moody, 'Maximum Flow Rate of a Single Component, Two-Phase Mixture', Transactions of ASME, Ser C, 87 (1965). pp. 134-142.

8. L. R. Baker Jr. and L. C. Just, "Studies of Metal-Water Reactions at High Temperature, III", ANL-6548, May 1962

9. MELCOR 1.8.1 Code Manual, Sandia National Laboratories, June, 1991.

10. Report for Nordic SIK 2.3 Project: Application of Codes MAAP, MELCOR and SCDAP/5 For TVO NPP.

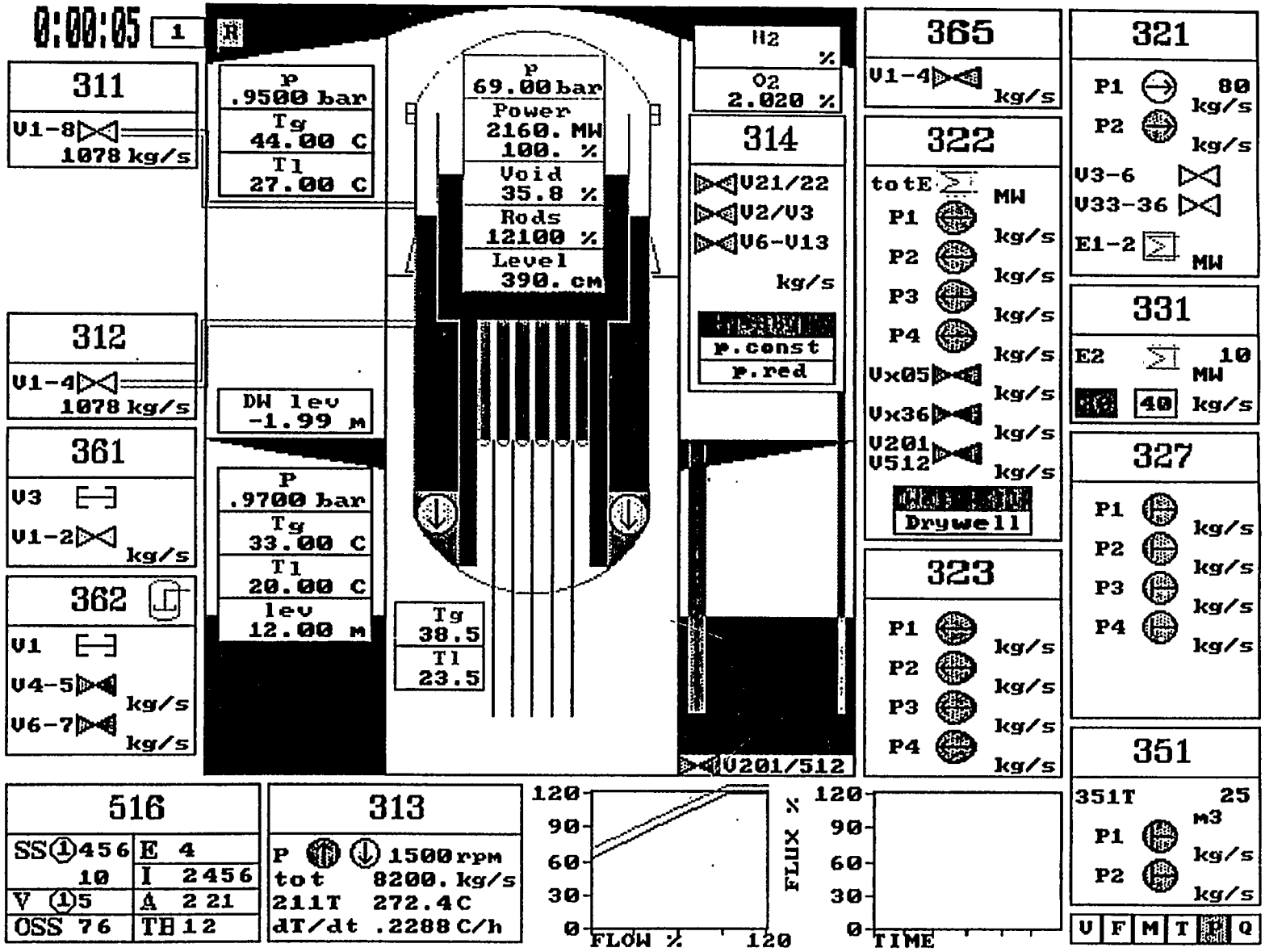
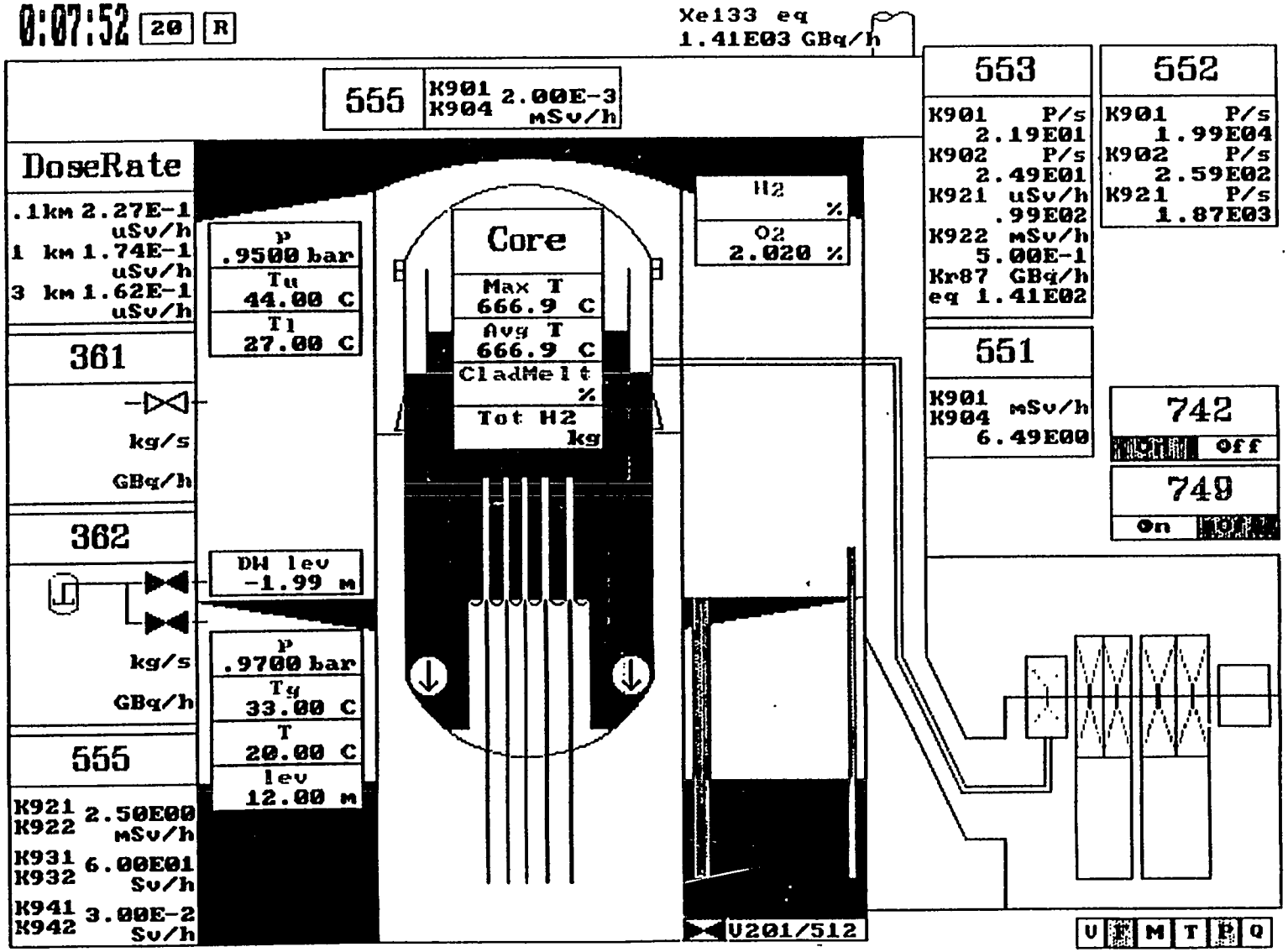


Figure 1 PCTRAN-TVO NSSS and containment systems.



2446

Figure 2 PCTRAN-TVO Radiation Monitoring system.

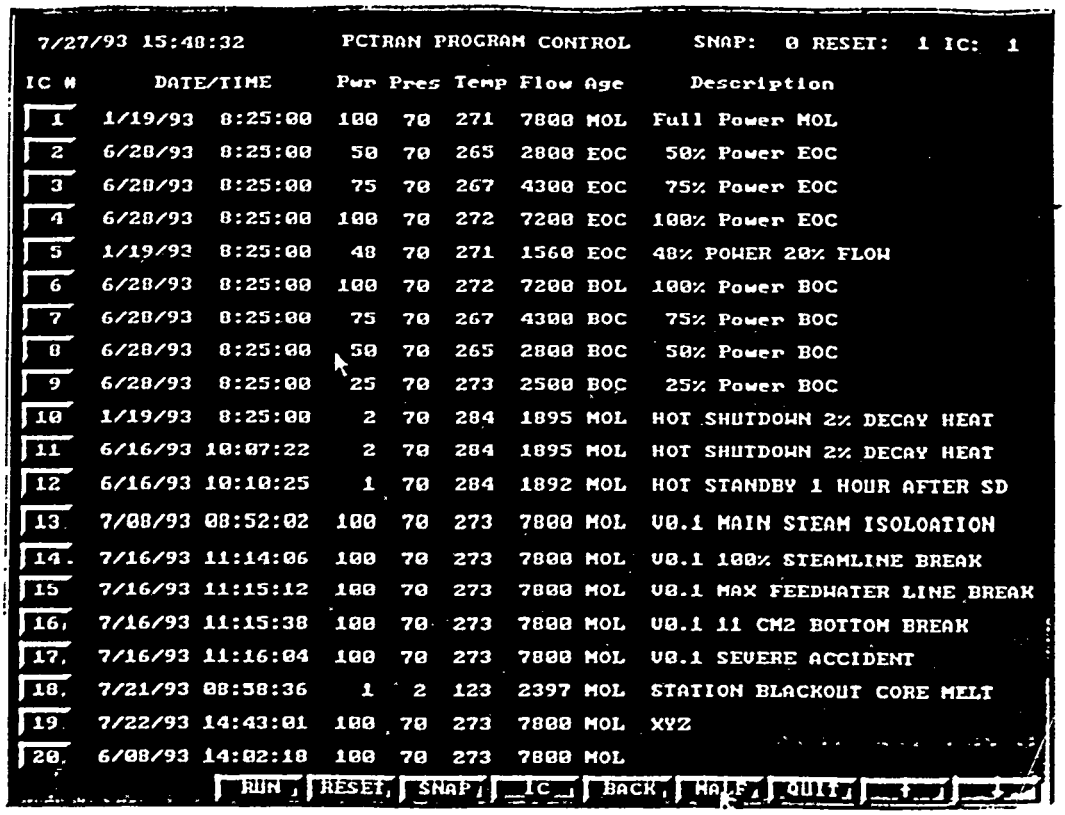


Figure 3 PCTRAN-TVO Initial Condition Lišt and Program Menu.

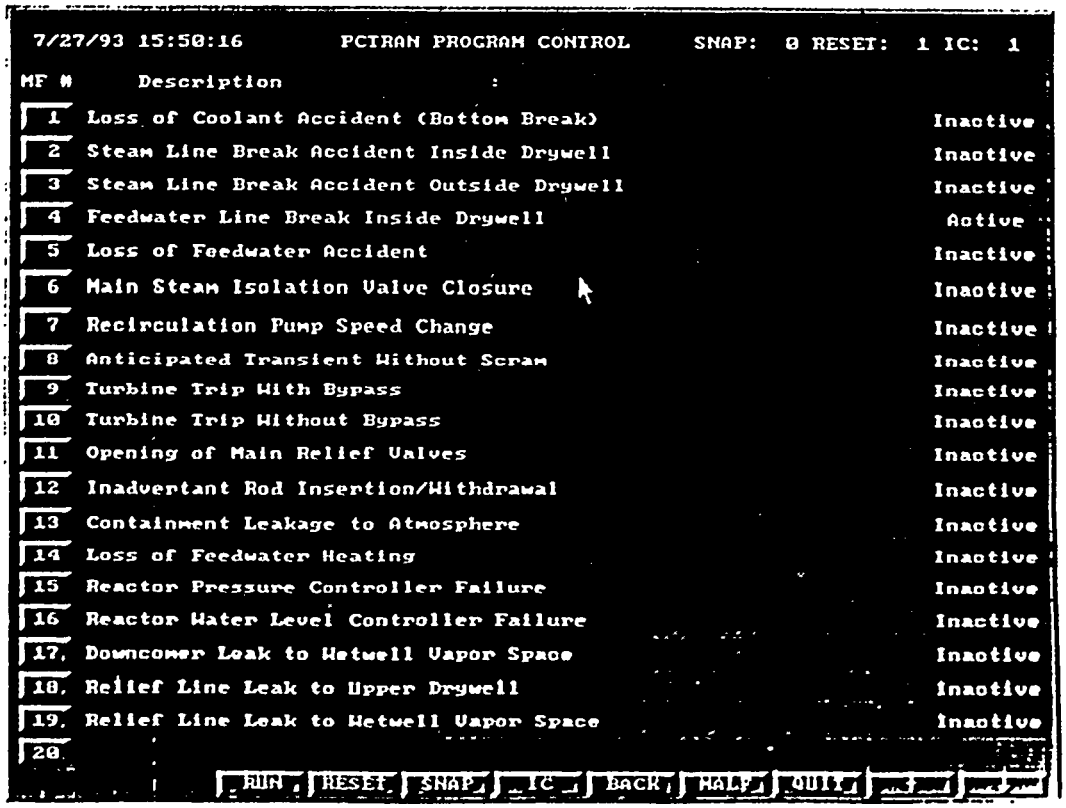


Figure 4 PCTRAN-TVO Malfunction List.

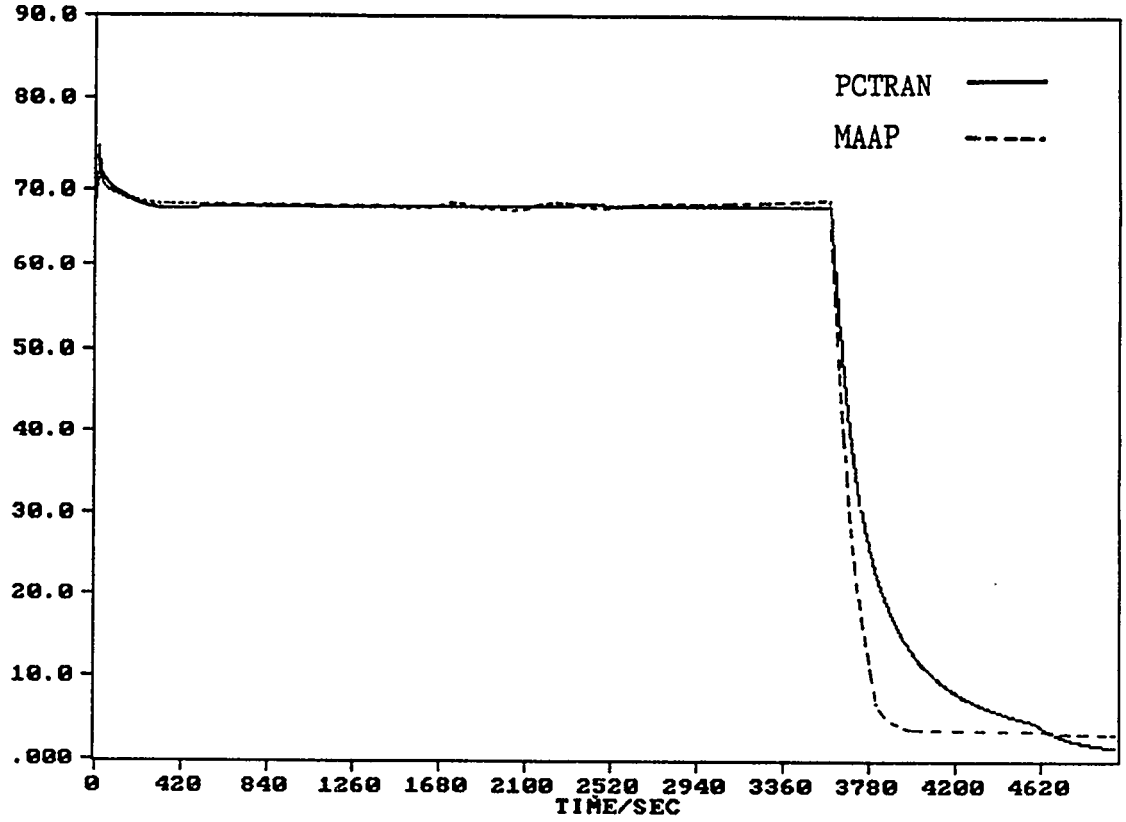


Figure 5 Station blackout, Reactor Pressure (Bar).

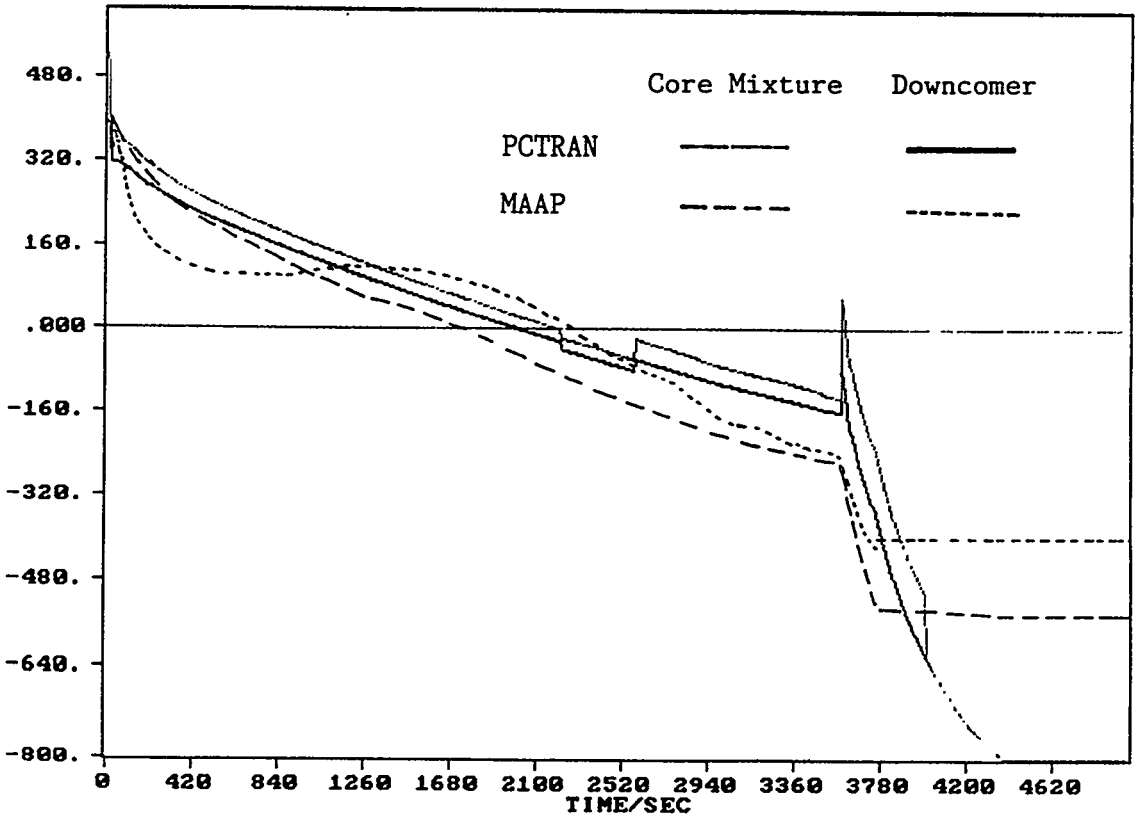


Figure 6 Station blackout, Reactor water level (cm TAF).

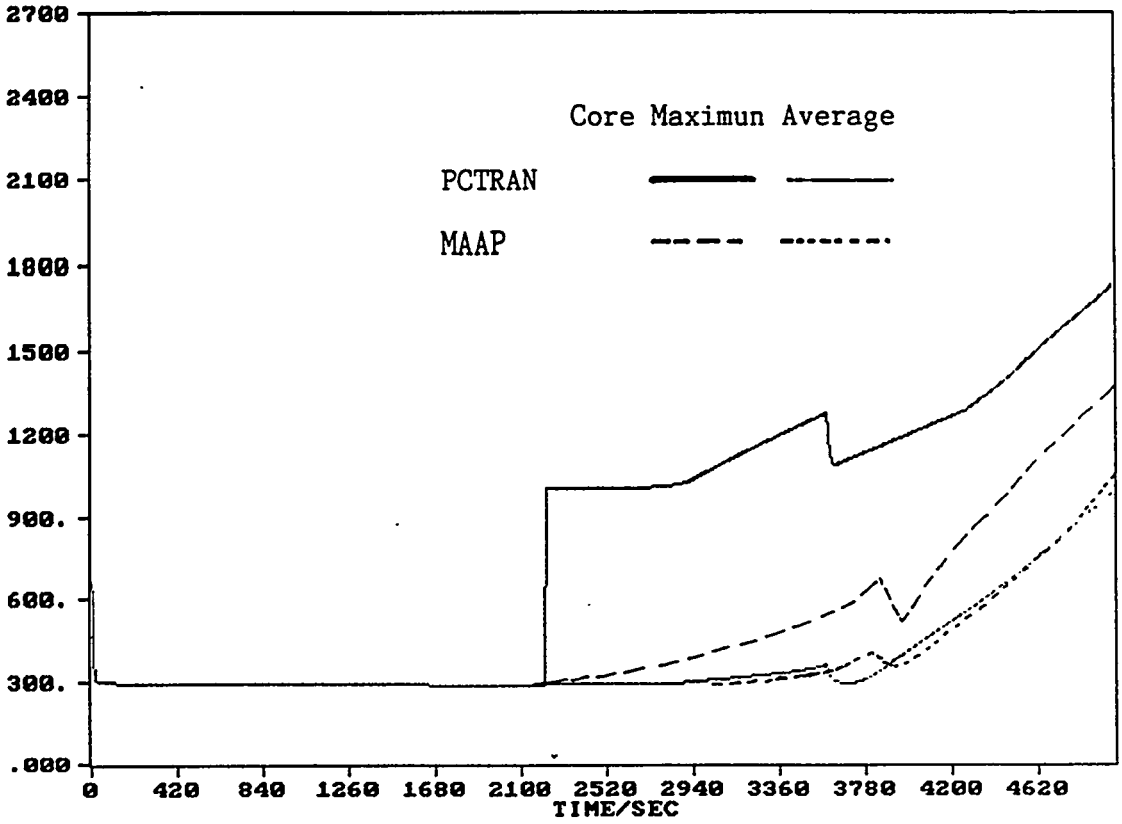


Figure 7 Station blackout, Core fuel temperatures, (°C).

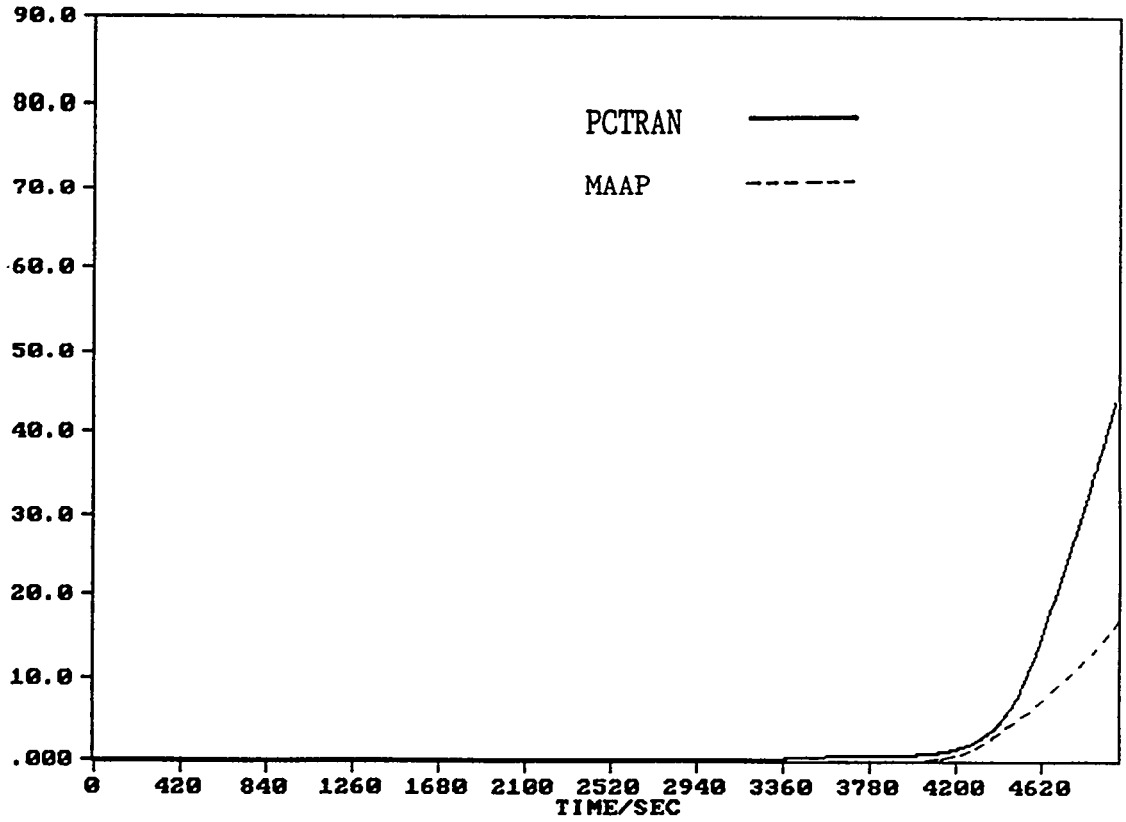


Figure 8 Station blackout, Total hydrogen generation (Kg).

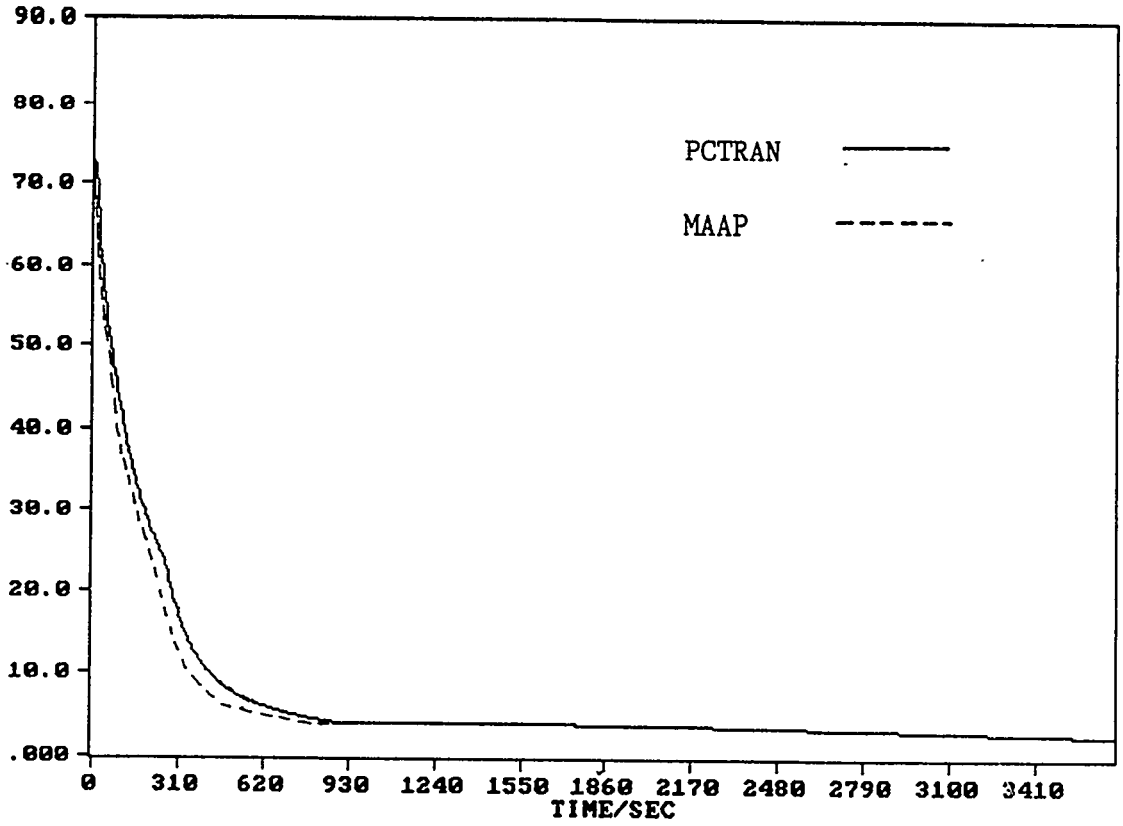


Figure 9 Steamline break without cooling, Reactor pressure (Bar).

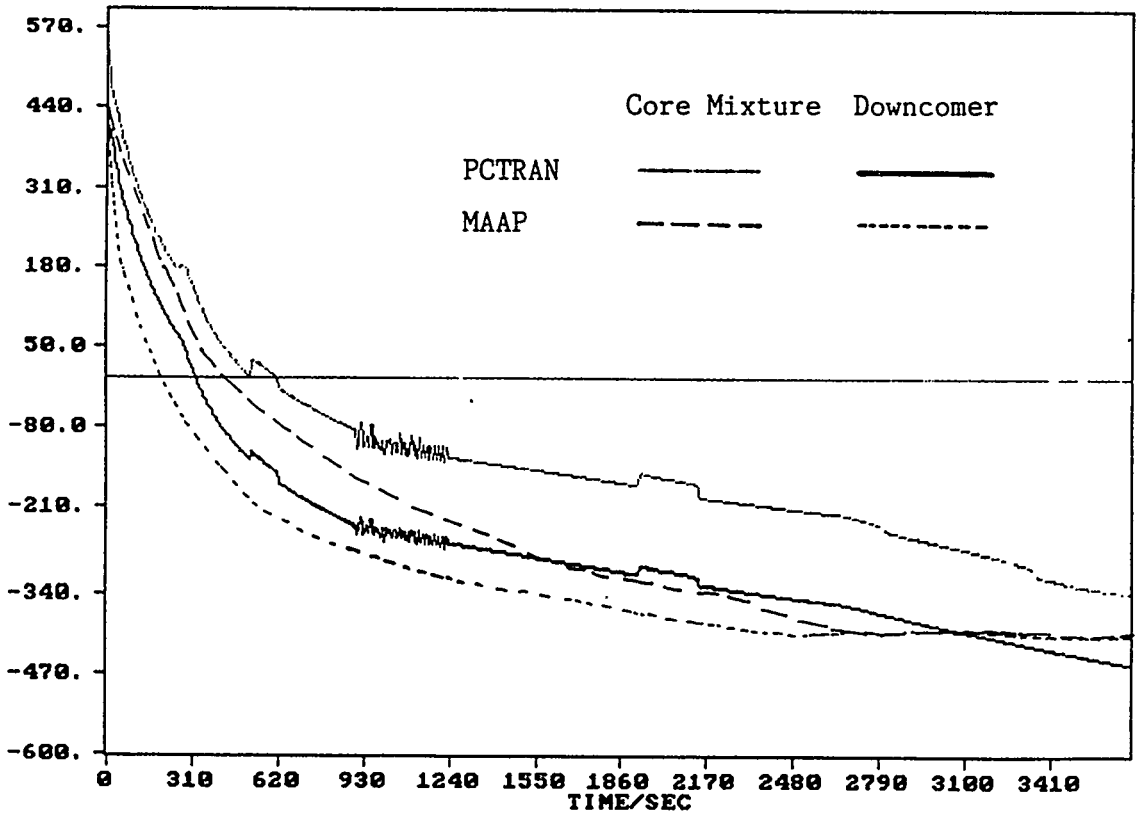


Figure 10 Steamline break without cooling, Core water level (cm).

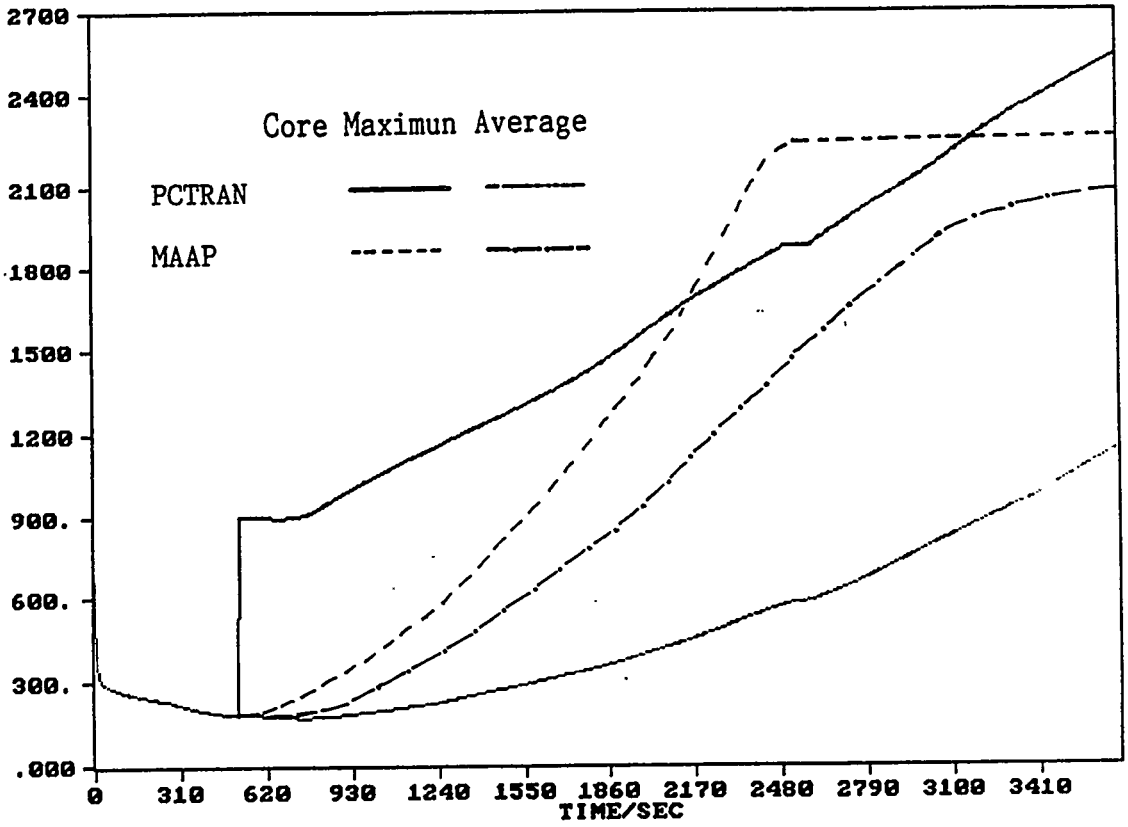


Figure 11 Steamline break without cooling, (°C).

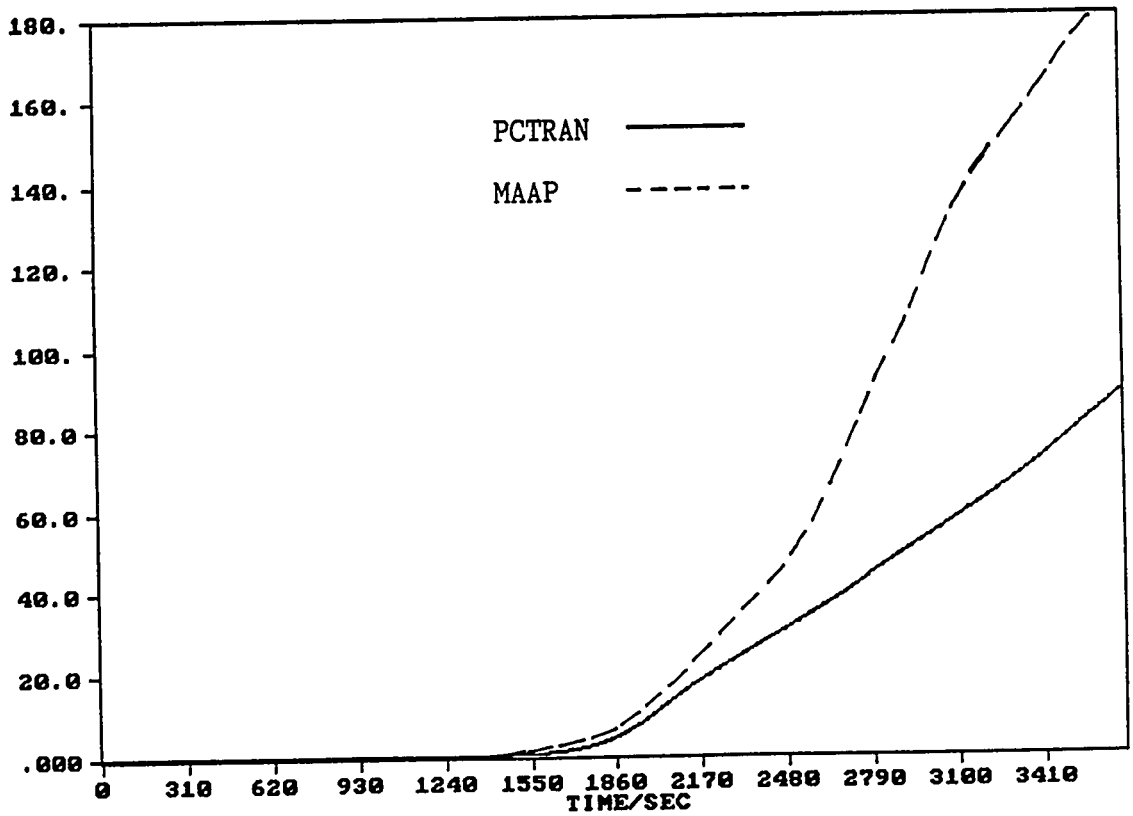


Figure 12 Steamline break without cooling, Total hydrogen generation (Kg).

AUTHORS INDEX

A

Abdelmessih, A.H. 264
Addabbo, C. 2159
Adomaitis, E. 3083
Akagane, K. 2994
Akiyama, M. 1653
Aksan, N. 2079, 2280, 2303
Aksan, S. N. 2904
Aksenova, A.E. 865
Aktas, B. 2035
Alemberti, A. 2869
Al-Falahi, S. 2263
Almenas, K. 1418
Allison, C.M. 1851
Analytis, G.Th. , 2011, 2067, 2079, 2654
Anderson, M. 1519
Andersson, N. G. 2895
Andreani, M. 1249, 2079
Angelini, S. 1754
Anghaie, S. 1997
Anglart , H. 673
Annunziato, A. 2159
Araya, F. 1169
Arnoux-Guisse, F. 2250
Aritomi, M. 875

B

Babelli, I. 947, 1272
Bacchiani, M. 2869
Balasubramaniam, V. 1380
Balino, J. 462
Banas, A.O. 284
Banati, J. 1116
Bang, K.H. 1677
Banerjee, S. 434
Baratta, A.J. 978
Barthel, V. 1456
Bartkus, G. 3083
Bartsoen, L. 2704
Barre, F. , 750, 2045
Baytas, A.C. 720
Bazin, P. 815
Beckjord, E. 1
Belov, V. A. 1555
Benet, L. V. 1443
Bengaouer, A. 815
Bertrand, C. 2250
Bertodano, M.L. 1272
Bestion, D. 2222
Blinkov, V.N. 967
Boatwright, W.J. 1083
Bobkov, V.P. 2539
Boldyrev, A. V 1914
Bonnet, J. M. 1958
Bonnin, O 2250
Boyack, B.E. , 1100, 1153
Boyer, B. D. 2185
Brauner, N. 192
Briere, E. 736
Brockmeir, U. 1830
Brown, N.W. 2470
Brun, P. 1351
Bui, V.A. 1809

C

Camelo, E. 111
Caroli, C. 1443
Carpentino, F.L. 21
Carrica, P. 462, 2453, 3218
Caruso, A. 1489
Carver, M.B. 284
Centner, B. 2704
Chae, H. T. 2786
Chaigne, G. 1351
Chang, J.S. 574
Chang, S. K. 2428
Chen, G. 1997
Chen, N. C. J. 2335
Chen, X. 1586
Chen, X.M. 377, 933

Cheng, X. 846
Cheng, S.C. 2583
Cheng, Z. 3093
Cherbonnel, C. 1489
Chetal, S. C. 1361, 1380
Chiang, J-H 875
Cho, J.H. 336
Choe, W.G. 1083
Chu, C. C. 2359
Chudanov, V.V. 865
Chun, M.-H. 93
Chung, B. J. 1477
Chung, M.K. 986
Cizek, J. 2112, 2636
Clausse, A. 231, 2453, 2762, 3218, 3232
Coddington, P. 1249
Cognet, G. 1797
Conway, L.E. 2869
Cornet, P. 1443
Corradini, M.L. 1501, 1519, 1637, 1728, 1743, 1779, 2240
Coste, P. 1456, 2222
Coulon, N. 1443

D

Dasaradhi, S. 2924
Daubert, O. 2250
D'Auria, F. 2146, 2303, 2904
Davis, K.L. 1851
Dehbi, A. 402
de Cachard, F. 166
de Crecy, F., 2045, 2480
Deguchi, A. 2721
Delgadino, G. 462
Delmastro, D.F. 3232
Deryugin, A. I. 1914
Deslandes, H. 1456
DeVore, C.V. 1083
DiMarco, P. 3218
Dinh, T.N. 827, 1809
Doerffer, S. 2583
Domoradov, A. 1090
Dor, I. 750
Dorning, J.J. 2677
Doubek, M. 2815
Dougherty, T.J. 3197
Dowlati, R. 1272
Driscoll, M.J. 1224
Durin, M. 1574

E

El-Genk, M.S. 353
Elkassabgi, Y. 2924
Elia, Jr., F.A. 336
Erbacher, F.J. 846
Ezsol, Gy. 2102

F

Fakory, M.R. 1982
Falkov, A. A. 2384
Farahani, A.A. 1728, 1779
Feltus, M.A. 1127
Finjakin, A. 1090
Firnhaber, M. 1830
Flour, I. 1489
Forsyth, D.R. 696
Fox, R. J. 1501
Franchello, G. 648
Fraser, D.W.H. 264
Frogheri, M. 2146
Frohlich, G. 1607
Fukahori, T. 2994
Fuketa, T. 2957
Fukuda, K. 554
Fujii, Y. 804, 1663
Furuya, M. 923

G

Gabrianovich, B.N. 711
Gango, P. 1535, 3120
Garnier, J. 2519
Gautier, G.M. 1196
Gauvain, J. 1574
Geffraye, G. 815
Georgevich, V. 2957, 2977, 3028, 3052
Glaeser, H. 2203, 2303, 2904
Glebov, A.G. 353

Gracyalny, E. 2240
Grassi, W. 3218
Green, J. 1418
Groeneveld, D.C. 2583
Gu, C-Y 3153
Guentay, S. 402
Guellouz, M.S. 2738
Guido-Lavalle, G. , 231, 2762

H

Haapelehto, T. 770, 2806
Hadaller, G.I. 2608
Hagen, S. 1830
Hama, K. 1333
Hamaguchi, H. 212
Han, J.T. 1272
Hanninen, M. 2263
Harkins, C.K. 2003
Harmony, S.C. 1100
Harrison, J.F. 1083
Harvel, G.D. 574
Hassan, Y.A. 434, 497, 591, 3073
Hata, K. 1333
Hayes, R.C. 2608
Hecker, M. 2250
Hejzlar, P. 1224
Hemstrom, B. 2895
Henderson, P. 1797
Herer, C. 2519
Herrero, V.A. 2762
Hiltbrand, D.W. 1083
Hochreiter, L.E. 43
Hofmann, F. 2250
Hofmann, P. 1830
Hohmann, H. 1688, 1712
Hohorst, J.K. 1851
Hongisto, O. 1535
Hori, K. 574
Hosokawa, S. 804
Huang, H. C. 2428
Huhtiniemi, I.K. 1712
Hwang, S. T. 2169

I

Ibrahim, W. A. 3073
Ieda, Y. 1313
Ikeda, T. 1972
Inada, F. 923
Inoue, A. 1663
Ishida, N. 487
Ishii, M. 947, 1272
Ishijima, K. 2957
Iwamura, T. 1169
Iwashige, K. 1972

J

Jacob, M.C. 21
Jacobson, S. 2895
Jafri, T. 3197
Juanico, L.E. 3232
Juhel, D. 2480
Jun, B. J. 2786

K

Kainulainen, S. 854
Kajiwara, H. 2021
Kalli, H. 299, 2146, 2834
Kamide, H. 1313
Kang, C. S. 1477
Kao, S. P. 2428
Karasulu, M. 911
Karlsson, R. 2895
Karoutas, Z. 3153
Karve, A.A. 2677
Karwat, H. 248
Kasinathan, N. 1361
Kawahara, A. 2721
Kawaji, M. 478
Kawanishi, K. 574
Kelly, A.E. 2003
Khodjaev, I.D. 1139
Kim, H. 2786
Kim, M.H. 1677
Kim, S. 2773
Kim, S.H. 2957, 2977, 3028, 3052
Kim, S.W. 1889

Kim, Y.-S. 93
Kiso, Y. 2994
Kisselev, A.E. 1914
Kirillov, P.L. 2558, 2916
Klingenfus, J. 1069
Klingenfus, J.A. 2410
Knebel, J. U. 1407
Kobayashi, J. 1313
Kodama, J. 804
Kodaira, T. 2957
Kok, H. V. 2884
Kondo, S. 1302
Korsun, A.S. 711
Korteniemi, V. 770
Kouhia, J. 299, 854, 2806, 2834
Kozina, N.V. 2539
Kramerov, A.J. 967
Krauss, T. , 603
Kuhn, S.Z. 312
Kurul, N. 673, 1889
Kuul, V. S. 2384

L

Lahey, Jr., R.T. 49, 1889, 1930
Larrauri, D. 736
Laugier, E. 2119
Laurinat, J.E. 514
Leduc, C. 1456
Lee, B.-R. 93
Lee, J. B. 2786
Lee, K-W 2489
Lee, S. J. 1863
Lee, S-Y 2489
Lemekha, A.V. 1914
Lemonnier, H. 111
Leonardi, M. 2146
Lepekhin, A.N. 2384
Levin, A.E. (2) 1231, 1291
Lider, S. 978
Lillington, J. 2904
Lime, J.F., 1100, 1153
Linca, A. 1607
Lischer, D.J. 336
Lombardi, C. 2506
Lorencez, C. 478
Lu, D. 1302
Lucas, A. T. 2941
Lundstrom, P. 1535

Mc

McDonald, J.M. 532
McDuffey, J. 131
McPherson, G.D. 1291

M

Macian, R. 2669
Madni, I. K. 2349
Magallon, D. 1688, 1712
Magnaud, J. P. 1443
Mahaffy, J.H. 2035, 2669
Majed, M. 2608
Maron, D.M. 192
Marshall, T.D. 532
Masson, V. 3218
Matsui, G. 3142
Matuszkiewicz, A. 781
Matsuzaki, M. 1663
Medich, C. 2841, 2869
Menant, B. 1324
Menna, J.D. 514
Melnikov, V. 508
Meyer, L. , 603
Midvidy, W. 781
Miettinen, A. 2146
Minagawa, H. 804
Monji, H. 3142
Moreau, G. -M. 1881
Moraga, F. 1930
Mori, M. 875
Morii, T. 1653
Moskalev, A. 1090
Mudde, R. F. 2884
Muftuoglu, A.K. 1127
Munther, R. 299
Murao, Y., 478, 1169

N

Nair, S 947

Nakamori, N. 804
Nam, H.-Y. 93
Neitzel, H.J. 846
Nguyen, T. Q. 2112
Nigmatulin, B.I. 508, 967, 1555
Nigmatulin, R.I., 49, 141
Nik, N. 911
Nimokata, H. 1398
Ninokata, H. 2721
Nithianandan, C.K. 2410
No, H.C. 986
Noe, H. 1324
Norback, G. 2608
Nourbakhsh, H.P. 3093
Nourgaliev, R.R. 827, 1809
Nylund, O. 673

O

Ochterbeck, J. 111
Ogura, K. 2021
Ohashi, H. 1653
Okamoto, K 497, 591
Ohshima, H. 1313
Okkonen, T. 1809
Olive, J. 736
Ousaka, A.
Ozawa, M. 487

P

Palagin, A.V. 1914
Palazov, V.V. 423
Park, G-C 2169, 2773
Park, H.S. 1743
Park, J.-W. 76
Park, R.J. 1863
Parlatan, Y. 2185
Perneczky, L. 2102
Pernsteiner, A.P. 1501
Parrish, K.R. 1046
Paul, P.K. 514
Pernica, R. 2636
Perret, C. 2045
Pershukov, V.A. 1555
Peterson, P.F., 312, 933, 1501
Petit, M. 1574
Petry, A. 1090
Pichon, P. 815
Pigny, S. 1881
Piplica, E.J. 43
Philip, O.G. 497, 591
Po, L-C 2438
Pochard, R. 2303, 2904
Podowski, M.Z. 673, 1003, 1889, 1930
Pokharna, H. 1272
Pokusaev, B.G. 1032
Polyansky, G.N. 2384
Porkholm, K. 2263
Poskas, P. 3083
Pribaturin, N.A. 1032
Purhonen, H. 2146, 2834
Puustinen, M. 770

Q

R

Radet, J. 2119
Rajakumar, A. 1361
Rajan, S.R. 911
Ransom, V.H. 1272
Raussi, P. 854
Raymond, P. 2621
Refling, J.G. 978
Reilly, S.S. 2410
Revankar, S.T. 1272
Richards, C. 2303
Rigamonti, M. 2869
Ris, V.V. 1555
Ritterbusch, S.E. 21
Rizwan-uddin 2677
Robinson, G.E. 978
Rohatgi, U.S. 2185
Rosa, M. 1003
Rouge, S. 1949
Rovinsky, Y. 192
Ruan, Y.Q. 248
Ruggles, A.E. 131, 2470

S

Saarenpaa, T. 2438
Sakaguchi, T. 212, 804
Sakurai, A. 554, 1333
Samoilov, O.B. 2384
Sanz, D. 231
Saphier, D. 2621
Sawada, T. 1398
Schindler, M. 1607
Schmidl, W.D. 497, 591
Schmitt, B. 1022
Schneider, R.E. 21
Schoen, B. 2856
Scholin, B. 3153
Schrock, V.E. 312, 377, 933
Schwirian, R.E. 696
Sehgal, B.R. 827
Seo, J.K. 2169
Selmer-Olsen, S. 111
Selivanov, Y.F. 2916
Sencar, M. 2280
Shamoun, B.I. 1637
Shimizu, A. 1398
Shiotsu, M. 554, 1333
Shoukri, M. 3175
Sidenkov D.V. 1555
Siefken, L.J. 1851
Sienicki, J. J. 2359
Sim, S. K. 1863
Simoneau, J. P. 1324
Simonin, O. 1489
Sjoberg, A. 2303, 2904
Smirnov, E.M. 1555
Smith, R.J. 2003
Smogalev, I.P. 2558
Souyri, A. 2519
Solvik, G.C. 2185
Song, C.H. 986
Sonnenburg, H.G. 423
Soyama, K. 2957
Spencer, B.W. 2359
Spindler, B. 1881
Stadtke, H. 648
Steiner, J.L. 1100
Steinhoff, F. 2203
Stekelenburg, A.J.C. 2785
Stern, F. 2608
Strizhov, V.F. 865
Stumpf, H.J. 1100
Sulfredge, C.D. 3003
Sun, C. 750
Sung, Y. 2112
Syri, .S. 627
Szabados, L. 2102

T

Tabata, H. 875
Takaguchi, M. 3142
Takahashi, M. 1663
Takemoto, T. 875
Takeuchi, Y. 1333
Takizawa, A. 1302, 2021
Taleyarkhan, R.P. 2957, 2977, 3028, 3052
Tapucu, A. 781
Tavoularis, S. 2738
Tarantini, M. 2841
Teresaka, H. 2021
Teschendorff, V. 2203
Teyssedou, A. 781
Theofanous, T.G. 627, 1535, 1586, 1754
Tikhonenko, L.K. 967
Tirkkonen, H. 2438
Todreas, N.E. 1224
Trambauer, K. 1830
Tsiklauri, G. 1022
Tucker, R. F. 2924
Tuomisto, H. 1535
Tuunanen, J. 423
Tye, P. 781
Tyler, T.N. 2669

U

Ubra, O. 2815
Ueda, H. 2021
Ueno, T. 804
Umekawa, H. 487
Umminger, K. J. 2856
Unrau, D. 284

Ushakov, P.A. 711

V

Vabishchevich, P.N. 865
Vaidyanathan, G. 1361, 1380
Valenti, S. N. 2957, 2977, 3028, 3052
Valentin, B. 1351
Vanhoenacker, L. 2704
van der Hagen, T.H.J.J. 2785, 2884
Van Hove, W. 2704
Van Laeken, K. 2704
Vasil'ev, A.D. 2470
Velusamy, K. 1380
Vescovi, O. 2869
Veshchunov, M.S. 1914
Vilemas, J. 3083
Vinberg, A.A. 1555
Vinogradov, V.N. 2539
Virtanen, E. 2806
Viskanta, R. 1272
Vitruk, S.G. 711
Volchek, A M. 1914

W

Weber, P. 2856
Wang, W. 1272
Watson, R.D. 532
Wendel, M.W. 2335, 2470
Williams, P.T. 2941
Wiman, P. 2608
Wissinger, G. 1069
Worth, B. 648

X

Xiang, J. Y. 2977

Y

Yacout, A.M. 2394
Yamshchikov, N.Y. 1914
Yang, B.W. 3197
Yang, Y.H. 1653
Yang, J.Y. 2169
Yang, W.S. 2394
Yasuo, A. 923
Yefanov, A.D. 2916
Yegorova, L. 1830
Yoder, G.L. 2335, 2924
Yoo, K. J. 1863
Yoshino, M. 2994
Youchison, D.L. 532
Yuann, R.Y. 377
Yuen, W.W. 1586, 1754

Z

Zaichik, L.I. 1555
Zabiego, M. 1797
Zeitoun, O. 3175
Zhou, Z. 888
Zyatnina, A.O. 2539

NRC FORM 335 (2-89) NRCM 1102, 3201, 3202

U.S. NUCLEAR REGULATORY COMMISSION

BIBLIOGRAPHIC DATA SHEET

(See instructions on the reverse)

1. REPORT NUMBER (Assigned by NRC, Add Vol., Supp., Rev., and Addendum Numbers, If any.)
NUREG/CP-0142
Vol. 3

2. TITLE AND SUBTITLE
Proceedings of the 7th International Meeting on Nuclear Reactor Thermal-Hydraulics
NURETH-7

Sessions 12 - 16

3. DATE REPORT PUBLISHED
MONTH: September | YEAR: 1995

4. FIN OR GRANT NUMBER

5. AUTHOR(S)
Compiled by R. C. Block and F. Feiner, Northeastern New York Chapter, American Nuclear Society

6. TYPE OF REPORT
Conference Proceedings

7. PERIOD COVERED *(Inclusive Dates)*

8. PERFORMING ORGANIZATION – NAME AND ADDRESS *(If NRC, provide Division, Office or Region, U.S. Nuclear Regulatory Commission, and mailing address; if contractor, provide name and mailing address.)*
Compiled by Northeastern New York Chapter, American Nuclear Society

9. SPONSORING ORGANIZATION – NAME AND ADDRESS *(If NRC, type "Same as above"; if contractor, provide NRC Division, Office or Region, U.S. Nuclear Regulatory Commission, and mailing address.)*

American Nuclear Society
555 N. Kensington Avenue
La Grange Park, IL 60525

American Institute of Chemical Engineers
345 East 47th Street
New York, NY 10017-2392

American Society of Mechanical Engineers
345 East 47th Street
New York, NY 10017-2392

Canadian Nuclear Society
144 Front Street West
Suire 725
Toronto, Ontario, Canada M5J2L7

European Nuclear Society
Secretariat: Monbijoustrasse 5
P.O. Box 5032
CH-3001 Berne, Switzerland

Atomic Energy Society of Japan
No. 1-13, 1-chome
Shimbashi, Minato-ku
Tokyo 105, Japan

Japan Society of Multiphase Flow
Prof. Akimi Serizawa
Department of Nuclear Engineering
Yoshida, Sakyo, Kycto 606-01
Japan

Division of Systems Technology
Office of Nuclear Regulatory Researc..
U.S. Nuclear Regulatory Commission
Washington, DC 20555-0001

10. SUPPLEMENTARY NOTES

11. ABSTRACT *(200 words or less)*

This volume includes papers presented at the 7th International Meeting on Nuclear Reactor Thermal-Hydraulics (NURETH-7) September 10-15, 1995 at Saratoga Springs, N.Y. The following subjects are discussed: progress in analytical and experimental work on the fundamentals of nuclear thermal-hydraulics, the development of advanced mathematical and numerical methods, and the application of advancements in the field in the development of novel reactor concepts. Also combined issues of thermal-hydraulics and reactor/power-plant safety, core neutronics and/or radiation.

12. KEY WORDS/DESCRIPTORS *(List words or phrases that will assist researchers in locating the report.)*
thermal-hydraulics, reactor/power-plant safety, core neutronics and/or radiation

13. AVAILABILITY STATEMENT
unlimited

14. SECURITY CLASSIFICATION
(This Page)
unclassified
(This Report)
unclassified

15. NUMBER OF PAGES

16. PRICE